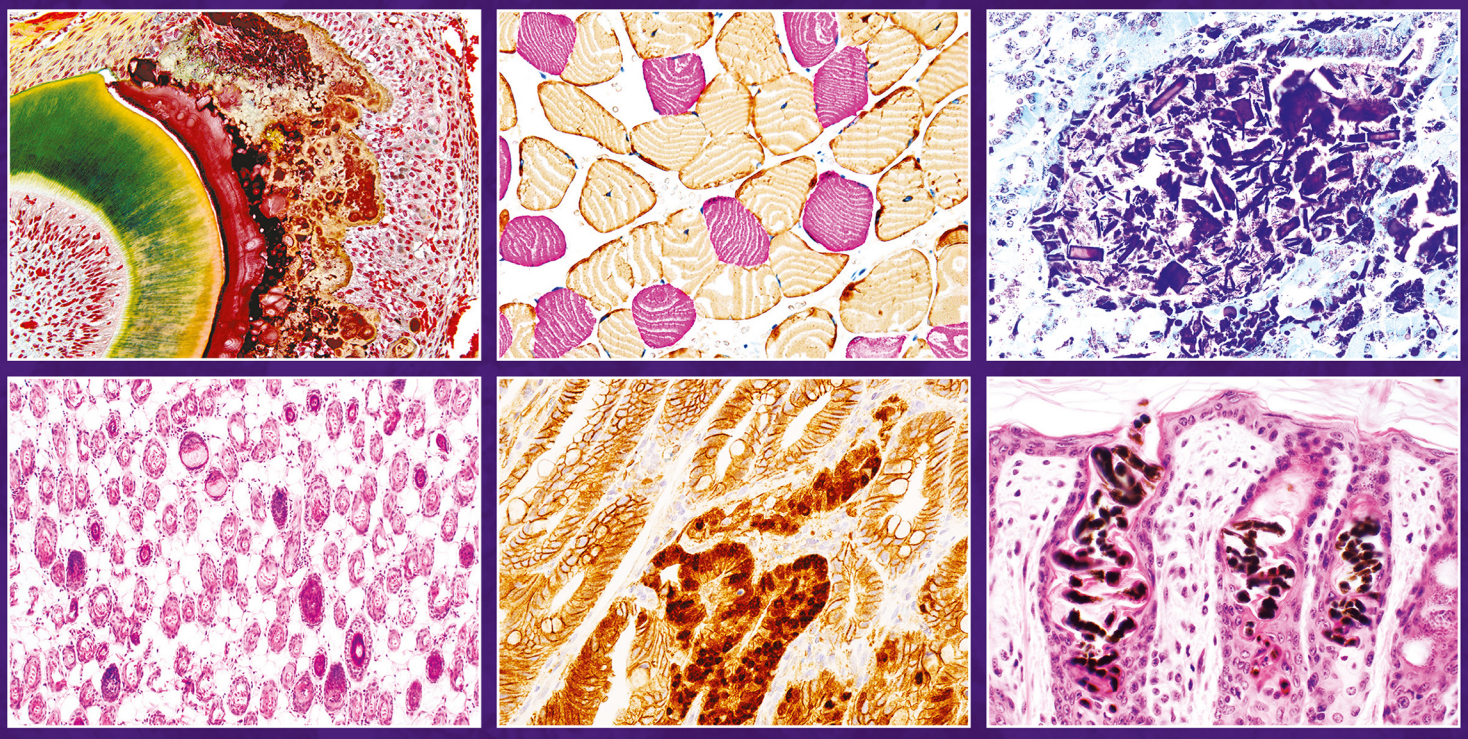
EDITED BY JOHN P. SUNDBERG,
PETER VOGEL, AND JERROLD M. WARD

PATHOLOGY OF GENETICALLY ENGINEERED AND OTHER MUTANT MICE



WILEY Blackwell

Pathology of Genetically Engineered and Other Mutant Mice

Vet-ebooks.com

Pathology of Genetically Engineered and Other Mutant Mice

Edited by

John P. Sundberg, DVM, PhD, Dipl. ACVP
The Jackson Laboratory
Bar Harbor, ME, USA
Department of Dermatology
Vanderbilt University Medical Center
Nashville, TN, USA

Peter Vogel, DVM, PhD, Dipl. ACVP
Pathology Department
St. Jude Children's Research Hospital
Memphis, TN, USA

Jerrold M. Ward, DVM, PhD, Dipl. ACVP, Fellow IATP
Global VetPathology
Montgomery Village, MD, USA

WILEY Blackwell

Vet-ebooks.com

This edition first published 2022
© 2022 John Wiley & Sons, Inc.

All rights reserved. No part of this publication may be reproduced, stored in a retrieval system, or transmitted, in any form or by any means, electronic, mechanical, photocopying, recording or otherwise, except as permitted by law. Advice on how to obtain permission to reuse material from this title is available at http://www.wiley.com/go/permissions.

The right of John P. Sundberg, Peter Vogel, and Jerrold M. Ward to be identified as the authors of the editorial material in this work has been asserted in accordance with law.

Registered Office
John Wiley & Sons, Inc., 111 River Street, Hoboken, NJ 07030, USA

Editorial Office
111 River Street, Hoboken, NJ 07030, USA

For details of our global editorial offices, customer services, and more information about Wiley products visit us at www.wiley.com.

Wiley also publishes its books in a variety of electronic formats and by print-on-demand. Some content that appears in standard print versions of this book may not be available in other formats.

Limit of Liability/Disclaimer of Warranty
The contents of this work are intended to further general scientific research, understanding, and discussion only and are not intended and should not be relied upon as recommending or promoting scientific method, diagnosis, or treatment by physicians for any particular patient. In view of ongoing research, equipment modifications, changes in governmental regulations, and the constant flow of information relating to the use of medicines, equipment, and devices, the reader is urged to review and evaluate the information provided in the package insert or instructions for each medicine, equipment, or device for, among other things, any changes in the instructions or indication of usage and for added warnings and precautions. While the publisher and authors have used their best efforts in preparing this work, they make no representations or warranties with respect to the accuracy or completeness of the contents of this work and specifically disclaim all warranties, including without limitation any implied warranties of merchantability or fitness for a particular purpose. No warranty may be created or extended by sales representatives, written sales materials or promotional statements for this work. The fact that an organization, website, or product is referred to in this work as a citation and/or potential source of further information does not mean that the publisher and authors endorse the information or services the organization, website, or product may provide or recommendations it may make. This work is sold with the understanding that the publisher is not engaged in rendering professional services. The advice and strategies contained herein may not be suitable for your situation. You should consult with a specialist where appropriate. Further, readers should be aware that websites listed in this work may have changed or disappeared between when this work was written and when it is read. Neither the publisher nor authors shall be liable for any loss of profit or any other commercial damages, including but not limited to special, incidental, consequential, or other damages.

Library of Congress Cataloging-in-Publication Data

Names: Sundberg, John P., editor. |Vogel, Peter, editor. | Ward, Jerrold Michael., editor.
Title: Pathology of genetically engineered and other mutant mice / edited by John P. Sundberg, Peter Vogel, Jerrold M. Ward.
Other titles: Pathology of genetically engineered mice
Description: Second edition. | Hoboken, NJ : Wiley-Blackwell, 2022. | Preceded by Pathology of genetically engineered mice / Jerrold M. Ward ... [et al.]. 1st ed. 2000. | Includes bibliographical references and index.
Identifiers: LCCN 2021009923 (print) | LCCN 2021009924 (ebook) | ISBN 9781119624578 (cloth) | ISBN 9781119624585 (adobe pdf) | ISBN 9781119624592 (epub)
Subjects: MESH: Mice, Transgenic–abnormalities | Disease Models, Animal
Classification: LCC RB125 (print) | LCC RB125 (ebook) | NLM QY 60.R6 | DDC 636.089/607–dc23
LC record available at https://lccn.loc.gov/2021009923
LC ebook record available at https://lccn.loc.gov/2021009924

Cover Design: Wiley
Cover Images: © John P. Sundberg, Peter Vogel, Jerrold M. Ward

Set in 9.5/11.5pt STIXTwoText by Straive, Pondicherry, India

10 9 8 7 6 5 4 3 2 1

Vet-ebooks.com

Contents

List of Contributors *vii*
Preface and Acknowledgments *x*

1 Introduction to Mouse Pathology *1*
Jerrold M. Ward, Peter Vogel, and John P. Sundberg

2 The Mouse Online: Open Mouse Biology and Pathology Data Resources for Biomedical Research *6*
Dale A. Begley, Paul N. Schofield, and John P. Sundberg

3 Mouse Genetic Nomenclature: The Underpinning of Mouse Genetics *22*
John P. Sundberg, Dale A. Begley, Melissa L. Berry, Michelle N. Perry, David Shaw, and Paul N. Schofield

4 Discovering and Validating Mouse Models of Human Diseases: The Cinderella Effect *39*
John P. Sundberg, Jerrold M. Ward, Peter Vogel, and Paul N. Schofield

5 Embryos, Placentas, and Neonates *48*
Brad Bolon and Jerrold M. Ward

6 Ciliopathies *72*
Peter Vogel and Laura J. Janke

7 Hematopoietic and Lymphoid Tissues *82*
Harm HogenEsch and John P. Sundberg

8 Mouse Hematolymphoid Neoplasms *97*
Jerold E. Rehg

9 Immunodeficient and Humanized Mice *132*
Sara F. Santagostino, Sébastien Monette, Alessandra Piersigilli, Virginia L. Godfrey, and Harm HogenEsch

10 Skin, Hair, and Nails *159*
John P. Sundberg, Lloyd E. King, Jr, and Raoul V. Kuiper

11 Mammary Gland *213*
Alexander D. Borowsky and Robert D. Cardiff

12 The Respiratory Tract *237*
Jerrold M. Ward and John P. Sundberg

13 The Gastrointestinal Tract *259*
Jerrold M. Ward, Piper M. Treuting, and M. Kay Washington

Vet-ebooks.com

14 Cardiovascular System *284*
Kathleen L. Gabrielson, Akash Behera, Polina Sysa-Shah, Tyler J. Creamer, and Timothy K. Cooper

15 Liver and Pancreas *307*
Maria L.Z. Dagli, Lucas M. Chaible, and Katja Steiger

16 Neuromuscular System *336*
Peter Vogel, Laura J. Janke, and Heather W. Sheppard

17 Endocrine System *355*
Krista M. D. La Perle

18 Kidney and Urinary Bladder *378*
Jeffrey B. Kopp, Avi Z. Rosenberg, Cory F. Brayton, Jeffrey I. Everitt, and Jerrold M. Ward

19 Female Reproductive System *403*
Darlene Dixon and Alexander Yu. Nikitin (In Memory of Dr. Joel Mahler)

20 Male Reproductive System *431*
Sue E. Knoblaugh, Hibret A. Adissu, Colin McKerlie, and Robert D. Cardiff

21 Nervous System *462*
Jessica M. Snyder, Katherine N. Gibson-Corley, and Enrico Radaelli

22 Eye and Ear *493*
Heather W. Sheppard, Laura J. Janke, Jerold E. Rehg, and Peter Vogel

23 Bones and Teeth *520*
Peter Vogel, John P. Sundberg, and Cheryl Ackert-Bicknell

Index *541*

Vet-ebooks.com

List of Contributors

Cheryl Ackert-Bicknell, PhD
Department of Orthopedics
School of Medicine
University of Colorado
Aurora, CO, USA

Hibret A. Adissu, DVM, MSc, PhD, DVSc, Dipl. ACVP
Pathology, Early Development
Covance, Inc.
Chantilly, VA, USA

Dale A. Begley, PhD
The Jackson Laboratory
Bar Harbor, ME, USA

Akash Behera, BS
College of Natural Sciences
University of Massachusetts Amherst
Amherst, MA, USA

Melissa L. Berry, MS, MBA
The Jackson Laboratory
Bar Harbor, ME, USA

Brad Bolon, DVM, MS, PhD, Dipl. ACVP, Dipl. ABT, Fellow ATS, Fellow IATP, Fellow RCPath
GEMpath Inc.
Longmont, CO, USA

Alexander D. Borowsky, MD, Dipl. ABPath
Department of Pathology and Laboratory Medicine
Center for Immunology and Infectious Diseases
Center for Genomic Pathology
University of California, Davis
Davis, CA, USA

Cory F. Brayton, DVM, Dipl. ACVP, Dipl. ACLAM
Department of Molecular and Comparative Pathology
School of Medicine
Johns Hopkins University
Baltimore, MD, USA

Robert D. Cardiff, MD, PhD, Dipl. ABPath
Department of Pathology and Laboratory Medicine
Center for Immunology and Infectious Diseases
Center for Genomic Pathology
University of California, Davis
Davis, CA, USA

Lucas M. Chaible, PhD
Laboratory of Experimental and Comparative Oncology
School of Veterinary Medicine and Animal Science
University of Sao Paulo
Sao Paulo, SP, Brazil

Timothy K. Cooper, DVM, PhD, Dipl. ACVP
Laulima Government Solutions – Contractor Supporting
National Institute of Allergy and Infectious Diseases, NIH
Integrated Research Facility
Division of Clinical Research
Frederick, MD, USA

Tyler J. Creamer, PhD
Departments of Surgery and Genetic Medicine
School of Medicine
Johns Hopkins University
Baltimore, MD, USA

Maria L.Z. Dagli, DVM, MSc, PhD, Fellow IATP
Laboratory of Experimental and Comparative Oncology
Department of Pathology
School of Veterinary Medicine and Animal Science
University of Sao Paulo
Sao Paulo, SP, Brazil

Darlene Dixon, DVM, PhD, Dipl. ACVP, Fellow, IATP
Molecular Pathogenesis Group
NTP Laboratory
NIEHS
Research Triangle Park, NC, USA

Jeffrey I. Everitt, DVM, Dipl. ACVP, Dipl. ACLAM
Department of Pathology
Duke University School of Medicine
Durham, NC, USA

Vet-ebooks.com

Kathleen L. Gabrielson, DVM, PhD, Dipl. ACVP
Departments of Molecular and Comparative Pathology
Pathology and Oncology and Environmental Health Engineering
School of Medicine and Bloomberg School of Public Health
Johns Hopkins University
Baltimore, MD, USA

Katherine N. Gibson-Corley, DVM, PhD, Dipl. ACVP
Department of Pathology, Microbiology and Immunology
Vanderbilt University Medical Center
Nashville, TN, USA

Virginia L. Godfrey, DVM, PhD, Dipl. ACVP
Division of Comparative Medicine
Department of Pathology and Laboratory Medicine
School of Medicine
University of North Carolina
Chapel Hill, NC, USA

Harm HogenEsch, DVM, PhD, Dipl. ACVP
Department of Comparative Pathobiology
College of Veterinary Medicine
Purdue University
West Lafayette, IN, USA

Laura J. Janke, DVM, PhD, Dipl. ACVP
Pathology Department
St. Jude Children's Research Hospital
Memphis, TN, USA

Lloyd E. King, Jr., MD, PhD, Dipl. DP
Department of Dermatology
Vanderbilt University Medical Center
Nashville, TN, USA

Sue E. Knoblaugh, DVM, Dipl. ACVP
Comparative Pathology & Digital Imaging Shared Resource
Department of Veterinary Biosciences
College of Veterinary Medicine
The Ohio State University
Columbus, OH, USA

Jeffrey B. Kopp, MD, Dipl. ABIM (Nephrology)
Kidney Diseases Branch
NIDDK
National Institutes of Health
Bethesda, MD, USA

Raoul V. Kuiper, PhD, DVM, Dipl. ECVP
Department of Laboratory Medicine
Karolinska University Hospital Huddinge
Stockholm, Sweden

Krista M. D. La Perle, DVM, PhD, Dipl. ACVP
Comparative Pathology & Digital Imaging Shared Resource
Department of Veterinary Biosciences
College of Veterinary Medicine
Columbus, OH, USA

Colin McKerlie, DVM, DVSc, MRCVS
Translational Medicine Research Program
The Hospital for Sick Children
Toronto, Canada
and
Faculty of Medicine
Department of Pathobiology & Laboratory Medicine
University of Toronto
Toronto, Canada

Sébastien Monette, DMV, MVSc, Dipl. ACVP
Laboratory of Comparative Pathology
Memorial Sloan Kettering Cancer Center
The Rockefeller University
Weill Cornell Medicine
New York, NY, USA

Alexander Yu. Nikitin, MD, PhD
Department of Biomedical Sciences
NYS College of Veterinary Medicine
Cornell University
Ithaca, NY, USA

Michelle N. Perry, PhD
Mouse Genome Informatics
The Jackson Laboratory
Bar Harbor, ME, USA

Alessandra Piersigilli, DVM, PhD, Dipl. ECVP
Drug Safety Research & Evaluation
Takeda Pharmaceuticals International Co.
Cambridge, MA, USA

Enrico Radaelli, DVM, PhD, Dipl. ECVP
Department of Pathobiology
School of Veterinary Medicine
University of Pennsylvania
Philadelphia, PA, USA

Jerold E. Rehg, DVM, Dipl. ACVP, Dipl. ACLAM
Pathology Department
St. Jude Children's Research Hospital
Memphis, TN, USA

Vet-ebooks.com

Avi Z. Rosenberg, MD, PhD, Dipl. ABPath
Division of Kidney-Urologic Pathology
Department of Pathology
Johns Hopkins Medical Institutions
Baltimore, MD, USA

Sara F. Santagostino, DVM, PhD, Dipl. ACVP
Department of Safety Assessment
Genentech, Inc.
South San Francisco, CA, USA

Paul N. Schofield, PhD
Department of Physiology, Development and Neuroscience
University of Cambridge
Cambridge, UK

David Shaw, PhD
The Jackson Laboratory
Bar Harbor, ME, USA

Heather W. Sheppard, DVM, PhD, Dipl. ACVP
Pathology Department
St. Jude Children's Research Hospital
Memphis, TN, USA

Jessica M. Snyder DVM, MS, Dipl. ACVIM and Dipl. ACVP
Department of Comparative Medicine
School of Medicine
University of Washington
Seattle, WA, USA

Katja Steiger, DVM, PD, Dr. Med. Vet. Habil., FTA Pathology
Comparative Experimental Pathology
Institute of Pathology, School of Medicine
Technical University of Munich (TUM)
Munich, Germany

John P. Sundberg, DVM, PhD, Dipl. ACVP
The Jackson Laboratory
Bar Harbor, ME, USA
and
Department of Dermatology
Vanderbilt University Medical Center
Nashville TN, USA
and
North Woods Mouse Pathology
Southwest Harbor, ME, USA

Polina Sysa-Shah, MD
Department of Urology
School of Medicine
Johns Hopkins University
Baltimore, MD, USA

Piper M. Treuting, DVM, MS, Dipl. ACVP
Non-clinical Sciences
Seattle Genetics
Bothell, WA, USA

Peter Vogel, DVM, PhD, Dipl. ACVP
Pathology Department
St. Jude Children's Research Hospital
Memphis, TN, USA

Jerrold M. Ward, DVM, PhD, Dipl. ACVP, Fellow IATP
Global VetPathology
Montgomery Village, MD, USA

M. Kay Washington, MD, PhD, Dipl. ABPath
Department of Pathology, Microbiology and Immunology
Vanderbilt University Medical Center
Nashville, TN, USA

Vet-ebooks.com

Preface and Acknowledgments

The editors of this book want to take this opportunity to acknowledge and thank our wives for supporting us through this process. Beth Sundberg, Jane Vogel, and Ann Ward supported us as we wrote our respective and coauthored chapters, and as we reviewed all the submissions from the numerous experts who carefully drafted the chapters that follow. This was a large undertaking by all involved, and we believe that this book will serve as a resource for many years to come to assist scientists in the development and interpretation of mouse models for the study of human diseases.

The pathologists and other scientists who wrote these chapters while examining the mice, overseeing necropsies, and evaluating the histologic sections of tissues of interest, need to take this opportunity to thank the laboratory animal staff including veterinarians and animal care technicians who managed these mouse colonies, the necropsy/laboratory technicians who performed the postmortem examinations and collected tissues for a variety of histological and molecular assays, as well as the histologists who processed the tissues, prepared sections, and stained them with a variety of histochemical stains and immunological markers. The end result of these largely anonymous contributions have been the excellent histologic sections all authors photographed. We also would like to thank all of our collaborators over the years who allowed us to participate with them on the many experiments using mice for studying the causes and mechanisms of both human and animal disease, and the search for effective disease therapies and methods of prevention experiments. In addition, the Wiley publication staff was invaluable for creation of this book. We greatly appreciate their help.

The purpose of this book is to provide a broad overview on how pathologists phenotype mutant and wild-type (without an induced or natural gene mutation) mice and compare them to human diseases. Each chapter covers one organ or organ system with a brief overview of the anatomy, but more importantly, specifics on tissue collection, processing, and special stains or assays used to analyze that particular organ. Each chapter is written by one or more experts on that organ. In so doing, this book provides a useful starting point for investigators working with mice, be they experts or neophytes.

Nomenclature is a critical aspect of pathological description. Pathologists learn to critically utilize very specific medical terms to describe gross and histologic features of lesions and that is evident throughout this book. However, equally important when working with mice, humans, rats, and many other laboratory species, is the species-specific nomenclature for genes and proteins. Reviews, especially books, should compile information on specific topics to provide an up-to-date overview, including using current molecular nomenclature. While this is required by most journals, few editors or reviewers pay much attention to nomenclature accuracy. Because we felt this was such an important and largely overlooked topic, there is a detailed chapter on this subject in this book. The editors made a decided effort to review all chapters not only for accuracy of the pathological descriptions and terms but also for molecular nomenclature. Ultimately, the chapter authors were free to decide whether or not to use the current terms, including listing the specific allelic mutations they were discussing, and most did. We want to specifically thank Michelle Perry, David Shaw, and Dale Begley from the Mouse Genome Informatics Database group at the Jackson Laboratory for following up on all of our inquiries to make sure we did our best to get the nomenclature correct. This included in a number of cases getting new names assigned to mouse mutant alleles that were recently published.

The real value for updating genetic nomenclature became obvious in many of the chapters as they were being reviewed. Defining an animal model of a human disease depends on closely matching the disease features (phenotypes) between the animal under investigation (the mouse) and humans in particular. Over the years, lab names were given to the animals, often indicating something about their phenotype(s). These names became embedded within "the field" to the point they were considered to be standard names. The mouse genetic community many years ago set up the *International Committee on Standardized Genetic Nomenclature for Mice* (http://www.informatics.jax.org/mgihome/nomen/inc.shtml). This is housed at the Jackson Laboratory within the Mouse Genome Informatics Database (MGI), but the committee consists of geneticists from around the world. They have sought to regularly review and adjust genetic nomenclature as new information is published on genes, biological pathways, and gene functions. In so doing, names change over the years. MGI maintains this information, which

Vet-ebooks.com

includes reported allelic mutations and links to many of the publications about that mutant mouse line. The surprise that came up consistently in all chapters was that as the mutant gene became known, and the names updated, it was obvious that not only did the mouse model often closely resemble the human disease, but since human genetic nomenclature had followed a similar course with updates in names, in most cases the orthologous gene was mutated in both species, an important point in validating the disease model.

It has been an amazing opportunity to follow the development of mouse models from the earliest days of spontaneous mutations occurring in mouse colonies, induced mutations using radiation or chemical mutagenesis, to the introduction of transgenic technology, then targeted mutagenesis (knock-out mouse technology), to CRISPR/Cas9, and beyond. Parallel to the advances in molecular technology has been refinement of histopathological approaches beyond H&E and special stained sections to immunofluorescence, immunohistochemistry, *in situ* hybridization, and transcriptome analysis on organs and now to single cells. Despite all these advances, histopathology will always be a backbone for characterizing the biology and pathology of animals including humans. We have seen refinements on all fronts resulting in excellent models for human diseases for dissecting molecular mechanisms to running preclinical trials. This book reflects the current state of the art in pathology phenotyping of mouse models, and we hope will lay the groundwork for many discoveries yet to come.

Vet-ebooks.com

1

Introduction to Mouse Pathology

Jerrold M. Ward, Peter Vogel, and John P. Sundberg

The Use of Mice in Medical Research

There has been a large increase in the use of mice in both basic and translational medical research over the past 20 years, as evidenced by the increase in retrievable references using "mice" as a keyword in PubMed from 29 029 publications in 1998 to 79 858 in 2018, and over 1.6 million in the entire PubMed database. Mice have been used for both basic and translational (formerly applied) research. Much of this important work is sponsored by the National Institutes of Health (NIH) in the United States. Mice have been used to study basic biological processes, embryo development, genetic disorders, infectious diseases, degenerative diseases, toxicology, carcinogenesis, and aging, often by organ system or tissue. Many Nobel Prize awardees in Physiology or Medicine have used mice in research leading to their honors. Much of this research has been greatly valued for the training of future scientists, discovery of new diseases, understanding the mechanism of disease in mice and other animals, including humans, and in the treatment and prevention of disease in mice and humans [1–8]. Histopathology may be included in the mouse research, but often it is not, or not by someone trained and competent in pathology [9]. The value of pathology has been proven for diagnosis and understanding normal biology and abnormal biology (pathology) of cells, tissues, and organs in all species. Comparative pathology spans all species of animals. But some investigators do not understand the value of pathology, as a discipline, in experimental studies with mice. This book intends to promote the value of mouse pathology in medical research aimed at the discovery of the causes, prevention, and therapy of diseases in both humans and other animals.

Understanding Diseases Found in Mutant Animals

Naturally occurring and induced changes in genes often result in a specific phenotype at the clinical and histopathological levels. The cause of this phenomenon is that genes have specific functions that play a role in the normal homeostasis of cells, tissues, and organs. A genetically engineered mouse (GEM) line represents a tool to investigate the effects resulting from the partial or complete loss of gene function or the gain of normal or abnormal functions. The genes are often found to function in specific cellular organelles and biochemical/molecular pathways important for normal biological functions (Figure 1.1) [10]. Cells involved in common gene functions can be single cell types in single tissues, multiple cells types in a single tissue, or multiple cells types in multiple tissues. Gene expression can also be induced in specific cells and tissues by normal and abnormal body functions, or by exposure to external factors such as drugs, infectious agents, environmental modifications, and ingested foods.

Mutant mice often exhibit histopathological changes (lesions) in tissues and organs that are associated with gene function, but the ultimate clinical phenotype can be influenced by various factors. Much of the histopathology found in mutant mice is in the usual spectrum of degenerative, inflammatory, proliferative, and neoplastic changes also found in nonmutant mice. Nouvelle lesions do occur commonly in some lines of mutant mice. These include unique developmental changes, cellular morphological changes, patterns of lesions, types of proliferative lesions, and often strain specific cancer types. These may be due to specific naturally occurring mutations (polymorphisms) in genes

Pathology of Genetically Engineered and Other Mutant Mice, First Edition. Edited by John P. Sundberg, Peter Vogel, and Jerrold M. Ward.
© 2022 John Wiley & Sons, Inc. Published 2022 by John Wiley & Sons, Inc.

Vet-ebooks.com

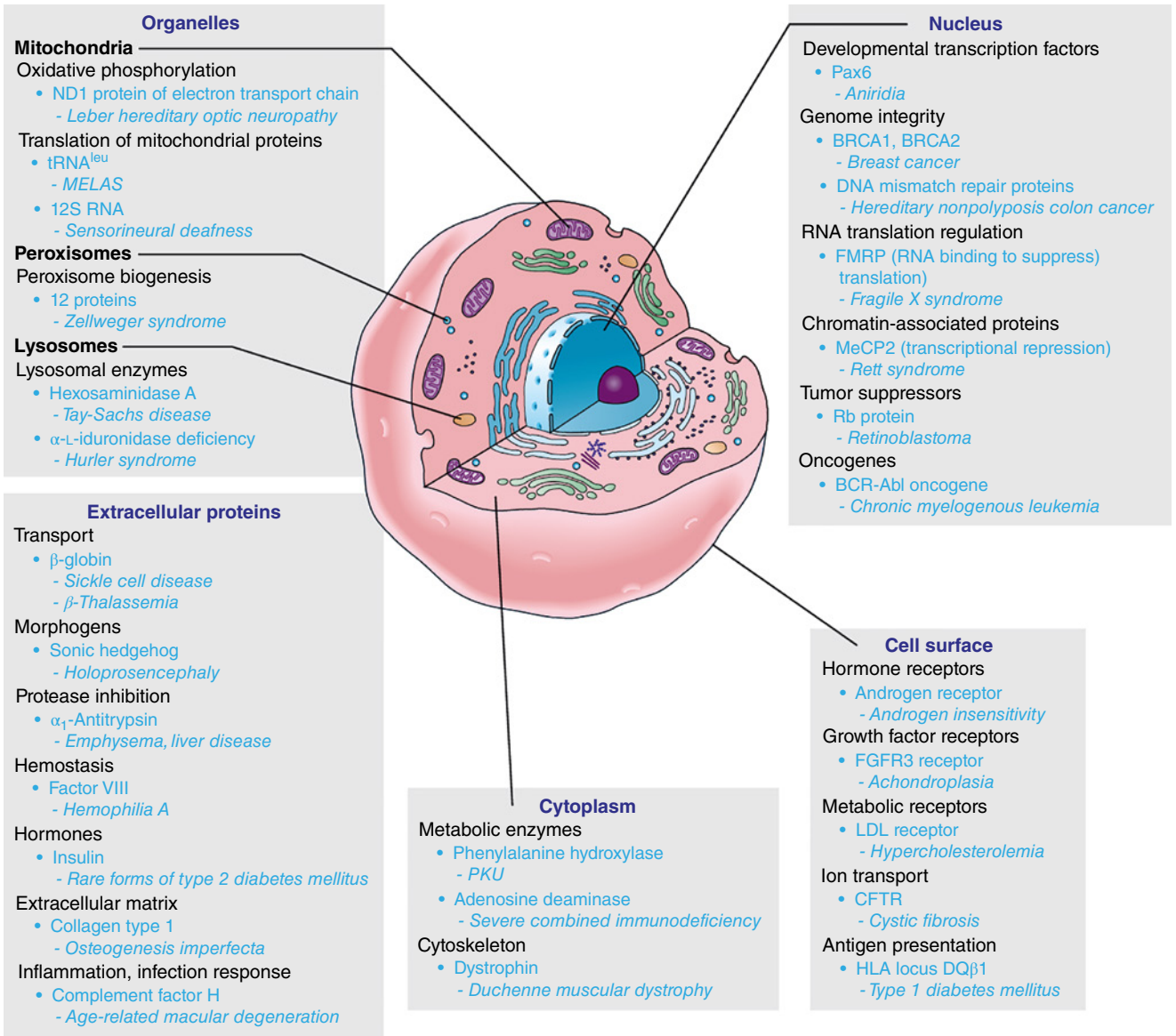


Figure 1.1 Classes of proteins associated with human genetic diseases. Source: Nussbaum (2007). Reprinted with permission of Elsevier

that can serve as genetic based models for disease. Spontaneous mutants made up the bulk of mouse models until the advent first of radiation and then chemical mutagenesis programs. The spectrum of spontaneous lesions is noted in each organ-specific chapter. Often the lesions are identical or very similar to those associated human genetic disorders, but they also may vary from human lesions. The genetic background of the mice often plays a role in spontaneous as well as induced disease phenotypes.

Mouse Pathology – Nomenclature

The pathology of mice in research was first led by Thelma Dunn and Harold Stewart at the National Cancer Institute (NCI) at the NIH [11–13]. Both were MD pathologists who applied general rules of human pathology diagnosis to mice when possible. Although mouse pathology nomenclature does not follow any official designation, two organizations (INHAND; https://www.toxpath.org/inhand.asp and National Cancer Institute Mouse Models of Cancer Consortium Tumor Pathology Nomenclature) have provided international nomenclatures for specific tissues [2, 14]. Other published guides are included in each appropriate organ chapter [15, 16]. Many books and refereed publications on mouse pathology provide valuable information for pathologists and scientists [12, 17–35] as well as web sites (https://ntp.niehs.nih.gov/nnl; http://www.informatics.jax.org/frithbook; http://eulep.pdn.cam.ac.uk/~skinbase/index.php). Importantly, many of these references involve both DVMs and MDs, pathologists, and basic scientists, who integrate mouse and human disease nomenclature together to be state-of-the-art. The pathology nomenclature used in this

Vet-ebooks.com

book generally reflects the NCI tumor pathology and INHAND general pathology nomenclatures. There are, however, no international or national standards for nomenclature that must be followed. These published nomenclatures are merely guidelines for use by scientists, pathologists, and journals. Each chapter author considered these guidelines and noted appropriate references for each organ and tissue.

Mouse Genetic Nomenclature

In contrast to pathology nomenclature, mouse genetic nomenclature is standardized. Chapter 3 focuses on the details of the nomenclature system and discusses how it was developed. While the authors and editors have, for the most part, updated the nomenclature, not all authors were willing to do so. Regardless, one can and should use the Mouse Genome Informatics website to verify all genes and alleles, as discussed in the Chapter 3, to make sure they are working with the correct nomenclature and allelic mutations.

Tumor Pathology

It is known in human and mouse pathology that cancer pathogenesis follows a scheme of molecular pathogenesis and an associated histopathogenesis [14, 16, 36]. There have been numerous publications on the role of specific genes in tumor pathogenesis in humans and animals. It is not the intention of this book to review the role of all genes for which published information on mouse cancer models is available, but rather to provide samples of some of the more common and important genes that play important roles. GEM may involve a single gene and attempt to mimic the human genetic disorder, or GEM may represent non-familial genetic changes in the pathways to disease including cancer. Tumor frequency data in wild-type control mice, especially in aging studies, have often been reported in various strains and stocks [1, 7, 23, 35, 37, 38]. While these reports provide general background information on the frequency of cancer types in a wildtype inbred strain, the actual frequency will vary based on substrain, husbandry, and other factors, necessitating the use of adequate numbers of control mice for studies on frequency of cancers in GEMs.

Immunohistochemistry (IHC), Scoring, Image Analysis, and Other Supportive Research Pathology Techniques

A variety of special pathology techniques are important adjuncts to mouse research. These include immunohistochemistry (IHC), *in situ* hybridization (ISH), ultrastructure, imaging, image analysis, artificial intelligence, machine learning, and a variety of molecular techniques. Most chapters will include examples of these for the various tissues. Some publications offer reviews of the use of IHC in mice [39–42] and Internet sites offer IHC protocols (http://tumor.informatics.jax.org/mtbwi/index.do, https://www.niehs.nih.gov/research/resources/protocols/protocols-immuno/index.cfm) and whole slide images (http://tumor.informatics.jax.org/mtbwi/lymphomaPathology.jsp).

Histopathology scoring (grading) of lesion type and severity can often be used for mouse models of disease, genetics, and preclinical development for drugs [6, 34, 43–45]. Examples are given in some chapters. The newer fields of image analysis, artificial intelligence, and machine learning are growing quickly [46, 47] and allow scientific analysis of quantitative pathology data.

Publication of Erroneous Pathology Data: Inadvertent Fraud?

Publications involving mice and other animals sometimes include histopathology figures that do not show what is described in the figure legend and/or text [2, 48, 49]. This problem has occurred most often in publications that do not appear to include a pathologist as a co-author, and in journals that are not pathology-based. The absence of pathology support at a research institution may be due to cost, lack of pathology staff, and/or the desire of a scientist and his staff to attempt pathology on their own ("Do It yourself pathology") [50]. These publications containing clearly erroneous findings may be due to lack of pathologists as reviewers of the submitted manuscript and/or a lack of the journal reviewers and editors who understand the value of accurate histopathology description and interpretation. Emails to authors and editors involved with the publication usually evoke no responses, and rarely concern even if there is a response. The only solution is for scientists and journals to understand the importance of pathology as a critically important medical specialty as part of doing research using mice.

Overall Organization of the Book

The *Pathology of Genetically-engineered Mice (GEM) and Other Mutant Mice* is organized into introductory chapters on concepts on the use of mice in biomedical research and the critical need to include mouse pathology expertise. The mouse pathology chapters, by organ system or other topics, are generally organized into sections on anatomy and histology, special necropsy organ protocols, aging/spontaneous strain specific lesions, GEM, and references. The reference listings are not an extensive review of the topic since there are thousands of such references, but they do include recent reviews and relevant classic and current publications. Tables and figures call attention to important information on the mice and their applications.

Vet-ebooks.com

Acknowledgments

The editors wish to thank the lead and co-authors of all chapters for their valuable contributions and interactions with the editors.

This work was supported grants from the National Institutes of Health (R01-CA089713 and P30-CA034196 to JPS).

References

1 Brayton, C.F., Boyd, K.L., Everitt, J.L. et al. (2018). An introduction to pathology in biomedical research: a mission-critical specialty for reproducibility and rigor in translational research. *ILAR J.* 59 (1): 1–3.
2 Cardiff, R.D., Ward, J.M., and Barthold, S.W. (2008). 'One medicine—one pathology': are veterinary and human pathology prepared? *Lab. Invest.* 88 (1): 18–26.
3 Holland, E.C. (ed.) (2004). *Mouse Models of Human Cancer*. Hoboken, NJ: Wiley-Liss.
4 Proetzel, G. and Wiles, M.V. (eds.) (2016). *Mouse Models for Drug Discovery: Methods and Protocols*, 2e. New York, NY: Humana Press.
5 Schofield, P.N., Ward, J.M., and Sundberg, J.P. (2016). Show and tell: disclosure and data sharing in experimental pathology. *Dis. Models Mech.* 9 (6): 601–605.
6 Sundberg, J.P., Silva, K.A., Li, R. et al. (2004). Adult-onset alopecia areata is a complex polygenic trait in the C3H/HeJ mouse model. *J. Invest. Dermatol.* 123 (2): 294–297.
7 Sundberg, J.P., Berndt, A., Sundberg, B.A. et al. (2016). Approaches to investigating complex genetic traits in a large-scale inbred mouse aging study. *Vet. Pathol.* 53 (2): 456–467.
8 Treuting, P.M., Snyder, J.M., Ikeno, Y. et al. (2016). The vital role of pathology in improving reproducibility and translational relevance of aging studies in rodents. *Vet. Pathol.* 53 (2): 244–249.
9 Barthold, S.W., Borowsky, A.D., Brayton, C. et al. (2007). From whence will they come? – a perspective on the acute shortage of pathologists in biomedical research. *J. Vet. Diagn. Invest.* 19 (4): 455–456.
10 Nussbaum, R.L., McInnes, R.R., and Willard, H.F. (2007). *Thompson & Thompson Genetics in Medicine*, 7e. Philadelphia, PA: Saunders/Elsevier.
11 Dunn, T.B. (1949). Some observations on the normal and pathologic anatomy of the kidney of the mouse. *J. Natl. Cancer Inst.* 9 (4): 285–301.
12 Dunn, T.B. (1958). Morphology and pathology of reticular neoplasms in the mouse: relationship to man. *Ann. N. Y. Acad. Sci.* 76 (3): 619–628.
13 Grady, H.G. and Stewart, H.L. (1940). Histogenesis of induced pulmonary tumors in strain A mice. *Am. J. Pathol.* 16 (4): 417–432.5.
14 Cardiff, R.D., Anver, M.R., Boivin, G.P. et al. (2006). Precancer in mice: animal models used to understand, prevent, and treat human precancers. *Toxicol. Pathol.* 34 (6): 699–707.
15 Elmore, S.A., Cardiff, R., Cesta, M.F. et al. (2018). A review of current standards and the evolution of histopathology nomenclature for laboratory animals. *ILAR J.* 59 (1): 29–39.
16 Cardiff, R.D. and Borowsky, A.D. (2010). Precancer: sequentially acquired or predetermined? *Toxicol. Pathol.* 38 (1): 171–179.
17 Barthold, S.W., Griffey, S.M., and Percy, D.H. (2016). *Pathology of Laboratory Rodents and Rabbits*, 4e. Ames, IA: Wiley-Blackwell.
18 Cheville, N.F. (2009). *Ultrastructural Pathology*. Ames, IA: Wiley-Blackwell.
19 Fox, J.G., Barthold, S.W., Davisson, M.T. et al. (eds.) (2006). *The Mouse in Biomedical Research: History, Wild Mice, and Genetics*, 2e. Burlington, MA: Academic Press.
20 Haines, D.C., Chattopadhyay, S., and Ward, J.M. (2001). Pathology of aging B6; 129 mice. *Toxicol. Pathol.* 29 (6): 653–661.
21 Hedrich, H.J. (ed.) (2012). *The Laboratory Mouse*, 2e. Amsterdam: Academic Press.
22 Jones, T.C., Ward, J.M., Mohr, U., and Hunt, R.D. (eds.) (1990). *Monographs on Pathology of Laboratory Animals: Hematopoietic System*. Berlin: Springer-Verlag.
23 Maronpot, R.R. (ed.) (1999). *Pathology of the Mouse*. Vienna, IL: Cache River Press.
24 Mohr, U. (ed.) (2001). *International Classification of Rodent Tumors: The Mouse*. Berlin: Springer.
25 Mohr, U., Dungworth, D.L., Capen, C.C. et al. (eds.) (1996). *Pathology of the Aging Mouse*., Vols. 1 and 2. Washington DC: ILSI Press.
26 Ruberte, J., Carretero, A., and Navarro, M. (eds.) (2017). *Morphological Mouse Phenotyping: Anatomy, Histology and Imaging*. Amsterdam: Academic.
27 Scudamore, C.L. (ed.) (2014). *A Practical Guide to the Histology of the Mouse*. Oxford: Wiley-Blackwell.
28 Sundberg, J.P. and Boggess, D. (2000). *Systematic Approach to Evaluation of Mouse Mutations*. Boca Raton, FL: CDC Press.
29 Sundberg, J.P. and Ichiki, T. (eds.). *Genetically Engineered Mice Handbook*. Boca Raton,FL: CRC Press.
30 Frith, C.H. and Ward, J.M. (1988). *Color Atlas of Neoplastic and Non-neoplastic Lesions in Aging Mice*. Amsterdam: Elsevier.
31 Turner, P.V., Brash, M.L., and Smith, D.A. (2017). *Pathology of Small Animal Pets*. Wiley-Blackwell.
32 Wallig, M.A., Haschek, W.M., Rousseaux, C.G. et al. (eds.) (2018). *Fundamentals of Toxicologic Pathology*, 3e. London: Academic Press.

Vet-ebooks.com

33 Smith, R.S., John, S.W.M., Nishina, P.M., and Sundberg, J.P. (eds.) (2002). *Systematic Evaluation of the Mouse Eye*. Boca Raton, FL: CRC Press.

34 Sundberg, J.P., Elson, C.O., Bedigian, H., and Birkenmeier, E.H. (1994). Spontaneous, heritable colitis in a new substrain of C3H/HeJ mice. *Gastroenterology* 107 (6): 1726–1735.

35 Ward, J.M., Mahler, J.F., Maronpot, R.R., and Sundberg, J.P. (eds.) (2000). *Pathology of Genetically Engineered Mice*. Ames, IA: Iowa State University Press.

36 Ward, J.M. and Treuting, P.M. (2014). Rodent intestinal epithelial carcinogenesis: pathology and preclinical models. *Toxicol. Pathol.* 42 (1): 148–161.

37 Radaelli, E., Castiglioni, V., Recordati, C. et al. (2016). The pathology of aging 129S6/SvEvTac mice. *Vet. Pathol.* 53 (2): 477–492.

38 Harbison, C.E., Lipman, R.D., and Bronson, R.T. (2016). Strain- and diet-related lesion variability in aging DBA/2, C57BL/6, and DBA/2xC57BL/6 F1 mice. *Vet. Pathol.* 53 (2): 468–476.

39 Mikaelian, I., Nanney, L.B., Parman, K.S. et al. (2004). Antibodies that label paraffin-embedded mouse tissues: a collaborative endeavor. *Toxicol. Pathol.* 32 (2): 181–191.

40 Janardhan, K.S., Jensen, H., Clayton, N.P., and Herbert, R.A. (2018). Immunohistochemistry in investigative and toxicologic pathology. *Toxicol. Pathol.* 46 (5): 488–510.

41 Ward, J.M. and Rehg, J.E. (2014). Rodent immunohistochemistry: pitfalls and troubleshooting. *Vet. Pathol.* 51 (1): 88–101.

42 Rehg, J.E. and Ward, J.M. (2017). Application of immunohistochemistry in toxicologic pathology of the hematopoietic system. In: *Immunopathology in Toxicology and Drug Development* (ed. G.A. Parker), 489–561. Springer.

43 Meyerholz, D.K. and Beck, A.P. (2018). Fundamental concepts for semiquantitative tissue scoring in translational research. *ILAR J.* 59 (1): 13–17.

44 Bleich, A., Mahler, M., Most, C. et al. (2004). Refined histopathologic scoring system improves power to detect colitis QTL in mice. *Mamm. Genome* 15 (11): 865–871.

45 Jurisic, G., Sundberg, J.P., Bleich, A. et al. (2010). Quantitative lymphatic vessel trait analysis suggests *Vcam1* as candidate modifier gene of inflammatory bowel disease. *Genes Immun.* 11 (3): 219–231.

46 Turner, O.C., Aeffner, F., Bangari, D.S. et al. (2020). Society of toxicologic pathology digital pathology and image analysis special interest group article*: opinion on the application of artificial intelligence and machine learning to digital toxicologic pathology. *Toxicol. Pathol.* 48 (2): 277–294.

47 Aeffner, F., Zarella, M.D., Buchbinder, N. et al. (2019). Introduction to digital image analysis in whole-slide imaging: a white paper from the digital pathology association. *J. Pathol. Inform.* 10: 9.

48 Ward, J.M., Schofield, P.N., and Sundberg, J.P. (2017). Reproducibility of histopathological findings in experimental pathology of the mouse: a sorry tail. *Lab. Anim. (NY).* 46 (4): 146–151.

49 Wolf, J.C. and Maack, G. (2017). Evaluating the credibility of histopathology data in environmental endocrine toxicity studies. *Environ. Toxicol. Chem.* 36 (3): 601–611.

50 Ince, T.A., Ward, J.M., Valli, V.E. et al. (2008). Do-it-yourself (DIY) pathology. *Nat. Biotechnol.* 26 (9): 978–979.

Vet-ebooks.com

2

The Mouse Online: Open Mouse Biology and Pathology Data Resources for Biomedical Research

Dale A. Begley, Paul N. Schofield, and John P. Sundberg

Introduction

Large collections of data and resources are available online, ranging from genomic and gene expression databases (GXDs) to archives of experimental data, phenotype data, and bioresources such as strains, cell lines, and tissues. While many core resources contain multispecies data and are good sources for mouse information, this review will cover some of the major websites that provide access to mouse-centric databases (Table 2.1) and how they can be used to assist with analysis of normal, abnormal, or mutant mice.

Databases fall into two main categories; those where data are gathered, expertly curated, and presented by the database project itself, often integrating data from several sources and analytical tools. The second type of database acts as an archival platform to which data are uploaded by users, often with minimal curation. There are several examples of hybrids of various proportions where uploads are solicited by the database, curated to a different degree, and presented with core data sourced and validated by the database staff. Curated databases may also be long-term repositories or archives of legacy datasets. Data resources are generally funded out of project/program grants and core institutional funding. The degree of currency and the depth of curation often depends on funding and funding sustainability. Metrics and indicators for database description, and to a degree for assessing database quality, can be found in ELIXIR [1], as the criteria developed for qualification as an ELIXIR core database are widely applicable. A good source of rapidly accessible core information about databases is the annual database issue of *Nucleic Acids Research*. Databases present their core activities and modes of access in the papers but also publish updates as significant developments are achieved. It is always useful to browse this issue when looking for new sources of data.

FAIR Data Access and Databases of Databases

The move to make scientific data openly discoverable, accessible, and useable has led to the formalization of the principles of open data, known as FAIRsharing [2]. Data has to be free, accessible, interoperable, and reusable. Increasingly databases are trying to comply with the FAIR semantic and access technical requirements as part of data discovery and interoperability, and many databases now provide access computationally through an Application Programming Interface (API) as well as through Hypertext Markup Language (HTML), together with complete data dumps and data reports. Searching using standardized semantics and ontologies provides very powerful ways of searching databases, and for databases such as MouseMine it is possible to use very powerful SPARQL Protocol and RDF (Resource Description Framework) Query Language (SPARQL) queries.

Along with standardization of database structures and access goes formalization of standards, essential for interoperability and data aggregation. Different communities have established specific standards for metadata, minimal information (MI) for reporting (MI standards), and other data structures. These standards and the characteristics of databases can now be found in databases of databases such as the very useful FAIRsharing database. FAIRsharing lists and describes standards used in databases but also the type of data and importantly the species. Currently, FAIR sharing lists 90 databases either dedicated to the mouse or with specifically mouse data [2].

The Re3data repository [3] lists 57 mouse data resources, interestingly with limited overlap with those from FAIRsharing, indicating the usefulness of looking at as many metaresources as possible. Of course, many databases, particularly small but often valuable ones, are not listed in these resource repositories. It is one aim in this

Pathology of Genetically Engineered and Other Mutant Mice, First Edition. Edited by John P. Sundberg, Peter Vogel, and Jerrold M. Ward.
© 2022 John Wiley & Sons, Inc. Published 2022 by John Wiley & Sons, Inc.

Vet-ebooks.com

Table 2.1 Websites with information useful for phenotyping mutant laboratory mice.

Website name	Address	Data resource
Alliance of Genome Resources	https://www.alliancegenome.org	Identification of animal models for human disease
Atlas of mouse cardiovascular development	https://www.devbio.pitt.edu/research/atlas-mouse-cardiovascular-development	Atlas of the mouse cardiovascular system using EFIC
Bonebase	http://www.bonebase.org	Variation in bone mass using μCT and histomorphometry for KOMP mice
Emouseatlas	https://www.emouseatlas.org/emap/home.html	Mouse embryonic anatomy and development
GUDMAP	https://www.gudmap.org	Urogenital and prostate development with a collection of immunohistochemical, histological, and immunofluorescence images, and gene expression data
International Mouse Phenotyping Consortium (IMPC)	https://www.mousephenotype.org	Summaries of phenotyping of genetically engineered mice in the KOMP program
Monarch	https://monarchinitiative.org	Identification of animal models for human disease
Mouse Brain Atlas	https://developingmouse.brain-map.org, https://mouse.brain-map.org	High-resolution physical atlases of the adult and embryonic mouse brains
Mouse Genome Informatics	http://www.informatics.jax.org	Large datasets on mice, genetics, inbred strains, mutant lines, etc.
Mouse Genome Informatics SNP Database	http://www.informatics.jax.org/snp	Single nucleotide polymorphisms for inbred strains
MouseMine	http://www.mousemine.org/mousemine/begin.do	Comparative human and mouse data
Mouse Models of Human Cancer Database (MMHCD)	http://tumor.informatics.jax.org/mtbwi/index.do	Mouse models of human cancer data and images
Mouse Phenome Database	https://phenome.jax.org	Variety of data on studies that compare inbred strains
MUTAGENETIX	https://mutagenetix.utsouthwestern.edu	Immunological phenotypes of single gene mouse mutants produced by ENU mutagenesis
National Toxicology Program Neoplastic Lesion Atlas	https://ntp.niehs.nih.gov/nnl/index.htm	Atlas of images and descriptions on nonneoplastic lesions in rats and mice
Noah's Arkive	http://noahsarkive.cldavis.org/cgi-bin/show_image_info_page.cgi	Images of lesions from many different species
Online Mendelian Inheritance in Man (OMIM)	https://www.ncbi.nlm.nih.gov/omim	Summaries with references on genetic based diseases in humans with reference to animal models
Pathbase, The European Mouse Pathology Database	http://www.pathbase.net	Images of lesions found in mice (spontaneous, genetically engineered, etc.)
PATHBIO	http://www.pathbio.org	Training modules, X-ray atlas, lymphatic mapping atlas, images of inbred strain specific diseases
Sanger Mouse SNP Database	https://www.sanger.ac.uk/sanger/Mouse_SnpViewer/rel-1505	Single nucleotide polymorphisms for 36 inbred strains
Skinbase	http://eulep.pdn.cam.ac.uk/~skinbase/index.php	Subdirectory of Pathbase focusing on normal and abnormal skin phenotypes in mice

Vet-ebooks.com

chapter to introduce some of these smaller databases that are nevertheless very valuable.

Many archival databases and some reference resources are very dependent on users to curate, correct uploads, and to give them added value for a community. Databases run for the use of specific communities can provide a high degree of added value at low cost and contribute heavily to scientific sustainability. Image databases especially fall into this category and in particular need new material from experts in the field to constantly expand the resource and accurately curate the material. Pathologists can use these resources as legacy tools for extra photomicrographs they take while working up new models or defining spontaneous diseases in colonies. Such additional images can be referenced in the primary publication as being publicly available on the websites, which usually is very well received by journals and reviewers on future grant applications. Many of the current public repositories will not accept files of the size of zoomable histopathology images and limited user uploads. This, together with payment to commercial repositories is a specific problem for very image intensive histopathology and cell biology data.

General Information on Inbred Laboratory Mice

Mouse Genome Informatics (http://www.informatics.jax.org)

The Mouse Genome Informatics (MGI) international database resource is the most comprehensive collection of information on mouse biology available today. It is the first place one should go to when searching for information on the mouse or even just searching for a mouse. MGI is an integrated collection of databases providing access to comprehensive information on genetics, genomics, and biology of the laboratory mouse. Data in MGI are obtained by direct expert curation of published literature and importation of large-scale datasets from other data resources. The Mouse Genome Database (MGD) [4] is the core resource for general mouse information in MGI. MGD contains information on mouse genes, strains, phenotypes, mutant alleles, sequences/single nucleotide polymorphisms (SNP), vertebrate homology, and mouse models of human disease. MGD also is the source for official gene, allele, and mouse strain nomenclature using International Committee on Standardized Nomenclature for Mice standards (see Chapter 3 for details on nomenclature). The GXD [5] contains information on gene expression in the developing mouse including immunohistochemistry, immunofluorescence, and *in situ* hybridization images. The CrePortal contains data on *cre*-recombinase expressing mice with a large library of images [6]. The Gene Ontology (GO) project provides functional annotations for mouse gene products [7–11]. The Mouse Models of Human Cancer database (MMHC) contains information on inbred mouse strains, genetically engineered mouse (GEM) models, [12–15] and patient derived xenograft (PDX) models of human cancer [16]. This database is particularly useful for pathologists and is described in detail below. Databases in the MGI consortium that contain images are the MGD, the MMHC, and the GXD.

MouseMine (http://www.mousemine.org/mousemine/begin.do)

MouseMine [17] is a data warehouse resulting from a collaboration between the Intermine project at the University of Cambridge and The Jackson Laboratory MGI group. MouseMine contains a subset of data from MGI, focused on genomics, strain, and allele annotations curated by MGI, such as GO [7–11] and Mutant Phenotype using Mouse Phenotype Ontology [18]. Specifically, it is focused on comparative human and mouse data and contains a great deal of information annotated to standard human ontologies such as the Disease Ontology [19] and the Human Phenotype Ontology [20]. It is cross-referenced to Online Mendelian Inheritance in Man (OMIM) [21] (see below) and other external resources. A full list of the data in MouseMine can be found at http://www.mousemine.org/mousemine/dataCategories.do. One of the strengths of MouseMine is that it is possible to carry out very sophisticated queries, to integrate the results of MouseMine queries with user data, and to combine the outputs of multiple queries. It also offers web services over an API to provide programmatic access to MGI data.

Monarch (https://monarchinitiative.org)

Monarch [22] aims to provide a formally integrated resource pulling together data from model organisms such as the mouse, and from humans, through alignment of genotypes, variants, diseases, and phenotypes. The focus is on using formally defined phenotypes to support identification of animal models for human disease. The database pulls data from wide range of sources (Figure 2.1) and provides powerful methods for data exploration. Data can be accessed through an API and RESTful web services.

Alliance of Genome Resources (https://www.alliancegenome.org)

The Alliance of Genome Resources is a consortium of six model organism databases (MODs) and the (GO) consortium. The purpose of the alliance is to provide a central data resource that provides a common user interface to query genomic data and integrates the data from different organisms allowing this data to be viewed in a consistent manner. The Alliance also provides links back to the primary data in many cases. The ability to compare common data across multiple model organisms in an integrated manner is a very useful and powerful tool [23]. The MGD is one of the founding members of the Alliance.

Vet-ebooks.com

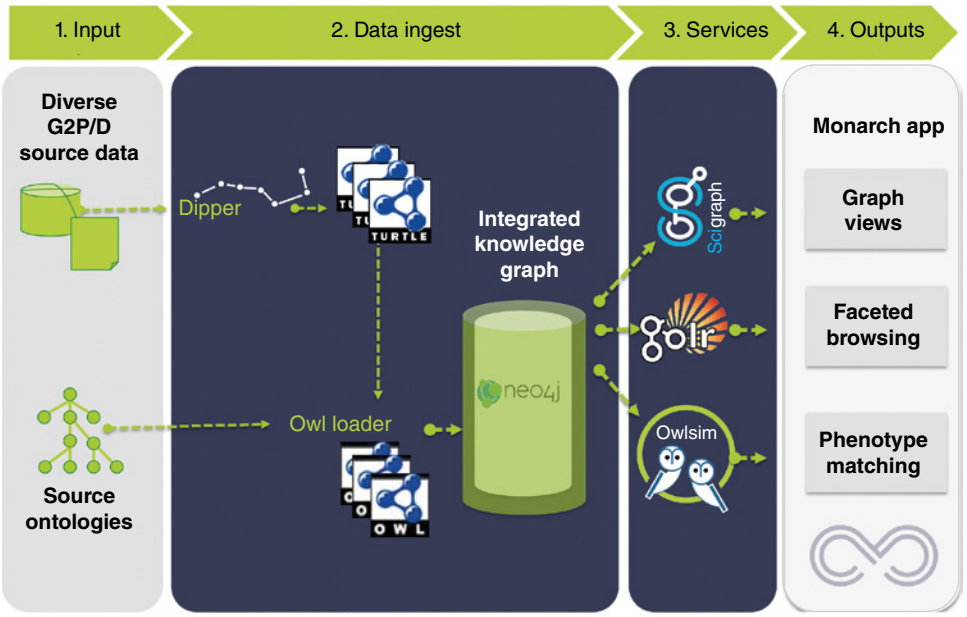


Figure 2.1 **Data integration strategy for Monarch**. Data, mainly "genotype-to-phenotype," are gathered from a wide range of databases and parsed so that they can be organized into an integrated knowledge graph based on the 35 underlying ontologies used by Monarch describing for example genotype–phenotype relations, diseases, and gene properties. The knowledge graph can then be browsed, searched, or semantic similarity between entities calculated to look for related diseases or mutant strains, for example, where the relationship had previously not been noticed. The databases integrated by Monarch can be found on https://monarchinitiative.org/about/data-sources. Source: Image reproduced with permission from Monarch.

Mouse Models of Human Cancer Database (MMHC, Formerly Mouse Tumor Biology Database) (http://tumor.informatics.jax.org/mtbwi/index.do)

The Mouse Models of Human Cancer Database is one of the core databases included in the MGI consortium. Unlike Pathbase (see below), which covers all types of lesions diagnosed in laboratory mice, this website focuses on cancer and hyperplastic lesions in mice (Figure 2.2). Much of the database is built around data and the literature such that the images are supplemental to the enormous amount of data on strain specific lesions, genes known to cause specific types of cancer, and how this information relates to human cancer [12, 24–29]. A recent change has been to integrate photomicrographs of human cancers into the database for more direct anatomic comparisons. Also, MMHC contains datasets and webpages focused on specific topics, such as skin cancers [15], lymphomas [13], and a list of antibodies tested in mice with conditions tested under and results [30]. Whole slide scanned images of the lymphomas with immunohistochemistry demonstrate how to subtype the lesions can be accessed in this database [13]. The lymphoma digital slide (whole slide images) collection originates from the NCI Mouse Models of Cancer Consortium workshop on Hematopoietic Tumors (http://tumor.informatics.jax.org/mtbwi/lymphomaPathology.jsp) [31, 32]. Lung cancers and hyperplasias were whole-slide scanned from a large-scale aging program looking at lesions in 31 inbred mouse strains [33, 34]. Current projects include developing a training module to aid pathologists in the interpretation and grading of non-melanoma skin cancers in mice caused by UV light, two-stage chemical carcinogenesis, papillomavirus, or those that arise in production colonies spontaneously. As PDX (cancers resected from patients and transplanted into immunodeficient mice) have become a major research tool, these too are included in this database [16].

The histopathology images included in MMHC are curated from the primary literature, when given permission by the publisher, and from direct submissions from researchers and large-scale projects.

As of January 2020, MMHC contains over 6400 photomicrographs, both histological and immunohistochemical. These images are attached to detailed information on the tumor diagnosis, strain, genetics, original reference, treatment, and human lesion the strain models. Images also contain annotations from the submitting author/pathologist if the image is a direct submission or notes from the curated reference that are relevant to the image.

Mouse Genome Informatics SNP Database (http://www.informatics.jax.org/snp)

This is another search capability of MGI. It allows researchers to ask how inbred mouse strains differ from each other at the molecular level by enabling queries of SNP data for 88 strains of mice obtained from NCBI's dbSNP resource (Build 142) [35, 36]. Users can query by gene, proximity to gene, and strain and results can be sorted by dbSNP Function Classes or by Strain, and drag columns to reposition strains of interest [37].

Vet-ebooks.com

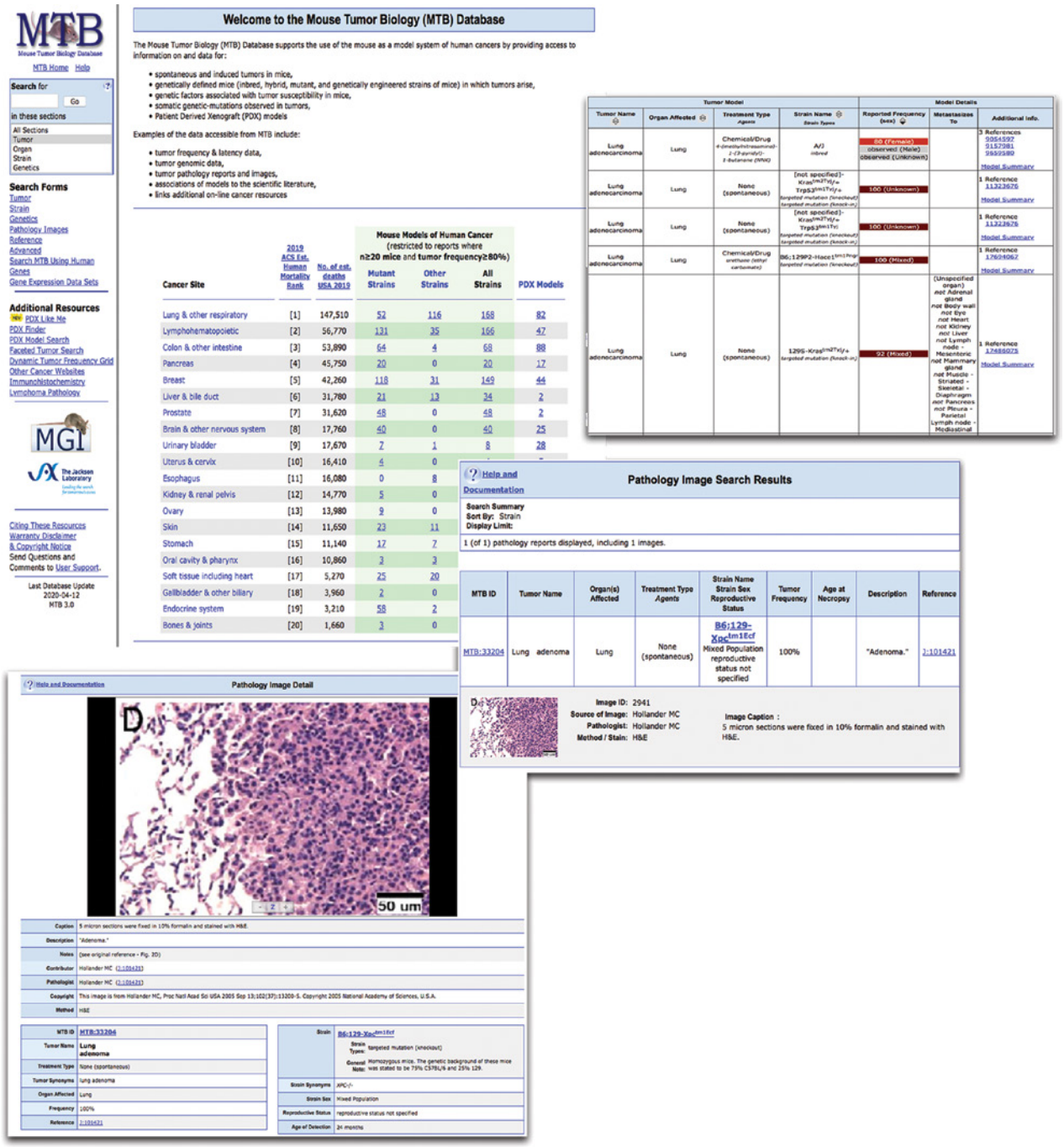


Figure 2.2 **The Mouse Models of Human Cancer Database (MMHC), formerly Mouse Tumor Biology Database (MTB).** Data on frequency and types of cancer in inbred strains and following manipulation (genetically or chemically), photomicrographs, and references are available on this website. Source: Images were retrieved from the Mouse Models of Human Cancer Database (MMHC, formerly MTB), Mouse Genome Informatics, The Jackson Laboratory, Bar Harbor, Maine. World Wide Web (URL: http://tumor.informatics.jax.org) (April 2020).

Sanger Mouse SNP Database (https://www.sanger.ac.uk/sanger/Mouse_SnpViewer/rel-1505)

This is similar to the MGI SNP database but provides specific annotation on a more limited number of inbred strains. This resource has sequence data on 36 inbred strains representing strains most commonly used in biomedical research today to those with great genetic diversity [38, 39]. The strains were sequenced and annotated, and base changes, relative to the C57BL/6J reference strain as well as predicted effect of changes are listed. This information can be useful when one suspects a molecular difference in a gene in an inbred strain with a specific lesion associated with a known genetic mutation. One example came from the observation of ectopic

Vet-ebooks.com

mineralization in several inbred mouse strains in an aging study that resembled, to various degrees, lesions observed in B6.Cg-*Abcc6*^{tm1Jfk} (ATP-binding cassette, sub-family C [CFTR/MRP], member 6) null mice, a mouse model for human pseudoxanthoma elasticum (PXE) [40]. Four strains were found to have the same SNP in the *Abcc6* gene that was predicted to have a major effect and later confirmed to function as a hypomorphic mutation (Table 2.2) [41–43].

While often assumed that the reference strain (C57BL/6J) is wild type for the gene under investigation, it may actually be the abnormal gene in the reference strain. An example is alcohol dehydrogenase 7 (*Adh7*, formerly called *Adh4*, that is no longer listed in the Sanger SNP database). As shown in Table 2.3, there are two SNPs predicted to be missense mutations with significant effects [44]. However, the strains listed (129, C3H/HeJ, DBA/2J, and KK/HlJ) are actually wild type and the C57BL/6J (reference strain) and C57BL/6NJ are the hypomorphic mutant strains. This change partially explains alopecia and dermatitis that is a strain specific phenotype in most B6 substrains [45].

Table 2.2 SNP comparison between inbred strains for the *Abcc6* gene. A search of the Sanger Mouse SNP database (17 January 2020) revealed a single base difference predicted to be a missense mutation (yellow) that has a predicted significant effect (*). Note that not all of the 129 substrains carry this allele.

Gene	Chromosome	Position	dbSNP	Reference	129P2/OlaHsd	129S1/SvImJ	129S5SvEvBrd	C3H/HeJ	C57BL/6NJ	DBA/2J	KK/HiJ
Abcc6	7	45,979,026	rs32751584	T	C	C	C	C	-	C	C
Abcc6	7	45,979,027	rs32751586	G	-	A	A	A	-	A	A
Abcc6	7	45,979,329	rs52492784	T	C	C	C	C	-	C	C
Abcc6	7	45,979,332	rs255648560	C	T	-	-	-	-	-	-
Abcc6	7	45,979,342	rs52081041	T	C	C	C	C	-	C	C
Abcc6	7	45,979,350	rs52476049	T	C	C	C	C	-	C	C
Abcc6	7	45,979,428	rs32751588	T	C	C	C	C	-	C	c
Abcc6	7	45,979,479	rs226776926	A	G	G	G	G	-	G	G
Abcc6	7	45,979,481	rs245254287	T	C	C	C	C	-	C	C
Abcc6	7	45,979,483	rs215733716	C	T	T	T	T	-	T	T
Abcc6	7	45,979,503	rs47309606	A	G	G	G	G	-	G	G
Abcc6	7	45,979,518	rs32751593	T	C	C	C	C	-	C	C
Abcc6	7	45,979,519	rs49208795	G	T	-	-	-	-	-	-
Abcc6	7	45,979,526	rs50146914	A	G	G	G	G	-	G	G
Abcc6	7	45,979,719	rs32752395	C	-	T*	T*	T*	-	T*	T*
Abcc6	7	45,979,850	-	T	C	-	-	-	-	-	-
Abcc6	7	45,980,046	rs32752398	C	T	-	-	-	-	-	-
Abcc6	7	45,980,047	rs32752399	G	-	A	A	A	-	A	A
Abcc6	7	45,980,124	rs32752401	T	C	C	C	C	-	C	C
Abcc6	7	45,980,195	rs31113325	C	T	T	T	T	-	T	T
Abcc6	7	45,980,274	rs216152409	A	G	G	G	G	-	G	G
Abcc6	7	45,980,412	rs31560978	C	T	-	-	-	-	-	-
Abcc6	7	45,980,427	rs32352446	G	A	-	-	-	-	-	-
Abcc6	7	45,980,475	rs31369566	A	G	-	-	-	-	-	-
Abcc6	7	45,980,499	rs49424268	T	C	-	-	-	-	-	-

Vet-ebooks.com

Table 2.3 **Polymorphisms in *Adh7*.** Two SNP in the *Adh7* gene (formerly called *Adh4*) are predicted to be missense mutations (yellow) with a significant effect (*) in many inbred strains. However, actually this is only true for the reference strain (C57BL/6J) and the closely related substrain (C57BL/6NJ). Those predicted to have significant effects are in fact the wild type alleles.

Gene	Chromosome	Position	dbSNP	Reference	129P2/OlaHsd	129S1/SvImJ	129S5SvEvBrd	C3H/HeJ	C57BL/6NJ	DBA/2J	KK/HiJ
0610031O16Rik	3	138,221,632	rs30512262	G	C	C	C	C	-	C	C
0610031O16Rik	3	138,222,187	rs30594157	T	C	C	C	C	-	C	C
0610031O16Rik	3	138,223,190	rs30907305	G	A	A	A	A	-	A	A
0610031O16Rik	3	138,223,276	rs49048350	A	T	T	T	T	-	T	T
0610031O16Rik	3	138,223,314	rs48657115	T	G	G	G	G	-	G	G
0610031O16Rik	3	138,223,345	rs49621707	A	T	T	T	T	-	T	T
0610031O16Rik	3	138,223,449	rs47855194	C	T	T	T	T	-	T	T
0610031O16Rik	3	138,223,512	rs46440580	T	C	C	C	C	-	C	C
Adh7	3	138,223,922	rs13468441	C	T*	T*	T*	T*	-	T*	T*
0610031O16Rik	3	138,224,573	rs50005056	C	T	T	T	T	-	T	T
0610031I16Rik	3	138,224,578	rs46271260	A	G	G	G	G	-	G	G
0610031O16Rik	3	138,225,390	rs30170105	T	C	C	C	C	-	C	C
0610031O16Rik	3	138,225,871	rs30695413	G	A	A	A	-	-	A	A
0610031O16Rik	3	138,226,121	rs31386034	A	C	~	C	C	-	~	~
0610031O16Rik	3	138,226,125	rs31000950	C	G	G	G	G	-	G	G
0610031O16Rik	3	138,226,160	rs30901573	G	-	-	-	A	-	-	-
Adh7	3	138,226,410	rs31091615	A	G*	G*	G*	G*	-	G*	G*
0610031O16Rik	3	138,228,417	rs30262949	T	C	C	C	C	-	C	A
0610031O16Rik	3	138,228,503	rs50248152	G	A	A	A	A	-	A	G
0610031O16Rik	3	138,228,653	rs31428790	A	G	G	G	G	-	G	G
0610031O16Rik	3	138,228,722	rs30904366	A	G	G	G	G	-	G	G
Adh7	3	138,231,370	-	T	g		~		-		
Adh7	3	138,231,388	rs50766077	C	A	A	A	A	-	A	A
Adh7	3	138,231,410	rs46894990	A	G	G	G	G	-	G	G
Adh7	3	138,231,427	rs46279078	T	A	A	A	A	-	A	A

Large Scale Mutagenesis

International Mouse Phenotyping Consortium (IMPC; https://www.mousephenotype.org)

Many pharmaceutical companies have created large number of mutant mice, some using large scale, high throughput methods to both create and phenotype the mice generated. However, their goals were very drug oriented and proprietary. Only now, many years later are some of the results becoming publicly available from such projects as those done by Lexicon [46]. An alternative approach was to systematically create null mutations in all known protein-coding genes in the mouse and utilize a systematic and standardized phenotyping protocol. The International Mouse Phenotyping Consortium (IMPC) was developed to meet this objective [47]. While initially a variety of recombineering methods were used, now null mutations are created using CRISPR/Cas9. The goal is to inactivate approximately 20 000 genes one at a time on a standardized inbred strain (C56BL/6N). Attempts at overall standardization enable comparison of results creating in a sense an encyclopedia on gene function inferred from knockout phenotypes. However, there are variations between the environments at different participating

Vet-ebooks.com

institutions and different substrains of C57BL/6N are used. For example, some use a substrain where the *Crb1*^{rd8} allele causing a retinal phenotype in C57BL/6N mice was corrected using TALEN-mediated homology-directed repair [48]. This website provides deep summaries of the data by gene, together with primary data that is also accessible through the IMPC API web services. At the time of writing, 6440 knockouts have been phenotyped for more than 600 parameters in embryonic and adult life. A schematic of the phenotyping pipeline is shown in Figure 2.3.

Large numbers of radiographs and histopathology images are available on IMPC together with embryo images using different modes of imaging. Histopathology images are available on https://www.mousephenotype.org/data/landing_pages/histopath for 580 genes and, where changes were diagnosed, use the combination of mouse pathology ontology (MPATH) and mouse anatomy ontology (MA) ontology terms as used in Pathbase (Figure 2.4). Embryos, as part of the embryonic lethality program, are visualized using OPT, micro CT, and whole mounts, including LacZ expression reporters. Volumetric data are available from the micro CT and images through the dedicated embryo viewer (https://www.mousephenotype.org/data/embryo_imaging). Radiographs were taken at week 14 and a standard set of orientations and organs displayed (see https://www.mousephenotype.org/impress/ProcedureInfo?action=list&procID=556).

The website is set up such that IMPC data can be used in a variety of ways, such as to investigate basic biology mechanisms that can lead to new therapeutic targets or to narrow down a suspected list of genes in patients. As with the Lexicon studies, the IMPC has and continues to make discoveries related to a wide variety of diseases [50–53].

MUTAGENETIX (https://mutagenetix.utsouthwestern.edu)

MUTAGENETIX is a database of immunological phenotypes of single gene mouse mutants produced by ENU mutagenesis. It currently contains data generated by the

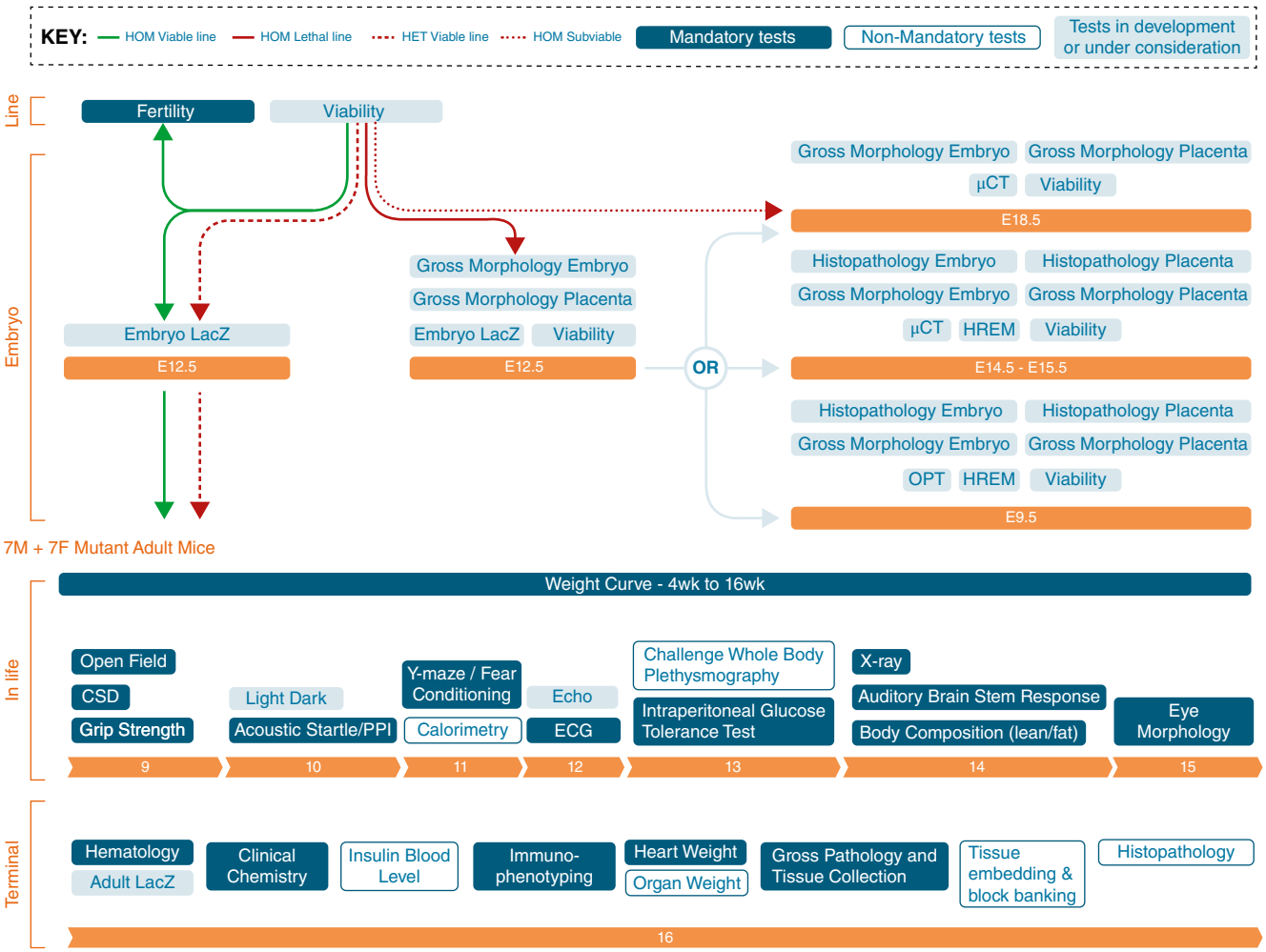


Figure 2.3 **IMPC phenotyping pipelines for adult mice (17 weeks) and embryos.**

Vet-ebooks.com



Figure 2.4 **The histopathology browser for the IMPC database**. Data can be searched for by gene and, where phenotyping of the strain has been completed, users can find data from individual mice, with zygosity of the knockout and in many cases, a diagnostic assessment with lesion and anatomical location derived from the MPATH and MA ontologies and used combinatorially. There are also estimates of severity and microanatomical qualifiers. The use of the ontologies in this way is described in Elmore et al. [49]. Selected hematoxylin and eosin stained images are available.

Vet-ebooks.com

Beutler Lab at the University of Texas Southwestern Medical Center and the Goodnow Lab at the Australian National University and provides access to strains maintained at these centers. The immunological data are very rich and the site contains information about protocols and breeding procedures that are very valuable. Note that incidental, nonimmunological phenotypes are also described for some mutations, such as growth, skin, and endocrine phenotypes. The site is updated regularly (https://mutagenetix.utsouthwestern.edu) [54, 55].

Background Strain Comparison Studies

Mouse Phenome Database (https://phenome.jax.org)

The Mouse Phenome Database (MPD) was originally envisioned as a site to host data on comparative studies that utilized multiple inbred strains. It provided a repository for the primary data. As the site evolved, the data could be manipulated to generate a variety of tables to define quantitative differences for specific phenotypes between strains. Today, the site has been refined enabling integration of genomic and phenomic data by providing access to primary experimental data, well-documented data collection protocols, and a variety of tools to analyze these datasets. Investigators worldwide provided the data on this site which represent a broad scope of disease-related characteristics in the inbred mouse strains to variations in behavior, morphological, and physiological differences in naive mice and those exposed to drugs, environmental agents, or other manipulations [56].

Mouse Pathology Image (Histopathology) Resources

Pathbase, the European Mouse Pathology Database (http://www.pathbase.net)

Pathbase is a community resource for images of all types of lesions and normal tissues from laboratory mice [57, 58]. Pathologists from all over the world, not just Europe, provide photomicrographs of lesions diagnosed in laboratory mice. While initially the goal was to illustrate lesions in genetically engineered mice, this website has evolved to include all types of mouse diseases as well as normal tissues including large collections of images from aged inbred mouse strain studies [33]. These data are curated in an ontology built around the Mouse Anatomy (MA) [59] and Mouse Pathology (MPATH) [60] ontologies, with more refinement for selected organs, such as skin [61]. This enables rapid retrieval of histologic images. In fact, if one integrates this into a diagnostic database, one can use the diagnostic term to go to Pathbase to look up the definition of the term and then access images of lesions with that diagnosis provided by numerous pathologists from around the world, something called the "virtual second opinion" [62]. Integration of the Mouse Anatomy and Pathology Ontologies into diagnostic laboratory software sets up a controlled vocabulary that enables consistent data searches to enable high-level computational analysis of the dataset [62, 63].

National Toxicology Program Neoplastic Lesion Atlas (https://ntp.niehs.nih.gov/nnl/index.htm)

The National Toxicology Program Atlas of Nonneoplastic Lesions in Rats and Mice is a publicly accessible resource built around the goal of identifying potential human carcinogens in rodent bioassays. Nonneoplastic diseases are also a major cause of morbidity and mortality in humans. This atlas provides diagnostic guidelines for histologic lesions in both rats and mice. This was built around an effort to maintain consistency with lesion terminology through the creation of the International Harmonization of Nomenclature and Diagnostic Criteria (INHAND) monograph series [64, 65] and classification systems in textbooks [66, 67]. A web resource for INHAND can be found on https://www.toxpath.org/inhand.asp.

The database is organized by major organ systems (alimentary, cardiovascular, endocrine, hematopoietic, hepatobiliary, immune, integumentary, musculoskeletal, nervous, reproductive [female and male], respiratory, special senses, and urinary) and within each category are a limited number of examples of lesions with a representative image. This is useful for getting started to gain a basic understanding of lesions, terms, and definitions. Unfortunately, while aimed at standardizing toxicology diagnoses, it does not embrace the complexity of human disease making it relatively superficial and not helpful to define a mouse model for a human disease.

Noah's Arkive, Charles Louis Davis, and Samuel Wesley Thompson Foundation for the Advancement of Veterinary and Comparative Pathology (http://noahsarkive.cldavis.org/cgi-bin/show_image_info_page.cgi)

Noah's Arkive was developed in the early 1980s as *The International Veterinary Pathology Slide Bank* to serve as a repository of slides (2×2 color transparencies) contributed by individuals and institutions worldwide. In 1986, this slide archive was made available in a digitized format, on laser videodisks. In 2010, Noah's Arkive was launched as a single web-based resource. Images cover a broad variety of species not just laboratory mice. As such, it is a powerful resource for comparing lesions between species when working up a new mouse model. When looking up lists of images (7 February 2020), searching just for mouse, there were 141 pages with 100 entries (often with more than one image per entry) per page listed.

Vet-ebooks.com

Organ/Disease Specific Resources

Most websites are generic providing examples of lesions or models that cover a broad range of topics and organ systems. However, most investigators focus on a particular disease or group of diseases or specific anatomic sites. Several organ/disease specific websites are listed below that remain active and are maintained at the time of this writing. These sites come and go so one is best advised to do a search under the disease or organ of interest. Many of the disease sites one finds are for patient advocacy groups (foundations) that often provide both patient information and sometimes a review or relevant research that may involve mouse models. While a useful source of information for experts in the field, these resources do not often provide detail on non-human animal models as they are aimed more at support of the clinical practice and medical research communities. Other sites have been developed by investigators working with specific models or fine-tuning discoveries in the many large-scale mutant producing programs. Several are provided below.

Bone Diseases: Skeletal Phenotyping of IMPC/KOMP Mice (http://www.bonebase.org)

The Knockout Mouse Program (KOMP) is a United States initiative in collaboration with the International Knockout Mouse Consortium (IKMC) to generate a large number of laboratory mice with a single gene inactivated (null mouse) eventually for all protein coding genes, one at a time. A collaboration between investigators at several institutions have been systematically analyzing bones in C57BL/6NJ mice generated by KOMP. This is not one of the primary sites generating and phenotyping these mutant mice, but rather a group specializing in detailed analysis of subtle abnormalities only of bones. The group is focused on screening gene knockout mice for variation in bone mass using μCT and histomorphometry to systematically analyze mice generated from the various KOMP primary sites [68].

Skin Diseases: Skinbase (http://eulep.pdn.cam.ac.uk/~skinbase/index.php)

While there initially was a group that systematically reviewed skin, hair, and nails in KOMP mice [53, 69], this was discontinued. Some examples of skin phenotypes in mice with spontaneous single gene mutations are available as whole slide scans on Skinbase, a subdirectory of Pathbase (http://www.pathbase.net). This site also has labeled images of normal skin, hair follicles, and nails to explain normal anatomy of these structures. Pathbase itself has thousands of tiff files on normal and abnormal examples in mice from wild type inbred strains to spontaneous single gene mutations in mice, to mutations caused by a variety of man-made methods (radiation, chemical mutagenesis, and genetically engineered mice).

GenitoUrinary Development Molecular Anatomy Project (GUDMAP) (https://www.gudmap.org)

GenitoUrinary Development Molecular Anatomy Project (GUDMAP) is a consortium of laboratories working to provide the scientific and medical community with tools to facilitate research on the GenitoUrinary (GU) tract. This resource is effectively a toolkit for the study of the mammalian urogenital system with a great deal of information on mouse mutants, tools, and strains. It presents a very significant educational resource for urogenital and prostate development, together with a collection of immunohistochemical, histological, and immunofluorescence images, and gene expression data for the mouse GU tract [70].

Mouse Brain Atlas (https://developingmouse.brain-map.org, https://mouse.brain-map.org)

The mouse brain atlas is part of the Allen Brain Atlas project (https://portal.brain-map.org) and presents high-resolution physical atlases of the adult and embryonic mouse brains based on histological sections annotated to gene expression at cellular resolution. The atlas has an interactive viewer with annotations based on a high-resolution ontology for brain anatomy. There is also an atlas of the mouse spinal cord with an expression color map and serial histological sections. This is a powerful set of tools for the anatomy and molecular anatomy of the mouse brain and, for example, allows users to search for different anatomic regions with similar patterns of gene expression. There is related single cell data on morphology, gene expression, and single cell electrophysiology together with access to electrophysiological models. These data are all accessible through an API as well as a web interface [71].

Atlas of Mouse Cardiovascular Development (https://www.devbio.pitt.edu/research/atlas-mouse-cardiovascular-development)

This site presents a developmental atlas of the mouse cardiovascular system using episcopic fluorescence image capture (EFIC) imaging from E9.5 to term. Embryo sections are available in multiple orientations and can be viewed using a fly-through interactive viewer. Some examples of EFIC 3D reconstructions are provided showing a variety of congenital cardiovascular anomalies seen in several knockout and ENU-induced mouse mutants [72, 73].

Mouse/Human Disease Phenotype Databases

The connection between a mouse model and a corresponding human disease can be difficult to identify. MGI has multiple resources that allow for the identification of human disease models. MGD has the Human–Mouse: Disease Connection (HMDC) that enables searches for potential

Vet-ebooks.com

mouse models, candidate genes, and similarity between mouse models and human patients. Gene entries in MGD have links to predicted vertebrate orthologs in other species databases including Homologene, HGNC, OMIM, and Entrez Gene. MMHC contain tumor phenotypes from potential human disease models including human corresponding examples.

Online Mendelian Inheritance in Man (OMIM) (https://www.ncbi.nlm.nih.gov/omim)

OMIM is a comprehensive database on human genes and genetic disorders and has been publicly available since 1987 [74]. OMIM is continually updated from the public literature and has links to other species databases. OMIM is the internet version of the multivolume book titled *Mendelian Inheritance in Man* by Victor McCusik [75] and is based at Johns Hopkins University. OMIM entries are classified using a standardized system of MIM numbers (denoting genetic classifications) and OMIM disorder codes (indicating loci associated genetic based diseases). OMIM concentrates on the genotype/phenotype relationship. OMIM entries contain text summaries of associated clinical features, molecular genetics, references, clinical synopses, phenotypic series the entry belongs to, and multiple graphic representations of the data [74]. Information and references on various animal models, including those in mice, that mimic or are confirmed orthologs is provided.

Emouseatlas (https://www.emouseatlas.org/emap/home.html)

The Emouseatlas focuses on embryonic development of the laboratory mouse [76–81]. This website has four modules. EMA (Mouse Anatomy Atlas) covers mouse embryonic anatomy, ontology, and staging. Ehistology is an histology atlas of embryonic development that includes classic whole embryo images produced by Prof. Mathew Kaufman, used in his book *Atlas of Mouse Development* [82]. Emage covers mouse gene expression in embryos. Elearning provides tutorials to provide training on key principals of embryonic development.

Finding Mouse Models

While one can read a paper and contact the corresponding author to try to obtain mice to develop a colony for research, there are always concerns about real availability, time to get the mice, genetic quality (is the strain really what it is claimed to be?), pathogen status, and many other variables. Fortunately, a large number of commercial and nonprofit institutions have set up repositories to obtain, standardize, and distribute mice world-wide. Some are listed in Table 2.4. Information provided on the websites can be quite detailed and specific while others can be limited to the degree that sometimes the specific mutation in the gene is not known. However, careful study of the literature provides a lot of the information needed to make an informed decision.

An alternative approach is to do your initial searches on MGI (http://www.informatics.jax.org, described above). This website is not a mouse repository. However, if you look up your gene of interest (under the header Genes and then search for the gene of interest in the Genes and Marker Query) you end up at a Gene Detail page. On the lower right side is a category "All mutations and alleles" with a number. If you click on that (or the specific type listed below) you will get a listing of all published alleles with the correct (at the time of viewing) gene and allele symbol with a short summary. Click on the link to the allele of interest and you will get more information on that allele. At the bottom of the page, just above the reference list, is a section "Find Mice

Table 2.4 Sources of mouse models for human diseases.

Vendor	Website address
Charles River Laboratory	https://www.criver.com/products-services/find-model
Envigo	https://www.envigo.com/p/research-models/browse
Hilltop Lab Animals	http://hilltoplabs.com
Infrafrontier	https://www.infrafrontier.eu
Janvier Labs	https://www.janvier-labs.com
Knockout Mouse Project (KOMP) Repository	https://www.komp.org
MRC Harwell Institute	https://www.har.mrc.ac.uk
Mutant Mouse Resource and Research Centers	https://www.mmrrc.org/catalog/StrainCatalogSearchForm.php
Simonsen Laboratories	http://www.simlab.com
The European Conditional Mouse Mutagenesis Program	https://www.mousephenotype.org/about-impc/about-ikmc/eucomm
The Jackson Laboratory	https://www.jax.org/mouse-search
Taconic Biosciences	https://www.taconic.com/find-your-model

Vet-ebooks.com

IMSR". Click on that link and it will take you to the International Mouse Strain Resource (IMSR) or you can go to their site directly from the start (http://www.findmice.org). This will tell you where in the world the mice are currently available from.

Use of Mouse Pathology Resources on Line; Citations, and Licenses

The availability of the wide range of resources discussed in this chapter is subject to the constraints of funding and user interactions, and there will inevitably be turnover as existing databases cease and new ones emerge. Funding patterns are very different for all of the resources discussed above, some are well-funded and supported institutionally, while others run on a wing and a prayer. The importance of even small databases to particular specialties or communities is, however, not necessarily related to their scale or the size of their funding and it is the role that they play which is important.

What makes a data resource succeed is interaction with its users. Submission of data for those that act as archives, feedback, and contact for all, but specifically making sure that databases are cited in papers if they were used in the work, even though images may not have been actually included in papers. The use of data resources far outstrips citations; this is a known aspect of running databases, yet funding agencies like to see citations and this will help the database you use to stay afloat. All databases have advice on how to cite them and we would encourage everyone in the community to remember to cite databases that have been of use in training or in writing original manuscripts.

The second issue of note is the license under which images and data are distributed. Most data and images are distributed under a Creative Commons CC-BY license that permits data to be used, redistributed, and modified as long as the original source is always cited. The CC-BY-ND, that is less often used, prohibits the making of derivatives so that means that you cannot redistribute the image modified in any way. Finally, CC-0 is effectively a waiver on rights so that the image or data are distributed to the public domain. These licenses are legally actionable, though the authors are currently unaware of any actions being taken under these licenses for histopathology images. It is, however, useful to know what each means and act accordingly. We would encourage all data and images put into the public domain to be released according to, at least, a CC-BY license if not CC-0, for the benefit of the community.

Acknowledgments

This work was supported in part by a grant from the Erasmus + Knowledge Alliance of the Education, Audiovisual and Culture Executive Agency (EACEA) of the European Union (Reference Number 600803-EPP-1-2018-1-ES-EPPKA2) and grants from the National Institutes of Health (CA089713 and CA034196).

References

1 Durinx, C., McEntyre, J., Appel, R. et al. (2017). Identifying ELIXIR core data resources. *F1000 Res.* 5: 2422.
2 Sansone, S.A., McQuilton, P., Rocca-Serra, P. et al. (2019). FAIRsharing as a community approach to standards, repositories and policies. *Nature Botechnol.* 37 (4): 358–367.
3 Pampel, H., Vierkant, P., Scholze, F. et al. (2013). Making research data repositories visible: the re3data.org registry. *PLoS One* 8 (11): e78080.
4 Bult, C.J., Blake, J.A., Smith, C.L. et al., Mouse Genome Database Group (2019). Mouse Genome Database (MGD) 2019. *Nucleic Acids Res.* 47 (D1): D801–D806.
5 Smith, C.M., Hayamizu, T.F., Finger, J.H. et al. (2019). The mouse Gene Expression Database (GXD): 2019 update. *Nucleic Acids Res.* 47 (D1): D774–D779.
6 Heffner, C.S., Herbert Pratt, C., Babiuk, R.P. et al. (2012). Supporting conditional mouse mutagenesis with a comprehensive cre characterization resource. *Nat. Commun.* 3: 1218.
7 Lovering, R.C., Roncaglia, P., Howe, D.G. et al. (2018). Improving interpretation of cardiac phenotypes and enhancing discovery with expanded knowledge in the Gene Ontology. *Circ Genom Precis Med.* 11 (2): e001813.
8 Hill, D.P., D'Eustachio, P., Berardini, T.Z. et al. (2016). Modeling biochemical pathways in the gene ontology. *Database* 2016: baw126.
9 Gene Ontology, C., Blake, J.A., Dolan, M. et al. (2013). Gene Ontology annotations and resources. *Nucleic Acids Res.* 41 (Database issue): D530–D535.
10 Thomas, P.D., Wood, V., Mungall, C.J. et al., Gene Ontology Consortium (2012). On the use of gene ontology annotations to assess functional similarity among orthologs and paralogs: a short report. *PLoS Comput. Biol.* 8 (2): e1002386.
11 Blake, J.A. and Harris, M.A. (2008). The Gene Ontology (GO) project: structured vocabularies for molecular biology and their application to genome and expression analysis. *Curr. Protoc. Bioinformatics*;Chapter 7:Unit 7.2.
12 Krupke, D.M., Begley, D.A., Sundberg, J.P. et al. (2017). The Mouse Tumor Biology Database: a comprehensive resource for mouse models of human cancer. *Cancer Res.* 77 (21): e67–e70.
13 Begley, D.A., Sundberg, J.P., Krupke, D.M. et al. (2015). Finding mouse models of human lymphomas and leukemia's using the Jackson laboratory mouse tumor biology database. *Exp. Mol. Pathol.* 99 (3): 533–536.

Vet-ebooks.com

14 Bult, C.J., Krupke, D.M., Begley, D.A. et al. (2015). Mouse Tumor Biology (MTB): a database of mouse models for human cancer. *Nucleic Acids Res.* 43 (Database issue): D818–D824.

15 Begley, D.A., Krupke, D.M., Neuhauser, S.B. et al. (2014). Identifying mouse models for skin cancer using the Mouse Tumor Biology Database. *Exp. Dermatol.* 23 (10): 761–763.

16 Conte, N., Mason, J.C., Halmagyi, C. et al. (2019). PDX Finder: a portal for patient-derived tumor xenograft model discovery. *Nucleic Acids Res.* 47 (D1): D1073–D1079.

17 Motenko, H., Neuhauser, S.B., O'Keefe, M., and Richardson, J.E. (2015). MouseMine: a new data warehouse for MGI. *Mamm. Genome* 26 (7–8): 325–330.

18 Smith, C.L. and Eppig, J.T. (2015). Expanding the mammalian phenotype ontology to support automated exchange of high throughput mouse phenotyping data generated by large-scale mouse knockout screens. *J. Biomed. Semantics* 6: 11.

19 Bello, S.M., Shimoyama, M., Mitraka, E. et al. (2018). Disease Ontology: improving and unifying disease annotations across species. *Dis. Model. Mech.* 11 (3): dmm032839.

20 Kohler, S., Doelken, S.C., Mungall, C.J. et al. (2014). The Human Phenotype Ontology project: linking molecular biology and disease through phenotype data. *Nucleic Acids Res.* 42 (Database issue): D966–D974.

21 Amberger, J.S., Bocchini, C.A., Scott, A.F., and Hamosh, A. (2019). OMIM.org: leveraging knowledge across phenotype-gene relationships. *Nucleic Acids Res.* 47 (D1): D1038–D1043.

22 Mungall, C.J., McMurry, J.A., Kohler, S. et al. (2017). The Monarch Initiative: an integrative data and analytic platform connecting phenotypes to genotypes across species. *Nucleic Acids Res.* 45 (D1): D712–D722.

23 Alliance of Genome Resources Consortium (2019). The Alliance of Genome Resources: building a modern data ecosystem for model organism databases. *Genetics* 213 (4): 1189–1196.

24 Begley, D.A., Krupke, D.M., Neuhauser, S.B. et al. (2012). The Mouse Tumor Biology Database (MTB): a central electronic resource for locating and integrating mouse tumor pathology data. *Vet. Pathol.* 49 (1): 218–223.

25 Begley, D.A., Krupke, D.M., Vincent, M.J. et al. (2007). Mouse Tumor Biology Database (MTB): status update and future directions. *Nucleic Acids Res.* 35 (Database issue): D638–D642.

26 Bult, C.J., Krupke, D.M., Sundberg, J.P., and Eppig, J.T. (2000). Mouse tumor biology database (MTB): enhancements and current status. *Nucleic Acids Res.* 28 (1): 112–114.

27 Krupke, D.M., Begley, D.A., Sundberg, J.P. et al. (2008). The Mouse Tumor Biology database. *Nat. Rev. Cancer* 8 (6): 459–465.

28 Krupke, D.M., Naf, D., Vincent, M.J. et al. (2005). The Mouse Tumor Biology Database: integrated access to mouse cancer biology data. *Exp. Lung Res.* 31 (2): 259–270.

29 Naf, D., Krupke, D.M., Sundberg, J.P. et al. (2002). The Mouse Tumor Biology Database: a public resource for cancer genetics and pathology of the mouse. *Cancer Res.* 62 (5): 1235–1240.

30 Mikaelian, I., Nanney, L.B., Parman, K.S. et al. (2004). Antibodies that label paraffin-embedded mouse tissues: a collaborative endeavor. *Toxicol. Pathol.* 32 (2): 181–191.

31 Morse, H.C. 3rd, Anver, M.R., Fredrickson, T.N. et al. (2002). Bethesda proposals for classification of lymphoid neoplasms in mice. *Blood* 100 (1): 246–258.

32 Kogan, S.C., Ward, J.M., Anver, M.R. et al. (2002). Bethesda proposals for classification of nonlymphoid hematopoietic neoplasms in mice. *Blood* 100 (1): 238–245.

33 Sundberg, J.P., Berndt, A., Sundberg, B.A. et al. (2011). The mouse as a model for understanding chronic diseases of aging: the histopathologic basis of aging in inbred mice. *Pathobiol. Aging Age Relat. Dis.* 1: 7179.

34 Berndt, A., Cario, C.L., Silva, K.A. et al. (2011). Identification of *Fat4* and *Tsc22d1* as novel candidate genes for spontaneous pulmonary adenomas. *Cancer Res.* 71 (17): 5779–5791.

35 NCBI Resource Coordinators (2016). Database resources of the National Center for Biotechnology Information. *Nucleic Acids Res.* 44 (D1): D7–D19.

36 NCBI Resource Coordinators (2015). Database resources of the National Center for Biotechnology Information. *Nucleic Acids Res.* 43 (Database issue): D6–D17.

37 Blake, J.A., Eppig, J.T., Kadin, J.A. et al. (2017). Mouse Genome Database (MGD)-2017: community knowledge resource for the laboratory mouse. *Nucleic Acids Res.* 45 (D1): D723–D729.

38 Keane, T.M., Goodstadt, L., Danecek, P. et al. (2011). Mouse genomic variation and its effect on phenotypes and gene regulation. *Nature* 477 (7364): 289–294.

39 Yalcin, B., Wong, K., Agam, A. et al. (2011). Sequence-based characterization of structural variation in the mouse genome. *Nature* 477 (7364): 326–329.

40 Klement, J.F., Matsuzaki, Y., Jiang, Q.J. et al. (2005). Targeted ablation of the *Abcc6* gene results in ectopic mineralization of connective tissues. *Mol. Cell. Biol.* 25 (18): 8299–8310.

41 Berndt, A., Li, Q., Potter, C.S. et al. (2013). A single-nucleotide polymorphism in the *Abcc6* gene associates with connective tissue mineralization in mice similar to targeted models for pseudoxanthoma elasticum. *J. Invest. Dermatol.* 133 (3): 833–836.

42 Li, Q., Guo, H., Chou, D.W. et al. (2014). Mouse models for pseudoxanthoma elasticum: genetic and dietary modulation of the ectopic mineralization phenotypes. *PLoS One* 9 (2): e89268.

43 Li, Q., Philip, V.M., Stearns, T.M. et al. (2019). Quantitative trait locus and integrative genomics revealed candidate modifier genes for ectopic mineralization in mouse models of pseudoxanthoma elasticum. *J. Invest. Dermatol.* 139 (12): 2447–2457.e7.

44 Dolney, D.E., Szalai, G., and Felder, M.R. (2001). Differences in charge and kinetic properties of alcohol dehydrogenase 4 from C57BL/6 mice compared to other inbred strains are associated with a cysteine120 to arginine120 substitution. *Biochem. Genet.* 39 (7–8): 239–250.

Vet-ebooks.com

45 Sundberg, J.P., Taylor, D., Lorch, G. et al. (2011). Primary follicular dystrophy with scarring dermatitis in C57BL/6 mouse substrains resembles central centrifugal cicatricial alopecia in humans. *Vet. Pathol.* 48 (2): 513–524.

46 Brommage, R., Powell, D.R., and Vogel, P. (2019). Predicting human disease mutations and identifying drug targets from mouse gene knockout phenotyping campaigns. *Dis. Mod. Mech.* 12 (5): dmm038224.

47 Meehan, T.F., Conte, N., West, D.B. et al. (2017). Disease model discovery from 3,328 gene knockouts by The International Mouse Phenotyping Consortium. *Nat. Genet.* 49 (8): 1231–1238.

48 Low, B.E., Krebs, M.P., Joung, J.K. et al. (2014). Correction of the *Crb1*^{rd8} allele and retinal phenotype in C57BL/6N mice via TALEN-mediated homology-directed repair. *Invest. Ophthalmol. Vis. Sci.* 55 (1): 387–395.

49 Elmore, S.A., Cardiff, R., Cesta, M.F. et al. (2018). A review of current standards and the evolution of histopathology nomenclature for laboratory animals. *ILAR J.* 59 (1): 29–39.

50 Dickinson, M.E., Flenniken, A.M., Ji, X. et al. (2016). High-throughput discovery of novel developmental phenotypes. *Nature* 537 (7621): 508–514.

51 Moore, B.A., Leonard, B.C., Sebbag, L. et al. (2018). Identification of genes required for eye development by high-throughput screening of mouse knockouts. *Commun. Biol.* 1: 236.

52 Rozman, J., Rathkolb, B., Oestereicher, M.A. et al. (2018). Identification of genetic elements in metabolism by high-throughput mouse phenotyping. *Nat. Commun.* 9 (1): 288.

53 Sundberg, J.P., Dadras, S.S., Silva, K.A. et al. (2017). Systematic screening for skin, hair, and nail abnormalities in a large-scale knockout mouse program. *PLoS One* 12 (7): e0180682.

54 Wang, T., Bu, C.H., Hildebrand, S. et al. (2018). Probability of phenotypically detectable protein damage by ENU-induced mutations in the Mutagenetix database. *Nat. Commun.* 9 (1): 441.

55 Wang, T., Zhan, X., Bu, C.H. et al. (2015). Real-time resolution of point mutations that cause phenovariance in mice. *Proc. Natl. Acad. Sci. U.S.A.* 112 (5): E440–E449.

56 Bogue, M.A., Philip, V.M., Walton, D.O. et al. (2020). Mouse Phenome Database: a data repository and analysis suite for curated primary mouse phenotype data. *Nucleic Acids Res.* 48 (D1): D716–D723.

57 Schofield, P.N., Bard, J.B., Boniver, J. et al. (2004). Pathbase: a new reference resource and database for laboratory mouse pathology. *Radiat. Prot. Dosim.* 112 (4): 525–528.

58 Schofield, P.N., Gruenberger, M., and Sundberg, J.P. (2010). Pathbase and the MPATH ontology. Community resources for mouse histopathology. *Vet. Pathol.* 47 (6): 1016–1020.

59 Hayamizu, T.F., Mangan, M., Corradi, J.P. et al. (2005). The Adult Mouse Anatomical Dictionary: a tool for annotating and integrating data. *Genome Biol.* 6 (3): R29.

60 Schofield, P.N., Sundberg, J.P., Sundberg, B.A. et al. (2013). The mouse pathology ontology, MPATH; structure and applications. *J. Biomed. Semantics* 4 (1): 18.

61 Fisher, H.M., Hoehndorf, R., Bazelato, B.S. et al. (2016). DermO; an ontology for the description of dermatologic disease. *J. Biomed. Semantics* 7: 38.

62 Sundberg, B.A., Schofield, P.N., Gruenberger, M., and Sundberg, J.P. (2009). A data-capture tool for mouse pathology phenotyping. *Vet. Pathol.* 46 (6): 1230–1240.

63 Sundberg, J.P., Sundberg, B.A., and Schofield, P. (2008). Integrating mouse anatomy and pathology ontologies into a phenotyping database: tools for data capture and training. *Mamm. Genome* 19 (6): 413–419.

64 Keenan, C.M., Baker, J.F., Bradley, A.E. et al. (2015). International Harmonization of Nomenclature and Diagnostic Criteria (INHAND) progress to date and future plans. *Toxicol. Pathol.* 28 (1): 51–53.

65 Keenan, C.M., Baker, J., Bradley, A. et al. (2015). International Harmonization of Nomenclature and Diagnostic Criteria (INHAND): progress to date and future plans. *Toxicol. Pathol.* 43 (5): 730–732.

66 Maronpot, R.R., Boorman, G.A., and Gaul, B.W. (1999). *Pathology of the Mouse*. Vienna, IL: Cache River Press.

67 Suttie, A.W., Leininger, J.R., and Bradley, A.E. (2017). *Boorman's Pathology of the Rat*, 2e. San Diego: Academic Press.

68 Rowe, D.W., Adams, D.J., Hong, S.H. et al. (2018). Screening gene knockout mice for variation in bone mass: analysis by μCT and histomorphometry. *Curr. Osteoporos Rep.* 16 (2): 77–94.

69 DiTommaso, T., Jones, L.K., Cottle, D.L. et al. (2014). Identification of genes important for cutaneous function revealed by a large scale reverse genetic screen in the mouse. *PLoS Genet.* 10 (10): e1004705.

70 Harding, S.D., Armit, C., Armstrong, J. et al. (2011). The GUDMAP database – an online resource for genitourinary research. *Development* 138 (13): 2845–2853.

71 Lein, E.S., Hawrylycz, M.J., Ao, N. et al. (2007). Genome-wide atlas of gene expression in the adult mouse brain. *Nature* 445 (7124): 168–176.

72 Krishnan, A., Samtani, R., Dhanantwari, P. et al. (2014). A detailed comparison of mouse and human cardiac development. *Pediatr. Res.* 76 (6): 500–507.

73 Talman, V., Teppo, J., Poho, P. et al. (2018). Molecular atlas of postnatal mouse heart development. *J. Am. Heart Assoc.* 7 (20): e010378.

74 Amberger, J.S., Bocchini, C.A., Schiettecatte, F. et al. (2015). OMIM.org: Online Mendelian Inheritance in Man (OMIM(R)), an online catalog of human genes and genetic disorders. *Nucleic Acids Res.* 43 (Database issue): D789–D798.

75 McKusick, V.A. (2007). Mendelian Inheritance in Man and its online version, OMIM. *Am. J. Hum. Genet.* 80 (4): 588–604.

76 Armit, C., Richardson, L., Venkataraman, S. et al. (2017). eMouseAtlas: an atlas-based resource for understanding mammalian embryogenesis. *Dev. Biol.* 423 (1): 1–11.

77 Armit, C., Richardson, L., Hill, B. et al. (2015). eMouseAtlas informatics: embryo atlas and gene expression database. *Mamm. Genome* 26 (9–10): 431–440.

Vet-ebooks.com

78 Richardson, L., Graham, L., Moss, J. et al. (2015). Developing the eHistology Atlas. *Database* 2015: bav105.
79 Graham, E., Moss, J., Burton, N. et al. (2015). The atlas of mouse development eHistology resource. *Development* 142 (14): 2545.
80 Stevenson, P., Richardson, L., Venkataraman, S. et al. (2011). The BioMart interface to the eMouseAtlas gene expression database EMAGE. *Database* 2011: bar029.
81 Armit, C., Venkataraman, S., Richardson, L. et al. (2012). eMouseAtlas, EMAGE, and the spatial dimension of the transcriptome. *Mamm. Genome* 23 (9–10): 514–524.
82 Kaufman, M.H. (1992). *The Atlas of Mouse Development*. London: Academic Press.

Vet-ebooks.com

3

Mouse Genetic Nomenclature: The Underpinning of Mouse Genetics

John P. Sundberg, Dale A. Begley, Melissa L. Berry, Michelle N. Perry, David Shaw, and Paul N. Schofield

Introduction

Pathologists are meticulous about the accurate use of nomenclature when making a diagnosis, even though there are often numerous synonyms for the disease under investigation. Debates about the specificity of diagnostic terms and the consequences, particularly for genetics, of differences in nosological preferences, can be critical in coming to an understanding of disease etiology and prognosis. For example, differences in "lumping" and "splitting" diagnoses [1] can make the difference between discovering and missing a Genome Wide Association Study (GWAS) signal [2]. In spite of this, few pathologists and researchers are as careful about the accurate use of mouse genetic nomenclature, yet this is as important to the description of a novel mouse model for a human disease as the pathologic description of the lesions.

Systematic genetic nomenclature expresses, in a succinct and precise way, the background of the strain under investigation, the presence of complex sequence variants of many types, and the genetic relationship of one strain to another. Understanding the fundamentals of genetic terminology is a key skill needed to design and interpret experiments using laboratory mice, and a critical part of reporting and sharing results and resources. This has a huge impact on reproducibility as well as accuracy of interpretation, and is a very important part of making data FAIR (https://en.wikipedia.org/wiki/FAIR_data) as it uses community agreed norms for the exchange and interpretation of information [3].

This chapter provides an overview of the various types of mouse strains (inbred, recombinant inbred, congenic, consomic, hybrid, and others [Table 3.1]), outbred stocks, and mutations (spontaneous or engineered) and how their symbols reflect what they are and how they were made. Methods for creating genetically engineered mice are numerous and rapidly changing [4], so they will not be covered here other than in providing information on the currently used genetic designations for the mice created.

Why Use Standardized Nomenclature?

Even before the days of easy access to computers and search algorithms, words were created to reflect specific things. In medicine, for example Latin was adopted in Europe as a language commonly understood in many countries with their own languages and with defined, agreed meanings – a *lingua franca*. In so doing, clinicians could communicate reliably with each other through time and across locations. The same is true for mouse genetic nomenclature (Table 3.2). This has become more important when exchanging and aggregating information between international databases to access, analyze, and distribute data. Searches can only be accurately completed when words, or gene and protein symbols, are written correctly and have semantic consistency. Some databases, such as that of the Sanger Mouse Genomes Project (http://www.sanger.ac.uk/sanger/Mouse_SnpViewer), will only work if the correct current gene symbol is entered. If your search returns "The gene you selected is not in the database," it may mean that you entered the wrong symbol or the name/symbol has been changed and is no longer in use. For example, if you search for *p53* in this database, it returns the response above as the correct current term is *Trp53* (Figure 3.1).

The Mouse Genome Informatics Database (MGI, www.informatics.jax.org), fortunately, associates synonyms, the unofficial symbols used in publications, with their official nomenclature. Therefore, a search for the commonly used symbol for the gene mutated in publications can be used to find the currently used correct gene and allele symbol. Figure 3.2 illustrates how this can be used to identify the correct allele for *Cdx2* in a paper.

International committees were organized to standardize genetic nomenclature for rodents (http://www.informatics.jax.org/mgihome/nomen/short_gene.shtml), humans (https://www.genenames.org/about/guidelines/#!/#tocAnchor-1-29), and other species. The MGI database provides detailed information on this subject for mice (http://www.

Pathology of Genetically Engineered and Other Mutant Mice, First Edition. Edited by John P. Sundberg, Peter Vogel, and Jerrold M. Ward.
© 2022 John Wiley & Sons, Inc. Published 2022 by John Wiley & Sons, Inc.

Vet-ebooks.com

Table 3.1 Types of mouse strains.

Inbred mice: 20 generations of brother X sister matings using mice of disparate or even unknown backgrounds
F1 hybrid mice: Progeny of two inbred strains
F2 hybrid mice: Progeny of a female and male of the same F1 hybrid lineage
Recombinant inbred (RI) mice: 20 generations of brother X sister matings from parents of different inbred strains
Recombinant congenic mice: Two inbred strains are crossed followed by several backcrosses to one of the parental strains. The resulting mice are then inbred without selection
Collaborative Cross (CC) mice: Modified RI lines using parents from 8 genetically diverse inbred strains
Congenic mice: Moving a defined genetic interval from one inbred strain to another inbred strain
Consomic mice: A strain in which one intact chromosome from the donor strain is transferred to a host strain (one line is created for each chromosome)
Conplastic mice: Backcrossing the nuclear genome from one inbred strain into the cytoplasm of another inbred strain (mitochondrial parent is always the female parent during the backcross)

Table 3.2 Standardized nomenclature.

Advantages
Provides a unique identifier
Standardizes spelling for accurate retrieval
Conveys the maker and technology used to create mutations and strains
Can communicate detailed genetic background information
Disadvantages
Sometimes complex
Sometimes incomplete information
Uses
Publications (most journals require use of official standardized symbols)
Accurate ordering (to make sure that you get what you think you really ordered!)
Correct breeding (facilities management)
Maintain master pedigree and records

informatics.jax.org/mgihome/nomen/index.shtml) and The Jackson Laboratory also offers a quick guide to nomenclature (https://www.jax.org/jax-mice-and-services/customer-support/technical-support/genetics-and-nomenclature). This system has been in use and evolving for over 80 years [5]. One goal of these committees is to provide concise, precise, and unique gene symbols and names (Figure 3.3). Mouse genetic nomenclature continues to evolve to accommodate the ever-increasing complexity of functional genomics as well as the genetically engineered mice created, reflecting the biotechnology that made these advances possible.

In the early development of the Mouse Genome Database and MGI (see Chapter 2), italics and Greek letters could not always be used online and be retrieved by different computers, browsers, or software versions. Thus, in many databases, gene symbols are not italicized, and Greek letters are replaced by the modern English alphabet. Periods and commas could not always be visualized on computer screens so commas were replaced by semi-colons, a critical problem when dealing with congenic strains, as discussed below. Gene names and symbols also changed over time to reflect new discoveries and to more accurately place them in molecular pathways or with genes of similar structure and function. In spite of all of this, MGI constantly maintains the most up-to-date nomenclature that can be searched using all previously assigned or published symbols (Figure 3.2). It is important to look for and use the most current symbol as, over time, the same symbol may have been used by different laboratories for many different genes. For example, *p38* currently is the synonym for 13 different genes on 10 different chromosomes (Figure 3.3).

Standardized strain names inform readers of the specific strain type (inbred, hybrid, outbred, etc.), genetic background, source (vendor or research laboratory), and the mutation(s) carried by the mice used in a study. This information is critical for accurate reporting and scientific reproducibility. But where to start and how to understand and use this information? This chapter will discuss basic mouse genetics as it relates to the nomenclature used at the time of writing.

Inbred Mice

Inbreeding is well known to concentrate deleterious mutations. Most commonly inbreeding depression is due to the creation of homozygous recessive pathogenic or maladaptive genotypes but also loss of the fitness advantage of heterozygosity due to overdominance.

Most people are familiar with the "Royal disease," hemophilia B, that affected males of European royalty (https://www.sciencemag.org/news/2009/10/case-closed-famous-royals-suffered-hemophilia#:~:text=Now%2C%20new%20DNA%20analysis%20on,subtype%20known%20as%20hemophilia%20B.&text=Such%20was%20the%20case%20with,heir%20to%20the%20Russian%20throne). The same thing happens with laboratory mice. However, with a uniform genetic background combined with strict environmental controls and pathogen free status it is possible to minimize variables to test very specific parameters in a statistically efficient way. It is easier to identify a genetic component to a trait when the population under investigation is effectively one of 150 identical twins rather than 150 unrelated individuals. This comes at a cost (Table 3.3); many lines are lost during inbreeding as they can be hard to maintain due to poor breeding efficiency and impacted by strain-specific genetic diseases, all of which lead to increased expense compared to use of outbred mice. For example, the commonly

Vet-ebooks.com

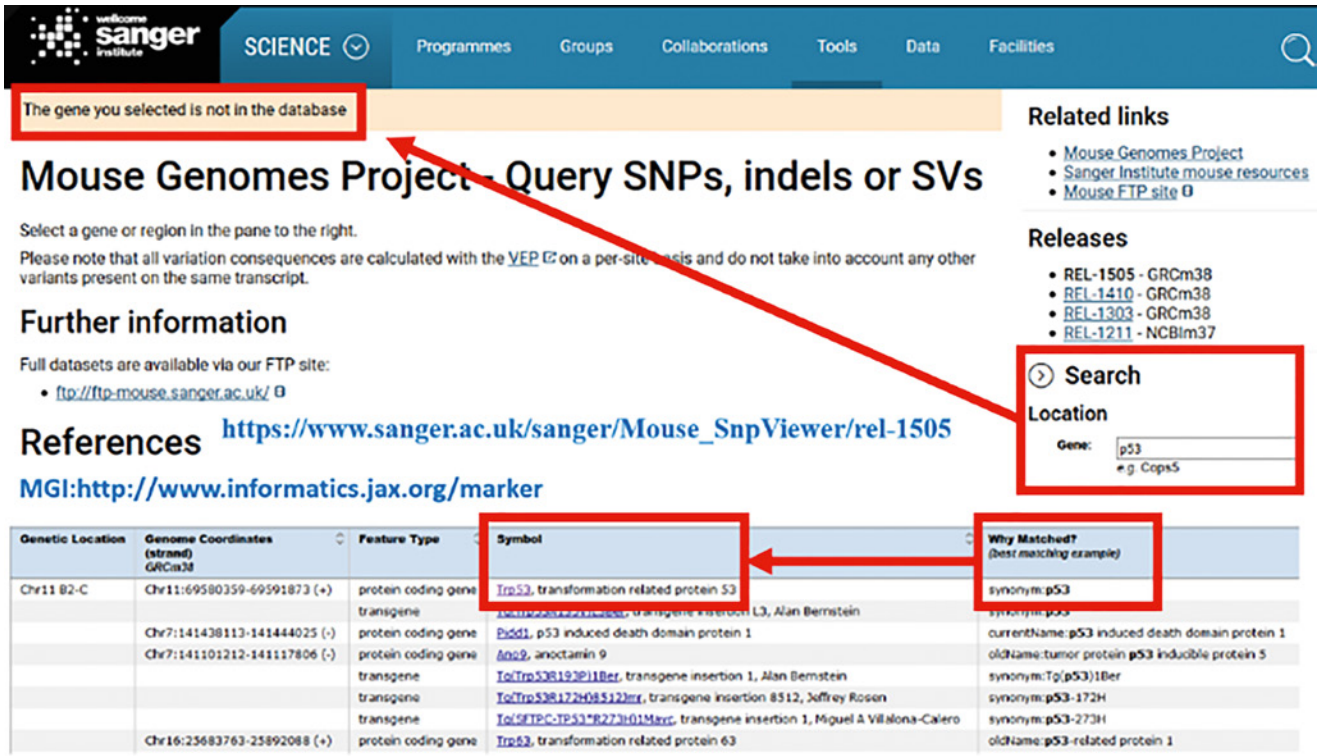


Figure 3.1 **Top, searching *p53* SNPs reveals "The gene you selected is not in the database."** An MGI search (bottom) reveals the current, correct symbol is *Trp53* which does yield data in the Sanger database. Source: Wellcome Sanger Institute.

used C3H/HeJ inbred strain has a short breeding time (around five months of age) due to the females having a high frequency of ovarian cysts and tumors [6]. There are, however, some advantages of specifically outbred populations such as the Collaborative Cross discussed below.

Inbred strains are developed by first mating a female (note that in mouse genetics, the female information is usually listed first) and male of disparate or even unknown backgrounds. From their progeny, one breeding pair is selected for breeding, and again one breeding pair is selected from their offspring. This is repeated for 20 generations (written F20 for filial generation 20) at which point the genome is mathematically about 99% homogeneous at all loci. At this point, the mice produced are considered to be an incipient inbred strain, and at F60, a fully inbred strain. In the process, many sublines will not reproduce, produce nonviable progeny, or develop other phenotypic problems making them difficult to maintain.

The first inbred strain, the DBA, was begun in 1909 by C.C. Little, the founder of The Jackson Laboratory (http://www.informatics.jax.org/morsebook/chapters/russell.shtml). These mice were produced by crosses with a stock of mice that carried three different coat colors, dilute (*d*), brown (*b*), and non-agouti (*a*), the letters of which designated the genes for these different colors [7]. This provides insight into the inbred strain names. The names are always in capital letters and not italicized and can represent coat color (C57BL where BL stands for black), origin of the strain or the person who created it (SJL: Swiss, Jim Lambert), or the phenotype (NOD: non-obese diabetic or NON: non-obese non-diabetic). The line numbers were designated by the creator of the line. For example, C.C. Little mated female 57 and female 58 to male 52 (line C descended from Lathrop's stock) resulting in the C57 and C58 lines (http://www.informatics.jax.org/morsebook/chapters/russell.shtml). A laboratory (lab) code is a 1–5 letters long symbol representing an investigator or institution that is registered with the Institute for Laboratory Animal Research (ILAR). Lab codes are assigned to alleles and strains to designate who made them (Table 3.4).

While the full-inbred strain designation is important, many of the most commonly used inbred strain names have been assigned official abbreviations (Figure 3.4), to incorporate in derivative strains as described below. Many investigators use abbreviations, often incorrectly, in their publications. Some of the most common mistakes are to use B for BALB/cJ (correct is C) or B6 for any undefined C57BL substrain. Thus, it is often best for investigators to use official strain designations in the methods section of a publication.

Hybrid Mice (F1 and F2)

A cross of two unrelated inbred mice (for example, A/J × BALB/cByJ) produces pups that are all identically 50% maternal genome and 50% paternal genome with no

Vet-ebooks.com

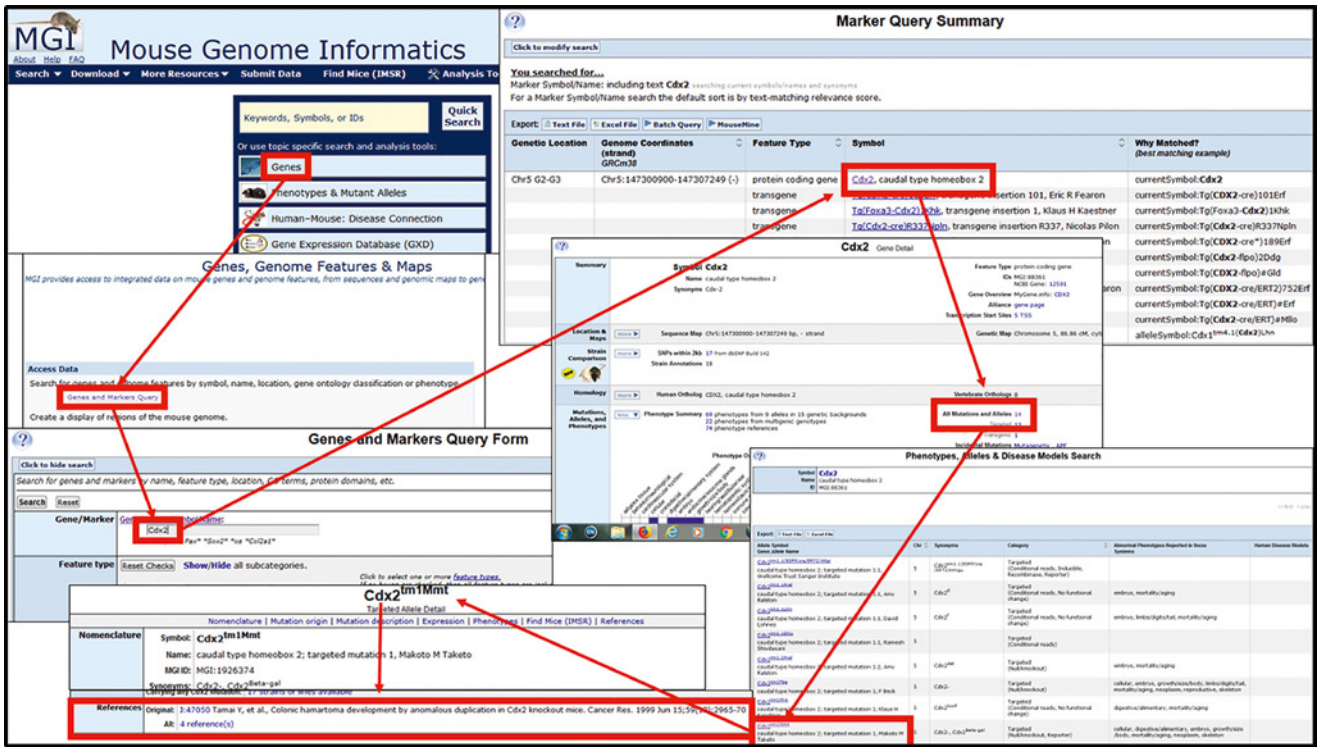


Figure 3.2 **Finding the gene and allele symbol on Mouse Genome Informatics.** One of the chapter authors inquired about how to find the correct allele symbol to use relative to a specific reference (Source: Tamai Y, Nakajima R, Ishikawa T, Takaku K, Seldin MF, **Taketo MM**. Colonic hamartoma development by anomalous duplication in *Cdx2* knockout mice. Cancer Res. 1999 Jun 15;59(12):2965-70). Go to the Mouse Genome Informatics home page (http://www.informatics.jax.org/) and select "Gene." The link goes to "Genes, Genome Features & Maps." Then select "Genes and Marker Query." In the Gene/Marker query box, enter the gene symbol or mutant mouse name, in this case *Cdx2* was entered. Note, while gene symbols should be in italics no italics are given on this website or many other websites. This will give you all the genes for which this is part of the symbol or where *Cdx2* was used as a synonym at some point in time. Selecting *Cdx2* will yield the "Gene Detail" page. In the lower right area is the link to find all 14 of the currently reported allelic mutations (as of 1 May 2020) or the number of specific types of mutations. By selecting "All Mutations and Alleles" a summary field will appear. But which one is correct? By looking at the **last author on the reference** it is obvious from the summary. This is confirmed by selecting "*Cdx2*^{tm1Mmt}" to reveal the data sheet on this specific allelic mutation. At the bottom of the field is the reference that is the original reference provided. Source: The Jackson Laboratory.

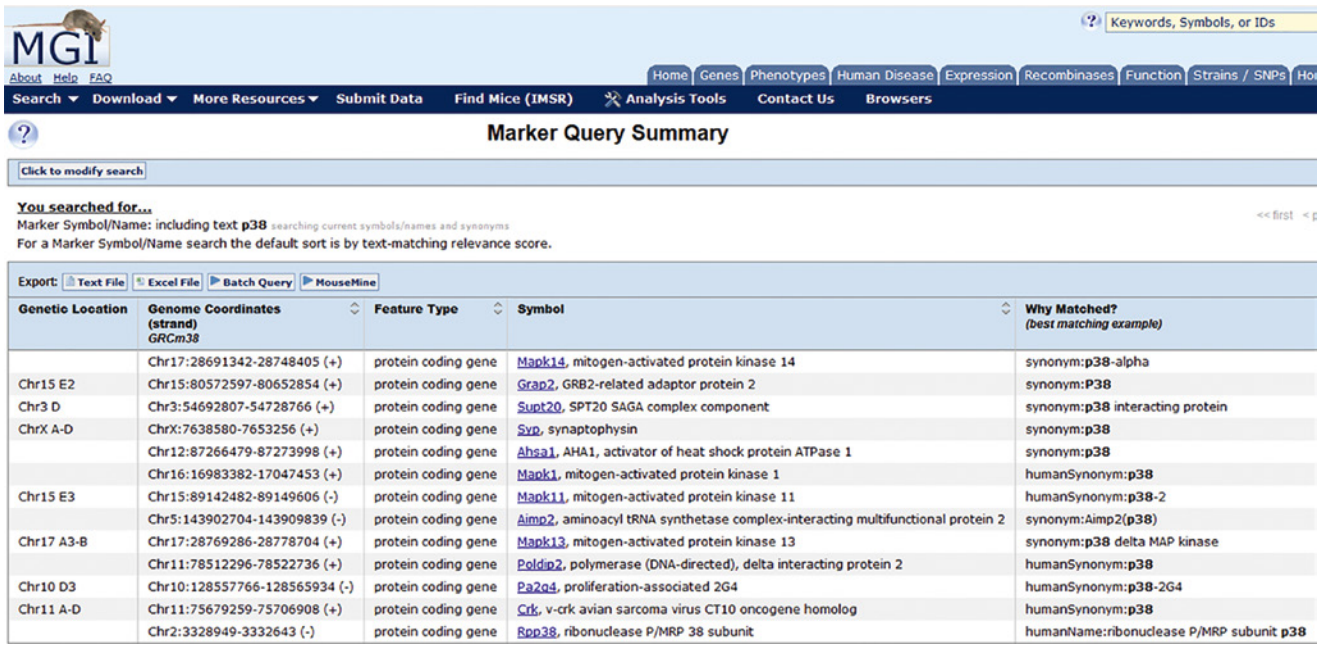


Figure 3.3 **Current symbols assigned to a variety of unrelated genes originally published as *p38*.** If one searches for the gene symbol *p38* the results indicate numerous genes on different chromosomes that at one time were all called *p38*. The new names not only separate out the different genes but also reflect to a degree what is currently known about the gene function. By following the links you can obtain much more detail on each gene, the number and details on allelic mutations, and links to the original and many subsequent publications on the topic (MGI accessed 22 April 2020).

Vet-ebooks.com

Table 3.3 Inbred strains of mice.

Advantages
Genetic and phenotypic uniformity (smaller numbers needed)
Well characterized (pathology and physiology)
For most standard inbred strains >200 generations
Ideal controls (both biological and sequencing)
Permits clear genetic mapping
Enables identification of modifier genes
Disadvantages
Not as robust (smaller, lower reproductive performance [fecundity], shorter lifespan)
Strain-specific characteristics (deleterious mutations causing strain specific diseases)
Expensive (when difficult to maintain)
Uses
Widely used in all types of research
Models for human disease
Background for mice with spontaneous and induced mutations

Table 3.4 Inbred strain nomenclature.

C57BL/6J or C57BL/10J
C57BL is the parental strain name (since C57BL/6J is the actual strain name)
6 or **10** indicate the substrain line number (C57BL/10J are prone to serious heart disease not seen in C57BL/6J) [8]
J indicates the breeder (The Jackson Laboratory) of these substrains
C3H/HeJ or C3H/HeN
C3H is the strain generated by Strong from a cross of Bagg albino with DBA
He is the substrain from the W.E. Heston laboratory at the National Cancer Institute
J indicates the subline received from Heston then bred by The Jackson Laboratory
N indicates the substrain bred at the National Institutes of Health

An inbred strain is designated in capital letters.
A substrain is identified using a forward slash (/) after the strain name followed by a lab code of the strain breeder.
Further substrains derived from the founder add to the end of the lab code of subsequent breeders without another forward slash.
Note that C3H/HeJ has a mutation in the *Tlr4* gene making it highly susceptible to gram negative bacterial infection while the C3H/HeN substrain is wildtype for *Tlr4*.

A/J x BALB/cByJ
↓
(A/J x BALB/cByJ)F1 or ACByJF1

ACByJF1 x ACByJF1
↓
ACByJF2

A = A/J abbreviation, female first.
CByJ = BALB/cByJ abbreviation, male second.
F1 or F2 = 1st or 2nd filial generation.

Figure 3.4 Nomenclature for hybrid stocks.

Table 3.5 Examples of inbred strain abbreviations.

129P3/J = 129P3
129S1/SvImJ = 129S1
A/HeJ = AHe
A/J = A
AKR/J = AK
BALB/cByJ = CByJ
BALB/cJ = C
C57BL = B
C57BL/6J = B6
C57BL/6JEi = B6Ei
C57BL/6NJ = B6NJ
C57BL/10J = B10
C57BR/cdJ = BR
C57L = L
CBA/CaJ = CBACa
CBA/J = CBA
C3H/HeJ = C3
C3HeB/FeJ = C3Fe
DBA/1J = D1
DBA/2J = D2
NZB/BINJ = NZB
NZW/LacJ = NZW
RIIIS/J = R3
SJL/J = SJL or J
SWR/J = SW

recombination between any of the chromosomes. This is called the first filial or F1 hybrid generation and is named by putting the maternal then paternal parental strain names in parentheses separated by a lower case x, to represent cross, and followed by F1, (A/J x BALB/cByJ)F1 (Figure 3.4). This can be abbreviated using the strain abbreviations (Table 3.5) and dropping the parentheses and x, ACByJF1 in this case (Figure 3.4). Aside from spontaneous mutations arising in that single generation, all pups from all litters of such a cross should be genetically identical and have hybrid vigor, which is increased fecundity and overall health resulting, in part, from the loss of homozygosity of detrimental recessive alleles. Additionally, F1 hybrid mice can generally accept tissue transplants from either parent (Table 3.6). Unlike inbred

Vet-ebooks.com

Table 3.6 F1 and F2 hybrid mice.

F1 hybrids	F2 hybrids
Advantages	*Advantages*
Genetic and phenotypic uniformity	Hybrid vigor
Contains a 50 : 50 mix of both parental strains	F2 hybrids do not have 50 : 50 mix but do have some mice in the population homozygous for some alleles and are valuable as a population for mutant gene mapping
Hybrid vigor	
Accepts transplants of tissue from mice of either parental strain	
Disadvantage	*Disadvantages*
Not self-perpetuating	Not self-perpetuating
	Genotype and phenotype NOT uniform
	Parental strains most likely reject tissue transplants
Uses	*Use*
Radiation research	Control for many targeted ("knockout") mutations on a mixed B6; 129
Behavioral research	
Bioassays of nutrients, drugs, pathogens, or hormones	
Transplant recipients	
Background for transgenics and some deleterious mutations	

strains, F1 hybrid mice are not self-perpetuating because at meiosis each germ cell will have a unique set of recombinations between each of the two parental chromosomes, except for the sex chromosomes outside of the pseudoautosomal region.

Sibling breeding F1 hybrid mice for one generation produces an F2 hybrid population (Figure 3.4), and continued inbreeding after that eventually leads to the creation of recombinant inbred strains (see below). The F2 hybrid population also has hybrid vigor, but is distinct from the F1 hybrid population because meiosis has resulted in recombinations between the parental chromosomes such that there may be some homozygosity in a minority of the segregating alleles. This makes an F2 hybrid population a tremendous tool for mapping, especially for mapping recessive mutations. For example, if an interesting phenotype is observed in an inbred strain, such as an abnormal hair coat, hair interior defect (*hid*) in all AKR/J mice, these animals can be crossed with another inbred strain, such as BALB/cByJ, that has normal hair (Figure 3.5). As *hid* in this example is an autosomal recessive mutation, the obligate heterozygous F1 progeny of this cross will all have a normal hair coat. When these heterozygous progeny are intercrossed to create F2 hybrids, 25% of these mice are expected to have the abnormal hair phenotype. The genetic interval carrying the mutant sequence derives from AKR/J so by screening the DNA from the mutant and unaffected mice in the population with molecular markers distributed evenly across all chromosomes, a pattern emerges in which markers specific to AKR/J and not BALB/cByJ skew to increased homozygosity in the region of the genome specific to the mutation. Usually this works relatively quickly to identify the region in which the mutated gene is located. However, in this particular case, less than 15% of the F2 mice were affected (Table 3.7) due to modifier genes in BALB/cByJ. Similar crosses with other strains resulted in the expected 25% distribution. This illustrates two points, the deviation from Mendelian expectation due to modifiers and the value of doing mapping crosses with different inbred strains, which in this instance identified different genetic intervals that together reduced the interval and the number of candidate genes (Figure 3.6) [9, 10].

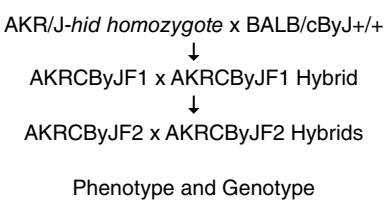


Figure 3.5 Setting up a mapping cross using F1 and F2 hybrids.

Backcrossing an F1 hybrid to one of the parents, instead of sibling intercrossing, is the initial process in the creation of a congenic, consomic, or conplastic strain, and such an N2 population is a useful tool for mapping dominant mutations. Some mutations or transgenes are adequately deleterious to overall health that they cannot be maintained on an inbred background and instead require hybrid vigor. Such mutants are maintained by breeding to an F1 hybrid at each generation or through outcross–intercross to an F1 hybrid. One complicated example of this is B6EiC3Sn *a*/*A*-Ts(17^{16})65Dn/J [11]. This chromosomal aberration was induced in DBA/2J inbred mice, but is detrimental to health and causes male sterility so in order to successfully maintain a colony a female carrier is bred to a (C57BL/6JEiJ x C3H/HeSnJ)F1/J male at each generation. There is no punctuation in the genetic background of the strain name, B6EiC3Sn, and the presence of the DBA/2J contribution is omitted from the nomenclature for simplicity and must be found in sources outside of the strain nomenclature.

Vet-ebooks.com

Table 3.7 Breeding data used to identify the gene responsible for the hair interior defect phenotype.

AKR/J-*hid** homozygote crossed with	Total progeny	Normal mice	Affected mice	Affected (%)	X^2	*p*-Value
BALB/cByJ	260	222	38	**14.62**	5.92	0.025–0.010
C57BL/6J	430	330	100	23.26	0.220	0.500–0.750
CAST/EiJ	339	255	84	24.78	0.003	>0.900
C3H/HeJ	248	191	57	22.98	0.170	0.500–0.750
FVB/NJ	272	205	67	24.63	0.006	>0.900
Total F2 mice	1549	1203	346			

* AKR/J-*hid* was the original designation until the gene responsible was identified. Because the gene was identified with a different phenotype earlier, the allele is officially *Soat1*^{ald} not *Soat1*^{hid}.

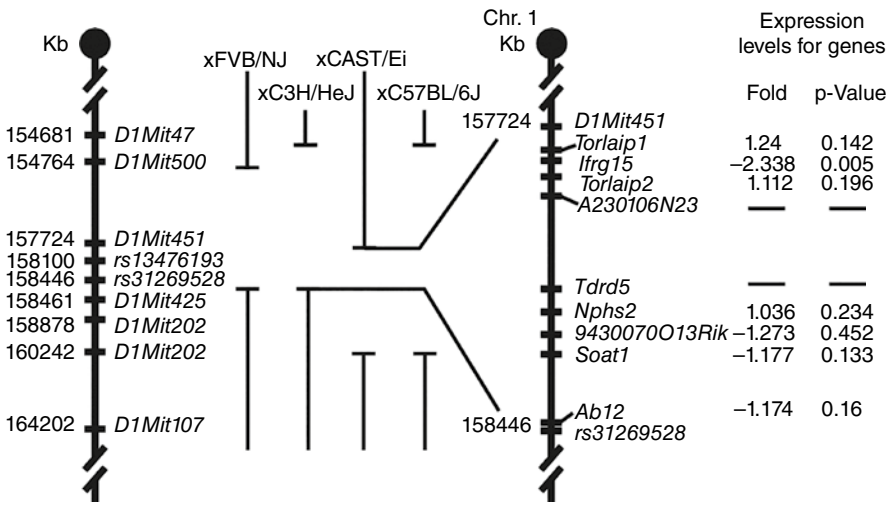


Figure 3.6 Crossing AKR/J mice with more than one inbred strain to map the mutant gene locus. By using the shortest interval between different crosses, the list of candidate genes could be reduced. Sequencing then only had to be done on a few genes to identify the mutant gene responsible for the hair interior defect phenotype. Sources: Based on Giehl KA et al. [9].

Some mutations are maintained on a background in which the genetic contributions of two inbred strains are segregating. The retarded hair growth (in ornithine aminotransferase, *Oat*^{rhg}) mutation arose spontaneously in AKR/J and was later outcrossed to C57BL/6JEi and subsequently maintained by sibling intercrossing [12, 13]. Thus, the genetic background consists of contributions from both AKR/J and C57BL/6JEi segregating at each generation. A semicolon between the strain abbreviations is used to represent this situation, B6Ei;AKR-*Oat*^{rhg}/J. If more than two inbred strains contribute to the genetic background of a strain, then it is simply called a stock, such as STOCK *Noto*^{tc}/J (notochord homeobox gene, truncate mutation). The truncate mutation arose spontaneously in the F4 generation of a cross between a C3H female and a Swiss outbred male. It was subsequently bred to BALB/cHu and again to C3H before being inbred for more than 80 generations [14]. The STOCK is in capital letters designating inbred, and there is no hyphen between STOCK and the allele symbol. The strain could have been assigned a unique inbred strain name, such as TC/J, but was instead designated as a STOCK. When stock is in lower case, it indicates that the segregating population has not reached F20.

Recombinant Inbred (RI) and Recombinant Congenic Mice

One variation of inbred mice is the creation of recombinant inbred (RI) mice. In this case, two different inbred strains are crossed to produce F1 progeny. As with creating inbred strains, breeding pairs of these F1 progeny are crossed to create an F2 population and then one pair is selected for breeding in this and each subsequent generation until at 20 consecutive generations of breeding (F20) from a single brother–sister pair a new inbred strain is created, which has approximately 50% of its DNA derived from each of the original parental inbred strains. The generation of many separate recombinant inbred strains from the same parental inbred strains creates a panel of recombinant inbred stains, each of which has an array of unique DNA recombinations and therefore unique subset of parental DNA segments. Recombinant inbred strains are named with a pair of 1- or 2-letter strain abbreviation codes representing the original parental inbred strains (Figure 3.3) with the female founder strain first, followed by an X for the cross, then the male founder strain abbreviation followed by a slash, a number to indicate the specific line and then the laboratory code for

Vet-ebooks.com

Table 3.8 Recombinant inbred and recombinant congenic strain designation.

BXD31/TyJ	AcB51/Prgs
B = C57BL/6J	**A** = backcross to A/J
X = cross	**c** = recombinant congenic cross
D = DBA/2J	**B** = C57BL/6J
31 = RI line number	**51** = recombinant congenic line number
Ty = Lab that created the line (Benjamin Taylor)	**Prgs** = Lab that created the line (Philippe Gros)
J = Subsequent breeder of the strain, The Jackson Laboratory	

who made the strain (Table 3.8). The higher the number of strains in a recombinant inbred panel, the potentially more valuable the collection due to the increased number of recombination sites available for comparison across the panel.

The Jackson Laboratory Repository distributes more than 125 BXD RI lines and there are many more in private laboratories. Many of these BXD RI lines have been sequenced and annotated. Using websites, such as GeneNetwork (www.genenetwork.org) [15], it is possible to use these mice for localizing, if not necessarily identifying, the gene(s) responsible for a disease, response to a treatment, or for any phenotype observed in one of the parental strains but not the other. For example, if the primary gene responsible for a disease in DBA/2J mice is known, such as a hypomorphic allele of *Abcc6* that causes pseudoxanthoma elasticum, and the gene is wildtype in C57BL/6J, by first identifying all the BXD lines that are homozygous for the D2 mutant allele, one can then select only those mice, phenotype them, and rapidly identify narrow genetic intervals from which to generate a small list of candidate disease modifier genes [16] (Figure 3.7). Other RI lines exist for a variety of crosses that can be used in a similar manner.

A variation on the RI line is the recombinant congenic strains that are created by crossing two inbred strains followed by one or several backcrosses to one of the parental strains. The resulting mice are then inbred without selection. Recombinant congenic strains are also named using 1- or 2-letter strain abbreviation codes representing the parental strains, but a lower case c for congenic, not an X, separates them and the first strain listed is the host strain, that to which the backcrossing is done, and the strain symbol following the c is the donor strain, that contributing the least amount to the total genetic background. The AcB51/Pgrs recombinant congenic strain was generated by Dr. Philippe Gros by backcrossing (A/J x C57BL/6J)F1 to A/J for two consecutive generations then sibling inbreeding to generate a panel of recombinant consomics including this, line 51.

Collaborative Cross (CC) Mice

Another variation of RI lines is the Collaborative Cross. This is a complex set of crosses using eight different inbred strains that represent a great deal of genetic diversity [17, 18]. The goal was to create over 1000 new inbred strains. Due to reproductive failure and low viability of many strains, the current goal is to create 200 strains. These mice present with great phenotypic variability, a reflection of the great genetic diversity. These can be used to screen for specific phenotypes [19, 20]. When a large enough cohort are examined, phenotyped, and genotyped using the Mouse Universal Genotyping Array (Single Nucleotide Polymorphism [SNP] Array), it is possible to identify candidate gene regions and even the gene(s) responsible for the phenotype [21].

Collaborative Cross mice are designated by CC for Collaborative Cross, the line number, forward slash, and the lab that created it followed by the laboratory that currently maintains it. For example, CC001/UncJ (stock number 021238) is line number one, generated at the University of North Carolina, and currently maintained and distributed by The Jackson Laboratory.

Congenic Mice

When a genetic mutation arises spontaneously or is created in a specific mouse strain and the investigator wants to characterize it on another inbred strain, this can be accomplished by a modification of inbreeding to create what is called a congenic strain (Table 3.9). For example, if you have an albino (white) strain carrying a single gene mutation, specifically a recessive mutation such as hairless on the HRS/J inbred strain (donor strain), and want to move it onto a predominantly C57BL/6J background (host strain), one parent from each strain is mated together to create F1 hybrids (see below). These F1 progeny are intercrossed to create F2 mice, ideally but not always 25% of which will be homozygous for the recessive hairless mutant allele. Only the mutant mice are then crossed back (backcrossed) to C57BL/6J mice to produce the N2 generation. This is repeated 10 times (N10) to create a fully congenic mouse strain [22, 23], with congenic nomenclature permitted to be used at N5. At N10, the strain will be mathematically >99% host background. Unfortunately, there will always be some of the parental strain DNA flanking the gene selected for, known as the congenic interval, and the possibility of trace amounts of donor sequence elsewhere in the genome. The more backcrosses to B6, the smaller this congenic interval should become and the lower the likelihood of traces of donor sequence but the genetic background will never entirely become B6. Creating a group of congenic strains on the same host background controls for phenotypic variability caused by genetic background in comparative or combinatorial assessments of mutation-induced phenotypes.

This description is only true for recessive mutations that cannot be genotyped and even in those instances, a handful

Vet-ebooks.com

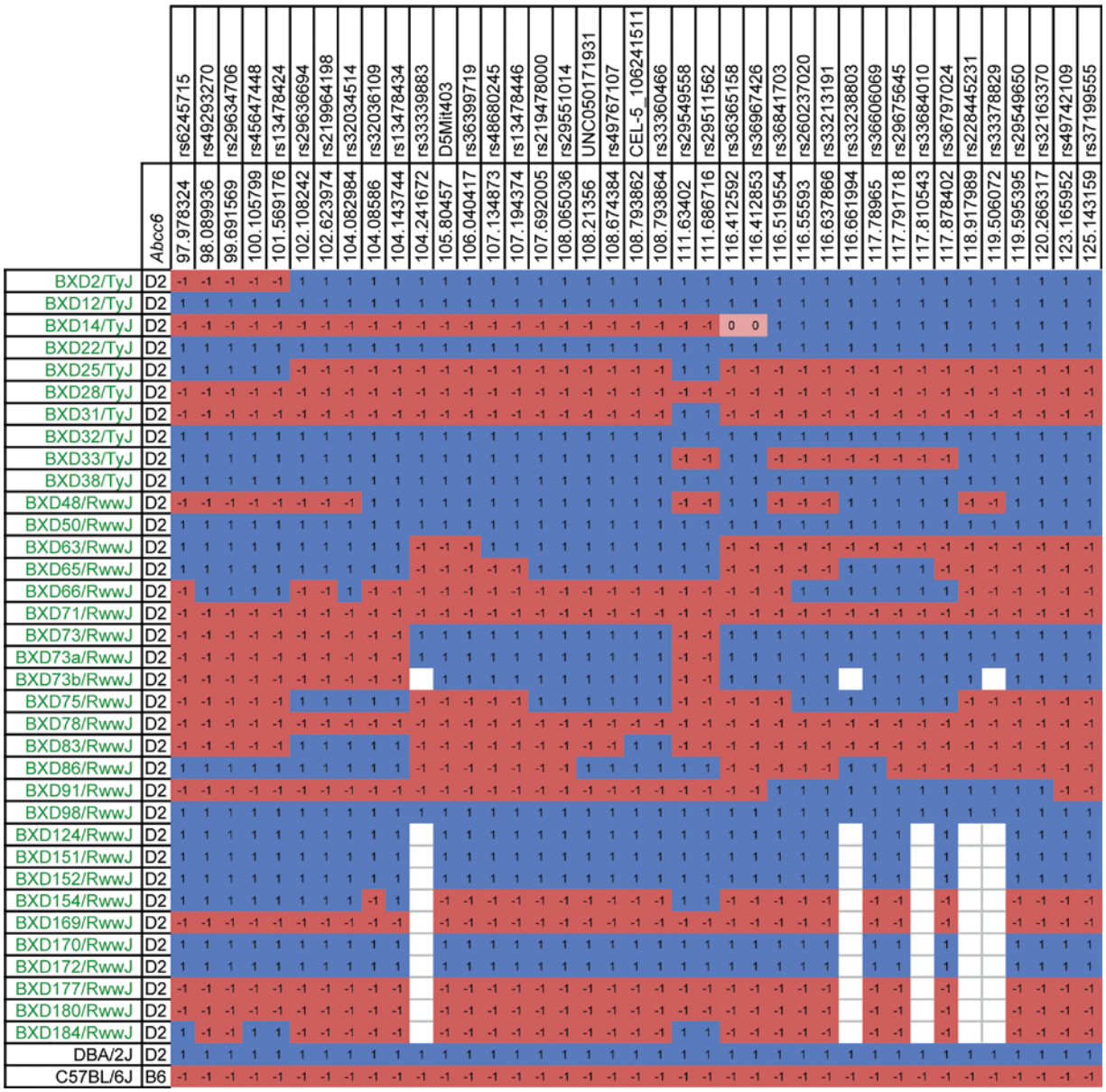


Figure 3.7 **Using recombinant inbred lines to narrow candidate gene intervals using WWW.GeneNetwork.org** The BXD lines on the left are all homozygous for the hypomorphic *Abcc6* allele from DBA/2J. One quantitative trait locus interval has a mixture of DBA/2J (blue) and C57BL/6J (red) DNA. By phenotyping the mice, it is possible to narrow the interval to identify the modifier gene. Source: Generated by Dr. Jason Bubier 4 May 2020; WWW.GeneNetwork.org.

of researchers might go straight to N2 before the intercross, especially if it is a homozygote that cannot be used to breed. Dominant mutations or alleles that can be genotyped do not require the intercross step so can be repeatedly backcrossed at each generation.

Nomenclature for congenic strains begins with a standard abbreviation for the host strain (Table 3.4), followed by a period (.) to indicate congenicity, then the standard abbreviation for the donor strain, then a hyphen, then the allele(s) or congenic interval transferred, then a forward slash (/), and then laboratory code of the investigator in whose laboratory the congenic was completed. For example, a mutation in the sodium channel, voltage-gated, type VIII, alpha gene (*Scn8a*^{8J}) was induced using *N*-ethyl-*N*-nitrosourea (ENU) in the C57BL/6J background and was backcrossed onto C3HeB/FeJ in the laboratory of Dr. Wayne Frankel so the strain name is C3Fe.B6-*Scn8a*^{8J}/Frk [24]. In the strain B6.C3-*Pde6b*^{rd1} *Hps4*^{le}/J both the phosphodiesterase 6B, cGMP, rod receptor, β-polypeptide retinal degeneration one allele (*Pde6b*^{rd1}) and HPS4, biogenesis of lysosomal organelles complex 3 subunit 2 light-ear allele (*Hps4*^{le}) were transferred in a single congenic interval from Chromosome

Vet-ebooks.com

Table 3.9 Congenic strains.

Advantages
Genetic and phenotypic uniformity
Reduce experimental variability
Can transfer most mutations onto a different genetic background
Allows examination of modifier genes
Can maintain mutation or transgene homozygously and use inbred as control
Disadvantages
Generation time (two to three years to N10 or longer if ovarian graft to immunodeficient mouse used; can reduce time with speed congenics)
Phenotype may change on different genetic background
Linked genes may confuse experimental findings

5 of a mutant subline of C3H/HeJ onto C57BL/6J. The congenic interval can also be represented not by the allele(s) of interest but by the most proximal and distal markers identified in the donor interval, such as in the strain B6.129S1-(rs13480546-rs13480629)/Kjn [25]. If two alleles of interest from separate genetic origins are combined into one congenic strain or if the precise origins of the donor sequence are not known, then there is no single donor strain that can be put after the period so that complex genomic donor source is represented as "Cg." The Tg(Ins2-rtTA)2Doi transgenic mice were generated by microinjection into (C57BL/6J x SJL/J)F1 hybrid mice then backcrossed onto a NOD host to generate the congenic named NOD.Cg-Tg(Ins2-rtTA)2Doi/Doi [26], in which the Cg is used because it is unknown whether the congenic interval derives from C57BL/6J or SJL/J. If the source of the desired donor sequence does not come from a strain that is a pure inbred, but rather contains contributions from a source different from the host background or the donor congenic interval, then that strain information can be represented in parentheses after the donor strain abbreviation. Thus, if it were known that Tg(Ins2-rtTA)2Doi inserted into C57BL/6J-derived sequence in the original F1 hybrid, and not into SJL/J-derived sequence, then the strain name of the congenic would be NOD.B6(SJL)-Tg(Ins2-rtTA)2Doi/Doi. This allows the reader to see at a glance that there is a possibility that some small amounts of SJL/J-derived sequence exist in the strain. In the example of NOD.129S4(B6)-*Art2a*^{tm1Fkn} *Art2b*^{tm1Fkn}/Lt it is immediately clear that both targeted alleles were generated in 129S4, at least one, if not both, were bred at least once to C57BL/6J, and then both were backcrossed onto NOD, either together or separately then bred together [27]. If there are more than one additional sources of trace contribution to the genetic background, aside from the donor, then Cg is entered into the parentheses to represent this. For example, NOD.129P2(Cg)-*Il10*^{tm1Cgn} *Il4*^{tm1Cgn}/Dvs had C57BL/6J and C57BL/10J in part of the genetic lineage so the potential contributions from those backgrounds are captured in the (Cg) [28]. Another example of a congenic strain in which the donor origin is represented by "Cg" is B6.Cg-*Kitl*^{Sl} *Krt71*^{Ca}/J, a C57BL/6J host congenic for both *Kitl*^{Sl}, which arose in C3H/He, and *Krt71*^{Ca}, which arose in a Swiss stock [29].

As illustrated in the above examples, more than one gene can be selected for in the congenic breeding process, especially if molecular markers are available so that each generation can be screened. The entire process is speeded up if markers for the host strain are identified on all chromosomes and selected for during the inbreeding process, to create what are termed speed congenics.

The advantage of creating congenic strains is that the gene of interest is now on the inbred strain the investigator wants to work with. The disadvantage is that there is always some remaining DNA from the donor strain around the gene that has been moved and potentially elsewhere in the genome. The more the strain is backcrossed to the new strain, the smaller this interval is, but some donor DNA still remains, and may be in small segments of forced heterozygosity not linked to the congenic interval. Endonuclease-mediated technology can be used to replicate the same allele sequence in different inbred strains, which eliminates the problem of flanking donor sequence in the congenic interval and saves years of breeding.

There are also a group of strains generated by the outcross of a coisogenic mutant subline followed by backcrossing to the original inbred strain in order to return to something close the original genetic background. This can occur by error or by necessity, such as when the chimeric founder of a targeted mutation created in an ES cell derived from 129S6/SvEvTac is bred to C57BL/6NTac to select mice with an agouti coat color, indicative of transmission from 129S6. If it is desirable to assess the phenotype of the allele on a 129S6 background, then repeated backcrossing to that original background can produce something similar to a congenic in that it is predominantly 129S6 but may carry traces of C57BL/6NTac sequence even though the interval surrounding the mutation is 129S6. Such a strain would be named 129S6(B6NTac)-*Gene*^{tm1Lab}/Lab with the abbreviation of the predominant strain followed by the abbreviation of the potentially contaminating strain in parentheses. This nomenclature says at a glance that this is not a congenic strain (no period), the allele did not originate in C57BL/6NTac, but rather in 129S6-derived sequence, but that some contribution from C57BL/6NTac may be present in the genome. This nomenclature is only used after five backcross generations. Prior to that the correct strain nomenclature would be 129S6;B6NTac-*Gene*^{tm1Lab}/Lab.

Consomic Mice

Consomic strains have one intact chromosome from the donor strain transferred to a host background through repeated backcrossing, similar to congenic mice, but with careful screening at each generation for a fully intact specific donor chromosome. The strain nomenclature for consomic strains places the donor strain as a superscript to the transferred chromosome. The strain C57BL/6J-Chr 1$^{PWD/Ph}$/Fore

Vet-ebooks.com

had Chromosome 1 from the inbred strain PWD/Ph bred onto a C57BL/6J host background by Dr. Jiri Forejt, whose laboratory code is Fore. A complete set of consomic strains, in which each chromosome from the donor strain is separately transferred to the same host background in a panel of separate strains, provides a unique tool for mapping mutations and modifiers.

These types of mice can be quite valuable when multiple congenic strains are created, each carrying the same single gene mutation. If each strain develops different lesions or different levels of severity of lesions, then one can integrate this type of strain into the analysis. For example, a spontaneous hypomorphic allele of laminin gamma 2 (*Lamc2*^{jeb}) resulted a model for non-Herlitz Junctional Epidermolysis Bullosa, a blistering skin disease. Five congenic strains homozygous for this mutation revealed very different onset and severity of blistering disease and other lesions [30]. By crossing the congenic strains, several quantitative trait loci (QTLs) were identified, one major modifier gene on chromosome 19. By creating B6 and C57BL/6J-Chr 19$^{PWD/Ph}$/ForeJ congenic strains that were both homozygous for *Lamc2*^{jeb} (on Chromosome 1), these mice could be crossed and each time rearrangements only occurred on Chromosome 19, thereby shortening the interval when selecting for disease severity. In so doing, it was possible to reduce the genetic interval to 1 megabase thereby identifying the binding region of *Col17a1* as the major modifier gene [31].

Conplastic Mice

Conplastic strains have been created by backcrossing the nuclear genome from one inbred strain into the cytoplasm of another in which the mitochondrial parent is always the female parent during the backcrossing program. The strain designation is the nuclear genome strain-mt$^{\text{cytoplasmic genome strain}}$. For example, C57BL/6J-mt$^{A/J}$/Na is a strain with the nuclear genome derived from C57BL/6J and the cytoplasmic genome from A/J, which was created by crossing male C57BL/6J mice with A/J females [32]. Their female progeny were repeatedly backcrossed to male C57BL/6J. As with congenic strains, a minimum of 10 backcross generations are required.

Outbred Mice

Wild mouse populations are generally not inbred, and some populations have great genetic diversity between individuals. Exceptions occur when there is severe geographical isolation in which gene diversity is mixed but less so than in large free-ranging populations. The result of outbreeding is various degrees of genetic and therefore phenotypic variability between individuals (Table 3.10). Since human populations, in general, are outbred, properly maintained outbred mouse stocks can, in many ways, be better models for the general human population for identifying population outliers/rare susceptibility in toxicology and other types of studies. One big advantage of outbred stocks is that fecundity, reproductive efficiency, is usually quite high compared to inbred animals. This translates to lower costs to produce large numbers of animals in a short period of time. The major disadvantage is that because of the high phenotypic variability between individuals, large numbers need to be used to generate valid results, and the colony size and breeding schemes necessary to prevent inbreeding are large and more complex. This variability severely limits the ability to do highly refined research to ask very specific genetic and environmental questions about effects on disease or other phenotypes. But if the goal is to look for rare events, such as adverse drug reactions, these types of mice might better reflect the response in humans. This depends, of course, on breadth of alleles in the starting population and the rigor with which the outbred population is maintained. Defined outbred stocks are closed colonies, and inadvertent selection for fecundity, size, or health are selective pressures that reduce the genetic diversity of the population, as is any passage through a genetic bottleneck such as can occur during rederivation.

Table 3.10 Outbred mouse stocks.

Advantages
High genetic and phenotypic variability
Can be more reflective of the general outbred human population
Robust (high fecundity)
Inexpensive
Disadvantages
Large numbers needed for analysis
High variability in results
Uses
Widely used in all types of research
Models for human disease with variability between patients (population outliers)

One of the most commonly used outbred stocks is Crl:CD1 mice from Charles River Laboratories. This and other related "Swiss"-derived stocks originated from seven females and two males were sent from a non-inbred albino stock of Dr. Andre de Coulon at Centre Anticancereux Romand, Lausanne, Switzerland to Clara J. Lynch at Rockefeller University in the United States in 1926. These mice were further developed into the Hauschka Ha/ICR stock, which was initiated in 1948 at the Institute for Cancer Research (ICR) in Philadelphia. In 1959, a colony of mice, then maintained at Roswell Park Memorial Institute, were send to Charles River designated as HaM/ICR (https://www.criver.com/sites/default/files/resources/CD-1IGSMouseModelInformationSheet.pdf). Today on the Charles River website you will find various trade names for different colonies of these mice including CD1-Elite (SOPF) or CD1-Elite Mouse. However, the correct formal nomenclature for the stock is

Vet-ebooks.com

Crl:CD1. While it is commonly used as an outbred stock, the genetic diversity from the small number of albino progenitors used and variability of sublines passed between institutions make this not the best example of an outbred stock.

Fzt:DU provides a better example of an outbred stock [33]. This population was generated by crossing four other outbred stocks and four disparate inbred strains together to produce eight founder populations of 15 litters and then a careful breeding rotation was followed to maximize the allele frequencies in the population.

Various breeding strategies have been reported in the literature for maintaining maximal genetic diversity in an outbred stock and all require a large population with a set rotation of breeding interactions. Random breeding places selective pressures on the population, most notably for a preference of increased fecundity, but has been used in some outbred stocks, and sibling breeding must be avoided. The nomenclature for outbred stocks begins with the laboratory code of the researcher who bred it followed by a colon followed by upper case stock name of two to four letters representing the population. Some outbred populations have been generated around a particular mutation in order to assess that phenotype in a diverse genetic setting. J:NU is an outbred stock bred around the nude (*Foxn1*^{nu}) mutation. Crl:SKH1-*Hr*^{hr} is an outbred stock commonly used for UV light carcinogenesis studies because they have a high frequency for developing aggressive squamous cell carcinomas compared to other inbred strains carrying the hairless mutation [23]. The nomenclature (Crl:SKH1-*Hr*^{hr}) again reflects the breeder (Crl), outbred strain (SKH1), and the specific allelic mutation *Hr*^{hr}.

Diversity Outbred (DO) Mice

While there is genetic diversity in the outbred stocks described above, over time the genetic diversity will decrease without a very large colony maintained by a careful breeding scheme to avoid inbreeding. In addition, because each mouse is unique, there are no relevant control animals or sequenced reference genomes. These factors present significant difficulties in using outbred stocks. To address these issues and further expand genetic diversity, another approach was taken in recent years. As described above, the Collaborative Cross strains were developed using a mix of eight inbred strains that represented the most genetic diversity possible with existing inbred strains at the time. In the process of producing these mice, an alternative approach was developed in which 144 partially inbred Collaborative Cross strains, at generations ranging from F4 to F12, were maintained by randomized outcrossing, to create a novel population of mice, the Diversity Outbred stock, in which each individual mouse had an equal amount of DNA from all the progenitor strains, but all in a unique mix [34]. Each mouse is phenotypically and genetically different from the next and resulting in a huge variation in phenotypes. Large SNP genotyping arrays make it possible to phenotype large numbers of these mice that share the same phenotype and identify the candidate genes that might cause the problem [35–37].

Nomenclature for the Diversity Outbred stocks follows that of outbred stocks, J:DO, where J is the breeder, The Jackson Laboratory in this example, and DO stands for Diversity Outbred.

Nomenclature for Normal and Mutated Genes

Spontaneous mutations, including sequence variants, copy number variants, small indels, and multigenic chromosomal aberrations constantly arise in colonies but at relatively low rates so they are often missed unless a careful screening program is in place to identify them. This is called genetic drift and can be a major problem for large production colonies. There is also the real potential problem of genetic contamination, where strains are inadvertently mixed. To minimize and control these problems, two approaches are used in large production colonies: the Genetic Stability Program (GSP) (*Methods for maintaining genetic stability of inbred animal strains* (https://www.jax.org/jax-mice-and-services/find-and-order-jax-mice/why-jax-mice/patented-genetic-stability-program) US 7592501 [22 September 2009]; SG 119769; CN 200480023858.4 [23 June 2010]; AU [11 November 2010]; US 8110721 [7 February 2012]; JP 5072359 [31 August 2012]; USA 8552254 [8 September 2013]) and a genetic quality control program [37]. GSP essentially resets the genetic drift back to an arbitrary start point every ~5 generations by the use of a large pool of inbred embryos to replace the Founder stock. Genetic quality control programs regularly screen breeders at the top and sample the bottom of the production chain for a variety of molecular markers (SNPs) and phenotypes [38]. Newer methods, built around SNPs, utilize MiniMUGA Genotyping Arrays [38]. Prior to polymerase chain reaction (PCR), a variety of diagnostic screens (enzyme assays) and tail skin grafts were used (https://resources.jax.org/misc/jax-handbook-genetically-standardized-mice).

Spontaneous mutations can be recessive, semi-dominant, or dominant and can be true nulls, hypomorphic alleles, or gain-of-function mutations. Some result from retrovirus integration events, such as the hairless allele (*Hr*^{hr}) discussed above [39]. Radiation and chemical mutagenesis are also used to create mutations in mice without targeting specific genes, although specific phenotypes may be the focus. Genetically engineered mice can be created by transgenesis, recombineering, or nuclease mediated approaches. While many engineered mutations are called knockouts, not all are true nulls so this term has to be used carefully.

Spontaneous Mutations in Mice

Spontaneous mutations have traditionally been named for the readily observable phenotype(s) they initially present. In the pre-genomic era chromosomes were defined in large part by the linkage maps of phenotypic mutants. The gene(s)

Vet-ebooks.com

impacted by a spontaneous mutation are not initially known, and the symbol for such a heritable phenotypic marker is italicized and all lower case for recessive mutations, such as *bg* for beige, *ob* for obese, and *d* for dilute. The first letter of the symbol is in upper case for dominant or semi-dominant mutations, such as *Tr* for trembler. When the impacted gene is identified, if the mutation is a molecular lesion in only one gene, then the original marker symbol becomes a superscript of that gene for the allele symbol, $Lyst^{bg}$, Lep^{ob}, $Myo5a^{d}$, and $Pmp22^{Tr}$, respectively. Although gene symbols may change over time as the function and ontology of the gene is better understood, other than becoming a superscript of the gene, the allele symbol remains the same as does the allele name. For example the commonly used nude mouse gene name has changed considerably over time (Table 3.11). For mice, the gene symbol has the first letter capitalized and subsequent letters in lower case, all in italics. Hyphens are avoided except to depict new alleles of the initial phenotypic mutation (Table 3.12). For example, while interleukin 10 is commonly written in journals as IL-10, the correct gene symbol would be *Il10* and protein symbol would be IL10. Human gene symbols are essentially the same as for mice except the human gene symbols are all in capital letters and italicized. Greek letters are not used at all, only Roman letters and Arabic numbers. For example, interferon gamma is *Ifng*. The protein coded for by this gene is listed in capital letters with no italics (IFNG) for both mouse and human proteins.

Non-engineered Induced Mutations

The system for naming chemically or radiation-induced mutations is similar to that for spontaneous mutations, except that while many are initially assigned phenotypic names and corresponding symbols, some are instead assigned program accession numbers. One example of this is *nmf12*, which was the 12th characterized ENU induced mutation in the neuroscience mutagenesis facility (nmf) at The Jackson Laboratory. Once the underlying mutation was found to be a H716R point substitution in the gene MER proto-oncogene tyrosine kinase, the symbol changed to $Mertk^{nmf12}$ [40].

Radiation-induced mutations have also often been assigned phenotypic names, such as disproportionate micromelia ($Col2a1^{Dmm}$), but because radiation-induced mutations often impact more than one gene, the mutation symbol is in those instances not superscripted to a single gene symbol. A.G. Searle reported several phenotypic mutants generated in neutron irradiation experiments, one of which caused severe ocular colobomas in heterozygotes and was therefore named coloboma, with the symbol *Cm* [41, 42]. When this mutation was determined to be a multigenic deletion encompassing 29 genes the symbol remained *Cm* but the name changed from coloboma to coloboma deletion region. The symbol and name could have been changed to follow chromosomal aberration nomenclature for deletions, but because of the long history of this mutation in the literature this was not done.

Table 3.11 Evolution of the nomenclature for nude.

nu original mutation symbol
D11Bhm185e, Hfh11, whn- early gene symbols
Foxn1 (current gene symbol, forkhead box N1)
$Foxn1^{nu}$ current allele symbol for the nude allelic mutation

Table 3.12 Nomenclature for spontaneous mouse mutations.

C57BL/6J-$Lyst^{bg\text{-}J}$/J C57BL/6J-$Pax3^{Sp\text{-}d}$/J
C57BL/6J = Inbred strain carrying the mutation
Lyst = Lysosomal trafficking regulator (gene name, italics)
bg-J = Allele symbol for beige Jackson. Note the first letter in the allele (*bg-J*) is lower case indicating it is recessive
C57BL/6J-$Pax3^{Sp\text{-}d}$/J
C57BL/6J = Inbred strain carrying the mutation
Pax3 = Paired box 3 (gene name, italics)
Sp-d = Allele symbol for delayed splotch. Note the first letter in the allele (*Sp-d*) is upper case indicating dominant or semi-dominant

Chromosomal Aberration Nomenclature

Mutations that include more than one gene or alter chromosomal organization are often, but not always, assigned symbols and names that indicate this. The symbol begins with an indicator of the nature of the mutation followed by details about the chromosomal location of the mutation in parentheses followed by a line number and lab code of the laboratory that identified it. The most common types of chromosomal aberrations are multigenic deletions, but we include here a short list of examples of a few other important types:

Del(10)77H: Deletion in Chromosome 10 that was the 77th deletion identified at Harwell (http://www.informatics.jax.org/accession/MGI:5314347).

Del(5Letm1-Htt)1Jcs: Deletion in Chromosome 5 from the gene *Letm1* to the gene *Htt* that was the first made by Dr. John Schimenti (http://www.informatics.jax.org/accession/MGI:3798057).

Dp(7Sult1a1-Spn)7Yah: Duplication in Chromosome 7 from the gene *Sult1a1* to the gene *Spn* that was the seventh duplication made by Dr. Yann Herault (http://www.informatics.jax.org/accession/MGI:6342919).

In(5)2Rk: Inversion in Chromosome 5 that was the 5th inversion generated by Dr. Thomas Roderick (http://www.informatics.jax.org/accession/MGI:3789592).

Rb(11.16)2H: Robertsonian translocation between Chromosomes 11 and 16 that was the second Robertsonian

Vet-ebooks.com

translocation generated at Harwell (http://www.informatics.jax.org/accession/MGI:104106).

T(12;16)1Cje: Reciprocal translocation between Chromosomes 12 and 16 that was the first reciprocal translocation generated by Dr. Charles Epstein (http://www.informatics.jax.org/accession/MGI:1860491).

While chromosomal aberrations were traditionally generated primarily through radiation experiments, modern genetic engineering techniques permit more engineered strategies [43]. Transgenic insertions are also a form of chromosomal aberration, and they are covered in the "Genetically Engineered Mice" section.

Genetically Engineered Mice

There are three basic types of genetically engineered mice: transgenic, targeted, and endonuclease-mediated. Different nomenclature is used to distinguish these.

Transgenic mice can be created to overexpress a gene, express a gene not normally found in mice (green fluorescent protein [GFP] from jellyfish), conditionally express genes, and many other engineered approaches not found normally in nature.

Transgenic nomenclature can be complex, especially as some transgenes still use older formats (Table 3.13). All transgenes begin with Tg followed by information in parentheses then a founder line number and lab code. If a single gene driven by its own promoter is inserted, then the information in the parentheses is simply that gene symbol, not italicized. The information in the parentheses begins with the promoter, a hyphen, then information about the expressed sequence(s). For example, C57BL/6J-Tg(Mt1-Tnfsf4)1Pgn/Pgn has a transgenic insertion of mouse tumor necrosis factor (ligand) superfamily, member 4 (*Tnfsf4*) gene under the control of the metallothionine promoter coisogenic on the C57BL/6J background and is the first transgenic line with these components made by Dr. Beverly Paigen [44].

Table 3.13 Nomenclature for transgenic mice.

FVB/NJ-Tg(KRT14-HPV18E7)CSun/Sun
FVB/NJ = genetic background of the strain
Tg = Transgene insertion
KRT14 = Human KRT14 promoter
HPV18E7 = Human papillomavirus 18 E7 gene
C = transgenic line
Sun = strain lab code, John P. Sundberg
B6N.Cg-Tg(KRT14-cre)1Amc/J
B6N = Congenic host strain carrying the allele, C57BL/6N
Cg = donor strain is not known (C57BL/6 x CBA)F1
Tg = Transgene insertion
KRT14 = Human keratin 14 gene
cre = cre-recombinase expressing
1Amc = line 1, Andrew P. McMahon
J = strain lab code, The Jackson Laboratory

Targeted, Endonuclease-Mediated, Enhancer or Gene Trap, Transposon-Induced, and Transgenic Mutations

Targeted mutations were initially generated to produce mutant mice with inactivation of one specific gene, the so-called "knockout" mouse lines. Targeted mutations can also have a foreign gene or gene segment inserted into a target gene, resulting in expression of the foreign gene under control of the endogenous promoter. These are termed "knock-in" mutations. In these cases, the inserted gene symbol is included in parentheses as part of the targeted allele symbol. However, reporter symbols, such as GFP, are not included in allele symbols. Details describing the specifics of knock-in constructs should be provided in databases or publications, and not in the nomenclature.

In the targeted knock-in mutation $En1^{tm1(Otx2)Wrst}$, the coding region of the engrailed 1 gene (*En1*) was replaced by the orthodenticle homeobox 2 (*Otx2*) gene, originating from the W. Wurst laboratory [45]. For the Cd19 antigen targeted knock-in mutation $Cd19^{tm1(cre)Cgn}$, *cre*-recombinase was inserted in-frame in exon 1 [46]. The allele expresses *cre*-recombinase specifically in B-lineage cells throughout development. The apolipoprotein E targeted knock-in mutation ($Apoe^{tm1(APOE*2)Mae}$) has a DNA fragment containing exons 2–4 of a human *APOE2* isoform replacing the equivalent portion of the mouse *Apoe* gene. The human protein is expressed from this allele and the endogenous mouse protein is undetectable.

When a targeting vector is used to generate multiple germline-transmissible alleles, such as in the *cre-Lox* system, the original knock-in of *loxP* would follow the regular *tm* designation rules. If a second heritable allele was then generated after mating with a *cre*-recombinase transgenic mouse, it would retain the parental designation followed by a decimal point and serial number. For example, $Tfam^{tm1Lrsn}$ designates a targeted mutation where *loxP* was inserted into the transcription factor A, mitochondrial (*Tfam*) gene [47]. $Tfam^{tm1.1Lrsn}$ (note: tm1Lrsn vs. tm1.1Lrsn) designates the derivative germline transmissible allele generated after mating with a *cre*-recombinase transgenic mouse. Note that somatic events generated in offspring from a $Tfam^{tm1Lrsn}$ bearing mouse and a *cre*-recombinase transgenic that cause disruption of *Tfam* in selective tissues would not be part of strain nomenclature.

Mutagenesis using targeted endonuclease-cleavage technologies (CRISPR, Zinc Finger endonuclease, or TALEN) create site-targeted genomic changes by either non-homologous end joining resulting in random indels (insertion/deletions),

Vet-ebooks.com

or homologous recombination with a donor plasmid to generate specific sequence alterations (floxed, point mutations, insertion of exogenous sequence, etc.). While there is no standard for naming endonuclease-mediated mutations across species, mouse, rat, and *Xenopus* designate such mutation with "em" [48] followed with the serial number of endonuclease-mediated mutation for the generating laboratory, and the ILAR-registered laboratory code (e.g. *Abcb1a*^{em1Sbkv} for endonuclease-mediated mutation 1 from the laboratory of Dr. Sergei B Koralov in adenosine triphosphate (ATP)-binding cassette, sub-family B [MDR/TAP], member 1A gene) [49]. Endonuclease-mediated mutation nomenclature mirrors targeted allele nomenclature in regard to inserted expressed sequences (http://www.informatics.jax.org/mgihome/nomen/gene.shtml#endim). When endonuclease-mediated mutations are used to produce multigenic mutations either through direct targeting or recombination between previously targeted sites, chromosomal aberration nomenclature is used in the absence of a marker designating the region affected (to be added to the nomen webpage). For example, Del(5Kit-Nmu)2Staka (deletion, Chr 5, Satoru Takahashi 2) describes the 1.07 Mb deletion produced by CRISPR/Cas targeting of a region 240 kb upstream of *Kit* and 81 kb downstream of *Nmu* [50].

Gene trap alleles are produced by random integration of constructs containing splice acceptors and other sequences that prematurely terminated transcription disrupting gene expression [51]. Alleles generated by the integration of a gene trap are represented with "Gt," the mutant cell line in parenthesis, and ILAR-registered laboratory code. For example, in *Dnajb9*$^{Gt(KST256)Byg}$ (gene trap KST256 from BayGenomics in *DnaJ* heat shock protein family [Hsp40] member B9), a gene trap with a splice donor and β-galactosidase gene is inserted into intron producing a hypomorphic allele [52].

Enhancer traps are specialized transgenes. One utility of these transgenes is in creating *cre*-recombinase driver lines. Enhancer traps of this type that are currently being created may include a minimal promoter, introns, a *cre*-recombinase cassette (sometimes fused with another element such as ERT2), and polyA sites from different sources. Nomenclature for these enhancer traps consists of 4 parts as follows: Et, prefix for enhancer trap; *cre* recombinase cassette, portion in parentheses (for example, cre, icre, or cre/ERT2 [if fused with ERT2]); line number or serial number to designate lab trap number or serial number; Lab code: ILAR code identifying the creator of this enhancer trap; Examples include: Et(icre)754Rdav (for Enhancer trap 754, Ron Davis) and Et(cre/ERT2)2047Rdav (for Enhancer trap 2047, Ron Davis) [53].

Transposon-induced mutations utilize transposases (e.g. sleeping beauty) to mobilize integrated transposon concatemers flanked by long terminal repeats (LTR) to insert into small base pair recognition sequences [54]. When integration of the transposon does not disrupt the LTR, these elements can be remobilized and "hop" into different sites located either on the same chromosome or a different one. Transposons can insert sequences to be expressed as well as disrupting gene expression at integration site. Transposon-induced alleles are denoted with "Tn," the transposon concatemer (specifying the transposase), a line number (followed by a period "." and additional serial number in the case of remobilization), and ILAR-registered laboratory code. In the transposon-induced mutation *Slc16a10*$^{Tn(sb\text{-}lacZ,GFP)1.4Tcb}$ (line 4 containing reintegration of a sleeping beauty-specific transposon that expressed lacZ and GFP from Dr. Thomas Brodnicki), transposition of the expression cassette into intron 1 produces a null allele [55].

In many cases, a large number of transgenic lines are made from the same gene construct and only differ by tissue specificity of expression. The most common of these are transgenes that use reporter constructs or recombinases (e.g. GFP, *lacZ*, *cre*), where the promoter should be specified as the first part of the gene insertion designation, separated by a hyphen from the reporter or recombinase designation. The SV40 large T antigen is another example. The use of promoter designations is helpful in such cases. Examples include Tg(Wnt1-LacZ)206Amc, in which the mouse has a *LacZ* transgene with a wingless-type mouse mammary tumor virus (MMTV) integration site family, member 1 (*Wnt1*) promoter, from mouse line 206 created in the laboratory of Andrew McMahon [56]. Another example is Tg(Zp3-cre)3Mrt in which the *cre* transgene has a zona pellucida glycoprotein 3 (*Zp3*) promoter, the third transgenic mouse line from the laboratory of Gail Martin [57].

Summary

Mouse genetic nomenclature can be confusing at first, and is often considered to be unimportant by investigators. However, there are many sources of help and support, discussed above, and the effort needed to become fluent in the language of strains and mutants is much less than the potential effort needed to rescue badly planned experiments or recoup the costs involved in using the wrong mice. It is also essential for the replication of experiments, both yours and those whose resources you intend to use, and the sharing of your data. We hope that this commentary lays out clearly why an appreciation and functional knowledge of nomenclature is not only helpful but essential for those using mice as a model system.

Acknowledgments

This work was supported in parts by grants from the National Institutes of Health (R01 CA089713 and HG000330).

Vet-ebooks.com

References

1 McKusick, V.A. (1969). On lumpers and splitters, or the nosology of genetic disease. *Perspect Biol. Med.* 12 (2): 298–312.
2 Simon-Sanchez, J. and Gasser, T. (2015). Parkinson disease GWAS: the question of lumping or splitting is back again. *Neurology* 84 (10): 966–967.
3 Schofield, P.N., Bubela, T., Weaver, T. et al. (2009). Post-publication sharing of data and tools. *Nature* 461 (7261): 171–173.
4 Low, B.E., Kutny, P.M., and Wiles, M.V. (2016). Simple, efficient CRISPR-Cas9-mediated gene editing in mice: strategies and methods. *Methods Mol. Biol.* 1438: 19–53.
5 Snell, G.D. (1941). *Biology of the Laboratory Mouse*, 1e. New York, NY: McGraw-Hill.
6 Husler, M.R., Beamer, W.G., Boggess, D. et al. (1998). Neoplastic and hyperplastic lesions in aging C3H/HeJ mice. *J. Exp. Anim. Sci.* 38 (4): 165–180.
7 Sundberg, J.P., King, L.E. Jr., Bosenberg, M. et al. (2020). Animal models of skin disease. In: *McKee's Pathology of the Skin with Clinical Correlations. 2*, 5e (eds. E. Calonje, T. Brenn, A.H. Lazar and S.D. Billings), 1895–1917. China: Elsevier.
8 Li, Q., Berndt, A., Sundberg, B.A. et al. (2016). Mouse genome-wide association study identifies polymorphisms on chromosomes 4, 11, and 15 for age-related cardiac fibrosis. *Mamm Genome.* 27 (5-6): 179–190. https://doi.org/10.1007/s00335-016-9634-y. Epub 2016 Apr 28.
9 Giehl, K.A., Potter, C.S., Wu, B. et al. (2009). Hair interior defect in AKR/J mice. *Clin. Exp. Dermatol.* 34 (4): 509–517.
10 Wu, B., Potter, C.S., Silva, K.A. et al. (2010). Mutations in sterol O-acyltransferase 1 (*Soat1*) result in hair interior defects in AKR/J mice. *J. Invest. Dermatol.* 130 (11): 2666–2668.
11 Davisson, M.T., Schmidt, C., Reeves, R.H. et al. (1993). Segmental trisomy as a mouse model for Down syndrome. *Prog. Clin. Biol. Res.* 384: 117–133.
12 Bisaillon, J.J., Radden, L.A. 2nd, Szabo, E.T. et al. (2014). The retarded hair growth (*rhg*) mutation in mice is an allele of ornithine aminotransferase (*Oat*). *Mol. Genet. Metabol. Rep.* 1: 378–390.
13 Fox, S. and Eicher, E.M. (1978). The retarded hair growth (*rhg*) mutation in mice is an allele of ornithine aminotransferase (*Oat*). *Mouse News Lett.* 58: 47.
14 Griffen, A. (1951). *tc* – truncate. *Mouse News Lett.* 5: 31.
15 Mulligan, M.K., Mozhui, K., Prins, P., and Williams, R.W. (2017). GeneNetwork: a toolbox for systems genetics. *Methods Mol. Biol.* 1488: 75–120.
16 Li, Q., Philip, V.M., Stearns, T.M. et al. (2019). Quantitative trait locus and integrative genomics revealed candidate modifier genes for ectopic mineralization in mouse models of pseudoxanthoma elasticum. *J. Invest. Dermatol.* 139 (12): 2447–2457. e7.
17 Chesler, E.J., Miller, D.R., Branstetter, L.R. et al. (2008). The Collaborative Cross at Oak Ridge National Laboratory: developing a powerful resource for systems genetics. *Mamm. Genome* 19 (6): 382–389.
18 Philip, V.M., Sokoloff, G., Ackert-Bicknell, C.L. et al. (2011). Genetic analysis in the Collaborative Cross breeding population. *Genome Res.* 21 (8): 1223–1238.
19 Graham, J.B., Thomas, S., Swarts, J. et al. (2015). Genetic diversity in the collaborative cross model recapitulates human West Nile virus disease outcomes. *mBio* 6 (3): e00493–e00415.
20 Zeiss, C.J., Gatti, D.M., Toro-Salazar, O. et al. (2019). Doxorubicin-induced cardiotoxicity in Collaborative Cross (CC) mice recapitulates individual cardiotoxicity in humans. *G3* 9 (8): 2637–2646.
21 Gralinski, L.E., Ferris, M.T., Aylor, D.L. et al. (2015). Genome wide identification of SARS-CoV susceptibility loci using the Collaborative Cross. *PLoS Genet.* 11 (10): e1005504.
22 Konger, R.L., Derr-Yellin, E., Hojati, D. et al. (2016). Comparison of the acute ultraviolet photoresponse in congenic albino hairless C57BL/6J mice relative to outbred SKH1 hairless mice. *Exp. Dermatol.* 25 (9): 688–693.
23 Voigt, A.Y., Michaud, M., Tsai, K.Y. et al. (2019). Differential hairless mouse strain-specific susceptibility to skin cancer and sunburn. *J. Invest. Dermatol.*
24 Papale, L.A., Beyer, B., Jones, J.M. et al. (2009). Heterozygous mutations of the voltage-gated sodium channel SCN8A are associated with spike-wave discharges and absence epilepsy in mice. *Hum. Mol. Genet.* 18 (9): 1633–1641.
25 Johnson, K.R., Tian, C., Gagnon, L.H. et al. (2017). Effects of *Cdh23* single nucleotide substitutions on age-related hearing loss in C57BL/6 and 129S1/Sv mice and comparisons with congenic strains. *Sci. Rep.* 7: 44450.
26 Thomas, M.K., Devon, O.N., Lee, J.H. et al. (2001). Development of diabetes mellitus in aging transgenic mice following suppression of pancreatic homeoprotein IDX-1. *J. Clin. Invest.* 108 (2): 319–329.
27 Ohlrogge, W., Haag, F., Lohler, J. et al. (2002). Generation and characterization of ecto-ADP-ribosyltransferase ART2.1/ART2.2-deficient mice. *Mol. Cell. Biol.* 22 (21): 7535–7542.
28 Serreze, D.V., Chapman, H.D., Post, C.M. et al. (2001). Th1 to Th2 cytokine shifts in nonobese diabetic mice: sometimes an outcome, rather than the cause, of diabetes resistance elicited by immunostimulation. *J. Immunol.* 166 (2): 1352–1359.
29 Dunn, L.C. (1937). Caracul, a dominant mutation. *J. Heredity.* 28: 334.
30 Bubier, J.A., Sproule, T.J., Alley, L.M. et al. (2010). A mouse model of generalized non-Herlitz junctional epidermolysis bullosa. *J. Invest. Dermatol.* 130 (7): 1819–1828.
31 Sproule, T.J., Bubier, J.A., Grandi, F.C. et al. (2014). Molecular identification of collagen 17a1 as a major genetic modifier of laminin gamma 2 mutation-induced junctional epidermolysis bullosa in mice. *PLoS Genet.* 10 (2): e1004068.

Vet-ebooks.com

32 Nadeau, J.H., Singer, J.B., Matin, A., and Lander, E.S. (2000). Analysing complex genetic traits with chromosome substitution strains. *Nat. Genet.* 24 (3): 221–225.

33 Dietl, G., Langhammer, M., and Renne, U. (2004). Model simulations for genetic random drift in the outbred strain Fzt:DU. *Arch. Anim. Breed* 47 (6): 595–604.

34 Svenson, K.L., Gatti, D.M., Valdar, W. et al. (2012). High-resolution genetic mapping using the mouse diversity outbred population. *Genetics* 190 (2): 437–447.

35 French, J.E., Gatti, D.M., Morgan, D.L. et al. (2015). Diversity outbred mice identify population-based exposure thresholds and genetic factors that influence benzene-induced genotoxicity. *Environ. Health Perspect.* 123 (3): 237–245.

36 Broman, K.W., Gatti, D.M., Svenson, K.L. et al. (2019). Cleaning genotype data from diversity outbred mice. *G3* 9 (5): 1571–1579.

37 Recla, J.M., Bubier, J.A., Gatti, D.M. et al. (2019). Genetic mapping in diversity outbred mice identifies a *Trpa1* variant influencing late-phase formalin response. *Pain* 160 (8): 1740–1753.

38 Sigmon, J.S., Blanchard, M.W., Baric, R.S. et al. (2020). Content and performance of the MiniMUGA genotyping array, a new tool to improve rigor and reproducibility in mouse research. *Genetics* 216 (4): 905–930. https://doi.org/10.1534/genetics.120.303596.

39 Stoye, J.P., Fenner, S., Greenoak, G.E. et al. (1988). Role of endogenous retroviruses as mutagens: the hairless mutation of mice. *Cell* 54 (3): 383–391.

40 Maddox, D.M., Hicks, W.L., Vollrath, D. et al. (2011). An ENU-induced mutation in the Mertk gene ($Mertk^{nmf12}$) leads to a slow form of retinal degeneration. *Invest. Ophthalmol. Vis. Sci.* 52 (7): 4703–4709.

41 Theiler, K. and Varnum, D.S. (1981). Development of coloboma (*Cm*/+), a mutation with anterior lens adhesion. *Anat. Embryol. (Berl).* 162 (1): 121–126.

42 Hess, E.J., Jinnah, H.A., Kozak, C.A., and Wilson, M.C. (1992). Spontaneous locomotor hyperactivity in a mouse mutant with a deletion including the Snap gene on chromosome 2. *J. Neurosci.* 12 (7): 2865–2874.

43 Birling, M.C., Schaeffer, L., Andre, P. et al. (2017). Efficient and rapid generation of large genomic variants in rats and mice using CRISMERE. *Sci. Rep.* 7: 43331.

44 Wang, X., Ria, M., Kelmenson, P.M. et al. (2005). Positional identification of TNFSF4, encoding OX40 ligand, as a gene that influences atherosclerosis susceptibility. *Nat. Genet.* 37 (4): 365–372.

45 Broccoli, V., Boncinelli, E., and Wurst, W. (1999). The caudal limit of *Otx2* expression positions the isthmic organizer. *Nature* 401 (6749): 164–168.

46 Rickert, R.C., Rajewsky, K., and Roes, J. (1995). Impairment of T-cell-dependent B-cell responses and B-1 cell development in CD19-deficient mice. *Nature* 376 (6538): 352–355.

47 Larsson, N.G., Wang, J., Wilhelmsson, H. et al. (1998). Mitochondrial transcription factor A is necessary for mtDNA maintenance and embryogenesis in mice. *Nat. Genet.* 18 (3): 231–236.

48 Knowlton, M.N. and Smith, C.L. (2017). Naming CRISPR alleles: endonuclease-mediated mutation nomenclature across species. *Mamm. Genome* 28 (7–8): 367–376.

49 Cao, W., Kayama, H., Chen, M.L. et al. (2017). The xenobiotic transporter *Mdr1* enforces T cell homeostasis in the presence of intestinal bile acids. *Immunity* 47 (6): 1182–1196. e10.

50 Mizuno, S., Takami, K., Daitoku, Y. et al. (2015). Peri-implantation lethality in mice carrying megabase-scale deletion on 5qc3.3 is caused by *Exoc1* null mutation. *Sci. Rep.* 5: 13632.

51 Friedel, R.H. and Soriano, P. (2010). Gene trap mutagenesis in the mouse. *Methods Enzymol.* 477: 243–269.

52 Fritz, J.M., Dong, M., Apsley, K.S. et al. (2014). Deficiency of the BiP cochaperone ERdj4 causes constitutive endoplasmic reticulum stress and metabolic defects. *Mol. Biol. Cell* 25 (4): 431–440.

53 The Jackson Laboratory. (2009). Large-scale enhancer trap project to generate transgenic cre alleles by Ron Davis at Baylor University [Internet]. http://www.informatics.jax.org (accessed 04 March 2021).

54 Li, L., Liu, P., Sun, L. et al. (2016). PiggyBac transposon-based polyadenylation-signal trap for genome-wide mutagenesis in mice. *Sci. Rep.* 6: 27788.

55 Elso, C.M., Chu, E.P., Alsayb, M.A. et al. (2015). Sleeping beauty transposon mutagenesis as a tool for gene discovery in the NOD mouse model of type 1 diabetes. *G3* 5 (12): 2903–2911.

56 Echelard, Y., Vassileva, G., and McMahon, A.P. (1994). Cis-acting regulatory sequences governing Wnt-1 expression in the developing mouse CNS. *Development* 120 (8): 2213–2224.

57 Lewandoski, M., Wassarman, K.M., and Martin, G.R. (1997). *Zp3-cre*, a transgenic mouse line for the activation or inactivation of loxP-flanked target genes specifically in the female germ line. *Curr. Biol.* 7 (2): 148–151.

Vet-ebooks.com

4

Discovering and Validating Mouse Models of Human Diseases: The Cinderella Effect

John P. Sundberg, Jerrold M. Ward, Peter Vogel, and Paul N. Schofield

Introduction

Historically, animal models (regardless of species) of human diseases were identified and proposed empirically. Namely the best fit was based largely on clinical similarities between the human and animal disease (Figure 4.1). This concept of "best fit," or the "Cinderella Effect," [1] has evolved considerably with the advance of technology to include direct correlations at the level of the genetic variation found in humans with specific diseases.

However, access to advanced technology does not guarantee the identification and development of valid animal models. In fact, without critical observation and proper experimental design, misinterpretation of experiment results can derail the valuable contribution that might be obtained from the use of animal models. In a relatively recent example, an investigation on inflammation compared eight-week-old C57BL/6J male mice (one inbred strain, one sex, one age) with a heterogeneous group of outbred human patients up to 55 years of age with blunt trauma, burns, and bacterial endotoxin responses. The results showed consistency in the overall transcriptional response in humans, but major differences when compared to those seen in a mouse model, which led the authors to conclude that mouse models were without value [2]. This paper caused a sensation in lay media (http://www.nytimes.com/2013/02/12/science/testing-of-some-deadly-diseases-on-mice-mislead-report-says.html?smid=pl-share) as well as scientific circles. However, re-evaluation of the data revealed important areas of similarity [3]. Because the transcriptome data used in that study were available in publicly accessible databases, other groups were able to reanalyze the data and showed that mouse and human comparative studies were valuable even in this model [3, 4]. This change in interpretation, still debated, reflects a fundamental experimental design flaw in the study that led to the misinterpretations, namely "comparing apples to oranges" [4] and whether mouse and human diseases can be compared or not. One human, or even one group of humans, is unlikely to accurately model all humans, which is the lesson learned from approaches to personalized medicine [5]. One should not be surprised to find that young laboratory mice of a single strain, a single sex (the genetic equivalent of a single individual or a group of identical twins), and exposed to experimental insults, does not mirror the inflammatory response of a heterogeneous human adult population of mixed ages and both sexes. It is a general point that multiple inbred strains or outbred strains need to be used when attempting to model human disease [6]. Therefore, careful comparison at the most basic levels are necessary to accurately create and validate animal models for human diseases. This applies to genetic-based diseases as well. Definitions of human diseases include common, often characteristic lesions, as well as less frequent to rare lesions (subtypes of the disease). These can be conceptually presented as a Gaussian curve with each bar representing a subgroup of any particular disease (Figure 4.2). Inbred mouse strains essentially present as an infinite number of one individual with both sexes due to their genetic homogeneity. As such, each inbred strain carrying a defined mutation may represent a model of one subtype of the human disease not all subtypes. Some strains may exhibit the common or characteristic lesion while others do not.

Real examples of this were exemplified by creating a null mutation in the epidermal growth factor receptor gene (*Egfr*^{tm1Dwt}). When this allele was moved by breeding onto other strains to create hybrid stocks, a variety of phenotypes were observed, ranging from embryonic lethality at 4–11.5 days post conception (DPC) to live births with runting (Figure 4.3) [7, 8]. While this is an interesting observation, the question is really how can these observations help us to better understand human diseases. An example of how this phenomenon can explain the human disease subtypes came via a spontaneous hypomorphic allele of the laminin gamma 2 gene (*Lamc2*^{jeb}) in mice. When the gene was mapped by crossing the parental strain with five other inbred strains, in the process of creating five new congenic strains, a large variation in phenotypes was evident [9]. Skin fragility (blister formation) was a feature on all backgrounds, characteristic of junctional epidermolysis bullosa. However, on one background, nail abnormalities were observed. Mapping for these quantitative differences revealed the collagen 17A1

Pathology of Genetically Engineered and Other Mutant Mice, First Edition. Edited by John P. Sundberg, Peter Vogel, and Jerrold M. Ward.
© 2022 John Wiley & Sons, Inc. Published 2022 by John Wiley & Sons, Inc.

Vet-ebooks.com

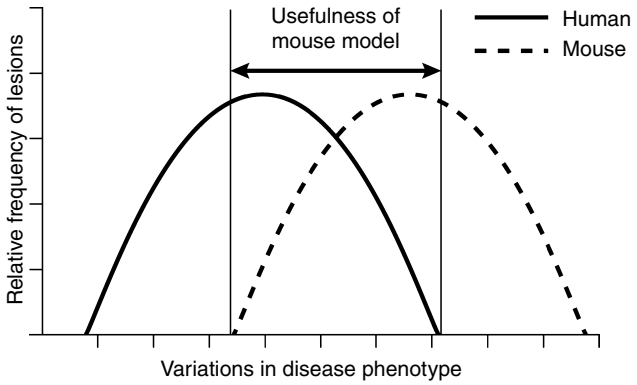


Figure 4.1 Nonhuman (including mouse) models were historically compared empirically to human diseases. Diseases present a variety of phenotypes and severity levels in a mixed population, as it does with a human population as illustrated by the Gaussian curve. Where the lesions (phenotypes) overlapped was where they were considered to be potentially useful as models. Many did not hold up over time.

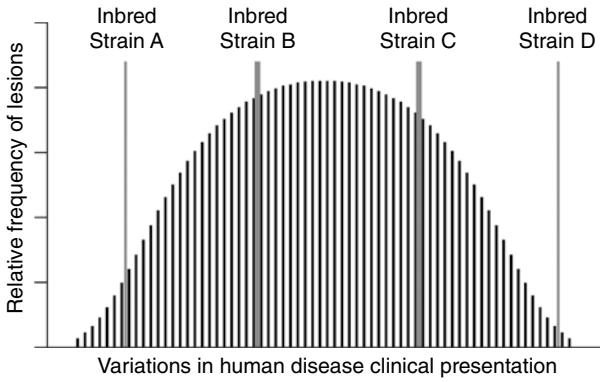


Figure 4.2 Human population response to disease is often highly variable between individuals. By contrast, inbred mice carrying the same genetic mutation are more monomorphic and can present as a specific subtype of the human disease.

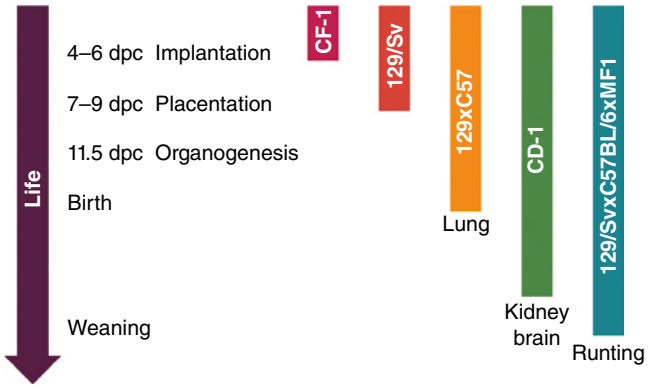


Figure 4.3 Effect of strain on phenotype for a single gene mutation. A classic example of the effect of an inbred strain background on phenotype was when the epidermal growth factor receptor null mutation (*Egfr*^{tm1Dwt}) was transferred by breeding onto different hybrid genetic backgrounds. Sources: Based on Threadgill et al. [7] and Sibilia and Wagner [8].

(*Col17a1*) was a major modifier gene that resulted in the mice having nail dystrophy, a feature of one subtype of the human disease [10]. A second gene was later identified that explained the musculoskeletal weakness in another subtype of this human disease (Sproule and Sundberg, unpublished work). Figure 4.4 illustrates how using websites that define specific features of subtypes of a human disease can facilitate phenotyping mouse models to understand the underlying genetics behind these variations.

Basic Concepts of Defining a Mouse Model for a Human Disease

There are numerous criteria needed to make an animal model for a human disease, many of which were standardized in a fascicle series edited by George Migaki during the 1970s–1990s (Table 4.1) [11]. Models can be built on spontaneous or induced mutations, or those experimentally generated by various methods (including chemicals, infectious and physical agents, surgery, etc.). Simply finding a case or case series is a start but, ideally, the model should be reproducible either by breeding or by using some type of manipulation [12]. Sometimes a model may combine an underlying genetic lesion with an additional challenge such as infection, aging, or high fat diet to manifest its full range of phenotypes. An example of this would be the feeding of high-fat diets to mice to understand the genetics of atherosclerosis [13]. Furthermore, the model should be readily available for other scientists to validate and utilize. Single gene mutations in mice, which result in a genetically reproducible disease, have been the cornerstone of mouse genetics and models for more than a century. However, the locus or allele heterogeneity in human genetic disorders also makes a specific gene mutation mouse model useful for perhaps that human equivalent but not necessarily for all human forms of a monogenic disease.

Mouse models, as well as other species used as models, should have some or many of the clinical and pathological features of the human disease to which they are compared. Where these features overlap were historically considered to be where the models were useful (Figure 4.1).

An informative example of the complexity of phenotype-genotype relationships in both mice and humans, and the consequent difficulty in establishing a model, can be found in CHARGE syndrome [14]. CHARGE syndrome is an extremely phenotypically diverse syndrome with coloboma, heart defects, choanal atresia, retardation (of growth or development), genitourinary malformation, and ear abnormalities, being the most common phenotypes. The phenotypic variability raises the question as to whether this is indeed a genetic or a clinical definition of the syndrome, suggesting that the phenotypic clusters could be due to multiple genetic origins. As it turned out, the identification of the *CHD7* gene in humans lead to huge simplification of the understanding of the syndrome and identified at least some allelic:phenotypic spectrum relationships [15]. This stimulated the investigation of

Vet-ebooks.com

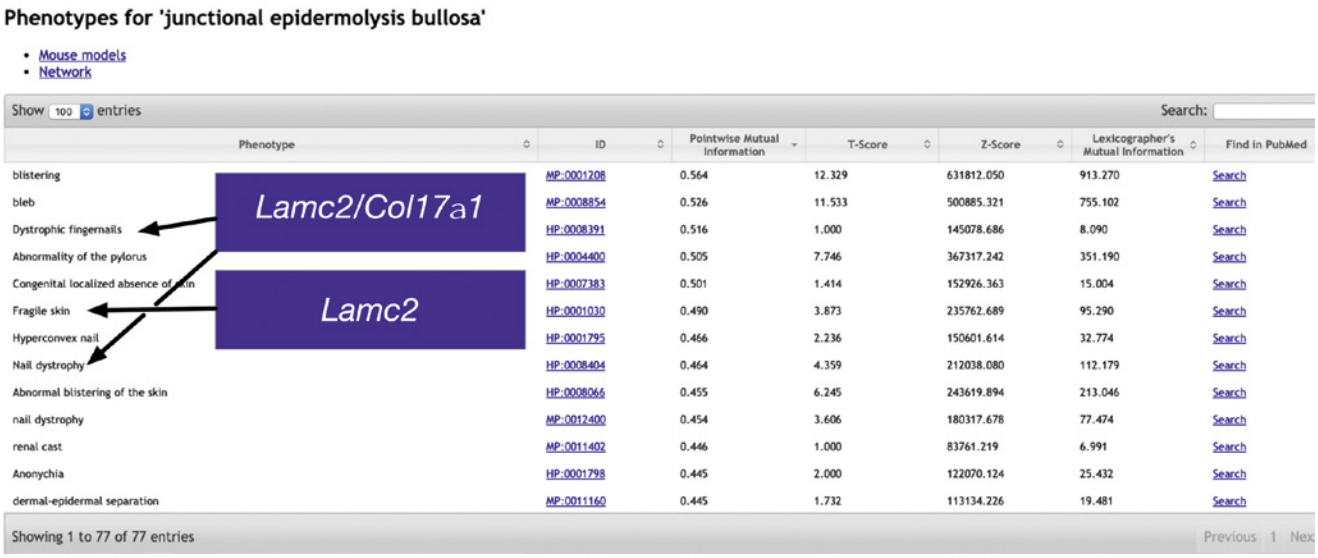


Figure 4.4 **Mouse models identify subtypes of junctional epidermolysis bullosa**. A spontaneous hypomorphic allele of *Lamc2*^{jeb} had different phenotypes when moved to different congenic backgrounds. Using this observation the underlying gene for each variation was identified. The range of phenotypes of junctional epidermolysis bullosa were gathered from the literature by text mining using disease labels from the DERMO ontology and accessed through the Aber OWL skin disease phenotypes database. Source: http://aber-owl.net/aber-owl/diseasephenotypes.

Table 4.1 Criteria for accurately defining an animal model, regardless of how it was created, for a human disease.

1) Accurately recapitulates the clinical and pathological features of the human disease (responds to similar drugs in both species).
2) Primary molecular defect similar (ideally similar or identical mutation in the same).
3) Readily available to other investigators:
   a) Genetic, breed mice to produce more as needed.
   b) Repository for archiving model for public distribution.
   c) Experimental induction easily done if not a genetic-based model.
4) Reproducibility (stability of model, inbred strains).
5) Genetic manipulability (arsenal of genetic tools).

Source: Based on Scarpelli et al. [11].

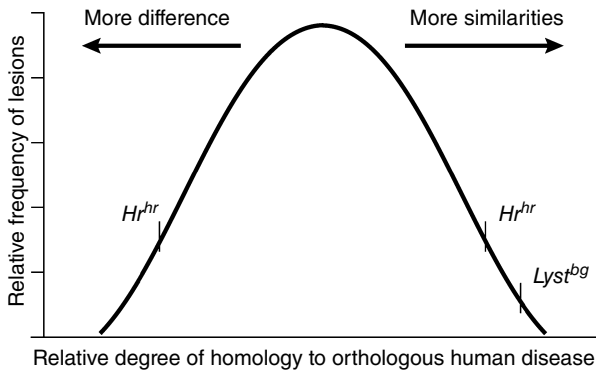


Figure 4.5 **Fitting mouse models to the concepts of human disease**. The mouse beige mutation (*Lyst*^{bg}) was found early on to be a good model for Chediak-Higashi syndrome in humans. By contrast, the mild form of the hairless gene (*Hr*^{hr}) mutation was considered 30 years ago to be a model for normal human skin and was used for sun screen testing.

mouse *N*-ethyl-*N*-nitrosourea (ENU) mutations showing related phenotypes in balance function, and the identification of mouse mutants in *Chd7* but which nonetheless did not model all of the phenotypes seem in humans [16]. The building of mouse models since that initial discovery has generated very valuable and useful strains for the understanding of both genotype/phenotype relationships, together with the mechanisms underlying them, but there still does not exist a single mutation on a single background that completely recapitulates all of the phenotypes expressed in CHARGE allelic series [17]. This example illustrates how identification of models through phenotype similarity can be extremely difficult, but that modeling of a restricted set of phenotypes can be scientifically extremely useful [18].

Some monogenic mouse mutations have features that are essentially identical to or at least very similar to those seen in humans with the same disease. An excellent example is the beige mouse [19] (one of many mammalian species [20, 21] that have mutations in the lysosomal trafficking regulator [*Lyst*^{bg}] gene) as a model for Chediak-Higashi syndrome in humans (Figure 4.5), which can be called a phylogenetically valid model.

One of the big problems with working up (phenotyping) new mutants is that investigators often focus only on the organ or disease process, or molecular pathway of interest rather than do complete analysis of the animal. This results in incomplete definition of the mouse making accurate

Vet-ebooks.com

comparisons to the proposed human disease. Likewise, this is often the problem when defining the human disease, where clinical specialists focus on their area of interest and ignore other organ systems. Combined, this becomes the proverbial blind men describing the elephant [22].

By contrast, before the gene responsible for the hairless mouse was identified, many investigators used it as a model for "normal human skin" because the mice lacked hair as adults, making it useful for topical drug or ultraviolet light carcinogenesis studies. The more severe allelic mutation, rhino (Hr^{rh}) was used for testing drugs, such as retinoic acid analogs, for treating wrinkles [23–26]. Other than being without hair neither were accurate models for normal human skin, but lesions were later shown to be a model for human papular atrichia [27, 28]. The orthologous human disease was eventually identified [29] as was the gene, which allowed direct comparisons between the correct human disease with the correct mouse model [29–34]. This has been the case for numerous single mutant gene mouse models where finding the underlying gene allowed for accurate comparisons with human patients with mutations in the orthologous gene (Figure 4.6).

The one gene–one disease concept remains an oversimplification of disease. Maintaining a single gene mutation as a colony on an inbred strain minimizes variability (a relatively reproducible model) but does not eliminate it within that strain as the mice are not absolutely identical genetically [35]. Many diseases have a sexual dichotomy, and environmental effects, such as diet, can result in different phenotypes at different institutions [36]. Moving the mutation from one inbred strain onto another strain (creating congenic strains) can result in loss to exaggeration of the phenotype, or even to a different phenotype due to the effects of modifier genes or gene redundancy. For example, mouse models of human cancer genes often result in a mouse model with a similar but not identical phenotype [37], where mouse genetic background may play a role in the phenotype. *Trp53* null mutant mice (allele not designated) developed high rates of mammary tumors when bred on the BALB/cMed background but not C57BL/6 or 129/Sv congenic backgrounds, indicating a more complicated genetic predisposition toward mammary tumorigenesis than only mutations in this one gene [38]. These concepts are discussed in detail in Chapter 3, Genetics. However, these observations explain the inability of one inbred mouse strain carrying one or more mutated genes to model all variations seen in human patients. This is because humans are, for the most part, outbred and live in a relatively "dirty" environment. One concern raised about mouse models has been that mice cannot be good models of human disease because they live in environmentally controlled housing (boxes) under pathogen-free conditions with abundant food, water, and access to good veterinary care. When one steps back and looks at how humans exist in a modern society, they too live in a box with many of the same benefits as mice [39].

Genocopies, defined as mutations in differing genes that result in a similar phenotype in humans or mice, further complicate matching mouse genetic-based diseases with those found in human populations. Such is the case for genes that are receptors, ligands, or that interfere with the kinetics of these interactions, exemplified by anhidrotic ectodermal dysplasia models (the tabby–crinkled–downless syndrome or mimics, see Chapter 10 on Skin for more details) [40, 41]. Similarly, ectopic mineralization of soft tissues is a complicated process involving numerous genes that, when mutated, can result in overlapping phenotypes because they are part of a complex molecular network [42]. As molecular pathways or networks are further refined, not only do protein–protein interactions become better defined but also candidate genes for similar diseases are identified that can then be mutated in mice to determine biologically if this is actually the case.

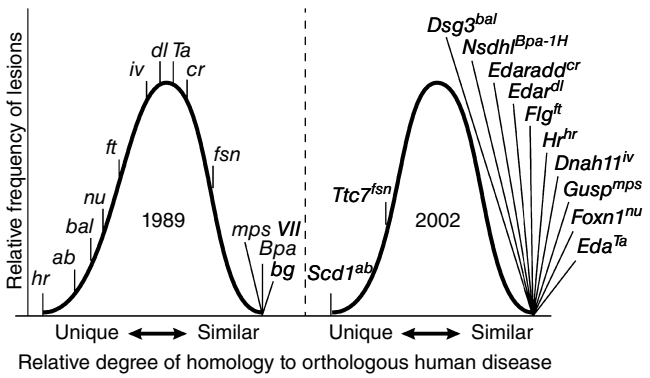


Figure 4.6 **Validation of mouse models over time.** In 1989 few mouse models accurately reflected human diseases. This changed just a few years later, in 2002, as genetic mutations in specific genes were identified in both mice and humans that allowed more accurate comparisons.

Large-Scale Mutagenesis Projects to Discover New Mouse Models

The traditional approach to determining gene function has been to work up spontaneous mutations in mice. An example was the allelic series of desmoglein 4 (*Dsg4*) mutations found first in mice [43, 44]. These were initially compared to human Netherton's syndrome because occasionally abnormal hairs (trichorrhexis invaginata), pathognomonic for Netherton's syndrome, were found in these mice. However, the mutated gene in human Netherton's syndrome was later found to be serine peptidase inhibitor, Kazal type 5 (*SPINK5*) [45], which did not map to the location of the mouse mutation, making it obvious that another mechanism was involved. Desmoglein 4 was later identified as the genetic basis of the mouse lanceolate hair phenotype. Soon thereafter, the orthologous human disease was found to be the result of mutations in the human *DSG4* gene [46]. Not only was the mouse disease identified first, but by finding more than one disease had a so-called "pathognomonic lesion," it demonstrated how that concept, of a lesion specific for a disease, can be misleading.

Vet-ebooks.com

Another example where the concept of "pathognomonic lesion" is an over-simplification is with hair disease characterized by decreased levels of sulfur containing proteins (trichothiodystrophy, illustrated in Chapter 10, Skin). Trichothiodystrophy was a term used for a specific human disease [47, 48]. Hair shaft structural defects are quite common in mice with a number of mutations and most have low sulfur levels, making that a phenotype not, a pathognomic lesion. Trichothiodystrophy is now considered to be a heterogeneous group of autosomal recessive disorders that share sulfur-deficient brittle hairs in humans [49]. Many of these defects are due to mutations in specific keratin genes or genes that regulate keratin expression (such as the forkhead box N1 gene causing the nude mouse [*Foxn1*^{nu}] and human ortholog [*FOXN1*]), especially the hard keratins that are high in sulfur containing amino acids [50].

Two main strategies to generate mouse models at scale have been developed based on forward and reverse genetics. The aim of both being to make mutations experimentally, and then characterize the resulting phenotypes.

The forward genetic approaches define the phenotype and aim to identify mouse orthologs of genes responsible for human disorders through cross-species phenotypic similarity. These can utilize mice carrying spontaneous mutations [51], those that are the result of chemical mutagenesis [52–56] or other means, such as radiation induced mutation. In addition to identifying null gene mutations, forward genetics approaches often identify hypomorphic, gain-of function, and dominant-negative mutations. For example, The Jackson Laboratory utilized whole-exome sequencing to identify the genes responsible for numerous spontaneous mutations in 124 inbred mouse strains [57, 58].

Such programs, especially ENU, have proved their long-term success but depend very much on having targeted phenotype screens that can be carried out at high throughput and strategies for recovery of the mutated gene. This has become much easier with the development of next-generation sequencing technologies and successful sperm freezing techniques. Two of the first projects were set up in 1997 at the Helmholtz Institute in Munich and the Medical Research Council (MRC) Mammalian genome unit in the United Kingdom. These have been followed by similar projects in Australia, the United States, and Japan and to date more than 20 projects have been run worldwide [59, 60]. These projects have yielded a steady stream of novel mouse models, often generating very useful allelic series across a wide range of domains [55]. Particularly notable is the innate immunity screen set up in Bruce Beutler's laboratory with an innovative methodology for rapidly identifying the mutated allele associated with an immunological phenotype [53].

The work involved in identifying mutant alleles from ENU screens gave rise to the second strategy for randomized mutation – that of using insertional mutagenesis making use of the insertion of transposons, such as Sleeping Beauty or Piggy-Bac, which has high mutagenesis efficiency and makes recovery of mutant alleles relatively straightforward [61].

The most comprehensive strategy, however, has been a reverse genetic strategy to individually knockout every protein-coding gene in the mouse genome one by one, and to phenotype the subsequent strains. The first of these very ambitious projects began in 2007 with the International Knockout Mouse Consortium using a set of tailored constructs for embryonic stem cell (ES cell) mediated homologous recombination, which has been followed up by the use of the much faster CRISPR/Cas9 technology which has sped up this process and completely replaced the various molecular technologies that generated traditional null mutations. CRISPR/Cas9 is capable of generating very precise mutations that can and do mimic polymorphisms found in human populations [42, 62–65].

Unfortunately, results often varied between laboratories, most likely due to differences in environment, genetic background, and experimental approaches. Moreover, many laboratories lacked pathology support. The transition to large scale, partially blind approaches using more standardized methodologies, has greatly expanded and speeded up this process. Early, large-scale, industrialized programs were designed to identify novel drug targets but also proved useful in predicting human disease mutations [66]. Currently the international public sector program, the US NIH Knockout Mouse Program (KOMP) and the International Mouse Phenotyping Consortium (IMPC), has systematically inactivated one gene at a time with a standardized phenotyping program [67]. Development of the comprehensive high throughput phenotyping has been critical in using these mutants to discover information about gene function and to establish new mouse models for human diseases [67, 68] To date more than 18 000 genes have been conditionally knocked out and more than 6000 of these mutant ES cells turned into mouse strains and phenotyped [69]. Combined, these programs have identified many new diseases in mice and humans [70–73].

The importance of phenotype in the approach to model discovery is critical and this has consequently lead to computational approaches to identify candidate genes for human diseases from mouse mutants by comparing phenotypes of patients with unknown lesions, to those of mice with known knockouts. Advances in biosemantics have led to the development of several platforms supporting this approach, based on semantic similarity between phenotypes of two or more species [74–76]. While the approach is able to recapitulate known gene–phenotype relationships most of the time, there remains some concern about the ability of such algorithms to identify new genes due to perceived overfitting of training sets. In addition, the IMPC report that comparing phenotypes from International Knockout Mouse Consortium (IKMC) mutants, made on a C57BL/6N background, to those already in the mouse genome informatics (MGI) database created through hypothesis-driven research showed that only 40% had any phenotype in common at all [68]. While this figure could be due to incomplete or biased phenotyping by investigators, or incorrect phenotyping calls by the IMPC, the likelihood is that it represents strain background effects, an issue that reinforces the need for careful and detailed phenotyping on multiple backgrounds in order to find useful models.

Vet-ebooks.com

From Human Polymorphism to Mouse Models

Some from the clinical genetics community, seeing successes from genome-wide association studies (GWAS), claim that with modern genetics and next generation sequencing "the model for the human is now the human" and the use of other organisms is redundant. However, when combined with human genetic studies, such as GWAS for complex genetic diseases, it is now possible to reverse engineer mouse models from development toward validation of the human discoveries. This has been ongoing for many years using traditional recombineering approaches. For example, mutations in the *Abcc6*, ATP-binding cassette, sub-family C (CFTR/MRP), member and member 6 (*ABCC6*) gene were identified by several groups to cause pseudoxanthoma elasticum (PXE) in humans, a systemic disease characterized by ectopic mineralization. Two groups made null mutations of this gene in mice that recapitulated many of the phenotypes seen in humans [77, 78]. Many other genes produce genocopies of ectopic mineralization, and the discovery of four inbred strains with the same spontaneous *Abcc6* hypomorphic allele but very different severity of PXE lesions [79] revealed many modifier genes in the mouse and by extension in humans [42].

Complex human genetic diseases, such as psoriasis, have been difficult to model in mice [80]. However, GWAS studies identified several single nucleotide polymorphisms in the caspase recruitment domain family, member 14 (*CARD14*) gene [81, 82]. One of these single nucleotide polymorphism (SNPs) was reproduced by three different laboratories in mice, all of which recapitulated the skin disease [83–85]. One lab made the second allelic mutation, which did not have any effect [85]. These are a few of many examples where genetic engineering in mice can either validate or fail to match molecular discoveries in human patient cohorts.

New Mouse Genetic Tools

The power of mouse genetics is being increasingly exploited, for example by using the resources of inbred strains which are now being used to construct genetic reference populations, such as the Collaborative Cross [86], which mimics the genetic complexity of human populations and the Diversity Outcross mice, a stock of truly outbred mice derived from the incipient inbred collaborative cross strains [87], that can provide defined heterozygosity. Together with the ability to manipulate the genome through reverse genetics, these novel mouse genetic tools provide complementarity to human clinical and genetic studies never before available. Medicine will continue to face major challenges for which mouse models will prove to be invaluable; for example, the ability to predict whether a particular individual will develop one or more of hundreds of different diseases for which they carry predisposing alleles, the accurate prediction of risk or prognosis or a particular disease in an individual and the prioritization of the many candidate genes arising from GWAS studies [88–90]. Success in translational research depends on the combined efforts of investigators in the laboratory and clinic to create the ideal slippers (mice) for Cinderella to go to the Ball.

Patient Derived Xenograft (PDX) Models

Mouse cancer models, be they spontaneous, induced by a variety of means, or genetically engineered, have been invaluable as tools to dissect underlying mechanisms of disease. However, they have had a smaller impact on translational studies to directly impact cancer treatment in humans. Development of refined immunodeficient mouse models [64, 91] has enabled engraftment of human cancer cells into these mice providing a tool to directly assess the human cancers in this xenograft model. These patient derived xenografts (PDX models) are used for target-validation and drug-assessment studies [92].

Acknowledgments

The authors thank Zoe Reifsneider for her help in preparing the graphics. This work was supported in part by grants from the National Institutes of Health (R13 OD010920, to JPS and JMW; R01-CA089713 and P30-CA034196 to JPS) and the European Union (Teacher, Erasmus+ Programme of the Commission of the European Union H2020, 600803-EPP-1-2018-1-ES-EPPKA2; to JPS, PNS, and PV).

References

1 Sundberg, J.P., Roopenian, D.C., Liu, E.T., and Schofield, P.N. (2013). The Cinderella effect: searching for the best fit between mouse models and human diseases. *J. Invest. Dermatol.* 133 (11): 2509–2513.

2 Seok, J., Warren, H.S., Cuenca, A.G. et al. (2013). Genomic responses in mouse models poorly mimic human inflammatory diseases. *Proc. Natl. Acad. Sci. U.S.A.* 110 (9): 3507–3512.

3 Takao, K. and Miyakawa, T. (2015). Genomic responses in mouse models greatly mimic human inflammatory diseases. *Proc. Natl. Acad. Sci. U.S.A.* 112 (4): 1167–1172.

4 Shay, T., Lederer, J.A., and Benoist, C. (2015). Genomic responses to inflammation in mouse models mimic humans: we concur, apples to oranges comparisons won't do. *Proc. Natl. Acad. Sci. U.S.A.* 112 (4): E346.

Vet-ebooks.com

5 Lu, Y.F., Goldstein, D.B., Angrist, M., and Cavalleri, G. (2014). Personalized medicine and human genetic diversity. *Cold Spring Harb. Perspect. Med.* 4 (9): a008581.

6 Selman, C. and Swindell, W.R. (2018). Putting a strain on diversity. *EMBO J.* 37 (22): e100862. https://doi.org/10.15252/embj.2018100862.

7 Threadgill, D.W., Dlugosz, A.A., Hansen, L.A. et al. (1995). Targeted disruption of mouse EGF receptor: effect of genetic background on mutant phenotype. *Science* 269 (5221): 230–234.

8 Sibilia, M. and Wagner, E.F. (1995). Strain-dependent epithelial defects in mice lacking the EGF receptor. *Science* 269 (5221): 234–238.

9 Bubier, J.A., Sproule, T.J., Alley, L.M. et al. (2010). A mouse model of generalized non-Herlitz junctional epidermolysis bullosa. *J. Invest. Dermatol.* 130 (7): 1819–1828.

10 Sproule, T.J., Bubier, J.A., Grandi, F.C. et al. (2014). Molecular identification of collagen 17a1 as a major genetic modifier of laminin gamma 2 mutation-induced junctional epidermolysis bullosa in mice. *PLoS Genet.* 10 (2): e1004068.

11 Scarpelli, D.G., Capen, C.C., Cork, L.C. et al. (1985). Animal models of human disease. In: (ed. G. Migaki), 302–321. Washington, DC: Armed Forces Institute of Pathology.

12 McElwee, K.J., Boggess, D., King, L.E. Jr., and Sundberg, J.P. (1998). Experimental induction of alopecia areata-like hair loss in C3H/HeJ mice using full-thickness skin grafts. *J. Invest. Dermatol.* 111 (5): 797–803.

13 Nishina, P.M., Verstuyft, J., and Paigen, B. (1990). Synthetic low and high fat diets for the study of atherosclerosis in the mouse. *J. Lipid Res.* 31 (5): 859–869.

14 Hudson, A., Trider, C.-L., and Blake, K. (2017). CHARGE syndrome. *Pediatr. Rev.* 38 (1): 56.

15 Jongmans, M.C.J., Admiraal, R.J., van der Donk, K.P. et al. (2006). CHARGE syndrome: the phenotypic spectrum of mutations in the *CHD7* gene. *J. Med. Genet.* 43 (4): 306–314.

16 Bosman, E.A., Penn, A.C., Ambrose, J.C. et al. (2005). Multiple mutations in mouse *Chd7* provide models for CHARGE syndrome. *Hum. Mol. Genet.* 14 (22): 3463–3476.

17 van Ravenswaaij-Arts, C. and Martin, D.M. (2017). New insights and advances in CHARGE syndrome: diagnosis, etiologies, treatments, and research discoveries. *Am. J. Med. Genet. C Semin. Med. Genet.* 175 (4): 397–406.

18 Gage, P.J., Hurd, E.A., and Martin, D.M. (2015). Mouse models for the dissection of *CHD7* functions in eye development and the molecular basis for ocular defects in CHARGE syndrome. *Invest. Ophthalmol. Vis. Sci.* 56 (13): 7923–7930.

19 Lutzner, M.A., Lowrie, C.T., and Jordan, H.W. (1967). Giant granules in leukocytes of the beige mouse. *J. Hered.* 58 (6): 299–300.

20 Penner, J.D. and Prieur, D.J. (1987). A comparative study of the lesions in cultured fibroblasts of humans and four species of animals with Chediak-Higashi syndrome. *Am. J. Med. Genet.* 28 (2): 445–454.

21 Penner, J.D. and Prieur, D.J. (1987). Interspecific genetic complementation analysis with fibroblasts from humans and four species of animals with Chediak-Higashi syndrome. *Am. J. Med. Genet.* 28 (2): 455–470.

22 Schofield, P.N., Vogel, P., Gkoutos, G.V., and Sundberg, J.P. (2012). Exploring the elephant: histopathology in high-throughput phenotyping of mutant mice. *Dis. Models Mech.* 5 (1): 19–25.

23 Mezick, J.A., Bhatia, M.C., and Capetola, R.J. (1984). Topical and systemic effects of retinoids on horn-filled utriculus size in the rhino mouse. A model to quantify "antikeratinizing" effects of retinoids. *J. Invest. Dermatol.* 83 (2): 110–113.

24 Ashton, R.E., Connor, M.J., and Lowe, N.J. (1984). Histologic changes in the skin of the rhino mouse (Hr^{rh}/Hr^{rh}) induced by retinoids. *J. Invest. Dermatol.* 82 (6): 632–635.

25 Bryce, G.F., Bogdan, N.J., and Brown, C.C. (1988). Retinoic acids promote the repair of the dermal damage and the effacement of wrinkles in the UVB-irradiated hairless mouse. *J. Invest. Dermatol.* 91 (2): 175–180.

26 Kligman, L.H. (1989). Prevention and repair of photoaging: sunscreens and retinoids. *Cutis* 43 (5): 458–465.

27 Sundberg, J.P., Dunstan, R.W., and Compton, J.G. (1989). Hairless mouse, HRS/J *hr/hr*. In: *Integument and Mammary Glands Monographs on Pathology of Laboratory Animals* (eds. T.C. Jones, U. Mohr and R.D. Hunt), 192–197. Heidelberg: Springer-Verlag.

28 Sundberg, J.P., Price, V.H., and King, L.E. Jr. (1999). The "hairless" gene in mouse and man. *Arch. Dermatol.* 135 (6): 718–720.

29 Ahmad, W., Faiyaz ul Haque, M., Brancolini, V. et al. (1998). Alopecia universalis associated with a mutation in the human hairless gene. *Science* 279 (5351): 720–724.

30 Ahmad, W., Irvine, A.D., Lam, H. et al. (1998). A missense mutation in the zinc-finger domain of the human hairless gene underlies congenital atrichia in a family of Irish travellers. *Am. J. Hum. Genet.* 63 (4): 984–991.

31 Ahmad, W., Panteleyev, A.A., Henson-Apollonio, V. et al. (1998). Molecular basis of a novel rhino (hr^{rhChr}) phenotype: a nonsense mutation in the mouse hairless gene. *Exp. Dermatol.* 7 (5): 298–301.

32 Ahmad, W., Panteleyev, A.A., Sundberg, J.P., and Christiano, A.M. (1998). Molecular basis for the rhino ($Hr^{rh\text{-}8J}$) phenotype: a nonsense mutation in the mouse hairless gene. *Genomics* 53 (3): 383–386.

33 Panteleyev, A.A., Ahmad, W., Malashenko, A.M. et al. (1998). Molecular basis for the rhino Yurlovo ($hr^{(rhY)}$) phenotype: severe skin abnormalities and female reproductive defects associated with an insertion in the hairless gene. *Exp. Dermatol.* 7 (5): 281–288.

34 Panteleyev, A.A., Paus, R., Ahmad, W. et al. (1998). Molecular and functional aspects of the hairless (*Hr*) gene in laboratory rodents and humans. *Exp. Dermatol.* 7 (5): 249–267.

35 Tuttle, A.H., Philip, V.M., Chesler, E.J., and Mogil, J.S. (2018). Comparing phenotypic variation between inbred and outbred mice. *Nat. Methods* 15 (12): 994–996.

Vet-ebooks.com

36 McElwee, K.J., Niiyama, S., Freyschmidt-Paul, P. et al. (2003). Dietary soy oil content and soy-derived phytoestrogen genistein increase resistance to alopecia areata onset in C3H/HeJ mice. *Exp. Dermatol.* 12 (1): 30–36.

37 Ward, J.M. and Devor-Henneman, D.E. (2004). Mouse models of human familial cancer syndromes. *Toxicol. Pathol.* 32 (Suppl 1): 90–98.

38 Kuperwasser, C., Hurlbut, G.D., Kittrell, F.S. et al. (2000). Development of spontaneous mammary tumors in BALB/c *p53* heterozygous mice. A model for Li-Fraumeni syndrome. *Am. J. Pathol.* 157 (6): 2151–2159.

39 Sundberg, J.P. and Schofield, P.N. (2018). Living inside the box: environmental effects on mouse models of human disease. *Dis. Models Mech.* 11 (10): dmm035360. https://doi.org/10.1242/dmm.035360.

40 Sofaer, J.A. (1969). Aspects of the tabby-crinkled-downless syndrome. II. Observations on the reaction to changes of genetic background. *J. Embryol. Exp. Morphol.* 22 (2): 207–227.

41 Sofaer, J.A. (1969). Aspects of the tabby-crinkled-downless syndrome. I. The development of tabby teeth. *J. Embryol. Exp. Morphol.* 22 (2): 181–205.

42 Li, Q., Philip, V.M., Stearns, T.M. et al. (2019). Quantitative trait locus and integrative genomics revealed candidate modifier genes for ectopic mineralization in mouse models of pseudoxanthoma elasticum. *J. Invest. Dermatol.* 139 (12): 2447–2457.e7.

43 Montagutelli, X., Hogan, M.E., Aubin, G. et al. (1996). Lanceolate hair (*lah*): a recessive mouse mutation with alopecia and abnormal hair. *J. Invest. Dermatol.* 107 (1): 20–25.

44 Sundberg, J.P., Boggess, D., Bascom, C. et al. (2000). Lanceolate hair-J (*lahJ*): a mouse model for human hair disorders. *Exp. Dermatol.* 9 (3): 206–218.

45 Chavanas, S., Bodemer, C., Rochat, A. et al. (2000). Mutations in SPINK5, encoding a serine protease inhibitor, cause Netherton syndrome. *Nat. Genet.* 25 (2): 141–142.

46 Kljuic, A., Bazzi, H., Sundberg, J.P. et al. (2003). Desmoglein 4 in hair follicle differentiation and epidermal adhesion: evidence from inherited hypotrichosis and acquired pemphigus vulgaris. *Cell* 113 (2): 249–260.

47 Price, V.H., Odom, R.B., Ward, W.H., and Jones, F.T. (1980). Trichothiodystrophy: sulfur-deficient brittle hair as a marker for a neuroectodermal symptom complex. *Arch. Dermatol.* 116 (12): 1375–1384.

48 Gummer, C.L., Dawber, R.P., and Price, V.H. (1984). Trichothiodystrophy: an electron-histochemical study of the hair shaft. *Br. J. Dermatol.* 110 (4): 439–449.

49 Metze, D. and Oji, V. (2020). Disorders of keratinization. In: *McKee's Pathology of the Skin. 1*., 5e (eds. E. Calonje, T. Brenn, A. Lazar and S.D. Billings), 53–117. China: Elsevier.

50 Mecklenburg, L., Paus, R., Halata, Z. et al. (2004). FOXN1 is critical for onycholemmal terminal differentiation in nude (*Foxn1*) mice. *J. Invest. Dermatol.* 123 (6): 1001–1011.

51 Davisson, M.T., Bergstrom, D.E., Reinholdt, L.G., and Donahue, L.R. (2012). Discovery genetics – the history and future of spontaneous mutation research. *Curr. Protoc. Mouse Biol.* 2: 103–118.

52 Probst, F.J. and Justice, M.J. (2010). Mouse mutagenesis with the chemical supermutagen ENU. *Methods Enzymol.* 477: 297–312.

53 Arnold, C.N., Barnes, M.J., Berger, M. et al. (2012). ENU-induced phenovariance in mice: inferences from 587 mutations. *BMC Res. Notes* 5: 577.

54 Sabrautzki, S., Rubio-Aliaga, I., Hans, W. et al. (2012). New mouse models for metabolic bone diseases generated by genome-wide ENU mutagenesis. *Mamm. Genome* 23 (7-8): 416–430.

55 Potter, P.K., Bowl, M.R., Jeyarajan, P. et al. (2016). Novel gene function revealed by mouse mutagenesis screens for models of age-related disease. *Nat. Commun.* 7: 12444.

56 Wang, T., Bu, C.H., Hildebrand, S. et al. (2018). Probability of phenotypically detectable protein damage by ENU-induced mutations in the Mutagenetix database. *Nat. Commun.* 9 (1): 441.

57 Fairfield, H., Srivastava, A., Ananda, G. et al. (2015). Exome sequencing reveals pathogenic mutations in 91 strains of mice with Mendelian disorders. *Genome Res.* 25 (7): 948–957.

58 Palmer, K., Fairfield, H., Borgeia, S. et al. (2016). Discovery and characterization of spontaneous mouse models of craniofacial dysmorphology. *Dev. Biol.* 415 (2): 216–227.

59 Andrews, T.D., Whittle, B., Field, M.A. et al. (2012). Massively parallel sequencing of the mouse exome to accurately identify rare, induced mutations: an immediate source for thousands of new mouse models. *Open Biol.* 2 (5): 120061. https://doi.org/10.1098/rsob.120061.

60 Gondo, Y. (2008). Trends in large-scale mouse mutagenesis: from genetics to functional genomics. *Nat. Rev. Genet.* 9 (10): 803–810.

61 Chang, H., Pan, Y., Landrette, S. et al. (2019). Efficient genome-wide first-generation phenotypic screening system in mice using the piggyBac transposon. *Proc. Natl. Acad. Sci. U.S.A.* 116 (37): 18507–18516.

62 Birling, M.C., Herault, Y., and Pavlovic, G. (2017). Modeling human disease in rodents by CRISPR/Cas9 genome editing. *Mamm. Genome* 28 (7-8): 291–301.

63 Brehm, M.A., Wiles, M.V., Greiner, D.L., and Shultz, L.D. (2014). Generation of improved humanized mouse models for human infectious diseases. *J. Immunol. Methods* 410: 3–17.

64 Hosur, V., Low, B.E., Avery, C. et al. (2017). Development of humanized mice in the age of genome editing. *J. Cell. Biochem.* 118 (10): 3043–3048.

65 Low, B.E., Krebs, M.P., Joung, J.K. et al. (2014). Correction of the *Crb1*^{rd8} allele and retinal phenotype in C57BL/6N mice via TALEN-mediated homology-directed repair. *Invest. Ophthalmol. Vis. Sci.* 55 (1): 387–395.

66 Brommage, R., Powell, D.R., and Vogel, P. (2019). Predicting human disease mutations and identifying drug targets from mouse gene knockout phenotyping campaigns. *Dis. Models Mech.* 12 (5).

Vet-ebooks.com

67 Bradley, A., Anastassiadis, K., Ayadi, A. et al. (2012). The mammalian gene function resource: the International Knockout Mouse Consortium. *Mamm. Genome* 23 (9-10): 580–586.

68 Meehan, T.F., Conte, N., West, D.B. et al. (2017). Disease model discovery from 3,328 gene knockouts by The International Mouse Phenotyping Consortium. *Nat. Genet.* 49 (8): 1231–1238.

69 Kaloff, C., Anastassiadis, K., Ayadi, A. et al. (2016). Genome wide conditional mouse knockout resources. *Drug Discovery Today* 20: 3–12.

70 Dickinson, M.E., Flenniken, A.M., Ji, X. et al. (2016). High-throughput discovery of novel developmental phenotypes. *Nature* 537 (7621): 508–514.

71 Moore, B.A., Leonard, B.C., Sebbag, L. et al. (2018). Identification of genes required for eye development by high-throughput screening of mouse knockouts. *Commun. Biol.* 1: 236.

72 Rozman, J., Rathkolb, B., Oestereicher, M.A. et al. (2018). Identification of genetic elements in metabolism by high-throughput mouse phenotyping. *Nat. Commun.* 9 (1): 288.

73 Sundberg, J.P., Dadras, S.S., Silva, K.A. et al. (2017). Systematic screening for skin, hair, and nail abnormalities in a large-scale knockout mouse program. *PLoS One* 12 (7): e0180682.

74 Smedley, D., Oellrich, A., Köhler, S. et al. (2013). PhenoDigm: analyzing curated annotations to associate animal models with human diseases. *Database* 2013: bat025. https://doi.org/10.1093/database/bat025.

75 Hoehndorf, R., Schofield, P.N., and Gkoutos, G.V. (2013). An integrative, translational approach to understanding rare and orphan genetically based diseases. *Interface Focus* 3 (2): 20120055.

76 Hoehndorf, R., Schofield, P.N., and Gkoutos, G.V. (2011). PhenomeNET: a whole-phenome approach to disease gene discovery. *Nucleic Acids Res.* 39 (18): e119.

77 Klement, J.F., Matsuzaki, Y., Jiang, Q.J. et al. (2005). Targeted ablation of the *Abcc6* gene results in ectopic mineralization of connective tissues. *Mol. Cell. Biol.* 25 (18): 8299–8310.

78 Gorgels, T.G., Hu, X., Scheffer, G.L. et al. (2005). Disruption of *Abcc6* in the mouse: novel insight in the pathogenesis of pseudoxanthoma elasticum. *Hum. Mol. Genet.* 14 (13): 1763–1773.

79 Berndt, A., Li, Q., Potter, C.S. et al. (2013). A single-nucleotide polymorphism in the *Abcc6* gene associates with connective tissue mineralization in mice similar to targeted models for pseudoxanthoma elasticum. *J. Invest. Dermatol.* 133 (3): 833–836.

80 Hawkes, J.E., Adalsteinsson, J.A., Gudjonsson, J.E., and Ward, N.L. (2018). Research techniques made simple: murine models of human psoriasis. *J. Invest. Dermatol.* 138 (1): e1–e8.

81 Jordan, C.T., Cao, L., Roberson, E.D. et al. (2012). Rare and common variants in *CARD14*, encoding an epidermal regulator of NF-kappaB, in psoriasis. *Am. J. Hum. Genet.* 90 (5): 796–808.

82 Jordan, C.T., Cao, L., Roberson, E.D. et al. (2012). PSORS2 is due to mutations in *CARD14*. *Am. J. Hum. Genet.* 90 (5): 784–795.

83 Mellett, M., Meier, B., Mohanan, D. et al. (2018). *CARD14* gain-of-function mutation alone is sufficient to drive IL-23/IL-17-mediated psoriasiform skin inflammation in vivo. *J. Invest. Dermatol.* 138 (9): 2010–2023.

84 Wang, M., Zhang, S., Zheng, G. et al. (2018). Gain-of-function mutation of *Card14* leads to spontaneous psoriasis-like skin inflammation through enhanced keratinocyte response to IL-17A. *Immunity* 49 (1): 66–79. e5.

85 Sundberg, J.P., Pratt, C.H., Silva, K.A. et al. (2019). Gain of function p.E138A alteration in *Card14* leads to psoriasiform skin inflammation and implicates genetic modifiers in disease severity. *Exp. Mol. Pathol.* 110: 104286.

86 Threadgill, D.W. and Churchill, G.A. (2012). Ten years of the collaborative cross. *G3* 2 (2): 153–156.

87 Svenson, K.L., Gatti, D.M., Valdar, W. et al. (2012). High-resolution genetic mapping using the Mouse Diversity outbred population. *Genetics* 190 (2): 437–447.

88 Schofield, P.N., Hoehndorf, R., and Gkoutos, G.V. (2012). Mouse genetic and phenotypic resources for human genetics. *Hum. Mutat.* 33 (5): 826–836.

89 Lehner, B. (2013). Genotype to phenotype: lessons from model organisms for human genetics. *Nat. Rev. Genet.* 14 (3): 168–178.

90 Cox, R.D. and Church, C.D. (2011). Mouse models and the interpretation of human GWAS in type 2 diabetes and obesity. *Dis. Models Mech.* 4 (2): 155–164.

91 Shultz, L.D., Keck, J., Burzenski, L. et al. (2019). Humanized mouse models of immunological diseases and precision medicine. *Mamm. Genome* 30 (5-6): 123–142.

92 Bernards, R., Jaffee, E., Joyce, J.A. et al. (2020). A roadmap for the next decade in cancer research. *Nat. Cancer.* 1: 12–17.

Vet-ebooks.com

5

Embryos, Placentas, and Neonates

Brad Bolon and Jerrold M. Ward

Introduction

Comparative pathologists who evaluate adult mice can phenotype developing mice as well. However, new practitioners will need to attain familiarity with unusual anatomic features, physiological processes, and lesion patterns that are the norm in embryos and neonates. Most investigators approach histopathological evaluation of late-stage embryos (gestational day [GD] 15.5 or older), neonates, and juveniles (up to postnatal day [PND] 42) with confidence due to anatomic similarities between these developmental stages and adult mice. This assurance fades when the rapidly evolving morphology of earlier embryos and their extra-embryonic membranes needs to be characterized.

This chapter offers a brief introduction to key anatomical and pathophysiological concepts in prenatal and early postnatal mice. More detailed coverage of specific mouse developmental anatomy and pathology topics is available in other books [1–5], book chapters [6–9], anatomic atlases [10–15], major review articles [16–27], and websites [15, 28–30].

Four-Dimensional Anatomy of the Developing Mouse

Stages of mouse development are defined in terms of major events in four dimensions: length, width, breadth, and time (Figure 5.1). Specific stages typically are assigned using the Theiler staging (TS) system based on visible anatomic landmarks [11, 15, 29, 31, 32]. Timing for each event varies by up to 12 hours among strains with different genetic backgrounds [33, 34]. Furthermore, the developmental stages in any litter differ by between 10 to 24 hours for the oldest and youngest embryos (Figure 5.2) [2, 11, 33]. Accordingly, developmental stage is not equal to developmental age for prenatal mice. *In utero* age is assigned as either "days *post coitum*" (dpc) or as "gestational day" (GD, often referred to as "embryonic day" [E]). When using the GD (or E) timing convention, it is imperative that investigators note whether the day of conception is counted as GD0 or GD1 since this choice will dramatically impact the times assigned to developmental landmarks. The convention used in this chapter is that the presence of a vaginal plug is designated as 0 dpc (or GD0).

Developmental Events in Embryos and Neonates

In mice, conception for all members of a litter occurs on average at GD0.5. At about GD1.0, the free-floating zygotes (i.e. one-celled embryos) begin the first of multiple rounds of cell division as they travel down the oviduct. Embryos enter the uterus at about GD2.5 as morulae (solid multicelled masses) and evolve into blastocysts with an off-center, fluid-filled cavity at about GD3.0. Dilation of this cavity is accompanied by differentiation of the first embryonic tissues: the inner cell mass (ICM), a crescentic group of pluripotent stem cells at one pole that will become the embryo proper, and the trophectoderm, which forms the outer wall of the blastocyst and will differentiate into the extra-embryonic membranes (i.e. placenta). Evolution from morula to blastocyst is accompanied by increased activity of the embryonic genome and substantial strain-specific metabolic changes.

Embryos implant in the uterine wall at about GD4.5. Prior to implantation, cross-talk between the uterine wall and blastocyst results in production of a highly permeable, well-vascularized endometrial layer, termed "decidua," that promotes embryo attachment and survival [35, 36]. The decidual reaction provides the primary means for sustaining the embryos until they form their own placenta. Upon implantation, the trophectoderm proliferates, invades the decidua, and then differentiates into syncytiotrophoblasts (which border the maternal tissue) and cytotrophoblasts (which envelop the ICM). Reciprocal interactions between the embryos and decidua are essential in maintaining pregnancy [37, 38].

By GD5.0, the implanted round blastocyst morphs into an elongated "egg cylinder," and distinct embryonic and

Pathology of Genetically Engineered and Other Mutant Mice, First Edition. Edited by John P. Sundberg, Peter Vogel, and Jerrold M. Ward.
© 2022 John Wiley & Sons, Inc. Published 2022 by John Wiley & Sons, Inc.

Vet-ebooks.com

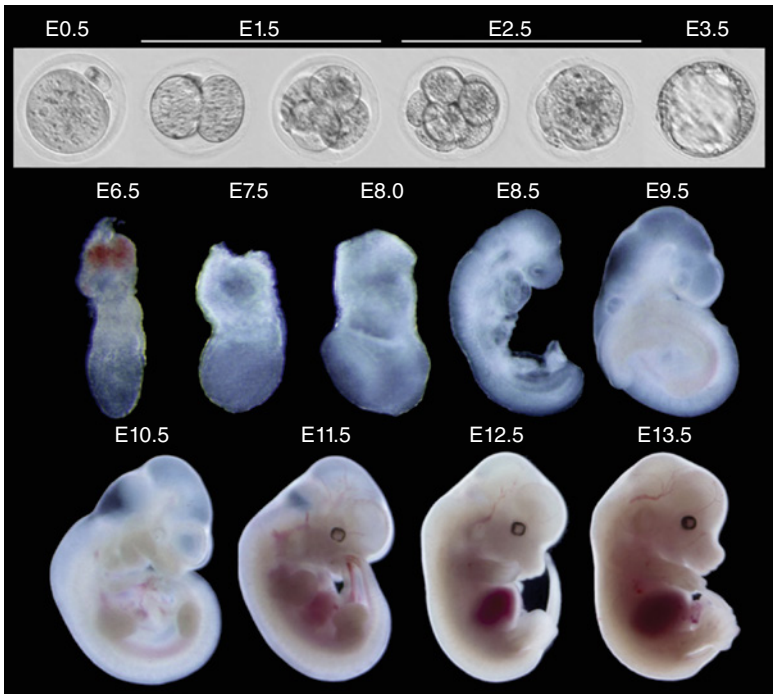


Figure 5.1 Composite image of embryonic mouse developmental stages from just after conception (at embryonic day [E] 0.5, in upper left) throughout preimplantation (E1.5 to E3.5, remainder of upper row) and during early postimplantation (E6.5) to mid-gestation (E13.5). Source: Dr. Yi Zhang, Harvard Medical School and the Howard Hughes Medical Institute.



Apparent age: GD13
Chronological age: GD13

Apparent age: GD12
Chronological age: GD13

Figure 5.2 Mouse embryo littermates with a shared chronological age at gestational day (GD) 13 but having anatomic features demonstrating different developmental stages: GD13 (Theiler stage [TS] 21) on the left as shown by discrete linear gray rays denoting the sites of future digit separation on the paddle-shaped forepaw (F) and hind paw (H) limb buds, but GD12 (TS20) on the right as shown by the absence of digital rays on the forelimb buds. Digital rays usually form on the forelimb bud at about GD12.3 and on the hind limb bud at about GD12.8. Source: Bolon and La Perle [89] with permission of CRC Press.

placental features begin to form. At this stage, the ectoplacental cone appears as a triangle of extra-embryonic tissue that invades the mesometrial decidua at one pole of the egg cylinder. Simultaneously, the ICM differentiates into the epiblast, an outer layer of columnar cells that will give rise to three embryonic germ layers (ectoderm, mesoderm, and endoderm) as well as some extra-embryonic ectoderm and mesoderm, and the hypoblast, a thin inner layer of cuboidal cells that will produce the yolk sac (YS) endoderm and some extra-embryonic mesoderm. Generation of germ layers by the epiblast begins on GD6.0 with the ectoderm and endoderm, with formation of the mesoderm (a process called "gastrulation") beginning at about GD6.5 and lasting until about GD7.5.

Organogenesis begins at about GD7.5 and lasts until GD15.0. During this portion of embryonic development, all major organ precursors (termed "anlagen") undergo initial specification and generation. Organ structures and the external appearance of the embryo only approximate the adult conformation at the end of organogenesis. Different organs, and parts of organs, are initiated at different "critical periods" throughout this time range so that the developmental path for most organs extends across several days [39]. These critical periods represent times of intense cell proliferation, migration, and differentiation, and thus define organ-, region-, and cell type-specific times of heightened vulnerability to endogenous and exogenous insults [40, 41]. An oft forgotten fact is that for some organs, such as brain and

Vet-ebooks.com

lymph nodes, critical periods occur not only during gestation but also after birth [42, 43].

The last few days of gestation (GD15.0 to term) and the first few days after birth (up to PND7 or so) correspond to the fetal period in primate embryos. This phase represents a period of organ growth. With some exceptions, organs acquire their adult appearance at this time, although function often is decreased in neonatal and juvenile animals relative to adult systems.

Developmental Events in Placentation

The placenta is the first organ created by a newly implanted embryo (GD5.0), although its form varies considerably until the definitive placenta (DP) becomes active (GD12.5). The placenta acts as an interface for exchanging gases and organic molecules between the embryonic and maternal circulations, a hormone source that regulates maternal processes need to sustain pregnancy, and a protective environment for embryonic survival and growth. The decidua also serves as a barrier to reduce immunogenicity of embryonic proteins. The structure, function, and molecular signature of the placenta is revised greatly over time in response to the growing embryo's evolving metabolic demands [4, 16, 17, 44, 45].

The YS is the first functional placenta (Figure 5.3). It forms shortly after implantation and acts until about GD10.5 as the sole means of gas exchange (by diffusion) and macromolecular transfer (by trophoblast phagocytosis, a process termed "histiotrophic nutrition") [45, 46]. The YS also serves as the main hematopoietic organ in embryos from about GD8 to GD11 by virtue of the "blood islands" that form at multiple sites near YS blood vessels [8].

At about GD12.5, the DP becomes the main functionally mature placenta (Figure 5.4). This transition is required to provide enhanced blood flow for increased nutrient exchange (a process termed "hemotrophic nutrition"). The mouse DP is a discoid, trihemochorial, chorioallantoic-derived interface. A discoid arrangement indicates that the region for gas and nutrient exchange is a discrete mass rather than spread over the entire placental surface, while the trihemochorial organization means that maternal blood runs in blood-filled labyrinth trophoblast-lined channels lacking an endothelial lining (termed "sinusoids") and embryonic blood flows through a dense labyrinth comprised of embryonic endothelial-lined embryonic capillaries that are surrounded by one to three embryonic trophoblast layers. The chorioallantoic derivation means that the DP originates from both chorionic plate (extra-embryonic ectoderm) and allantois (extra-embryonic mesoderm) [45].

The late-gestation placenta consists of multiple distinct regions, which are discerned based on their location and distinct cell composition (Figures 5.3–5.5). The amnion is a thin, translucent membrane that envelops the embryo. The next membrane further from the embryo is the YS, which now is highly vascular and covered on its outer surface by an acellular matrix termed Reichert's membrane (RM). The allantois is a thin, irregular column extending from the

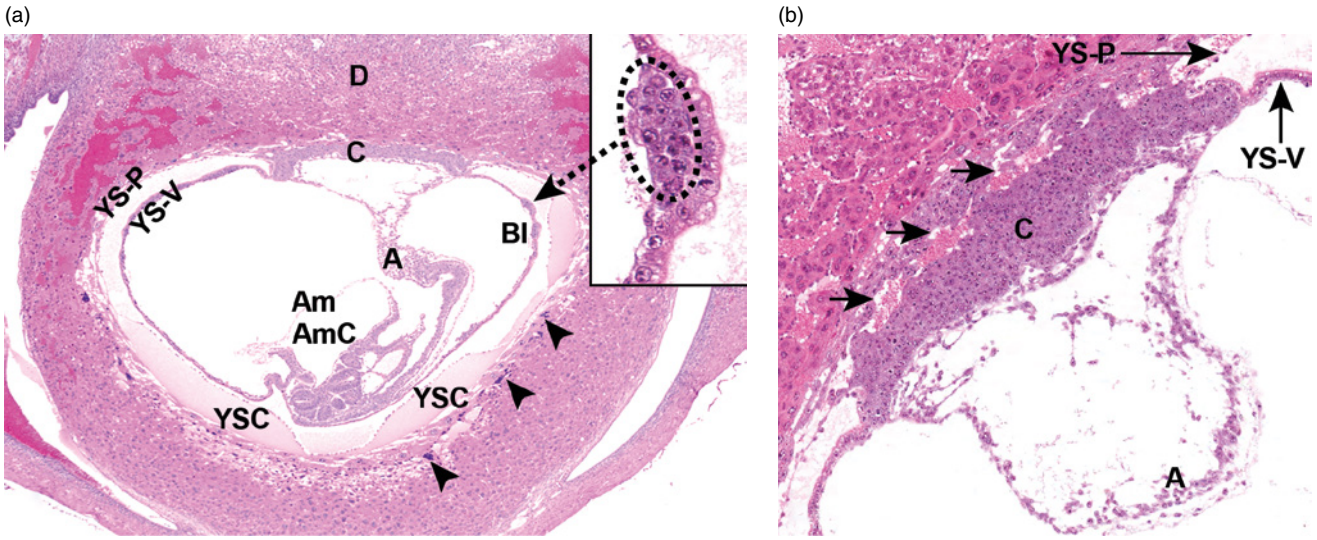


Figure 5.3 The early placenta (shown here at GD8.5) consists chiefly of maternal decidua (D) and the embryonic yolk sac (YS), separated at their interface by trophoblast giant cells (arrowheads). The YS consists of visceral (inner, YS-V) and parietal (outer, YS-P) layers. Blood islands (BI, circled in inset of Panel (a)) form in the YS-V as the source of primitive hematopoietic cell precursors. The YS-P rests atop Reichert's membrane, a rodent-specific tough basement membrane that is not visible here. The allantois (A) is a mesodermal projection (i.e. the nascent umbilical cord) connecting the caudal end of the embryo proper to the flat, broad epithelial plate known as the chorion (C), which forms centrally at the base of the embryonic placenta. The amnion (Am) is a thin membrane that eventually will envelop the entire embryo. Short arrows (in (b)) indicate large embryonic blood vessels in the chorion that connect to umbilical cord blood vessels. Abbreviations: AmC = amniotic cavity, YSC = yolk sac cavity. Stain: H&E. Sources: Bolon [96] with permission of Elsevier, and Bolon and Ward [39] with permission of CRC Press.

Vet-ebooks.com

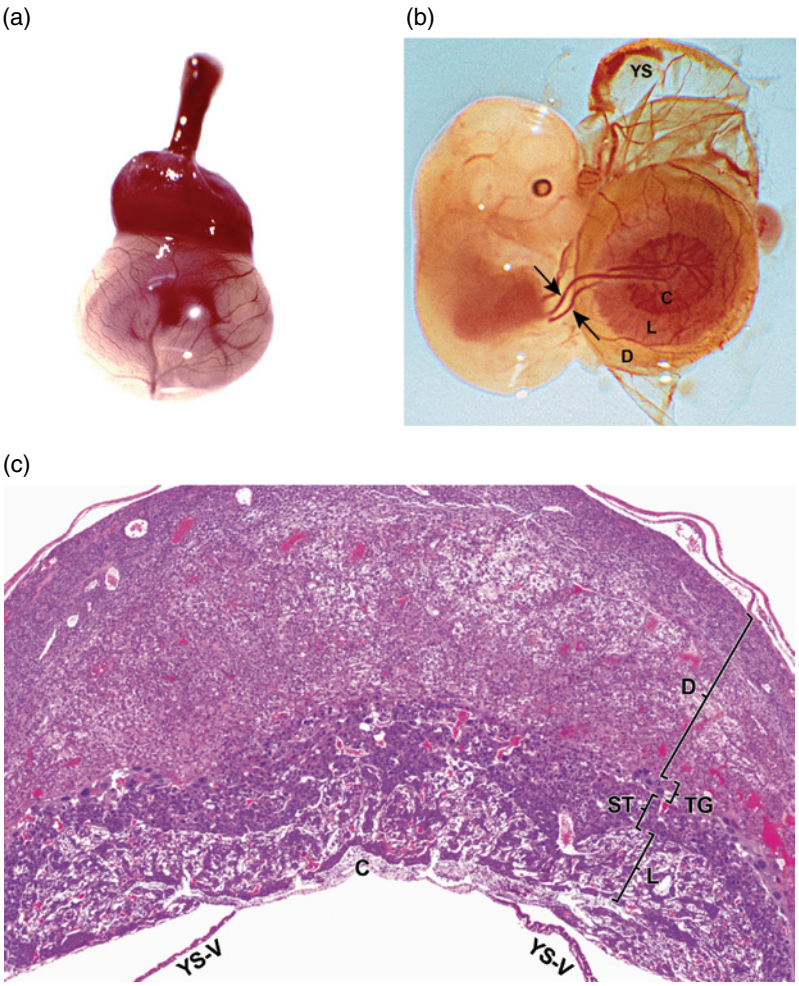


Figure 5.4 The definitive placenta forms fully by GD12.5 (Panel (a)), appearing while intact as a discoid, highly vascularized mass capping the mesometrial pole of the thin, highly vascularized, translucent yolk sac (YS). After dissection (Panel (b)), the discoid cap at GD12.5 may be seen to consist of three concentric zones: the chorion (C) centrally, to which the umbilical blood vessels (arrows) are anchored; labyrinth (L); and decidua (D). Microscopically when viewed in mid-axial cross-section (Panel (c)), the definitive placenta at GD12.5 displays many cytoarchitecturally distinct structures, the chief of which are the labyrinth, junctional zone (comprised of the spongiotrophoblast [ST] and trophoblast giant cell [TG] layers), and decidua. Other abbreviation: YS-V = visceral portion of the yolk sac. Stain (Panel (c)): H&E. Sources: Ward and Devor-Henneman [44] with permission of Iowa State University Press, and Bolon and Ward [39] with permission of CRC Press.

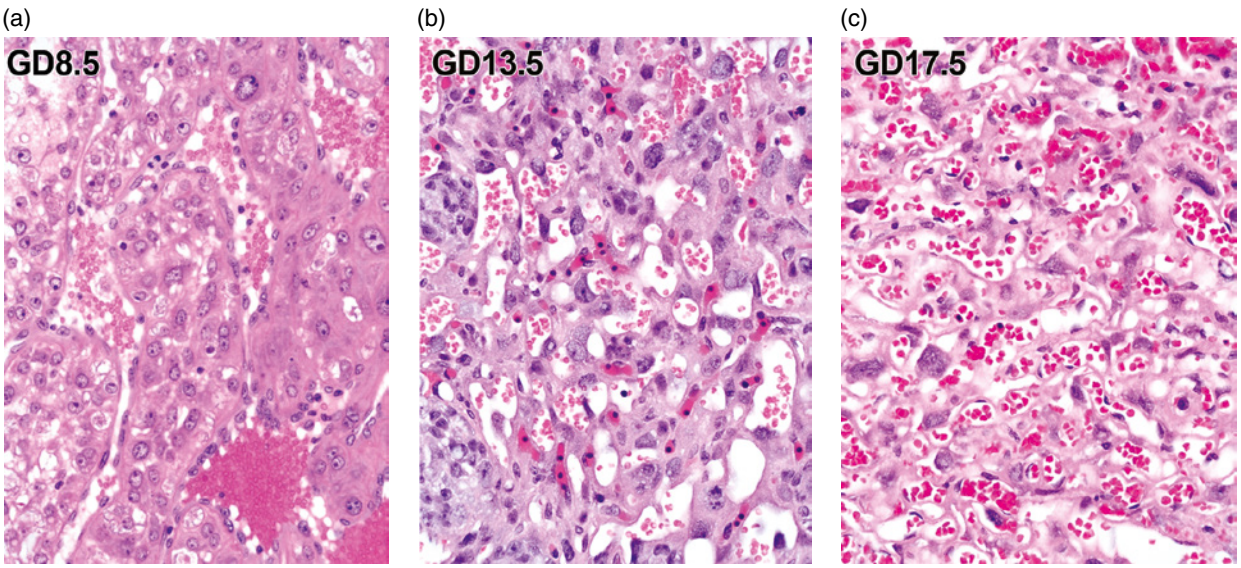


Figure 5.5 The labyrinth of the placenta (shown here for wild-type CD-1 mice) evolves over time. Early in development (GD8.5, in (a)), this zone consists of dense trophoblast cords separated by large, trophoblast-lined maternal blood spaces (MBS or "sinusoids") that are packed with non-nucleated red blood cells (RBCs). In mid-gestation (GD13.5, in (b)), the definitive placenta exhibits many tortuous, thin-walled, closely apposed vascular channels, of two kinds: embryonic blood spaces (EBS) lined by endothelial cells and containing a mixture of primitive (large-diameter, nucleated) and definitive (small-diameter, non-nucleated) RBCs, and MBS lined by three embryo-derived trophoblast layers but not endothelium and containing only definitive RBCs. Near term (GD17.5, in (c)), both EBS and MBS contain large numbers of definitive RBCs. Stain: H&E. Source: Bolon and Ward [39] with permission of CRC Press.

Vet-ebooks.com

ventral abdomen to the flat bottom surface of the DP disc; this allantoic bridge eventually forms the umbilical cord. The DP disc is partitioned into distinct areas. The chorion is the red central plaque that serves as the site where the allantois fuses. The labyrinth is a dense spongy mesh covering the chorion. The labyrinth consists of embryonic capillaries and maternal sinusoids arranged in tortuous, parallel channels to maximize countercurrent blood flow for the most efficient nutrient transfer [47]. The labyrinth represents about 50% of the DP mass once the organ reaches its maximal size at about GD12.5. The junctional zone (JZ) is the middle layer located between the labyrinth and uterine wall. Blood vessels in the JZ contain only maternal blood. A trophoblast giant cell layer sits atop the JZ as a discontinuous, thin border that abuts the decidua basalis. As gestation progresses, the outer layers contain growing numbers of periodic acid Schiff (PAS)-positive glycogen cells [48]. Specific trophoblast populations in the DP exhibit distinct patterns of molecular expression, which can shift over the course of gestation.

The maternal immune response against the embryo is restrained by the presence of a transient immune-modulating structure in the decidua of mice and rats designated variously as the decidualized mesometrial triangle, mesometrial lymphoid aggregates of pregnancy (MLAp), or metrial gland (Figure 5.6) [49–52]. This metrial "gland" isn't really a gland but an area of the placenta composed of arteriolar-like blood vessels and abundant uterine natural killer (uNK) cells (also called granulated metrial gland [GMG] cells). These uNK cells are maternal bone marrow-derived, perforin-positive leukocytes that express NK cell biomarkers [52, 53]. The uNK cell population and the entire metrial gland begin to regress by mid-gestation.

Placental size differs among mouse strains. Outbred ICR (Institute of Cancer Research) mice have placentas that are

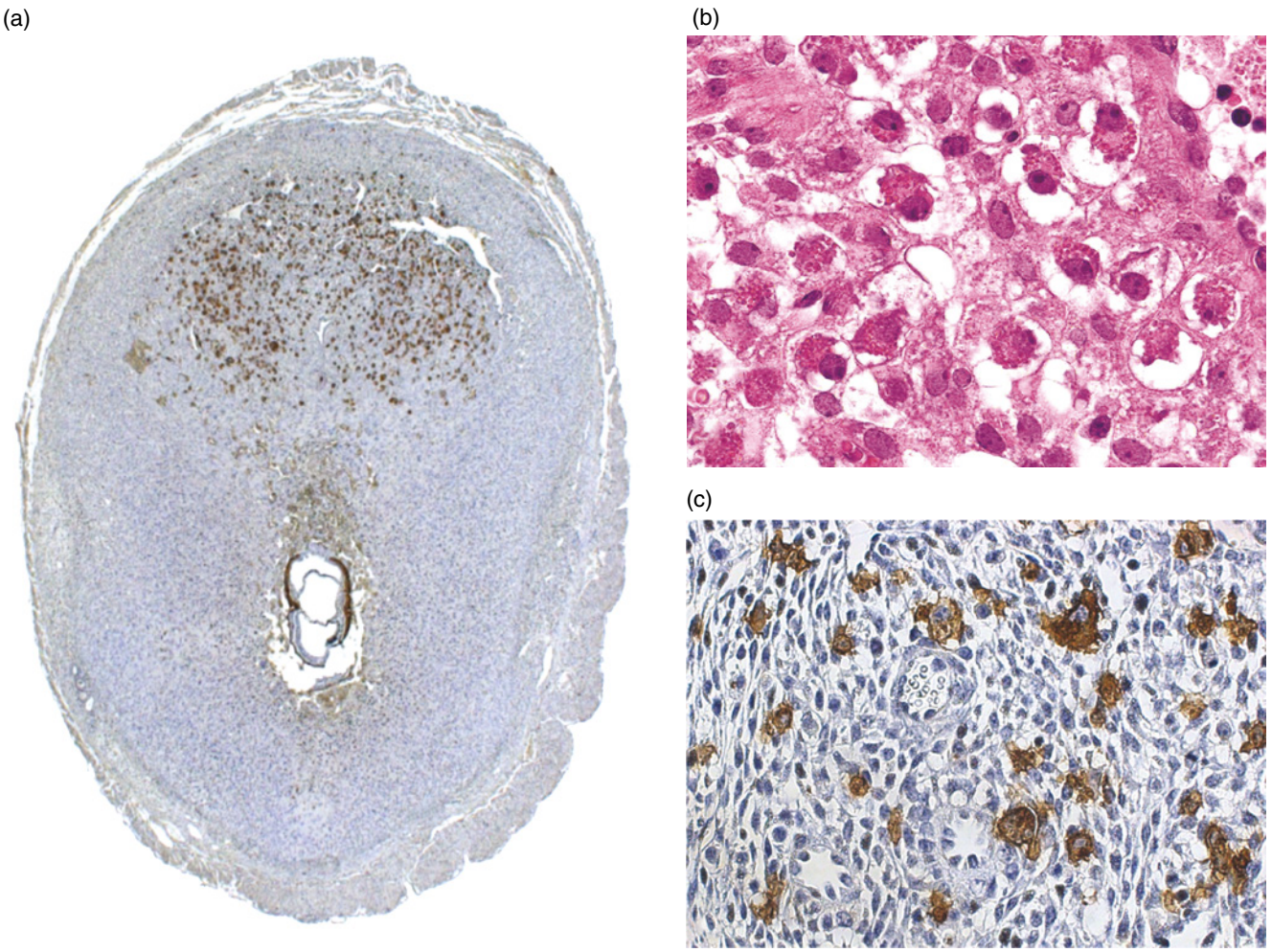


Figure 5.6 The nascent metrial gland (also designated the mesometrial lymphoid aggregate of pregnancy), shown here at GD8.5 (Panel (a)), appears as a dense collection of granulated metrial gland (GMG) cells (Panel (b); also called uterine natural killer [uNK] cells, Panel (c)) that surrounds large maternal blood vessels in the mesometrial decidua. Lectin histochemistry for the uNK cell marker *Dolichos biflorus* agglutinin (DBA) lectin (Panels (a) and (c)). Stain (panel (b)): H&E. Sources: Dr. Bruno Zavan, University of Alfenas, Brazil, and from Bolon [96] with permission of Elsevier.

Vet-ebooks.com

about 25% larger than those of age-matched inbred C57BL/6J (B6) mice. This discrepancy is correlated with embryonic growth as ICR embryos are approximately 25% bigger than age-matched B6 embryos [54]. A similar placental size increase of 20% has been reported in hybrid mice, where embryos are larger relative to those generated by the inbred C57BL/Mcl or C3H/BiMcl parental strains [55], and even larger increases have been described in cloned mice [56]. Strain differences in placental biology are not limited to structural effects, as metabolic capacities and pathways in placental tissue also vary among mouse strains [57].

Technical Considerations for Pathologic Evaluation of Developing Mice

The plan for pathologic evaluation for any phenotyping project in developing mice will utilize techniques comparable to those applied when examining adult mice. However, the choice of methods will depend on several factors unique to prenatal and early postnatal animals, including the developmental age of the subjects, the presumed timing of the lethal event(s), and in many instances the expertise and interest of the investigators and cost. In general, the initial pathologic evaluation of a novel phenotype will center on known anatomic, clinical, and molecular pathology procedures [5, 58]. For prenatal phenotypes, both the embryo and placenta must be examined since developmental and lethal events may occur in either or both of these specimens.

An important consideration for success in mouse developmental pathology is a sufficient degree of prior knowledge and experience by the morphologist. Developmental pathology is an endeavor where DIY ("do it yourself") assessments [59] are rarely efficient or effective, and often are incorrect or misleading. Substantial money, time, and animals will likely be wasted if individuals with limited or no foundation in mouse developmental biology and pathology attempt to lead a developmental pathology project.

Noninvasive Imaging of Developing Mice

The traditional basis for characterizing structural changes in embryonic lethal and neonatal lethal phenotypes in mice has concentrated on qualitative macroscopic and light microscopic analysis, supplemented as needed by quantitative measurements of organ dimensions [60, 61], volumes [62], or cell numbers [48]. Historically, these strategies have been undertaken at one or more specific time points and have been complicated by some degree of sample destruction (e.g. via continuous or interval ["step"] sectioning to make multiple μm-thick, two-dimensional [2D] tissue slices) and subsequent three-dimensional [3D] tissue reconstruction (e.g. by mental or physical realignment ["stacking"] many 2D tissue slices). In recent decades, the advent of noninvasive imaging methods for rodents has been adapted to allow one-time or serial evaluation of adult [63] and developing [22, 64, 65] mice. These technologies facilitate the digitized, relatively high-resolution, 2D and 3D macroscopic and microscopic analysis of anatomic features and/or functional attributes without destroying or greatly distorting the specimen (Figure 5.7). Key modalities include computer-assisted tomography (CAT or μCT), confocal microscopy, echocardiography, magnetic resonance microscopy (MRM), optical coherence tomography (OCT), and ultrasound biomicroscopy (UBM), among others [66–69]. These noninvasive imaging techniques will not replace standard microscopy since both light and electron microscopy afford higher resolution of cell and tissue architecture. Instead, the use of imaging techniques provides the best data when employed in tandem with conventional pathology techniques.

Anatomic Pathology Evaluation of Developing Mice

For prenatal phenotypes, the first task is to measure maternal total body weight and then count the numbers of total and viable conceptuses (i.e. embryo/placental units) as well as abnormal and resorbed implantation sites. For isolated embryos and neonates, relevant individual animal characteristics are recorded including sex (based on anogenital distance; Figure 5.8), body weight, and/or crown/rump length as well as the kind and severity of external gross defects. The embryos and neonates then are relegated to different subgroups for conventional necropsy to harvest tissues (Figure 5.9), free-hand sectioning of the torso (Figure 5.10) and head (Figure 5.11) in multiple planes to view organs *in situ* to find gross internal defects, double staining to highlight skeletal (bone and cartilage) differentiation (Figure 5.12), or fixation to permit histopathological evaluation [70]. Placentas should be fixed together with their embryos.

Histological processing is a key step in preparing the tissues of developing mice for microscopic evaluation. The choice or processing techniques depend on the age of the animal and the types of tissues that need to be preserved. Commonly, fixation is done by immersion, which is simple and rapid, but perfusion fixation may be needed to preserve deep, dense tissues that degenerate quickly, such as bone marrow and brain [58, 71]. For early embryos, tissues generally are fixed by immersion in neutral buffered 10% formalin (NBF), Bouin's solution, or modified Davidson's solution. All three of these solutions penetrate well, and both Bouin's and modified Davidson's solutions harden soft embryonic tissues so that they may be handled for macroscopic evaluation. For late-stage embryos (GD14.0 and later) and neonates, the same three fixatives still may be used, but for NBF the thick skin will needed to be opened (usually by a long slit in the ventral thoracic and abdominal regions) to permit penetration. Tissue dehydration and clearing, embedding media, and routine staining protocols for use with embryos and

Vet-ebooks.com

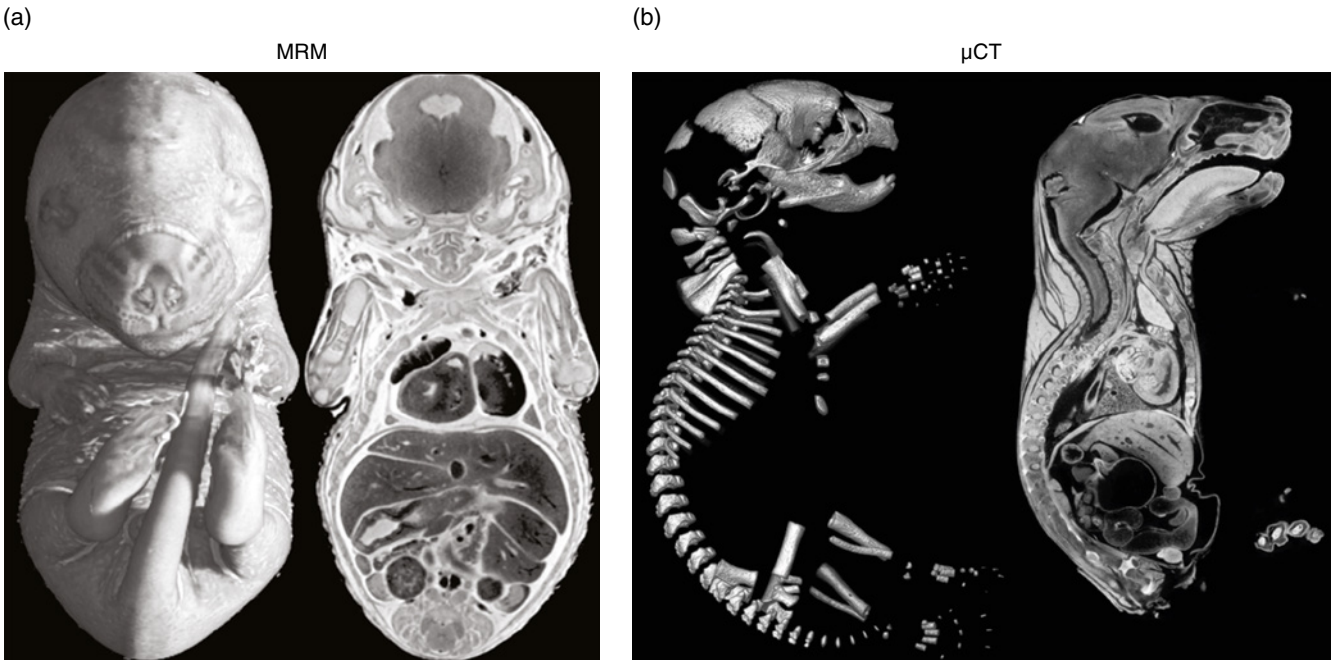


Figure 5.7 Noninvasive imaging modalities are useful means for characterizing developmental phenotypes in embryonic mice. Panel (a): Magnetic resonance microscopy (MRM) of a GD17.5 mouse embryo showing volume-rendered composite (left) and "dissected" images acquired at 20-μm resolution using a magnetic field strength of 9.4T [18]. Panel (b): Microscopic computer-assisted tomography (μCT) of a neonatal (PND0) mouse demonstrating differential highlighting of bone (left, unstained specimen) or soft tissues (right, sample processed with the proprietary Virtual Histology™ staining protocol [Numira Biosciences, Inc., Salt Lake City, UT, USA]). Sources: MRM image from Dr. G. A. Johnson, Duke University and μCT image from Numira Biosciences, Inc.; both images reproduced from Bolon et al. [67] by permission of CRC Press.

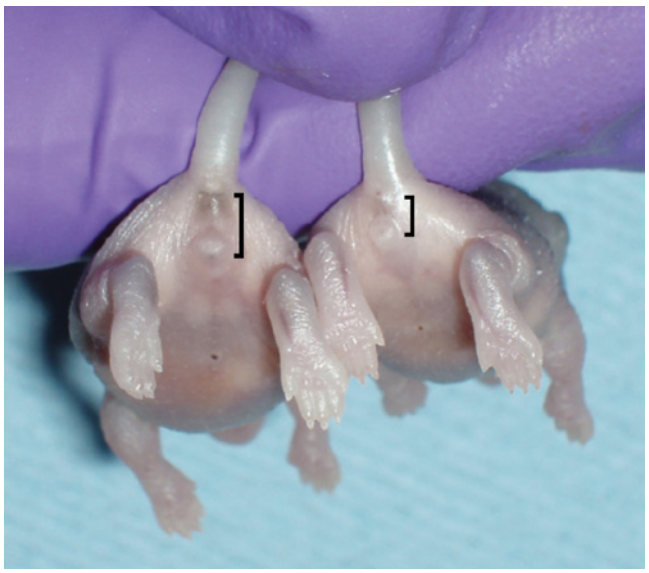


Figure 5.8 Sex differentiation of neonatal (PND1) mice using anogenital distances (brackets), which are longer in males (left) relative to females (right). Source: Dr. Cynthia Besch-Williford, IDEXX and Newbigging et al. [70] with permission of CRC Press.

neonates generally are equivalent to those used for adult tissues [72]. The two biggest differences between embryos and neonates vs. adults are that gentle decalcification is required for all samples of developing mice beginning at GD15.5 and later due to progressive skeletal mineralization, and that all embryos and neonates should be either serial- or step-sectioned to ensure that all major organs and tissues are available for microscopic evaluation. A useful strategy is to stain every fifth or tenth serial section with hematoxylin and eosin (H&E) while allocating the other sections for molecular biomarkers. When step-sectioning, the interval between steps needed to ensure that all major organs are sampled effectively varies with the developmental stage of the animal. In our experience, suitable intervals between steps are between 25 to 50 μm at GD5.5–6.5, 75 to 100 μm at GD7.0–8.0, and 150 to 250 μm at GD9.5–10.5. For older embryos and neonates, the presence of major viscera can be verified on the block face when sectioning. Greater cellular detail may be visible, particularly in very young embryos (GD8.5 or earlier), if samples are post-fixed by immersion in 1% osmium tetroxide for one to two hours followed by embedding in hard plastic resin. Smaller embryos, especially preimplantation embryos (GD0.5–GD4.0) are pre-embedded in 1% agar (in distilled water) following fixation to minimize cell trauma during processing [72].

Histopathologic evaluation is a critical element in phenotyping embryos and neonates since microscopic findings often represent the only evidence of a new phenotype [73]. The first step of the examination is to assess sections at low magnification (i.e. using objectives ranging from 1× to 5×) to observe the general appearance of differentiated organs (Figure 5.13). This portion of the analysis will detect obvious

Vet-ebooks.com

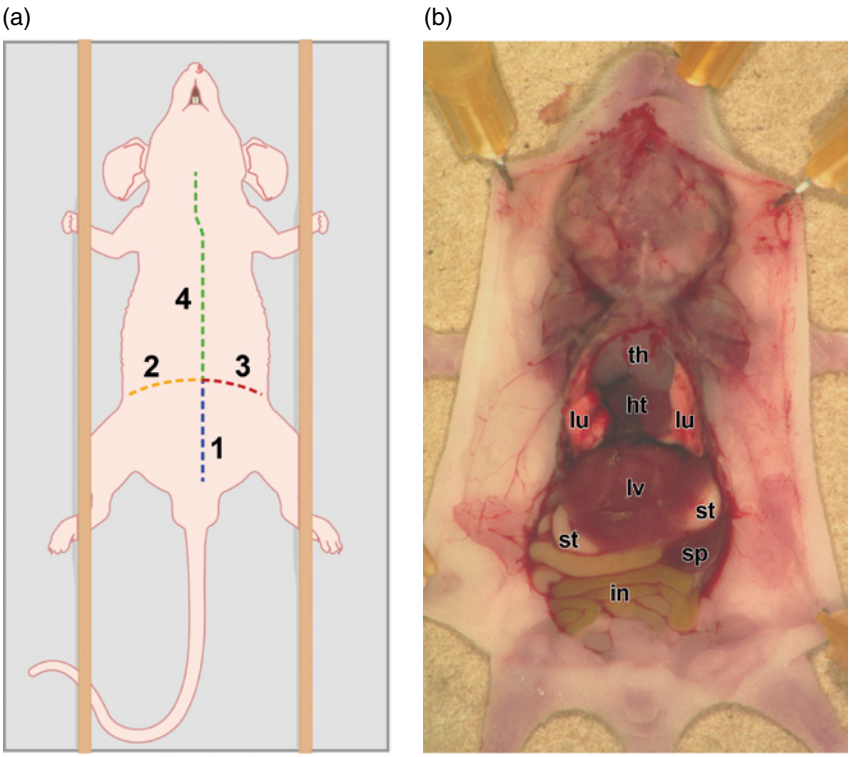


Figure 5.9 Schematic diagram showing necropsy approach for neonatal and juvenile mice. The animal is placed in dorsal recumbency, and the limbs are secured to maintain the "splayed" position. Panel (a): Organs are exposed with four cuts (made in numerical order) through the body wall. The curved arc represented by cuts "2" and "3" follows the contour of the diaphragm, which separates the thoracic cavity (located under "4") from the abdominal cavity (found under "1"). Panel (b): Photograph demonstrating the location of principal viscera in the thoracic and abdominal cavities of a juvenile (10-day-old) mouse as viewed from the ventral aspect. Abbreviations: ht = heart, in = intestine, lv = liver, lu = lung, sp = spleen, st = stomach, th = thymus. Sources: Diagram, prepared by Tim Vojt, The Ohio State University, is from Newbigging et al. [70] with permission of CRC Press; photograph from Bolon et al. [58] with permission of John Wiley & Sons.

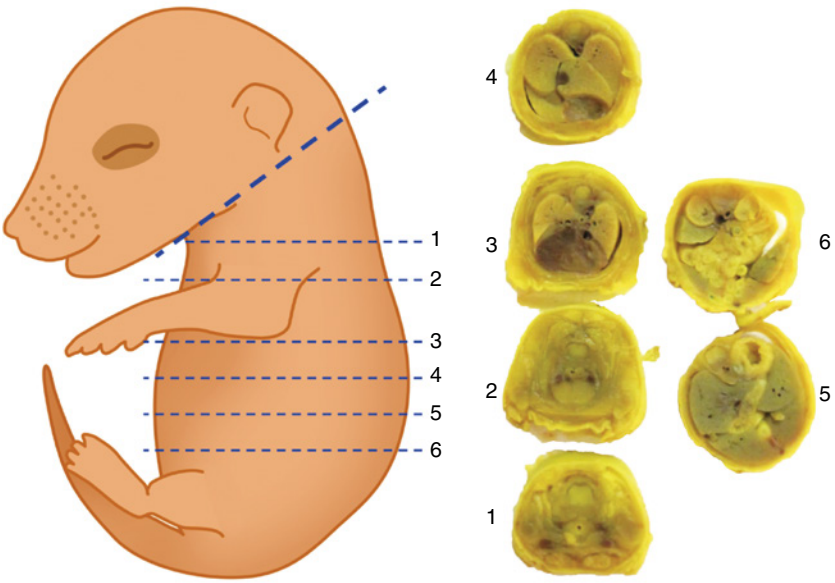


Figure 5.10 Sectioning (Wilson's) technique to allow macroscopic evaluation of defects in large internal organs of near-term (GD17 and older) mouse embryos and neonates. The schematic diagram (left panel) demonstrates the placement of freehand incisions to expose internal organs. Numbers of the dashed lines in the diagram correspond to the numbered planes in the labeled torso blocks (right panel) of a near-term embryo that had been fixed in Bouin's solution. Tissue blocks may be processed subsequently for histopathological assessment. Sources: Diagram (by Tim Vojt, The Ohio State University) and photograph (by Dr. Elizabeth R. Magden, Colorado State University) both from Newbigging et al. [70] with permission of CRC Press.

Vet-ebooks.com

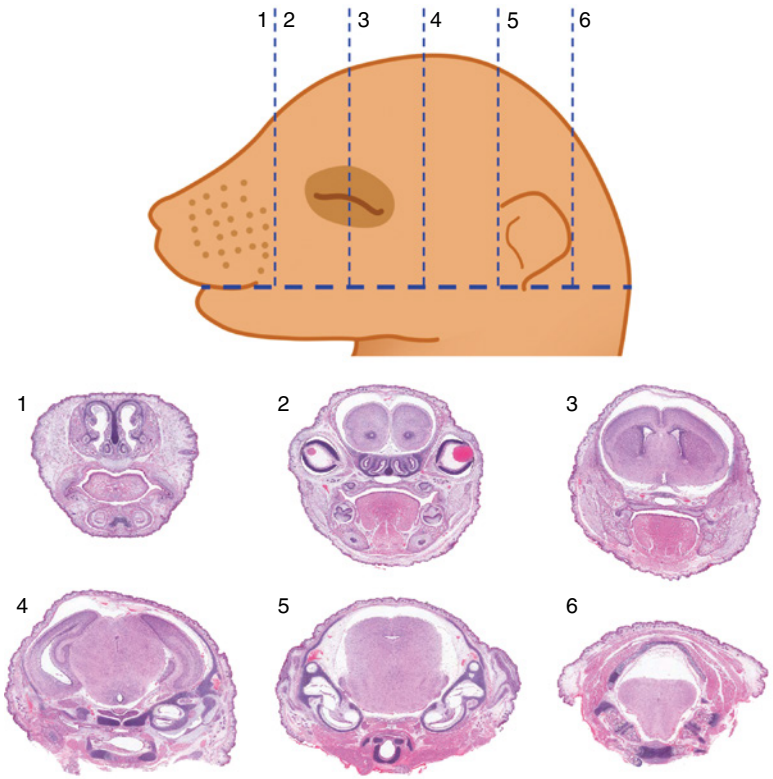


Figure 5.11 Sectioning (Wilson's) technique to allow macroscopic evaluation of brain defects in near-term (GD17 and older) mouse embryos and neonates. The numbers identify the position of the tissue block located between two adjacent incisions (dashed lines). Should a microscopic examination of the blocks be desired, the cut surface closest to the number identifying the block should be placed "down" in the cassette. Tissue processing: Bouin's fixation, paraffin embedding, H&E staining. Stain: H&E. Source: Diagram by Tim Vojt, The Ohio State University; all images from Newbigging et al. [70] with permission of CRC Press.

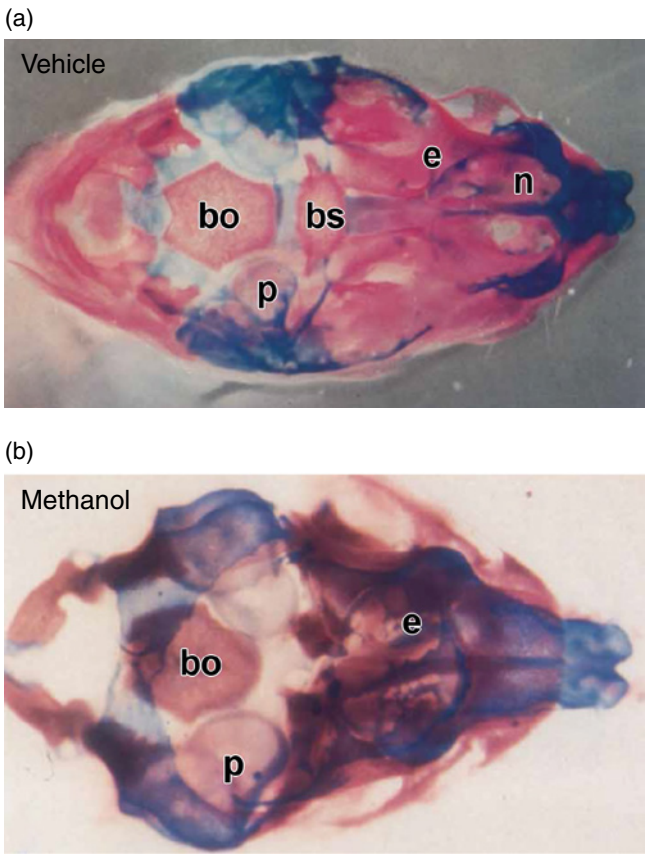


Figure 5.12 Skeletal double staining may be used to characterize axial patterning defects in near-term mouse embryos (here GD17) and neonates, with Alcian blue utilized to highlight cartilage while Alizarin red is used to show bone. Panel (a): Vehicle-treated embryo with normal basal cranial structures. Panel (b): Methanol-exposed exencephalic embryo (following maternal inhalation throughout neurulation [GD7–9]) showing malformed basal cranium bones exhibiting less cartilage to bone conversion. Abbreviations: bs = basisphenoid, bo = basioccipital, e = ethmoid, n = nasal, p = petrous temporal bone. Source: Bolon et al. [97] with permission of John Wiley & Sons.

Vet-ebooks.com



Figure 5.13 Developmental anatomy of a wild-type GD16.0 mouse embryo demonstrating the anatomic relationship of key structures when viewed in mid-axial section. Major organs are specified during organogenesis (the period from approximately GD8.0 to GD15.0), and near-term are fairly easy to recognize with the aid of well-annotated developmental anatomy atlases and their similarity to adult positions and contours. Major exceptions to this rule are the cerebellum (arrow) and lymph nodes, for which anlagen (organ primordia) form prenatally while the bulk of differentiation occurs after birth. Stain: H&E.

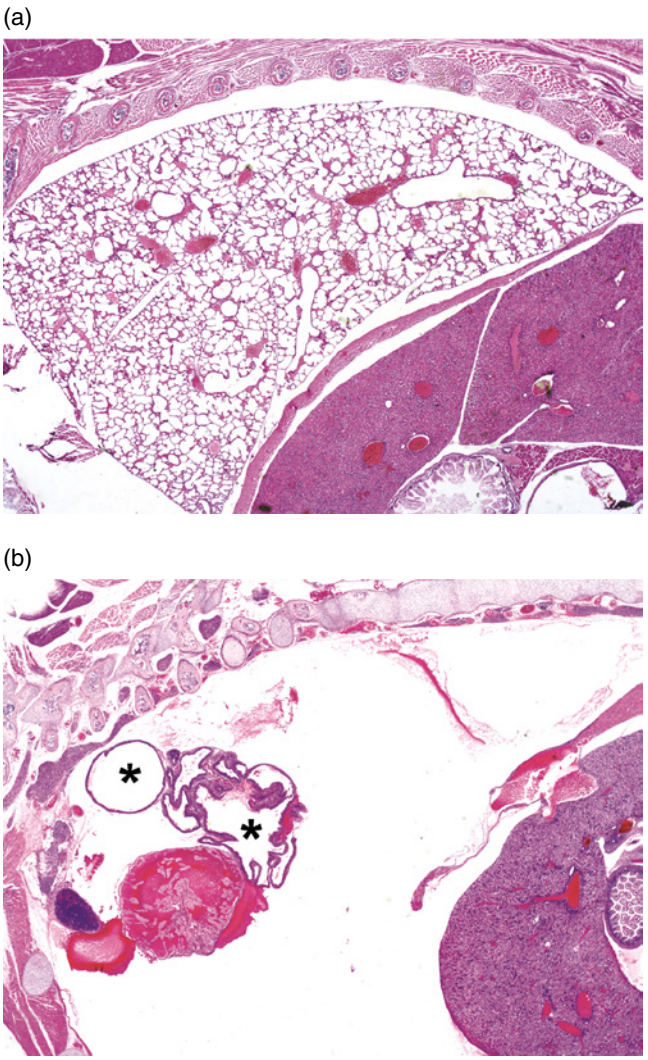


Figure 5.14 Missing structures represent a special situation in developmental pathology. In some cases, their absence is obvious – as is seen here by comparing the normal appearance of expanded air spaces in the lung parenchyma of a wild-type (WT) mouse neonate (Panel (a)) to the thoracic cavity of an NK2 homeobox 1 (*Nkx2-1*^{tm1Shk}) null mutant (KO) mouse neonate, which lacks all lung tissue except some cystic remnants (asterisks) representing aborted lobar development (Panel (b)). The absence of smaller organs or individual cell populations may be more subtle, and the tendency of the mind to "fill in" missing features may lead to a missed phenotype if the phenotypic evaluation is undertaken in a cursory manner. Stain: H&E.

developmental defects in tissues and organs. Special care must be taken to recognize the absence of any missing structures, which may be obvious but sometimes is not (Figure 5.14) [74, 75]. The second step is to assess tissue features at intermediate magnification (4× to 20×) to further define potential target cell populations in affected organs. This task requires detailed understanding of the unique cytoarchitectural features of each region and its major cell types across many stages of prenatal and postnatal development – knowledge that can only be gained by experience. The third step of a well-designed histopathologic analysis is to fully describe the nature of the structural defects at the organ, cellular, and (if necessary) subcellular levels, using both routinely stained (H&E) and specially processed sections (e.g. to demonstrate molecular biomarkers, especially utilizing immunohistochemistry [IHC]). A successful phenotypic evaluation for prenatal and neonatal mice often will require comparison of possible lesions to normal structures shown in a well-illustrated and highly annotated rodent developmental anatomy atlases [11–15].

Readouts for mouse developmental pathology endpoints may be confined to qualitative scores (i.e. "normal" or "abnormal") and detailed descriptions of lesion, but in many cases, potential developmental phenotypes are better judged by assigning semi-quantitative lesion scores [76]. A common scoring scheme typically includes multiple tiers: within normal limits (score = 0), or minimal (1+), mild (2+), moderate (3+), or marked (4+) lesions. Each tier must be founded on

Vet-ebooks.com

well-defined criteria, which generally should be stated explicitly in publications to ensure their reproducibility by investigators seeking to interpret or replicate the results.

Clinical Pathology Evaluation of Developing Mice

Many mouse developmental pathology assessments are limited to anatomic pathology evaluation of macroscopic and microscopic defects. Clinical pathology analysis for mouse developmental pathology experiments usually is confined to hematology (in whole blood), clinical chemistry (in serum), or organ cytology. These samples are collected due to the common role of cardiovascular dysfunction and hematopoietic defects in developmental lethal phenotypes [8, 77]. Common tests performed for mouse developmental pathology projects, since they need only a small blood sample, are an automated complete blood count (CBC) and a limited chemistry battery (albumin, blood urea nitrogen, calcium, glucose, phosphorus, total protein).

Blood collection for developing mice typically is undertaken as a terminal procedure since embryos and neonates have a very small blood volume. Common sampling options are decapitation and cardiac puncture [58, 77]. Blood is harvested into standard collection tubes (e.g. Microtainer®). Greater blood volumes may be obtained from outbred mouse stocks relative to smaller inbred strains. In our experience, enough blood may be harvested from a single neonatal mouse (1.5 g or larger in weight) to permit either a CBC or a serum chemistry battery, but not both. Alternatively, collection of blood in a tube containing potassium or sodium ethylenediaminetetraacetic acid (EDTA) as an anti-coagulant may allow measurement of both a CBC (from whole blood) and a very few chemistry values (from plasma obtained by centrifugation of the sample). For small subjects (embryos from GD15 to term), sample volumes typically need to be extended either by mixing whole blood with an equal volume of physiologic saline (pH 7.4) or by pooling blood or plasma samples from mice that have an identical genotype and/or that received the same treatment. In our experience, pooling blood from two (at GD18.5) to four (at GD15.0) embryos will provide enough sample for either a CBC or a chemistry battery, but not both.

When investigating some lethal phenotypes, cytological assessment of isolated cells may be necessary to define the pathogenesis [58]. Cytological evaluations permit assessment of cellular and subcellular features at high resolution. Techniques such as smears for blood and bone marrow and either squash or touch preparations for organs with dense parenchyma like liver, spleen, and thymus are particularly useful in this regard. In general, results from cytological methods should be interpreted along with findings from conventional histopathological evaluation so that both tissue organization and individual cell characteristics can be assessed. For most embryo phenotyping projects, microscopic examination of tissue sections is used for the initial screen for both cell and tissue lesions, while cytological methods are employed as a secondary procedure when warranted to better understand the nature of the changes first identified by histopathologic analysis of cells within the context of their usual tissue organization.

Pathologic Patterns in Mouse Embryos and Neonates

Gene targeted (null mutant or "knockout" [KO]) mouse embryos, and less often transgenic mouse embryos, develop abnormal organ- or tissue-specific lesions due to the functional abnormalities arising from altering the role of the genetically engineered gene at different stages of normal development. In large-scale knockout mouse programs, about 30% of all inactivated genes lead to developmental embryonic defects at various stages of gestation [78, 79]. In one study of 242 developmental lethal knockout mouse lines, 44% of lethal events occurred before GD9.5, 17% from GD9.5–12.5, 4% from GD12.5–18.5, and 36% from GD15.5 to weaning [78]. The specific developmental defect(s) in the 242 lines were not determined.

The stage at which injury (lack of normal development of the entire embryo, or specific tissues or organs) occurs will determine the outcome of developing mice (Table 5.1). For harm prior to implantation (i.e. before GD4.5), significant interference to normal development usually will lead to death of the embryo, while modest effects may engender developmental delays but minor consequences or no overt abnormalities. Such delays may undergo complete or partial compensatory repair as the remaining pluripotent stem cells restore lost tissue. Gross abnormalities ("birth defects" seen during gestation) most commonly result from damage incurred after implantation (GD5.0) but before the end of organogenesis (GD15.0), with the character of the malformation determined by the timing of the insult relative to various organ-specific "critical periods." For injury after organogenesis is finished (i.e. GD15.0 through the neonatal period), the embryo may exhibit slow growth or develop cell type- or tissue-specific histopathological changes and/or functional abnormalities rather than gross defects; the exceptions to this rule are structures like the cerebellum and hippocampus that undergo major peaks of cell proliferation after birth. Embryonic lethality may result from many different causes, but common aberrations that reliably lead to death are decreased circulation (e.g. heart and/or vascular defects any time during gestation) and reduced oxygen exchange (e.g. erythrocyte deficiencies or hemorrhagic diatheses or placental insufficiency, especially occurring late in gestation).

Gross developmental defects that occur as spontaneous background lesions vary in frequency and severity among wild-type (WT) mouse strains and lines. Minor incidental anomalies like renal pelvic cavitation (physiological hydronephrosis) and extra or wavy ribs are common (from 5% to

Vet-ebooks.com

Table 5.1 Common embryonic or neonatal defects leading to lethality.

Developmental stage	Developmental days when damage occurs	Target site for mutation or toxicant	Developmental outcome	Developmental timing of lethality
Preimplantation	GD0–3.5	Any cells (totipotent or pluripotent)	Embryonic death (no visible implantation sites)	GD1.0–4.0
Postimplantation	GD4.5–5.0	Any cells (pluripotent)	Embryonic death (no visible implantation sites)	GD5.0–5.5
Gastrulation	GD6.5–9.0	Altered germ layers or body plan	Embryonic death (empty implantation sites)	GD6.0–7.5
Early organogenesis	GD8.0–10.5	Cardiovascular or central nervous system defects, abnormal erythropoiesis	Mid-gestational death due to cardiovascular or hematopoietic insufficiency	GD10.0–13.0
Late organogenesis	GD11.0–15.0	Defects in many organs, abnormal erythropoiesis, delayed growth	Mid- to late-gestational death due to cardiovascular or hematopoietic insufficiency	GD13.0–16.0
Near-term growth spurt	GD15.5–18.5	Altered cardiovascular function, abnormal erythropoiesis, delayed growth	Late-gestational or perinatal death due to cardiovascular or hematopoietic insufficiency (or edema or hemorrhage)	GD16.0 to PND0.5
Early neonatal	PND0	Abnormal cardiovascular, central nervous system, cutaneous, musculoskeletal, or pulmonary function	Insufficiencies in circulation or respiration (inability to breath)	PND0–0.5
Late neonatal	PND0.5–2.0	Abnormal cardiovascular, gastrointestinal, metabolic, or neural functions	Insufficiencies in digestion or suckling (inability to feed)	PND1.0–2.5
Juvenile	PND2.5–28	Abnormal hematopoietic, immune, metabolic, or renal functions	Sustained anemia, abnormal immune function, metabolic or renal insufficiencies	PND3.0–28

GD = gestational day (where GD0 is the vaginal plug-positive day), PND = postnatal day.

35% of animals) since they do not impact embryonic viability [80]. Major malformations like cleft palate and neural tube defects have low background frequencies (typically 0.5% or less) since they are lethal. An individual may harbor one or several minor or major abnormalities.

Frequencies of both minor and major defects may be increased by genetic manipulation, infections, or exposure to teratogens. Nearly 5000 abnormal phenotypes have been identified in mutant mouse embryos [79, 81], most of which are associated with monogenic null mutations ("knockouts"). Induced developmental defects have been reported in approximately 30% of genetically engineered knockout mice [78]. Bacterial and viral infections that can cross the placenta may lead to substantial tissue destruction of the embryo, placenta, or both. Numerous toxicants are capable of producing developmental phenotypes in rodents including agricultural and industrial chemicals, drugs, metals, and physical agents (heat and radiation) [82]. The kind of phenotype elicited by a genetic mutation or toxicant exposure will depend on where and when during development the gene normally performs its function. For example, in the brain anomalies in the cerebral cortex tend to arise from genetic defects that arise during mid-gestation while abnormalities in the cerebellum – which develops late in gestation and after birth in rodents [42] – typically involve genetic dysfunction late in gestation or after birth. Knowledge of normal spatial and temporal patterns of gene expression during development is instrumental in allowing developmental pathologists to define potential target organs and more efficiently characterize developmental phenotypes. In general, the frequency and severity of developmental phenotypes will vary among litters, and among individuals of comparably treated litters. The variation in stages of embryo degeneration, necrosis and death, no matter the etiology, may be seen grossly [83] (Figure 5.15).

Microscopic lesions of many cell types, and tissues and organs may be identified when phenotyping the tissues from developing mice. Identification of normal cell and tissue features for developing rodents is simple thanks to several detailed developmental atlases [7, 11, 12, 14, 15, 84–86]. A full appreciation of histopathologic changes for developmental phenotypes often requires that the histogenesis of the lesions be explored by serial evaluation of embryos at several times (e.g. serial days). For example, cardiac defects that initially produce gross structural malformations and/or histopathological abnormalities and altered circulation in the heart may lead over time to secondary lesions in other highly vascularized organs such as liver (congestion followed by necrosis) and lungs (right-sided congestion) (Figure 5.16).

Vet-ebooks.com

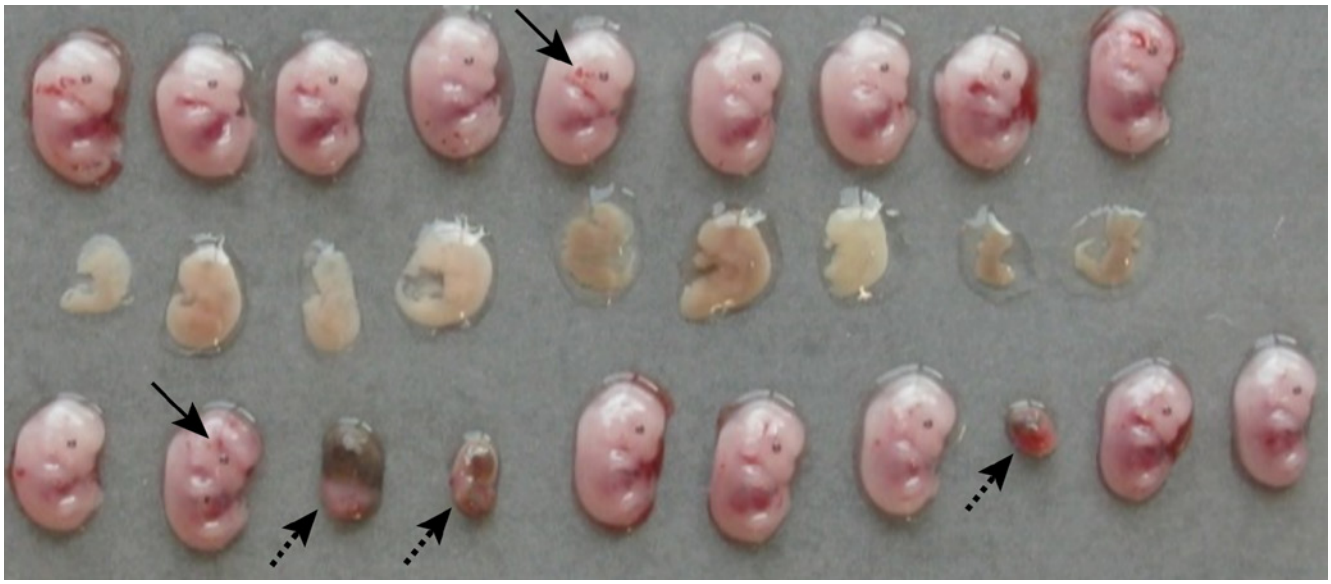


Figure 5.15 Comparison of variable lesion progression in three litters of wild-type GD13.5 mouse embryos at four days following maternal Zika virus infection. Several phenotypes are evident, and often cluster in particular litters. Acute death soon after exposure (based on conceptus size) resulted in embryonic resorption (as shown in the bottom row by small, oval, discolored implantation site remnants [arrowheads with dotted lines]). Slightly later embryonic death led to diffuse embryonic necrosis or autolysis rather than resorption (indicated in the middle row by uniform pallor, the absence of a pigmented eye primordium, and indistinct body contours). Other embryos appear to be viable (based on their similar, age-appropriate size and anatomic features), but some exhibit focal acute hemorrhage (arrowheads with solid lines) as either a delayed effect of the virus or more likely an artifact of slight trauma encountered during necropsy. Source: Szaba et al. [83] by permission of the Authors under a Creative Commons 4.0 International License.

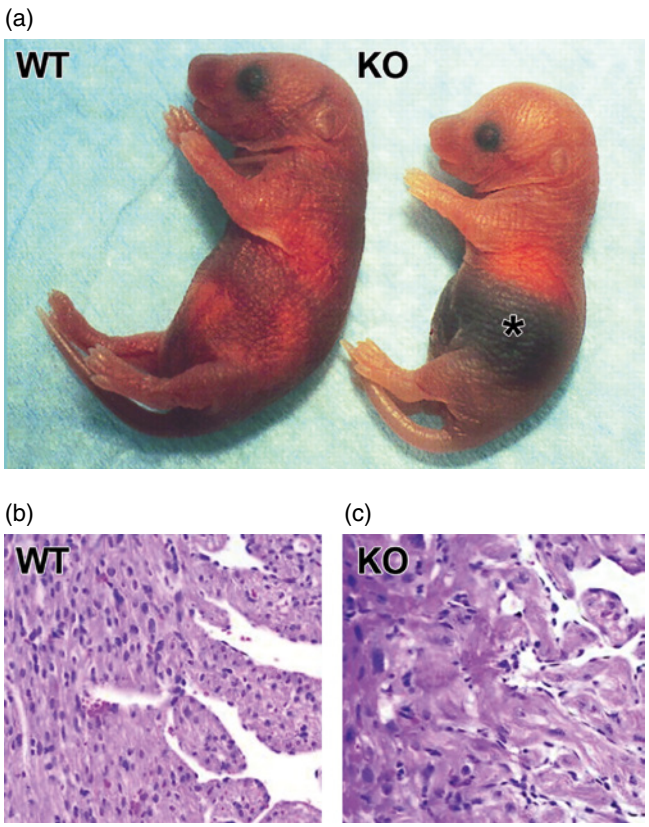


Figure 5.16 Developmental phenotypes resulting from circulatory disturbances may present as macroscopic or microscopic lesions. Panel (a): Relative to a wild-type (WT) littermate, knockout (KO) neonates at PND0 that lack the gene for non-muscle myosin heavy chain II-B (*Myh10*^{tm2Rsad}) have congestive heart failure that leads to a reduced body size, pallor (indicative of poor perfusion), and a dark band (asterisk) in the abdomen (due to chronic hepatic congestion). Relative to the WT animal (Panel (b)), the microscopic lesions in the KO animal (Panel (c)) stem from myocardial dysgenesis (shown by the larger size and random arrangement of ventricular myofibers). Stain: H&E. Source: Tullio et al [98] with permission of the U.S. National Academy of Sciences.

Vet-ebooks.com

Several gross and microscopic patterns occur commonly in development phenotypes that arise during gestation (Figure 5.17). Cell *degeneration* (potentially reversible) and/or *necrosis* (irreversible) may be evident and often presents as organs with aberrant cellular features (for degeneration) or that are small (for either, but especially for necrosis). *Heterotopiae* are clusters of ectopic (displaced) cells that usually indicate prior abnormalities in migration. *Kinetic defects* appear as a surplus or dearth in either proliferation or programmed cell death (PCD) for a particular population. Any or all of these intrinsic mechanisms as well as other extrinsic tissue changes like *hemorrhage* may produce gross defects. In general, *inflammation* is not a prominent tissue response in mouse embryos since the immune system is functionally immature until fairly late in gestation or after birth. The gross appearance of the uterus and implantation sites (Figure 5.17a) as well as the microscopic lesion spectrum in a dying embryo varies with the tissue or organ involved (Table 5.1), but once viability is lost, the microscopic pattern invariably will include first focal or multifocal necrosis in various organs (Figure 5.17e) and then diffuse end-stage necrosis of all organs (Figure 5.17d,f). Nonviable conceptuses grossly will appear as small implantation sites either lacking an embryo (a finding termed a "resorption," and typically appearing as a pale, dark green, or purple tissue mass) or with cloudy intra-amniotic fluid surrounding a white, friable embryo (Figure 5.17b,d).

Many different developmental disturbances may lead to neonatal lethality. Death within one to two hours of birth is a reliable indicator of functional or structural defects that prevent effective oxygen uptake and distribution. Commonly affected systems in this regard include the heart and vessels, lungs, hematopoietic tissue (red blood cells), and brain (respiratory centers). Mice can be born without an intact brain, endocrine glands, limbs, lungs, and skin because these organs are not needed for viability *in utero*, but only after birth. Acute but slower death (i.e. 6–36 hours after birth) typically results from impaired energy metabolism (especially glucose utilization) or suckling difficulties (Figure 5.18). The pathogenesis of these effects may be simple and obvious (e.g. small or no lung lobes), but often the cause is associated with subtle (e.g. reduced neurons in brainstem centers that control respiration) or no (e.g. altered neurotransmission in synapses of respiratory muscles) structural lesions. For this reason, investigations of developmental lethal phenotypes require a team approach.

For mutant mouse lines, the time of death may be probed further by evaluating the genotype of viable embryos and neonates. The first clue that a given genotype may be responsible for an embryonic or neonatal lethal phenotype often is an altered Mendelian ratio and/or a decrease in the expected litter size (Figure 5.17a) [87]. The developmental stage at which lethality occurs may be estimated by the gross appearance of abnormal individuals relative to the expected appearance of developmental stage-matched embryos or neonates. If all implantation sites contain structurally normal embryos with a wild-type (WT) or heterozygous (HET) genotype, then the null mutant ("knockout" [KO]) embryos likely died prior to implantation (i.e. before GD4.5). If some implantation sites contain no embryo or a small dead embryo, then the KO embryos likely expired during initial early organogenesis before generation of the DP (i.e. between GD8.5–9.5). If implantation sites at mid-gestation (i.e. GD12.5) include apparently normal KO embryos, then the embryo lethal phenotype likely is expressed near or just after birth. Dead pups often are eaten immediately by the dam, so harvesting embryos right before birth (i.e. GD17.5–18.5) might be required to confirm that animals were viable throughout gestation. Given this spectrum of time-dependent defects, most developmental pathologists tend to perform the initial evaluation to characterize a genetically engineered lethal phenotype by examining litters toward the end of gestation (between GD16.0–18.5; Figure 5.19) or at weaning (PND21; Figure 5.20) [22, 88, 89]. If necessary to pinpoint the time of death and/or characterize the phenotype, follow-up examinations usually are conducted by working backward at two-day intervals during gestation (GD14, GD12, GD10, etc.) or two- to three-day intervals between birth and weaning (PND18, PND15, PND12, PND9, PND6, PND4, PND2) until viable but affected individuals are observed.

For developmental toxicity studies, the developmental outcome also is predicted chiefly by the timing of exposure relative to critical periods of development. However, other factors also play a role in the vulnerability of developing mice. For example, some strains have an inherently higher sensitivity to some forms of birth defects because their background incidence is high (e.g. A/J mice and cleft palates [90, 91], SWV [Swiss Webster Vancouver] mice and neural tube closure defects [92]). This strain-specific sensitivity usually is for a specific spectrum of birth defects and/or teratogenic agents, and not for all kinds of malformations and teratogens generally. Similarly, male and female embryos may respond differently to toxicants based on their proximity to littermates of the opposite sex during gestation and the nutritional status of the dam. Therefore, the pathologist will need to be familiar with the background strain sensitivity as well as the specific intrauterine environment experienced by the embryo prior to performing developmental pathology evaluations.

In the simplest scenario, a lethal developmental phenotype will reliably produce a common spectrum of lesions affecting the same organs in all individuals with a given genetic mutation or that were exposed to a particular dose of toxicant. However, in many cases (for mutant lines and infectious diseases more so than toxicant exposures), lethal phenotypes exhibit variable penetrance, with some embryos exhibiting substantial defects and/or death early in development while a few live well after birth. Typically, no explanation can be defined to account for the differing penetrance, although factors like the genetic background, gene dosage, and maternal age commonly are implicated. The pathologist's role in such investigations is to properly describe the lesions associated with lethality, and to record any shifts in the lesion constellation noted in the long-term survivors.

Vet-ebooks.com

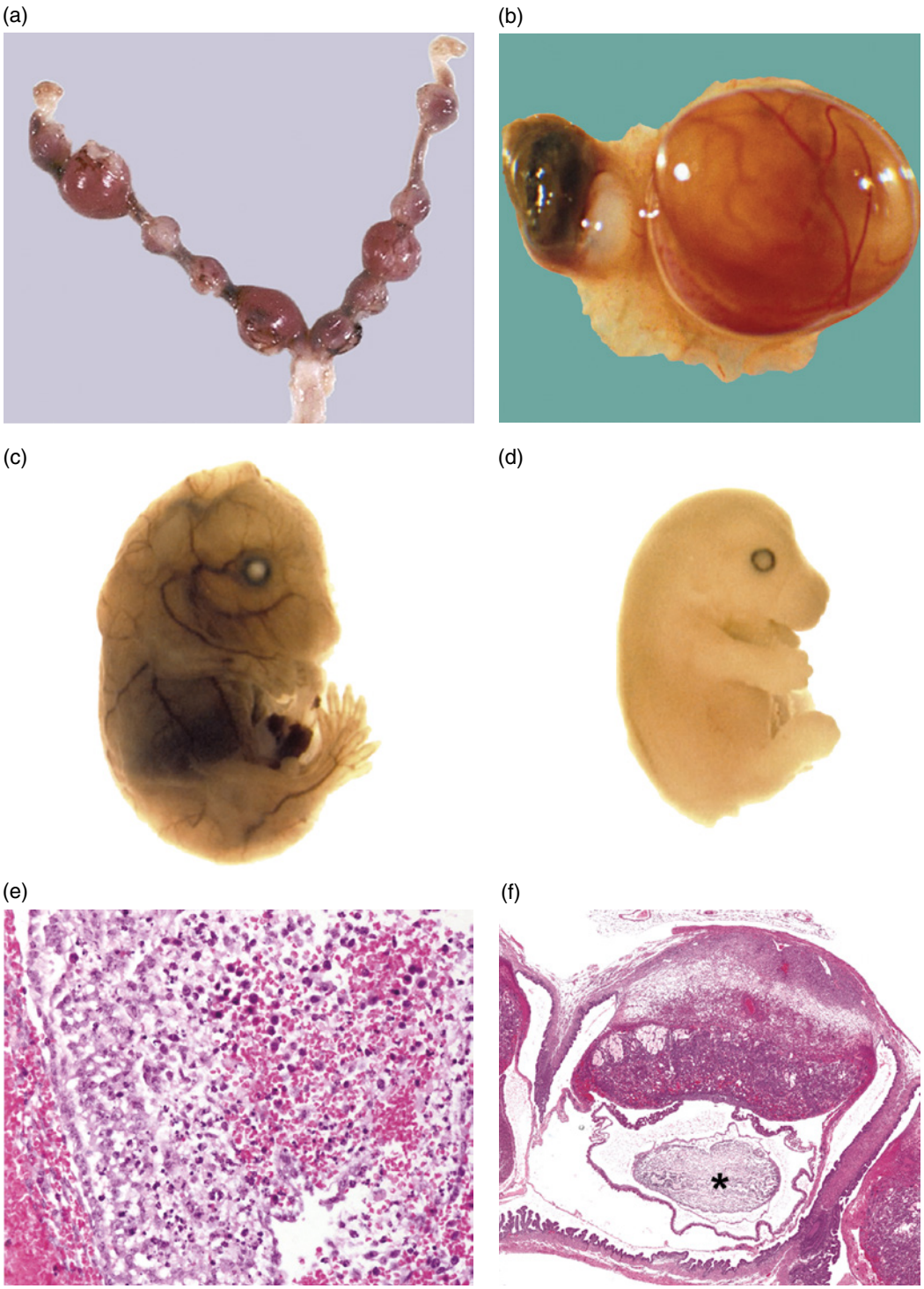


Figure 5.17 Embryonic death is demonstrated by a spectrum of macroscopic and microscopic changes. Panel (a): Gravid uterus at GD10.0 in which all but three implantation sites exhibit various degrees of regression (termed "resorption"). Panel (b): An isolated implantation site at GD15.0 in which a dead (pale) embryo is obscured by opaque, red-tinged amniotic fluid (i.e. containing increased protein and cells, including blood). A viable wild-type GD14.5 embryo (Panel (c)) with tan skin and many branching blood vessels is contrasted to a white, avascular, wild-type littermate (Panel (d)) that died at approximately GD13.5 (as shown by the obvious albeit short digits on the forepaw and digital rays (which arise about GD12.8) but very minimal digits on the hind paw). The grossly visible pallor corresponds to diffuse necrosis microscopically. Panel (e): Focal necrosis and acute hemorrhage in a GD13.5 embryo are the first harbingers of imminent embryonic death. Panel (f): Diffuse necrosis leading to death in a GD13.5 embryo (asterisk) is a consequence of widespread primary placental necrosis and acute hemorrhage at four days following maternal Zika virus infection; placental failure in this model causes embryonic death but not embryonic infection. Stain (panels (e) and (f)): H&E. Sources: Ward and Devor-Henneman [44] with permission of Iowa State University Press, Bolon and Ward [39] with permission of CRC Press, and Szaba et al. [83] by permission of the Authors under a Creative Commons 4.0 International License.

Vet-ebooks.com

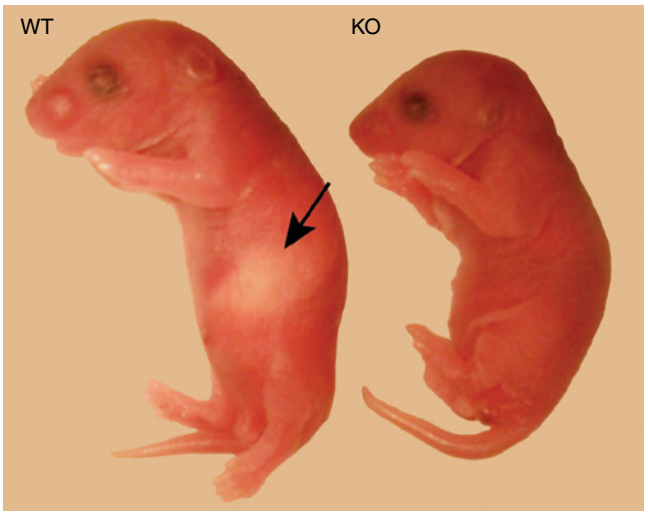


Figure 5.18 A common cause of neonatal lethality is inability to suckle, which is shown by the inability to discern a "milk spot" (milk-engorged stomach [arrow]) through the left abdominal wall. Relative to wild-type (WT) littermates, knockout mice lacking the gene for cardiotrophin-like cytokine (*Clcf1*^{tm1Zou}) die by PND1 from dehydration and starvation resulting from deficient numbers of brainstem neurons needed to mediate nursing. Source: Zou et al. [99] by courtesy of Sage Publications.

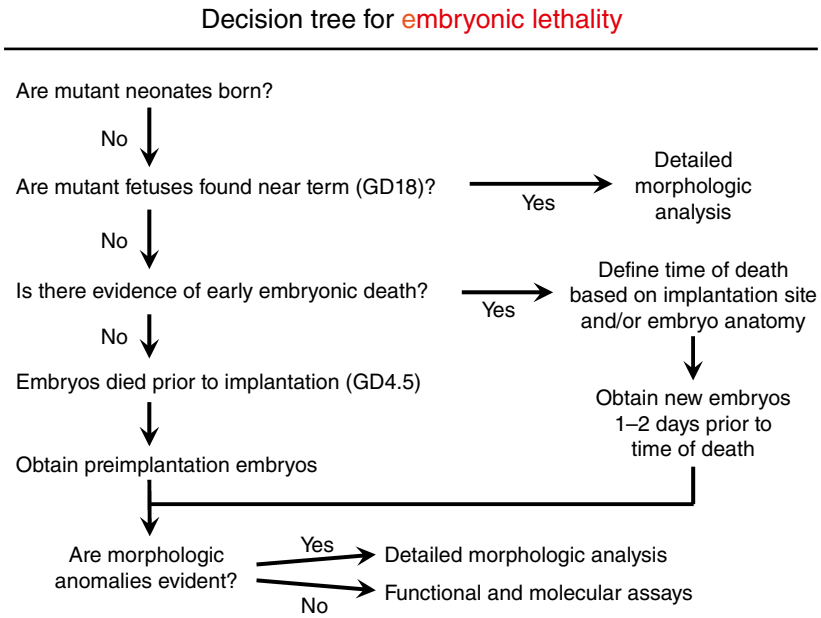


Figure 5.19 An outcome-oriented decision tree for evaluating embryonic lethal phenotypes in developing mice. The initial analysis is performed near term (gestational day [GD] 17.5–18.5). If necessary, one or more follow-up experiments may be needed earlier in gestation, usually either moving backward in two-day intervals (GD16, GD14, GD12, GD10. . .) or selecting a new time point based on the external features of regressing implantation sites or dead embryos.

Pathologic Patterns in Mouse Placenta

The placenta is the first part of the conceptus that will be available for macroscopic evaluation, and it should be subjected to histopathological evaluation during investigations of embryonic lethality. The reasons for including this organ in the assessment are that many genes are expressed in both embryo and the embryonic portion of the placenta, and that abnormal placental development will lead soon thereafter to embryonic death even in the absence of lesions in the embryo proper [83]. About 650 abnormal placental phenotypes have been reported in mutant mouse embryos [93].

Since a properly conducted developmental pathologic evaluation should include an assessment of this organ, the placenta should be evaluated grossly before the embryo examination begins [94]. This placental review may be limited to rapid observations of size, shape, and color as many placental conditions present as alterations in these parameters; gross defects in placenta often are indicative of obvious embryonic defects as well (Figure 5.21). In some cases, placental weights may be obtained to discern more subtle

Vet-ebooks.com

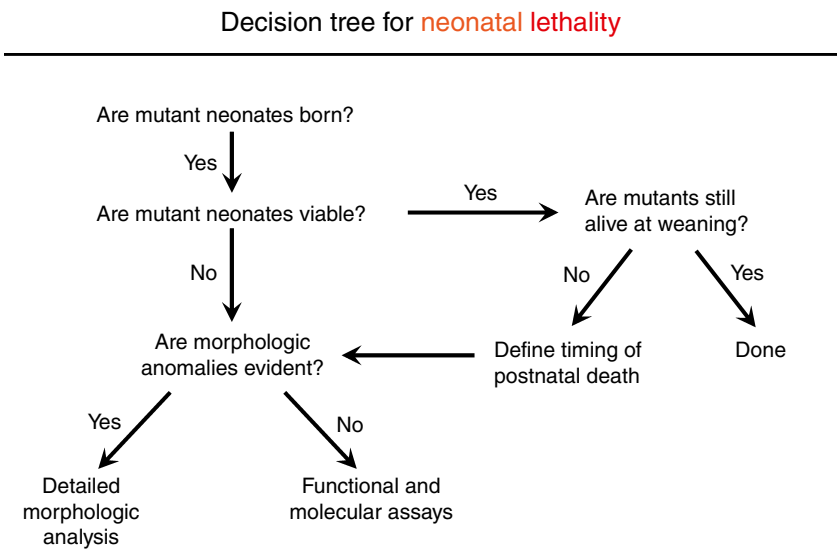


Figure 5.20 An outcome-oriented decision tree for evaluating neonatal and juvenile lethal phenotypes. The initial analysis is performed at weaning (postnatal day [PND] 21–22). If necessary, one or more follow-up studies may be needed at earlier postnatal time points, moving backward in three-day intervals during the late juvenile period (PND18, PND15, PND12, PND9, PND6) and then at one- or two-day intervals through the early juvenile and neonatal periods (PND4, PND, PND1). Source: Based on ref [22, 88, 89]

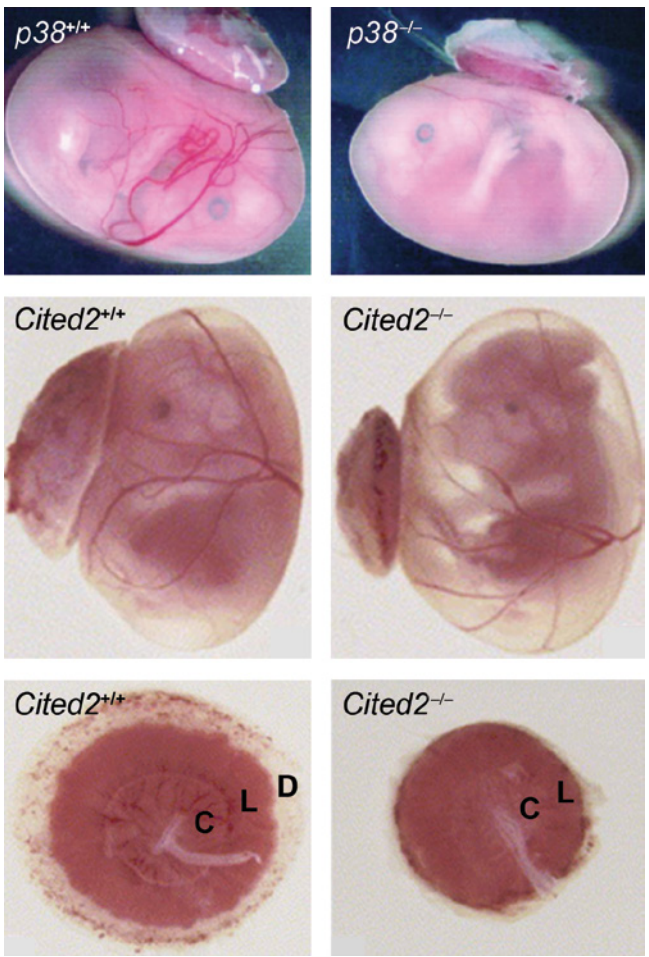


Figure 5.21 Placental dysfunction relative to wild-type littermates (left column) may be observed macroscopically in knockout mice (right column) by reductions in vascularity of the yolk sac (top row) or size (i.e. hypoplasia, middle and bottom rows) of the definitive placenta. Findings may be visible from the side (upper two rows) or base (bottom row). Abbreviations: +/+ = wild-type, −/− = knockout, C = chorion, D = decidua, L = labyrinth. *Sources: Mapk14*^{tm1Mka} (*p38α* knockout) mice from Tamura et al. [100], and *Cited2*^{tm1Ipmb} (*Cited2* knockout) mice from Withington et al. [101] with the permission of Elsevier.

Vet-ebooks.com

variations in mass. For more extensive review and photodocumentation, the placenta typically should be placed in a buffered saline solution to prevent drying and collapse. In general, however, the placenta should be assessed and then quickly fixed to prevent excessive autolysis of this highly vascular organ.

Histopathological assessment of the placenta typically is performed on NBF-fixed, paraffin-embedded, H&E-stained tissue sections, with serial sections used as needed to explore the expression of cell type-specific molecular markers. Bouin's solution also may be used as a placental fixative (since embryos and placentas typically are fixed in a single container, and Bouin's penetrates older embryos better than NBF). However, Bouin's solution tends to rupture erythrocytes and destroys some fragile antigens, so this fixative should be employed with discretion for this organ. The key to successful histopathological evaluation of placenta is that the pathologist must be familiar with the laminar organization and cell populations within the various portions of the placenta (especially YS and the DP) during both early and late stages of gestation. In particular, the early placenta consists largely of a thick mass of maternal decidua encompassing a thin layer of trophectoderm (GD4.5–7.0); transitions to a thin undulating YS separated from a modest decidual margin by a thin layer of trophoblast giant cells in mid-gestation (GD7.5–10.5); and then assumes a mature DP conformation with thick inner labyrinth, middle JZ with spongiotrophoblast nearest the labyrinth and trophoblast giant cells peripherally, and outer decidual rim (at GD12.5 and later).

Patterns of placental lesions leading to embryo mortality vary depending on the timing of the lethal event (Table 5.2 and Figure 5.22) [16, 17, 94, 95]. Early placental-based lethality commonly involves either circulatory dysfunction in the YS with endothelial and/or hematopoietic disruption, leading to embryonic death between GD8.5–10.0, or failure of chorioallantoic fusion (i.e. umbilical cord formation) with embryonic death from GD9.5–11.0. Later placental-based lethality typically results from malformed placental labyrinth due to faulty differentiation of one or more labyrinthine trophoblast lineages, leading to embryonic death occurring from GD13–16. In many cases, the precise cause and mechanism cannot be defined, so a generic diagnosis of "small labyrinth" is applied as a nonspecific end-stage finding [17]. Disrupted formation of the placental labyrinth is by far the most frequent mechanism responsible for placental failure in mice. For example, lesions in the labyrinth due to gene inactivation or viral infection of endothelium [83] include trophoblast hyperplasia with mitotic figures (Figure 5.23a) and embryonic endothelial cell necrosis (Figure 5.23b); these changes may lead to placental failure and embryonic death. If an embryo dies during gestation and placental development is normal until the embryo dies, the placenta will regress as seen initially by necrotic debris within embryonic blood vessels in the labyrinth, which represents evidence of dead cells arriving from the dying embryo (Figure 5.23c), followed by focal hemorrhage and focal necrosis of the placental tissue (Figure 5.23d).

Table 5.2 Common placental defects leading to embryonic lethality. Source: Based on [16, 5, 95]

Affected structure	Gross findings	Histopathological findings	Proposed defect	Developmental timing of lethality
Decidua (maternal)	Reduced amount	Decreased cells and vascular density	Diminished cell production	Variable (usually prior to GD10.5)
Yolk sac (primitive placenta)	Reduced size	Fewer and smaller blood vessels and blood islands	Abnormal vasculogenesis and primitive hematopoiesis	GD8.5–10.0
Chorioallantois (umbilical cord)	Non-fusion of allantois to chorion	Non-fusion of allantois to chorion	Absence of umbilical cord, abnormal vasculogenesis of placenta	GD9.5–11.0
Labyrinth (definitive placenta)	Altered placental size (smaller or larger)	Reduced or enhanced numbers of one or multiple trophoblast lineages	Abnormal differentiation and expansion of trophoblasts, hemorrhage	GD9.0–12.5
			Abnormal organization of the labyrinth layers	GD13.0–16.0

GD = gestational day (where GD0 is the vaginal plug-positive day).

Vet-ebooks.com

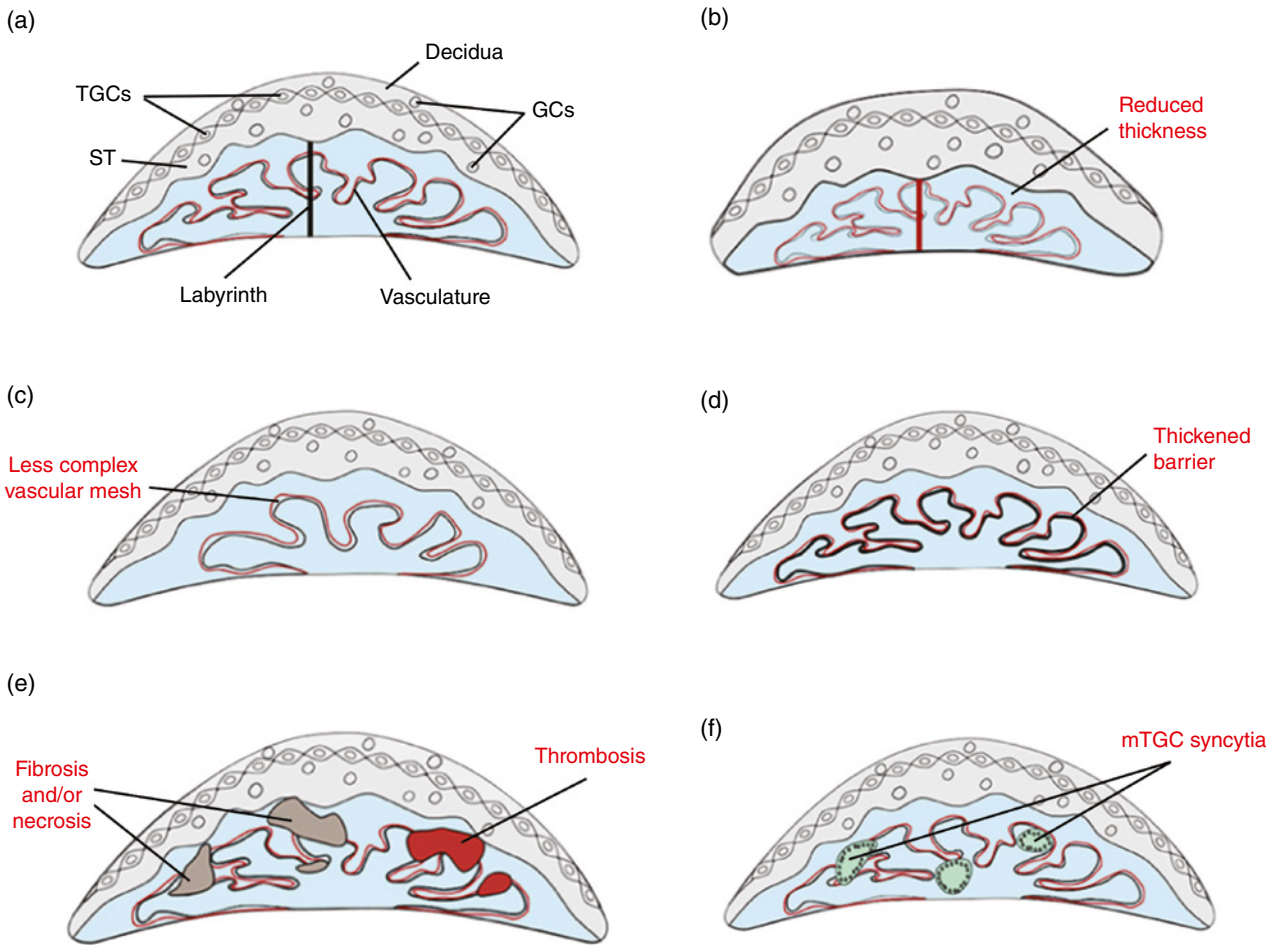


Figure 5.22 Schematic representation of structurally distinct lesion patterns whereby placental labyrinth dysfunction leads to intrauterine growth restriction (IUGR) or embryonic lethality. In a **normal placenta** (a), the labyrinth (long black vertical bar) is the largest zone permitting exchange of gases and nutrients between the embryonic blood spaces (EBS) and maternal blood spaces (MBS). **Reduced labyrinth volume** (b, small red vertical bar) or **reduced vascular complexity** (c) typically indicate decreased numbers and/or altered organization of EBS and/or MBS, thus decreasing the vascular surface area available for exchange. **Interhemal barrier defects** (d) generally reflect abnormal density and/or function of one or more embryonic trophoblast layers, thereby increasing the tissue thickness across which nutrients and gases must be transported. **Tissue or vascular disruption** (e), such as local or multifocal fibrosis or necrosis and/or intravascular thrombosis, may both block blood flow and destroy vascular surface area needed for gas and nutrient exchange. **Multinucleated trophoblast giant cell** (mTGC) **formation** (f) results from a trophoblast differentiation defect in which improper cell fusion disturbs labyrinth organization. Source: Woods et al. [95]. License under a Creative Commons 4.0 International License.

Vet-ebooks.com

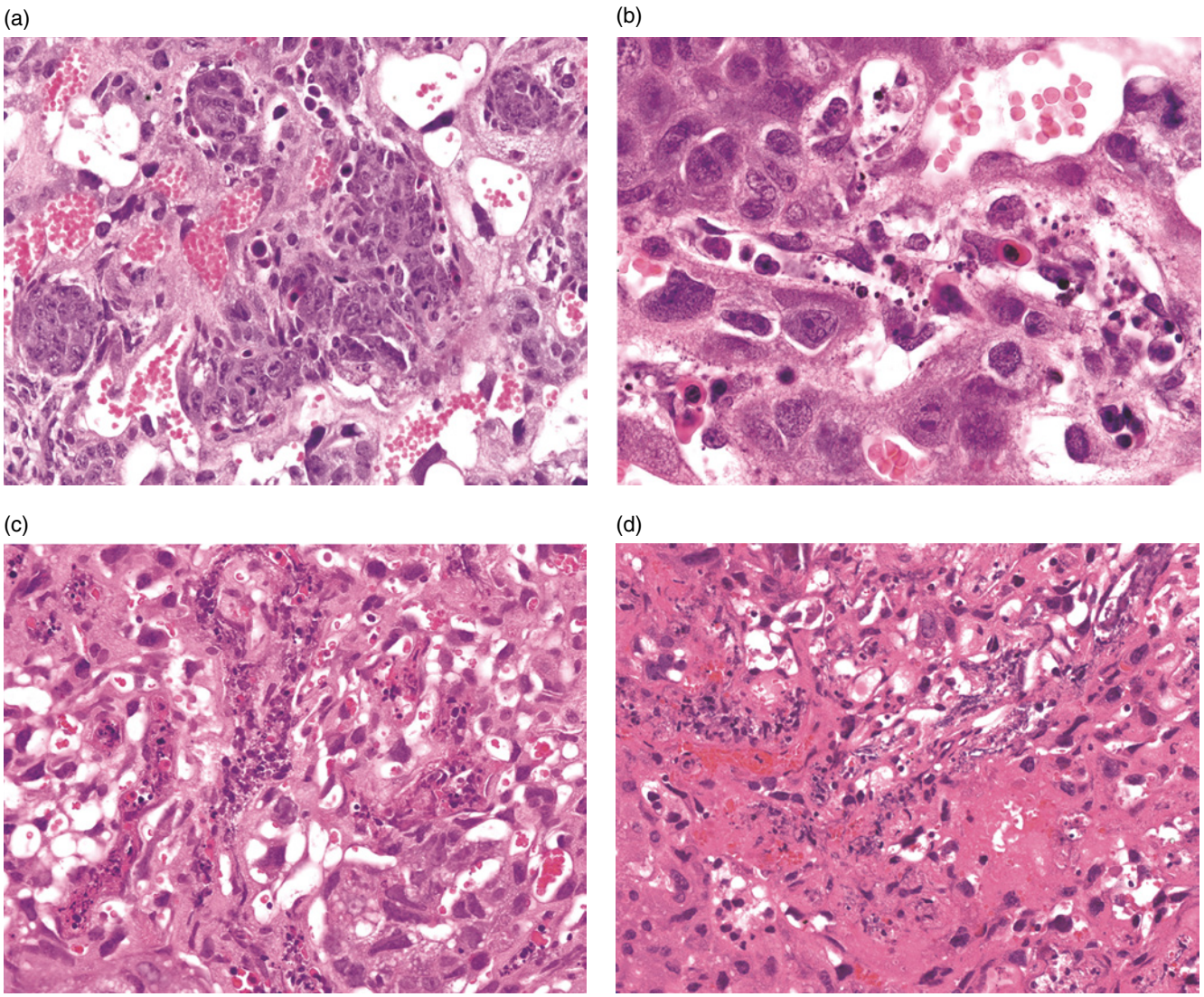


Figure 5.23 Common lesions in the placental labyrinth of mouse embryos may affect specific cell lineages or all cell populations in a region. Panel (a): Trophoblast hyperplasia appears as coalescing aggregates of plump basophilic cells, some of which contain mitotic figures. Panel (b): Virus-induced endothelial cell necrosis in embryonic blood spaces (EBS) presents as abundant cell debris in vascular channels that also contain a few large-diameter, nucleated erythrocytes. Panel (c): The EBS are packed with long, linear plugs of necrotic debris, which represent emboli of degenerating cells arising from the dying embryo. Panel (d): Widespread necrosis, hemorrhage, and fibrin deposition blurs the labyrinth structure and effaces many EBS. Stain: H&E.

Summary

Developmental phenotypes in embryonic and neonatal mice may be evaluated readily by comparative pathologists using routine macroscopic (gross observations and measurements of whole-animal or organ dimensions, volumes, or weights) and microscopic (light microscopy) techniques. If available, interpretation of such conventional endpoints is aided substantially by integration with other classes of data such as digital files acquired by noninvasive imaging or molecular expression profiles obtained from homogenized tissue samples or specially stained tissue sections. Lesions in embryos (and/or placentas) and neonates exhibit different patterns depending on when during development damage occurs in the conceptus. Genetic mutations, infectious agents, and toxicants all can adversely impact developing tissues, and can elicit comparable patterns of cell and tissue damage. The rapid anatomic and biochemical evolution in both space and time that takes place throughout the course of development ensures that the analysis of a potential lethal phenotype usually will be a complicated endeavor, requiring both patience and skill in designing the analytical strategy. Successful projects require an initial determination of the time of death followed by identification and detailed characterization of anatomic changes, functional abnormalities, and their molecular bases. Investigators should be prepared to acknowledge that a certain number of projects ultimately may fail to determine a cause for the developmental lethality.

Vet-ebooks.com

References

1 Theiler, K. (1972). *The House Mouse: Development and Normal Stages from Fertilization to 4 Weeks of Age*. Berlin: Springer-Verlag.
2 Rugh, R. (1990). *The Mouse. Its Reproduction and Development*. Oxford: Oxford University Press.
3 Rossant, J. and Tam, P.P.L. (2002). *Mouse Development: Patterning, Morphogenesis, Organogenesis*. San Diego, CA: Academic Press.
4 Croy, B.A., Yamada, A.T., DeMayo, F.J., and Adamson, S.L. (2014). *The Guide to Investigation of Mouse Pregnancy*. London: Academic Press (Elsevier).
5 Bolon, B. (2015). *Pathology of the Developing Mouse: A Systematic Approach*. Boca Raton, FL: CRC Press/Taylor & Francis.
6 Gossler, A. (1992). Early mouse development. In: *Early Embryonic Development of Animals* (ed. W. Hennig), 151–201. Berlin: Springer-Verlag.
7 Kaufman, M.H. (2007). Mouse embryology: research techniques and a comparison of embryonic development between mouse and man. In: *The Mouse in Biomedical Research: History, Wild Mice, and Genetics*, 2e, vol. 1 (eds. J.G. Fox, S.W. Barthold, M.T. Davisson, et al.), 165–209. San Diego, CA: Academic Press/Elsevier.
8 Boyd, K.L. and Bolon, B. (2010). Embryonic and fetal hematopoiesis. In: *Schalm's Veterinary Hematology*, 6e (eds. D.J. Weiss and K.J. Wardrop), 3–7. Ames, IA: Wiley Blackwell.
9 Nieman, B.J. and Turnbull, D.H. (2010). Ultrasound and magnetic resonance microimaging of mouse development. *Methods Enzymol.* 476: 379–400.
10 Theiler, K. (1989). *The House Mouse: Atlas of Embryonic Development*. New York: Springer-Verlag.
11 Kaufman, M.H. (1992). *The Atlas of Mouse Development*, 2e. San Diego, CA: Academic Press.
12 Jacobwitz, D.M. and Abbott, L.C. (1998). *Chemoarchitectonic Atlas of the Developing Mouse Brain*. Boca Raton, FL: CRC Press.
13 Paxinos, G., Halliday, G., Watson, C. et al. (2007). *Atlas of the Developing Mouse Brain at E17.5, P0, and P6*. San Diego, CA: Academic Press (Elsevier).
14 Schambra, U.B. (2007). Electronic prenatal mouse brain atlas. http://www.epmba.org (accessed 15 July 2021).
15 EMAP (2013). e-Mouse Atlas, v3.5. http://www.emouseatlas.org/emap/home.html (accessed 15 July 2021).
16 Rossant, J. and Cross, J.C. (2001). Placental development: lessons from mouse mutants. *Nat. Rev. Genet.* 2 (7): 538–548.
17 Watson, E.D. and Cross, J.C. (2005). Development of structures and transport functions in the mouse placenta. *Physiology* 20: 180–193.
18 Petiet, A.E., Kaufman, M.H., Goddeeris, M.M. et al. (2008). High-resolution magnetic resonance histology of the embryonic and neonatal mouse: a 4D atlas and morphologic database. *Proc. Natl. Acad. Sci. U.S.A.* 105 (34): 12331–12336.
19 Savolainen, S.M., Foley, J.F., and Elmore, S.A. (2009). Histology atlas of the developing mouse heart with emphasis on E11.5 to E18.5. *Toxicol. Pathol.* 37 (4): 395–414.
20 Crawford, L.W., Foley, J.F., and Elmore, S.A. (2010). Histology atlas of the developing mouse hepatobiliary system with emphasis on embryonic days 9.5–18.5. *Toxicol. Pathol.* 38 (6): 872–906.
21 Bolon, B., Couto, S., Fiette, L., and Perle, K.L. (2012). Internet and print resources to facilitate pathology analysis when phenotyping genetically engineered rodents. *Vet. Pathol.* 49 (1): 224–235.
22 Ward, J.M., Elmore, S.A., and Foley, J.F. (2012). Pathology methods for the evaluation of embryonic and perinatal developmental defects and lethality in genetically engineered mice. *Vet. Pathol.* 49 (1): 71–84.
23 Swartley, O.M., Foley, J.F., Livingston, D.P. 3rd et al. (2016). Histology atlas of the developing mouse hepatobiliary hemolymphatic vascular system with emphasis on embryonic days 11.5–18.5 and early postnatal development. *Toxicol. Pathol.* 44 (5): 705–725.
24 Chen, V.S., Morrison, J.P., Southwell, M.F. et al. (2017). Histology atlas of the developing prenatal and postnatal mouse central nervous system, with emphasis on prenatal days E7.5 to E18.5. *Toxicol. Pathol.* 45 (6): 705–744.
25 Elmore, S.A., Kavari, S.L., Hoenerhoff, M.J. et al. (2019). Histology atlas of the developing mouse urinary system with emphasis on prenatal days E10.5–E18.5. *Toxicol. Pathol.* 47 (7): 865–886.
26 Furukawa, S., Tsuji, N., and Sugiyama, A. (2019). Morphology and physiology of rat placenta for toxicological evaluation. *J. Toxicol. Pathol.* 32 (1): 1–17.
27 Elmore, S.A., Cochran, Z., Bolon, B. et al. (2021). Histology atlas of the developing mouse placenta. *Toxicol. Pathol.* (in press).
28 Clancy, B., Charvet, C.J., Darlington, R.B. et al. (2013). Translating time (across developing mammalian brains). http://translatingtime.net (accessed 15 March 2020).
29 Hill, M.A. (2014). Mouse development. University of New South Wales. https://embryology.med.unsw.edu.au/embryology/index.php/Mouse_Timeline_Detailed (accessed 15 July 2021).
30 Sulik, K.K. and Bream, P.R.J. Embryo images: normal and abnormal mammalian development. Chapel Hill, NC: University of North Carolina. Not given. http://www.med.unc.edu/embryo_images/ (accessed 15 July 2021).
31 Butler, H. and Juurlink, B.H.J. (1987). *An Atlas for Staging Mammalian and Chick Embryos*. Boca Raton, FL: CRC Press.
32 Kaufman, M.H. and Bard, J.B.L. (1999). *The Anatomical Basis of Mouse Development*. San Diego, CA: Academic Press.
33 Thiel, R., Chahoud, I., Jürgens, M., and Neubert, D. (1993). Time-dependent differences in the development of somites of four different mouse strains. *Teratog., Carcinog., Mutagen.* 13 (6): 247–257.

Vet-ebooks.com

34 Malle, D., Economou, L., Sioga, A. et al. (2004). Somitogenesis in different mouse strains. *Folia Anat.* 32 (1): 5–10.

35 Paria, B.C., Lim, H., Das, S.K. et al. (2000). Molecular signaling in uterine receptivity for implantation. *Semin. Cell Dev. Biol.* 11 (2): 67–76.

36 Ramathal, C.Y., Bagchi, I.C., Taylor, R.N., and Bagchi, M.K. (2010). Endometrial decidualization: of mice and men. *Semin. Reprod. Med.* 28 (1): 17–26.

37 Spencer, T.E. and Bazer, F.W. (2004). Conceptus signals for establishment and maintenance of pregnancy. *Reprod. Biol. Endocrinol.* 2: 49.

38 O'Neill, C., Li, Y., and Jin, X.L. (2012). Survival signaling in the preimplantation embryo. *Theriogenology* 77 (4): 773–784.

39 Bolon, B. and Ward, J.M. (2015). Anatomy and physiology of the developing mouse and placenta. In: *Pathology of the Developing Mouse: A Systematic Approach* (ed. B. Bolon), 39–98. Boca Raton, FL: CRC Press (Taylor & Francis).

40 Warkany, J. (1971). Sensitive or critical periods in teratogenesis: uses and abuses of embryologic timetables. In: *Congenital Malformations* (ed. J. Warkany), 49–52. Chicago, IL: Year Book Medical Publishing, Inc.

41 Daston, G.P. and Manson, J.M. (1995). Critical periods of exposure and developmental outcome. *Inhalation Toxicol.* 7 (6): 863–871.

42 Rodier, P.M. (1980). Chronology of neuron development: animal studies and their clinical implications. *Dev. Med. Child Neurol.* 22 (4): 525–545.

43 Turgeon, B. and Meloche, S. (2009). Interpreting neonatal lethal phenotypes in mouse mutants: insights into gene function and human diseases. *Physiol. Rev.* 89 (1): 1–26.

44 Ward, J.M. and Devor-Henneman, D.E. (2000). Gestational mortality in genetically engineered mice: evaluating the extraembryonal embryonic placenta and membranes. In: *Pathology of Genetically Engineered Mice* (eds. J.M. Ward, J.F. Mahler, R.R. Maronpot, et al.), 103–122. Ames, IA: Iowa State University Press.

45 Georgiades, P., Ferguson-Smith, A.C., and Burton, G.J. (2002). Comparative developmental anatomy of the murine and human definitive placentae. *Placenta* 23 (1): 3–19.

46 Jollie, W.P. (1990). Development, morphology, and function of the yolk-sac placenta of laboratory rodents. *Teratology* 41 (4): 361–381.

47 Adamson, S.L., Lu, Y., Whiteley, K.J. et al. (2002). Interactions between trophoblast cells and the maternal and fetal circulation in the mouse placenta. *Dev. Biol.* 250 (2): 358–373.

48 Coan, P.M., Conroy, N., Burton, G.J., and Ferguson-Smith, A.C. (2006). Origin and characteristics of glycogen cells in the developing murine placenta. *Dev. Dyn.* 235 (12): 3280–3294.

49 Pijnenborg, R. (2000). The metrial gland is more than a mesometrial lymphoid aggregate of pregnancy. *J. Reprod. Immunol.* 46 (1): 17–19.

50 Ain, R. and Soares, M.J. (2004). Is the metrial gland really a gland? *J. Reprod. Immunol.* 61 (2): 129–131.

51 Croy, B.A., van den Heuvel, M.J., Borzychowski, A.M., and Tayade, C. (2006). Uterine natural killer cells: a specialized differentiation regulated by ovarian hormones. *Immunol. Rev.* 214 (1): 161–185.

52 Picut, C.A., Swanson, C.L., Parker, R.F. et al. (2009). The metrial gland in the rat and its similarities to granular cell tumors. *Toxicol. Pathol.* 37 (4): 474–480.

53 Croy, B.A., Zhang, J., Tayade, C. et al. (2010). Analysis of uterine natural killer cells in mice. *Methods Mol. Biol.* 612: 465–503.

54 Plaks, V., Sapoznik, S., Berkovitz, E. et al. (2011). Functional phenotyping of the maternal albumin turnover in the mouse placenta by dynamic contrast-enhanced MRI. *Mol. Imag. Biol.* 13 (3): 481–492.

55 McLaren, A. (1965). Genetic and environmental effects on foetal and placental growth in mice. *J. Reprod. Fertil.* 9: 79–89.

56 Tanaka, S., Oda, M., Toyoshima, Y. et al. (2001). Placentomegaly in cloned mouse concepti caused by expansion of the spongiotrophoblast layer. *Biol. Reprod.* 65 (6): 1813–1821.

57 George, J.D. and Manson, J.M. (1986). Strain-dependent differences in the metabolism of 3-methylcholanthrene by maternal, placental, and fetal tissues of C57BL/6J and DBA/2J mice. *Cancer Res.* 46 (11): 5671–5675.

58 Bolon, B., Newbigging, S., and Boyd, K.L. (2017). Pathology evaluation of developmental phenotypes in neonatal and juvenile mice. *Curr. Protoc. Mouse Biol.* 7 (3): 191–219.

59 Ince, T.A., Ward, J.M., Valli, V.E. et al. (2008). Do-it-yourself (DIY) pathology. *Nat. Biotechnol.* 26 (9): 978–979. discussion 9.

60 Bolon, B., Garman, R., Jensen, K. et al. (2006). A 'best practices' approach to neuropathologic assessment in developmental neurotoxicity testing—for today. *Toxicol. Pathol.* 34 (3): 296–313.

61 Coan, P.M., Ferguson-Smith, A.C., and Burton, G.J. (2004). Developmental dynamics of the definitive mouse placenta assessed by stereology. *Biol. Reprod.* 70 (6): 1806–1813.

62 Weninger, W.J. and Geyer, S.H. (2008). Episcopic 3D imaging methods: tools for researching gene function. *Curr. Genomics* 9 (4): 282–289.

63 Ruberte, J., Carretero, A., and Navarro, M. (2017). *Morphological Mouse Phenotyping: Anatomy, Histology and Imaging*. San Diego, CA: Academic Press (Elsevier).

64 Tobita, K., Liu, X., and Lo, C.W. (2010). Imaging modalities to assess structural birth defects in mutant mouse models. *Birth Defects Res. C Embryo Today* 90 (3): 176–184.

65 Cleary, J.O., Modat, M., Norris, F.C. et al. (2011). Magnetic resonance virtual histology for embryos: 3D atlases for automated high-throughput phenotyping. *NeuroImage* 54 (2): 769–778.

66 Yu, Q., Leatherbury, L., Tian, X., and Lo, C.W. (2008). Cardiovascular assessment of fetal mice by in utero echocardiography. *Ultrasound Med. Biol.* 34 (5): 741–752.

Vet-ebooks.com

67 Bolon, B., Gabrielson, K., Cole, S. et al. (2015). Three-dimensional imaging in mouse developmental pathology studies. In: *Pathology of the Developing Mouse: A Systematic Approach* (ed. B. Bolon), 275–290. Boca Raton, FL: CRC Press (Taylor & Francis).

68 Hsu, C.W., Wong, L., Rasmussen, T.L. et al. (2016). Three-dimensional microCT imaging of mouse development from early post-implantation to early postnatal stages. *Dev. Biol.* 419 (2): 229–236.

69 Raghunathan, R., Singh, M., Dickinson, M.E., and Larin, K.V. (2016). Optical coherence tomography for embryonic imaging: a review. *J. Biomed. Opt.* 21 (5): 50902.

70 Newbigging, S., Ward, J.M., and Bolon, B. (2015). Necropsy sampling and data collection for studying the anatomy, histology, and pathology of mouse development. In: *Pathology of the Developing Mouse: A Systematic Approach* (ed. B. Bolon), 133–173. Boca Raton, FL: CRC Press (Taylor & Francis).

71 McKerlie, C., Newbigging, S., and Wood, G.A. (2015). Mouse developmental pathology assessments in high-throughput phenogenomic facilities. In: *Pathology of the Developing Mouse: A Systematic Approach* (ed. B. Bolon), 377–404. Boca Raton, FL: CRC Press (Taylor & Francis).

72 Bolon, B., Duryea, D., and Foley, J.F. (2015). Histotechnological processing of developing mice. In: *Pathology of the Developing Mouse: A Systematic Approach* (ed. B. Bolon), 195–210. Boca Raton, FL: CRC Press (Taylor & Francis).

73 Adissu, H.A., Estabel, J., Sunter, D. et al. (2014). Histopathology reveals correlative and unique phenotypes in a high-throughput mouse phenotyping screen. *Dis. Models Mech.* 7 (5): 515–524.

74 Kimura, S., Hara, Y., Pineau, T. et al. (1996). The *T/ebp* null mouse: thyroid-specific enhancer-binding protein is essential for the organogenesis of the thyroid, lung, ventral forebrain, and pituitary. *Genes Dev.* 10 (1): 60–69.

75 Min, H., Danilenko, D.M., Scully, S.A. et al. (1998). *Fgf-10* is required for both limb and lung development and exhibits striking functional similarity to Drosophila branchless. *Genes Dev.* 12 (20): 3156–3161.

76 Gibson-Corley, K.N., Olivier, A.K., and Meyerholz, D.K. (2013). Principles for valid histopathologic scoring in research. *Vet. Pathol.* 50 (6): 1007–1015.

77 Boyd, K.L., Bolon, B., and Bounous, D.I. (2015). Clinical pathology analysis in developing mice. In: *Pathology of the Developing Mouse: A Systematic Approach* (ed. B. Bolon), 175–193. Boca Raton, FL: CRC Press (Taylor & Francis).

78 Dickinson, M.E., Flenniken, A.M., Ji, X. et al. (2016). High-throughput discovery of novel developmental phenotypes. *Nature* 537 (7621): 508–514. (Corrigendum: *Nature* **51** (7680): 398, 2017).

79 International Mouse Phenotyping Consortium (IMPC) (2020). Pheno(type) search results: embryo. https://www.mousephenotype.org/data/search?term=embryo&type=pheno (accessed 15 July 2021).

80 Palmer, A.K. (1972). Sporadic malformations in laboratory animals and their influence on drug testing. In: *Drugs and Fetal Development* (eds. M.A. Klingberg, A. Abramovici and J. Chemke), 45–60. New York: Plenum Press.

81 The Jackson Laboratory. Mouse phenome database - lethal phenotypes during embryogenesis 2001–2020. http://www.informatics.jax.org/vocab/mp_ontology/MP:0005380 (accessed 15 March 2020).

82 Shepard, T.H. and Lemire, R.J. (2010). *Catalog of Teratogenic Agents*, 13e. Baltimore, MD: Johns Hopkins University Press.

83 Szaba, F.M., Tighe, M., Kummer, L.W. et al. (2018). Zika virus infection in immunocompetent pregnant mice causes fetal damage and placental pathology in the absence of fetal infection. *PLoS Pathog.* 14 (4): e1006994.

84 Kaufman, M., Nikitin, A.Y., and Sundberg, J.P. (2010). *Histologic Basis of Mouse Endocrine System Development: A Comparative Analysis* (ed. J.P. Sundberg). Boca Raton, FL: CRC Press (Taylor & Francis Group).

85 Baldock, R., Bard, J.B., Davidson, D.R., and Morriss-Kay, G. (2016). *Kaufman's Atlas of Mouse Development Supplement: With Coronal Sections*. San Diego, CA: Academic Press (Elsevier).

86 Parker, G.A. and Picut, C.A. (2016). *Atlas of Histology of the Juvenile Rat*. San Diego, CA: Academic Press (Elsevier).

87 Papaioannou, V.E. and Behringer, R.R. (2012). Early embryonic lethality in genetically engineered mice: diagnosis and phenotypic analysis. *Vet. Pathol.* 49 (1): 64–70.

88 Wendling, O., Teletin, M., Ghyselinck, N.B., and Mark, M. (2011). Une procédure dédiée au phénotypage de souris porteuses de mutations ciblées, létales in utero ou à la naissance ("A procedure dedicated to the phenotyping of mice carrying targeted mutations, lethal *in utero* or at birth") [original in French]. *Rev. Fr. Histotechnol.* 24 (1): 47–57.

89 Bolon, B. and La Perle, K.D.M. (2015). Principles of experimental design for mouse developmental pathology studies. In: *Pathology of the Developing Mouse: A Systematic Approach* (ed. B. Bolon), 117–132. Boca Raton, FL: CRC Press (Taylor & Francis).

90 Diewert, V.M. and Pratt, R.M. (1981). Cortisone-induced cleft palate in A/J mice: failure of palatal shelf contact. *Teratology* 24 (2): 149–162.

91 Diewert, V.M. (1982). A comparative study of craniofacial growth during secondary palate development in four strains of mice. *J. Craniofacial Genet. Dev. Biol.* 2 (4): 247–263.

92 Hovland, D.N.J., Machado, A.F., Scott, W.J.J., and Collins, M.D. (1999). Differential sensitivity of the SWV and C57BL/6 mouse strains to the teratogenic action of single administrations of cadmium given throughout the period of anterior neuropore closure. *Teratology* 60 (1): 13–21.

93 The Jackson Laboratory. Mouse phenome database - prenatal lethality due to placental pathology 2001–2020. http://www.informatics.jax.org/searches/Phat.cgi?id=MP:0001711 (accessed 15 July 2021).

Vet-ebooks.com

94 Bolon, B. and Ward, J.M. (2015). Pathology of the placenta. In: *Pathology of the Developing Mouse: A Systematic Approach* (ed. B. Bolon), 355–376. Boca Raton, FL: CRC Press (Taylor & Francis).

95 Woods, L., Perez-Garcia, V., and Hemberger, M. (2018). Regulation of placental development and its impact on fetal growth—new insights from mouse models. *Front. Endocrinol.* 9: 570.

96 Bolon, B. (2014). Pathology analysis of the placenta. In: *The Guide to Investigations of Mouse Pregnancy* (eds. B.A. Croy, A.T. Yamada, F. DeMayo and S.L. Adamson), 175–188. San Diego, CA: Academic Press (Elsevier).

97 Bolon, B., Welsch, F., and Morgan, K.T. (1994). Methanol-induced neural tube defects in mice: pathogenesis during neurulation. *Teratology* 49 (6): 497–517.

98 Tullio, A.N., Accili, D., Ferrans, V.J. et al. (1997). Nonmuscle myosin II-B is required for normal development of the mouse heart. *Proc. Natl. Acad. Sci. U. S. A.* 94 (23): 12407–12412.

99 Zou, X., Bolon, B., Pretorius, J.K. et al. (2009). Neonatal death in mice lacking cardiotrophin-like cytokine (CLC) is associated with multifocal neuronal hypoplasia. *Vet. Pathol.* 46 (3): 514–519.

100 Tamura, K., Sudo, T., Senftleben, U. et al. (2000). Requirement for p38a in erythropoietin expression: a role for stress kinases in erythropoiesis. *Cell* 102 (2): 221–231.

101 Withington, S.L., Scott, A.N., Saunders, D.N. et al. (2006). Loss of *Cited2* affects trophoblast formation and vascularization of the mouse placenta. *Dev. Biol.* 294 (1): 67–82.

Vet-ebooks.com

6

Ciliopathies

Peter Vogel and Laura J. Janke

Introduction

Cilia are exceptionally complex microtubule-based organelles that are present on the surface of almost every type of cell as either multiple motile cilia or individual nonmotile primary/sensory cilia. Dysfunctional cilia result in diseases termed ciliopathies, the number of which is continually increasing. Research on genetically engineered mice is facilitating the discovery of novel ciliopathies and the functions of the ciliary proteins involved [1]. Primary/sensory cilia are present on almost all cell types, whereas motile cilia are generally restricted to the respiratory tract, ependymal cells in the brain, reproductive tract, and the embryonic node. Primary/sensory cilia play key roles in a wide range of developmental and cellular functions, including cell-cycle regulation and planar cell polarity, as well as photo-, mechano-, and chemo-sensation. Motile cilia move fluids over epithelial surfaces and as flagella, propel spermatozoa. The sensory cilia integrate critical signaling pathways involved in development and differentiation, with the sensory primary cilium essentially acting as a cell antenna that contains and integrates critical components of the sonic hedgehog (SHH), wingless-type mouse mammary tumor virus (MMTV) integration site family (WNT), Hippo, Notch, and mechanistic target of rapamycin kinase (mTOR) signaling pathways, among others [2]. For example, the hedgehog (HH) pathway is involved in the developmental patterning of many tissues, including the neural tube and limb buds [3], and defective HH signaling is strongly linked to the development of ciliopathies.

Given their nearly ubiquitous distribution and diverse functions, defects in proteins required for the biogenesis and/or function of these extremely complex multifunctional organelles have been linked to an ever expanding and heterogeneous group of inherited ciliopathies [4–6]. It is important for mouse pathologists to recognize the pleomorphic disease phenotypes that are indicative of a ciliary dysfunction because the pathologist is frequently the only research team member that evaluates the whole animal [7], and mutations affecting the several hundred genes involved in the biogenesis and function of cilia make ciliopathies surprisingly common.

The essential functions of cilia are reflected by the significant number of highly conserved genes in the ciliary proteome (ciliome). For example, many conserved structural and intraflagellar transport (IFT) proteins that are present in *Chlamydomonas reinhardtii* have made this single-cell green algae a very useful model for identifying ciliary proteins and processes in motile cilia. In the evolution of multicellular animals, the sensory primary cilia provided the means of intercellular communication required to coordinate the growth, patterning, and differentiation of cells [8] and for sensing environmental stimuli [9]. The localization of HH, G protein-coupled receptors (GPCRs), and transient receptor potential (TRP) channels to cilia began before the origin of animals [10]. The continually expanding ciliome includes over a thousand different proteins [11], and hundreds of these have already been localized to the ciliary/flagellar axoneme, ciliary root, centriole, basal body transition zone, IFT proteins, ciliary membrane, central pair, axoneme, or ciliary tip in humans and mice [12, 13].

These structures have specific functions within the cilium – the basal body is involved in early ciliogenesis, the transition zone functions in ciliary gating, and the IFT enables cargo trafficking and signaling. Some receptors and pathways are localized to one of these specific areas, whereas others affect multiple processes within the cilia. For example, the HH receptor Patched1 (*Ptch1*) is located on primary cilia [14] and the levels of HH and other signaling molecules on the ciliary membrane are affected by both trafficking via IFT and gating at the transition zone. In addition, several so called second-order ciliopathies have been identified; these are

Pathology of Genetically Engineered and Other Mutant Mice, First Edition. Edited by John P. Sundberg, Peter Vogel, and Jerrold M. Ward.
© 2022 John Wiley & Sons, Inc. Published 2022 by John Wiley & Sons, Inc.

Vet-ebooks.com

caused by dysfunction or loss of nonciliary proteins that are nevertheless required for ciliary biogenesis/function [15].

Although the cilium is contiguous with the rest of the cell, its contents and membrane must be functionally separate from the rest of the cell in order for it to function as a cellular antenna. To maintain the distinct compartmentalization of ciliary components, a specialized transition zone surrounding the base of the cilium controls which proteins can enter and exit the cilium, and also forms a diffusion barrier for membrane-associated soluble proteins [16]. Numerous mutations affecting transitional zone proteins have been identified in both motile and nonmotile cilia.

Cilia can be classified on the basis of their number (multiple vs. single), their motility (motile vs. immotile), and by the presence or lack of central microtubule singlets within the core of the cilium (axoneme). In all cilia, the axoneme is made up of nine radially arranged microtubules that originate from the basal body. Motile cilia typically have two central microtubule singlets and axonemal inner and outer dynein arms that power ciliary movement, forming a 9+2 pattern. The motile cilia and flagella are responsible for sperm locomotion and the generation of extracellular fluid flow [17], whereas the nonmotile primary cilia are sensory, which requires the localization of specific signal transduction machinery to cilia [8]. In contrast, axonemes in nonmotile cilia lack the central pair and thus have a 9+0 arrangement of microtubules.

Identifying the pleomorphic phenotypes indicative of a ciliopathy requires careful examination of mice at time of necropsy and under the microscope. The ciliopathy-associated phenotypes that are best identified grossly include hydrocephalus, craniofacial and skeletal defects, and laterality defects. Histology is used to identify lesions such as rhinosinusitis, otitis media, spermatozoal flagellar defects, and brain malformations. Other symptoms that may be the result of ciliary dysfunction include behavioral disorders, deafness, and obesity. However, since these disorders can have underlying pathogenetic mechanisms that do not involve cilia, they generally must be accompanied by one or more other cilia-related phenotypes to be recognized as potential ciliopathies. Although motile and sensory cilia sometimes have overlapping effects on embryonic development or adult tissue homeostasis [5], the phenotypes of most ciliopathies are conveniently categorized as involving predominantly motile or sensory cilia.

Motile Ciliopathies

Motile cilia (including flagella) exhibit wave-like or beating motions that are powered by the molecular motor dynein. Motile cilia are present in the respiratory tract, ependymal cells in the brain, reproductive tract, and embryo. While formation of a single cilium is a complex process depending on hundreds of proteins, multiciliated cells must develop a complex network of properly oriented cilia that beat in coordinated fashion in order to generate continuous fluid flow in the brain ventricles, nasal and pulmonary airways, oviduct/epididymis, and embryonic node. Defective motile cilia cause primary ciliary dyskinesias (PCDs), which are typically characterized by chronic rhinosinusitis, pulmonary infections, otitis media, impaired fertility, and hydrocephalus [18–20]. Interestingly, bronchiectasis and pulmonary infections are typical signs of motile ciliary defects in humans but these lesions are absent in mice, whereas hydrocephalus is rare in affected humans but common in mice [21]. Defective motile cilia in the embryonic node lead to laterality defects such as *situs inversus* and heterotaxy in both mice and humans [22]. Mutations in genes that encode axonemal dynein subunits and dynein motor assembly proteins account for fewer than two-thirds of PCD cases, indicating that many motile cilia gene mutations causing these diseases remain to be discovered [23].

Rhinosinusitis and Otitis Media

Suppurative rhinosinusitis is the most characteristic and consistent finding in mice with dysfunctional motile cilia or PCD. Ciliary dysfunction reduces the ability of the mucociliary clearance mechanism to remove secretions and infectious agents from mucosal surfaces, which results in the accumulation of exudates and promotes secondary bacterial infections and suppurative inflammation (Figure 6.1). When mucociliary clearance is impaired in humans [20], chronic otitis media, rhinitis, sinusitis, and recurrent infections of the lower respiratory tract can result in irreversible bronchiectasis [24, 25].

In mice, PCD lesions are characterized by accumulations of mucus and mucopurulent exudates in the nasal passageways and sinuses, which are frequently accompanied by chronic-active inflammation in the nasal submucosa. The high prevalence of suppurative otitis media in affected mice is most likely the result of impaired mucociliary function

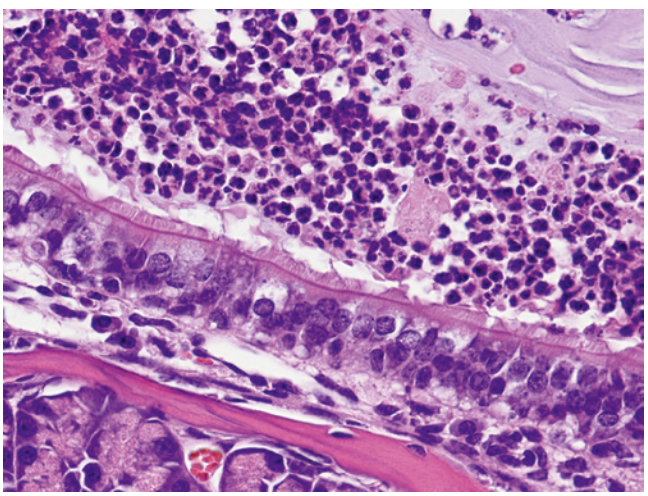


Figure 6.1 **Nasal epithelium**. Motile cilia are present on respiratory epithelium but are dysfunctional, resulting in suppurative rhinosinusitis.

Vet-ebooks.com

within the Eustachian tubes. In contrast to PCD in humans, respiratory tract lesions in mice are limited to the nasal passageways and sinuses, and they appear to be completely resistant to the severe pulmonary lesions that typically develop in humans with PCD [21, 26, 27].

Hydrocephalus

Young mice that develop hydrocephalus before their cranial sutures close typically present with an enlarged, domed head (Figure 6.2), but the majority of cases have milder disease that may not be evident until the head is sectioned. Hydrocephalus may be caused by a blockage of the normal flow of cerebrospinal fluid (CSF), a failure of absorption of CSF, or least commonly, an overproduction of CSF. Although there are many different potential causes of hydrocephalus, a motile ciliopathy is most likely involved when the brain lesion is accompanied by rhinosinusitis, defective spermatozoa, or laterality defects. Abnormal or deficient motility of ependymal cilia during brain morphogenesis clearly contributes to the development of hydrocephalus in many mice [28]. The synchronous beat of ependymal cilia that line the ventricles and interventricular connections generates a directional flow of CSF which has been termed "ependymal flow" [29], which may be required to maintain the patency of the aqueduct. The absence of ependymal flow during early postnatal brain development has been linked to secondary aqueduct stenosis [29].

However, congenital hydrocephalus in mice is a complex polygenic trait, and its development is strongly influenced by the presence of strain-specific genetic modifiers. For example, hydrocephalus is a relatively common finding in C57BL/6 mice, and it has been observed that *Del(1)Brk* (formerly *nm1054*) [30] and *Fyn*-deficient mice on C57BL/6 backgrounds develop severe hydrocephalus, while mutants on 129 or mixed background showed either mild or no hydrocephalus [30, 31]. Similarly, hydrocephalus develops in L1-deficient mice only after backcrossing to the C57BL/6 strain, with the mutation eventually becoming embryonic lethal after several backcrosses [32]. Taken together, these findings suggest that C57BL/6 already carry mutant alleles that predispose them to having dysfunctional motile cilia and thus to developing hydrocephalus and other motile ciliopathies. Although most cases of hydrocephalus can be linked to dysfunctional motile cilia, it is clear that primary cilia are involved in cellular signal pathways expressed during early brain development that can result in hydrocephalus when disrupted. The previously described L1-deficient mutant mice develop severe hydrocephalus that does not involve either aqueduct stenosis or ultrastructural abnormalities of ependymal cells or cilia lining the lateral ventricles or the aqueduct [33].

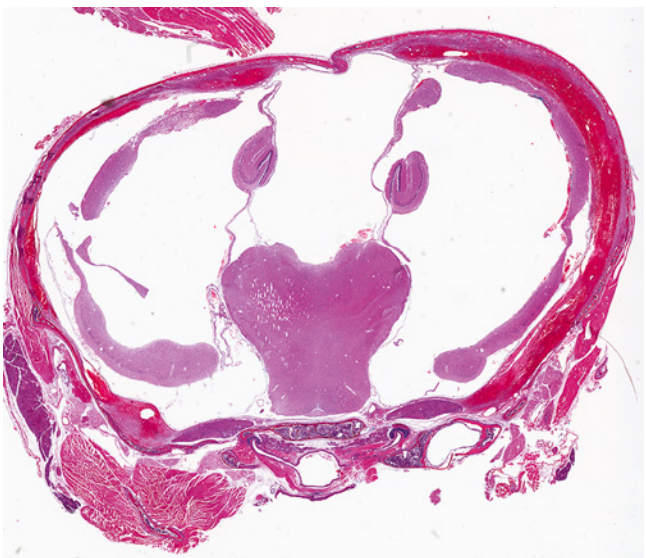


Figure 6.2 **Brain hydrocephalus**. Ependymal ciliary dysfunction often results in severe dilatation of the ventricles in the brain.

Laterality Defects

Laterality defects can only be identified on gross exam, and prosectors need to be alert because these phenotypes are surprisingly easy to overlook during necropsies, especially since fewer than 50% of the homozygous mice will display any *situs* phenotype in most affected lines. One critical role for cilia is the specification of the left–right (LR) body axis during development. Motile cilia alongside the embryonic node, a cup-shaped structure on the ventral surface of the developing embryo, generate a flow that is detected by sensory cilia within the node [34], with both types of cilia required for normal left–right axis patterning [27]. Defects in motile cilia are likely when the laterality defects are accompanied by rhinosinusitis, male infertility, or hydrocephalus, whereas the absence of these lesions is suggestive of a sensory ciliopathy [27]. The term *situs solitus* is used to describe the normal left–right (LR) asymmetry in the positioning of internal organs [35, 36], while a mirror image reversal of organ positioning is called *situs inversus* [37, 38]. The terms *situs ambiguus* or heterotaxy are used to describe other variations in organ placement due to abnormal left–right patterning during embryonic development.

Infertility

In male mice, infertility is often a consequence of defective biogenesis or function of the motile spermatozoal flagellum [39]. Many flagellar defects are visible by light microscopy [40] and may be accompanied by other lesions commonly associated with dysfunctional motile cilia [41] (Figure 6.3). In contrast, fertility is generally not impaired in female mice with motile cilia deficiencies, despite the presence of ciliated epithelium of the oviduct. These findings are consistent with those in humans with PCD, where reduced fertility in men with PCD is attributed to dysmotility of spermatozoa and/or reduced sperm count, while lack of ciliary motility in the

Vet-ebooks.com

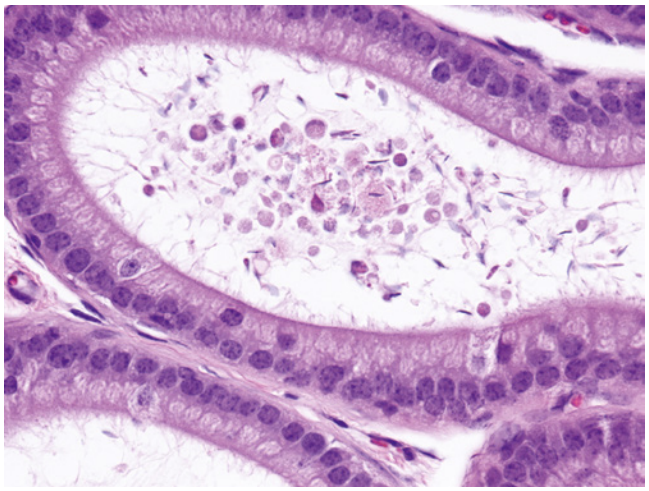


Figure 6.3 **Epididymis**. Flagellar defects or dysfunction are common causes of male infertility.

Fallopian tubes of women does not appear to have a major effect on fertility [42]. Although cilia-related infertility is usually associated with dysfunctional motile cilia, defective immotile sensory cilia are also involved in some cases [43].

Sensory Ciliopathies

The immotile/primary cilia are present on almost all types of cells, and their primary function is to transduce signals from the environment or surrounding cells. For many decades after their discovery, it was thought that the immotile primary cilia were purely vestigial organelles. However, it is now clear that defects in immotile primary cilia, which have a variety of different sensory functions [44], can cause myriad inherited diseases that simultaneously involve several different organ systems and thus display pleiotropic phenotypes. These diseases range from severe developmental defects resulting in embryonic or perinatal lethality to diseases such as polycystic kidney disease (PKD), retinal degeneration, hepatic and pancreatic cysts, skeletal anomalies, brain malformations such as microcephaly and cerebellar dysplasia, and left–right axis defects. Ciliopathies are also associated with other types of lesions affecting the eye, central nervous system (CNS), liver, and pancreas.

The sensory functions of primary cilia depend on the coordinated trafficking and temporal localization of specific receptors and their associated signal transduction modules in the cilium. Primary cilia sense and transduce environmental signals via several signaling pathways, including HH, GPCR, WNT, receptor tyrosine kinase, and transforming growth factor β (TGFβ)/bone morphogenetic protein (BMP) signaling [8]. The central importance of these pathways in regulating key processes in development and tissue homeostasis account for the pleomorphic developmental disorders and diseases that accompany primary cilia defects [45]. The role of primary cilia in HH signaling is probably the best understood at this time. There are three major protein ligands in the HH system: SHH, Indian Hedgehog (IHH), and Desert Hedgehog (DHH). Of these, SHH signaling is critical to spatial patterning of the neuroepithelium, cellular identity in the CNS, axonal guidance, wiring of the neural network, and neuronal activity. Primary cilia defects in mice with mutations in SHH are associated with several defects in brain development, such as defective neural patterning, cerebellar hypoplasia, and defective hippocampal neurogenesis. IHH and DHH are both essential for normal craniofacial development, and mutations in several HH-related ciliary proteins result in skeletal and craniofacial deformities [46].

Cystic Kidney Diseases

PKDs were the first to be linked definitively to defects in primary immotile cilia. Recognition that polycystin 1 (PKD1), polycystin 2 (PKD2), and nephrocystin 1 (NPHP1) proteins were all localized to the primary cilium/basal body/centrosome provided the first evidence that dysfunctional primary cilia could be involved in the pathogenesis of PKD and nephronophthisis (NPHP) [47, 48]. Since then mutations in dozens of other cilia-related genes have been directly linked to the development of cystic kidney diseases [49]. The primary cilium on renal tubular epithelial cells projects into the urinary space and appears to act as a mechanosensor in detecting the flow of urine and thereby influencing renal cell division [50]. The primary cilium also regulates the orientation of cell division and disrupted planar cell polarity signaling also contributes to renal cystogenesis [51]. PKD is characterized by grossly enlarged kidneys, due to markedly dilated renal tubules lined by epithelial cells showing increased mitotic activity (Figure 6.4). In contrast, the polycystic kidneys in NPHP are essentially normal or reduced in size, with low mitotic rates and increased apoptosis of renal tubular epithelium [52] (Figure 6.5).

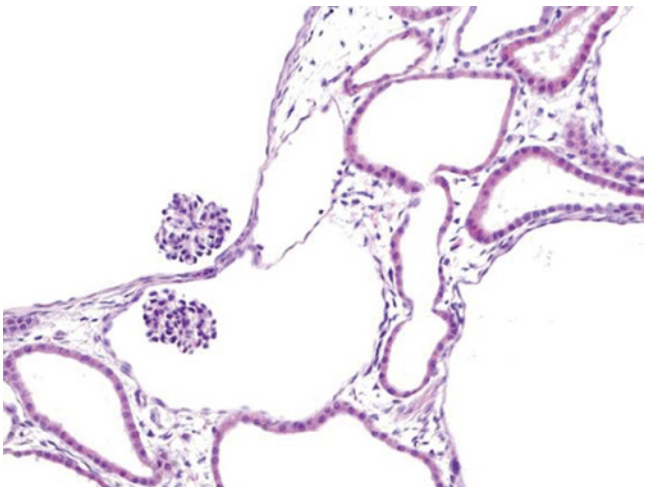


Figure 6.4 **Polycystic kidney disease**. Dilatation of renal tubules in an enlarged kidney due to proliferation of renal epithelium is associated with dysfunctional primary cilia.

Vet-ebooks.com

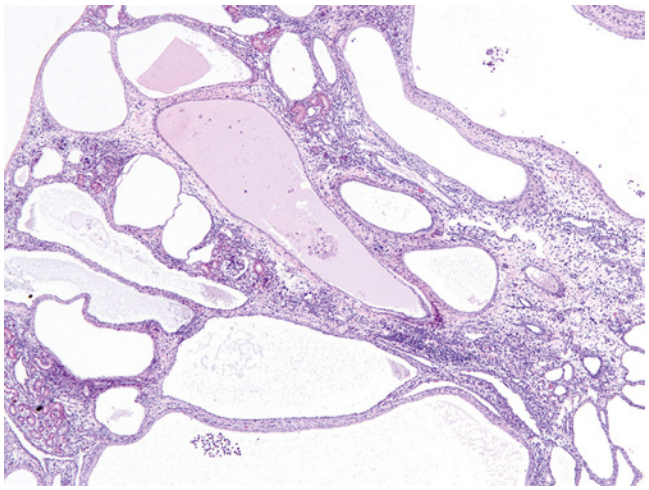


Figure 6.5 **Nephronophthisis**. Cystic tubules with interstitial inflammation and fibrosis in a normal sized kidney are associated with attrition of renal epithelium due to dysfunctional primary cilia.

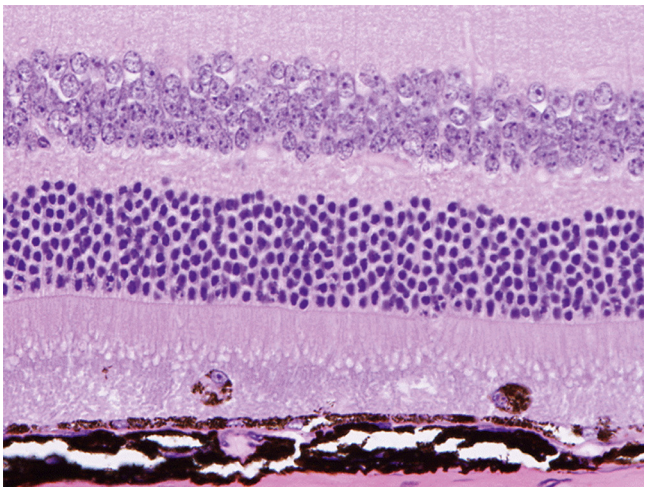


Figure 6.6 **Eye**. Macrophages within the outer segment of photoreceptor are present at the earlier stages of retinal degeneration.

Retinal Degeneration

Retinal degeneration is the most common manifestation of ciliary dysfunction in the eye, although coloboma and microphthalmia can occur in some ciliopathies as a result of defective HH signaling. In the retinal photoreceptor cells, modified primary cilia form the photoreceptor outer segments and express proteins that are specialized for phototransduction. The outer segments are specialized sensory cilia, and deficient morphogenesis and/or dysfunction of these sensory cilia caused by mutations in a wide range of photoreceptor-specific and ciliary genes can result in inherited retinal degenerations [53]. Almost all of the proteins involved in maintenance of the outersegment and phototransduction (most notably rhodopsin) are synthesized in the inner segment and must be transported to the outer segment via the connecting cilium. As a result, the efficient transport of cargo along the connecting cilium is essential for the assembly and maintenance of the photoreceptor outer segment. Mutations in several genes that encode proteins localized to the connecting cilium and/or its basal body can disrupt this process of intersegmental transport and result in the mislocalization of outer segment proteins and disorganization of the outer segments [54–58], which often precedes photoreceptor degeneration [59, 60]. In addition, the axoneme of the connecting cilium extends into the OS and is thought to establish the proper alignment of the membranous disks containing rhodopsin and other proteins required for phototransduction [61].

Histology is a very sensitive and specific method for detecting retinopathies. In normal mouse eyes, subretinal macrophages are absent or very rare, the inner and outer segments of the photoreceptors appear in organized columns and are of approximately equal length, and the outer nuclear layer is thicker than the inner nuclear layer. Almost all disruptions affecting the development or function of outer segments will lead to degeneration of photoreceptors, which can be detected histologically even at early stages by the appearance or any combination of the following changes: increased numbers of subretinal macrophages (Figure 6.6), disrupted/thin outer segments, or reduced thickness of the outer nuclear layer (consisting of photoreceptor nuclei; Figure 6.7).

Heart Defects

Careful gross examination of the heart and great vessels should be included when phenotyping any genetically engineered mouse line showing decreased viability [62, 63]. Cilia play a key role in cell signaling pathways that regulate the development of the heart and large blood vessels, particularly those involved in left–right patterning. Although *situs inversus totalis* is generally asymptomatic, complex congenital cardiac

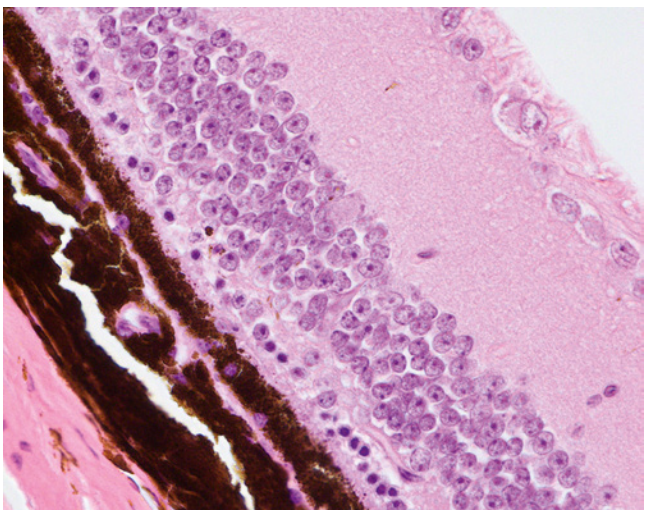


Figure 6.7 **Eye**. Advanced retinal degeneration there is characterized by a marked reduction in the thickness of the outer nuclear layer photoreceptors.

Vet-ebooks.com

defects and transposition of the great vessels of the heart are often associated with *situs ambiguus* or heterotaxy [64–66]. Interestingly, humans with congenital heart disease show a high prevalence of ciliary dysfunction and *de novo* ciliary mutations, suggesting that ciliary functions other than left–right positioning may be involved [67].

Skeletal Defects

Ciliopathies affecting skeletal development most often appear as malformed ribs, polydactyly, brachydactyly, shortened long bones, and cone-shaped epiphyses. Disruption of HH signaling regulation leads to multiple bone diseases [68] and many of the mutated genes associated with these skeletal defects encode proteins involved ciliary transport and thus HH signaling [69, 70]. SHH is a major morphogen during early stages of embryonic limb development, while IHH has a key role in endochondral ossification.

The high prevalence of skeletal and craniofacial malformations in ciliopathies [71] stems from the key role of HH signaling during the development of bone and the craniofacial complex. [72]. In both humans and mice, craniofacial malformations often manifest as micrognathia [73]. Any lines with newborn mice that show signs of impaired feeding or breathing should be carefully examined for the presence of ciliopathy-related craniofacial malformations such as micrognathia and cleft palate. Dysfunctional HH signaling is also linked to the development of polydactyly in Bardet–Biedl, oral–facial–digital, Senior–Løken, and Meckel–Gruber syndromes, via the ciliary role in HH signaling [74]. In mice, polydactyly has been linked to mutations in IFT genes in mice [75], as primary cilia are required for cells to respond to SHH mediators [76]. Polydactyly is another ciliopathy-related skeletal defect that should be identified in live mice or at time of necropsy.

To augment gross necropsy findings, whole-mount skeletal staining is recommended to confirm and better characterize any suspected skeletal defects. Detailed protocols for whole-mount skeletal staining of embryos which highlight cartilage using Alcian Blue and mineralized bone with Alizarin Red S are available [77].

Brain Malformations

Hydrocephalus is the most common CNS disorder caused by defective cilia, but ciliary involvement should be considered in any mice displaying brain malformations. Neurons and astrocytes have a single nonmotile primary cilium [78]. These cilia have critical roles in neurogenesis [79–81] and CNS development [82]. Normal CNS development is dependent on neuronal migration, which is a complex process involving signaling molecules that integrate intercellular signals with cytoskeletal proteins to initiate migration and nucleokinesis, which include neurotrophins, glutamate receptors, and peroxisome-derived factors [83]. Dysfunctional primary cilia are responsible for many neurodevelopmental disorders [82], with the cerebellar malformations associated with Joubert syndrome (JBTS), Meckel–Gruber syndrome (MKS) and Bardet–Biedl syndrome (BBS) providing the most conspicuous examples [84]. Mice with a conditional deletion of *270049A03Rik* (formerly *Talpid3*) in the CNS display the hallmark signs of JBTS, which include progressive ataxia, cerebellar hypoplasia, and abnormal decussation of the superior cerebellar peduncles [85].

Deafness

Deafness is associated with several ciliopathies, but the lesions in the inner ear are not detectable by light microscopy. Each sensory hair cell in the cochlea has a single transient nonmotile cilium (kinocilium) located at its apex. This so-called kinocilium disappears by 12 days postpartum in mice and was long believed to be a transient embryonic organelle without any functional significance. However, kinocilia are required for correct polarization of sensory hair cells in the organ of Corti during development. The kinocilium initially occupies a central position on the sensory hair cell before migrating to the periphery where it is critical for the maturation and correct orientation of stereocilia [86]. There are several recessive mutations in CDC14 cell division cycle 14A (*Cdc14a*) that result in substantial perinatal lethality in mice, but the deafness and male infertility (abnormal morphology and motility of spermatozoa) phenotypes mirror those seen in humans with mutant *CDC14A* genotypes [87]. Despite the absence of light microscopic lesions in the cochlea in these cases, the deafness phenotype with concurrent defects affecting spermatozoa flagella would point toward a ciliopathy.

Anosmia

The primary cilia projecting from the surface of the olfactory epithelium utilize GPCRs on the ciliary membrane to detect and transduce signals from odorants [88]. The dysfunction or mislocalization of ciliary proteins and/or the loss of cilia will prevent olfaction [89], and mice lacking functional cilia on their olfactory neuroepithelium are anosmic [90]. Certain types of inherited anosmias may be accompanied by severely reduced ciliated borders over the olfactory neuroepithelium [91], but most defects involving the structure or signaling functions of olfactory receptors are not detectable by light microscopy or associated with degeneration or apoptosis of olfactory sensory neurons [89].

Obesity

Some ciliopathies in both humans and mice are associated with hyperphagia and obesity (e.g. Bardet–Biedl Syndrome, Alström Syndrome) [92]. Several mouse models recapitulate the human phenotypes and have proven useful in elucidating how sensory cilia influence appetite and the pathogenesis of obesity [93]. The sensory cilia on paraventricular nucleus neurons appear to control appetite by detecting signals from the arcuate nucleus. The tubby bipartite transcription factor

Vet-ebooks.com

(*Tub*^{tub}) mutant mouse, which develops progressive obesity and blindness, has defective trafficking of ciliary GPCRs in hypothalamic neurons [94]. Heterozygous mice hypomorphic for *Rpgrip1l* are leptin-resistant, hyperphagic, and obese. The distribution and responses of leptin receptors in sensory cilia of hypothalamic neurons are abnormal in *Rpgrip1l*^{tm1Urt} mice [95]. Similarly, obese and hyperphagic *Ankrd26Gt(XK525) Byg* mice have defective primary cilia in the hypothalamic paraventricular nucleus [92]. Again, since there are many different underlying mechanisms that can contribute to the development of obesity, other cilia-related phenotypes must be present to suspect a ciliopathy.

Genetic Background Effects

Cilia are incredibly complex organelles whose biogenesis and functions involve the interactions of many different genes (multigenicity). As a result, ciliopathies are phenotypically and genetically heterogeneous. Mutations involving a single gene can produce very different phenotypes depending on genetic background which introduces the varying effects of gene modifiers, gene redundancy, and allelism [15]. The modifier roles of specific alleles [96, 97] and multiprotein modules further illustrate the complexity of interactions between ciliary proteins [98].

For example, in both human and mouse PKD, genetic background effects modulate the renal and extrarenal phenotypes [99, 100]. For example, *Tmem67bpck* mice show a less severe kidney phenotype in a mixed background than they do in B6 or C3H/HeJ congenic lines [101]. The same mice on a B6 genetic background have a higher incidence of hydrocephalus, most likely due to underlying defects in ciliary structure/function [21]. Mouse strain-dependent genetic background effects can influence the incidence of hydrocephalus in PCD mouse models. For example, *Del(1)1Brk* mutant mice on a B6 background usually die within the first week of life due to severe hydrocephalus, whereas mutants on a 129 background develop either mild or no hydrocephalus, indicating the presence of varying genetic modifiers in the different mouse strains [30].

Although mutations in a particular ciliopathy gene may present with a consistent phenotype, it is common for genetic modifiers to alter some of the clinical features observed within syndromes [102]. Clearly, some of the differences reported between mice and humans with mutations in syntenic genes are due to species-specific differences in expression profiles, and/or the presence of compensatory proteins developed during divergent evolution of the species [57]. The extreme complexity of ciliary structures and functions undoubtedly accounts for most of the inter- and intraspecies variation in phenotypic expression. Physiological differences between these species may also greatly influence the phenotypic outcome.

Different mutations in a specific gene can produce a wide spectrum of overlapping clinical phenotypes. For example, different mutations within the human *NPHP11/MKS3/TMEM67* genes can give rise to mild (NPHP), intermediate (JBTS), or severe (MKS) phenotypes [103]. Mutations involving multiple genes can be involved in individuals with Bardet–Biedl syndrome [104], and different mutations at the same locus of a single gene (CEP290) can result in three distinct disease syndromes (BBS, MKS, and NPHP) [1].

Finally, it is important to know that truncating mutations often cause severe developmental defects that result in prenatal and perinatal mortality, whereas hypomorphic mutations are more likely to cause organ specific diseases that are degenerative rather than developmental [105]. Since complete loss of ciliopathy-associated genes often results in early lethality, it may be necessary to generate mice carrying hypomorphic alleles with a range of strengths in order to model ciliopathies [1]. The genetic mechanisms that underlie ciliary functions and thus determine ciliopathy phenotypes are extremely complex, with gene locus heterogeneity, allelic effects, and modifier genes all contributing to influence both the type and severity of disease, and pleiotropic phenotypes [106]. To further complicate matters, a growing number of ciliopathies can be classified as second order ciliopathies [15]. These include ciliopathies that are caused by mutations in genes encoding proteins not present in cilia, but that do influence cilia formation or functions. For example, there are motile ciliopathies resulting from mutations affecting specific nonciliary proteins involved in the cytosolic assembly of axonemal dynein complexes before they are imported into cilia [15].

References

1 Norris, D.P. and Grimes, D.T. (2012). Mouse models of ciliopathies: the state of the art. *Dis. Models Mech.* 5 (3): 299–312.

2 Singla, V. and Reiter, J.F. (2006). The primary cilium as the cell's antenna: signaling at a sensory organelle. *Science* 313 (5787): 629–633.

3 Briscoe, J. and Therond, P.P. (2013). The mechanisms of Hedgehog signalling and its roles in development and disease. *Nat. Rev. Mol. Cell Biol.* 14 (7): 416–429.

4 Wallmeier, J., Nielsen, K.G., Kuehni, C.E. et al. (2020). Motile ciliopathies. *Nat. Rev. Dis. Primers* 6 (1): 77.

5 Kempeneers, C. and Chilvers, M.A. (2018). To beat, or not to beat, that is question! The spectrum of ciliopathies. *Pediatr. Pulmonol.* 53 (8): 1122–1129.

6 Davis, E.E. and Katsanis, N. (2012). The ciliopathies: a transitional model into systems biology of human genetic disease. *Curr. Opin. Genet. Dev.* 22 (3): 290–303.

Vet-ebooks.com

7 Schofield, P.N., Vogel, P., Gkoutos, G.V., and Sundberg, J.P. (2012). Exploring the elephant: histopathology in high-throughput phenotyping of mutant mice. *Dis. Models Mech.* 5 (1): 19–25.

8 Goetz, S.C. and Anderson, K.V. (2010). The primary cilium: a signalling centre during vertebrate development. *Nat. Rev. Genet.* 11 (5): 331–344.

9 Bloodgood, R.A. (2010). Sensory reception is an attribute of both primary cilia and motile cilia. *J. Cell Sci.* 123 (Pt 4): 505–509.

10 Sigg, M.A., Menchen, T., Lee, C. et al. (2017). Evolutionary proteomics uncovers ancient associations of cilia with signaling pathways. *Dev. Cell* 43 (6): 744–62 e11.

11 Heydeck, W., Fievet, L., Davis, E.E., and Katsanis, N. (2018). The complexity of the cilium: spatiotemporal diversity of an ancient organelle. *Curr. Opin. Cell Biol.* 55: 139–149.

12 Christie, K.R. and Blake, J.A. (2018). Sensing the cilium, digital capture of ciliary data for comparative genomics investigations. *Cilia* 7: 3.

13 van Dam, T.J., Wheway, G., and Slaats, G.G., SYSCILIA Study Group et al. (2013). The SYSCILIA gold standard (SCGSv1) of known ciliary components and its applications within a systems biology consortium. *Cilia* 2 (1): 7.

14 Rohatgi, R., Milenkovic, L., and Scott, M.P. (2007). Patched1 regulates hedgehog signaling at the primary cilium. *Science* 317 (5836): 372–376.

15 Reiter, J.F. and Leroux, M.R. (2017). Genes and molecular pathways underpinning ciliopathies. *Nat. Rev. Mol. Cell Biol.* 18 (9): 533–547.

16 Goncalves, J. and Pelletier, L. (2017). The ciliary transition zone: finding the pieces and assembling the gate. *Mol. Cells* 40 (4): 243–253.

17 Satir, P. and Christensen, S.T. (2007). Overview of structure and function of mammalian cilia. *Annu. Rev. Physiol.* 69: 377–400.

18 Afzelius, B.A. (1976). A human syndrome caused by immotile cilia. *Science* 193 (4250): 317–319.

19 Afzelius, B.A. (1999). Asymmetry of cilia and of mice and men. *Int. J. Dev. Biol.* 43 (4): 283–286.

20 Fliegauf, M., Benzing, T., and Omran, H. (2007). When cilia go bad: cilia defects and ciliopathies. *Nat. Rev. Mol. Cell Biol.* 8 (11): 880–893.

21 Vogel, P., Read, R.W., Hansen, G.M. et al. (2012). Congenital hydrocephalus in genetically engineered mice. *Vet. Pathol.* 49 (1): 166–181.

22 Rott, H.D. (1979). Kartagener's syndrome and the syndrome of immotile cilia. *Hum. Genet.* 46 (3): 249–261.

23 Zariwala, M.A., Omran, H., and Ferkol, T.W. (2011). The emerging genetics of primary ciliary dyskinesia. *Proc. Am. Thorac. Soc.* 8 (5): 430–433.

24 Meeks, M. and Bush, A. (2000). Primary ciliary dyskinesia (PCD). *Pediatr. Pulmonol.* 29 (4): 307–316.

25 Geremek, M. and Witt, M. (2004). Primary ciliary dyskinesia: genes, candidate genes and chromosomal regions. *J. Appl. Genet.* 45 (3): 347–361.

26 Vogel, P., Hansen, G., Fontenot, G., and Read, R. (2010). Tubulin tyrosine ligase-like 1 deficiency results in chronic rhinosinusitis and abnormal development of spermatid flagella in mice. *Vet. Pathol.* 47 (4): 703–712.

27 Vogel, P., Read, R., Hansen, G.M. et al. (2010). Situs inversus in Dpcd/Poll−/−, Nme7−/−, and Pkd1l1−/− mice. *Vet. Pathol.* 47 (1): 120–131.

28 Banizs, B., Pike, M.M., Millican, C.L. et al. (2005). Dysfunctional cilia lead to altered ependyma and choroid plexus function, and result in the formation of hydrocephalus. *Development* 132 (23): 5329–5339.

29 Ibanez-Tallon, I., Pagenstecher, A., Fliegauf, M. et al. (2004). Dysfunction of axonemal dynein heavy chain Mdnah5 inhibits ependymal flow and reveals a novel mechanism for hydrocephalus formation. *Hum. Mol. Genet.* 13 (18): 2133–2141.

30 Lee, L., Campagna, D.R., Pinkus, J.L. et al. (2008). Primary ciliary dyskinesia in mice lacking the novel ciliary protein Pcdp1. *Mol. Cell. Biol.* 28 (3): 949–957.

31 Goto, J., Tezuka, T., Nakazawa, T. et al. (2008). Loss of Fyn tyrosine kinase on the C57BL/6 genetic background causes hydrocephalus with defects in oligodendrocyte development. *Mol. Cell. Neurosci.* 38 (2): 203–212.

32 Itoh, K., Cheng, L., Kamei, Y. et al. (2004). Brain development in mice lacking L1–L1 homophilic adhesion. *J. Cell Biol.* 165 (1): 145–154.

33 Rolf, B., Kutsche, M., and Bartsch, U. (2001). Severe hydrocephalus in L1-deficient mice. *Brain Res.* 891 (1–2): 247–252.

34 Nonaka, S., Tanaka, Y., Okada, Y. et al. (1998). Randomization of left–right asymmetry due to loss of nodal cilia generating leftward flow of extraembryonic fluid in mice lacking KIF3B motor protein. *Cell* 95 (6): 829–837.

35 Capdevila, J., Vogan, K.J., Tabin, C.J., and Izpisua Belmonte, J.C. (2000). Mechanisms of left–right determination in vertebrates. *Cell* 101 (1): 9–21.

36 Levin, M. (2005). Left–right asymmetry in embryonic development: a comprehensive review. *Mech. Dev.* 122 (1): 3–25.

37 Mercola, M. and Levin, M. (2001). Left–right asymmetry determination in vertebrates. *Annu. Rev. Cell Dev. Biol.* 17: 779–805.

38 Ramsdell, A.F. (2005). Left–right asymmetry and congenital cardiac defects: getting to the heart of the matter in vertebrate left–right axis determination. *Dev. Biol.* 288 (1): 1–20.

39 Escalier, D. (2006). Knockout mouse models of sperm flagellum anomalies. *Hum. Reprod. Update* 12 (4): 449–461.

40 Sironen, A., Shoemark, A., Patel, M. et al. (2020). Sperm defects in primary ciliary dyskinesia and related causes of male infertility. *Cell. Mol. Life Sci.* 77 (11): 2029–2048.

41 Inaba, K. and Mizuno, K. (2016). Sperm dysfunction and ciliopathy. *Reprod. Med. Biol.* 15 (2): 77–94.

42 Afzelius, B.A., Camner, P., and Mossberg, B. (1978). On the function of cilia in the female reproductive tract. *Fertil. Steril.* 29 (1): 72–74.

Vet-ebooks.com

43 Girardet, L., Augiere, C., Asselin, M.P., and Belleannee, C. (2019). Primary cilia: biosensors of the male reproductive tract. *Andrology* 7 (5): 588–602.

44 Berbari, N.F., O'Connor, A.K., Haycraft, C.J., and Yoder, B.K. (2009). The primary cilium as a complex signaling center. *Curr. Biol.* 19 (13): R526–R535.

45 Anvarian, Z., Mykytyn, K., Mukhopadhyay, S. et al. (2019). Cellular signalling by primary cilia in development, organ function and disease. *Nat. Rev. Nephrol.* 15 (4): 199–219.

46 Pan, A., Chang, L., Nguyen, A., and James, A.W. (2013). A review of hedgehog signaling in cranial bone development. *Front. Physiol.* 4: 61.

47 Olbrich, H., Fliegauf, M., Hoefele, J. et al. (2003). Mutations in a novel gene, NPHP3, cause adolescent nephronophthisis, tapeto-retinal degeneration and hepatic fibrosis. *Nat. Genet.* 34 (4): 455–459.

48 Otto, E.A., Schermer, B., Obara, T. et al. (2003). Mutations in INVS encoding inversin cause nephronophthisis type 2, linking renal cystic disease to the function of primary cilia and left-right axis determination. *Nat. Genet.* 34 (4): 413–420.

49 Loftus, H. and Ong, A.C. (2012). Cystic kidney diseases: many ways to form a cyst. *Pediatr. Nephrol.* 28: 33–49.

50 Raghavan, V. and Weisz, O.A. (2016). Discerning the role of mechanosensors in regulating proximal tubule function. *Am. J. Physiol. Renal Physiol.* 310 (1): F1–F5.

51 Luyten, A., Su, X., Gondela, S. et al. (2010). Aberrant regulation of planar cell polarity in polycystic kidney disease. *J. Am. Soc. Nephrol.* 21 (9): 1521–1532.

52 Vogel, P., Gelfman, C.M., Issa, T. et al. (2015). Nephronophthisis and retinal degeneration in tmem218−/− mice: a novel mouse model for Senior–Loken syndrome? *Vet. Pathol.* 52 (3): 580–595.

53 Bujakowska, K.M., Liu, Q., and Pierce, E.A. (2017). Photoreceptor cilia and retinal ciliopathies. *Cold Spring Harbor Perspect. Biol.* 9 (10): 1–27.

54 Chang, B., Khanna, H., Hawes, N. et al. (2006). In-frame deletion in a novel centrosomal/ciliary protein CEP290/NPHP6 perturbs its interaction with RPGR and results in early-onset retinal degeneration in the rd16 mouse. *Hum. Mol. Genet.* 15 (11): 1847–1857.

55 Westfall, J.E., Hoyt, C., Liu, Q. et al. (2010). Retinal degeneration and failure of photoreceptor outer segment formation in mice with targeted deletion of the Joubert syndrome gene, Ahi1. *J. Neurosci.* 30 (26): 8759–8768.

56 Won, J., Gifford, E., Smith, R.S. et al. (2009). RPGRIP1 is essential for normal rod photoreceptor outer segment elaboration and morphogenesis. *Hum. Mol. Genet.* 18 (22): 4329–4339.

57 Won, J., Marin de Evsikova, C., Smith, R.S. et al. (2011). NPHP4 is necessary for normal photoreceptor ribbon synapse maintenance and outer segment formation, and for sperm development. *Hum. Mol. Genet.* 20 (3): 482–496.

58 Zhao, Y., Hong, D.H., Pawlyk, B. et al. (2003). The retinitis pigmentosa GTPase regulator (RPGR)-interacting protein: subserving RPGR function and participating in disk morphogenesis. *Proc. Natl. Acad. Sci. U. S. A.* 100 (7): 3965–3970.

59 Insinna, C. and Besharse, J.C. (2008). Intraflagellar transport and the sensory outer segment of vertebrate photoreceptors. *Dev. Dyn.* 237 (8): 1982–1992.

60 Pazour, G.J., Baker, S.A., Deane, J.A. et al. (2002). The intraflagellar transport protein, IFT88, is essential for vertebrate photoreceptor assembly and maintenance. *J. Cell Biol.* 157 (1): 103–113.

61 Liu, Q., Lyubarsky, A., Skalet, J.H. et al. (2003). RP1 is required for the correct stacking of outer segment discs. *Invest. Ophthalmol. Visual Sci.* 44 (10): 4171–4183.

62 Campione, M. and Franco, D. (2016). Current perspectives in cardiac laterality. *J. Cardiovasc. Dev. Dis.* 3 (4): 1–18.

63 Tan, S.Y., Rosenthal, J., Zhao, X.Q. et al. (2007). Heterotaxy and complex structural heart defects in a mutant mouse model of primary ciliary dyskinesia. *J. Clin. Invest.* 117 (12): 3742–3752.

64 Bisgrove, B.W., Morelli, S.H., and Yost, H.J. (2003). Genetics of human laterality disorders: insights from vertebrate model systems. *Annu. Rev. Genomics Hum. Genet.* 4: 1–32.

65 Bohun, C.M., Potts, J.E., Casey, B.M., and Sandor, G.G. (2007). A population-based study of cardiac malformations and outcomes associated with dextrocardia. *Am. J. Cardiol.* 100 (2): 305–309.

66 Kennedy, M.P., Omran, H., Leigh, M.W. et al. (2007). Congenital heart disease and other heterotaxic defects in a large cohort of patients with primary ciliary dyskinesia. *Circulation* 115 (22): 2814–2821.

67 Klena, N.T., Gibbs, B.C., and Lo, C.W. (2017). Cilia and ciliopathies in congenital heart disease. *Cold Spring Harbor Perspect. Biol.* 9 (8): 1–18.

68 Yang, J., Andre, P., Ye, L., and Yang, Y.Z. (2015). The Hedgehog signalling pathway in bone formation. *Int. J. Oral Sci.* 7 (2): 73–79.

69 Halbritter, J., Bizet, A.A., Schmidts, M. et al. (2013). Defects in the IFT-B component IFT172 cause Jeune and Mainzer–Saldino syndromes in humans. *Am. J. Hum. Genet.* 93 (5): 915–925.

70 Schmidts, M., Frank, V., Eisenberger, T. et al. (2013). Combined NGS approaches identify mutations in the intraflagellar transport gene IFT140 in skeletal ciliopathies with early progressive kidney disease. *Hum. Mutat.* 34 (5): 714–724.

71 Zaghloul, N.A. and Brugmann, S.A. (2011). The emerging face of primary cilia. *Genesis* 49 (4): 231–246.

72 Schock, E.N. and Brugmann, S.A. (2017). Discovery, diagnosis, and etiology of craniofacial ciliopathies. *Cold Spring Harbor Perspect. Biol.* 9 (9): 1–14.

73 Adel Al-Lami, H., Barrell, W.B., and Liu, K.J. (2016). Micrognathia in mouse models of ciliopathies. *Biochem. Soc. Trans.* 44 (6): 1753–1759.

74 Marshall, W.F. (2008). The cell biological basis of ciliary disease. *J. Cell Biol.* 180 (1): 17–21.

75 Babbs, C., Furniss, D., Morriss-Kay, G.M., and Wilkie, A.O. (2008). Polydactyly in the mouse mutant Doublefoot

Vet-ebooks.com

involves altered Gli3 processing and is caused by a large deletion in cis to Indian hedgehog. *Mech. Dev.* 125 (5–6): 517–526.

76 Haycraft, C.J., Banizs, B., Aydin-Son, Y. et al. (2005). Gli2 and Gli3 localize to cilia and require the intraflagellar transport protein polaris for processing and function. *PLoS Genet.* 1 (4): e53.

77 Rigueur, D. and Lyons, K.M. (2014). Whole-mount skeletal staining. *Methods Mol. Biol.* 1130: 113–121.

78 Guemez-Gamboa, A., Coufal, N.G., and Gleeson, J.G. (2014). Primary cilia in the developing and mature brain. *Neuron* 82 (3): 511–521.

79 Breunig, J.J., Sarkisian, M.R., Arellano, J.I. et al. (2008). Primary cilia regulate hippocampal neurogenesis by mediating sonic hedgehog signaling. *Proc. Natl. Acad. Sci. U. S. A.* 105 (35): 13127–13132.

80 Han, Y.G., Spassky, N., Romaguera-Ros, M. et al. (2008). Hedgehog signaling and primary cilia are required for the formation of adult neural stem cells. *Nat. Neurosci.* 11 (3): 277–284.

81 Spassky, N., Han, Y.G., Aguilar, A. et al. (2008). Primary cilia are required for cerebellar development and Shh-dependent expansion of progenitor pool. *Dev. Biol.* 317 (1): 246–259.

82 Lee, J.E. and Gleeson, J.G. (2011). Cilia in the nervous system: linking cilia function and neurodevelopmental disorders. *Curr. Opin. Neurol.* 24 (2): 98–105.

83 Gressens, P. (2006). Pathogenesis of migration disorders. *Curr. Opin. Neurol.* 19 (2): 135–140.

84 Louie, C.M. and Gleeson, J.G. (2005). Genetic basis of Joubert syndrome and related disorders of cerebellar development. *Hum. Mol. Genet.* 14 (2): R235–R242.

85 Bashford, A.L. and Subramanian, V. (2019). Mice with a conditional deletion of Talpid3 (KIAA0586) – a model for Joubert syndrome. *J. Pathol.* 248 (4): 396–408.

86 Jones, C., Roper, V.C., Foucher, I. et al. (2008). Ciliary proteins link basal body polarization to planar cell polarity regulation. *Nat. Genet.* 40 (1): 69–77.

87 Imtiaz, A., Belyantseva, I.A., Beirl, A.J. et al. (2018). CDC14A phosphatase is essential for hearing and male fertility in mouse and human. *Hum. Mol. Genet.* 27 (5): 780–798.

88 McEwen, D.P., Jenkins, P.M., and Martens, J.R. (2008). Olfactory cilia: our direct neuronal connection to the external world. *Curr. Top. Dev. Biol.* 85: 333–370.

89 Jenkins, P.M., McEwen, D.P., and Martens, J.R. (2009). Olfactory cilia: linking sensory cilia function and human disease. *Chem. Senses* 34 (5): 451–464.

90 McIntyre, J.C., Davis, E.E., Joiner, A. et al. (2012). Gene therapy rescues cilia defects and restores olfactory function in a mammalian ciliopathy model. *Nat. Med.* 18 (9): 1423–1428.

91 Kulaga, H.M., Leitch, C.C., Eichers, E.R. et al. (2004). Loss of BBS proteins causes anosmia in humans and defects in olfactory cilia structure and function in the mouse. *Nat. Genet.* 36 (9): 994–998.

92 Acs, P., Bauer, P.O., Mayer, B. et al. (2015). A novel form of ciliopathy underlies hyperphagia and obesity in *Ankrd26* knockout mice. *Brain Struct. Funct.* 220 (3): 1511–1528.

93 Vaisse, C., Reiter, J.F., and Berbari, N.F. (2017). Cilia and obesity. *Cold Spring Harbor Perspect. Biol.* 9 (7): 1–13.

94 Mukhopadhyay, S. and Jackson, P.K. (2013). Cilia, tubby mice, and obesity. *Cilia* 2: 1.

95 Stratigopoulos, G., Burnett, L.C., Rausch, R. et al. (2016). Hypomorphism of *Fto* and *Rpgrip1l* causes obesity in mice. *J. Clin. Invest.* 126 (5): 1897–1910.

96 Khanna, H., Davis, E.E., Murga-Zamalloa, C.A. et al. (2009). A common allele in RPGRIP1L is a modifier of retinal degeneration in ciliopathies. *Nat. Genet.* 41 (6): 739–745.

97 Louie, C.M., Caridi, G., Lopes, V.S. et al. (2010). AHI1 is required for photoreceptor outer segment development and is a modifier for retinal degeneration in nephronophthisis. *Nat. Genet.* 42 (2): 175–180.

98 Rachel, R.A., May-Simera, H.L., Veleri, S. et al. (2012). Combining Cep290 and Mkks ciliopathy alleles in mice rescues sensory defects and restores ciliogenesis. *J. Clin. Invest.* 122 (4): 1233–1245.

99 Gattone, V.H. 2nd, MacNaughton, K.A., and Kraybill, A.L. (1996). Murine autosomal recessive polycystic kidney disease with multiorgan involvement induced by the *cpk* gene. *Anat. Rec.* 245 (3): 488–499.

100 Ricker, J.L., Gattone, V.H. 2nd, Calvet, J.P., and Rankin, C.A. (2000). Development of autosomal recessive polycystic kidney disease in BALB/c-cpk/cpk mice. *J. Am. Soc. Nephrol.* 11 (10): 1837–1847.

101 Cook, S.A., Collin, G.B., Bronson, R.T. et al. (2009). A mouse model for Meckel syndrome type 3. *J. Am. Soc. Nephrol.* 20 (4): 753–764.

102 Zaki, M.S., Sattar, S., Massoudi, R.A., and Gleeson, J.G. (2011). Co-occurrence of distinct ciliopathy diseases in single families suggests genetic modifiers. *Am. J. Med. Genet. Part A* 155A (12): 3042–3049.

103 Wolf, M.T. and Hildebrandt, F. (2011). Nephronophthisis. *Pediatr Nephrol.* 26 (2): 181–194.

104 Beales, P.L., Badano, J.L., Ross, A.J. et al. (2003). Genetic interaction of BBS1 mutations with alleles at other BBS loci can result in non-Mendelian Bardet–Biedl syndrome. *Am. J. Hum. Genet.* 72 (5): 1187–1199.

105 Hildebrandt, F., Benzing, T., and Katsanis, N. (2011). Ciliopathies. *N. Engl. J. Med.* 364 (16): 1533–1543.

106 Chaki, M., Hoefele, J., Allen, S.J. et al. (2011). Genotype–phenotype correlation in 440 patients with NPHP-related ciliopathies. *Kidney Int.* 80 (11): 1239–1245.

Vet-ebooks.com

7

Hematopoietic and Lymphoid Tissues

Harm HogenEsch and John P. Sundberg

Introduction

Hematopoiesis refers to the production of erythrocytes, leukocytes, and platelets from hematopoietic stem cells (HSCs), a population of self-renewing cells that can give rise to all blood cell lineages. HSCs are needed throughout the life of mice to maintain blood cell populations because of their relatively short lifespan. HSCs are found in the bone marrow and spleen of adult mice and can be recruited to other extramedullary tissues when there is increased demand for hematopoiesis.

The hemopoietic system is derived from the mesoderm in three waves during embryonal development. The first and second waves occur in the yolk sac of the embryo beginning at embryonal day (ED) 7, and generate blood cells that supply the developing embryo including macrophages involved in tissue remodeling [1]. The definitive HSCs, which can reconstitute the entire hematopoietic system of a lethally irradiated adult mouse, are generated in the third wave around ED 10.5 from the hemogenic endothelium of the dorsal aorta of the aorta-gonad-mesonephros (AGM) tissue. The generation of HSCs is dependent on proinflammatory cytokines secreted by macrophages in the arterial wall and by catecholamines supplied by the sympathetic nervous system in the developing embryo [2, 3]. The HSCs migrate from the AGM to the fetal liver where they undergo marked proliferation between ED 11 and ED 16. Additional HSCs are supplied to the fetal liver by the vitelline and umbilical arteries. From the fetal liver, HSCs move to the fetal spleen from around ED15.5 until a few weeks after birth. Hemopoietic stem cells in the spleen of adult mice are mostly committed to erythropoiesis. In addition, HSCs begin to populate the bone marrow starting at ED17.5. They undergo a rapid expansion in the bone marrow during the first three weeks after birth after which they become quiescent [1].

We describe here the pathology of the hemopoietic and lymphoid tissues with an emphasis on changes in mice with spontaneous and genetically engineered mutations. A detailed review of the pathology of these tissues in mice and rats was recently published as part of the INHAND Project (International Harmonization of Nomenclature and Diagnostic Criteria for Lesions in Rats and Mice) [4].

Bone Marrow

The bone marrow occupies the cavities of the trabecular meshwork of the axial and long bones. It is highly vascularized and supplied by nerves, but it lacks lymphatic drainage. The bone marrow forms a network of hemopoietic and nonhemopoietic cells, including endothelial cells, pericytes, fibroblasts, and osteoblasts. Together, these cells form a niche, a microenvironment for HSCs that controls their self-renewal and differentiation [5]. The HSCs generate progenitor cells that differentiate into erythrocytes, leukocytes, including immature B lymphocytes, and platelets. In addition to its major role in generating blood cells, the bone marrow is also the site where populations of plasma cells and memory T cells reside following their induction in secondary lymphoid organs.

Examination of bone marrow: Routine assessment of the bone marrow is performed on sections of bones following formalin fixation and decalcification. Decalcification is usually achieved with organic acids such as formic acid or with chelating agents such as ethylenediaminetetraacetic acid (EDTA) solution. The latter procedure takes longer but is preferred for immunohistochemistry because of enhanced antigen preservation. The knee joint with the distal femur and proximal tibia and sternum are good choices. Light microscopy of H&E-stained sections, preferably less than 4 μm thick, can assess overall cellularity, ratio of erythroid to myeloid precursors, and number of megakaryocytes. Examination of smears or cytospin preparations of bone marrow cells can provide a more detailed analysis of the cellular composition of the bone marrow. Cell suspensions can be obtained by flushing the long bones with a 25G needle and syringe after removing the ends (epi- and metaphyses). In depth analysis of the cellular composition of bone marrow and the different maturation stages of blood cell lineages

Pathology of Genetically Engineered and Other Mutant Mice, First Edition. Edited by John P. Sundberg, Peter Vogel, and Jerrold M. Ward.
© 2022 John Wiley & Sons, Inc. Published 2022 by John Wiley & Sons, Inc.

Vet-ebooks.com

requires flow cytometry of cells labeled with fluorochrome-conjugated antibodies.

Hypoplasia and aplasia: Mutations or chemical treatments that induce DNA damage or interfere with cell division will induce bone marrow aplasia, a general loss of all hematopoietic lineages. Hematopoietic cells are absent, and bone marrow space is filled with venous sinuses and a few adipocytes (Figure 7.1). Such changes are often associated with a reduction of the red pulp of the spleen. Loss of specific lineages may be seen with genetic deletion of growth factors. A selective decrease of erythropoiesis is associated with chronic inflammation. There is increased myelopoiesis and an increase of hemosiderin.

Hyperplasia: Increased numbers of hematopoietic cells may involve all or selected cell lineages. The hyperplasia is usually the result of increased demand induced by

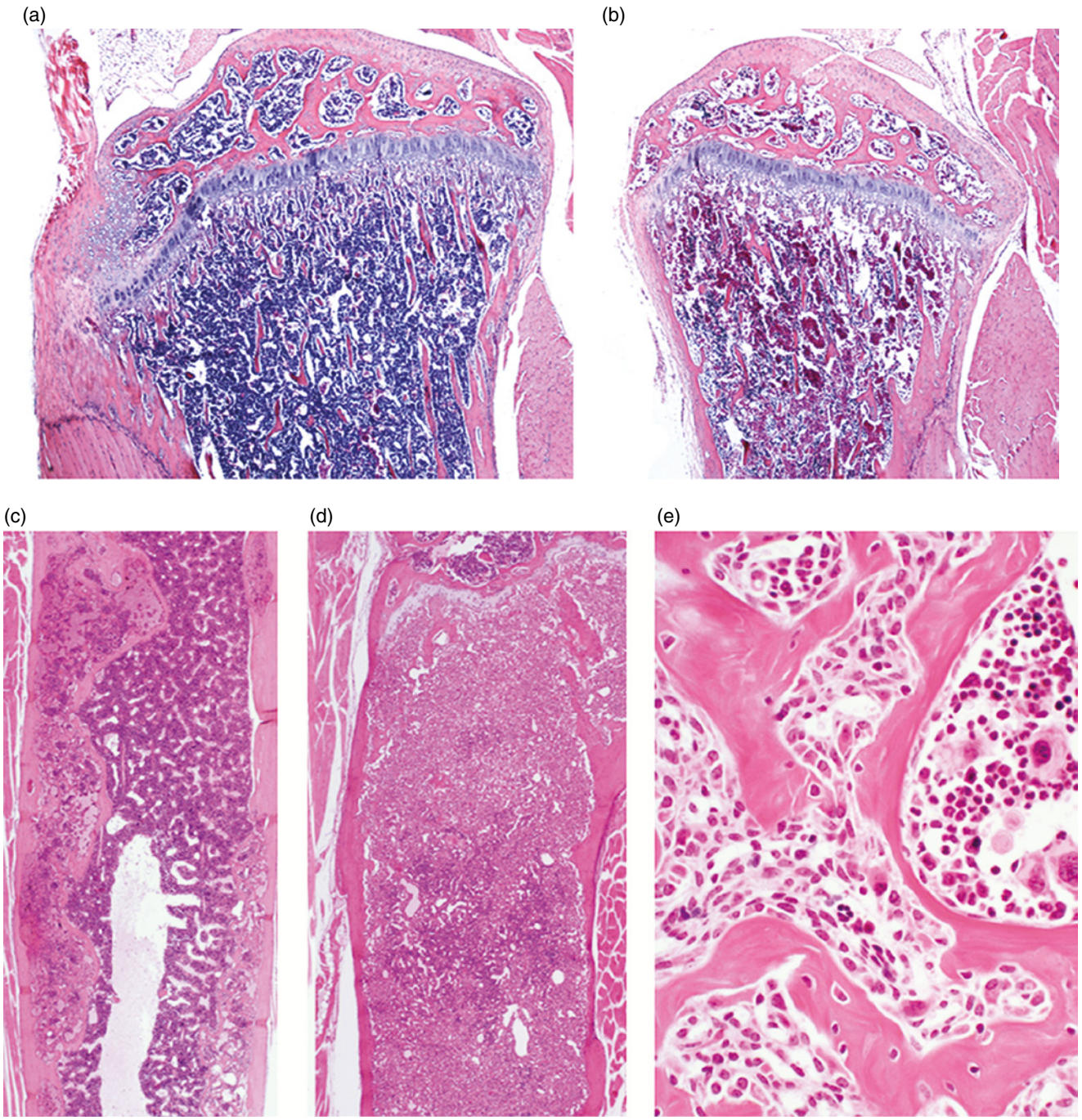


Figure 7.1 **Bone marrow**. Bone marrow hypoplasia four days after deletion of *Cul4A* in *Cul4a/Pcid2*^{tm2Ktc} mice (b) compared with C57BL/6J mice (a). (c) Fibro-osseous lesions in 821-day old female 129S1/SvlmJ and 427-day old female KK/H1J (d) mice. Higher magnification of fibro-osseous lesion (e).

Vet-ebooks.com

increased secretion of growth factors or cytokines, and is typically associated with increased extramedullary hematopoiesis (EMH) in the spleen and liver. An increase of erythropoiesis is caused by anemia and may be associated with megakaryocyte hyperplasia if there is loss of platelets. Increased myelopoiesis is often seen with chronic inflammation and can result in a dramatic shift of the myeloid:erythroid ratio.

Aging-associated changes: The overall cellularity of the bone marrow in old mice remains high at >90% in contrast to humans in which the hematopoietic cells are gradually replaced by adipocytes, although there are strain and regional differences in the distribution and accumulation of adipocytes. Aging is associated with an increased number of HSCs, increased myelopoiesis, and increased accumulation of plasma cells. The plasma cells promote myelopoiesis through the local secretion of inflammatory cytokines [6]. These changes may be difficult to assess in routine H&E sections of the bone marrow. Fibro-osseous lesions are proliferative alterations comprised of fibrovascular tissue intermixed with fine bone trabeculae in the bone marrow of aged mice (Figure 7.1). Although they replace hemopoietic tissue, the lesions are not sufficiently expansive to compromise the production of hemopoietic cells. Fibro-osseous lesions occur predominantly in female mice with a high incidence in B6C3F1 mice and in certain inbred strains including 129S1/SvImJ, KK/H1J, and NZW/LacJ [7–9].

Lymphoid Tissues

Lymphoid tissue can be divided into primary, secondary, and tertiary lymphoid tissues. The primary lymphoid organs are the sites of development and maturation of B and T lymphocytes. The developing B and T lymphocytes undergo somatic recombination of the immunoglobulin and T cell receptor gene segments resulting in a vast repertoire of antigen-specific receptors. This process is largely antigen-independent. The primary lymphoid organs in the mouse are the bone marrow for B cell development and the thymus for T cell development. The initiation of the adaptive immune response mediated by antibodies and T cells occurs in the secondary lymphoid organs which include the lymph nodes, white pulp of the spleen, and mucosa-associated lymphoid tissues. Mature, naïve B and T lymphocytes circulate through the secondary lymphoid organs which are connected via the lymphatic and blood circulation. Naïve lymphocytes enter the lymph nodes and mucosa-associated lymphoid tissues via high endothelial venules and leave via the efferent lymphatics. The spleen has open-ended arterioles that deliver lymphocytes to the marginal zone and red pulp. Lymphocytes leave the spleen primarily via the splenic vein. The restricted circulation pattern of naïve lymphocytes maximizes the chances that the few lymphocytes with receptors for a specific antigen will encounter that antigen which is delivered to the lymphoid tissues. Lymph nodes are strategically positioned throughout the body to capture antigens delivered via the afferent lymphatics from the tributary areas. Blood-borne antigens are captured by macrophages, B cells and dendritic cells in the marginal zone of the spleen and transported into the white pulp. The epithelium that overlies the mucosa-associated lymphoid tissues has specialized epithelial cells (M cells) that facilitate the uptake of antigens from the mucosal surface and transport them into the underlying lymphoid tissue.

Tertiary lymphoid organs develop at sites of chronic inflammation associated with infections, autoimmune disease, and cancer. The organization of tertiary lymphoid organs mimics that of secondary lymphoid organs with varying degrees of differentiation.

Primary Lymphoid Organs

The primary lymphoid organs in the mouse are the bone marrow for the antigen-independent generation of B cells and the thymus for T cells. The general assessment of bone marrow is described above. Microscopy of routinely stained sections of bone marrow does not provide specific information about the development of B cells. This requires isolation of bone marrow cells followed by labeling with appropriate reagents and analysis by flow cytometry.

Thymus

The thymus is a bi-lobed organ in the cranial mediastinum of the thoracic cavity. It is composed of a network of epithelial cells filled with developing T cells ("thymocytes") and fewer other hemopoietic cells. The epithelial cells are derived from the endoderm of the third pharyngeal pouch. The formation of the thymus starts around ED 11, and the initial population of the thymus by hemopoietic cells begins at ED 12. Under the influence of the transcription factor FOXN1, thymic epithelial precursor cells differentiate into cortical and medullary epithelial cells [10]. The cortex of the thymus is densely populated with immature T cells which obscure the presence of the cortical epithelial network on H&E sections. Macrophages containing apoptotic fragments of immature T cells ("tingible body macrophages") are scattered throughout the cortex. The medulla is less densely populated with more mature T cells intermixed with macrophages, dendritic cells, B cells, and eosinophils. The medullary epithelial cells are plump with more cytoplasm compared with the dendritic morphology of the cortical epithelial cells. Medullary epithelial cells undergo a maturation process and undergo cornification upon terminal differentiation. Hassall's (thymic) corpuscles are clusters of cornified epithelial cells that are typical of the thymic medulla. They are not as well organized and less prominent in commonly used strains of mice such as C57BL/6 and BALB/c as in humans and many other mammals. However, certain mouse strains including NZW/LacJ and NZBW F1 mice have many Hassall's corpuscles [11] (Figure 7.2).

Vet-ebooks.com

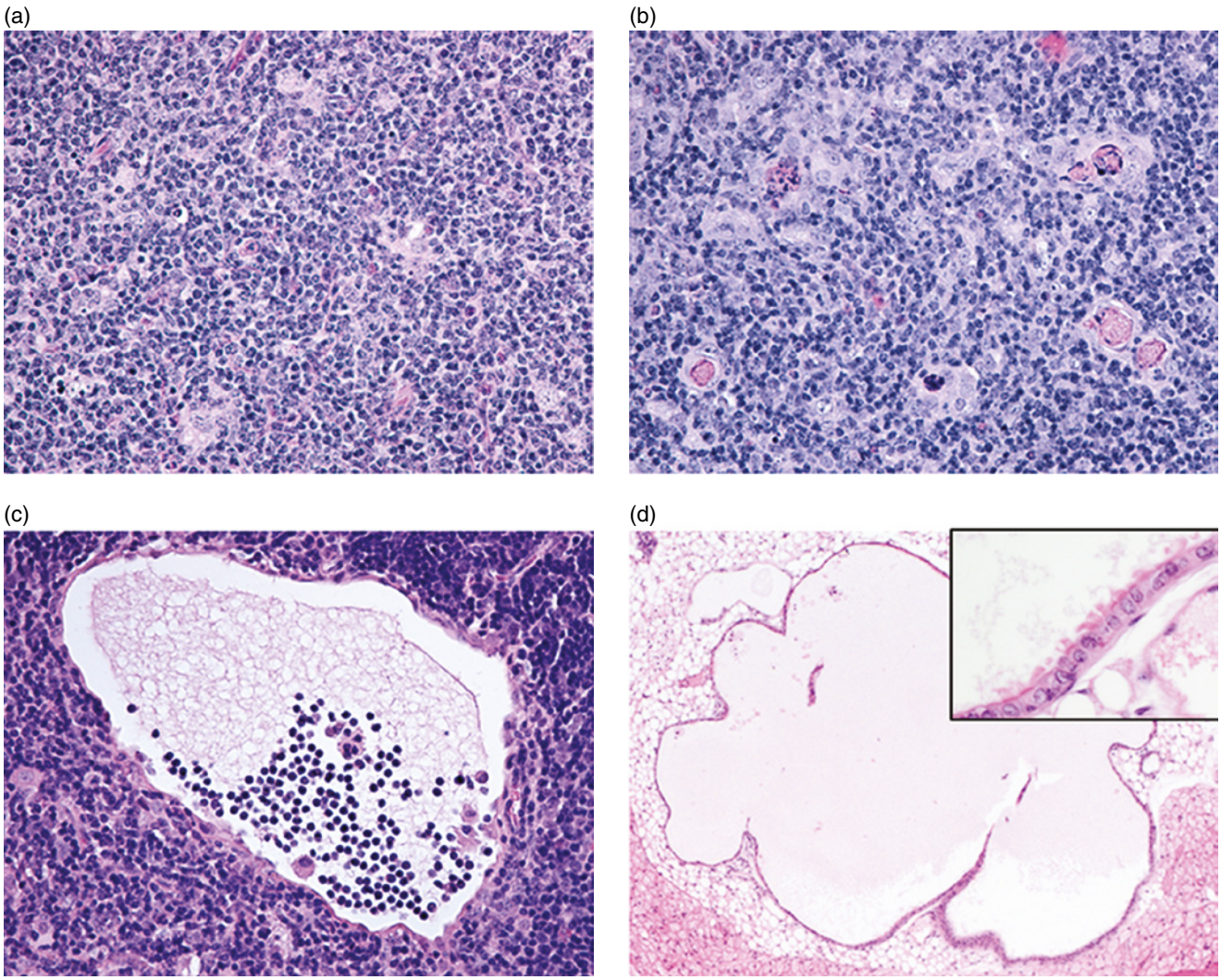


Figure 7.2 **Thymus**. (a, b). Medulla of thymus of a female C57BL/6J mouse (a) and a female NZW/LacJ mouse with prominent Hassall's corpuscles (b). (c) Cyst in thymus of a 24-week old CBA/2J mouse. (d) Cystic remnant in FOXN1-deficient NU/J mouse. Inset: higher magnification of ciliated epithelial cells.

Cervical thymus tissue may be found in up to 90% of mice depending on the genetic background. These are likely derived from remnants of thymic embryonal tissues that are left behind during the migration of primordial thymus from the pharyngeal region to the cranial mediastinum. The morphology ranges from small clusters of lymphocytes to well-differentiated tissue with a distinct medulla and cortex typical of the thymus.

The thymus plays a critical role in T cell development. Every day, approximately 100 precursor T cells enter the thymus from the bone marrow. Differentiation, positive and negative selection, and maturation of T cells occur as the precursors migrate from the outer cortex to the medulla. Approximately 1 million mature T cells leave the thymus daily via blood vessels at the corticomedullary junction.

Examination of the thymus: For routine examination, H&E slides prepared from cross sections of the thymus fixed in formalin will suffice. For more detailed investigation of the stromal and epithelial cell composition, immunohistochemistry with antibodies against specific cell populations is necessary. To examine the effect of changes on T lymphocyte development, flow cytometry with multiple fluorochrome-conjugated antibodies is required.

Aging-associated changes: The thymus reaches its maximum size of 25–45 mg at about 5–6 weeks of age. When mice reach sexual maturity, the thymus undergoes involution with a gradual loss of lymphocytes. The loss of parenchymal tissue is partially compensated by an increase of stromal cells. There are marked differences between mouse strains in the weight of the thymus and degree of involution [12].

Cysts: Cysts are typically found in the medulla and at the corticomedullary junction of the thymus. They are lined by ciliated or squamous cells and may contain proteinaceous fluid, lymphocytes, and dendritic cells

Vet-ebooks.com

(Figure 7.2). The prevalence of these cysts is age and strain-dependent.

Thymic hypoplasia and aplasia: The thymus and parathyroid glands are both derived from the endoderm of the third pharyngeal pouch. Neural crest-derived mesenchyme contributes to the migration and early formation of the thymus, but the thymus in young adult mice contains few if any neural crest-derived cells. Functional deletion of genes involved in the formation and patterning of the pharyngeal arches cause thymic aplasia or hypoplasia and frequently affect other tissues that are derived from these embryonal structures (Table 7.1). The most common defect in thymus development in humans is DiGeorge syndrome, caused by a deletion in chromosome 22q11.2, and characterized by cardiac and facial abnormalities and hypothyroidism. This chromosomal segment contains the *Tbx1* gene and deletion of this gene in mice recapitulates the features of DiGeorge syndrome. A more selective defect in thymus development is induced by deletion of *Foxn1*, which is the genetic defect in the nude mouse. As mentioned earlier, FOXN1 is critical for the differentiation and maturation of both cortical and medullary epithelial cells, and spontaneous or engineered deletion induces thymic aplasia with sometimes only a cystic remnant present in the cranial mediastinum (Figure 7.2). FOXN1 also plays a role in the formation of the hair shaft as this transcription factor regulates various keratin gene. Nude mice have hair follicles, but lack visible hair because of abnormal and fragile hair shafts (see Chapter 10 on skin, hair, and nail for details).

Mice with defects in the production of T lymphocytes have small thymuses comprised predominantly of epithelial and stromal cells with few lymphocytes. This includes mice with impaired formation of T cell receptors including mutations in the *Prkdc* gene that underlies the *scid* mutation [22], and in the *Rag1* or *Rag2* genes [23, 24], and mice with mutations in the *Il2rg* gene that encodes for the IL2 receptor common gamma chain (CD132) [25, 26].

Thymic hyperplasia: Focal hyperplasia of thymic epithelial cells has been reported in older B6C3F1 mice [27]. Focal lymphoid hyperplasia and development of follicles sometimes with germinal centers in the thymus medulla have been reported in NZB and NZBWF1 mice that are prone to systemic autoimmune disease similar to systemic lupus erythematosus [11, 28].

Secondary Lymphoid Organs

Lymph Nodes

Among invertebrate and vertebrate animals, lymph nodes are found only in mammals. Afferent lymph vessels collect lymph fluid from organs and tissues, which allows LNs to monitor peripheral tissues for infections and tissue damage and to act as a barrier to further dissemination of potential pathogens. Specialized mesenchymal stromal cells and endothelial cells secrete chemotactic factors that control the migration of lymphocytes that enter LNs via high endothelial venules and afferent lymph vessels. In this manner, LNs play an essential role in maximizing the chances for antigen to find the rare B and T lymphocytes that express the receptors for that specific antigen. The number of lymph nodes in mice raised in a clean environment is fairly constant with about 22 LNs found in specific locations [29].

Lymph node anlagen are formed as a result of interactions between lymphoid tissue organizer (LTo) cells and lymphoid tissue inducer (LTi) cells during ED14 to ED17 [30, 31]. Secretion of CXCL13 by LTo cells recruits LTi cells released from the fetal liver. Accumulation and activation of LTi cells results in further recruitment of LTi cells in a lymphotoxin and RANK-dependent manner followed by the recruitment of B and T lymphocytes and differentiation of stromal cells in subtypes that populate the different compartments of the lymph node. LTi cells are a type of innate lymphoid cells, whereas the LTo cells include mesenchymal stromal cells and lymphatic endothelial cells. The relative role of stromal

Table 7.1 Defects in thymus development in genetically engineered mice.

Targeted mutation (gene)	Thymus	Other defects	References
Eya1	Aplasia	Absence of ears, kidneys, parathyroid aplasia, thyroid hypoplasia	[13, 14]
Foxn1	Aplasia	Hair shaft defects	[15]
Hoxa3	Aplasia	Parathyroid aplasia, thyroid hypoplasia	[16]
Pax1	Hypoplasia	Skeletal defects	[17]
Pax3	Aplasia	Cardiac defects, parathyroid aplasia, thyroid aplasia, neural tube defects	[18]
Pax9	Aplasia	Parathyroid aplasia, skeletal defects, absence of teeth	[19]
Six1	Aplasia	Absence of kidneys, parathyroid aplasia, skeletal defects	[20]
Tbx1	Aplasia	Parathyroid aplasia, cardiac defects, skeletal defects, cleft palate	[21]

Vet-ebooks.com

LTo cells and lymphatic endothelial cells in the initiation of LN formation is controversial [30, 31]. Understanding the process of LN formation is clinically relevant because the same signals are thought to be involved in the generation of tertiary lymphoid tissues which can be found in cancer and chronic inflammatory lesions [32, 33].

Lymph nodes can be divided into the cortex, paracortex, and medulla. B cell follicles are located in the cortex and contain follicular dendritic cells, specialized stromal cells that retain immune complexes on their surface and play an important role in the affinity maturation and longevity of the humoral immune response. The paracortex is populated by T cells and dendritic cells, and contains the high endothelial venules that permit the extravasation of naïve B and T lymphocytes. The medulla is composed of medullary cords which contain macrophages and plasma cells, and medullary sinuses that converge into a single efferent lymphatic vessel. Antigens reach the lymph node via afferent lymphatics that open into the subcapsular sinus. The "floor" of the subcapsular sinus is lined by endothelial cells that limit diffusion of antigens into the underlying lymphoid tissue. At least five different types of macrophages can be identified in lymph nodes based on their localization and phenotype [34]. These are the subcapsular sinus macrophages, tingible body macrophages in germinal centers, T cell zone macrophages in the paracortex, and medullary cord and medullary sinus macrophages.

Examination of lymph nodes: Lymph nodes vary in size and degree of lymphocyte activation based on their location and exposure to antigens. The largest lymph nodes are those that drain the intestine. Because of their small size in the mouse, it is often necessary to use a dye to visualize and identify lymph nodes. This can be readily done by injection of Evans blue or Indian ink into the tributary area of the lymph node. For example, injection of Evans blue in the footpads of the hindlegs induces accumulation of the blue dye in the popliteal and iliac lymph nodes within 30 minutes. Systemic staining of lymph nodes can be accomplished by injection of 1% pontamine sky blue in the peritoneal cavity of mice. The dye stains connective tissues blue, but after about two weeks, the staining of the connective tissues has decreased and the dye selectively accumulates in lymph nodes throughout the body. Mutations in cytokine and cytokine receptor genes or transcription factors may lead to a selective or general absence of lymph nodes (Table 7.2).

For routine examination, H&E-stained sections of formalin-fixed lymph nodes that contain the cortex, paracortex, and medulla are adequate. It is important to recognize that multiple afferent lymph vessels enter the lymph node causing regional differences in the distribution of changes within a lymph node. Furthermore, differences in the angle at which lymph nodes are sectioned may give the wrong impression of changes in the size of the

Table 7.2 Defects in the development of secondary lymphoid tissues in genetically engineered mice.

			Lymph nodes		Mucosa-associated lymphoid tissues			Spleen		References
Category	**Targeted gene**	**Protein**	**PLN**	**MLN**	**PP**	**NALT**	**LDALT**	**GC**	**MZ**	
TNF-superfamily	*Tnf*	Tumor necrosis factor-alpha	+	+	+	+	+	–	⇓	[35]
	Lta	Lymphotoxin A	–	–	–	⇓	+	–	–	[36, 37]
	Ltb	Lymphotoxin B	–	+	–	⇓	+	–	–	[38, 39]
	Ltbr	Lymphotoxin-receptor	–	–	–	⇓	+	–	–	[40]
	Tnfsf11	Receptor-associated with NFkB-ligand (RANKL)	–	–	+	+	+	+	+	[41]
	Tnfrsf11a	Receptor-associated with NFkB (RANK)	–	–	+	+	+	+	+	[42]
Transcription factors	*Relb*	RELB	–	–	–	⇓	ND	–	–	[43]
	Nfkb2	NFKB2	–	+	–	–	ND	–	–	[43]
	Map3k14	NFkB-inducing kinase (NIK)	–	–	–	⇓	⇓	–	–	[44, 45]
	Id2	Inhibitor of DNA binding 2 (ID2)	–	–	–	–	+	+	+	[46]
	Rorg	RAR-related orphan receptor gamma (RORγ)	–	–	–	–	+	+	+	[47]
	Cbfb2	Core binding factor β2 (CBFβ2)	–	+	–	–	–	ND	ND	[48, 49]
Chemokine (receptor)	*Cxcl13*	CXCL13	⇓	–	⇓	⇓	+	–	+	[50]
	Cxcr5	CXCR5	⇓	–	⇓	⇓	ND	–	+	[50]

Vet-ebooks.com

different LN compartments. Immunohistochemistry and flow cytometry can be used to identify specific lymphocyte and macrophage subpopulations.

Lymphoid hypoplasia: Mutations that affect the production of lymphocytes in the primary lymphoid tissues result in greatly decreased numbers of lymphocytes in the lymph nodes and other secondary lymphoid tissues. Null mutations of *Foxn1* selectively affect the generation of T cells in the thymus and cause a marked decrease of lymphocytes in the paracortex of the lymph nodes (Figure 7.3). Mutations of the *Rag1*, *Rag2*, and *Prkdc* genes result in a lack of B and T cells, and the lymph nodes are largely devoid of lymphocytes (Figure 7.3). *Il2rg* mutations affect the production of lymphocytes as well as other immune cells. NOD.Cg-*Prkdc*^{scid} *Il2rg*^{tm1Wjl}/SzJ (NSG) mice have small rudimentary lymph nodes (Figure 7.3).

Reactive lymph node: As a physiologic response to antigenic stimulation, e.g. by injection of a vaccine or an infection, draining lymph nodes undergo a rapid increase in size as a result of increased blood supply, increased lymphocyte influx, and reduced egress of lymphocytes from the lymph node. Chemokines that reach the lymph node via afferent lymph vessels induce hypertrophy of high endothelial venules in the paracortex and increased extravasation of lymphocytes. This is followed by proliferation of lymphocytes resulting in expansion of the paracortex and increased size of follicles. The follicles are comprised of a germinal center surrounded by a mantle zone of recirculating resting B lymphocytes. The germinal center has a dark zone in which B cells undergo proliferation and a light zone in which B cells with high affinity receptors are selected and other B cells undergo apoptosis. Upon prolonged stimulation of lymph nodes, there may be a marked accumulation of plasma cells in the medullary cords.

Aging-associated changes: A detailed study of aging changes in the inguinal lymph node of C57BL/6J mice revealed a decrease of the percentage of T cells and increase of B cells in lymph nodes of old mice [51]. B cell follicles were less well defined, and there was a reduced number of follicular dendritic cells. There was an increased number of subcapsular sinus, medullary sinus, and medullary cord macrophages.

Amyloidosis. Accumulation of amyloid occurs most commonly in mesenteric lymph nodes. Amyloid appears as pale eosinophilic amorphous material in H&E-stained sections (Figure 7.4). Amyloid deposits first in the subcapsular sinus and may expand into the paracortex.

Sinus dilatation: Dilatation of the medullary sinuses is a common finding in the mesenteric and mediastinal lymph nodes of old mice. The sinuses contain proteinaceous fluid, lymphocytes, and macrophages.

Sinus erythrocytosis: The presence of erythrocytes in the subcapsular and medullary sinuses may be the result of antemortem hemorrhage in the tributary area or be caused by tissue manipulation and euthanasia especially in the bronchial and mediastinal lymph nodes when the mice are euthanized by CO_2 asphyxiation. In chronic hemorrhage, erythrocyte and hemosiderin-laden macrophages are typically present.

Angiomatous hyperplasia: This is a common finding in the mesenteric lymph nodes of old mice characterized by an increased number of endothelium-lined spaces in the cortex and medulla. The vessels may contain proteinaceous fluid and erythrocytes. There is no evidence that this lesion will progress to a neoplasm.

Pigmentation: Accumulation of hemosiderin and ceroid-lipofuscin is common in sinusoidal macrophages that drain areas of hemorrhage and inflammation. Melanin may be observed in skin-draining lymph nodes of black mice.

Macrophage hyperplasia: Diffuse or focal increases of the different macrophage populations may occur in lymph nodes as a result of influx from the blood or draining area or as a result of proliferation. A diffuse accumulation of subcapsular and medullary sinus macrophages is commonly referred to as sinus histiocytosis. The macrophages may contain pigment, red blood cells, or material injected in the tributary area such as mineral or oil from vaccine adjuvants (Figure 7.4).

Mucosa-Associated Lymphoid Tissues

The mucosa-associated lymphoid tissues are composed of the inductive sites for adaptive immune responses in the intestinal and upper respiratory tract. In the mouse, they include the Peyer's patches, solitary lymphoid follicles, and colonic lymphoid patches in the intestine, and the nasopharynx-associated lymphoid tissue (NALT) and lacrimal duct-associated lymphoid tissue (LDALT) in the nose (Figure 7.5). Mice do not have tonsils. Mucosa-associated lymphoid organs do not have afferent lymphatics, and antigens gain access to the lymphoid tissue from the mucosal surface via specialized epithelial cells (microfold or M cells). In addition, dendritic cells may extend dendritic processes between epithelial cells to sample the lumen of the intestinal and respiratory tract. M cells are derived from epithelial stem cells. Mature M cells are characterized electron microscopically by short, irregular microvilli and a thin brush border, and express glycoprotein 2 as a distinct surface marker [52]. The basolateral membrane of M cells is invaginated forming a pocket that often contains lymphocytes, macrophages, and dendritic cells. Antigens taken up by transcytosis through M cells are processed by dendritic cells and activate B and T cells in the underlying lymphoid tissue.

Examination of mucosa-associated lymphoid tissues: Peyer's patches can be observed and counted macroscopically in adult mice. However, for a detailed investigation of lymphoid tissues in the small intestine, the intestine should be cut in two pieces, and each piece rolled up in a cassette as a "Swiss roll". Serial longitudinal sections allow for a thorough examination of the intestine. The large intestine is first opened longitudinally to empty the contents and then rolled up in a cassette. To examine the development

Vet-ebooks.com

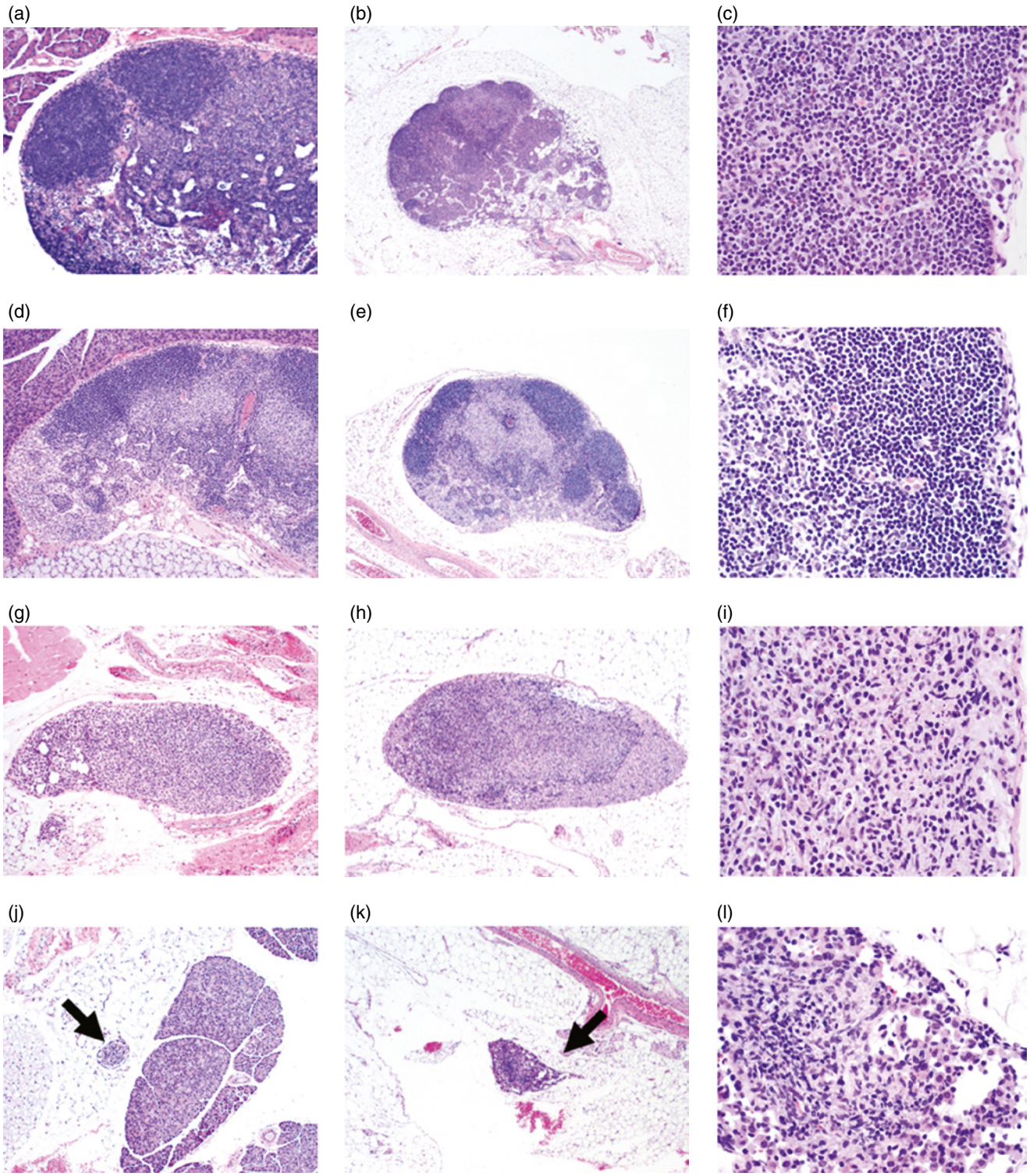


Figure 7.3 **Lymph nodes**. C57BL/6J (a–c), B6.Cg-*Foxn1*^{nu} (d–f), B6.129S7-*Rag1*^{tm1Mom} (g–i), and NOD.Cg-*Prkdc*^{scid} *Il2rg*^{tm1Wjl}/SzJ (NSG) mice (j–l). a, d, g, j – cervical lymph node; b, e, h, k – jejunal lymph node with higher magnification of subcapsular sinus and cortex (c, f, i, l). Arrows point to lymph nodes in NSG mice.

of Peyer's patches in late-stage embryos and newborn pups, whole mount immunohistochemistry can be performed [53]. Microscopic examination of the NALT and LDALT requires cross sections of the nose after fixation and decalcification of the head. A cross section just rostral of the first molar will include the NALT.

Vet-ebooks.com

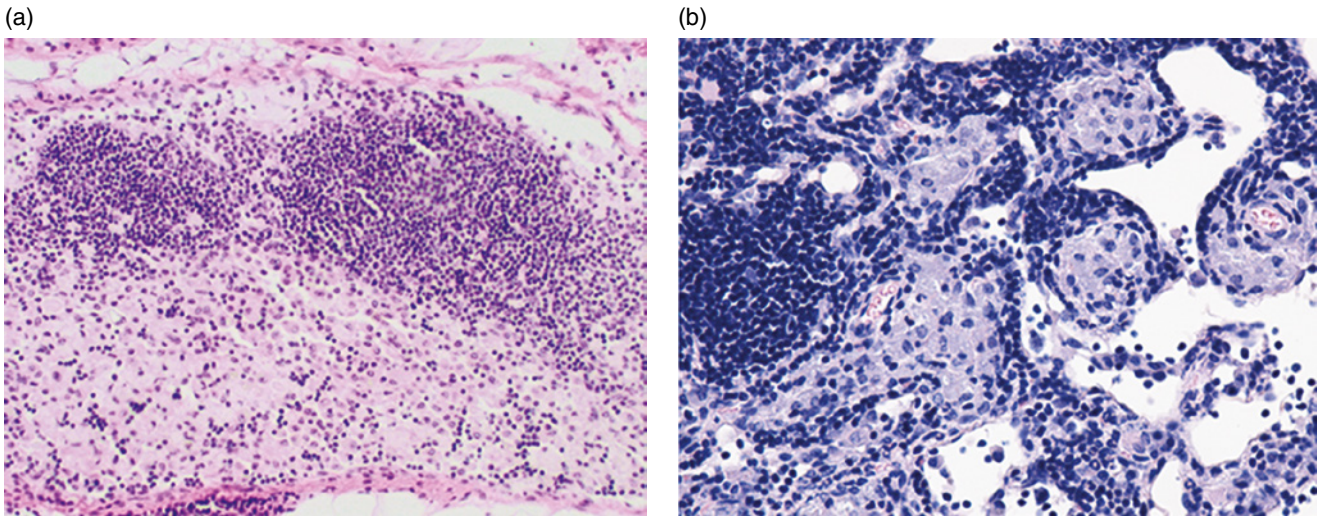


Figure 7.4 **Amyloid**. (a) Amyloid in mesenteric lymph node of 615-day old C57BL/6J mouse. (b) Macrophages with intracellular accumulation of aluminum adjuvant in medullary cords. Iliac lymph node of male CD-1 mouse after injection of an aluminum adjuvant.

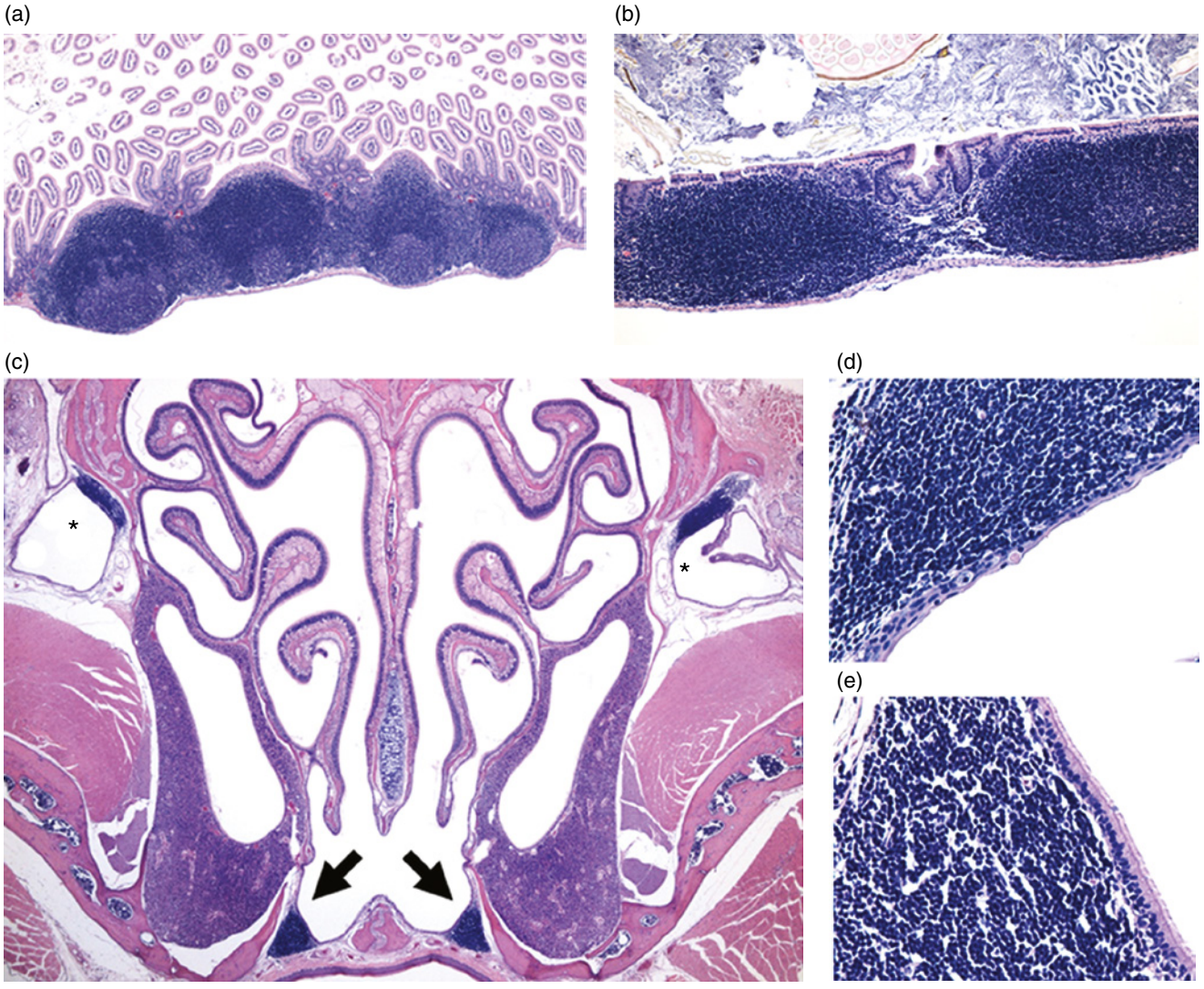


Figure 7.5 **Mucosal lymphoid tissues**. (a) Peyer's patch in C57BL/6J mouse. (b) Colonic lymphoid patch in C57BL/6J mouse. (c) Cross section of the nose of a CD-1 mouse. Arrows point to the nasopharynx-associated lymphoid tissue (NALT) and * identifies the lacrimal duct with the lacrimal duct-associated lymphoid tissue (LDALT). Higher magnification of the squamous epithelium overlying the LDALT (d) and ciliated epithelium overlying the NALT (e).

Vet-ebooks.com

Peyer's patches: Peyer's patches are located in the antimesenteric wall of the small intestine. The number of Peyer's patches varies between 6 and 10 depending on the mouse strain. Each Peyer's patch is composed of several lymphoid follicles [8–12] which extend from the submucosa into the lamina propria. The follicles have a prominent germinal center as a result of immune stimulation by antigens from the intestinal lumen, and are separated by small interfollicular areas which are analogous to the paracortex of lymph nodes and contain high endothelial venules. The formation of Peyer's patches begins before birth and continues in the first weeks after the pups are born. Several mutations are associated with a lack or reduced number and size of Peyer's patches (Table 7.2). In SHARPIN-deficient mice (*Sharpin*^{cpdm} and *Sharpin*$^{cpdm\text{-}Dem}$), Peyer's patches are initially formed and populated by B and T cells. However, lymphoid follicles are not formed, and the lymphoid tissues undergo regression at about two to three weeks of age resulting in the absence of Peyer's patches in adult mice [54]. The majority of lymphocytes in Peyer's patches are B cells. *Foxn1* mutant mice that lack T cells have well-developed Peyer's patches with sparsely populated interfollicular areas. Peyer's patches are absent from mice with null mutations in *Rag1*, *Rag2*, *Prkdc* and *Il2rg* genes, although anlagen of VCAM1-positive stromal cells could be detected in neonatal C.B17/Icr-SCID Jc mice [53]

Solitary intestinal lymphoid tissues (SILTs): These are individual follicles located in the lamina propria of the small and large intestine. They are formed after birth, but are considered secondary lymphoid tissues with a similar function to Peyer's patches. There are about 100–200 SILTs in the mouse intestine, the number depending on the mouse strain. Cryptopatches are small collections of leukocytes, about 80 μm in diameter, in the intestinal lamina propria that do not extend to the epithelium. Their cellular composition includes dendritic cells and innate lymphoid cells. Cryptopatches may represent immature forms of SILTs.

Large intestinal lymphoid tissue: There are two to five colonic patches in the colon of C57BL/6J mice. Each is composed of two large lymphoid follicles in the submucosa extending into the lamina propria of the colon separated by an interfollicular T cell area. M cells are present in the overlying mucosal epithelium. In addition, there are SILTs scattered throughout the lamina propria of the colon with increasing density toward the distal colon. Lymphoid patches similar to colonic patches are also present in the cecum and rectum.

Nasopharynx-associated lymphoid tissue: The NALT consists of two bilateral rows of five to six lymphoid follicles in the ventral meatus of the nasal cavity. The overlying epithelium consists of ciliated cells interspersed with M cells. The NALT is absent or hypoplastic in several mutant mouse strains (Table 7.2)

Lacrimal duct-associated lymphoid tissue: The LDALT consists of isolated lymphoid nodules in the propria mucosae of the lacrimal duct. They consist mostly of a B cell follicle with fewer T cells and dendritic cells. The overlying squamous epithelium contains M cells. Absence of the LDALT in selected mutant mouse strains has identified genes involved in the development of these lymphoid tissues (Table 7.2).

Spleen

The spleen is a slightly curved elongated organ on the left side of the stomach in the abdominal cavity. It is comprised of red pulp and white pulp surrounded by a thin fibroelastic capsule. The development of the spleen starts with the formation of the splanchnic mesodermal plate on ED 12. Defects in the formation and further development of this splenic anlage occur in mice with the dominant hemimelia mutation and mice with genetic deletion of the transcription factors NK3 homeobox 2 (*Nkx3-2*), transcription factor 21 (*Tcf21*), Wilms tumor 1 homolog (*Wt1*), NK2 homeobox 5 (*Nkx2-5*), and T cell leukemia homeobox 1 (*Tlx1*). These mice are asplenic, but also have other organ defects and usually die perinatally, with exception of TLX1-deficient mice which have a selective absence of the spleen. The formation of the white pulp is dependent on the secretion of chemokines that attract B cells into follicles (CXCL13) and T cells to the periarteriolar lymphocyte sheath (CCL19 and CCL21). The secretion of these chemokines relies on induction by lymphotoxin (a heterotrimer composed of LTA and LTB) and tumor necrosis factor (TNF) which activate the NF-κB signaling pathway when they engage with their receptors. The formation of the white pulp is disrupted when any of these factors are absent (Table 7.2). The separation of white pulp and red pulp is not complete until about two to three weeks postpartum.

The structure of the spleen is best understood in the context of the blood circulation. The splenic artery enters the spleen through the hilus and forms trabecular branches that extend into the parenchyma. Central arterioles branch off from the trabecular arteries and are surrounded by the lymphoid tissue that constitutes the white pulp. The arterioles terminate open-ended in the marginal sinus and the cords of the red pulp. The cords consist of fibroblasts and reticular fibers without an endothelial lining and are filled with red pulp macrophages. Blood percolates through the cords and collects in venous sinuses which merge into the splenic vein. The spleen lacks afferent lymphatics, but it does have efferent lymphatics. Red pulp macrophages phagocytize damaged or aged red blood cells and recycle iron. Plasma cells induced by immune responses in the white pulp localize in the red pulp. The red pulp of the adult mouse also contains hemopoietic stem cells and precursor cells representing all lineages.

The white pulp is comprised of the periarteriolar lymphocyte sheath populated mostly by T cells and dendritic cells, flanked by B cell follicles. The marginal zone is the outermost layer of the white pulp which is thin and fairly indistinct in H&E-stained sections. It is composed of an inner

Vet-ebooks.com

layer of metallophilic marginal zone macrophages, a marginal sinus lined by endothelial cells and an outer layer that contains marginal zone macrophages mixed with marginal zone B cells. The marginal zone is not fully formed until about three to four weeks of age.

Examination of the spleen: Routine examination is usually performed on two H&E-stained cross sections of the spleen. Immunohistochemistry is performed to identify specific regions of the white pulp such as the marginal zone, and specific cell populations.

Lymphoid hypoplasia: Similar to the lymph nodes, mutations that affect the production of lymphocytes result in greatly decreased numbers of lymphocytes in the white pulp. Null mutations of *Foxn1* cause a marked decrease of lymphocytes in the periarteriolar lymphocyte sheath (Figure 7.6). Mutations of the *Rag1*, *Rag2*, and *Prkdc* genes result in a lack of B and T cells, and the white pulp is markedly reduced in size and largely devoid of lymphocytes (Figure 7.6). *Il2rg* mutations affect the production of lymphocytes as well as other immune cells. NOD.Cg-*Prkdc*^{scid} *Il2rg*^{tm1Wjl}/SzJ (NSG) mice have very small rudimentary white pulp (Figure 7.6).

Aging-associated changes: The white pulp of older mice (>12 months of age) becomes increasingly disorganized with less clear separation of B and T cell areas [55]. B cell follicles are reduced in size and there is a reduction in the number and function of follicular dendritic cells. The marginal zone and metallophilic marginal zone macrophages no longer form a continuous cell layer [55, 56].

Amyloidosis: Amyloid in the spleen is usually AA-amyloid associated with chronic inflammation. Experimental models indicate that AA amyloid first accumulates in the marginal zone and is associated with loss of marginal zone macrophages [57]. As the amyloidosis increases in severity, deposits expand into the red pulp.

Pigment: The appearance of hemosiderin pigment is normal in the red pulp of the spleen. Red pulp macrophages are

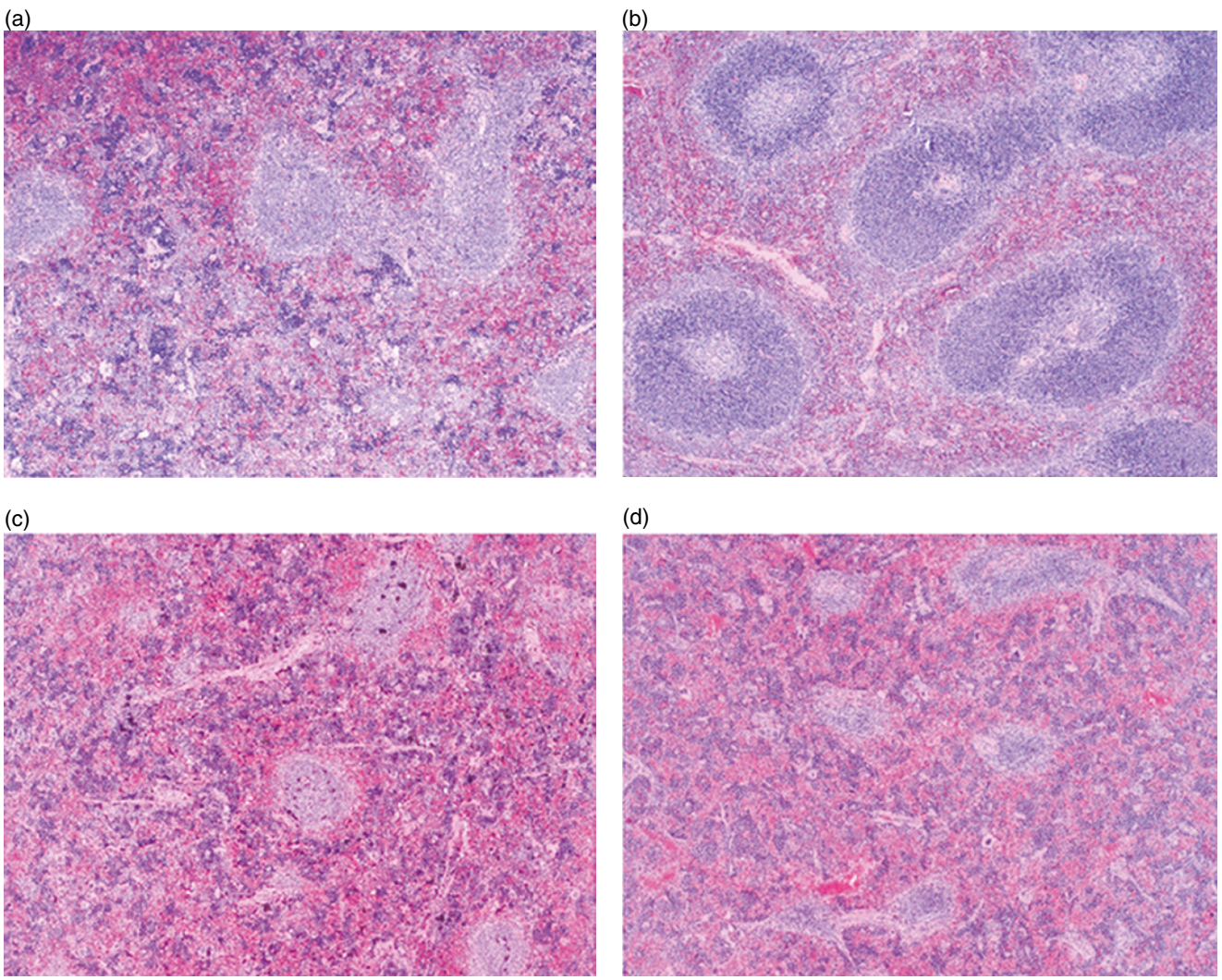


Figure 7.6 **Spleen**. Spleen of C57BL/6J (a), B6.Cg-*Foxn1*^{nu} (b), B6.129S7-*Rag1*^{tm1Mom} (c), and NOD.Cg-*Prkdc*^{scid} *Il2rg*^{tm1Wjl}/*SzJ* (NSG) mice (d).

Vet-ebooks.com

engaged in erythrophagocytosis and frequently contain hemosiderin. The amount of hemosiderin is greater in female mice, but varies by mouse strain. Hemosiderin can be distinguished from other pigments by Prussian blue staining (Figure 7.7). Lipofuscin-ceroid pigment may be observed in red pulp macrophages, but is less common than hemosiderin. In mice with black fur, the dorsal one-third of the spleen is often dark red to black as a result of accumulation of melanin. Light microscopically, dendritic melanocytes and melanin-laden macrophages are present in the red pulp, and occasionally in the white pulp (Figure 7.7).

Increased extramedullary hematopoiesis (EMH): While modest EMH is normal in the red pulp of the spleen of adult mice, increased EMH can lead to marked expansion of the red pulp and is a common cause of splenomegaly. The myeloid lineage predominates when there is inflammation in other organs, while hemorrhage and red blood cell destruction may lead to an increase of erythrocyte precursors and sometimes megakaryocytes.

Red pulp atrophy and hypoplasia: A reduced size of the red pulp may be seen in mice with blocks in cell division as a result of genetic mutations or chemical treatment.

Milky Spots

Milky spots are collections of leukocytes located just beneath the mesothelium in the omentum [58]. They are predominantly composed of macrophages and B1 B cells with fewer classical B2 B cells. They contain few T cells and lack a distinct T cell area that is present in other secondary lymphoid organs. Furthermore, follicular dendritic cells are absent from milky spots. Lymphoid structures similar to milky spots are found in pericardial, mediastinal, and mesenteric fat, and these are known as fat-associated lymphoid clusters (FALCs) [59]. The formation of milky spots and FALCs requires LTA and CXCL13, but is independent of lymphoid tissue-inducer cells. The number and size of milky spots and FALCs is increased by exposure to microbiota, suggesting that these tissues have features in common with both secondary and tertiary lymphoid tissues. Milky spots lack afferent lymphatics, and antigens enter via fenestrations in the overlying mesothelium. Inflammation and infections in the peritoneal cavity lead to a rapid increase of the number and size of milky spots as a result of an influx of peritoneal macrophages and recruitment of cells from the blood circulation. Immune responses can involve both B1 cells which differentiate into IgM and IgA-secreting plasma cells and conventional B and T cells.

Tertiary Lymphoid Organs

Organized lymphoid tissues can form at sites of chronic inflammation associated with autoimmune diseases, infections, and neoplasms (Figure 7.8). Immunohistochemistry can identify distinct T and B cell areas with high-endothelial venules, follicles with follicular dendritic cells and sometimes germinal centers. The same cytokines and chemokines that orchestrate the formation of secondary lymphoid organs play a role, but tertiary lymphoid organs are formed after birth and not at preselected sites [33]. The role of tertiary lymphoid organs in inflammation and cancer is not well established. Tertiary lymphoid organs associated with autoimmune inflammation are thought to contribute to the autoimmune response and be detrimental. However, tertiary lymphoid organs formed in the adventitial layer of the aorta in ApoE-deficient mice (B6.129P2-*Apoe*^{tm1Unc}/J) with atherosclerosis seem to have a beneficial effect as the atherosclerosis was more severe in mice in which the formation of the serosal lymphoid

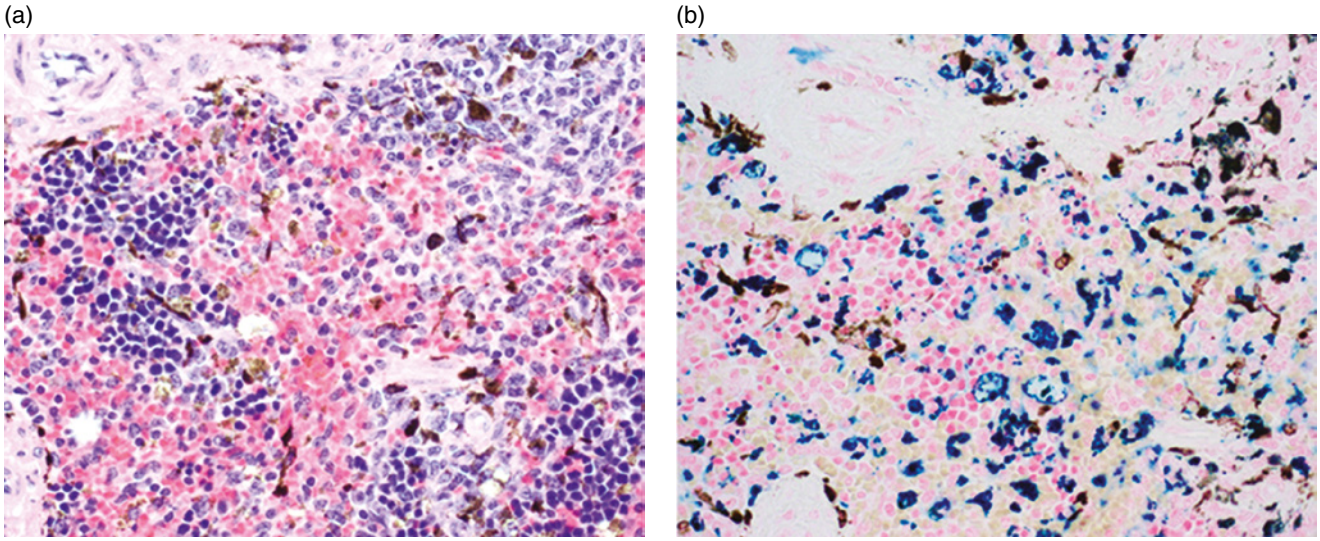


Figure 7.7 Melanin vs. hemosiderin. (a) Spleen of B6.Cg-*Prkdc*^{scid}/SzJ mouse with melanocytes and melanin-laden macrophages and hemosiderin. (b) Prussian blue stain distinguishes hemosiderin (blue) and melanin (dark brown) pigments.

Vet-ebooks.com

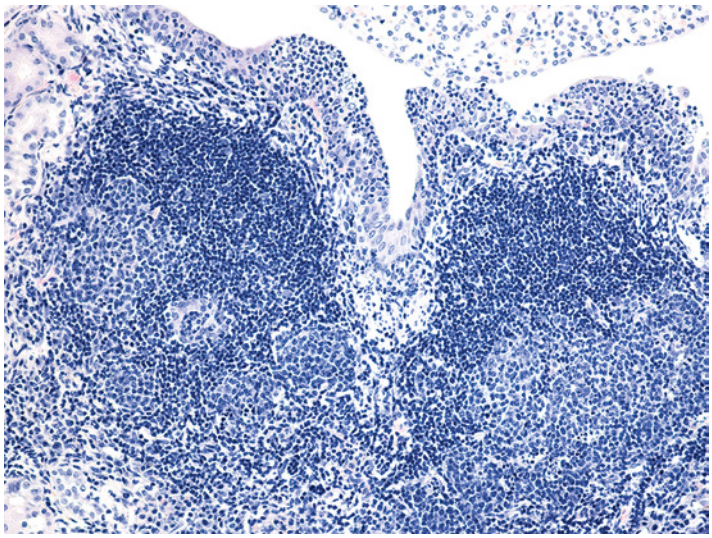


Figure 7.8 **Tertiary lymphoid structures**. Tertiary lymphoid tissue with two follicles with germinal centers in the kidney of a CD-1 mouse with chronic pyelonephritis.

tissue was blocked [60]. The presence of tertiary lymphoid organs in and near tumors is thought to increase the response to immunotherapy and to be a positive prognostic indicator [61].

Acknowledgments

This work was supported grants from the National Institutes of Health (R01-CA089713 and P30-CA034196 to JPS).

References

1 Gao, X., Xu, C., Asada, N., and Frenette, P.S. (2018). The hematopoietic stem cell niche: from embryo to adult. *Development* 145 (2): dev139691.

2 Fitch, S.R., Kimber, G.M., Wilson, N.K. et al. (2012). Signaling from the sympathetic nervous system regulates hematopoietic stem cell emergence during embryogenesis. *Cell Stem Cell* 11 (4): 554–566.

3 Mariani, S.A., Li, Z., Rice, S. et al. (2019). Pro-inflammatory aorta-associated macrophages are involved in embryonic development of hematopoietic stem cells. *Immunity* 50 (6): 1439–1452. e5.

4 Willard-Mack, C.L., Elmore, S.A., Hall, W.C. et al. (2019). Nonproliferative and proliferative lesions of the rat and mouse hematolymphoid system. *Toxicol. Pathol.* 47 (6): 665–783.

5 Pinho, S. and Frenette, P.S. (2019). Haematopoietic stem cell activity and interactions with the niche. *Nat. Rev. Mol. Cell Biol.* 20 (5): 303–320.

6 Pioli, P.D., Casero, D., Montecino-Rodriguez, E. et al. (2019). Plasma cells are obligate effectors of enhanced myelopoiesis in aging bone marrow. *Immunity* 51 (2): 351–366. e6.

7 Sass, B. and Montali, R.J. (1980). Spontaneous fibro-osseous lesions in aging female mice. *Lab. Anim. Sci.* 30 (5): 907–909.

8 Albassam, M.A., Wojcinski, Z.W., Barsoum, N.J., and Smith, G.S. (1991). Spontaneous fibro-osseous proliferative lesions in the sternums and femurs of B6C3F1 mice. *Vet. Pathol.* 28 (5): 381–388.

9 Berndt, A., Ackert-Bicknell, C., Silva, K.A. et al. (2016). Genetic determinants of fibro-osseous lesions in aged inbred mice. *Exp. Mol. Pathol.* 100 (1): 92–100.

10 Rodewald, H.R. (2008). Thymus organogenesis. *Annu. Rev. Immunol.* 26: 355–388.

11 de Vries, M.J. and Hijmans, W. (1967). Pathological changes of thymic epithelial cells and autoimmune disease in NZB, NZW and (NZB x NZW)F1 mice. *Immunology* 12 (2): 179–196.

12 Li, L., Hsu, H.C., Grizzle, W.E. et al. (2003). Cellular mechanism of thymic involution. *Scand. J. Immunol.* 57 (5): 410–422.

13 Xu, P.X., Adams, J., Peters, H. et al. (1999). Eya1-deficient mice lack ears and kidneys and show abnormal apoptosis of organ primordia. *Nat. Genet.* 23 (1): 113–117.

14 Xu, P.X., Zheng, W., Laclef, C. et al. (2002). Eya1 is required for the morphogenesis of mammalian thymus, parathyroid and thyroid. *Development* 129 (13): 3033–3044.

15 Nehls, M., Kyewski, B., Messerle, M. et al. (1996). Two genetically separable steps in the differentiation of thymic epithelium. *Science* 272 (5263): 886–889.

16 Manley, N.R. and Capecchi, M.R. (1998). Hox group 3 paralogs regulate the development and migration of the thymus, thyroid, and parathyroid glands. *Dev. Biol.* 195 (1): 1–15.

17 Dietrich, S. and Gruss, P. (1995). undulated phenotypes suggest a role of Pax-1 for the development of vertebral and extravertebral structures. *Dev. Biol.* 167 (2): 529–548.

18 Conway, S.J., Henderson, D.J., and Copp, A.J. (1997). Pax3 is required for cardiac neural crest migration in the mouse: evidence from the splotch (Sp2H) mutant. *Development* 124 (2): 505–514.

Vet-ebooks.com

19 Peters, H., Neubuser, A., Kratochwil, K., and Balling, R. (1998). Pax9-deficient mice lack pharyngeal pouch derivatives and teeth and exhibit craniofacial and limb abnormalities. *Genes Dev.* 12 (17): 2735–2747.

20 Laclef, C., Souil, E., Demignon, J., and Maire, P. (2003). Thymus, kidney and craniofacial abnormalities in Six 1 deficient mice. *Mech. Dev.* 120 (6): 669–679.

21 Jerome, L.A. and Papaioannou, V.E. (2001). DiGeorge syndrome phenotype in mice mutant for the T-box gene, Tbx1. *Nat. Genet.* 27 (3): 286–291.

22 Custer, R.P., Bosma, G.C., and Bosma, M.J. (1985). Severe combined immunodeficiency (SCID) in the mouse. Pathology, reconstitution, neoplasms. *Am. J. Pathol.* 120 (3): 464–477.

23 Mombaerts, P., Iacomini, J., Johnson, R.S. et al. (1992). RAG-1-deficient mice have no mature B and T lymphocytes. *Cell* 68 (5): 869–877.

24 Shinkai, Y., Rathbun, G., Lam, K.P. et al. (1992). RAG-2-deficient mice lack mature lymphocytes owing to inability to initiate V(D). *J. Rearrangement. Cell* 68 (5): 855–867.

25 DiSanto, J.P., Muller, W., Guy-Grand, D. et al. (1995). Lymphoid development in mice with a targeted deletion of the interleukin 2 receptor gamma chain. *Proc. Natl. Acad. Sci. U.S.A.* 92 (2): 377–381.

26 Cao, X., Shores, E.W., Hu-Li, J. et al. (1995). Defective lymphoid development in mice lacking expression of the common cytokine receptor gamma chain. *Immunity* 2 (3): 223–238.

27 Pearse, G. (2006). Histopathology of the thymus. *Toxicol. Pathol.* 34 (5): 515–547.

28 Burnet, F.M. and Holmes, M.C. (1964). Thymic changes in the mouse strain Nzb in relation to the auto-immune state. *J. Pathol. Bacteriol.* 88: 229–241.

29 Van den Broeck, W., Derore, A., and Simoens, P. (2006). Anatomy and nomenclature of murine lymph nodes: descriptive study and nomenclatory standardization in BALB/cAnNCrl mice. *J. Immunol. Methods* 312 (1–2): 12–19.

30 van de Pavert, S.A. and Mebius, R.E. (2010). New insights into the development of lymphoid tissues. *Nat. Rev. Immunol.* 10 (9): 664–674.

31 Onder, L. and Ludewig, B. (2018). A fresh view on lymph node organogenesis. *Trends Immunol.* 39 (10): 775–787.

32 Colbeck, E.J., Ager, A., Gallimore, A., and Jones, G.W. (2017). Tertiary lymphoid structures in cancer: drivers of antitumor immunity, immunosuppression, or bystander sentinels in disease? *Front. Immunol.* 8: 1830.

33 Buckley, C.D., Barone, F., Nayar, S. et al. (2015). Stromal cells in chronic inflammation and tertiary lymphoid organ formation. *Annu. Rev. Immunol.* 33: 715–745.

34 Bellomo, A., Gentek, R., Bajenoff, M., and Baratin, M. (2018). Lymph node macrophages: scavengers, immune sentinels and trophic effectors. *Cell. Immunol.* 330: 168–174.

35 Pasparakis, M., Alexopoulou, L., Episkopou, V., and Kollias, G. (1996). Immune and inflammatory responses in TNF alpha-deficient mice: a critical requirement for TNF alpha in the formation of primary B cell follicles, follicular dendritic cell networks and germinal centers, and in the maturation of the humoral immune response. *J. Exp. Med.* 184 (4): 1397–1411.

36 De Togni, P., Goellner, J., Ruddle, N.H. et al. (1994). Abnormal development of peripheral lymphoid organs in mice deficient in lymphotoxin. *Science* 264 (5159): 703–707.

37 Banks, T.A., Rouse, B.T., Kerley, M.K. et al. (1995). Lymphotoxin-alpha-deficient mice. Effects on secondary lymphoid organ development and humoral immune responsiveness. *J. Immunol.* 155 (4): 1685–1693.

38 Koni, P.A., Sacca, R., Lawton, P. et al. (1997). Distinct roles in lymphoid organogenesis for lymphotoxins alpha and beta revealed in lymphotoxin beta-deficient mice. *Immunity* 6 (4): 491–500.

39 Alimzhanov, M.B., Kuprash, D.V., Kosco-Vilbois, M.H. et al. (1997). Abnormal development of secondary lymphoid tissues in lymphotoxin beta-deficient mice. *Proc. Natl. Acad. Sci. U.S.A.* 94 (17): 9302–9307.

40 Futterer, A., Mink, K., Luz, A. et al. (1998). The lymphotoxin beta receptor controls organogenesis and affinity maturation in peripheral lymphoid tissues. *Immunity* 9 (1): 59–70.

41 Kong, Y.Y., Yoshida, H., Sarosi, I. et al. (1999). OPGL is a key regulator of osteoclastogenesis, lymphocyte development and lymph-node organogenesis. *Nature* 397 (6717): 315–323.

42 Dougall, W.C., Glaccum, M., Charrier, K. et al. (1999). RANK is essential for osteoclast and lymph node development. *Genes Dev.* 13 (18): 2412–2424.

43 Weih, F. and Caamano, J. (2003). Regulation of secondary lymphoid organ development by the nuclear factor-kappaB signal transduction pathway. *Immunol. Rev.* 195: 91–105.

44 Miyawaki, S., Nakamura, Y., Suzuka, H. et al. (1994). A new mutation, aly, that induces a generalized lack of lymph nodes accompanied by immunodeficiency in mice. *Eur. J. Immunol.* 24 (2): 429–434.

45 Fukuyama, S., Hiroi, T., Yokota, Y. et al. (2002). Initiation of NALT organogenesis is independent of the IL-7R, LTbetaR, and NIK signaling pathways but requires the Id2 gene and CD3(−)CD4(+)CD45(+) cells. *Immunity* 17 (1): 31–40.

46 Yokota, Y., Mansouri, A., Mori, S. et al. (1999). Development of peripheral lymphoid organs and natural killer cells depends on the helix-loop-helix inhibitor Id2. *Nature* 397 (6721): 702–706.

47 Sun, Z., Unutmaz, D., Zou, Y.R. et al. (2000). Requirement for RORgamma in thymocyte survival and lymphoid organ development. *Science* 288 (5475): 2369–2373.

48 Tachibana, M., Tenno, M., Tezuka, C. et al. (2011). Runx1/Cbfbeta2 complexes are required for lymphoid tissue inducer cell differentiation at two developmental stages. *J. Immunol.* 186 (3): 1450–1457.

49 Nagatake, T., Fukuyama, S., Sato, S. et al. (2015). Central role of core binding factor beta2 in mucosa-associated lymphoid tissue organogenesis in mouse. *PLoS One* 10 (5): e0127460.

Vet-ebooks.com

50 Ansel, K.M., Ngo, V.N., Hyman, P.L. et al. (2000). A chemokine-driven positive feedback loop organizes lymphoid follicles. *Nature* 406 (6793): 309–314.

51 Turner, V.M. and Mabbott, N.A. (2017). Structural and functional changes to lymph nodes in ageing mice. *Immunology* 151 (2): 239–247.

52 Terahara, K., Yoshida, M., Igarashi, O. et al. (2008). Comprehensive gene expression profiling of Peyer's patch M cells, villous M-like cells, and intestinal epithelial cells. *J. Immunol.* 180 (12): 7840–7846.

53 Adachi, S., Yoshida, H., Kataoka, H., and Nishikawa, S. (1997). Three distinctive steps in Peyer's patch formation of murine embryo. *Int. Immunol.* 9 (4): 507–514.

54 Seymour, R., Shirley, B.J., HogenEsch, H. et al. (2013). Loss of function of the mouse sharpin gene results in Peyer's patch regression. *PLoS One* 8 (2): e55224.

55 Aw, D., Hilliard, L., Nishikawa, Y. et al. (2016). Disorganization of the splenic microanatomy in ageing mice. *Immunology* 148 (1): 92–101.

56 Turner, V.M. and Mabbott, N.A. (2017). Influence of ageing on the microarchitecture of the spleen and lymph nodes. *Biogerontology* 18 (5): 723–738.

57 Lundmark, K., Vahdat Shariatpanahi, A., and Westermark, G.T. (2013). Depletion of spleen macrophages delays AA amyloid development: a study performed in the rapid mouse model of AA amyloidosis. *PLoS One* 8 (11): e79104.

58 Rangel-Moreno, J., Moyron-Quiroz, J.E., Carragher, D.M. et al. (2009). Omental milky spots develop in the absence of lymphoid tissue-inducer cells and support B and T cell responses to peritoneal antigens. *Immunity* 30 (5): 731–743.

59 Meza-Perez, S. and Randall, T.D. (2017). Immunological functions of the omentum. *Trends Immunol.* 38 (7): 526–536.

60 Hu, D., Mohanta, S.K., Yin, C. et al. (2015). Artery tertiary lymphoid organs control aorta immunity and protect against atherosclerosis via vascular smooth muscle cell lymphotoxin beta receptors. *Immunity* 42 (6): 1100–1115.

61 Sautes-Fridman, C., Petitprez, F., Calderaro, J., and Fridman, W.H. (2019). Tertiary lymphoid structures in the era of cancer immunotherapy. *Nat. Rev. Cancer* 19 (6): 307–325.

Vet-ebooks.com

8

Mouse Hematolymphoid Neoplasms

Jerold E. Rehg

Introduction and Overview of the Classification of Leukemias and Lymphomas in the Mouse

Leukemias and lymphomas result from the clonal expansion of myeloid or lymphoid precursors. Mouse myeloid leukemias arise from myeloid precursors residing in the bone marrow or spleen. Lymphoid leukemias and lymphomas arise from immature or mature lymphocytes of B-cell, T-cell, or natural killer (NK)-cell lineage at various stages of differentiation. B-cell and T-cell lymphomas are considered to recapitulate the stages of normal B-cell and T-cell differentiation. The differentiation of hematolymphoid neoplastic cells from their normal counterparts can be difficult because of their morphologic similarities. Bone marrow cytology and peripheral blood smears are helpful for leukemia assessment. Flow cytometry and immunohistochemistry (IHC) play a critical role in the diagnosis of myeloid or lymphoid leukemia and lymphomas.

Many mice with primary spontaneous leukemias have marked hepatosplenomegaly, with leukemic cells in the splenic red pulp and in the hepatic sinusoids and portal tracts. The leukemic mouse may or may not have a leukocytosis. Generally, mice with leukemia often have a pancytopenia or one or more cytopenias. Bone marrow should be used instead of the spleen for subclassification of leukemias because the spleen contains a mixture of leukemic and normal hematopoietic cells. Primary spontaneous lymphoid leukemias are not common in mice; however, around 30% of mouse lymphomas develop a leukemic phase. For there to be consistent interpretation of leukemogenic and lymphogenic research studies among different laboratories, a common nomenclature and classification is important. To this end, the Mouse Models of Human Cancers Consortium (MMHCC) established by the National Cancer Institute (NCI) proposed a classification for hematopoietic neoplasms and lymphoid neoplasms in mice; their recommendations are known as the Bethesda proposals [1, 2]. The two mouse Bethesda classifications model the human WHO classification of tumors of hematopoietic and lymphoid Tissues [3]. The classification discussed in this chapter models the Bethesda proposals and is based primarily on the morphology and immunophenotype of the neoplastic proliferations. The Bethesda classifications were established to standardize the characterization of mouse hematolymphoid neoplasms that occur under various conditions so that these entities could be compared to human hematolymphoid neoplasms and further our understanding of the pathogenesis of leukemogenesis. The markers used for immunophenotyping mouse hematopoietic and lymphoid cells and their neoplasms have been well described elsewhere [4–6].

In 1954, stromal tumors were classified as either Dunn's reticulum cell sarcoma type A (RCS type A) or Dunn's reticulum cell sarcoma type B (RCS type B) [7]. With the advent of more advanced diagnostic techniques, RCS type A was determined to be of histiocytic origin and was reclassified as histiocytic sarcoma (HS). RCS type B was subsequently determined to be a B-cell lymphoma. Although tumors of fibroblastic reticular cells have been reported in humans [8–10], they have yet to be documented in mice. However, clones of C57BL/6 nonneoplastic fibroblastic reticular cells have been immortalized and characterized [11]. In addition to the histiocyte (macrophage) stromal cells that are distributed in hematolymphoid and nonhematolymphoid organs, the epithelial reticular cells in the thymus can give rise to neoplasms. Like other stromal cells in lymphoid tissues, the thymic epithelial reticular cells support homing, proliferation, differentiation, and migration of T cells in the thymus. Consequently, abnormal proliferation of these stromal cells is often associated with increased proliferation of T lymphocytes. Therefore, neoplasms of the thymic epithelial reticular cells known as thymomas are composed of variable mixtures of epithelial cells and T lymphocytes, as reported in humans, mice, and other species.

The pathogenesis of spontaneous hematopoietic and lymphoid neoplasms in mice is not well defined. However, hematolymphoid neoplasms have been associated with endogenous mouse retroviruses and have been experimentally induced with chemical agents and irradiation [12–14]. Murine leukemia viruses can malignantly transform myeloid and/or lymphoid progenitors and have been critical to our understanding of the pathogenesis of hematolymphoid neoplasms because

Pathology of Genetically Engineered and Other Mutant Mice, First Edition. Edited by John P. Sundberg, Peter Vogel, and Jerrold M. Ward.
© 2022 John Wiley & Sons, Inc. Published 2022 by John Wiley & Sons, Inc.

Vet-ebooks.com

they have revealed many hitherto-unknown oncogenes involved in leukemogenesis. Genetically engineered mice (GEMs) carrying transgenes, targeted mutations (knock-out genes, knock-in genes), and mouse xenograft models have also provided valuable information regarding the pathogenesis of hematolymphoid neoplasms. Because the process of generating and characterizing GEMs can take several years, patient-derived xenografts (PDXs) of leukemias/lymphomas and gene-transfected human hematopoietic stem cell transplants in immunodeficient mice are rapidly becoming common models for studying oncogenesis [15, 16].

This chapter will address the morphologic and immunophenotypic markers that aid in diagnosing of mouse hematolymphoid neoplasms based on the recommendations of the NCI MMHCC, the experience of the author, and information from the literature. Flow cytometry immunophenotyping of neoplastic cells is the gold standard for characterizing leukemias; unfortunately, however, this is often not an option for veterinary pathologists, and IHC is necessary to characterize and diagnose the lineage of a leukemia/lymphoma in mice, as well as the lineage of human leukemia/lymphoma xenografts in mice.

Nonlymphoid Hematopoietic Neoplasms in Mice

Myeloid Leukemia (Granulocytic Leukemia, Myelogenous Leukemia, and Myelocytic Leukemia)

Definition: A leukemia consisting of numerous immature forms or blasts of granulocyte cells (neutrophils, eosinophils), but no monocytes.

Tissues involved: Myeloid leukemia may involve the bone marrow, spleen, liver, and other tissues, as well as the peripheral blood.

Morphology: Blasts and immature forms account for at least 20% of the cells in the blood, bone marrow, and/or spleen. Tissues, such as the liver, lymph nodes, and adrenal glands, may occasionally be involved. Mature granulocytes may or may not be evident. The blasts/immature forms are usually medium sized having round, slightly indented/kidney-shaped, ring (donut-shaped), or bilobed nuclei with dispersed nuclear chromatin and one or two nucleoli. The azurophilic granules in mice may not be visible in hematoxylin and eosin (H&E)–stained tissue. Consequently, the cytoplasm may or may not have a granular appearance. Occasionally, the blasts may be small with condensed chromatin, inconspicuous nucleoli, and scant cytoplasm, thus resembling lymphocytes. These cells do not stain with Sudan Black B or chloroacetate esterase (CAE).

Immunophenotype: The percentage of the leukemia cell population that expresses the myeloid (nonlymphoid bone marrow cell) markers CD34, CD117 (C-KIT), CD43, MPO, and/or lysozyme will vary depending on the maturation stage of the leukemic cells. Generally, the leukemia cells do not express CD3, PAX5, CD45R/B220, CD19, or TDT. However, it should be noted that expression of TDT, CD3, PAX5, and CD19 has been reported in some human myeloid leukemias. Whether similar alterations occur in mouse leukemias remains to be determined.

Differential diagnosis: The differential diagnosis includes erythroid leukemia, megakaryocytic leukemia, lymphoblastic lymphoma, and the leukemic phase of large-cell lymphoma. These diseases can be differentiated from one another by flow cytometry and/or IHC using a board panel of antibodies to myeloid markers (CD71, alpha-hemoglobin-stabilizing protein [AHSP], CD235A (glycophorin A), and TER119 for erythroid cells; MPO, lysozyme, GR1, and LY6G for granulocytes; CD68, and IBA1 for monocytes; CD41, CD61, Von Willebrand factor (VWF) or coagulation factor VIII (F8) for megakaryocytes) and lymphoid markers (CD3, PAX5) as discussed further in this chapter.

Conventional mice and mouse models: Myeloid leukemia occurs spontaneously in conventional aging mice, irradiated mice, and mice given xenobiotics. Mouse models of myeloid leukemia are far too numerous to address in detail here and have been discussed extensively in numerous publications [17–26] (see Table 8.1).

Myelomonocytic Leukemia

Definition: A leukemia characterized by the proliferation of immature forms of both neutrophils and monocytes. The peripheral blood or bone marrow and/or spleen have at least 20% blasts, at least 20% neutrophils and their precursors, and at least 20% monocytes and their precursors, or more than 20% of the neoplastic cells coexpress granulocyte and monocyte markers.

Tissues involved: Leukemia cells involve the bone marrow, spleen, and peripheral blood; they may infiltrate the liver, lymph nodes, and other tissues.

Morphology: In the mouse, immature cells with ring (donut-shaped) nuclear morphology occur in both the neutrophil and monocyte lineages [46]. Therefore, myelomonocytic leukemia is difficult to diagnose in the mouse based on morphology alone without immunophenotypic characterization of the neoplastic cells. The features of monocytes versus neutrophils have been described, but these alone do not enable unambiguous classification of cells with ring-shaped nuclei as being of neutrophilic or monocytic lineage. Ring monocytes have a broad nuclear ring with regular contours, and the diameter of the cytoplasmic center is smaller than the width of the ring. In contrast, ring neutrophil cells have a slender nuclear ring that is constricted and of irregular contour. The diameter of the cytoplasmic center of neutrophils is larger than the width of the ring. The immature forms of these lineages may have solid nuclear blasts. Such myeloblast nuclei are round or slightly indented, with fine chromatin and one or more prominent nucleoli. Monoblast nuclei are round, with fine chromatin and one or more large prominent nucleoli.

Immunophenotype: This leukemia variably expresses myeloid antigens (myeloperoxidase, LY6B, LY6G) and antigen

Vet-ebooks.com

Table 8.1 Myeloid leukemia associated with conventional mice and mouse models.

Type	Conventional	References	GEMs	References	Other models	References
Myeloid	Rare	[25, 26]	Tg *RUNXI-ETO* fusion gene Tg *FLT3-ITD* fusion gene Tg *MLL-AF9* fusion gene Tg *PML-RARa* fusion gene Tg *PLZF/RARa* fusion gene	[18, 19, 23, 24]	Irradiation; CBA, C3H/He, SJL/J Xenobiotics: AKR/J, DBA/2J, C3H/He, C57BL/6, SWR/J, Trp53KO Immunocompromised mice + XT: SCID (CB.17-*Prkdc*^{scid}/*Prkdc*^{scid}) NOD/SCID (NOD.Cg-*Prkdc*^{scid}/J), NSG (NOD.Cg-*Prkdc*^{scid} *Il2rg*^{tm1Wjl}/SzJ), NSG-SGM3 mice (NOD.Cg-*Prkdc*^{scid} *Il2rg*^{tm1Wjl} Tg(CMV-IL3,CSF2,KITLG)1Eav/MloySzJ) MuLV mice: AKXD23, C57BL/6, C3H, DBA, NFS, NIH Swiss, BXH2	[12–15, 17–19, 24]
Myelomonocytic	Rare, BALB/c	[27]	Tg *CBFB-MYH11* fusion gene Tg *MLL-ELL* fusion gene	[28–30]	MuLV mice: BXH-2 WEHI-3B BALB/c cell line	[18, 31]
Monocytic	Not known		*Pten* KO	[32]	Not known	
Erythroid	Rare	[33]	Tg *EWS-FLI1* fusion gene Tg *SPI-1*	[34, 35]	Friend MuLV-WBB6F1/J-*Kit*^{w}/*Kit*$^{w-v}$ (W/W^{v}) mice	[36]
Megakaryocytic	Not known		Tg *OTT-MAL* fusion gene Tg *NMP1*	[37, 38]	Irradiated C3H/HeMs mice MuL^{V+} NFS/N mice	[39]
Mast cell/basophil	Rare	[40]	*Gata1*$^{Plt13+}$ BALB/c mice	[41]	DBA/2NCrl mice + mouse P815 mast cell line NSG (NOD.Cg-*Prkdc*^{scid} *Il2rg*^{tm1Wj}) + human *Rosa*$^{KITD816V-Glu}$ cells	[42–45]

XT = xenotransplantations.

markers characteristic of monocytic differentiation, such as lysozyme C (LYZ1), CD68, IBA1 (AIF1, allograft inflammatory factor 1), and/or MAC2 (LGAL3, lectin, galactose binding, soluble 3). In some instances, myeloid and monocytic proteins may be coexpressed in the same cell. Residual nonleukemic populations of undifferentiated myeloid cells that express CD34, CD43, or CD117 are often present.

Differential diagnosis: The major differential diagnosis is myeloid leukemia, monocytic leukemia, or the myeloproliferative neoplasm (MPN) chronic myelomonocytic leukemia (CMML). The distinction from myeloid leukemia types is based on immunophenotypic findings and the percentage of monocytes. The distinction from monocytic leukemia is based on the percentage of immature myeloid cells, which are not a feature of monocytic leukemia. The distinction from CMML is based on the high percentage of blasts and immature monocyte forms in the bone marrow, which is not a feature of CMML.

Conventional mice and mouse models: Myelomonocytic leukemia is rare in most conventional mouse strains, but it has been described in BALB/c mice and GEMs [27–31] (see Table 8.1).

Monocytic Leukemia

Definition: Monocytic leukemia is a leukemia in which at least 20% of the bone marrow or splenic cells are monoblasts and immature forms and at least 80% of the marrow or splenic cells have monocytic features by morphology or immunophenotyping. If at least 80% of the monocytoid cells are immature monoblasts, the leukemia is considered monoblastic leukemia. If the monocytoid cells show evidence of maturation and less than 80% of the leukemic cells are monoblasts, the leukemia is considered a monocytic leukemia.

Tissues involved: Leukemia cells involve the bone marrow, spleen, and peripheral blood, and other tissues may have leukemic infiltrates.

Morphology: The bone marrow or spleen is hypercellular, with a predominant population of large cells with abundant cytoplasm. Monoblasts are large cells with round nuclei and abundant cytoplasm. The nucleus has reticular (lacy) chromatin and one or more nucleoli. The nuclei of monocytes are irregular and convoluted (folded, cerebriform), and the cytoplasm is paler than that of monoblasts. In the mouse,

Vet-ebooks.com

ring-shaped nuclei may be present (Figure 8.1). In smears, the cytoplasm of monoblasts and monocytes may contain vacuoles.

Immunophenotype: The leukemia cells generally lack CD34 expression but may express CD117. At present, there is no evidence that mouse monocytic leukemia cells express MPO. The leukemia cells commonly express CD68 and lysozyme, but these markers are relatively nonspecific. Although, CD163 is a specific marker for human monocytes, mouse monocytes do not express CD163. Mouse monocyte lineage cells also express IBA1 (Figure 8.2) and MAC2, and they may weakly express F4/80 (ADGRE1, adhesion G protein-coupled receptor E 1).

Differential diagnosis: The major differential diagnosis of monocytic leukemia includes minimally differentiated myeloid leukemia and myelomonocytic leukemia. Both of these leukemias have strong MPO expression, whereas monocytes are generally negative for MPO.

Conventional mice and mouse models: To date, spontaneous monocytic leukemia has not been documented in conventional mice. However, there is a report of disseminated monocytic leukemia involving multiple tissues in PTEN knock-out mice [32] (see Table 8.1).

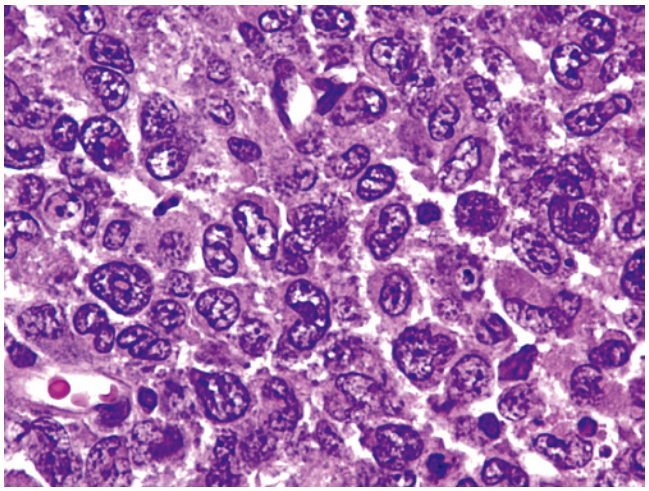


Figure 8.1 **Monocytic leukemia, H&E**. Spleen with blasts and immature forms having round, kidney-shaped and ring (donut-shaped) nuclei. The diameter of the cytoplasmic center of the donut cell is smaller than the width of the ring band, which is more consistent with a monocyte than a neutrophil.

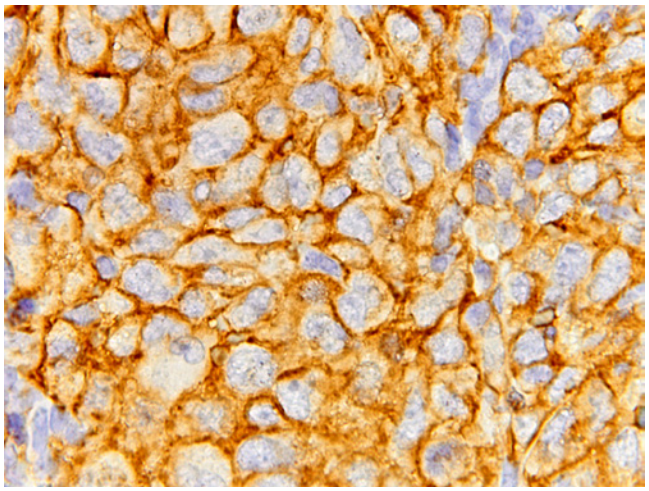


Figure 8.2 **Monocytic leukemia, IHC**. The cells in Figure 8.1 express the monocytic marker IBA1.

Erythroid Leukemia

Definition: Erythroid leukemia is characterized by at least 50% of the nucleated cell population being erythroid precursor cells.

Morphology: All maturation stages of the erythroid precursors may be present. The erythroid precursors are medium sized to large, with single, double, or multiple nuclei. The leukemia cells have round nuclei with fine chromatin and agranular, deeply basophilic cytoplasm (Figure 8.3). In some instances, the blasts resemble lymphoblasts.

Immunophenotype: The proerythroblasts may express CD43, CD44, CD45, CD117, and GATA1, but these antigens are not specific as they are also expressed by other myeloid and lymphoid neoplasms. It should also be noted that CD45 and CD117 expression decreases in the proerythroblasts as they mature. Erythroleukemias typically do not express antigens associated with myeloid cells (MPO, lysozyme, CD68, etc.) and lymphoid cells (PAX5, CD3). Erythroleukemias also typically lack expression of specific antigens associated with megakaryocytes (CD41, CD61, and VWF or F8).

However, CD235A (glycophorin A) (Figure 8.4) and TER119 are erythroid-specific antigens, and their intensity of expression increases with erythroid maturation. Consequently, the more immature forms are usually negative for these two markers or these antigens are expressed only weakly in a

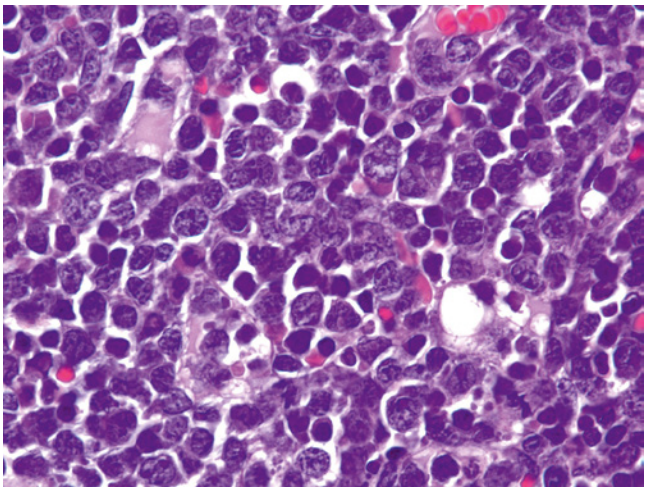


Figure 8.3 **Erythroleukemia, H&E**. Bone marrow with blasts and differentiating erythroid cells. All the leukemic cells have round nuclei, the large cells have basophilic cytoplasm and some of the small cells have pinkish cytoplasm suggestive of erythroid differentiation.

Vet-ebooks.com

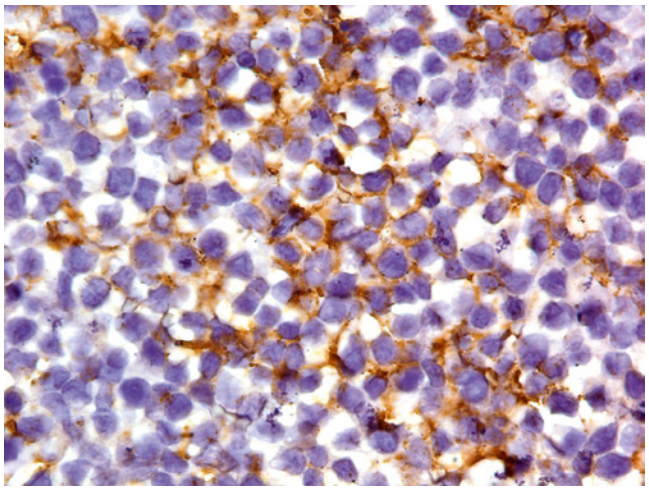


Figure 8.4 Erythroleukemia, IHC. The more differentiated cells in Figure 8.3 express CD235A (glycophorin A).

minority of blasts. Although the immunoreactivity for these two antigens may be detectible by flow cytometry, the intensity of expression on malignant erythroblasts is often below the level of detection by IHC [5, 34, 47]. However, alpha-hemoglobin-stabilizing protein/erythroid differentiation-related factor (AHSP/EDRF) is also a sensitive and specific marker of nucleated erythroid developmental stages, especially the early immature erythroid cells [48]. Because erythroid leukemias have variable expression of lineage antigens, it is essential for diagnosis to use a panel of antibodies that detect antigens expressed at various stages of maturation. Although CD71 is not a specific erythroid marker, it is uniformly expressed at high levels at all erythroid maturation stages [49]. Therefore, consideration should be given to including CD71 in an erythroid antibody panel.

Differential diagnosis: Erythroid leukemia without morphologic evidence of erythroid maturation may be difficult to differentiate from myeloid leukemia without maturation, megakaryoblastic leukemia, and, in some instances, lymphoblastic lymphoma. Furthermore, erythroleukemia and myeloid leukemia have been reported to occur in the same mouse, as have erythroleukemia and lymphoma. As a result of the multilineage nature of erythroleukemia, the leukemic cells may express MPO and erythroid markers, but the lack of MPO expression and lymphoid antigen expression, as detected by flow cytometry or IHC, will generally differentiate erythroleukemia from myeloid and lymphoma, respectively. Differentiating erythroleukemia and megakaryoblastic leukemia can be more difficult, especially in cases with concurrent erythroid–megakaryocytic involvement. However, with panels of antibodies specific for erythroid and megakaryocyte antigens, it is generally possible to distinguish between these two leukemias.

Conventional mice and mouse models: Erythroleukemia is rare in conventional mouse strains [33]. However, there are retroviral and GEM models of this leukemia [35, 36, 50] (see Table 8.1).

Megakaryocytic Leukemia

Definition: Megakaryocytic leukemia is a leukemia with at least 20% blasts of which at least 50% are of megakaryocytic lineage.

Morphology: Megakaryoblasts are of medium to large size (12–18 μm) with a round, irregular, or indented nucleus with reticular chromatin and one to three nucleoli. The cytoplasm is basophilic and agranular. The blasts can also be small, with a high nuclear-to-cytoplasmic ratio, and it is not uncommon for most of the leukemic cells to consist of small lymphoid-like blasts. Small and large blasts may be present in the same smear or tissue section, and there may be a mixture of blasts and maturing cells at different stages of differentiation (promegakaryocytes, megakaryocytes).

Differential diagnosis: Megakaryocytic leukemia can be difficult to differentiate from minimally differentiated myeloid leukemia, monocytic leukemia, and erythroleukemia based on morphology alone; immunophenotyping is required to differentiate between these leukemias.

Immunophenotype: Cells at all stages of megakaryocyte maturation may express CD34 in the mouse [5]. Megakaryoblasts, promegakaryocytes, and megakaryocytes do not express markers associated with myeloid differentiation (MPO) or monocyte differentiation (lysozyme, CD68, IBA1, and MAC2). Although erythroid cells and megakaryocytic cells both express nuclear GATA1, megakaryocytes do not express the erythroid-specific markers glycophorin A, TER119, or AHSP. However, megakaryocytic differentiating cells express CD41, CD61, and VWF or F8, which are not expressed by myeloid, monocytic, or erythroid differentiating cells.

Conventional mice and mouse models: Megakaryocytic leukemia as a spontaneous disease is rare in mice, but a low incidence has been described in GEM, mouse leukemia (MuL) virus infected mice and xenotransplants [15, 37–39] (see Table 8.1).

Mast Cell and Basophil Leukemia

Definition: A mast cell proliferation is considered a leukemia when at least 20% of the bone marrow, spleen, or blood cells are blast cells or immature forms with evidence of mast cell or basophil differentiation.

Morphology: The common mouse mast cells have abundant large, coarse, basophilic cytoplasmic granules (Figure 8.5), whereas it has been controversial whether mouse basophils have granules [51]. Some reports indicate that the granules in mouse basophils are loosely packed and few in number compared to those in mast cells [51, 52]. The granules of mast and basophil leukemic cells stain metachromatically with toluidine blue or Giemsa stains. The metachromatic granules of both cell types are water-soluble and can be diminished or totally abolished by conventional tissue processing, especially with an acidified decalcification solution. In some instances, either cell type may have insufficient cytoplasmic granules. Generally, basophils are lobated, whereas mast cells are mononucleated. However, in

Vet-ebooks.com

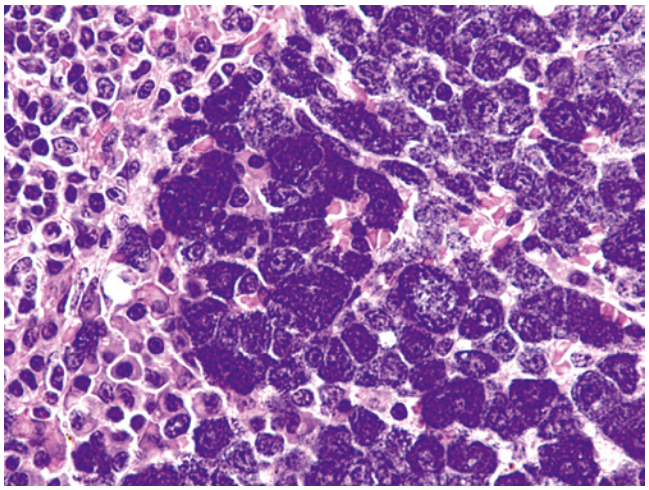


Figure 8.5 **Mast cell leukemia, H&E**. Spleen with small and large cells with basophilic cytoplasmic granules.

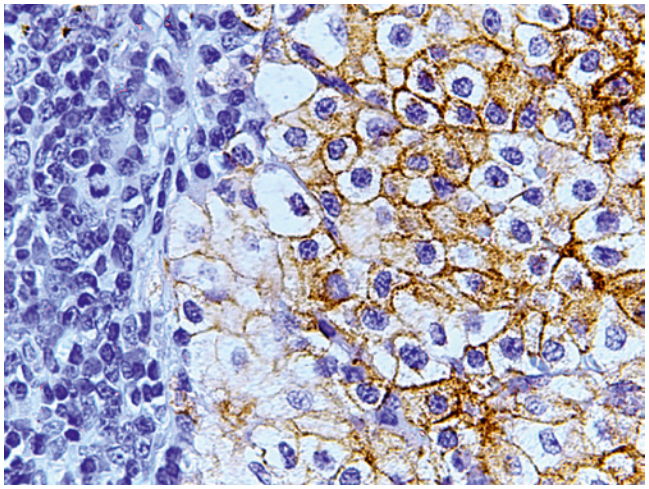


Figure 8.6 **Mast cell leukemia, IHC**. The cells in Figure 8.5 express CD117 (C-KIT) on their membrane, which is consistent with the cells being mast cells and not basophils.

some circumstances, mouse mast cells exhibit varied nuclear profiles, having both monolobed and polylobed nuclei [53]. Therefore, immunohistochemical and immunophenotype analysis may be the best means of determining whether a cell proliferation is of mast cell or basophil lineage.

Immunophenotype: Unlike mouse basophils, mouse mast cells express membrane CD34, CD117 (C-KIT, Figure 8.6), and cytoplasmic tryptase (tryptase beta-2 [TPSB2]). CD25 expression also helps to distinguish leukemic mast cells from nonneoplastic mast cells and leukemic basophils. However, mouse bone marrow and splenic basophils strongly express mast cell proteases 8 and 11, whereas mast cells do not express these proteases or express them only very weakly [54–56]. Therefore, cells that have morphologic features of mast cells or basophils and express MMCP-8 and MMCP-11 (*Prss34*; MGI: 2681414) but that are negative for CD117 expression are probably of basophil lineage.

Differential diagnosis: Basophil and mast cell blasts may resemble myeloid leukemia of neutrophil or eosinophil subtypes with minimal differentiation. However, with the use of a broad panel of antibodies specific for mast cell, basophil, and myeloid cell antigens, flow cytometry and IHC can determine whether a leukemia is of mast cell, basophil, or a myeloid cell–subtype lineage.

Conventional mice and mouse models: Spontaneous mast cell/basophil leukemia is rare in mice [40]. However, transgenic and transplantation mice models have been developed [40–45] (see Table 8.1).

Myeloid Proliferations (Nonreactive)

Definition: Spontaneous, nonreactive myeloid proliferations in mice have not been well described or characterized. However, in humans, they are considered clonal hematopoietic stem cell disorders characterized by increases in one or more myeloid lineages (erythroid, granulocytic, or megakaryocytic), resulting in peripheral blood erythrocytosis, granulocytosis, and/or thrombocytosis. Bone marrow or splenic fibrosis may ensue and lead to ineffective hematopoiesis and transformation to leukemia. In humans and mouse models, the fibrosis that often accompanies these complex MPNs is secondary to the abnormal release of cytokines from neoplastic and nonneoplastic cells in the bone marrow, which stimulates fibroblastic proliferation and connective tissue deposition. The human myeloproliferative disorders/diseases are now referred to as myeloproliferative neoplasms (MPNs). GEMs are used to model these MPNs, which can be divided into *BCR-ABL*–positive chronic myeloid (myelogenous) leukemia (CML) and *BCR-ABL*–negative MPNs, of which the most common are polycythemia vera (PV), essential thrombocythemia (ET), and primary myelofibrosis (PMF).

Tissues involved: Depending on the proliferative disease, the spleen, liver, bone marrow, and peripheral blood can be involved. In GEMs, the peripheral blood may not be involved, and the lesions that occur may vary with the mouse strain background. For instance, the JAK2V617F mutation, which occurs in all three of the common human MPNs, is associated with more prominent leukocytosis and bone marrow fibrosis in experimental Tg(JAK2*V617F)FF1 Rsko PV mice on the BALB/cAnTac strain background than in those on the C57BL/6NTac strain background [57].

Morphology: Diagnosing a myeloproliferative condition in mice requires the integration of complete blood count (CBC) data, blood and bone marrow smears, and tissue morphology. Depending on these findings, a myeloproliferation in a mouse can be designated as (i) myeloid proliferation, nonreactive; (ii) myeloproliferative disease–like; or (iii) myeloproliferative disease with features of a named human disease entity. If the proliferation is limited to increased nonlymphoid hematopoietic cells in the spleen and/or bone marrow without a cytosis in the blood, the designation "myeloid proliferation, nonreactive; genetic" should be considered. If, in addition to spleen and bone marrow involvement, the mouse also has increased blood erythrocytes, granulocytes, platelets, etc., then designating the

Vet-ebooks.com

proliferation as "myeloproliferative disease-like" would be appropriate. However, if the proliferation has features of a particular human MPN, designating it as a named human disease entity would be more appropriate, for example "myeloproliferative disease with features of polycythemia vera."

The following are morphologic features characteristic of the four most common MPNs in humans and in mouse models of MPNs. It is usually possible to distinguish these four types of myeloproliferations based on CBC data, blood smear morphology, and bone marrow histology. In humans, the morphologic features of megakaryocytes in these conditions are especially useful. Unfortunately, the histology of the megakaryocytes in the mouse models of these conditions is not well characterized. The features of mouse megakaryocytes and platelets vary between mouse strains, which might account for the limited descriptions of the megakaryocytes in the mouse models. Therefore, the following is based on WHO human criteria and on the limited reports derived from mouse models in an attempt to aid investigators in comparing their model to its human counterpart and the mouse literature [3, 58–60]. As the mouse spleen can also serve as a hematopoietic organ, the changes observed in the bone marrow in patients with these conditions may also be manifested in the spleen of mouse models.

CBC data and blood smear morphology:

- A marked leukocytosis largely due to neutrophils in different stages of maturation, with normal morphology and no significant dysplasia and associated with normal or slightly increased platelets, with or without anemia, and very few blasts is suggestive of a myeloproliferation with chronic myeloid leukemia features.
- A marked erythrocytosis with normocytic, normochromic RBCs, high hematocrit and hemoglobin, normal or increased platelets, and normal WBC or leukocytosis is suggestive of a myeloproliferation with PV features.
- A marked thrombocytosis with a normal or mildly elevated WBC count, normal RBC parameters, and normal or increased megakaryopoiesis is suggestive of a myeloproliferation with ET features.
- An anemia, thrombocytopenia, or a pancytopenia warrants examination of the spleen and bone marrow for increased fibrosis for further consideration of a myeloproliferation with PMF. Spleen and bone marrow fibrosis can also be indicative of the end stages of PV or ET myeloproliferation.
- A leukoerythroblastosis (circulating erythroblasts in association with immature myeloid cells) in the peripheral blood is a common finding in PMF in humans, but to date, it has not been described in corresponding mouse models.

Bone Marrow, Spleen, and Other Tissues

Chronic myeloid leukemia (CML): In the chronic phase of CML, the bone marrow and spleen are hypercellular as a result of the proliferation of granulocytes with a maturation pattern similar to that in the blood. The proliferation consists of mature granulocytes, typically neutrophils and metamyelocytes/myelocytes, with a marked increase in megakaryocytes that are smaller than those in PV, ET, and PMF [3, 61]. Blasts are rare and, if present, account for less than 3% of the total cells. The spleen and liver are enlarged. The splenic red pulp is expanded, and the white pulp is partially or completely replaced by mature and immature granulocytes. Similarly, immature and mature granulocytes infiltrate the hepatic sinusoids and portal triads. In some mouse models, the lungs are involved and perivascular macrophage infiltrates occur in the lung [61, 62].

Polycythemia vera: The spleen and/or bone marrow in PV are hypercellular as a result of trilineage hyperplasia of erythrocytes, granulocytes, and megakaryocytes, with RBCs and megakaryocytes being the most prominent. The megakaryocytes are small to medium sized, having hyperlobulated (staghorn-like) nuclei.

Essential thrombocythemia: The spleen and/or bone marrow in ET have normal cellularity, with a marked increase in megakaryocytes with large hyperlobulated (staghorn-like) nuclei and voluminous cytoplasm [58–60].

Primary myelofibrosis: The spleen and/or bone marrow in PMF vary depending on the stage of the proliferation at the time of examination. They may be hypercellular, with a leukocytosis and mild fibrosis, or hypocellular, with marked fibrosis. In either case, megakaryocytes are prominent, with an abnormal nuclear-to-cytoplasmic ratio and atypical features. Most megakaryocytes are large, but small ones may be present and can be detected with IHC. The megakaryocytes have hyperchromatic, hyperlobulated nuclei with bulbous, bulky (cloud-like), or balloon-shaped features [58].

As the MPNs age and progress, they may be characterized by bone marrow insufficiency due to fibrosis and osteosclerosis or by blast transformation that develops into leukemia involving the bone marrow and/or spleen. Acceleration of a blast phase into leukemia may be diagnosed when blasts/immature forms account for 20% or more of the WBCs in the blood or nonlymphoid cells in the bone marrow and/or spleen. The transformed blasts and the leukemias may arise from myeloid or lymphoid (B or T) lineages or from a combination of two of these [3, 61–64].

Immunophenotype: Immunophenotyping is of minimal relevance in diagnosing or differentiating the MPNs. However, flow cytometry and/or IHC with a panel of antibodies that includes antibodies to both myeloid-associated antigens (CD68, MPO, lysozyme C (LYZ1), CD41, CD71, and GATA1) and lymphoid-associated antigens (CD3, PAX5, and TDT) can help confirm an increase in blasts and identify their lineage in the blast transformation stage of the MPN. CBC data and blood smear morphology can provide direction as to prospective diagnostic differentials.

Differential diagnosis: Usually, evaluating the standard blood findings in conjunction with blood and bone marrow smears and histopathologic evaluation of the bone marrow, spleen, and liver is sufficient to determine which MPN is the appropriate diagnosis. However, the major challenge when diagnosing an MPN is to exclude a reactive leukocytosis, erythrocytosis, or thrombocytosis.

Vet-ebooks.com

Causes of reactive leukocytosis that need to be excluded include infection, inflammatory disorders, and neoplasms of any type.

Causes of reactive erythrocytosis that need to be excluded include anything that causes excess production of erythropoietin, be it genetic or nongenetic, such as hypoxia, cardiac disease, pulmonary disease, renal disease, hepatic disease, or erythropoietin-producing neoplasms. However, it should be noted that long-term hypoxia in mice can cause thrombocytopenia.

Causes of reactive thrombocytosis that need to be excluded are infections, inflammatory states, acute blood loss, iron deficiency, malignant neoplasms, and drugs [65].

Causes of reactive myelofibrosis that need to be excluded include inflammatory conditions or neoplasms that involve the bone marrow, as well as autoimmune diseases.

In human medicine, a patient's clinical history, including the laboratory blood parameters indicative of a PMN over an extended time, is particularly helpful in rendering an appropriate diagnosis. Unfortunately, when dealing with mice, a veterinary pathologist is limited to blood data and tissue associated with a specific time point. Consequently, when the blood analysis and tissue pathology yield findings of bone marrow insufficiency with marrow fibrosis and osteosclerosis, it may not be possible, without a history characteristic of a progressive myeloproliferation, to determine whether the condition is a PMF or whether the pathology is an end stage of one of the other three common MPNs.

Conventional mice and mouse models: There are no good descriptions in the literature characterizing spontaneous persistent myeloproliferations on a par with the entities in the 2017 WHO monograph. Except for the 2002 Bethesda workshop [2], there has been no detailed examination of a multitude of spontaneous myeloproliferations. However, there is accumulating evidence of an inherited susceptibility to MPNs in humans. Therefore, it is possible that one or more unrecognized inbred mouse strains can serve as spontaneous models of the MPNs.

Retroviral transduction, transgenic, knock-in, knock-out, and xenotransplant mouse models associated with various mouse strains have been developed to understand the molecular pathogenesis and therapeutic approaches for CML, PV, ET, and PMF [64, 66–68].

The *BCR-ABL* oncogene arises from a reciprocal translocation between human chromosomes 9 and 22. Many mouse models have been developed to determine how this oncogene results in CML and what therapies would be effective in replacing bone marrow transplantation [61, 63, 69, 70].

JAK2 gain-of-function mutations give rise to constitutively active JAK-STAT signaling, which accounts for most of the myeloproliferations characterized as PV, ET, or PMF in human patients. The *JAK2* V617F mutation is the most common molecular abnormality in *BCR-ABL*–negative MPNs: 95–98% of patients with PV and 50–60% of those with ET or PMF carry the mutation. The transgenic Tg(Vav1-JAK2*V617F)AZjz and Tg(H2-K^{b}Jak2*V617F)2Shmd mouse models have confirmed the role of the mutation in the pathogenesis of PV, ET, and PMF [58]. These findings have led to the development of additional mouse models to investigate how a single mutation contributes to the pathogenesis of different MPN diseases and the pathogenesis of PV, ET, and PMF in cases that lack the *Jak2* V617F mutation. Other mouse models have established a role for *Jak2* exon 12, calreticulin (*Calr*) gene mutations, and thrombopoietin (*Tpo*) receptor (*TpoR*) mutations in the development of MPNs [59, 60, 71, 72].

Myeloid Dysplasia

Definition: The myeloid dysplasias are a group of nonlymphoid hematopoietic stem cell diseases characterized by cytopenia and dysplasia (defective maturation) in one or more of the major nonlymphoid hematopoietic lineages. A cytopenia in at least one of the hematopoietic lineages is required for a diagnosis of myeloid dysplasia. In determining whether a mouse is cytopenic, it is important to be aware of the lower reference range of the hematopoietic parameters of your laboratory and to take into consideration the variations associated with strain and gender. Based on the criteria established by the histopathology subcommittee of the MMHCC [2], dysplasia is classified as myeloid dysplasia with two subclassifications: myelodysplastic syndrome (MDS) and cytopenia with increased blasts. However, if a mouse presents not only with cytopenias and dysplastic morphology but also has persistent neutrophilia, monocytosis, erythrocytosis, or thrombocytosis, a more appropriate classification may be myeloid dysplasia/MPN.

Tissues involved: Myeloid dysplasia in mice involves the peripheral blood, bone marrow, and spleen.

Morphology: To diagnose myeloid dysplasia, close examination of various hematopoietic samples is essential. Moreover, the normal ranges of different cellular elements within the different hematopoietic compartments in normal mice are important. When mice are monitored for features of myeloid dysplasia, peripheral blood samples should be examined at a series of time points. Unfortunately, a pathologist often has only one mouse or a few mice to assess at a given time point, which makes it more difficult to render a definitive diagnosis of myeloid dysplasia. Furthermore, peripheral blood assessments alone are insufficient to confirm myeloid dysplasia, and despite the peripheral blood cytopenia, thorough cytologic examination of a bone marrow smear and histologic examination of the bone marrow and spleen are required. Additional examination and histologic assessment of other tissues may also be required, especially if myeloid leukemia is suspected.

The defining criteria for myeloid dysplasia require the presence of cytopenia and the absence of evidence of a myeloproliferation in the form of erythrocytosis, leukocytosis, or thrombocytosis. The features considered to be evidence of dyspoiesis are indicated below. It should be kept in mind that a blood specimen exposed to anticoagulant for more than two hours often has unsatisfactory morphology.

Vet-ebooks.com

Erythroid features consistent with dyserythropoiesis include megaloblastic change (maturation of the cytoplasm preceding maturation of the nucleus), nuclear fragmentation, multinucleation, irregular nuclear contours, abnormal mitotic figures, and ring sideroblasts, but these are rare in the mouse. However, if sideroblasts are present, they are pathognomonic for dysplasia.

Neutrophil features consistent with dysgranulopoiesis include abnormal cytoplasmic maturation (pale basophilic cytoplasm in mature neutrophils) and abnormal nuclear maturation i.e. open chromatin in mature cells or lobated, as opposed to ring-shaped, nuclei.

Megakaryocyte features consistent with dysmegakaryocytosis include micromegakaryocytes (small oval nuclei in mature cytoplasm), large megakaryocytes with unlobated nuclei, large nuclei with bizarre hypersegmentation, and megakaryocytes with separated nuclei.

Bone marrow and spleen tissue sections give a general overview of the degree of involvement and specific histologic features. The bone marrow and spleen are generally hypercellular, and EMH is frequently evident in the spleen. The paradox of peripheral cytopenia despite a hypercellular bone marrow and spleen reflects premature loss of myeloid cells via apoptosis.

Cytopenia with increased blasts is a diagnostic classification recommended by the MMHCC when acute myeloid leukemia has been excluded and the animal has a cytopenia with at least 20% immature forms/blasts in the bone marrow and/or spleen and a lack of morphologic dysplasia features.

If a mouse has a disease with features of dysplasia and it very closely approximates a defined human MDS subtype, the MMHCC criteria indicate that the disease may be labeled myelodysplastic syndrome with features of a named human MDS.

Immunophenotype/histochemistry: Immunophenotype studies may demonstrate a decrease in or loss of normal myeloid maturation antigens or the presence of antigens not normally expressed. IHC may be helpful in order to

- exclude lymphoid origin of blasts with antibodies to CD3, CD45R/B220 (protein tyrosine phosphatase receptor type C, PTPRC), and PAX5;
- distinguish erythroid precursors with antibodies to the erythroid antigens CD71 and CD235A;
- quantify myeloid blasts/immature forms with antibodies to CD117, MPO, and CD68. CD34 is expressed not only in immature mouse megakaryocytes but also in more mature stages. Therefore, in the mouse, CD117 is recommended over CD34 for determining the total blasts/immature forms. Furthermore, CD117 is expressed not only by myeloblasts but also by proerythroblasts and promyelocytes. Consequently, its quantification provides a better estimate of the total blast/immature population;
- detect dysplastic or immature megakaryocytes, especially micromegakaryocytes, with antibodies to VWF, CD41, and CD61.

Histochemistry may also be helpful:

Iron stains can be used to identify ring sideroblasts, which are rare in mice but pathognomonic for dysplasia if present. Bone marrow smears or aspirates may be better than bone marrow tissue sections for detecting ring sideroblasts, because decalcification may leach out the iron.

PAS staining of erythroblasts may aid in assessing dyserythropoiesis characterized by erythroid cells with coarse or fine cytoplasmic granules.

Differential diagnosis: Morphologic features of dyspoiesis are subtler in mice than in humans and can be difficult to identify in mice. Consequently, it is often difficult to diagnose myeloid dysplasia in mice, and it must be differentiated from myeloid leukemia and MPNs.

If blasts and immature myeloid forms account for more than 20% of the total nucleated cells in the peripheral blood or bone marrow aspirate, as determined by flow cytometry or comparative blood or bone marrow smears, with or without morphologic dysplastic change, this is consistent with a myeloid leukemia diagnosis.

Cytopenia of one or more of the myeloid cell lineages is a hallmark of myeloid dysplasia, whereas an increase in one or more of the myeloid cells lineages in the peripheral blood is a feature of MPNs, as previously discussed. Therefore, a proliferative increase in myeloid cells without evidence of ring sideroblasts is suggestive of an MPN. Unfortunately, ring sideroblasts are rare in mice [2]. The diagnosis can be further complicated if overlapping features are present. For example, a myelodysplastic/myeloproliferative neoplasm (CML), a condition in which both dysplastic and proliferative features coexist, has been reported in a knock-out mouse model [73].

Conventional mice and mouse models: Dysplasia of the bone marrow elements occurs in old mice, and dyshematopoiesis has recently been recommended as the preferred term for these conditions in mice [74]. However, when there is a cytopenia in association with dysplasia in conventional or genetic engineered mice, the 2002 MMHCC subcommittee recommendations should be followed in classifying the condition [2].

Over 20 mouse models of myeloid dysplasia (MDS) have been described [75–77]. These mouse models include animals given mutagenic and carcinogenic agents; genetic models such as those involving retroviral transduction and transplantation; genetically engineered mouse hematopoietic cells, produced using transgenic, knock-out, or knock-in strategies; and PDXs in mice given human MDS cells. Various immunodeficient mice have been used for PDX MDS cell studies, but propagation of PDX MDS cells in most of these mice has been limited. Recently, NSG (NOD.Cg-*Prkdc*^{scid}/*Il2rgtm*/SzJ) and NSG-SGM3 (NOD.Cg-*Prkdc*^{scid} *Il2rg*^{tm1Wjl} Tg(CMV-IL3,CSF2,KITLG)1Eav/MloySzJ) mice with or without co-administration of human mesenchymal stromal cells have shown promise; a high percentage of the mice become engrafted with the human MDS cells, but the level of engraftment is only low to moderate [78, 79]. When dealing with PDX MDS, it is important to confirm that the engrafted cells have the same mutant allele burden as the patient's MDS cells to ensure that the engrafted cells did not arise from normal HSCs among the MDS cells. With all

Vet-ebooks.com

mouse MDS models, it is important to recapitulate the human condition, whereby the MDS model progresses to myeloid leukemia over time and the engrafted cells are transplantable to a second mouse, confirming the autotomy of the MDS cells associated with the mouse model. In the future, additional mouse models of MDS will be developed that will further our understanding of the evolutionary processes associated with the development of this complex heterogeneous group of human hematopoietic stem cell disorders with diverse phenotypes.

Nonlymphoid Hematopoietic Sarcomas

Myeloid Sarcoma

Definition: A myeloid sarcoma is a tumor mass consisting of myeloid blasts, with or without maturation that occurs at an anatomical site other than the bone marrow in a mouse that does not have a myeloid leukemia. In humans, myeloid sarcoma may be a manifestation of a myeloid leukemia.

Tissues involved: Myeloid sarcoma can arise in any extramedullary tissue.

Morphology: The most common type of myeloid sarcoma is the granulocytic sarcoma, which is composed of variable proportions of myeloblasts, neutrophil precursors, and mature neutrophils.

Immunophenotype: Most myeloid sarcomas express CD43. Immunoreactivity of tumor cells for CD43, but not for CD3 or PAX5, should prompt consideration of a myeloid sarcoma, and the tumor should be labeled with antibodies to MPO, lysozyme C, CD41, and CD71. Granulocytic myeloid sarcomas are immunoreactive for MPO and lysozyme C; erythrocytic sarcomas are immunoreactive for CD71; and megakaryocytic sarcomas are immunoreactive for CD41. The latter two types of sarcoma are rare.

Differential diagnosis: The major differential diagnosis in the mouse is lymphoblastic lymphoma and histiocytic sarcoma, and the tumor should be labeled with antibodies to CD3, PAX5, MPO, lysozyme C, CD68, IBA1, and CD163.

Myeloid sarcomas express neither the T-lymphoblastic lymphoma antigen CD3 nor the B-lymphoblastic lymphoma antigen PAX5. Myeloid sarcomas do not express CD68, IBA1, or CD163, but histiocytic sarcoma cells are immunoreactive for at least one of these macrophage (histiocyte) antigens.

Conventional mice and mouse models: Spontaneous myeloid sarcomas are rare in conventional mice, but they have been reported in GEM [80, 81] (see Table 8.2).

Histiocytic Sarcoma

Definition: Histiocytic sarcoma (HS) in the mouse has been known by several names, such as reticulum sarcoma type A, histiocytic lymphoma, malignant histiocytosis, and malignant

Table 8.2 Nonlymphoid hematopoietic sarcomas associated with conventional mice and mouse models.

Type	Conventional	References	GEMs	References	Other models	References
Myeloid	Rare, Crl:CD-1(ICR)	Charles River 2005 report	*Dnmt3a*+/− *Tet2*−/−	[80, 81]	ENU mutagenesis: SWR/J,DBA/J, BALB/cByJ	[12]
Histiocytic	Variable with gender, age, and strain C57Bl/6 > Balb/c, C3H, CBA	[25, 26, 82–85]	*p21*−/− *p53*−/−; +/− *Bax*−/− *Pten*−/− C*dkn2a* D*ok1*−/−, D*ok2*−/−, D*ok3*−/− C*yp1b*−/−	[86–90]	Xenobiotics	[91]
Dendritic cell	Not known		*Braf*^{CA}*Pten*$^{loxP/loPx}$Tg (*CD207-cre)*	[92]	FDC PDXs Malignant histiocytosis sarcoma virus	[93–95]
Langerhans cell histiocytosis	Not known		Tg Mushi mice Tg *Braf*^{CA}*Pten*$^{loxP/loxP}$ Tg *Lck-GM-CSF*	[92, 96, 97]	Not known	
Mast cell	Rare, <1%. Generally, >18 mo. old in strains A, BALB/cStCrIBR, B6C3F1, FVB/NJ	[40, 98–100]	Not known		Xenobiotics Irradiation MuLV Allotransplant	[40, 44, 45, 99, 101]

PDX = patient-derived xenografts, MuLV = murine leukemia virus.

Vet-ebooks.com

schwannoma [7, 82, 102, 103]. Immunohistochemical, immunological, and ultrastructural studies have demonstrated a histogenesis consistent with cells of the mononuclear phagocyte system, and the tumor is now referred to as histiocytic sarcoma [82, 83].

Tissues involved: In most mouse strains, the liver and uterus are the predilection sites for HS, but the lungs, spleen, lymph nodes, bone marrow, and other tissues may be involved [83–85].

Morphology: Histiocytic sarcomas are composed of large round or spindle-shaped cells with pale coalescing eosinophilic cytoplasm. Occasionally, an HS consists of both spindle and round cells. The nuclei are round, oval, irregular, elongated, folded, or indented, with vesicular chromatin and prominent nucleoli. Ring-shaped nuclei with a central opening are occasionally present. The growth pattern may be nodular or diffuse. Multinucleated giant cells are sometimes present in the neoplastic lesions. Small B or T lymphocytes may be scattered among the neoplastic histiocytes. Erythrophagocytosis and foci of hematopoiesis characterized by small nodules of myelocytic and erythrocytic cells dispersed among or surrounded by neoplastic histiocytes may be observed. The neoplastic cells in the liver often have a sinusoid growth pattern, whereas those in the lung have an intravascular and/or perivascular growth pattern. Lung involvement is common in mice with hepatic histiocytic sarcoma. It is also not uncommon for a HS in the uterus to have a spindle cell pattern rather than a round cell pattern. In some mice with HS, the proximal renal tubules have an increased number of intracytoplasmic eosinophilic hyaline granules, which are positive for lysozyme C. The intensity of the stain will depend on the tumor load. A tumor with HS morphology associated with strong lysozyme expression in the renal tubule cells is suggestive of, but not pathognomonic for HS because renal cell lysozyme expression has been associated with other neoplastic processes [104].

Immunophenotype: Histiocytic sarcoma cells commonly express, with variable intensity, one or more of the following macrophage markers: CD68, CD163, F4/80, IBA1, MAC2, and lysozyme C. It should be noted that F4/80 expression increases as cells mature from monocytes to tissue histiocytes. Consequently, in an HS composed of a mixture of spindle and round cells, the spindle cells will be F4/80 negative and the round cells will be F4/80 positive, suggesting that the tumor contains both immature and mature histiocytes. In rare instances, a uterine HS may express S100B.

Differential diagnosis: The differential diagnosis of HS includes diffused large B-cell lymphoma histiocytic-associated (DLBCL-HA) variant, composite HS/lymphoma, and mast cell tumor. The first of these can be problematic. A retrospective study found that only 33% of cases initially diagnosed as HS were confirmed to be HS, with half of the remainder being DLBCL-HA variants. Unlike DLBCL-HA, HS does not have a prominent population of large B cells. Mitotic figures are uncommon, but erythrophagocytosis is common. It can also be problematic to differentiate HS from a composite tumor composed of lymphoma and HS unless the two components have segregated as pure tumors in different tissues. Although HSs and mast cell tumors can occasionally mimic each other morphologically, IHC will readily differentiate the two neoplasms. Histiocytic sarcomas express proteins: F4/80 (ADGRE1, adhesion G protein-coupled receptor E 1), MAC2 (LGAL3, lectin, galactose binding, soluble 3), and IBA1 (AIF1, allograft inflammatory factor 1), whereas mast cell tumors express proteins: CD117, tryptase, mMCP1 (CCL2, chemokine [C-C motif] ligand 2), and mMCP4 (MCPT4, mast cell protease 4).

Conventional mice and mouse models: Histiocytic sarcoma occurs in various outbred and inbred mouse strains and GEM [25, 26, 81–91] (see Table 8.2).

Dendritic Cell Tumors/Histiocytosis

Definition: Dendritic cell tumors are related to several lineages of accessory antigen-presenting cells (dendritic cells) that have a role in phagocytosing and processing antigens and presenting them to lymphoid cells.

Tissues involved: Except for Langerhans cell sarcomas, which primarily involve the bone and skin, dendritic cell sarcomas, such as those developing from follicular dendritic cells, interdigitating cells, and fibroblastic reticular cells, primarily involve lymph nodes and the spleen. However, all of these dendritic sarcomas may involve extranodal tissues.

Morphology: Except in Langerhans cell histiocytosis (LCH) in which the cells have round-to-oval nuclei, the neoplastic cells associated with dendritic cell sarcomas are spindle-shaped cells arranged in fascicles, storiform patterns, and whorls. Mitotic cells and lymphocytes are variable in number.

Immunophenotype: No single marker identifies all dendritic cell subsets. Therefore, it is important to immunophenotype the cells by using a panel of antibodies that is appropriate to the cell in question and rigorously excludes other cell lineages [6].

Primary antigen markers for Langerhans cell sarcoma are langerin (CD207) and S100B protein. Unlike human Langerhans cells, mouse Langerhans cells do not express CD1A. Primary markers for follicular dendritic cell sarcoma are CD21/CD35 and podoplanin; primary markers for interdigitating dendritic cell sarcoma are S100B and fascin-1 (FSCN1, fascin actin-bundling protein 1), and primary markers for fibroblastic reticular cell sarcoma are SMA, desmin, and keratin (immunoreactivity is variable for keratin 8 (KRT8), keratin18 (KRT18), pan-keratin AE1/AE3).

Differential diagnosis: The various dendritic cell sarcomas require differentiation from one another and from thymomas, carcinomas, and, in some instances, lymphoma. Differentiation between these various entities requires IHC. A panel of antibodies to the various dendritic cells will aid in determining the lineage of a dendritic cell sarcoma. Thymomas and carcinomas express keratins (pan-keratin AE1/AE3, keratin 8 (KRT8), keratin 5 (KRT5), keratin 14 [KRT14]). Whereas dendritic cells do not. Dendritic cell sarcomas lack PAX5 and CD3 expression, but lymphomas express one or other of these lymphoid markers.

Vet-ebooks.com

Conventional mice and mouse models: Spontaneous dendritic cells or other antigen-presenting cells have not been reported in mice, but GEM, xenotransplant, and viral-induced models have been reported [92–97, 103] (see Table 8.2).

Mast Cell Neoplasms

Definition: Mouse mast cell proliferations have been known by several names, such as mastocytoma, mast cell sarcoma, malignant mastocytoma, malignant mastocytosis, and systemic mastocytosis. Mast tumors are rare in mice; consequently, their morphology and biologic behavior have not been well characterized. This has raised the question as to the appropriate terminology for these neoplasms in mice. Based on the few documented cases of such proliferations in mice, it has recently been recommended that a solitary mast cell tumor be classified as either a mast cell tumor, benign, or a mast cell tumor, malignant, with the latter having either solitary nodules or systemic diffuse features [74].

Tissues involved. Mast cells may involve the bone marrow, kidney, liver, lymph nodes, skin, and spleen.

Morphology: Benign mast cell tumors have a uniform appearance of compacted, nonencapsulated, well-circumscribed sheets of discrete cuboidal or rhomboid cells. The nuclei are round to oval and are centrally located. The nuclei may be difficult to see, depending on whether the cytoplasm is granular, hypogranular, or agranular. The granules in granulated mast cells stain red or blue with metachromatic stains. The cells of malignant mast cell tumors are atypical and often hypogranular, but with atypical granules. The nuclei are bizarre, bilobed, and/or polylobed. A malignant mast cell tumor has an infiltrative and destructive growth pattern.

Immunophenotype: The mouse has at least three types of mast cells: the connective tissue type and two mucosal subtypes [105]. One of the mucosal subtypes has large nonmetachromatic eosinophilic granules and is located predominantly within the mucosal epithelium and less frequently in the lamina propria. The author is not aware of tumors being associated with this subtype. The other mucosal mast cell subtype is located in the lamina propria, but it is infrequently seen with H&E staining. The two mucosal mast cell subtypes can be differentiated from one another and from the connective tissue type by IHC [6]. CD117 and CD34 are expressed in mouse mast cells throughout their development and maturation, but they are not specific for mast cells. Tryptase and mouse MCP4 are expressed by connective tissue and lamina propria mast cells, whereas mouse MCP1 is the most specific marker for the intraepithelial mucosal mast cells. Anti-CD117 and anti-tryptase antibodies also aid in determining whether the tumor cells are mast cells or basophils.

Differential diagnosis: Mast cell tumors may need to be differentiated from mast cell hyperplasia, basophil cell tumors, and histiocytic sarcomas.

Mast cell tumors are well-circumscribed, densely packed nodules or sheets of densely packed tumor cells with no connective tissue between the tumor cells, whereas foci of mast cell hyperplasia are loosely arranged collections of mast cells separated by connective tissue bundles. Hyperplastic mast cells do not have cellular atypia, whereas mast cell tumors may or may not have features of cellular atypia, such as binucleated or polynucleated cells.

Mast cell tumors are difficult to differentiate from basophil tumors based on morphologic criteria in tissue. Both cells may contain dark basophilic granules that may impede an adequate determination of whether the tumor cells are monolobed mast cells or bilobed basophils. These morphologic nuclear differences can be further blurred in pathologic conditions. Using IHC to detect expression of CD117, tryptase, and mouse MCP11 (mMCP11) by tumor cells is the best way to differentiate a mast cell tumor from a basophil tumor. Mast cells express CD117 and tryptase but do not express mMCP11, whereas basophils express MCP11, but do not generally express tryptase or CD117 [6].

Under some circumstances, mast cell tumors may be difficult to differentiate from histiocytic sarcoma based on morphologic criteria. However, these two tumors can be readily differentiated from one another with IHC. Mast cell tumors do not express the macrophage markers F4/80, MAC2, or IBA1, and histiocytic sarcomas do not express the mast cell markers CD117, tryptase, mMCP1, or mMCP4.

Conventional mice and mouse models: Foci of mast cell hyperplasia are common in mice of many strains and are frequently seen in lymph nodes, the mesentery, and other organs. It is not uncommon to see foci of mast cells at the periphery of solid tumors, especially those in the skin.

The incidence of spontaneous mast cell tumors in mice is reported to be less than 1%, and they generally occur in mice older than 18 months [40, 98–101] (see Table 8.2**)**.

Lymphoid Neoplasms

Overview of Lymphoid Neoplasm Classification

B-cell, T-cell, and NK cell neoplasms are clonal neoplasms of immature and mature B cells, T cells, and NK cells, respectively, at various stages of differentiation. B-cell neoplasms and T-cell neoplasms, in many instances, correlate with the developmental and differentiation stages of normal B and T cells. T cells and NK cells are closely related and share some immunophenotypic features. The heterogeneity and lineage plasticity seen with human B-cell and T-cell neoplasms have not been well documented in mice, but these possibilities need to be kept in mind when evaluating mouse lymphoid leukemias/lymphomas. Some mice, especially GEMs, may have parallel (composite) lymphomas of two different lineages or of two different morphologic classifications, with or without collision.

B-Cell Neoplasms

B-Cell Lymphoblastic Lymphoma/Leukemia (LBL)

Definition: B-cell lymphoblastic lymphoma (LBL) is a neoplasm originating from hematopoietic stem cells or precursor

Vet-ebooks.com

B-cells. Lymphoblasts can have variable morphology, and the histopathologies of B-lymphoblastic lymphoma and B-lymphoblastic leukemia are indistinguishable except for differences in tissue distribution. B-lymphoblastic lymphoma is more common than primary lymphoblastic leukemia in the mouse. Lymphoma is diagnosed when the lymphoblasts primarily involve extramedullary tissues and the lymphoblasts constitute less than 25% of the cells in the blood or bone marrow. The WHO states that when 25% or more of the cells in the blood or bone marrow are lymphoblasts, the appropriate term is leukemia. The MMHCC Bethesda proposals do not specify a blast percentage for diagnosing lymphoid leukemias. When there is a mass lesion(s) and lymphoblasts in the bone marrow, the distinction between lymphoma and leukemia is arbitrary. In leukemia, the bone marrow is almost always hypercellular, with normal marrow elements being replaced by a diffuse infiltrate of immature cells. With either lymphoma or leukemia, there can be significant involvement of the liver, the spleen, single or multiple lymph nodes, and the central nervous system (CNS), especially when there is a leukemia.

Tissues involved: B-lymphoblastic lymphoma involves the lymph nodes, spleen, liver, and/or other tissues. The bone marrow and peripheral blood are involved when the lymphoma progresses to a leukemic phase.

Morphology: B-lymphoblastic lymphomas/leukemias are composed of medium-sized cells with round-to-ovoid nuclei and scant cytoplasm. The nuclei have fine or dispersed (salt and pepper) chromatin and variable (one to three) or inconspicuous nucleoli. Single central nucleoli are more typical. Mitosis and tingible body macrophages with apoptotic bodies are abundant, imparting a starry sky appearance. Morphologically, there is no distinction between lymphoblastic lymphoma and lymphoblastic leukemia. Lymphoblastic lymphoma is much more common than primary lymphoblastic leukemia in mice; however, approximately 30% of B-cell lymphoblastic lymphomas develop a leukemic phase.

Immunophenotype: The antigens expressed in lymphoblastic lymphoma in mice, and their detection, are dependent upon the maturation stage of the B cells when they undergo transformation and whether flow cytometry or IHC is used to characterize the immunophenotype of the lymphoma [106].

Pro-B lymphoblastic lymphomas may be CD19+, CD43+/−, CD45R/B220+/−, CD117+/−, CD127 (IL7RA)+, LY6D+ (ThB)+, PAX5+, TDT+/−, cIgM–, and Ig light chain negative.
Pre-B lymphoblastic lymphomas may be CD19+, CD25+, CD43+/−, CD45R/B220+, CD117−, CD127 (IL7RA)+, LY6D (ThB)+, PAX5+, TDT−, cIgM+, and Ig light chain negative.

Note: The level of CD25 expression detected by flow cytometry in the mouse appears to be below the level of detection by IHC. It is not feasible to discern by IHC whether IgM is in the cytoplasm or on the surface of a lymphoblast. Consequently, to differentiate a pre-B lymphoblast from an immature transitional lymphocyte, it is necessary to determine whether a neoplastic B lymphocyte is expressing Ig light chain [5, 106–108]. An initial analysis for kappa light chain expression is recommended, because the percentage of lymphocytes expressing kappa light chain in adult mice is 10-fold higher than the percentage of lymphocytes expressing lambda light chain [109].

Differential diagnosis: B-cell and T-cell lymphoblastic lymphomas/leukemias are morphologically indistinguishable, and immunophenotyping is necessary to distinguish these two lineages. A large thoracic mass alone should not be used as the sole criterion for diagnosing a lymphoma as a T-cell lymphoblastic lymphoma. A B-lymphoblastic lymphoma arising in a mediastinal lymph node can invade the thymus, thereby giving the impression of the lymphoma being a thymic mass. Lymphoblastic lymphoma in the mouse also needs to be differentiated from a similar lymphoma that has been referred to as diffuse high-grade blastic B-cell lymphoma (DHGBL). DHGBL has also been referred to as DLBCL/LL (diffuse large B-cell lymphoma of lymphoblastic subtype) and as Burkitt-like lymphoma. Lymphoblastic lymphomas/leukemias of B-cell lineage express one or more of the B-cell markers listed above, and lymphoblastic lymphomas/leukemias of T-cell lineage express CD3, TDT, and, to varying degrees, CD2, CD4, CD8, CD5, and CD43.

Conventional mice and mouse models: As with most types of lymphoma, the incidence of B-lymphoblastic lymphoma varies with age and gender and they occur spontaneously, in GEM and MuL virus infected mice [104, 107, 110–118] (see Table 8.3).

Small B-Cell Lymphoma/Leukemia

Definition: Small cell lymphoma/leukemia is a neoplasm of well-differentiated lymphocytes. The term "small lymphocytic lymphoma" (SLL) is reserved for nonleukemic disease of secondary lymphoid tissues that may have a leukemic phase. Although there are cytologic similarities between mouse SLL and chronic lymphocytic leukemia (CLL) or SLL in humans, there are many differences with regard to organ involvement, histologic features, and blood involvement [118, 144].

Tissues involved: Small B-cell lymphoma/leukemia (B-SLL) primarily involves the lymph nodes and spleen; in advanced disease, the liver, kidneys, and peripheral blood may be involved.

Morphology: Small B-cell lymphoma cells are noncohesive, are of uniform small-to-medium size, and have round nuclei with densely clumped chromatin, inconspicuous nucleoli, and scant cytoplasm. The cells differ little from normal circulating small lymphocytes. Mitosis is rare. The spleen and lymph nodes are effaced by lymphoma cells; the liver and kidneys may be involved in advanced cases. Approximately 25–30% of cases develop a leukemic phase, and conversion to high-grade lymphoma may occur [1].

Immunophenotype: B-SLLs express the following antigen markers: CD19, CD45R/B220 (protein tyrosine phosphatase, receptor type, C, PTPRC), PAX5, CD5, CD43, and IgM.

Vet-ebooks.com

Differential diagnosis: Small B-cell lymphoma and small T-cell lymphoma (SLL) are morphologically similar and can be differentiated with flow cytometry or IHC. B-SLL cells express PAX5, T-SLL cells express CD3, and both cell populations are negative for TDT expression.

Conventional mice and mouse models: Spontaneous small cell lymphoma is uncommon, occurring in only a few strains at a low percentage in old mice, few MuL virus induced models and a few GEM [104, 119–124, 141] (see Table 8.3).

Splenic Marginal Zone Lymphoma

Definition: Splenic marginal zone lymphoma (MZL) is a B-cell neoplasm consisting of small lymphocytes that expand the splenic marginal zone with extension into the red pulp.

Tissues involved: MZL primarily involves the splenic marginal zone and the red pulp; occasionally, it will invade the follicle. MZL also involves the splenic hilar lymph node and the liver. Splenic MZL in humans commonly involves the bone marrow, but this feature has not been reported in mice and requires further investigation.

Morphology: Early in the disease, MZL is characterized by a substantial widening of the marginal zone in the absence of germinal center (GC) hyperplasia. The marginal zone cells at this stage have normal cytology of uniform shape and scant or clear cytoplasm, with the latter imparting a monocytoid appearance; mitosis is rare or absent. This stage is difficult to differentiate from marginal zone hyperplasia, emphasizing the importance of a comparison to concurrent controls. Subsequently, there are progressive changes in the morphologic features of the cytology and growth patterns. At an intermediate stage of progression, there is merging or bridging of the marginal zones and cellular atypia characterized by medium- to large-sized centroblast nuclei with nucleoli and occasional mitosis. When the lymphoma is at an advanced stage, the red pulp is completely replaced by large lymphoma cells that have vesicular nuclei, with or without prominent nucleoli, and moderate amounts of eosinophilic cytoplasm. Mitosis is common at this stage. In rare cases, the lymphoma cells invade the follicle and compress the PALS. Plasmacytic differentiation may also occur. Therefore, plasma cells may be associated with some MZLs. Although MZL is generally restricted to the spleen, metastasis to the liver and splenic hilar lymph nodes may occur.

Immunophenotype: Depending on whether the antigen expression is analyzed using flow cytometry or IHC, MZL may be CD5+/−, CD19+, CD45R/B220+/−, PAX5+, IgD−, IgM+/−, and kappa light chain positive. Recently, it has been suggested that the splenic MZLs reported in 1999 to be CD45R/220− and CD5+ were not MZLs but iNKT lymphomas [126, 160]. However, it has now been determined that CD45R/B220− MZLs express PAX5, which is consistent with these splenic tumors being of B-cell origin and, consequently, being MZLs [108].

Differential diagnosis: When splenic MZL metastasizes to other tissues, it is difficult to differentiate it from other small B-cell lymphomas. MZL and generally mantle cell lymphoma (MCL) are CD43–, whereas B-SLL are generally CD43+. If MZL involves the follicle, it must be differentiated from follicular lymphoma (FL). MZLs do not express follicle cell markers.

Conventional mice and mouse models: MZL occur in NZB, NFS/N^{V+}, AKXD recombinant inbred (RI) mice and *Trp53*−/− mice of C57BL/6 and other background strains. The mice are generally older than 12 months [118, 124–126]. NFS/N^{V+} (NFS/N mouse congenic for ecotropic murine leukemia viruses), AKXD mice are commonly used to assess which genes are associated with the development of specific types of hematolymphoid neoplasms) (see Table 8.3).

Mucosa-Associated Lymphoid Tissue Lymphoma

Definition: Mucosa-associated lymphoid tissue (MALT) lymphoma is an extranodal lymphoma that rarely arises directly from MALT but usually occurs as a result of a chronic inflammatory disorder at a site normally devoid of MALT.

Tissues involved: MALT lymphoma may involve the gastrointestinal tract (Peyer's patches), salivary glands, thyroid, respiratory tract, etc.

Morphology: MALT lymphomas consist morphologically of heterogeneous small B cells with centrocyte-like features (small cells with irregular nuclei, inconspicuous nucleoli, and pale cytoplasm), scattered immunoblasts and cells with centroblast-like features; occasionally, there is plasma cell differentiation. The neoplastic cells infiltrate the epithelium at the involved site, forming lymphoepithelial lesions. Like other small B-cell lymphomas, a MALT lymphoma can undergo transformation to a diffuse large B-cell lymphoma (DLBCL). Only when solid nodules or sheets of transformed cells are present should the lymphoma be considered to have transformed to a DLBCL.

Immunophenotype: MALT lymphoma cells are PAX5, CD45/B220, CD79A, and CD21 positive and CD3, CD5, and CD43 negative. The neoplastic cells typically express IgM and, less often, IgA; they are generally IgG and IgD negative.

Differential diagnosis: Based on its cytologic morphology, MALT lymphoma has similarities to reactive infiltrates in many organs, such as the salivary glands, and to FL of Peyer's patches. Lymphoepithelial lesions are characteristic of MALT lymphoma, unlike reactive inflammatory lesions in the salivary glands, thyroid glands, etc. IHC is helpful in differentiating Peyer's patch MALT lymphoma from Peyer's patch FL. The FL cells express one or both of the follicular cell markers BCL6 and peanut agglutinin (PNA), whereas MALT lymphoma cells express neither of these antigens.

Conventional mice and mouse models: Other than Peyer's patch MALT lymphoma, these tumors are rare in conventional mice. The fact that MALT lymphomas are not addressed in the MMHCC document [1] or in the recent International Harmonization of Nomenclature and Diagnostic Criteria for Lesions (INHAND) publication on the hematolymphoid system [74] attest to the rarity of these tumors in mice. GEM and bacterial induced models have been reported [127–129] (see Table 8.3).

Vet-ebooks.com

Table 8.3 B-cell lymphoid neoplasms associated with conventional mice and mouse models.

Type	Conventional	References	GEMs	References	Other models	References
B-lymphoblastic	CD-1, C57BL/6, C57BL/10, BALB/c, B6,129 NFS/N, SL/Kh	[104, 110–114]	Tg *IghMyc* Tg *Ebf1+/−Bcl-xL* Tg *BCR-ABL*	[115–117]	NFS/N^{V+} AKXD RI	[112, 118]
Small B-cell	Rare reports in CD-1, BALB/c, NZB, NZW	[104, 119–121]	Tg *IGH-TCL1A*	[122, 123]	NFS/N^{V+} AKXD RI Immunocompromised mice + XT	[118, 123, 124]
Splenic marginal zone	NZB	[125]	*Trp53−/−*	[126]	NFS/N^{V+} AKXD RI	[118, 124]
MALT	Rare	[74]	BALB/c *Plcg2*$^{Ali5+}$ Tg *APRIL C57BL/6*	[127, 128]	BALB/c + *Helicobacter* spp.	[129]
Mantle	Not known		Tg *IGH-CCND1* DTg *MYC/IL4* DTg *Myc-39RR/p53+/−* DTg *Myc/Cdk4*^{R24c}	[130–134]	Immunocompromised mice + XT	[123, 135–138]
Plasma cell	Rare, NZB, SJL/J	[139]	Tg *IL-6* C3H-*Fas*^{lpr} /*Fas*^{lpr}; C3H-*Fasl*^{gld}/*Fasl*^{gld} BAL/c-*Fasl*^{gld}/*Fasl*^{gld} *Igh-Myc*^{His}	[139, 140]	NFS^{V+} BALB/c/An, BALB/cJ, or NZB/BI, NZB/NIcr + pristane	[139, 141–143]
Follicular	BALB/cCrl, BALB/cAn C57BL/6, C3H, CD-1, CFW, DBA/2SJL/J, NZB	[25, 26, 104, 110, 141, 144, 145]	*Trp53−/−*; *Trp*53+/−, *Tet1−/−*, Tg *IGH-BCL-2,* Tg *Mcl1,* Tg *MLL-AF4* fusion gene Ing1−/−	[146–149]	AKXD RI NFS/$^{NV+}$	[118, 145]
DLBCL	BALB/cCrl, CFW	[110, 150]	*Bad−/−* Tg *BCL6*, *Trp53−/−* Tg *IGH-TCL1* Tg *IGH-MYC* *Cd21*$^{Cre/wt}$*; Myd88*$^{c\text{-}p.L252P/w}$	[150–157]	AKXD RI NFS/N^{V+}	[144, 150]
Diffuse high-grade blastic B-cell	CFW	[141, 150]	Tg *λMYC, Cdkn2a−/−*	[150]	AKXDR1 NFS/N^{V+}	[144, 150]
NK B-cell	SL/Kh × AKR/MEF1 (SLAKF1), C57BL/6	[70, 158]	Tg *HLA-DR4-H2-E*	[159]	None reported	

NFS/N^{V+} = NFS/N mouse congenic for ecotropic murine leukemia viruses, XT = xenotransplantation of patient derived tumor tissues or human cell lines, DTg = double transgenic.

Vet-ebooks.com

Mantle Cell Lymphoma

Definition: Mantle cell lymphoma (MCL) is a mature B-cell neoplasm. A t(11;14)(q13;32) translocation between *IGH* and *CYCLIN D* loci is the hallmark of human MCL, resulting in dysregulated expression of the cyclin CCND1 protein [161]. The cell of origin is unknown, but most tumors have unmutated Ig genes, suggesting that the cell of origin is a naive or extrafollicular B-cell type.

Tissues involved: In humans, lymph nodes are the most common organs involved, but extranodal sites such as the spleen and gastrointestinal tract can also be involved. Some GEM models have tissue involvement similar to that in patients, but in other GEM models, the spleen and bone marrow are the organs generally involved.

Morphology: MCL demonstrates a monomorphic proliferation with a vague nodular, diffuse, or mantle zone growth pattern. The lymphoma is composed of small- to medium-sized lymphocytes with irregular nuclear contours that resemble centrocytes, but there are two blastoid variants. The classic blastoid variant has lymphoblast-like nuclei, whereas the pleomorphic blastoid variant has large cleaved to oval nuclei, prominent nucleoli, and pale cytoplasm.

Immunophenotype: By flow cytometry and IHC, human and GEM MCLs are CD5+, CD19+, CD43−/+, PAX5+, $_{S}$IgM+, $_{S}$IgD+/−, and CCND1 (cyclin D1)+ and are negative for CD21, CD23, and BCL6.

Differential diagnosis: Based on morphology, classic MCL must be differentiated from small cell lymphoma, MZL, and small-cleaved FL.

Conventional mice and mouse models: MCL has not been reported to occur spontaneously in mice. However, GEM models, cell-line transplant models, and xenotransplant models have been described [130–138, 162, 163] (see Table 8.3).

Plasma Cell Neoplasms

Definition: Plasma cell neoplasms in the mouse are heterogeneous tumors consisting of mature plasma cells, immature plasma cells, or a mixture of the two. Histologically, based on the predominant morphologic features of the tumor nuclei, plasma cell tumors can be classified into three subtypes: plasmacytic plasmacytomas, immunoblastic plasmacytomas, and anaplastic plasmacytomas. It is often difficult to distinguish plasmablasts and immunoblasts, and the term "plasmablast" has been used in different scenarios, leading to much confusion and misunderstanding. Therefore, the term "immunoblast plasmacytomas" has been chosen to refer to the mouse plasmacytoma that has been classified by some investigators as plasmablastic plasmacytoma [139, 164].

Tissues involved: Plasmacytomas occur in the spleen, lymph nodes, bone marrow, liver, kidney, and intestinal tract.

Morphology: Plasmacytic plasmacytomas are composed predominantly of mature B cells that have small nuclei with peripheral clumped (clock-faced) chromatin, abundant basophilic cytoplasm, and a discernible Golgi apparatus. These cells are generally arranged in solid sheets, with rare mitoses and a scattering of immunoblasts and plasmablasts. Immunoblastic plasmacytoma consists of all stages of plasma cell differentiation, with immunoblasts and plasmablasts being the predominant cell types. The immunoblasts and plasmablasts vary in size. Their nuclei have open chromatin, thickened smooth or irregular nuclear membranes, and a single, large magenta nucleolus, and they contain abundant amphophilic cytoplasm. Mitoses and apoptosis are frequent. Unlike immunoblasts, most plasmablasts have round, eccentric nuclei and abundant cytoplasm, imparting plasma cell or plasmacytoid features. The cytoplasm is basophilic or pyroninophilic, with or without a perinuclear halo. In tissue sections, these distinctions are difficult to identify. Anaplastic plasmacytomas are a mixture of immunoblasts, plasmablasts, and large pleomorphic cells with bizarre, complex vesicular nuclei that have irregular, folded nuclear membranes imparting a horseshoe, kidney, or embryonal shape. Mitoses and apoptosis are frequent, and recognizable plasma cells are rare.

Immunophenotype: In plasma cells, the expression of the B-cell antigens PAX5, CD45R/B220, CD79A, and BCL6 is downregulated, whereas that of IRF4, CD138, and XBP1 is upregulated. Plasma cells also express CD43, but this is also commonly expressed in T cells. However, the T-cell marker CD3 is not expressed by plasma cells and, therefore, helps to differentiate the two. Although CD138 expression can differentiate plasmacytomas from most B-cell lymphomas and T-cell lymphomas, it does not differentiate plasma cell tumors from mouse B-cell lymphoblastic lymphomas (B-LBLs) or from many carcinomas because it is expressed by some of those tumors. Most plasmacytomas induced by IP injection of pristane express IgA, whereas most plasmacytomas unrelated to pristine induction express IgG.

Plasma cell neoplasms have the following immunoprofile by flow cytometry and/or IHC: CD138+, CD43+/−, IRF4+, XBP1+, cIg+; PAX5−, CD45R/B220−, CD79A−/+, and CD45 is generally negative.

Differential diagnosis: Plasmacytic plasmacytomas involving lymphoid tissues must be differentiated from reactive plasma cell hyperplasia. Reactive hyperplasias in lymphoid tissues such as lymph nodes and spleen usually feature numerous large, active germinal centers and increased myeloid cells.

Immunoblastic and anaplastic plasmacytomas can be difficult to distinguish from immunoblastic and anaplastic lymphomas of B- or T-cell lineages. These two plasmacytoma subtypes can also be difficult to distinguish from undifferentiated carcinoma, especially when they occur in the intestine. In most instances, an IHC panel consisting of antibodies to PAX5, CD45R/B220, CD3, IRF4, XBP1, and a keratin panel including pan-keratin AE1/AE3 will aid in differentiating plasmacytomas from lymphomas and carcinomas.

Conventional mice and mouse models: Plasma cell tumors are rare spontaneous tumors in SJL mice [139]. A variety of GEM and MuL virus and pristane-induced models have been developed [139–143] (see Table 8.3).

Follicular Lymphoma

Definition: Follicular lymphoma (FL) is a neoplasm of follicle center B cells that typically consists of transformed

Vet-ebooks.com

centrocytes (small-cleaved cells) and centroblasts (noncleaved cells). In the mouse, unlike in humans, FL does not generally have a follicular pattern, but it has an entirely diffuse pattern in the tissue.

Tissues involved: FL involves the lymph nodes, spleen, and gastrointestinal Peyer's patches. The bone marrow and CNS are occasionally involved. However, FL can occur at any extranodal site.

Morphology: Most cases of FL in the mouse have a diffuse rather than a follicular pattern, with effacement of the lymph node architecture. Morphologically, mouse FL (Figure 8.7) is more like the nodal diffuse variant of FL in humans. In neoplastic centrocyte (cleaved) cells, the nucleus is twice the size of a small lymphocyte and is elongated, irregular, twisted, or angular, with inconspicuous nucleoli. The chromatin is dispersed and paler than that of a small lymphocyte, imparting a grayish-blue appearance to the nucleus. The cytoplasm is scant and not apparent in H&E-stained tissue. The nucleus of a centroblast (noncleaved) cell is round to oval in shape and similar to or larger than a histiocyte in size; it has vesicular open chromatin and one or more nucleoli juxtaposed to the nuclear membrane. A narrow rim of cytoplasm surrounds the nucleus. In some instances, the neoplastic centrocytes may be more pleomorphic and the neoplastic centroblasts may vary in size and shape, have increased hyperchromatin, and be binucleated or lobulated. Mitosis is low, and tingible body macrophages and a starry sky appearance are absent or infrequent. Varying numbers of small T cells, histiocytes, and dendritic cells are often scattered among the neoplastic cells and, in some instances, plasma cell differentiation may be evident. Follicular dendritic cells are often not detected in the mouse because of the diffuse nature of FL in mice. The proportions of centrocytes and centroblasts vary, and the number of centroblasts per high power fields (hpf) is used in human cases to differentiate FL into low-grade and high-grade based on the predicted biological behavior. No studies have been conducted in mice to determine whether there is a biological behavior difference based on the level of centroblasts in FL. Consequently, in mice, it may be best to classify FL as either FL, centrocyte-dominant, or FL, centroblast-dominant. In both cases, the lymphoma would have the immunophenotype characteristic of an FL and would be considered FL, centrocyte dominant, if the centroblasts and immunoblasts constitute less than 50% of the population and FL, centroblast-dominant, if the centroblasts and immunoblasts constitute more than 50% of the population. In the spleen, FL generally does not involve the red pulp, and in the bone marrow, the aggregates of FL are located adjacent to bone trabeculae.

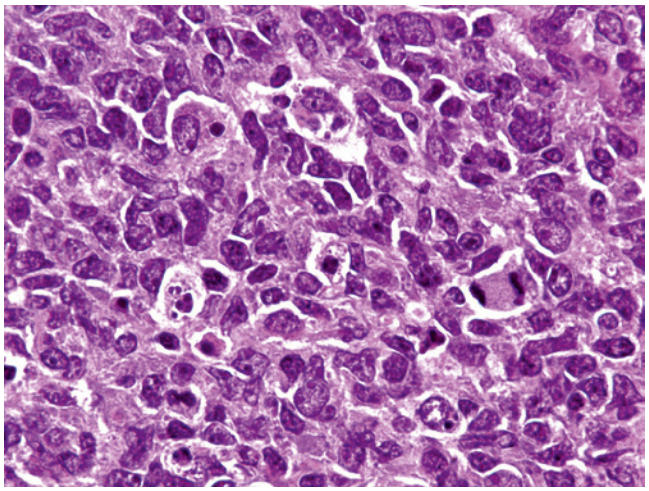


Figure 8.7 **Follicular lymphoma, H&E**. Lymph node with an abundance of centrocytes (cleaved) cells and a scattering of centroblasts (noncleaved) cells. The centrocytes have irregular twisted nuclei, whereas the centroblasts have round to oval nuclei that approximate the size of the tingle body macrophages.

Differential diagnosis: The differential diagnosis includes reactive hyperplasia, lymphoblastic lymphoma, DLBCL and its variants, and T-cell lymphoma.

- *Reactive hyperplasia*: In the mouse, germinal center polarization of centrocytes and centroblasts is often not readily apparent. Therefore, in the few instances in which FL in the mouse has a follicular pattern, it can be difficult to differentiate reactive germinal centers from neoplastic germinal centers based on whether there is distinct polarization. Human FL is BCL2 positive, whereas reactive hyperplasia is BLC2 negative, enabling differentiation of the two. However, mouse FL does not express BCL2. Consequently, BCL2 expression cannot be used to differentiate reactive hyperplasia from FL in the mouse. Because mouse mature B cells predominantly express the kappa immunoglobulin light chain, light chain restriction cannot be used to differentiate hyperplasia from lymphoma. Therefore, differentiation between these two entities in the mouse is dependent solely on morphologic criteria. Frequent mitosis and numerous tingible body macrophages are characteristic of germinal center hyperplasia, whereas mitoses are few or absent in FL. FL nodules lack a mantle zone, whereas a mantle zone is maintained in reactive follicular hyperplasia. Neoplastic centrocytes are present in interfollicular areas, but they are virtually never present in the interfollicular areas of reactive nodes. Therefore, expression of BCL6, a germinal center cell marker in cells in the interfollicular regions, is indicative of lymphoma. FL cells often extend into the pericapsular tissue of a lymph node, whereas tissue invasion is virtually absent with nodal reactive hyperplasia.
- *Lymphoblastic lymphoma*: In addition to having frequent mitosis and containing numerous tingible body macrophages, lymphoblastic lymphomas have a homogeneous population and an immunophenotype that differs from that of reactive hyperplasia or FL.
- *DLBCL*: Differentiating centroblast-dominant FL from DLBCL is more problematic, especially when only lymph nodes are involved. Splenic involvement can be helpful in differentiating DLBCL from FL. DLBCL generally involves the red pulp, whereas FL generally involves only the white

Vet-ebooks.com

pulp, with marked demarcation between the neoplastic white pulp and the uninvolved red pulp. Until differentiating molecular markers are identified for FL and DLBCL, it might not be possible to make this differentiation. However, in many instances, IHC will be helpful: A DLBCL that is not of follicular cell origin will label with antibody to IRF4, whereas a DLCBL composed of transformed FL cells will label with antibodies to BCL6 and PNA.

- *T-cell lymphoma*: IHC will aid in differentiating between FL and T-cell lymphomas with cleaved-appearing cells or those with centroblastic cells. The T-cell lymphoma cells will label with antibody to CD3, and the FL cells will label with antibodies to the B-cell markers CD45R/B220 or PAX5.

Immunophenotype: FL B cells express the pan-B antigens CD19, CD22, CD45R/B220, CD79A, and PAX5; the germinal center cell markers BCL6 (Figure 8.8) and PNA and surface immunoglobulin heavy chain, more commonly, IgM. IRF4 (MUM1) is not usually expressed in FL. Unlike human follicular cells, CD10 is not expressed by mouse follicular cells [165].

Conventional mice and mouse models: FL occurs spontaneously in a wide range of outbred and inbred mouse strains, as well as in many GEMs [25, 26, 104, 110, 118, 141, 144–149, 166] (see Table 8.3).

Diffuse Large B-Cell Lymphoma (DLBCL)

Definition: DLBCL is a proliferation of medium- to large-sized neoplastic B cells with nuclei that are the same size as or larger than a tissue macrophage, with a diffuse growth pattern. Morphologically, mouse DLBCLs have been classified as one of four variants: centroblastic, immunoblastic, anaplastic, and histiocytic associated [1]. Based on molecular and IHC studies, human DLBCLs have been divided into two subtypes: the germinal center B-cell (GC) subtype and the nongerminal center (NGC) subtype. Whether mouse DLBCLs can be divided into these two subtypes remains to be determined.

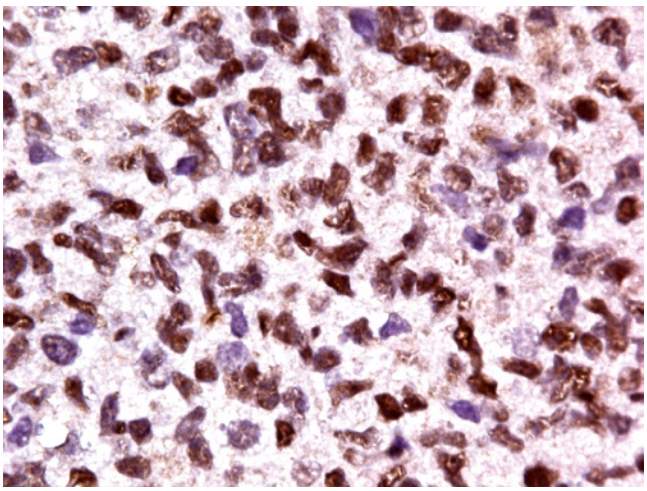


Figure 8.8 Follicular lymphoma, IHC. The neoplastic cells in Figure 8.7 express nuclear BCL6 a marker for germinal center cells.

Tissues involved: DLBCL involves the lymph nodes, spleen, and liver, but any extranodal tissue may be involved. The architecture of the spleen may be completely effaced, or the red pulp may be primarily involved. In other extranodal tissues, DLBCL may manifest as large masses or it may exhibit interstitial infiltrative growth, separating the normal structures of the tissue. Although the mediastinum is listed in the 2002 Bethesda classification as a primary site of DLBCL in the mouse, there are no reports of occurrence at this site in the literature [1].

Morphology: DLBCL typically replaces the normal architecture of the lymph node and extranodal tissue with a diffuse growth pattern. In high-grade, aggressive tumors, there may be a starry sky appearance with macrophages that contain phagocytic cellular debris (tingible bodies). The DLBCL cells are medium to large-sized lymphocytes with morphologic features of centroblasts, immunoblasts, or anaplastic cells. Variable numbers of small CD4+ T cells, macrophages, and, occasionally, plasma cells may be present in a DLBCL.

- *DLBCL centroblastic variant*: The cells of this variant are medium- to large-sized cells with round-to-oval vesicular nuclei that have multiple membrane-bound small nucleoli and a small rim of bluish amphophilic cytoplasm. This variant may be monomorphic or polymorphic, consisting of centroblasts, immunoblasts, and macrophages. Cells with multilobated vesicular nuclei are another form of large cells described in the centroblastic variant. It can be difficult to distinguish whether a cell is a centroblast, an immunoblast, or a cell having an indeterminate appearance between the two. Therefore, blasts (centroblasts, immunoblasts, and indeterminate cells) should account for 70–75% of the neoplastic cells, and there should be fewer immunoblasts than centroblasts. In some instances, the large lymphoma cells have angulated or cleaved nuclei requiring differentiation from FL.
- *DLBCL immunoblastic variant*: The cells of this variant are large, with round or oval nuclei, a single prominent amphophilic nucleolus, and abundant amphophilic cytoplasm. Although centroblasts may be present, immunoblasts should be the dominant cell.
- *DLBCL anaplastic variant*: This variant is composed of cells with bizarre pleomorphic (horseshoe, kidney, or embryonal shaped) nuclei, often with multinucleated forms and abundant cytoplasm (Figure 8.9).
- *DLBCL histiocytic-associated (HA) variant*: This variant is identified in the Bethesda proposal, but there are only a few reports of it, mostly from one investigator group. DLBCL-HA is composed of a mixture of neoplastic B cells and nonneoplastic histiocytes. Histiocytes (macrophages) make up 50–70% of the tumor, and neoplastic B cells admixed with a small number of T cells make up the remainder. In some instances, the histiocytes may obscure the neoplastic B cells. The histiocytes, which are large with abundant cytoplasm, are admixed with B cells with centroblastic and immunoblastic features. The growth pattern is mainly nodular rather than diffuse. DLBCL-HA commonly involves the spleen, lymph nodes, and liver. This variant is

Vet-ebooks.com

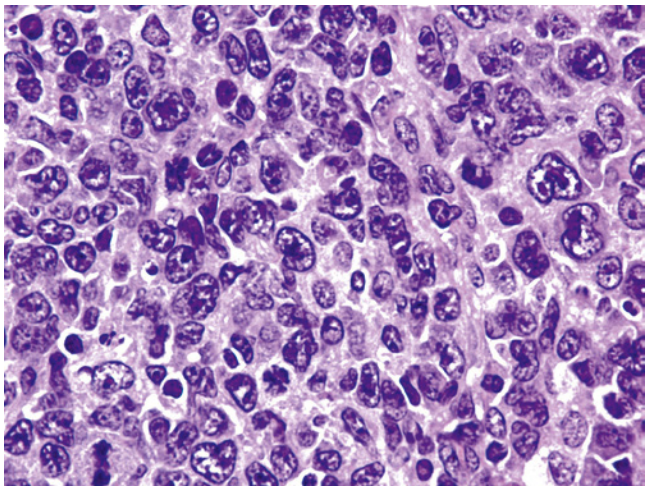


Figure 8.9 DLBCL, anaplastic variant, H&E. This lymphoma variant has hallmark cells with bizarre pleomorphic horseshoe-, kidney-, or embryonal-shaped nuclei that have a paranuclear eosinophilic region and abundant cytoplasm. Binucleated Reed–Sternberg-like cells are scattered cells among the neoplastic population.

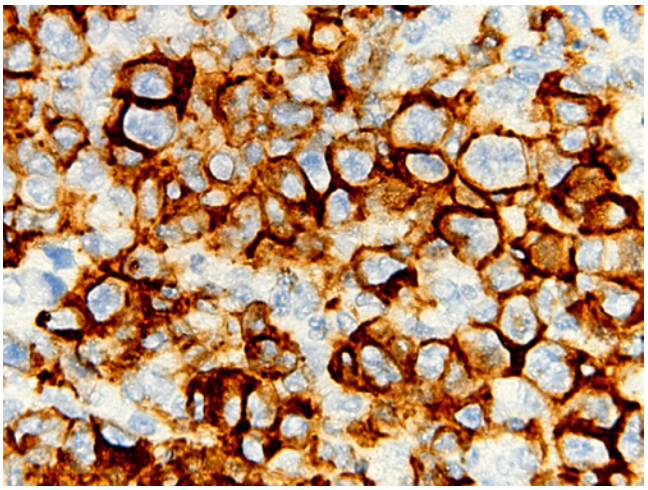


Figure 8.10 DLBCL, anaplastic variant, IHC. The neoplastic cells in Figure 8.9 express CD45R/B220 on their membrane.

rare in most mouse strains, but it is more common in the AKXD28/TyJ and AKXD1/TyJ RI mouse strains and, albeit less frequently, in NFS/N^{V+} mice [1, 118, 144, 150, 159].

Immunophenotype: DLBCL cells have one or more of the following antigen expression patterns, as detected by flow cytometry or IHC: CD22+, CD45R/B220+ (Figure 8.10), CD79A+, PAX5+, BCL6+/−, and IRF4+/−. Anaplastic cells may be CD30+. The tumor cells are also positive for surface and/or cytoplasmic heavy chain immunoglobulin. Cytoplasmic immunoglobulin is often present when a tumor exhibits plasma cell differentiation. The cells are more commonly positive for the IgM heavy chain than for IgG or IgA.

In DLBCL-HA, the histiocytes are immunoreactive for F4/80, MAC2, and lysozyme C, whereas the neoplastic B cells are PAX5+.

Differential diagnosis: In some instances, one or more of the DLBC variants can mimic a carcinoma or melanoma, but these neoplasms can be differentiated by IHC because carcinomas and melanomas are negative for CD45 and express their respective antigen markers, such as cytokeratin and S100B protein.

- *DLBCL centroblastic variant*: Although BCL6 may be expressed in both DLBCL and FL, DLBCL centroblasts are often positive for IRF4, whereas FL centroblasts do not commonly express IRF4.
- *DLBCL immunoblastic variant*: Immunoblasts are the dominant cells in the DLBCL immunoblastic variant, whereas immunoblasts are a minor component of FL. The DLBCL immunoblastic variant and immunoblastic plasmacytoma have similar morphology, but DLBCL immunoblasts do not express CD138 or CD43, both of which are commonly expressed in immunoblastic plasmacytoma.
- *DLBCL anaplastic variant*: The DLBCL anaplastic variant can be readily differentiated from anaplastic plasmacytoma and T-cell anaplastic lymphoma by IHC. DLBCL anaplastic lymphoma cells do not express CD138, CD43, or XBP1 that are commonly expressed in anaplastic plasmacytoma, nor do they express CD3, which is commonly expressed in T-cell anaplastic lymphoma.
- *DLBCL-HA variant*: The lack of a definite marker or molecular signature for transformed histiocytes that can differentiate neoplastic histiocytes from nonneoplastic histiocyte proliferation underlies the difficulty in differentiating DLBCL-HA from histiocytic sarcoma or a composite neoplasm consisting of an HS and a B-cell neoplasm in the same tissue. Lymphocytes are not a significant component of an HS, and when present, they lack neoplastic features. The presence of a significant quantity of neoplastic lymphocytes in a tumor that expresses macrophage markers suggests that the tumor is a DLBCL-HA or an HS/lymphoma composite tumor. At present, the only definitive means of differentiating DLBCL-HA from a composite HS/lymphoma is to examine multiple tissues histologically to determine whether pure populations of HS and lymphoma cells segregate out in one or more tissues. If some tissues have only histiocytes and other tissues have only lymphoma, this suggests that the neoplastic proliferation is a collision of two independent neoplasms.

Conventional mice and mouse models: DLBCL occurs in several conventional mouse strains and in various GEMs [26, 110, 118, 144, 149, 151–157, 166, 167]. The DLBCL-HA variant is rare is most mouse strains, but it is more common in the AKXD RI mouse strains and, albeit less frequently, in NFS/N^{V+} mice [1, 39, 144] (see Table 8.3).

Diffuse High-Grade Blastic B-Cell Lymphoma

Definition: Diffuse high-grade blastic lymphoma (DHGBL) is a highly aggressive neoplasm with morphologic features of lymphoblasts that is characterized by a uniform population of medium-sized B cells that are sIg+ and are associated with

Vet-ebooks.com

a high mitotic rate, apoptosis, and, occasionally, a leukemic phase. Lymphomas with these morphologic features are common in transgenic Tg(IghMyc)22Bri, transgene insertion 22, Ralph L. Brinster synonym: Emu-c-myc mouse models. In these models, the *Myc* gene is inserted into the IgH locus with a high incidence of B-cell lymphoma developing. The lymphomas that develop are a heterogeneous group and the lymphoma may be of an immature, transitional, or a mature B-cell. This lymphoma heterogeneity in Tg(IghMyc)22Bri transgenic mice with various C57BL/6J hybrid backgrounds is related to the mouse's age [154]. The Tg(IghMyc)22Bri lymphomas also vary in their BCL6 expression, and they may or may not have mutated IgV regions. Previously, this heterogeneous lymphoma group was designated as lymphoblastic-like lymphoma, Burkitt and Burkitt-like lymphoma, and DLBCL lymphoblastic-like [1, 118, 168]. Recently, it has been proposed that this sIg+ lymphoblastic-like lymphoma be classified as "diffuse high-grade blastic B-cell lymphoma (DHGBL)." Until recently, it was contended that mouse DHGBL had no human counterpart [150]. The 2017 WHO monograph includes a lymphoma that has been identified as high-grade B-cell lymphoma (HGBL), and there are two categories of HGBL: HGBL with *MYC* and HGBL, not otherwise specified (NOS). These two categories of human HGBL comprise lymphomas with overlapping lymphoblastic, DLBCL centroblastic, and Burkitt-like features. The WHO HGBL group has many of the features common to the lymphomas in the mouse DHGBL classification.

Tissues involved: DHGBL involves the lymph nodes, spleen, liver, and lungs. The neoplastic cells efface the normal lymph node architecture and often infiltrate the pericapsular tissue. The splenic red pulp and white pulp are diffusely infiltrated. Perivascular and peribronchiolar infiltrates of the lung and periportal liver infiltrates are common. In the leukemic phase, the bone marrow is involved.

Morphology: Many DHGBLs have the morphology of L3 lymphoblasts, consisting of uniform medium-sized cells with open nuclear chromatin, distinct nucleoli, and scant cytoplasm. There is a high mitotic rate and abundant apoptosis, and macrophages are present with phagocytic cytoplasmic debris (tingible bodies) that imparts a starry sky appearance (Figure 8.11).

Immunophenotype: DHGBL has a mature postgerminal center phenotype. The cells express CD19, CD45R/B220, CD79A, PAX5, sIgM, and surface kappa light chain (Figure 8.12), and they are BCL6+/−, IRF4+/−.

Differential diagnosis: DHGBLs can be difficult to differentiate from lymphoblastic lymphoma and centroblastic DLBCL based on morphologic features. However, B-lymphoblastic lymphomas do not exhibit surface immunoglobulins, and T-lymphoblastic lymphomas are CD3+ and generally TDT+. Centroblastic DLBCLs that are not of FL origin generally express IRF4 (interferon regulatory factor 4), lack cellular uniformity and have two or more nucleoli.

Conventional mice and mouse models: Lymphomas with the morphologic features of DHGBL occur in NFS/N^{V+}, CFW inbred and AKXD RI strains and at variable frequencies in many GEMs, especially those overexpressing *Myc* [141, 144, 150].

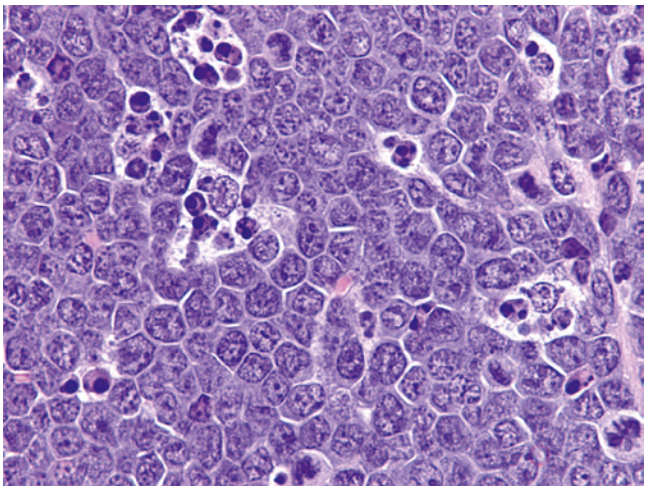


Figure 8.11 Diffuse high-grade blastic B-cell lymphoma, H&E. The lymphoma has a starry sky appearance and a uniform population of medium-sized cells with lymphoblast features of finely stippled chromatin and either inconspicuous or one or more small nucleoli and scant cytoplasm.

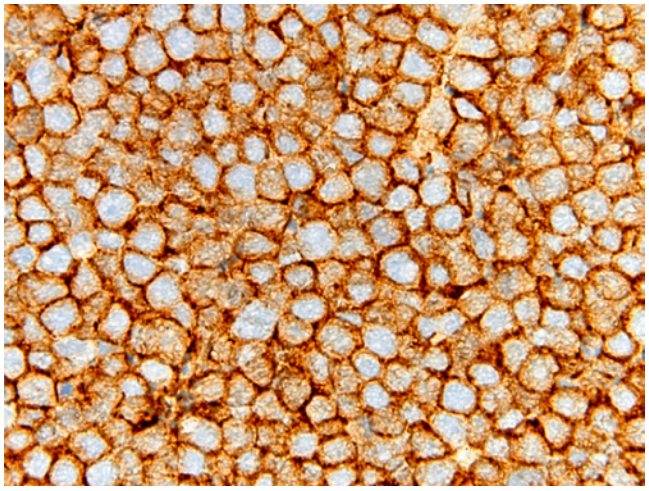


Figure 8.12 Diffuse high-grade blastic B-cell lymphoma, IHC. The neoplastic cells in Figure 8.11 label with kappa light chain consistent with the lymphoma cells not being precursor lymphoblasts.

Natural Killer B-Like (NKB) Cell Lymphoma

Definition and comment: Natural killer B-cell lymphoma is a neoplasm of cells that express both NK cell and B cell immunophenotypes. Recently, lymphocytes expressing the B-cell markers CD19, PAX5, and IgM and the NK cell markers NK1.1 and NKP46 were identified as a B-lymphocyte subpopulation in the spleen and lymph nodes of mice on the C57BL/6 background [70]. Although the cells lacked cytoplasmic cytotoxic granules when examined by electron microscopy, they were classified as NK-like B cells based on their immunophenotype. It is not apparent whether the NK-like B cells observed in this study were activated. Others have shown that nonactivated mouse NK cells, unlike human NK cells, have very few cytoplasmic granules and that activation is required for the cells to

Vet-ebooks.com

develop granular morphology [169]. Whether the lymphocytes called NK-like B cells and the NKB-like cell lymphoma cells are related and whether NK-like B cells are the cells of origin for NKB-like cell lymphoma remains to be determined.

Tissues involved: NKB-cell lymphoma primarily involves the spleen, lymph nodes, and liver, but the Peyer's patches are also frequently involved.

Morphology: NKB-like cell lymphoma has a diffuse growth pattern and consists of large cells with abundant pale cytoplasm and round and indented nuclei with two to four prominent nucleoli. Mitosis is mild to moderate.

Immunophenotype: NKB-like cell lymphoma cells express the B-cell markers CD5, CD45R/B220, CD79A, and IgM and the NK cell markers NK1.1, CD16, and the cytotoxic molecule lysozyme. The lymphoma also expresses high levels of the mRNAs for IL4, IFNG, and PRF1 (perforin-1). NKB-like cell lymphomas do not express the T-cell markers CD3, CD4, or CD8. The tumors have IgH and IgK gene rearrangements, confirming their clonal nature.

Differential diagnosis: The expression of NK cell markers by NKB-like cell lymphomas necessitates their differentiation from NK lymphomas and NKT lymphomas. Morphologically, they may be confused with B- or T-cell lymphoblastic lymphoma.

NKB-like cell lymphomas express B-cell markers, whereas NK cell lymphomas and NKT lymphomas generally do not. However, there are subsets of human and mouse NK cells and NKT cells, and their respective lymphomas that express the B-cell markers CD19, CD45R/B220, and CD79A, which can be a confounding factor in diagnosis [170–175]. Also, NK cell and NKT lymphomas generally express cytoplasmic CD3, whereas the NKB-like cell lymphomas do not express CD3. Therefore, it is recommended that CD3 and the B-cell marker PAX5 be used to differentiate NKB-like cell lymphomas from NK cell lymphomas or NKT lymphomas.

Although NKB-like cell lymphomas can share morphologic features with B-cell and T-cell lymphoblastic lymphomas (LBLs), they can be readily differentiated with flow cytometry or IHC. T-cell LBLs express CD3 and TDT, whereas NKB-like cell lymphomas express neither of these markers. NKB-like cell lymphomas express the NK cell markers NK1.1, lysozyme C, and perforin (PRF1), whereas B-cell LBLs express none of these antigen markers.

Conventional mice and mouse models: In 1999, lymphomas with a morphology and immunophenotype consistent with mature B cell and NK cell features were reported to occur in >90% of thymectomized SL/Kh×AKR/Ms F1 (SLAKF1) mice [158]. A lymphoma with similar features was described in a chimeric HLA-DR4-H2-E homozygous transgenic mouse [159] (see Table 8.3).

T-Cell Neoplasia

T-Cell Lymphoblastic Lymphoma/Leukemia (T-LBL)

Definition: T-cell lymphoblastic lymphoma, like B-cell LBL, is a neoplasm of hematopoietic stem cells, but it is characterized by an immature T-cell rather than a B-cell phenotype. Lymphoblasts can have variable morphology, and the histopathology of T-lymphoblastic lymphoma and T-lymphoblastic leukemia are indistinguishable, with the distinction being based on the distribution of tissue involvement. In the mouse, T-cell lymphoblastic lymphoma is more common than primary T-cell lymphoblastic leukemia. Lymphoma is diagnosed when the lymphoblasts primarily involve extramedullary tissues and account for less than 25% of the nucleated cells in the blood or bone marrow. The WHO states that when 25% or more of the cells in the blood and bone marrow are lymphoblasts, the appropriate term is leukemia. The MMHCC Bethesda proposal does not specify a percentage of blasts for diagnosing lymphoid leukemias. When there is a mass lesion(s) and lymphoblasts in the bone marrow, the distinction between lymphoma and leukemia is arbitrary. When a leukemia is involved, the bone marrow is almost always hypercellular, with normal bone marrow elements being replaced by a diffuse infiltrate of immature cells. With either lymphoma or leukemia, there can be significant involvement of organs, including the liver, the spleen, single or multiple lymph nodes, and the CNS.

Morphology: T-cell lymphoblastic lymphomas/leukemias are composed of medium-sized cells with round-to-ovoid nuclei and scant cytoplasm. The nuclei have fine or dispersed (salt and pepper) chromatin and variable (one to three) or inconspicuous nucleoli. Single central nucleoli are more typical. Mitosis is abundant, as are tingible body macrophages, imparting a starry sky appearance. Approximately, 30% of T-cell lymphoblastic lymphomas develop a leukemic phase.

Differential diagnosis: T-cell lymphoblasts tend to be more heterogeneous than B-cell lymphoblasts; however, with regard to size and nuclear morphology, B-cell and T-cell lymphoblastic lymphomas and leukemia are morphologically indistinguishable, and immunophenotyping is required to distinguish the two lineages. A large thoracic mass should not be used as the sole criterion for diagnosing a lymphoma as a T-cell lymphoblastic lymphoma. A B-lymphoblastic lymphoma arising in a mediastinal lymph node can invade the thymus, imparting the impression of the lymphoma being a thymic mass. Lymphoblastic lymphoma in the mouse must also be differentiated from a morphologically similar lymphoma/leukemia that has been referred to in this chapter as diffuse high-grade blastic B-cell lymphoma (DHGBL). It has also been referred to as diffuse large B-cell lymphoma of lymphoblastic subtype (DLBCL-LL) [118]. DHGBLs express mature B-cell antigens, whereas T-LBLs express CD3 and TDT.

Immunophenotype: The antigens expressed in lymphoblastic lymphoma reflect the various stages of T-cell maturation in the mouse, and their detection is dependent upon whether flow cytometry or IHC is used to characterize the immunophenotype of the lymphoma. T-cell lymphoblastic lymphomas in some mouse lines are of the late common thymocyte CD4+ CD8+ double-positive phenotype, but this has been documented in only a few strains, and additional documentation in more mouse strains is warranted. It should be noted that cytoplasmic CD3 expression is generally considered the first definitive marker of T-cell commitment and that mouse hematopoietic cells, unlike human hematopoietic cells, do not

Vet-ebooks.com

express CD1A [6]. It is also not uncommon for T-cell lymphoblastic lymphomas to lose one or more of the three immature T-cell markers, CD2, CD5, and CD7. Of all the T-cell markers, the most reliable marker for establishing T-cell lineage is CD3.

Pro-T lymphoblastic lymphomas are of the CD4− CD8− double-negative phenotype and have the following immunophenotype depending on the stage of maturation [6]: By flow cytometry or IHC: CD44+, CD25−/+, CD117+, CD5+/−, CD43+, CD90+/−, TDT+, PLZF+ (promyelocytic leukemia zinc finger), cCD3+ and CD2+/−. By flow cytometry only: CD7+/−.

Pre-T lymphoblastic lymphomas are of the CD4− CD8− double-negative phenotype and have the following immunophenotype depending on the stage of maturation [6]: By flow cytometry or IHC: CD44−, CD25+/−, CD117+/−, CD5+/−, CD43+, CD90+, TDT+, PLZF+, cCD3 and CD2+/−. By flow cytometry only: CD7+/−.

Common T-cell lymphoblastic lymphomas have a CD4+ CD8+ phenotype and have the following immunophenotype [6]: By flow cytometry or IHC: CD25+/−, CD5+/−, CD43+, TDT+, PLZF−, CD2+/−, cCD3. By flow cytometry alone: CD7+/−.

Conventional mice and mouse models: T-cell lymphoblastic lymphoma is a common lymphoma in some outbred and inbred mouse strains [26, 145, 176, 177] and a variety of GEM, allotransplant and xenotransplant models [22, 148, 178–184] (see Table 8.4).

Mature T-Cell Neoplasms

Small T-Cell Lymphoma (STL)

Definition: Small T-cell lymphoma (STL) is a neoplasm composed of monomorphic small mature T cells with a diffuse growth pattern.

Tissues involved: The thymus is not involved, but the lymph nodes, spleen, and liver are frequently involved [1, 74].

Morphology: The STL cells are small, uniform, and noncohesive. The neoplastic cells have round nuclei with clumped chromatin, inconspicuous nucleoli, and basophilic cytoplasm. The cells resemble normal circulating small lymphocytes.

Both STL and one variant of peripheral T-cell lymphoma (PTCL) are composed of small cells, but the small cells of STL have round nuclei with inconspicuous nucleoli, whereas the nuclei of the PTCL small-cell variant are generally irregular in shape with small nucleoli.

Immunophenotype: STL has a mature T-cell immunophenotype. The cells are CD3+ CD4+ or CD8+ CD5+ and negative for nuclear TDT, and they lack cytotoxic granules.

Differential diagnosis: STL and SBL are morphologically similar, but they can be differentiated from one another by flow cytometry or IHC. STL expresses CD3, SBL expresses PAX5, and both lymphomas are negative for TDT expression.

Conventional mice and mouse models: STL is a rare tumor in mouse strains, which might account for why it has not been well characterized and why some investigators consider it to be a lymphoma unique to the mouse with no human counterpart [1, 104] (see Table 8.4).

Peripheral T-Cell Lymphoma, NOS

Definition: Peripheral T-cell lymphoma (PTCL), NOS, is a heterogeneous category of postthymic mature T-cell lymphomas. Based on morphologic features, PTCL can be subclassified as PTCL, small cell; PTCL, mixed cell; or PTCL, large (immunoblastic) cell. Although T-cell lymphomas with these features occur in mice, and they have not been well characterized. The growth pattern is diffuse, with effacement of the nodal architecture, and the splenic infiltrates may form single or multiple discrete nodules, or the red pulp and white pulp may be diffusely involved.

Tissues involved: PTCLs involve the lymph nodes, spleen, liver, kidneys, and lungs; bone marrow may also be involved.

Morphology: PTCL, small cell, either has a monomorphic population consisting predominantly of small- to medium-sized cells with irregular (cleaved) or round nuclei with small nucleoli or the tumor population may be polymorphous with a background of eosinophils, macrophages, B-cells, and plasma cells (Figures 8.13–8.16).

PTCL, mixed cell, has a monomorphic or polymorphic population consisting of medium- and large-sized cells with irregular nuclei, prominent nucleoli, and abundant mitotic figures. Multilobated cells may be present.

PTCL, large (immunoblastic) cell, has a monomorphic or polymorphic population consisting predominantly of pleomorphic large cells, with prominent nucleoli and abundant mitotic figures (Figures 8.17 and 8.18). Multilobated cells may be present.

Immunophenotype: PTCLs have a mature T-cell immunophenotype. They commonly express the pan–T-cell–associated antigens (CD2, CD3, CD5, and CD7), which are detectable by IHC and/or flow cytometry. However, individual lymphomas may lack one or more of these markers. The lymphomas are CD4+ or CD8+, with the former being more common. CD8+ cells may also express granzyme B and/or perforin.

Differential diagnosis: PTCL, NOS, must be differentiated from FL and DLBCL. Both of these lymphomas are B-cell lymphomas and express pan–B-cell antigens.

Conventional mice and mouse models: A few lymphomas with small cell PCTL, and large (immunoblastic) PCTL have been described in CWD mice, and it is not uncommon for mature T-cell lymphoma to occur in tumor suppressor knockout mice [177]. Four GEM models have been used to understand the pathophysiology of PTCL [185–189] (see Table 8.4).

Anaplastic Large Cell Lymphoma

Definition: Anaplastic large cell lymphoma (ALCL) is defined by its morphology of large, anaplastic, sometimes Hodgkin and Reed–Sternberg (RS)–like cells with CD30 expression. Most cases of human ALCL are of T-cell or null-cell origin, whereas only a minority of cases show expression of B-cell differentiation antigens. In the fourth edition of the WHO Classification of Tumors of Hematopoietic and Lymphoid Tissues, this group of tumors in humans is divided into ALK (anaplastic lymphoma kinase)-positive and ALK-negative

Vet-ebooks.com

Table 8.4 T-cell lymphoid neoplasms associated with conventional mice and mouse models.

Type	Conventional	References	GEMs	References	Other models	References
T-lymphoblastic	AKR Balb/c Crl:CD1(ICR), C57BL/6 CWD	[26, 104, 145, 176, 177]	*Arf*−/− *Atm*−/− *Trp53*−/− *Pten*−/− *Runx1*$^{lacZ/lacZ}$ chimeras Tg *E2A-HLF* fusion gene Tg *E2A-PBXl* fusion gene, Tg *BCR-ABL* fusion gene, Tg *LMO2*, Tg *NOTCH1* KI *K-rasG12D* mutant	[22, 148, 178–180]	Immunocompromised mice + XT C.B-17/Icr-*Prkdc*$^{scid/scid}$, NOD.Cg-*Prkdc*^{scid}/J NOD.Cg-*Prkdc*^{scid} *Il2rg*^{tm1Wjl}/SzJ Notch 1 mouse all0 cell lines; allotumor grafts	[181–184]
Small T-cell	Rare	[1, 104]	Not known		Not known	
Peripheral T-cell	CWD	[177]	C3H/He-Tg (*LCKpr-BCL2)*36Sjk/J Tg *ITK-SYK*^{CD4Cre} SJL.129 Il21r*tm1Wlj* (Il21r−/−) *Snf5*$^{inv/-}$Mx-Cre *Rc3h1*$^{san/Rc3h1}$+	[185–189]	Not known	
Anaplastic large cell	Not known		See text narrative		Not known	
Granular lymphocytes		[190]		[191–194]	p53−/− (B6.129S2-Trp53$^{tm1Tyj/J}$)	[160]
Cytotoxic-T	Rare, BALB/c. OlaHsd					
NK/T	Not reported		Not reported			
NKT-like	Not reported		Tg FVB/N *Il15*			
NK	Not reported		Tg *Hmg1-C*			
Cutaneous T-cell	CD1 ICR (Tac:Icr:Ha)	[195, 196]	Tg *Il-15* Tg C57BL/6R26-Stat3c$^{fl\text{-}STOP+}$	[197–199]	Immunocompromised mice + XT: nude (Foxn1$^{Nu/Nu}$), CB-17 SCID beige (CB-17/lcr. Cg-Prkdc ^{scid} Lyst bg/ Crl), Rag2−/−; Il2rg−/− SCID (Prkdc^{scid} Prkdc^{scid}) NSG (NOD.Cg-*Prkdcscid Il2rg*^{tm1Wjl}/SzJ)	[197, 199–202]

XT = xenotransplantation.

ALCLs. Presently, it is not apparent whether a similar tumor occurs in any standard mouse strain or stock.

Morphology: This human tumor has a broad spectrum of morphologies. The cytologic/morphologic patterns consist of large cells, small cells, or a lymphohistiocytic mixture. All of the ALCL morphologic patterns have hallmark cells that, histologically, are large pleomorphic cells with eccentric kidney-shaped or horseshoe-shaped nuclei that have a paranuclear eosinophilic region and abundant amphophilic or eosinophilic cytoplasm.

Immunophenotype: There is currently no evidence as to whether any mouse tumors with anaplastic features express ALK. Therefore, the immunophenotype described here is based on the WHO classification of ALK-negative ALCL. All ALCLs have diffuse, strong expression of CD30, and they often express CD3. CD30 is expressed on the membrane and in the Golgi region. CD30+ cells often cluster around blood vessels. Most ALCLs are positive for epithelial membrane antigen (EMA; mucin 1, MUC1), and tumor cells are variably positive for CD4, CD5, and CD8. Most tumors exhibit positivity for TIA1 (cytotoxic granule-associated RNA binding protein 1), GZMB (granzyme B), and PRF1 (perforin 1).

Differential diagnosis: Morphologically, ALCL can mimic anaplastic DLBCL, immunoblastic PTCL, and a metastatic carcinoma. Whether a nongenetically engineered mouse ALCL would express ALK is not known. Therefore, based on

Vet-ebooks.com

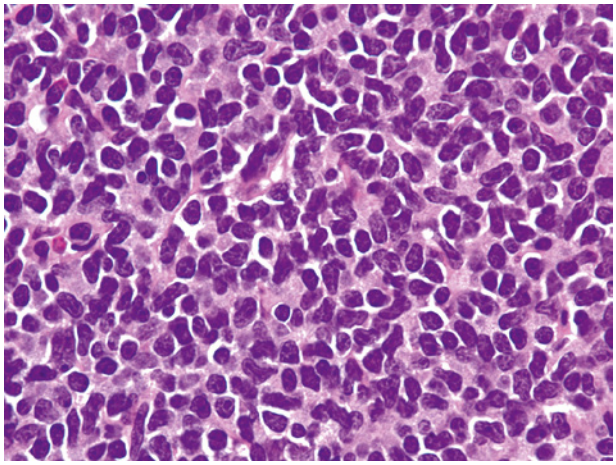


Figure 8.13 **Peripheral T-cell lymphoma (PTCL), small cell, H&E**. A nodal lymphoma with a monomorphic population consisting of small- to medium-sized cells with irregular (cleaved) or round nuclei.

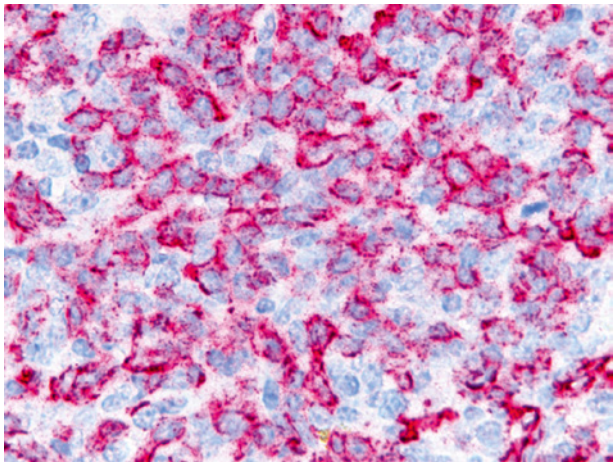


Figure 8.14 **PTCL, small cell, IHC**. The neoplastic cells in Figure 8.13 express CD3 on their membrane, but do not express cytotoxic molecules consistent with a small cell noncytotoxic PTCL.

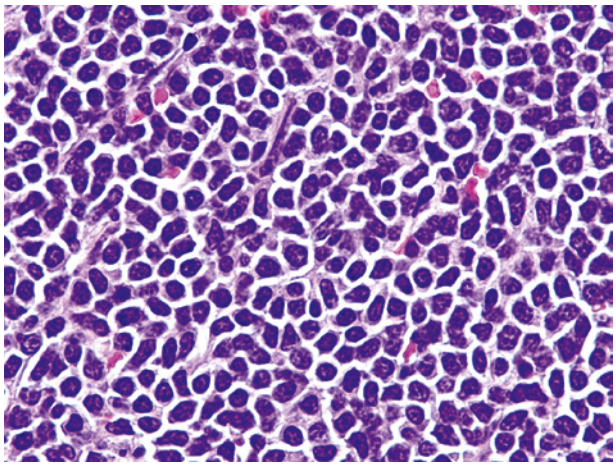


Figure 8.15 **PTCL, small cell, H&E**. A splenic lymphoma with a monomorphic population similar to the lymphoma in Figure 8.13, and the neoplastic cells also express CD3 and CD8 (not shown), consistent with a small cell PTCL.

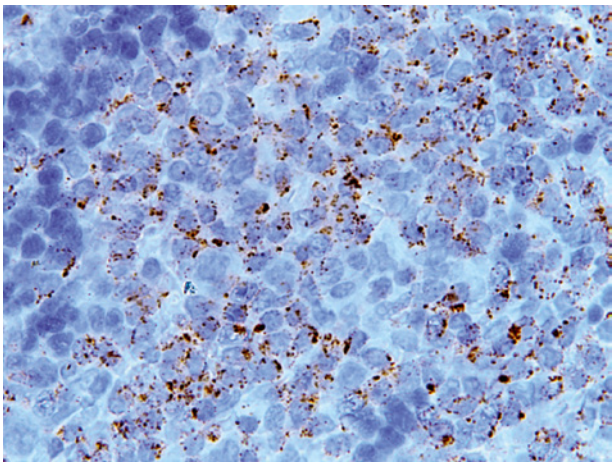


Figure 8.16 **PTCL, small cell, IHC**. The neoplastic cells in Figure 8.15 express the cytotoxic molecule perforin in their cytoplasm consistent with a cytotoxic PTCL.

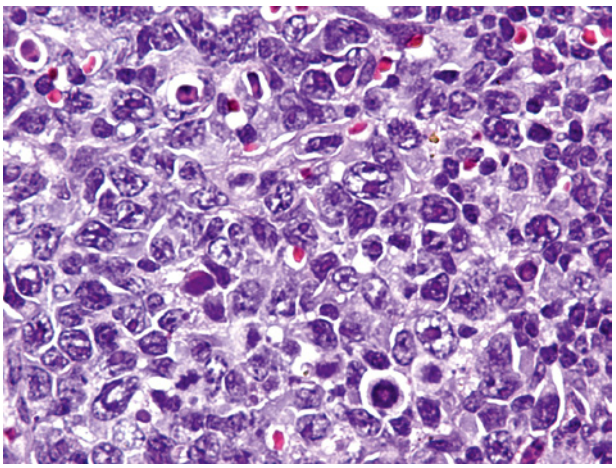


Figure 8.17 **PTCL, large cell, H&E**. A splenic lymphoma with a monomorphic population with immunoblast features consisting of medium to large pleomorphic cells with prominent central nucleoli.

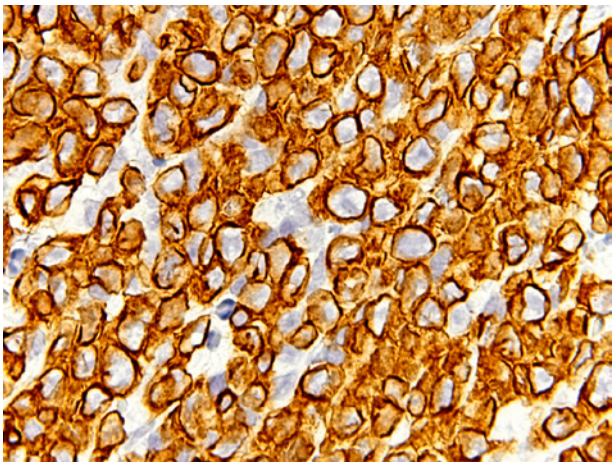


Figure 8.18 **PTCL, large cells, IHC**. The neoplastic cells in Figure 8.17 express membrane CD3 consistent with a large cell PTCL.

Vet-ebooks.com

the criteria for ALK-negative ALCL in humans, the differential diagnoses of a mouse tumor that has anaplastic features with hallmark cells include ALCL, anaplastic DLBCL, and immunoblastic PTCL. Anaplastic DLBCLs generally express more than one of the B-cell markers CD19, CD45R/B220, CD79A, and PAX5, and only rarely do they express CD30, whereas ALCLs are diffusely CD30+ CD3+/−, and they do not express any B-cell markers. Although some immunoblastic PTCLs may express CD30, the expression is patchy, whereas ALCL CD30 expression is diffuse and strong. Unlike metastatic carcinomas, ALCLs do not express keratins.

Conventional mice and mouse models: As previously stated, there is no evidence that CD30+ anaplastic large-cell lymphomas occur spontaneously in conventional mice, but multiple GEM models have been reported in the literature. Eleven ALK fusion partners have been described in human ALCL tumors, and the choice of promoter and the level of fusion protein expression have been problematic for determining the oncogene outcome. Many of the ALK transgenic mouse models develop B-cell lymphomas and plasma cell tumors [203–205]. Consequently, it has been suggested that the nucleophosmin–ALK (NPM–ALK) fusion models (Tg(Vav1-NPM1/ALK)1Sudt, Tg(Cd4-NPM/ALK)N1Ingh, Tg(tetO-NPM1/ALK,-luc)2Gde, Tg(tetO-TPM3/ALK,-luc)2Gde) preferentially transform the B lineage in mice, in contrast to the T-lineage tumors more typical of human ALK+ ALCLs. However, a minority of human ALK+ ALCLs are of B-cell lineage. CD30+ T-cell lymphoma development does occur in some NPM–ALK transgenic mouse models, but most of these lymphomas have an immunophenotype and/or morphology of T-cell lymphoblastic lymphoma [206–209]. Although ALCL is considered a mature T-cell lymphoma, a recent mouse ALCL model with hallmark cells suggests that ALCL may initially arise in the thymus [210].

Granular Lymphocyte Lymphoma/Leukemia

Definition and comment: Granular lymphocyte lymphoma/leukemia is a group of lymphomas associated with neoplastic proliferations of NK cells, NK/T cells, or cytotoxic T cells. All three cell types have similar cytotoxic granules. Unlike normal or neoplastic NK cells, which do not express surface CD3, normal NK/T cells and cytotoxic T cells commonly do express surface CD3, but it is not uncommon for neoplastic T cells to lose expression of surface T-cell antigens. Consequently, when an NK/T-cell lymphoma or cytotoxic T-cell lymphoma does not express CD3, it is extremely difficult to differentiate it from an NK cell lymphoma because NK/T-cell lymphomas may also express NK cell markers and cytotoxic T-cell lymphomas may coexist with an NK cell lymphoma. Although cytotoxic T-cell lymphoma does occur in mice, it is rare [190]. However, NK/T-cell and NK cell lymphomas have not been reported to occur as spontaneous neoplasms in conventional mouse strains. Therefore, the following is based on what is known from lymphomagenesis studies in GEMs. In most GEMs, the lymphoma/leukemia is induced by the overexpression of IL15 by various means [191–193, 211, 212].

There is also a report of NK/T-cell lymphoma arising in B6.129S2-*Trp53*^{tm1Tyj}/J (*Trp53*-null) mice [160]. It is now recognized that NK/T cells in the mouse can be divided into two subtypes, CD1D-dependent and CD1D-independent NK/T cells, which are known, respectively, as invariant NK/T cells and NKT-like cells [213, 214]. Invariant NK/T cells in the mouse predominantly express CD4, whereas the mouse NKT-like cells predominantly express CD8. Therefore, the lymphomas/leukemias in the FVB/N IL15 transgenic mouse (Tg(H2-D-Il15)3304Clgr) studies are probably composed of CD1D-independent CD8+ NKT-like cells. However, based on the expression of PLZF and/or CD45/B220, the NK/T-cell lymphomas reported in theses *Trp53*-null mice and in the HMG1-C/T transgenic mice (strain not reported) are probably of the CD1D-dependent NK/T subtype [160, 194]. CD45R/B220, a B-cell marker, is known to be expressed in subsets of NK cells [6].

Tissues involved: Granular lymphocyte lymphomas involve the lymph nodes, spleen, liver, lungs, kidneys, bone marrow, and peripheral blood.

Morphology: Cytotoxic T-cell, NK/T-cell, and NK cell lymphomas consist of diffuse infiltrates that efface the normal architecture. The neoplastic cells have small, medium, or large-sized nuclei with coarse chromatin and moderate cytoplasm. The architecture of the spleen and liver is often effaced with nodular or diffuse neoplastic cellular infiltrates.

Immunophenotype: The NK cell and NK/T-cell lymphomas in these studies were positive for the NK cell antigens: NK1.1 (strain-dependent), natural cytotoxicity triggering receptor 1 (NCR 1, NKp46) and, variably, CD49B. Some of these lymphomas express CD45R/B220. CD1D-independent NKT-like lymphomas/leukemias were positive for surface CD3, CD5, CD8 CD43, CD44, TCRB, and granzyme B but negative for CD4. The CD1D-dependent iNKT lymphomas/leukemias were CD3+, CD44+, CD45R/B220+, PD-1+, and PLZF+. They were predominantly CD4− CD8− double negative, CD4 weak, or CD8 weak. NK cells express cytoplasmic CD3 epsilon, but not surface CD3 or CD5.

Cytotoxic T-cell lymphomas are positive for surface and cytoplasmic CD3, CD5, CD8, CD43, and cytotoxic molecules but negative for NK1.1 and CD49B. It should be noted that NK1.1 is not expressed in all mouse strains and that subsets of NK and NK/T cells have been reported to be positive for CD45R/B220 [5].

Differential diagnosis: Cytotoxic T-cell lymphomas can morphologically mimic mature B-cell lymphomas, noncytotoxic CD8+ PTCLs, NK/T-cell lymphomas, and NK cell lymphomas. Unlike mature B-cell lymphomas, cytotoxic T-cell lymphomas express the T-cell antigens CD3, CD4, or CD8 and cytotoxic molecules. Unlike NK/T-cell and NK cell lymphomas, cytotoxic T-cell lymphoma cells do not express the NK antigen markers NK1.1, NKP46, or CD49B (DX5). Unlike NK cell lymphoma, NK/T-cell lymphomas express CD5 and surface CD3; the iNKT lymphomas express cytoplasmic PLZF; and the NKT-like lymphomas express surface CD8 [160, 191, 192].

Conventional mice and mouse models: Granular lymphocyte lymphomas are rare in conventional mice, but GEM models for NK/T lymphomas have been reported (see Table 8.4).

Vet-ebooks.com

Cutaneous T-Cell Lymphoma (CTCL)

Definition: Cutaneous T-cell lymphoma (CTCL) is a general term for mature T-cell lymphomas that involve the skin. CTCL may be a primary skin lymphoma or a secondary skin lymphoma arising from a disseminated multisystemic PTCL. There are several subtypes of primary CTCL in humans, including mycosis fungoides (MF), MF variants, Sezary syndrome, and CD8+ cytotoxic T-cell lymphoma. CTCL is very rare in the mouse, and characterization of the few known mouse cases has been limited.

Tissues involved: As a rule, CTCL is limited to the skin; however, with time, some may disseminate and involve the lymph nodes, spleen, liver, kidneys, lungs, and blood.

Morphology: All of the mouse CTCL subtypes described in the literature are characterized by epidermal infiltrates of small- to medium-sized mature T cells with irregular (cerebriform) nuclei and scant cytoplasm. As the lymphoma progresses, the neoplastic cells may have medium-sized to large cerebriform nuclei. Based on the mouse and the WHO reports, each of the subtypes has features that are unique to that subtype, as described below.

- *Mycosis fungoides (MF)*: The epidermotropic neoplastic lymphocytes are aligned along the basal layer, and they may form round, compacted intra-epidermal aggregates called Pautrier microabscesses. The latter are characteristic of MF, but they are infrequent. Hair follicles and adnexal structures may be involved. In addition to epidermal lymphocytes, MF is characterized by a polymorphic dermal infiltrate of lymphoma cells, normal lymphocytes, histiocytes, and eosinophils. The dermal infiltrate may be patchy, multifocal, or diffuse and become band-like (lichenoid) in the papillary dermis. The disease is generally limited to the skin, with variable distribution, but it can progress with wide dissemination to the lymph nodes, spleen, liver, kidneys, lungs, and peripheral blood.
- *Pagetoid reticulosis*: In this MF variant, the epidermis is hyperkeratotic and, in addition to the neoplastic cell alignment along the basal layer, there is extensive diffuse neoplastic cell infiltration of the epidermis. The neoplastic infiltrates are restricted to the epidermis, and extracutaneous dissemination is not a feature of this subtype.
- *Sezary syndrome*: This is the leukemic counterpart of MF and has not been reported to occur spontaneously in mice, but a mouse model has been reported [200]. The skin lesion is similar to MF with epidermal and dermal infiltrates of T lymphocytes with small and large cerebriform nuclei. Neoplastic lymphocytes in the blood are required for a diagnosis of Sezary syndrome. Effacement of lymph nodes is common, but other organ involvement is not common.
- *Cutaneous CD8+ cytotoxic lymphoma*: The morphology of the skin lesion is similar to that of MF or pagetoid reticulosis.

Immunophenotype. The typical phenotype of MF and its variants is CD2+, CD3+, CD4+, CD5+, CD8−, TCRB+, and TCRG−. The cells are more often negative than positive for CD7 and may or may not express CD30. On rare occasions, the immunophenotype of the neoplastic cells may be CD4− CD8−, or CD8+. Cytotoxic granule-associated proteins may or may not be expressed, but more commonly are not. The phenotype of the CD8+ cytotoxic T-cell lymphoma is CD2+/−, CD3+, CD4−, CD5−/+, CD7+, CD8 +, TIA1+, granzyme b−/+, perforin−/+ TCRB+, and TCRG−.

Differential diagnosis: Many types of lymphocytic interface dermatitis simulate CTCLs, histologically requiring differentiation from CTCLs. Inflammatory dermatitides do not have Pautrier microabscesses, and their nuclei are round and smaller than the irregular cerebriform nuclei seen in MF and its variants. The nuclei of CTCL cells in the epidermis and dermis are of the same size, whereas the lymphocyte nuclei in the epidermis of inflammatory dermatoses are smaller than those in the dermis. The presence of apoptosis and dyskeratotic cells in the basilar layer of the epidermis is more characteristic of an inflammatory dermatitis than of a CTCL.

PTCL can present in the skin, necessitating differentiation from CTCLs. Unlike CTCL, which is multifocal and involves both the epidermis and dermis, PTCL metastasis to the skin is generally focal and confined to the dermis.

Differentiation of CD8+ cutaneous cytotoxic lymphoma from the other CTCL types, such as MF and its variants, may be very difficult if not impossible when the pathogenic lymphocyte associated with MF or its variants is a CD8+ cell.

Conventional mice and mouse models: A CTCL with features of MF has been reported in an ICR mouse, and a CTCL with features of pagetoid reticulosis, MF variant, has been reported in a CD1 mouse [195, 196]. These two CTCLs expressed CD3, but no further characterization has been reported. Several transgenic, syngeneic, and xenogeneic mouse models of various CTCLs have been developed to understand further the biology of these lymphomas with regard to their development, progression, and treatment [197–202] (see Table 8.4).

Thymus Neoplasms

Definition: Thymoma is a tumor of the thymic epithelium, regardless of the presence, absence, or abundance of lymphocytes. In the past, mouse thymomas were classified into three main histologic groups, epithelial, mixed, and lymphoid dominant, depending on the relative preponderance of epithelial cells and lymphocytes. Based on their biological behavior, all human thymomas are considered malignant; however, the biological behavior of these rare tumors with variable morphologic features in mice is not well defined. Therefore, it has recently been recommended that thymomas in the mouse be classified as benign or malignant based on their morphologic and invasive features and that they be subclassified as epithelial type or spindeloid type based on their growth patterns [74].

Tissues involved: The thymus is the primary tissue in which thymomas develop, but malignant thymomas may spread through the capsule and into the fat around the thymus or they may metastasize to other organs.

Morphology: The epithelial elements exhibit various morphologies, including squamous or glandular appearance or the formation of rosettes or spindle cells, which may be localized or dispersed among lymphoid cells. The lymphocytes are nonneoplastic and have the morphology of normal thymocytes. The tumor may be solitary or multifocal with a

Vet-ebooks.com

nodular pattern or it may be composed of cellular sheets. In the epithelial thymoma type, the neoplastic epithelial cells constitute 80% of the tumor. In the spindeloid thymoma type, the neoplastic cells are fusiform and can mimic mesenchymal cells with a sarcoma growth pattern.

In benign thymoma, the epithelial component does not have atypical features or mitosis, but there may be a slight local infiltration of the thymic capsule. In malignant thymoma, the epithelial component has atypical features consisting of large round or spindle cells with vesicular nuclei and prominent nucleoli, and there may be extensive invasion beyond the capsule into the surrounding fat and thoracic organs. The tumor may also metastasize to thoracic and extrathoracic organs.

Immunophenotype. The epithelial cells express pan–keratin A1/A3. If they are of cortical origin, they express keratin 8 (KRT8), whereas if they are of medullary origin, they generally express keratins 5 (KRT5) and 14 (KRT14) [215]. The lymphocytes are a mixture of cells that express CD4 or CD8 and/or cells that are double-positive for CD4 and CD8 as well as expressing TDT.

Differential diagnosis: Thymomas may resemble entities such as thymic epithelial hyperplasia, lymphoid hyperplasia, squamous cell carcinoma, lymphoma, and malignant mesothelioma.

- *Epithelial hyperplasia*: Thymic epithelial cell hyperplasia is found in the medulla and may be focal to diffuse. The epithelial cells form tubules, ribbons or cords, and cystic structures, which may contain eosinophilic secretory material. Pleomorphic variations of thymic epithelial hyperplasia can be similar to the cellular forms of thymoma. Consequently, thymic epithelial cell hyperplasia may be difficult to distinguish cytologically from benign thymoma. However, hyperplasias are not nodular, do not compress the surrounding tissue, and do not invade the capsule, whereas benign thymomas are nodular and compressive. Malignant thymomas are invasive and may have distant metastasis.
- *Lymphoid hyperplasia*: Unlike thymomas, thymic lymphoid hyperplasia lesions do not have an epithelial component, and medullary lymphoid hyperplasia is often characterized by follicle formation, with or without germinal centers.
- *Squamous cell carcinoma*: Differentiating squamous cell carcinoma from malignant epithelial thymoma with squamous differentiation may be difficult when the thymoma lacks a lymphoid component, and there is no evidence of an extrathymic primary squamous cell carcinoma [74].
- *Lymphoma*: Lymphoma involving the thymus lacks an epithelial cell component, and the neoplastic lymphocytes are large with nuclear atypia, whereas the lymphocytes of a lymphocyte-predominant thymoma are small and do not have nuclear atypia [74].
- *Malignant mesothelioma*: Both thymomas and mesotheliomas show morphologic diversity with epithelial, spindled, and mixed epithelial/spindled components. Lymphocytes may also be associated with both tumors, but the presence of TDT+ or CD4+ CD8+ double-positive cells is indicative of a thymic epithelial tumor. In contrast, nuclear calbindin2 expression favors malignant mesothelioma.

Conventional mice and mouse models: Thymomas are uncommon in all conventional strains of mice [99, 216]. However, thymic tumors referred to as thymomas have been induced by injecting of 7,12-dimethylbenz[a]anthracene (DMBA) into the thymus of newborn mice from various inbred and F1 hybrid mouse strains. However, it has never been confirmed that the cells of these tumors were epithelial cells [217]. Neonatal C3H/Fg virus 2 (Bittner virus) mice injected with polyomavirus develop nonneoplastic lymphocyte-associated, keratin-positive, spindeloid thymomas [218]. SV40 T-antigen transgenic mice have been used in multiple studies in attempt to produce thymomas. Because of insufficient promoters, thymic hyperplasia was the only thymic abnormality in these mice. Whereas, transgenic C57BL/6J mice carrying the SV40 large T antigen transgene developed thymic changes that progressed from hyperplasia and benign thymoma to malignant thymoma after 23 weeks of age. The malignant thymomas were of the epithelial type or the spindeloid type, and some tumors had a mixture of epithelial and spindeloid features [219].

Final Considerations

When assessing mouse hematopoietic proliferations, caution is required in diagnosing a hematopoietic neoplasm when an infection or a nonhematopoietic tumor is evident. Reactive processes such as extramedullary hematopoiesis, especially in the spleen, and leukemoid reactions in the peripheral blood can be difficult to distinguish from neoplasms. Therefore, evidence that a hematopoietic proliferation is neoplastic should include the absence of an infectious or inflammatory disease and the lack of a nonhematopoietic tumor in the mouse. It is also important that the mouse has had adequate food and water intake and that it has not been treated with drugs or toxins that affect the hematopoietic system. Furthermore, Ig heavy chain receptor or T-cell receptor rearrangement is generally considered evidence of a monoclonal proliferation and that the proliferation is a neoplasm. However, when genetically engineered changes in a mouse are sufficient to cause disease, it may be impossible to establish the monoclonality of a tumor, i.e. the tumor may be nonclonal or polyclonal. Consequently, it may be necessary to resort to other methods, such as determining the proviral integration status or transplanting the tumor into a recipient mouse. Demonstrating that a neoplasm is transplantable usually provides evidence that a tumor has an autonomous malignant nature. However, caution is warranted because some benign tumors can be transplanted, and some malignant neoplasms fail to be transplanted. In some instances, normal hematopoietic stem cells within the original tumor may replace the transplanted tumor. Therefore, it is important to confirm that a recipient tumor has the same genetic markers as the original tumor. Mouse models featuring xenotransplants of human tumor cells have an additional problem in that the xenotransplant may be replaced or infiltrated by neoplastic mouse hematolymphoid cells that arise

Vet-ebooks.com

within the recipient mouse. Therefore, it is important to ensure the tumor in the recipient mouse is of human origin and that it has not been replaced or infiltrated by mouse neoplastic cells of a hematopoietic or lymphocyte lineage [184].

CRISPR/Cas9, a powerful genome-editing tool, has provided a futuristic approach to developing mouse models needed for the study of complex gene modifications. This tool will enable investigators to develop mouse models with cooperating mutations in cytokine signaling, recapitulating the combinations of mutations observed in patients, and thus generate the most appropriate humanized mouse models.

In summary, traditional, genetically engineered, xenogeneic, and humanized mouse models will continue to be important for revealing the biology of carcinogenesis. Understanding the morphology, immunophenotype, and diagnostic criteria of tumors, as described in this chapter, will be essential to characterizing the hematolymphoid proliferations that develop in these mouse models and to continued progress in our understanding of the pathogenesis, treatment, and prevention of cancer.

Acknowledgments

The author thanks Drs. Peter Vogel, Laura Janke, and Teresa Santiago for their critical review of the chapter. The author also thanks Keith A. Laycock, PhD, ELS, for scientific editing of the manuscript.

References

1 Morse, H.C. 3rd, Anver, M.R., Fredrickson, T.N. et al. (2002). Bethesda proposals for classification of lymphoid neoplasms in mice. *Blood* 100 (1): 246–258.

2 Kogan, S.C., Ward, J.M., Anver, M.R. et al. (2002). Bethesda proposals for classification of nonlymphoid hematopoietic neoplasms in mice. *Blood* 100 (1): 238–245.

3 Swerdlow SH, Campo E, Harris NL, Jaffe ES, Pileri SA, Stein H, Thiele J. *WHO Classification of Tumours of Hematopoietic and Lymphoid Tissues*,4, revised fourth edition. Tumours WCo, editor. Lyon: WHO; 2017, 586.

4 Kunder, S., Calzada-Wack, J., Hölzlwimmer, G. et al. (2007). A comprehensive antibody panel for immunohistochemical analysis of formalin-fixed, paraffin-embedded hematopoietic neoplasms of mice: analysis of mouse specific and human antibodies cross-reactive with murine tissue. *Toxicol. Pathol.* 35 (3): 366–375.

5 Rehg, J.E., Bush, D., and Ward, J.M. (2012). The utility of immunohistochemistry for the identification of hematopoietic and lymphoid cells in normal tissues and interpretation of proliferative and inflammatory lesions of mice and rats. *Toxicol. Pathol.* 40 (2): 345–374.

6 Rehg, J.E. and Ward, J.M. (2017). Application of immunohistochemistry in toxicologic pathology of the hematolymphoid system. In: *Immunopathology in Toxicology and Drug Development Molecular Integrative Toxicology*, vol. 1 (ed. G. Parker), 489–561. New York, NY: Springer Nature.

7 Dunn, T.B. (1954). Normal and pathologic anatomy of the reticular tissue in laboratory mice, with a classification and discussion of neoplasms. *J. Natl. Cancer Inst.* 14 (6): 1281–1433.

8 Jones, D., Amin, M., Ordonez, N.G. et al. (2001). Reticulum cell sarcoma of lymph node with mixed dendritic and fibroblastic features. *Mod. Pathol.* 14 (10): 1059–1067.

9 Andriko, J.W., Kaldjian, E.P., Tsokos, M. et al. (1998). Reticulum cell neoplasms of lymph nodes: a clinicopathologic study of 11 cases with recognition of a new subtype derived from fibroblastic reticular cells. *Am. J. Surg. Pathol.* 22 (9): 1048–1058.

10 Martel, M., Sarli, D., Colecchia, M. et al. (2003). Fibroblastic reticular cell tumor of the spleen: report of a case and review of the entity. *Hum. Pathol.* 34 (9): 954–957.

11 Ng, C.T., Nayak, B.P., Schmedt, C., and Oldstone, M.B.A. (2012). Immortalized clones of fibroblastic reticular cells activate virus-specific T cells during virus infection. *Proc. Natl. Acad. Sci. U.S.A.* 109 (20): 7823–7828.

12 Fenske, T.S., McMahon, C., Edwin, D. et al. (2006). Identification of candidate alkylator-induced cancer susceptibility genes by whole genome scanning in mice. *Cancer Res.* 66 (10): 5029–5038.

13 Rivina, L., Davoren, M., and Schiestl, R.H. (2014). Radiation-induced myeloid leukemia in murine models. *Hum. Genomics* 8 (1): 13.

14 Janke, M.R., Baty, J.D., and Graubert, T.A. (2013). SWR/J mice are susceptible to alkylator-induced myeloid leukemia. *Blood Cancer J.* 3 (11): e161.

15 Mambet, C., Chivu-Economescu, M., Matei, L. et al. (2018). Murine models based on acute myeloid leukemia-initiating stem cells xenografting. *World J. Stem Cells* 10 (6): 57–65.

16 Lampreht Tratar, U., Horvat, S., and Cemazar, M. (2018). Transgenic mouse models in cancer research. *Front. Oncol.* 8: 268.

17 Rithidech, K.N., Cronkite, E.P., and Bond, V.P. (1999). Advantages of the CBA mouse in leukemogenesis research. *Blood Cells Mol. Dis.* 25 (1): 38–45.

18 McCormack, E., Bruserud, O., and Gjertsen, B.T. (2005). Animal models of acute myelogenous leukaemia – development, application and future perspectives. *Leukemia* 19 (5): 687–706.

19 McCormack, E., Bruserud, O., and Gjertsen, B.T. (2008). Review: genetic models of acute myeloid leukaemia. *Oncogene* 27 (27): 3765–3779.

20 Fortier, J.M. and Graubert, T.A. (2010). Murine models of human acute myeloid leukemia. *Cancer Treat. Res.* 145: 183–196.

21 Zuber, J., Radtke, I., Pardee, T.S. et al. (2009). Mouse models of human AML accurately predict chemotherapy response. *Genes Dev.* 23 (7): 877–889.

Vet-ebooks.com

22 Jacoby, E., Chien, C.D., and Fry, T.J. (2014). Murine models of acute leukemia: important tools in current pediatric leukemia research. *Front. Oncol.* 4: 95.

23 Almosailleakh, M. and Schwaller, J. (2019). Murine models of acute myeloid leukaemia. *Int. J. Mol. Sci.* 20 (2): 453.

24 Skayneh, H., Jishi, B., Hleihel, R. et al. (2019). A critical review of animal models used in acute myeloid leukemia pathophysiology. *Genes (Basel)* 10 (8): 614.

25 Frith, C.H. and Wiley, L.D. (1981). Morphologic classification and correlation of incidence of hyperplastic and neoplastic hematopoietic lesions in mice with age. *J. Gerontol.* 36 (5): 534–545.

26 Frith, C.H., Ward, J.M., and Chandra, M. (1993). The morphology, immunohistochemistry, and incidence of hematopoietic neoplasms in mice and rats. *Toxicol. Pathol.* 21 (2): 206–218.

27 Warner, N.L., Moore, M.A.S., and Metcalf, D. (1969). A transplantable myelomonocytic leukemia in BALB/c mice: cytology, karyotype, and muramidase content 23. *J. Natl. Cancer Inst.* 43 (4): 963–982.

28 Castilla, L.H., Garrett, L., Adya, N. et al. (1999). The fusion gene Cbfb-MYH11 blocks myeloid differentiation and predisposes mice to acute myelomonocytic leukaemia. *Nat. Genet.* 23 (2): 144–146.

29 Lavau, C., Luo, R.T., Du, C., and Thirman, M.J. (2000). Retrovirus-mediated gene transfer of MLL-ELL transforms primary myeloid progenitors and causes acute myeloid leukemias in mice. *Proc. Natl. Acad. Sci. U.S.A.* 97 (20): 10984–10989.

30 Luo, R.T., Lavau, C., Du, C. et al. (2001). The elongation domain of ELL is dispensable but its ELL-associated factor 1 interaction domain is essential for MLL-ELL-induced leukemogenesis. *Mol. Cell. Biol.* 21 (16): 5678–5687.

31 Murphy, W.H., Urnovitz, H.B., Maryanski, J.L., and Abrams, G.D. (1978). Characterization of transplantable myelomonocytic leukemia WEHI-3B in syngeneic BALB/c mice. *Proc. Soc. Exp. Biol. Med.* 157 (4): 556–564.

32 Yu, H., Li, Y., Gao, C. et al. (2010). Relevant mouse model for human monocytic leukemia through Cre/lox-controlled myeloid-specific deletion of PTEN. *Leukemia* 24 (5): 1077–1080.

33 Frith, C.H., McConnell, R.F., and Johnson, A.N. (1990). Erythroleukemia in a mouse. *Lab. Anim. Sci.* 40 (4): 418–419.

34 Torchia, E.C., Boyd, K., Rehg, J.E. et al. (2007). EWS/FLI-1 induces rapid onset of myeloid/erythroid leukemia in mice. *Mol. Cell. Biol.* 27 (22): 7918–7934.

35 Kosmider, O., Denis, N., Lacout, C. et al. (2005). Kit-activating mutations cooperate with Spi-1/PU.1 overexpression to promote tumorigenic progression during erythroleukemia in mice. *Cancer Cell* 8 (6): 467–478.

36 Subramanian, A., Teal, H.E., Correll, P.H., and Paulson, R.F. (2005). Resistance to friend virus-induced erythroleukemia in W/W(v) mice is caused by a spleen-specific defect which results in a severe reduction in target cells and a lack of Sf-Stk expression. *J. Virol.* 79 (23): 14586–14594.

37 Mercher, T., Raffel, G.D., Moore, S.A. et al. (2009). The OTT-MAL fusion oncogene activates RBPJ-mediated transcription and induces acute megakaryoblastic leukemia in a knockin mouse model. *J. Clin. Invest.* 119 (4): 852–864.

38 Sportoletti, P., Varasano, E., Rossi, R. et al. (2013). The human NPM1 mutation A perturbs megakaryopoiesis in a conditional mouse model. *Blood* 121 (17): 3447–3458.

39 Hao, X., Shin, M.S., Zhou, J.X. et al. (2006). Histologic and molecular characterizations of megakaryocytic leukemia in mice. *Leuk. Res.* 30 (4): 397–406.

40 Deringer, M.K. and Dunn, T.B. (1947). Mast-cell neoplasia in mice. *J. Natl. Cancer Inst.* 7 (4): 289–298.

41 Metcalf, D., Majewski, I., Mifsud, S. et al. (2007). Clonogenic mast cell progenitors and their excess numbers in chimeric BALB/c mice with inactivated GATA-1. *Proc. Natl. Acad. Sci. U.S.A.* 104 (47): 18642–18647.

42 Demehri, S., Corbin, A., Loriaux, M. et al. (2006). Establishment of a murine model of aggressive systemic mastocytosis/mast cell leukemia. *Exp. Hematol.* 34 (3): 284–288.

43 Bibi, S., Zhang, Y., Hugonin, C. et al. (2016). A new humanized in vivo model of KIT D816V+ advanced systemic mastocytosis monitored using a secreted luciferase. *Oncotarget* 7 (50): 82985–83000.

44 Dunn, T.B. and Potter, M. (1957). A transplantable mast-cell neoplasm in the mouse. *J. Natl. Cancer Inst.* 18 (4): 587–601.

45 Rask-Nielsen, R. and Christensen, H.E. (1963). Studies on a transplantable mastocytoma in mice. I. Origin and general morphology. *J. Natl. Cancer Inst.* 30: 743–761.

46 Biermann, H., Pietz, B., Dreier, R. et al. (1999). Murine leukocytes with ring-shaped nuclei include granulocytes, monocytes, and their precursors. *J. Leukocyte Biol.* 65 (2): 217–231.

47 Kina, T., Ikuta, K., Takayama, E. et al. (2000). The monoclonal antibody TER-119 recognizes a molecule associated with glycophorin A and specifically marks the late stages of murine erythroid lineage. *Br. J. Haematol.* 109 (2): 280–287.

48 Raess, P.W., Paessler, M.E., Bagg, A. et al. (2012). α-Hemoglobin-stabilizing protein is a sensitive and specific marker of erythroid precursors. *Am. J. Surg. Pathol.* 36 (10): 1538–1547.

49 Dong, H.Y., Wilkes, S., and Yang, H. (2011). CD71 is selectively and ubiquitously expressed at high levels in erythroid precursors of all maturation stages: a comparative immunochemical study with glycophorin A and hemoglobin A. *Am. J. Surg. Pathol.* 35 (5): 723–732.

50 Cmarik, J. and Ruscetti, S. (2010). Friend spleen focus-forming virus activates the tyrosine kinase sf-Stk and the transcription factor PU.1 to cause a multi-stage erythroleukemia in mice. *Viruses* 2 (10): 2235–2257.

51 Lee, J.J. and McGarry, M.P. (2007). When is a mouse basophil not a basophil? *Blood* 109 (3): 859–861.

52 Metcalf, D., Ng, A.P., Baldwin, T.M. et al. (2013). Concordant mast cell and basophil production by

Vet-ebooks.com

individual hematopoietic blast colony-forming cells. *Proc. Natl. Acad. Sci. U.S.A.* 110 (22): 9031–9035.

53 Gurish, M.F., Friend, D.S., Webster, M. et al. (1997). Mouse mast cells that possess segmented/multi-lobular nuclei. *Blood* 90 (1): 382–390.

54 Ugajin, T., Kojima, T., Mukai, K. et al. (2009). Basophils preferentially express mouse mast cell protease 11 among the mast cell tryptase family in contrast to mast cells. *J. Leukocyte Biol.* 86 (6): 1417–1425.

55 Yamagishi, H., Mochizuki, Y., Hamakubo, T. et al. (2011). Basophil-derived mouse mast cell protease 11 induces microvascular leakage and tissue edema in a mast cell-independent manner. *Biochem. Biophys. Res. Commun.* 415 (4): 709–713.

56 Tsutsui, H., Yamanishi, Y., Ohtsuka, H. et al. (2017). The basophil-specific protease mMCP-8 provokes an inflammatory response in the skin with microvascular hyperpermeability and leukocyte infiltration. *J. Biol. Chem.* 292 (3): 1061–1067.

57 Wernig, G., Mercher, T., Okabe, R. et al. (2006). Expression of Jak2V617F causes a polycythemia vera-like disease with associated myelofibrosis in a murine bone marrow transplant model. *Blood* 107 (11): 4274–4281.

58 Shide, K., Shimoda, H.K., Kumano, T. et al. (2008). Development of ET, primary myelofibrosis and PV in mice expressing JAK2 V617F. *Leukemia* 22 (1): 87–95.

59 Li, J., Prins, D., Park, H.J. et al. (2018). Mutant calreticulin knockin mice develop thrombocytosis and myelofibrosis without a stem cell self-renewal advantage. *Blood* 131 (6): 649–661.

60 Balligand, T., Achouri, Y., Pecquet, C. et al. (2020). Knock-in of murine Calr del52 induces essential thrombocythemia with slow-rising dominance in mice and reveals key role of Calr exon 9 in cardiac development. *Leukemia* 34 (2): 510–521.

61 Pear, W.S., Miller, J.P., Xu, L. et al. (1998). Efficient and rapid induction of a chronic myelogenous leukemia-like myeloproliferative disease in mice receiving P210 bcr/abl-transduced bone marrow. *Blood* 92 (10): 3780–3792.

62 Daley, G.Q., Van Etten, R.A., and Baltimore, D. (1991). Blast crisis in a murine model of chronic myelogenous leukemia. *Proc. Natl. Acad. Sci. U.S.A.* 88 (24): 11335–11338.

63 Gishizky, M.L., Johnson-White, J., and Witte, O.N. (1993). Efficient transplantation of BCR-ABL-induced chronic myelogenous leukemia-like syndrome in mice. *Proc. Natl. Acad. Sci. U.S.A.* 90 (8): 3755–3759.

64 Sontakke, P., Jaques, J., Vellenga, E., and Schuringa, J.J. (2016). Modeling of chronic myeloid leukemia: an overview of in vivo murine and human xenograft models. *Stem Cells Int.* 2016: 1625015.

65 Vo, Q.T. and Thompson, D.F. (2019). A review and assessment of drug-induced thrombocytosis. *Ann. Pharmacother.* 53 (5): 523–536.

66 Li, J., Kent, D.G., Chen, E., and Green, A.R. (2011). Mouse models of myeloproliferative neoplasms: JAK of all grades. *Dis. Models Mech.* 4 (3): 311.

67 Mullally, A., Lane, S.W., Brumme, K., and Ebert, B.L. (2012). Myeloproliferative neoplasm animal models. *Hematol. Oncol. Clin. N. Am.* 26 (5): 1065–1081.

68 Dunbar, A., Nazir, A., and Levine, R. (2017). Overview of transgenic mouse models of myeloproliferative neoplasms (MPNs). *Curr. Protoc. Pharmacol.* 77: 14.40.1–14.40.19.

69 Kelliher, M.A., McLaughlin, J., Witte, O.N., and Rosenberg, N. (1990). Induction of a chronic myelogenous leukemia-like syndrome in mice with v-abl and BCR/ABL. *Proc. Natl. Acad. Sci. U.S.A.* 87 (17): 6649–6653.

70 Wang, S., Xia, P., Chen, Y. et al. (2016). Natural killer-like B cells prime innate lymphocytes against microbial infection. *Immunity* 45 (1): 131–144.

71 Shide, K., Kameda, T., Yamaji, T. et al. (2017). Calreticulin mutant mice develop essential thrombocythemia that is ameliorated by the JAK inhibitor ruxolitinib. *Leukemia* 31 (5): 1136–1144.

72 Lanikova, L., Babosova, O., and Prchal, J.T. (2019). Experimental modeling of myeloproliferative neoplasms. *Genes* 10 (10): 813.

73 Wu, M.-Y., Eldin, K.W., and Beaudet, A.L. (2008). Identification of chromatin remodeling genes Arid4a and Arid4b as leukemia suppressor genes. *J. Natl. Cancer Inst.* 100 (17): 1247–1259.

74 Willard-Mack, C.L., Elmore, S.A., Hall, W.C. et al. (2019). Nonproliferative and proliferative lesions of the rat and mouse hematolymphoid system. *Toxicol. Pathol.* 47 (6): 665–783.

75 Beachy, S.H. and Aplan, P.D. (2010). Mouse models of myelodysplastic syndromes. *Hematol. Oncol. Clin. N. Am.* 24 (2): 361–375.

76 Beurlet, S., Chomienne, C., and Padua, R.A. (2013). Engineering mouse models with myelodysplastic syndrome human candidate genes; how relevant are they? *Haematologica* 98 (1): 10–22.

77 Tan, S., Smeets, M., Chalk, A. et al. (2016). Insights into myelodysplastic syndromes from current preclinical models. *World J. Hematol.* 5 (1): 1–22.

78 Li, X. and Deeg, H.J. (2014). Murine xenogeneic models of myelodysplastic syndrome: an essential role for stroma cells. *Exp. Hematol.* 42 (1): 4–10.

79 Rouault-Pierre, K., Mian, S.A., Goulard, M. et al. (2017). Preclinical modeling of myelodysplastic syndromes. *Leukemia* 31 (12): 2702–2708.

80 Cole, C.B., Russler-Germain, D.A., Ketkar, S. et al. (2017). Haploinsufficiency for DNA methyltransferase 3A predisposes hematopoietic cells to myeloid malignancies. *J. Clin. Invest.* 127 (10): 3657–3674.

81 Wang, J., Zhaoyi, M., Joamg, Y. et al. (2020). Characteristics of myeloid sarcoma in mice and patients with *TET2* deficiency. *Oncol. Lett.* 19: 3789–3798.

82 Frith, C.H., Davis, T.M., Zolotor, L.A., and Townsend, J.W. (1980). Histiocytic lymphoma in the mouse. *Leuk. Res.* 4 (6): 651–662.

Vet-ebooks.com

83 Frith, C.H. (1990). Histiocytic sarcoma, mouse. In: *Monographs on Pathology of Laboratory Animals. Hemopoietic System* (eds. T.C. Jones, J.M. Ward, U. Mohr and R.D. Hunt), 58–65. Berlin, Heidelberg, New York: Sorubger-Verlag.

84 Turusov, V.S. (1994). Histiocytic sarcoma. *IARC Sci. Publ.* 111: 671–680.

85 Lacroix-Triki, M., Lacoste-Collin, L., Jozan, S. et al. (2003). Histiocytic sarcoma in C57BL/6J female mice is associated with liver hematopoiesis: review of 41 cases. *Toxicol. Pathol.* 31 (3): 304–309.

86 Martín-Caballero, J., Flores, J.M., García-Palencia, P., and Serrano, M. (2001). Tumor susceptibility of p21(Waf1/Cip1)-deficient mice. *Cancer Res.* 61 (16): 6234–6238.

87 Eischen, C.M., Rehg, J.E., Korsmeyer, S.J., and Cleveland, J.L. (2002). Loss of Bax alters tumor spectrum and tumor numbers in ARF-deficient mice. *Cancer Res.* 62 (7): 2184–2191.

88 Carrasco, D.R., Fenton, T., Sukhdeo, K. et al. (2006). The PTEN and INK4A/ARF tumor suppressors maintain myelolymphoid homeostasis and cooperate to constrain histiocytic sarcoma development in humans. *Cancer Cell* 9 (5): 379–390.

89 Ward, J.M., Nikolov, N.P., Tschetter, J.R. et al. (2004). Progressive glomerulonephritis and histiocytic sarcoma associated with macrophage functional defects in CYP1B1-deficient mice. *Toxicol. Pathol.* 32 (6): 710–718.

90 Mashima, R., Honda, K., Yang, Y. et al. (2010). Mice lacking Dok-1, Dok-2, and Dok-3 succumb to aggressive histiocytic sarcoma. *Lab. Invest.* 90 (9): 1357–1364.

91 Hirata, A., Tsukamoto, T., Yamamoto, M. et al. (2007). Early development of histiocytic sarcomas in p53 knockout mice treated with N-bis(2-hydroxypropyl)nitrosamine. *Oncol. Rep.* 18 (4): 755–761.

92 Nelson, D.S., Marano, R.L., Joo, Y. et al. (2019). BRAF V600E and Pten deletion in mice produces a histiocytic disorder with features of Langerhans cell histiocytosis. *PLoS One* 14 (9): e0222400.

93 Kiyuna, T., Murakami, T., Tome, Y. et al. (2016). High efficacy of tumor-targeting Salmonella typhimurium A1-R on a doxorubicin- and dactolisib-resistant follicular dendritic-cell sarcoma in a patient-derived orthotopic xenograft PDOX nude mouse model. *Oncotarget* 7 (22): 33046–33054.

94 Oshiro, H., Tome, Y., Kiyuna, T. et al. (2019). Temozolomide targets and arrests a doxorubicin-resistant follicular dendritic-cell sarcoma patient-derived orthotopic xenograft mouse model. *Tissue Cell* 58: 17–23.

95 Leenen, P.J.M., Bechan, G.I., Melis, M. et al. (2010). Heterogeneity in a mouse model of histiocytosis: transformation of Langerin+ dendritic cells, macrophages, and precursors. *J. Leukocyte Biol.* 87 (5): 949–958.

96 Steiner, Q.-G., Otten, L.A., Hicks, M.J. et al. (2008). in vivo transformation of mouse conventional CD8alpha+ dendritic cells leads to progressive multisystem histiocytosis. *Blood* 111 (4): 2073–2082.

97 van Nieuwenhuijze, A.E., Coghill, E., Gray, D. et al. (2014). Transgenic expression of GM-CSF in T cells causes disseminated histiocytosis. *Am. J. Pathol.* 184 (1): 184–199.

98 Frith, C.H., Sprowls, R.W., and Breeden, C.R. (1976). Mast cell neoplasia in mice. *Lab. Anim. Sci.* 26 (3): 478–481.

99 Haseman, J.K., Hailey, J.R., and Morris, R.W. (1998). Spontaneous neoplasm incidences in Fischer 344 rats and B6C3F1 mice in two-year carcinogenicity studies: a National Toxicology Program update. *Toxicol. Pathol.* 26 (3): 428–441.

100 Sundberg, J.P., Berndt, A., Sundberg, B.A. et al. (2016). Approaches to investigating complex genetic traits in a large-scale inbred mouse aging study. *Vet. Pathol.* 53 (2): 456–467.

101 Dunn, T.B. (1968). Mast cell neoplasms of mice. *Natl. Cancer Inst. Monogr.* 32: 285–287.

102 Stewart, H.L., Deringer, M.K., Dunn, T.B., and Snell, K.C. (1974). Malignant schwannomas of nerve roots, uterus, and epididymis in mice. *J. Natl. Cancer Inst.* 53 (6): 1749–1758.

103 Löhler, J., Franz, T., Klingler, K. et al. (1987). Retrovirus-induced malignant histiocytosis in mice: a model for the human disease. *Haematol. Blood Transfus.* 31: 448–449. https://doi.org/10.1007/978-3-642-72624-8_96. PMID: 3443405.

104 Rehg, J.E., Rahija, R., Bush, D. et al. (2015). Immunophenotype of spontaneous hematolymphoid tumors occurring in young and aging female CD-1 mice. *Toxicol. Pathol.* 43 (7): 1025–1034.

105 Vogel, P., Janke, L., Gravano, D.M. et al. (2018). Globule leukocytes and other mast cells in the mouse intestine. *Vet. Pathol.* 55 (1): 76–97.

106 Janke, L.J., Mullighan, C.G., Dang, J., and Rehg, J.E. (2019). Immunophenotyping of murine precursor B-cell leukemia/lymphoma: a comparison of immunohistochemistry and flow cytometry. *Vet. Pathol.* 56 (6): 950–958.

107 Fredrickson, T.N., Morse, H.C. 3rd, Yetter, R.A. et al. (1985). Multiparameter analyses of spontaneous nonthymic lymphomas occurring in NFS/N mice congenic for ecotropic murine leukemia viruses. *Am. J. Pathol.* 121 (2): 349–360.

108 Rehg, J.E. and Sundberg, J.P. (2008). Utility of antiPax5 in the diagnosis of lymphoproliferative disorders and neoplasia in mice. *Comp. Med.* 58 (3): 246–252.

109 Woloschak, G.E. and Krco, C.J. (1987). Regulation of kappa/lambda immunoglobulin light chain expression in normal murine lymphocytes. *Mol. Immunol.* 24 (7): 751–757.

110 Pattengale, P.K. and Frith, C.H. (1983). Immunomorphologic classification of spontaneous lymphoid cell neoplasms occurring in female BALB/c mice. *J. Natl. Cancer Inst.* 70 (1): 169–179.

111 Wright, J.A., Horne, M., and Stewart, M.G. (1991). An immunohistochemical study of spontaneous lymphomas in the C57B1/10J mouse. *J. Comp. Pathol.* 104 (2): 211–222.

Vet-ebooks.com

112 Fredrickson, T.N., Morse, H.C., and Rowe, W.P. (1984). Spontaneous tumors of NFS mice congenic for ecotropic murine leukemia virus induction loci2. *J. Natl. Cancer Inst.* 73 (2): 521–524.

113 Yamada, Y., Matsushiro, H., Ogawa, M.S. et al. (1994). Genetic predisposition to pre-B lymphomas in SL/Kh strain mice. *Cancer Res.* 54 (2): 403–407.

114 Haines, D.C., Chattopadhyay, S., and Ward, J.M. (2001). Pathology of aging B6;129 mice. *Toxicol. Pathol.* 29 (6): 653–661.

115 Adams, J.M., Harris, A.W., Pinkert, C.A. et al. (1985). The c-myc oncogene driven by immunoglobulin enhancers induces lymphoid malignancy in transgenic mice. *Nature* 318 (6046): 533–538.

116 Hauer, J., Borkhardt, A., Sánchez-García, I., and Cobaleda, C. (2014). Genetically engineered mouse models of human B-cell precursor leukemias. *Cell Cycle* 13 (18): 2836–2846.

117 Ramírez-Komo, J.A., Delaney, M.A., Straign, D. et al. (2017). Spontaneous loss of B lineage transcription factors leads to pre-B leukemia in Ebf1(+/−)Bcl-x(L)(Tg) mice. *Oncogenesis* 6 (7): e355.

118 Morse, H.C. 3rd, Qi, C.F., Chattopadhyay, S.K. et al. (2001). Combined histologic and molecular features reveal previously unappreciated subsets of lymphoma in AKXD recombinant inbred mice. *Leuk. Res.* 25 (8): 719–733.

119 Slavin, S. and Strober, S. (1978). Spontaneous murine B-cell leukaemia. *Nature* 272 (5654): 624–626.

120 Okada, T., Takiura, F., Tokushige, K. et al. (1991). Major histocompatibility complex controls clonal proliferation of CD5+ B cells in H-2-congenic New Zealand mice: a model for B cell chronic lymphocytic leukemia and autoimmune disease. *Eur. J. Immunol.* 21 (11): 2743–2748.

121 Scaglione, B.J., Salerno, E., Balan, M. et al. (2007). Murine models of chronic lymphocytic leukaemia: role of microRNA-16 in the New Zealand Black mouse model. *Br. J. Haematol.* 139 (5): 645–657.

122 Bichi, R., Shinton, S.A., Martin, E.S. et al. (2002). Human chronic lymphocytic leukemia modeled in mouse by targeted TCL1 expression. *Proc. Natl. Acad. Sci. U.S.A.* 99 (10): 6955–6960.

123 Patten, C.L. and Cutucache, C.E. (2016). Murine models of splenic marginal zone lymphoma: a role for Cav1? *Front. Oncol.* 6: 258.

124 Hartley, J.W., Chattopadhyay, S.K., Lander, M.R. et al. (2000). Accelerated appearance of multiple B cell lymphoma types in NFS/N mice congenic for ecotropic murine leukemia viruses. *Lab. Invest.* 80 (2): 159–169.

125 Yumoto, T., Yoshida, Y., Yoshida, H. et al. (1980). Prelymphomatous and lymphomatous changes in splenomegaly of New Zealand Black mice. *Acta Pathol. Jpn.* 30 (2): 171–186.

126 Ward, J.M., Tadesse-Heath, L., Perkins, S.N. et al. (1999). Splenic marginal zone B-cell and thymic T-cell lymphomas in p53-deficient mice. *Lab. Invest.* 79 (1): 3–14.

127 Gossmann, J., Stolte, M., Lohoff, M. et al. (2016). A gain-of-function mutation in the Plcg2 gene protects mice from *Helicobacter felis*-induced gastric MALT lymphoma. *PLoS One* 11 (3): e0150411.

128 Floch, P., Izotte, J., Guillemaud, J. et al. (2017). A new animal model of gastric lymphomagenesis: APRIL transgenic mice infected by *Helicobacter* species. *Am. J. Pathol.* 187 (7): 1473–1484.

129 O'Rourke, J.L., Dixon, M.F., Jack, A. et al. (2004). Gastric B-cell mucosa-associated lymphoid tissue (MALT) lymphoma in an animal model of '*Helicobacter heilmannii*' infection. *J. Pathol.* 203 (4): 896–903.

130 Ford, R.J., Shen, L., Lin-Lee, Y.C. et al. (2007). Development of a murine model for blastoid variant mantle-cell lymphoma. *Blood* 109 (11): 4899–4906.

131 Beltran, E., Fresquet, V., Martinez-Useros, J. et al. (2011). A cyclin-D1 interaction with BAX underlies its oncogenic role and potential as a therapeutic target in mantle cell lymphoma. *Proc. Natl. Acad. Sci. U.S.A.* 108 (30): 12461–12466.

132 Fiancette, R., Rouaud, P., Vincent-Fabert, C. et al. (2011). A p53 defect sensitizes various stages of B cell development to lymphomagenesis in mice carrying an IgH 3' regulatory region-driven c-myc transgene. *J. Immunol.* 187 (11): 5772–5782.

133 Vincent-Fabert, C., Fiancette, R., Rouaud, P. et al. (2012). A defect of the INK4-Cdk4 checkpoint and Myc collaborate in blastoid mantle cell lymphoma-like lymphoma formation in mice. *Am. J. Pathol.* 180 (4): 1688–1701.

134 Rouaud, P., Fiancette, R., Vincent-Fabert, C. et al. (2012). Mantle cell lymphoma-like lymphomas in c-myc-3'RR/p53+/− mice and c-myc-3'RR/Cdk4R24C mice: differential oncogenic mechanisms but similar cellular origin. *Oncotarget* 3 (5): 586–593.

135 Bryant, J., Pham, L., Yoshimura, L. et al. (2000). Development of intermediate-grade (mantle cell) and low-grade (small lymphocytic and marginal zone) human non-Hodgkin's lymphomas xenotransplanted in severe combined immunodeficiency mouse models. *Lab. Invest.* 80 (4): 557–573.

136 M'Kacher, R., Farace, F., Bennaceur-Griscelli, A. et al. (2003). Blastoid mantle cell lymphoma: evidence for nonrandom cytogenetic abnormalities additional to t(11;14) and generation of a mouse model. *Cancer Genet. Cytogenet.* 143 (1): 32–38.

137 Klanova, M., Soukup, T., Jaksa, R. et al. (2014). Mouse models of mantle cell lymphoma, complex changes in gene expression and phenotype of engrafted MCL cells: implications for preclinical research. *Lab. Invest.* 94 (7): 806–817.

138 Zhang, L., Nomie, K., Zhang, H. et al. (2017). B-cell lymphoma patient-derived xenograft models enable drug discovery and are a platform for personalized therapy. *Clin. Cancer Res.* 23 (15): 4212–4223.

139 Qi, C.-F., Zhou, J.X., Lee, C.H. et al. (2007). Anaplastic, plasmablastic, and plasmacytic plasmacytomas of mice:

Vet-ebooks.com

relationships to human plasma cell neoplasms and late-stage differentiation of normal B cells. *Cancer Res.* 67 (6): 2439–2447.

140 Park, S.S., Kim, J.S., Tessarollo, L. et al. (2005). Insertion of c-Myc into Igh induces B-cell and plasma-cell neoplasms in mice. *Cancer Res.* 65 (4): 1306–1315.

141 Morse, H.C. 3rd, McCarty, T., Qi, C.-F. et al. (2003). B lymphoid neoplasms of mice: characteristics of naturally occurring and engineered diseases and relationships to human disorders. *Adv. Immunol.* 81: 97–121.

142 de Jong, D. and Janz, S. (2010). Anaplastic plasmacytoma of mouse—establishing parallels between subtypes of mouse and human plasma cell neoplasia. *J. Pathol.* 221 (3): 242–247.

143 Potter, M. (2003). Neoplastic development in plasma cells. *Immunol. Rev.* 194: 177–195.

144 Janz, S., Morse, H.C., and Teitell, M. (2008). Mouse models of human mature B-cell and plasma cell neoplasms. In: *Mouse Models of Human Blood Cancers, Basic Research and Preclinical Applications* (ed. S. Li), 178–226. New York, NY: Springer Science+Business Media, LLC.

145 Pattengale, P.K. and Taylor, C.R. (1983). Experimental models of lymphoproliferative disease. The mouse as a model for human non-Hodgkin's lymphomas and related leukemias. *Am. J. Pathol.* 113 (2): 237–265.

146 Chen, W., Li, Q., Hudson, W.A. et al. (2006). A murine Mll-AF4 knock-in model results in lymphoid and myeloid deregulation and hematologic malignancy. *Blood* 108 (2): 669–677.

147 Kichina, J.V., Zeremski, M., Aris, L. et al. (2006). Targeted disruption of the mouse ing1 locus results in reduced body size, hypersensitivity to radiation and elevated incidence of lymphomas. *Oncogene* 25 (6): 857–866.

148 Donehower, L.A., Harvey, M., Vogel, H. et al. (1995). Effects of genetic background on tumorigenesis in p53-deficient mice. *Mol. Carcinog.* 14 (1): 16–22.

149 Ramezani-Rad, P. and Rickert, R.C. (2017). Murine models of germinal center derived-lymphomas. *Curr. Opin. Immunol.* 45: 31–36.

150 Morse, H.C., Ward, J.M., and Teitell, M. (2010). Mouse models of human B lymphoid neoplasms. In: *The Lymphoid Neoplasms* (eds. T. MI, K. Bhatia, P. Boffetta, et al.), 281–293. London: Taylor & Francis Group.

151 Qi, C.F., Hori, M., Coleman, A.E. et al. (2000). Genomic organisation and expression of BCL6 in murine B-cell lymphomas. *Leuk. Res.* 24 (8): 719–732.

152 Cattoretti, G., Pasqualucci, L., Ballon, G. et al. (2005). Deregulated BCL6 expression recapitulates the pathogenesis of human diffuse large B cell lymphomas in mice. *Cancer Cell* 7 (5): 445–455.

153 Ranger, A.M., Zha, J., Harada, H. et al. (2003). Bad-deficient mice develop diffuse large B cell lymphoma. *Proc. Natl. Acad. Sci. U.S.A.* 100 (16): 9324–9329.

154 Mori, S., Rempel, R.E., Chang, J.T. et al. (2008). Utilization of pathway signatures to reveal distinct types of B lymphoma in the Emicro-myc model and human diffuse large B-cell lymphoma. *Cancer Res.* 68 (20): 8525–8534.

155 Knittel, G., Liedgens, P., Korovkina, D. et al. (2016). B-cell-specific conditional expression of Myd88p.L252P leads to the development of diffuse large B-cell lymphoma in mice. *Blood* 127 (22): 2732–2741.

156 Kohnken, R., Porcu, P., and Mishra, A. (2017). Overview of the use of murine models in leukemia and lymphoma research. *Front. Oncol.* 7: 22.

157 Green, M.R., Vicente-Dueñas, C., Romero-Camarero, I. et al. (2014). Transient expression of Bcl6 is sufficient for oncogenic function and induction of mature B-cell lymphoma. *Nat. Commun.* 5: 3904.

158 Lu, L.M. and Hiai, H. (1999). Mixed phenotype lymphomas in thymectomized (SL/Kh x AKR/Ms) F1 mice. *Jpn. J. Cancer Res.* 90 (11): 1218–1223.

159 Raffegerst, S.H., Hoelzlwimmer, G., Kunder, S. et al. (2009). Diverse hematological malignancies including Hodgkin-like lymphomas develop in chimeric MHC class II transgenic mice. *PLoS One* 4 (12): e8539.

160 Bachy, E., Urb, M., Chandra, S. et al. (2016). CD1d-restricted peripheral T-cell lymphoma in mice and humans. *J. Exp. Med.* 213 (5): 841–857.

161 Swerdlow, S., Campo, E., Seto, M., and Muller-Hermelink, H. (2017). Mantle cell lymphoma. In: *WHO Classification of Tumours of Haematopoietic and Lymphoid Tissues*, 4e (eds. S.H. Swerdlow, E. Campo, N.L. Harris, et al.), 285–290. Lyon: IARC.

162 Body, S., Esteve-Arenys, A., Recasens-Zorzo, C. et al. (2018). A mouse model of disseminated mantle cell lymphoma highlights a lack of activity of estrogen receptor beta agonists toward tumor burden. *Leuk. Lymphoma* 59 (7): 1726–1729.

163 Smith, M.R., Joshi, I., Jin, F., and Al-Saleem, T. (2006). Murine model for mantle cell lymphoma. *Leukemia* 20 (5): 891–893.

164 Balagué, O. and Martínez, A. (2015). What is a plasmablast? A commentary to: "plasmablastic lymphoma versus diffuse large B-cell lymphoma with plasmablastic differentiation: proposal for a novel diagnostic scoring system" by Sonja Catharina Boy et al. *J. Hematopathol.* 8 (2): 51–52.

165 Kalled, S.L., Siva, N., Stein, H., and Reinherz, E.L. (1995). The distribution of CD10 (NEP 24.11, CALLA) in humans and mice is similar in non-lymphoid organs but differs within the hematopoietic system: absence on murine T and B lymphoid progenitors. *Eur. J. Immunol.* 25 (3): 677–687.

166 Donnou, S., Galand, C., Touitou, V. et al. (2012). Murine models of B-cell lymphomas: promising tools for designing cancer therapies. *Adv. Hematol.* 2012: 701704.

167 Coles, A.H., Marfella, C.G.A., Imbalzano, A.N. et al. (2008). p37Ing1b regulates B-cell proliferation and cooperates with p53 to suppress diffuse large B-cell lymphomagenesis. *Cancer Res.* 68 (21): 8705–8714.

168 Kovalchuk, A.L., Qi, C.F., Torrey, T.A. et al. (2000). Burkitt lymphoma in the mouse. *J. Exp. Med.* 192 (8): 1183–1190.

Vet-ebooks.com

169 Fehniger, T.A., Cai, S.F., Cao, X. et al. (2007). Acquisition of murine NK cell cytotoxicity requires the translation of a pre-existing pool of granzyme B and perforin mRNAs. *Immunity* 26 (6): 798–811.

170 Soma, L., Wu, D., Chen, X. et al. (2015). Apparent CD19 expression by natural killer cells: a potential confounder for minimal residual disease detection by flow cytometry in B lymphoblastic leukemia. *Cytometry B Clin. Cytometry* 88 (2): 145–147.

171 Korol, C., Rossi, J., Sanz, M., and Bernasconi, A. (2015). NK cells expressing the B cell antigen CD19: expanding the phenotypical characterization and the potential consequences from misinterpretation of this subset population. *Cytometry B Clin. Cytometry* 88 (6): 358–360.

172 Blakolmer, K., Vesely, M., Kummer, J.A. et al. (2000). Immunoreactivity of B-cell markers (CD79a, L26) in rare cases of extranodal cytotoxic peripheral T- (NK/T-) cell lymphomas. *Mod. Pathol.* 13 (7): 766–772.

173 Yao, X., Teruya-Feldstein, J., Raffeld, M. et al. (2001). Peripheral T-cell lymphoma with aberrant expression of CD79a and CD20: a diagnostic pitfall. *Mod. Pathol.* 14 (2): 105–110.

174 Blasius, A.L., Barchet, W., Cella, M., and Colonna, M. (2007). Development and function of murine B220+CD11c+NK1.1+ cells identify them as a subset of NK cells. *J. Exp. Med.* 204 (11): 2561–2568.

175 Vosshenrich, C.A.J., Lesjean-Pottier, S., Hasan, M. et al. (2007). CD11cloB220+ interferon-producing killer dendritic cells are activated natural killer cells. *J. Exp. Med.* 204 (11): 2569–2578.

176 Metcalf, D. (1966). Histologic and transplantation studies on preleukemic thymus of the AKR mouse. *J. Natl. Cancer Inst.* 37 (4): 425–442.

177 Thomas, C.Y., Buxton, V.K., Roberts, J.S. et al. (1989). Phenotypic heterogeneity of spontaneous lymphomas of CWD mice. *Blood* 73 (1): 240–247.

178 Barlow, C., Hirotsune, S., Paylor, R. et al. (1996). Atm-deficient mice: a paradigm of ataxia telangiectasia. *Cell* 86 (1): 159–171.

179 Kundu, M., Compton, S., Garrett-Beal, L. et al. (2005). Runx1 deficiency predisposes mice to T-lymphoblastic lymphoma. *Blood* 106 (10): 3621–3624.

180 You, Q., Su, H., Wang, J. et al. (2018). Animal models of T-cell acute lymphoblastic leukemia: mimicking the human disease. *J. BioX Res.* 1 (1): 32–40.

181 Custer, R.P., Bosma, G.C., and Bosma, M.J. (1985). Severe combined immunodeficiency (SCID) in the mouse. Pathology, reconstitution, neoplasms. *Am. J. Pathol.* 120 (3): 464–477.

182 Prochazka, M., Gaskins, H.R., Shultz, L.D., and Leiter, E.H. (1992). The nonobese diabetic scid mouse: model for spontaneous thymomagenesis associated with immunodeficiency. *Proc. Natl. Acad. Sci. U.S.A.* 89 (8): 3290–3294.

183 Lin, Y.-W., Nichols, R.A., Letterio, J.J., and Aplan, P.D. (2006). Notch1 mutations are important for leukemic transformation in murine models of precursor-T leukemia/lymphoma. *Blood* 107 (6): 2540–2543.

184 Tillman, H., Janke, L.J., Funk, A. et al. (2020). Morphologic and immunohistochemical characterization of spontaneous lymphoma/leukemia in NSG mice. *Vet. Pathol.* 57 (1): 160–171.

185 Linette, G.P., Hess, J.L., Sentman, C.L., and Korsmeyer, S.J. (1995). Peripheral T-cell lymphoma in lckpr-bcl-2 transgenic mice. *Blood* 86 (4): 1255–1260.

186 Pechloff, K., Holch, J., Ferch, U. et al. (2010). The fusion kinase ITK-SYK mimics a T cell receptor signal and drives oncogenesis in conditional mouse models of peripheral T cell lymphoma. *J. Exp. Med.* 207 (5): 1031–1044.

187 Cutucache, C.E. and Herek, T.A. (2016). Burrowing through the heterogeneity: review of mouse models of PTCL-NOS. *Front. Oncol.* 6: 206.

188 Roberts, C.W., Leroux, M.M., Fleming, M.D., and Orkin, S.H. (2002). Highly penetrant, rapid tumorigenesis through conditional inversion of the tumor suppressor gene Snf5. *Cancer Cell* 2 (5): 415–425.

189 Allchin, R.L., Kelly, M.E., Mamand, S. et al. (2019). Structural and diffusion weighted MRI demonstrates responses to ibrutinib in a mouse model of follicular helper (Tfh) T-cell lymphoma. *PLoS One* 14 (4): e0215765.

190 Beyersdorf, N., Werner, S., Wolf, N. et al. (2011). Characterization of a new mouse model for peripheral T cell lymphoma in humans. *PLoS One* 6 (12): e28546.

191 Fehniger, T.A., Suzuki, K., VanDeusen, J.B. et al. (2001). Fatal leukemia in interleukin-15 transgenic mice. *Blood Cells Mol. Dis.* 27 (1): 223–230.

192 Yokohama, A., Mishra, A., Mitsui, T. et al. (2010). A novel mouse model for the aggressive variant of NK cell and T cell large granular lymphocyte leukemia. *Leuk. Res.* 34 (2): 203–209.

193 Mishra, A., Liu, S., Sams, G.H. et al. (2012). Aberrant overexpression of IL-15 initiates large granular lymphocyte leukemia through chromosomal instability and DNA hypermethylation. *Cancer Cell* 22 (5): 645–655.

194 Baldassarre, G., Fedele, M., Battista, S. et al. (2001). Onset of natural killer cell lymphomas in transgenic mice carrying a truncated HMGI-C gene by the chronic stimulation of the IL-2 and IL-15 pathway. *Proc. Natl. Acad. Sci. U.S.A.* 98 (14): 7970–7975.

195 Abbott, D.P., Masson, M.T., and Bonnet, M.C. (1991). A condition resembling pagetoid reticulosis in a laboratory mouse. *Lab. Anim.* 25 (2): 153–155.

196 Lohmiller, J.J., Swing, S.P., Valli, V.E.O., and Li, X. (1999). Epidermotropic lymphoma (mycosis fungoides) in an ICR mouse. *Contemp. Top. Lab. Anim. Sci.* 38 (5): 47–49.

197 Mishra, A., La Perle, K., Kwiatkowski, S. et al. (2016). Mechanism, consequences, and therapeutic targeting of abnormal IL15 signaling in cutaneous T-cell lymphoma. *Cancer Discovery* 6 (9): 986–1005.

198 Fanok, M.H., Sun, A., Fogli, L.K. et al. (2018). Role of dysregulated cytokine signaling and bacterial triggers in the pathogenesis of cutaneous T-cell lymphoma. *J. Invest. Dermatol.* 138 (5): 1116–1125.

199 Wu, X. and Hwang, S.T. (2018). A microbiota-dependent, STAT3-driven mouse model of cutaneous T-cell lymphoma. *J. Invest. Dermatol.* 138 (5): 1022–1026.

Vet-ebooks.com

200 Doebbeling, U. (2010). A mouse model for the Sézary syndrome. *J. Exp. Clin. Cancer Res.* 29 (1): 11.

201 Thaler, S., Burger, A.M., Schulz, T. et al. (2004). Establishment of a mouse xenograft model for mycosis fungoides. *Exp. Dermatol.* 13 (7): 406–412.

202 van der Fits, L., Rebel, H.G., Out-Luiting, J.J. et al. (2012). A novel mouse model for Sézary syndrome using xenotransplantation of Sézary cells into immunodeficient RAG2(−/−) γc(−/−) mice. *Exp. Dermatol.* 21 (9): 706–709.

203 Turner, S.D. and Alexander, D.R. (2005). What have we learnt from mouse models of NPM-ALK-induced lymphomagenesis? *Leukemia* 19 (7): 1128–1134.

204 Giuriato, S., Foisseau, M., Dejean, E. et al. (2010). Conditional TPM3-ALK and NPM-ALK transgenic mice develop reversible ALK-positive early B-cell lymphoma/leukemia. *Blood* 115 (20): 4061–4070.

205 Kuefer, M.U., Look, A.T., Pulford, K. et al. (1997). Retrovirus-mediated gene transfer of NPM-ALK causes lymphoid malignancy in mice. *Blood* 90 (8): 2901–2910.

206 Chiarle, R., Gong, J.Z., Guasparri, I. et al. (2003). NPM-ALK transgenic mice spontaneously develop T-cell lymphomas and plasma cell tumors. *Blood* 101 (5): 1919–1927.

207 Lange, K., Uckert, W., Blankenstein, T. et al. (2003). Overexpression of NPM-ALK induces different types of malignant lymphomas in IL-9 transgenic mice. *Oncogene* 22 (4): 517–527.

208 Jäger, R., Hahne, J., Jacob, A. et al. (2005). Mice transgenic for NPM-ALK develop non-Hodgkin lymphomas. *Anticancer Res.* 25 (5): 3191–3196.

209 Shoumariyeh, K., Schneider, N., Poggio, T. et al. (2019). A novel conditional NPM-ALK-driven model of CD30+ T-cell lymphoma mediated by a translational stop cassette. *Oncogene* https://doi.org/10.1038/s41388-019-1058-1.

210 Malcolm, T.I.M., Villarese, P., Fairbairn, C.J. et al. (2016). Anaplastic large cell lymphoma arises in thymocytes and requires transient TCR expression for thymic egress. *Nat. Commun.* 7: 10087.

211 Fehniger, T.A., Suzuki, K., Ponnappan, A. et al. (2001). Fatal leukemia in interleukin 15 transgenic mice follows early expansions in natural killer and memory phenotype CD8+ T cells. *J. Exp. Med.* 193 (2): 219–231.

212 Yu, J., Mitsui, T., Wei, M. et al. (2011). NKp46 identifies an NKT cell subset susceptible to leukemic transformation in mouse and human. *J. Clin. Invest.* 121 (4): 1456–1470.

213 Godfrey, D.I., MacDonald, H.R., Kronenberg, M. et al. (2004). NKT cells: what's in a name? *Nat. Rev. Immunol.* 4 (3): 231–237.

214 Eberl, G., Lees, R., Smiley, S.T. et al. (1999). Tissue-specific segregation of CD1d-dependent and CD1d-independent NK T cells. *J. Immunol.* 162 (11): 6410–6419.

215 Lee, E.N., Park, J.K., Lee, J.-R. et al. (2011). Characterization of the expression of cytokeratins 5, 8, and 14 in mouse thymic epithelial cells during thymus regeneration following acute thymic involution. *Anat. Cell Biol.* 44 (1): 14–24.

216 Pearse, G. (2006). Histopathology of the thymus. *Toxicol. Pathol.* 34 (5): 515–547.

217 Stutman, O., Yunis, E.J., and Good, R.A. (1968). Carcinogen-induced tumors of the thymus. I. Restoration of neonatally thymectomized mice with a functional thymoma. *J. Natl. Cancer Inst.* 41 (6): 1431–1452.

218 Hoot, G.P. and Kettman, J.R. (1989). Primary polyoma virus-induced murine thymic epithelial tumors. A tumor model of thymus physiology. *Am. J. Pathol.* 135 (4): 679–695.

219 Lee, S., Jang, J., Seo, J. et al. (1997). Thymic tumor progression in SV40T transgenic mice model. In: *Epithelial Tumors of the Thymus; Pathology, Biology, Treatment* (eds. A. Marx and H. Muller-Hermelink), 135–153. New York, New York: Springer Science+Business Media.

Vet-ebooks.com

9

Immunodeficient and Humanized Mice

Sara F. Santagostino, Sébastien Monette, Alessandra Piersigilli, Virginia L. Godfrey, and Harm HogenEsch

Introduction

Immunological studies in mutant mice have contributed immensely to our understanding of the immune system. Spontaneous mutations arising in inbred strains of mice and later the creation of genetically engineered mice have provided critical new insights that formed the foundations of our knowledge of the immune system and the immune response to infections and neoplasms. However, translation of discoveries made in mice to human patients has been challenging and resulted in costly failures in drug development. Anatomical, genetic, and physiological differences between mice and humans extend to the immune system [1]. Immunodeficient mice have been used to graft human tumor cell lines and primary tumor samples. The first patient-derived xenograft experiment, involving a human colon carcinoma transplanted in a nude mouse, was described in 1969 [2] shortly after the report of thymic aplasia in this mutant mouse [3]. To better study the interaction between tumors and the immune system, scientists have attempted to create humanized mice in which certain types of hematopoietic cells are replaced with human cells. Such mice have found applications not only in cancer research but also in the study of infectious and immune-mediated diseases [4, 5].

Over 30 spontaneous mutations in inbred strains of mice that lead to functional immune defects were reviewed in 1987 [6]. Since then, additional phenotypes have been described as a result of naturally occurring mutations, including alymphoplasia (mice lacking lymph nodes and Peyer's patches due to a mutation in *Map3k14*) [7] and chronic proliferative dermatitis (mice lacking follicles and germinal centers due to a mutation in the *Sharpin* gene) [8]. Many other mice with immune system abnormalities have been created through genetic engineering [9]. This chapter focuses on immunodeficient mice that are commonly used in preclinical biomedical research (Table 9.1).

Nude Mice

Nude mice (*Foxn1*$^{nu/nu}$) fail to express the transcription factor FOXN1 which is essential for the differentiation of thymic epithelial cells from endodermal precursor cells of the third endopharyngeal pouch and their function in guiding T cell development. A cystic vestige of the thymus may be present in the cranial mediastinum [10]. The mice lack grossly visible hair because of defective development of hair shafts and have abnormal nails and vibrissae [11, 12]. The thymic and cutaneous phenotypes are the results of altered regulation of keratin and keratin-associated protein expression levels [13]. The mice are severely deficient in T cells, although functional T cells can be detected in older mice. Lymphoid hypoplasia of T cell areas in secondary lymphoid organs such as the periarteriolar lymphocyte sheath of the spleen, paracortex of the lymph node, and interfollicular areas of Peyer's patches is seen.

Nude mice have increased macrophage and natural killer (NK) cell activity [6, 14]. The acceptance rate of xenografts and response to therapies is variable and dependent on the inbred strains or outbred stocks on which this mutation is placed [15, 16]. Although mice with more severe immunodeficiencies are available, nude mice remain popular because of the relatively low cost and ease of visualization and measurement of tumors implanted underneath the skin.

Prkdc^{scid}, *Rag1* and *Rag2*-Deficient, and *Lyst*^{bg} Mice

Severe combined immunodeficiency (SCID) (*Prkdc*^{scid}) mice are deficient in B and T cells because of a mutation in protein kinase, DNA-activated, catalytic (PRKDC) subunit. PRKDC is a component of a multiprotein DNA repair complex that is involved in somatic recombination events of the immunoglobulin and T cell receptor loci required for expression of functional antibody and T cell receptor molecules.

Pathology of Genetically Engineered and Other Mutant Mice, First Edition. Edited by John P. Sundberg, Peter Vogel, and Jerrold M. Ward.
© 2022 John Wiley & Sons, Inc. Published 2022 by John Wiley & Sons, Inc.

Vet-ebooks.com

Table 9.1 Common genetic mutations in immunodeficient strains used in biomedical research.

Common name of strain/stock	Mutation(s)	T cells	B cells	Innate lymphoid cells (other than NK)	NK cells	Macrophages	Hemolytic complement (C5)	Comments
Nude (multiple strains/stocks)	*Foxn1*^{nu}	–	+	+	+[a]	+	+	
scid (multiple strains)	*Prkdc*^{scid}	– (leaky)	– (leaky)	+	+[a]	+	+	Radiosensitive; short life span (40–80 wk; thymic lymphoma)
Rag1 deficient (multiple strains)	*Rag1*^{tm1Mom}	–	–	+	+[a]	+	+	
Rag2 deficient (multiple strains)	*Rag* ^{tm1Fwa}	–	–	+	+[a]	+	+	
NOD *scid*	*Prkdc*^{scid}	– (leaky)	–	+	⇓	⇓	–	Radiosensitive; short life span (37 weeks; thymic lymphoma); *Sirpa*-allele[b]
scid beige	*Prkdc*^{scid}, *Lyst*^{bg}	–	–	+	⇓[c]	+	+	Radiosensitive
IL2RG chain deficient	*Il2rg*^{tm1Wjl}	⇓	⇓ (B2)[d]	–	–	+	+	
NSG	*Prkdc*^{scid}, *Il2rg*^{tm1Wjl}	–	–	–	–	⇓	–	Radiosensitive; *Sirpa*-allele[b]
NOG	*Prkdc*^{scid}, *Il2rg*^{tm1Sug}	–	–	–	–	⇓	–	Radiosensitive; *Sirpa*-allele[b]
NRG	*Rag1*^{tm1Mom}, *Il2rg*^{tm1Wjl}	–	–	–	–	⇓	–	*Sirpa*-allele[b]
BRG	*Rag2*^{tmFwa1}, *Il2rg*^{tm1Sug}	–	–	–	–	⇓	+	

[a] Strain-related variability exists.
[b] "Don't eat me" signal.
[c] Present with severely reduced activity (functionally inactive).
[d] Conventional B cells.

Vet-ebooks.com

However, with age, an increasing number of functional B and T cells, and immunoglobulin production are observed in *scid* mice. This phenomenon is known as leakiness and indicates that somatic recombination can occur in the absence of PRKDC, although at reduced rate. The incidence of leakiness is generally high on the C57BL/6J and BALB/cByJ backgrounds, while it remains low on the C3H/HeSnJSmn background [17]. By eight months of age, nearly all *Prkdc*^{scid} mice have detectable concentrations of serum IgM. Myeloablation by total-body irradiation (TBI) of recipient mice is commonly performed prior to transplantation of human hematopoietic cells. As DNA repair is necessary to protect cells from radiation injury, lack of efficient DNA repair makes the *Prkdc*^{scid} mice much more sensitive to radiation. RAG1 and RAG2 are essential components of the multiprotein recombinase complex that catalyzes somatic recombination of the immunoglobulin and T cell receptor loci. Mice that lack *Rag1* or *Rag2* null mutations have no functional B and T cells. In contrast to *Prkdc*^{scid} mice, *Rag* ^{tm1Mom} and *Rag2* ^{tm1Fwa} mice are not leaky and do not have increased sensitivity to radiation.

Prkdc^{scid}, *Rag1*^{tm1Mom}, and *Rag2*^{tm1Fwa} mice have similar changes in the thymus and secondary lymphoid organs, including severe and diffuse lymphoid hypoplasia [18] and a small thymic anlage composed of epithelial cells. Mucosal lymphoid tissues are absent.

The *Lyst*^{bg} mutation causes defective lysosomal trafficking resulting in a condition in mice that closely resembles Chediak–Higashi syndrome in humans, which is caused by a mutation of the human ortholog *LYST*. Immune defects include decreased NK cell and granulocyte activity [19, 20]. This mutation has been crossed with *Prkdc*^{scid} mice to create strains known as SCID beige, such as CB17.Cg-*Prkdc*^{scid}*Lyst*$^{bg\text{-}J}$/Crl. Phenotypes resulting from *Lyst*^{bg} in these mice also include abnormal melanosomes causing the beige hair coat color and giant lysosome formation in numerous cell types [21], including renal tubular cells and leukocytes in which cytoplasmic inclusions representing giant lysosomes can be observed on histology and blood smears, respectively (Figure 9.1).

Immunodeficient mouse mutants obtained by classical gene targeting or, more recently, by the CRISPR/Cas9 system (FVB-*Rag2*^{em1Hwl}, B6-*Rag2*^{em2Hwl}, and BALB/c- *Prkdc*^{em1Hwl}) share similar immunodeficient phenotypes [22].

NOD-*Prkdc*^{scid} Mice

Crossing *Prkdc*^{scid} mice with nonobese diabetic NOD/ShiLtJ (NOD) mice greatly reduces the leakiness and combines adaptive immune system deficiencies with several defects in the innate immune system including a lack of complement component C5 and decreased NK cell and macrophage function [23]. In addition, the NOD mouse expresses an allelic variant of signal regulatory protein alpha (SIRPA, also known as CD172A). This protein is expressed on macrophages and other myeloid cells and is a receptor for CD47 expressed by many cell types [24]. Engagement of CD47 by SIRPA suppresses phagocytosis ("don't eat me" signal). The common variant of mouse SIRPA does not recognize CD47 expressed on human cells, but the NOD allele does [24]. This prevents phagocytosis of human cells engrafted in NOD.Cg-*Prkdc*^{scid} (NOD-*scid*) mice and results in an increased engraftment rate.

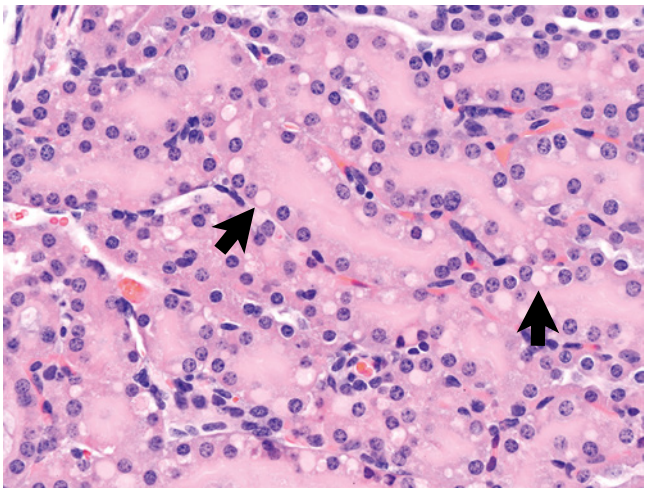


Figure 9.1 Kidney of a CB17.Cg-*Prkdc*^{scid}*Lyst*^{bg}-J/Crl mouse. Renal tubules contain numerous intracytoplasmic eosinophilic inclusions representing giant lysosomes (arrows), a phenotype resulting from the *Lyst*^{bg} mutation and frequently observed in beige and SCID beige strains. Hematoxylin and eosin (HE) staining. Source: Courtesy of S. Monette, MSKCC (unpublished).

IL-2RG-Deficient Mice

Interleukin-2 receptor gamma chain (IL-2RG, also known as CD132) is an essential component of the receptors for IL-2, IL-4, IL-7, IL-9, IL-15, and IL-21. The absence of a functional IL-2RG results in severe defects in B and T cell development, absence of NK cells and other innate lymphoid cells [25–27]. These mice have been crossed with *Prkdc*^{scid}, *Rag1*^{tm1Mom}, *Rag2*^{tm1Fwa} and NOD/ShiLt mice to create highly immunodeficient mice with a high acceptance rate of human cells and tissues.

The NOD.Cg-*Prkdc*^{scid} *Il2rg*^{tm1Wjl} (NSG) mice, the NODShi.Cg-*Prkdc*^{scid}*Il2rg*^{tm1Su} (NOG), and the C;129S4-*Rag2*^{tm1Flv}*Il2rg*^{tm1Flv} (BRG) mice have different *Il2rg* alleles resulting in a similar phenotype. NOG mice have a truncated intracytoplasmic domain of the IL-2RG and therefore permits cytokine binding but no signaling [28]; conversely, the IL-2RG in NSG and BRG mice is lacking. Representative morphologic features of hematolymphoid organs in NSG mice are shown in Figures 9.2–9.4.

B6-*Il2rg*^{em1Hwl} mice generated via CRISPR/Cas9 system have a unique phenotype, with a lack of mature B cells, increased number of T cells, and detectable serum IgM [22].

Vet-ebooks.com

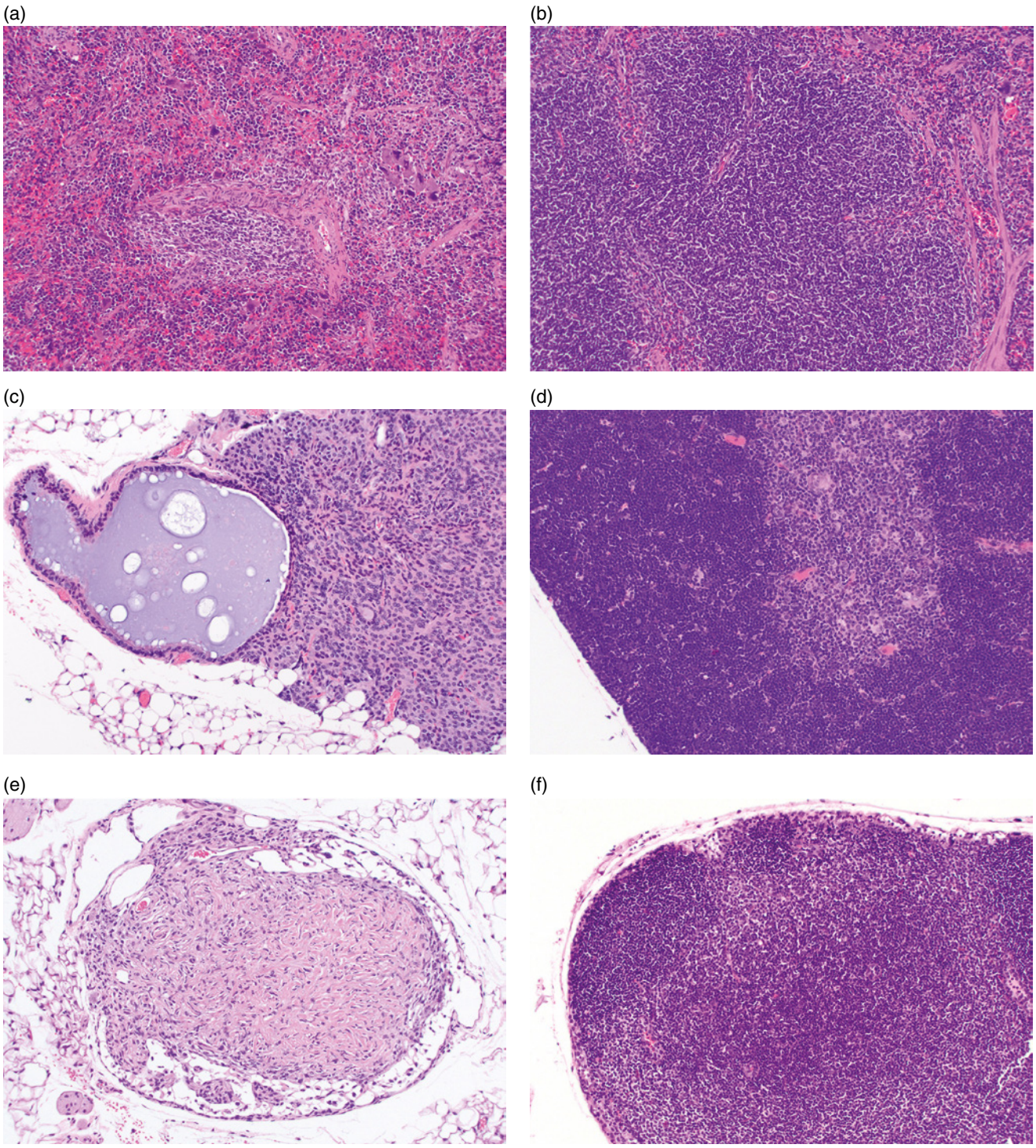


Figure 9.2 **Representative sections of lymphoid organs**. The spleen (a), thymus (c), and mesenteric lymph node (e) of NOD.Cg-*Prkdc*^{scid} *Il2rg*^{tm1Wjl} (NSG) mice lack discernible lymphoid cells and structures that are typically seen in immunocompetent C57BL/6J mice (spleen, b; thymus, d; mesenteric lymph node, f). Additionally, cystic epithelial structures may be observed in the thymus of NSG mice (c). HE staining. Source: Courtesy of S. Monette, MSKCC (unpublished).

Vet-ebooks.com

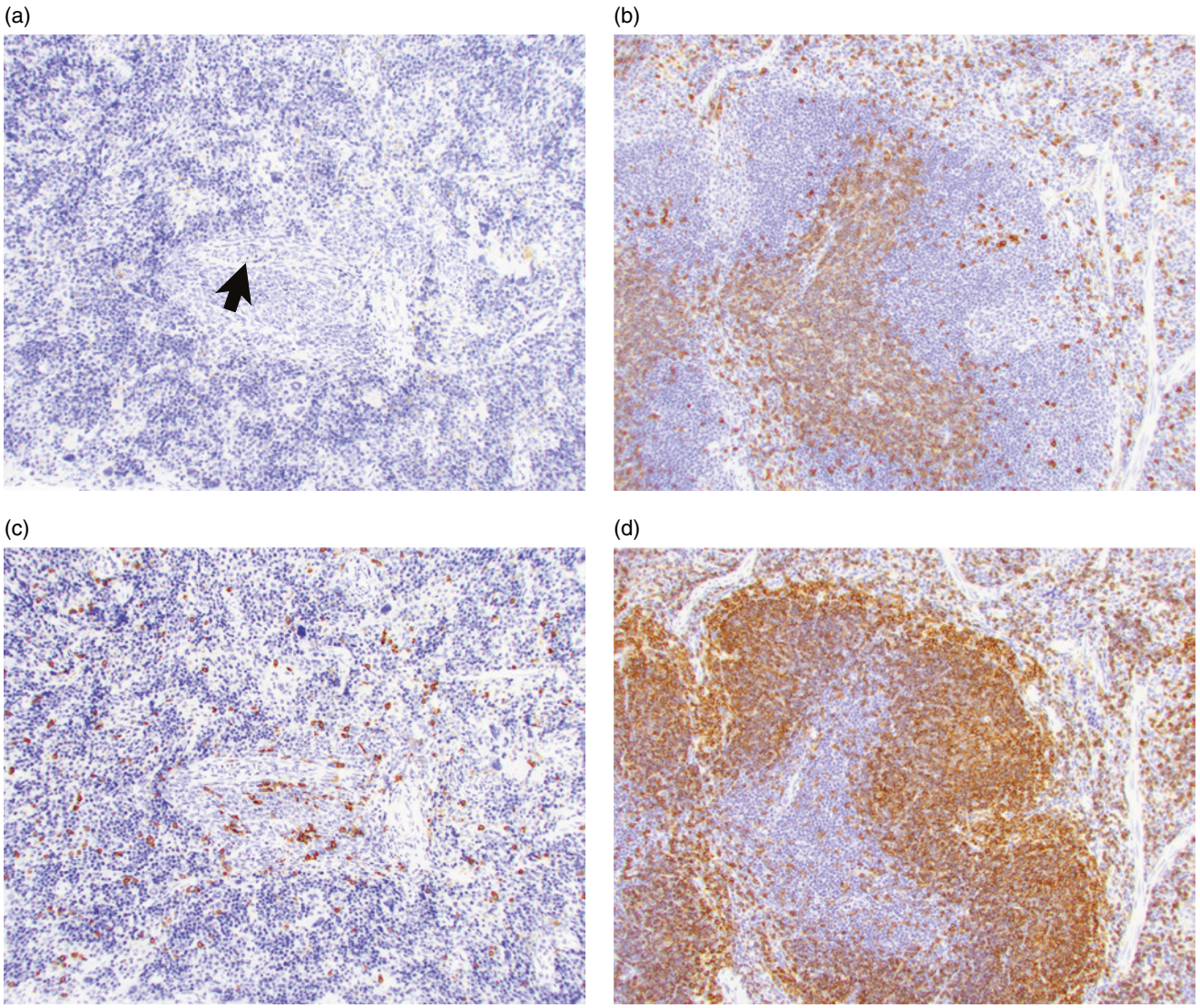


Figure 9.3 **Representative sections of spleen**. The spleen of NOD.Cg-*Prkdc*^{scid} *Il2rg*^{tm1Wjl} mice (left column) contains severely reduced numbers of lymphocytes typically seen in immunocompetent C57BL/6J mice (right column), and minimally developed white pulp centered on arterioles (arrow). IHC staining, CD3 for T cells (a, b), B220 for B cells (c, d). Source: Courtesy of S. Monette, MSKCC (unpublished).

Uses of Immunodeficient Mouse Models

Xenotransplants of Solid and Hematopoietic Human Patient-Derived Tumors or Neoplastic Cell Lines

Patient-derived xenografts (PDX) and implants of human neoplastic cell lines are a tool used to overcome the translational gap between the biology of spontaneous and induced mouse tumors and that one of human neoplasms [29]. Both methods rely upon the engraftment of human cells or small fragments of surgically resected tumors into a mouse recipient (Figure 9.5). The characterization of the human tumor tissue before and after the engraftment provides important information about the fitness of the tumor and its biology, including the response to different therapeutics. PDX models have the potential to determine the effects of single-agent treatment and combination therapies. PDX models aid in the therapeutic decision-making and offer improved preclinical modeling for personalized therapy by acting as unique testing platforms for the engraftment of tumors from specific patients [30]. Thanks to their small size, short life span, affordable costs, and inbred genetics and genetic homologies with humans, mice are good recipients for PDX models. Implants of human-derived tumor cells into a mouse

Vet-ebooks.com

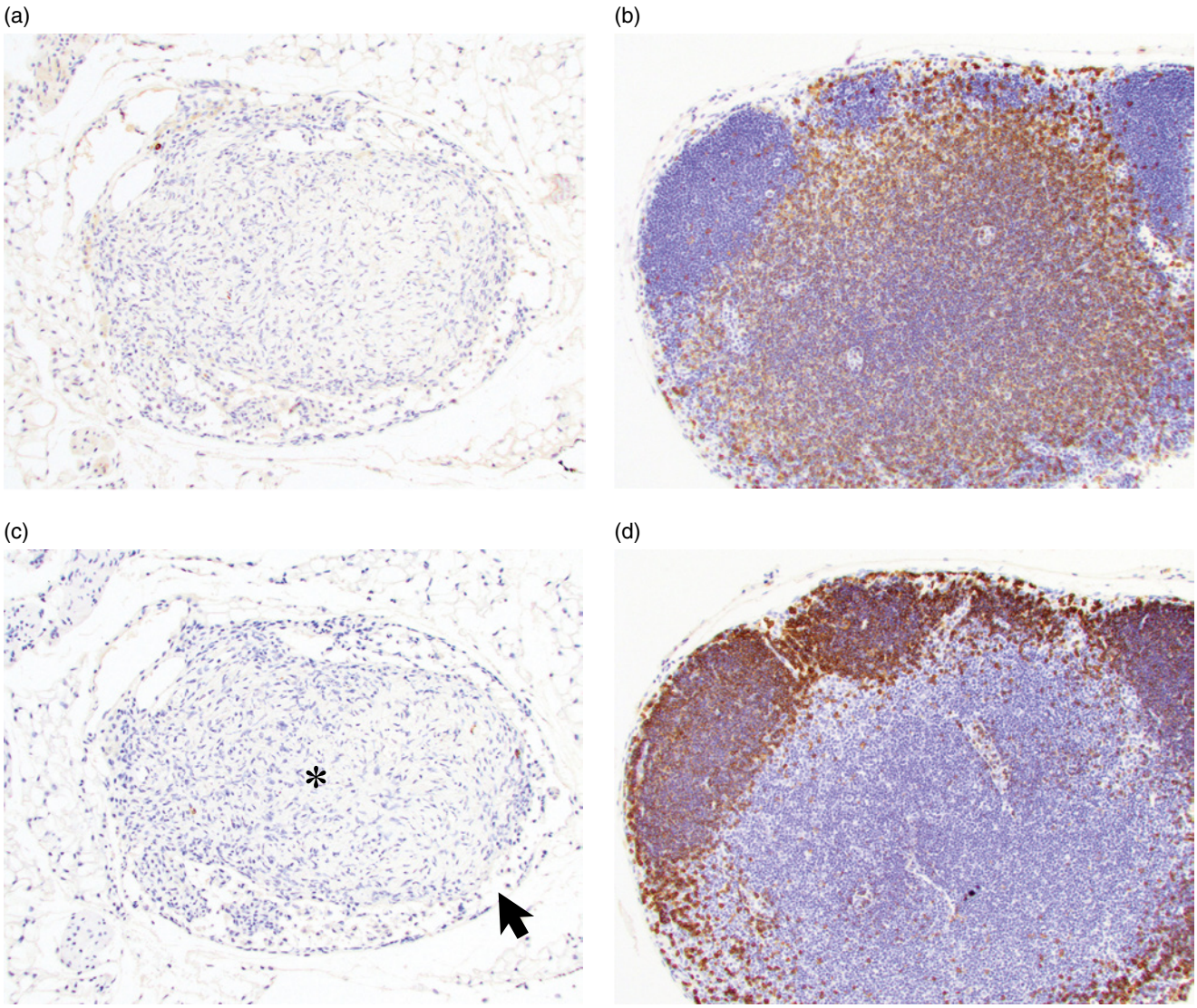


Figure 9.4 **Representative sections of lymph node**. The cortical and medullary structures of the mesenteric lymph nodes are not appreciable in NOD.Cg-*Prkdc*^{scid} *Il2rg*^{tm1Wjl} mice (left column) compared to the typical nodal structure seen in immunocompetent C57BL/6J mice (right column), and lymphocytes are extremely rare or absent, although lymph node stroma (asterisk) and subcapsular sinuses are observed (arrow). IHC staining, CD3 for T cells (a, b), B220 for B cells (c, d). Source: Courtesy of S. Monette, MSKCC (unpublished).

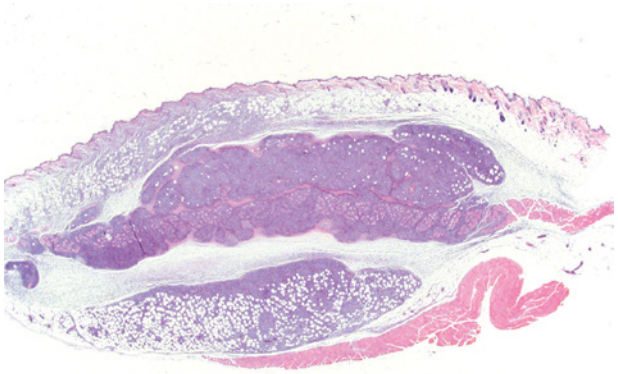
recipient can yield variable amounts and types of data that are influenced by the factors listed below (also see Table 9.2).

Source of tumor material: Tumor samples to generate PDX models can be obtained from surgical resections, biopsies, autopsies, and fluids collections [30]. Aside from immediate availability of tumor specimens from selected patients in hospital settings, human xenograft material and mice carrying xenografts are available from a number of vendors for research purposes. PDX models can be identified and requested through online databases (http://tumor.informatics.jax.org/mtbwi/pdxSearch.do; http://www.pdxfinder.org). Selection criteria to identify the optimal specimens include information on the anatomic system and cancer of interest, stage, treatment status, molecular and genomic characteristics, and providers.

Tissue preservation and transfer: For PDX models, timely tissue transfer from the patient to the mouse is crucial as prolonged tissue ischemia impairs engraftment [31]. While cryopreservation is commonly used to store tissues and cells even in large repositories and allow a variety of different lesions to be readily available, some methods for cryopreservation can impact cell viability [32]. Ice crystals can form when standard freezing is used, resulting in cell damage and cell death. As part of tumor heterogeneity, various clones can tolerate temperature changes differently; the same applies to the infiltrating inflammatory cells [33]. Applying

Vet-ebooks.com

(a)



(b)

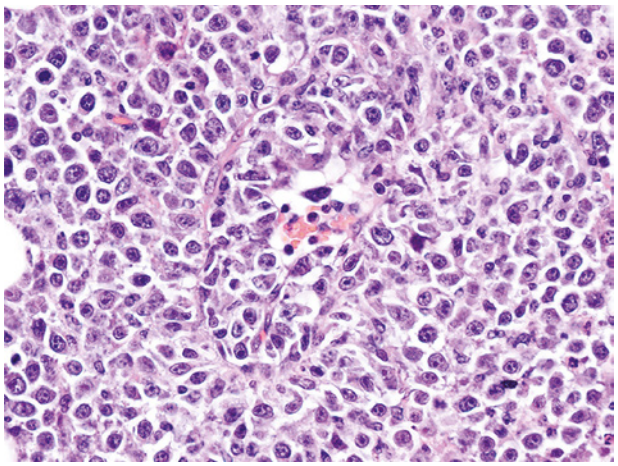


Figure 9.5 **Heterotopic implantation (subcutis)**. A patient-derived lymphoma implanted in the subcutis of in an immunodeficient mouse (a). The neoplastic population is composed of pleomorphic round cells with frequent mitotic figures (b). HE staining. Source: Courtesy of A. Piersigilli, WCM (unpublished data).

Table 9.2 A comparison of advantages and disadvantages offered by PDX models and implants of cell lines.

PDX	Cell line xenografts
Source of material	*Source of material*
Tumor fragments obtained surgically or at autopsy	Immortalized cell lines maintained *in vitro*
Cell suspensions from cavitary fluids	
Blood/bone marrow aspirates	
Advantages	*Advantages*
Genetic and phenotypic heterogeneity (representative of the single patient)	Requires low level of immunodeficiency for engraftment
Includes tumor microenvironment (in bioptic fragments)	Standardized and homogeneous features
	Abundant published information on commonly used cell lines (commercial cell lines)
	Readily available and in large amounts (commercial cell lines)
	Limited invasiveness of the implantation procedure
	High engraftment rate
	Short latency between implantation and tumor development (days)
	Synchronous tumors (similar rate growth within multiple primary tumors in the same mouse or across a given cohort of mice engrafted at the same time)
	Ease to manipulate *in vitro* (genetic mutation, gene reporters, bioluminescent tags, etc.)
	Inexpensive
Disadvantages	*Disadvantages*
Requires high level of immunodeficiency for engraftment	Loss of morphologic and biologic features of the original tumor due to serial passages *in vitro*
Variable biologic behavior	Poorly representative of the biology of tumor of origin
Invasive procedure for implantation of tumor fragment samples	Lack of tumor donor microenvironment
Possibility to alter the tumor engraftment and tumor associated inflammatory infiltrate	Possible contamination with bacteria or other cell types affecting the behavior of the primary tumor cells
Limited availability of material	Large necrotic areas
Limited information	
Variable engraftment (timely tissue transfer, cryopreservation technique, etc.)	
Long latency between implantation and tumor development (weeks/months)	
Expensive passaging and banking is complex and expensive	
Large necrotic areas	
Multiple tumor clones with different fitness compared to a monotypic cell line	

Source: Adapted from Uthamanthil and collaborators [30].

Vet-ebooks.com

cold temperature for cryopreservation introduces a selective pressure on the tumor cell pool, allowing survival of only those clones that tolerate low temperature, significantly modifying molecular and phenotypic aspects of the original tumor [33]. The antigenicity of tissues is also impacted by the technique used for cryopreservation [34]. This can potentially have implications in tumor immunotherapy studies using cryopreserved PDX samples. While these factors could similarly influence the preservation of cell lines, a clear understanding of the parameters responsible for engraftment failure in mice implanted with cell lines is lacking.

Tumor intrinsic factors: The nature of tumor cells can impact PDX engraftment rates. High-grade primary malignancies and their metastases tend to more easily engraft [35, 36] than low-grade lesions, which have a limited success rate and/or require special conditions for engraftment [37]. Additionally, certain primary tumor types (e.g. colon adenocarcinomas, oral squamous cell carcinomas, and hepatocellular carcinomas) have a relatively more successful and consistent engraftment rate [36, 38, 39], while primary or metastatic prostate cancers are more challenging [40, 41]. Another limiting factor for PDX models is the presence of donor-derived T lymphocytes in the transplanted tissue. These lymphocytes have the ability to proliferate and induce a life-threatening xenogeneic graft-versus-host disease (GVHD) reaction [42]. In PDX models, cancer therapy in the patient prior to sampling can influence the engraftment success. Chemotherapeutic agents can act on tumor clone selection and favor the emergence of minor clones, often more aggressive, with a higher engraftment rate [30]. Furthermore, xenograft acute lymphoid leukemias (ALL) are frequently established from minor genetic subclones with less resemblance to the tumor population at the time of diagnosis in patients [43].

Implantation route: The engraftment rate depends greatly on the site of implantation of the cells or tissue fragment. Overall, implantation can be *orthotopic,* when the lesion is placed in the organ or tissue of origin of the neoplasm (e.g. human pancreatic cancer implanted into the mouse pancreas) or *heterotopic*, when the implantation site does not match the tissue of origin of the tumor (e.g. human pancreatic cancer into the subcutis). The orthotopic implant provides a more faithful niche or microenvironment to the xenograft, with greater chances to recapitulate molecular and biological aspects of the interplay between the tumor and the surrounding tissue [44]. For breast cancer, implantation into the inguinal fat pads seems to be correlated to higher engraftment rates compared to thoracic pads, confirming the fundamental importance of the microenvironment [45]. Furthermore, invasiveness and metastatic potential of the engrafted tumor can be influenced by the implantation site. As an example, intraductal injection of breast cancer tissue has been shown to yield invasive carcinomas as opposed to implantation of tumor fragments in the mammary fat pad [46].

Differences exist also in terms of treatment responses, with more translational power of data acquired from tumors implanted orthotopically [47]. Heterotopic implantation allows easy monitoring of the tumor longitudinally. However, the effect of the recipient stroma on tumor growth and behavior is amplified when implanted subcutaneously, as this microenvironment differs from the microenvironment of the tissue of origin. In some instances, implantation within visceral organs yields a much better engraftment. For example, by virtue of the highly vascularized nature of the kidney, the renal capsule provides some advantages compared to the subcutis [48]. However, implantation into visceral organs is clearly more invasive as it requires surgery leading to local inflammation with possible impact on the recipient and on the tumor itself [49]. Further, longitudinal monitoring of tumor growth becomes more challenging as it requires *in vivo* imaging equipment and trained personnel.

Mouse recipient: Immunodeficient mice offer a higher engraftment rate as the immune response mounted against the xenograft is limited or absent. Humanization of these models results in mice that model a competent human immune system capable of mounting anticancer immune responses. Such models have enhanced translational value and may be particularly useful for studying immunotherapeutic interventions. Although immunodeficient mice appear to be more versatile and permissive recipients, they can pose several issues. As commonly used mice are inbred, the diversity in the human population is not reflected. Additionally, variations in the diet, water quality, microbiome, environment temperatures, and enrichment programs may cause differences in tumor engraftment and growth rate between institutions [30]. Although xenograft tumor are generally implanted into immunodeficient mice, a few examples of implants in immunocompetent mice are available [50]. Despite the differences between the human and mouse immune system, and a high rate of graft rejection, mouse recipients with intact immune system allow the assessment of the dynamics between the immune response and the xenografted tumor [51].

Immunologic Reactions Against Transplanted Tumors

In PDX models, cotransplanted immune cells of B and T lineages can also react against tumor antigens and result in partial of complete effacement of the engrafted tumors. Unsuccessful melanoma engraftment associated with severe effacement of tumor xenografts by donor immune cells has been seen in mice engrafted with melanoma [42]. Although a definitive mechanism has not been discovered yet, the highly permissive recipient microenvironment of the immunodeficient mouse recipients could have contributed to select tumor clones able to mount an effective humoral immunity. In fact, as previously mentioned, variation in the spectrum of tumor-associated antigens and unmasking of novel antigens are frequently encountered in the context of xenotransplantation, and may play a role on the onset of such lesions [42].

Vet-ebooks.com

Humanized Mice

The term "humanized" mice has been used to describe immunodeficient mice engrafted with human hematopoietic cells and tissues that generate functional human immune system components [4]. Beginning with engraftment of human fetal liver and thymus into C.B-17-*Prkdc*^{scid} mice that resulted in transient human CD4+ and CD8+ T cells [52], these models have been greatly refined over the past decades to support a wide variety of human hematopoietic populations (Figure 9.6).

A typical procedure for generation of hematopoietic humanized mice includes selection of the appropriate immunodeficient mouse strain, a mild myeloablative treatment such as sublethal irradiation, and injection of purified CD34+ human hematopoietic stem cells (HSCs) with or without surgical implantation of human fetal liver and/or thymus to support the development of all lineages of human hematopoietic cells. Sources of CD34+ human stem cells include bone marrow, umbilical cord blood, and fetal liver, each with its own unique characteristics and varied potential for engraftment of different of hematopoietic lineages [53]. Receptivity of the mouse host has improved by combining inherent strain characteristics such as the reduced NK cell activity in NOD/ShiLt mice (compared to C.B17-scid mice) with spontaneous or targeted mutations in the interleukin-2 receptor common γ chain (*IL2rg*), and transgenes for human cytokines such as kit ligand (KITL, formerly called stem cell factor, SCF), colony stimulating factor 2 (granulocyte-macrophage) (CSF2, formerly granulocyte/macrophage colony-stimulating factor GM-CSF), and interleukin-3 (IL-3). The resulting NOD.Cg*Prkdc*^{scid}*Il2rg*^{tm1Wjl}Tg(CMV-IL3,CSF2, KITLG)1Eav/MloySz (NSG-SGM3) mouse supports development of human myeloid and dendritic cells, as well as more functional B and T lymphocytes, allowing both innate and adaptive immune responses from the human cells [54–56]. At least 12 variants of the NSG strain that include various other transgenes or targeted mutations have been created, resulting in modulation of engraftment of human hematopoietic cells or of the occurrence of GVHD (reviewed in [57]).

In addition to providing a model system to study human stem cells, hematopoiesis, and immunobiology, the humanized mouse has created a critical small animal model for the study of human-specific infectious agents targeting immune cells such as HIV, Epstein–Barr virus (EBV), Dengue virus, and *Salmonella enterica* serovar Typhi (*Salmonella typhi*). Other human-specific agents have additional tissue tropisms such as the need for human hepatocytes for hepatitis viruses and *Plasmodium falciparum* [58]. This multitissue need is met by creating double-chimeric mice with both humanized hematopoietic systems and mouse-human livers [59]. In this model, the NOD-*Rag1*^{null} *IL2rg*^{null} (NRG) mice lacking fumarylacetoacetate hydrolase (*Fah*^{em1Mvw}), the gene mutation causing hereditary tyrosinemia type I, receive intrasplenic injections of human CD34+ cells and adult human hepatocytes [60]. This double-chimeric model allows hepatitis virus infections to be studied in the presence of an autologous human immune response [54].

Common Lesions in Immunodeficient Mice

Experimentally Induced Lesions

Xenogeneic GVHD

GVHD is an immune-mediated condition that occurs when donor T cells recognize recipient tissues as foreign

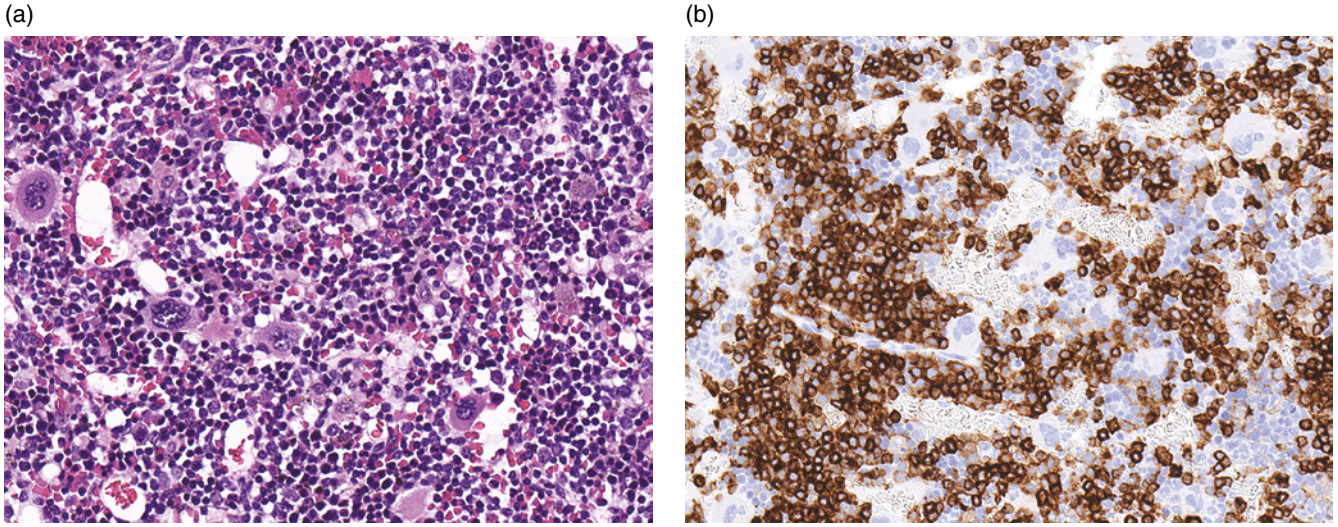


Figure 9.6 Bone marrow of a NOD.Cg-*Prkdc*^{scid} *Il2rg*^{tm1Wjl} mouse engrafted with human CD34+ hematopoietic stem cells. HE (a) and IHC staining for human-specific CD45-leukocyte common antigen (LCA) to show the degree of bone marrow chimerism (b). Mice were conditioned with busulfan 24 hours before transplantation. Source: Courtesy of E. Radaelli, University of Pennsylvania (unpublished).

Vet-ebooks.com

and induce tissue injury [42]. Allogeneic graft-versus-host disease (aGVHD) is a common adverse event following hematopoietic cell transplantation in human patients, and this can be modeled by the transfer of bone marrow between mice of different immunocompetent strains. In immunodeficient mouse models, the engraftment of human T cells through xenotransplantation of primary tumor samples PDXs containing cotransplanted human lymphoid cells, HSCs and human peripheral-blood mononuclear cells (hPBMCs) to create humanized mice can give rise to the human-into-mouse xenogeneic graft-versus-host disease (xGVHD).

The relative resistance of CBySmn.Cg-*Prkdc*^{scid} mice to GVHD is attributed to their residual innate immune system [61]. Susceptibility of NOD.Cg-*Prkdc*^{scid} and H-2^{d}-*RAG2*^{null}*Il2rg*^{null} mice to xGVHD requires sublethal TBI and relatively large doses of hPBMCs [61]. In NSG and NOG mice, the development of xGVHD occurs more readily with small doses of hPBMCs administered [61, 62]. The occurrence of xGVHD is a common limitation of these models and may introduce a confounding experimental variable.

Clinical findings occurring with xGVHD include prominent alopecia especially around the muzzle, the eyes and the ventrum, dry eyes, lethargy, and progressive wasting [42] (Santagostino, unpublished). Histologically, similarly to human a GVHD, hallmarks of xGVHD include interface dermatitis and hepatitis, as well as similar interface patterns on oral mucosal membranes [42, 63]. Cutaneous lesions are characterized by mononuclear cell infiltrates (primarily human T cells) abutting the basement membrane (Figure 9.7) and the adnexal units, epidermal vacuolar changes, keratinocyte apoptosis, and adnexal atrophy. In the liver, mononuclear cell infiltrates surround portal tracts and often breach through the limiting plates where they are associated with apoptotic hepatocytes. Multisystemic inflammatory perivascular and interstitial lymphocytic infiltrates composed of human T cells with or without associated tissue damage are seen mostly in lungs, spleen, kidneys, thyroid gland, salivary and lacrimal glands, and Harderian glands (Santagostino, unpublished). In contrast with human aGVHD, the gastrointestinal tract in mouse xGVHD is mostly spared [62] (Santagostino, unpublished).

Epstein–Barr Virus Induced Lymphoma

The unexpected occurrence of B cell lymphoma of human origin has been observed in various PDX cancer models in NSG and NOG mice, such as hepatocellular and prostatic carcinoma and melanoma models [42, 64, 65]. Evidence of EBV RNA within lymphoma cells was demonstrated by in situ hybridization (ISH), suggesting causation. Latent asymptomatic EBV infection is highly prevalent in humans, and the virus is known to contribute to posttransplant lymphoproliferative disorders, including B cell lymphoma in immunocompromised humans. It appears that the presence

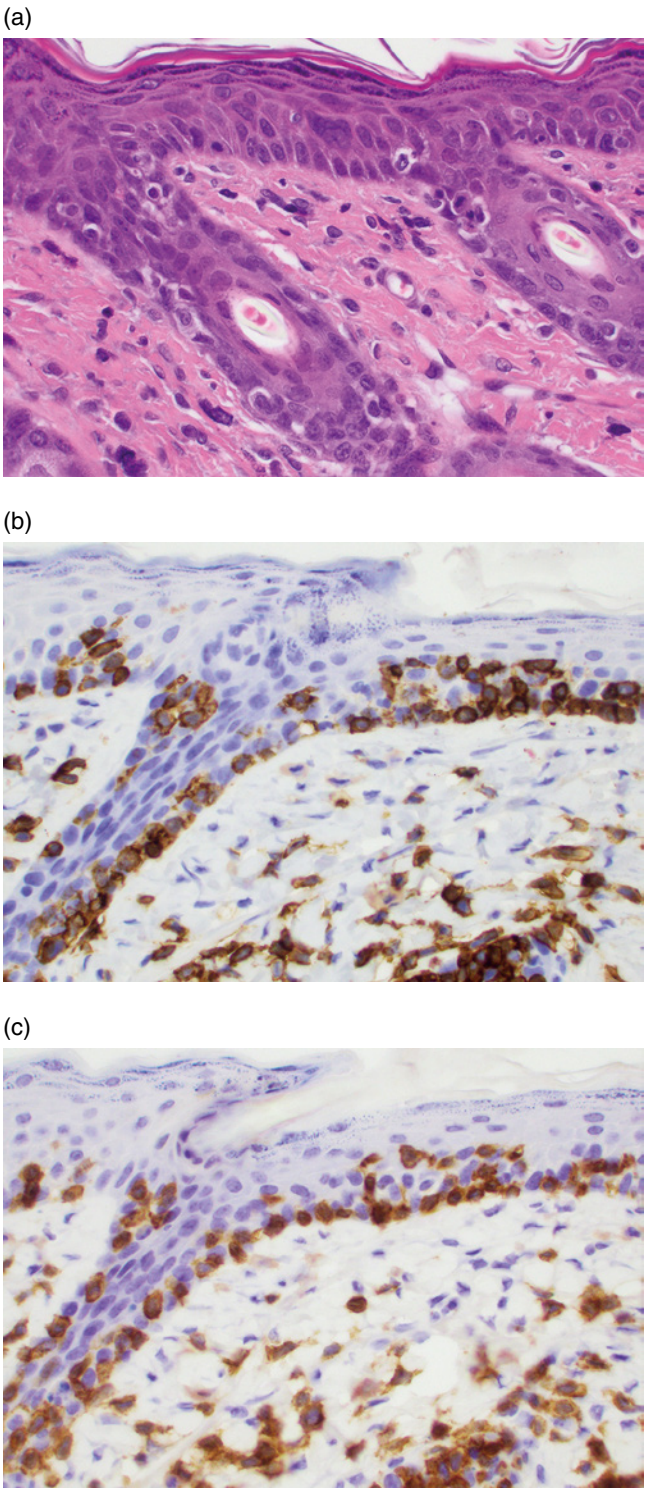


Figure 9.7 Skin of a NOD.Cg-*Prkdc*^{scid} *Il2rg*^{tm1Wjl} mouse. Inflammatory cells abutting the basement membrane and infiltrating the basal layer of the epidermis are present. The findings are consistent with an interface dermatitis. HE staining (a). Cellular infiltrates cells are positive for human CD45 (b) and CD3 (c). Source: Courtesy of S. Monette, MSKCC (unpublished).

Vet-ebooks.com

of normal human B cells and latent EBV infection in PDXs of any cancer type may result in a similar phenomenon in highly immunodeficient mice. In these cases, lymphoma is observed at the PDX implantation site, alone or in combination with the expected neoplasm, and metastatic lymphoma at distant sites may also be present. The lesions are classified as a diffuse large B cell lymphoma of human origin based on morphology and expression of human-specific immunohistochemistry (IHC) markers (CD45, CD19, CD20) (Figure 9.8). The lymphoma may be misinterpreted as the expected tumor model if histopathologic examination is not performed.

Posthematopoietic Transplant Bone Marrow Failure

As described earlier, TBI followed by hematopoietic cell transfer is commonly performed in immunodeficient mice. Failure of hematopoietic cells engraftment resulting in bone marrow failure is an occasional cause of unexpected morbidity and mortality in such studies [66, 67]. This complication may be caused by inadequate administration technique or insufficient number or quality of transferred cells. Marked anemia, leukopenia, and thrombocytopenia are typically noted on complete blood count. Lesions may include generalized pallor of the carcass, petechial hemorrhages, and severely decreased or absent hematopoietic cellularity in the bone marrow and splenic red pulp. When severe neutropenia occurs, septicemia is a common complication, usually caused by opportunists such as *Enterococcus faecalis* and *Staphylococcus xylosus*, and histopathology reveals abundant multisystemic intravascular bacterial colonies in the absence of an inflammatory response (Figure 9.9).

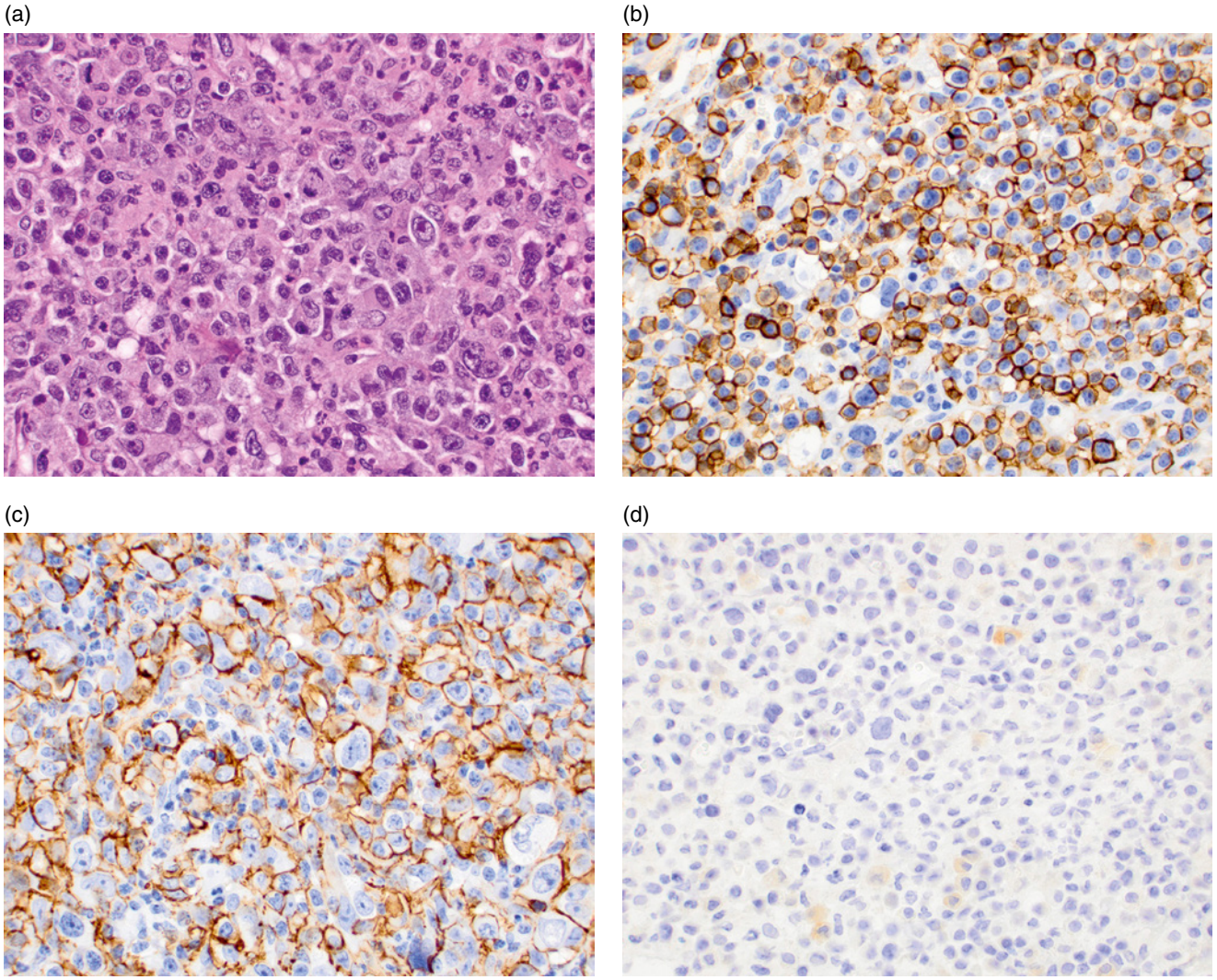


Figure 9.8 Diffuse large B cell lymphoma of human origin that occurred at the subcutaneous PDX implantation site of a human urothelial carcinoma in a NOD.Cg-*Prkdc*^{scid} *Il2rg*^{tm1Wjl} mouse. HE (a) and IHC staining for human CD45 (b), human CD20 (c), and CD3 (d). Source: Courtesy of S. Monette, MSKCC (unpublished).

Vet-ebooks.com

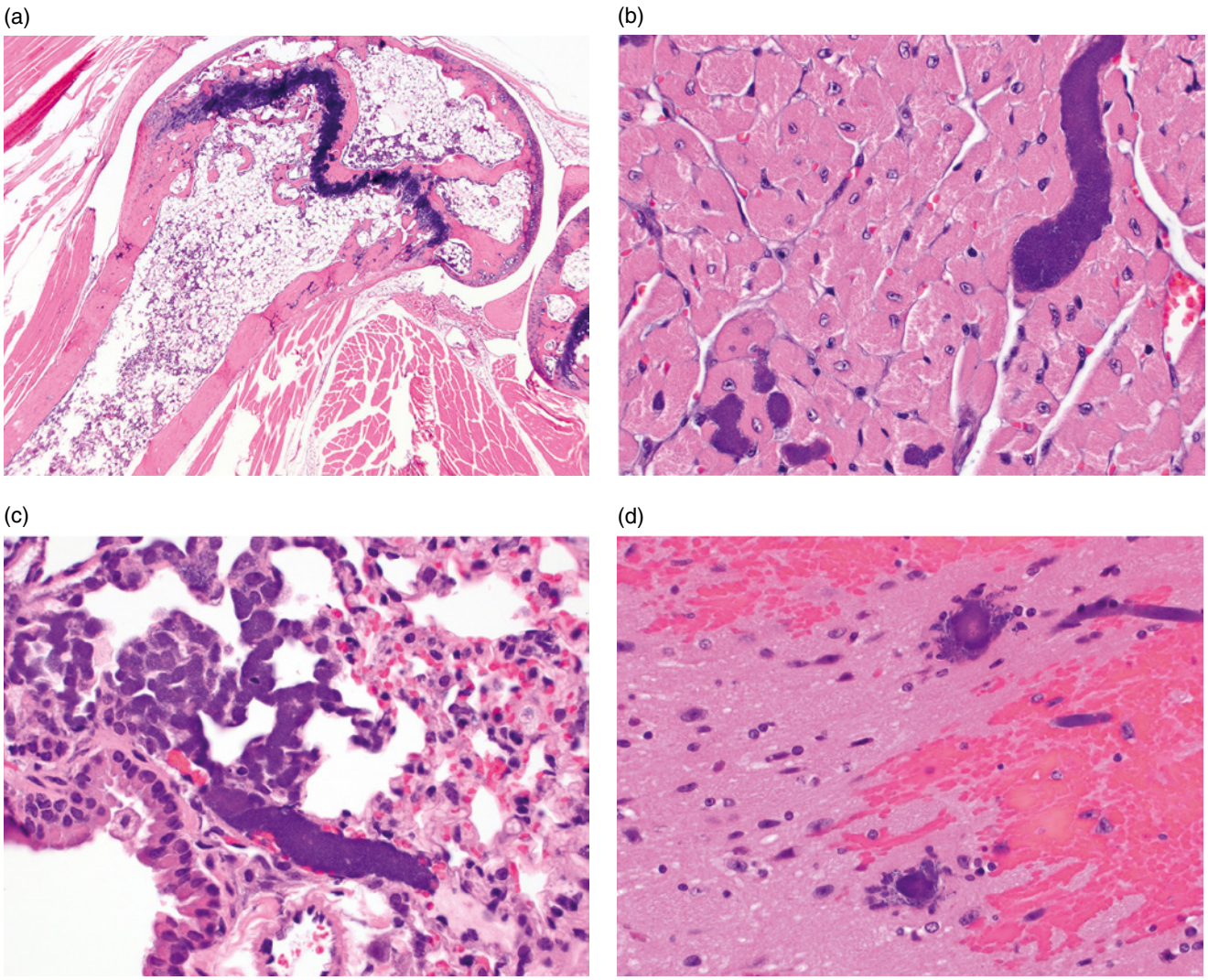


Figure 9.9 Bone marrow failure with secondary septicemia after irradiation and hematopoietic cell transfer that failed to engraft in a NOD.Cg-*Prkdc*^{scid} *Il2rg*^{tm1Wjl} mouse. Severe hypocellularity of the bone marrow (a), bacterial emboli without inflammatory response in multiple organs (heart – b; lungs – c; brain – d) and cerebral hemorrhages (d) are noted. HE staining. Source: Courtesy of S. Monette, MSKCC (unpublished).

Naturally Occurring Lesions – Infectious and Parasitic

Recently Recognized and Emerging Diseases in Immunodeficient Mice

With the increased use of highly immunodeficient mice, there is growing evidence of novel or previously unrecognized opportunistic bacterial, viral, and parasitic diseases. The defective immune system of these animals and the exposure to various environmental conditions have created a favorable milieu for such emerging diseases. Furthermore, both the experimental manipulations and the transfer of biological material can inadvertently serve as vectors for pathogens. Prior to the widespread use of highly immunodeficient strains some of these infectious agents were unknown or their importance as disease agents in mice was not recognized. For these reasons, the presence of some of these agents in mouse colonies has not typically been monitored by rodent biosecurity programs until recently. Thus, they remain a significant potential cause of disease in immunodeficient mice at this time.

Mouse Kidney Parvovirus (MKPV, aka Murine Chapparvovirus – MuCPV)

For over 40 years, a nephropathy characterized by intranuclear inclusion bodies within renal tubules has been reported in immunocompetent (ICR) and immunodeficient (CBySmn.CB17-*Prkdc*^{scid}/J, NOD.CB17-*Prkdc*^{scid}, and B6.129S7-*Rag*^{1tm1Mom}/J) mice [68, 69]. A more severe form of this inclusion body nephropathy (IBN) characterized by chronic progressive tubular injury leading to chronic kidney disease, renal failure, and spontaneous unexpected morbidity and

Vet-ebooks.com

mortality has been described in *Rag1* deficient and NSG mice [70, 71].

The etiologic agent of IBN was recently identified by metagenomic analysis as a novel parvovirus that is genetically highly divergent from previously known murine parvoviruses. The virus found in laboratory mice was named mouse kidney parvovirus (MKPV) [71] and a virus that was nearly identical genetically was concurrently and independently discovered in wild mice and named murine chapparvovirus (MuCPV) [72]. Both viruses belong to the recently created species *Rodent chaphamaparvovirus 1* [73]. Transmission of MKPV occurs through fecal-oral or urinary-oral route by cohousing and soiled bedding transfer [71]. The virus displays a highly preferential tropism for the kidneys, where persistent viral replication occurs in renal tubules; minimal viral replication occurs in other tissues [72]. While only subclinical infection, seroconversion, and mild renal lesions have been reported in immunocompetent mice, MKPV persistently infects highly immunodeficient mouse strains and leads to chronic kidney disease with significant morbidity and mortality [70, 71] (Figure 9.10). A major commercial diagnostic laboratory has reported an overall sample prevalence of 5.1% in their client-submitted fecal polymerase chain reaction (PCR) samples, including a prevalence of 9.4% in samples from immunocompetent mice [72]. Of note, lethal renal disease caused by MKPV has been documented in ICR sentinel mice with severely limited microbiome (altered Schaedler flora) (Godfrey, unpublished). Therefore, the exclusion of this agent from immunodeficient mouse colonies is desirable.

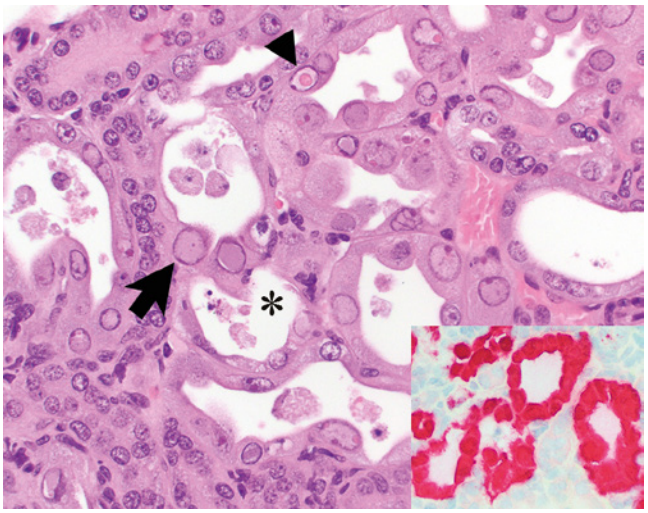


Figure 9.10 Kidney with inclusion body nephropathy caused by mouse kidney parvovirus (MKPV) in a NOD.Cg-*Prkdc*^{scid} *Il2rg*^{tm1Wjl} mouse. Renal tubular cells display karyomegaly with numerous large pale amphophilic (arrow), and fewer small eosinophilic intranuclear inclusions (arrowhead), and tubular necrosis (asterisk). HE staining. MKPV RNA was detected by in situ hybridization in tubular cells displaying karyomegaly (inset). Source: Courtesy of S. Monette, MSKCC (unpublished).

Clostridioides difficile

Clostridioides difficile is a Gram-positive, anaerobic, spore-forming, rod-shaped bacterium. The pathogenicity loci of clinically significant *C. difficile* strains encode toxins primarily responsible for its pathological features [74]. Two major exotoxins, consistently produced in toxigenic strains, include toxin A, an enterotoxin, and toxin B, an inflammatory cytotoxin [74].

Experimentally naive immunocompetent mice are generally refractory to natural infection and clinical disease [75–77]. Protective commensal bacteria present in these mice likely inhibit *C. difficile* growth [78]. Experimentally, the susceptibility of mice to *C. difficile* infection is induced by disrupting the microbiota through antibiotic treatment prior to spore administration, while the use of axenic mice does not require antibiotic pretreatment [79].

Antimicrobial treatment induces dysbiosis and decreases "colonization resistance" through decreased competition and increased metabolites and nutrients availability (e.g. proline), supporting growth of opportunistic bacteria that normally exist in small numbers [80]. Beside lasting antibiotic treatment, long-term exposure to the bacterium may lead to disease eventually.

Lethal spontaneous outbreaks of *C. difficile* enterotoxemia caused by the hypervirulent multilocus sequence type (MLST) group, which is associated with high lethality in antibiotic-treated mouse models and humans [81], have been reported in immunodeficient mice with and without previous antibiotic treatment [82]. Three clinical syndromes of peracute death; severe diarrhea leading to euthanasia or death; and mild-to-moderate diarrhea followed by recovery were reported. Similar to community-acquired infections in humans, female mice were more frequently clinically affected than males. In clinically affected mice, the cecum appears enlarged, empty, and edematous (Figure 9.11). The

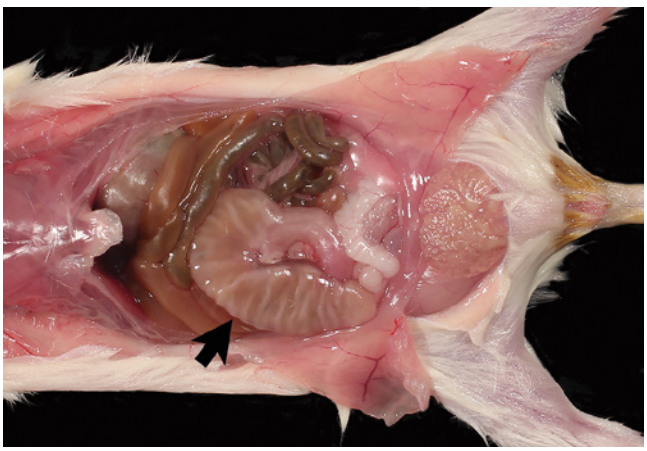


Figure 9.11 Macroscopic appearance of the gastrointestinal tract in a NOD.Cg-*Prkdc*^{scid} *Il2rg*^{tm1Wjl} mouse with *C. difficile* enterotoxemia. The cecum appears enlarged, empty, and edematous (arrow). Source: Courtesy of A. Piersigilli, WCM (unpublished).

Vet-ebooks.com

most common microscopic lesion was necrotizing and neutrophilic typhlo-colitis with numerous Gram-positive rods along intact and damaged mucosal surfaces (Figure 9.12). Pseudomembranes and erosive inflammatory mucosal lesions ("volcano lesions") were variably present. Submucosal edema was seen in both sub- and clinically affected animals. A comparison of *C. difficile*-induced lesions in different mouse strains is reported in Table 9.3.

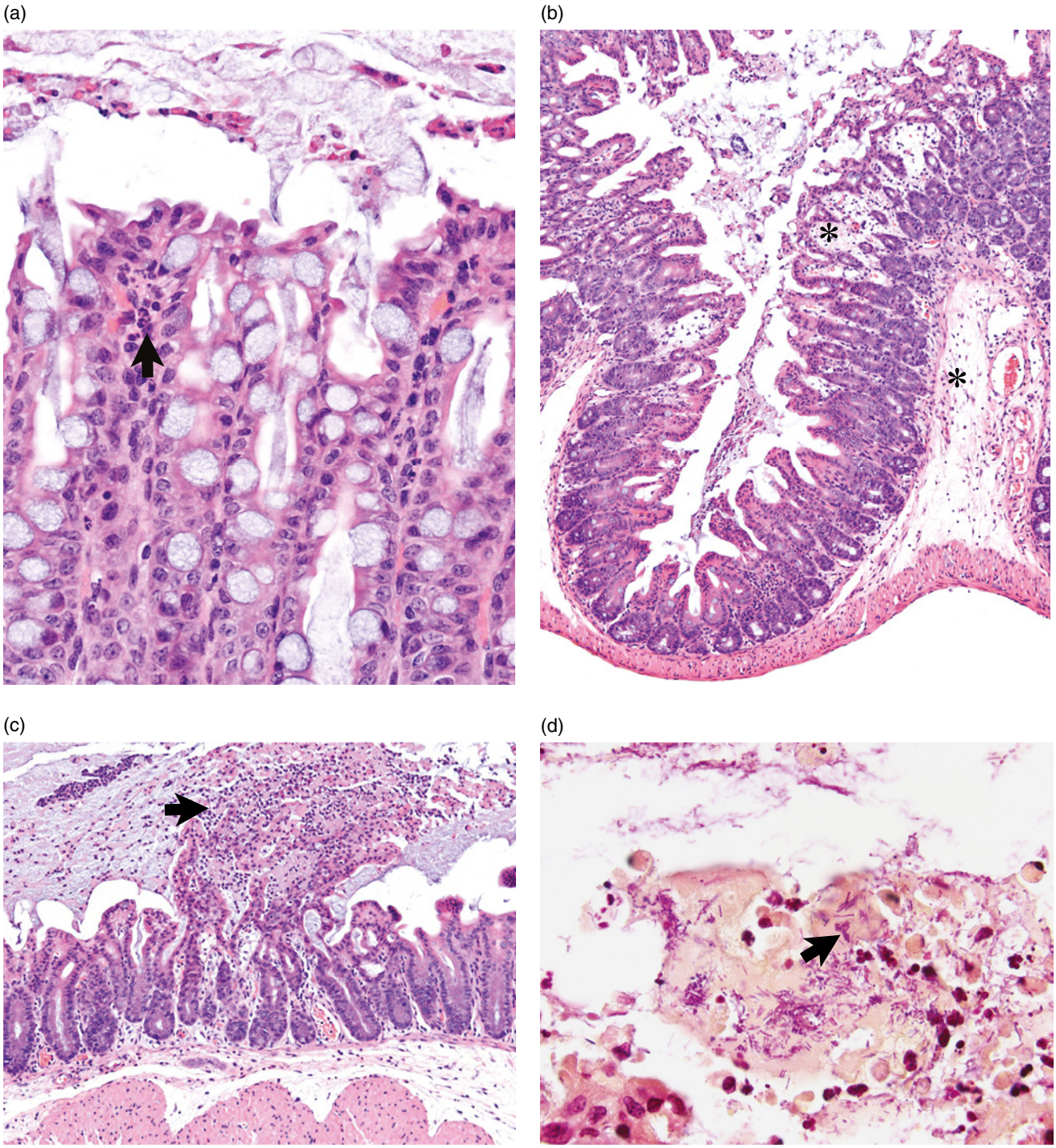


Figure 9.12 **Superficial necrotizing colitis caused by *C. difficile*.** Multifocal mucosal necrosis and infiltration by neutrophils are located within the lamina propria (arrow) (a) of a NOD.Cg-*Prkdc*^{scid} *Il2rg*^{tm1Wjl} mouse. Necrotizing typhlitis (b) with debris and bacterial colonies within the lumen, and mucosal and submucosal edema (asterisks) was also noted. In addition, "volcano" lesions (c), consisting of vertical accumulation of necrotic debris and degenerated neutrophils (arrow), are visible within the colon. HE staining (a–c). Gram staining (d) highlights *C. difficile* rods admixed with degenerated enterocytes; endospore are visible (arrow). Source: Courtesy of A. Piersigilli, WCM (unpublished).

Vet-ebooks.com

Table 9.3 *Clostridioides difficile*-induced lesions in different mouse strains.

Mouse strain	C57BL/6J	C57BL/6J	C3SnSmn.CB17-*Prkdc*^{scid}/J	NOD.Cg-*Prkdc*^{scid} *Il2rg*^{tm1Wjl}/SzJ (NSG); NOD.CB17-*Prkdc*^{scid}/NCrCrl (NOD scid)
Experimental manipulation	Autoimmune encephalomyelitis	Pre- and perinatal methyl-donor supplementation diet	Naïve	Naïve
Antibiotic treatment	No	No	No	Amoxicillin-treated NSG mice
Isolated *C. difficile*	Toxins A and B	Toxins A and B	Toxin A	Toxins A and B
Clinical signs	Lethargy; hunched posture; abdominal distention; lack of defecation; mortality	Hunched posture; lethargy; dyspnea and mucoid stool with perineal staining	Soft feces	Diarrhea; hunched posture; weight loss
Gross pathology	Ceco-colic distention with fecal impaction	Not reported	Edematous cecum, red discoloration of cecal serosa	Cecal/colonic edema; abnormal intestinal content; serosal red discoloration
Histopathology	Ulcerative and proliferative typhlocolitis with submucosal edema; pseudomembrane formation; infiltration of neutrophils; and macrophages	Severe necrotizing typhlocolitis with pseudomembrane formation and submucosal edema	Cecal and colonic submucosal edema; infiltration of neutrophils and mononuclear cells; luminal Gram-positive rods	Typhlocolitis with necrosis, pseudomembrane formation and volcano lesions; Gram-positive rods; submucosal edema; infiltration of neutrophils and mononuclear cells
References	[75]	[77]	[76]	[82]

Vet-ebooks.com

Innate and adaptive immunity are essential in controlling *C. difficile* proliferation and toxin production; thus, highly immunodeficient mouse strains are more susceptible and the clinical outcome of enterotoxemia is worse [82].

Burkholderia spp.

The genus *Burkholderia* represents a rapidly expanding group of Gram-negative bacilli. Over 80 species that are adapted to a wide range of environments can affect plants, animals, and humans [83]. These bacteria survive harsh conditions thanks to their metabolic versatility, virulence factors, and ability to form biofilms [84].

The *Burkholderia cepacia* complex (Bcc), which includes more than 20 species of bacilli, and *Burkholderia gladioli* contribute to cause life-threatening infections in human patients affected by cystic fibrosis and chronic granulomatous disease [83, 85]. Rodents can act as asymptomatic carriers of *Burkholderia* sp. However, no screening methods are regularly in place to exclude these agents from laboratory animal facilities, thus immunocompromised mice may be exposed to them. Inappropriate husbandry conditions and contamination of drinking water have been recently associated with outbreaks of *B. gladioli* or members of the *Bcc* in colonies of B6.129S-*Cybb*^{tm1Din}/J, CB17.Cg-*Prkdc*^{scid}*Lyst*$^{bg\text{-}J}$/Crl, NSG, C57BL/6J-*Rag1*^{tm1Mom}, B6.129S6-*Rag2*^{tm1Fwa}N12, and C;129S4-*Rag2*$^{tm1.1Flv}$ *Il2rg*$^{tm1.1Flv}$/J mutant mice [86–88]. Clinically, head tilt, circling, spinning, dehydration, and lethargy were described. Lesions included suppurative otitis media, labyrinthitis, encephalitis, and necrosuppurative hepatitis.

Candida spp.

Candida spp. are trimorphic commensal fungi that colonize the skin and mucosal surfaces of humans and other animals [89]. Initiation of infections usually requires disruption of the host immune status, barrier function, or local microenvironment (including microbiota) [90]. Macrophages and neutrophils play an essential role in the host defense against candidiasis [91]. While NK cells are not required for defense against intravenous infection in immunocompetent animals, NSG mice display increased susceptibility to infection due to their lack of NK cells [92].

Inbred mouse strains vary widely and a variable innate susceptibility to systemic candidiasis exist among common inbred mouse strains without the need of immunosuppression [93, 94]. While the lack of complement component C5 renders mice highly susceptible to infection, the presence of *Candida albicans* resistance genes (*Carg3* and *Carg4*) also modulates the susceptibility [94]. Mouse models of candidiasis are developed either by infecting immunocompromised animals or animals pretreated with antimicrobials or other therapies [93, 95].

In athymic beige mice, a progressive systemic infection in *C. albicans*-colonized mice occurred 12–16 weeks after mucosal infection, with yeast and hyphal organisms found in the palate, tongue, esophagus, and stomach [96]. Yeasts, septate hyphae, and pseudohyphae morphologically compatible with *Candida* spp. have been reported in NSG mice affected by chronic dermatitis due to ectoparasite burden [70]. Naturally occurring *Candida glabrata* infections have been reported in NSG mice (Godfrey, unpublished) (Figure 9.13).

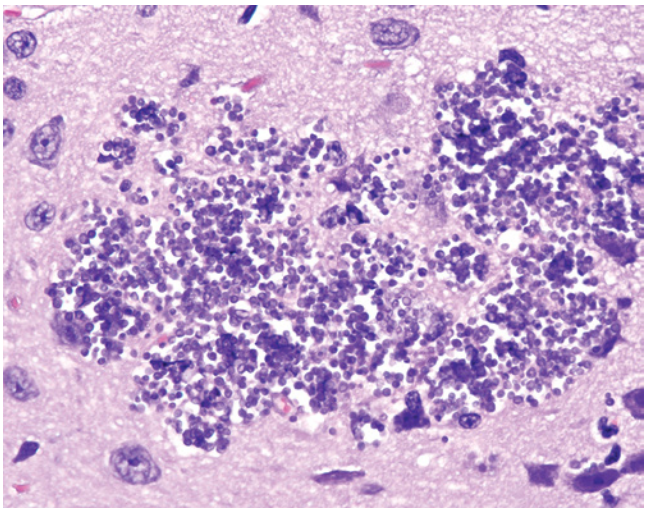


Figure 9.13 **Naturally occurring *Candida glabrata* infection in the brain of a humanized NOD.Cg-*Prkdc*^{scid} *Il2rg*^{tm1Wjl} mouse**. HE staining. Source: Courtesy of VL Godfrey, UNC School of Medicine (unpublished).

Demodex musculi

Six species of Demodex mites have been reported in *Mus musculus,* but *Demodex musculi* is the only species that has been identified in laboratory mice. Until recently, *D. musculi* has not been considered a significant parasite of laboratory mice, and screening and exclusion of this parasite has not been performed in most colonies. While infestation in most strains results in a low mite burden and remains subclinical, infestations causing clinical signs and lesions of dermatitis associated with high numbers of mites have been reported in several immunocompromised mouse strains including *Stat6*^{tm1Gru}/*Cd28*^{tm1Mak} [97], NSG, C;129S4-*Rag2*$^{tm1.1Flv}$ *Il2rg*$^{tm1.1Flv}$/J, BALB/c-Tg(*DO11.10)Il13*^{tm} [98], and TRP1/TCR mice (Figure 9.14) [99]. Until recently, *D. musculi* has rarely been reported in laboratory mice, but evidence suggests that it may have easily gone undetected due to inadequate testing methods and is likely more prevalent than previously recognized [100]. Data from recently developed PCR screening suggest a prevalence of 10–30% in academic colonies [101]. Significant serum IgE elevation has been shown in several strains, including immunocompetent strains with subclinical infestation, suggesting that *D. musculi* may impact reproducibility of immunologic research [102].

Historically Recognized Pathogens

While the prevalence of pathogens in laboratory mice has changed over time and many historically recognized rodent

Vet-ebooks.com

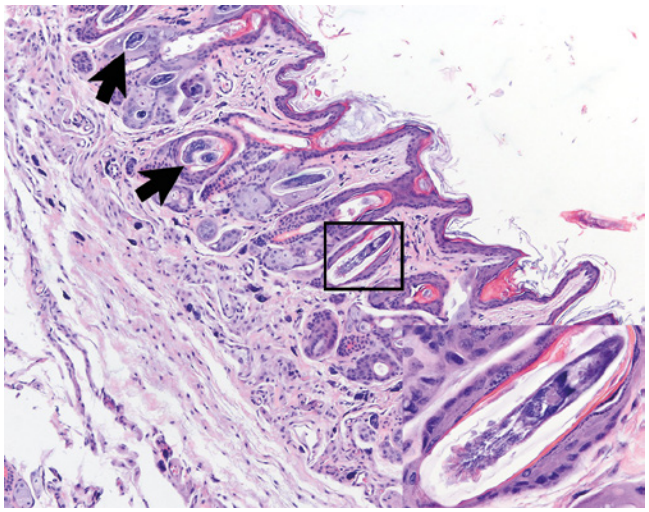


Figure 9.14 ***Demodex musculi*** **infestation in a NOD.Cg-*Prkdc*^{scid} *Il2rg*^{tm1Wjl} mouse**. Note numerous mites in hair follicles and sebaceous glands (arrows). Magnified mite in inset show typical *Demodex* morphology. HE staining. Source: Courtesy of S. Monette, MSKCC (unpublished).

pathogens are no longer present in modern research colonies due to improved biosecurity and husbandry conditions, immunodeficient mice are exquisitely susceptible to diseases induced by primary pathogens and opportunists. While immunocompetent mice may act as mere subclinical carriers for pathogens and do not display any discernible lesions, the same agents can cause morbidity and mortality in highly immunocompromised animals. A description of findings in immunocompromised strain is presented in Table 9.4.

Mouse hepatitis virus (MHV, family Coronaviridae) encompasses numerous strains with different tissue tropism and pathogenicity due to the high rate of mutation and recombination. Respiratory strains, defined as "polytropic," replicate and are cytolytic in the upper respiratory tract mucosa, although can disseminate and replicate in vascular endothelium and several parenchymal tissues in immunocompromised or genetically susceptible mice [103]. Resistance to the infection, efficacy of the mounted immune response and disease severity are strain-related [103]. Enterotropic strains rarely infect tissue or cell types other than enterocytes, even in immunodeficient mice, although T cells are required to prevent viral dissemination [104].

Although mice were long thought to not be naturally infected by papillomaviruses, an outbreak occurred in a colony of nude mice (NMRI-*Foxn1*^{nu}/*Foxn1*^{nu}) [109]. Transmission studies indicated that a pan T-cell deficiency was needed for mice to develop lesions; however, strain susceptibility differences possibly due to differences in NK cell levels between the different immunodeficient strains also constitute underlying contributing factors [110]. Lesions induced by this virus included exophytic papillomas on the muzzle and tail skin, invasive endophytic trichoblastomas on the skin in the lumbar region, and sessile vaginal papillomas (see Chapter 10 – Skin, Hair, and Nails).

Murine Norovirus (MNV) has a high seroprevalence in many mouse colonies due to its high persistence in the environment and low infective dose. Clinical disease has been described only in mouse strains lacking components of the innate immune system.

Mammalian orthoreovirus infects a wide range of mammals including humans and mice, although the virus is very

Table 9.4 Historically recognized pathogens – effects in immunodeficient mouse strains.

Pathogens	Pathologic findings	References
Mouse hepatitis virus (MHV)	Respiratory strains: cytolytic lesions (liver, lymphoid organs, bone marrow); syncitia (endothelium); granulomatous peritonitis and pleuritis in *Ifng*^{tm1Ts} mice; chronic wasting disease; demyelinating lesions in *Fox1*^{nu} mice Enteric strains: gastrointestinal lesions in B6.129S2-Igh-6^{tm1Cgn} mice; multisystemic lethal dissemination in B6.129P2-*Tcrb*^{tm1Mom} *Tcrd*^{tm1Mom} mice	[103, 104]
Murine norovirus	Infects and replicates in mouse antigen-presenting dendritic cells (DCs) and macrophages Can cross the intestinal epithelium by transcytosis (M cell luminal cargo) Splenomegaly and/or hepatic pale spots in *Rag1*^{tm1Mom}*Stat1*^{tm1Rds} mice Lethal infection reported in immunodeficient mice with altered innate immune system (including *Rag2*^{tm1Fwa}*Stat1*^{tm1Rds}, *Ifngr1*^{tm1Agt}*Ifnar1*^{tm1Agt}, *Stat1*^{tm1Rds}, and *Stat1*^{tm1Rds}*Eif2ak2*^{tm1Cwe} mice): encephalitis, vasculitis (cerebral vessels), meningitis, hepatitis, pneumonia Antibiotic treatment results in reduced intestinal MNV yield	[105–108]
Mouse papillomavirus (MmuPV1)	Multiple cutaneous papillomas around the mouth and nose In T cell-deficient mice, experimental transmission to the skin induces proliferative lesions (papillomas and trichoblastomas); genetic background influences susceptibility	[109, 110]

Vet-ebooks.com

Table 9.4 (Continued)

Pathogens	Pathologic findings	References
Mouse Sendai virus (Mouse Parainfluenza virus type 1)	Wasting disease, bronchopneumonia, rhinitis, and otitis media in nude mice Genetic differences in susceptibility among mouse strains Severe pneumonia with proliferative "adenomatoid-like" lesions and delayed viral clearance in immunodeficient mice (especially T-cell deficient mice)	[111]
α-Hemolytic *Streptococcus viridans*	Bacteremia in CB17.Cg-*Prkdc*^{scid}*Lyst*$^{bg\text{-}J}$/Crl mice	[112]
Corynebacterium bovis	Hyperkeratotic dermatitis in adult *Foxn1*^{nu}, *Prkdc*^{scid}, and NSG mice Mortality in suckling immune-deficient mice Can influence growth of human xenografts	[103, 113]
Helicobacter sp.	Proliferative typhlitis colitis, rectal prolapse, hepatic necrosis with limited inflammation in several immunodeficient mice *H. hepaticus*: intestinal carcinoma in *Il10*^{tm1Cgn} *and Rag2*^{tm1Fwa} mice	[114]
Paecilomyces sp., Aspergillus fumigatus, Rhizopus sp.	Suppurative and necrotizing pneumonia in *Cybb*^{tm1Din} mice	[115]
Pasteurella pneumotropica (*Rodentibacter* spp.)*, Staphylococcus aureus and xylosus*	Abscesses, cellulitis in *Cybb*^{tm1Din} mice *S. xylosus*-induced severe dermatitis with alopecia, crusts, and scaly skin in knockout mice carrying the *Rag1*^{tm1Mom} and *Map3k8*^{tm1Pnt} alleles Botryomycosis: folliculitis and furunculosis of the muzzle in nude mice	[103, 116, 117]
Pseudomonas aeruginosa, Klebsiella spp.*, E. coli, Enterococcus* spp.	Suppurative and necrotizing pneumonia in *Cybb*^{tm1Din} mice Sepsis, abscesses, meningoencephalitis in B6.129P2(SJL)-*Myd88*$^{tm1.1Defr}$ mice Pyogranulomatous hepatitis and nephritis in *Ncf1*null mice *Klebsiella oxytoca*: spontaneous chronic otitis media in C3H/HeJ mice due to a spontaneous mutation (*Tlr4*$^{Lps\text{-}d}$) and pyelonephritis in NSG mice	[115, 118–120](Godfrey, unpublished)
Staphylococcus sp.	Dermatitis, conjunctivitis in BALB/c-*Prkdc*^{scid}	(Godfrey, unpublished)
Candida glabrata	Granulomatous otitis media and interna, nephritis, encephalomyelitis in NSG and NRG-*Akita* mice (NOD.Cg-*Rag1*^{tm1Mom}*Ins2AkitaIl2rg*^{tm1Wjl}/SzJ)	(Godfrey, unpublished)
Pneumocystis murina	Hunched posture, dry skin, ruffle coat, dyspnea, weight loss, decreased breeding performance, death (in immunodeficient mice) Interstitial pneumonia and exudative alveolitis with fungal organisms In *Prkdc*^{scid} mice, *P. murina* spreads to bone marrow, heart, liver, and spleen *Pneumocystis*-infected mice:⇑ IL-17A/IL-10; ⇑ Th17 cells in the lung	[103, 121, 122]

rare in modern mouse colonies and generally not a significant health concern [123]. However, recent outbreaks have been reported in NSG mice in which PDX tumor seeds were identified as the source of the virus [124]. In immunodeficient mice, the infection is multisystemic, may be acute or chronic, and causes inflammatory and necrotizing lesions (Figure 9.15) in the brain, heart, lymphoid tissues, liver, pancreas, adrenal gland, and spinal cord and thrombosis with ischemic necrosis of extremities [103, 124–126].

Pasteurella pneumotropica (now reclassified within the new genus *Rodentibacter*) and *Staphylococcus aureus* are the most prevalent bacterial agents isolated in laboratory mice [123, 127], and can cause suppurative lesions and abscess formation in immunodeficient mice [128–130]. The number of reports of opportunistic infections by other common bacterial species of the genera *Klebsiella* and *Pseudomonas* is relatively low. However, some strains that have mutations in toll-like receptor 4 (*Tlr4*) are highly susceptible to gram negative infections [131].

Ubiquitous opportunistic organisms such as the fungi *Pneumocystis* spp. have the ability to replicate in the lungs of both immunocompromised and immunocompetent animals and humans in a species-specific manner [132] (Figure 9.16). Outbreaks of pneumocystosis previously reported as caused by *Pneumocystis carinii* in immunodeficient mice (e.g. *scid* or nude) were actually caused by *Pneumocystis murina* [103].

Biological materials used for experimental purpose can harbor a variety of viruses and bacteria of mouse or other origins. In immunocompromised mice, the engraftment of tumors or tumor cell lines could represent an opportunity for infectious agents to colonize the host and multiply in the absence of a viable immune response [133]. Administration of *Mycoplasma arginini*-contaminated cells to *Prkdc*^{scid} mice caused arthritis and other clinical illnesses [134]. Viruses including lymphocytic choriomeningitis virus (LCMV), lactic dehydrogenase elevating virus (LDEV), reoviruses, parvoviruses, and coronaviruses have been identified as contaminating agents [135, 136].

Vet-ebooks.com

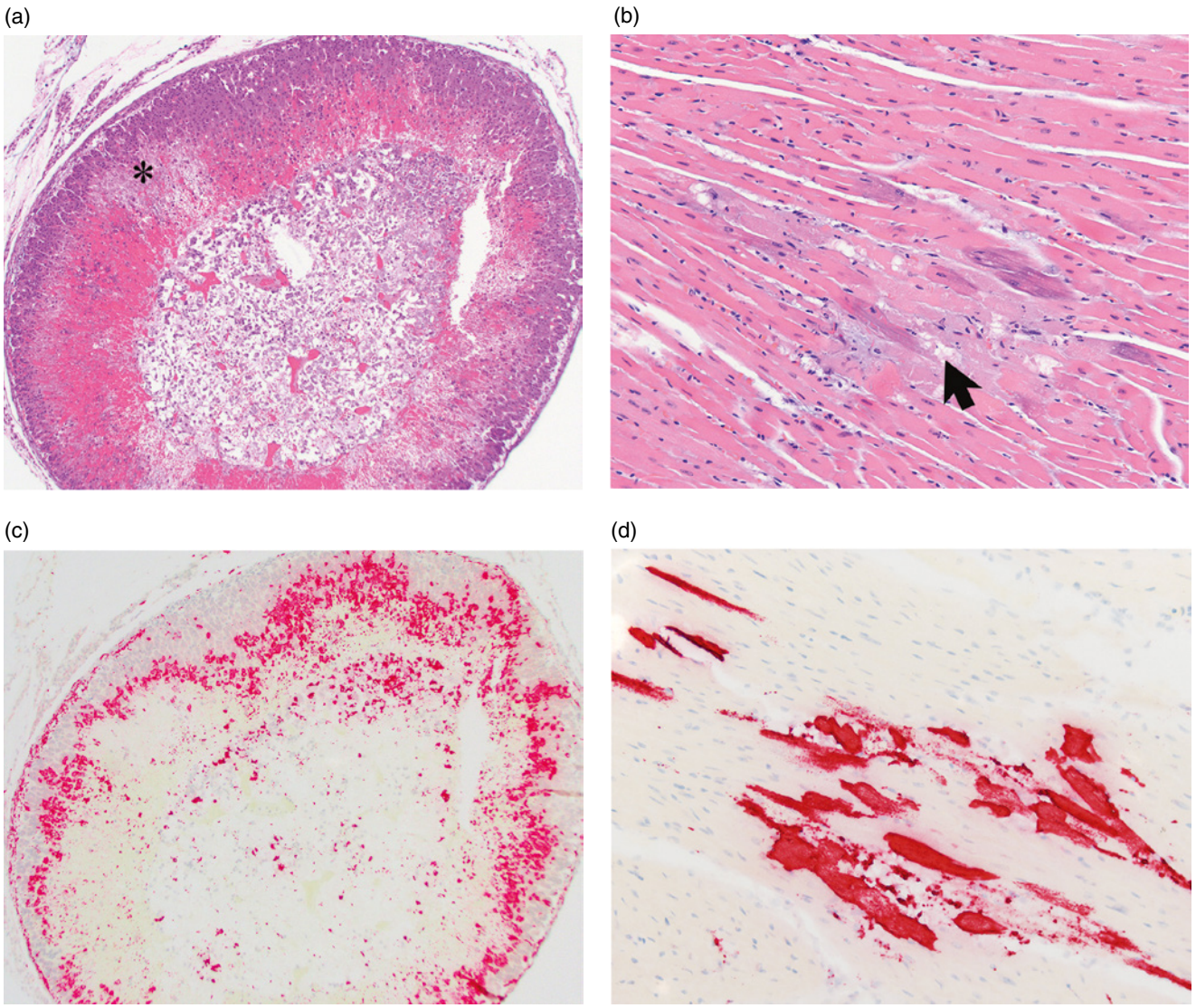


Figure 9.15 **Natural mammalian orthoreovirus infection in a NOD.Cg-*Prkdc*^{scid} *Il2rg*^{tm1Wjl} mouse acquired from an implanted PDX.** Multisystemic necrotizing lesions were observed. Adrenocortical necrosis (asterisk) (a) and myocardial necrosis and mineralization (arrow) (b) are shown. HE staining. Intralesional orthoreoviral RNA was observed on in situ hybridization in both organs (adrenal gland – c; heart – d). Source: Courtesy of S. Monette, MSKCC (unpublished).

Naturally Occurring Lesions – Noninfectious or Parasitic

Neoplastic, degenerative, and miscellaneous background lesions in immunodeficient mouse strains and stocks are listed in Table 9.5. Briefly, a low predisposition for spontaneous tumors has been described for NSG mice [139]. Mammary carcinomas have been reported in aged NSG mice and in NOD and NOD-derived strains [70, 139, 151], in addition to lymphomas, osteosarcomas, and many epithelial, mesenchymal, and endocrine tumors [70, 140, 151–153]. Incidence of thymic lymphomas varies between immunodeficient strains, with high incidence reported primarily in NOD *scid* mice [137]. NOD.Cg-*Prkdc*^{scid} mice appear to have similar lesions as *Prkdc*^{scid}, *Rag1*^{tm1Mom}, and *Rag2* ^{tm1Fwa} mice, except for a greater incidence of thymic lymphomas which greatly reduces the lifespan (average of 37 weeks) [23].

Published information on background lesions of nude mice of different strains and stocks is limited. Unlike some other immunodeficient strains, nude mice do not appear predisposed to develop lymphoma at a higher incidence than thymus bearing mice of corresponding genetic background [145]. Glomerulonephritis with secondary anasarca (Figure 9.17) is a relatively common cause of morbidity and mortality in aged nude mice [146].

Vet-ebooks.com

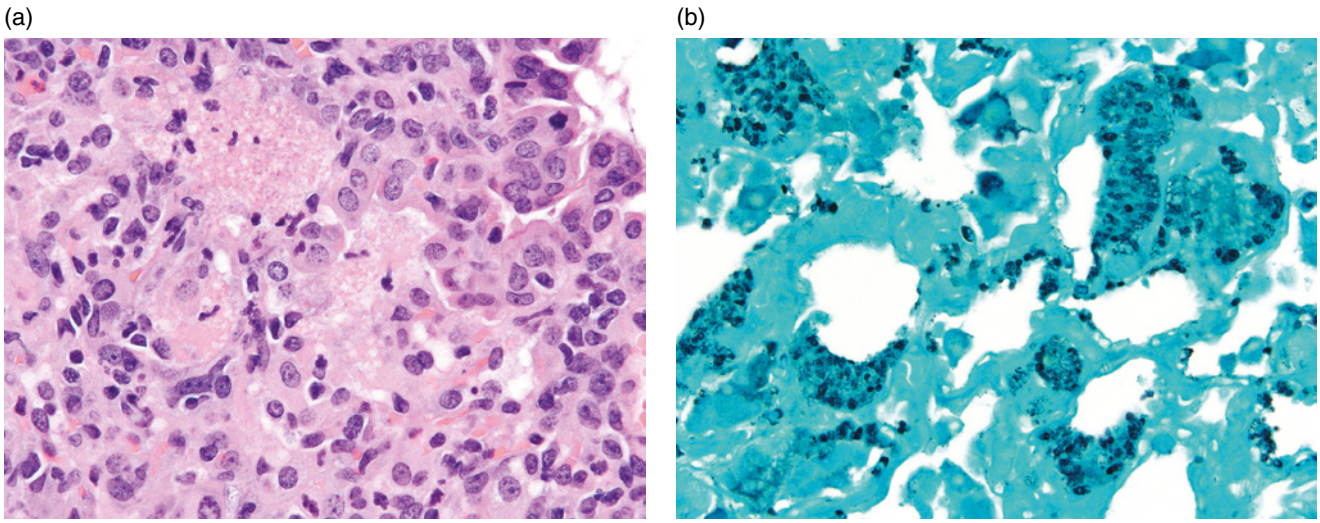


Figure 9.16 ***Pneumocystis murina*** **infection in a NOD.Cg-*Prkdc*^{scid} *Il2rg*^{tm1Wjl} mouse**. Pulmonary alveoli are filled with fungal organisms. HE (a) and Grocott (b) staining. Source: Courtesy of A. Piersigilli, WCM (unpublished).

Table 9.5 Neoplastic, degenerative, and miscellaneous lesions in immunodeficient mouse strains.

Common name of strain/stock	Reported lesions	Spontaneous lymphomas	References
NOD *scid*	*Nonneoplastic, degenerative, and miscellaneous* Incisor abnormalities after nonmyeloablative irradiation	Thymic lymphomas; high incidence	[137, 138]
NSG	*Neoplastic (other than lymphomas; old mice)* Mammary gland: high incidence; carcinomas Female reproductive tract: granulosa cell tumors, endometrial stromal polyps, parietal yolk sac carcinomas, leiomyosarcomas, leiomyomas, neuroendocrine carcinomas (mesometrium) Low incidence of tumors of bone, liver, gastrointestinal tract, lung, skin, Harderian gland, and adrenal gland *Nonneoplastic, degenerative, miscellaneous (old mice)* Uterus: endometrial cystic glandular dilation or hyperplasia, hemosiderosis, ⇓ ovarian follicles Adrenal glands: ceroid, subcapsular hyperplasia Skeletal system: hyperostoses (calvaria, nasal bone), DJD, intervertebral disc disease Other organs: kidney (chronic nephropathy), heart (progressive cardiomyopathy)	Lymphoma, HS; low incidence No thymic lymphomas	[70, 139, 140]

(*Continued*)

Vet-ebooks.com

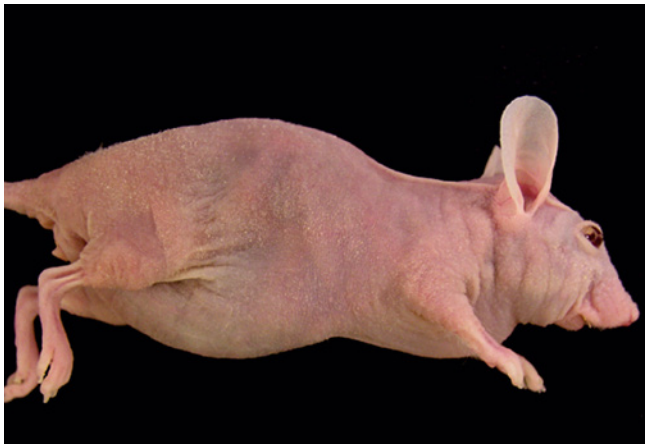
Table 9.5 (Continued)

Common name of strain/stock	Reported lesions	Spontaneous lymphomas	References
NOG		Thymic lymphomas; low incidence	[141]
Rag1 and *Rag2* deficient (multiple strains)		Thymic lymphomas and B cell lymphomas in NOD·129S7(B6)-*Rag1*^{tm1Mom}/J mice and knockout mice carrying the *Rag2*^{tm1Fwa} mutant allele on a NOD background; increased incidence	[142, 143]
BALB *scid*	*Neoplastic (other than lymphomas)* Pulmonary adenoma, mammary carcinoma	Thymic lymphomas; high incidence	[18]
Scid beige	*Nonneoplastic, degenerative, and miscellaneous* Lung: spontaneous alveolar lipoproteinosis with marked increases in phosphatidylcholine and surfactant proteins A and B. Also described in CB.17-*Prkdc*^{scid}/*Prkdc*^{scid} mice		[144]
Nude (multiple strains/stocks)	*Neoplastic (other than lymphomas)* Outbred stock on Swiss background: Spontaneous neoplasia in 2.1% of mice, including pulmonary adenoma *Nonneoplastic, degenerative, and miscellaneous* Kidney: glomerulonephritis; strain/stock not specified Cecum and colon: proliferative typhlocolitis with multinucleated giant cells in Hsd:Athymic Nude-*Foxn1*^{nu} Eye: foreign body conjunctivitis in Cby.Cg-*Foxn1*^{nu} caused by bedding material due to the lack of eyelashes Lymph node: sinus ectasia ("cystic" lymph nodes); strain/stock not specified Testis: seminiferous tubule degeneration BALB/cSlc-^{nu} in KSN/Slc and Crl:CD1-*Foxn1*^{nu}. Increased incidence compared to thymus-bearing mice of corresponding genetic backgrounds	Lymphomas and HS; low incidence	[145–150]

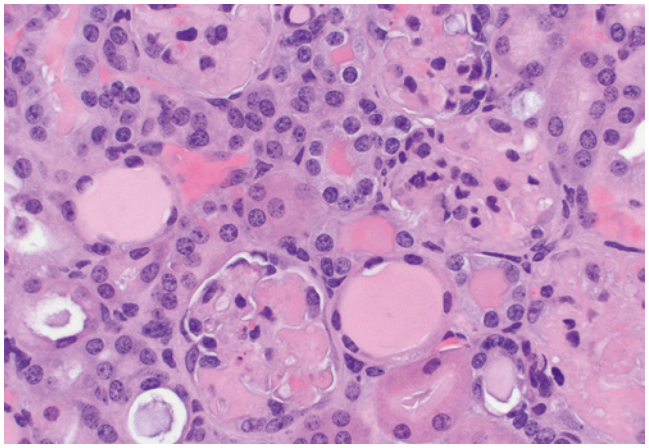
DJD = degenerative joint disease, HS = histiocytic sarcoma.

Vet-ebooks.com

(a)



(b)



(c)

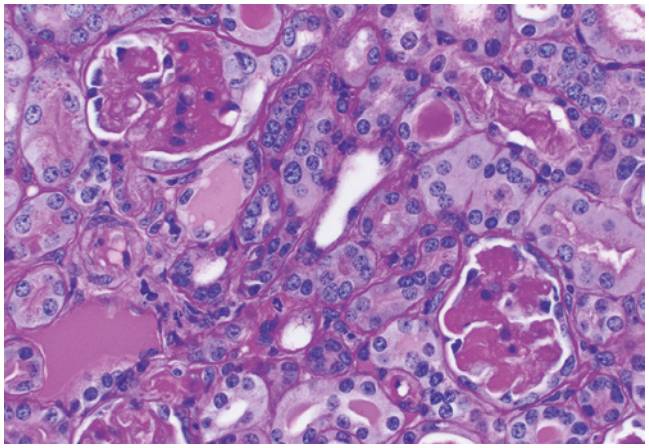


Figure 9.17 **Naturally occurring glomerulonephritis in an athymic nude mouse, Crl:NU(NCr)-*Foxn1*^{nu}.** There is generalized subcutaneous edema (anasarca) (a). Glomeruli are expanded by an abundant eosinophilic material on HE staining (b); the material is also Periodic acid-Schiff (PAS)-positive (c) and negative for Congo Red (not shown). Glomerular synechia and tubular luminal proteinaceous casts are also observed. Source: Courtesy of S. Monette, MSKCC (unpublished).

References

1 Mestas, J. and Hughes, C.C.W. (2004). Of mice and not men: differences between mouse and human immunology. *J. Immunol.* 172 (5): 2731–2738.

2 Rygaard, J. and Poulsen, C.O. (1969). Heterotransplantation of a human malignant tumor to "nude" mice. *Acta Pathol. Microbiol. Scand.* 77 (4): 758–760.

3 Pantelouris, E.M. (1968). Absence of thymus in a mouse mutant. *Nature* 217 (5126): 370–371.

4 Shultz, L.D., Brehm, M.A., Garcia-Martinez, J.V., and Greiner, D.L. (2012). Humanized mice for immune system investigation: progress, promise and challenges. *Nat. Rev. Immunol.* 12 (11): 786–798.

5 Shultz, L.D., Keck, J., Burzenski, L. et al. (2019). Humanized mouse models of immunological diseases and precision medicine. *Mamm. Genome* 30 (5–6): 123–142.

6 Shultz, L.D. and Sidman, C.L. (1987). Genetically determined murine models of immunodeficiency. *Annu. Rev. Immunol.* 5 (1): 367–403.

7 Shinkura, R., Kitada, K., Matsuda, F. et al. (1999). Alymphoplasia is caused by a point mutation in the mouse gene encoding Nf-κb-inducing kinase. *Nat. Genet.* 22 (1): 74–77.

8 Seymour, R.E., Hasham, M.G., Cox, G.A. et al. (2007). Spontaneous mutations in the mouse Sharpin gene result in multiorgan inflammation, immune system dysregulation and dermatitis. *Genes Immun.* 8 (5): 416–421.

9 Seymour, R., Sundberg, J.P., and Hogen Esch, H. (2006). Abnormal lymphoid organ development in immunodeficient mutant mice. *Vet. Pathol.* 43 (4): 401–423.

10 Dooley, J., Erickson, M., Roelink, H., and Farr, A.G. (2005). Nude thymic rudiment lacking functional foxn1 resembles respiratory epithelium. *Dev. Dyn.* 233 (4): 1605–1612.

11 Mecklenburg, L., Nakamura, M., Sundberg, J.P., and Paus, R. (2001). The nude mouse skin phenotype: the role of *Foxn1* in hair follicle development and cycling. *Exp. Mol. Pathol.* 71 (2): 171–178.

12 Mecklenburg, L., Paus, R., Halata, Z. et al. (2004). FOXN1 is critical for onycholemmal terminal differentiation in nude (*Foxn1*) mice. *J. Invest. Dermatol.* 123 (6): 1001–1011.

13 Baxter, R.M. and Brissette, J.L. (2002). Role of the nude gene in epithelial terminal differentiation. *J. Invest. Dermatol.* 118 (2): 303–309.

14 Herberman, R.B. and Holden, H.T. (1979). Natural killer cells as antitumor effector cells. *J. Natl. Cancer Inst.* 62 (3): 441–445.

15 HogenEsch, H. and Nikitin, A.Y. (2012). Challenges in pre-clinical testing of anti-cancer drugs in cell culture and in animal models. *J. Controlled Release* 164 (2): 183–186.

16 Liang, Y., Silva, K.A., Kennedy, V., and Sundberg, J.P. (2011). Comparisons of mouse models for hair follicle reconstitution. *Exp. Dermatol.* 20 (12): 1011–1015.

Vet-ebooks.com

17 Nonoyama, S., Smith, F.O., Bernstein, I.D., and Ochs, H.D. (1993). Strain-dependent leakiness of mice with severe combined immune deficiency. *J. Immunol.* 150 (9): 3817–3824.

18 Custer, R.P., Bosma, G.C., and Bosma, M.J. (1985). Severe combined immunodeficiency (SCID) in the mouse. Pathology, reconstitution, neoplasms. *Am. J. Pathol.* 120 (3): 464–477.

19 Talmadge, J.E., Meyers, K.M., Prieur, D.J., and Starkey, J.R. (1980). Role of NK cells in tumour growth and metastasis in beige mice. *Nature* 284 (5757): 622–624.

20 Jones-Carson, J., Vazquez-Torres, A., and Balish, E. (1995). Defective killing of *Candida albicans* hyphae by neutrophils from beige mice. *J. Infect. Dis.* 171 (6): 1664–1667.

21 Oliver, C. and Essner, E. (1973). Distribution of anomalous lysosomes in the beige mouse: a homologue of Chediak–Higashi syndrome. *J. Histochem. Cytochem. Off. J. Histochem. Soc.* 21 (3): 218–228.

22 Lee, J.H., Park, J.-H., Nam, T.-W. et al. (2018). Differences between immunodeficient mice generated by classical gene targeting and CRISPR/Cas9-mediated gene knockout. *Transgenic Res.* 27 (3): 241–251.

23 Shultz, L.D., Schweitzer, P.A., Christianson, S.W. et al. (1995). Multiple defects in innate and adaptive immunologic function in NOD/LtSz-scid mice. *J. Immunol.* 154 (1): 180–191.

24 Takenaka, K., Prasolava, T.K., Wang, J.C.Y. et al. (2007). Polymorphism in Sirpa modulates engraftment of human hematopoietic stem cells. *Nat. Immunol.* 8 (12): 1313–1323.

25 Cao, X., Shores, E.W., Hu-Li, J. et al. (1995). Defective lymphoid development in mice lacking expression of the common cytokine receptor γ chain. *Immunity* 2 (3): 223–238.

26 DiSanto, J.P., Müller, W., Guy-Grand, D. et al. (1995). Lymphoid development in mice with a targeted deletion of the interleukin 2 receptor gamma chain. *Proc. Natl. Acad. Sci. U.S.A.* 92 (2): 377–381.

27 Ohbo, K., Suda, T., Hashiyama, M. et al. (1996). Modulation of hematopoiesis in mice with a truncated mutant of the interleukin-2 receptor gamma chain. *Blood* 87 (3): 956–967.

28 Walsh, N.C., Kenney, L.L., Jangalwe, S. et al. (2017). Humanized mouse models of clinical disease. *Annu. Rev. Pathol.* 12: 187–215.

29 Quandt, D., Fiedler, E., Boettcher, D. et al. (2011). B7-h4 expression in human melanoma: its association with patients' survival and antitumor immune response. *Clin. Cancer Res. Off. J. Am. Assoc. Cancer Res.* 17 (10): 3100–3111.

30 Uthamanthil, R., Tinkey, P., and de Stanchina, E. (2016). Patient Derived Tumor Xenograft Models Promise, Potential and Practice, p. 460. Elsevier.

31 Guerrera, F., Tabbò, F., Bessone, L. et al. (2016). The influence of tissue ischemia time on RNA integrity and patient-derived xenografts (PDX) engraftment rate in a non-small cell lung cancer (NSCLC) biobank. *PLoS One* 11 (1): e0145100.

32 Baust, J.M., Van Buskirk, R., and Baust, J.G. (2000). Cell viability improves following inhibition of cryopreservation-induced apoptosis. *in vitro Cell Dev. Biol. Anim.* 36 (4): 262–270.

33 Le Gallo, M., de la Motte Rouge, T., Poissonnier, A. et al. (2018). Tumor analysis: freeze-thawing cycle of triple-negative breast cancer cells alters tumor CD24/CD44 profiles and the percentage of tumor-infiltrating immune cells. *BMC Res. Notes* 11 (1): 401.

34 Ingham, E., Matthews, J.B., Kearney, J.N., and Gowland, G. (1993). The effects of variation of cryopreservation protocols on the immunogenicity of allogeneic skin grafts. *Cryobiology* 30 (5): 443–458.

35 Némati, F., Sastre-Garau, X., Laurent, C. et al. (2010). Establishment and characterization of a panel of human uveal melanoma xenografts derived from primary and/or metastatic tumors. *Clin. Cancer Res.* 16 (8): 2352–2362.

36 Bertotti, A., Migliardi, G., Galimi, F. et al. (2011). A molecularly annotated platform of patient-derived xenografts ("xenopatients") identifies HER2 as an effective therapeutic target in cetuximab-resistant colorectal cancer. *Cancer Discov.* 1 (6): 508–523.

37 Bagnara, D., Kaufman, M.S., Calissano, C. et al. (2011). A novel adoptive transfer model of chronic lymphocytic leukemia suggests a key role for T lymphocytes in the disease. *Blood* 117 (20): 5463–5472.

38 Sun, S. and Zhang, Z. (2016). Patient-derived xenograft platform of OSCC: a renewable human bio-bank for preclinical cancer research and a new co-clinical model for treatment optimization. *Front. Med.* 10 (1): 104–110.

39 Gu, Q., Zhang, B., Sun, H. et al. (2015). Genomic characterization of a large panel of patient-derived hepatocellular carcinoma xenograft tumor models for preclinical development. *Oncotarget* 6 (24): 20160–20176.

40 Russell, P.J., Russell, P., Rudduck, C. et al. (2015). Establishing prostate cancer patient derived xenografts: lessons learned from older studies. *The Prostate* 75 (6): 628–636.

41 Williams, E.S., Rodriguez-Bravo, V., Rodriquez-Bravo, V. et al. (2015). Generation of prostate cancer patient derived xenograft models from circulating tumor cells. *J. Vis. Exp.* (105): 53182.

42 Radaelli, E., Hermans, E., Omodho, L. et al. (2015). Spontaneous post-transplant disorders in NOD.Cg-*Prkdcscid Il2rgtm1Sug*/JicTac (NOG) mice engrafted with patient-derived metastatic melanomas. *PLoS One* 10 (5): e0124974.

43 Clappier, E., Gerby, B., Sigaux, F. et al. (2011). Clonal selection in xenografted human T cell acute lymphoblastic leukemia recapitulates gain of malignancy at relapse. *J. Exp. Med.* 208 (4): 653–661.

44 Mattie, M., Christensen, A., Chang, M.S. et al. (2013). Molecular characterization of patient-derived human pancreatic tumor xenograft models for preclinical and translational development of cancer therapeutics. *Neoplasia* 15 (10): 1138–1150.

Vet-ebooks.com

45 Fleming, J.M., Miller, T.C., Meyer, M.J. et al. (2010). Local regulation of human breast xenograft models. *J. Cell. Physiol.* 224 (3): 795–806.

46 Vockentanz, L. and Nopora, A. (2016). Development of next-generation breast cancer PDX models by applying intra mammary fat pad and intraductal tumor transfer [abstract]. In: Proceedings of the AACR Special Conference: Patient-Derived Cancer Models: Present and Future Applications from Basic Science to the Clinic, 11–14 February. New Orleans, LA. Philadelphia (PA): AACR; Clin Cancer Res 2016;22(16_Suppl):Abstract nr B28.

47 Wilmanns, C., Fan, D., O'Brian, C.A. et al. (1992). Orthotopic and ectopic organ environments differentially influence the sensitivity of murine colon carcinoma cells to doxorubicin and 5-fluorouracil. *Int. J. Cancer* 52 (1): 98–104.

48 Hidalgo, M., Amant, F., Biankin, A.V. et al. (2014). Patient-derived xenograft models: an emerging platform for translational cancer research. *Cancer Discov.* 4 (9): 998–1013.

49 Predina, J., Eruslanov, E., Judy, B. et al. (2013). Changes in the local tumor microenvironment in recurrent cancers may explain the failure of vaccines after surgery. *Proc. Natl. Acad. Sci. U.S.A.* 110 (5): E415–E424.

50 Garcia, C., Dubois, L.G., Xavier, A.L. et al. (2014). The orthotopic xenotransplant of human glioblastoma successfully recapitulates glioblastoma-microenvironment interactions in a non-immunosuppressed mouse model. *BMC Cancer* 14: 923.

51 Basel, M.T., Narayanan, S., Ganta, C. et al. (2018). Developing a xenograft human tumor model in immunocompetent mice. *Cancer Lett.* 412: 256–263.

52 McCune, J.M., Namikawa, R., Kaneshima, H. et al. (1988). The SCID-hu mouse: murine model for the analysis of human hematolymphoid differentiation and function. *Science* 241 (4873): 1632–1639.

53 Nicolini, F.E., Cashman, J.D., Hogge, D.E. et al. (2004). NOD/SCID mice engineered to express human IL-3, GM-CSF and steel factor constitutively mobilize engrafted human progenitors and compromise human stem cell regeneration. *Leukemia* 18 (2): 341–347.

54 Brehm, M.A., Wiles, M.V., Greiner, D.L., and Shultz, L.D. (2014). Generation of improved humanized mouse models for human infectious diseases. *J. Immunol. Methods* 410: 3–17.

55 Jangalwe, S., Shultz, L.D., Mathew, A., and Brehm, M.A. (2016). Improved B cell development in humanized NOD-*scid IL2Rγnull* mice transgenically expressing human stem cell factor, granulocyte-macrophage colony-stimulating factor and interleukin-3. *Immun. Inflammation Dis.* 4 (4): 427–440.

56 Coughlan, A.M., Harmon, C., Whelan, S. et al. (2016). Myeloid engraftment in humanized mice: impact of granulocyte-colony stimulating factor treatment and transgenic mouse strain. *Stem Cells Dev.* 25 (7): 530–541.

57 Curran, M., Mairesse, M., Matas-Céspedes, A. et al. (2020). Recent advancements and applications of human immune system mice in preclinical immuno-oncology. *Toxicol. Pathol.* 48 (2): 302–316.

58 Grompe, M. and Strom, S. (2013). Mice with human livers. *Gastroenterology* 145 (6): 1209–1214.

59 Vercauteren, K., de Jong, Y.P., and Meuleman, P. (2015). Animal models for the study of HCV. *Curr. Opin. Virol.* 13: 67–74.

60 Wilson, E.M., Bial, J., Tarlow, B. et al. (2014). Extensive double humanization of both liver and hematopoiesis in FRGN mice. *Stem Cell Res.* 13 (3 Pt A): 404–412.

61 Ito, R., Katano, I., Kawai, K. et al. (2009). Highly sensitive model for xenogenic GVHD using severe immunodeficient NOG mice. *Transplantation* 87 (11): 1654–1658.

62 King, M.A., Covassin, L., Brehm, M.A. et al. (2009). Human peripheral blood leucocyte non-obese diabetic-severe combined immunodeficiency interleukin-2 receptor gamma chain gene mouse model of xenogeneic graft-versus-host-like disease and the role of host major histocompatibility complex. *Clin. Exp. Immunol.* 157 (1): 104–118.

63 Shulman, H.M., Kleiner, D., Lee, S.J. et al. (2006). Histopathologic diagnosis of chronic graft-versus-host disease: National Institutes of Health consensus development project on criteria for clinical trials in chronic graft-versus-host disease: II. Pathology working group report. *Biol. Blood Marrow Transplant.* 12 (1): 31–47.

64 Chen, K., Ahmed, S., Adeyi, O. et al. (2012). Human solid tumor xenografts in immunodeficient mice are vulnerable to lymphomagenesis associated with Epstein–Barr virus. *PLoS One* 7 (6): e39294.

65 Wetterauer, C., Vlajnic, T., Schüler, J. et al. (2015). Early development of human lymphomas in a prostate cancer xenograft program using triple knock-out immunocompromised mice. *The Prostate* 75 (6): 585–592.

66 Duran-Struuck, R. and Dysko, R.C. (2009). Principles of bone marrow transplantation (BMT): providing optimal veterinary and husbandry care to irradiated mice in BMT studies. *J. Am. Assoc. Lab. Anim. Sci.* 48 (1): 11–22.

67 Gugel, M., Lertpiriyapong, K., White, J. et al. (2017). Acute morbidity and mortality in highly immunocompromised mice following irradiation and hematopoietic cell line injection. *J. Am. Assoc. Lab. Anim. Sci.* 56 (5): 574–694.

68 Baze, W.B., Steinbach, T.J., Fleetwood, M.L. et al. (2006). Karyomegaly and intranuclear inclusions in the renal tubules of sentinel ICR mice (*Mus musculus*). *Comp. Med.* 56 (5): 435–438.

69 McInnes, E., Bennett, M., O'Hara, M. et al. (2015). Intranuclear inclusions in renal tubular epithelium in immunodeficient mice stain with antibodies for bovine papillomavirus type 1 L1 protein. *Vet. Sci.* 2 (2): 84–96.

70 Santagostino, S.F., Arbona, R.J.R., Nashat, M.A. et al. (2017). Pathology of aging in NOD *scid* gamma female mice. *Vet. Pathol.* 54 (5): 855–869.

Vet-ebooks.com

71 Roediger, B., Lee, Q., Tikoo, S. et al. (2018). An atypical parvovirus drives chronic tubulointerstitial nephropathy and kidney fibrosis. *Cell* 175 (2): 530. 543.e24.

72 Lee, Q., Padula, M.P., Pinello, N. et al. (2020). Murine and related chapparvoviruses are nephro-tropic and produce novel accessory proteins in infected kidneys. *PLoS Pathog.* 16 (1): e1008262.

73 Pénzes, J.J., Söderlund-Venermo, M., Canuti, M. et al. (2020). Reorganizing the family Parvoviridae: a revised taxonomy independent of the canonical approach based on host association. *Arch. Virol.* 165 (9): 2133–2146.

74 Abt, M.C., McKenney, P.T., and Pamer, E.G. (2016). *Clostridium difficile* colitis: pathogenesis and host defence. *Nat. Rev. Microbiol.* 14 (10): 609–620.

75 Koya, V., Campbell, A.M., McLaughlin, P.J. et al. (2012). Outbreak of abdominal distension and obstipation in a C57BL/6J experimental autoimmune encephalomyelitis study. *Vet. Pathol.* 49 (3): 528–531.

76 Kawano, A., Ikeda, M., Iritani, R. et al. (2007). Colitis associated with *Clostridium difficile* in specific-pathogen-free C3H-scid mice. *J. Vet. Med. Sci.* 69 (9): 973–975.

77 Mau, T., Eckley, S.S., Bergin, I.L. et al. (2019). Outbreak of murine infection with *Clostridium difficile* associated with the administration of a pre- and peri-natal methyl-donor diet. *mSphere* 4: e00138-19. http://biorxiv.org/lookup/doi/10.1101/565762.

78 Etienne-Mesmin, L., Chassaing, B., Adekunle, O. et al. (2018). Toxin-positive *Clostridium difficile* latently infect mouse colonies and protect against highly pathogenic *C. difficile*. *Gut* 67 (5): 860–871.

79 Hutton, M.L., Mackin, K.E., Chakravorty, A., and Lyras, D. (2014). Small animal models for the study of *Clostridium difficile* disease pathogenesis. *FEMS Microbiol. Lett.* 352 (2): 140–149.

80 Fletcher, J.R., Erwin, S., Lanzas, C., and Theriot, C.M. (2018). Shifts in the gut metabolome and *Clostridium difficile* transcriptome throughout colonization and infection in a mouse model. *mSphere* 3 (2): e00089-18. https://msphere.asm.org/content/3/2/e00089-18.

81 Lewis, B.B., Carter, R.A., Ling, L. et al. (2017). Pathogenicity locus, core genome, and accessory gene contributions to *Clostridium difficile* virulence. *mBio* 8 (4): e00885-17. https://mbio.asm.org/content/8/4/e00885-17.

82 Ma, K.G.L., Lertpiriyapong, K., Piersigilli, A. et al. (2020). Outbreaks of typhlocolitis caused by hypervirulent group ST1 *Clostridioides difficile* in highly immunocompromised strains of mice. *Comp. Med.* 70 (3): 277–290.

83 Depoorter, E., Bull, M.J., Peeters, C. et al. (2016). *Burkholderia*: an update on taxonomy and biotechnological potential as antibiotic producers. *Appl. Microbiol. Biotechnol.* 100 (12): 5215–5229.

84 Mahenthiralingam, E., Urban, T.A., and Goldberg, J.B. (2005). The multifarious, multireplicon *Burkholderia cepacia* complex. *Nat. Rev. Microbiol.* 3 (2): 144–156.

85 Porter, L.A. and Goldberg, J.B. (2011). Influence of neutrophil defects on *Burkholderia cepacia* complex pathogenesis. *Front. Cell Infect. Microbiol.* 1: 9.

86 Collymore, C., Giuliano, F., and Banks, K.E. (2019). Head tilt in immunodeficient mice due to contamination of drinking water by *Burkholderia gladioli*. *J. Am. Assoc. Lab. Anim. Sci.* 58 (2): 246–250.

87 Kain, M., Martin, H., Michel, A. et al. (2018). Multiple cases of otitis media in immunocompromised mice linked to *Burkholderia gladioli*. *J. Am. Assoc. Lab. Anim. Sci.* 57: 534–642.

88 Foley, P.L., Lipuma, J.J., and Feldman, S.H. (2004). Outbreak of otitis media caused by *Burkholderia gladioli* infection in immunocompromised mice. *Comp. Med.* 54 (1): 93–99.

89 Bastidas, R.J. and Heitman, J. (2009). Trimorphic stepping stones pave the way to fungal virulence. *Proc. Natl. Acad. Sci. U.S.A.* 106 (2): 351–352.

90 Jabra-Rizk, M.A., Kong, E.F., Tsui, C. et al. (2016). *Candida albicans* athogenesis: fitting within the host-microbe damage response framework. *Infect. Immun.* 84 (10): 2724–2739.

91 Netea, M.G., Brown, G.D., Kullberg, B.J., and Gow, N.A.R. (2008). An integrated model of the recognition of *Candida albicans* by the innate immune system. *Nat. Rev. Microbiol.* 6 (1): 67–78.

92 Quintin, J., Voigt, J., van der Voort, R. et al. (2014). Differential role of NK cells against *Candida albicans* infection in immunocompetent or immunocompromised mice. *Eur. J. Immunol.* 44 (8): 2405–2414.

93 Godfrey, V. (2007). Fungal diseases in laboratory mice. In: The Mouse in Biomedical Research, Chapter 20, 2e (eds. J.G. Fox, M.T. Davisson, F.W. Quimby, et al.), 507–515. Burlington: Academic Press.

94 Radovanovic, I., Mullick, A., and Gros, P. (2011). Genetic control of susceptibility to infection with *Candida albicans* in mice. *PLoS One* 6 (4): e18957.

95 Kobayashi-Sakamoto, M., Tamai, R., Isogai, E., and Kiyoura, Y. (2018). Gastrointestinal colonisation and systemic spread of *Candida albicans* in mice treated with antibiotics and prednisolone. *Microb. Pathog.* 117: 191–199.

96 Cantorna, M.T. and Balish, E. (1990). Mucosal and systemic candidiasis in congenitally immunodeficient mice. *Infect. Immun.* 58 (4): 1093–1100.

97 Liu, Q., Arseculeratne, C., Liu, Z. et al. (2004). Simultaneous deficiency in CD28 and STAT6 results in chronic ectoparasite-induced inflammatory skin disease. *Infect. Immun.* 72 (7): 3706–3715.

98 Smith, P.C., Zeiss, C.J., Beck, A.P., and Scholz, J.A. (2016). *Demodex musculi* infestation in genetically immunomodulated mice. *Comp. Med.* 66 (4): 278–285.

99 Nashat, M.A., Luchins, K.R., Lepherd, M.L. et al. (2017). Characterization of *Demodex musculi* infestation, associated comorbidities, and topographic distribution in a mouse strain with defective adaptive immunity. *Comp. Med.* 67 (4): 315–329.

Vet-ebooks.com

100 Nashat, M.A., Ricart Arbona, R.J., Riedel, E.R. et al. (2018). Comparison of diagnostic methods and sampling sites for the detection of *Demodex musculi*. *J. Am. Assoc. Lab. Anim. Sci.* 57 (2): 173–185.

101 Gugel, M., Ricart-Arbona, R., Schietinger, A. et al. (2018). Characterizing the murine immune response following infestation with *Demodex musculi*. *J. Am. Assoc. Lab. Anim. Sci.* 57 (5): 534–642. p. 620.

102 Gugel, M., Ricart-Arbona, R., Daniels, K. et al. (2019). Mite burden and immunologic response to *Demodex musculi* in Swiss Webster, BALB/cAnNCrl, and C57BL/6NCrl mice. *J. Am. Assoc. Lab. Anim. Sci.* 58 (5): 607–726. p. 681.

103 Barthold, S., Griffey, S., and Percy, D. (2016). Pathology of Laboratory Rodents and Rabbits, p. 384, 4e. Ames, IA: Wiley Blackwell.

104 Compton, S.R., Ball-Goodrich, L.J., Johnson, L.K. et al. (2004). Pathogenesis of enterotropic mouse hepatitis virus in immunocompetent and immunodeficient mice. *Comp. Med.* 54 (6): 681–689.

105 Ward, J.M., Wobus, C.E., Thackray, L.B. et al. (2006). Pathology of immunodeficient mice with naturally occurring murine norovirus infection. *Toxicol. Pathol.* 34 (6): 708–715.

106 Karst, S.M. (2003). STAT1-dependent innate immunity to a Norwalk-like virus. *Science* 299 (5612): 1575–1578.

107 Karst, S.M., Wobus, C.E., Goodfellow, I.G. et al. (2014). Advances in norovirus biology. *Cell Host Microbe* 15 (6): 668–680.

108 Jones, M.K., Watanabe, M., Zhu, S. et al. (2014). Enteric bacteria promote human and mouse norovirus infection of B cells. *Science* 346 (6210): 755–759.

109 Ingle, A., Ghim, S., Joh, J. et al. (2011). Novel laboratory mouse papillomavirus (MusPV) infection. *Vet. Pathol.* 48 (2): 500–505.

110 Sundberg, J.P., Stearns, T.M., Joh, J. et al. (2014). Immune status, strain background, and anatomic site of inoculation affect mouse papillomavirus (MmuPV1) induction of exophytic papillomas or endophytic trichoblastomas. *PLoS One* 9 (12): e113582.

111 Percy, D.H., Auger, D.C., and Croy, B.A. (1994). Signs and lesions of experimental Sendai virus infection in two genetically distinct strains of SCID/beige mice. *Vet. Pathol.* 31 (1): 67–73.

112 Percy, D.H. and Barta, J.R. (1993). Spontaneous and experimental infections in scid and scid/beige mice. *Lab. Anim. Sci.* 43 (2): 127–132.

113 Vedder, A.R., Miedel, E.L., Ragland, N.H. et al. (2019). Effects of *Corynebacterium bovis* on engraftment of patient-derived chronic-myelomonocytic leukemia cells in NSGS mice. *Comp. Med.* 69 (4): 276–282.

114 Fox, J.G., Ge, Z., Whary, M.T. et al. (2011). *Helicobacter hepaticus* infection in mice: models for understanding lower bowel inflammation and cancer. *Mucosal Immunol.* 4 (1): 22–30.

115 Bingel, S.A. (2002). Pathology of a mouse model of x-linked chronic granulomatous disease. *Contemp. Top. Lab. Anim. Sci.* 41 (5): 33–38.

116 Pizzolla, A., Hultqvist, M., Nilson, B. et al. (2012). Reactive oxygen species produced by the NADPH oxidase 2 complex in monocytes protect mice from bacterial infections. *J. Immunol.* 188 (10): 5003–5011.

117 Acuff, N.V., LaGatta, M., Nagy, T., and Watford, W.T. (2017). Severe dermatitis associated with spontaneous *Staphylococcus xylosus* infection in *Rag*$^{-/-}$*Tpl2*$^{-/-}$ mice. *Comp. Med.* 67 (4): 344–349.

118 Villano, J.S., Rong, F., and Cooper, T.K. (2014). Bacterial infections in Myd88-deficient mice. *Comp. Med.* 64 (2): 110–114.

119 MacArthur, C.J., Pillers, D.-A.M., Pang, J. et al. (2008). Gram-negative pathogen *Klebsiella oxytoca* is associated with spontaneous chronic otitis media in Toll-like receptor 4-deficient C3H/HeJ mice. *Acta Otolaryngol.* 128 (2): 132–138.

120 Foreman, O., Kavirayani, A.M., Griffey, S.M. et al. (2011). Opportunistic bacterial infections in breeding colonies of the NSG mouse strain. *Vet. Pathol.* 48 (2): 495–499.

121 Dagnæs-Hansen, F. and Poulsen, K. (2011). *Pneumocystis murina* infection in immunodeficient mice in a closed barrier unit: a case report |. *Scand. J. Lab. Anim. Sci.* 38 (2): 91–96.

122 Rong, H.-M., Qian, X.-J., Zhang, C. et al. (2019). IL-17 inversely correlated with IL-10 via the STAT3 gene in *Pneumocystis*-infected mice. *Mediators Inflamm.* 2019: 6750861. https://www.hindawi.com/journals/mi/2019/6750861.

123 Pritchett-Corning, K.R., Cosentino, J., and Clifford, C.B. (2009). Contemporary prevalence of infectious agents in laboratory mice and rats. *Lab. Anim.* 43 (2): 165–173.

124 Mangosing, S., Ricart Arbona, R., Monette, S., and Lipman, N. (2019). Iatrogenic reovirus infection in highly immunocompromised mice. *J. Am. Assoc. Lab. Anim. Sci.* 58 (5): 607–726.

125 Nicklas, W., Bleich, A., and Mähler, M. (2012). Viral infections of laboratory mice. In: The Laboratory Mouse, Chapter 3.2, 2e (ed. H.J. Hedrich), 427–480. Waltham, MA: Elsevier.

126 Loken, S.D., Norman, K., Hirasawa, K. et al. (2004). Morbidity in immunosuppressed (SCID/NOD) mice treated with reovirus (dearing 3) as an anti-cancer biotherapeutic. *Cancer Biol. Ther.* 3 (8): 734–738.

127 Carty, A.J. (2008). Opportunistic infections of mice and rats: Jacoby and Lindsey revisited. *ILAR J.* 49 (3): 272–276.

128 Franklin, C.L. (2006). Microbial considerations in genetically engineered mouse research. *ILAR J.* 47 (2): 141–155.

129 Treuting, P.M., Clifford, C.B., Sellers, R.S., and Brayton, C.F. (2012). Of mice and microflora: considerations for genetically engineered mice. *Vet. Pathol.* 49 (1): 44–63.

130 Adhikary, S., Bisgaard, M., Dagnæs-Hansen, F., and Christensen, H. (2017). Clonal outbreaks of [*Pasteurella*] *pneumotropica* biovar Heyl in two mouse colonies. *Lab. Anim.* 51 (6): 613–621.

131 Bleich, A., Kirsch, P., Sahly, H. et al. (2008). *Klebsiella oxytoca*: opportunistic infections in laboratory rodents. *Lab. Anim.* 42 (3): 369–375.

Vet-ebooks.com

132 Chabé, M., Aliouat-Denis, C.-M., Delhaes, L. et al. (2011). Pneumocystis: from a doubtful unique entity to a group of highly diversified fungal species. *FEMS Yeast Res.* 11 (1): 2–17.

133 Peterson, N.C. (2008). From bench to cageside: risk assessment for rodent pathogen contamination of cells and biologics. *ILAR J.* 49 (3): 310–315.

134 Dodd, J., Kelleher, R., Menon, M., and Besch-Williford, C. (2003). *Mycoplasma arginini* -associated septic arthritis and wasting in SCID mice. *Contemp. Top. Lab. Anim. Sci.* 42 (4): 66.

135 Dykewicz, C.A., Dato, V.M., Fisher-Hoch, S.P. et al. (1992). Lymphocytic choriomeningitis outbreak associated with nude mice in a research institute. *J. Am. Med. Assoc.* 267 (10): 1349–1353.

136 Nicklas, W., Kraft, V., and Meyer, B. (1993). Contamination of transplantable tumors, cell lines, and monoclonal antibodies with rodent viruses. *Lab. Anim. Sci.* 43 (4): 296–300.

137 Brayton, C.F., Treuting, P.M., and Ward, J.M. (2012). Pathobiology of aging mice and GEM: background strains and experimental design. *Vet. Pathol.* 49 (1): 85–105.

138 Larsen, S.R., Kingham, J.A., Hayward, M.D., and Rasko, J.E.J. (2006). Damage to incisors after nonmyeloablative total body irradiation may complicate NOD/SCID models of hemopoietic stem cell transplantation. *Comp. Med.* 56 (3): 209–214.

139 Shultz, L.D., Lyons, B.L., Burzenski, L.M. et al. (2005). Human lymphoid and myeloid cell development in NOD/LtSz-scid IL2R gamma null mice engrafted with mobilized human hemopoietic stem cells. *J. Immunol.* 174 (10): 6477–6489.

140 Tillman, H., Janke, L.J., Funk, A. et al. (2020). Morphologic and immunohistochemical characterization of spontaneous lymphoma/leukemia in NSG mice. *Vet. Pathol.* 57 (1): 160–171.

141 Yasuda, M., Ogura, T., Goto, T. et al. (2017). Incidence of spontaneous lymphomas in non-experimental NOD/Shi-scid, IL-2Rγ^{null} (NOG) mice. *Exp. Anim.* 66 (4): 425–435.

142 Chiu, P.P.L., Ivakine, E., Mortin-Toth, S., and Danska, J.S. (2002). Susceptibility to lymphoid neoplasia in immunodeficient strains of nonobese diabetic mice. *Cancer Res.* 62 (20): 5828–5834.

143 Shultz, L.D., Lang, P.A., Christianson, S.W. et al. (2000). NOD/LtSz-*Rag1*^{null} mice: an immunodeficient and radioresistant model for engraftment of human hematolymphoid cells, HIV infection, and adoptive transfer of NOD mouse diabetogenic T cells. *J. Immunol.* 164 (5): 2496–2507.

144 Braun, A., Ernst, H., Schaudien, D. et al. (2012). The respiratory tract. In: The Laboratory Mouse, Chapter 2.7, 2e (ed. H.J. Hedrich), 271–311. Waltham, MA: Elsevier.

145 Sharkey, F.E. and Fogh, J. (1979). Incidence and pathological features of spontaneous tumors in athymic nude mice. *Cancer Res.* 39 (3): 833–839.

146 Viguera, C., Ward, J.M., Nims, R.M. et al. (1978). Clinical and pathologic conditions of female nude (athymic) mice in two conventional maintained colonies. *J. Am. Vet. Med. Assoc.* 173 (9): 1198–1201.

147 Bazille, P.G., Walden, S.D., Koniar, B.L., and Gunther, R. (2001). Commercial cotton nesting material as a predisposing factor for conjunctivitis in athymic nude mice. *Lab. Anim.* 30 (5): 40–42.

148 Economopoulos, V., Noad, J.C., Krishnamoorthy, S. et al. (2011). Comparing the MRI appearance of the lymph nodes and spleen in wild-type and immuno-deficient mouse strains. *PLoS One* 6 (11): e27508.

149 Itoh, M., Kokudo, Y., Sakamoto, Y., and Takeuchi, Y. (1997). Spontaneous degeneration of testicular germ cells in congenitally athymic nude mice of four strains: a light microscopical observation. *J. Androl.* 18 (6): 672–680.

150 Casey, K.M., Johnson, A.L., Hunrath, M.N. et al. (2019). Proliferative typhlocolitis with multinucleated giant cells: a nonspecific enteropathy in immunodeficient sentinel mice. *Vet. Pathol.* 56 (1): 157–168.

151 Leiter, E. (1993). The NOD mouse: a model for analyzing the interplay between heredity and environment in development of autoimmune disease. *ILAR News* 35 (1): 4–14.

152 Kavirayani, A.M. and Foreman, O. (2010). Retrospective study of spontaneous osteosarcomas in the nonobese diabetic strain and nonobese diabetic-derived substrains of mice. *Vet. Pathol.* 47 (3): 482–487.

153 Kavirayani, A.M., Sundberg, J.P., and Foreman, O. (2012). Primary neoplasms of bones in mice: retrospective study and review of literature. *Vet. Pathol.* 49 (1): 182–205.

Vet-ebooks.com

10

Skin, Hair, and Nails

John P. Sundberg, Lloyd E. King, Jr, and Raoul V. Kuiper

Introduction

The skin is the largest of the intermediate sized organs, at least in terms of mass [1], and it performs a variety of functions (Table 10.1) [2]. Covering the exterior of the body, skin features such as hair texture, color, hair loss (alopecia), as well as lesions such as ulcers, scaly skin, are readily observed. As a physiological interface between the organism's inner workings and the outside environment, skin and its derivatives often provide the first display of the general physical condition of an animal. Not only do skin disorders have major potential impact on the animal's physiology, but changes in the skin and hair can also reflect general physiological homeostasis, and genetic status. In mice, nails are small and abnormalities are less easily identified unless major, such as massively overgrown nails (onychogryphosis).

The earliest sources of mice that spontaneously reproduce cutaneous abnormalities were those carrying naturally occurring mutations (see Chapter 3). When in otherwise good health, their appearance caused many mutant mice with cutaneous abnormalities, especially hair color and texture, to be raised as pets as illustrated on many websites (www.fancymice.info, www.petmousefanciers.com). Today, highly inbred uniform strains of mutant mice, available in biorepositories worldwide (see Chapter 2), include those with skin and hair abnormalities, and facilitate accurate analysis and identification of responsible genes. Mice carrying mutations in the same (orthologous) genes while recapitulating a human phenotype provide valuable cross-species support for the underlying genetic cause for human disease [3]. Modern molecular approaches to partially (hypomorphic allele) or completely (null allele) inactivate a single gene, impose local and temporal control over expression (conditional and inducible alleles), and create orthologous mutations to those found in human patients, further help address which gene(s) is/are functionally responsible for the detected alterations and validate candidate genes and potential models for human disorders. Today, candidate gene variants identified in human genome wide association studies (GWAS) or next-generation sequencing of families with rare diseases can be replicated in mice using clustered regularly interspaced short palindrome repeats (CRISPR)/CRISPR-associated protein 9 (Cas9) to validate or invalidate the discovery. For example, when *CARD14* was identified as being important in the pathogenesis of psoriasis, the precise mouse ortholog was created by more than one lab group, each using different methods, resulting in mice with a psoriasis-like phenotype [4–6]. Only one out of two identified single nucleotide polymorphisms (SNPs) resulted in a skin phenotype in mice similar to the human disease, demonstrating the discoveries in humans can be validated or invalidated using the mouse [6].

Mutations in various genes involved in related functions tend to result in similar phenotypes (genocopies). Detailed evaluation of genocopies is a powerful approach to define how each gene/protein functions within a molecular pathway. A classic example is provided by inactivating mutations in the transforming growth factor alpha pathway. Two induced null mutations of transforming growth factor alpha ($Tgfa^{tm1Ard}$ and $Tgfa^{tm1Unc}$) were found to be allelic with the spontaneous waved 1 ($Tgfa^{wa1}$) mutation, and all resulted in mice with wavy hair [7, 8]. Another spontaneous mutation, waved 2 ($Egfr^{wa2}$), clinically very similar to waved 1, was determined to be a mutation of the epidermal growth factor receptor gene *Egfr*, for which TGFA is an activating ligand [9].

While some mutations have no obvious effects [10], in others, phenotypes can vary dramatically because of the type of mutation within a gene, or the genetic background of the strain the mutation occurs in or is transferred onto (see Chapter 3 on genetics). Some mutations, such as spontaneous and induced mutations in the desmoglein 3 (*Dsg3*) gene, cause a similar pemphigus vulgaris-like disease regardless of background strain or exon mutated (see below) [11, 12]. In other cases, there may be marked variability between alleles within a single gene, or the same allele in different congenic strains. For example, the $Egfr^{tm1Dwt}$ null mutation has marked phenotypic variation dependent on strain background (see Figure 4.3) [13–15]. Another example is the spontaneous hypomorphic allele of laminin gamma 2 ($Lamc2^{jeb}$) [16] that causes blistering skin disease with affected mice surviving to

Pathology of Genetically Engineered and Other Mutant Mice, First Edition. Edited by John P. Sundberg, Peter Vogel, and Jerrold M. Ward.
© 2022 John Wiley & Sons, Inc. Published 2022 by John Wiley & Sons, Inc.

Vet-ebooks.com

Table 10.1 Functions of the skin.

Barrier: Physical, percutaneous absorption, chemical. Ultraviolet radiation protection
Endocrine: Vitamin D metabolism
Immunological: Acquired and innate (antimicrobial peptides, cytokines)
Mechanical: Stretch and compression
Repair injury or damage
Sensory and autonomic functions
Sociosexual communication
Thermoregulation

Source: Based on Chuong et al. (2002).

adulthood while the null allele (*Lamc2*^{tm1Uit1}) [17] is a neonatal lethal mutation. Moving the former hypomorphic allele, *Lamc2*^{jeb}, onto different inbred backgrounds to create congenic strains revealed major changes in disease severity, partially due to a *Col17a1* hypomorphic allelic mutation in some of the strains [18]. While these types of findings were observed for decades from studying many different mouse mutations, only more recently have investigators utilized the power of mouse genetics to identify modifying genes to explain the subtypes in the orthologous human disease (see Chapter 4). Similar approaches will reveal further genetic basis for phenotypic variability in humans affected by closely resembling genodermatoses.

Targeted mutagenesis studies often utilize C57BL/6 and 129 strains, for both of which there are many substrains, each with their own set of peculiarities. This can create additional complications for investigators comparing lesions associated with similar mutations created in different laboratories [19]. For example some, but not all, of the 129 strains have a hypomorphic allele of the ATP-binding cassette, subfamily C (CFTR/MRP), member 6 (*Abcc6*) gene (Figure 2.1), a mutation that results in ectopic mineralization (pseudoxanthoma elasticum) [20]. This can result in inaccurate phenotyping of null mutations in other genes that also affect mineralization, such as 5′ nucleotidase (*Nt5e*^{tm1Jgsc}), unless the mutant *Abcc6* allele is replaced with the wildtype allele [21]. Also, multifactorial disorders like ulcerative dermatitis in B6 strains vary dramatically in severity and frequency among different C57BL/6 substrains [22]. Knowing as much as possible about each inbred strain used, including common and rare background diseases, can help with the interpretation of phenotypes.

This chapter provides examples of spontaneous and induced mutant mice that illustrate general types of abnormalities in skin and its appendages. Categorizing (skin) phenotypes facilitates identification of diseases in humans and domestic animals for which the mutant mouse presents a potential orthologous model. Grouping of phenotypes, also helps identify those phenotypic mimics (genocopies) that are key to unravel complex molecular pathways controlled by hitherto seemingly unrelated genes and better understand the pathogenesis of the disease.

This chapter is not designed to be comprehensive, but rather representative of disease groups to help investigators structure their approach to the complexity of phenotyping the skin and adnexa in newly developed mutants.

Normal Anatomy and Embryology of Mouse Skin, Hair, and Nails

In order to define lesions in mutant mice, one must first understand basic anatomy and physiology of the organ system under investigation. The embryology, anatomy, and physiology of normal mammalian skin, hair, and nails are deceptively complex and cannot be completely described in this chapter. The reader is referred to comprehensive reviews elsewhere [23–29]. In brief, from early embryogenesis the hair follicle develops from a simple two to three cell layer structure (placode) into a complex multilayered hair follicle and sebaceous gland (Figure 10.1) [23, 30–33]. Hair follicle density increases during embryonic life [34]. The epithelial/mesenchymal interactions that induce the hair bulge, hair follicle elongation, and ultimately hair shaft development are described elsewhere in detail [27, 35, 36]. Melanization of the hair bulb and shaft first occurs during the final stages at a time when the first hair shaft is formed [27]. In general, all of the pigment in mouse skin is present in the midregion of the mature plucked hair shaft with little or no melanin present in the interfollicular epidermis (IFE), unlike in human skin. This feature of mouse skin is often a cause for alarm when shaving heavily pigmented mice, such as a C57BL/6J mouse that have black hair. The skin color of these mice ranges from dark to light gray, almost pink, often in blotches (Figure 10.2) [37]. As the pigment is produced and transferred to the hair shaft exclusively during anagen (actively growing hair shafts), only anagen hair follicles are pigmented. In normal mice, there is no interfollicular epidermal pigmentation in the truncal skin [37]. Early hair follicle cycles follow a wave pattern from head to tail that accounts for the pattern described above in shaved mice [38, 39]. Thus, skin color can be used as an indicator for hair cycle stage [37, 40, 41].

At birth, the truncal epidermis is quite thick, but it rapidly thins around the first two weeks of life (Figures 10.1–10.3) [42–44]. Different hair follicles producing different hair types develop at different embryologic stages (Figure 10.1c) [45–48]. Development of hair follicles continues to full anagen by one-week *postpartum*. By the end of the second week of life, follicles enter catagen during which the bulb regresses and moves closer to the surface, leaving a trail of apoptotic cells of the deep portion of the hair follicle. This is a very short transition phase, one to two days in duration, to the resting, or telogen phase and it represents the end of embryonic hair development. Like the epidermis, the dermis is relatively thick during the first two weeks of life and then thins to the adult state. However, the hypodermal fat layer varies in thickness as hair follicle length increases in anagen

Vet-ebooks.com

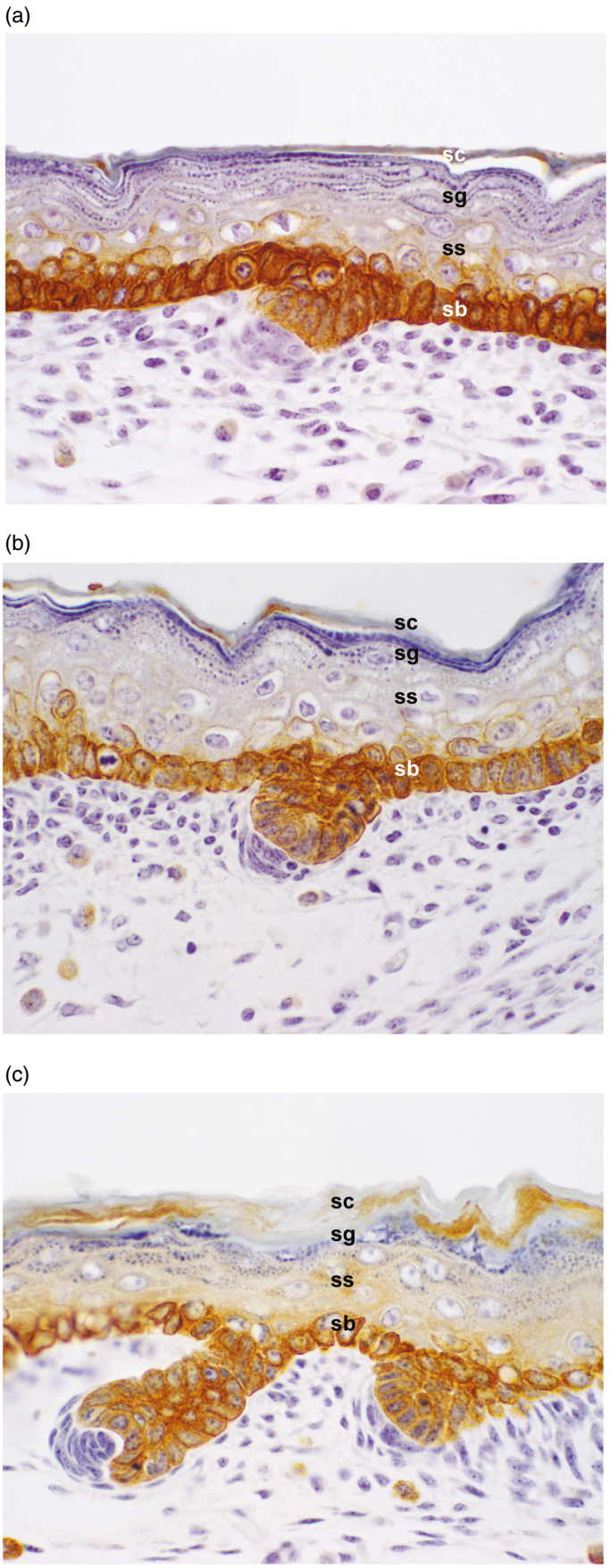


Figure 10.1 **Embryonic hair follicle development**. The epidermis is relatively thick near the end of embryogenesis and during the first two weeks of life at which point it becomes very thin. Hair follicles develop from placodes (accumulation of specialized fibroblasts forming the dermal papilla beneath the epidermis). Keratin 5 (KRT5) labels basal and hair follicle cells but not fibroblasts. Follicle development is illustrated in C57BL/6J mice at 17.5 dpc (a), 18.5 dpc (b), and one day of age (c). At these stages, the epidermis has already stratified (stratum basale [sb], stratum spinosum [ss], stratum granulosum [sg], and stratum corneum [sc]). Note by 18.5 dpc follicles can be observed at different developmental stages which are follicles that produce different hair types.

Vet-ebooks.com

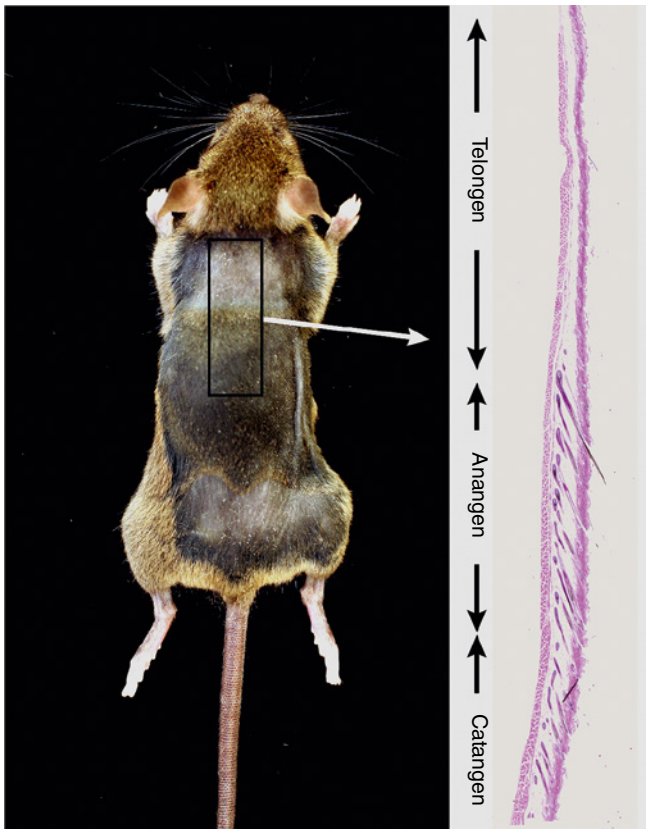


Figure 10.2 **Gross differences in hair cycle stage**. An agouti C3H/HeJ shaved mouse exhibits pale skin in telogen but pigmented skin in areas of anagen and early catagen. Adjacent histologic section illustrates the long anagen stage follicles from where the skin pigmentation begins.

and decreases in telogen (Figure 10.3) [49–52]. The hair cycles in young mice in a wave beginning cranially and progressing in a somewhat irregular pattern caudally [53]. In adults, the hair follicles cycle in patches but still in an anterior to posterior manner. Humans have a hair wave during embryogenesis, but, in contrast to the mouse, humans have a mosaic pattern of hair cycling as adults [28]. When comparing mutant and control mouse skin, it is of paramount importance to match hair cycle stage to avoid the common misinterpretation that any difference seen in skin thickness is due to the mutation being investigated and not differences in the hair cycle stage [37]. Examples where this was not done are commonly found in the literature [54, 55]. Furthermore, prominent apoptosis in certain stages of catagen can be misinterpreted to be necrosis in toxicology studies if one is not aware that this can be normal.

Various hair shaft types are found in different regions on the body of the mouse, as is also the case in humans and most other mammals (Table 10.2). For the most commonly studied hairs, those of the trunk (body or pelage hairs), four types are recognized morphologically (Figure 10.4) [45, 56]. Further distinct hairs and follicles include vibrissae on the muzzle, around the eyes, and above the feet (Figure 10.5A–C), tail skin hair (Figure 10.5D–F), cilia on eyelids (Figure 10.6A), hairs around the ears (Figure 10.6C), and perianal hairs (Figure 10.6D) [26]. The length of the hair shaft is primarily determined by the length of the hair cycle and varies with the different hair types.

The normal adult hair follicle is a very complicated structure that develops into an elongated production unit to form the hair shaft (anagen) and then undergoes apoptosis and collapse (catagen) to form a tiny resting structure (telogen) until the growth phase (anagen) starts all over again. Examples of hair follicles at anagen, catagen, and telogen are shown in Figure 10.3. The deepest part of the anagen follicle is bulbous in appearance and known as the hair bulb (Figure 10.7). It consists of layers of epithelial cells that surround a core of specialized fibroblasts known by the historical term as the dermal papilla [57]. The term "dermal papilla" is commonly used by researchers working on hair follicle biology; however, some dermatologists consider the dermal papilla to relate to the upper part of the dermis where it lies between rete ridges in human skin, a configuration not found in mice. For this reason, some use the term "follicular papilla" [58]. The epithelial part of the hair bulb differentiates to form a number of layers. The basement membrane, forming the outer junction of the follicle with the dermis, becomes very hyalinized and prominent during catagen and is called the glassy membrane. The epithelial layers adjacent to this membrane form the outer root sheath, which can be identified using keratins 5 (KRT5) and 14 (KRT14) as immunohistochemical (IHC) markers for basal keratinocytes (Figures 10.1 and 10.8).

Keratin 6A (KRT6A; Figure 10.8) is a marker for the inner bulge cells that secrete BMP6 and FGF18 [59]. These cells contain many stem cell regulators, are derived from the outer root sheath (ORS) [59], and, as such, are neither companion layer nor simply differentiated ORS. These inner bulge KRT6A positive cells also anchor the hair follicle to the club hair and are involved in shedding hair during late exogen [60, 61]. Keratin 6A positive companion layer cells are a useful histologic marker to delineate the border between outer and inner root sheaths [11]. Mouse keratin-specific antibodies can be very useful for defining affected cell layers in some mutant mice [11, 62]. The inner root sheath can be differentiated into two layers based on anatomical features evident in their descriptive names concerning cytoplasmic granules: pale epithelial or Henle's (outer layer) and granular epithelial or Huxley's (inner) layers, respectively [63, 64]. These inner root sheath layers are covered by a thin layer of cells, the cuticle of the inner root sheath, that interlocks with the cuticle of the hair shaft (Figure 10.9), thus firmly attaching the hairshaft to the skin. By interlocking these layers, keep the hair shaft firmly attached to the skin. The hair shaft consists of epithelial cells that form a cortex and medulla. The hair shaft is formed from a conical cluster of keratinocytes located directly above the dermal papilla called the hair matrix [65, 66]. The size, shape, tinctorial characteristics, cytoplasmic granules, and other features change along the developing hair shaft as it approaches the epidermis. These gradual changes make interpretation of tangential and transverse sections difficult [67, 68].

Vet-ebooks.com

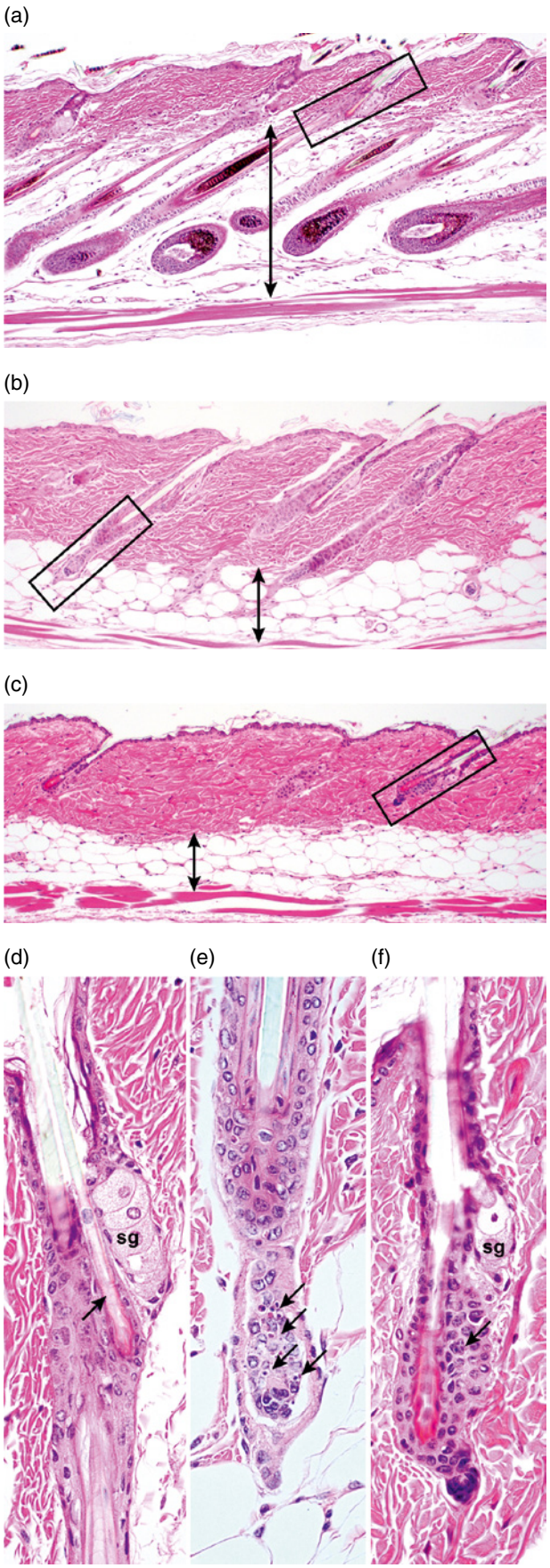


Figure 10.3 **Major stages of the hair cycle in adult C57BL/6NJ mice**. While substages have been defined, the primary hair cycle stages are the actively growing phase that produces the hair shaft, anagen (a, d), the involution stage, catagen (b, e), and the resting stage, telogen (c, f). Note how the hypodermal fat layer varies considerably between the stages (double-headed arrow, a–c). In the anagen follicle, the club hair from the previous hair cycle is pushed to the side, not forced out (arrow, d). During catagen, there is massive apoptosis and contraction of the lower portion of the hair follicle (arrows, e). In telogen, the bulge region is easily seen. The bulge cells have convoluted nuclei (arrow, f). The sebaceous glands empty via a duct into the infundibulum (sg, d, f).

Vet-ebooks.com

Table 10.2 Comparisons of structures and functions of skin and adnexa between humans and mice.

Criteria	Mouse	Human
Epidermal thickness of adult body skin	10–15 µm	50–100 µm
Epidermal thickness of thick skin	Eyelid (50–60 µm) Foot pad (150–400 µm), Muzzle (20–30 µm) Tail (70–80 µm)	Palms of hands, soles of feet (300–400 µm)
Hair types: body	Auschene Awl Guard Zigzag	Terminal Vellus
Hair types: other	Cilia (eyelashes) Ear hair Perianal hair Tail hair Vibrissae (specialized somatosensory organ with blood filled sinus found in facial skin/ muzzle and distal limbs)	Axillary hair Cilia (eyelashes) Eyebrows Facial (beard, mustache) Pubic hair
Emergence of hair	5 d postpartum	19–21 weeks gestation
Hair cycle	Wave pattern in young mice; zones in adults	Wave pattern in fetus; mosaic pattern in adult
Tail and tail hairs	Yes	Not present
Sebaceous glands	Yes	Yes
Modified sebaceous glands	Clitoral gland Meibomian glands Perianal gland Preputial gland Zymbal's gland	Ceruminous glands Meibomian glands
Eccrine glands	Yes, footpads only	Yes (entire body including soles and palms)
Apocrine sweat glands	Mice do not have apocrine sweat glands. Mammary glands are modified apocrine glands.	Yes, axilla, genito-anal region, ceruminous glands, mammary glands
Nails	Yes, distal digits	Yes, distal digits

General mechanisms of normal nail unit formation are described in reviews for mouse, human, and domestic animals [28, 63, 69, 70]. The nail plate is produced by the nail matrix at the proximal end [70] and remains firmly attached to the nail bed epidermis until, at the hyponychium, the nail bed keratinocytes transition to form a stratum granulosum and stratum corneum, allowing the nail plate to separate from the nail bed. The epidermis reflects beneath the nail unit to form the foot pad through which the eccrine gland ducts penetrate to allow secretions from these glands to reach the skin surface (Figure 10.6B) [69].

Practical Guidelines for the Biological Characterization of a New Mutation

Mice, like other mammals, undergo major changes in their lives that may affect or reflect the phenotype of a mutation. These hallmark transitions can provide points to focus systematic investigations, while knowledge of specific age-related changes of the organ system under investigation will define a second set of observation points. Hallmark transitions and phases include birth, weaning (3–4 weeks), sexual maturity (puberty, 6–8 weeks), sexual quiescence (6–8 months), and geriatric stages (2 years +) (Figure 10.10a) [71, 72]. The age range provided reflects strain specific differences, usually related to how long strains remain fecund [73]. However, it is best to define specific ages and use these consistently for comparison between studies. Mice of geriatric age are rarely studied, as the cost of maintaining mice to old age is often prohibitive, or, as is frequently the case, mutants under investigation have reduced life span and never reach this age.

An alternative approach to timed observations is to determine when clinical lesions are first evident and subsequently select ages earlier (to determine the pattern of histologic lesion development) and later (to follow the terminal features of the disease) (Figure 10.10b). For example, alopecia areata is a very late onset autoimmune disease that in mice can be initiated with full thickness skin grafts. Lesions can

Vet-ebooks.com

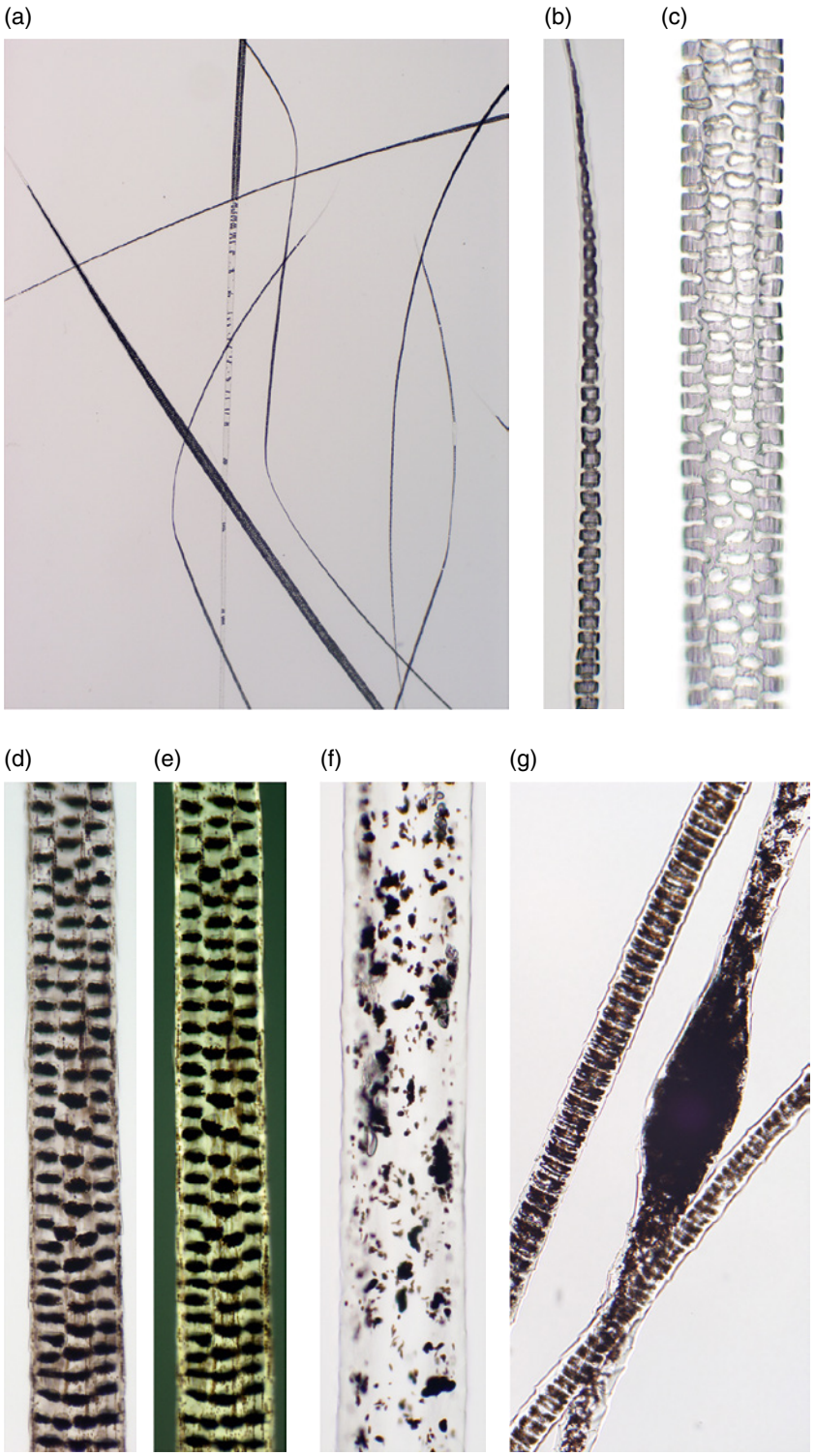


Figure 10.4 **Evaluation of plucked hair**. Hair can be manually plucked from a mouse, placed on a clean slide, and cover slipped with mounting media to create a permanent, flat sample. Most hairs are zigzag, named for their shape due to sharp bends (a). Zigzag hairs are long, thin, and have a single column of fat filled cells resulting in a septate pattern (b). By contrast, the very large, wide, and straight guard hairs have multiple layers of cells called a septulate pattern (c, BALB/cByJ albino). Pigmented mice such as C57BL/6J (d) have melanin granules within the cells of the medulla. The same hair evaluated by polarized light (e). A guard hair from an *SB/LeJ-Foxq1*^{sa} *Lyst*^{bg} satin, beige mouse (f) reveals loss of the medullary structure (satin phenotype) and abnormal clumping of melanin granules (beige phenotype). Other mutants, such as *Krt75*^{tm1Der} have some normal hair shafts while others have various degrees of swelling, loss of structure, and breakage (g).

Vet-ebooks.com

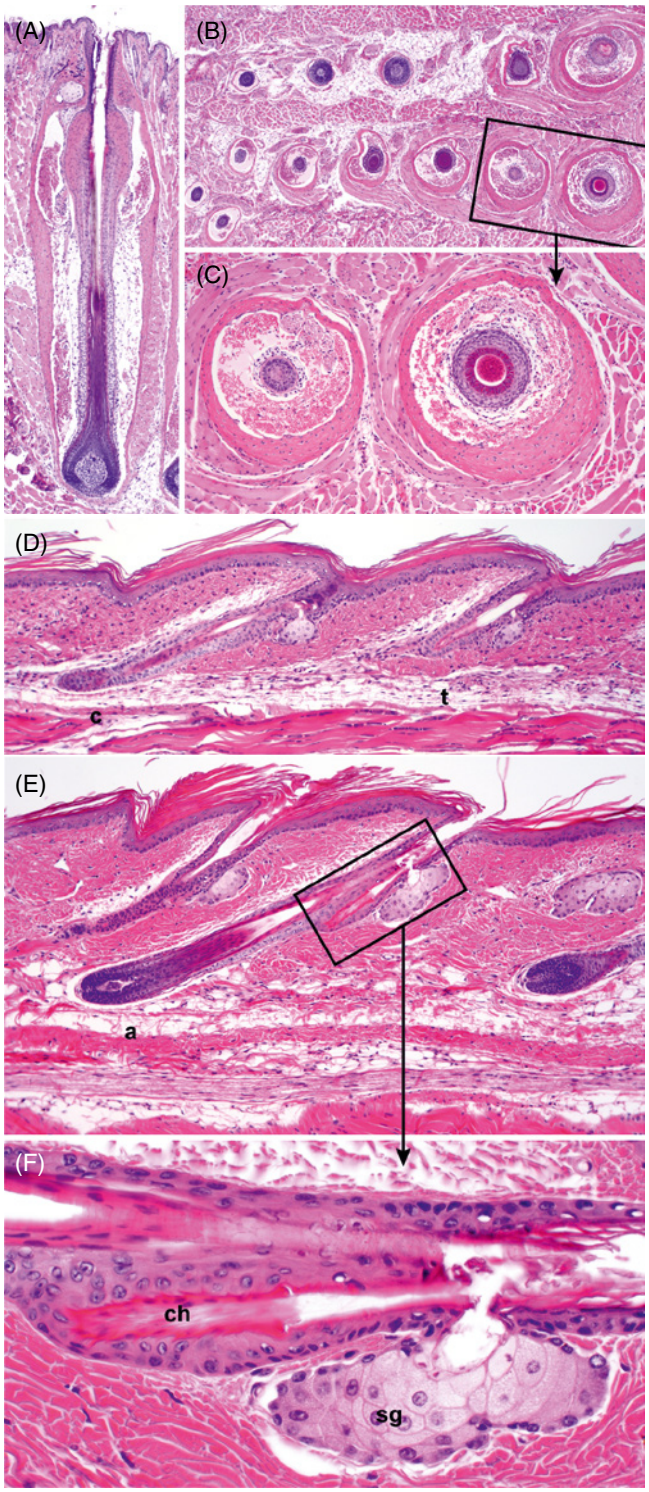


Figure 10.5 **Vibrissae and tail hair follicles.** Vibrissae follicles (A–C) are large hair follicles with sebaceous glands that form in a matrix pattern on the muzzle but also above the eyes and around the feet. They have a large blood filled sinus (s) and nerves making them somatosensory organs. The tail skin is thicker than truncal skin (D, E). Hair follicles are short, usually found in prolonged telogen (D; t) but can be found in catagen (D; c) or anagen (E; a). They have sebaceous glands (sg) adjacent to a club hair (ch) in this figure (F).

be followed at five-week intervals after skin grafting (Figure 10.11) [74]. At the other end of the spectrum is the chronic proliferative dermatitis mutant mouse (*Sharpin*^{cpdm}), where mice have to be euthanized at 10 weeks of age due to extensive cutaneous ulceration. Evaluating mice at two-week intervals from birth until euthanasia provided details on the pathogenesis (Figure 10.12) [75].

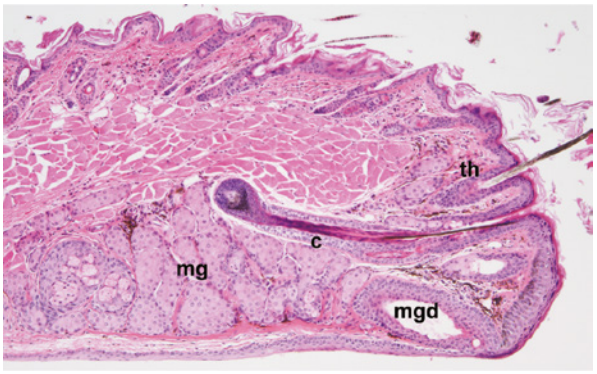
Skin and its appendages undergo very dramatic changes during the first three weeks of life as described above. To evaluate subtle changes associated with development and hair cycle, skin is collected at three-day intervals during the first three weeks of life. This can be modified based on the mutant strain being studied as some mutations affect one site, such as the ears, while others may be limited to the trunk. The numbers of mice in these studies can easily become quite large. Using inbred mice maintained in a clean, environmentally controlled, pathogen-free facility, with appropriate (littermate) controls allows one to keep the numbers of mice from which tissues are sampled to a reasonable minimum of three mutants and three controls for each sex (12 mice per time point). Those collected for the major life changes (birth, weaning, puberty, and adulthood) should have complete sets of organs sampled for comprehensive histological evaluation (see below) [76], while sampling at time points for refined skin and appendage evaluation can be limited to collection of selected skin at defined anatomic sites. Skin should be sampled at multiple standardized sites for both groups. Use of the same individual for repeated biopsies over time can reduce the numbers of animals used but could have other problematic consequences. Mice prone to blistering diseases could develop severe ulcers necessitating euthanasia. Mutant mice can develop exacerbation of the skin lesions following trauma, such as a biopsy. This is called a positive Köbner reaction and can be an issue with some of the scaly skin mutations [77, 78]. The Köbner reaction describes exacerbation of a skin lesion by relatively mild trauma, such as a psoriasis flare following tape stripping [79].

Mouse lines carrying inducible conditional reporter transgenes may provide dynamic information on cell origin and lesion development without the need for repeated sampling. This can be facilitated using inducible mutants with reporter genes or cell transfer studies using donors ubiquitously expressing markers such as green fluorescent protein with immunohistochemistry directed at the marker [80].

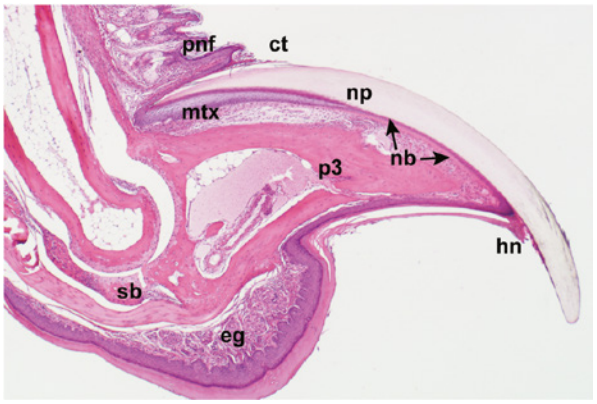
Kinetic studies on cell proliferation can be done by intraperitoneal injection of mice with 50 µg/g body weight of bromodeoxyuridine (BRDU) one hour (for mice over 12 days of age or 2 hours for newborns to 7 days of age) prior to euthanasia. Initial screening can be done of histologic samples stained with hematoxylin and eosin while kinetic analyses of the same samples can be done at later times by recutting the block and labeling them using immunohistochemistry [81]. Positive nuclei can be counted per millimeter if the skin is prepared flat and measured or per 1000 nuclei in a layer or area. Other markers include

Vet-ebooks.com

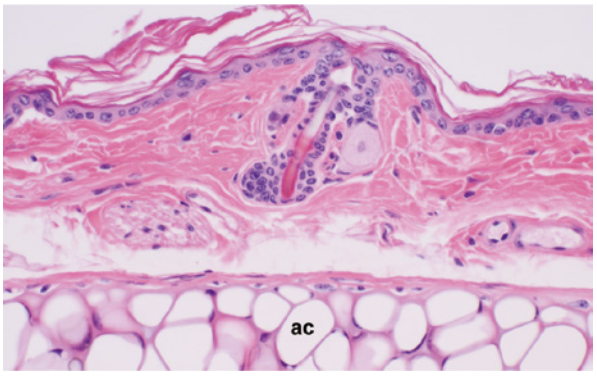
(A)



(B)



(C)



(D)

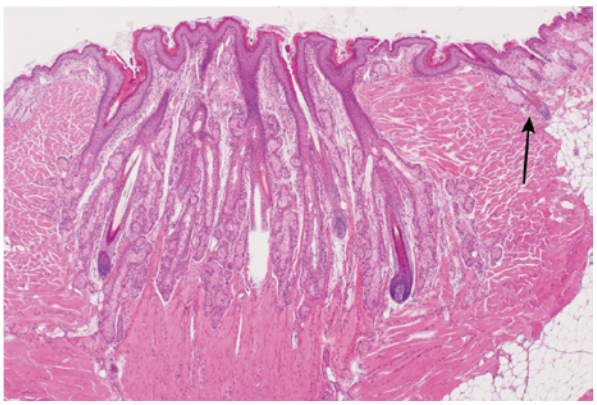


Figure 10.6 **Specialized hairs and nail**. Cilia (c) in the eyelid have their own sebaceous gland and duct exiting into the hair follicle (A). By contrast, the meibomian gland (mg) has its own duct. The cilia (c) are much larger than surrounding truncal hair (th). The nail unit (B) has a proximal nail fold (pnf), cuticle (ct), matrix (mtx), forming the nail plate (np) attached to the nail bed (nb), separating at the hyponychium (hn). Eccrine glands (eg) are located under the footpads. Auricular (ear) hairs (C) are usually found in telogen in skin overlying the auricular cartilage (ac). Perianal hairs (D) form around the anus. These are very large hair follicles with large sebaceous glands compared to the surrounding truncal hair follicles (arrow).

Vet-ebooks.com

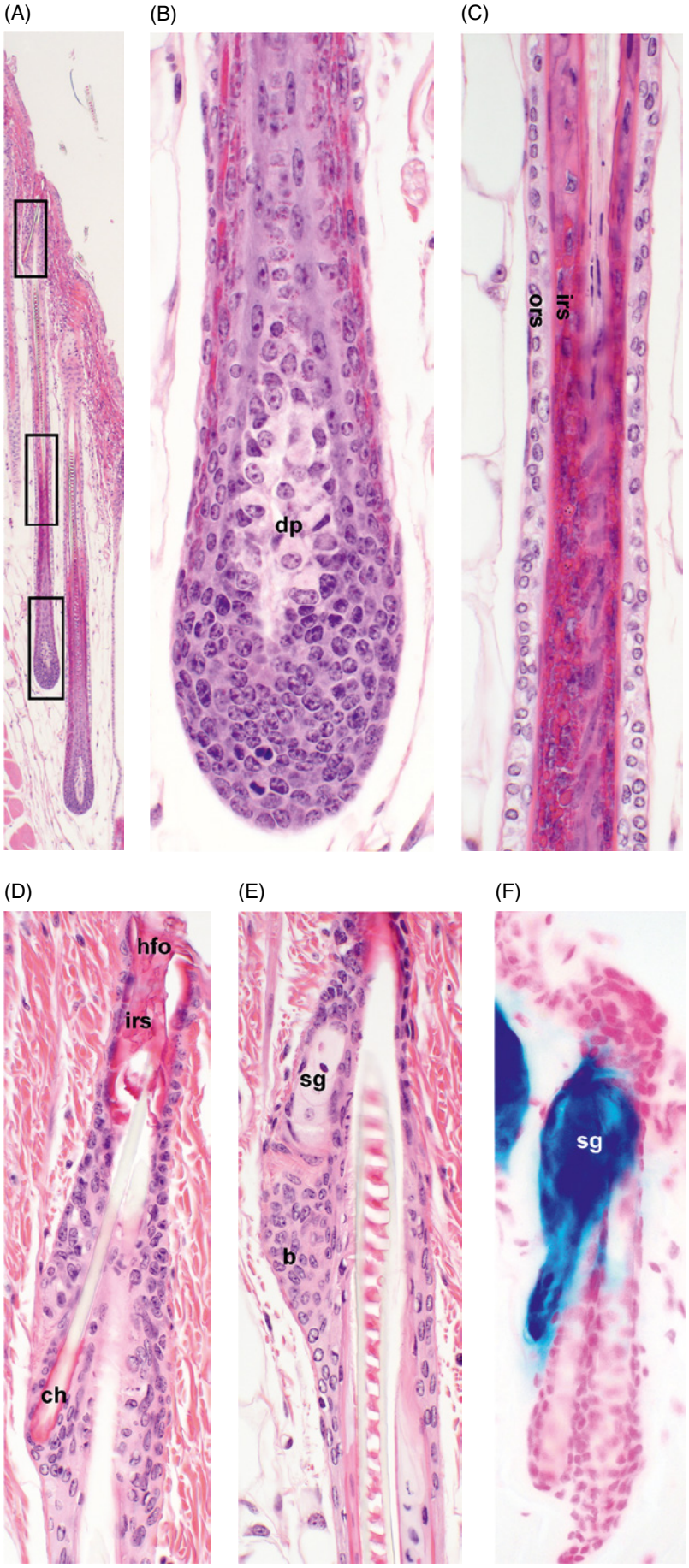


Figure 10.7 Normal late anagen truncal hair follicle. Low magnification (A) reveals the length of the follicle in an adult B6N(Cg) male. The bulb (B) is at the base surrounding the dermal papilla (dp). The mid region of the follicle (C) reveals the distinct outer root sheath (ors) and inner root sheath (irs). Near the skin surface, the old club hair (ch) is pushed to the side (D). Sebum contains enzymes that degrade the inner root sheath (irs) (D) enabling the hair shaft to exit the hair follicular ostium (hfo). The sebaceous gland (sg) is located above the bulge (b) where the hair follicle stem cells are located (E). The sebaceous gland is labeled in blue using a B6N(Cg)-*Far2*$^{tm2b(KOMP)}$Wst12J LacZ reporter (F).

Vet-ebooks.com

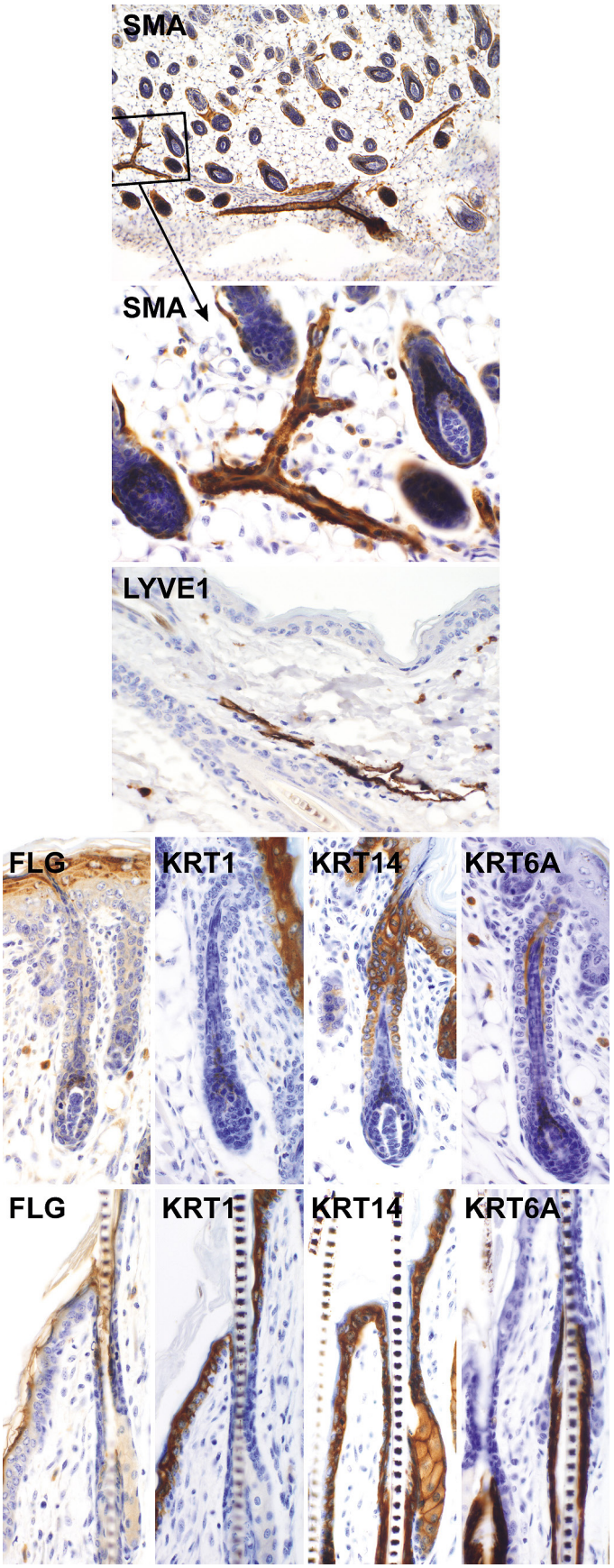


Figure 10.8 **Commonly used markers for skin.** Smooth muscle actin (SMA) is a good marker for arterial walls (and arrector pili muscles) and LYVE1 for lymphatic endothelium. For the epidermis filaggrin (FLG) and loricrin (LOR, not shown) label the stratum granulosum, keratin 1 (KRT1) and its pair (KRT10, not shown) label suprabasal keratinocytes, keratin 14 (KRT14) and its pair (KRT5, not shown) label basal cells and hair follicle epithelium, and keratin 6a (KRT6A) labels the companion layer of the hair follicle. The differential expression is more evident in two-day-old mouse skin (top row) where the epidermis is much thicker than in older mice, such as 15-day-old mice shown here (bottom row).

Vet-ebooks.com

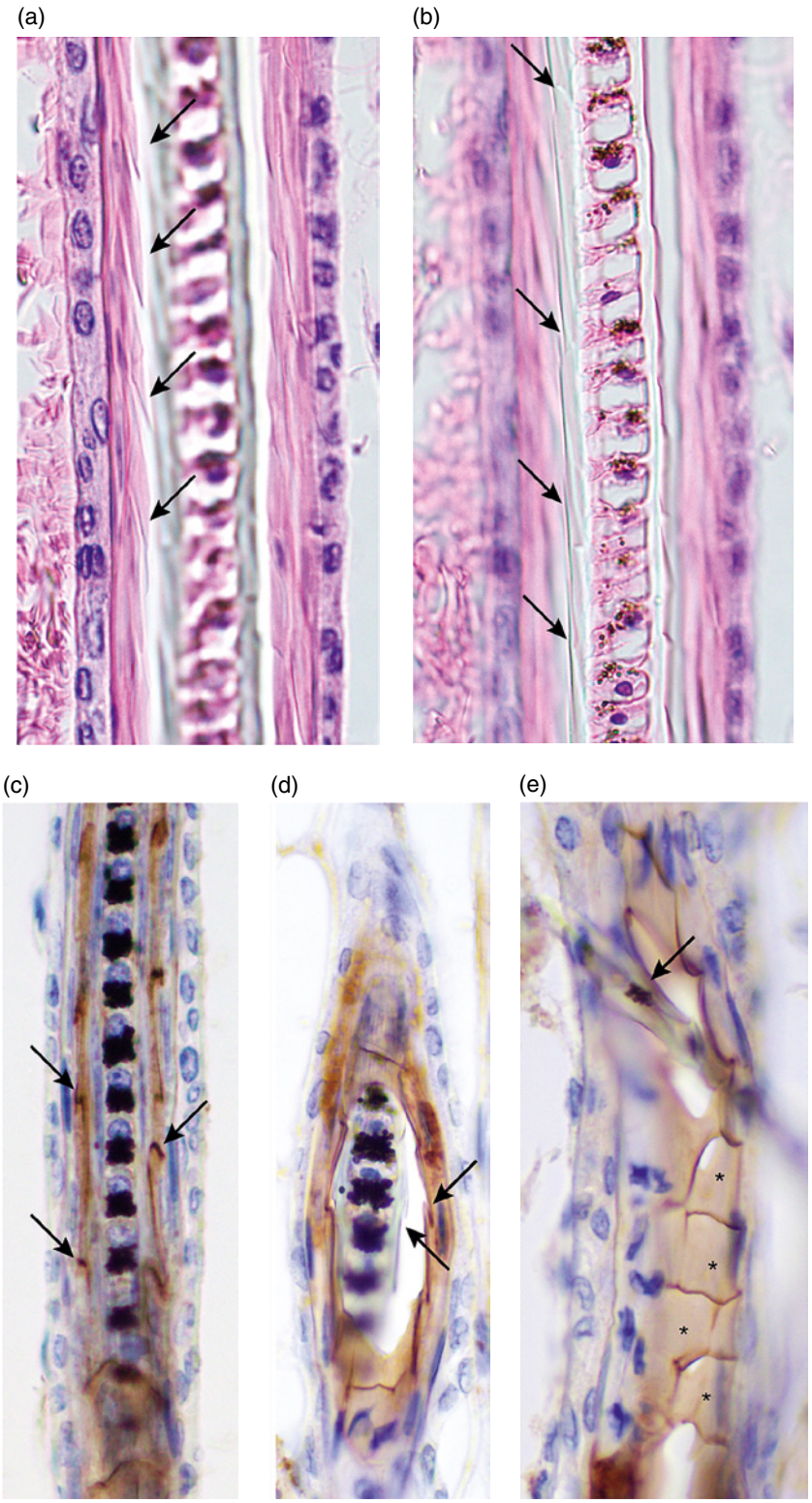


Figure 10.9 **Interdigitation of the cuticle layers**. The cuticle of the inner root sheath (a, arrows) forms scale-like structures that are angled down relative to the epidermis. By contrast, the cuticle of the hair shaft (b, arrows) forms scale-like structures that are angled up toward the epidermis. Where they intersect, they form a tight-fitting attachment that reduces avulsion of the hair shaft from the hair follicle (H&E stain with the condenser removed). The hair follicle cuticle is labeled brown (c–e, IHC, desmoglein 4 (DSG4)). Note where the hair shaft is separated from the hair follicle (d), the cuticle of the hair shaft is clear (unlabeled), while the cuticle of the inner root sheath is positive for DSG4. The shape of the cuticle (asterix) is seen where the section missed the hair shaft which is pulled out of the section (e, arrow).

Vet-ebooks.com

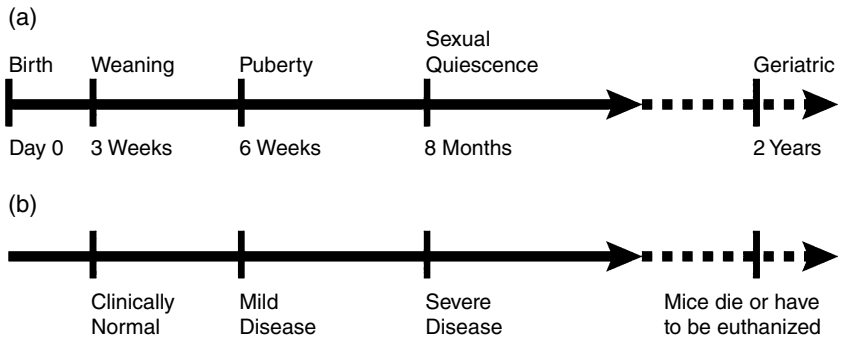


Figure 10.10 **Selecting ages for phenotyping**. Set ages based on normal developmental stages (a) utilize a standard, reproducible approach. However, focusing on disease onset and then defining specific time points before and after clinical features become evident (b) can be an effective alternative. Source: Based on Sundberg et al. (1998).

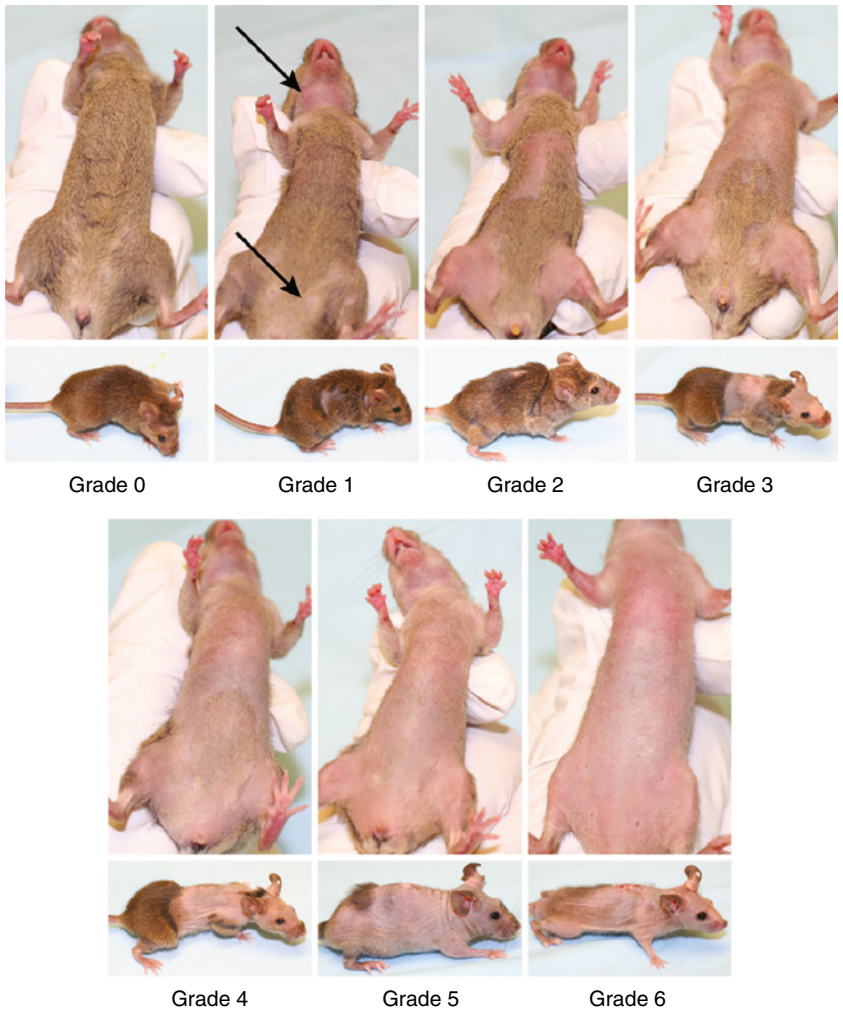


Figure 10.11 **Disease progression of alopecia areata**. Full thickness skin grafts from C3H/HeJ mice with alopecia areata to naive mice result in progressive hair loss over a 20-week time period. Mice can be evaluated for mechanisms of disease progression at 5-week intervals. Alternatively, efficacy of drugs can be graded based on degree of hair loss at specific times.

Vet-ebooks.com

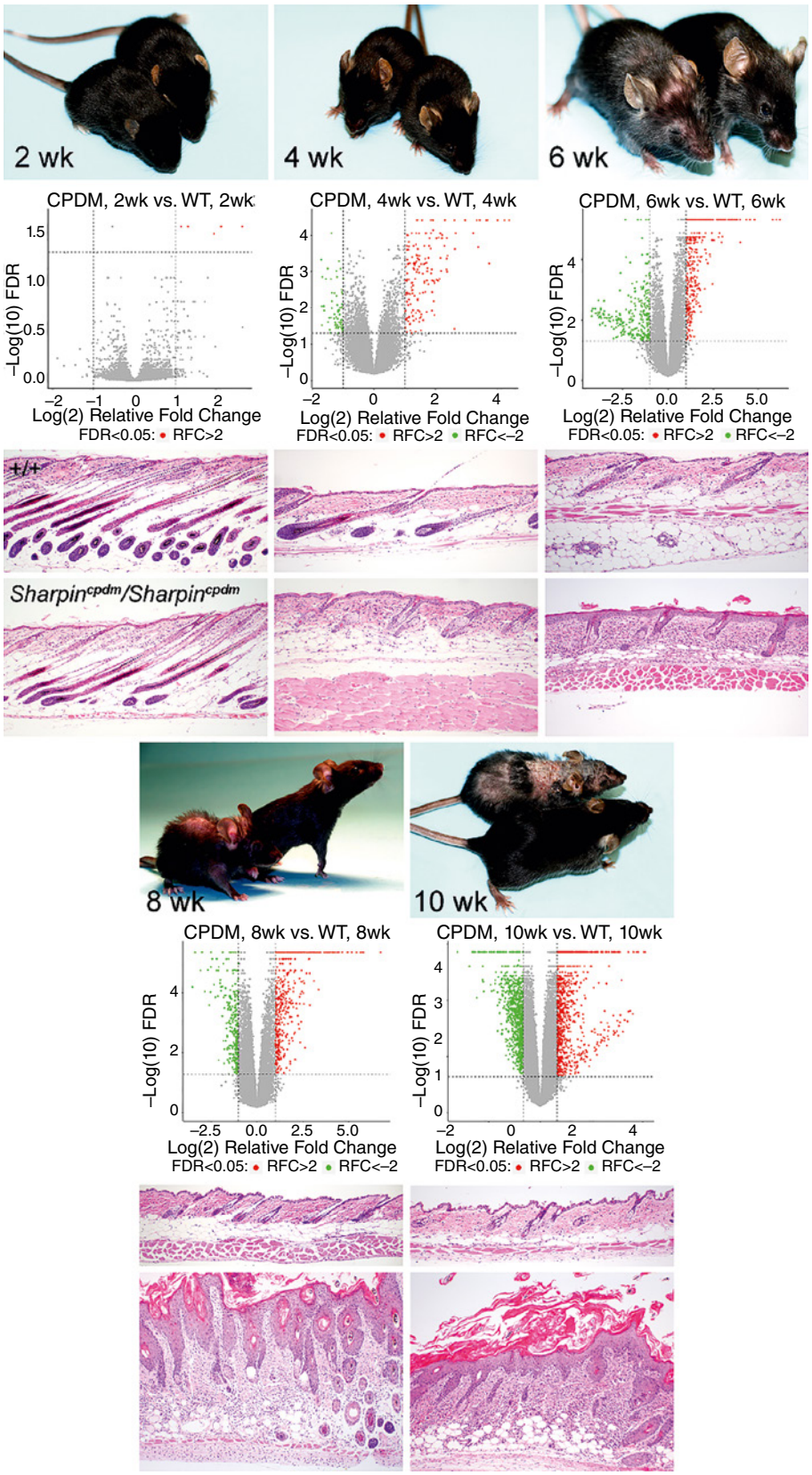


Figure 10.12 **Disease progression of dermatitis in *Sharpin*^{cpdm} mice**. Mutant mice appear to be normal at two weeks of age. Proliferative and ulceractive skin disease can be investigated at two week intervals to follow gross, (top row), transcriptome (second row), and histologic changes. Source: Potter, Wang, Silva, et al. (2014).

Vet-ebooks.com

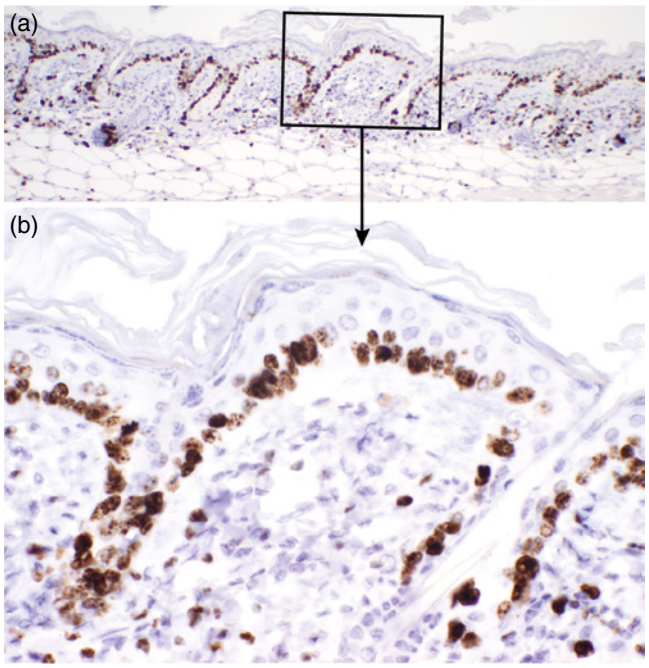


Figure 10.13 **Proliferation rates of skin**. Brown labeled nuclei in a *Sharpin*^{cpdm} mouse with scaly skin disease. Immunohistochemistry can be used to detect KI67 protein expressed in all active stages of the cell cycle except resting cells (G0).

KI67 [82] (Figure 10.13) and proliferating cell nuclear antigen (PCNA). Similarly, markers for apoptosis, such as cleaved caspase 3 can be used [83].

Complete, full organ system necropsy methods vary between laboratories but procedures for mice and other rodents have been detailed elsewhere [71, 76]. Mice can be euthanized by numerous methods depending upon institutional regulations that often follow recommendations made by regulatory agencies [84].

Skin is collected from the dorsal and ventral thoracic region, eyelids, ear, muzzle, tail, and footpads because each anatomic site is functionally different both at the molecular [74, 85] and morphological level (thickness of the epidermis: thin on the body and thick on the footpads; types of hair follicles (four types on the body; vibrissae on the head and above the feet, ear hair, tail hair, etc.)). Although dorsal and ventral skin cannot easily be differentiated histologically when normal, the other skin sites can be. For this reason, one can place dorsal skin with tail and ear skin into one histological processing cassette. Ventral skin is processed in a cassette together with muzzle and eyelid skin. Footpads with eccrine glands are processed separately since they have a very different consistency and the samples may include phalangeal bones. Both vertical and horizontal sections can be prepared for dorsal and ventral skin as is commonly done with human skin [67, 86]. More general necropsy procedures for collection of all organs are described elsewhere [76, 87, 88]. All tissues should be handled delicately to avoid crushing artifact that will be obvious during, and interfere with, microscopic evaluation.

Skin should be laid out flat, epidermal (haired) surface up, on an unlined index type card or aluminum foil. The hair can be left on or removed, depending upon the ability of the histology laboratory technicians and goals of the study. Mice can be shaved and/or depilated at the time of necropsy with minimal change in histologic features or epitope expression patterns for keratins compared with haired skin samples (Sundberg, unpublished data). The skin should be oriented on the card or foil in a head to tail (cranial-caudal) fashion and labeled (in pencil) as such, along with where the skin came from. When the tissue is trimmed, it should be cut in the cranial-caudal orientation (lengthwise) to follow the lay of the hair, which reflects the angle of the follicle within the skin. This will maximize the chances of obtaining vertical versus oblique sections of the hair follicles. Alternatively, tissues can be oriented using a dissection microscope, one paraffin block at a time, to obtain high-quality vertical hair follicle sections. Another approach is to lay a 1 cm^2 piece of skin flat in a cassette and section it from the top down to create horizontal sections. These are useful for scanning to find isolated lesions when abnormalities do not affect every hair follicle (Figure 10.14). Since the dermis will adhere to the card or foil tissues can be placed in the same receptacle with fixative regardless of the anatomic site as long as each is labeled. Most pen ink will wash off the cards in the water-based fixatives so pencil is necessary to maintain a legible label.

Tissue fixation is as critical as tissue collection. A large number of fixatives are available, each with their own advantages and disadvantages. Water-based (neutral buffered 10% formalin) or acid–alcohol-based (Fekete's Solution) formaldehyde containing fixatives yield fine detail in well-preserved specimens while also maintaining many epitopes for IHC studies (tumor.informatics.jax.org) [89]. Other fixatives commonly used include 4% paraformaldehyde and Bouin's solutions. Bouin's solution tends to hyalinize the dermal connective tissue, which can be less than optimal for evaluation. Acid fixatives are often avoided when molecular studies are planned due to degradation of nucleic acids; however, testing should be done in advance to determine if the fixative will be useful for the assays that will be used. In spite of this concern, *in situ* hybridization and quantitative real-time polymerase chain reaction assays were done successfully using acid containing fixatives [90, 91]. All organs should be routinely fixed by immersion overnight, ideally trimmed the following day, and transferred to 70% ethanol or whatever methods used by the histology lab that will process the samples. In addition to hematoxylin and eosin (H&E) staining for routine evaluation, serial sections of skin can be stained with Masson's trichrome (for scarring), Verhöeff-van Gieson (for elastic fibers), or periodic acid-Schiff (PAS; to highlight basement membrane, fungi, glycogen, glycoproteins, and glycolipids), and von Kossa (for mineralization) stains, among others [92].

Skin can also be frozen for use in various biochemical, molecular, or immunofluorescence studies. Frozen sections lack detail but maintain epitopes for IHC studies. Lipids can

Vet-ebooks.com

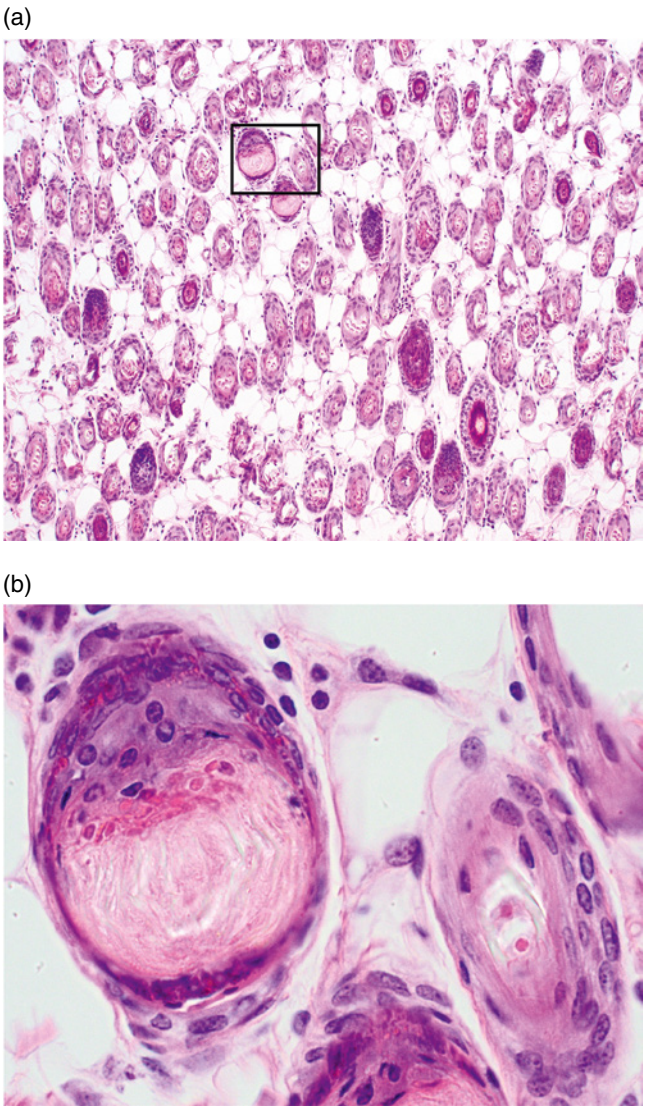


Figure 10.14 **Horizontal sections**. Most skin sections are evaluated as vertical sections. However, laying the sample flat during embedment and cutting into the skin from the top down yields this type of horizontal section. One can quickly scan the section to identify defective hair follicles (a, boxed area enlarged in b) as in this DBA/1/LacJ-*Dsg4*^{Lahl} mouse.

be detected in frozen sections using oil red O, Sudan black, osmium, and other stains [92]. A 1.5 cm × 2.0 cm section of skin is removed from the dorsal surface of the mouse at a standardized location, usually at the dorsal interscapular region (tissue overlying the shoulders). This skin is trimmed to approximately 0.3 × 1.5 cm to form strips that run lengthwise from the head to the tail to properly orient hair follicles. The strips of skin are placed on a piece of aluminum foil and a bead of optimal cutting temperature (OCT) solution (Miles Inc., Elkhart, IN, USA) is run along one edge. The foil is then dipped into liquid nitrogen to instantly freeze the samples. Once frozen, samples are quickly removed from the foil and placed on edge in a clear plastic mold (HistoPrep disposable base molds, Fisher Scientific, Pittsburgh, PA, USA) filled with OCT solution. The mold is then placed back into the liquid nitrogen and allowed to freeze. Frozen molds are wrapped in foil and stored at −80° C until needed. Both the molds and the foil are labeled with the accession number used for the animal being necropsied.

In situ hybridization techniques can utilize tissues collected in fixatives routinely used for histopathology. However, use of some fixatives can be associated with high background signals. A number of commercial kits are now available where most methods are standardized. Manufacturers often recommend specific fixatives that they optimized for use with their kits.

For molecular studies (gene mapping), spleen, liver, and kidneys are routinely removed at necropsy, snap frozen in liquid nitrogen in screw capped plastic vials (NUNC tubes, Nalgen Nunc International, Denmark), and stored at –80 °C for subsequent DNA extraction. Collecting multiple tissues and especially storing them in separate freezers provides backup should one set be destroyed or not be useful for whatever reason.

Transmission electron microscopy can be a useful adjunct to standard histological studies. However, the relatively high cost of processing and viewing specimens warrants its judicious use. Skin is fixed for 18 hours in 2.5% glutaraldehyde in 0.1 M cacodylate buffer, pH 7.4, and postfixed for 18 hours in aqueous 1% osmium or ruthenium tetroxide. Tissues are stained *en bloc* with 2% uranyl acetate in 10% ethanol and further dehydrated in a graded ethanol series. Samples embedded in Spurrs–Mollenhauer resin are polymerized at 65 °C for 48 hours. Ultrathin sections are collected, stained with uranyl acetate and lead citrate, and examined in a transmission electron microscope [93].

Hair shafts are quite hard when processed for transmission electron microscopy by themselves in plastic blocks. During sectioning, the hair shafts usually get removed leaving only holes in the plastic sections. Processing the hair samples in a boiling water bath for six hours in 5–10 ml of 50 mM sodium phosphate (pH 7.9), 2% SDS, and 20 mM dithiothreitol, rinsed briefly in distilled water, followed by routine fixation and processing allows the hair shafts to become more soft so that longitudinal sections can be obtained with high levels of detail [94–96].

Scanning electron microscopy can be performed on amputated nails, skin biopsy punches, skin excised surgically at the time of necropsy, and on plucked hairs. One concern often raised by dermatologists is that manual plucking of hair will, by itself, cause artifacts. Physicians are used to performing hair trichograms where human hairs (in anagen) are removed with hemostats, which does cause damage to the hair shafts. Adult mice are usually in prolonged telogen so simply pulling the hairs gently will remove them without creating artifacts. Alternatively or in addition to plucked hairs, at the time of necropsy, 1.5–2.0 cm^2 samples of mouse skin can be removed from mutant and control mice. The samples are placed, connective tissue side down, on dry nylon mesh, and immersed in cold 2.5%

Vet-ebooks.com

glutaraldehyde in 0.1 M cacodylate buffer. In addition, during necropsy a front and rear foot can be amputated at the carpus/tarsus and prepared in a similar manner. After overnight fixation at 4 °C, samples are washed twice with 0.1 M cacodylate buffer and postfixed in 0.5% osmium tetroxide in 0.1 M cacodylate buffer. Some of the skin samples can be freeze fractured in liquid nitrogen and then processed. Samples are subsequently dehydrated in a series of graded ethanols to 100%. After three changes in 100% ethanol, the samples are critical point dried, attached to aluminum stubs with silver adhesive, and sputter coated with 15 nm of gold. Samples are examined in a scanning electron microscope operated at 10 kV. Plucked hairs from mice are directly mounted onto aluminum stubs with double stick tape. Hair samples are sputter coated with gold and examined as described above [93, 97].

Categories of Disease of the Skin and Adnexa

Hair Color (Pigmentation) Mutations

Coat color variations have been the single most important driver for selective breeding of mice since ancient history. Mapping the albino (tyrosinase [Tyr^{c}]) and pink-eyed dilution (oculocutaneous albinism II [$Oca2^{p}$]) mutations to the same chromosome marked the first linkage of traits in the post-Mendelian era [98], and coat color played a major role in the subsequent construction of a linkage map of the mouse genome. Regulation of coat color is complex and detailed reviews are available [99–101]. Here, we highlight some of the coat color variations revealing wider functional alterations, allowing these mice to be selected as models for (human) disease.

Hair color depends on amount and type of pigment, pigment granule size, shape, distribution, and other structural features influencing reflection and refraction of light. A large number of mouse strains with different coat colors are available for investigation. The arguably most prominent variation is total absence of pigment, albinism, associated with mutations in the gene coding for tyrosinase (*Tyr*) in the melanocytes. Albinism is epistatic, the situation in which the effect of one phenotype (due to a single genetic mutation) is dominant over the effect of other genes affecting the phenotype. $Tyr^{c/c}$ mice will lack pigment and be albino regardless of other coat color alleles. Absence of melanin pigment *per se* is associated with a number of human disorders, including oculocutaneous albinism type 1 (OCA1), which may be associated with vision problems and increased damage in tissues exposed to sunlight. In contrast to mutations in *Tyr*, mutations in the gene for melanogenesis-associated transcription factor (*Mitf*), affect melanocyte differentiation and numbers in affected tissues more extensively. Associated phenotypes include variably reduced coat and iris pigmentation, microphthalmia, sensorineural hearing loss (specific melanocytes, the striate intermediate cells, play a role in cochlear signal transduction), and an increased sensitivity for melanoma development. In humans, disruptions of *MITF* are associated with a very similar spectrum of abnormalities for which these mice have served as experimental models [102].

Tyrosinase-related protein 1 (*Tyrp1*) is a catalase encoded by the B-locus, functioning in melanin synthesis downstream of tyrosinase. The dominant wildtype allele (*B*) produces black eumelanin, while the recessive allele (*b*) produces brown eumelanin, making a mouse harboring the $Tyrp1^{b/b}$ genotype cinnamon brown due to the occurrence of yellow-banded brown hairs. Other variants exist. Human manifestations of *TYRP1* mutations include oculocutaneous albinism type 3 [103] and Melanesian blond hair [104]. Further melanin modifying loci include the P-locus (pink eye dilution, coding for a protein regulating melanosome pH during melanogenesis and causing oculocutaneous albinism type 2, $Oca2^{p}$), and the D (dilute) locus, coding for myosin VA ($Myo5a^{d}$), a motor protein that regulates melanin dispersion within the melanocyte before transfer to keratinocytes. Similarly mutated alleles in the human orthologous loci result in a milder variant oculocutaneous albinism (OCA type 2) and a diluted pigmentation (Griscelli syndrome), respectively [101, 105].

Mutations that affect melanin distribution and quality while driving broader pleiotropic effects include beige (lysosomal trafficking regulator, $Lyst^{bg}$; see Chapter 7 for immunological effects) and mottled (ATPase, Cu^{++} transporting alpha polypeptide, $Atp7a^{Mo}$). Coat colors of these mice reflect generalized conditions that are orthologous to the human diseases Chediak–Higashi Syndrome [106] and Menkes syndrome [107], respectively. The mouse beige mutation was first discovered in C3H/RI mice, an agouti (brown) strain with a coat color dilution [108], hence, the name beige for light brown. Carriers of remutations (C57BL/6J-$Lyst^{bg\text{-}J}$/J) [109] and congenic strains (B6.C3Rl-$Lyst^{bg}$/J) on C57BL/6 substrains have a coat color dilution from the parental black to what is described as charcoal. The full phenotype is due to the formation of abnormal giant lysosomal granules in all tissues with granule-containing cells resulting in a systemic disease, including immunodeficiency. By contrast, Menkes syndrome is another generalized disease with hair abnormalities as well as many systemic effects including neurological defects, caused by disorders of copper transport [110]. Multiple remutations at these loci (*Lyst* has 64 and *Atp7a* has 126 allelic mutations listed; www.informatics.jax.org, 3 November 2020) result in mice with various modifications of the phenotype, providing good examples of how a single disease with variations in presentation can be the result of different mutations in the same gene. There are many other genes that have a similar pattern of causing a pigmentation change that reflects systemic disease. The Kit ligand was formerly known as steel factor [111] because of coat color dilution in mice that were mutant for the encoding gene $Kitl^{Sl}$, which is a component in an essential stem cell signaling pathway [112].

Vet-ebooks.com

In the mouse hair follicle, pigmentation follows an exact sequence of interactions between melanocytes and the dermal papilla [113, 114]. Pigment production during anagen is further periodically modulated by a number of loci regulating expression of the nonagouti protein at the A locus. (Non-)agouti acts in the hair follicles, primarily affecting the relative amount and distribution of yellow pigment (pheomelanin) and black/brown pigment (eumelanin) in hair. Wildtype mice have banded hairs whereby a band of black melanin resides at the top of the hair followed by yellow melanin in the middle and ending with black pigment near the end of the hair shaft. The switch from eu- to pheomelanogenesis is regulated by a number of genes, namely pro-opiomelanocortin-alpha (*Pomc*/*α-Msh*), melanocortin 1 receptor (*Mc1r*), nonagouti (*A*), mahogunin ring finger 1 (*Mgrn1*), and attractin (*Atrn*). Eumelanin synthesis is promoted when pro-opiomelanocortin (POMC) binds to the MC1R receptor, which in turn leads to the activation of the cyclic adenosine monophosphate (cAMP) pathway and eumelanin synthesis. Pheomelanin is synthesized when the nonagouti signal protein is expressed and interacts with MC1R and ATRN to inhibit the cAMP pathway [114–116]. Viable yellow (A^{vy}) [117] is an allelic variant at the A locus that renders the tightly regulated periodic expression of the nonagouti protein highly sensitive to DNA methylation. The resulting variation of coat color in mice has been proposed as an indicator of general genome methylation status [118].

Gradual loss of hair pigmentation is most obvious in aging black mice, such as C57BL/6 strains. A number of genes and molecular pathways have been implicated in mouse hair graying including anti-apoptotic factors (*Bcl2*), hair follicle stem cell-associated collagens (*Col17a1*), melanocyte transcription factors (*Mitf, Sox10*), paracrine signaling pathways (*Notch, Tgfb, Wnt3a/Ctnnb1*), signal transduction kinases (*Braf, Raf1*). One genetically engineering mouse (GEM) hair graying model (Tg(Dct-Sox10)CF1-10Pav) [119, 120] features premature differentiation of melanocyte stem cells within their niche, to produce ectopic pigmentation within the stem cell compartment of the hair upon their activation at anagen. These ectopically pigmented stem cells do not persist with hair cycling such that as this stem cell pool is exhausted hairs become devoid of pigment resulting in gray hairs. In addition, this varied based on strain background [121]. Using this transgenic model, the authors determined that stress-induced hair graying was the result of activation of the sympathetic nerves that innervate the melanocyte stem cell niche [122].

Graying related to age and accelerated aging in association with the DNA damage response (with ionizing radiation or mutations in *Atm, Xpd*) [99, 120, 123–129] is associated with generalized stem cell depletion that includes melanocytes in the skin. Features of accelerated aging have been described in detail for xeroderma pigmentosum (XP) models of pigmented mice. $Ercc2^{tm2(ERCC2)Jhjh}$ mice, an orthologous model for xeroderma pigmentosum group D show accelerated white spotting of body hair. As explained above, the IFE of pigmented mice is normally devoid of pigment, and abnormal pigmentation typical of XP in human glabrous skin was not noted in the IFE of these mice, illustrating how mouse pigmentation features may be selectively permissive for features of the human phenotype. In contrast, hyperpigmentation of the mouse IFE, in association with loss of hairs and pigment redistribution was observed in mice carrying the nonannotated allelic variant adrenocortical dysplasia (Acd^{acd}), coding for the ACD shelterin complex subunit and telomerase recruitment factor. These mice have severe hair follicle defects associated with hyperpigmentation of the remaining IFE [130, 131], while also showing dysplasia/hypoplasia of the adrenal cortex that gave the gene its name. Inactivating mutations in human *ACD* result in a disease called autosomal dominant dyskeratosis congenita 6.

Pigment can also be lost by physical destruction of melanocyte stem cells. Freeze branding has long been used as a means of identification for (pigmented) domestic animals (e.g. in the form of alphanumeric code or symbols). A similar approach has been used to test whether pigmentation is part of the underlying cause for (autoimmune) skin disorders. Alopecia areata is a cell-mediated autoimmune disease that targets anagen stage hair follicles; recovered areas often have white hair. Whether white hairs were spared or not could be tested in a mouse model either using albino mice, that have melanosomes but not melanin pigment (several albino strains do develop alopecia areata) [132], or by eliminating melanocyte stem cells by freeze branding, which did not prevent those areas from developing hair loss [133].

Sebaceous and Eccrine Gland Defects and Scarring Alopecias

The sebaceous glands produce a variety of lipids (wax esters, saturated fatty acids, diacylglycerol, triacylglycerol, cholesterol esters, glycerophosphocholine, ceramide, sphingomyelin, and acylcarnitine, and many others) [134] creating a film that functions to soften the skin and provide a hydrophobic barrier that reduces dehydration of the epithelia [135–137]. Mice have five types of sebaceous glands or modified sebaceous glands. These include (i) sebaceous glands of the hair follicles (pilosebaceous unit; Figures 10.5–10.7); (ii) meibomian glands in the eyelids (Figure 10.6A); (iii) preputial (males) or clitoral (females) glands adjacent to the prepuce or vulva, respectively; (iv) Zymbal's glands adjacent to the external ear canal (Figure 10.15); and (v) perianal glands (Figure 10.6D) which are part of the perianal hair pilosebaceous unit [28].

The five types of sebaceous glands share similar cytologic and architectural features but vary in size and where their ducts empty. Reserve cells, the transient amplifying cells that differentiate into sebocytes, form a crescent of flattened, hyperchromatic cells around the gland. These cells presumably differentiate from the bulge region stem cells, located immediately below the sebaceous gland along the hair shaft. The reserve cells differentiate into polygonal cells with abundant, finely vacuolated cytoplasm, the sebocytes. The

Vet-ebooks.com

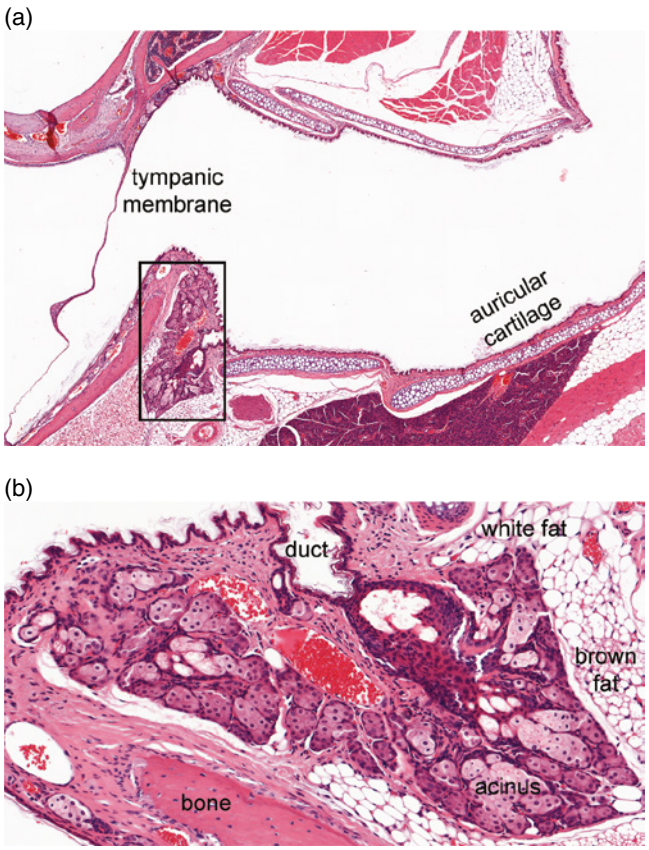


Figure 10.15 **Zymbal's gland**. The Zymbal's gland is located at the base of the ear distal to the tympanic membrane. This is a modified sebaceous gland with numerous acini consisting of sebocytes that discharge their contents into a stratified squamous epithelial lined duct continuous with the external ear canal.

differentiated cells are excreted *in toto* (holocrine) and rupture to release their oily contents. The size of the sebaceous glands of the pilosebaceous unit varies with the stage of the mouse hair cycle. The glands associated with hair follicles are generally larger during telogen and smaller during middle and late anagen [49, 50]. For this reason, it is imperative to compare glands between mutant and control in age and sex-matched mice, while also the hair cycle is locally at similar stage to avoid misinterpretations.

Sebaceous glands of the hair follicles empty, via a short duct, directly into the piliary canal. Meibomian glands, located adjacent to cilia in the eyelids, have separate ducts from follicles that empty directly onto the mucocutaneous junction of the eyelid, providing a hydrophobic barrier that prevents loss of the tear film, thus keeping the cornea and conjunctiva from drying [138]. Preputial and clitoral glands are large glands that have stratified squamous epithelium lined ducts within the gland that often enlarge and efface the gland as mice age [139]. Zymbal's glands empty directly into the ear canal. Perianal glands are large sebaceous glands that empty directly into the piliary canal of the large perianal hair follicles.

Eccrine glands are one of two types of sweat gland, and these are only located within the dermis of footpads in mice. They differ in many ways from human eccrine glands and as such have not been the focus of much comparative research [140]. The eccrine glands consist of cuboidal cells arranged in small islands with a tortuous, long duct leading to the epidermal surface. Eccrine gland secretions and excretions soften and lubricate the skin and regulate body temperature [135, 141, 142]. Mice do not have apocrine sweat glands, although female mice do have an extensive network of mammary glands, which are considered to be modified apocrine glands.

Mutations affecting sebaceous glands typically target fatty acid metabolism that in skin is unique to sebocytes, disrupting production and release of the sebum. Examples include targeted mutation of Perilipin 2 (*Pln2*^{tm1Chan}) [143], Fatty-acyl CoA reductase 2 (*Far2*$^{tm2b(KOMP)Wtsi}$/2J) [134], and groups of spontaneous and genetically engineered null alleles of the Stearoyl-CoA desaturase-1 gene (*Scd1*, Figure 10.16a–g) [144, 145] and Gasdermin A3 (*Gsdma3*, Figure 10.16h) [146, 147] as well as many others [148]. These mice have illustrated the role of sebum in controlling the barrier around emerging hair fibers. Dysfunctional sebaceous glands may play a prominent role in the development of scarring alopecias (Figure 10.16g, h) [145, 149–151].

Primary cicatricial (scarring) alopecias (PCAs) in humans are a diverse group of spontaneous diseases that have a common endpoint, a follicular scar. Most PCAs are defined as being various types of inflammatory skin diseases (Table 10.3), some of which overlap or occur concurrently, but little is really known about their initial cause or even if they have a genetic basis [151, 156]. An evolving theme in human PCAs is that sebaceous glands are involved in the pathogenesis of some forms of scarring alopecia even in clinically unaffected sites. This hypothesis [150] first came from observations on sebaceous adenitis in dogs [160]. An increasing number of simple autosomal recessive mutations that affected sebaceous glands resulting in similar end-stage disease were subsequently identified in inbred laboratory mice (Table 10.3).

The asebia mouse (*Scd1*^{ab}; and subsequent allelic mutations in this gene), which, more correctly, was the first hypoplastic sebaceous gland mouse model (Figure 10.16a–g), provided the prototype pathogenesis for PCA [145]. The first allele was discovered in 1965 [161]. Eighteen different allelic mutations or gene trap embryonic stem cells are currently available (www.informatics.jax.org, 3 November 2020). Mice with mutations in this gene have been used for over 50 years to study sebaceous gland function [162]. Identification of the mutated gene, stearoyl-Coenzyme A desaturase 1 (*Scd1*) [144], followed by detailed phenotyping [145] suggested that secretions from the sebaceous gland do not degrade the hair follicle inner root sheath adequately, and the growing hair follicle and shaft cannot push the shaft out at a normal rate. When the follicles enter catagen, they fail to contract normally such that telogen follicles are unusually long, often being misdiagnosed as

Vet-ebooks.com

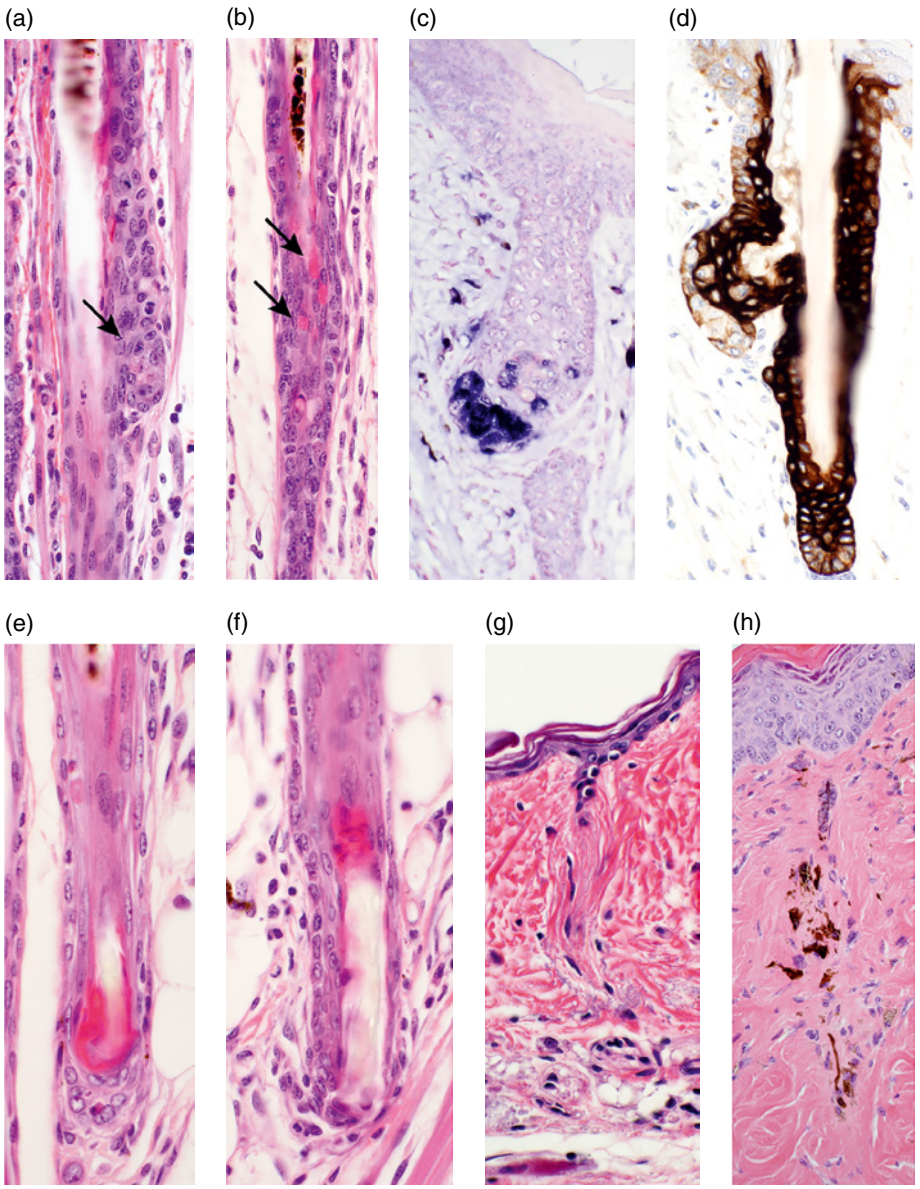


Figure 10.16 **Primary cicatricial (scarring) alopecia**. A number of mutations in genes that affect regulation of lipid metabolism result in abnormal sebaceous glands (a, b, arrow; DBA1LacJ-*Scd1*$^{ab2J/ab2J}$). Brightly eosinophilic cytoplasm in sebocytes can be a subtle indicator of abnormality (b, arrows). Sebaceous glands are small and sometimes indistinct (c, adipophilin IHC; d, KRT17 IHC; DBA1LacJ-*Scd1*^{ab2J}). Failure of the inner root sheath to degrade completely leads to excessively long anagen follicles and persistent, long telogen follicles (e; DBA1LacJ-*Scd1*^{ab2J}) leading to follicular rupture (f, DBA1LacJ-*Scd1*^{ab2J}) foreign body granulomas, and ultimately follicular scars (g, AB/LeJ-*Scd1*^{abJ}; h, C57BL/6J- *Gsdma3*^{Bsk}).

prolonged anagen. When they occasionally rupture, contents of the follicle trigger an intense acute dermal inflammation that develops into a trichogranulomatous response that eventually resolves by formation a follicular scar. Studies with asebia mice pioneered the field and led to the hypothesis that sebaceous gland defects are critical in some, but not all, forms of cicatricial alopecia [145, 149, 150]. Work in asebic (hyposebic) *Scd1*^{tm1Wst} null mice provided mechanistic evidence that the absence of palmitoleic acid prohibits posttranslational *O*-palmitoleoylation of WNT3A protein, that is essential for WNT3A/CTNNB1 signaling to stem cells regulating the epidermal barrier, hair cycle, and sebaceous gland development. Substitution with an artificial lipid barrier prevents excessive transepidermal water loss, normalizes thermogenesis and metabolic parameters, and activates the hair-bulge progenitor cells to produce a regular hair cycle in these mice [163].

A number of other single gene mutant mice were identified that develop various degrees of follicular scarring similar to the prototypical asebia mice. A phenotype similar to asebia was found in mice with a mutation in the Gasdermin A3 gene (*Gsdma3*) (Figure 10.16h); the first one described

Vet-ebooks.com

Table 10.3 Classification of primary scarring (cicatricial) alopecias.

Inflammation	Mouse and dog models	Human primary scarring alopecia
Lymphocytic	MRL/MpJ-*Fas*^{lpr}, NZBNZWF1, and fluorouracil induced lupus in mice [152]	Chronic cutaneous lupus erythematosus [153]
	Peroxisome proliferator activated receptor gamma (*Pparg*) mutations [154, 155]	Lichen planopilaris (LPP) which includes classic LPP, frontal fibrosing alopecia, and Graham–Little syndrome [156, 157]
	NA	Pseudopelade (Brocq)
	B6 alopecia and dermatitis [22]	Central centrifugal cicatricial alopecia (CCCA)
	NA	Alopecia mucinosa
	NA	Keratosis follicularis spinulosa decalvans
Neutrophilic	NA	Folliculitis decalvans
	Possibly spermidine/spermine N1-acetyl transferase 1 (*Sat1*) mutations in mice [158]	Dissecting cellulitis/folliculitis (perifolliculitis abscedens et suffodiens)
Mixed	NA	Folliculitis (acne) keloidalis
	Necrotizing dermatitis and folliculitis in Herpesvirus saimiri 1 (HVS1) infected BALB/c mice [159]	Folliculitis (acne) necrotica
	NA	Erosive pustular dermatosis
Nonspecific	Stearoyl-CoA desaturase 1 (Scd1) [145] Gasdermin 3 (*Gsdma3*) mutations [146, 147] Sebaceous adenitis in dogs [160]	Sebaceous gland abnormalities (primary or secondary)

NA = no models currently available.

being called defolliculated (*Gsdma3*^{Dfl}) [146]. There are now 15 known allelic mutations in this mouse gene (www.informatics.jax.org, 3 May 2020). A number of additional genes mutated in mice have been identified naturally or created by genetic engineering with similar sequelae. However, not all mutations in genes that are normally expressed in the sebaceous gland cause primary scarring alopecias. For example, mice with mutations in sterol *O*-acyltransferase 1 (*Soat1*^{ald}) [164–166], melanocortin 5 receptor (*Mc5r*^{tm1Cone}) [167], and stearoyl-coenzyme A desaturase 3 (*Scd3*) [168] do not exhibit follicular scarring, yet all these genes are expressed in the sebaceous gland. By contrast, abnormalities in hair follicle development that are not primarily related to sebaceous gland (dys)function, illustrated by mouse models such as hair patches (*Tal1*^{Hpt}) [164, 169] and disheveled hair and ears (*Lmna*^{Dhe}) [170], may ultimately lead to PCA-like alopecia. These observations illustrate the variety of different genes and molecular pathways that can be involved in PCAs thus complicating accurate diagnosis and prognosis in human patients. Phenomewide association (PheWAS – a method to examine many different phenotypes to determine which are associated with a given genetic variant) in large human repositories, identified polymorphisms in the peroxisome proliferator activated receptor gamma (PPARG) gene as being associated with PCA. Utilizing the Tg(Krt15-cre/PGR)22Cot/J and *Pparg*^{tm1Rev} compound mutant conditional system to exclusively inactivate *Pparg* in the skin, a mouse model for lichen planopilaris (the most frequent primary PCA in humans) was created [154, 155].

B6 alopecia and dermatitis or ulcerative dermatitis is a strain-specific background disease that develops as a result of a primary follicular dystrophy resulting in a form of scarring alopecia that closely resembles human central centrifugal cicatricial alopecia (Figure 10.17a–d). Some have attributed this simply to barbering because hair can be found embedded around the teeth (Figure 10.17e), while the latter commonly occurs in all inbred mice with or without alopecia [139, 171]. All major C57BL/6 substrains develop this to various degrees due to a hypomorphic mutation in their alcohol dehydrogenase 7 (*Adh*7, formerly called *Adh4*) gene affecting processing of retinoic acid (RA), while most other inbred strains are wild type and process RA normally [22]. Commercial mouse diets have fortified levels of vitamin A, some approaching toxic levels. B6 mice, with reduced ability to degrade RA due to this mutation, are susceptible to vitamin A toxicity that causes a variety of skin problems. Frequency of disease can be increased by increasing vitamin A levels in the diet [172]. Penetrance of disease varies between B6 substrains because of variations in gene expression of other proteins involved with retinoic acid metabolism and function, such as DHRS9 [22]. Lesions are due to defects in the hair shaft (follicular dystrophy) resulting in perforation of the deformed hair shaft through the hair follicle wall inducing a foreign body reaction (Figure 10.17f–j) [22]. Pruritus results in erosions and ulcers that heal by pseudoepitheliomatous

Vet-ebooks.com

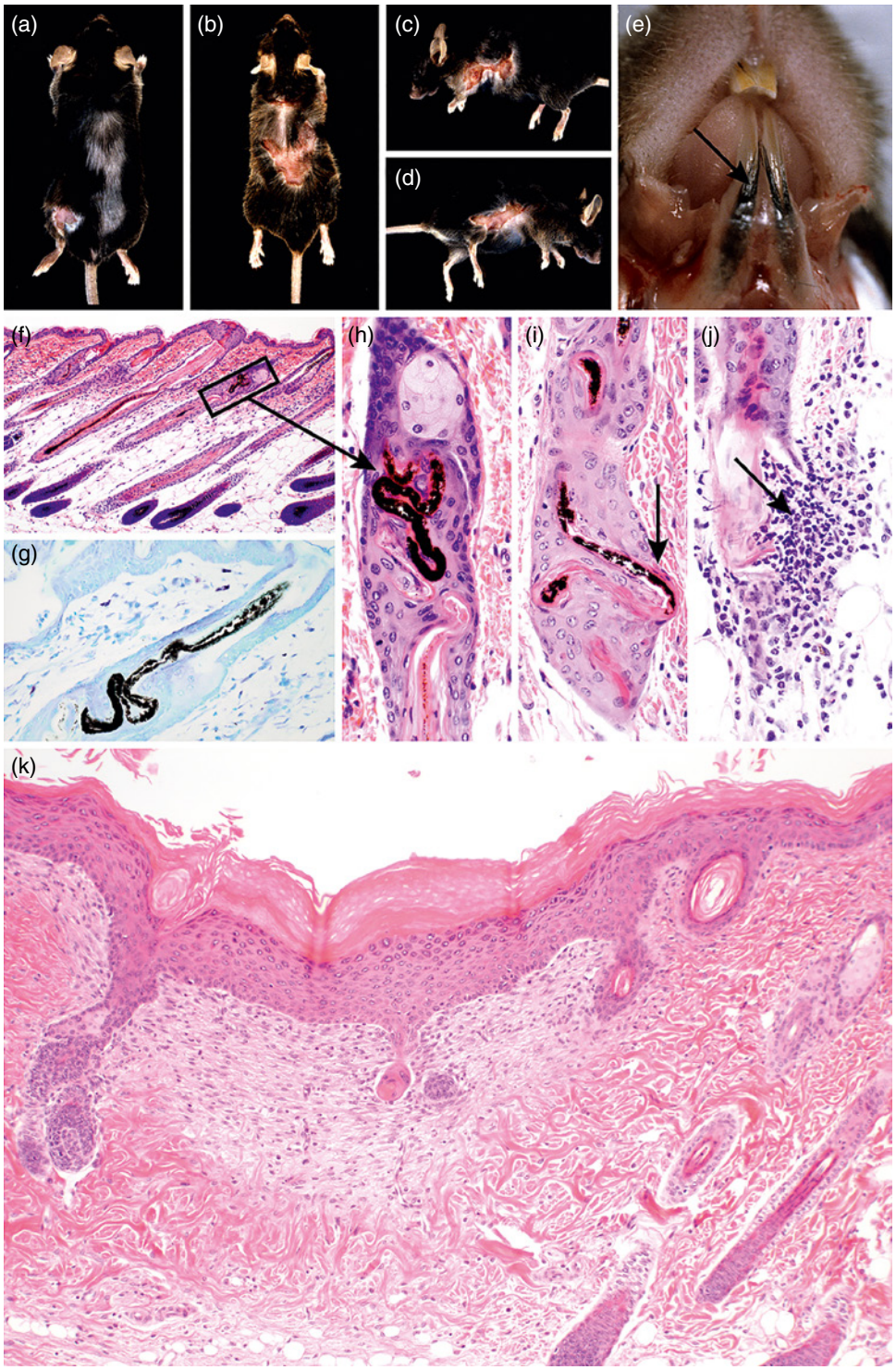


Figure 10.17 **B6 alopecia and dermatitis**. C57BL/6 substrains are prone to develop focal to locally extensive alopecia (a). Hair may regrow if there is no damage to the bulge region, or lesions progress to severe ulcerative dermatitis (b–d) secondary to pruritus. Hair impacted around teeth has been suggested as an indicator of barbering (e, arrow). Gross lesions are associated with primary follicular dystrophy that begins with failure of the inner root sheath to degrade normally (f, h) which in turn may lead to a deformed hairshaft that may penetrate the root sheath (i). Acute inflammation ensues (j) that may progress to a trichogranuloma. Ulcerated lesions may show pseudoepitheliomatous hyperplasia, abundant granulation tissue, and may heal with formation of dermal scars (k). Mast cells are not increased in the dermis as long as the deformed hair shaft remains within the immune privileged hair follicle (g, toluidine blue stain).

Vet-ebooks.com

hyperplasia (Figure 10.17k). This can be misinterpreted to be the phenotype of the mutation under investigation, which it may be, or the mutation effect can make this sporadic lesion become quite frequent. Details of the follicular dystrophy and hair shaft abnormalities need to be carefully scrutinized to differentiate these events.

Single gene mutations may affect a subset of sebaceous glands. Besides an extensive range of skeletal deformities in these mice, of the skin appendages in *Hoxd13*^{spdh} mutants preputial and clitoral glands are specifically lacking [173, 174], reflecting major developmental and biochemical differences among the five groups of glands in spite of morphologic similarities.

Some mouse mutants, lacking meibomian glands, also lack eccrine glands (i.e. crinkled, *Edaradd*^{cr}; downless, *Edar*^{dl}; sleek, *Edar*^{dlSlk}; and tabby, *Eda*^{Ta}) [175–181]. These "tabby mimics" provide a group of genocopies of the human disease anhidrotic ectodermal dysplasia and share mutations in the homologous genes, coding for ectodermal dysplasia A protein (EDA), its receptor (EDAR), or the EDAR (ectodysplasin-A receptor)-associated death domain (EDARADD). EDA is a member of the TNF family of ligands expressed by keratinocytes and involved in the epidermal-dermal signaling that drives skin appendage development. The tabby mutation has been defined in the gene coding for EDA, located on the X chromosome in both mice and humans [176, 181–183], while the other loci, crinkled, and downless, are autosomal mutations resulting in genocopies of the disease except for the X-linked inheritance [175, 179, 180]. Targeted mutation of *Traf6*, a more ubiquitously expressed member of the tumor necrosis factor (TNF) family, resulted in a comparable phenotype in skin [184]. Thus, identification of the mutated genes and their function helps define not only the biochemical pathways involved in this disease but also the normal physiology of eccrine glands.

Mutations that affect only eccrine glands are extremely rare. A complex transgenic line that included the SV40 antigen (Tag) and the rat C3(1) prostatein promoter resulted in heterotopic endochondral ossification with mixed tumor formation affecting the eccrine glands. When these mice were crossed with Tabby mice that lacked eccrine glands no lesions developed [185] thereby demonstrating the value of confirming the origin of the lesions by crossing the GEM with a spontaneous mutant that lacked eccrine glands.

Hair Follicle Cycling and Structural Defects of Hair Shafts

Hair Cycle

Early hair cycles in the mouse progress in a synchronous wave from the head to the tail [36, 38, 39, 52, 53]. Hair from the first embryonic cycle emerges at five days postpartum, and the hair shafts are shed at the end of the embryonic hair stage, to be replaced by hair of the first postnatal cycle. This is best illustrated by mice with various dysfunctional alleles of the hairless (*Hr*) gene, including those commonly known as the hairless (*Hr*^{hr}) and rhino (*Hr*^{rh}) allelic mutations, which have different degrees of severity of clinical and histologic features [186]. In these mutant mice, the bulge region (where stem cells are located) fails to reassociate with the dermal (follicular) papilla, resulting in an abortive first postnatal hair cycle. Thus, complete hair loss progresses in a single wave from muzzle to tail as the embryonic hair is shed around three weeks of age (Figure 10.18) [187–189]. *Hr* mutant mice are an orthologous model for human atrichia with papular lesions in which the same gene is mutated [190, 191]. However, function of the encoded protein (lysine demethylase and nuclear receptor corepressor) is pleiotropic and the phenotype is further complicated with genocopies including ornithine decarboxylase transgenic lines [192, 193], vitamin D receptor null mice [194], and other mutations in various genes in the putrescine pathway. Hairless mice are commonly used to test sunscreen efficacy and safety but response to UV light can be markedly different based on the genetic background, even when the same hairless allele is used (see below) [195].

Hair follicle cycle duration is a major determinant for hair length, and genes modifying the hair cycle have been the focus as potential candidates for hair growth regulation [35, 196–207]. Loss of function mutations in the gene for fibroblast growth factor 5 (*Fgf5*) causes prolonged hair growth (Figure 10.19a) [208]. *Fgf5* null mutations turned out to be allelic with angora (*Fgf5*^{go}), a mutant mouse that has a three-day prolongation of the hair growth phase resulting in long hair [43]. *FGF5* inactivating mutations in humans cause prolonged anagen and resulting trichomegaly (long hairs of several types), while exposure of isolated hair follicles to FGF5 caused onset of catagen [209]. Other studies have implicated additional members of this family of cytokines [210, 211].

Excessively long hair due to extensions of the hair cycle may occur regionally, such as long hair on the pinnae in hairy ears (*Eh*) mutant mouse (Figure 10.19B) [212]. In other examples of regionally abnormally long hair, this may reflect an atypical follicle type for that location. Koala mutant mice (*In(15)rH*) somewhat resemble the Australian marsupials by that name, being light gray in color and sporting hairy ears. However, hairs covering the ears in these mutant mice are structurally similar to body hairs and their longer phenotype actually reflects heterotopic follicle development rather than prolonged anagen [213].

Mice have a variety of distinct hair types depending upon their anatomic location (Table 10.2). Some mutants have thin hair coat because specific hair shaft types do not develop. Examples include long hair mice (*lgh*) that lack zig zag hairs [214], downless (*Edar*^{dl}), crinkled (*Edaradd*^{cr}), sleek (*Edar*$^{Dl\text{-}slk}$), tabby (*Eda*^{Ta}) that lack tail hairs (and eccrine glands as described above) [32, 175, 179, 215], and opossum (*Sox18*$^{Ra\text{-}Op}$) with affected zigzag hairs [216–218]. Others may have reduced numbers of follicles [219].

The hair cycle may be affected at specific stages targeted as part of broader hair follicle disorders. C3H/HeJ mice develop alopecia areata as a cell-mediated autoimmune disease that targets late anagen and early catagen stage truncal hair follicles. While cytotoxic responses directed against cells forming

Vet-ebooks.com

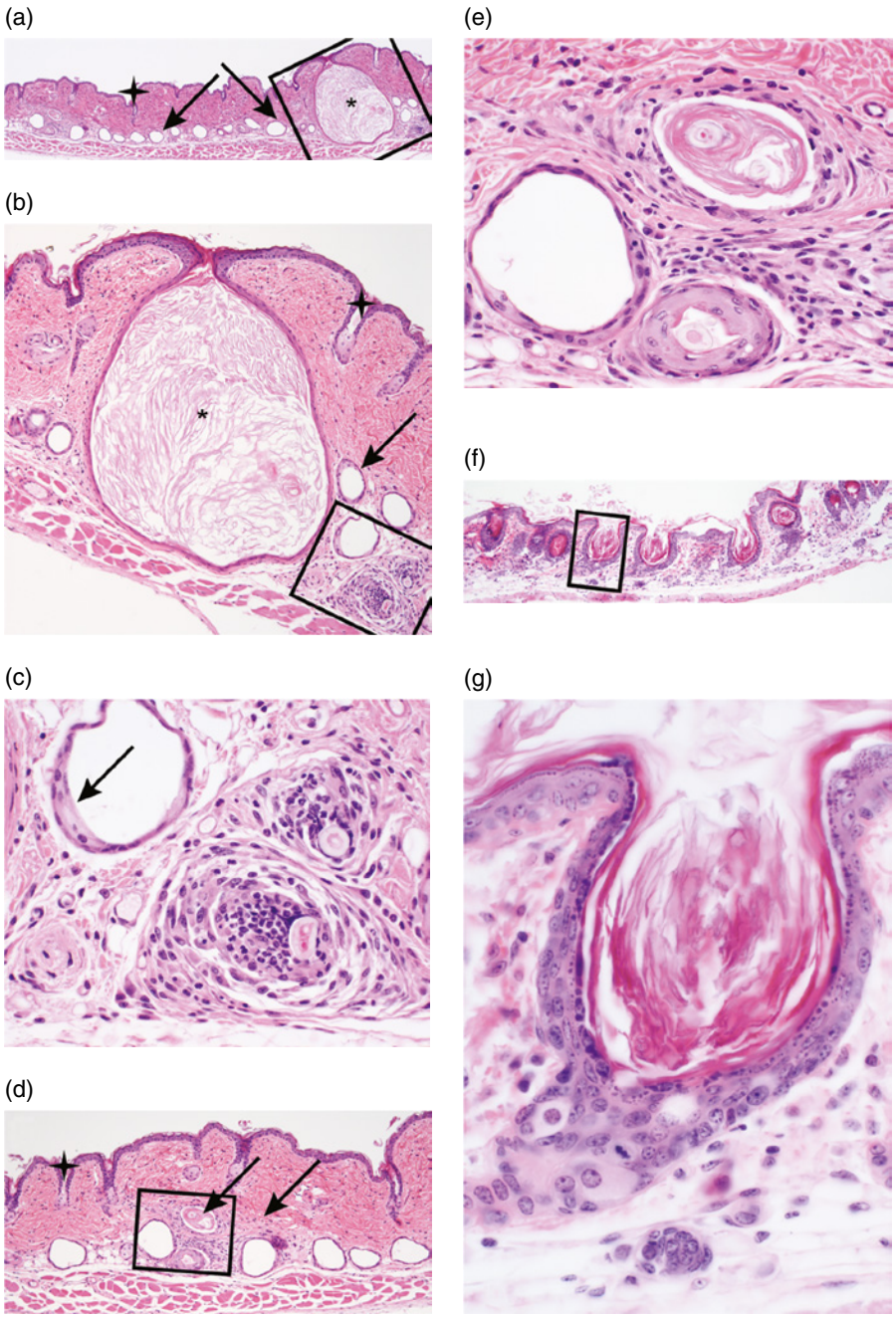


Figure 10.18 **Hairless allelic mutations**. B6.Cg mice homozygous for the hairless allele of the hairless gene (Hr^{hr}) have very small utricles (a, b, c, dilated infundibulae, star) and relatively small deep dermal cysts (a, b, d, arrows). Occasional large utricles (a, b, *) filled with cornified material are present. Deep dermal cysts may show sebaceous gland differentiation within the cyst wall (c, arrow). Ruptured cysts, some containing remnants of hair shafts, may cause pyogranulomas (c) to granulomas with fibrosis (e). Mice carrying the rhino allele of hairless, the clinically more severe form with marked skin folding (as in this 26 day old RH/LeJ-$Hr^{hr\text{-}J}$ female, e, f), show large utricles (f, g). Large, deep dermal cysts develop as they age. Boxed areas are enlarged to show details.

the hair cortex result in deformity of the hair shafts that break off when they emerge, findings indicate that cytokines such as members of the transforming growth factor beta (TGFB) family by themselves can initiate catagen, thus shortening anagen and contributing to alopecia [220–222]. As such, these mice with a complex polygenic disease fall into hair cycle, hair structure, and autoimmune categories.

Hair Texture Abnormalities and Hair Shaft Structural defects

Mice may have a developed coat with cycling hair follicles, but cyclic deviations can result in periodic structural changes to the hair shaft resulting in aberrant coat texture. The best characterized texture mutations are the spontaneous mutations known as waved 1 (transforming growth factor alpha,

Vet-ebooks.com

(a)

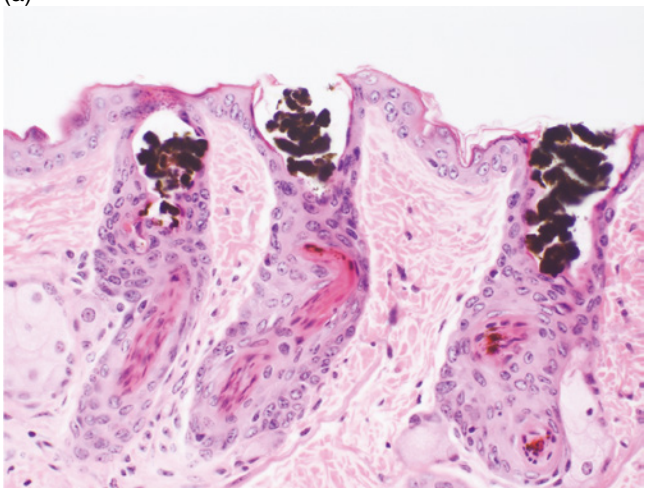


(b)



Figure 10.19 **Excessive hair growth**. The angora (a, C57BL/6J-*Fgf5*^{go} top, wildtype bottom) and hairy ears (b, B6By.Cg-*Eh*/J top, wildtype bottom) are examples of two mutations that result in hairs longer than normal because the anagen hair grows for a longer period of time than in normal mice or typical for the location.

(a)



(b)

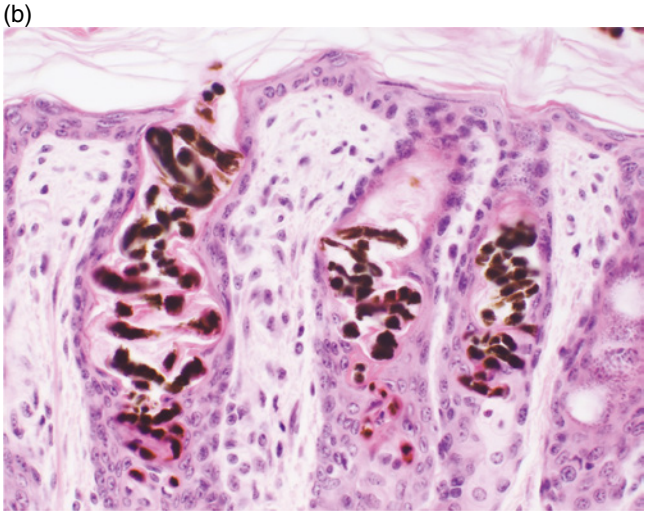


Figure 10.20 **Follicular dystrophy genocopies**. Severe twisting of weak, deformed hair shafts are very similar between B6.Cg-*Hoxc13*^{tm1Mrc} (a) and B6.Cg-*Foxn1*^{nu} (b) mutant mice making them genocopies, similar phenotypes due to mutations in totally different genes. Similar lesions can be found in human patients with mutations in these genes. Source: Pratt, Potter, Fairfield, et al. (2015).

Tgfa^{wa1}) and waved 2 (epidermal growth factor receptor, *Egfr*^{wa2}) that are each allelic with null mutations at the *Tgfa* and *Egfr* loci as described above [7–9]. Additional mutations with wavy hair have been found or created and the genes responsible for the phenotypes identified include waved 3 (protein phosphatase 1, regulatory subunit 13 like, *Ppp1r13l*^{wa3}) [223], waved with open eyelids (a disintegrin and metallopeptidase domain 17, *Adam17*^{woe}) [224], and many others.

Hair shaft defects can result in inferior structural integrity and breakage. Phenotypic presentations vary from subtle in histologic sections to overt phenotypes like nude (*Foxn1*^{nu}) (Figure 10.20a) [97, 225], homeobox C13 (*Hoxc13*^{tm1Mrc}) (Figure 10.20b) [226], shaven (*Sha*) [227], or naked (*N*) [228] in which shafts twist and deform within the follicle or as the shaft emerges [56]. *Foxn1* and *Hoxc13* mutations were first worked out in the mouse and later human cases were identified with very similar phenotypes due to mutations in the orthologous human genes (*FOXN1* and *HOXC13*) [226, 229–233]. Many of these, such as nude, have decreased levels of sulfur containing proteins (trichothiodystrophy) [97]. Trichothiodystrophy was a term coined initially for a specific human disease [234, 235], but trichothiodystrophy is now considered to be a heterogeneous group of autosomal recessive disorders that share sulfur-deficient brittle hairs [236]. Similar findings in mice, in which mutants with deformed hair often have low levels of sulfur-containing proteins, indicate that this is an example of a phenotype rather than a clinical diagnosis in both species, and probably most mammalian species. Many of these defects are due to mutations in keratin genes or genes that regulate keratin expression,

Vet-ebooks.com

especially the hard keratins that are rich in sulfur containing amino acids [97, 237, 238].

Other mutant mice have hair shaft abnormalities that result in periodic deformities (swellings) along an otherwise normal appearing hair shaft, a defect called monilithrix in humans [239]. For example, a number of allelic mutations in the desmoglein 4 gene result in swellings along the hair shaft. The first allele discovered was named lanceolate hair (*Dsg4*^{lah}) because the hair shafts often broke at these areas of deformity forming a structure that resembled a lance head on a spear [240]. More recently, new allelic mutations have hair shafts that break at weak points without forming the lance head-like structure (Berry and Sundberg, unpublished data), a feature that more closely resembles the human disease called localized autosomal recessive hypotrichosis (LAH), with the abbreviation reflecting the *Dsg4* mutation (lanceolate hair, *lah*) first identified in the mouse [3]. In all of these allelic mutations, as the hair cycle changes from late anagen to early catagen, these localized deformities become severe generalized follicular dystrophy involving the entire hair follicle (Figure 10.21). Desmoglein 4 is an adhesion molecule so it was not surprising to find genocopies in other mice with mutations in adhesion molecules also involved in formation and function of the desmosome [241]. Clinical alopecia results when the emerging hair shafts readily break off at the weakened spots.

Proliferative Skin Diseases

As described in the anatomy and development section above, mouse truncal skin is relatively thick for the first two weeks of life, more like human skin, but then thins out and remains remarkably thin throughout adult life. A number of genetic or environmentally induced diseases in mice result in marked thickening of the epidermis with or without a prominent inflammatory component. The two classic disease types in humans with proliferative skin lesions are psoriasis for an inflammation-driven disease and ichthysosis for a noninflammatory disease. Mouse skin disease with these general features have, therefore, been broadly classified as psoriasiform or ichthyosiform, respectively [242]. This general concept helps investigators design both characterization and mechanistic studies with new mouse models.

Psoriasiform Dermatitis

Human psoriasis is a very complex polygenic disease with a variety of forms [243]. As such, it was long assumed that a good mouse model would never be identified and in many respects that has remained the case. As discussed in the Chapters 3 and 4, it is hard, if not impossible, to accurately model a complex genetic disease in a species with a heterogeneous genetic background (humans) with a single gene mutation in one inbred mouse strain. However, based on the basic characteristics of psoriasis, epidermal proliferation with orthokeratosis driven by lymphocytes, a large number of mouse models have been found spontaneously or created using genetic engineering [244–252]. In addition, chemically induced models using Imiquimod [253] or human skin xenografts [249, 250, 254] have been developed. While all of these models have shortcomings, a great deal has been learned about the pathogenesis of this broad group of diseases and several are regularly used for preclinical trials. Two spontaneous single gene mutations are presented to illustrate how initial observations of psoriasiform dermatitis were later dissected and the value or lack of value of the models revealed.

Flaky skin was the name of the initial autosomal recessive allelic mutation that arose spontaneously in A/J mice [255] that developed a psoriasiform dermatitis [44]. The mutated gene was eventually identified as tetratricopeptide repeat domain 7 (*Ttc7*^{fsn}) [256]. Affected mice developed marked epidermal hyperplasia, orthokeratotic hyperkeratosis, and had a positive Koebner reaction. However, the mice did not respond to cyclosporine treatment and have subsequently been bypassed by newer models [251].

A spontaneous mutation in the mouse *Sharpin* gene (*Sharpin*^{cpdm}) was initially published as having psoriasiform dermatitis (Figure 10.12) [257–259]. Mice developed progressive epidermal hyperplasia associated with prominent keratinocyte apoptosis with a mixed inflammatory cell infiltration in the dermis consisting largely of neutrophils and eosinophils. This was later determined to be an autoinflammatory disease [75] resembling human hypereosinophilic syndrome [260]. This model has inspired extensive research in regulation of inflammation through the nuclear factor kappa-light-chain-enhancer of activated B cells (NF-κB) pathway using mouse embryonic fibroblasts [261], but using a *Sharpin* conditional null (B6(Cg)-*Tyr*$^{c-2J}$ *Sharpin*$^{tm1.1Sun}$/Sun) demonstrated that the gene functions primarily in the epidermis [262].

Neither of these serve as good models for psoriasis, but as some of the earliest of the general models, many other features were evident that allowed investigation such as increased dermal vascularization [263] and increase in dermal mast cells [264] or negative features such as lymphocytes not playing a role in the pathogenesis of the skin disease [75]. Taken together these and the many subsequent models for psoriasiform dermatitis have greatly expanded knowledge about the complexity of these types of diseases.

Ichthyosiform Dermatoses

Ichthysosis is a general category for a heterogeneous group of skin diseases, predominantly characterized by permanent and generalized abnormalities in keratinization, ranging in humans from mild dry skin (xerosis) to diffuse, severe scaly lesions. Nearly 40 distinct types of ichthyosiform dermatosis are reported in humans with one or more mutated genes associated (Table 10.4) [236]. A variety of allelic mutations in mice are available for most of the genes identified in these human diseases. Quite a few have been matched to specific human diseases, but many more have skin abnormalities that have not been investigated and compared completely to

Vet-ebooks.com

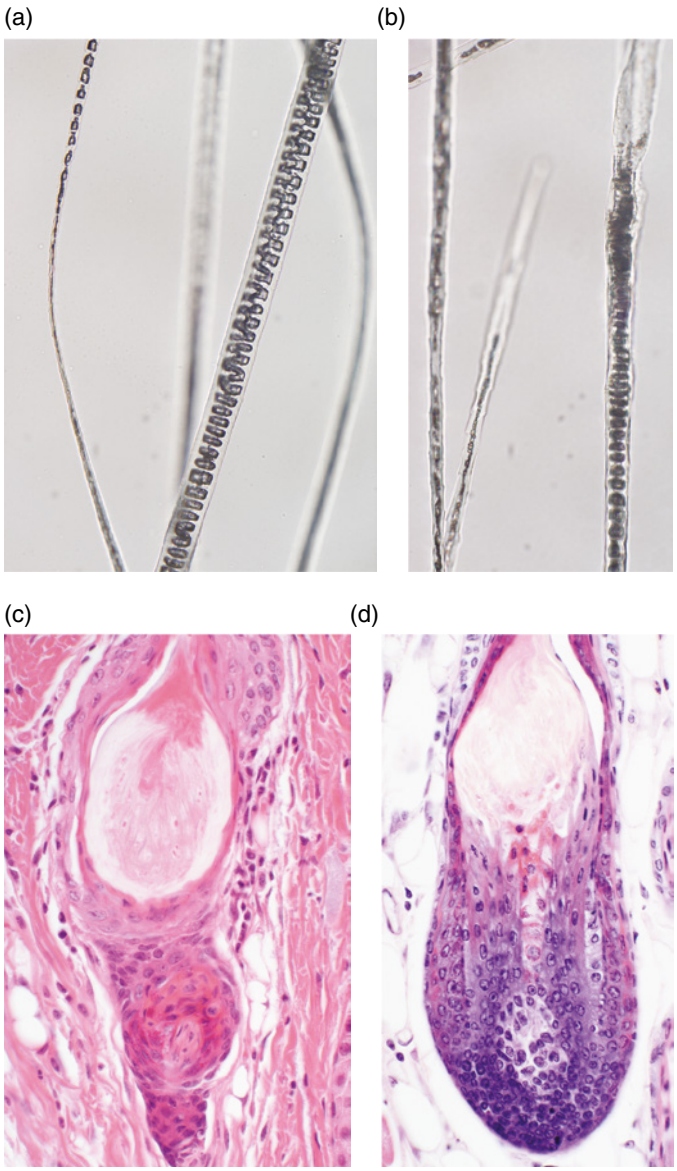


Figure 10.21 **Hair structural defects**. Mice carrying a mutation in the desmoplakin gene (ruffled, *Dsp*^{ruf}), that codes for a protein in desmosomes, results in to develop defective hair shafts that are structurally unsound and break off at the skin surface. Normal hair (a) compared to *Dsp*$^{ruf/ruf}$ hair that is disintegrating and breaking off (b). The defective ends in tissue sections resemble spearheads (c, d) that are very similar to the phenotype observed in desmoglein 4 mutant mice called lanceolate hair (*Dsg4*^{lah}, not shown).

the various human diseases. As such, models probably exist for most, if not all of the currently defined forms of ichthyosis (Table 10.4).

A number of spontaneous mouse models were described over the years based on clinical and histological similarities to human ichthyosiform dermatosis. The mouse ichthyosis mutant (lamin B receptor, *Lbr*^{ic}) was first described in 1948 [265] and subsequent allelic mutations all result in adults with short, fine hair coats with various degrees of density to alopecia based on the genetic background. The epidermis is mildly thickened (orthokeratotic hyperkeratosis) and can develop hard scales. Infundibulae of hair follicles are ectatic [266]. These mice were subsequently found to resemble Pelger–Huët anomaly, where human patients also have mutations in the lamin B receptor [267, 268].

The flaky tail mutant mouse had mild scaling and flaking of the tail in the first weeks of life. This was found to be a model for ichthysosis vulgaris and determined to be due to a mutation in the filaggrin gene (*Flg*^{ft}) [269, 270]. However, the real value of these mice became evident as the role of filaggrin in barrier formation and atopic dermatitis was unraveled [270, 271]. With the discovery of the many of the genes responsible for ichthyosiform diseases in humans combined with genetic engineering to inactivate the orthologous genes in mice as well as the large-scale mutagenesis and knockout mouse projects, many of the human scaly skin

Vet-ebooks.com

Table 10.4 Human ichthyosiform dermatoses and mouse orthologs.

Human disease	Human gene	Mouse ortholog[a]
Ichthyosis vulgaris	*FLG*	*Flg*^{ft}
Nonsyndromic recessive X-linked ichthysosis	*STS*	None[b]
Lamellar ichthysosis	*TGM1, NIPAL4, ALOX12B, ABCA12, PNPLA1, CERS3, LIPH*	*Tgm1*^{tm1Kfyn}, *Nipal4*^{tm1Akih}, *Alox12b*$^{tm1.1Krie}$, *Abca12*^{el12}, *Abca12*^{smsk}, *Abca12*^{tm1Lex}, *Abca12*^{tm1Shzu}, *Pnpla1*$^{tm1a(KOMP)Wtsi}$, *Cers3*$^{tm1.1Rsnd}$, *Liph*^{tm1Aoki},
Congenital ichthyosiform erythroderma	*ALOXE3, ALOX128, ABCA12, CYPAF22, NIPLA1, CERS3, LIPH*	*Abca12*^{el12}, *Abca12*^{smsk}, *Abca12*^{tm1Lex}, *Abca12*^{tm1Shzu}, *Krt2*^{Mhdadsk2}
Self-healing collodion baby	*TGM1, ALOXE3, ALOX12B*	None
Acral self-healing collodion baby	*TGM1*	None
Bathing suit ichthyosis	*TGM1*	None
Harlequin ichthyosis	*ABCA12*	None
Epidermolytic ichthyosis	*KRT1, KRT10*	*Krt1*^{Mhdadsk12}
Superficial epidermolytic ichthyosis	*KRT2*	None
Annular epidermolytic ichthyosis	*KRT1, KRT10*	None
Congenital reticular ichthyosiform erythroderma	*KRT10*	None
Ichthyosis Curth–Macklin	*KRT1*	None
Autosomal recessive epidermolytic ichthyosis	*KRT10*	*Krt10*^{tm1Tmm}
Loricrin keratoderma	*LOR*	*Lor*^{tm1Der}
Erythrokeratodermia variabilis	*GJB3, GJB4*	*Gjb3*$^{tm2.1Kwi}$
Inflammatory peeling skin disease	*CDSN*	None
Exfoliative ichthyosis	*CSTA*	None
Keratosis linearis-ichthyosis congenital-keratoderma	*POMP*	None
Recessive X-linked ichthyosis	*STS*	None
Ichthyosis follicularis alopecia photophobia	*MBTPS2*	None
Conradi–Hunermann–Happle syndrome	*EBP*	None
Netherton syndrome	*SPINK5*	*Spink5*^{m1Btlr}, *Spink5*^{tm1Drh}, *Spink5*^{tm1Hov}, *Spink5*$^{Tn(Pgk2-sb10,sb-Tyr)1498Ove}$
Severe dermatitis-multiple allergies-metabolic wasting	*DSG1*	None
Ichthyosis with hypotrichosis	*ST14*	None
Neonatal ichthyosis-sclerosing cholangitis	*CLDN1*	None
Refsum syndrome	*PHYH, PEX7*	*Phyh*^{tm1Safe}
Multiple sulfatase deficiency	*SUMF1*	None
Gaucher syndrome type 2	*GBA*	*Gba*^{tm1Nsb}, *Gba*^{tm2Karl}
Sjögren–Larsson syndrome	*ALDH3A2*	None
Dorfman–Chanarin syndrome	*ABHD5*	None
Trichothiodystrophy	*C7ORF11, ERCC2, ERCC3, GTF2H5, TTDA*	*Ercc2*^{tm1Jhjh}, *Ercc2*$^{tm2(ERCC2)Jhjh}$
Cerebral dysgenesis–neuropathy-ichthyosis–palmoplantar keratoderma	*SNAP29*	*Snap29*$^{tm1b(EUCOMM)Wtsi}$, *Snap29*$^{tm1c(EUCOMM)Wtsi}$
Arthrogryposis–renal-dysfunction–cholestasis	*VPS33B*	*Vps33b*$^{tm1.1Arte}$, *Vipas39*$^{tm1c(KOMP)Mbp}$
Keratitis ichthyosis deafness	*GJB2*	*Gjb2*$^{tm2.2Kwi}$
ELOVL4 deficiency	*ELOVL4*	*Elovl4*^{tm1Kzh}, *Elovl4*^{tm1Wked}

(*Continued*)

Vet-ebooks.com

Table 10.4 (Continued)

Human disease	Human gene	Mouse ortholog[a]
Mental retardation–enteropathy-deafness–neuropathy–ichthyosis–keratoderma	*AP1S1*	None
Ichthyosis prematurity syndrome	*SLC27A4*	None

[a] Mouse Genome Informatics (http://www.informatics.jax.org/marker) accessed on 19 May 2020. References are available on that website for these allelic mutations and many others.
[b] None indicates no specific model for the disease is listed in MGI at the time searched. Many allelic mutations exist for these genes, but phenotypes have not been matched to specific human diseases. Many have nondefined skin abnormalities.
Source: Metze et al. (2020). Reprinted with permission of Elsevier.

diseases now have good mouse models or will as these are more thoroughly analyzed and compared with the specific human diseases (Table 10.4)

Autoimmune Skin Diseases

There are autoimmune diseases that affect the skin, hair, and nails. Each can be, and often is, placed in more than one group. For example pemphigus vulgaris is discussed under bullous and acantholytic diseases because, while in humans this is a humoral autoimmune disease, in the mouse it is due to a null mutation in the responsible gene, desmoglein 3. Alopecia areata is often classified as a nonscarring alopecia or among diseases of hair in dermatology text books [272].

If there are inflammatory cells in the skin associated with other changes, a basic question is whether the inflammation is driving the lesion, or if inflammation is the result of the lesion. The elegance of mouse models is that once a stable colony is established, the changes can be studied in detail sequentially to determine which come(s) first, inflammation before the other lesions or the other way around. In addition, there are a large number of inbred strains that carry broad immunodeficiencies or very specific ones that enable one to investigate the role of the immune system in the pathogenesis of the disease. This can be done using full thickness skin grafts [273, 274], breeding, or even infection studies [85]. These types of studies can be refined using cell transfer of specific subsets of immune cells [74, 275, 276] to define the details of the pathogenesis.

Alopecia areata is a spontaneous, cell-mediated, autoimmune disease that affects many species of mammals [277]. In all species hair loss waxes and wanes, it appears, often as a circular lesion (alopecia areata), expands, contracts, and may disappear altogether [220]. In many cases, the alopecia can expand to involve large areas of the body, eventually involving the head (alopecia totalis), or the entire body (alopecia universalis) and various other patterns as well (Figure 10.11). While antibodies may develop against hair proteins in both mice and humans [278], these were shown to be secondary due to epitope spreading [74]. While $CD4^+$ and $CD8^+$ T cells are usually found around or in anagen stage hair follicles in affected mice and humans, a subset of $CD8^+$ $NKG2D^+$ T cells are now considered to be the effector cells that cause follicular dystrophy that results in formation of deformed hair shafts that break off at the skin surface (Figure 10.22) [220, 221, 279]. Alopecia areata has proven to be a very complex polygenic disease in both mice [280, 281] and humans [282].

Skin Cancers

Cancer-like Epidermal Response to Injury (Pseudoepitheliomatous/Pseudocarcinomatous Hyperplasia)

Response to injury (i.e. trauma or topical application of irritants) of mouse epidermis, although similar to that of other mammals, has several species-specific features. Mouse skin does not respond to injury by producing rete ridges. This feature may be a reflection of the high hair follicle density in mouse skin. In addition, pseudoepitheliomatous (also called pseudocarcinomatous) hyperplasia adjacent to ulcers in mouse skin can become prominent enough to be misinterpreted as a papilloma (pseudopapilloma) or carcinoma at both gross and microscopic levels (Figure 10.17). Changes in keratin gene expression, as revealed by alterations in IHC labeling patterns, cannot be used to differentiate these events. These biochemical features are discussed in greater detail elsewhere [283–286].

Various degrees of acanthosis (thickening of the viable cell layers) and orthokeratosis (thickening of the stratum corneum without nuclear retention) may be focal (healing ulcer, such as severe cases of B6 ulcerative dermatitis) or diffuse (irritant application). These epidermal changes can involve and extend from the hair follicles to cover large beds of granulation tissue. Chronic applications of irritants such as phorbol esters may produce foci of parakeratosis (retention of the keratinocyte nuclei into the stratum corneum). Terminal differentiation markers (loricrin, LOR; filaggrin, FLG; and keratins 1 and 10, KRT1 and KRT10) are not identifiable in foci of parakeratosis [283, 286].

Spontaneous Nonmelanoma Skin Cancers in Mice

Disease surveillance of mouse colonies invariably identifies a relatively low frequency of spontaneous cancers in mice (Figures 10.23–10.26; however, the frequency increases with

Vet-ebooks.com

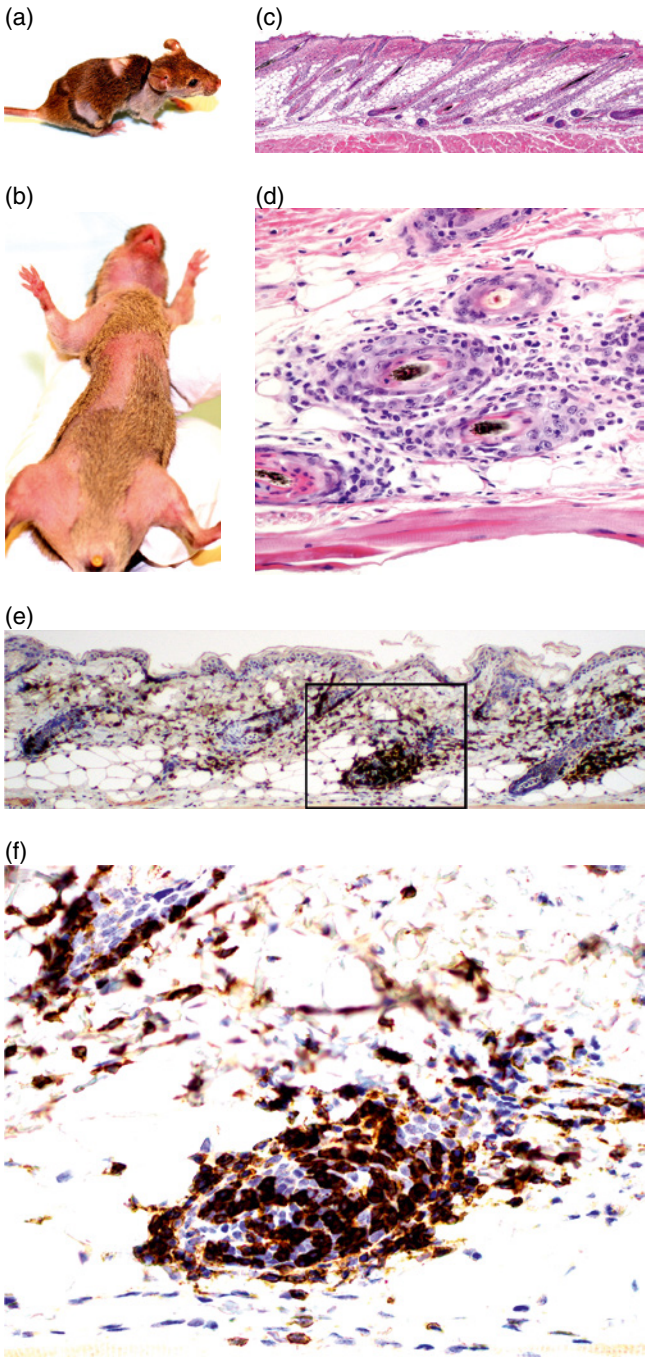


Figure 10.22 **Alopecia areata**. Bald patches of skin are evident on the dorsal (a) and ventral (b) surface. Histologically, there is a mixed inflammatory cell infiltrate, primarily consisting of lymphocytes, in and around anagen stage hair follicles (c, d). The majority are $CD4^+$ (not shown) and $CD8^+$ (e, f) T cells.

age [139, 287]). Spontaneous melanomas are extremely rare in laboratory mice (see below). Lymphomas are relatively common in many inbred strains resulting in massively enlarged lymph nodes. Although rare, involvement of the skin can be found. Hemangiomas and hemangiosarcomas tend to be isolated systemic findings especially in older mice, but they do arise in the skin. Mast cell tumors are very rare but in an aging study were found primarily in FVB/NJ mice [139]. Spindle cell neoplasms often look relatively similar histologically, but IHC evaluation can be variable making diagnosis difficult (Sundberg unpublished data). Trichoepitheliomas are relatively rare but can be difficult to distinguish from some types of mammary cancer in which there is squamous metaplasia resembling abortive hair follicles. Criteria to distinguish the two include to find the trichoepithelioma involving hair follicles and location on the epidermal side of the panniculus carnosus muscle.

Two-stage Chemical Carcinogenesis

The study of two-stage cutaneous chemical carcinogenesis utilized laboratory mice for decades. The most common and potent phorbol ester used for initiation is 12-O-tetradecanoylphorbol-13-acetate (TPA) followed long term with dimethylbenzanthracene (DMBA), both diluted in acetic acid and applied topically to shaved skin. Selective breeding resulted in the development of mice sensitive to carcinogens (SENCAR mice), initially as an outbred stock. A number of inbred strains were developed including the super SENCAR, and SENCAR lines A, B, and C strains [288–292]. Identification of a single-base pair mutation in the *Hras1* gene at codon 61 led to the development of transgenic lines using keratin promoters in the epidermis, some of which were used in chemical carcinogenesis screening [293–298].

Inspired by similarities of lesions caused in the skin by chemical carcinogens with those caused by papillomaviruses in mammals including mice (see below), lesions were screened, but no virus was identified [299, 300]. There are strain variations in frequency, severity, and histologic type of tumors. Examples of the various cancer types identified in a number of inbred strains utilizing the same carcinogenesis protocol are summarized (Table 10.5) [300].

UV Light-Induced Carcinogenesis

UV light-induced skin cancer has been a long used model for human skin cancer [301]. The hairless mouse, particularly the outbred Crl:SKH1-Hr^{hr} stock, has been favored because of the high frequency of invasive squamous cell carcinomas and the less severe sunburn/skin ulceration that these mice develop. Unfortunately, since most GEM are maintained on various B6 inbred backgrounds, SKH1 mice have limited value for molecular dissection of carcinogenesis. While an inbred SKHIH/Sprd strain was created, it still had little value for breeding with B6 mutant mice due to genetic diversity. Furthermore, these mice are no longer available [302]. To circumvent this genetic problem, a B6.Cg congenic strain was developed carrying the same hairless allelic mutation to provide a more useful genetic model. Unfortunately, these mice developed very few invasive squamous cell carcinomas but did develop very severe sunburn and extensive cutaneous ulcers, exemplifying the effect of background strain genetics on carcinogenesis [195, 303–305].

Vet-ebooks.com

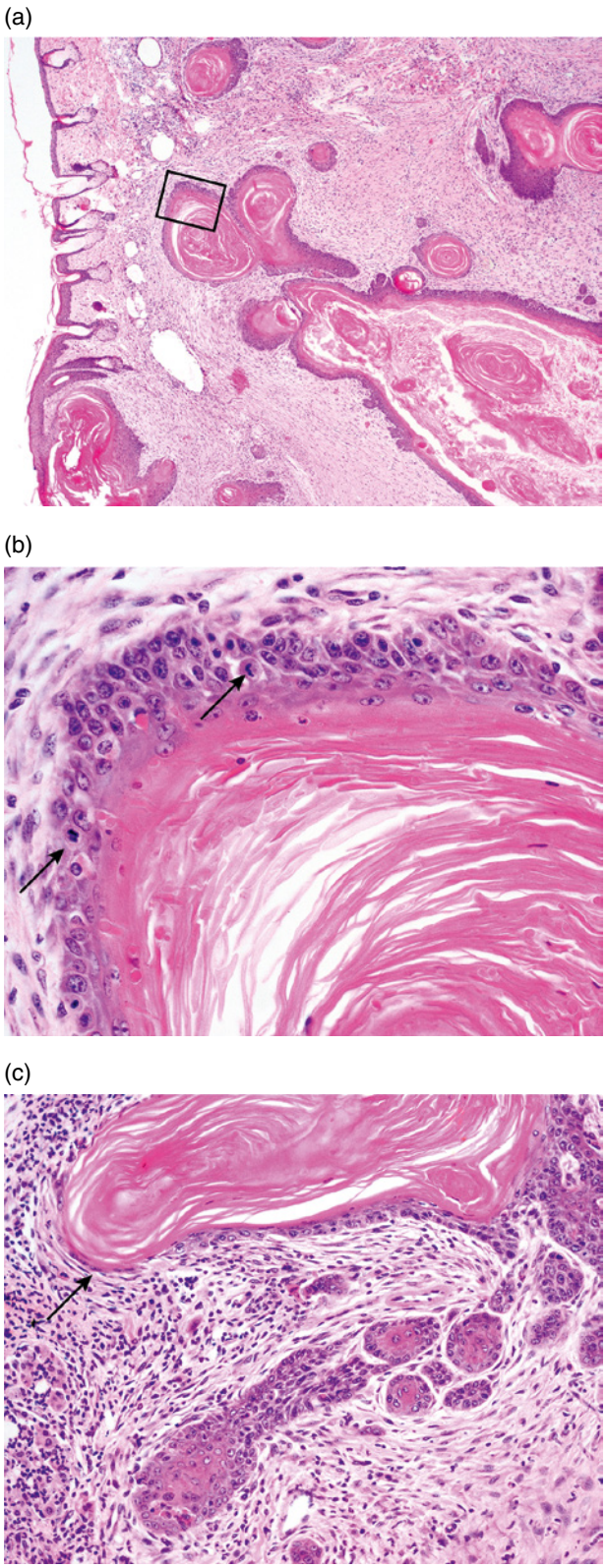


Figure 10.23 Spontaneous trichepithelioma in an HRS/J male. Multiple cysts filled with abrupt cornification are found in the dermis surrounded by fibrosis and inflammation (a, b) secondary to cyst rupture (c). Enlarged box (b) illustrates numerous mitotic figures (arrows) and ghost cells. Rupture of the cyst (arrow, c) results in fibrosis and acute inflammation.

The skin lesions induced in the Crl:SKH1-Hr^{hr} stock are complicated to interpret. However, a grading scheme has been developed that provides a guide to evaluating results (Table 10.5) [301]. Examples of the variety of lesions are illustrated (Figure 10.27).

Papillomaviruses

Papillomaviruses naturally induce papillomas, squamous cell carcinomas, and other types of nonmelanoma skin cancers in most if not all mammalian species, birds, and reptiles [306, 307]. Rodents are no exception, but papillomavirus-induced skin cancer in laboratory mice was not confirmed until a novel papillomavirus (MmuPV1) was discovered in the hair follicles of T-cell deficient nude mice [308, 309]. This novel mouse papillomavirus appeared to reside within the hair follicle epithelium, as was first demonstrated with cat papillomaviruses [310, 311] and later human papillomaviruses [312]. While laboratory mice were known to spontaneously develop a variety of skin cancer types [26] when treated with chemical carcinogens [299, 300] or UV light [195, 301], the papillomavirus infections only resulted in cancer when immunodeficient mice were infected, specifically those with pan-T cell deficiencies [85]. Different types of lesions developed at different anatomic sites. Exophytic papillomas developed in the skin of the muzzle and tail, sessile papillomas developed in the vagina, and invasive trichoblastomas developed on skin in the lumbar region. Histologically, the benign lesions had koilocytes (hollow or pale cells, pathognomonic changes consisting of cell swelling, loss of staining of the cytoplasm, and sometimes the presence of intranuclear inclusions that contained virus-like particles as demonstrated by transmission electron microscopy) [85, 308]. The trichoblastomas were locally invasive growing directly off the bulge region of the hair follicles with large irregular nuclei, scant cytoplasm, and abundant mitotic figures (Figure 10.28).

Before the laboratory mouse papillomavirus was identified, the common approach using mice to study the pathogenesis of human papillomavirus infections was to make transgenic mice with various parts of the human virus. While some of these were very useful, resulting in skin and cervical cancer [313–315], others produced unexpected results, such as cataracts [316]. Many such models were developed and some are still used.

Mouse Models of Melanoma

Spontaneous neoplasia in mice arising from malignant transformation of melanocytes is uncommon (Figure 10.29) [91]. Except for the tail, mice generally lack melanocytes at the dermal-epidermal junction in interfollicular skin. The B16 melanoma model was established by Fidler [317] as a cell line that would metastasize to the lungs in mice. It has become a widely used model systems for melanoma. Various cell lines were developed by investigators that had different metastatic potential [318]. Ultraviolet (UV) radiation is perhaps the most important environmental exposure leading to

Vet-ebooks.com

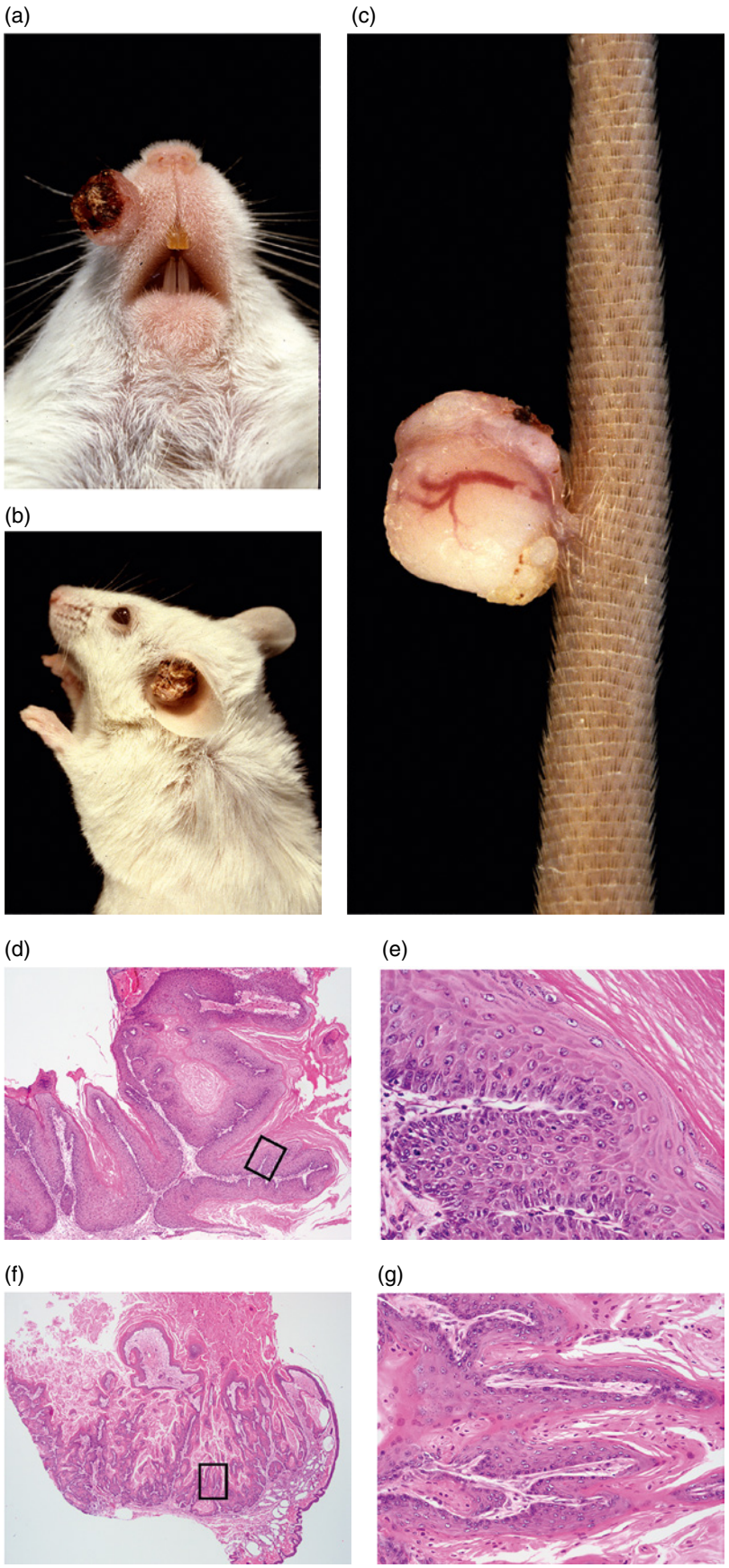


Figure 10.24 Spontaneous papillomas in mice. Spontaneous papillomas are found occasionally in production and research colonies on the muzzle (a) and ear (b) of BALB/cJ and tail (c) on DBA/2J mice as well as other sites. Papillomas are benign epidermal tumors that can rise above the level of the skin (exophytic; d, e) or form a cup-like depression in the skin (endophytic; f, g) lesion. Both are characterized by epithelial proliferation on thin fibrovascular stalks in finger-like projections. These are negative for papillomavirus antigens and DNA in specific pathogen-free (SPF) colonies.

Vet-ebooks.com

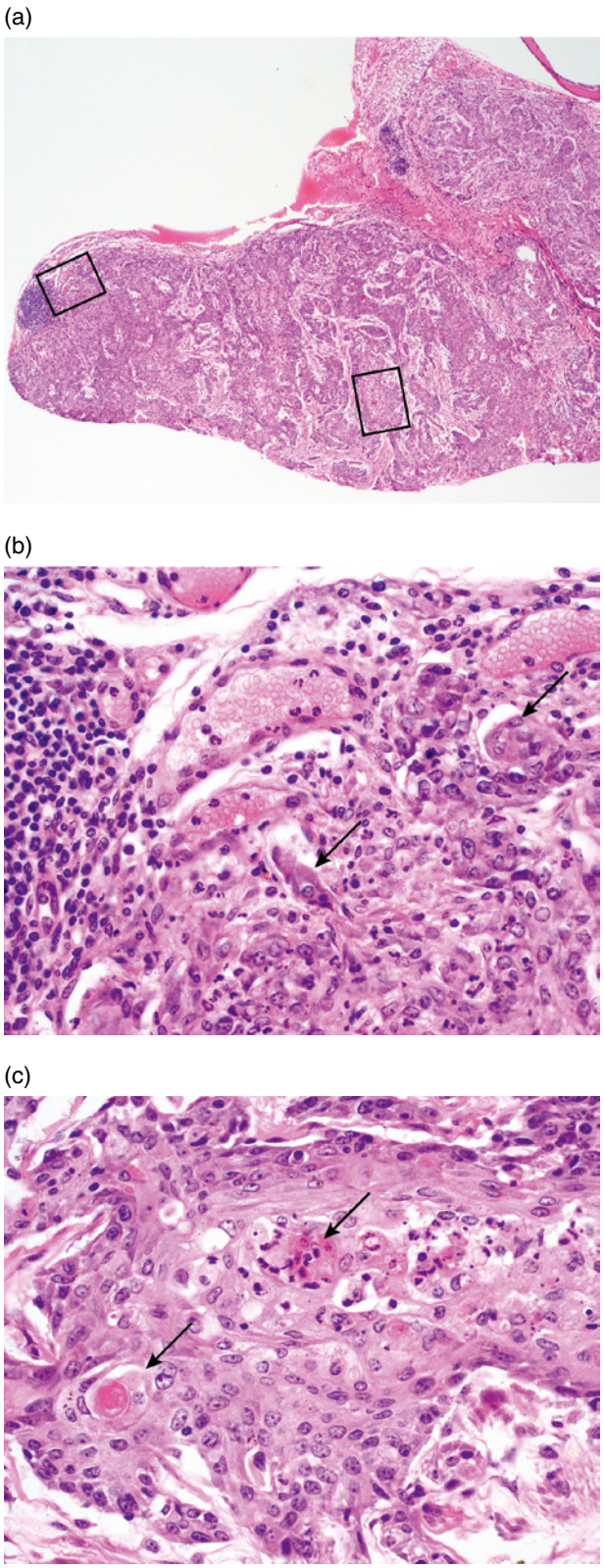


Figure 10.25 **Spontaneous squamous cell carcinoma.** An aggressive squamous cell carcinoma on the head invades through bone (a). Lymphoid nodules are present (box to the left). Adjacent to the lymphoid nodule, there is lymphatic invasion (arrows, b). In the center (box), there is evidence of limited differentiation into epithelial pearls (arrows, c) characteristic of a squamous cell carcinoma.

melanoma in humans. Chronic, repetitive exposure to UV light in mice results in cutaneous malignant tumors, most of which were squamous cell carcinomas, occasional cutaneous sarcomas, and rarely resulted in melanoma [301]. However, exposing genetically engineered mice to UV light has provided very useful models [319]. With the exception of the *Mitf* gene, spontaneous alleles increasing melanoma frequency are also rare, and nonsurgical approaches to modeling melanoma in mice have relied on genetic engineering as reviewed [320, 321] and summarized below.

Transgene expression can be directed to melanocytes with a high level of specificity making use of promoters within the melanogenesis pathway, which is unique to melanocytes. Examples include promoter/enhancer constructs from the tyrosinase (*Tyr*) and dopachrome tautomerase (*Dct*) genes. Outside the melanogenesis pathway, micropthalmia associated transcription factor (*Mitf*) has also been utilized [320]. Examples of (proto)oncogenes giving rise to melanomas when expressed in melanocytes include SV40 T antigens [322], Ret proto-oncogene (*Ret*) [323], Harvey rat sarcoma virus oncogene (*Hras*) [324], neuroblastoma ras oncogene (*Nras*) [325], Braf transforming gene (*Braf*) [325], and hepatocyte growth factor (*HGF*) [326]. Although not all of these transgenes/oncogenes play a major role in human melanoma, collectively they enable the study of melanoma formation and progression in genetically engineered mouse models.

Melanocyte-specific inducible *cre*-recombinase transgenic alleles (*Tyr-cre/ERT2*) allow further refined spatial, and temporal, control over melanocyte specific recombination/expression by topical administration of 4-hydroxytamoxifen. This approach has been used to study genetic changes commonly observed in human melanoma, including the *BRAF*V600E, *NRAS*Q61K, and loss of phosphatase and tensin homolog (*PTEN*), cyclin dependent kinase inhibitor 2A (*CDKN2A*), transformation related protein 53 (*TP53*), and neurofibromin 1 (*NF1*), alone, or in combination [327–330]. Without other genetic changes, constitutive activation of *Braf* causes transient proliferation of dermal melanocytes mimicking the growth dynamics of human melanocytic nevi, which frequently show activation of *Braf* as the only genetic change. Additional loss of tumor suppressors such as mouse *Pten*, *Cdkn2a*, or *Trp53* results in melanoma formation with various numbers of tumors developing in each mouse. The combination of constitutively active *Braf* and loss of *Pten* resulted in particularly aggressive disease; adding spatial and temporal control allows for restricted tumor formation while retaining sufficient unaffected skin for comparative use [327, 328].

Bullous and Acantholytic Skin Diseases: Pemphigus, Pemphigoid, and Epidermolysis Bullosa

The bullous or blistering skin diseases of mammals involve proteins that provide adhesion between cells (primarily desmosome and hemidesmosomal proteins) or those that make

Vet-ebooks.com

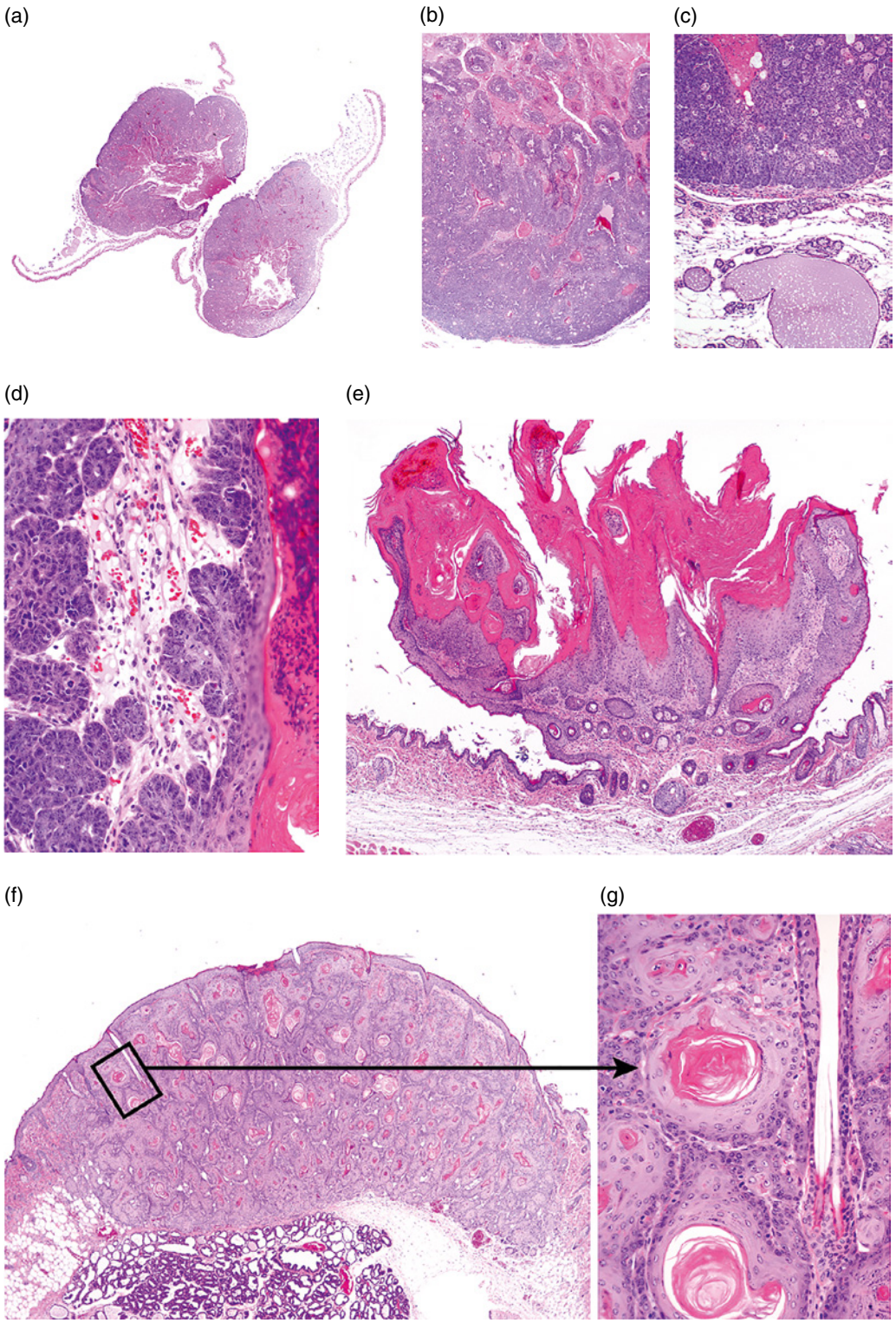


Figure 10.26 **Spontaneous nonmelanoma skin cancer**. Some mutant strains, such as B6.129P2-*Apoe*^{tm1Unc}/J, spontaneously develop a variety of skin cancers such as endophytic (inverted) papillomas filled with cornified material (a) and lined by papillomas (b), solid regions with sebaceous differentiation (c), to areas that appear to be invading locally (d). Other lesions are more typical exophytic papillomas (e) or trichofolliculomas (f, g) forming abortive hair follicles.

Vet-ebooks.com

Table 10.5 Nonmelanoma skin cancers in mice by induction method.

Spontaneous skin tumors	Two-stage chemical carcinogenesis	UV light carcinogenesis	Mouse papillomavirus infection
Epidermal inclusion cyst	Follicular papillomas	Premalignant papillomas Grades 1, 2, and 3	Exophytic papilloma
Trichoepithelioma	Mixed papillomas	Malignant microinvasive squamous cell carcinoma Grades 1, 2, and 3	Sessile papilloma
Spindle cell tumors	Fibropapillomas	Fully invasive squamous cell carcinoma	Trichoblastoma
Exophytic papillomas	Exophytic papillomas	Spindle cell/anaplastic tumor	
Hyperkeratotic exophytic papillomas	Hyperkeratotic exophytic papillomas		
Invasive squamous cell carcinomas	Invasive squamous cell carcinomas		
Mast cell tumor	Mast cell tumor		
Hemangioma, hemangiosarcoma			

Source: Based on Sundberg et al. (1997).

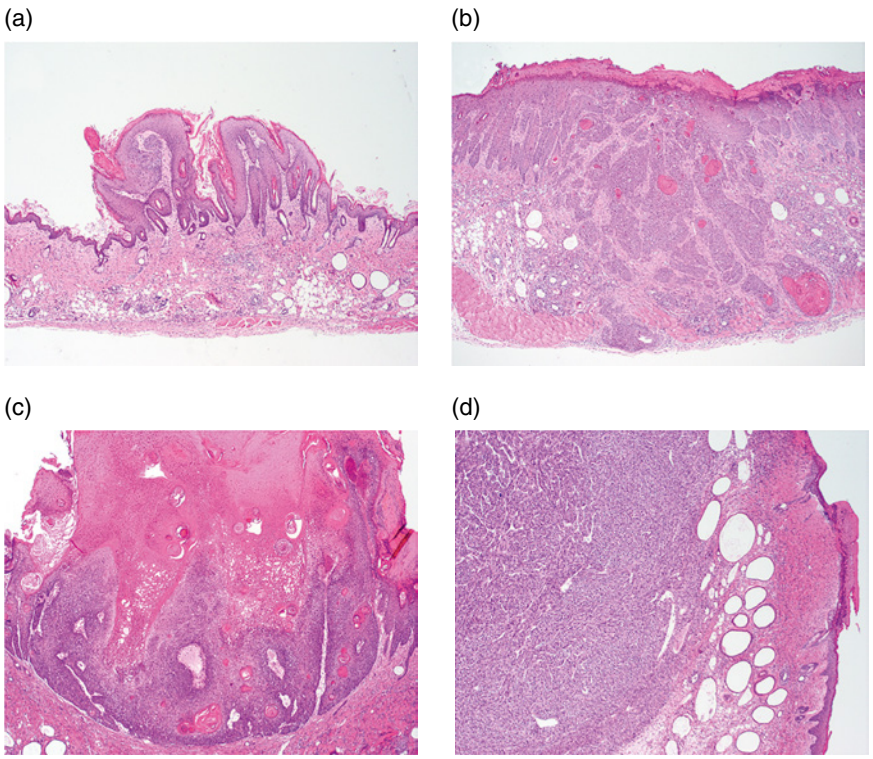


Figure 10.27 **UV light-induced skin tumors**. Outbred Crl:SKH1-*Hr*^{hr} hairless mice are uniquely sensitive to UV light-induced carcinogenesis. A wide variety of tumor types develop including exophytic papillomas (a), invasive squamous cell carcinomas (b), endophytic papillomas (that tend toward low-grade squamous cell carcinomas; c), and occasionally poorly differentiated spindle cell tumors (d, negative for keratins).

up the cytoskeletal system (such as keratin proteins). The first spontaneous mutation in the mouse that resulted in blister formation involved balding (*bal*) and subsequently two allelic mutations, balding-2J and balding-Pas [11, 331, 332]. Concurrently, targeted mutagenesis studies for the desmoglein 3 (*Dsg3*) gene created a fourth allelic mutation and verified that all four were due to mutations within the same gene with the same resulting phenotype (Figure 10.30) [12]. Desmoglein 3 is part of the adhesion molecule matrix that connects the basal cells to the rest of the epidermis and holds

Vet-ebooks.com

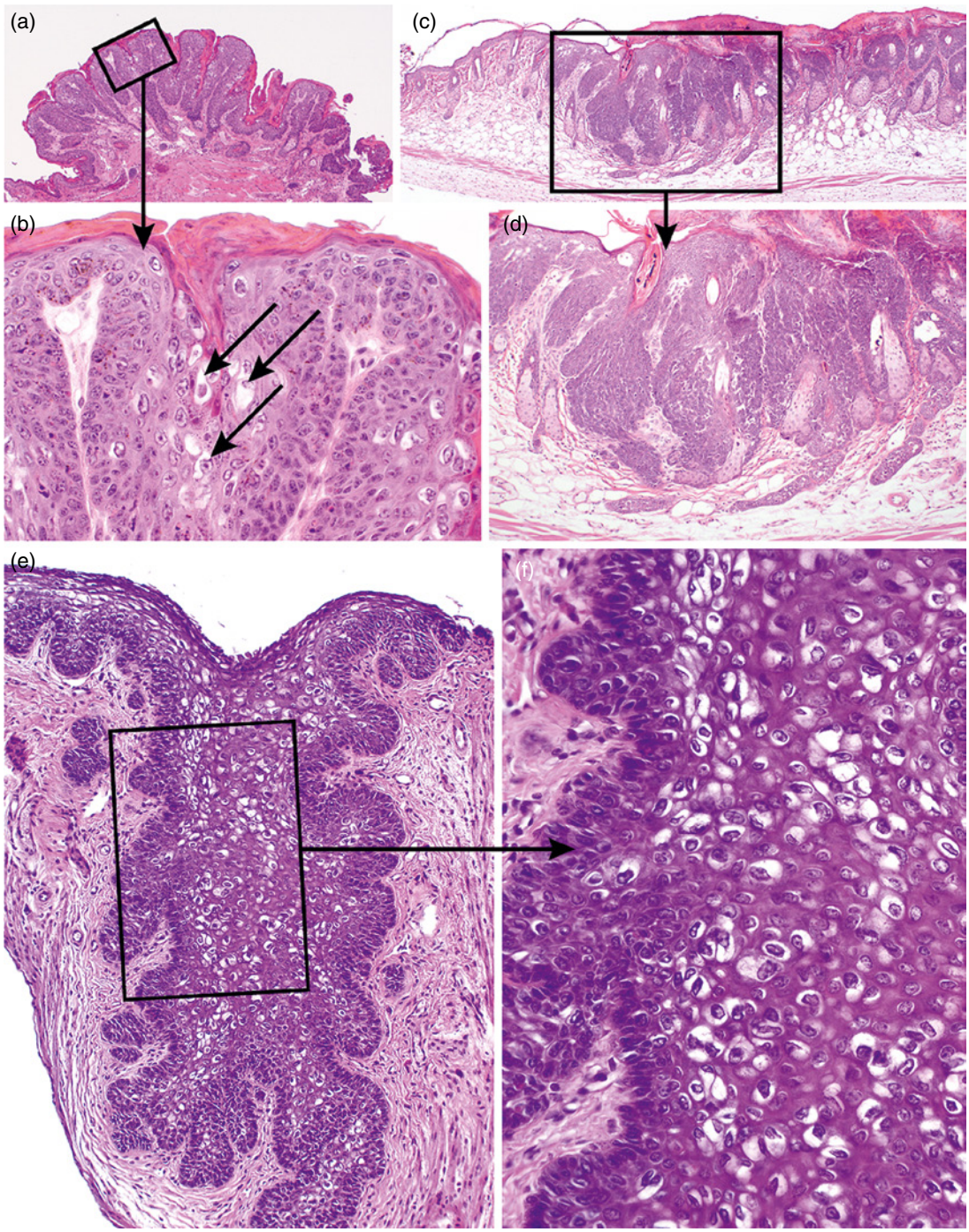


Figure 10.28 **Mouse papillomavirus (MmuPV1) infection**. MmuPV1 causes benign papillomas with koilocytosis (clear or pale cells, cytopathologic effect of a productive viral infection) on the muzzle and tail (a, b, arrows), invasive trichoblastomas (c, d) in the lumbar truncal skin, and sessile to invasive appearing lesions in the vagina (e, f, note koilocytosis) in B6.Cg-*Foxn1*^{nu} nude mice.

the root sheaths of the hair follicle together. Loss of function causes suprabasal vesicles and blisters or entire loss of the follicle, respectively, leaving the classic "tombstone-like" appearance of the basal cells. Induced mutations in other structural genes have resulted in creation of additional blistering phenotypes. The problem with these null mutations in *Dsg3* is that pemphigus vulgaris in humans, and many other mammals is a humoral autoimmune disease due to production of inactivating autoantibodies against DSG3 [333, 334]. Recent studies indicate the disease can be subtyped by the types of autoantibodies produced to DSG3 and other desmogleins [335]. The DSG3 null mice can be used to induce antibodies by various methods in mice with normal DSG3 that can then be used to reproduce a disease more clinically

Vet-ebooks.com

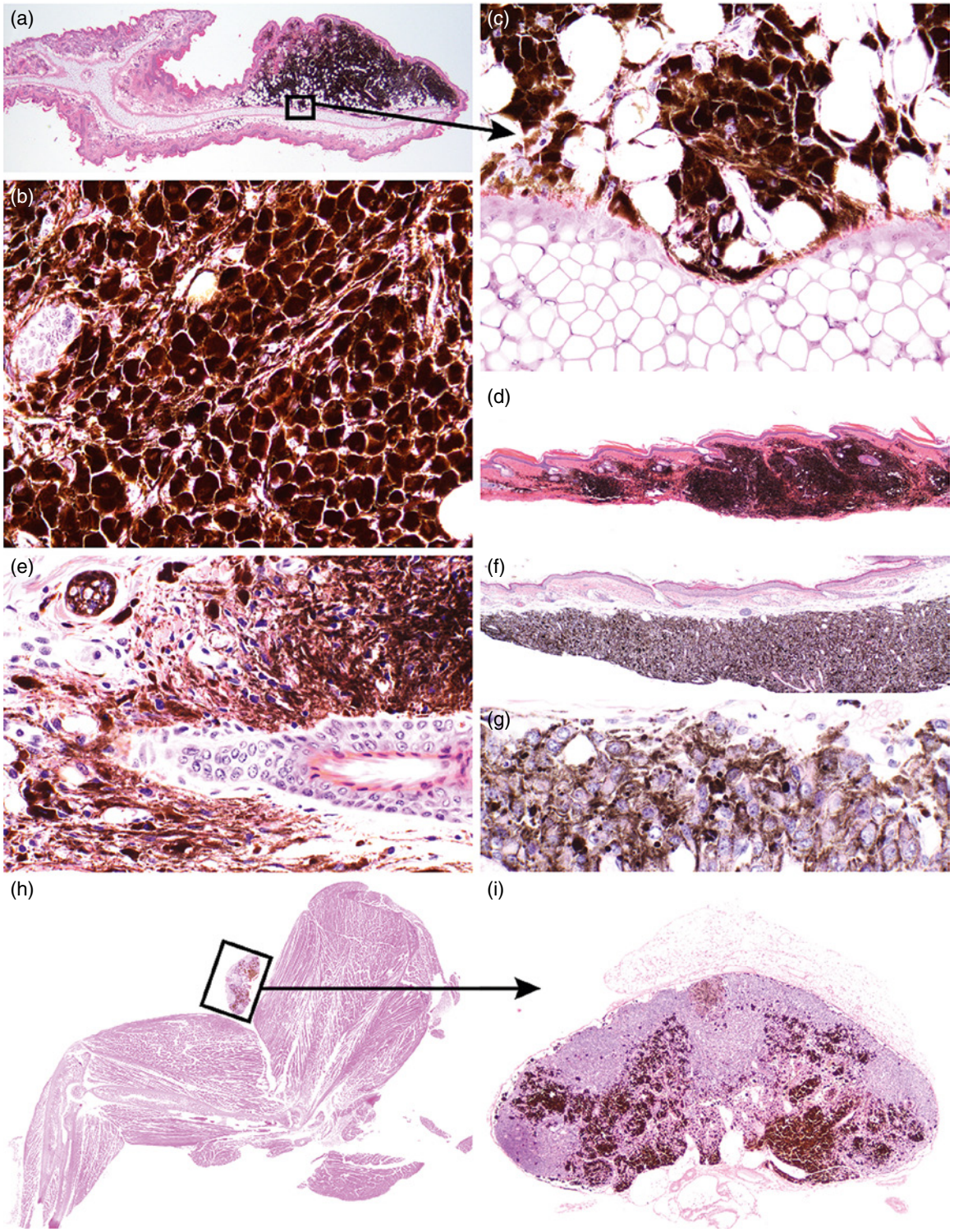


Figure 10.29 **Spontaneous pigmented epithelioid melanocytoma**. Melanomas very rarely arise spontaneously in laboratory mice. Lesions arise on the ears (a–c; C3H/HeJ 301 day old female), tail (d, e; LTB6 Cg line adult female), as well as visceral organs. Some of these can be easily transplanted into histocompatible mice to reproduce in a reliable manner primary melanomas (f, g; LT/SvEiJ 596 day old female) and metastases, such as shown here in the popliteal lymph node (h, i; LT/SvEiJ 596 day old female).

relevant to human pemphigus vulgaris [336–338]. Pemphigus vulgaris serves as a prototypical model, but there are other forms of pemphigus and pemphigoid due to mutations in other genes [334]. Two *Dsg3* transgenic lines (*Dsg3ΔN* [339] and Tg(KRT1-DSG3)1Dga [340]) resulted in aberrant organization of desmosomes and thickened scaly skin.

Vet-ebooks.com

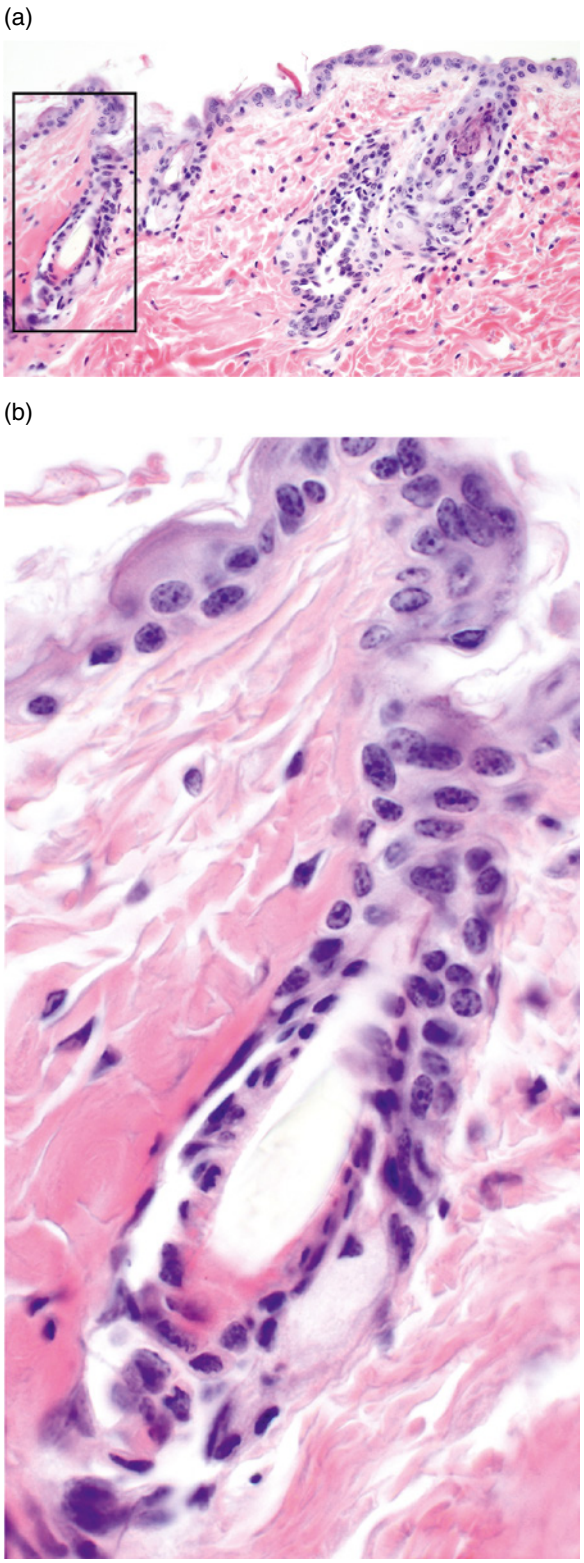


Figure 10.30 **Pemphigus vulgaris**. Blister formation within the epidermis and hair follicles involves the desmoglein genes. While pemphigus vulgaris is a humoral autoimmune disease in humans and many other mammals, both spontaneous (a, b, *Dsg3*$^{bal\text{-}Pas}$) and targeted null mutations (not shown) are available. Lesions are easiest to identify in hair follicles where separation occurs at the level of the companion layer (a, b). In areas of thick epidermis, there is separation above the stratum basale with a "tombstone effect" of the basal cells.

Epidermolysis bullosa is another group of blistering skin diseases that involve keratins and other cellular proteins as well as adhesion molecules that form the basement membrane (Table 10.6). These groups of diseases are considered, for the most part, to each be monogenetic diseases (one mutated gene causing a specific disease). While there is usually one mutated gene with a major effect, modification of its effects by other genes explains subtypes often seen in human patients. This is best exemplified by the spontaneous mutation in laminin gamma 2 (*Lamc2*^{jeb}) that causes a condition similar to non-Herlitz junctional epidermolysis bullosa [16]. Homozygous mutant mice develop severe dermal-epidermal separation leading to ulceration, especially where the epidermis is thick (tail, ear, and foot pads). Severity varied dramatically between congenic strains created to be homozygous for this mutation. Quantitative trait locus analysis not only revealed mutations in collagen 17a1 (*Col17a1*) and a second unpublished genetic mutation accounted for these variations but also each alone added an additional phenotype that defined the clinical variations seen in human patients [18].

One complaint about mouse models for epidermolysis bullosa has been that most null mutants die *in utero* or soon after birth making them of little value. While this is true for the *Lamc2*^{tm1Uit} null allele [17], the *Lamc2*^{jeb} junctional epidermolysis bullosa model is a hypomorphic allele and the mice survive (Figure 10.31) [16]. Thus, different allelic mutations in the primary gene responsible for the disease will have very severe or mild effects. It is likely that humans conceive embryos with null mutations in the genes causing various forms of epidermolysis bullosa that are resorbed and never born. Failure to find live births with null mutations in humans does not mean they do not occur. These can be created and investigated using mouse models and many have been (Table 10.6) [341]. Details and references can be found in Mouse Genome Informatics online (www.informatics.jax.org, 19 May 2020).

Structural and Growth Defects in Nails

Nails cover the distal phalanx of each digit providing both protection and a gripping device. The gross and microscopic structure superficially appears to be very different in the mouse compared with man; however, the only real difference is that the nail plate in mice tends to be laterally compressed forming a semiconical structure rather than a flat plate resulting in a claw-like structure. As mouse nail units are much smaller than human nail units, side-by-side comparisons illustrated at different magnifications to include the entire nail facilitates a perception of differences. When viewed at the same magnification, the specific structures are very similar microanatomically (Figure 10.6) and similar protein markers are located in the same structures in both species [69].

Routine gross and histologic evaluation of young mice from many inbred strains revealed few, if any abnormalities of the nail unit [342] (Sundberg, unpublished data). However, in a large-scale aging study of 30 inbred strains, two nail abnormalities were identified histologically that

Vet-ebooks.com

Table 10.6 Mouse models for the various forms of human Epidermolysis Bullosa.

Gene	Symbol	No. Alleles[a]	Type	Survival
Epidermolysis bullosa simplex				
Keratin 5	*Krt5*^{tm1Tmm}	10	Tm	Neonatal death
Keratin 14	*Krt14*^{tm1Der}	16	Tm not specified	Neonatal death
Keratin 14	*Krt14*^{tm1Efu}	16	Tm null	Neonatal death
Keratin 14	*Krt14*^{tm2Der}	16	Tm conditional	Live to adulthood
Epidermolysis bullosa simplex with muscular dystrophy and pyloric atresia				
Plectin	*Plec*^{tm1Gwi}	34	Tm null	Neonatal death
Plectin	*Plec*^{tm2Gwi}	34	Tm null	Neonatal death
Plectin	*Plec*$^{tm7.1Gwi}$	34	Tm hypomorph	Live to adulthood
Plectin	*Plec*^{tm4Gwi}	34	Tm conditional	Normal
Epidermolysis bullosa simplex with pyloric atresia				
Integrin beta 4	*Itgb4*^{tm1Fgg}	10	Tm null	Neonatal death
Integrin beta 4	*Itgb4*^{tm1Mfel}	10	Tm conditional	Normal
Integrin beta 4	*Itgb4*^{tm2Son}	10	Tm conditional	Normal
Junctional epidermolysis bullosa, Herlitz Type				
Integrin alpha 6	*Itga6*^{tm1Egl}	62	Tm null	Neonatal death
Integrin alpha 6	*Itga6*^{tm2Egl}	62	Tm conditional	Normal
Integrin beta 4	*Itgb4*^{tm1Efu}	10	Tm null	Neonatal death
Laminin alpha 3	*Lama3*^{tm1Arte}	15	Tm conditional	Normal
Laminin beta 3	*Lamb3*^{IAP}	8	Spontaneous	Neonatal death
Laminin beta 3	*Lamb3*$^{tm1.1Hosc}$	8	Tm hypomorph	Neonatal death
Laminin gamma 2	*Lamc2*^{tm1Uit}	14	Tm null	Neonatal death
Junctional epidermolysis bullosa, non-herlitz type				
Collagen, type XVII, alpha 1	*Col17a1*^{tm1Shzu}	7	Tm null	20% survival
Laminin alpha 3	*Lama3*^{tm1Crt}	15	Tm null	Neonatal death
Laminin gamma 2	*Lamc2*^{jeb}	14	Spontaneous hypomorph	Live to adult but varies by strain
Recessive dystrophic epidermolysis bullosa				
Collagen, type VII, alpha 1	*Col7a1*^{tm1Uit}	12	Tm null	Neonatal death
Collagen, type VII, alpha 1	*Col7a1*^{tm1Lbt}	12	Tm hypomorph	Early death
Collagen, type VII, alpha 1	*Tg(CMV-COL7A1)1Shzu*	4 Tg	Tg	Live to 6 mo
Collagen, type VII, alpha 1	*Tg(Col1a2-COL7A1)1Shzu*	4 Tg	Tg	Live to 6 mo
Collagen, type VII, alpha 1	*Tg(KRT14-COL7A1)1Shzu*	4 Tg	Tg	Live to 6 mo
Collagen, type VII, alpha 1	*Tg(KRT14-COL7A1*)1Shzu*	4 Tg	Tg	Live to 6 mo
Kindler syndrome				
Fermitin family homolog 1	*Fermt1*^{tm1Ref}	6	Tm null	Neonatal death

Tm = targeted mutant (knockout), Tm null = true knockout, Tm conditional = *cre*-recombinase, Tg = transgenic, hypomorph = hypomorphic allele, not a complete null

[a] Number of Allelic Mutations listed in Mouse Genome Informatics (http://www.informatics.jax.org, 18 May 2020)

were missed at the time of necropsy, emphasizing the necessity of histologic evaluation of these small structures. Several inbred strains, but especially NON/ShiLtJ mice, developed acute to chronic inflammation due to rotation of the third phalangeal bone through the hyponychium resulting in ulceration, inflammation, and osteolysis. Ultimately, the nail plate was lost resulting in metaplasia of the nail matrix and nail bed causing severe orthokeratotic hyperkeratosis replacing the nail plate (Figure 10.32). This recapitulates some features of laminitis in horses [343]. A somewhat similar disorder was noted in aging DBA/1J mice that was proposed as a model for psoriatic arthritis [344].

Vet-ebooks.com

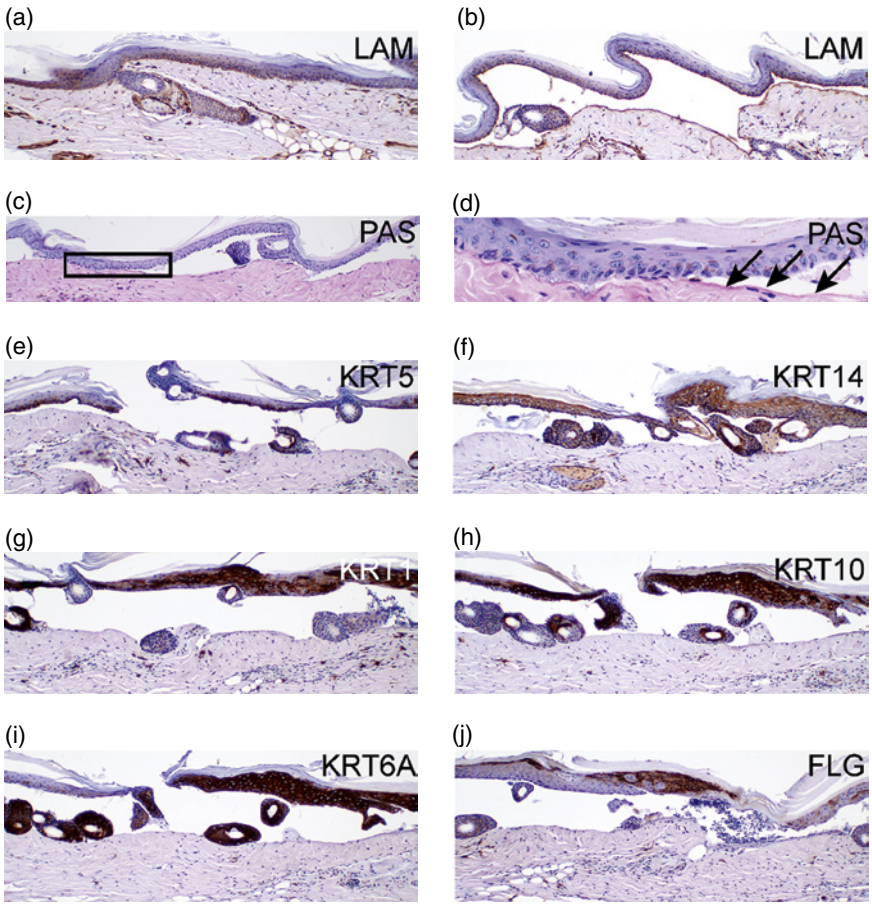


Figure 10.31 **Junctional epidermolysis bullosa**. The *Lamc2*$^{jeb/jeb}$ hypomorphic mutant has separation of the epidermis from the dermis at the basement membrane that closely resembles human junctional epidermolysis bullosa. Changes can be seen in tail skin relative to the wildtype (a) for expression of laminin (LAM, b), staining with periodic acid Schiff (PAS) for the basement membrane (c, boxed area enlarged in d, pink line, arrow), keratins 5 (KRT5, e) and 14 (KRT14, f) for basal cells, keratins 1 (KRT1, g) and 10 (KRT10, h) for suprabasal cells, keratin 6A for hyperplastic keratinocytes (KRT6A, i), and filaggrin for granular cells (FLG, j).

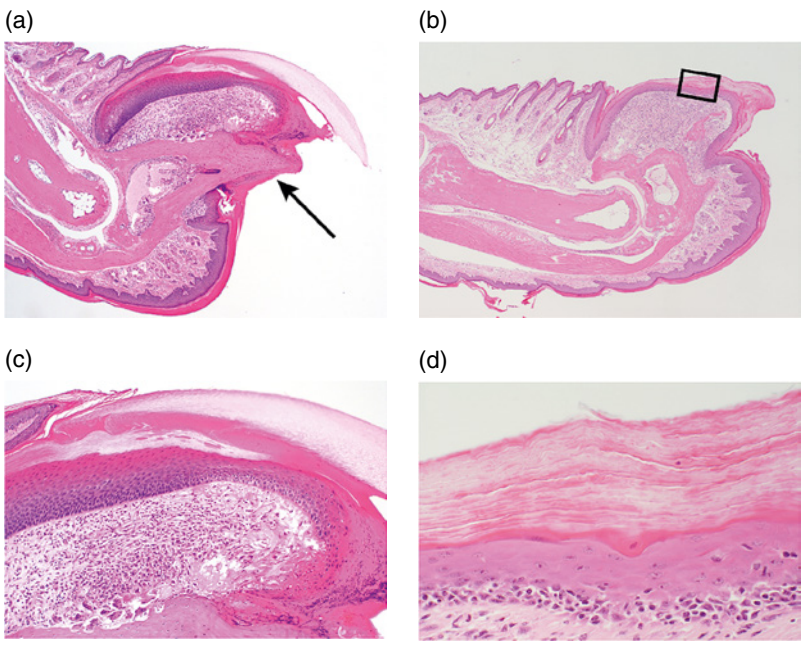
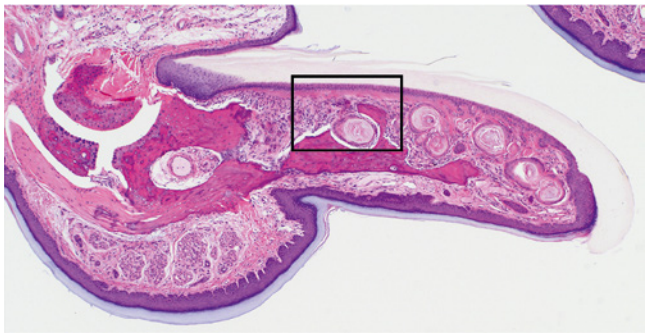


Figure 10.32 **Nail dystrophy with rotation of P3 in NON/ShiLtJ mice**. A common spontaneous aging change in this strain is rotation of the distal phalanx (P3) penetrating the hyponychium (a, arrow, b) resulting in hemorrhage and fluid buildup under the nail plate causing separation. The nail plate becomes friable and the underlying nail bed undergoes metaplasia resembling nail matrix in areas (c, d). The bone undergoes secondary resorption as noted by abundant osteoclasts.

Vet-ebooks.com

(a)



(b)

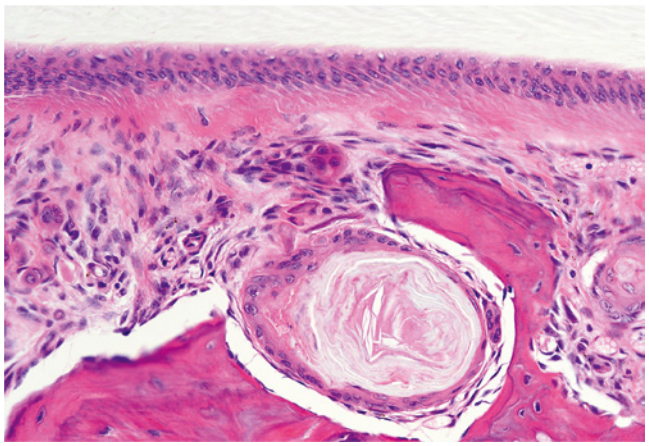


Figure 10.33 **Subungual intraosseous cysts in old mice**. This is a rare spontaneous lesion seen in most strains of mice (a, b). Similar lesions are found in many species including humans. They consist of stratified squamous epithelial lined cysts filled with cornified material extending down from the nail bed and forming cysts into the underlying bone as seen here. Boxed area in (a) is enlarged in (b).

A second spontaneous lesion observed in the 30 strain aging study was sporadic, subungual epidermoid inclusion cysts, rare lesions seen in humans and other mammals [343] (Figure 10.33).

Defects of nails are a common problem that occur in some human skin and hair diseases such as alopecia areata [345] and psoriasis [346] for which there are proposed mouse models with nail abnormalities [132, 347]. Spontaneous mutations such as hairless (Hr^{hr}) and ichthyosis ($Lbr^{ic\text{-}J}$) in mice cause severely overgrown and curved nails [186, 266, 348]. Similar gross changes occur in a number of transgenic [349] and targeted mouse mutations [350]. Complete destruction of the nail plate and bed may occur as a sequelae to loss of sensation as is the case with the nerve growth factor receptor null mutation [351]. These mice traumatize their nails when feeding on wire mesh or grooved metal feed hoppers embedded in the cage lids. As the mice age, the lesions result in complete loss of the nail with ulcerations and secondary infections of the remaining soft tissues. More subtle lesions, such as longitudinal striations on the nails of flaky skin (*fsn*) mice, may only be identified by scanning electron microscopy [347]. Failure of digits to develop with or without deformed nails can be found in GEMs that involve genes that regulate limb development [226, 352–357], keratins or genes that regulate keratin expression [97, 226, 358, 359], or cell adhesion [360]. Detailed evaluation of mouse nails should be included in routine characterization studies of new mutations, especially when nail defects are a feature of potentially analogous human diseases.

Summary

Mouse dermatology has changed from a peculiar hobby of mouse fanciers in the early 1900s to a highly sophisticated experimental system that opens a gateway to understanding the details of human skin diseases from the molecular level through to testing novel therapeutic compounds and regimens. This chapter provides an overview of the diversity of mutant mice available, suggested or proven models for specific human diseases, and examples of how these mice can be used to investigate diseases of specific aspects of the integument be they epidermis, dermis, pilosebaceous units, various glands, or nails.

Acknowledgments

The authors thank Zoe Reifsneider for her help preparing the figures used in this chapter; Nicholas Gott and Elaine Bechteld for histology and immunohistochemistry.

This publication was supported grants from the National Institutes of Health (R01-CA089713 to John P. Sundberg [JPS]) and Teacher, Erasmus+ Programme of the Commission of the European Union H2020 (PATHBIO to JPS). Dr. R. Kuiper was supported by an American Hair Research Society Mentorship grant. The Jackson Laboratory Shared Services were supported in part by Basic Cancer Center Core Grant from the National Cancer Institute (P30-CA034196).

References

1 Goldsmith, L.A. (1990). My organ is bigger than your organ. *Arch. Dermatol. Res.* 126 (3): 301–302.

2 Chuong, C.M., Nickoloff, B.J., Elias, P.M. et al. (2002). What is the 'true' function of skin? *Exp. Dermatol.* 11 (2): 159–187.

3 Kljuic, A., Bazzi, H., Sundberg, J.P. et al. (2003). Desmoglein 4 in hair follicle differentiation and epidermal adhesion: evidence from inherited hypotrichosis and acquired pemphigus vulgaris. *Cell* 113 (2): 249–260.

Vet-ebooks.com

4 Mellett, M., Meier, B., Mohanan, D. et al. (2018). CARD14 gain-of-function mutation alone is sufficient to drive IL-23/IL-17-mediated psoriasiform skin inflammation in vivo. *J. Invest. Dermatol.* 138 (9): 2010–2023.

5 Wang, M., Zhang, S., Zheng, G. et al. (2018). Gain-of-function mutation of *Card14* leads to spontaneous psoriasis-like skin inflammation through enhanced keratinocyte response to IL-17A. *Immunity* 49 (1): 66–79. e5.

6 Sundberg, J.P., Pratt, C.H., Silva, K.A. et al. (2019). Gain of function p.E138A alteration in *Card14* leads to psoriasiform skin inflammation and implicates genetic modifiers in disease severity. *Exp. Mol. Pathol.* 110: 104286.

7 Luetteke, N.C., Lee, D.C., Palmiter, R.D. et al. (1993). Regulation of fat and muscle development by transforming growth factor alpha in transgenic mice and in cultured cells. *Cell Growth Differ.* 4 (3): 203–213.

8 Mann, G.B., Fowler, K.J., Gabriel, A. et al. (1993). Mice with a null mutation of the TGF alpha gene have abnormal skin architecture, wavy hair, and curly whiskers and often develop corneal inflammation. *Cell* 73 (2): 249–261.

9 Luetteke, N.C., Phillips, H.K., Qiu, T.H. et al. (1994). The mouse waved-2 phenotype results from a point mutation in the EGF receptor tyrosine kinase. *Genes Dev.* 8 (4): 399–413.

10 Colucci-Guyon, E., Portier, M.M., Dunia, I. et al. (1994). Mice lacking vimentin develop and reproduce without an obvious phenotype. *Cell* 79 (4): 679–694.

11 Montagutelli, X., Lalouette, A., Boulouis, H.J. et al. (1997). Vesicle formation and follicular root sheath separation in mice homozygous for deleterious alleles at the balding (bal) locus. *J. Invest. Dermatol.* 109 (3): 324–328.

12 Koch, P.J., Mahoney, M.G., Ishikawa, H. et al. (1997). Targeted disruption of the pemphigus vulgaris antigen (desmoglein 3) gene in mice causes loss of keratinocyte cell adhesion with a phenotype similar to pemphigus vulgaris. *J. Cell Biol.* 137 (5): 1091–1102.

13 Miettinen, P.J., Berger, J.E., Meneses, J. et al. (1995). Epithelial immaturity and multiorgan failure in mice lacking epidermal growth factor receptor. *Nature* 376 (6538): 337–341.

14 Threadgill, D.W., Dlugosz, A.A., Hansen, L.A. et al. (1995). Targeted disruption of mouse EGF receptor: effect of genetic background on mutant phenotype. *Science* 269 (5221): 230–234.

15 Sibilia, M. and Wagner, E.F. (1995). Strain-dependent epithelial defects in mice lacking the EGF receptor. *Science* 269 (5221): 234–238.

16 Bubier, J.A., Sproule, T.J., Alley, L.M. et al. (2010). A mouse model of generalized non-Herlitz junctional epidermolysis bullosa. *J. Invest. Dermatol.* 130 (7): 1819–1828.

17 Meng, X., Klement, J.F., Leperi, D.A. et al. (2003). Targeted inactivation of murine laminin gamma2-chain gene recapitulates human junctional epidermolysis bullosa. *J. Invest. Dermatol.* 121 (4): 720–731.

18 Sproule, T.J., Bubier, J.A., Grandi, F.C. et al. (2014). Molecular identification of collagen 17a1 as a major genetic modifier of laminin gamma 2 mutation-induced junctional epidermolysis bullosa in mice. *PLoS Genet.* 10 (2): e1004068.

19 Simpson, E.M., Linder, C.C., Sargent, E.E. et al. (1997). Genetic variation among 129 substrains and its importance for targeted mutagenesis in mice. *Nat. Genet.* 16 (1): 19–27.

20 Berndt, A., Li, Q., Potter, C.S. et al. (2013). A single-nucleotide polymorphism in the *Abcc6* gene associates with connective tissue mineralization in mice similar to targeted models for pseudoxanthoma elasticum. *J. Invest. Dermatol.* 133 (3): 833–836.

21 Li, Q., Price, T.P., Sundberg, J.P., and Uitto, J. (2014). Juxta-articular joint-capsule mineralization in CD73 deficient mice: similarities to patients with *NT5E* mutations. *Cell Cycle* 13 (16): 2609–2615.

22 Sundberg, J.P., Taylor, D., Lorch, G. et al. (2011). Primary follicular dystrophy with scarring dermatitis in C57BL/6 mouse substrains resembles central centrifugal cicatricial alopecia in humans. *Vet. Pathol.* 48 (2): 513–524.

23 Mann, S.J. (1962). Prenatal formation of hair follicle types. *Anat. Rec.* 144: 135–142.

24 Holbrook, K.A. (1991). Structure and function of the developing human skin. In: *Physiology, Biochemistry, and Molecular Biology of the Skin* (ed. L.A. Goldsmith), 63–110. New York, NJ: Oxford University Press.

25 Holbrook, K.A. and Smith, L.T. (1993). Morphology and connective tissue: structure of the skin and tendon. In: *Connective Tissue and its Heritable Disorders Molecular, Genetic, and Medical Aspects* (eds. P.M. Royce and B. Steinmann), 51–71. New York, NY: Wiley-Liss.

26 Sundberg, J.P., Hogan, M.E., and King, L.E. Jr. (1996). Normal biology and aging changes in skin and hair. In: *Pathobiology of the Aging Mouse*, vol. 2 (eds. U. Mohr, D.L. Dungworth, C.C. Capen, et al.), 303–323. Washington, DC: ILSI Press.

27 Paus, R., Muller-Rover, S., Van Der Veen, C. et al. (1999). A comprehensive guide for the recognition and classification of distinct stages of hair follicle morphogenesis. *J. Invest. Dermatol.* 113 (4): 523–532.

28 Sundberg, J.P., Booth, C.J., Nanney, L.B. et al. (2018). Skin and adnexa. In: *Comparative Anatomy and Histology a Mouse, Rat, and Human Atlas*, 2e (eds. P. Treuting, S.M. Dintzis, C.W. Frevert, et al.), 511–542. Amsterdam: Elsevier.

29 Sundberg, J.P., King, L.E. Jr., Bosenberg, M. et al. (2020). Animal models of skin disease. In: *McKee's Pathology of the Skin with Clinical Correlations*, 5e, vol. 2 (eds. E. Calonje, T. Brenn, A.H. Lazar and S.D. Billings), 1895–1917. China: Elsevier.

Vet-ebooks.com

30 Gruneberg, H. (1943). The development of some external features in mouse embryos. *J. Hered.* 34: 88–92.

31 Hardy, M.H. (1949). The development of mouse hair in vitro with some observations on pigmentation. *J. Anat.* 83 (4): 364–384, 3 pl.

32 Falconer, D.S., Fraser, A.S., and King, J.W. (1951). The genetics and development of 'crinkled', a new mutant in the house mouse. *J. Genet.* 50 (2): 324–344.

33 Slee, J. (1962). Developmental morphology of the skin and hair follicles in normal and in 'ragged' mice. *J. Embryol. Exp. Morphol.* 10: 507–529.

34 Claxton, J.H. (1966). The hair follicle group in mice. *Anat. Rec.* 154 (2): 195–207.

35 Chiang, C., Swan, R.Z., Grachtchouk, M. et al. (1999). Essential role for sonic hedgehog during hair follicle morphogenesis. *Dev. Biol.* 205 (1): 1–9.

36 Plikus, M.V., Widelitz, R.B., Maxson, R., and Chuong, C.M. (2009). Analyses of regenerative wave patterns in adult hair follicle populations reveal macro-environmental regulation of stem cell activity. *Int. J. Dev. Biol.* 53 (5–6): 857–868.

37 Sundberg, J.P. and Silva, K.A. (2012). What color is the skin of a mouse? *Vet. Pathol.* 49 (1): 142–145.

38 Plikus, M.V. and Chuong, C.M. (2008). Complex hair cycle domain patterns and regenerative hair waves in living rodents. *J. Invest. Dermatol.* 128 (5): 1071–1080.

39 Plikus, M.V., Baker, R.E., Chen, C.C. et al. (2011). Self-organizing and stochastic behaviors during the regeneration of hair stem cells. *Science* 332 (6029): 586–589.

40 Andreasen, E. (1953). Cyclic changes in the skin of the mouse. *Acta Pathol. Microbiol. Scand.* 32 (1): 157–164.

41 Trachy, R.E., Fors, T.D., Pickart, L., and Uno, H. (1991). The hair follicle-stimulating properties of peptide copper complexes. Results in C3H mice. *Ann. N.Y. Acad. Sci.* 642: 468–469.

42 Sundberg, J.P., Boggess, D., Sundberg, B.A. et al. (1993). Epidermal dendritic cell populations in the flaky skin mutant mouse. *Immunol. Invest.* 22 (5): 389–401.

43 Sundberg, J.P., Rourk, M.H., Boggess, D. et al. (1997). Angora mouse mutation: altered hair cycle, follicular dystrophy, phenotypic maintenance of skin grafts, and changes in keratin expression. *Vet. Pathol.* 34 (3): 171–179.

44 Sundberg, J.P., France, M., Boggess, D. et al. (1997). Development and progression of psoriasiform dermatitis and systemic lesions in the flaky skin (*fsn*) mouse mutant. *Pathobiology* 65 (5): 271–286.

45 Dry, F.W. (1926). The coat of the mouse (*Mus musculus*). *J. Genet.* 16: 287–340.

46 Trigg, M.J. (1972). Hair growth in mouse mutants affecting coat texture. *J. Zool. Lond.* 168: 165–198.

47 Fraser, A.S. (1951). Growth of the mouse coat. *J. Exp. Zool.* 117: 15–29.

48 Yamakado, M. and Yohro, T. (1979). Subdivision of mouse vibrissae on an embryological basis, with descriptions of variations in the number and arrangement of sinus hairs and cortical barrels in BALB/c (*nu*/+; nude, *nu*/*nu*) and hairless (*hr*/*hr*) strains. *Am. J. Anat.* 155 (2): 153–173.

49 Chase, H.B., Montagna, W., and Malone, J.D. (1953). Changes in the skin in relation to the hair growth cycle. *Anat. Rec.* 116 (1): 75–81.

50 Chase, H.B. (1954). Growth of the hair. *Physiol. Rev.* 34 (1): 113–126.

51 Chase, H.B. (1955). The physiology and histochemistry of hair growth. *J. Soc. Cosmet. Chem.* 6: 9–14.

52 Straile, W.E., Chase, H.B., and Arsenault, C. (1961). Growth and differentiation of hair follicles between periods of activity and quiescence. *J. Exp. Zool.* 148: 205–221.

53 Chase, H.B. and Eaton, G.J. (1959). The growth of hair follicles in waves. *Ann. N.Y. Acad. Sci.* 83: 365–368.

54 Levkovich, T., Poutahidis, T., Smillie, C. et al. (2013). Probiotic bacteria induce a 'glow of health'. *PLoS One* 8 (1): e53867.

55 Neutelings, T., Nusgens, B.V., Liu, Y. et al. (2015). Skin physiology in microgravity: a 3-month stay aboard ISS induces dermal atrophy and affects cutaneous muscle and hair follicles cycling in mice. *NPJ Microgravity* 1: 15002.

56 Sundberg, J.P. and Hogan, M.E. (1994). Hair types and subtypes in the laboratory mouse. In: *Handbook of Mouse Mutations with Skin and Hair Abnormalities: Animal Models and Biomedical Tools* (ed. J.P. Sundberg), 57–68. Boca Raton, FL: CRC Press.

57 Jamieson, W.A. (1888). *Diseases of the Skin*. Philadelphia, PA: J. B. Lippincott Co.

58 Williams, D., Profeta, K., and Stenn, K.S. (1994). Isolation and culture of follicular papillae from murine vibrissae: an introductory approach. *Br. J. Dermatol.* 130 (3): 290–297.

59 Hsu, Y.C., Pasolli, H.A., and Fuchs, E. (2011). Dynamics between stem cells, niche, and progeny in the hair follicle. *Cell* 144 (1): 92–105.

60 Higgins, C.A., Westgate, G.E., and Jahoda, C.A. (2009). From telogen to exogen: mechanisms underlying formation and subsequent loss of the hair club fiber. *J. Invest. Dermatol.* 129 (9): 2100–2108.

61 Higgins, C.A., Westgate, G.E., and Jahoda, C.A. (2011). Modulation in proteolytic activity is identified as a hallmark of exogen by transcriptional profiling of hair follicles. *J. Invest. Dermatol.* 131 (12): 2349–2357.

62 HogenEsch, H., Boggess, D., and Sundberg, J.P. (1999). Changes in keratin and filaggrin expression in the skin of chronic proliferative dermatitis (*cpdm*) mutant mice. *Pathobiology* 67 (1): 45–50.

63 Calhoun, M.L. and Stinson, A.W. (1981). Integument. In: *Textbook of Veterinary Histology* (eds. H.D. Dellmann and E.M. Brown), 378–411. Philadelphia, PA: Lea & Febiger.

64 Bloom, W. and Fawcett, D.W. (1968). *Textbook of Histology*. Philadelphia, PA: W. B. Saunders.

65 Parakkal, P.F. (1969). The fine structure of anagen hair follicle of the mouse. *Adv. Biol. Skin* 9: 441–469.

Vet-ebooks.com

66 Sperling, L.C. (1991). Hair anatomy for the clinician. *J. Am. Acad. Dermatol.* 25 (1 Pt 1): 1–17.

67 Headington, J.T. (1984). Transverse microscopic anatomy of the human scalp. A basis for a morphometric approach to disorders of the hair follicle. *Arch. Dermatol.* 120 (4): 449–456.

68 Bergfeld, W.F. (1990). Noninflammatory reactions of the pilosebaceous unit and disorders of the hair shaft. In: *Pathology of the Skin* (eds. E.R. Farmer and A.F. Hood), 941–951. Norwalk, CT: Appelton and Lange.

69 Fleckman, P., Jaeger, K., Silva, K.A., and Sundberg, J.P. (2013). Comparative anatomy of mouse and human nail units. *Anat. Rec. (Hoboken).* 296 (3): 521–532.

70 Takeo, M., Chou, W.C., Sun, Q. et al. (2013). *Wnt* activation in nail epithelium couples nail growth to digit regeneration. *Nature* 499 (7457): 228–232.

71 Sundberg, J.P. and Boggess, D. (2000). *Systematic Approach to Evaluation of Mouse Mutations*, 199 p. Boca Raton, FL: CRC Press.

72 Sundberg, J.P., Montagutelli, X., and Boggess, D. (1998). Systematic approach to evaluation of mouse mutations with cutaneous appendage defects. In: *Cutaneous Appendages* (ed. M. Chuong), 421–435. Austin, TX: Molecular Biology Intelligence Unit I, R.G. Landes Company.

73 Green, M.C. and Witham, B.A. (1991). *Handbook on Genetically Standardized Jax Mice*, 4e. The Jackson Laboratory: Bar Harbor, ME.

74 Carroll, J.M., McElwee, K.J., Lloyd, E.K. et al. (2002). Gene array profiling and immunomodulation studies define a cell-mediated immune response underlying the pathogenesis of alopecia areata in a mouse model and humans. *J. Invest. Dermatol.* 119 (2): 392–402.

75 Potter, C.S., Wang, Z., Silva, K.A. et al. (2014). Chronic proliferative dermatitis in *Sharpin* null mice: development of an autoinflammatory disease in the absence of B and T lymphocytes and IL4/IL13 signaling. *PLoS One* 9 (1): e85666.

76 Silva, K. and Sundberg, J.P. (2012). Necropsy methods. In: *The Laboratory Mouse*, 2e (ed. H.J. Hedrich), 779–806. Amsterdam: AP, Elsevier.

77 Sundberg, J.P., Beamer, W.G., Shultz, L.D., and Dunstan, R.W. (1990). Inherited mouse mutations as models of human adnexal, cornification, and papulosquamous dermatoses. *J. Invest. Dermatol.* 95 (5 Suppl): 62S–63S.

78 Nanney, L.B., Sundberg, J.P., and King, L.E. (1996). Increased epidermal growth factor receptor in *fsn/fsn* mice. *J. Invest. Dermatol.* 106 (6): 1169–1174.

79 Weiss, G., Shemer, A., and Trau, H. (2002). The Koebner phenomenon: review of the literature. *J. Eur. Acad. Dermatol. Venereol.* 16 (3): 241–248.

80 Liang, Y., Silva, K.A., Kennedy, V., and Sundberg, J.P. (2011). Comparisons of mouse models for hair follicle reconstitution. *Exp. Dermatol.* 20 (12): 1011–1015.

81 Smith, R.S., Martin, G., and Boggess, D. (2000). Kinetics and morphometrics. In: *Systematic Approach to Evaluation of Mouse Mutations* (eds. J.P. Sundberg and D. Boggess). Boca Raton, FL: CRC Press.

82 Scholzen, T. and Gerdes, J. (2000). The Ki-67 protein: from the known and the unknown. *J. Cell. Physiol.* 182 (3): 311–322.

83 Liang, Y. and Sundberg, J.P. (2011). SHARPIN regulates mitochondria-dependent apoptosis in keratinocytes. *J. Dermatol. Sci.* 63 (3): 148–153.

84 Leary, S., Underwood, W., Anthony, R. et al. *AVMA Guidelines for the Euthanasia of Animals*: 2020 Edition, 2020. Schaumburg, IL: American Veterinary Medical Association.

85 Sundberg, J.P., Stearns, T.M., Joh, J. et al. (2014). Immune status, strain background, and anatomic site of inoculation affect mouse papillomavirus (MmuPV1) induction of exophytic papillomas or endophytic trichoblastomas. *PLoS One* 9 (12): e113582.

86 Whiting, D.A. (1990). The value of horizontal sections of scalp biopsies. *J. Cut Aging Cosmet. Dermatol.* 1: 165–173.

87 Feldman, D.B. and Seely, J.C. (1988). *Necropsy Guide to Rodents and the Rabbit*. Boca Raton, FL: CRC Press.

88 Knoblaugh, S.E. and Randolph-Habecker, J. (2018). Necropsy and histology. In: *Comparative Anatomy and Histology A Mouse, Rat, and Human Atlas*, 2e (eds. P.M. Treuting, S.M. Dintzis and K.S. Montine), 23–51. London: Academic Press.

89 Mikaelian, I., Nanney, L.B., Parman, K.S. et al. (2004). Antibodies that label paraffin-embedded mouse tissues: a collaborative endeavor. *Toxicol. Pathol.* 32 (2): 181–191.

90 Sundberg, J.P., Boggess, D., Bascom, C. et al. (2000). Lanceolate hair-J (*lahJ*): a mouse model for human hair disorders. *Exp. Dermatol.* 9 (3): 206–218.

91 Dadras, S.S., Silva, K.A., King, L.E. Jr., and Sundberg, J.P. (2014). Transplantable malignant melanoma in LT.B6 congenic mice resembling pigmented epithelioid melanocytoma in humans. *J. Invest. Dermatol.* 134 (6): 1772–1775.

92 Luna, L.G. (1968). *Manual of Histologic Staining Methods of the Armed Forces Institute of Pathology*. New York, NY: Blakiston Division, McGraw-Hill.

93 Bechtold, L.S. (2000). Ultrastructural evaluation of mouse mutations. In: *Systematic Characterization of Mouse Mutations* (eds. J.P. Sundberg and D. Boggess), 121–129. Boca Raton, FL: CRC Press.

94 Rice, R.H., Bradshaw, K.M., Durbin-Johnson, B.P. et al. (2012). Differentiating inbred mouse strains from each other and those with single gene mutations using hair proteomics. *PLoS One* 7 (12): e51956.

95 Rice, R.H., Wong, V.J., Pinkerton, K.E., and Sundberg, J.P. (1999). Cross-linked features of mouse pelage hair resistant to detergent extraction. *Anat. Rec.* 254 (2): 231–237.

96 Rice, R.H., Wong, V.J., Williams, M.L. et al. (1999). Hair shaft defects visualized after detergent extraction. *Exp. Dermatol.* 8 (4): 308–310.

Vet-ebooks.com

97 Mecklenburg, L., Paus, R., Halata, Z. et al. (2004). FOXN1 is critical for onycholemmal terminal differentiation in nude (*Foxn1*) mice. *J. Invest. Dermatol.* 123 (6): 1001–1011.

98 Haldane, J.B.S., Sprunt, A.D., and Haldane, N.M. (1915). Reduplication in mice. *J. Genet.* 5: 133–135.

99 Barsh, G.S. (1996). The genetics of pigmentation: from fancy genes to complex traits. *Trends Genet.* 12 (8): 299–305.

100 Baxter, L.L., Hou, L., Loftus, S.K., and Pavan, W.J. (2004). Spotlight on spotted mice: a review of white spotting mouse mutants and associated human pigmentation disorders. *Pigment Cell Res.* 17 (3): 215–224.

101 Reissmann, M. and Ludwig, A. (2013). Pleiotropic effects of coat colour-associated mutations in humans, mice and other mammals. *Semin. Cell Dev. Biol.* 24 (6–7): 576–586.

102 George, A., Zand, D.J., Hufnagel, R.B. et al. (2016). Biallelic mutations in *MITF* cause coloboma, osteopetrosis, microphthalmia, macrocephaly, albinism, and deafness. *Am. J. Human Genet.* 99 (6): 1388–1394.

103 Boissy, R.E., Zhao, H., Oetting, W.S. et al. (1996). Mutation in and lack of expression of tyrosinase-related protein-1 (*TRP-1*) in melanocytes from an individual with brown oculocutaneous albinism: a new subtype of albinism classified as "OCA3". *Am. J. Human Genet.* 58 (6): 1145–1156.

104 Kenny, E.E., Timpson, N.J., Sikora, M. et al. (2012). Melanesian blond hair is caused by an amino acid change in *TYRP1*. *Science* 336 (6081): 554.

105 Menasche, G., Ho, C.H., Sanal, O. et al. (2003). Griscelli syndrome restricted to hypopigmentation results from a melanophilin defect (GS3) or a *MYO5A* F-exon deletion (GS1). *J. Clin. Invest.* 112 (3): 450–456.

106 Oliver, C. and Essner, E. (1973). Distribution of anomalous lysosomes in the beige mouse: a homologue of Chediak-Higashi syndrome. *J. Histochem. Cytochem.* 21 (3): 218–228.

107 Sundberg, J.P. (1994). The mottled (*Mo*), blotchy (Mo^{blo}), brindled (Mo^{br}), dappled (Mo^{dp}), mosaic (Mo^{ms}), tortoiseshell (Mo^{to}), and viable brindled (Mo^{vbr}), chromosome X. In: *Handbook of Mouse Mutations with Skin and Hair Abnormalities: Animal Models and Biomedical Tools* (ed. J.P. Sundberg), 359–369. Boca Raton, FL: CRC Press.

108 Kelly, E.M. (1957). Beige, *bg*. *Mouse News Lett.* 16: 36.

109 Lane, P.W. (1962). *bg*-beige and bg^{2J} – beige-2J. *Mouse News Lett.* 26: 35.

110 Kaler, S.G. (1993). ATP7A-related copper transport disorders. In: *GeneReviews((R))* (eds. M.P. Adam, H.H. Ardinger, R.A. Pagon, et al.). Seattle, WA: University of Washington.

111 Sarvella, P.A. and Russell, L.B. (1956). Steel, a new dominant gene in the house mouse. *J. Hered.* 47: 123–128.

112 Li, H. and Hou, L. (2018). Regulation of melanocyte stem cell behavior by the niche microenvironment. *Pigment Cell Melanoma Res.* 31 (5): 556–569.

113 Slominski, A. and Paus, R. (1993). Melanogenesis is coupled to murine anagen: toward new concepts for the role of melanocytes and the regulation of melanogenesis in hair growth. *J. Invest. Dermatol.* 101 (1 Suppl): 90S–97S.

114 Slominski, A., Wortsman, J., Plonka, P.M. et al. (2005). Hair follicle pigmentation. *J. Invest. Dermatol.* 124 (1): 13–21.

115 Oyehaug, L., Plahte, E., Vage, D.I., and Omholt, S.W. (2002). The regulatory basis of melanogenic switching. *J. Theor. Biol.* 215 (4): 449–468.

116 Steingrimsson, E., Copeland, N.G., and Jenkins, N.A. (2006). Mouse coat color mutations: from fancy mice to functional genomics. *Dev. Dyn.* 235 (9): 2401–2411.

117 Dickies, M.M. (1962). A new viable yellow mutation in the house mouse. *J. Hered.* 53: 84–86.

118 Cropley, J.E., Suter, C.M., Beckman, K.B., and Martin, D.I. (2006). Germ-line epigenetic modification of the murine A vy allele by nutritional supplementation. *Proc. Natl. Acad. Sci. U.S.A.* 103 (46): 17308–17312.

119 Hakami, R.M., Hou, L., Baxter, L.L. et al. (2006). Genetic evidence does not support direct regulation of *EDNRB* by *SOX10* in migratory neural crest and the melanocyte lineage. *Mech. Dev.* 123 (2): 124–134.

120 Harris, M.L., Buac, K., Shakhova, O. et al. (2013). A dual role for *SOX10* in the maintenance of the postnatal melanocyte lineage and the differentiation of melanocyte stem cell progenitors. *PLos Genet.* 9 (7): e1003644.

121 Harris, M.L., Levy, D.J., Watkins-Chow, D.E., and Pavan, W.J. (2015). Ectopic differentiation of melanocyte stem cells is influenced by genetic background. *Pigment Cell Melanoma Res.* 28 (2): 223–228.

122 Zhang, B., Ma, S., Rachmin, I. et al. (2020). Hyperactivation of sympathetic nerves drives depletion of melanocyte stem cells. *Nature* 577 (7792): 676–681.

123 Aubin-Houzelstein, G., Djian-Zaouche, J., Bernex, F. et al. (2008). Melanoblasts' proper location and timed differentiation depend on Notch/RBP-J signaling in postnatal hair follicles. *J. Invest. Dermatol.* 128 (11): 2686–2695.

124 Moriyama, M., Osawa, M., Mak, S.S. et al. (2006). *Notch* signaling via *Hes1* transcription factor maintains survival of melanoblasts and melanocyte stem cells. *J. Cell Biol.* 173 (3): 333–339.

125 Nishimura, E.K., Granter, S.R., and Fisher, D.E. (2005). Mechanisms of hair graying: incomplete melanocyte stem cell maintenance in the niche. *Science* 307 (5710): 720–724.

126 Rabbani, P., Takeo, M., Chou, W. et al. (2011). Coordinated activation of Wnt in epithelial and melanocyte stem cells initiates pigmented hair regeneration. *Cell* 145 (6): 941–955.

127 Schouwey, K., Delmas, V., Larue, L. et al. (2007). Notch1 and Notch2 receptors influence progressive hair graying in a dose-dependent manner. *Dev. Dyn.* 236 (1): 282–289.

128 Tanimura, S., Tadokoro, Y., Inomata, K. et al. (2011). Hair follicle stem cells provide a functional niche for melanocyte stem cells. *Cell Stem Cell* 8 (2): 177–187.

Vet-ebooks.com

129 Valluet, A., Druillennec, S., Barbotin, C. et al. (2012). B-Raf and C-Raf are required for melanocyte stem cell self-maintenance. *Cell Rep.* 2 (4): 774–780.

130 Beamer, W.G., Sweet, H.O., Bronson, R.T. et al. (1994). Adrenocortical dysplasia: a mouse model system for adrenocortical insufficiency. *J. Endocrinol.* 141 (1): 33–43.

131 Sundberg, J.P., Orlow, S.J., Sweet, H.O., and Beamer, W.G. (1994). The adrenocortical dysplasia (*acd*) mutation, chromosome 8. In: *Handbook of Mouse Mutations with Skin and Hair Abnormalities: Animal Models and Biomedical Tools* (ed. J.P. Sundberg), 159–164. Boca Raton, FL: CRC Press.

132 McElwee, K.J., Boggess, D., Miller, J. et al. (1999). Spontaneous alopecia areata-like hair loss in one congenic and seven inbred laboratory mouse strains. *J. Invest. Dermatol. Symp. Proc.* 4 (3): 202–206.

133 McElwee, K.J., Silva, K., Beamer, W.G. et al. (2001). Melanocyte and gonad activity as potential severity modifying factors in C3H/HeJ mouse alopecia areata. *Exp. Dermatol.* 10 (6): 420–429.

134 Sundberg, J.P., Shen, T., Fiehn, O. et al. (2018). Sebaceous gland abnormalities in fatty acyl CoA reductase 2 (*Far2*) null mice result in primary cicatricial alopecia. *PLoS One* 13 (10): e0205775.

135 Briggs, O.M. (1987). Practical small animal dermatology. I: structure and function of the skin. *J. S. Afr. Vet. Assoc.* 58 (4): 229–231.

136 Strauss, J.S., Downing, D.T., Ebling, F.J. et al. (1991). Sebaceous glands. In: *Physiology, Biochemistry, and Molecular Biology of the Skin* (ed. L.A. Goldsmith), 712–740. New York, NY: Oxford University Press.

137 Fluhr, J.W., Mao-Qiang, M., Brown, B.E. et al. (2003). Glycerol regulates stratum corneum hydration in sebaceous gland deficient (asebia) mice. *J. Invest. Dermatol.* 120 (5): 728–737.

138 Smith, R.S., Sundberg, J.P., and John, S.W.M. (2000). The anterior segment and ocular adnexae. In: *Systematic Evaluation of the Mouse Eye Anatomy, Pathology, and Biomethods* (eds. R.S. Smith, S.W.M. John, P.M. Nishina and J.P. Sundberg), 3–23. Boca Raton, FL: CRC Press.

139 Sundberg, J.P., Berndt, A., Sundberg, B.A. et al. (2016). Approaches to investigating complex genetic traits in a large-scale inbred mouse aging study. *Vet. Pathol.* 53 (2): 456–467.

140 Bovell, D.L. (2018). The evolution of eccrine sweat gland research towards developing a model for human sweat gland function. *Exp. Dermatol.* 27 (5): 544–550.

141 Munger, B.L. and Brusilow, S.W. (1971). The histophysiology of rat plantar sweat glands. *Anat. Rec.* 169 (1): 1–21.

142 Taylor, D.K., Bubier, J.A., Silva, K.A., and Sundberg, J.P. (2012). Development, structure, and keratin expression in C57BL/6J mouse eccrine glands. *Vet. Pathol.* 49 (1): 146–154.

143 Dahlhoff, M., Pfister, S., Blutke, A. et al. (2014). Peri-conceptional obesogenic exposure induces sex-specific programming of disease susceptibilities in adult mouse offspring. *Biochim. Biophys. Acta* 1842 (2): 304–317.

144 Zheng, Y., Eilertsen, K.J., Ge, L. et al. (1999). *Scd1* is expressed in sebaceous glands and is disrupted in the asebia mouse. *Nat. Genet.* 23 (3): 268–270.

145 Sundberg, J.P., Boggess, D., Sundberg, B.A. et al. (2000). Asebia-2J ($Scd1^{ab2J}$): a new allele and a model for scarring alopecia. *Am. J. Pathol.* 156 (6): 2067–2075.

146 Porter, R.M., Jahoda, C.A., Lunny, D.P. et al. (2002). Defolliculated (*dfl*): a dominant mouse mutation leading to poor sebaceous gland differentiation and total elimination of pelage follicles. *J. Invest. Dermatol.* 119 (1): 32–37.

147 Lunny, D.P., Weed, E., Nolan, P.M. et al. (2005). Mutations in gasdermin 3 cause aberrant differentiation of the hair follicle and sebaceous gland. *J. Invest. Dermatol.* 124 (3): 615–621.

148 Ehrmann, C. and Schneider, M.R. (2016). Genetically modified laboratory mice with sebaceous glands abnormalities. *Cell. Mol. Life Sci.* 73 (24): 4623–4642.

149 Stenn, K.S. (2001). Insights from the asebia mouse: a molecular sebaceous gland defect leading to cicatricial alopecia. *J. Cutaneous Pathol.* 28 (9): 445–447.

150 Stenn, K.S., Sundberg, J.P., and Sperling, L.C. (1999). Hair follicle biology, the sebaceous gland, and scarring alopecias. *Arch. Dermatol.* 135 (8): 973–974.

151 Sundberg, J.P., Hordinsky, M.K., Bergfeld, W. et al. (2018). Cicatricial Alopecia Research Foundation meeting, May 2016: progress towards the diagnosis, treatment and cure of primary cicatricial alopecias. *Exp. Dermatol.* 27 (3): 302–310.

152 Furukawa, F. and Yoshimasu, T. (2005). Animal models of spontaneous and drug-induced cutaneous lupus erythematosus. *Autoimmune Rev.* 4 (6): 345–350. https://doi.org/10.1016/j.autrev.2005.01.006.

153 Uva, L., Miguel, D., Pinheiro, C. et al. (2012). Cutaneous manifestations of systemic lupus erythematosus. *Autoimmune Dis.* 2012: 834291. https://doi.org/10.1155/2012/834291.

154 Karnik, P., Tekeste, Z., McCormick, T.S. et al. (2009). Hair follicle stem cell-specific PPARgamma deletion causes scarring alopecia. *J. Invest. Dermatol.* 129 (5): 1243–1257.

155 Mirmirani, P. and Karnik, P. (2009). Lichen planopilaris treated with a peroxisome proliferator-activated receptor gamma agonist. *Arch. Dermatol.* 145 (12): 1363–1366.

156 Olsen, E., Stenn, K., Bergfeld, W. et al. (2003). Update on cicatricial alopecia. *J. Invest. Dermatol. Symp. Proc.* 8 (1): 18–19.

157 Tee, W.S. and Shapiro, J. (2015). Scarring alopecias: a trichologic emergency. *Semin. Cutan. Med. Surg.* 34 (2): 76–80. https://doi.org/10.12788/j.sder.2015.0130.

158 Gimelli, G., Giglio, S., Zuffardi, O. et al. (2002). Gene dosage of the spermidine/spermine N(1)-acetyltransferase (*SSAT*) gene with putrescine accumulation in a patient with a Xp21.1p22.12 duplication and keratosis follicularis

Vet-ebooks.com

spinulosa decalvans (KFSD). *Hum Genet.* 111 (3): 235–241. https://doi.org/10.1007/s00439-002-0791-6.

159 Breshears, M.A., Eberle, R., and Ritchey, J.W. (2001 Jul). Characterization of gross and histological lesions in Balb/c mice experimentally infected with herpesvirus saimiri 1 (HVS1). *J Comp Pathol.* 125 (1): 25–33. https://doi.org/10.1053/jcpa.2001.0473.

160 Pedersen, N.C., Brucker, L., Tessier, N.G. et al. (2015). The effect of genetic bottlenecks and inbreeding on the incidence of two major autoimmune diseases in standard poodles, sebaceous adenitis and Addison's disease. *Canine Genet. Epidemiol.* 2: 14.

161 Gates, A.H. and Karasek, M. (1965). Hereditary absence of sebaceous glands in the mouse. *Science* 148 (3676): 1471–1473.

162 Schneider, M.R. (2015). Fifty years of the asebia mouse: origins, insights and contemporary developments. *Exp. Dermatol.* 24 (5): 340–341.

163 Stoffel, W., Schmidt-Soltau, I., Jenke, B. et al. (2017). Hair growth cycle is arrested in SCD1 deficiency by impaired Wnt3a-palmitoleoylation and retrieved by the artificial lipid barrier. *J. Invest. Dermatol.* 137 (7): 1424–1433.

164 Sundberg, J.P. (1994). *Handbook of Mouse Mutations with Skin and Hair Abnormalities: Animal Models and Biomedical Tools*, 544 p. Boca Raton, FL: CRC Press.

165 Giehl, K.A., Potter, C.S., Wu, B. et al. (2009). Hair interior defect in AKR/J mice. *Clin. Exp. Dermatol.* 34 (4): 509–517.

166 Wu, B., Potter, C.S., Silva, K.A. et al. (2010). Mutations in sterol O-acyltransferase 1 (*Soat1*) result in hair interior defects in AKR/J mice. *J. Invest. Dermatol.* 130 (11): 2666–2668.

167 Chen, W., Kelly, M.A., Opitz-Araya, X. et al. (1997). Exocrine gland dysfunction in MC5-R-deficient mice: evidence for coordinated regulation of exocrine gland function by melanocortin peptides. *Cell* 91 (6): 789–798.

168 Dahlhoff, M., Camera, E., Schafer, M. et al. (2016). Sebaceous lipids are essential for water repulsion, protection against UVB-induced apoptosis and ocular integrity in mice. *Development* 143 (10): 1823–1831.

169 Hosur, V., Cox, M.L., Burzenski, L.M. et al. (2013). Retrotransposon insertion in the T-cell acute lymphocytic leukemia 1 (*Tal1*) gene is associated with severe renal disease and patchy alopecia in Hairpatches (*Hpt*) mice. *PLoS One* 8 (1): e53426.

170 Odgren, P.R., Pratt, C.H., Mackay, C.A. et al. (2010). Disheveled hair and ear (*Dhe*), a spontaneous mouse *Lmna* mutation modeling human laminopathies. *PLoS One* 5 (4): e9959.

171 Sundberg, J.P., Rozell, B., and Everts, H. (2011). Association between hair-induced oronasal inflammation and ulcerative dermatitis in C57BL/6 mice. *Comp. Med.* 61 (3): 204–205. author reply 5.

172 Everts, H.B., Silva, K.A., Montgomery, S. et al. (2013). Retinoid metabolism is altered in human and mouse cicatricial alopecia. *J. Invest. Dermatol.* 133 (2): 325–333.

173 Johnson, K.R., Sweet, H.O., Donahue, L.R. et al. (1998). A new spontaneous mouse mutation of *Hoxd13* with a polyalanine expansion and phenotype similar to human synpolydactyly. *Hum. Mol. Genet.* 7 (6): 1033–1038.

174 Cocquempot, O., Brault, V., Babinet, C., and Herault, Y. (2009). Fork stalling and template switching as a mechanism for polyalanine tract expansion affecting the DYC mutant of *HOXD13*, a new murine model of synpolydactyly. *Genetics* 183 (1): 23–30.

175 Crocker, M. and Cattanach, B.M. (1979). The genetics of Sleek: a possible regulatory mutation of the tabby-crinkled-downless syndrome. *Genet. Res.* 34 (3): 231–238.

176 Ferguson, B.M., Brockdorff, N., Formstone, E. et al. (1997). Cloning of Tabby, the murine homolog of the human *EDA* gene: evidence for a membrane-associated protein with a short collagenous domain. *Hum. Mol. Genet.* 6 (9): 1589–1594.

177 Gruneberg, H. (1966). The molars of the tabby mouse, and a test of the 'single-active X-chromosome' hypothesis. *J. Embryol. Exp. Morphol.* 15 (2): 223–244.

178 Gruneberg, H. (1971). The glandular aspects of the tabby syndrome in the mouse. *J. Embryol. Exp. Morphol.* 25 (1): 1–19.

179 Sofaer, J.A. (1969). Aspects of the tabby-crinkled-downless syndrome. II. Observations on the reaction to changes of genetic background. *J. Embryol. Exp. Morphol.* 22 (2): 207–227.

180 Sofaer, J.A. (1969). Aspects of the tabby-crinkled-downless syndrome. I. The development of tabby teeth. *J. Embryol. Exp. Morphol.* 22 (2): 181–205.

181 Srivastava, A.K., Pispa, J., Hartung, A.J. et al. (1997). The Tabby phenotype is caused by mutation in a mouse homologue of the *EDA* gene that reveals novel mouse and human exons and encodes a protein (ectodysplasin-A) with collagenous domains. *Proc. Natl. Acad. Sci. U.S.A.* 94 (24): 13069–13074.

182 Monreal, A.W., Zonana, J., and Ferguson, B. (1998). Identification of a new splice form of the *EDA1* gene permits detection of nearly all X-linked hypohidrotic ectodermal dysplasia mutations. *Am. J. Hum. Genet.* 63 (2): 380–389.

183 Bayes, M., Hartung, A.J., Ezer, S. et al. (1998). The anhidrotic ectodermal dysplasia gene (*EDA*) undergoes alternative splicing and encodes ectodysplasin-A with deletion mutations in collagenous repeats. *Hum. Mol. Genet.* 7 (11): 1661–1669.

184 Naito, A., Yoshida, H., Nishioka, E. et al. (2002). TRAF6-deficient mice display hypohidrotic ectodermal dysplasia. *Proc. Natl. Acad. Sci. U.S.A.* 99 (13): 8766–8771.

185 Maroulakou, I.G., Shibata, M.A., Anver, M. et al. (1999). Heterotopic endochondrial ossification with mixed tumor formation in C3(1)/Tag transgenic mice is associated with elevated TGF-beta1 and BMP-2 expression. *Oncogene* 18 (39): 5435–5447.

186 Sundberg, J.P. (1994). The hairless (*hr*) and rhino (hr^{rh}) mutations, chromosome 14. In: *Handbook of Mouse Mutations with Skin and Hair Abnormalities Animal*

Vet-ebooks.com

Models and Biomedical Tools (ed. J.P. Sundberg), 291–312. Boca Raton, FL: CRC Press.

187 Sundberg, J.P., Roop, D.R., Dunstan, R. et al. (1991). Interaction between dermal papilla and bulge: the rhino mouse mutation as a model system. *Ann. N.Y. Acad. Sci.* 642: 496–499.

188 Panteleyev, A.A., Ahmad, W., Malashenko, A.M. et al. (1998). Molecular basis for the rhino Yurlovo ($Hr^{(rhY)}$) phenotype: severe skin abnormalities and female reproductive defects associated with an insertion in the hairless gene. *Exp. Dermatol.* 7 (5): 281–288.

189 Panteleyev, A.A., Paus, R., Ahmad, W. et al. (1998). Molecular and functional aspects of the hairless (*hr*) gene in laboratory rodents and humans. *Exp. Dermatol.* 7 (5): 249–267.

190 Sundberg, J.P., Price, V.H., and King, L.E. Jr. (1999). The "hairless" gene in mouse and man. *Arch. Dermatol.* 135 (6): 718–720.

191 Ahmad, W., Irvine, A.D., Lam, H. et al. (1998). A missense mutation in the zinc-finger domain of the human hairless gene underlies congenital atrichia in a family of Irish travellers. *Am. J. Hum. Genet.* 63 (4): 984–991.

192 Megosh, L., Gilmour, S.K., Rosson, D. et al. (1995). Increased frequency of spontaneous skin tumors in transgenic mice which overexpress ornithine decarboxylase. *Cancer Res.* 55 (19): 4205–4209.

193 Clifford, A., Morgan, D., Yuspa, S.H. et al. (1995). Role of ornithine decarboxylase in epidermal tumorigenesis. *Cancer Res.* 55 (8): 1680–1686.

194 Bikle, D.D., Elalieh, H., Chang, S. et al. (2006). Development and progression of alopecia in the vitamin D receptor null mouse. *J. Cell. Physiol.* 207 (2): 340–353.

195 Voigt, A.Y., Michaud, M., Tsai, K.Y. et al. (2019). Differential hairless mouse strain-specific susceptibility to skin cancer and sunburn. *J. Invest. Dermatol.*

196 Botchkarev, V.A., Botchkarev, N.V., Albers, K.M. et al. (1998). Neurotrophin-3 involvement in the regulation of hair follicle morphogenesis. *J. Invest. Dermatol.* 111 (2): 279–285.

197 Botchkarev, V.A., Welker, P., Albers, K.M. et al. (1998). A new role for neurotrophin-3: involvement in the regulation of hair follicle regression (catagen). *Am. J. Pathol.* 153 (3): 785–799.

198 Lindner, G., Botchkarev, V.A., Botchkareva, N.V. et al. (1997). Analysis of apoptosis during hair follicle regression (catagen). *Am. J. Pathol.* 151 (6): 1601–1617.

199 Maurer, M., Handjiski, B., and Paus, R. (1997). Hair growth modulation by topical immunophilin ligands: induction of anagen, inhibition of massive catagen development, and relative protection from chemotherapy-induced alopecia. *Am. J. Pathol.* 150 (4): 1433–1441.

200 Paus, R., Foitzik, K., Welker, P. et al. (1997). Transforming growth factor-beta receptor type I and type II expression during murine hair follicle development and cycling. *J. Invest. Dermatol.* 109 (4): 518–526.

201 Schilli, M.B., Ray, S., Paus, R. et al. (1997). Control of hair growth with parathyroid hormone (7-34). *J. Invest. Dermatol.* 108 (6): 928–932.

202 Combates, N.J., Chuong, C.M., Stenn, K.S., and Prouty, S.M. (1997). Expression of two Ig family adhesion molecules in the murine hair cycle: DCC in the bulge epithelia and NCAM in the follicular papilla. *J. Invest. Dermatol.* 109 (5): 672–678.

203 Cotsarelis, G. (1997). The hair follicle: dying for attention. *Am. J. Pathol.* 151 (6): 1505–1509.

204 Matzuk, M.M., Lu, N., Vogel, H. et al. (1995). Multiple defects and perinatal death in mice deficient in follistatin. *Nature* 374 (6520): 360–363.

205 Guo, L., Degenstein, L., and Fuchs, E. (1996). Keratinocyte growth factor is required for hair development but not for wound healing. *Genes Dev.* 10 (2): 165–175.

206 Guo, L., Yu, Q.C., and Fuchs, E. (1993). Targeting expression of keratinocyte growth factor to keratinocytes elicits striking changes in epithelial differentiation in transgenic mice. *EMBO J.* 12 (3): 973–986.

207 Blessing, M., Nanney, L.B., King, L.E. et al. (1993). Transgenic mice as a model to study the role of TGF-beta-related molecules in hair follicles. *Genes Dev.* 7 (2): 204–215.

208 Hebert, J.M., Rosenquist, T., Gotz, J., and Martin, G.R. (1994). FGF5 as a regulator of the hair growth cycle: evidence from targeted and spontaneous mutations. *Cell* 78 (6): 1017–1025.

209 Higgins, C.A., Petukhova, L., Harel, S. et al. (2014). FGF5 is a crucial regulator of hair length in humans. *Proc. Natl. Acad. Sci U.S.A.* 111 (29): 10648–10653.

210 Rosenquist, T.A. and Martin, G.R. (1996). Fibroblast growth factor signalling in the hair growth cycle: expression of the fibroblast growth factor receptor and ligand genes in the murine hair follicle. *Dev. Dyn.* 205 (4): 379–386.

211 Danilenko, D.M., Ring, B.D., Yanagihara, D. et al. (1995). Keratinocyte growth factor is an important endogenous mediator of hair follicle growth, development, and differentiation. Normalization of the *nu/nu* follicular differentiation defect and amelioration of chemotherapy-induced alopecia. *Am. J. Pathol.* 147 (1): 145–154.

212 Mentzer, S.E., Sundberg, J.P., Awgulewitsch, A. et al. (2008). The mouse hairy ears mutation exhibits an extended growth (anagen) phase in hair follicles and altered *Hoxc* gene expression in the ears. *Vet. Dermatol.* 19 (6): 358–367.

213 Fantauzzo, K.A., Tadin-Strapps, M., You, Y. et al. (2008). A position effect on *TRPS1* is associated with Ambras syndrome in humans and the Koala phenotype in mice. *Hum. Mol. Genet.* 17 (22): 3539–3551.

Vet-ebooks.com

214 Sweet, H.O., Davisson, M.T., Akeson, E.C., and Harris, B.H. (1989). Long hair (*lgh*). *Mouse News Lett.* 83: 166–167.

215 Vielkind, U. and Hardy, M.H. (1996). Changing patterns of cell adhesion molecules during mouse pelage hair follicle development. 2. Follicle morphogenesis in the hair mutants, Tabby and downy. *Acta Anat. (Basel).* 157 (3): 183–194.

216 Mann, S.J. (1963). The phenogenetics of hair mutants in the house mouse: opossum and ragged. *Genet. Res.* 4: 1–11.

217 Pennisi, D., Gardner, J., Chambers, D. et al. (2000). Mutations in *Sox18* underlie cardiovascular and hair follicle defects in ragged mice. *Nat. Genet.* 24 (4): 434–437.

218 Villani, R., Hodgson, S., Legrand, J. et al. (2017). Dominant-negative *Sox18* function inhibits dermal papilla maturation and differentiation in all murine hair types. *Development* 144 (10): 1887–1895.

219 Sellheyer, K., Bickenbach, J.R., Rothnagel, J.A. et al. (1993). Inhibition of skin development by overexpression of transforming growth factor beta 1 in the epidermis of transgenic mice. *Proc. Natl. Acad. Sci. U.S.A.* 90 (11): 5237–5241.

220 Sundberg, J.P., Cordy, W.R., and King, L.E. Jr. (1994). Alopecia areata in aging C3H/HeJ mice. *J. Invest. Dermatol.* 102 (6): 847–856.

221 Pratt, C.H., King, L.E. Jr., Messenger, A.G. et al. (2017). Alopecia areata. *Nat. Rev. Dis. Primers.* 3: 17011.

222 Soma, T., Tsuji, Y., and Hibino, T. (2002). Involvement of transforming growth factor-beta2 in catagen induction during the human hair cycle. *J. Invest. Dermatol.* 118 (6): 993–997.

223 Herron, B.J., Rao, C., Liu, S. et al. (2005). A mutation in NFkB interacting protein 1 results in cardiomyopathy and abnormal skin development in wa3 mice. *Hum. Mol. Genet.* 14 (5): 667–677.

224 Hassemer, E.L., Le Gall, S.M., Liegel, R. et al. (2010). The waved with open eyelids (*woe*) locus is a hypomorphic mouse mutation in *Adam17*. *Genetics* 185 (1): 245–255.

225 Mecklenburg, L., Nakamura, M., Sundberg, J.P., and Paus, R. (2001). The nude mouse skin phenotype: the role of *Foxn1* in hair follicle development and cycling. *Exp. Mol. Pathol.* 71 (2): 171–178.

226 Potter, C.S., Pruett, N.D., Kern, M.J. et al. (2011). The nude mutant gene *Foxn1* is a HOXC13 regulatory target during hair follicle and nail differentiation. *J. Invest. Dermatol.* 131 (4): 828–837.

227 Sundberg, J.P. (1994). The shaven (*Sha*) mutation, chromosome 15. In: *Handbook of Mouse Mutations with Skin and Hair Abnormalities: Animal Models and Biomedical Tools* (ed. J.P. Sundberg), 431–436. Boca Raton, FL: CRC Press.

228 Sundberg, J.P. (1994). The naked (*N*) mutation, chromosome 15. In: *Handbook of Mouse Mutations with Skin and Hair Abnormalities: Animal Models and Biomedical Tools* (ed. J.P. Sundberg), 371–377. Boca Raton, FL: CRC Press.

229 Adriani, M., Martinez-Mir, A., Fusco, F. et al. (2004). Ancestral founder mutation of the nude (*FOXN1*) gene in congenital severe combined immunodeficiency associated with alopecia in southern Italy population. *Ann. Hum. Genet.* 68 (Pt 3): 265–268.

230 Nehls, M., Pfeifer, D., Schorpp, M. et al. (1994). New member of the winged-helix protein family disrupted in mouse and rat nude mutations. *Nature* 372 (6501): 103–107.

231 Lin, Z., Chen, Q., Shi, L. et al. (2012). Loss-of-function mutations in *HOXC13* cause pure hair and nail ectodermal dysplasia. *Am. J. Human Genet.* 91 (5): 906–911.

232 Farooq, M., Kurban, M., Fujimoto, A. et al. (2013). A homozygous frameshift mutation in the *HOXC13* gene underlies pure hair and nail ectodermal dysplasia in a Syrian family. *Human Mutat.* 34 (4): 578–581.

233 Ali, R.H., Habib, R., Ud-Din, N. et al. (2013). Novel mutations in the gene *HOXC13* underlying pure hair and nail ectodermal dysplasia in consanguineous families. *Br. J. Dermatol.* 169 (2): 478–480.

234 Price, V.H., Odom, R.B., Ward, W.H., and Jones, F.T. (1980). Trichothiodystrophy: sulfur-deficient brittle hair as a marker for a neuroectodermal symptom complex. *Arch. Dermatol.* 116 (12): 1375–1384.

235 Gummer, C.L., Dawber, R.P., and Price, V.H. (1984). Trichothiodystrophy: an electron-histochemical study of the hair shaft. *Br. J. Dermatol.* 110 (4): 439–449.

236 Metze, D. and Oji, V. (2020). Disorders of keratinization. In: *McKee's Pathology of the Skin*, 5e, vol. 1 (eds. E. Calonje, T. Brenn, A. Lazar and S.D. Billings), 53–117. China: Elsevier.

237 Baxter, R.M. and Brissette, J.L. (2002). Role of the nude gene in epithelial terminal differentiation. *J. Invest. Dermatol.* 118 (2): 303–309.

238 Mecklenburg, L., Tychsen, B., and Paus, R. (2005). Learning from nudity: lessons from the nude phenotype. *Exp. Dermatol.* 14 (11): 797–810.

239 Whiting, D.A. and Howsden, F.L. (1996). *Color Atlas of Differential Diagnosis of Hair Loss*, 101 p. Cedar Grove, NJ: Canfield Publishing.

240 Montagutelli, X., Hogan, M.E., Aubin, G. et al. (1996). Lanceolate hair (*lah*): a recessive mouse mutation with alopecia and abnormal hair. *J. Invest. Dermatol.* 107 (1): 20–25.

241 Pratt, H.C., Potter, C.S., Fairfield, H. et al. (2015). *Dsp*^{rul}: a spontaneous mouse mutation in desmoplakin as a model of Carvajal-Huerta syndrome. *Exp. Mol. Pathol.* 98 (2): 164–172.

Vet-ebooks.com

242 Sundberg, J.P. and King, L.E. Jr. (2000). Skin and its appendages: normal anatomy and pathology of spontaneous, transgenic, and targeted mutant mice. In: *Pathology of Genetically Engineered Mice*, 1e (eds. J.M. Ward, J.F. Mahler, R.R. Maronpot and J.P. Sundberg), 183–215. Ames, IA: Iowa State University Press.

243 Greb, J.E., Goldminz, A.M., Elder, J.T. et al. (2016). Psoriasis. *Nat. Rev. Dis. Primers.* 2: 16082.

244 Gudjonsson, J.E., Johnston, A., Dyson, M. et al. (2007). Mouse models of psoriasis. *J. Invest. Dermatol.* 127 (6): 1292–1308.

245 Luo, T., Ma, Y., and Wei, W. (2020). Murine models of psoriasis and its applications in drug development. *J. Pharmacol. Toxicol. Methods* 101: 106657.

246 Wagner, E.F., Schonthaler, H.B., Guinea-Viniegra, J., and Tschachler, E. (2010). Psoriasis: what we have learned from mouse models. *Nat. Rev. Rheumatol.* 6 (12): 704–714.

247 Danilenko, D.M. (2008). Review paper: preclinical models of psoriasis. *Vet. Pathol.* 45 (4): 563–575.

248 Schon, M.P. (2008). Animal models of psoriasis: a critical appraisal. *Exp. Dermatol.* 17 (8): 703–712.

249 Mizutani, H., Yamanaka, K., Konishi, H., and Murakami, T. (2003). Animal models of psoriasis and pustular psoriasis. *Arch. Dermatol. Res.* 295 (Suppl 1): S67–S68.

250 Hawkes, J.E., Adalsteinsson, J.A., Gudjonsson, J.E., and Ward, N.L. (2018). Research techniques made simple: murine models of human psoriasis. *J. Invest. Dermatol.* 138 (1): e1–e8.

251 Bochenska, K., Smolinska, E., Moskot, M. et al. (2017). Models in the research process of psoriasis. *Int. J. Mol. Sci.* 18 (12): 2514. https://doi.org/10.3390/ijms18122514.

252 Nakajima, K. and Sano, S. (2018). Mouse models of psoriasis and their relevance. *J. Dermatol.* 45 (3): 252–263.

253 Flutter, B. and Nestle, F.O. (2013). TLRs to cytokines: mechanistic insights from the imiquimod mouse model of psoriasis. *Eur. J. Immunol.* 43 (12): 3138–3146.

254 Salgado, G., Ng, Y.Z., Koh, L.F. et al. (2017). Human reconstructed skin xenografts on mice to model skin physiology. *Differentiation* 98: 14–24.

255 Sundberg, J.P., Kenty, G.A., Beamer, W.G., and Adkison, D.L. (1992). Forestomach papillomas in flaky skin and steel-Dickie mutant mice. *J. Vet. Diagn. Invest.* 4 (3): 312–317.

256 Helms, C., Pelsue, S., Cao, L. et al. (2005). The Tetratricopeptide repeat domain 7 gene is mutated in flaky skin mice: a model for psoriasis, autoimmunity, and anemia. *Exp. Biol. Med. (Maywood).* 230 (9): 659–667.

257 HogenEsch, H., Gijbels, M.J., Offerman, E. et al. (1993). A spontaneous mutation characterized by chronic proliferative dermatitis in C57BL mice. *Am. J. Pathol.* 143 (3): 972–982.

258 Gijbels, M.J., Zurcher, C., Kraal, G. et al. (1996). Pathogenesis of skin lesions in mice with chronic proliferative dermatitis (*cpdm/cpdm*). *Am. J. Pathol.* 148 (3): 941–950.

259 Seymour, R.E., Hasham, M.G., Cox, G.A. et al. (2007). Spontaneous mutations in the mouse *Sharpin* gene result in multiorgan inflammation, immune system dysregulation and dermatitis. *Genes Immun.* 8 (5): 416–421.

260 Liang, Y., Seymour, R.E., and Sundberg, J.P. (2011). Inhibition of NF-kappaB signaling retards eosinophilic dermatitis in SHARPIN-deficient mice. *J. Invest. Dermatol.* 131 (1): 141–149.

261 Ikeda, F., Deribe, Y.L., Skanland, S.S. et al. (2011). SHARPIN forms a linear ubiquitin ligase complex regulating NF-kappaB activity and apoptosis. *Nature* 471 (7340): 637–641.

262 Sundberg, J.P., Pratt, C.H., Goodwin, L.P. et al. (2020). Keratinocyte-specific deletion of SHARPIN induces atopic dermatitis-like inflammation in mice. *PLoS One* 15 (7): e0235295.

263 Hogenesch, H., Sola, M., Stearns, T.M. et al. (2016). Angiogenesis in the skin of SHARPIN-deficient mice with chronic proliferative dermatitis. *Exp. Mol. Pathol.* 101 (3): 303–307.

264 Peuhu, E., Salomaa, S.I., De Franceschi, N. et al. (2017). Integrin beta 1 inhibition alleviates the chronic hyperproliferative dermatitis phenotype of SHARPIN-deficient mice. *PLoS One* 12 (10): e0186628.

265 Carter, T.C. and Phillips, R.S. (1950). Ichthyosis, a new recessive mutant in the house mouse. *J. Hered.* 41: 297–300.

266 Sundberg, J.P. and Pittelkow, M.R. (1994). The ichthyosis (*ic*) mutation, chromosome 1. In: *Handbook of Mouse Mutations with Skin and Hair Abnormalities: Animal Models and Biomedical Tools* (ed. J.P. Sundberg), 327–335. Boca Raton, FL: CRC Press.

267 Hoffmann, K., Dreger, C.K., Olins, A.L. et al. (2002). Mutations in the gene encoding the lamin B receptor produce an altered nuclear morphology in granulocytes (Pelger-Huet anomaly). *Nat. Genet.* 31 (4): 410–414.

268 Shultz, L.D., Lyons, B.L., Burzenski, L.M. et al. (2003). Mutations at the mouse ichthyosis locus are within the lamin B receptor gene: a single gene model for human Pelger-Huet anomaly. *Hum. Mol. Genet.* 12 (1): 61–69.

269 Presland, R.B., Boggess, D., Lewis, S.P. et al. (2000). Loss of normal profilaggrin and filaggrin in flaky tail (*ft/ft*) mice: an animal model for the filaggrin-deficient skin disease ichthyosis vulgaris. *J. Invest. Dermatol.* 115 (6): 1072–1081.

270 Fallon, P.G., Sasaki, T., Sandilands, A. et al. (2009). A homozygous frameshift mutation in the mouse *Flg* gene facilitates enhanced percutaneous allergen priming. *Nat. Genet.* 41 (5): 602–608.

271 Moniaga, C.S., Egawa, G., Kawasaki, H. et al. (2010). Flaky tail mouse denotes human atopic dermatitis in the steady state and by topical application with *Dermatophagoides pteronyssinus* extract. *Am. J. Pathol.* 176 (5): 2385–2393.

272 Restrepo, R. and Calonje, E. (2020). Diseases of the hair. In: *McKee's Pathology of the Skin with Clinical*

Vet-ebooks.com

Correlations, 5e, vol. 2 (eds. E. Calonje, T. Brenn, A.J. Lazar and S.D. Billings), 1051–1128. China: Elsevier.

273 Sundberg, J.P., Dunstan, R.W., Roop, D.R., and Beamer, W.G. (1994). Full-thickness skin grafts from flaky skin mice to nude mice: maintenance of the psoriasiform phenotype. *J. Invest. Dermatol.* 102 (5): 781–788.

274 McElwee, K.J., Boggess, D., King, L.E. Jr., and Sundberg, J.P. (1998). Experimental induction of alopecia areata-like hair loss in C3H/HeJ mice using full-thickness skin grafts. *J. Invest. Dermatol.* 111 (5): 797–803.

275 McElwee, K.J., Freyschmidt-Paul, P., Hoffmann, R. et al. (2005). Transfer of CD8(+) cells induces localized hair loss whereas CD4(+)/CD25(−) cells promote systemic alopecia areata and CD4(+)/CD25(+) cells blockade disease onset in the C3H/HeJ mouse model. *J. Invest. Dermatol.* 124 (5): 947–957.

276 Wang, E.H.C., Khosravi-Maharlooei, M., Jalili, R.B. et al. (2015). Transfer of alopecia areata to C3H/HeJ mice using cultured lymph node-derived cells. *J. Invest. Dermatol.* 135 (10): 2530–2532.

277 Sundberg, J.P., McElwee, K., Brehm, M.A. et al. (2015). Animal models for alopecia areata: what and where? *J. Invest. Dermatol. Symp. Proc.* 17 (2): 23–26.

278 Tobin, D.J., Sundberg, J.P., King, L.E. Jr. et al. (1997). Autoantibodies to hair follicles in C3H/HeJ mice with alopecia areata-like hair loss. *J. Invest. Dermatol.* 109 (3): 329–333.

279 de Jong, A., Jabbari, A., Dai, Z. et al. (2018). High-throughput T cell receptor sequencing identifies clonally expanded CD8+ T cell populations in alopecia areata. *JCI Insight* 3 (19): e121949. https://doi.org/10.1172/jci.insight.121949.

280 Sundberg, J.P., Silva, K.A., Li, R. et al. (2004). Adult-onset alopecia areata is a complex polygenic trait in the C3H/HeJ mouse model. *J. Invest. Dermatol.* 123 (2): 294–297.

281 Sundberg, J.P., Boggess, D., Silva, K.A. et al. (2003). Major locus on mouse chromosome 17 and minor locus on chromosome 9 are linked with alopecia areata in C3H/HeJ mice. *J. Invest. Dermatol.* 120 (5): 771–775.

282 Petukhova, L., Duvic, M., Hordinsky, M. et al. (2010). Genome-wide association study in alopecia areata implicates both innate and adaptive immunity. *Nature* 466 (7302): 113–117.

283 Conti, C., Binder, R., and Sundberg, J.P. (1996). Histological, biochemical, and molecular evolution of skin lesions using a two-stage chemical carcinogenesis protocol. In: *Pathobiology of the Aging Mouse*, vol. 2 (eds. U. Mohr, D.L. Dungworth, C.C. Capen, et al.), 359–368. Washington, DC: ILSI Press.

284 Aldaz, C.M., Conti, C.J., Larcher, F. et al. (1988). Sequential development of aneuploidy, keratin modifications, and gamma-glutamyltransferase expression in mouse skin papillomas. *Cancer Res.* 48 (11): 3253–3257.

285 Roop, D.R., Krieg, T.M., Mehrel, T. et al. (1988). Transcriptional control of high molecular weight keratin gene expression in multistage mouse skin carcinogenesis. *Cancer Res.* 48 (11): 3245–3252.

286 Sundberg, J.P., Erickson, A.A., Roop, D.R., and Binder, R.L. (1994). Ornithine decarboxylase expression in cutaneous papillomas in SENCAR mice is associated with altered expression of keratins 1 and 10. *Cancer Res.* 54 (5): 1344–1351.

287 Sundberg, J.P. (1996). Spontaneous skin neoplasms in inbred laboratory mice. In: *Pathobiology of the Aging Mouse*, vol. 2 (eds. U. Mohr, D.L. Dungworth, C.C. Capen, et al.), 339–350. Washington, DC: ILSI Press.

288 Gimenez-Conti, I.B., Bianchi, A.B., Fischer, S.M. et al. (1992). Dissociation of sensitivities to tumor promotion and progression in outbred and inbred SENCAR mice. *Cancer Res.* 52 (12): 3432–3435.

289 Stern, M.C., Gimenez-Conti, I.B., and Conti, C.J. (1995). Genetic susceptibility to papilloma progression in SENCAR mice. *Carcinogenesis* 16 (8): 1947–1953.

290 Stern, M.C. and Conti, C.J. (1996). Genetic susceptibility to tumor progression in mouse skin carcinogenesis. *Prog. Clin. Biol. Res.* 395: 47–55.

291 Hennings, H., Lowry, D.T., Yuspa, S.H. et al. (1997). New strains of inbred SENCAR mice with increased susceptibility to induction of papillomas and squamous cell carcinomas in skin. *Mol. Carcinog.* 20 (1): 143–150.

292 Stern, M.C., Gimenez-Conti, I.B., Budunova, I. et al. (1998). Analysis of two inbred strains of mice derived from the SENCAR stock with different susceptibility to skin tumor progression. *Carcinogenesis* 19 (1): 125–132.

293 Spalding, J.W., Momma, J., Elwell, M.R., and Tennant, R.W. (1993). Chemically induced skin carcinogenesis in a transgenic mouse line (TG.AC) carrying a v-Ha-ras gene. *Carcinogenesis* 14 (7): 1335–1341.

294 Hansen, L.A. and Tennant, R. (1994). Focal transgene expression associated with papilloma development in v-Ha-ras-transgenic TG.AC mice. *Mol. Carcinog.* 9 (3): 143–154.

295 Hansen, L.A., Spalding, J.W., French, J.E., and Tennant, R.W. (1995). A transgenic mouse model (TG.AC) for skin carcinogenesis: inducible transgene expression as a second critical event. *Prog. Clin. Biol. Res.* 391: 223–235.

296 Cannon, R.E., Spalding, J.W., Trempus, C.S. et al. (1997). Kinetics of wound-induced v-Ha-ras transgene expression and papilloma development in transgenic Tg.AC mice. *Mol. Carcinog.* 20 (1): 108–114.

297 Blanchard, K.T., Ball, D.J., Holden, H.E. et al. (1998). Dermal carcinogenicity in transgenic mice: relative responsiveness of male and female hemizygous and homozygous Tg.AC mice to 12-O-tetradecanoylphorbol 13-acetate (TPA) and benzene. *Toxicol. Pathol.* 26 (4): 541–547.

298 Thompson, K.L., Rosenzweig, B.A., and Sistare, F.D. (1998). An evaluation of the hemizygous transgenic Tg.

Vet-ebooks.com

AC mouse for carcinogenicity testing of pharmaceuticals. II. A genotypic marker that predicts tumorigenic responsiveness. *Toxicol. Pathol.* 26 (4): 548–555.

299 Sundberg, J.P., Binder, R.L., Maurer, J.K. et al. (1990). Absence of papillomavirus in skin tumors induced in SENCAR mice by a two-stage carcinogenesis protocol. *Carcinogenesis* 11 (2): 341–344.

300 Sundberg, J.P., Sundberg, B.A., and Beamer, W.G. (1997). Comparison of chemical carcinogen skin tumor induction efficacy in inbred, mutant, and hybrid strains of mice: morphologic variations of induced tumors and absence of a papillomavirus cocarcinogen. *Mol. Carcinog.* 20 (1): 19–32.

301 Benavides, F., Oberyszyn, T.M., VanBuskirk, A.M. et al. (2009). The hairless mouse in skin research. *J. Dermatol. Sci.* 53 (1): 10–18.

302 Perez, C., Parker-Thornburg, J., Mikulec, C. et al. (2012). SKHIN/Sprd, a new genetically defined inbred hairless mouse strain for UV-induced skin carcinogenesis studies. *Exp. Dermatol.* 21 (3): 217–220.

303 Konger, R.L., Derr-Yellin, E., Hojati, D. et al. (2016). Comparison of the acute ultraviolet photoresponse in congenic albino hairless C57BL/6J mice relative to outbred SKH1 hairless mice. *Exp. Dermatol.* 25 (9): 688–693.

304 Kitajima, T., Iwashiro, M., Kuribayashi, K., and Imamura, S. (1995). Effect of parent genetic background on latency and antigenicity of UV-induced tumors originating in F1 hybrids. *Exp. Dermatol.* 4 (1): 42–45.

305 Naito, M. and DiGiovanni, J. (1989). Genetic background and development of skin tumors. *Carcinog Compr. Surv.* 11: 187–212.

306 Sundberg, J.P. (1987). Papillomavirus infections in animals. In: *Papillomaviruses and Human Disease* (eds. S.K. GL and L.G. Koss), 40–103. Heidelberg: Springer-Verlag.

307 Sundberg, J.P., Van Ranst, M., and Jenson, A.B. (1996). The nonhuman (animal) papillomaviruses: host range, epitope conservation, and molecular diversity. In: *Human Papillomavirus Infections in Dermatology and Venereology* (eds. G. Gross and G. von Krogh), 47–68. Boca Raton, FL: CRC Press.

308 Ingle, A., Ghim, S., Joh, J. et al. (2011). Novel laboratory mouse papillomavirus (MusPV) infection. *Vet. Pathol.* 48 (2): 500–505.

309 Joh, J., Jenson, A.B., King, W. et al. (2011). Genomic analysis of the first laboratory-mouse papillomavirus. *J. Gen. Virol.* 92 (Pt 3): 692–698.

310 Carney, H.C., England, J.J., Hodgin, E.C. et al. (1990). Papillomavirus infection of aged Persian cats. *J. Vet. Diagn. Invest.* 2 (4): 294–299.

311 Sundberg, J.P., Van Ranst, M., Montali, R. et al. (2000). Feline papillomas and papillomaviruses. *Vet. Pathol.* 37 (1): 1–10.

312 Kohler, A., Forschner, T., Meyer, T. et al. (2007). Multifocal distribution of cutaneous human papillomavirus types in hairs from different skin areas. *Br. J. Dermatol.* 156 (5): 1078–1080.

313 Tinsley, J.M., Fisher, C., and Searle, P.F. (1992). Abnormalities of epidermal differentiation associated with expression of the human papillomavirus type 1 early region in transgenic mice. *J. Gen. Virol.* 73 (Pt 5): 1251–1260.

314 Song, S., Pitot, H.C., and Lambert, P.F. (1999). The human papillomavirus type 16 E6 gene alone is sufficient to induce carcinomas in transgenic animals. *J. Virol.* 73 (7): 5887–5893.

315 Rademacher, B.L., Matkowskyj, K.A., LaCount, E.D., and Carchman, E.H. (2019). Topical application of a dual PI3K/mTOR inhibitor prevents anal carcinogenesis in a human papillomavirus mouse model of anal cancer. *Eur. J. Cancer Prev.* 28 (6): 483–491.

316 Ghim, S., Jenson, A.B., Bubier, J.A. et al. (2008). Cataracts in transgenic mice caused by a human papillomavirus type 18 E7 oncogene driven by KRT1-14. *Exp. Mol. Pathol.* 85 (2): 77–82.

317 Fidler, I.J. (1973). Selection of successive tumour lines for metastasis. *Nat. New Biol.* 242 (118): 148–149.

318 Giavazzi, R. and Decio, A. (2014). Syngeneic murine metastasis models: B16 melanoma. *Methods Mol. Biol.* 1070: 131–140.

319 Day, C.P., Marchalik, R., Merlino, G., and Michael, H. (2017). Mouse models of UV-induced melanoma: genetics, pathology, and clinical relevance. *Lab. Invest.* 97 (6): 698–705.

320 Damsky, W.E. Jr. and Bosenberg, M. (2010). Mouse melanoma models and cell lines. *Pigment Cell Melanoma Res.* 23 (6): 853–859.

321 Zaidi, M.R., Davis, S., Noonan, F.P. et al. (2011). Interferon-gamma links ultraviolet radiation to melanomagenesis in mice. *Nature* 469 (7331): 548–553.

322 Bradl, M., Klein-Szanto, A., Porter, S., and Mintz, B. (1991). Malignant melanoma in transgenic mice. *Proc. Natl. Acad. Sci. U.S.A.* 88 (1): 164–168.

323 Umansky, V. and Sevko, A. (2013). Ret transgenic mouse model of spontaneous skin melanoma: focus on regulatory T cells. *Pigment Cell Melanoma Res.* 26 (4): 457–463.

324 Nogueira, C., Kim, K.H., Sung, H. et al. (2010). Cooperative interactions of PTEN deficiency and RAS activation in melanoma metastasis. *Oncogene* 29 (47): 6222–6232.

325 Conde-Perez, A. and Larue, L. (2014). Human relevance of NRAS/BRAF mouse melanoma models. *Eur. J. Cell Biol.* 93 (1–2): 82–86.

326 Noonan, F.P., Dudek, J., Merlino, G., and De Fabo, E.C. (2003). Animal models of melanoma: an HGF/SF transgenic mouse model may facilitate experimental access to UV initiating events. *Pigment Cell Res.* 16 (1): 16–25.

327 Dankort, D., Curley, D.P., Cartlidge, R.A. et al. (2009). Braf(V600E) cooperates with *Pten* loss to induce metastatic melanoma. *Nat. Genet.* 41 (5): 544–552.

328 Dhomen, N., Reis-Filho, J.S., da Rocha, D.S. et al. (2009). Oncogenic *Braf* induces melanocyte senescence and melanoma in mice. *Cancer Cell.* 15 (4): 294–303.

Vet-ebooks.com

329 Damsky, W., Micevic, G., Meeth, K. et al. (2015). *mTORC1* activation blocks *BrafV600E*-induced growth arrest but is insufficient for melanoma formation. *Cancer Cell.* 27 (1): 41–56.

330 Maertens, O., Johnson, B., Hollstein, P. et al. (2013). Elucidating distinct roles for *NF1* in melanomagenesis. *Cancer Discov.* 3 (3): 338–349.

331 Davisson, M.T., Cook, S.A., Johnson, K.R., and Eicher, E.M. (1994). Balding: a new mutation on mouse chromosome 18 causing hair loss and immunological defects. *J. Hered.* 85 (2): 134–136.

332 Sundberg, J.P. (1994). The balding (*bal*) mutation, chromosome 18. In: *Handbook of Mouse Mutations with Skin and Hair Abnormalities: Animal Models and Biomedical Tools* (ed. J.P. Sundberg), 187–191. Boca Raton, FL: CRC Press.

333 Wolff, P.L., Garden, J.M., Marder, R. et al. (1986). Pemphigus vulgaris in a pigtail macaque. *J. Am. Vet. Med. Assoc.* 189 (9): 1220–1221.

334 Calonje, E., Brenn, T., Lazar, A.J., and Billings, S.D. (2020). Acantholytic disorders. In: *McKee's Pathology of the Skin with Clinical Correlations*, vol. 1 (eds. E. Calonje, T. Brenn, A.J. Lazar and S.D. Billings), 171–200. China: Elsevier.

335 Amagai, M., Tsunoda, K., Zillikens, D. et al. (1999). The clinical phenotype of pemphigus is defined by the anti-desmoglein autoantibody profile. *J. Am. Acad. Dermatol.* 40 (2 Pt 1): 167–170.

336 Amagai, M. (2008). Pemphigus vulgaris and its active disease mouse model. *Curr. Dir. Autoimmun.* 10: 167–181.

337 Ohyama, M., Amagai, M., Tsunoda, K. et al. (2002). Immunologic and histopathologic characterization of an active disease mouse model for pemphigus vulgaris. *J. Invest. Dermatol.* 118 (1): 199–204.

338 Ohyama, M., Ota, T., Aoki, M. et al. (2003). Suppression of the immune response against exogenous desmoglein 3 in desmoglein 3 knockout mice: an implication for gene therapy. *J. Invest. Dermatol.* 120 (4): 610–615.

339 Allen, E., Yu, Q.C., and Fuchs, E. (1996). Mice expressing a mutant desmosomal cadherin exhibit abnormalities in desmosomes, proliferation, and epidermal differentiation. *J. Cell Biol.* 133 (6): 1367–1382.

340 Merritt, A.J., Berika, M.Y., Zhai, W. et al. (2002). Suprabasal desmoglein 3 expression in the epidermis of transgenic mice results in hyperproliferation and abnormal differentiation. *Mol. Cell. Biol.* 22 (16): 5846–5858.

341 Natsuga, K., Shinkuma, S., Nishie, W., and Shimizu, H. (2010). Animal models of epidermolysis bullosa. *Dermatol. Clin.* 28 (1): 137–142.

342 Sundberg, J.P., Dadras, S.S., Silva, K.A. et al. (2017). Systematic screening for skin, hair, and nail abnormalities in a large-scale knockout mouse program. *PLoS One* 12 (7): e0180682.

343 Linn, S.C., Mustonen, A.M., Silva, K.A. et al. (2019). Nail abnormalities identified in an ageing study of 30 inbred mouse strains. *Exp. Dermatol.* 28 (4): 383–390.

344 Lories, R.J., Matthys, P., de Vlam, K. et al. (2004). Ankylosing enthesitis, dactylitis, and onychoperiostitis in male DBA/1 mice: a model of psoriatic arthritis. *Ann. Rheum. Dis.* 63 (5): 595–598.

345 Chelidze, K. and Lipner, S.R. (2018). Nail changes in alopecia areata: an update and review. *Internatl. J. Dermatol.* 57 (7): 776–783.

346 Ventura, A., Mazzeo, M., Gaziano, R. et al. (2017). New insight into the pathogenesis of nail psoriasis and overview of treatment strategies. *Drug Des. Dev. Ther.* 11: 2527–2535.

347 Morita, K., Hogan, M.E., Nanney, L.B. et al. (1995). Cutaneous ultrastructural features of the flaky skin (*fsn*) mouse mutation. *J. Dermatol.* 22 (6): 385–395.

348 Sundberg, J.P., Dunstan, R.W., and Compton, J.G. (1989). Hairless mouse, HRS/J *hr/hr*. In: *Integument and Mammary Glands Monographs on Pathology of Laboratory Animals* (eds. T.C. Jones, U. Mohr and R.D. Hunt), 192–197. Heidelberg: Springer-Verlag.

349 Soler, A.P., Gilliard, G., Megosh, L.C., and O'Brien, T.G. (1996). Modulation of murine hair follicle function by alterations in ornithine decarboxylase activity. *J. Invest. Dermatol.* 106 (5): 1108–1113.

350 Jiang, R., Lan, Y., Norton, C.R. et al. (1998). The *slug* gene is not essential for mesoderm or neural crest development in mice. *Dev. Biol.* 198 (2): 277–285.

351 Lee, K.F., Li, E., Huber, L.J. et al. (1992). Targeted mutation of the gene encoding the low affinity NGF receptor p75 leads to deficits in the peripheral sensory nervous system. *Cell* 69 (5): 737–749.

352 Salzgeber, B. and Guenet, J.L. (1984). Studies on "repeated epilation" mouse mutant embryos: II. Development of limb, tail, and skin defects. *J. Craniofac. Genet. Dev. Biol.* 4 (2): 95–114.

353 Chen, H., Lun, Y., Ovchinnikov, D. et al. (1998). Limb and kidney defects in *Lmx1b* mutant mice suggest an involvement of LMX1B in human nail patella syndrome. *Nat. Genet.* 19 (1): 51–55.

354 Spielmann, M., Kakar, N., Tayebi, N. et al. (2016). Exome sequencing and CRISPR/Cas genome editing identify mutations of *ZAK* as a cause of limb defects in humans and mice. *Genome Res.* 26 (2): 183–191.

355 Kimura, S., Saitsu, H., Schaumann, B.A. et al. (2010). Rudimentary claws and pigmented nail-like structures on the distal tips of the digits of *Wnt7a* mutant mice: Wnt7A suppresses nail-like structure development in mice. *Birth Defects Res. A Clin. Mol. Teratol.* 88 (6): 487–496.

356 Jumlongras, D., Bei, M., Stimson, J.M. et al. (2001). A nonsense mutation in *MSX1* causes Witkop syndrome. *Am. J. Hum. Genet.* 69 (1): 67–74.

Vet-ebooks.com

357 Frojmark, A.S., Schuster, J., Sobol, M. et al. (2011). Mutations in Frizzled 6 cause isolated autosomal-recessive nail dysplasia. *Am. J. Hum. Genet.* 88 (6): 852–860.

358 Chen, J., Jaeger, K., Den, Z. et al. (2008). Mice expressing a mutant *Krt75* (*K6hf*) allele develop hair and nail defects resembling pachyonychia congenita. *J. Invest. Dermatol.* 128 (2): 270–279.

359 Cui, C.Y., Klar, J., Georgii-Heming, P. et al. (2013). Frizzled6 deficiency disrupts the differentiation process of nail development. *J. Invest. Dermatol.* 133 (8): 1990–1997.

360 McMillan, J.R. and Shimizu, H. (2001). Desmosomes: structure and function in normal and diseased epidermis. *J. Dermatol.* 28 (6): 291–298.

Vet-ebooks.com

11

Mammary Gland

Alexander D. Borowsky and Robert D. Cardiff

Introduction

The domestic house mouse (*Mus musculus domesticus*) was one of the first animal models used for the experimental study of cancer. The first mention of mammary cancer in mice, in the English literature, was in 1854 by Crisp. He reported a " . . .hard scirrhus-like tumor" upon the pectoral muscle [1]. By the 1890s, many European laboratories were using colonies of "fancy" mice to study breast cancer [1]. The first systematic pathology study of mouse mammary tumors was by published by Apolant in 1907 [1]. Haaland published the first English language study of the pathology of mouse mammary cancers in 1911 [1].

However, the transplantable Jensen cell line (1903) [1] and inbred mouse lines by Little and Tyzzer (1916) [1] laid the foundations for experimental mammary cancer research (Ewing 1919) [1]. These studies mark the beginning of experimental cancer research (Foulds 1945) [1]. The discovery of the Milk Agent (1934) [1], with confirmation that the milk agent was a virus, was another major step forward. The test-by-transplantation (T-by-T) brought new insights and invigorated breast cancer research in the era from 1950s to 1970s [2] with experimental evidence that the hyperplastic alveolar nodules are, indeed, preneoplastic [2].

The advent of molecular analysis and gene manipulation heralded a new era of mouse mammary gland research. The genetic modification of the inbred mouse was the most notable advent. This technology was enthusiastically adopted by the scientific community as the new "Koch's Postulates" [3]. Now, the biological potential of every candidate oncogene and tumor suppressor can be experimentally tested and validated in a mammalian animal, the mouse. The initial publication of this new technology in mouse mammary model came from Stewart et al. [4] in 1984 and led to the infamous Oncomouse patent [5]. Stewart's paper was followed by a plethora of mouse models of human breast cancer, now numbering in the hundreds. Unfortunately, many of these articles are coauthored by scientists and pathologists with little or no experience with mouse models, anatomy, histology, or pathology [6, 7]. Thus, many of the next generation have perpetuated numerous mistakes and misconceptions. We offer this practical guide to assist in your study of the mouse mammary gland pathology.

Anatomy, Histology, and Biology of Mouse Mammary Glands

First, the mouse is a mammal and not a human. Mice can be a very useful for modeling human mammary gland biology and its diseases, primarily cancer. A "model" animal has one or more attributes that approximate the human condition, in this case, the human breast. Therefore, the investigator needs to define the shared attribute, or attributes, desired. The limitation of any model is that it rarely contains all the attributes of the human. Your evaluation of the model and the attribute(s) will need to consider these limitations. For example, the breast is an appendage unique to primates [8]. Domestic animals used for milk production have similar appendages, udders, anatomically located near to the groin. So mice do not have breasts per se. However, the mouse and human, as with all mammals, share the organ named mammary gland.

The mammary glands of all mammals are formed from the milk line that extends bilaterally from the neck to the vulva (scrotum) [9]. The milk line condenses during embryogenesis to form placodes. The mouse forms five to six placode (right/left) pairs along the milk line also called the mammary anlage. These structures develop mammary buds [10]. The mammary glands extend from the mammary bud into the surrounding mammary fat pad. The growing edge of the mammary ductal tree contains the growth structure, the terminal end bud (TEB). The mouse TEB has been used as the prototype of mammalian mammary gland development [11].

The mammary tree, in most strains, "fills" the fat pad by six–eight weeks of age. The "tree" extends to the perimeter

Pathology of Genetically Engineered and Other Mutant Mice, First Edition. Edited by John P. Sundberg, Peter Vogel, and Jerrold M. Ward.
© 2022 John Wiley & Sons, Inc. Published 2022 by John Wiley & Sons, Inc.

Vet-ebooks.com

of the fat pad and is embedded in abundant, functionally important, adipose tissue [12]. The mammary fat pad is a specialized stroma compartment that forms developmentally before the mammary bud begins to elongate. The mammary ducts form a branching, "tree-like," structure. The number and types of branches are important to note in assessing mammary growth and development [13]. An extensive literature describes the effect of a variety of genes on mammary gland development [14]. The mature quiescent mouse mammary gland has ducts but no terminal ductal lobular units (TDLUs) such as found in the rat and human [9]. The mature, quiescent, ducts terminate in blunt ends and not TEB [9]. The formation of Lobulo-alveolar units, that then resemble the human TDLU, begins with pregnancy and ends with lactation that fills the fat pads with alveoli. Involution occurs rapidly following separation of the pups and the gland regresses to its former tree-like structure. The estrus cycle has a minor effect on the mammary gland but, generally, these minor changes cannot be used to accurately predict estrus stages.

Various genetic, metabolic, and nutritional factors influence mammary growth and development as well as lactation and postlactational involution [13]. Pregnancy and prelactation takes three weeks. Most weanlings can be removed from the nursing female after three weeks of age resulting in involution that takes two to three days for the gland to regress and remodel to a relatively normal state [13].

Mammary Gland Biology

The mammary gland biology has been extensively studied using mice [15, 16]. Normal growth and development, with an emphasis upon percent fat pad filled and branching morphogenesis, is generally considered an important metric [17]. Lactation and involution have also been studied [15, 18], even in genetically engineered mice (GEM) [19]. The mammary gland has also been featured in studies of aging [20]. Early stem cell research featured the mouse mammary gland [21]. This literature is useful in considering various abnormalities in GEM models [22]. A case study is provided in the closing section of this chapter as an example of the utilization of the multiple techniques.

Pathology of the Mammary Gland

Clinical veterinary and human pathology consists primarily of recognition of patterns of disease using the tools of histopathology/light microscopy, immunohistochemistry (IHC), and, increasingly, molecular (DNA and RNA) evaluation. Descriptions of these patterns are used to develop diagnostic criteria specific to disease nomenclature. This allows consistent and comparable application of standard or experimental therapies and subsequent outcome assessment. In mouse models, experimental pathology can be used to evaluate the dynamic functional properties of these disease states/diagnostic categories (Table 11.1). This is the science of pathobiology.[1]

Pathobiologists are essential for evaluating the experiment. We are responsible for interpreting the morphological origin, evolution, and outcome of the genetic engineer's experiments. This involves understanding the experimental details and interpreting the results. However, our responsibility goes further. We must validate, curate, and organize the data. As the person who sees the variety of GEM models within each institution, we are required to keep and organize our experiences for future use. We have recorded some of the guidelines to help in this task [7, 23–28].

The "spontaneous" tumors of the mouse mammary gland were first described by Crisp and then classified by Apolant and Haaland [1]. Thelma Dunn and colleagues provided a classification of the "spontaneous" mouse mammary tumor virus (MMTV)-induced mammary tumors that is still accurate but now has more modern terms [29]. Wisely, she avoided the then-current clinical breast cancer nomenclature and designated the tumors with an alphabetical nomenclature [1]. The two most common spontaneous tumors represent 90% of mouse mammary virus (MTV)-induced mammary tumors. These are called Type A and Type B tumors.[2] Both can be metastatic. The Type A tumor of Dunn is a micro-acinar biphasic tumor with both luminal and myoepithelial cells. The Type B tumor is a more solid tumor also biphasic and lined with prominent large basal myoepithelial cells. Modern molecular biology has demonstrated that these tumors are caused by direct or indirect (cis–trans) insertion-activation of the exogenous MMTV into the mouse DNA. Here they activate the *Wnt* or *Fgf* pathways. Interestingly, experimental insertion of the *Wnt* genes into a GEM results in generation of Type A and Type B tumors [1]. A third spontaneous tumor type also typically seen in virus-free mice treated with chemical carcinogens forms squamous cysts with smaller lesions referred to as "Squamous Nodules." Although chemical carcinogens most commonly are found to mutate oncogenic *Ras*, these lesions have also been associated with activation of the *Wnt* pathways [30].

[1] Two types of pathologists exist. One names the lesions and the other seeks to understand the biology of the lesion. The first is a diagnostician and has value. The second is a pathobiologist and a discovery pathologist who tries to understand the mechanisms. Most scientists view us as diagnosticians who names their particular lesions and rarely discusses their experiments with the pathologist. Worse yet, are those who make their own interpretations, D.I.Y. (Do-It-Yourself) pathology [6]. As a result, we constantly see misleading interpretations in the literature and, in some cases, major mistakes of interpretation. *Untrained or inexperienced investigators frequently bring the pathology specimens to the pathologists only upon completion of the study. The pathologist is then put "on the spot" trying to interpret poorly designed experiments and/or poorly sampled specimens.* In reading this, we implore you to be a pathobiologist or find someone who is.

[2] No relation to the human "Luminal A" or "Luminal B" intrinsic subtypes.

Vet-ebooks.com

Neoplastic Progression

One of the most important experimental questions that can be studied in mice, but cannot be studied with cell culture or xenograft studies, involves progression of normal or tumor susceptible epithelium to *in situ* and invasive carcinoma. The first experimental model of a stepwise progression in the mammary gland was DeOme's T-by-T in the mouse in 1958 [31, 32]. Although the concept of an *in situ* precursor had been introduced earlier [33, 34], DeOme's studies defined a biological and experimental two-step process in the neoplastic progression of the mammary tumors, (i) Nodulogenesis and (ii) Tumorigenesis [35, 36]. DeOme's student, Sefton Wellings, careful study of human breast whole mounts applied the concept of a nonobligate precursor to human breast cancer in 1975 [32].

The more recent GEM tumorigenesis also appears to go through a similar evolutionary process to DeOme's nodulogenesis to tumorigenesis model [31]. DeOme experimentally proved that nodulogenesis and tumorigenesis were independent processes. The T-by-T (see Cartoon 1) involves surgical clearing the mammary fat pad by removing the mammary tissue. This creates a "gland free" transplantation site. Then, small fragments of normal, nodular, or tumor tissue are transplanted into the gland cleared fat pad. All three-tissue type transplants will recapitulate their native growth pattern. Most importantly, both the nodular and "normal gland" are contact inhibited and remain flat while the tumor transplants grow in three dimensions. Neither nodules nor normal gland will grow when transplanted directly into the subcutaneous fat. However, malignant tissues will grow when transplanted in exogenous sites. The flat nodular outgrowths will undergo focal tumor development with time, which becomes a palpable tumor. Transplants of normal duct do not become tumors. Thus, the malignant potential any suspected nodule should be experimentally tested and proven using the T-by-T (Figure 11.1).

The formal T-by-T has been applied to GEM in a limited number of cases [38, 39]. Importantly, the transplants using *Wnt*1-induced lesions did not result in overt malignancy [39]. Likewise, after transplantation, many dysplasias have not proven to be premalignant. However, most investigators have assumed that focal dysplastic foci observed at early time points associated are obvious malignancies. Thus, the notion that such lesions are always "precancers" has not been experimentally defended or validated. With this in mind, various consensus groups have recommended the term "mammary intraepithelial neoplasm" (MIN) as a broad designation for focal epithelial dysplasias [40].

Ironically, the medical community has only recently recognized that many of the so-called "DCIS" lesions do not portend malignancy and such representations has led to the conundrum of "Over-diagnoses and Over-treatment" [41]. Eventually, the research scientist will be required to develop experimental proof, in GEM, of the biological potential of these lesions.

As of now, MIN (Figure 11.2) is defined as any focal lesion with dysplastic epithelial cells [40, 42]. The definition predicts that some such lesions will become invasive cancers. In fact, most GEM mammary cancers are associated with adjacent MIN-like lesions. The T-by-T experimentally defines MIN as an abnormal tissue that will grow when transplanted into a gland cleared mammary fat pad but will not grow when transplanted into the subcutaneous tissues. Cancers (malignant neoplasms) emerge out of transplanted MIN, will grow in three dimensions, become easily palpable, and grow in subcutaneous tissues (Figure 11.1).

Mammary Tumor Invasion and Metastases

Some inexperienced observers see the expansile (pushing) margins of many mouse mammary tumors and consider the lesions to be noninvasive "adenomas" (Figure 11.3). However, these lesions frequently have distant metastases. Some tumors are known to metastasize via the venous blood supply as "noninvasive intravascular metastases" (Figure 11.4) [43]. This appears to be a phenomenon tumor cell "embolism" to the lung, from tumors without the ability to reinvade out of the blood vessels.

Spontaneous (virus-induced) mouse mammary tumors metastasize to the lungs with a prevalence as high as 70% in some strains [44]. In contrast, human breast cancer is notorious for lymphatic spread, which presages hematogenous dissemination to multiple organs including the lungs. Lymphatic metastases in mice have been seen, but are rare events. In many cases, direct extensions of tumor into a regional lymph node has been misinterpreted to represent lymphatic spread. This is one of the major pathobiological differences between mouse mammary cancers and breast cancers in humans. However, this distinction is rarely mentioned. Clinical staging of breast cancer is based primarily on the detection of cancer in the local and regional lymph nodes. Although the mouse has an extensive lymphatic system, lymph node involvement is vanishingly rare in mice. Two of the earliest mentions of pulmonary metastases in mice by Livingood (1899) and Haaland (1911) have illustrations and camera-lucida images of intravascular pulmonary metastases [1]. Vaage presented the most extensive modern analysis of the biology of mouse metastases [44]. Tarin took the circulating mouse mammary cancers into early recognition of similar occurrences in humans [45].

Genetic Engineering of Mouse Mammary Gland

The mouse mammary gland was one of the first organs targeted in the new world of genetic engineering [4]. The "Oncomouse" patent was largely based on the induction of mammary tumors

Vet-ebooks.com

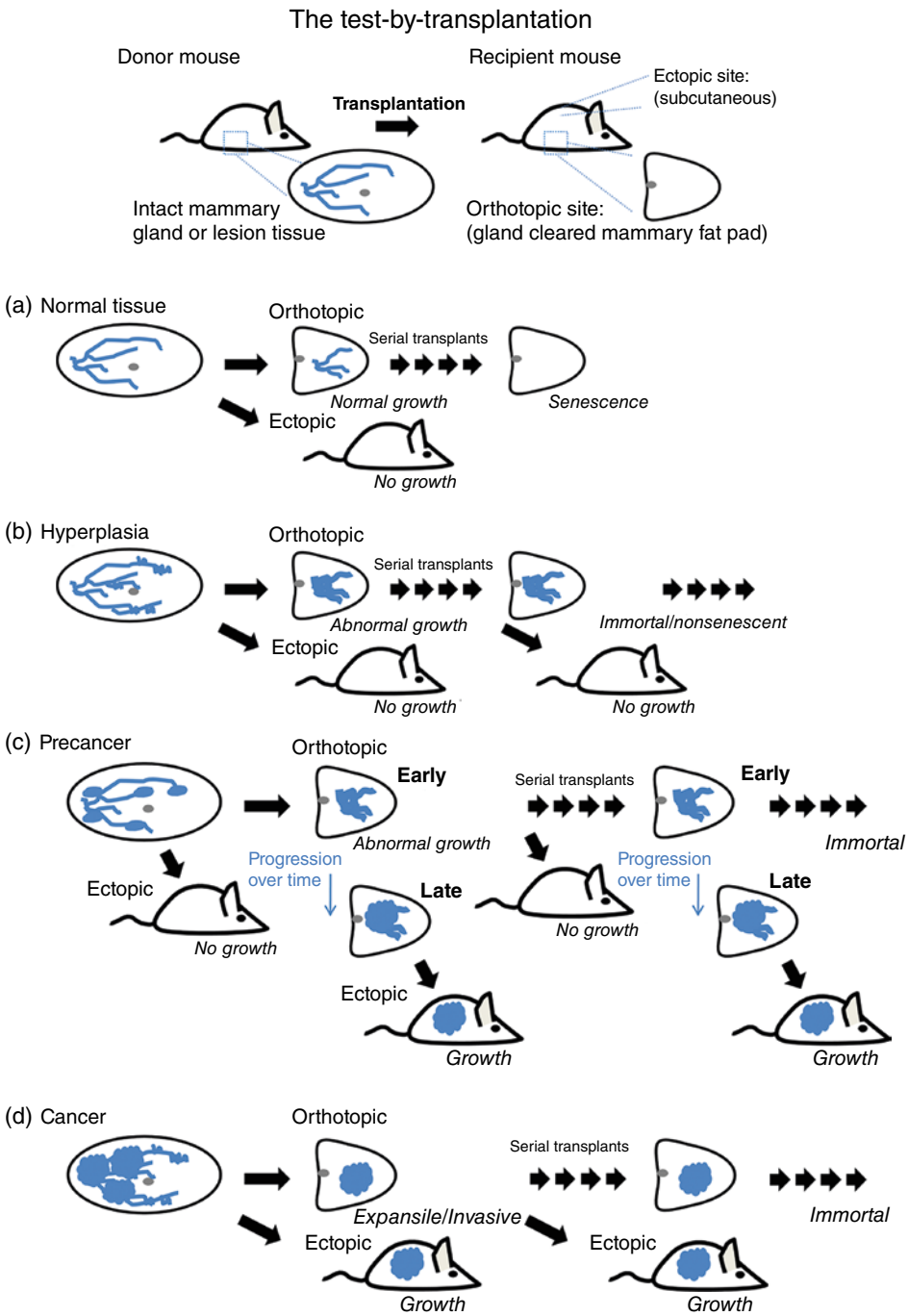


Figure 11.1 **The test by transplantation**. Transplantation in orthotopic or ectopic sites provides an experimental definition for normal (a), hyperplastic (b), precancer (c), or cancer (d) in mammary epithelial tissues. Fresh tissue fragments can be harvested from a "donor" mouse and transplanted into a "recipient" mouse, either in the orthotopic site – a gland-cleared mammary fat pad – where the tissue proximal to the lymph node in the inguinal mammary stroma is removed at three weeks of age; or in an ectopic site such as subcutaneous stroma. (a) Normal tissue transplanted into the orthotopic site yields a normal gland outgrowth, but does not grow ectopically. After sequential "serial" transplant generations, the normal tissue will senesce, eventually resulting in no outgrowth. (b) Hyperplasias, in contrast, will not senesce after multiple serial transplant generations, but they still will not grow ectopically. (c) Precancer tissues are defined by immortal growth in serial transplantation, but they are also defined by a progression to a lesion that will grow ectopically. (d) Cancer tissues, meanwhile, are consistently able to grow in either the orthotopic or ectopic site Based on.

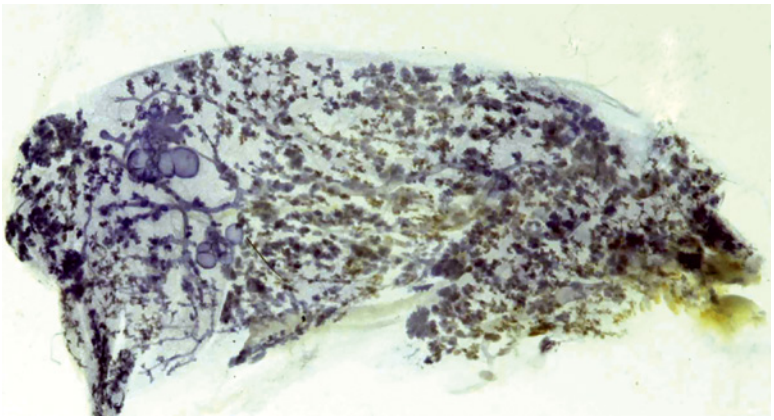
Vet-ebooks.com

Table 11.1 Breast cancer genes and mouse models.

Gene	Human genetics	Human comparative subtype	Category	Model		
				MU phenotype	Image	PMID
Erbb2, receptor tyrosine kinase 2 Synonym: HER-2	Gene amplification/alternative splice/mutations	HER2	Receptor tyrosine kinase	Nodular-solid	11.5a	1887859
Apc, APC, WNT signaling pathway regulator	Inherited or somatic mutation	Basal	Cytoskeleton control	Pilar/biphasic		11309311
Brca1, breast cancer 1, early onset	Inherited or somatic mutation	Basal	DNA repair	Poorly differentiated		30674894
Cdh1, cadherin 1	Inherited or somatic mutation	Luminal B/lobular	Cell adhesion	Lobular Ca	11.8d	17097565
Chek2, checkpoint kinase 2	Inherited or somatic mutation	Basal/metaplastic	DNA mitotic factor	Adenosquamous		16488990
Stat1, signal transducer and activator of transcription 1	Somatic truncating mutations	Luminal B	Signal transducer and activator of transcription	Alveolar solid	11.7	28865492
Fgfr1, fibroblast growth factor receptor 1	Amplification/alternative splice/upregulated	Basal/metaplastic	Growth factor	Biphasic/heterogeneous		20501844
Myc, myelocytomatosis oncogene	Gene amplification	Basal	DNA-binding factor for transcription	Solid/large cell	11.5b	1887859
Trp53, transformation-related protein 53	Inherited (Li-Fraumeni) or somatic mutation	Basal/Metaplastic	DNA transcription	Biphasic/heterogeneous	11.5d	22173978
PIK3CA^{E545K}	Inherited (Cowden's) or somatic mutation	Basal/metaplastic	Tumor suppressor, signal transduction	Adenomyoepithelioma	11.7b	24080956
Prlr, prolactin receptor	Somatic mutations (Heterozygous truncating with STAT1 loss)	Luminal B	Hormone receptor	Alveolar solid		27681435
Pten, phosphatase and tensin homolog	Inherited (Cowden's) or somatic mutation	Basal/metaplastic	Tumor suppressor dual-specificity phosphatase	Biphasic/heterogeneous	11.9b	22949413
Tg(MMTV-PyVT)634Mul, Polyoma middle T viral antigen	Viral molecular mimic of HER2/EGFR	HER2	Signal transduction	Cystic/solid nodular	11.9e,f	12213737
Ras, resistance to audiogenic seizures	Amplification/somatic activating mutation	Basal	Signaling	Small cell, metaplastic		1887859
Wnt-10b	Activity	Basal/metaplastic	Developmental signaling	Type A	11.5	6855600
Fgf3, fibroblast growth factor 3	Activity	Basal/metaplastic	Growth factor	Pilar/biphasic		12165853

Vet-ebooks.com

(a)



(b)

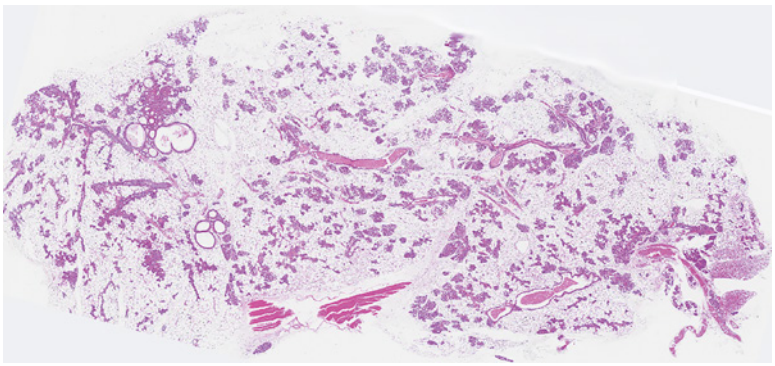


Figure 11.2 **Whole Mount Subgross and Histology.** Whole slide images of the left #1 mammary fat pad from a 119-week old nulliparous129S6/*SvEvTac-Stat1*^{tm1Rds} (Stat1-null) female mouse showing the three dimensional hematoxylin stained whole mount (a) and a 10-µm section stained with hematoxylin and eosin (b). The image (a) shows all the atypical features in the mammary gland. Some features, such as the two cystic areas appear in both images. However, many of the features are not present in the 10-µm section. The image (b) length measures 11 mm.

in mice [5]. Since then genetic engineering has been used study mammary embryogenesis, development [8, 15], lactation [13, 19], involution [18], stem cells [14, 46], carcinogenesis, aging [20], and other phenomena. These studies far exceed the scope of this chapter. However, the pathologist needs to be aware of the range and depth of this research.

Promoters

To a certain extent, the tumor phenotype has been independent of the promoter used to drive the gene. However, most tissue-specific promoters, such as the mouse mammary tumor virus (*MMTV*) long terminal repeat (*LTR*; viral), whey acidic protein (*Wap*; milk), or keratin (*Krt*; structural), are mammary gland targeted [47, 48]. Gordon Hager's mouse mammary tumor virus long terminal repeat (MMTV-LTR) construct is the most frequently used promoter [49]. The *MMTV-LTR* has a variety of open reading frames and endogenous response elements that deal with super antigens and dexamethasone response [50]. Devoid of additional viral genomic components, the *MMTV-LTR* serves as very specific,[3] highly active mammary epithelial cell promoter with transcriptional activity within a few days of birth in mature luminal as well as luminal progenitor cells. In recent years, scientists have introduced increasingly complex and inducible promoters or knock out (KO) systems that promote or KO genes in unique cellular subsets resulting in differing phenotypes for the same gene. It is fascinating to see different tumor phenotypes emerge using the same gene but a different promoter [51–53]. The lesson for the pathologist is to be certain that the promoter system is identified for each experiment.

Oncogenes and Tumor Suppressors

In general, activated oncogenes lead to cancer. The activation is accomplished by gene over expression or mutation. The process can be a prolonged process depending on the "strength" of the oncogene. The T50 (time when 50% of the

[3] There is additional *MMTV-LTR* activity in salivary gland, Harderian gland, T cells, and some macrophages.

Vet-ebooks.com

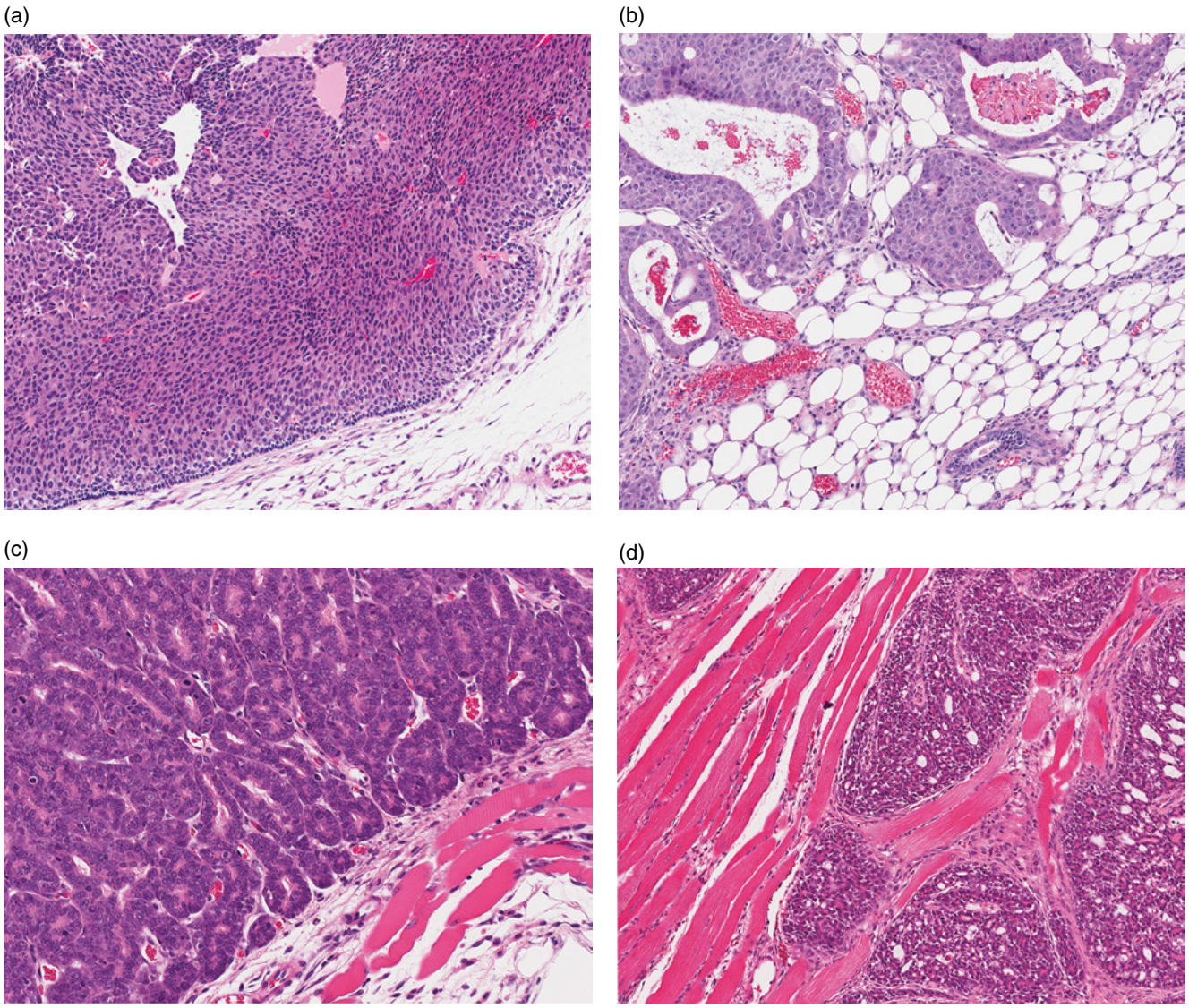


Figure 11.3 **Invasion vs. Expansion**. These images illustrated growth patterns commonly found in GEM mammary cancers. (a) *cNeu* tumor with expansile margins. Note the compression of host tissue by the expanding tumor. (b) *Stat*1 KO tumor with invading margin. Note the invading tumor cells separate the surrounding adipocytes. (c) *Wnt10b* tumor with expansile margins compressing the surrounding fat pad. Note the compression of adipose tissue and skeletal muscle. (d) A similar *Wnt10b* invading between skeletal muscle fibers.

animals have tumors) varies from 6 to 124 weeks [20]. The *MMTV-LTR:Polyoma Middle T* (FVB/N-Tg(MMTV-PyVT) 634Mul/J)[4] transgenic mouse is, by far, the most popular GEM because the mice develop premalignant masses by three weeks of age and develop tumors by six weeks of age and metastasis shortly thereafter [20]. Therefore, almost all experiments are completed within a relatively short period (one postdoc's lifetime). In contrast, the next most popular model, the Pds5bTg(Wap-ERBB2)229Wzw/J Tg(MMTVneu)202Mul/J compound mutant on a mixed genetic background (formerly called *cNeu*/*Her2*) with a T50 around 25 weeks [14]. Thus, the investigator using FVB/N--Tg(MMTVneu)202Mul/J mice [54] needs to plan to hold mice for 12–18 months for an accurate T50. This is expensive in both time and money. Hence, the popularity of the *MMTV-PyMT* models.

Oncogene Addiction and Nononcogene Addiction (NOA)

The investigator has been able control the chronology of oncogenesis with the development of inducible promoter systems. Tumors can be induced at the convenience of the investigator [47]. Better yet, the oncogenic stimulus can be removed and the tumor "deinduced." Amazingly, in many cases, the deinduced tumors completely regress. This

[4] FVB/N-Tg(MMTV-PyVT)634Mul/J.

Vet-ebooks.com

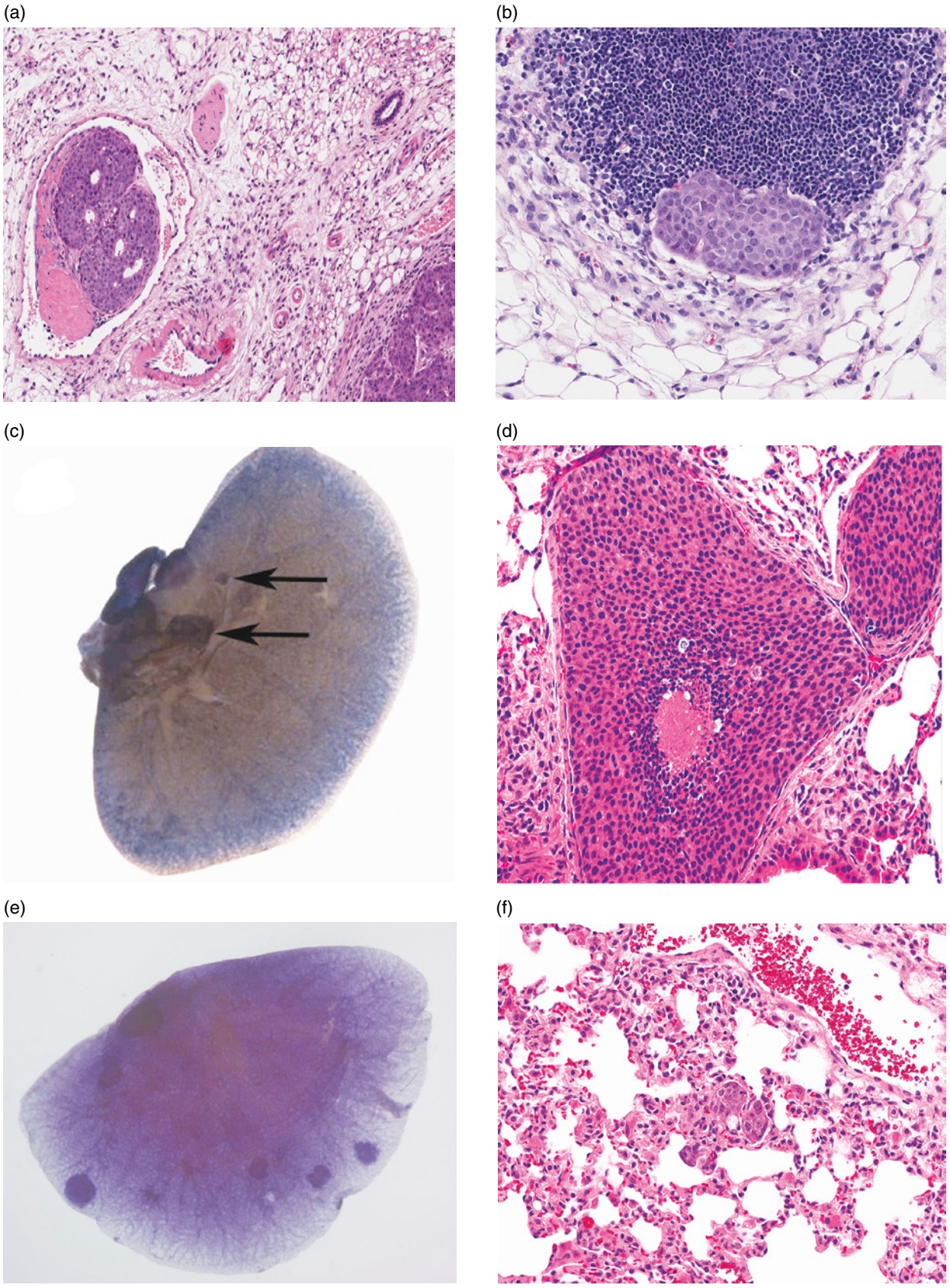


Figure 11.4 **Metastasis**. These images illustrate various sites and modes of metastatic disease. (a) An intravascular metastasis from *Stat1* KO tumor. The tumor cells are attached to a fibrin clot and surrounded by a rim of endothelial cells. The vessel has a second endothelial layer and some RBCs. (b) Lymph node with a metastasis from another *Stat1* KO tumor. Note that the metastatic cells are in the subcapsular sinus; this sinus is the sight of most nodal metastases in both mouse and human. (c) A whole mount of a lung in a *cNeu* tumor bearing mouse with a large (central) hilar metastasis (epithelial Lower Arrow). (d) A microscopic image of a similar metastasis for a *cNeu* tumor in the main stem pulmonary veins. Note the two layers of endothelial cells. One layer surrounding the tumor embolus. The second layer lining the pulmonary vein. (e) A whole mount of a lung in a tumor-bearing *Stat1* KO mouse with small peripheral micrometastases. (f) Histological image of one micro metastasis in lung of a tumor-bearing *Stat1* KO mouse.

Vet-ebooks.com

dependence of the tumor on oncogene expression is called "oncogene addiction." It gave hope that, by simply preventing the expression of the inciting oncogene, one could effectively treat cancer [55]. However, it was soon learned that many of the tumors reappeared, frequently with a completely different tumor phenotype (metaplasia) [56]. In a like manner, tumor suppressor genes also lead to a form of addiction [55, 57]. The tumor suppressor genes lead to neoplasia only after being disabled, mutated, or removed. The prime example is a mutation of transformation-related protein 53 (*Trp53*). The tumor phenotypes of *Trp53* mutations alone can lead to heterogeneous tumors that reflect the secondary oncogenic hit [55, 58]. If the immunohistochemical identification of mutant nuclear TRP53 is used as an indicator numerous other GEM examples exist [59, 60]. The escape from the presumed addiction is often accompanied by the emergence of the tumor in another cell type. In other words, the neoplastic cells exhibit a remarkable plasticity known as metaplasia.

Metaplasia

Metaplasia is defined as a change of one cell type to another cell type. A number of metaplastic changes from normal basal and luminal epithelium are found in the GEM mammary gland. For example, small squamous nodules are frequently found in mammary glands of multiparous females [61]. These lesions are generally not neoplastic and do not grow upon transplantation.

However, the metaplastic changes found in the context of morphological MIN and tumors are of primary concern. The ultimate endpoint of the metaplastic process appears to be a complete transition from an epithelial phenotype to a spindle cell, vimentin-expressing phenotype. These are called epithelial–mesenchymal transition (EMT) phenotype tumors [62]. Generally, the spindle cells of these tumors will express both keratins and vimentin [62].

However, assuming that the mammary gland is limited to basal and luminal cells, other metaplastic phenotypes appear. Since the mammary gland is a skin appendage, squamous cell lesions are the most frequent metaplastic tumor type. Tumors in the *Apc-Wnt* pathways are particularly squamous and have other dermoid features [63]. We have also seen tumors with sebaceous and endothelial metaplasia. EMT in GEM tumors frequently involves a mutant *Trp53* that is easily detected using IHC [59].

Host and Environmental Factors

Host and environmental factors play an important role in the interpretation of results. For example, in mouse mammary tumor biology, parity is a major factor. Multiparous females with MMTV infection or the MMTV promoter will develop more tumors than nulliparous females. The *MMTV-LTRs* have complex structures with various hormone response elements, negative response elements, and open reading frames [49]. Most notorious is a dexamethasone response element that is on the most commonly used *MTV-LTR* promoter [49]. Thus, any experiment using the *MTV-LTR*, or other hormone-sensitive promoter, is directly affected by pregnancy and lactogenic hormones. This includes the majority of current models in use.

Standard pronuclear injection to introduce DNA constructs encoding the tissue-specific strong promoters designed to express the gene(s) in the mammary epithelium results in random insertion sites. These sites often have multiple tandem repeats of the construct inserted at one or more loci in the genome [64]. As a result, different founder lines (derived from individual pronuclei) have unpredictable transgene expression levels due to positional effects of the genome. Sometimes a founder phenotype is lost, when screening maintains a silent rather than active locus of insertion [65]. Improved techniques for more consistent and dependable transgene expression have been developed. The most common is homologous recombination into a known tried and true permissive locus, such as the *Rosa26* locus [66], and has proven to be useful for large constructs [67]. In order to improve upon the ability to regulate expression, a variety of inducible promoter systems allow temporal and, to some extent, expression level control of the transgene. For example, the "TET ON" system has been successfully introduced in a mammary-specific fashion by use of a dual construct where the mammary-specific promoter drives expression of the reverse Tet transactivator (rTTA) and the transgene/oncogene is controlled by a strong promoter including the Tet operon. Exogenous administration of tetracycline (doxycycline) usually in the food or water of the animal induces transgene expression, which is turned off when the tetracycline is removed. Such systems are prone to some "leaky" expression but nonetheless have proven to be powerful and robust models to answer "timing" questions as well as potential for resetting transgene expression to more physiologic levels [37, 68]. Finally, a variety of multiconstruct conditional systems have been developed allowing a temporal on switch (floxed stop cassette) [69, 70], off switch (floxed transgene) or more complex recombinations using tissue-specific promoters to express a recombinase (e.g. *cre*-recombinase) [67] or even an exogenously activatable form of the recombinase (e.g. *cre*-ert2).

Investigators developing GEM have, in general, ignored strain differences while celebrating their engineering triumphs. The early pioneers frequently used cross (or mixed) breeds and rarely bred their lines to homogeneity. The animals were carefully bred only when transferred to an established facility such as JAX. The pioneering work of Kent Hunter demonstrated that the same oncogene, in different mouse strains resulted in different tumoral natural histories [71, 72]. Further, some investigators have mistaken the idiosyncrasies of a given strain as a result of their molecular manipulations. For example, different colonies of the FVB mouse strain exhibit abnormal lobuloalveolar development in multiparous females [61, 73, 74]. FVB strains also seems to be prone to pituitary adenomas [74]. This trait leads to a relatively high incidence of mammary abnormalities, including mammary tumors. As a result, pituitaries need to be

Vet-ebooks.com

examined in studies involving older populations of FVB mice. Another common error has been mistaking the pulmonary bronchioalveolar adenomas occurring in older females for metastases [75]. In general, the investigator and pathologist need to know the details of their strains and their genetic crosses. Studies with mixed strain backgrounds are particularly problematic. Investigators often incorrectly believe that the segregation of a GEM allele among littermates, screened as either positive or negative for the allele (a variety of crosses are possible, e.g. Aa x aa; AA x aa; or even AA x Aa), (see Chapter 3 for more details). These strain-dependent differences and modifier genes can have major effects on tumor latency and phenotype [72].

As implied, age and parity are important factors to consider in the evaluation of an experimental cohort. Many studies use "historical" controls. Changes in environment and factors such as diet can have an enormous effect on experiments. One of the best documented involved a dietary change to a soy based-diet that effected tumor incidence [76]. We also have observed a change in colony venue at one university led to granulomatous infections by rat round worms that mimicked intestinal tumors. Almost every experienced veterinarian can relate such horror stories associated with environmental change [77].

GEM Mammary Tumors

How to Evaluate a Model

A good model should be approximations of reality that are testable, predictive, can falsify a hypothesis, and share one or more attributes of reality. A valid model has one or more of the desired attributes. In contrast to the human disease, mouse models are testable by direct experimentation. We have a limited ability to test hypotheses directly in humans. We are primarily limited to observation, demographics, epidemiology, and statistical analysis of heterogeneous populations (guilt-by-association). In contrast, a mouse model provides a relatively homogeneous population that is available for observation and genetic manipulation. Molecular-based hypotheses can be tested by genetic engineering. Biological hypotheses can be tested with syngeneic and orthotopic transplantation.

Many approaches have been used for choosing a model including the modern genomic perspective [78]. The review by Swiatnicki and Andrechek have thoroughly discussed the many analytical tools now available for molecular, genomic, proteomic, genetic, and metabolomic analysis of GEM [47]. However, this chapter is about the pathobiology of the models and shared with those of us who are responsible for evaluating the morphology and biology of the animal models.

The pathologist's role is primarily in obtaining and analyzing the morphology of appropriate biological samples. However, relatively untrained personnel perform 90% of the contacts with the animals [7, 79–81]. So the pathologists are frequently limited to an advisory role and microscopic examination. Thus, the staff will frequently become a critical part the quality of your experimental observations [6, 80].

The genetic engineer and cancer biologist will always ask if their mouse model resembles the human disease. This places the pathologist in a difficult position. What is a model and how close does the model resemble the human disease? A model has one or more attributes that resemble the human condition. The more attributes the "closer" the model; so the pathologist needs to know which attributes interest the investigator. Sometimes, the interests of the investigator are not met. As a result, other extremely valuable attributes are overlooked.

Pathology

Terminology, Classification, and Description

The nomenclature and terminology used to classify both human and mouse mammary epithelial neoplasms has been informed and shaped by the molecular analysis. Tumors of the mouse and human mammary glands appear to arise from a multipotential mammary epithelial precursor cell capable of differentiating into both basal/myoepithelial and luminal epithelial cells [47]. Mammary tumors are not composed of a single uniform cell population, but instead differentiate via progenitor populations into basal-like and/or luminal-like lineages. Differentiation is further stratified, for clinical therapy decisions based upon the presence or absence drug "targetable" expression of HER2/ERBB2 and hormone receptors (estrogen and progesterone receptors). A major goal of improving breast cancer treatment, therefore, is to find new targets in the tumors that do not express HER2 or hormone receptors, the so-called "triple negative" (TN) breast cancers. Fortunately, the majority of GEM tumors are HER2 and hormone receptor negative.

The molecular simplification of breast cancer stratification has improved our understanding that there are "cancers" with very limited malignant potential that contribute to the overdiagnosis and overtreatment conundrum [41]. Understanding of the biological potential encoded in the histopathology of the human disease cannot be experimentally tested in patients. We would not leave untreated a "cancer" that we hypothesize is nonmalignant in order to prove (or disprove) the hypothesis. These hypotheses and overdiagnosis issues will be addressed, as in the past, through experimentally derived understanding of the biology in the mouse.

The comparative pathologists are at the center of this dilemma [80]. We are frequently pressed by the biological and clinical scientists to match their GEM to the human disease. In order to address this demand, complex systems of nomenclature have been developed to assure that the same words are applied to the same phenomena [28, 29, 42, 82]. The International Harmonization of Nomenclature and Diagnostic Criteria for Lesions (INHAND) project has published detailed descriptions and criteria for diagnosing

Vet-ebooks.com

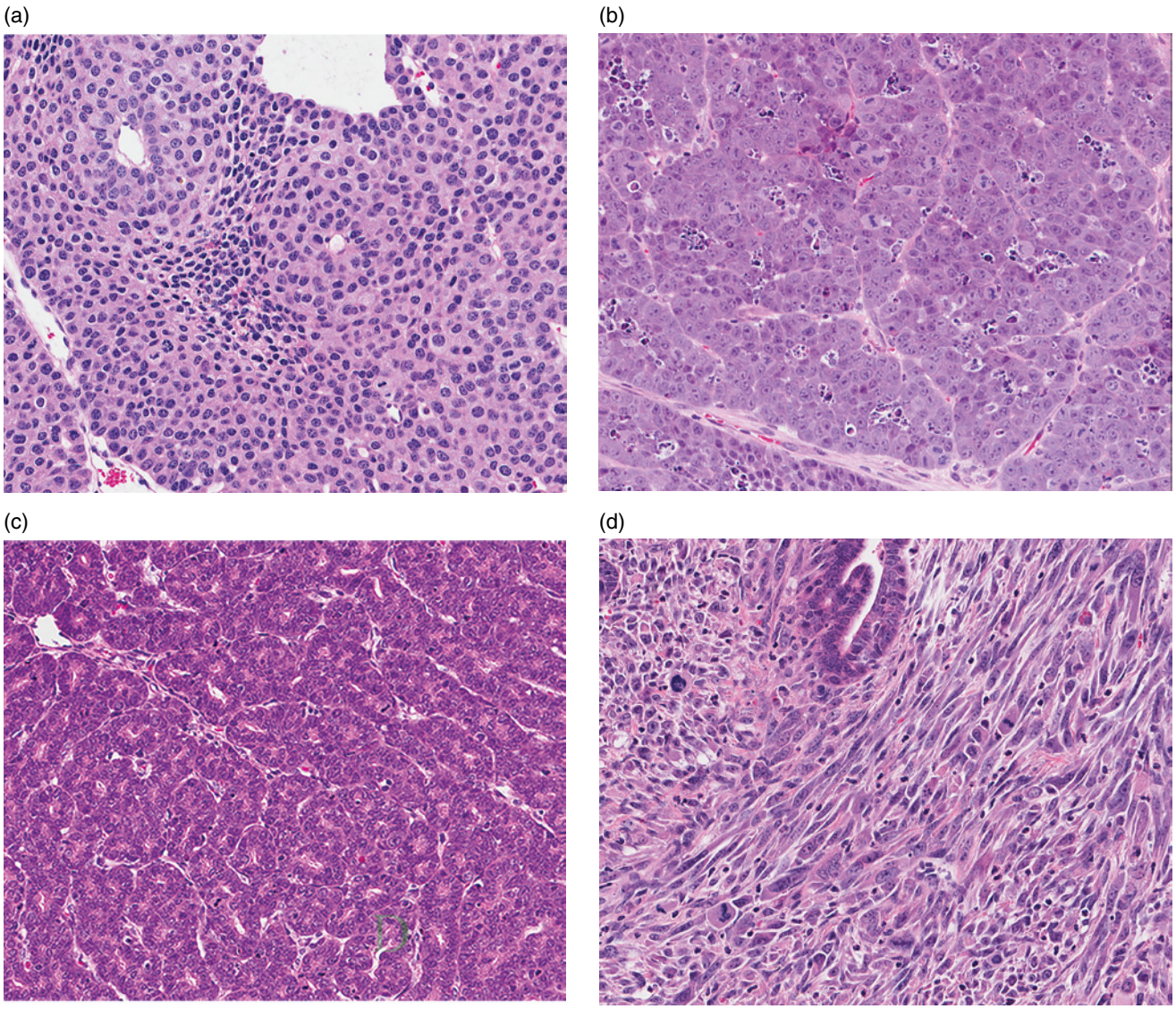


Figure 11.5 **Rogues Gallery of GEM tumor phenotypes**. Each image is selected to show the most common or the "Signature" phenotype tumor associated with a particular genotype. Note that when the signature phenotype is recognized, the genotype is generally associated. However, many, if not all, genotypes have multiple phenotype tumors. (a) The solid nodular phenotype in a cNeu (FVB/N-Tg(MMTV-Erbb2*-cre)1Mul/J) mouse. (b) The large cell phenotype typical of *Myc*. Note the abundant bluish cytoplasm, large pale nuclei and numerous clusters of apoptotic cells (pedigree unknown). (c) Microacinar (Dunn type A) tumor induced in a *Wnt10b* mutant mouse (MMTV-Wnt10bTG). (d) The spindle cell (EMT) phenotype in a *Trp53* knock out mouse. Note the gland like epithelial element (*Trp53*-null; *Trp53*^{tm1Tyj}).

rodent mammary gland pathology [80]. Although informative and useful guides to terminology and classification, these efforts are not sufficiently detailed. They sometimes overlook significant morphological features that provide important clues to mouse mammary tumor biology.

Genotypes Predict Phenotypes

The activated oncogene influences the tumor phenotype. By simply looking at many of the tumor phenotypes, the pathologist can predict which genes are involved [83, 84]. For example, insertion of *Wnt* genes leads to classical Type A (Figure 11.5a) and Type B (Figure 11.6d) tumor phenotypes[5] described by Thelma Dunn and associated with insertion activation by MMTV [84]. Squamous tumors are also associated with *Wnt, Apc*, and/or *Ras* activation (Figure 11.6c) [63]. *cNeu* tumors are typically solid nodular and *Myc* tumors large cell neoplasms with blue cytoplasm (Figure 11.5b). *Stat1* null associated tumors provide a completely different "large clear

[5] These are not the same as the "luminal A" and "luminal B" intrinsic subtypes of breast cancer defined by gene expression. They are among the patterns of mammary neoplasms, often complex, multilineage lesions that arise spontaneously in mice, as described by Thelma Dunn.

Vet-ebooks.com

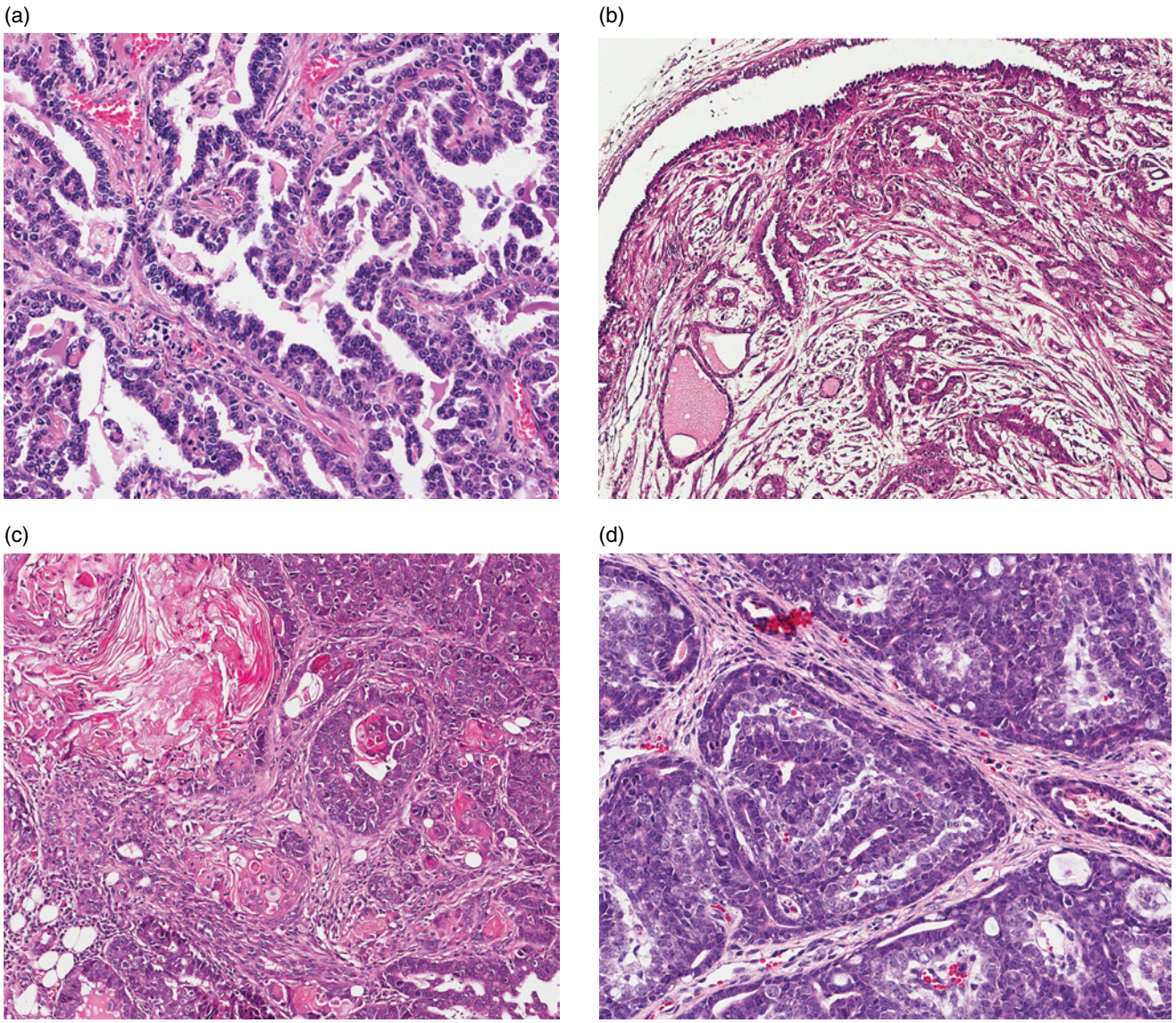


Figure 11.6 **Other GEM Phenotypes**. (a) Papillary mammary tumor from a GEM Notch mouse (Notch3β-geo/β-geo). (b) The edge of a large adenomyoepithelioma from a Pi3kinase mutant animal (PIK3CA H1047R-KRT8-creERT2). (c) An adenosquamous carcinoma, illustrating a phenotype common to *Ras*, *Wnt*, and other genes. This example is in a WAP-Cre H1047R. (d) A tubular, type B of Dunn tumor illustration the large pale myoepithelial cells.

cell" ER^+ tumor type (Figure 11.7) [85]. Various mutations of either *Pik3* kinase or *Pten* typically results in development of adenomyoepitheliomas (Figure 11.6b) [29, 52, 53].

However, different promoters driving the same oncogene can develop different tumor phenotypes. For example, the multinodular rosettes are unique to *Lgr5*-promoted *Pi3kca* mutant mice but not found in *Pi3kca* mice promoted by *Ck8--cre* or other promoters [52, 53]. Without a doubt, these morphological variations have significant biological and molecular implications but are currently of little interest to the clinician.

These tumor phenotypes are "Signature" phenotypes. When one observes them, one can be assured that a particular gene set is involved. However, tumor phenotypes in any given genotype can vary considerably [86]. It is now becoming apparent that metaplasia plays an important role in the end-point tumor phenotypes [87]. This process typically involves phenotype changes toward an increasingly primitive cell type, sometimes called the mammary epithelial progenitor cell. The endpoint is the spindle cell carcinoma, also known as the carcinosarcomas or EMT phenotype tumors (Figure 11.5d). The TRP53 protein is frequently mutated in these EMT type tumors and can be detected with immunohistochemical labeling [59].

Mouse Comparisons with Human (Table 11.1)

Clearly, humans and mice both develop mammary cancers. Humans have a molecular or gene-based origin. Mice develop spontaneous mammary cancers associated with a virus and experimentally with exposure to carcinogens or

Vet-ebooks.com

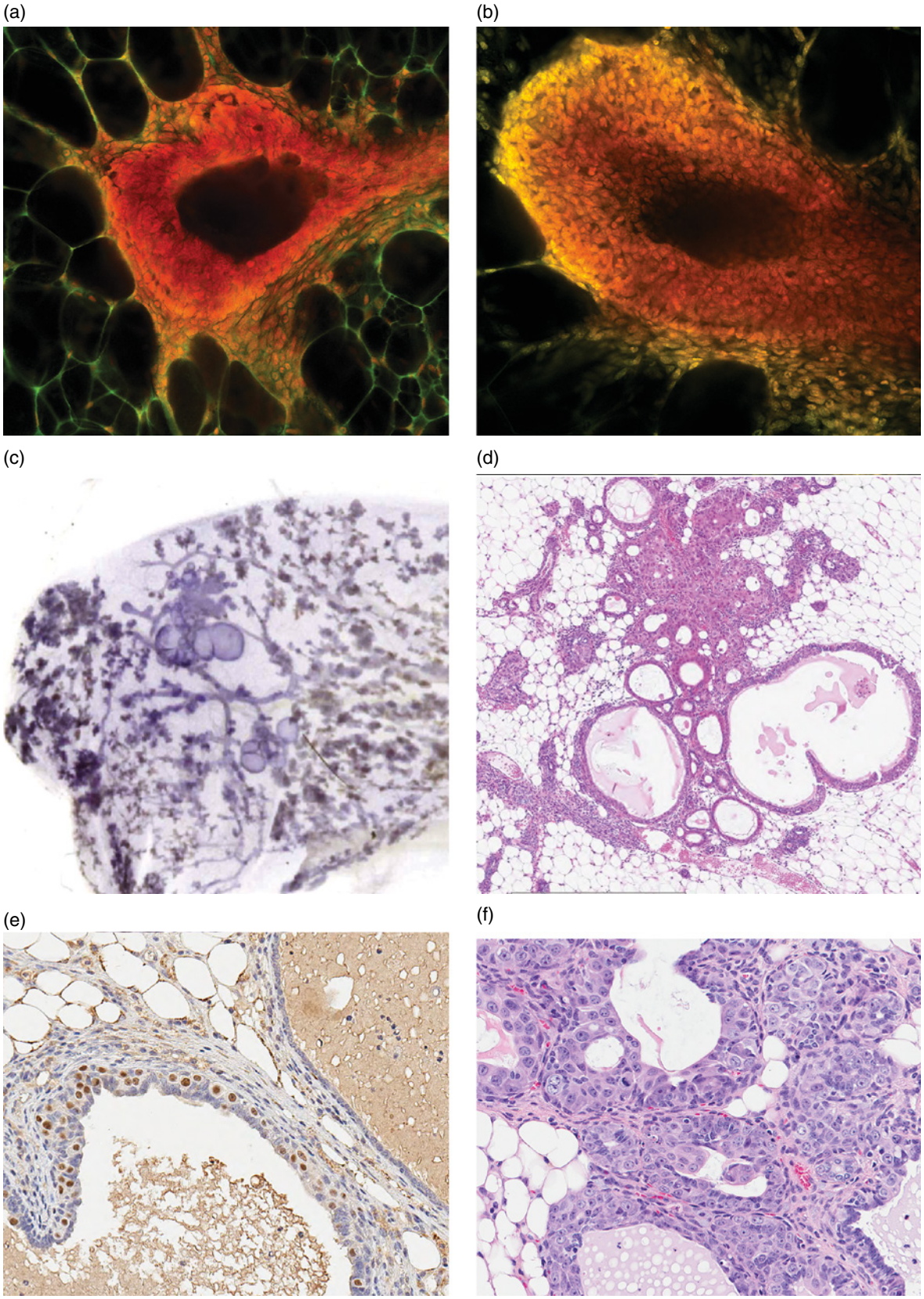


Figure 11.7 **Case study**. (a-b) LS-TAFI 3D image of a *Stat1* null terminal end bud. Note that the body is larger than the normal TEB in figure (a) and the connective tissue adjacent to the head lacks inflammatory cells. However, the inflammatory cells accumulate around the neck. (c) A whole mount of the #4 mammary gland in a *Stat1* KO showing multiple lesions including several cysts. (d) A histology image showing the cysts that are in figure (c). Note that the cells are relatively large. (e) A histological image showing two major ducts IHC labeled for FOXA1. Note that the upper right duct is lined by smaller NORMAL ductal epithelial cells that do not stain for FOXA1. The lower left duct has numerous isolated cells with abundant pale cytoplasm and FOXA1 positive nuclei (LOP cells). (f) A MIN from a *Stat1* KO mammary gland illustrating the cytological details of LOP cells.

Vet-ebooks.com

genetic engineers. The cells of the mammary glands in both species are identical types [9]. Molecular analysis in humans shows the cells have a similar origin and developmental trajectory. Molecular manipulation demonstrates that mutated genes from human when activated in mouse result in tumors [88]. Thus, we have fulfilled a modified version Koch's postulates for cancer, whereby isolation of the *oncogene* rather than the infectious agent from the human disease, and introduction of that human oncogene in a mouse cell/tissue recapitulates the disease seen in the human [5]. More intriguing, when limited microscopic fields are compared, the human and mouse tumors are morphologically inseparable [60, 89–94]. The GEM provides very revealing models.

It is true that we clever pathologists can find microscopic fields in human tumors that resemble one or more mouse models (Figure 11.8). And vice versa, one can match a phenotypic attribute from a mouse tumor with a comparable attribute in some human breast cancer. However, this matching of images is, realistically, a futile comparison. It takes little reflection to realize that one is comparing reproducible events in a highly inbred animal (the mouse) with a well-defined genotype to a sporadic occurrence in an individual from a highly heterogeneous population and with a poorly defined but highly individualized genotype. The task is even greater when one witnesses that the mouse tumors can exhibit wildly different phenotypes in the same inbred hosts induced by the same oncogene. Our odds for homogeneity get even lower when one observes that MIN isolated from the same mammary gland in the same animal can exhibit different biological behaviors [38]. Therefore, we need to be careful with morphological comparisons. However, as always, the biology counts.

The anatomy of the human breast differs from the mouse mammary gland. One important aspect of the anatomy is the rich lymphatics with lymph nodes that drain various parts of the human breast. The human lymphatic system commonly contains metastatic breast cancers. As indicated above, the mouse mammary gland also has a lymphatic system which, in contrast to the human, is rarely used as a metastatic route.

At the histological level, human normal and cancerous mammary cells are larger than mouse. However, the most obvious difference is that mouse mammary glands and their cancers rarely have extensive fibrosis. In contrast, the human mammary gland is usually encased in connective tissue and most breast cancers are characterized as fibrous masses.

GEM MIN

By consensus, the foci of small dysplastic nodules found in the GEM mammary gland are designated as MINs [40, 42].[6] This designation was developed in consensus meetings which objected to using the standard mouse nomenclature of hyperplastic alveolar nodule (HAN) as outmoded and inaccurate. Therefore, "MIN" has been applied to focal areas of intraepithelial dysplastic growth in the mouse mammary gland. This term avoided using terms such as precancerous or carcinoma *in situ* that might be pejorative without formal evidence. Since they occur in GEM, the pathologist can apply a guilt-by-association diagnosis and describe them on a morphological basis [95]. However, as discussed, this could be misleading without formal experimental proof (Figure 11.1) (T-by-T) [96, 97]. The outcome is monitored over time and with serial transplantation. Tumors grow at once in all transplantation sites. MIN are contact inhibited and take weeks for tumors to emerge from them.

As a practical matter, MIN lesions generally appear before the development of tumors. Thus, the appearance of focal dysplasias can be used to predict a pending tumor onset. This can be very useful in colony management.

Examination of tissues adjacent to the tumors will usually reveal small focal areas of dysplastic growth without invasion. These focal dysplasias are also found in regions without tumors. However, many investigators are only interested in the tumors, and only sample the tumors but not the tumor-free mammary gland. In our experience, inexperienced scientists will purposely dissect the host tissues from the tumor. This ignores the most important biological interactions between the malignancy and the host. We ask our contributing scientist to provide the host tissue surrounding the tumor.

Metastasis

Metastasis from the mouse mammary tumors generally goes to the lung (Figure 11.4). Two metastatic mechanism exist. The pathologist needs to know about and search for each. The most common is micrometastasis (Figure 11.4e,f). This form is probably the result of invasion of individual cells into the stroma, escorted by macrophages to the vessels, and vascular transport to the lungs where they are trapped in the peripheral pulmonary vasculature [98]. The second route is via "invasion-independent metastasis" in which large chunks of tumor cells float through the vessels and clog the central pulmonary vessels (Figure 11.4a,c,d) [43, 44, 99]. Many of these types of embolic metastases are encased in an endothelial layer. This results in two layers of endothelium at the site of pulmonary metastases (Figure 11.4d). One layer of endothelium from the neoplasm, and the other is pulmonary endothelium.

Metaplasia

Metaplasia is one of the "causes" of variation in tumor phenotype in any one genotype. The practice of leaving tumors to grow until their size reaches "institutional Animal Care and Use Committee guidelines" can result in metaplastic changes in the tumor phenotype. Thus, these older, larger tumors frequently have morphological

[6] MIN is also used in the gastrointestinal pathology designate multiple intestinal neoplasia model in mice, microsatellite instability in genetics, and in $Apc^{Min/+}$ as a gene designation.

Vet-ebooks.com

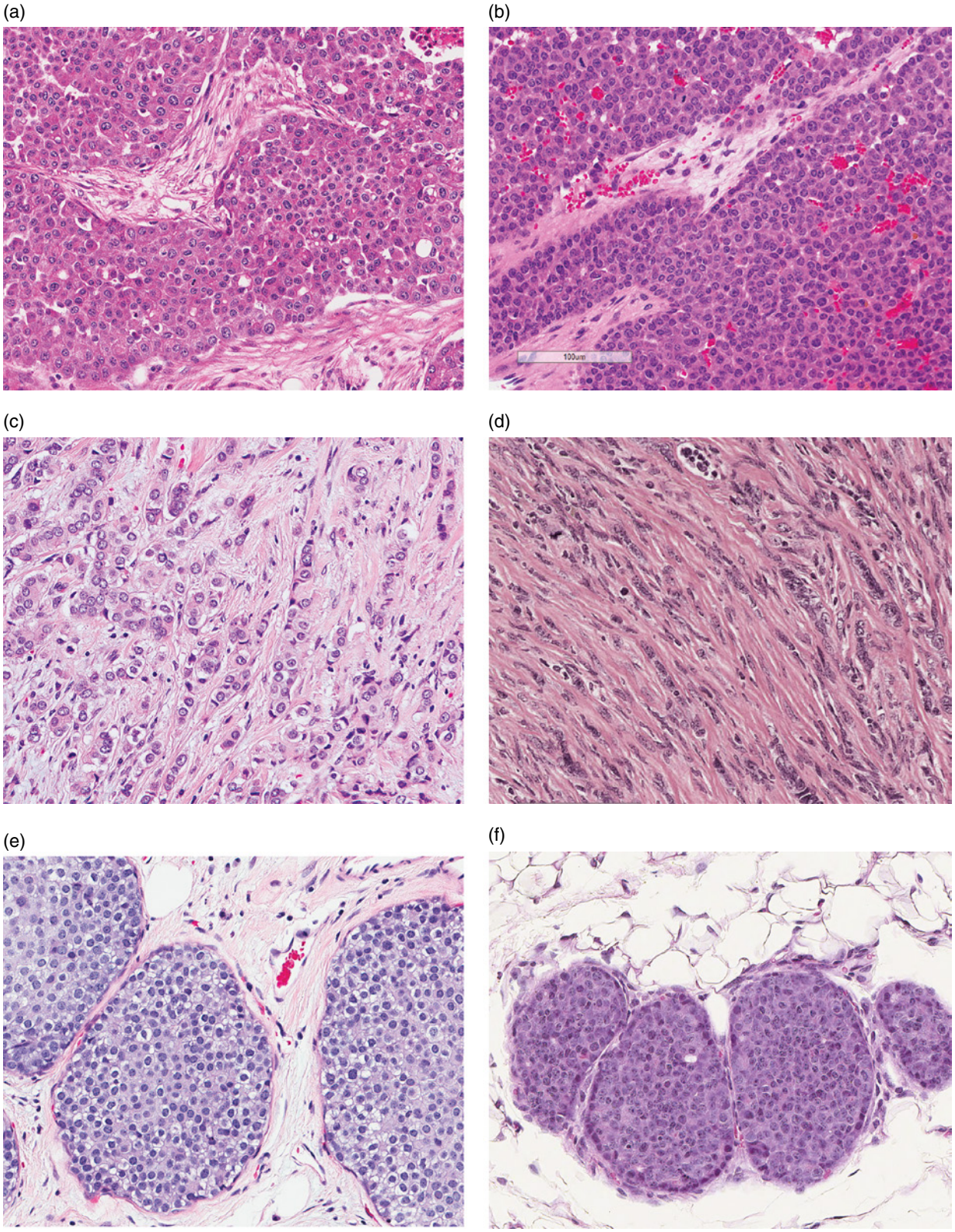


Figure 11.8 **Human-mouse comparisons**. Although the biology of mouse mammary tumorigenesis demonstrates close homology with the human disease, pathologist are always asked if the tumors "look like" human cancers. This figure provides some human-mouse "look a likes." Can you distinguish between mouse and human tumors in these comparisons? Images (a) and (b): Solid cords with fibrosis. (c) and (d): Single file strands of cells in a dense connective tissue. (e) and (f): Solid, nodular nests of cells without invasion.
Answers: Mouse (a), (d), (f), Human (b), (c), (e)
The full genotypes of (b), (c), and (e) are unknown. The mouse genotypes are the following:
(Please look these up in MGI and put in the correct nomenclature so we know what you are talking about)
(a): cNeu NDL (FVB/N-Tg(MMTV-ErbB2*)NDL2-5Mul)
(d): Trp53 null x CDh1 Null
(f): cNeu (NDL FVB/N-Tg(MMTV-ErbB2*)NDL2-5Mul)

Vet-ebooks.com

features that do not represent the original neoplasm. Again, this phenomenon is probably due to metaplastic changes in the cell population. A common example of epithelial metaplasia in mouse mammary tumors is squamous metaplasia. Squamous metaplasia also seems to correlate with tissue necrosis and healing. Another example is development of spindle cell tumors or EMT phenotype tumors (Figure 11.5d). Spindle cells, or carcinosarcomas, are particularly common in transplants from tissue culture cells [100]. In our experience, many of the serially transplanted mouse mammary tumors used in immunotherapy experiments are no longer epithelial tumors but spindle cell EMT tumors [100].

Important Techniques for the Evaluation of the Mammary Gland

An exhaustive library of methods and materials is available for the newcomer to mammary biology and pathology. We have listed several [7, 13, 22, 23, 27, 101–104]. Based on the above discussion, every mammary gland investigator and/or their pathologist need to master two techniques: Preparation of Mammary Gland Whole Mounts (Figure 11.2) and Mammary Gland Transplantation (Figure 11.1). Many descriptions of these two techniques are available and, in current times, a number of videos describing these methods are also available. Herein, we will discuss some of the problems observed when inexperienced, undertrained personnel are given the tasks.

Gross examination: The mouse mammary glands are arrayed along the milk line and lay in the subcutaneous tissue. Most mice can be gently held by the scruff of the neck and the 10–12 (depending on the mouse strain) easily identified by the nipples and palpated. The majority of GEM tumors initially arise beneath the nipples. Therefore, first palpate around each nipple. Most models exhibit tumor asymmetry with the neck and thoracic glands developing tumors before the inguinal glands. Some investigators, in palpating the first and second glands, mistake the salivary glands as mammary masses.

Tissue sampling: The mammary gland is an endocrine end organ. As such, it is very susceptible to alterations in other organs. Therefore, it is important to do a comprehensive necropsy, sampling, and saving other organs. The reproductive system with ovaries and vagina are of particular interest because they are indicators of estrus.

Other organs such as the Harderian glands are often enlarged in GEM experiments directed toward the mammary gland [105]. Most mouse mammary metastases are found in the lungs [44]. On the other hand, local lymph nodes are known to be occasional metastatic sites. Bulbourethral glands have been mistaken for #5 mammary tumors. The list can go further, but it is always wise to do a comprehensive necropsy for the model.

Preparation of Mammary Gland Whole Mounts

A good mammary gland whole mount can be stretched out on a glass microscopic slide, stained, and viewed in three dimensions under a dissecting microscope. This view provides a global, three-dimensional understanding of the mammary gland architecture. It is essential in understanding mammary growth and development, mammary abnormalities, and neoplastic development. Without the use of 3D whole mounts, critical but subtle morphological clues can be easily overlooked (Figures 11.2 and 11.9).

The most common errors by inexperienced dissectors are the lack of adequate spreading of the gland, reliance on a single gland sample, and inadequate "clearing" of the mammary gland.

The mammary gland is anatomically within a mammary fascia that needs to be recognized and utilized. The dissection should begin with an incision peripheral to the gland itself. The gland is embedded in this fascia on all surfaces, much like being in a sleeping bag. Removing the mammary glands from the lower surface of the skin, or the body wall, involves cutting peripheral to the gland itself to free the mammary fascia. The operator can then lift the edge of the fascia to dissect under the back (skin) side with a blunt instrument or with iridectomy scissors.

The number four glands (inguinal) are most frequently used for most studies. However, tumor formation and other interesting phenotypes occur more frequently in the upper three (thoracic) mammary glands. The thoracic glands are more difficult to dissect and spread and frequently ignored by the neophyte. The most common problem is the removal of the pectoral muscles from between the #3 and #2 glands. Recognizing the muscle and separating it from the mammary gland fascia takes experience and concerted effort. If the muscle is submitted with the glands, the sample is frequently crushed into a roll instead of being spread. While some detail can be seen in such preparations, the muscle obscures the field. Such samples demonstrate a lack of understanding of mouse mammary gland anatomy and biology.

Poor spreading of the gland results in overlapping ducts or tightly packed ducts. The experienced investigator will gently lay the fresh mammary fat pad containing the mammary gland on a flat surface such as a glass microscope slide. Then, grasping the edge of the mammary fascia with a fine-toothed forceps, gently tease the fascia toward the edge of the slide. One generally needs to tease around all four edges.

Some investigators are content to leave the sample on the slide during fixation and find it convenient to finish the staining for subgross examination on one slide. However, this can lead to uneven penetration and fixation, creating uneven distribution of the IHC labeling. In general, the mammary gland will stiffen in a couple of hours in formalin and may then be removed from the slide to more thoroughly fix the entire gland.

Vet-ebooks.com

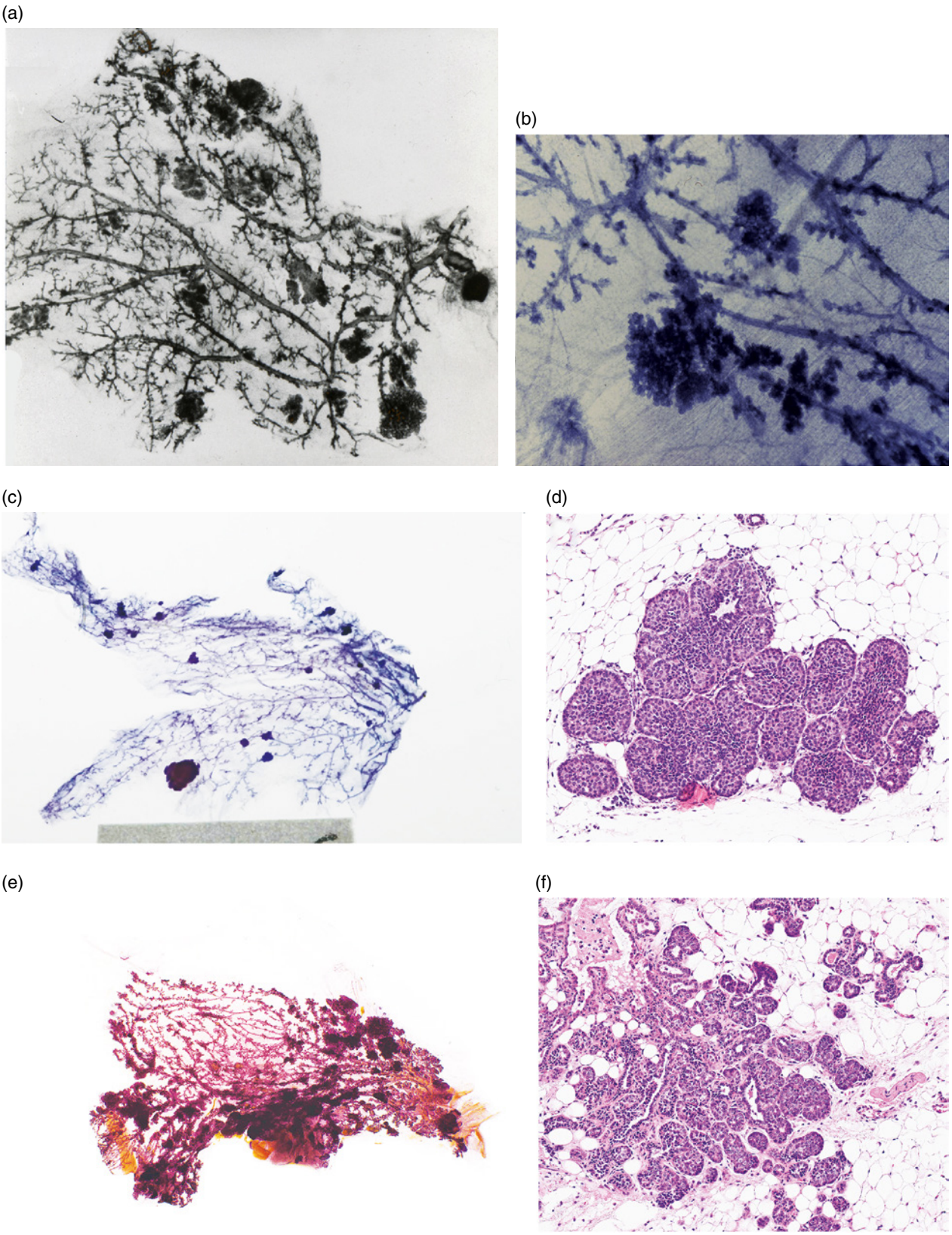


Figure 11.9 **Mammary Intraepithelial Neoplasia (MIN).** This figure illustrates the whole mount (a, c, e) and microscopic (b, d, f) images of precancerous lesions in MMTV-infected mice (a, b) (BALB/cfC3H), c, d: cNeu mice (FVB/N-Tg(MMTV-ErbB2*)NDL2-5Mul) and e, f: Polyoma Middle T FVB/N-Tg(MMTV-PyVT)634Mul/J mice. Note how the nonpalpable focal lesions stand out from the normal mammary background whole mounts and invasive lesions observed microscopically.

Vet-ebooks.com

Preparation of Lung Whole Mounts

The search for pulmonary metastases is essential for evaluation and interpretation of the biology of all mouse mammary cancers. Commonly, gross examination and a 10-µm microscopic sections are used to document and characterize pulmonary metastases. However, the more thorough approach is to inflate the lungs and examine them in three dimensions as whole mounts (Figure 11.4). A comprehensive guidelines for this procedure is available [106]. The location and nature of the metastases are generally visible in the whole mount. Subsequent histological examination can be used to confirm that the lesions are either peripheral microscopic metastases or the larger central embolic metastases. In some studies, the type of metastases proved to be critical [107].

Fixation and Processing

Tissue fixation and processing generally are standard techniques in established pathology laboratories. Occasionally, an investigator will find some reason to deviate from the routine neutral buffered 10% formalin fixation with paraffin embedding and hematoxylin and eosin (H&E) staining. The pathologist needs to be aware of how alternate fixatives and processing may affect the morphology and histochemistry of the samples [24–26, 71]. For example, alcohol fixation obliterates the anti-estrogen receptor IHC labeling and connective tissue stains more intensely red. Zinc fixatives, once touted for labeling immunocytes, are hypertonic and result in distorted histology. The litany can go on. Therefore, the pathologist has to be aware of the fixative used by the investigator. Alternatively, some IHC methods work better or only in specific fixatives, mandating optimizing methods prior to setting up a study.

Immunohistochemistry (IHC)

The investigators are often doing their own in-lab immunohistochemistry. Unfortunately, they are also interpreting (misinterpreting) the results [77]. Some labs do not run appropriate standards or positive and negative IHC controls. Fixation and processing can alter interpretation [71].

Mammary Gland Transplantation

A short history of the technique and other "*Mus* Musings" was published by Larry Young, one of the giants of the trade [108]. The T-by-T must be carried out in a gland-free mammary fat pad (Figure 11.1). Thus, the first step is to prepare a "gland cleared" mammary fat pad, the transplantation site. This site usually uses the number 4 mammary fat pads. The mammary bud originates from the underside of the nipple and does not extend into the fat pad until around the fourth week of life. Therefore, the surgical removal of the gland is performed on three-week-old females.

The proximal (nipple) end of the mammary fat pad of a three week old is removed by first identifying the veins and lymph node of the pad. The area between the lymph node and the nipple can be surgically removed, or cauterized, removing the immature, mammary tree. This creates a "gland free" mammary fat pad at the distal end to the pad. The transplantation is usually done at the time of "gland clearing." Alternately, the transplant may be delayed to use a more developed transplantation site.

The transplanted animals are then held and later examined for transplant outgrowths and/or tumors [31]. As illustrated (Figure 11.1), the experimental proof of biological potential depends on whether or not the tissue has malignant potential.

Transplantation can be used to evaluate mammary gland development [109] and the neoplastic potential of different mammary lesions [40]. Examples of complex analysis of multiple variables in mammary development in GEM and wild-type mice can be viewed elsewhere [13, 15].

The major use of the T-by-T has been in evaluating the neoplastic potential of a given mammary lesion [97]. Malignant tissue will grow in subcutaneous, nonmammary sites. However, normal duct will not grow outside of the mammary fat pad. Normal mammary gland transplants will fill the fat pad with a morphologically normal mammary tree. The transplanted mammary tree can be serial transplanted three or four times but begins to die back, an experiment in senescence of normal mammary epithelium.

In contrast, the premalignant HAN will not grow in ectopic sites, such as subcutaneous transplantation but will grow in the gland-cleared mammary fat pads. Generally, the MIN outgrowths are flat and contact inhibited to the limits of the fat pad [110]. MIN outgrowths do not senesce have been consecutively transplanted for many generations and years. They will develop tumors in a portion of the transplant. The tumors can be transplanted like any other malignancy.

Thus, the T-by-T has provided experimental proof of the premalignant state of the HAN and GEM. It supports the concept that DCIS in humans is a premalignant intermediate to breast cancer.

Host Response

The host response and the microenvironment are becoming increasingly important in assessing mammary gland neoplasia. At one level, many GEM tumors are expansile and do not elicit a substantial host response (Figure 11.1). They are classified as "immunologically ignorant" or "immune deserts." In contrast, some GEM mammary carcinomas elicit a marked host response. In the majority of these, however, very few of the immune cells penetrate into the tumor parenchyma. This pattern is referred to as an "excluded infiltrate" where although the host immune system is recruited to the site of tumor, the effector immune cells are prevented somehow of close interaction within the tumor. At a rudimentary level, the histopathological description should include an essential classification of the presence or absence of inflammation and the extent to which the inflammatory cells invade the tumor parenchyma. The responses have been classified no

Vet-ebooks.com

inflammation ("immunologically ignorant"), "excluded infiltrate," and "persisting immunity" with infiltration of the tumor parenchyma. Immune reactions can be characterized by the preponderance of cell types involved. In an effective anti-tumor response, $CD8^+$ T cells and macrophages are the commonest pattern, sometimes with remarkable $CD8^+$ T cell infiltration density. Neutrophils can sometimes be seen, in a more acute inflammatory pattern, but the initiators and effect of this type of reaction are less well understood. Eosinophils are thought to be a more important immune effector in mice than in humans, though there is evidence for eosinophilic responses in cancer in both species [111].

Case Study: 129S6/*SvEvTac-Stat1*^{tm1Rds} Mammary Biology and Tumorigenesis (Figures 11.2, 11.7, and 11.10)

We considered a number of different approaches for introducing the many different aspects of mammary biology that deserve your attention. However, each factor involves multiple technologies and diverse biologies that would consume too many pages. Instead, we provide a case study that includes factors such as developmental defects, mammary epithelium, the immune system, bone marrow, endocrine system, host responses, adipose tissue, the gynecological system, neoplasia, aging, and more. It illustrates the role of pathology in accessing these factors. This is the study of the remarkable *Stat1* null GEM (129S6/SvEvTac-*Stat1*^{tm1Rds}).

In 1996, a scientific team headed by Dr. R.D. Schreiber described a null mutation of the signal transducer and activator of transcription 1 (*Stat1*) gene in 129S6/SvEvTac mice [112]. They observed:

> Here we report the generation and characterization of mice deficient in STAT1. STAT1-deficient mice show no overt developmental abnormalities, but display a complete lack of responsiveness to either IFNα or IFNγ and are highly sensitive to infection by microbial pathogens and viruses. In contrast, these mice respond normally to several other cytokines that activate STAT1 in vitro.

A number of studies aimed at characterizing the defect followed with an emphasis on IFNG and NK cells [113, 114]. These mice were also used to document the effects of *Stat1* deletion on chemically induced tumor development. They became vital to Schreiber's classical immune-surveillance and immune-editing studies [115, 116].

Meanwhile, astute animal caretakers at Taconic observed that the Taconic *Stat1* null mice were developing spontaneous mammary gland tumors. Note that it was not a highly trained scientist who made the discovery, but an astute staff person who actually handled the mice. After establishing that the tumors were not viral-induced, Dr. Schreiber contacted the University of California, Davis (UCD) Mutant Mouse Pathology Lab.

Three tumors were sent to UCD in August 2002. The pathologist immediately informed Drs. Chan and Schreiber that, in our extensive experience with GEM mammary tumors, the tumor phenotypes were unique and not virus-induced. The spontaneous tumors in *Stat1* null females proved to be ER^+, PR^+, $FOXA1^+$ (Put all in caps if this is for IHC (protein) not transcript data) hormone sensitive [117]. This led to the very interesting collaboration exploring multiple variables described below.

Mammary Growth and Development

Dr. Jane Chen, Lab Chief, noticed that some of the 129S6/SvEvTac-*Stat1*^{tm1Rds} mice were runted and their mammary gland development stunted [109]. This was another key observation by someone who directly handled the mice. This led to a systematic search for the source of the underdevelopment. Another mammary biologist, Dr. Hidetoshi Mori noticed and documented that the TEBs were also abnormal (Figure 10.9a). Reciprocal transplants suggested that the KO fat pad and not the KO epithelium is defective. This deficiently could be overcome with a lactogenic hormone cocktail that included prolactin. Reciprocal bone marrow transplants into irradiated mice eliminated the hematopoietic system as the cause. Then, SSM2 cell line derived from a 129S6/SvEvTac-*Stat1*^{tm1Rds} KO tumor grew better in the WT animals than the KO hosts. This observation suggested that growth factors from the fat pads were important. Their cytokine profile was abnormally low. The low cytokine levels in the KO fat pads were restored by injection of the lactogenic hormone cocktail.

Tumorigenesis in aging females: The 129S6/SvEvTac-*Stat1*^{tm1Rds} develop tumors with a prolonged T50 of 91weeks in nulliparous females [20, 117, 118]. Multiparity lowers the T50 to 74 weeks. About 84% of the tumors occur in the thoracic glands. The pattern of preneoplastic lesions suggests isolated ductal branches are involved. The precancer and cancer cells are unique with large oval pale cytoplasm (LOP Cells) and large oval nuclei with prominent nuclei. The LOP cells have ER^+, PR^+, and $FOXA1^+$ nuclei (Figures 11.2 and 11.7). Additional abnormalities in the aged populations are present with a particularly abnormal reproductive tract including cystic ovaries.

Host response: The *Stat1* KO precancers and cancers are surrounded by a heavy host response composed of macrophages and T-cells. The analysis of this response demonstrated that the inflammation, although dense, surrounded the tumors but was excluded from the tumor (Figure 11.10). Using the SSM2 cell line, the tumor cells were found to secrete both macrophage migration-promoting and macrophage-inhibiting factors resulting in the "immune exclusion" phenotype [115].

Vet-ebooks.com

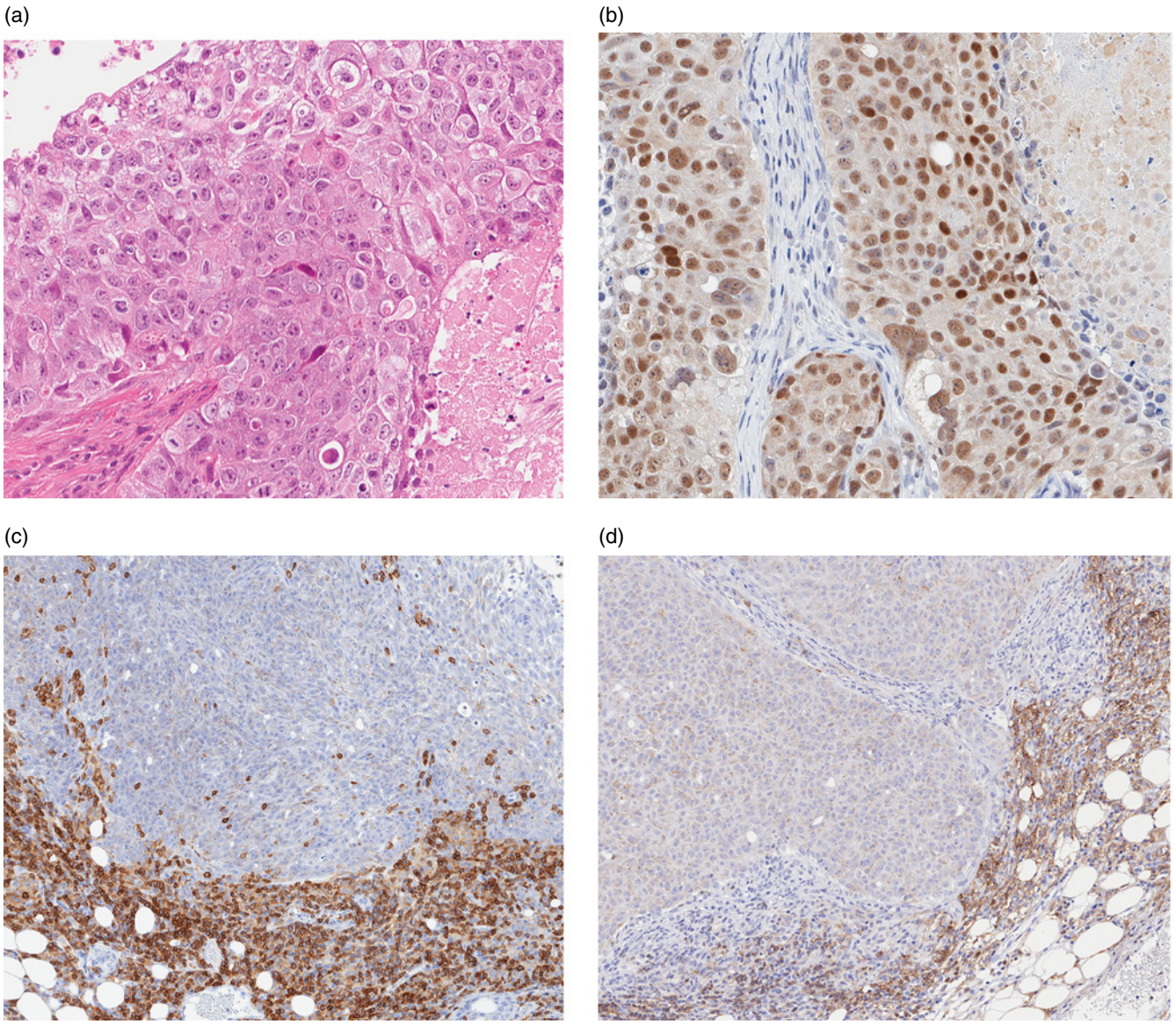


Figure 11.10 **Case study**. (a) A histological image of an HE stained *Stat1* KO tumor illustrating the large pale cells with abundant cytoplasm. (b) A FOXA1 IHC label of the tumor shown in figure (a). (c) The IHC label for F4/80 positive macrophages surrounding a *Stat1* KO tumor. Note that the macrophages form a very dense coat around the tumor but are excluded and do not penetrate the tumor. (d) The IHC label for CD3 positive lymphocytes (T cells) surrounding the same *Stat1* KO tumor. The T cells are excluded.

Molecular analysis: The molecular analyses of the primary tumors did not lead to a specific profile. However, subsequent molecular analysis has demonstrated (i) *Sox3* is involved [119] and (ii) the KO tumors have a mutant prolactin receptor [120].

Summary

129S6/SvEvTac-*Stat1*^{tm1Rds} mammary tumorigenesis is associated with important pathological features that make this model comparable to ER^{+} human luminal breast cancers. These include ductal origin, topographical asymmetry, age-related ablation of the ovaries, endocrine regulation, host immune response, and tumor-secreted factors. This model also uniquely reflects host–tumor relationships in an aging host.

This case study illustrates the role of pathology and the use of a numerous techniques documenting a complex tumor biology. An animal model, developed to study immunology, develops a complex of developmental defects and unusual mammary tumors that could have been overlooked or misinterpreted. However, careful attention to the biology, led by astute staff members, and discovery-intent pathobiologists reveals a unique, multifactorial tumor biology.

Vet-ebooks.com

Internet Resources

Journal of Mammary Biology and Neoplasia:
A scholarly review journal with articles by experts since 1996 (https://link.springer.com/journal/10911/volumes-and-issues)
Mammary Gland Whole Mounts:
https://bio-protocol.org/e2915
https://www.jove.com/video/55796/sectioning-mammary-gland-whole-mounts-for-lesion-identification
Inflating Mouse Lung:
https://www.ncbi.nlm.nih.gov/pmc/articles/PMC4692577/
Mouse Pathology:
https://www.jax.org/research-and-faculty/resources/mouse-disease-information-system
http://spectrum.ucdavis.edu/Welcome.php (enter as Guest/guest, Collection of whole slide images from Mouse Models of Human Cancers Consortium)
http://www.pathbase.net/Links/index.php (European archives)
https://www.proteinatlas.org/search/mouse (quick guide to mouse IHC)

References

1 Cardiff, R.D. and Kenney, N. (2007). Mouse mammary tumor biology: a short history. *Adv. Cancer Res.* 98: 53–116.
2 Cardiff, R.D. and Kenney, N. (2011). A compendium of the mouse mammary tumor biologist: from the initial observations in the house mouse to the development of genetically engineered mice. *Cold Spring Harbor Perspect. Biol.* 3 (6): 1–11.
3 Daley, G.Q. (1993). Animal models of BCR/ABL-induced leukemias. *Leuk. Lymphoma* 11 (Suppl 1): 57–60.
4 Stewart, T.A., Pattengale, P.K., and Leder, P. (1984). Spontaneous mammary adenocarcinomas in transgenic mice that carry and express MTV/myc fusion genes. *Cell* 38 (3): 627–637.
5 Salvi, M. (2001). Transforming animal species: the case of 'oncomouse'. *Sci. Eng. Ethics* 7 (1): 15–28.
6 Ince, T.A., Ward, J.M., Valli, V.E. et al. (2008). Do-it-yourself (DIY) pathology. *Nat. Biotechnol.* 26 (9) 978–9; discussion 9.
7 Cardiff, R.D. (2009). How to phenotype a mouse. *Dis. Models Mech.* 2 (7–8): 317–321.
8 Ackerman, A.B., Kessler, G., Gyorfi, T. et al. (2007). Contrary view: the breast is not an organ per se, but a distinctive region of skin and subcutaneous tissue. *Am. J. Dermatopathol.* 29 (2): 211–218.
9 Cardiff, R.D., Jindal, S., Treuting, P.M. et al. (2018). Mammary gland. In: *Comparative Anatomy and Histology: A Mouse, Rat, and Human Atlas*, xviii, 487–509, 2e (eds. P.M. Treuting, S.M. Dintzis and K.S. Montine). London: Elsevier/Academic Press.
10 Mikkola, M.L. and Millar, S.E. (2006). The mammary bud as a skin appendage: unique and shared aspects of development. *J. Mammary Gland Biol. Neoplasia* 11 (3): 187–203.
11 Paine, I.S. and Lewis, M.T. (2017). The terminal end bud: the little engine that could. *J. Mammary Gland Biol. Neoplasia* 22 (2): 93–108.
12 Hovey, R.C. and Aimo, L. (2010). Diverse and active roles for adipocytes during mammary gland growth and function. *J. Mammary Gland Biol. Neoplasia* 15 (3): 279–290.
13 Richert, M.M., Schwertfeger, K.L., Ryder, J.W., and Anderson, S.M. (2000). An atlas of mouse mammary gland development. *J. Mammary Gland Biol. Neoplasia* 5 (2): 227–241.
14 Frank-Kamenetskii, A. and Booth, B.W. (2019). Redirecting Normal and cancer stem cells to a mammary epithelial cell fate. *J. Mammary Gland Biol. Neoplasia* 24 (4): 285–292.
15 Rudolph, M.C., McManaman, J.L., Hunter, L. et al. (2003). Functional development of the mammary gland: use of expression profiling and trajectory clustering to reveal changes in gene expression during pregnancy, lactation, and involution. *J. Mammary Gland Biol. Neoplasia* 8 (3): 287–307.
16 Plaut, K. and Carraway, K.L. (2002). Preface: evolution and comparative biology of the mammary gland. *J. Mammary Gland Biol. Neoplasia* 7 (3): 223–224.
17 Blacher, S., Gerard, C., Gallez, A. et al. (2016). Quantitative assessment of mouse mammary gland morphology using automated digital image processing and TEB detection. *Endocrinology* 157 (4): 1709–1716.
18 Stein, T., Salomonis, N., and Gusterson, B.A. (2007). Mammary gland involution as a multi-step process. *J. Mammary Gland Biol. Neoplasia* 12 (1): 25–35.
19 Palmer, C.A., Neville, M.C., Anderson, S.M., and McManaman, J.L. (2006). Analysis of lactation defects in transgenic mice. *J. Mammary Gland Biol. Neoplasia* 11 (3): 269–282.
20 Mori, H., Cardiff, R.D., and Borowsky, A.D. (2018). Aging mouse models reveal complex tumor-microenvironment interactions in cancer progression. *Front. Cell Dev. Biol.* 6: 35.
21 Chepko, G. and Smith, G.H. (1999). Mammary epithelial stem cells: our current understanding. *J. Mammary Gland Biol. Neoplasia* 4 (1): 35–52.
22 Green, J.E. (2012). *Genetically Engineered Mice for Cancer Research Design, Analysis, Pathways, Validation and Pre-Clinical Testing*, 632. New York/Dordrecht/Heidelberg/London: SpringerLink.
23 Cardiff, R.D., Miller, C.H., and Munn, R.J. (2014). Analysis of mouse model pathology: a primer for studying the anatomic pathology of genetically engineered mice. *Cold Spring Harbor Protoc.* 2014 (6): 561–580.

Vet-ebooks.com

24 Cardiff, R.D., Miller, C.H., and Munn, R.J. (2014). Manual immunohistochemistry staining of mouse tissues using the avidin-biotin complex (ABC) technique. *Cold Spring Harbor Protoc.* 2014 (6): 659–662.

25 Cardiff, R.D., Miller, C.H., and Munn, R.J. (2014). Manual hematoxylin and eosin staining of mouse tissue sections. *Cold Spring Harbor Protoc.* 2014 (6): 655–658.

26 Cardiff, R.D., Miller, C.H., and Munn, R.J. (2014). Mouse tissue fixation. *Cold Spring Harbor Protoc.* 2014 (5): 522–524.

27 Cardiff, R.D., Miller, C.H., and Munn, R.J. (2014). Limited mouse necropsy. *Cold Spring Harbor Protoc.* 2014 (5): 518–521.

28 Cardiff, R.D., Miller, C.H., Munn, R.J., and Galvez, J.J. (2014). Structured reporting in anatomic pathology for coclinical trials: the caELMIR model. *Cold Spring Harbor Protoc.* 2014 (1): 32–43.

29 Rudmann, D., Cardiff, R., Chouinard, L. et al. (2012). Proliferative and nonproliferative lesions of the rat and mouse mammary, Zymbal's, preputial, and clitoral glands. *Toxicol. Pathol.* 40 (6 Suppl): 7S–39S.

30 Currier, N., Solomon, S.E., Demicco, E.G. et al. (2005). Oncogenic signaling pathways activated in DMBA-induced mouse mammary tumors. *Toxicol. Pathol.* 33 (6): 726–737.

31 Cardiff, R.D. and Borowsky, A.D. (2011). Precancer: sequentially acquired or predetermined? In: *Pre-Invasive Disease: Pathogenesis and Clinical Management* (ed. R.C. Fitzgerald), 131–150. New York: Springer.

32 Wellings, S.R., Jensen, H.M., and Marcum, R.G. (1975). An atlas of subgross pathology of the human breast with special reference to possible precancerous lesions. *J. Natl. Cancer Inst.* 55 (2): 231–273.

33 Foulds, L. (1965). Multiple etiologic factors in neoplastic development. *Cancer Res.* 25 (8): 1339–1347.

34 Foulds, L. (1964). Some general principles of neoplastic development. *Acta Unio Int. Contra Cancrum* 20: 663–666.

35 Blair, P.B. and DeOme, K.B. (1961). Mammary tumor development in transplanted hyperplastic alveolar nodules of the mouse. *Proc. Soc. Exp. Biol. Med.* 108: 289–291.

36 DeOme, K.B., Faulkin, L.J. Jr., Bern, H.A., and Blair, P.B. (1959). Development of mammary tumors from hyperplastic alveolar nodules transplanted into gland-free mammary fat pads of female C3H mice. *Cancer Res.* 19 (5): 515–520.

37 D'Cruz, C.M., Gunther, E.J., Boxer, R.B. et al. (2001). c-MYC induces mammary tumorigenesis by means of a preferred pathway involving spontaneous Kras2 mutations. *Nat. Med.* 7 (2): 235–239.

38 Maglione, J.E., Moghanaki, D., Young, L.J. et al. (2001). Transgenic Polyoma middle-T mice model premalignant mammary disease. *Cancer Res.* 61 (22): 8298–8305.

39 Lin, T.P., Guzman, R.C., Osborn, R.C. et al. (1992). Role of endocrine, autocrine, and paracrine interactions in the development of mammary hyperplasia in Wnt-1 transgenic mice. *Cancer Res.* 52 (16): 4413–4419.

40 Cardiff, R.D., Anver, M.R., Boivin, G.P. et al. (2006). Precancer in mice: animal models used to understand, prevent, and treat human precancers. *Toxicol. Pathol.* 34 (6): 699–707.

41 Mukhtar, R.A., Wong, J.M., and Esserman, L.J. (2015). Preventing overdiagnosis and overtreatment: just the next step in the evolution of breast cancer care. *J. Natl. Compr. Cancer Netw.* 13 (6): 737–743.

42 Cardiff, R.D., Anver, M.R., Gusterson, B.A. et al. (2000). The mammary pathology of genetically engineered mice: the consensus report and recommendations from the Annapolis meeting. *Oncogene* 19 (8): 968–988.

43 Oshima, R.G., Lesperance, J., Munoz, V. et al. (2004). Angiogenic acceleration of Neu induced mammary tumor progression and metastasis. *Cancer Res.* 64 (1): 169–179.

44 Vaage, J. and Harlos, J.P. (1987). Spontaneous metastasis from primary C3H mouse mammary tumors. *Cancer Res.* 47 (2): 547–550.

45 Tarin, D. (1985). Clinical and experimental studies on the biology of metastasis. *Biochim. Biophys. Acta* 780 (3): 227–235.

46 Bruno, R.D. and Smith, G.H. (2011). Functional characterization of stem cell activity in the mouse mammary gland. *Stem Cell Rev. Rep.* 7 (2): 238–247.

47 Swiatnicki, M.R. and Andrechek, E.R. (2019). How to choose a mouse model of breast cancer, a genomic perspective. *J. Mammary Gland Biol. Neoplasia* 24 (3): 231–243.

48 Shen, Q. and Brown, P.H. (2005). Transgenic mouse models for the prevention of breast cancer. *Mutat. Res.* 576 (1–2): 93–110.

49 Huang, A.L., Ostrowski, M.C., Berard, D., and Hager, G.L. (1981). Glucocorticoid regulation of the Ha-MuSV p21 gene conferred by sequences from mouse mammary tumor virus. *Cell* 27 (2 Pt 1): 245–255.

50 Hsu, K., Lee, Y.K., Chew, A. et al. (2017). Inherently variable responses to glucocorticoid stress among endogenous retroviruses isolated from 23 mouse strains. *Biochim. Biophys. Acta, Mol. Basis Dis.* 1863 (10 Pt B): 2594–2600.

51 Meyer, D.S., Koren, S., Leroy, C. et al. (2013). Expression of PIK3CA mutant E545K in the mammary gland induces heterogeneous tumors but is less potent than mutant H1047R. *Oncogenesis* 2: e74.

52 Meyer, D.S., Brinkhaus, H., Muller, U. et al. (2011). Luminal expression of PIK3CA mutant H1047R in the mammary gland induces heterogeneous tumors. *Cancer Res.* 71 (13): 4344–4351.

53 Koren, S., Reavie, L., Couto, J.P. et al. (2015). PIK3CA(H1047R) induces multipotency and multi-lineage mammary tumours. *Nature* 525 (7567): 114–118.

54 Ursini-Siegel, J., Schade, B., Cardiff, R.D., and Muller, W.J. (2007). Insights from transgenic mouse models of ERBB2-induced breast cancer. *Nat. Rev. Cancer* 7 (5): 389–397.

55 Couto, S.S., Bolon, B., and Cardiff, R.D. (2012). Morphologic manifestations of gene-specific molecular alterations ("genetic addictions") in mouse models of disease. *Vet. Pathol.* 49 (1): 116–129.

56 Moody, S.E., Perez, D., Pan, T.C. et al. (2005). The transcriptional repressor Snail promotes mammary tumor recurrence. *Cancer Cell* 8 (3): 197–209.

57 Cardiff, R.D., Couto, S., and Bolon, B. (2011). Three interrelated themes in current breast cancer research: gene addiction, phenotypic plasticity, and cancer stem cells. *Breast Cancer Res.* 13 (5): 216.

Vet-ebooks.com

58 Berman, J.J., Albores-Saavedra, J., Bostwick, D. et al. (2006). Precancer: a conceptual working definition – results of a Consensus Conference. *Cancer Detect. Prev.* 30 (5): 387–394.

59 Piersigilli, A., Borowsky, A.D., Chen, Q. et al. (2015). Current concepts and new insights from mouse models of mammary tumors on epithelial mesenchymal transition and its synergy with mutant p53. *J. Anal. Oncol.* 4 (4): 191–206.

60 Borowsky, A., Galvez, J., Munn, R., and Cardiff, R. (2003). Comparative pathology of mouse models of human cancers. *Comp. Med.* 53 (3): 248–249.

61 Nieto, A.I., Shyamala, G., Galvez, J.J. et al. (2003). Persistent mammary hyperplasia in FVB/N mice. *Comp. Med.* 53 (4): 433–438.

62 Cardiff, R.D. (2010). The pathology of EMT in mouse mammary tumorigenesis. *J. Mammary Gland Biol. Neoplasia* 15 (2): 225–233.

63 Miyoshi, K., Rosner, A., Nozawa, M. et al. (2002). Activation of different Wnt/beta-catenin signaling components in mammary epithelium induces transdifferentiation and the formation of pilar tumors. *Oncogene* 21 (36): 5548–5556.

64 Penzvalto, Z., Chen, J.Q., Tepper, C.G. et al. (2019). A syngeneic ErbB2 mammary cancer model for preclinical immunotherapy trials. *J. Mammary Gland Biol. Neoplasia* 24 (2): 149–162.

65 Siegel, P.M., Ryan, E.D., Cardiff, R.D., and Muller, W.J. (1999). Elevated expression of activated forms of Neu/ErbB-2 and ErbB-3 are involved in the induction of mammary tumors in transgenic mice: implications for human breast cancer. *EMBO J.* 18 (8): 2149–2164.

66 Friedrich, G. and Soriano, P. (1991). Promoter traps in embryonic stem cells: a genetic screen to identify and mutate developmental genes in mice. *Genes Dev.* 5 (9): 1513–1523.

67 Boone, P.G., Rochelle, L.K., Ginzel, J.D. et al. (2019). A cancer rainbow mouse for visualizing the functional genomics of oncogenic clonal expansion. *Nat. Commun.* 10 (1): 5490.

68 Moody, S.E., Sarkisian, C.J., Hahn, K.T. et al. (2002). Conditional activation of Neu in the mammary epithelium of transgenic mice results in reversible pulmonary metastasis. *Cancer Cell* 2 (6): 451–461.

69 Vinall, R.L., Chen, J.Q., Hubbard, N.E. et al. (2012). Initiation of prostate cancer in mice by Tp53R270H: evidence for an alternative molecular progression. *Dis. Models Mech.* 5 (6): 914–920.

70 Dunbar, M.E., Dann, P., Brown, C.W. et al. (2001). Temporally regulated overexpression of parathyroid hormone-related protein in the mammary gland reveals distinct fetal and pubertal phenotypes. *J. Endocrinol.* 171 (3): 403–416.

71 Cardiff, R.D., Hubbard, N.E., Engelberg, J.A. et al. (2013). Quantitation of fixative-induced morphologic and antigenic variation in mouse and human breast cancers. *Lab. Invest.* 93 (4): 480–497.

72 Lifsted, T., Le Voyer, T., Williams, M. et al. (1998). Identification of inbred mouse strains harboring genetic modifiers of mammary tumor age of onset and metastatic progression. *Int. J. Cancer* 77 (4): 640–644.

73 Wakefield, L.M., Thordarson, G., Nieto, A.I. et al. (2003). Spontaneous pituitary abnormalities and mammary hyperplasia in FVB/NCr mice: implications for mouse modeling. *Comp. Med.* 53 (4): 424–432.

74 Radaelli, E., Arnold, A., Papanikolaou, A. et al. (2009). Mammary tumor phenotypes in wild-type aging female FVB/N mice with pituitary prolactinomas. *Vet. Pathol.* 46 (4): 736–745.

75 Nikitin, A.Y., Alcaraz, A., Anver, M.R. et al. (2004). Classification of proliferative pulmonary lesions of the mouse: recommendations of the mouse models of human cancers consortium. *Cancer Res.* 64 (7): 2307–2316.

76 Yang, X., Edgerton, S.M., Kosanke, S.D. et al. (2003). Hormonal and dietary modulation of mammary carcinogenesis in mouse mammary tumor virus-c-erbB-2 transgenic mice. *Cancer Res.* 63 (10): 2425–2433.

77 Ward, J.M., Schofield, P.N., and Sundberg, J.P. (2017). Reproducibility of histopathological findings in experimental pathology of the mouse: a sorry tail. *Lab Anim.* 46 (4): 146–151.

78 Borowsky, A.D. (2011). Choosing a mouse model: experimental biology in context – the utility and limitations of mouse models of breast cancer. *Cold Spring Harbor Perspect. Biol.* 3 (9): a009670.

79 Cardiff, R.D. (2007). Pathologists needed to cope with mutant mice. *Nature* 447 (7144): 528.

80 Cardiff, R.D., Ward, J.M., and Barthold, S.W. (2008). 'One medicine - one pathology': are veterinary and human pathology prepared? *Lab. Invest.* 88 (1): 18–26.

81 Schofield, P.N., Brown, S.D., Sundberg, J.P. et al. (2009). PRIME importance of pathology expertise. *Nat. Biotechnol.* 27 (1): 24–25.

82 Elmore, S.A., Cardiff, R., Cesta, M.F. et al. (2018). A review of current standards and the evolution of histopathology nomenclature for laboratory animals. *ILAR J.* 59 (1): 29–39.

83 Rosner, A., Miyoshi, K., Landesman-Bollag, E. et al. (2002). Pathway pathology: histological differences between ErbB/Ras and Wnt pathway transgenic mammary tumors. *Am. J. Pathol.* 161 (3): 1087–1097.

84 Cardiff, R.D. and Munn, R.J. (1998). The histopathology of transgenes and knockouts in the mammary gland. In: *Advances in Oncobiology*, vol. 2 (eds. E.E. Bittar, G. Heppner, W.P. Peters and D.W. Visscher), 117–202. JAI Press Inc.

85 Mori, H., Chen, J.Q., Cardiff, R.D. et al. (2017). Pathobiology of the 129:Stat1 −/− mouse model of human age-related ER-positive breast cancer with an immune infiltrate-excluded phenotype. *Breast Cancer Res.* 19 (1): 102.

86 Hollern, D.P., Swiatnicki, M.R., and Andrechek, E.R. (2018). Histological subtypes of mouse mammary tumors reveal conserved relationships to human cancers. *PLoS Genet.* 14 (1): e1007135.

87 McCarthy, A., Savage, K., Gabriel, A. et al. (2007). A mouse model of basal-like breast carcinoma with metaplastic elements. *J. Pathol.* 211 (4): 389–398.

Vet-ebooks.com

88 Cardiff, R.D., Bern, H.A., Faulkin, L.J. et al. (2002). Contributions of mouse biology to breast cancer research. *Comp. Med.* 52 (1): 12–31.

89 Cardiff, R.D., Wagner, U., and Hennighausen, L. (2000). Mammary cancer in humans and mice: a tutorial for comparative pathology. The CD-ROM. *J. Mammary Gland Biol. Neoplasia* 5 (2): 243–244.

90 Cardiff, R.D. (2003). Mouse models of human breast cancer. *Comp. Med.* 53 (3): 250–253.

91 Cardiff, R.D. (1998). Are the TDLU of the human the same as the LA of mice? *J. Mammary Gland Biol. Neoplasia* 3 (1): 3–5.

92 Cardiff, R.D., Wagner, U., and Hennighausen, L. (2001). Mammary cancer in humans and mice: a tutorial for comparative pathology. *Vet. Pathol.* 38 (4): 357–358.

93 Cardiff, R.D. and Wellings, S.R. (1999). The comparative pathology of human and mouse mammary glands. *J. Mammary Gland Biol. Neoplasia* 4 (1): 105–122.

94 Derksen, P.W., Liu, X., Saridin, F. et al. (2006). Somatic inactivation of E-cadherin and p53 in mice leads to metastatic lobular mammary carcinoma through induction of anoikis resistance and angiogenesis. *Cancer Cell* 10 (5): 437–449.

95 Cardiff, R.D., Moghanaki, D., and Jensen, R.A. (2000). Genetically engineered mouse models of mammary intraepithelial neoplasia. *J. Mammary Gland Biol. Neoplasia* 5 (4): 421–437.

96 Cardiff, R.D., Rosner, A., Hogarth, M.A. et al. (2004). Validation: the new challenge for pathology. *Toxicol. Pathol.* 32 (Suppl 1): 31–39.

97 Cardiff, R.D. and Borowsky, A.D. (2010). Precancer: sequentially acquired or predetermined? *Toxicol. Pathol.* 38 (1): 171–179.

98 Dovas, A., Patsialou, A., Harney, A.S. et al. (2013). Imaging interactions between macrophages and tumour cells that are involved in metastasis in vivo and in vitro. *J. Microsc.* 251 (3): 261–269.

99 Sugino, T., Kusakabe, T., Hoshi, N. et al. (2002). An invasion-independent pathway of blood-borne metastasis: a new murine mammary tumor model. *Am. J. Pathol.* 160 (6): 1973–1980.

100 Watson, K.D., Lai, C.Y., Qin, S. et al. (2012). Ultrasound increases nanoparticle delivery by reducing intratumoral pressure and increasing transport in epithelial and epithelial-mesenchymal transition tumors. *Cancer Res.* 72 (6): 1485–1493.

101 Abate-Shen, C., Politi, K., Chodosh, L.A., and Olive, K.P. (2014). *Mouse Models of Cancer: A Laboratory Manual*, xiv, 521p. Cold Spring Harbor, New York: Cold Spring Harbor Laboratory Press.

102 Ip, M.M. and Asch, B.B. (2012). *Methods in Mammary Gland Biology and Breast Cancer Research*. New York, USA: Springer.

103 Lewis, M.T. and Porter, W.W. (2009). Methods in mammary gland biology and breast cancer research: an update. *J. Mammary Gland Biol. Neoplasia* 14 (4): 365.

104 Treuting, P.M., Dintzis, S.M., Frevert, C.W. et al. (2012). *Comparative Anatomy and Histology: A Mouse and Human Atlas*, xii, 461 p, 1e. Amsterdam/Boston, MA: Elsevier/Academic Press.

105 Thomas, H., Hanby, A.M., Smith, R.A. et al. (1996). An inbred colony of oncogene transgenic mice: diversity of tumours and potential as a therapeutic model. *Br. J. Cancer* 73 (1): 65–72.

106 Morton, J. and Snider, T.A. (2017). Guidelines for collection and processing of lungs from aged mice for histological studies. *Pathobiol. Aging Age Relat. Dis.* 7 (1): 1313676.

107 Siegel, P.M., Shu, W., Cardiff, R.D. et al. (2003). Transforming growth factor beta signaling impairs Neu-induced mammary tumorigenesis while promoting pulmonary metastasis. *Proc. Natl. Acad. Sci. U.S.A.* 100 (14): 8430–8435.

108 Young, L.J. (2008). Mus tales: a hands-on view. *J. Mammary Gland Biol. Neoplasia* 13 (3): 343–349.

109 Chen, J.Q., Mori, H., Cardiff, R.D. et al. (2015). Abnormal mammary development in 129:STAT1-null mice is stroma-dependent. *PLoS One* 10 (6): e0129895.

110 Ornitz, D.M., Cardiff, R.D., Kuo, A., and Leder, P. (1992). Int-2, an autocrine and/or ultra-short-range effector in transgenic mammary tissue transplants. *J. Natl. Cancer Inst.* 84 (11): 887–892.

111 Hegde, P.S., Karanikas, V., and Evers, S. (2016). The where, the when, and the how of immune monitoring for cancer immunotherapies in the era of checkpoint inhibition. *Clin. Cancer Res.* 22 (8): 1865–1874.

112 Meraz, M.A., White, J.M., Sheehan, K.C. et al. (1996). Targeted disruption of the Stat1 gene in mice reveals unexpected physiologic specificity in the JAK-STAT signaling pathway. *Cell* 84 (3): 431–442.

113 O'Shea, J.J., Gadina, M., and Schreiber, R.D. (2002). Cytokine signaling in 2002: new surprises in the Jak/Stat pathway. *Cell* 109 (Suppl): S121–S131.

114 Ramana, C.V., Gil, M.P., Schreiber, R.D., and Stark, G.R. (2002). Stat1-dependent and -independent pathways in IFN-gamma-dependent signaling. *Trends Immunol.* 23 (2): 96–101.

115 Vesely, M.D. and Schreiber, R.D. (2013). Cancer immunoediting: antigens, mechanisms, and implications to cancer immunotherapy. *Ann. N.Y. Acad. Sci.* 1284: 1–5.

116 Dunn, G.P., Ikeda, H., Bruce, A.T. et al. (2005). Interferon-gamma and cancer immunoediting. *Immunol. Res.* 32 (1–3): 231–245.

117 Chan, S.R., Vermi, W., Luo, J. et al. (2012). STAT1-deficient mice spontaneously develop estrogen receptor alpha-positive luminal mammary carcinomas. *Breast Cancer Res.* 14 (1): R16.

118 Mori, H. and Cardiff, R.D. (2016). Methods of immunohistochemistry and immunofluorescence: converting invisible to visible. *Methods Mol. Biol.* 1458: 1–12.

119 Chan, S.R., Rickert, C.G., Vermi, W. et al. (2014). Dysregulated STAT1-SOCS1 control of JAK2 promotes mammary luminal progenitor cell survival and drives ERalpha(+) tumorigenesis. *Cell Death Differ.* 21 (2): 234–246.

120 Griffith, O.L., Chan, S.R., Griffith, M. et al. (2016). Truncating prolactin receptor mutations promote tumor growth in murine estrogen receptor-alpha mammary carcinomas. *Cell Rep.* 17 (1): 249–260.

Vet-ebooks.com

12

The Respiratory Tract

Jerrold M. Ward and John P. Sundberg

Introduction

The respiratory tract includes the upper (nose, sinuses, pharynx, and larynx) and lower (trachea and lung) tracts. It serves as the entry way and portal for air with oxygen needed for body functions. The nasal cavity also serves as a clearance for inhaled foreign materials and the sense of smell (olfaction). It is susceptible to many insults including infectious agents and toxins. Genetically-engineered mice (GEM) have been used to study the development, susceptibility to disease, and genetic diseases of the respiratory tract.

The Upper Respiratory Tract

Anatomy and Histology

The anatomy and histology of the mouse nose, sinuses, pharynx, and larynx are well described. Necropsy and trimming protocols are defined for histopathology [1, 2]. Trimming protocols include whole head sectioning [3]. The nose is composed of the nasal passage, nasal turbinates, paranasal sinuses, and olfactory organs. Nasal associated lymphoid tissue (NALT) is found in mice. The nose serves as a filtering system for inhaled air and particles found in the environment. The olfactory epithelium is important for smell and has recently assumed a region for concern in coronavirus infection of the epithelium and brain in animals and humans [4].

Developmental Defects

When evaluating mice with skeletal and, in particular, head abnormalities, it is important to screen for cleft palates which may or may not be part of the phenotype [5]. Cleft palates can result in aspiration pneumonia. With the exception of C3H/HeJ mice, one of the few strains that commonly get aspiration pneumonia, this should be rarely, if ever seen in routine screening of sick mice without other problems (Sundberg unpublished observations).

Abnormalities in the upper respiratory track have long been a focus for the development of mouse models, especially cleft palate, as this is a frequent multifactorial human congenital anomaly. This should be an obvious gross lesion that might be found during routine necropsy of a sick mouse or as part of a detailed evaluation. Although it can be easily overlooked at the gross level, it may still be found by histologic evaluation. A number of reviews document various mouse models although one stated "Human and mouse facial traits are utterly dissimilar. However, embryonic development of the lip and palate are strikingly similar in both species, making the mouse a model of choice to study their normal and abnormal development" [6]. Contrary to this statement, a later review by the same author stated "This small mammal's (*mouse*) usefulness in cleft lip and palate research stems not only from the striking anatomical and molecular similarities of lip and palate development between human and mouse embryos, but also from its amenability to experimental and genetic manipulation" [7]. These contradictory comments reflect better understanding over time of the complexity of anterior-specific palatal fusion in mammals. Many genes exert various degrees of effects on this process. A combination of discovery in single mutant studies, transcriptome studies, and human genetic analyses have yielded many candidate genes, molecular pathways, and GEMs [8, 9]. When searching for cleft palate in Mouse Genome Informatics (MGI) (searched 5 January 2021), 659 genotypes with 853 annotations were displayed revealing the molecular complexity of this seemingly simple abnormality. Genes and specific allelic mutations are listed providing a massive list.

Pathology of the Nose

Spontaneous lesions in the mouse nose are generally mild in young animals and age-related lesions may be more severe including focal inflammation, hyalinosis (Figure 12.1), and rare tumors. Hyalinosis will be discussed in "The Lung" section. The nose is very important in inhalation toxicology studies and is well studied by toxicologic pathologists [1]. The nose is also important in experimental infections of the

Pathology of Genetically Engineered and Other Mutant Mice, First Edition. Edited by John P. Sundberg, Peter Vogel, and Jerrold M. Ward.
© 2022 John Wiley & Sons, Inc. Published 2022 by John Wiley & Sons, Inc.

Vet-ebooks.com

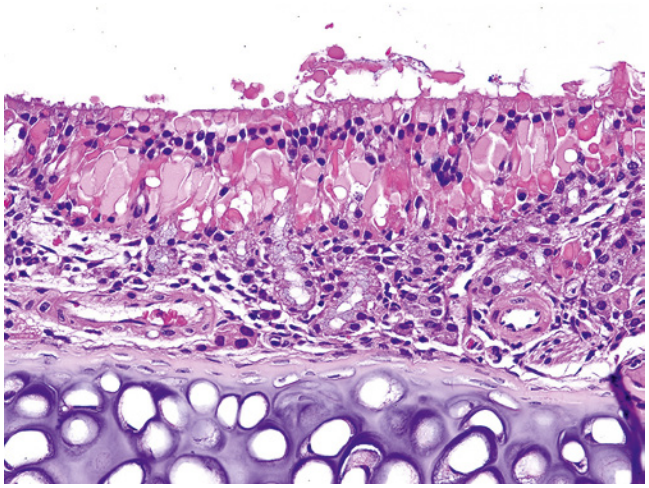


Figure 12.1 Nasal hyalinosis. Eosinophilic protein inclusions and a few intracellular crystals can be seen in the olfactory epithelium of an aging mouse.

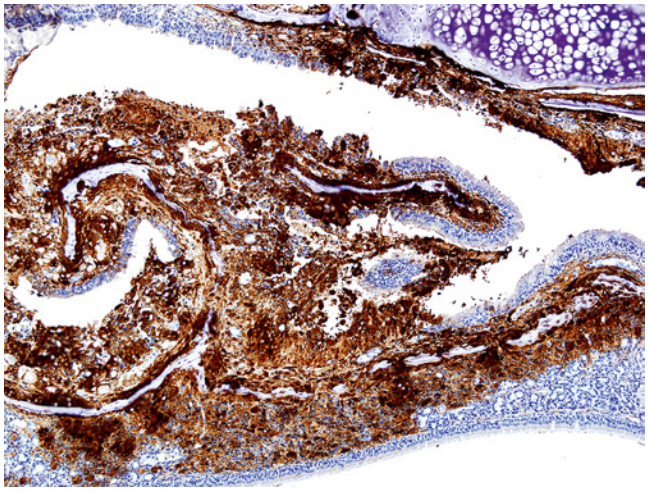


Figure 12.2 Massive nasal poxvirus infection of the nasal cavity. [10]. Intranasal infection with an engineered vaccinia virus seven days post infection with viral antigen in epithelium and nasal exudate. Rabbit antisera from whole virus.

respiratory tract but is often ignored in research studies of lung diseases. Olfactory and respiratory epithelium are often infected by the respiratory coronaviruses and other viruses [4, 10]. It was also identified as a major site of a massive poxvirus infection, whereas the lesions resulted in illness and death of the mice but had been ignored as a possible site of infection previously (Figure 12.2) [10]. It is most likely that the nasal epithelium is very much an under recognized site of respiratory viral and other infections.

The Lung

Anatomy and Histology

Mouse lung anatomy and histology are well described [1, 11, 12]. The mouse lung has five lobes (left, accessory, right cranial, right middle, right caudal) (Figure 12.3). The trachea branches into the bronchi and bronchioles. Histologically, the lung parenchyma includes smaller airways, bronchioles, and alveoli. The mouse lung has large pulmonary veins with cardiac myocytes in its walls; smaller veins may have no cardiac myocytes cells. Cardiac myocytes may be more prominent in the lung veins of some strains of mice. Bronchioalveolar stem cells (BASCs) have been described in the lung [13, 14]. The parenchymal cell types are noted in Table 12.1. Mouse lungs have no bronchial-associated lymphoid tissue (BALT) but foci of lymphocytes (mostly B cells) may be induced by experimentally procedures and are termed iBALT (Figure 12.4) [15].

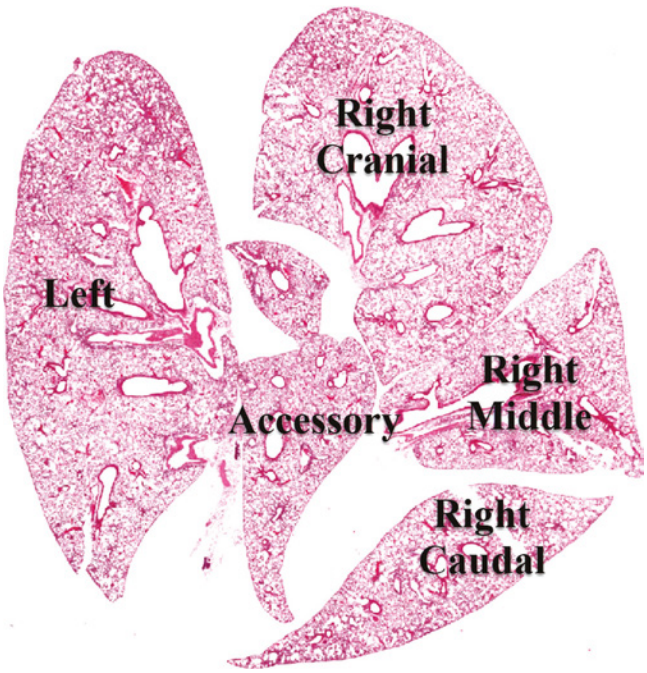


Figure 12.3 Whole lung infused with formalin. Left, right, and accessory lobes are identified and uniformly expanded.

Lung Necropsy and Histology Protocols

It is important to prepare lungs at necropsy for proper inflation, subsequent fixation, trimming, and processing [16]. If lungs are not inflated, the histology of the alveoli will not be optimal and interpretation of lesions will be difficult. Bronchiolar-alveolar lavage (BAL) can often wash out inflammatory cells from airways and alveoli although some pathologists note that it does not harm histopathology. Others prefer intravascular perfusion of the fixative but this procedure produces a different normal histologic appearance than by infusing fixative into the trachea [17]. Fixatives include the most common neutral buffered 10% formalin but others may be used including Bouin's solution, Fekete's solution, and 4% paraformaldehyde. Detailed lung intubation with fixative at necropsy has been described by mouse lung scientists measuring alveolar volume and other parameters [16, 18]. In these cases, an exact solution

Vet-ebooks.com

Table 12.1 Antibodies used to evaluate mouse lung by immunohistochemistry in neutral buffered 10% formalin fixed, paraffin embedded sections.

Cell type	Antigen	Other terms used	Antibody source
Club cell	SCGB1A1	Clara cell antigen, uteroglobin (UG), CC10, CC16, CCSP, Clara cell secretory protein, secretoglobin, blastokinin	Santa Cruz CC10 (E-11): sc-365 992
Alveolar Type I cell (AT1)	PDPN	Gp36, T1a, T1 alpha	Abcam Recombinant Anti-Podoplanin/gp36 (ab256559)
Alveolar Type II cell (AT2)	SFTPD SFTPC	Sfpd, Sftp4, SP-D Bricd6, pro-SpC, Sftp2, Sftp-2, SPC, SP-C, SAP, SP-D, pSPC, SFTPC,	Santa Cruz SP-D (IVG8): sc-52731
Club cell and Alveolar Type II cell (AT2)	NKX2-1	T/EBP, thyroid-specific enhancer-binding protein, thyroid transcription factor-1, Ttf-1, Titf1, TTF-1	Santa Cruz TTF-1 Antibody (8G7G3/1): sc-53136, Abcam TTF1 (ab227652)
Alveolar macrophages	YM1 (CHIL3)	Ym1, Chil3l3	R&D Systems AF2446, Abcam ab227110
Alveolar macrophages	F4/80 (ADGRE1)	DD7A5-7, EGF-TM7, Emr1, F4/80, Ly71, TM7LN3	ThermoFisher BM8
Alveolar macrophages	CD68 (Cd68)	gp110, Lamp4, macrosialin, Scard1	Abcam ab125212
Basal cells	TRP63, KRT5	Trp63, Keratin 5	Abcam Anti-p63 (ab124762), Abcam Anti-Cytokeratin 5 (ab52635)
Neuroendocrine cells	Calcitonin, CGRP (CALCA)	alpha CGRP, CA, Calc, Cgrp, Ct, CT, Ctn	Sigma-Aldrich C8198
Goblet cells	MUSC5AC	Mucin 5	Abcam Anti-Mucin 5AC – (ab212636)
Tuft cells	DCLK1	Dclk1	Abcam Anti-DCAMKL1 (ab106635)
Ciliated cells	FOXJ1, Alpha Tubulin	FoxJ1, Tuba1a	Abcam – anti-FoxJ1 [EPR21874] Abcam anti-FoxJ2 (ab235445), LSBio Mouse anti-Chicken Alpha Tubulin LS-C142821

[a] Synonyms as listed in Mouse Genome Informatics gene detail page (www.informatics.jax.org, accessed 23 December 2020). Other examples (common names) added as well.

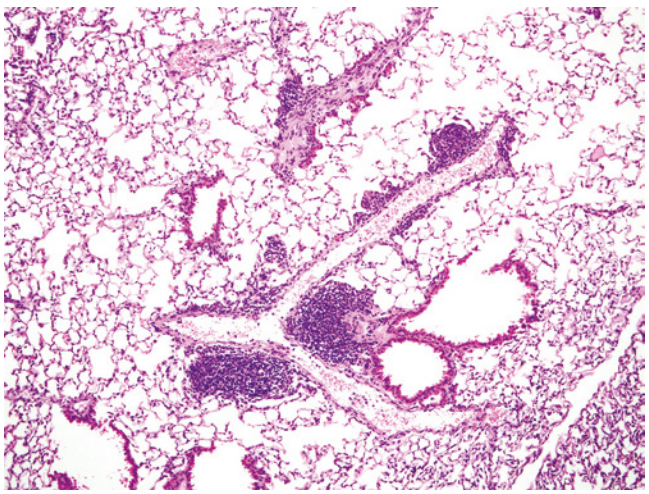


Figure 12.4 **iBALT in mouse lung**. Perivascular and bronchiolar lymphoid nodules are seen.

pressure, a ring stand with fixative 25 cm above the level of the mouse, and intratracheal application is required to prepare lungs with diffuse and equal inflation of alveoli. After 20–30 minutes of the pressure, the trachea can be tied off and lungs placed in the container with fixative. Most investigators, often not pathologists, however, do not use this exacting method for histopathology, but should do so to create a uniform whole lung section with all lobes visible (Figure 12.3), or a complete whole lung section but not of all lobes (Figure 12.5) and allow for optimal lung histopathology interpretation. The lung can be embedded whole with the largest surface down after flattening, including the heart in the block, which may allow for better whole lung sections (Figure 12.5). After fixation, all lung lobes can also be dissected and embedded individually (Figure 12.6). Unfortunately, in research studies involving mouse lung, investigators prefer to use specific lobes for their laboratory analysis and utilize a lobe, especially the largest left lobe, for histopathology, which often does not allow for lung inflation. If only one lobe is fixed for histopathology, the lung lobe is

Vet-ebooks.com

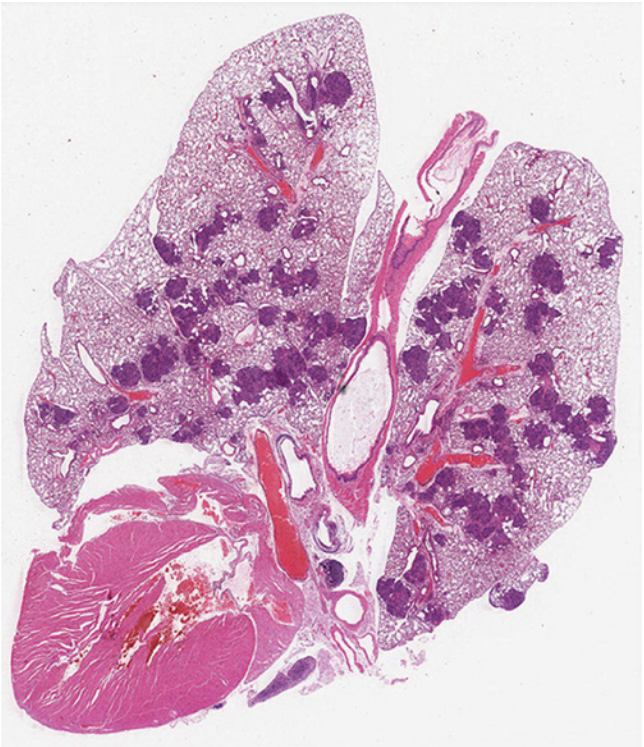


Figure 12.5 **Perfused lung embedded with heart**. Note lobes shown are uniformly dilated and lesions caused by an infectious agent are distributed throughout the lung.

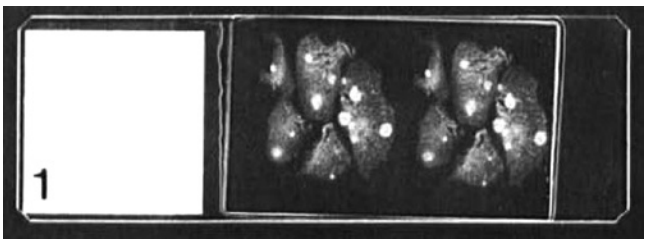


Figure 12.6 **Individual lung lobes for embedding**. The fixed lung lobes were individually embedded and sectioned.

often atelectatic since it was not inflated with fixative, which makes for difficult histopathology evaluation. We encourage investigators to allow for extra mice for complete lung inflation and histopathology of the entire lung or even inflate the left lobe if other lobes are used for lab work. After fixation, one may also dissect each lobe and embed each lobe separately with its longest side down, all in one block. Aged mouse lungs can also have specific lung protocols [19].

Immunohistochemistry of the Lung

The localization of antigens (usually gene protein products) in lung has been documented by many investigators [20–24]. Commonly used antibodies are noted in Table 12.1. Several figures in this chapter show antigens in normal lung cells (Figure 12.7) and in lesions.

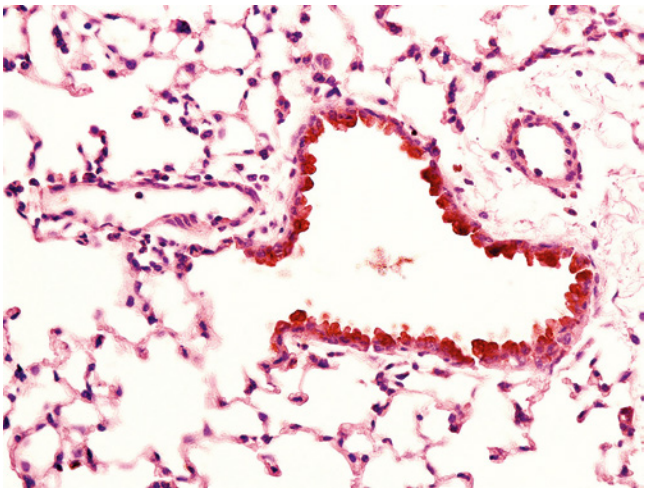


Figure 12.7 **SCGB1A1 in bronchiolar club cells**. The club cell antigen is present in all cells.

Lung Development

Development of the mouse lung involves many important genes [25], and 255 mouse genotypes with abnormal lung development have been reported (abnormal lung development Mammalian Phenotype Term [MP:0001176] [jax.org]). As examples of the phenotypes found, inactivation of *Nkx2-1* (*Nkx2-1*^{tm1Shk}) results in dead mice at birth due to lack of normal lungs, which originate from defects in pulmonary branching during mid-gestation and ends in the large pulmonary cysts without alveoli at birth [26]. Newborn mice (*Cyp1a2*^{tm1Gonz}) die after breathing a few times at birth due to an unknown cause [27]. Further study of neonatal lethal *Ndn*^{tm2Stw} mutant mice, also dying at birth after a few breaths, revealed that *Ndn* brain expression in the pre-Botzinger complex, the respiratory rhythm-generating center, was reduced [28] and obviously control of respiration was inconsistent with life. This phenotype mimics Prader–Willi syndrome in humans. Another neonatal lethality in *Abcb11*^{tm1Wng} mutant mice revealed that due to pulmonary bile acids as a key factor in the disruption of the structure of pulmonary surfactant, the mice developed atelectasis-producing pulmonary hypoxia, which recapitulates the neonatal respiratory distress of human intrahepatic cholestasis of pregnancy (ICP) [29]. Viable *Tomm5*$^{Gt(OST44663)Lex}$ mutant mice that survived birth developed organizing pneumonia (bronchiolitis obliterans) [30]. These cases show the variation in lung phenotypes due to gene inactivation important in mouse embryos for normal lung development.

Congenital Diaphragmatic Hernia

Congenital diaphragmatic hernia (CDH) in humans is relatively common and often lethal in which patients have diaphragmatic structural defects and pulmonary hypoplasia and hypotension. There are surgical and chemical methods to study CDH in animal models. A review of candidate genes

Vet-ebooks.com

when mutated did produce CDH (alleles here listed as models in MGI) including Wilms tumor 1 homolog (*Wt1*$^{tm1.1Ndha}$, *Wt1*^{tm1Jae}), slit guidance ligand 3 (*Slit3*$^{Gt(OST106158)Lex}$, *Slit3*$^{tm1.1Dor}$, *Slit3*^{tm1Dor}), zinc finger protein, multitype 2 (*Zfpm2*^{lil}; formerly *Fog2*), GATA binding protein 4 (*Gata4*$^{tm1.1Sad}$, *Gata4*$^{tm1.2Sad}$, *Gata4*$^{tm1.2Wtp}$), platelet derived growth factor receptor, alpha polypeptide (*Pdgfra*^{tm2Sor}), and potentially others [31].

Genetic studies on groups of affected human patients confirmed the genetic basis of the disease and have identified several candidate genes including nuclear receptor subfamily 2, group F, member 2 (*NR2F2*, formerly *COUP-TFII*) [32]. Of the 12 mutant mouse alleles listed in MGI, only *Nr2f2*$^{tm2.1Tsa}$ is listed as a mouse model for human CDH [33]. In another genetic approach, gene expression changes during the development of the mouse diaphragm were used to identify pre B cell leukemia homeobox 1 (*Pbx1*) as a candidate gene for CDH [34]. Homozygous nulls (*Pbx1*^{tm1Mlc}) died at E15/16 due to severe hypoplasia or aplasia of multiple organs in a study that focused on skeletal patterning and programming chondrocyte proliferation [35]. Because this was in the candidate gene region, mutant mice were examined and found to have previously undetected diaphragmatic defects [34]. While only a small number of mutant mice were examined, a variety of defects were observed including left-sided posterolateral defects with an intact membrane but absent musculature, herniation of the fundus of the stomach into the thorax, and abnormal muscular patterning. There are 32 additional allelic mutations of *Pbx* listed in MGI, none of which are listed as models for CDH but may have lesions if evaluated.

Approaches to Phenotyping the Respiratory System

If young or adult mice are observed in respiratory distress, a variety of problems should be investigated in addition to primary defects in the lungs. Infectious disease processes can be a problem even in high-level barrier facilities. With the myriad of mice carrying immunodeficiencies, infectious diseases can be of mouse or human (caretaker) origin. Botryomycosis, pyogranulomas with characteristic Splendore–Hoeppli phenomenon (immune complexes) caused by *Staphylococcus* spp., sometimes of human origin, gain entrance via foreign bodies (food) around teeth (periodontitis) that can spread to the lungs in a military distribution. While not uncommon in mice carrying mutations such as cytochrome b-245, beta polypeptide (*Cybb*^{tm1Din}), once established in a colony, wildtype mice can become infected. Another example is *Pneumocystis* infection. Often associated with specific types of immunodeficiencies, *Pneumocystis* spp. infection of lungs was long considered a diagnostic feature of severe combined immunodeficiency in many species before assays were readily available to determine immune status or to identify the pathogen [36]. This subject is discussed along with other infectious agents in Chapter 9. More subtle infections can involve opportunistic pathogens such as *Klebsiella oxytoca* in mice carrying very mild immune abnormalities such as C3H/HeJ mice with spontaneous mutations in toll-like receptor 4 (*Tlr*$^{Lps-d}$) [37, 38]. Gross lesions range from subtle to severe (red, firm, fibrin deposition) depending on the severity and cause. In all these cases aseptic culture is recommended along with other assays as indicated. PCR testing is now a routine for *Pneumocystis* that cannot be cultured.

Other causes of dyspnea include obstruction, such as mucus plugging associated with ciliopathies (see Chapter 6 for details), tumors (cancer to inflammatory polyps), to primary structural defects affecting the palate or diaphragm. These latter two have a genetic basis for which there are now numerous models and discussed later in the chapter.

Pathology of the Lung

Human respiratory tract diseases include congenital diseases, infections, obstructive diseases, occupational diseases, interstitial lung disease, hypertension, and tumors. Many of these human conditions do not exist spontaneously in mice but can be induced by various experimental methods or genetic engineering.

Spontaneous Lung Lesions in Mice

Young mice in specific pathogen free (SPF) facilities usually have no lung lesions. Occasional facilities will have mice with foci of lymphocytes (BALT or iBALT) suggesting endemic infection with an infectious agent, despite negative diagnostic assays (Figure 12.4). In one episode at a major research institution, one animal room had lesions of allergic pneumonitis in sentinel mice, with foci of macrophages and eosinophils in lungs (J. Ward, unpublished). It was thought to be an allergen in the bedding but the cause was never identified.

Lung lesions are commonly found in aging mice. Crystalline pneumonia (hyalinosis) and crystals in inflammatory alveolar macrophages occur in many conditions in mice including aging mice of some strains, genetic models, inflammatory models, and tumors [39–41]. Hyalinosis was found in wild type and mutant mice, also in the stomach, the nasal cavity, and other tissues of some strains [40, 42]. Mouse strain 129S4/SvJae has a high incidence in aging mice [39]. Grossly one or more lobes appear diffusely or focally pale, even around lung tumors (Figure 12.8). The lesions are also histologically diffuse, lobular, or focal in distribution depending in part on the mouse strain or mutant and the age of the mouse (Figure 12.9). Lesions are initially found within individual lung macrophages (Figure 12.10). The process appears to be an over-production of CHIL3 protein (*Chil3*, formerly called *Ym1*) in response to abnormal synthesis in some cases due to mutations in *Ptpn6* (*Ptpn6*^{me}; the motheaten mouse) [43–45], *Ncf1* (*Ncf1*^{m1J}) [46], *Hpse*^{tm1Jpli} [47] or *Lat*^{tm1Les} [48], and due to other causes [49]. The protein is seen in the cytoplasm and intracytoplasmic and extracellular crystals (Figure 12.11).

Vet-ebooks.com

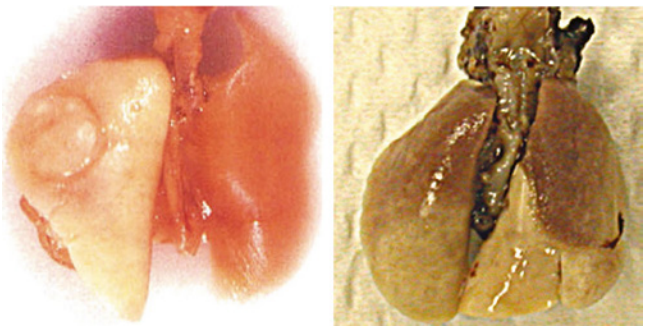


Figure 12.8 Gross necropsy findings of pulmonary hyalinosis (crystalline pneumonia). Note the pale lung around the lung tumor on left and pale areas towards distal portions of lung on right.

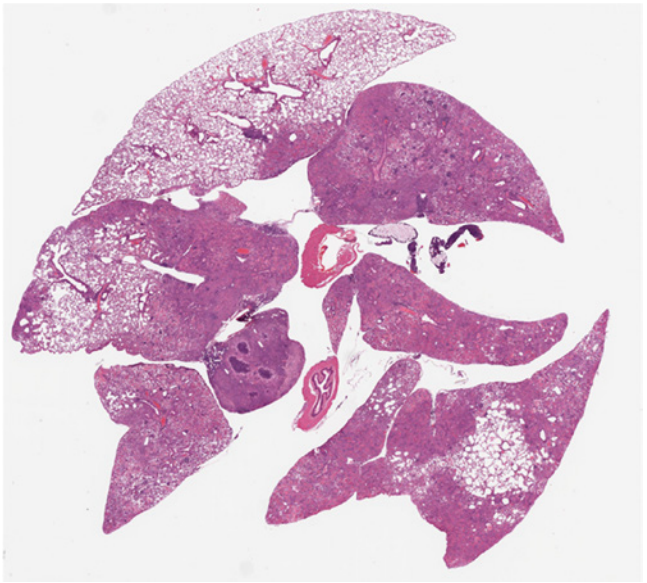


Figure 12.9 Whole lung section with crystalline pneumonia. The lesions are diffuse in some lobes and focal abscesses can be seen in an *Ncf1*^{m1J} homozygous mutant mouse.

There are various types of morphological crystals in lung macrophages and sometimes in other tissues. Crystals can be small (Figure 12.12) or large and needle-like (Figure 12.13), or intracellular parallel collections (Figure 12.14). Ultrastructure reveals thin needle-like crystals in some cells (Figure 12.15). When the cell produces an excess of protein and crystals, it may become necrotic and free crystals and masses of crystals can be seen in alveoli and bronchioles.

High frequency of pulmonary hyalinosis is often found adjacent to spontaneous or induced lung tumors, or from the causes of the inflammation including parasitic and allergic or other types of inflammation. Alternative activation of macrophages appears to be the pathway involved [49].

In inhalation experiments where drops of test material are placed on or in the external nasal meatus, plant

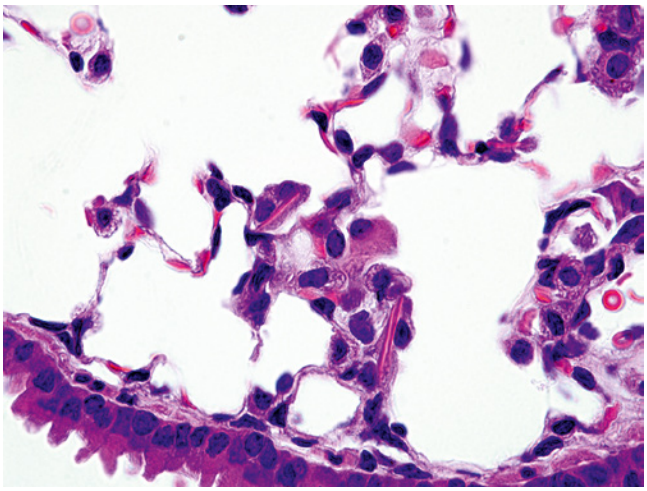


Figure 12.10 Early lung lesions of an *Ncf1*^{m1J} homozygous mutant mouse. There are increased numbers of alveolar macrophages along the alveolar walls and within alveoli, some with needle-like eosinophilic crystals.

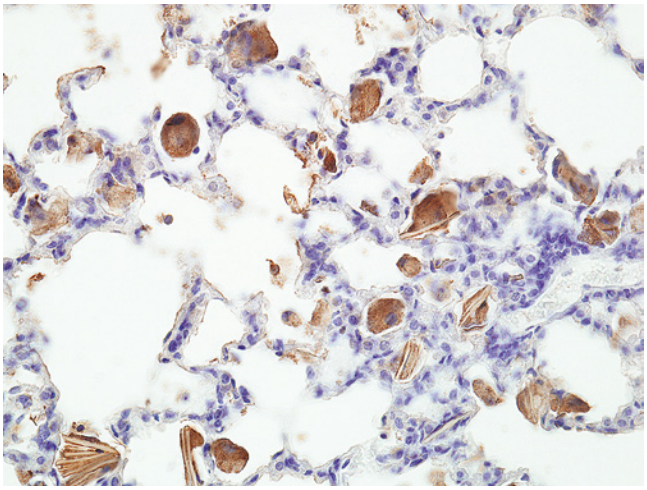


Figure 12.11 CHIL3 in alveolar macrophages. Early lesions of hyalinosis in an *Ncf1*^{m1J} mutant mouse with protein within macrophages and along crystals. Rabbit antiserum against CHIL3 peptides.

material (probably from food), or material present in the inoculum, may end up in the lungs as a foreign body reaction (Figure 12.16). The lesions may be single or multiple.

Disease Models

Scoring of Lung Lesions

Scoring (grading) of lung lesions is often used for mouse models of disease. Various lung lesion scoring methods have been used [50–53]. In the authors experience, one's personal preference usually is based on consideration of the published

Vet-ebooks.com

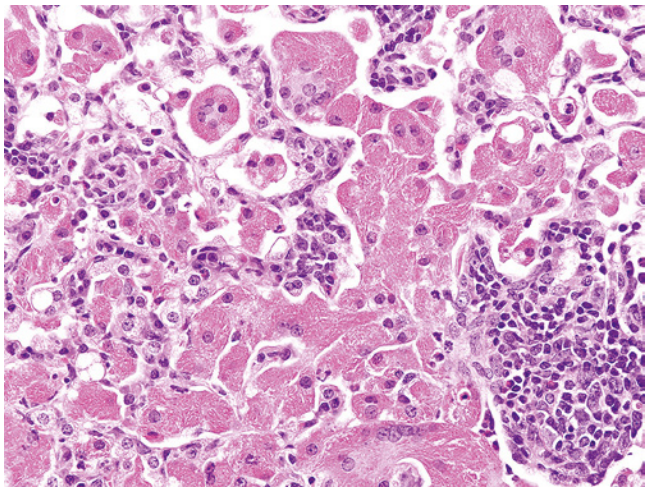


Figure 12.12 Alveolar macrophages in a *Lat*^{tm1Les} homozygous mutant mouse. Note the thin small needle-like crystals in the eosinophilic cytoplasm.

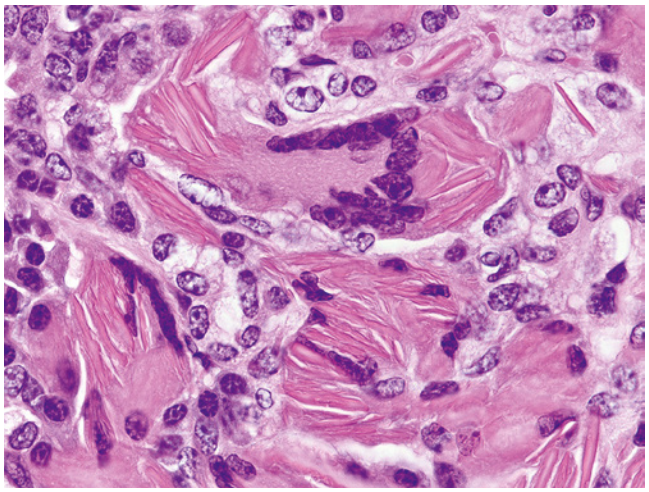


Figure 12.13 Alveolar macrophages in an *Ncf1*^{m1J} homozygous mutant mouse. Multinucleated giant macrophages with larger crystals than those shown in Figure 12.12.

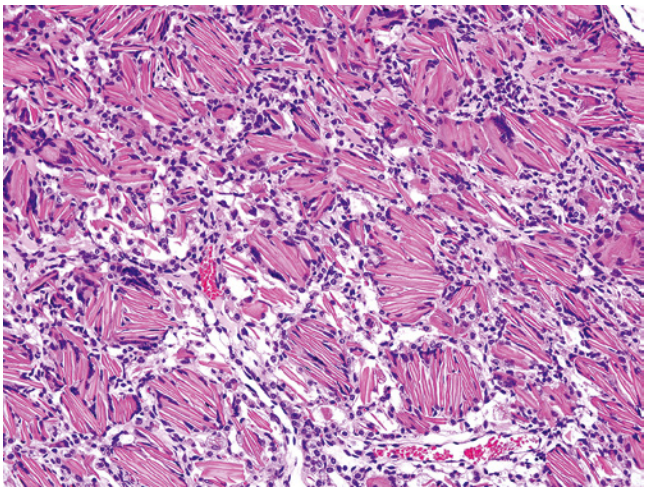


Figure 12.14 Alveolar macrophages in an *Ncf1*^{m1J} homozygous mutant mouse. Lower magnification of the lung showing multinucleated giant macrophages with larger crystals than those shown in Figures 12.12 and 12.13.

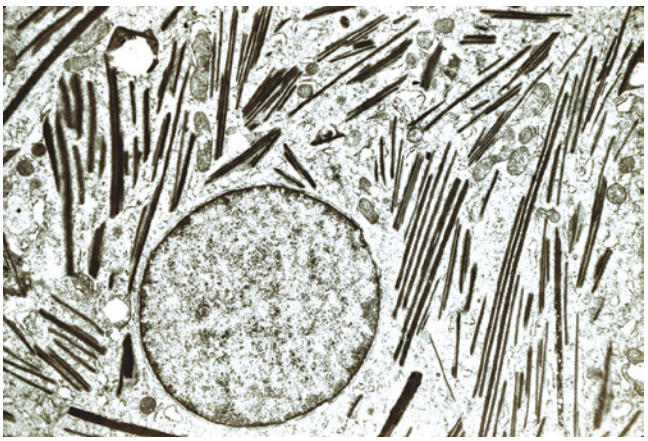


Figure 12.15 Electron micrograph of the CHIL3 crystals. Note the thin needle-like crystals in the alveolar macrophage.

suggestions. A big problem is sampling of the lung since pathologists providing support to investigators often have no input into the initial study design. They often get only a lobe that is not inflated. It is best to get a whole lung section or, if not possible, an entire lung lobe such as the larger left lobe, inflated if possible. Discussion of the protocol with the investigator provides optimal support from the pathologist. Scored lesions for coronavirus and influenza infections may include those lesions noted below and also others including edema, hemorrhage, hyaline membranes, inflammation of various types, thrombi, Type II cell hyperplasia, and syncytia, fibrosis [50, 51]. A total lung score can also be established including consideration of all relevant lung lesions seen. This is obviously best done with a whole lung section. Toxic lesions may follow rodent toxicologic pathology and human pathology guidelines [54, 55]. Diffuse alveolar damage has been reported for SARS CoV2 infection in mice, but lesions are not well described and not exactly the same nor as severe as those in humans. Image analysis has been also used for experimental lung lesions in mice [56, 57].

Infectious Disease Models

Mice may be infected experimentally with various viruses, bacteria, or other agents by intranasal, intratracheal, or oropharyngeal aspiration [58] and other routes of infection. The distribution of the infectious material in the lung may vary from centrilobular (Figure 12.17), lobular (Figure 12.18), and diffuse (Figures 12.5 and 12.19). The oropharyngeal method may distribute infectious agents more uniformly in the lung [58] (Figure 12.5). The morphologic type of lesions and its pathogenesis depends on the etiologic agent, dose of

Vet-ebooks.com

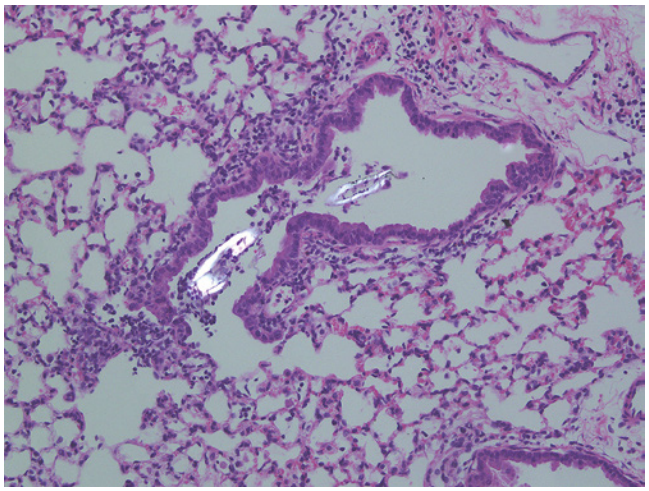


Figure 12.16 Foreign material in bronchiole. After intranasal administration of a virus in a solution seven days previously, there are inflammatory cells seen within the lumen of the airway and alveoli and also peribronchiolar. Plant material is seen with polarized light.

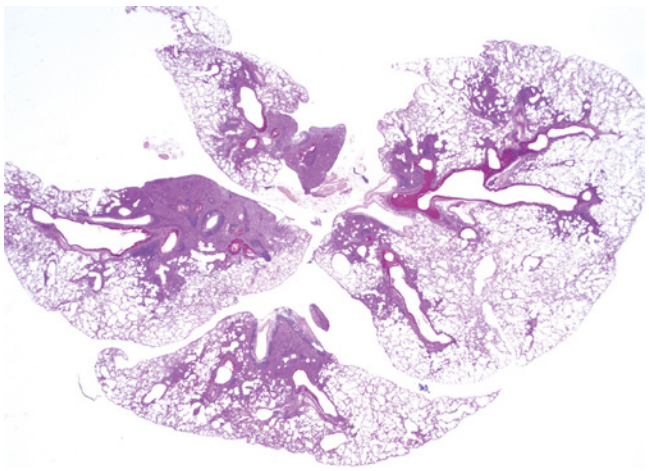


Figure 12.17 Centrilobular distribution of induced inflammatory lesions. Nine days postnasal exposure of a virus.

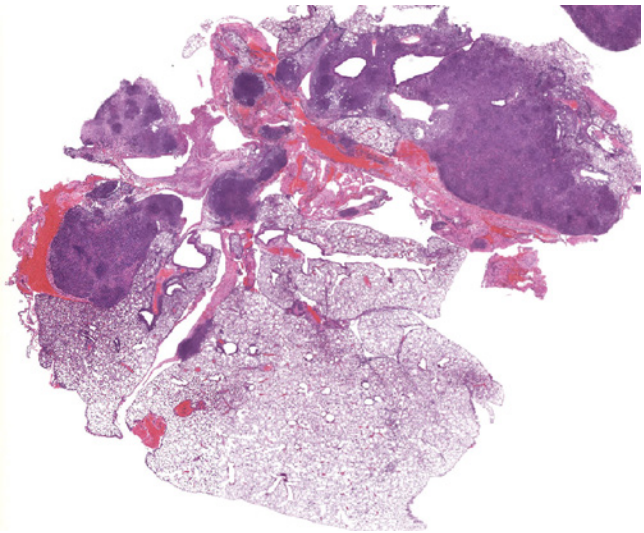


Figure 12.18 Lobular distribution of induced lesions. Fifteen days postnasal infection with SARS CoV in a 129S6/SvEv-*Stat1*^{tm1Rd} mouse. Lesions are pyogranulomas. See Figure 12.30.

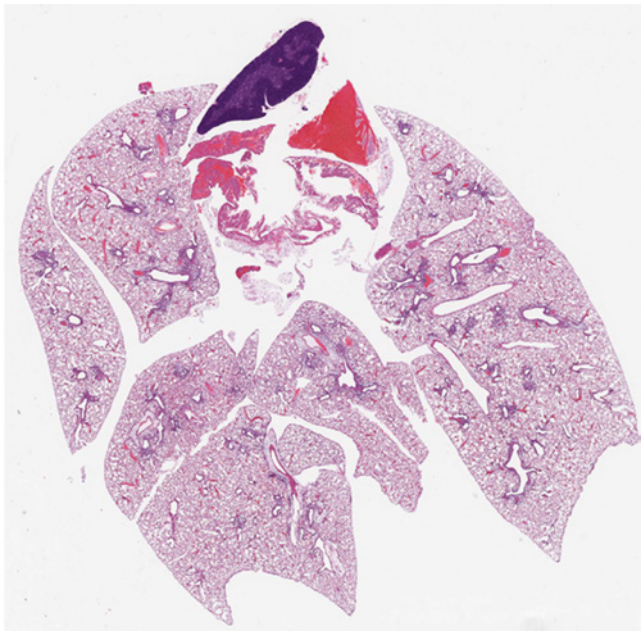


Figure 12.19 Diffuse distribution of induced lesions. Five days postnasal infection of SARS CoV in a 129S6/SvEv-*Stat1*^{tm1Rds} mouse. Only small bronchiolar and peribronchiolar lesions can be seen as very small darker areas throughout the lung. There is no alveolar involvement. Same group as in Figure 12.20 and also compare with normal lung in Figure 12.3.

the agent, time post infection, and mouse strain, stock, or GEM. Influenza viruses [59–61] and SARS CoV [62, 63] viruses are most popular for study. The earliest studies involved Sendai virus, which was common in mouse colonies over 30 years ago [64, 65]. Most recently, for the respiratory coronaviruses, GEM, involving immune system genes, are often used for studying the pathogenesis of viral infections [66, 67].

Spontaneous and viral induced lung infections generally show viral infection of nasal epithelium, tracheal, bronchial, and bronchiolar epithelial cells (Figures 12.20–12.22). Bronchiolar necrosis (Figure 12.23) occurs followed quickly by epithelial hyperplasia (Figure 12.24). Some viruses, including influenza viruses, SARS CoV2, and parainfluenza viruses (PVM, pneumonia virus of mice) [68], readily infect AT1 and AT2 cells (Figures 12.21 and 12.25), causing alveolitis and interstitial pneumonia (Figure 12.26), which leads to more severe clinical and lung disease. After viral clearance, if the mouse survives, there is alveolar regeneration, epithelialization (Figure 12.27), and chronic inflammation (iBALT), as remnants of infection. In SARS CoV2 infection, B6.Cg-Tg (K18-hACE2)2Prlmn/J transgenic mice develop

Vet-ebooks.com

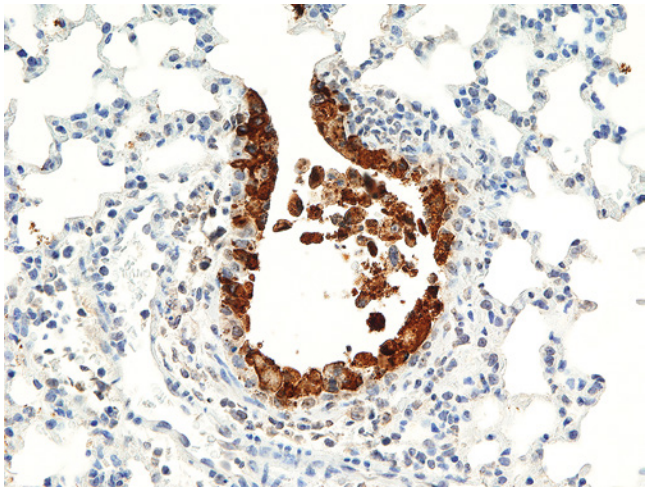


Figure 12.20 **Viral antigen in bronchiolar epithelium**. SARS CoV in bronchiolar club cells, three days post infection. Hyperimmune mouse serum.

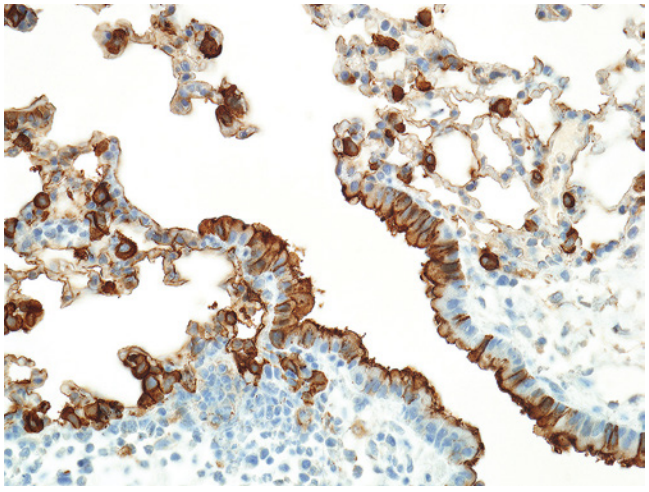


Figure 12.21 **Viral antigen in bronchiolar club cells and alveolar cells**. Day 8 after exposure to pneumonia virus of mice.

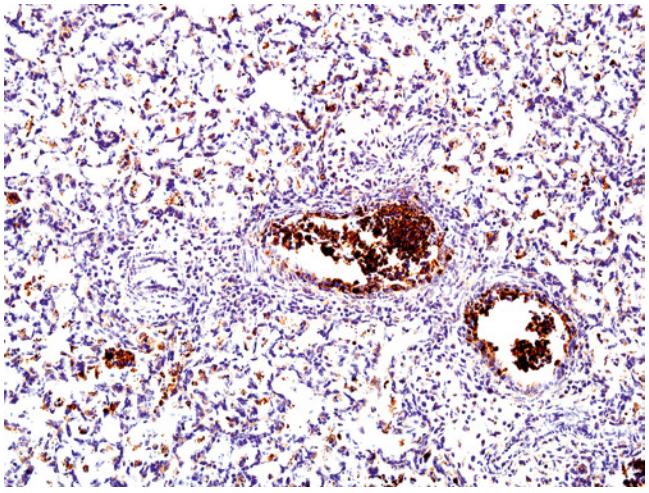


Figure 12.22 **H5N1 influenza viral antigen in lung**. Day 2 after infection in BALB/cAnNTac mice. Note antigen in bronchioles and alveoli.

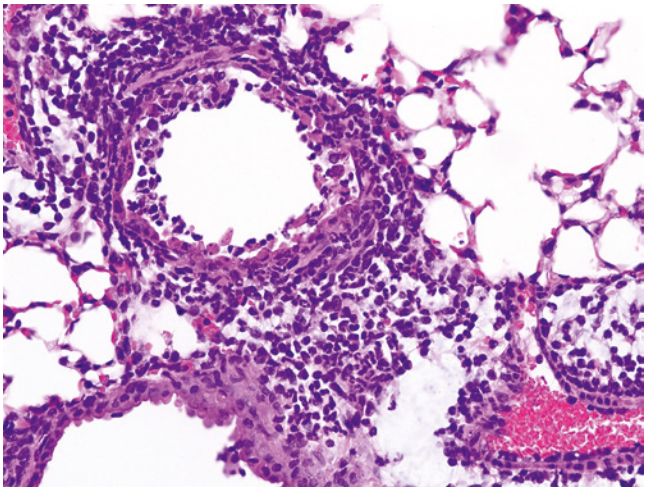


Figure 12.23 **Acute viral lesions in a bronchiole**. There is necrosis of bronchiolar epithelium and peribronchiolar and perivascular inflammation in a 129S6/SvEv-*Stat1*^{tm1Rds} mouse on day 3 after infection by SARS CoV, Urbani strain.

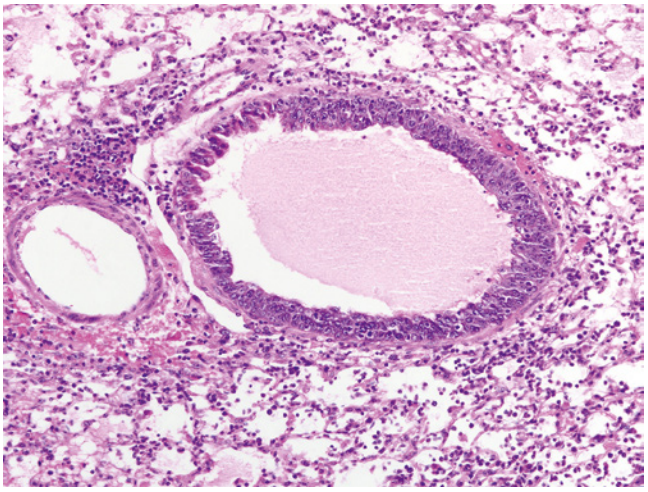


Figure 12.24 **Bronchiolar hyperplasia**. Hyperplastic club cells after naturally occurring Sendai virus infection. Note alveolar inflammation.

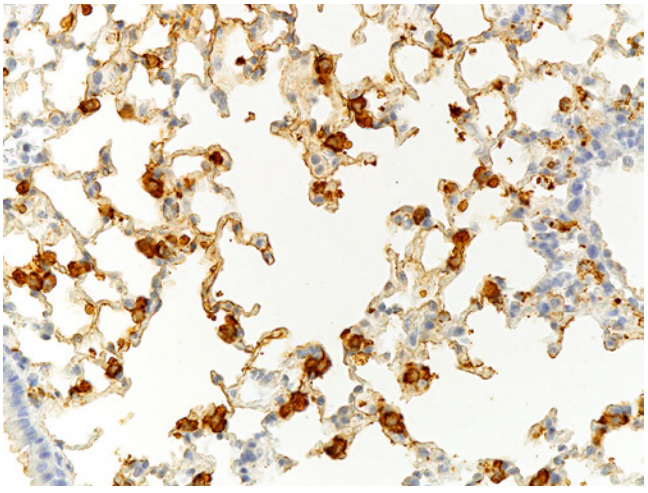


Figure 12.25 **Viral antigen in alveolar cells**. Mice infected with pneumonia virus of mice (PVM) shows antigen in alveolar Type II cells and macrophages. Rabbit antiserum to PVM G.

Vet-ebooks.com

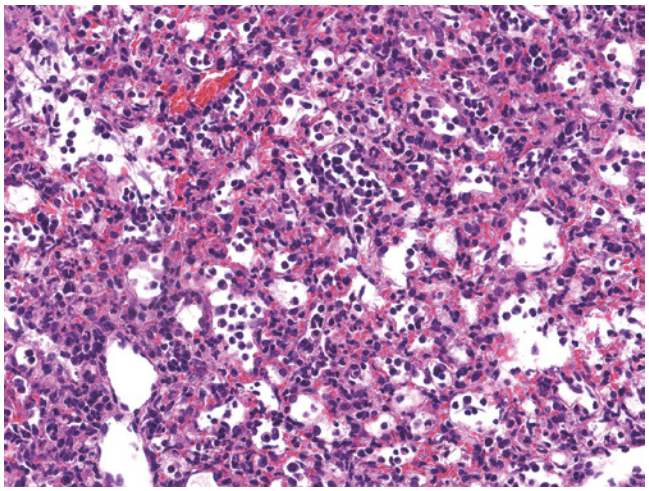


Figure 12.26 **Interstitial pneumonia**. Alveolar walls are thickened, and inflammatory cells are within alveoli. Lung of a B6.Cg-Tg(K18-hACE2)2Prlmn/J mouse, seven days post SARS CoV2 infection. Source: Joe Golden and Curtis Cline [69].

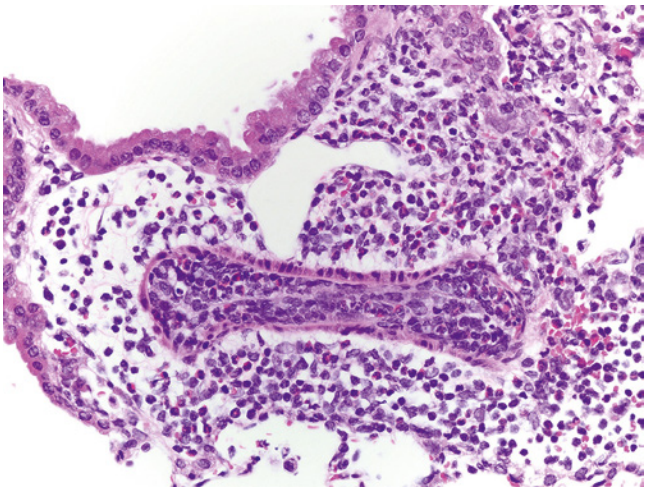


Figure 12.28 **Migration of leukocytes from arteriole into lung**. Leukocytes are within lumen and wall of arteriole two days post viral infection. Perivascular and peribronchiolar inflammatory cells are seen.

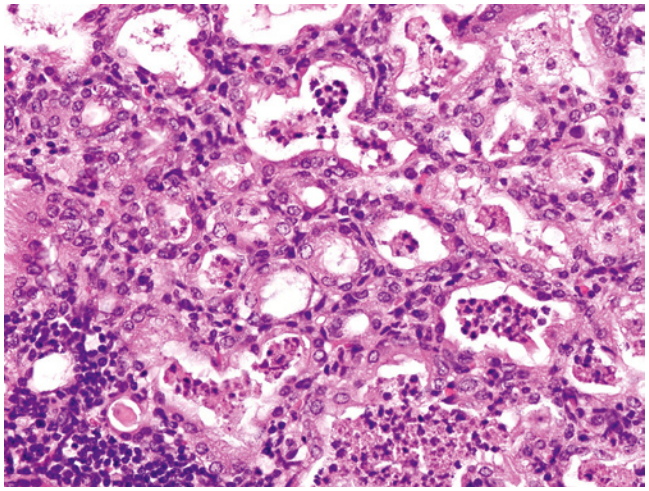


Figure 12.27 **Alveolar bronchiolization**. Naturally-occurring chronic Sendai virus infection. Cuboidal cells line alveoli with inflammatory cells within alveoli.

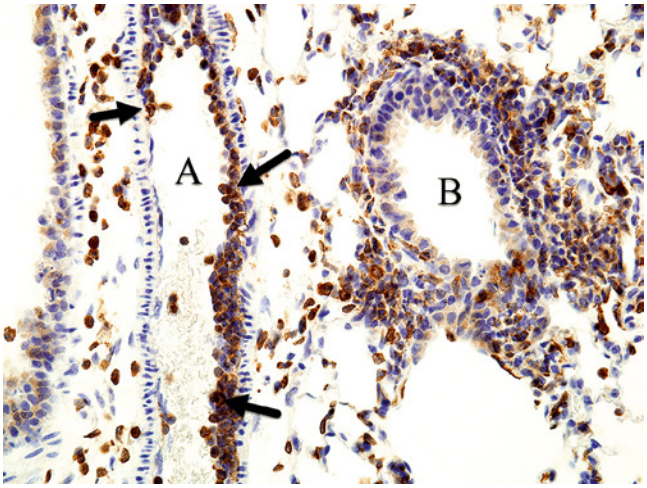


Figure 12.29 **Vasculitis**. Migration (arrows) of $CD3^+$ lymphocytes through wall of arteriole into lung. Two days post SARS CoV infection.

the most extensive and advanced alveolar lesions (Figure 12.26) for mouse models also with clinical illness and clinical signs [69].

Other common lung lesions in viral infections include migration of leukocytes (T cells and other cells) from arterioles (Figure 12.28) with subsequent perivascular cuffing with T cells (Figure 12.29). Vascular thrombi, hyaline membranes, and diffuse alveolar damage have been reported in some SARS CoV2 mouse models [69, 70].

Occasionally experimental lung infection causes unusual findings, especially in GEM used to study disease pathogenesis. STAT1 is a transcription factor active in interferon signaling. *Stat1* null mice are more susceptible to SARS CoV, SARS CoV2, and influenza viral infections [66, 71]. In the case of SARS CoV, infection of *Stat1* null mice (129S6/SvEv-*Stat1*^{tm1Rds}) results in typical initial lung viral infection of airway epithelium but the normal viral clearance in the lungs does not occur. Nine days post infection, the development of pyogranulomatous lesions occurs in the lung (Figure 12.30), liver, spleen, and peritoneal cavity, as in feline infectious peritonitis, also a coronavirus infection [66]. The lesions contain abundant virus in macrophages around the zone of central necrosis and many peripheral plasma cells (Figure 12.31), suggesting a role of the immune response in the lesion development. Similar more severe infections and diseases were found in infection of *Stat1* null mice in Influenza A/PR/8/34 H1N1 infection but pyogranulomas were not reported [71].

Vet-ebooks.com

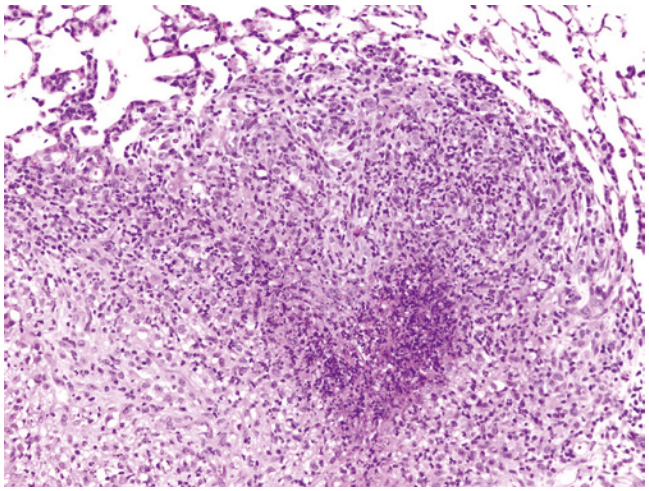


Figure 12.30 Pyogranuloma in the lung. A large lesion with central necrosis surrounded by macrophages in a 129S6/SvEv-*Stat1*^{tm1Rds} mouse 14 days post infection with SARS CoV.

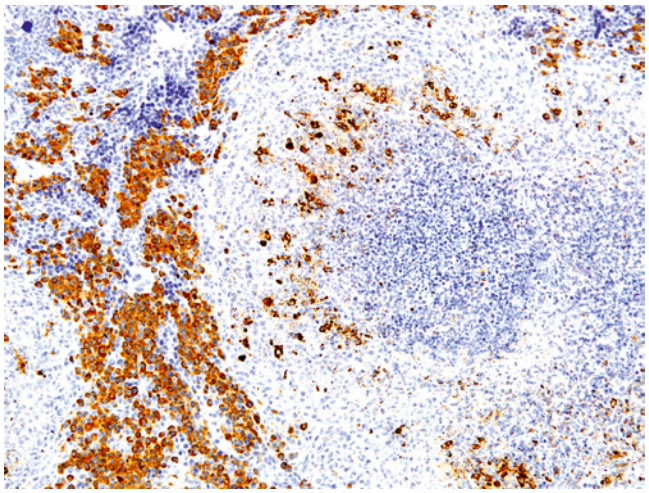


Figure 12.31 SARS CoV antigen in macrophages in a pyogranuloma as in Figure 12.30. Inner ring of cells are macrophages around a focus of necrosis. Outer ring are plasma cells, reacting to the secondary antibody.

Vaccine development often includes the use of mouse models of infection. In the case of SARS CoV2 [72] and respiratory syncytial viruses (RSVs) [73], these models play important roles determining the success or failure of vaccination. Some vaccines for RSV cause more severe disease, and mice have been used to study the mechanisms and for appropriate vaccine development [74, 75]. Vaccines for human tuberculosis infections have limited efficacy but recent studies have developed more effective vaccines using mice as models [76]. Attenuated organisms in mouse models have provided recent advances for vaccination against tuberculosis [77].

Mouse Models of Human Pulmonary Genetic Disorders

Inherited disorders in humans include surfactant dysfunction disorders, alpha-1-antitrypsin deficiency (AAT) deficiency, and cystic fibrosis (*CFTR* gene) [78, 79]. Surfactant dysfunction disorders have caused death in infancy (*SFTPB*, *SFTPC*, *ABCA3*, *NKX2-1*), chronic disease in infants (*ABCA3*, *SFTPC*, *NKX2-1*), and chronic lung disease and fibrosis in adults (*SFTPC*) [78]. Mouse models for these are noted in Table 12.2. However, the lesions in a GEM are often not the same as in humans but the lung can be the primary target site in GEM. *Nkx2-1* mouse mutants die at birth due to development lung defects [26], while *NKX2-1* mutant humans die in infancy [78]. It was reported that *Sftpc*^{tm1Swg} mice are normal at birth and have no lung lesions as do mutant humans with chronic pneumonitis of infancy [78, 80], but transgenic mice have been created to study the function of the protein in pulmonary fibrosis [80].

MGI (www.informatics.jax.org) is a good resource to search for genes that are associated with human lung diseases by searching for genes or the human diseases. While this may not contain all the genes/models, it is a living resource, meaning a team of curators constantly updates the database (Table 12.3). Many of the groups of diseases, such as primary ciliary dyskinesia, are discussed in this book, for example, Chapter 6, Ciliopathies.

Mice carrying one or more mutations, either spontaneous or genetically engineered, may have pulmonary lesions as a primary or secondary event. Most investigators focusing on a specific organ may or may not review all organs, including the lungs. Thus, it is likely many more mutant mice have lung abnormalities than are reported. GEM may reflect many aspects of the human disease or may not show any similarities and even show normal lung histology. An example is cystic fibrosis. Mutations in the human cystic fibrosis transmembrane conductance regulator (*CFTR*) gene result in cystic fibrosis (CF), a disease characterized by decreased mucociliary clearance, bacterial colonization, and chronic neutrophil-dominated inflammation [77]. While the pulmonary lesions are the most serious, this is a systemic disease.

The upper respiratory tract in many of the CF mouse models resemble that of humans [81, 82]. However, none of the *Cftr* mutant mice developed pulmonary disease without challenge, limiting their usefulness [83]. MGI lists 14 targeted mutations in the mouse ortholog (*Cftr*) gene as a model for human CF (out of 26 alleles listed, not all of which have been created and phenotyped; search 5 January 2021). A βENaC-Tg (B6.Cg-Tg(Scgb1a1-Scnn1b)6608Bouc/J) transgenic mouse with airway-specific overexpression of the epithelial Na+ channel (ENaC, now called sodium channel, nonvoltage-gated 1 beta, SCNN1B) was developed as another method to mimic CF ion transport pathophysiology in the lung [82]. Other CF models have also been developed [83].

Secondary pulmonary involvement can be obvious, such as metastatic lesions from distant primary cancers. By contrast, more obscure secondary effects can reflect genes that

Vet-ebooks.com

Table 12.2 Examples of genetic based human lung diseases for which mouse models have been identified or created.

Disease	Mouse models	Associated genes from mouse models	Associated human genes
Chronic obstructive pulmonary disease	22	*Bloc1s6, Fbn1, Fut8, Itgb6, Jun, Kl, Mus81, Ptma, Serpina1, Smo, Tg(Actb-Ptma)T12Clwu, Tg(HP-MMP1a)34-1Cha, Tg(Msr1-MMP9)#Apar, Tg(tetO-PLAGL2)P3Ysy, Tlr4*	*HMOX1, MMP1*
Cystic fibrosis	19	*Cftr, Scnn1b, Tg(Scgb1a1-Scnn1b)6608Bouc*	*CFTR, FCGR2A, TGFB1*
Desquamative interstitial pneumonia	1	*Sftpc*	
Idiopathic interstitial pneumonia	1	*Sftpc*	
Idiopathic pulmonary fibrosis	2	*Fosl2, Tg(H2-K-Fosl2,EGFP)13Wag, Tg(SFTPC-Tnf)2Pva, Tnf*	*MUC5B, SFTPA2, SFTPC, TERT*
Interstitial lung disease	3	*Fosl2, Tg(H2-K-Fosl2,EGFP)13Wag, Tg(SFTPC-Tnf)2Pva, Tg(tetO-TGFA)22.1Kor, Tnf*	*MUC5B, SFTPA2, SFTPC, TERT*
Joubert syndrome 26	1	*Katnip*	*KATNIP*
Junctional epidermolysis bullosa Herlitz type	4	*Itga6, Lamb3, Lamc2*	*LAMA3, LAMB3, LAMC2*
Kabuki syndrome	1	*Kmt2d*	*KDM6A, KMT2D*
Kleefstra syndrome 1	2	*Ehmt1*	*EHMT1*
Lethal congenital glycogen storage disease of heart	2	*Tg(Myh6-PRKAG2*T400N)1Feah, Tg(Myh6/tetO-PRKAG2*N488I)1Chib*	*PRKAG2*
Lethal restrictive dermopathy	4	*Fst, Slc27a4*	*LMNA, ZMPSTE24*
Lung adenocarcinoma	2	*Tg(SFTPC-env)1Yhch, Tg(tetO-Kras2)12Hev*	
Lung benign neoplasm	2	*Tg(tetO/CMV-KRAS*G12C)9.1Msmi*	
Newborn respiratory distress syndrome	4	*Epas1, Ndst1, Vegfa*	
Obstructive lung disease	22	*Bloc1s6, Fbn1, Fut8, Itgb6, Jun, Kl, Mus81, Ptma, Serpina1, Smo, Tg(Actb-Ptma)T12Clwu, Tg(HP-MMP1a)34-1Cha, Tg(Msr1-MMP9)#Apar, Tg(tetO-PLAGL2)P3Ysy, Tlr4*	*HMOX1, MMP1*
Pleuropulmonary blastoma	2	*Fgf9, Tg(tetO-Fgf9,-EGFP)#Dor, Yy1*	*DICER1*
Pneumonia	1	*Sftpc*	
Primary ciliary dyskinesia 1	3	*Dnai1*	*DNAI1*
Primary ciliary dyskinesia 21	2	*Drc1*	*DRC1*
Primary pulmonary hypertension	12	*Adora2a, Bmpr2, Pparg, Smad9, Tg(Lck-Tnfsf4)1Nish, Tg(Scgb1a1-IL6)9Flv, Tg(Tagln-SLC6A4)#Edd, Tg(tetO-Bmpr2*R899X)#Jwst, Tg(tetO-BMPR2*T504)1Jwst, Tnfsf4, Vip*	*BMPR2, CAV1, KCNK3, SMAD9*
Pulmonary alveolar proteinosis	7	*Abca3, Csf2, Csf2rb*	*ABCA3, CSF2RA, CSF2RB, SFTPB, SFTPC*
Pulmonary blastoma	2	*Fgf9, Tg(tetO-Fgf9,-EGFP)#Dor, Yy1*	*DICER1*
Pulmonary emphysema	22	*Bloc1s6, Fbn1, Fut8, Itgb6, Jun, Kl, Mus81, Ptma, Serpina1, Smo, Tg(Actb-Ptma)T12Clwu, Tg(HP-MMP1a)34-1Cha, Tg(Msr1-MMP9)#Apar, Tg(tetO-PLAGL2)P3Ysy, Tlr4*	
Pulmonary fibrosis	3	*Fosl2, Tg(H2-K-Fosl2,EGFP)13Wag, Tg(SFTPC-Tnf)2Pva, Tg(tetO-TGFA)22.1Kor, Tnf*	*MUC5B, SFTPA2, SFTPC, TERT*
Respiratory failure	4	*Epas1, Ndst1, Vegfa*	
Trichorhinophalangeal syndrome type I	1	*Trps1*	*TRPS1*

Source: Based on Mouse Genome Informatics website (http://www.informatics.jax.org/humanDisease.shtml).

Vet-ebooks.com

Table 12.3 Examples of mouse genes that when mutated create models for genetic based human lung diseases.

Gene/allele name	Human disease models
Abca3^{tm1frm}, *Abca3*^{tm1Holz}, *Abca3*^{tm1Nina}	Pulmonary alveolar proteinosis
Atf2^{tm1Sis}	Meconium aspiration syndrome
Bloc1s6^{pa}	Hermansky–Pudlak syndrome 9, pulmonary emphysema
Cftr^{tm1Hgu}	Cystic fibrosis
Col1a1$^{tm1(CAG-EGFR*T790M*C797S*L858R)Mje}$	Lung cancer
Col1a1$^{tm4(CAG-FGFR2_iII1b*K660N)Kkw}$	Lung cancer
Csf2^{tm1Ard}, *Csf2*^{tm1Mlg}	Pulmonary alveolar proteinosis
Csf2rb^{tm1Mur}	Pulmonary alveolar proteinosis
Dpp4$^{tm1(DPP4)Vlcg}$	Middle East respiratory syndrome
Epas1^{tm1Pec}	Newborn respiratory distress syndrome
Fbn1^{Tsk}	Marfan syndrome, pulmonary emphysema
Foxm1^{tm1Rhc}	Lung cancer
Fut8^{tm1Nta}	Pulmonary emphysema
Gt(ROSA)26Sor$^{tm1(Smo/EYFP)Amc}$	Pulmonary emphysema
Itgb6^{tm1Des}	Asthma, pulmonary emphysema
Jun^{tm4Wag}	Pulmonary emphysema
Kl^{kl}	Pulmonary emphysema
Kras^{tm1Bbd}, *Kras*^{tm2Bbd}, *Kras*^{tm2Tyj},	Lung cancer
Mus81^{tm1Esse}	Pulmonary emphysema
Ndst1^{tm1Ekf}, *Ndst1*^{tm1Hgx}	Newborn respiratory distress syndrome
Robo1^{tm1Phr}	Lung cancer
Serpina1^{em1Chmu}, *Serpina1*^{em2Chmu},	Pulmonary emphysema
Sftpc^{tm1Swg}	Desquamative interstitial pneumonia
Tg(Actb-Ptma)T12Clwu	Pulmonary emphysema
Tg(H2-K-Fosl2,EGFP)13Wag	Idiopathic pulmonary fibrosis
Tg(Lck-Tnfsf4)1Nish	Primary pulmonary hypertension
Tg(SFTPC-Tnf)2Pva	Idiopathic pulmonary fibrosis

Source: Data obtained from Mouse Genome Informatics (http://www.informatics.jax.org/) by searching Phenotypes/Diseases: lung disease (15 Dec 2020).

affect metabolism that have systemic effects. Examples include genes that when mutated dysregulate mineral metabolism resulting in ectopic calcification in many organs including lungs (Figure 12.32). *Abcc6*, *Enpp1*, *Klotho*, *Fam23*, and many others now listed in the ectopic mineralization network fall into this category. These are discussed in detail in other chapters in this book. More importantly, mutations in these and other genes can be spontaneous and fixed within inbred strains, such as a hypomorphic allele of *Abcc6* in C3H/HeJ (and other C3H substrains), DBA/2J, KK/HIJ, and most 129 substrains [84, 85], the phenotypes of which will interfere with analyzing mice carrying other mutations that affect calcium metabolism unless this allele is corrected (by CRISPR/Cas9) [86] or replaced by breeding [87]. Therefore, it is imperative to understand the common and rare strain specific lesions in the mice you are

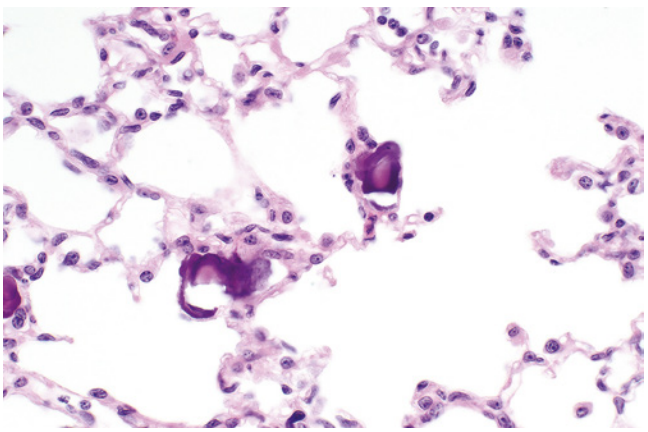


Figure 12.32 **Ectopic mineralization**. Foci of mineralization can be found scattered throughout the lung in a 65-day old male KKB6BC mouse due to a hypomorphic mutation in the *Abcc6* gene.

Vet-ebooks.com

working with [42]. Chapter 2 on databases provides details on how to find this type of information.

Asthma

Asthma, a chronic inflammatory immune-related disease of the airways, is caused by inhaled allergens, results in reversible airway obstruction associated with an eosinophilic inflammation of the airways, airway hyper-responsiveness, and remodeling. It is a common respiratory problem in humans resulting in high healthcare costs for severely affected patients. Mouse models provide tools to investigate the pathophysiology of this disease and for preclinical models for efficacy testing of new candidate pharmaceuticals. Since mice do not usually spontaneously develop asthma, an artificial asthmatic-like reaction is induced in the airways using an inhaled allergen including chicken egg ovalbumin (OVA), house dust mite, other parasites, birch pollen extract, *Aspergillus fumigatus*, or ragweed allergens [60, 88]. Viral infection and vaccine immunization can also induce an asthma-like syndrome [60, 75, 89, 90]. Allergic mouse models often produce eosinophilic inflammation, vasculitis, and mucous metaplasia of airways (Figures 12.33 and 12.34).

These allergens induce type-2 inflammation, which is associated with allergic/eosinophilic asthma in humans. The allergen, sensitization and challenge protocol, and inbred strain used all influence the model. Mouse strains commonly used include A/J, BALB/c, and C57BL/6 [91–93]. One of the real values of GEMs for investigating the pathogenesis of asthma are the large diversity of mice on various inbred and congenic backgrounds carrying immunodeficiencies (see Chapters 7 and 9).

Pulmonary Fibrosis Models

While a variety of mouse models are available for idiopathic pulmonary fibrosis (IPF) [80], few, if any, develop spontaneous pulmonary fibrosis. Based on disease surveillance observation in the Jackson Laboratory's production colonies, C3H/HeJ is one of the few strains prone to aspiration pneumonia that can result in fibrosis if the mice survive (J.P. Sundberg, unpublished). Possibly due to the high level of mouse husbandry (HEPA filtered air, pathogen free status, controlled food, water, and bedding, etc.), pulmonary fibrosis is rare in mice. In a 28 inbred strain aging study we found pulmonary fibrosis only occasionally as a minor lesion in 12 strains with no sexual dichotomy [42].

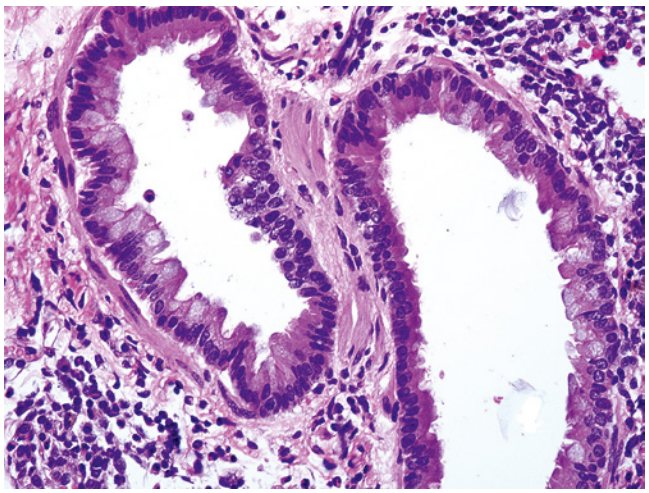


Figure 12.33 Club cell mucous metaplasia. Note the variable mucus in each club cell. Seven days after OVA exposure.

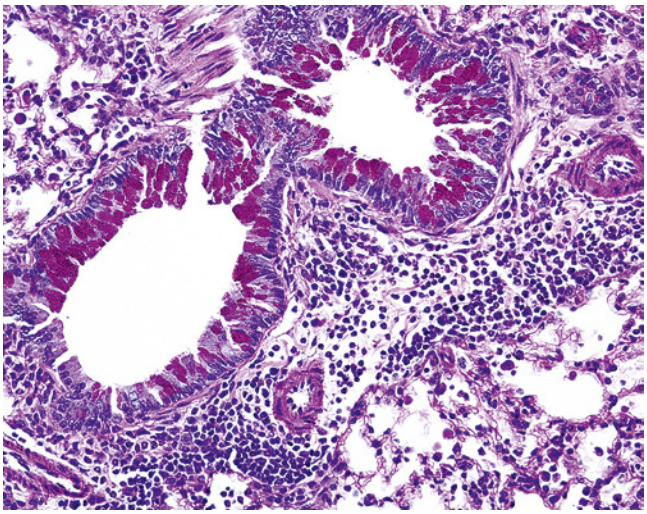


Figure 12.34 PAS stain of club cell mucous metaplasia. OVA model with peribronchiolar and perivascular cuffs containing many eosinophils.

Human pulmonary fibrosis is a severe, progressive disease resulting in airspace destruction by abnormal fibroblast proliferation and deposition of collagen-rich extracellular matrix. Although linked to exposure to radiation, minerals, metals, or smoke, for many cases the primary cause and predisposition remains unknown, i.e. IPF.

Genetic variants in a number of genes, presumably related to lung epithelial injury repair mechanisms and host defense, have been implicated as directly or indirectly causing IPF. A subset of IPF cases are inherited in an autosomal dominant manner; this syndrome is known as Familial Interstitial Pneumonia (FIP) and results in cases of pulmonary fibrosis that are clinically and histopathologically indistinguishable from cases that appear to be sporadic. Human whole exome sequencing (WES) approaches identified disease-associated novel and rare variants (RVs) in several genes that are potentially causative for human FIP. Of those genes reviewed a number of mutations were created in mice including mutations in *Sftpa*, *Terc*, and *Tert* [80]. Many of these models indirectly affect IPF by targeting inflammatory pathways, such as TGFA and NFKB, thereby regulating inflammation rather than being direct, single gene mutations that cause reproducible IPF in the mouse. In addition, these models do not spontaneously develop pulmonary fibrosis, but must be extensively treated to induce the disease state.

Vet-ebooks.com

Bleomycin is used experimentally to induce pulmonary fibrosis in mice [94]. The lesion tends to be focal and not diffuse (Figure 12.35). Recent studies have used machine learning to evaluate mouse lungs after bleomycin treatment [95]. This is one tool used to test GEM compared with wildtype control mice for IPF. However, there is a great deal of variation in response among inbred strains with some, such as C57BL/6 being highly susceptible, DBA/2 and Swiss mice intermediate responders, and BALB/c, BALB/cBy, and C3Hf/Kam being very resistant [96, 97]. Genetic studies indicated that bleomycin-induced pulmonary fibrosis is a heritable trait in mice controlled by a few genetic loci [98].

More recent studies indicating numerous genes are involved in bleomycin susceptibility in mice [98–100]. From these types of studies, both creation of mutations based on human genome wide association study (GWAS) studies and mapping studies done using highly susceptible or resistant inbred strains, it is possible to identify specific genes that regulate response to bleomycin [101, 102].

Lung Tumors

Lung cancer in humans is associated with cigarette, cigar, and pipe smoking, secondhand smoke, family history, HIV infection, environmental factors including radiation, workplace exposure to various chemicals, and other factors (http://www.cancer.gov/types/lung). Recently, electronic cigarette smoke was found to induce lung tumors in mice [103]. Somatic mutations in the *TP53*, *EGFR*, and *KRAS* genes are common in human lung cancers, while most lung cancers are not related to heritable genetic changes (https://medlineplus.gov/genetics/condition/lung-cancer/#causes). Squamous cell carcinomas show *TP53* mutations, adenocarcinomas *KRAS* and *EGFR* mutations, and small cell carcinoma with *RB1* and *TP53* mutations and *MYC* amplifications [104].

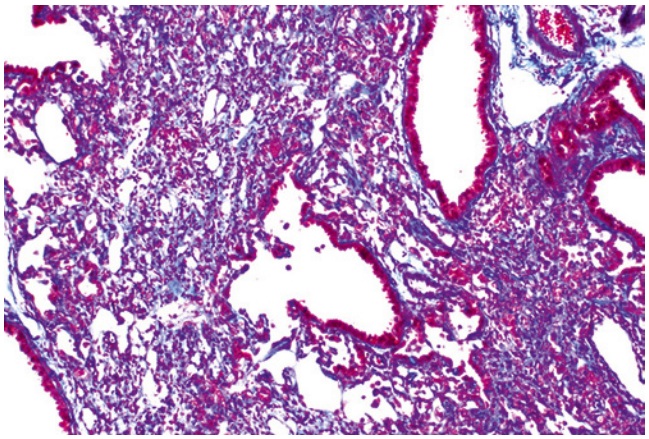


Figure 12.35 Fibrosis, alveolar. Masson's trichrome stain shows abundant collagen present (blue staining), 21 days after initial exposure to bleomycin.

Lung Tumors in Mice

Lung tumors are common spontaneous tumors in many strains of mice [42, 105, 106] and can be induced by chemicals [107, 108] and genetic engineering [109, 110]. The vast majority of the spontaneous lung tumors arise from alveolar type II cells [20, 22, 23] but others may arise from other lung cell types. Transcriptome analysis of spontaneous mouse lung tumors has been reported and compared with human lung tumors [24]. The classification of proliferative lung lesions was reviewed by the NCI mouse models of human cancer consortium [109] and others [110–112].

A recent review of lung tumors in GEM reveals lung adenocarcinoma models by targeting single or combined driver mutations to cells of origin, often AT2 cells and less so BASC (Table 12.4) [110, 113]. Most of these tumors involve *Kras* (*Kras*^{G12D}), *Ccsp*, and *Trp53* genetics. Tumors associated with *Kras* mutations may also arise from different cell types in mouse lung [114]. For some types of GEM, and especially in FVB.Cg-Tg(Scgb1a1-rtTA)1Jaw/J mice, a severe diffuse alveolar Type II cell proliferation occurs as a precursor to adenomas and carcinomas [115]. Lung squamous cell carcinoma mouse models were shown to involve *Ikka*, *Lkb*, *Pten*, and *Cdkn2b* genes [110]. Small cell lung cancer (SCLC) mouse models mostly involved *Trp53* and *Rb1* [110]. Many of these tumors arise from neuroendocrine cells. There are 368 mouse genotypes with increased lung tumors incidences (increased lung tumor incidence Mammalian Phenotype Term (MP:0008014) (jax.org)) and Mouse Models of Human Cancer Database (MMHCdb) (jax.org).

The National Cancer Institute (NCI) mouse models of cancer consortium have published a mouse lung tumor nomenclature (Table 12.5) [109]. For the most common alveolar tumor, the earliest lesions arise from alveolar type II cell hyperplasia (Figure 12.36), expressing Type II cell antigens, including NK2 homeobox 1 (NKX2-1, formerly TTF-1) (Figure 12.37), which leads to adenomas (Figure 12.38) [20]. Adenocarcinomas often develop in adenomas (Figure 12.39) in spontaneous tumors, chemically induced tumors, and by genetic engineering but also may arise *de novo* especially in some types of GEM. The foci of adenocarcinoma in the adenoma may have an increased cell proliferation rate as shown by Ki67 (*Mki67*) immunohistochemistry (IHC; Figure 12.40).

In specific types of GEM, the entire lung shows many foci of alveolar Type II cell hyperplasia leading to adenoma formation (Figure 12.41). The best example of this diffuse and multifocal histogenesis was described in FVB.Cg-Tg (Scgb1a1-rtTA) 1Jaw/J mice [115]. There was diffuse AT2 cell focal and diffuse hyperplasia and multiple adenomas with proliferative cells expressing *Sftpc* (Figure 12.41). In some *Kras*^{G12D} models, papillary hyperplasia of bronchiolar Club cells (Figure 12.42) may lead to tumors but often does not. Papillary lesions reveal SFTPC expression (Figure 12.43) but tumors do not (Figures 12.43 and 12.44). Tumors have various degrees of labeling for SFTPC. Adenocarcinomas may develop from adenomas and have variable histologic patterns even in the same tumor (Figure 12.45). Squamous cell carcinomas may arise from squamous metaplasia in

Vet-ebooks.com

Table 12.4 Examples of lung tumors from targeting single or combined driver mutations.

Tumor type	Cell type	Genetics	Inducer
Adenocarcinoma	AT2	*LSL-KrasG12D IN*	IN AdCre
	AT2	*CCSP-rtTA; Trp53F/F; KrasLSL-G12D/+*	Dox
	Club cell	*LSL-KrasG12D; Trp53Flox/+; CC10CreER/+; Rosa26R-fGFP*	Tam
	AT2	*CCSP-rtTA; TetO-EGFRL858R*	Dox
Squamous cell carcinoma	Lung cells	*PtenF/F;Lkb1F/F*	IN AdCre
	Lung cells	*Lori-IKKα; IkkαKA/KA*	Transgenic expression IKKα in Loripos cells; *Ikkα* germline mutation
	Lung cells	*Sox2CreER; Rosa26LSL-Sox2-IRES-GFPF/F; Nkx2-1F/F*	Tam
Small cell carcinoma	NE	*Trp53F/F;Rb1F/F IT*	IT Ad5-CGRP-Cre
	NE	*Trp53F/F;Rb1F/F;PtenF/+*	IT Ad5-CMV-Cre
	NE	*Trp53F/F;Rb1F/F;Fgfr1K656E*	IT Ad5-CGRP-Cre

NE = neuroendocrine, AT2 = alveolar Type II cell, Dox = doxycycline, Tam = tamoxifen, IN = intranasal, IT = intratracheal.
Source: Adapted from Ferone [110].

Table 12.5 Classification of proliferative lung lesions of mice.

1. Epithelial
1.1. Hyperplasia
1.1.1. Epithelial
1.1.1.1. Airways (bronchi, bronchioles)
1.1.1.2. Alveoli (alveolar Type I and II cells)
1.1.2. Neuroendocrine
1.2. Tumors
1.2.1. Benign
1.2.1.1. Papilloma
1.2.1.2. Adenoma
1.2.1.2.1. Solid
1.2.1.2.2. Papillary
1.2.1.2.3. Mixed subtypes
1.2.2. Preinvasive lesions
1.2.2.1. Squamous dysplasia
1.2.2.2. Atypical adenomatous hyperplasia
1.2.2.3. Diffuse pulmonary neuroendocrine cell hyperplasia
1.2.3. Malignant
1.2.3.1. Squamous cell carcinoma
1.2.3.2. Adenocarcinoma
1.2.3.2.1. Papillary
1.2.3.2.2. Acinar
1.2.3.2.3. Solid

Table 12.5 (Continued)

1.2.3.2.4. Mixed subtypes
1.2.3.2.5. Not otherwise specified, NOS
1.2.3.3. Adenosquamous carcinoma
1.2.3.4. Neuroendocrine carcinoma (small cell)
1.2.3.5. Carcinoma, other
1.2.3.6 Carcinosarcoma (Epithelial-Mesenchymal (EMT)
2. Soft tissue
3. Mesothelial
4. Lymphoproliferative
5. Secondary (metastatic)
6. Unclassified/miscellaneous
7. Tumor-like lesions

Modifiers – Modifiers should be used when sufficient information is available on the location and cell origin of the lesions including bronchial, bronchiolar, Club cell, neuroendocrine, alveolar Type I cell (AT1), alveolar Type II cell (AT2), as indicated in the table.
Source: Modified from Nikitin [109].

bronchi and bronchioles (Figure 12.46), especially when induced by carcinogens. More recently, BASCs at the bronchioalveolar junction [13] may develop into papillary and other tumor types in mice [110]. Neuroendocrine tumors (small cell carcinomas) in GEM (Figure 12.47) resemble those of humans [116]. The lung is also a common site of metastasis of primary tumors especially in GEM from mouse prostate, pancreas, liver, and other tissues (Figure 12.48).

Vet-ebooks.com

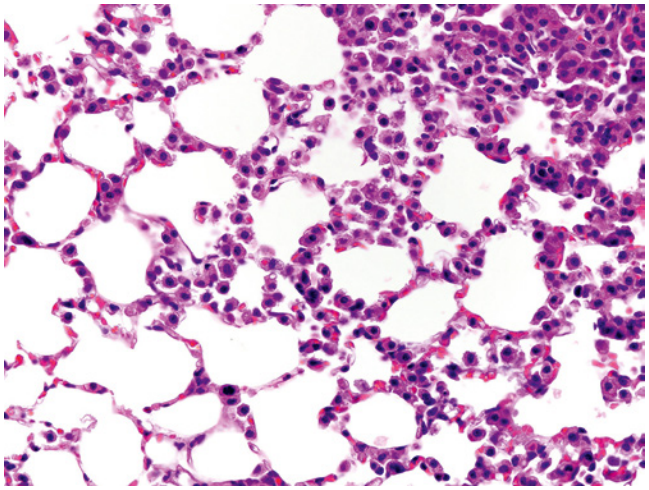


Figure 12.36 **Hyperplasia, alveolar**. Alveolar Type II cell (AT2) hyperplasia in a *Kras* lung tumor model.

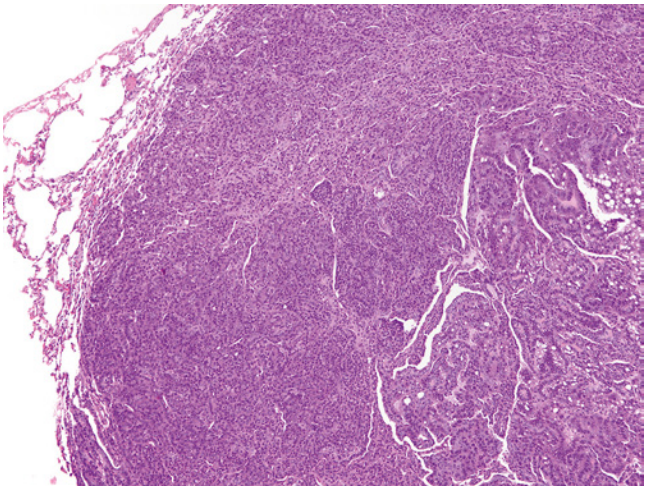


Figure 12.39 **Adenocarcinoma (right side) in an adenoma**. Note the papillary lesions. Induced by vinyl carbamate.

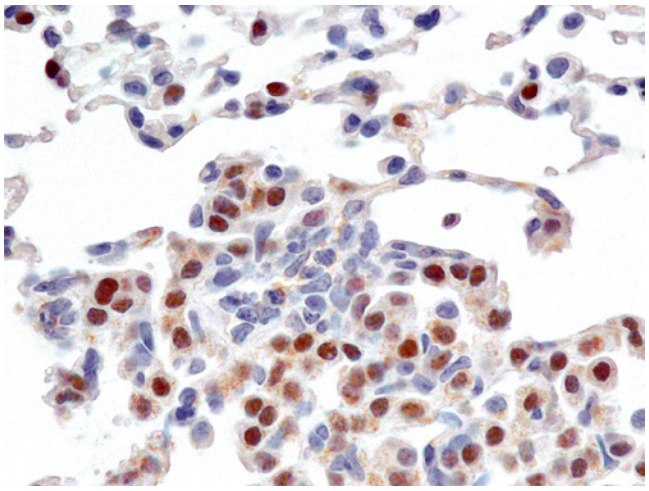


Figure 12.37 **Hyperplasia, alveolar Type II cells (AT2)**. TTF1 antigen (NKX2-1) nuclear labeling. Note adjacent normal AT2 cells (top) are also reactive.

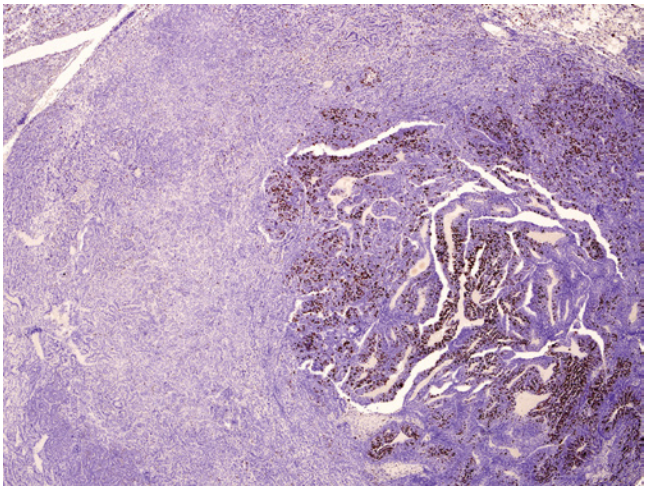


Figure 12.40 **Cell proliferation in the adenocarcinoma developing in an adenoma**. Ki67 (*Mki67*) is abundant in the focus of adenocarcinoma.

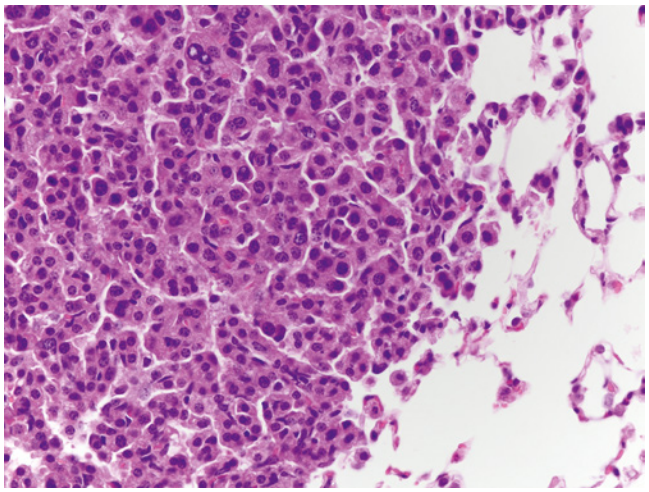


Figure 12.38 **Adenoma, alveolar Type II cell (AT2)**. The tumor cells are uniform in morphology.

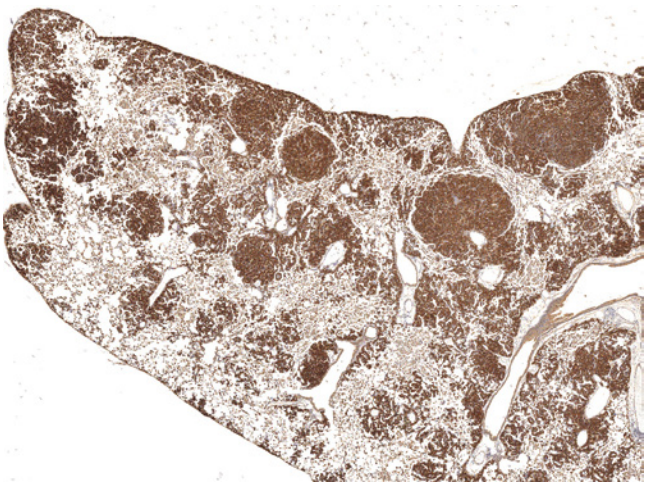


Figure 12.41 **Alveolar Type II cell (AT2) antigen (SFTPD)**. The antigen can be seen within hyperplastic alveolar lesions and adenomas in a *Egfr*$^{L858R\text{-}T790M}$*;Ccsp-rtTA* mouse.

Vet-ebooks.com

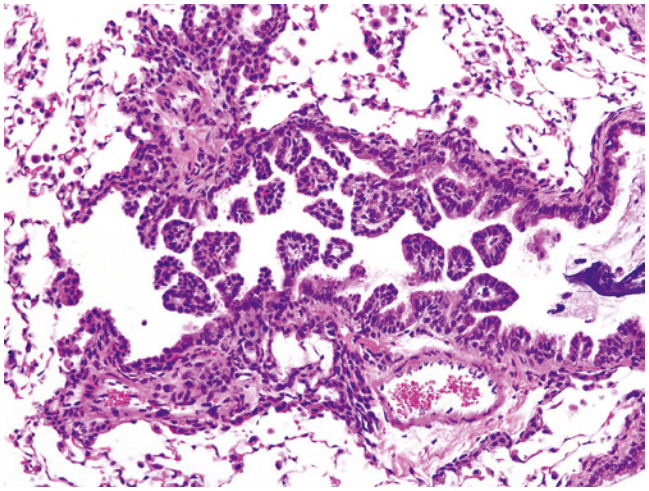


Figure 12.42 **Papillary bronchiolar hyperplasia**. Multiple lesions in the bronchiole in a *Ccsp-cre-Rosa/LSL-Kras*^{G12D} mutant.

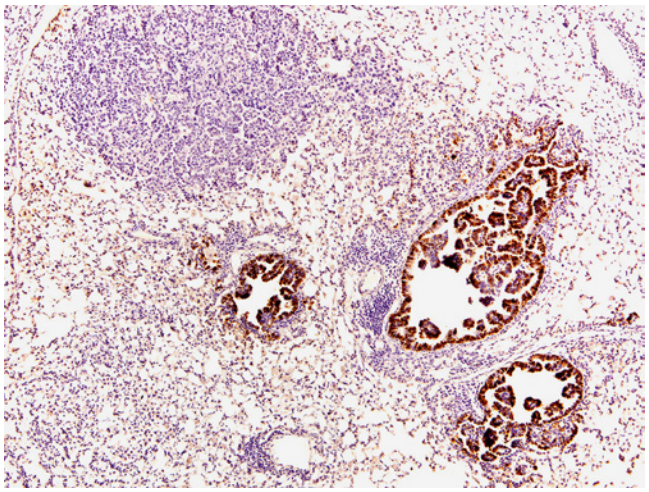


Figure 12.43 **SCGB1A1 antigen in papillary hyperplasia**. Note the adenoma and alveolar hyperplasias are negative. *Ccsp-cre-Rosa/LSL-Kras*^{G12D} mutant.

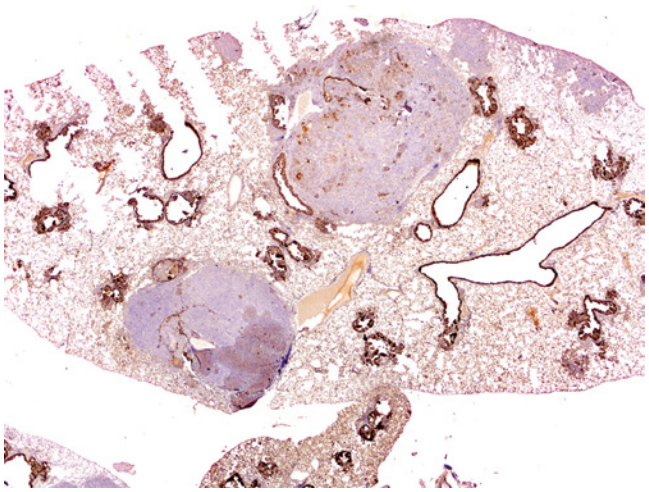


Figure 12.44 SCGB1A1 antigen in bronchioles. Note lack of labeling in adenomas. *Ccsp-cre-Rosa/LSL-Kras*^{G12D} mutant.

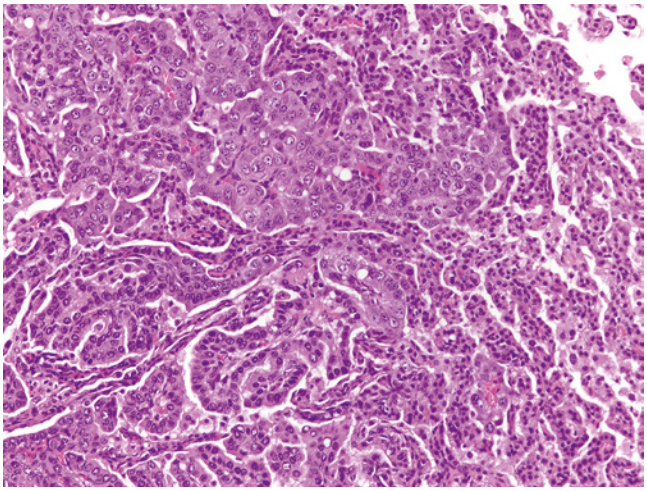


Figure 12.45 **Adenocarcinoma**. Solid and papillary patterns can be seen.

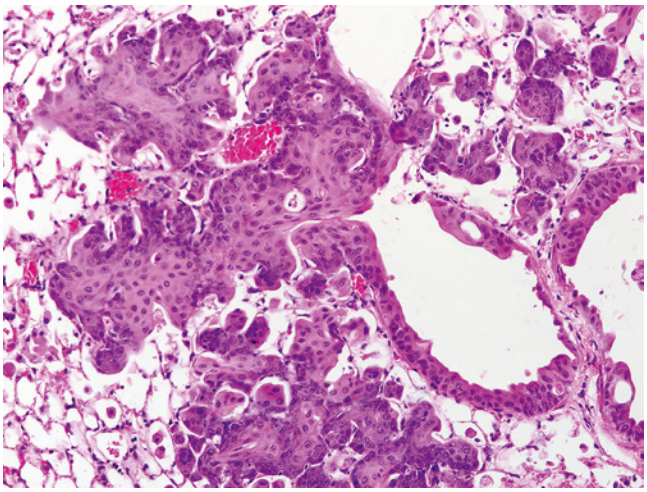


Figure 12.46 **Squamous metaplasia**. Squamous lesions in bronchiole and alveoli.

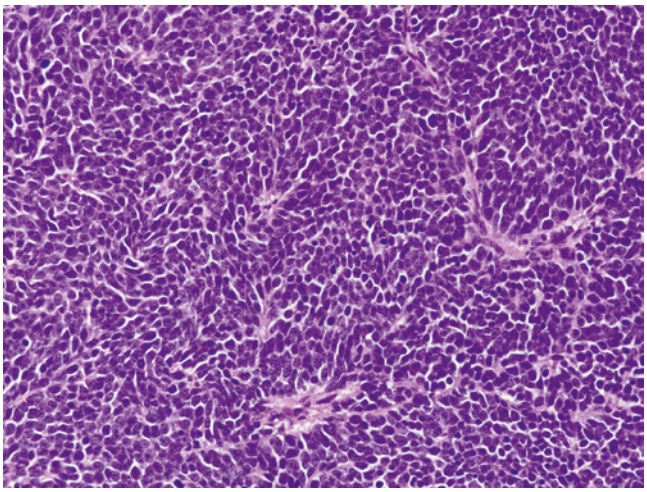


Figure 12.47 **Neuroendocrine carcinoma**. Small cell carcinoma in a mutant mouse. Note scant cytoplasm.

Vet-ebooks.com

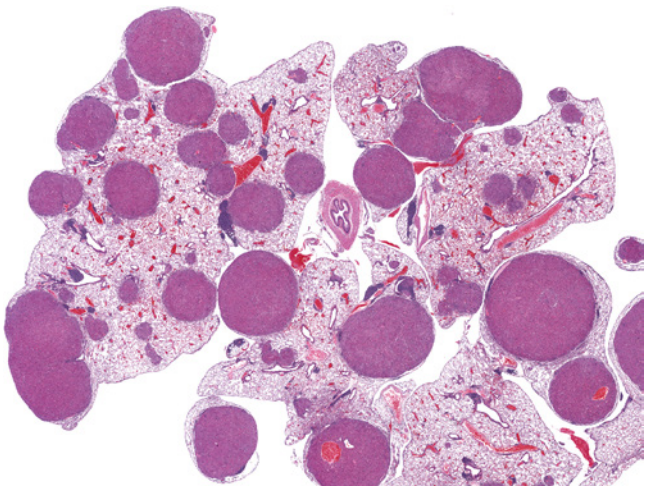


Figure 12.48 **Metastatic liver tumors in lung**. Note many tumor nodules of various sizes from primary hepatocellular carcinoma.

References

1 Harkema, J.R., Nikula, K.J., and Haschek, W.M. (2018). Respiratory system. In: *Fundamentals of Toxicologic Pathology*, 3e (eds. M.A. Wallig, W.M. Haschek, C.G. Rousseaux, et al.), 351–393. London: Elsevier.

2 Harkema, J.R., Carey, S.A., Wagner, J.G. et al. (2018). Nose, sinus, pharynx and larynx. In: *Comparative anatomy and histology: a mouse, rat and human atlas* (eds. P.M. Treuting, S.M. Dintzis and K.S. Montine), 89–114. London: Elsevier.

3 Knoblaugh, S.E. and Randolph-Habecker, J. (2018). Necropsy and histology. In: *Comparative Anatomy and Histology*, 2e (eds. P.M. Treuting, S.M. Dintzis and K.S. Montine), 23–51. London: Elsevier.

4 Zheng, J., Wong, L.R., Li, K. et al. (2020). COVID-19 treatments and pathogenesis including anosmia in K18-hACE2 mice. *Nature* 9.

5 Odgren, P.R., Pratt, C.H., Mackay, C.A. et al. (2010). Disheveled hair and ear (*Dhe*), a spontaneous mouse *Lmna* mutation modeling human laminopathies. *PLoS One*. [Research Support, N.I.H., Extramural] 5 (4): e9959.

6 Gritli-Linde, A. (2008). The etiopathogenesis of cleft lip and cleft palate: usefulness and caveats of mouse models. *Curr. Top Dev. Biol.* 84: 37–138.

7 Gritli-Linde, A. (2012). The mouse as a developmental model for cleft lip and palate research. *Front Oral Biol.* [Research Support, Non-U.S. Gov't] 16: 32–51.

8 Juriloff, D.M. and Harris, M.J. (2008). Mouse genetic models of cleft lip with or without cleft palate. *Birth Defects Res. A Clin. Mol. Teratol.* 82 (2): 63–77.

9 Suzuki, A., Abdallah, N., Gajera, M. et al. (2018). Genes and microRNAs associated with mouse cleft palate: a systematic review and bioinformatics analysis. *Mech. Dev.* 150: 21–27.

10 Sood, C.L., Ward, J.M., and Moss, B. (2008). Vaccinia virus encodes I5, a small hydrophobic virion membrane protein that enhances replication and virulence in mice. *J. Virol.* 82 (20): 10071–10078.

11 Meyerholz, D.K., Suarez, C.J., Dintziz, S.M., and Frevert, C.W. (2018). Respiratory System. In: *Comparative Anatomy and Histology: A Mouse, Rat and Human Atlas* (eds. P.M. Treuting, S.M. Dintzis and K.S. Montine), 147–162. London: Elsevier.

12 Ruberte, J., Carretero, A., and Navarro, M. (eds.) (2017). *Morphological Mouse Phenotyping: Anatomy, Histology and Imaging*. Amsterdam: Academic.

13 Jones-Freeman, B. and Starkey, M.R. (2020). Bronchioalveolar stem cells in lung repair, regeneration and disease. *J. Pathol.* 252 (3): 219–226.

14 Fernanda de Mello Costa, M., Weiner, A.I., and Vaughan, A.E. (2020). Basal-like progenitor cells: a review of dysplastic alveolar regeneration and remodeling in lung repair. *Stem Cell Reports* 15 (5): 1015–1025.

15 Randall, T.D. (2010). Bronchus-associated lymphoid tissue (BALT) structure and function. *Adv. Immunol.* 107: 187–241.

16 Van Winkle, L.S., Kelty, J.S., and Plopper, C.G. (2017). Preparation of specific compartments of the lungs for pathologic and biochemical analysis of toxicologic responses. *Curr. Protoc. Toxicol.* 71: 24.5.1–24.5.6.

17 Davenport, M.L., Sherrill, T.P., Blackwell, T.S., and Edmonds, M.D. (2020). Perfusion and inflation of the mouse lung for tumor histology. *J. Vis. Exp.* 162.

18 Limjunyawong, N., Mock, J., and Mitzner, W. (2015). Instillation and fixation methods useful in mouse lung cancer research. *J. Vis. Exp.* (102): e52964.

19 Morton, J. and Snider, T.A. (2017). Guidelines for collection and processing of lungs from aged mice for histological studies. *Pathobiol. Aging Age Relat. Dis.* 7 (1): 1313676.

20 Rehm, S., Devor, D.E., Henneman, J.R., and Ward, J.M. (1991). Origin of spontaneous and transplacentally induced mouse lung tumors from alveolar type II cells. *Exp. Lung Res.* 17 (2): 181–195.

Vet-ebooks.com

21 Rehm, S. and Ward, J.M. (1989). Quantitative analysis of alveolar type II cell tumors in mice by whole lung serial and step sections. *Toxicol. Pathol.* 17 (4 Pt 2): 737–742.

22 Rehm, S., Ward, J.M., ten Have-Opbroek, A.A. et al. (1988). Mouse papillary lung tumors transplacentally induced by N-nitrosoethylurea: evidence for alveolar type II cell origin by comparative light microscopic, ultrastructural, and immunohistochemical studies. *Cancer Res.* 48 (1): 148–160.

23 Ward, J.M., Singh, G., Katyal, S.L. et al. (1985). Immunocytochemical localization of the surfactant apoprotein and Clara cell antigen in chemically induced and naturally occurring pulmonary neoplasms of mice. *Am. J. Pathol.* 118 (3): 493–499.

24 Pandiri, A.R., Sills, R.C., Ziglioli, V. et al. (2012). Differential transcriptomic analysis of spontaneous lung tumors in B6C3F1 mice: comparison to human non-small cell lung cancer. *Toxicol. Pathol.* 40 (8): 1141–1159.

25 Bird, A.D., McDougall, A.R., Seow, B. et al. (2015). Glucocorticoid regulation of lung development: lessons learned from conditional GR knockout mice. *Mol. Endocrinol.* 29 (2): 158–171.

26 Kimura, S., Hara, Y., Pineau, T. et al. (1996). The T/ebp null mouse: thyroid-specific enhancer-binding protein is essential for the organogenesis of the thyroid, lung, ventral forebrain, and pituitary. *Genes Dev.* 10 (1): 60–69.

27 Pineau, T., Fernandez-Salguero, P., Lee, S.S. et al. (1995). Neonatal lethality associated with respiratory distress in mice lacking cytochrome P450 1A2. *Proc. Natl. Acad. Sci. U.S.A.* 92 (11): 5134–5138.

28 Ren, J., Lee, S., Pagliardini, S. et al. (2003). Absence of *Ndn*, encoding the Prader-Willi syndrome-deleted gene necdin, results in congenital deficiency of central respiratory drive in neonatal mice. *J. Neurosci.* 23 (5): 1569–1573.

29 Zhang, Y., Li, F., Wang, Y. et al. (2015). Maternal bile acid transporter deficiency promotes neonatal demise. *Nat. Commun.* 6: 8186.

30 Vogel, P., Read, R.W., Rehg, J.E., and Hansen, G.M. (2013). Cryptogenic organizing pneumonia in *Tomm5*(−/−) mice. *Vet. Pathol.* 50 (1): 65–75.

31 van Loenhout, R.B., Tibboel, D., Post, M., and Keijzer, R. (2009). Congenital diaphragmatic hernia: comparison of animal models and relevance to the human situation. *Neonatology* 96 (3): 137–149.

32 Longoni, M., High, F.A., Qi, H. et al. (2017). Genome-wide enrichment of damaging de novo variants in patients with isolated and complex congenital diaphragmatic hernia. *Hum. Genet.* 136 (6): 679–691.

33 Takamoto, N., You, L.R., Moses, K. et al. (2005). COUP-TFII is essential for radial and anteroposterior patterning of the stomach. *Development* 132 (9): 2179–2189.

34 Russell, M.K., Longoni, M., Wells, J. et al. (2012). Congenital diaphragmatic hernia candidate genes derived from embryonic transcriptomes. *Proc. Natl. Acad. Sci. U.S.A.* 109 (8): 2978–2983.

35 Selleri, L., Depew, M.J., Jacobs, Y. et al. (2001). Requirement for Pbx1 in skeletal patterning and programming chondrocyte proliferation and differentiation. *Development* 128 (18): 3543–3557.

36 Shultz, L.D., Schweitzer, P.A., Hall, E.J. et al. (1989). Pneumocystis carinii pneumonia in *scid/scid* mice. *Curr. Top Microbiol. Immunol.* 152: 243–249.

37 Dumont, F. and Barrois, R. (1976). Electrokinetic properties of splenic lymphocytes from the low-lipopolysaccharide responder C3H/HeJ mice. *Folia Biol (Praha).* 12 (3): 145–150.

38 Bleich, A., Kirsch, P., Sahly, H. et al. (2008). *Klebsiella oxytoca*: opportunistic infections in laboratory rodents. *Lab. Anim.* 42 (3): 369–375.

39 Hoenerhoff, M.J., Starost, M.F., and Ward, J.M. (2006). Eosinophilic crystalline pneumonia as a major cause of death in 129S4/SvJae mice. *Vet. Pathol.* 43 (5): 682–688.

40 Ward, J.M., Yoon, M., Anver, M.R. et al. (2001). Hyalinosis and Ym1/Ym2 gene expression in the stomach and respiratory tract of 129S4/SvJae and wild-type and CYP1A2-null B6, 129 mice. *Am. J. Pathol.* 158 (1): 323–332.

41 Haines, D.C., Chattopadhyay, S., and Ward, J.M. (2001). Pathology of aging B6;129 mice. *Toxicol. Pathol.* 29 (6): 653–661.

42 Sundberg, J.P., Berndt, A., Sundberg, B.A. et al. (2016). Approaches to investigating complex genetic traits in a large-scale inbred mouse aging study. *Vet. Pathol.* 53 (2): 456–467.

43 Green, M.C. and Shultz, L.D. (1975). Motheaten, an immunodeficient mutant of the mouse I. Genetics and pathology. *J. Hered.* 66 (5): 250–258.

44 Guo, L., Johnson, R.S., and Schuh, J.C. (2000). Biochemical characterization of endogenously formed eosinophilic crystals in the lungs of mice. *J. Biol. Chem.* 275 (11): 8032–8037.

45 Ward, J.M. (1978). Pulmonary pathology of the motheaten mouse. *Vet. Pathol.* 15 (2): 170–178.

46 Liu, Q., Cheng, L.I., Yi, L. et al. (2009). p47phox deficiency induces macrophage dysfunction resulting in progressive crystalline macrophage pneumonia. *Am. J. Pathol.* 174 (1): 153–163.

47 Waern, I., Jia, J., Pejler, G. et al. (2010). Accumulation of Ym1 and formation of intracellular crystalline bodies in alveolar macrophages lacking heparanase. *Mol. Immunol.* 47 (7–8): 1467–1475.

48 Zhang, W., Trible, R.P., and Samelson, L.E. (1998). LAT palmitoylation: its essential role in membrane microdomain targeting and tyrosine phosphorylation during T cell activation. *Immunity* 9 (2): 239–246.

49 Zhu, W., Lonnblom, E., Forster, M. et al. (2020). Natural polymorphism of Ym1 regulates pneumonitis through alternative activation of macrophages. *Sci. Adv.* 6 (43): eaba9337.

50 Meyerholz, D.K. and Beck, A.P. (2018). Fundamental concepts for semiquantitative tissue scoring in translational research. *ILAR J.* 59 (1): 13–17.

51 Meyerholz, D.K. and Beck, A.P. (2020). Histopathologic evaluation and scoring of viral lung infection. *Methods Mol. Biol.* 2099: 205–220.

52 Meyerholz, D.K., Sieren, J.C., Beck, A.P., and Flaherty, H.A. (2018). Approaches to evaluate lung inflammation in translational research. *Vet. Pathol.* 55 (1): 42–52.

Vet-ebooks.com

53 Klopfleisch, R. (2013). Multiparametric and semiquantitative scoring systems for the evaluation of mouse model histopathology – a systematic review. *BMC Vet. Res.* 9: 123.

54 Renne, R., Brix, A., Harkema, J. et al. (2009). Proliferative and nonproliferative lesions of the rat and mouse respiratory tract. *Toxicol. Pathol.* 37 (7 Suppl): 5S–73S.

55 Matute-Bello, G., Downey, G., Moore, B.B. et al. (2011). An official American Thoracic Society workshop report: features and measurements of experimental acute lung injury in animals. *Am. J. Respir. Cell Mol. Biol.* 44 (5): 725–738.

56 Dietert, K., Nouailles, G., Gutbier, B. et al. (2018). Digital image analyses on whole-lung slides in mouse models of acute pneumonia. *Am. J. Respir. Cell Mol. Biol.* 58 (4): 440–448.

57 Vasilescu, D.M., Klinge, C., Knudsen, L. et al. (2013). Stereological assessment of mouse lung parenchyma via nondestructive, multiscale micro-CT imaging validated by light microscopic histology. *J. Appl. Physiol.* 114 (6): 716–724.

58 Schully, K.L., Bell, M.G., Ward, J.M., and Keane-Myers, A.M. (2014). Oropharyngeal aspiration of *Burkholderia mallei* and *Burkholderia pseudomallei* in BALB/c mice. *PLoS One* 9 (12): e115066.

59 Kuiken, T., van den Brand, J., van Riel, D. et al. (2010). Comparative pathology of select agent influenza a virus infections. *Vet. Pathol.* 47 (5): 893–914.

60 Han, M., Rajput, C., Ishikawa, T. et al. (2018). Small animal models of respiratory viral infection related to asthma. *Viruses* 10 (12): 682. https://doi.org/10.3390/v10120682.

61 Sell, S., McKinstry, K.K., and Strutt, T.M. (2019). Mouse models reveal role of T-cytotoxic and T-reg cells in immune response to influenza: implications for vaccine design. *Viruses* 11 (1): 52. https://doi.org/10.3390/v11010052.

62 Gurumurthy, C.B., Quadros, R.M., Richardson, G.P. et al. (2020). Genetically modified mouse models to help fight COVID-19. *Nat. Protoc.* 15 (12): 3777–3787.

63 Hewitt, J.A., Lutz, C., Florence, W.C. et al. (2020). ACTIVating resources for the COVID-19 pandemic: in vivo models for vaccines and therapeutics. *Cell Host Microbe* 28 (5): 646–659.

64 Ward, J.M. (1974). Naturally occurring Sendai virus disease of mice. *Lab. Anim. Sci.* 24 (6): 938–942.

65 Ward, J.M., Houchens, D.P., Collins, M.J. et al. (1976). Naturally-occurring Sendai virus infection of athymic nude mice. *Vet. Pathol.* 13 (1): 36–46.

66 Frieman, M.B., Chen, J., Morrison, T.E. et al. (2010). SARS-CoV pathogenesis is regulated by a STAT1 dependent but a type I, II and III interferon receptor independent mechanism. *PLoS Pathog.* 6 (4): e1000849.

67 Hassert, M., Geerling, E., Stone, E.T. et al. (2020). mRNA induced expression of human angiotensin-converting enzyme 2 in mice for the study of the adaptive immune response to severe acute respiratory syndrome coronavirus 2. *PLoS Pathog.* 16 (12): e1009163.

68 Buchholz, U.J., Ward, J.M., Lamirande, E.W. et al. (2009). Deletion of nonstructural proteins NS1 and NS2 from pneumonia virus of mice attenuates viral replication and reduces pulmonary cytokine expression and disease. *J. Virol.* 83 (4): 1969–1980.

69 Golden, J.W., Cline, C.R., Zeng, X. et al. (2020). Human angiotensin-converting enzyme 2 transgenic mice infected with SARS-CoV-2 develop severe and fatal respiratory disease. *JCI Insight.* 5 (19): e142032.

70 Dinnon, K.H. 3rd, Leist, S.R., Schafer, A. et al. (2020). A mouse-adapted model of SARS-CoV-2 to test COVID-19 countermeasures. *Nature* 586 (7830): 560–566.

71 Lee, B., Gopal, R., Manni, M.L. et al. (2017). STAT1 is required for suppression of type 17 immunity during influenza and bacterial superinfection. *Immunohorizons* 1 (6): 81–91.

72 Corbett, K.S., Edwards, D.K., Leist, S.R. et al. (2020). SARS-CoV-2 mRNA vaccine design enabled by prototype pathogen preparedness. *Nature* 586 (7830): 567–571.

73 Zheng, Y., Bian, L., Zhao, H. et al. (2020). Respiratory syncytial virus F subunit vaccine with AS02 adjuvant elicits balanced, robust humoral and cellular immunity in BALB/c mice. *Front. Immunol.* 11: 526965.

74 Hijano, D.R., Vu, L.D., Kauvar, L.M. et al. (2019). Role of type I interferon (IFN) in the respiratory syncytial virus (RSV) immune response and disease severity. *Front. Immunol.* 10: 566.

75 Altamirano-Lagos, M.J., Diaz, F.E., Mansilla, M.A. et al. (2019). Current animal models for understanding the pathology caused by the respiratory syncytial virus. *Front. Microbiol.* 10: 873.

76 Kramnik, I. and Beamer, G. (2016). Mouse models of human TB pathology: roles in the analysis of necrosis and the development of host-directed therapies. *Semin. Immunopathol.* 38 (2): 221–237.

77 Martinot, A.J., Blass, E., Yu, J. et al. (2020). Protective efficacy of an attenuated Mtb DeltaLprG vaccine in mice. *PLoS Pathog.* 16 (12): e1009096.

78 Dishop, M.K. (2017). Congenital, developmental, and inherited disorders. In: *Pulmonary Pathology* (eds. D.S. Zander and C.F. Farver), 42–60. Philadelphia: Elsevier.

79 Alapati, D. and Morrisey, E.E. (2017). Gene editing and genetic lung disease. Basic research meets therapeutic application. *Am. J. Respir. Cell Mol. Biol.* 56 (3): 283–290.

80 Glasser, S.W. and Senft, A.P. (2011). Use of transgenic mouse models to understand the origins of familial pulmonary fibrosis. *Curr. Pharm. Biotechnol.* 12 (9): 1447–1454.

81 Lavelle, G.M., White, M.M., Browne, N. et al. (2016). Animal models of cystic fibrosis pathology: phenotypic parallels and divergences. *Biomed. Res. Int.* 2016: 5258727.

82 Zhou, Z., Duerr, J., Johnnesson, B. et al. (2011). The bENaC-0verexpressing mouse as a model of cystic fibrosis lung disease. *J. Cystic Fibrosis* 10 (Suppl 2): S172–S182.

83 Olivier, A.K., Gibson-Corley, K.N., and Meyerholz, D.K. (2015). Animal models of gastrointestinal and liver diseases. Animal models of cystic fibrosis: gastrointestinal, pancreatic, and hepatobiliary disease and pathophysiology. *Am. J. Physiol. Gastrointest. Liver Physiol.* 308 (6): G459–G471.

84 Berndt, A., Li, Q., Potter, C.S. et al. (2013). A single-nucleotide polymorphism in the *Abcc6* gene associates with connective tissue mineralization in mice similar to targeted models for pseudoxanthoma elasticum. *J. Invest. Dermatol.* 133 (3): 833–836.

Vet-ebooks.com

85 Klement, J.F., Matsuzaki, Y., Jiang, Q.J. et al. (2005). Targeted ablation of the *Abcc6* gene results in ectopic mineralization of connective tissues. *Mol. Cell. Biol.* 25 (18): 8299–8310.

86 Li, Q., Philip, V.M., Stearns, T.M. et al. (2019). Quantitative trait locus and integrative genomics revealed candidate modifier genes for ectopic mineralization in mouse models of pseudoxanthoma elasticum. *J. Invest. Dermatol.* 139 (12): 2447–2457. e7.

87 Li, Q., Price, T.P., Sundberg, J.P., and Uitto, J. (2014). Juxta-articular joint-capsule mineralization in CD73 deficient mice: similarities to patients with *NT5E* mutations. *Cell Cycle* 13 (16): 2609–2615.

88 Alessandrini, F., Musiol, S., Schneider, E. et al. (2020). Mimicking antigen-driven asthma in rodent models-how close can we get? *Front. Immunol.* 11: 575936.

89 Tseng, C.T., Sbrana, E., Iwata-Yoshikawa, N. et al. (2012). Immunization with SARS coronavirus vaccines leads to pulmonary immunopathology on challenge with the SARS virus. *PLoS One.* 7 (4): e35421.

90 Silveira, J.S., Antunes, G.L., Gassen, R.B. et al. (2019). Respiratory syncytial virus increases eosinophil extracellular traps in a murine model of asthma. *Asia Pac. Allergy* 9 (4): e32.

91 Maltby, S., Tay, H.L., Yang, M., and Foster, P.S. (2017). Mouse models of severe asthma: understanding the mechanisms of steroid resistance, tissue remodelling and disease exacerbation. *Respirology* 22 (5): 874–885.

92 Kumar, R.K., Herbert, C., and Foster, P.S. (2016). Mouse models of acute exacerbations of allergic asthma. *Respirology* 21 (5): 842–849.

93 Nials, A.T. and Uddin, S. (2008). Mouse models of allergic asthma: acute and chronic allergen challenge. *Dis. Models Mech.* 1 (4–5): 213–220.

94 Kurotani, R., Okumura, S., Matsubara, T. et al. (2011). Secretoglobin 3A2 suppresses bleomycin-induced pulmonary fibrosis by transforming growth factor beta signaling down-regulation. *J. Biol. Chem.* 286 (22): 19682–19692.

95 Bordag, N., Biasin, V., Schnoegl, D. et al. (2020). Machine learning analysis of the bleomycin mouse model reveals the compartmental and temporal inflammatory pulmonary fingerprint. *iScience* 23 (12): 101819.

96 Schrier, D.J., Kunkel, R.G., and Phan, S.H. (1983). The role of strain variation in murine bleomycin-induced pulmonary fibrosis. *Am. Rev. Respir. Dis.* 127 (1): 63–66.

97 Baecher-Allan, C.M. and Barth, R.K. (1993). PCR analysis of cytokine induction profiles associated with mouse strain variation in susceptibility to pulmonary fibrosis. *Reg. Immunol.* 5 (3–4): 207–217.

98 Haston, C.K., Amos, C.I., King, T.M., and Travis, E.L. (1996). Inheritance of susceptibility to bleomycin-induced pulmonary fibrosis in the mouse. *Cancer Res.* 56 (11): 2596–2601.

99 Lemay, A.M. and Haston, C.K. (2005). Bleomycin-induced pulmonary fibrosis susceptibility genes in AcB/BcA recombinant congenic mice. *Physiol. Genomics* 23 (1): 54–61.

100 Haston, C.K., Tomko, T.G., Godin, N. et al. (2005). Murine candidate bleomycin induced pulmonary fibrosis susceptibility genes identified by gene expression and sequence analysis of linkage regions. *J. Med. Genet.* 42 (6): 464–473.

101 Stefanov, A.N., Fox, J., Depault, F., and Haston, C.K. (2013). Positional cloning reveals strain-dependent expression of Trim16 to alter susceptibility to bleomycin-induced pulmonary fibrosis in mice. *PLoS Genet.* 9 (1): e1003203.

102 Paun, A., Lemay, A.M., Tomko, T.G., and Haston, C.K. (2013). Association analysis reveals genetic variation altering bleomycin-induced pulmonary fibrosis in mice. *Am. J. Respir. Cell Mol. Biol.* 48 (3): 330–336.

103 Tang, M.S., Wu, X.R., Lee, H.W. et al. (2019). Electronic-cigarette smoke induces lung adenocarcinoma and bladder urothelial hyperplasia in mice. *Proc. Natl. Acad. Sci. U.S.A.* 116 (43): 21727–21731.

104 Travis, W.D., Brambilla, E., Burke, A.P. et al. (2015). *WHO Classification of Tumours of the Lung, Pleura, Thymus and Hear*. Lyon: IARC.

105 Brayton, C.F., Treuting, P.M., and Ward, J.M. (2012). Pathobiology of aging mice and GEM: background strains and experimental design. *Vet. Pathol.* 49 (1): 85–105.

106 Tarone, R.E., Chu, K.C., and Ward, J.M. (1981). Variability in the rates of some common naturally occurring tumors in Fischer 344 rats and (C57BL/6N x C3H/HeN)F1 (B6C3F1) mice. *J. Natl. Cancer Inst.* 66 (6): 1175–1181.

107 Gold, L.S., Manley, N.B., Slone, T.H., and Ward, J.M. (2001). Compendium of chemical carcinogens by target organ: results of chronic bioassays in rats, mice, hamsters, dogs, and monkeys. *Toxicol. Pathol.* 29 (6): 639–652.

108 Pandiri, A. (2015). Comparative pathobiology of environmentally induced lung cancers in humans and rodents. *Toxicol. Pathol.* 43 (1): 107–114.

109 Nikitin, A.Y., Alcaraz, A., Anver, M.R. et al. (2004). Classification of proliferative pulmonary lesions of the mouse: recommendations of the mouse models of human cancers consortium. *Cancer Res.* 64 (7): 2307–2316.

110 Ferone, G., Lee, M.C., Sage, J., and Berns, A. (2020). Cells of origin of lung cancers: lessons from mouse studies. *Genes Dev.* 34 (15–16): 1017–1032.

111 Mohr, U. (2001). *International Classification of Rodent Tumors: The Mouse*, 474. Berlin: Springer.

112 Maronpot, R.R. (ed.) (1999). *Pathology of the Mouse*. Vienna, IL: Cache River Press.

113 Marjanovic, N.D., Hofree, M., Chan, J.E. et al. (2020). Emergence of a high-plasticity cell state during lung cancer evolution. *Cancer Cell.* 38 (2): 229–246. e13.

114 Sutherland, K.D., Song, J.Y., Kwon, M.C. et al. (2014). Multiple cells-of-origin of mutant K-Ras-induced mouse lung adenocarcinoma. *Proc. Natl. Acad. Sci. U.S.A.* 111 (13): 4952–4957.

115 Weaver, Z., Difilippantonio, S., Carretero, J. et al. (2012). Temporal molecular and biological assessment of an erlotinib-resistant lung adenocarcinoma model reveals markers of tumor progression and treatment response. *Cancer Res.* 72 (22): 5921–5933.

116 Gazdar, A.F., Savage, T.K., Johnson, J.E. et al. (2015). The comparative pathology of genetically engineered mouse models for neuroendocrine carcinomas of the lung. *J. Thorac. Oncol.* 10 (4): 553–564.

Vet-ebooks.com

13

The Gastrointestinal Tract

Jerrold M. Ward, Piper M. Treuting, and M. Kay Washington

Introduction

The gastrointestinal (GI) tract is composed of the stomach and the small and large intestines. The oral cavity and esophagus are not discussed here. The GI tract is the course of the food that enters the body through the mouth and after digestion, excretory products leave via the anus. Thus, it is exposed to exogenous substances from the environment and food supply, which may result in diseases and maintenance of normal life experiences.

Stomach

Anatomy and Histology

The mouse stomach is composed of the forestomach and glandular stomach. Detailed anatomy and histology have been reviewed [1–4]. The squamous epithelial lined esophagus empties into the squamous epithelial-lined forestomach. The glandular stomach is composed of the cardia, into which the esophagus enters, the corpus (fundus, body), and the pylorus. The limiting ridge forms the boundary at the glandular stomach, composed of the cardia, fundus, and antrum. Stem cells have been shown at the epithelial transition zone, at the junction of the forestomach, and cardiac glandular stomach [4] and may be the origin of some types of cancers.

Necropsy, Trimming, and Embedding Protocol

When opened at necropsy, the muscular layers of the stomach often contract and result in curling. Besides a usual method of opening and laying the stomach flat on paper or inflating the stomach with fixative and then placing it in the formalin jar, specialized methods for examining, opening, and preparing the stomach for fixation will produce the most optimal sections for histopathology, especially if the stomach is a target site. With one method [5], carefully remove the stomach from the esophagus, duodenum, omentum, and pancreas by cutting it from the esophagus on one end and duodenum on the other. Tie off both ends and gently fill with neutral buffered formalin to expand it to its approximate normal size. Let sit 5–10 minutes on the dissecting table. The inflation will make the muscle layers relax and the stomach will not curl up upon opening. After this time, make a cut along the longitudinal aspect (forestomach at the top and the glandular stomach in the middle and bottom) to open and place flat between two pieces of filter paper then stapled (Figure 13.1). Place in the jar with fixative. After several days, make 4–6 strips of representative areas of the stomach and place in 1–2 cassettes [5] and embed. Slides can show 4 flat sections or more on 1 slide and if necessary 2 on the second slide (Figure 13.2). Distribution of induced lesions is clearly shown (Figure 13.3). In another method the stomach is laid flat after opening, strips prepared, and place on flat index card for fixation, but the stomach often curls up prior to complete fixation [6–8].

Pathology of the Human Stomach

Disorders of the human stomach include developmental disorders, inflammatory, and infectious conditions, such as peptic ulcer disease and tumors [9]. The most common cause of human gastric lesions is infection with *Helicobacter pylori*, which produces a chronic gastritis that can lead to mucosal atrophy, intestinal metaplasia, and gastric carcinoma or lymphoma. Most of these conditions have no naturally-occurring mouse equivalent or are rare except when induced by experimental methods.

Pathology of the Mouse Stomach

The classification of spontaneous and induced lesions of the forestomach and glandular stomach of mice and rats has been described in an international nomenclature [10, 11] (https://ntp.niehs.nih.gov/nnl, http://www.informatics.jax.org/frithbook). The forestomach and glandular stomach of aging mice may have cystic glandular dilatation and hyperplasia, foci of chronic inflammation, erosion/ulcers, yeast infection, various bacteria on the epithelial surfaces, and hyalinosis. Genetically engineered mouse (GEM) often develops novel lesions not usually found in wild type mice.

Pathology of Genetically Engineered and Other Mutant Mice, First Edition. Edited by John P. Sundberg, Peter Vogel, and Jerrold M. Ward.
© 2022 John Wiley & Sons, Inc. Published 2022 by John Wiley & Sons, Inc.

Vet-ebooks.com

Hyalinosis in the mouse glandular stomach is characterized by epithelial cells with eosinophilic cytoplasm and intracellular and extracellular eosinophilic crystals of various sizes and shapes, but often rectangular (Figures 13.4–13.6). Hyalinosis is seen in low incidences in wild type mice of some strains and more commonly in some GEM lines [12] and in genetic mouse lung disorders. Because of the characteristic hyaline-like appearance of the protein responsible for the eosinophilic appearance, the lesions have been termed "hyalinosis," and this material can also be found in epithelium of bile ducts, gall bladder, pancreatic duct, nasal cavity, and other tissues. The lesions in mouse glandular stomach can be plaque-like and tumor-like (Figures 13.3 and 13.4). The protein has been identified as the gene product of *Chil3* (formerly *Ym1* and *Chil3l3*). The protein (CHIL3) can be localized in the epithelium by IHC and Dominici histochemistry (Figure 13.6). The cause of over-production of the protein has not been determined. The protein has been associated in various tissues with macrophages in inflammation with M2 alternatively activated macrophages (TH2) especially in experimental parasitic infections.

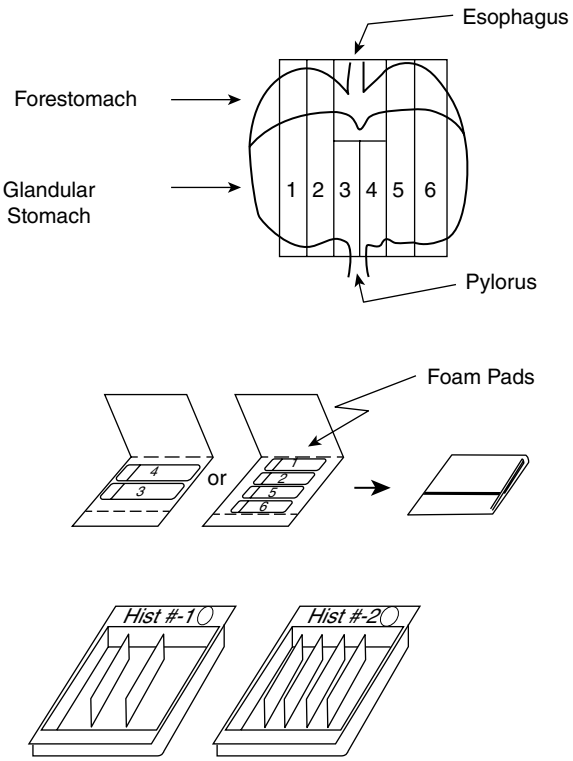


Figure 13.1 Trimming and embedding protocol for mouse stomach. The stomach is inflated with fixative, with its ends tied off, let sit for ten minutes and opened flat on filter or other paper, covered with another filter paper, and stapled for flat fixation, and later trimming. Source: Mahler [5].

Inflammation in mouse stomach is uncommon in control mice. Yeast (usually *Kazachstania pintolopesii*), found in some mouse colonies, may be found on the surfaces of the glandular epithelium (Figure 13.7), but inflammation usually does not usually accompany infection [13]. *Helicobacter* species may occur naturally in mouse stomach, but infections induced by *H. felis*, *H. pylori*, and *H. heilmannii* are common mouse models of the chronic inflammatory human disease [14, 15] and for adenocarcinoma [7, 8] or lymphoma [16, 17]. Chronic gastritis with proliferative lesions is often seen in chronic *Helicobacter* sp. infection in mouse stomach (Figure 13.8). Mucus metaplasia (Figures 13.8 and 13.9), epithelial hyperplasia (Figures 13.8–13.10), dysplasia (Figure 13.10), adenoma (Figures 13.11 and 13.12), adenocarcinoma (Figure 13.13), forestomach squamous cell carcinoma (Figure 13.14), and diverticula (herniation) are reported (Figures 13.15 and 13.16). A detailed gastric lesion classification has been described for *Helicobacter* spp. induced inflammatory and proliferative lesions [8]. Additional discussion of the lesions is found in the following text.

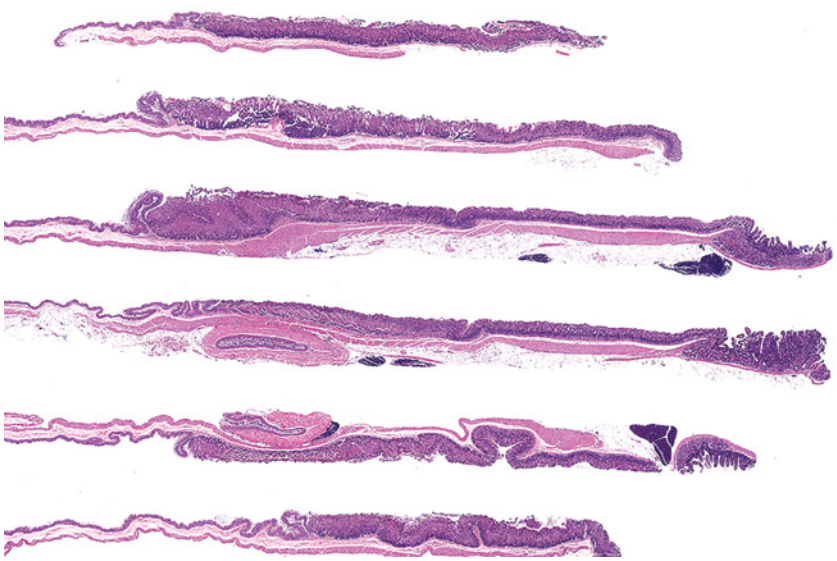


Figure 13.2 Example of 6 normal stomach sections from one mouse on one slide. Forestomach on left of each section.

Vet-ebooks.com

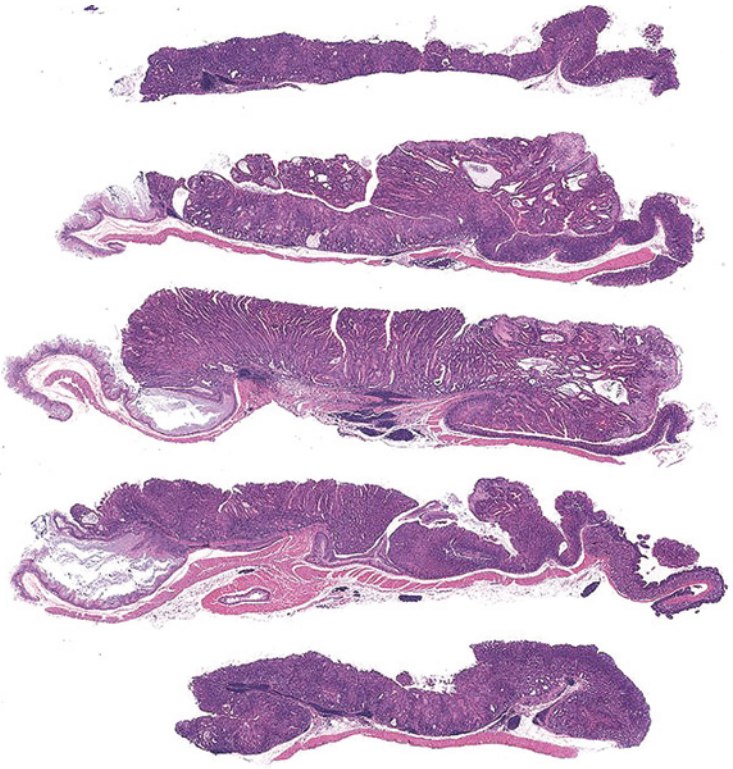


Figure 13.3 **Stomach from mouse with diffuse and focal gastric proliferative and inflammatory lesions**.

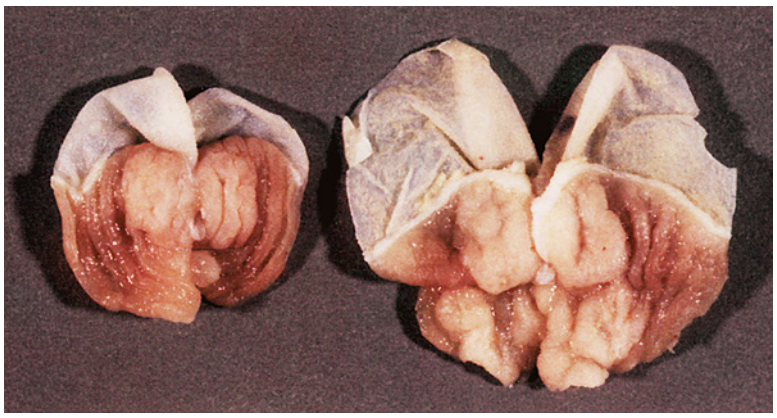


Figure 13.4 **Mouse stomachs with several glandular stomach hyperplastic plaques due to hyalinosis in a *Cyp1a2*^{tm1Gonz} mouse**.

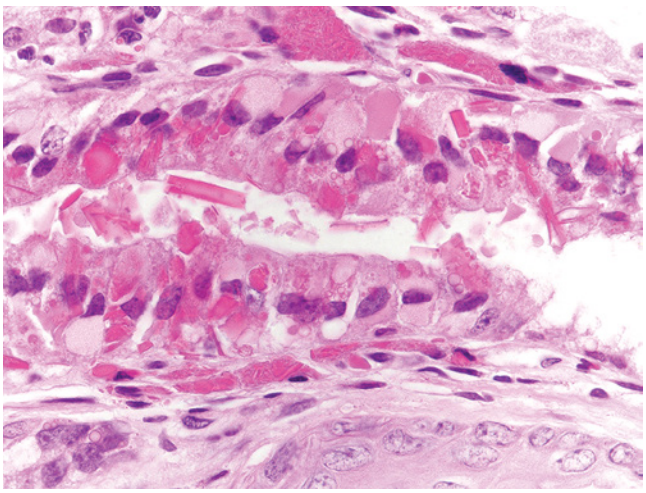


Figure 13.5 **Hyalinosis in glandular stomach**. There are intracellular and extracellular eosinophilic crystals (protein CHIL3).

Vet-ebooks.com

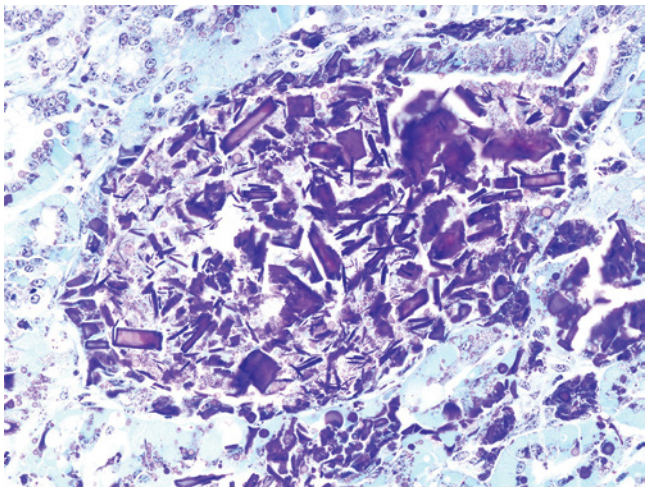


Figure 13.6 **Gastric crystals**. The CHIL3-containing gastric crystals of various sizes and shapes, Dominici stain.

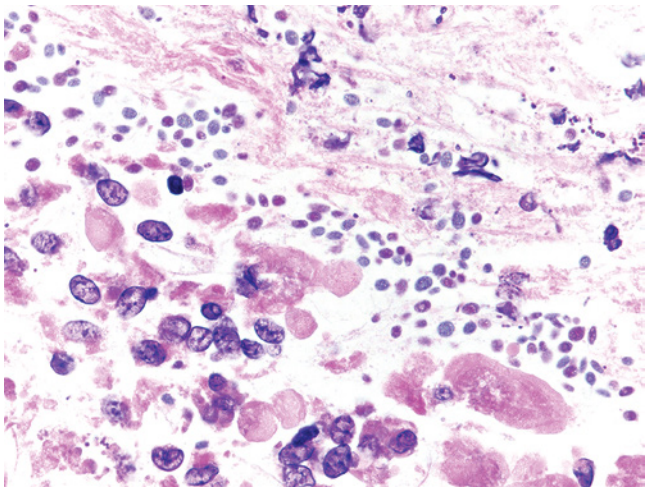


Figure 13.7 **Gastric yeast**. Many yeast, *Kazachstania pintolopesii*, are seen on the luminal glandular stomach surface.

Genetically Engineered Mice

Many genes have been shown to be involved with tumor induction in mouse stomach [18]. A variety of GEM have been created, some resembling human genetic disorders and others to show the role of genes in normal biology and carcinogenesis [5, 18]. Examples of mouse models of heritable and non-heritable human gastric disease are shown in Table 13.1 and in the Jackson Laboratory Phenotype Browser (http://www.informatics.jax.org/vocab/mp_ontology/MP:0000470).

Neoplasms and Other Proliferative Lesions

Human gastric diseases including Menetrier's disease and carcinomas are associated with several gene mutations (Table 13.1) [35]. The causes of gastric tumors in humans include *H. pylori* chronic infection, and in mice, at least 63 carcinogens [36–39] and genetic changes in mutant mice (Table 13.1) [3, 6, 15, 17–34]. These mutant mice have included those involving *Gf1*, *Cyp1A2*, *Tgfa*, *Igf1*, *Igfbp4*, alpha-Inhibin (*Inhba)*, SV40Tag (ATPase B), SV40Tag (amylase), *Ccnd1*, Papilloma virus 16 (HPV16) early region, Adenovirus 12 E1A, Adenovirus 12, Myxoma growth factor, Shope growth factor, *Men1* conditional/somatostatin null [5, 18], and other genes [26].

Experimental glandular stomach neoplasms seen in GEM or chronic *Helicobacter* sp. infection may develop through a sequence of preneoplastic and associated lesions in mouse stomach. For *Helicobacter* sp. infected mice, these lesions included chronic gastritis (Figure 13.8), atrophic gastritis, mucous metaplasia (Figure 13.9), hyalinosis (Figure 13.5), oxyntic atrophy, hyperplasia, pseudopyloric metaplasia and dysplasia (Figure 13.10), adenoma, and adenocarcinoma (Figures 13.12–13.14) [8]. Herniation (displacement of non-invasive glandular epithelium) may also be seen (Figures 13.15 and 13.16). Chronic *Helicobacter* spp. infection is a major contributing factor for human gastric cancer, but infection with *H. pylori* or *H. felis* in mice leads to few

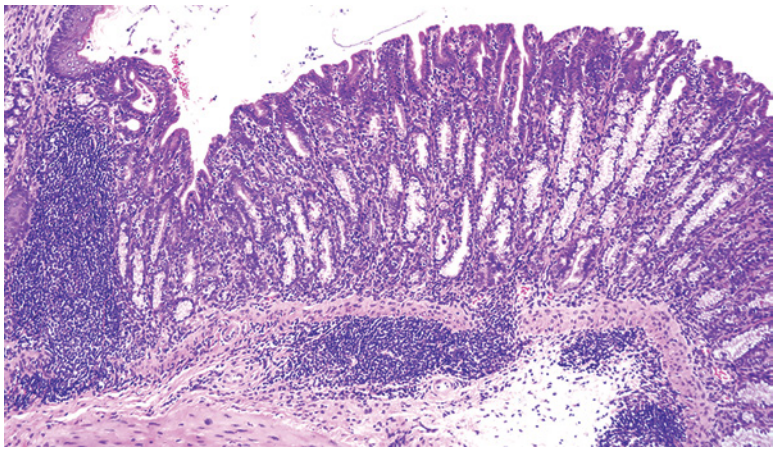


Figure 13.8 **Glandular stomach**. Chronic gastritis with diffuse epithelial hyperplasia and mucus metaplasia at the epithelial transition zone with the forestomach in mouse with chronic *H. pylori* infection.

Vet-ebooks.com

Figure 13.9 **Glandular stomach**. Mucus metaplasia, diffuse in hyperplastic gastric epithelium adjacent to the transition zone in mouse with *H. pylori* infection. PAS/Alcian Blue stain.

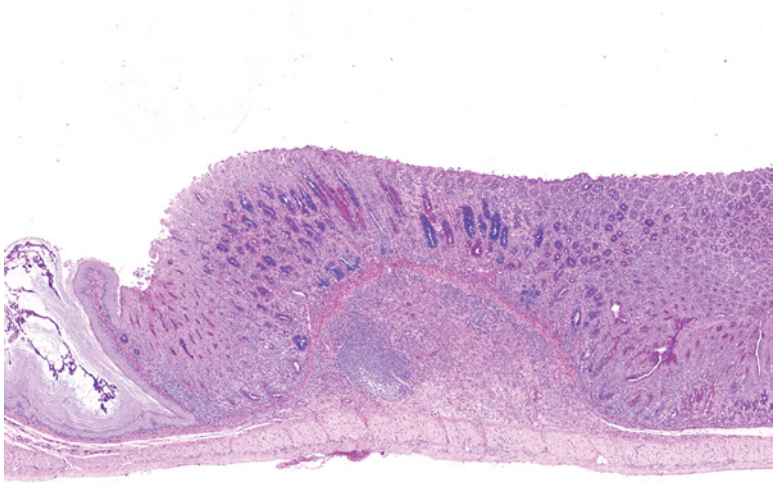


Figure 13.10 **Glandular stomach**. Focal gastric dysplasia in chronic gastritis in an *H. pylori*-infected mouse.

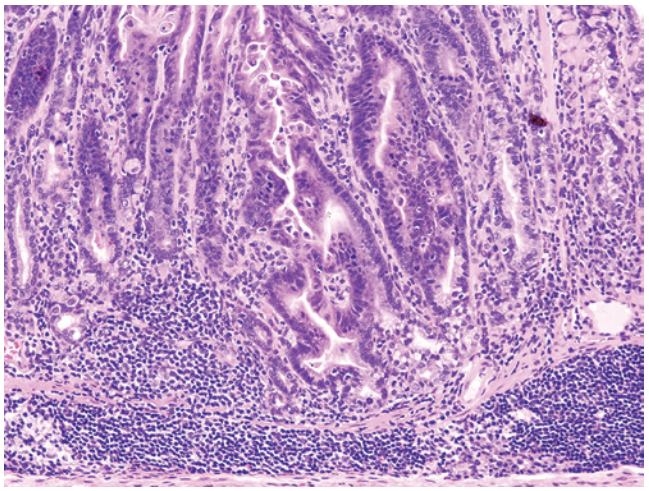
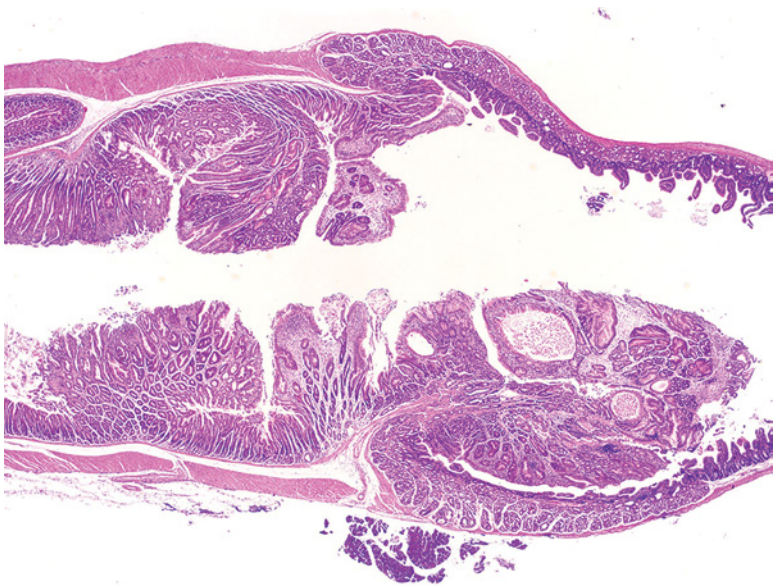


Figure 13.11 **Glandular stomach antrum**. Diffuse gastric hyperplasia and pyloric adenomas.



Vet-ebooks.com

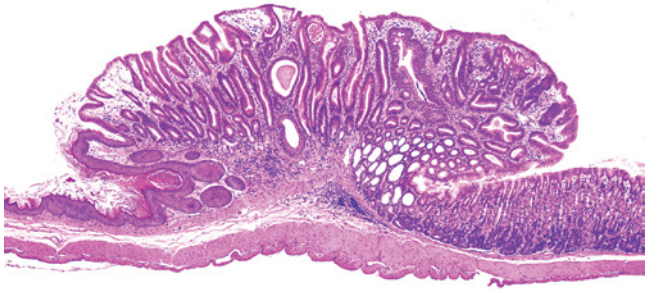


Figure 13.12 **Glandular stomach**. Single large gastric adenoma at the transition zone.

tumors or early invasive lesions, mostly in *H. felis* infected mice [7, 27]. More common are focal atypical hyperplasias or early infiltrative lesions. The gerbil may be a better model of *Helicobacter* spp.-induced gastric cancer.

In some GEM, multifocal or diffuse gastric mucosal hyperplasia and adenomas (Figure 13.12) are mostly seen [5], without carcinoma development at least if mice are not maintained until later in life [30]. Foveolar cell expansion with ectopic mucins, oxyntic atrophy, and pseudopyloric metaplasia in which the gastric corpus resembles that of the antrum was seen in some GEM, as potential precursors of adenocarcinoma (Figure 13.16) [25].

Carcinogenesis of the forestomach is usually due to chemical carcinogens [36] and follows a sequence of hyperplasia, atypical hyperplasia/dysplasia, papillomas, and squamous cell carcinomas (Figure 13.14).

Tumors of the glandular stomach are rare spontaneously. Spontaneous forestomach tumors in mice are rare except for papillomas in some mouse strains. Papillomatous hyperplasia of the limiting ridge is found in a number of single gene mutant mice with *Sharpin* [40] and *Ttc7* [41] or without (*Kitl*) [42] proliferative skin disease.

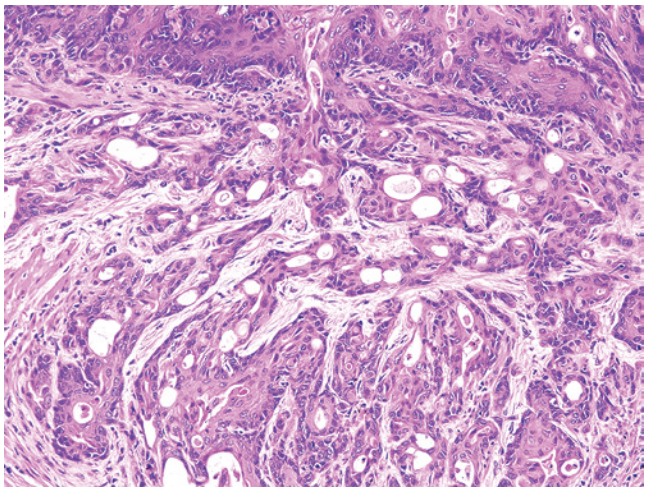


Figure 13.14 **Forestomach**. Squamous cell carcinoma.

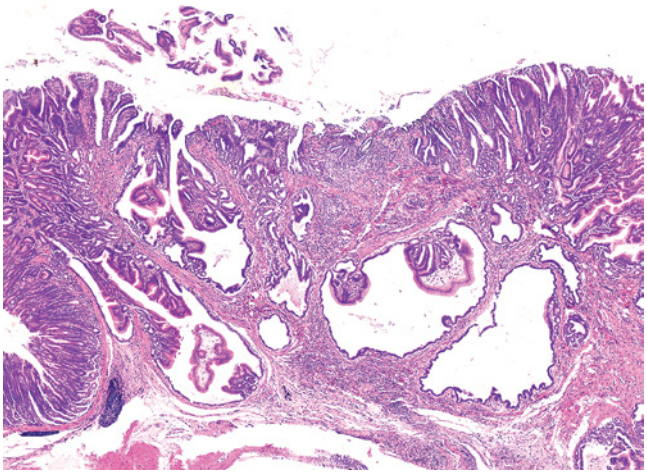


Figure 13.15 **Pylorus**. Atypical adenomatous hyperplasia with epithelial herniations in an I strain mouse.

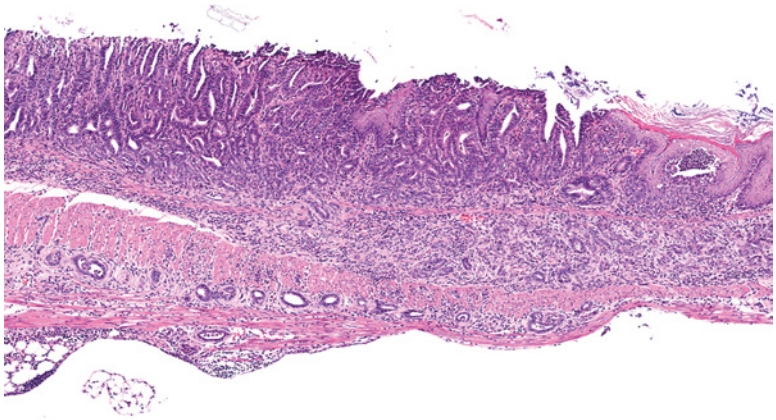


Figure 13.13 **Gastric adenocarcinoma invading through the layers of the stomach and to the serosa**. Note morphologic differences of the tumor in the different layers.

Vet-ebooks.com

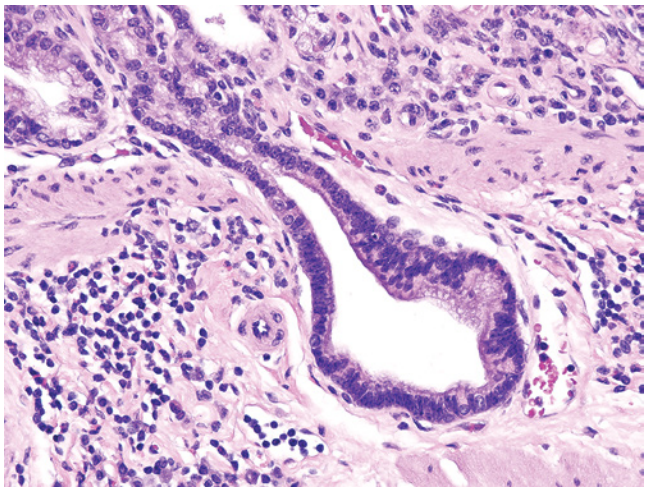


Figure 13.16 **Gastric herniation**. Arising as hyperplastic glands grow through the muscularis mucosa and later become cystic in a stomach with chronic *H. pylori* gastritis.

Primary gastric lymphomas have been reported in mice with chronic *H. felis* and *H. heilmannii* infections, but severe lymphoid lesions must be shown to be clonal [16, 17]. Other lymphomas affecting the stomach are often multicentric affecting many other organs.

Gastrointestinal stromal tumors (GISTs), often diagnosed as sarcomas, leiomyosarcomas, and other tumors, are found in mouse stomach, the small and large intestines of wild type mice [43], and mostly in the cecum of GEM [44, 45]. Tumor cells must show the biomarker *Kit* (CD117), which is expressed in the interstitial cells of Cajal. Gastric carcinoids (neuroendocrine tumors, NET) were found in *Men1* conditional/somatostatin null GEM [46] but are rare in mice, in general.

Cystic Proliferative Lesions in the Stomach and Intestine

Gastric herniation (also diagnosed by various authors of mouse pathology publications as mucosal herniation, hamartoma, cystic hyperplasia, adenomatous polyp, diverticulum, diverticulosis, pseudo-invasive lesion, and gastritis cystica profunda), often in the pylorus, was first described in strain I mice in 1937 [47] and rarely in other mouse strains and GEM [34, 48, 49]. It has not generally been shown to progress to malignancy although the lesions often appear similar to a well differentiated malignant tumor. Herniation can mimic adenocarcinoma but has differentiating features, in the glandular stomach (especially pylorus) and large intestine. In $Cdx2^{tm1Mmt}$ null mice, it has been shown to be a hamartoma, a development defect, by anomalous duplication in the *Cdx2* null [50]. That mechanism may also be true in the other mice. The epithelium lining the cysts is usually well differentiated, but cells are found in the various layers of the stomach or gut wall (Figure 13.15). In mice with chronic gastric *Helicobacter* spp. infection, herniation can be seen without a polypoid or tumor-like mass (Figures 13.15 and 13.16). In humans, a similar condition is most often found in the remnant stomach after gastric surgery and is termed gastritis cystica profunda. Intestinal mucosal herniation is discussed in more detail in the intestine section of this chapter.

The Small and Large Intestine

Normal Anatomy and Histology

The detailed anatomy and histology of the mouse intestine have been reviewed [2, 51]. The duodenum, jejunum, and ileum have differing histological appearance. Peyer patches are common in specific regions. The cecum is short, and the

Table 13.1 Examples of mouse models of heritable and non-heritable human gastric disease.

Disease-associated gene	Relevant human phenotype	Mouse phenotype	References
EGF	Menetrier's disease	Gastric hyperplasia	[19]
ATPase	Menetrier's disease	Gastric hyperplasia	[20]
TGF-α	Menetrier's disease	Gastric hyperplasia	[21]
BRAF	Cardio-facio-cutaneous (CFC) syndrome	Esophageal dilation, gastric hyperplasia	[22]
CDH1	Carcinoma, diffuse type	Foci, intramucosal ca, invasion, mets	[18, 23]
KRAS (G12D), *CHD*, *TRP53*	Carcinoma intestinal and diffuse type	Dysplasia, ca, mets, early deaths	[24]
PTEN	Cancer	Metaplasia	[25]
ANXA10	Diffuse type carcinoma	Diffuse type carcinoma	[26]
TNFSF13 (*APRIL*)	Gastritis, lymphoma	Lymphoma	[15, 17, 27, 28]
PTEN, *SMAD4*, *RNF43*, and *NF1*	Diffuse type carcinoma	Adenomas, diffuse carcinoma	[29, 30]
INS1, *NOD1*	*Helicobacter* sp. gastritis	Gastritis	[27, 31, 32]
GAST	No human disease	Chronic gastritis, antral carcinoma	[33]
A4GNT/CHST4	No human disease	Gastritis, dysplasia, adenocarcinoma	[34]

Vet-ebooks.com

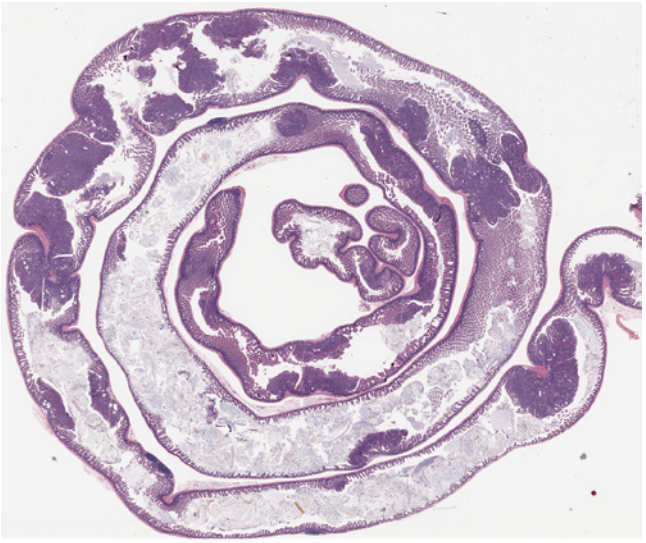


Figure 13.17 **Small intestinal gut roll**. Multiple lesions (dysplasias, microadenomas, and adenomas) can be seen in a *Apc*$^{Min+/-}$ mutant mouse, five months old.

ascending and descending colons lead into the rectum and anus. Lymphoid tissue is found in Peyer's patches in the small intestine and in lymphoid nodules in the cecum and colon [51].

Necropsy and Pathology Protocol

At necropsy, the small and large intestines may be dissected and observed by one of several methods depending on the type of study [52]. For any study, gut rolls of unopened or opened intestine may be used, which are good [53, 54], if done properly, to show many lesions and stages of the disease (Figures 13.17 and 13.18). But gut rolls are not optimal for the counting and measuring of gross findings, especially for cancer research studies, nor for the best sectioning of lesions. The authors prefer to open the entire gut longitudinally, carefully rinsing with physiological saline to remove ingesta and flattening the gut gently on towel, thin index card, or other paper. One can see the gross lesions, especially tumors, record their distribution, numbers, and measure sizes. Fixative in neutral buffered formalin produces good results, but some prefer Bouin's or other fixatives. For a thorough study of histopathology, after fixation one can trim each tumor in half with adjacent normal tissue and put both halves in one container (small vials are perfect) and prepare 1 block per tumor. Sampling of various anatomical areas of the small and large intestines by individual cross sections is also recommended especially for colitis models (Figure 13.19).

Pathology of the Human Intestine

Conditions affecting the small intestine in the human include congenital malformations and duplications;



Figure 13.18 **Large intestinal gut roll**. It is closed (a) and opened (b) with proximal colon (PC), mid colon (MC), distal colon (DC), and anus (A). Source: Treuting [51].

infectious, autoimmune, and allergic disorders; inflammatory bowel disease (IBD); vascular and neurogenic conditions; malabsorption; mechanical obstruction; and neoplasms. Congenital disorders include atresia/stenosis, Meckel's diverticulum, malrotation, and meconium ileus; the latter is associated with the genetic condition cystic fibrosis. In the large intestine, congenital disorders of

Vet-ebooks.com

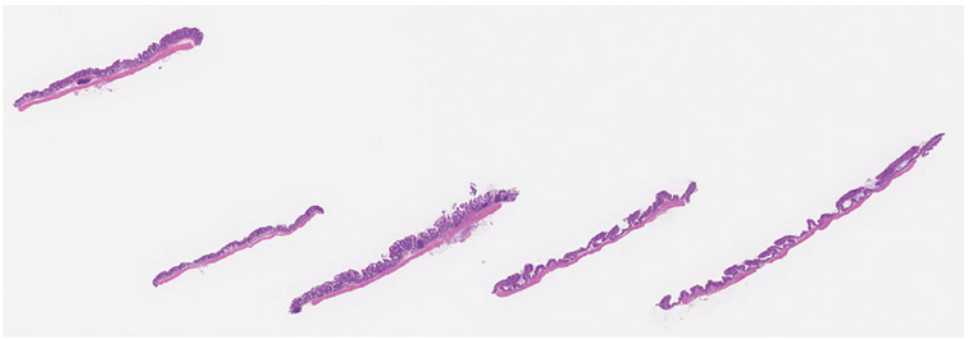


Figure 13.19 Colitis trim protocol. The first two sections of descending colon, one section of mid-colon, and two sections of ascending colon. Lesions of colitis, increase in thickness seen in some areas.

include Hirschsprung's disease (congenital megacolon), acquired megacolon, and anorectal malformations. Infectious colitis and inflammatory large bowel diseases such as ulcerative colitis and Crohn's disease occur as well as diverticulosis and vascular conditions. Solitary rectal ulcer syndrome due to rectal mucosal prolapse, and various benign and malignant neoplasms, most commonly colonic adenomas and adenocarcinoma, is found. Most of these conditions have no naturally-occurring mouse equivalent or are rare except when induced by experimental methods.

Histopathology of the Mouse Intestine

A complete nomenclature for rodent intestinal lesions has been published for use in toxicologic pathology and toxicology [10], and is best used for non-neoplastic lesions although many pathologists use their own preferred nomenclature for a mouse model, especially for grading/scoring lesions. Lesions in aging wild type mice are not common and include protozoal infection [55], amyloidosis in susceptible strains [56], inflammatory infiltrates, and duodenal polyps [56, 57]. Classification of neoplastic mouse intestinal lesions is discussed in the following text [10, 58–60]. The Jackson Laboratory Phenotype Browser reveals many references on mouse intestinal pathology (http://www.informatics.jax.org/vocab/mp_ontology/MP:0000477).

Mouse Models of Inflammatory Bowel Diseases and Related Diseases (Colitis Models)

In humans, IBD, most commonly Crohn's disease and ulcerative colitis, is a chronic relapsing inflammation of the gastrointestinal tract. While Crohn's disease may affect any part of the gastrointestinal tract and may cause fistulas and strictures, ulcerative colitis is localized to the mucosa of the large intestine. Human genes play a role in disease pathogenesis [61], and in experimental diseases in wild type mice and GEM [31, 62–72] have been used to study the role of these genes in mice (Table 13.2). While no one mouse model effectively recapitulates the complex and heterogeneous clinicopathogenic features of human IBD, each can provide a tool to dissect the molecular pathways underlying colitis. Models include those with epithelial integrity defects ("leaky guts") via chemical stripping of the epithelium (dextran sodium sulfate, DSS, and others), or via genetic defects. The role of the innate and adaptive immune response is examined in genetically modified mice (e.g. *Il10* null, *Rag2* null) and immunodeficient mice adoptive transferred with colitogenic T-cells. Model selection will depend on the particular research question and, as with any mouse model, the effect of background strain, environmental factors, and microflora on phenotype cannot be overstated. In order to attempt to mimic the various human colonic inflammatory disorders, mouse typhlocolitis can be induced by various methods, mostly by chemical irritants or toxins including DSS, without or with azoxymethane to induce tumors, trinitrobenzene sulfonic acid (TNBS), in immunodeficient mice infected with *Helicobacter* spp. [68] and other organisms, by transfers of immune cells and by other methods [52, 73–78]. The DSS model is by far the most popular model with over 3000 publications.

There are numerous genetically modified mouse colitis models, all with various degrees of the human disease and some that harbor genes present in susceptible humans (Table 13.1) [79]. The genetically susceptible strains may develop spontaneous colitis or may be synchronized or triggered with various inflammatory stimuli. The large number of human susceptibility genes (160) and GEM models (over 790) highlights the complexity of the pathogenesis of IBD [79–82].

Colitis Necropsy and Tumor Histopathology Protocols

Various necropsy protocols have been used for mouse colitis models [73, 76, 77, 83]. Sampling of various portions of the large bowel is most common but often not well described in publications. For colitis models, Swiss-roll preparation of the intestinal tract is one method of preparation that allows for examination of the entire section in a single slide, but artifacts are to be expected and additional sections may be required to assess [54, 84]. The Swiss-roll technique is relatively efficient at necropsy, where, prior to fixation, portions of the tract are rolled from proximal to distal (either opened

Vet-ebooks.com

Table 13.2 Role of genes in enteritis and colitis in humans and mice.

Disease-associated human gene	Relevant human phenotype	Mouse phenotype	Notes	References
NOD2 (*CARD15*), *CYBB*	Crohn's disease	Colitis	With bacteria, *Mucispirillum* sp.	[63]
ATG16L1	Crohn's disease	Colitis	With *Salmonella* sp.	[64, 65]
IL23R	Crohn's disease	Colitis	*Helicobacter hepaticus*, T cells	[66]
IRGM (*IFIM1*)	Crohn's disease	Colitis	DSS	[73]
ABCB1 (*MDR1*)	Ulcerative colitis (UC)	Colitis		[67]
IL10RA, *IL10*	UC	Colitis with *Helicobacter* sp.		[68]
PTPN2	UC	Systemic inflammation	No effect on DSS colitis	[69]
SPINT2 (*HAI2*)	Syndromic congenital tufting enteropathy	Enteropathy	Enteropathy In young mice	[70]
EPCAM (*TROP1*)	Congenital tufting enteropathy	Enteropathy, villous blunting, atrophy, colitis		[71]
WAS	Wiskott–Aldrich syndrome (with colitis)	Colitis, colon dysplasia adenocarcinoma	Disease only with *Helicobacter bilis*	[72]

or unopened) and placed into a cassette [77] (Figures 13.17 and 13.18). Alternatively, we favored the sampling of the large bowel for DSS induced colitis at specific locations including 2 from the proximal, one from the middle of the descending colon and 2 from the distal bowel (including rectum). In 1 paraffin block and a section on one slide, 5 colon sections can be placed in order (Figure 13.19). The sections can be cross sections or long sections about 0.5–1 cm in length. The cecum can be added on a separate slide, as 2 or more sections to include the lymphoid tissue. It was shown for one model that complete large bowel sampling was important for at least that model [83]. Ultimately, the needs of the study drive the tissue collection, trimming, embedding, and staining protocols. If a new model is used or one that requires evaluation of various anatomical areas of the colon, one can sample all areas before determining which area is most susceptible to induced lesions.

The histopathology of mouse colitis has been reported using various lesion scoring methods [28, 67, 73–75, 77, 83–91] and by image analysis [28]. There is no standard scoring method as the optimal system is driven by the study design and needs, and preference of the primary investigator and pathologist. Scored lesions may include extent of the involvement in the entire or portions of the colon, degree, and type of inflammation, erosion/ulceration, mucus loss, fibrosis, epithelial hyperplasia, squamous metaplasia, dysplasia, and cancer, and the use of IHC biomarkers. The regenerative epithelial lesions can be severe and the epithelial atypia of repair is often seen, even resembling that in preneoplastic lesions and neoplasias. Herniation of the inflamed and hyperplastic mucosa is a frequent event in mouse models due to the relatively thin submucosa. The regenerative dysplasia and herniations must be differentiated from neoplasia and invasion, and these are discussed under Pitfalls in Interpretation in the neoplasia section. Cancers found in these models are discussed in the intestinal tumor section.

Microbiota and Colitis

The influence of the microflora on colitis and colon cancer phenotype has been demonstrated in many colitis models as normal and other enteric bacteria are necessary to develop colitis [92]. Enteric bacteria as research tools are exemplified by *Helicobacter* spp. [93, 94].

Bacteria are used to drive typhlocolitis in susceptible genetic backgrounds emphasizing the role of the microbiota in disease and phenotype [94]. The role of the microbiota in development and progression of IBD is clearly established, yet there remains much to elucidate regarding the role of microbial communities, byproducts, or individual bacterial strains [95–97]. Additionally, the interactions between the microbiota, host immunity, and other environmental factors impact IBD in human and mouse models [96]. Globule leukocytes (mucosal mast cells) have been shown to play a role in some types of intestinal inflammation including allergic and parasite disease [98]. Gnotobiotic mice are useful models to assist in dissecting the impact of microbiota in colitis [99].

Human Intestinal Neoplasia

The majority of human intestinal tumors are found in the large bowel. The molecular underpinnings of colorectal carcinoma (CRC) in humans have been intensively studied, due to high prevalence, ready availability of preinvasive lesions, and existence of familial syndromes such as familial adenomatous polyposis (FAP) coli and Lynch syndrome

Vet-ebooks.com

Table 13.3 Common molecular pathways in human colorectal carcinogenesis.

Pathway	Chromosomal instability	Microsatellite instability	CpG island methylator phenotype
Frequency	~85% of CRCs	~15% of CRCs	~17% of CRCs (overlaps with MSI CRC)
Precursor lesion	Conventional adenoma	Serrated polyps (sessile serrated adenoma/lesion, traditional serrated adenoma, mixed polyps)	Serrated polyps (sessile serrated adenoma/lesion, traditional serrated adenoma, mixed polyps)
Genetic features	Mutation in *APC*, followed by mutations in oncogenes such as *TP53*, *KRAS*, *SMAD4*, and *PIK3CA*	Mutation in mismatch repair genes (*MLH1*, *MSH2*, *MSH6*, *PMS2)*, or hypermethylation of the *MLH1* promoter	Widespread hypermethylation of CpG island loci, with inactivation of tumor suppressor genes
Morphology	Conventional adenocarcinoma composed of large cribriform glands with luminal debris (dirty necrosis)	Mucinous or poorly differentiated carcinomas are more common; numerous tumor infiltrating lymphocytes	Mucinous carcinomas are common in CIMP-high MSI-H cancers but not in CIMP-H microsatellite stable cancers

Source: From Arends [61] and Ma [100].

(Tables 13.3 and 13.4). Most of the hereditary colorectal cancer syndromes are rare [61, 100, 108–110], with only a small percentage of human colorectal cancers arising in such a setting. For instance, one of the first of these to be recognized, FAP, due to germline mutation in the *APC* gene (WNT signaling pathway regulator), has an estimated carrier frequency in the general population of 1 in 1000. The most common, the Lynch syndrome, accounts for only 2–4% of human CRC [100]. However, elucidation of the contribution of specific genetic abnormalities has been aided by the generation of mutant and GEM models of these hereditary syndromes, such as the multiple intestinal neoplasia allelic mutation ($Apc^{Min/+}$) of the mouse *Apc* gene and the DNA mismatch repair deficiency models, as well as models that recapitulate somatic genetic features characterizing sporadic colorectal cancers.

Although human colorectal cancers are highly complex lesions genetically, most develop via a morphologically recognizable adenoma-carcinoma sequence that is associated often with specific genetic changes arising from conventional adenomas, sessile serrated adenomas (sessile serrated lesions), or traditional serrated adenomas [61]. Less is known about the pathogenesis of small intestinal carcinomas, but available data support a similar pathogenesis. Left-sided and rectal adenocarcinomas primarily develop through the conventional adenoma pathway, which accounts for about 70% of colorectal cancers, whereas many right-sided colonic adenocarcinomas develop in sessile serrated precursors. Molecular profiling has identified three main carcinogenesis pathways involving genetic instability in intestinal carcinomas: chromosomal instability, microsatellite instability (MSI), and the CpG island methylator phenotype (CIMP) (Table 13.3). The chromosomal instability pathway is the most common and is characterized by high levels of DNA copy number alterations and aneuploidy, and usually has alterations in the WNT pathway as a result of *APC* mutation. The MSI pathway is the result of somatic or germline mutation of one of the mismatch repair genes, resulting in a hypermutant condition resulting in mutations in a large number of genes and production of neoantigens provoking a host immune response. The CIMP results from an epigenetic alteration; this group of tumors overlaps with the MSI group but is due to hypermethylation of CpG dinucleotides in the promotor region of many genes, resulting in inactivation of tumor suppressor genes. The MSI and CpG island classifications are not mutually exclusive as subgroups of CIMP high and low tumors with proficient and deficient mismatch repair status may be identified; tumors in these groups often harbor BRAF mutations.

Mouse Models of Intestinal Cancer

Intestinal carcinogenesis was first induced in mice by chemical carcinogens, including azoxymethane, 1,2-dimethylhydrazine, chromium VI, capsaicin, captafol, captan, folpet, hexavalent chromium, *N*-ethyl-*N*-nitro-*N*-nitrosoguanidine; hydrogen peroxide; *N*-methyl-*N*-nitro-*N*-nitrosoguanidine; and *N*-(trichloromethylthio)phthalimide [36, 52, 111]; and later by genetic engineering (transgenic, knockout, conditional, and CRISPR mice) and chronic colitis [52, 75] [74]. Natural and induced *Apc* mouse mutants develop mostly small intestinal adenomas (Figure 13.20), while many GEM develop tumors in the colon only or also within the small intestine. Tumors in the small and large intestines may be found in lines of GEM including in mice modeled after human familial cancers (Table 13.4) [112]. More recently, GEM organoid models have been used [113]. The Mouse Models of Human Cancer Database maintained by The Jackson Laboratory contains information on several GEM models in a searchable database for a variety of tumor types (http://www.informatics.jax.org/vocab/mp_ontology/MP:0005381).

Intestinal cancers in humans are predominantly located in the colon and rectum, with small intestinal cancers much less common. In GEM models, some models such as

Vet-ebooks.com

Table 13.4 Examples of mouse models of human heritable cancer syndromes associated with intestinal cancer. Source: Based on [112]

Syndrome and inheritance	Human genes	Gastrointestinal cancers	Histologic features of human colorectal cancers	Mouse lesion	Representative GEM models [59, 60, 101]
Lynch syndrome (autosomal dominant)	*MLH1, MSH2, MSH6, PMS2, EPCAM*	Colorectal, small bowel, gastric, pancreatic	Poorly differentiated carcinoma, medullary carcinoma, mucinous carcinomas; numerous tumor-infiltrating lymphocytes	Small intestinal adenomas and adenoca	[59]
Familial adenomatous polyposis (FAP; autosomal dominant)	*APC*	Colorectal, small bowel, gastric	Cribriform morphology with intraluminal necrosis; carcinomas originate in adenomas	Intestinal adenomas; rarely adenoca	[60, 102–104]
Li Fraumeni syndrome (autosomal dominant)	*TP53*	Colorectal, gastric, pancreatic	Adenocarcinomas may arise in very small adenomas	Large intestine adenocarcinomas	[105]
Juvenile polyposis (autosomal dominant)	*SMAD4* *BMPR1A*	Colorectal, gastric, pancreatic	Carcinomas originate in juvenile polyps	Adenomas, adenoca, enhances DSS carcinogenesis	[89, 105]
Cowden or PTEN hamartoma tumor syndrome (autosomal dominant)	*PTEN+*	Colorectal	Carcinomas originate in hamartomatous polyps	Adenoca, some mucinous	[106]
Serrated polyposis	*RNF43;* other unidentified genes	Colorectal	Carcinomas originate in serrated polyps	Resembles serrated adenomas, adenoca	[107]

Vet-ebooks.com



Figure 13.20 **Colon**. Gross appearance of colon adenomas (polyps), azoxymethane-induced.

$Apc^{Min/+}$ exhibit a preponderance of tumors in the small bowel (Figure 13.17), while in others the tumors are mostly in the large intestine [102]. Most intestinal neoplasms in GEM are non-invasive precursor lesions, with few models developing deeply invasive or metastatic carcinomas [114].

Intestinal Tumor Pathology

Most colon tumors in humans arise in precursor lesions called adenomas (Table 13.5), which are often grossly detected by colon cancer screening methods [61, 115]. In contrast, in many mouse models of intestinal carcinogenesis, most of the mouse adenocarcinomas do not arise from grossly visible conventional adenomas but arise from non-invasive precursor lesions. The morphological appearances of a non-invasive lesion that may progress to an adenoma (Figure 13.20) (papillary, polypoid, sessile, or serrated) or invasive adenocarcinoma may be difficult to distinguish at the non-invasive stage, even by surface epithelial morphology. It is best to be conservative at the non-invasive stage unless one can demonstrate that these lesions do progress to invasive tumors in a mouse model. It was found in three GEM lines that non-invasive lesions had a different spectrum of gene mutations than did the invasive lesions [105]. Invasion of the stalk of adenomas in mice is not a common finding in mouse intestinal cancer models, but obviously may depend on the model (and mutations or genes involved). Invasion of *Apc* mouse adenomas can be found rarely mostly in older *APC* mutants.

Proliferative lesions of the colon in humans and mice are very similar in morphology and biology (and with similar or different genetic changes), but pathology terminology varies at least for the earliest lesions, known to be induced by carcinogens or genetic engineering in mice. In humans, the earliest adenomas are not visible on gross examination but can be identified even at the single crypt stage by their microscopic appearance. In mice, these microscopic only lesions are usually termed dysplasia for reasons noted in the following text (Table 13.5).

In humans, adenomas are further characterized by the degree of dysplasia they exhibit, as an indication of how far along the adenoma-carcinoma pathway they have progressed. Dysplasia is divided into low grade and high grade, based on nuclear cytology and polarity and architecture. Most adenomas in humans and rodents exhibit low-grade dysplasia (Figures 13.21 and 13.22). Because low-grade dysplasia is a defining characteristic of typical adenomas, the term adenoma with low-grade dysplasia is not used; rather, these lesions in humans are simply called adenomas or conventional adenoma because most will progress into grossly visible adenomas (Figure 13.20). In mice, a variety of alternative terms have been used for these early precursor lesions; these include atypical hyperplasia, gastrointestinal intraepithelial neoplasia, low- and high-grade dysplasia (Figures 13.21–13.24, 13.26, 13.27), and microadenomas (Figures 13.25 and 13.26) [10, 52, 59, 116]. The problem with diagnosing such small dysplastic lesions as adenomas in mice is that the active regenerative lesions after an intestinal irritant such as DSS, often with similar dysplastic epithelium to human adenomas, are also seen in mouse models of colitis and acute inactivation of genes, only days after treatment with the colon irritant (Figures 13.23 and 13.24). Some of the apparent regenerative lesions may have been diagnosed as microadenomas [117].

In a new mouse model, diagnoses should be conservative until proven progression, so that a diagnosis of dysplasia, low and high grade, is appropriate for microscopic lesions not grossly visible. When they are visible grossly (often 1 mm in size with one's eyes or a dissecting microscope) or they form a benign tumor (appearing nodular and compressed within the epithelium or growing into the gut lumen as an adenomatous lesion while still visible only on a microscopic level (Figure 13.25)), they should be diagnosed as adenomas (Figures 13.28 and 13.29), if not invasive. Similar criteria are used for other organ-specific adenoma and carcinoma precursor lesions [10, 52, 118]. Low-grade dysplasia in conventional human adenomas is characterized by tall columnar cells with elongated pencillate nuclei and increased nucleus-to-cytoplasm ratio. Although the nuclei are crowded and pseudostratified, there is no loss of nuclear polarity, i.e. the nuclei maintain their normal orientation with respect to the basement membrane. The adenomatous crypts are simple in outline and do not show cribriform architecture (gland-within-gland-formation), although in rodents, particularly in the small intestine, the adenomatous epithelium folds back upon itself and may mimic a more complex glandular structure.

In high-grade dysplasia of human colon adenomas, the adenomatous crypts are more crowded, display greater architectural complexity characterized by back-to-back glands with no intervening stroma, and show loss of nuclear polarity. Nuclei may be more rounded and overlapping, with clumped coarse chromatin. If the neoplastic cells break through the basement membrane to invade the lamina

Vet-ebooks.com

Table 13.5 Nomenclature of mouse glandular stomach and intestinal epithelial tumors and other epithelial proliferative lesions.

Diagnoses	Definition	Synonyms/notes
Hyperplasia, epithelial	Reactive/regenerative due to acute or chronic epithelial damage, focal, multifocal, or diffuse, may resemble pre-neoplastic lesions	Regenerative hyperplasia, often dysplastic, may be seen in rectal prolapse and after DSS colitis or other toxic lesions
Dysplasia, low or high grade	Microscopic lesion. When preneoplastic or precancerous it must be proven to progress to benign or malignant tumors	Gastrointestinal neoplasia (GIN), atypical hyperplasia, microadenoma, not having an adenomatous growth pattern
Microadenoma	A lesion not seen grossly, but has the same morphology and polypoid, sessile, or papillary growth pattern as a grossly visible adenoma. Must be shown to progress to a grossly visible adenoma	In humans, dysplasia, low or high grade. Sessile, polypoid, papillary, or serrated
Adenoma	Non-invasive epithelial neoplasm, with tubular, villous, sessile, or serrated gross and microscopic patterns lined by dysplastic epithelium. Also known as a polyp	The tumor epithelium may show low- or high-grade dysplasia. Adenomas are grossly visible and may be polypoid, papillary, sessile, or serrated. Carcinomas may arise in adenomas as manifested by true focal invasion of the stalk or arise from elsewhere in the adenoma but this process is less common in mice than in humans
Adenocarcinoma	Malignant epithelial neoplasm with invasive epithelial cells, invading through the muscularis mucosae, and/or submucosa, tunica muscularis or serosa. Tumor cells may be found in lymphatics. The earliest lesions will show a stromal and inflammatory response to invasive cells	Adenocarcinoma may be further characterized as papillary, tubular, tubulo-papillary, serrated, scirrhous, mucinous, signet ring cell, anaplastic, or neuroendocrine
Gastrointestinal stromal tumor (GIST)	Stromal tumor in wall of the stomach or intestine, derived from interstitial cells of Cajal. The majority express CD117 (*Kit*) by immunohistochemistry	Majority of intestinal sarcomas in mice
Neuroendocrine (NET) (carcinoid)	Tumor cells show neuroendocrine differentiation. Low-grade neoplasm previously termed carcinoid. The majority express synaptophysin	Found in stomach and intestine of GEM
Mucosal herniation	Found in glandular stomach or small or large intestine. Can form a diffuse lesion or a mass of well-differentiated neoplastic-like found in all layers of the stomach or intestine. Cystic lesions are common	Hamartoma, diverticulum, diverticulosis, pseudo-invasive lesion, adenomatous lesion, gastritis cystica profunda
Hyalinosis plaque	Found in stomach of aging mice and some mutant strains, epithelial hyperplasia producing hyaline protein product (CHIL3), often with intracellular and extracellular eosinophilic crystals	Hyperplastic plaque, hyalinosis, similar lesions may be found in pancreatic duct, bile ducts, gall bladder, ureter and nasal cavity
Intestinal or mucous metaplasia	Presence of cell types (e.g. goblet cells) not normally found in the mucosa at that site. Found in the glandular stomach of mice and associated with chronic inflammation and/or preneoplasia	In humans, found in chronic gastritis due to *Helicobacter pylori* or autoimmune gastritis. Considered the precursor lesion for some types of gastric adenocarcinoma

propria without involving deeper layers, the term intramucosal carcinoma is appropriate. Pitfalls in interpretation are discussed later.

Aberrant crypt foci (ACF) are microscopic lesions identified by examining methylene blue-stained intestinal mucosa under a dissecting microscope. The lesions have enlarged gaping crypt openings and may represent a variety of specific lesions. In humans ACF are classified on histologic examination as adenomas or hyperplastic polyps, but in the mouse, they are primarily minute adenomas/foci of dysplasia. Similarly, mucin-depleted foci have been described in azoxymethane-treated rat mouse models and typically represent small adenomas [119].

Adenomas in GEM vary in size from microscopic single crypt adenomas (Figure 13.25) to large pedunculated or sessile lesions (Figures 13.28 and 13.29) carpeting large areas of the intestine. Single crypt adenomas, dysplasias in mice (Figure 13.25), may be recognized on relatively low power by their blue appearance due to increased nucleus-to-cytoplasm ratio but in $Apc^{Min/+}$-related models, immunohistochemistry for beta catenin may be helpful in identifying these minute lesions by accumulation of nuclear and cytoplasmic

Vet-ebooks.com

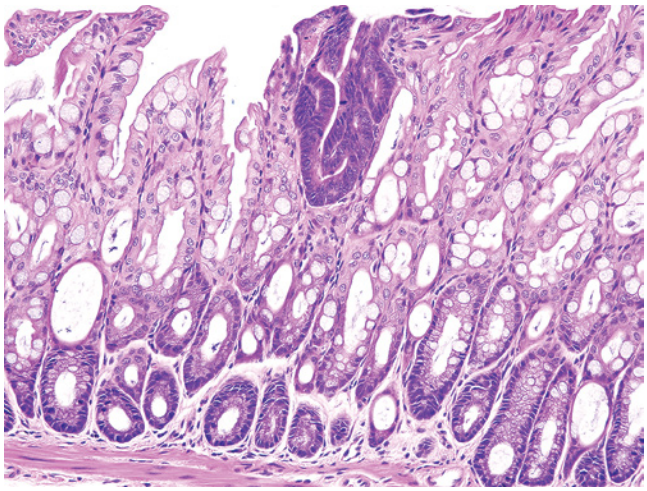


Figure 13.21 **Colon**. Focus of dysplasia. One crypt is involved.

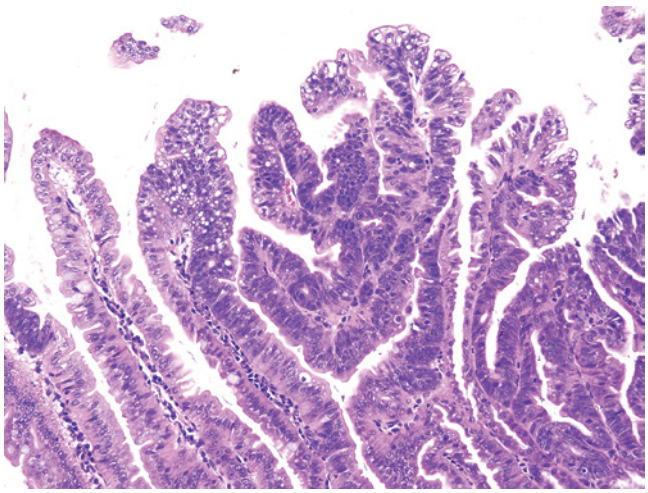


Figure 13.22 **Small intestine**. Focal dysplasia, multiple crypts. Hyperchromasia and abnormal growth patterns are evident.

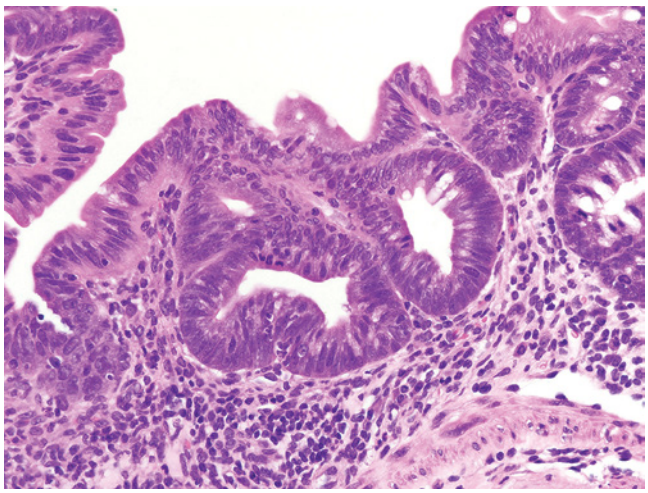


Figure 13.23 **Colon**. Multifocal hyperplasia with dysplasia in a regenerative colon with DSS colitis induced nine days earlier.

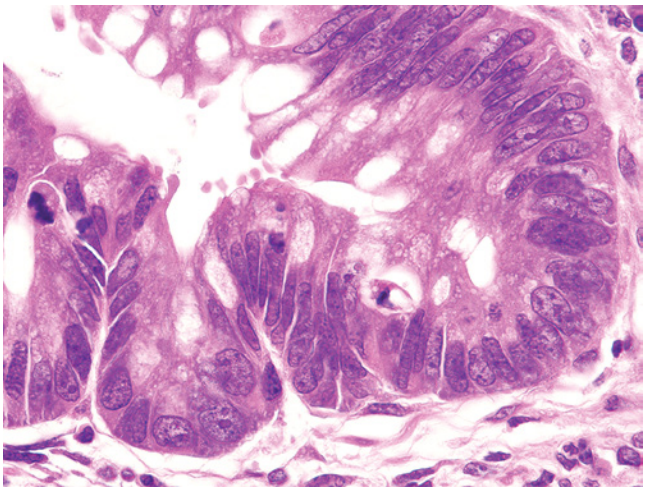


Figure 13.24 **Focus of colonic regenerative hyperplasia in induced colitis model**. Note low-grade dysplastic nuclei.

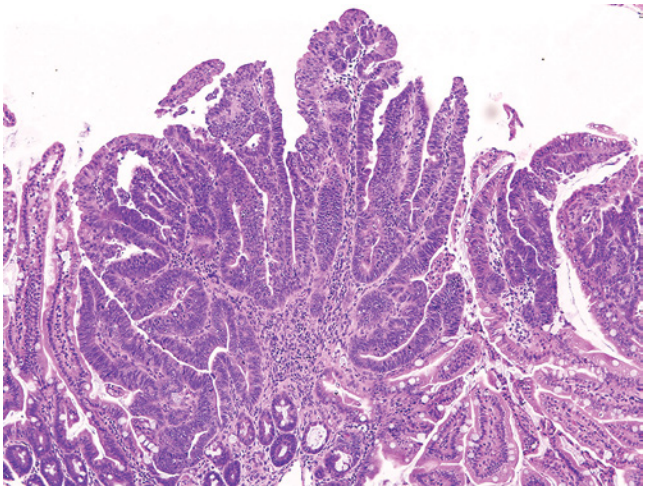


Figure 13.25 **Small intestine**. Microadenoma, with high-grade dysplasia.

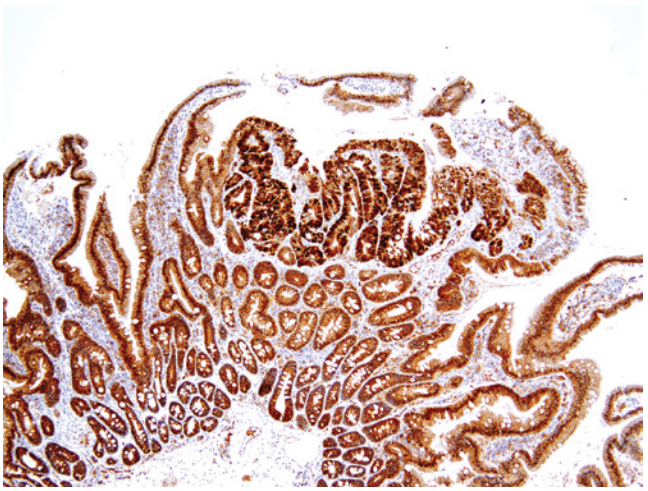


Figure 13.26 **Small intestine**. CTNNB1 in focal dysplasia. Nuclear staining in the dysplasia and cell membrane staining in the normal epithelium.

Vet-ebooks.com

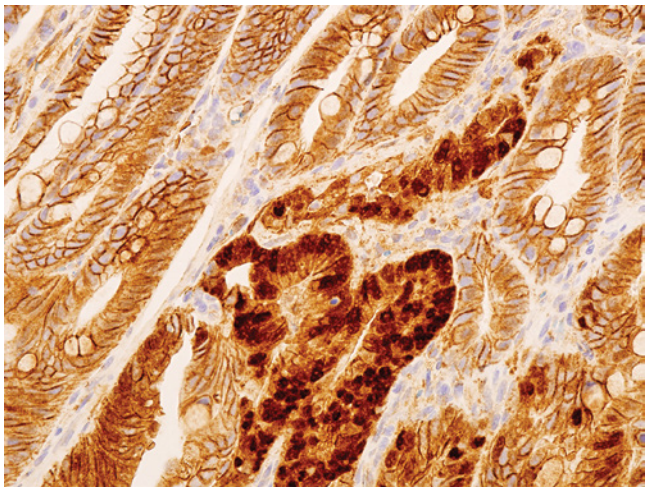


Figure 13.27 **Small intestine**. CTNNB1 in dysplasia. Note the nuclear and cytoplasmic staining in dysplasia and only membrane staining in the adjacent normal epithelium.

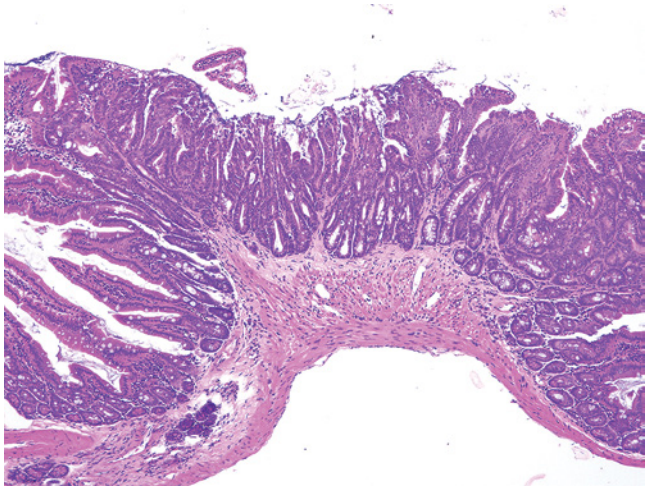


Figure 13.28 **Small intestine, adenoma, sessile**. No invasion is seen.

Ctnnb1 [116] compared with the antigen expressed only in the cell membrane of non-neoplastic intestinal epithelium (Figures 13.26 and 13.27).

Serrated adenomas in humans are divided into sessile serrated adenomas/lesions and traditional serrated adenomas [61]. The former lack nuclear features of conventional dysplasia but display abnormal architecture such as deep laterally branching crypts lined by serrated epithelium that extends to the crypt base. Traditional serrated adenomas are defined by the presence of ectopic crypts in a villiform pattern with pencillate nuclei. Most lesions described as "serrated" in GEM models [107] are hyperplastic lesions with villiform architecture and do not exactly resemble the serrated polyps found in humans. The term "serrated" should be reserved for lesions showing sawtooth or stellate architecture resembling the human serrated polyps [60].

Colon adenomas in humans may progress to adenocarcinomas (Figure 13.29). This progression is less common in mice and more often occurs in humans *de novo* from flat epithelium in mice (Figures 13.29–13.32). Invasive adenocarcinoma is characterized by the presence of neoplastic crypts or disorganized tumor cells extending through the muscularis mucosae into the submucosa or deeper layers of the bowel. The invasive glands are often angulated and associated with altered fibrotic stroma (desmoplasia, a reactive stroma), but the invasive front may have a pushing morphology, especially in mucinous lesions. A host inflammatory response to the invasive tumor is frequently present; this inflammatory response varies depending upon the GEM model. Adenocarcinomas are graded based on the degree of their resemblance to normal intestinal crypts. A three-tiered scheme (well, moderately, or poorly differentiated) is often used to classify human colorectal cancer, but two tiered schemes (low and high grade) in which well and moderately differentiated tumors are classified as low-grade and poorly differentiated tumors are classified as high grade are more reproducible. Well differentiated colorectal adenocarcinomas are composed of simple tubular glands. Most human cancers are classified as moderately differentiated, and consist of fused cribriform back-to-back glands, often containing luminal necrotic cellular debris ("dirty necrosis"). Poorly differentiated adenocarcinomas have a predominantly solid growth pattern, with little gland formation. Often carcinomas growing into the gut lumen have a different histologic pattern than the same tumor mass growing through the gut wall. The surface tumor cells are free to grow in a space while those in the wall meet a barrier of solid tissue, inflammatory cells, and stroma (Figures 13.33 and 13.34). This phenomenon is especially true for mucinous adenocarcinomas.

Adenocarcinomas are also subclassified based on histologic type. In mice, most intestinal adenocarcinomas are well differentiated adenocarcinomas that are not further classified as a special subtype except if unique types are found in specific mouse models, their morphological and biological characteristics have been reported. Metastases are not common but have been reported in mice [60] especially with the use of organoids [120]. Variant subtypes include signet ring cell carcinoma, a high-grade carcinoma in which a large intracellular mucin vacuole displaces the nucleus; and mucinous carcinoma, characterized by production of abundant extracellular mucin and mucus cysts (Figure 13.34). These mucinous adenocarcinomas are most commonly induced in colitis models. Medullary carcinoma, which nearly always shows high levels of MSI, grows in large sheets with numerous tumor-infiltrating lymphocytes; it is rare in humans and is rarely seen in GEM. Similarly, adenosquamous carcinoma is rare in humans but may occasionally be seen at the anorectal junction in GEM models. Another special subtype, high-grade neuroendocrine carcinoma, is a rare but aggressive cancer in humans [61] and is seldom encountered in GEM models of intestinal cancer [46]. Well differentiated NET (carcinoids) are more common in the small intestine compared with the large intestine in humans.

Diffuse multifocal origin of colonic adenocarcinomas associated with marked colitis and destruction of normal

Vet-ebooks.com

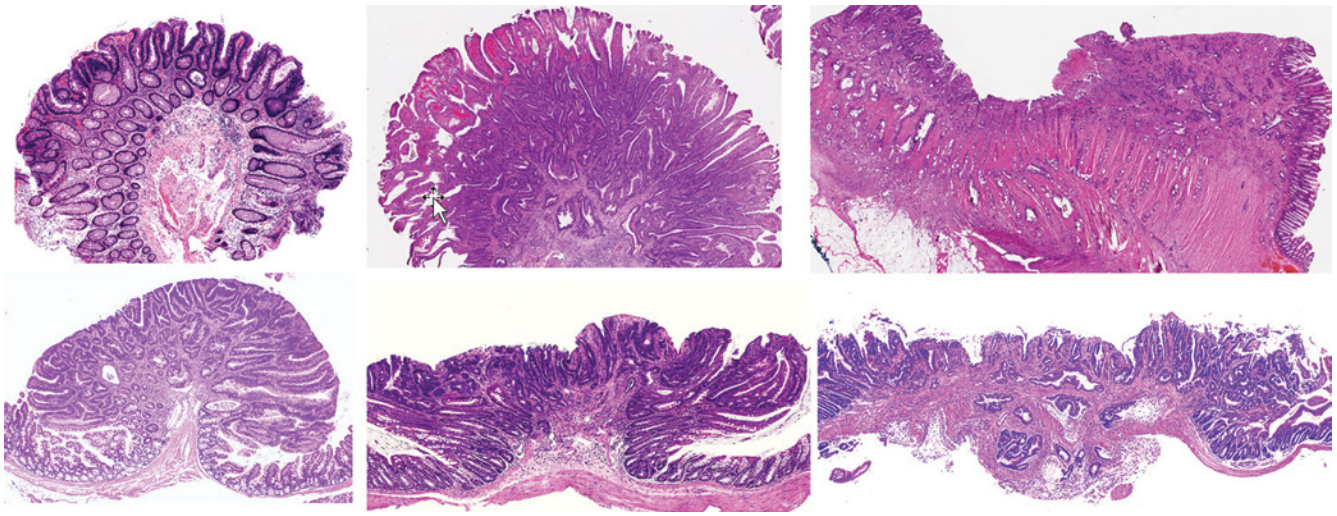


Figure 13.29 Comparative histogenesis of colon adenocarcinoma in humans (top 3 figures) and small intestinal adenocarcinoma in mice (lower 3). Adenomas (polyp) in left panel, early invasive adenocarcinomas in the middle panel, and highly invasive adenocarcinomas in the third panel. Source: Lower right mouse figure, Takeda [105].

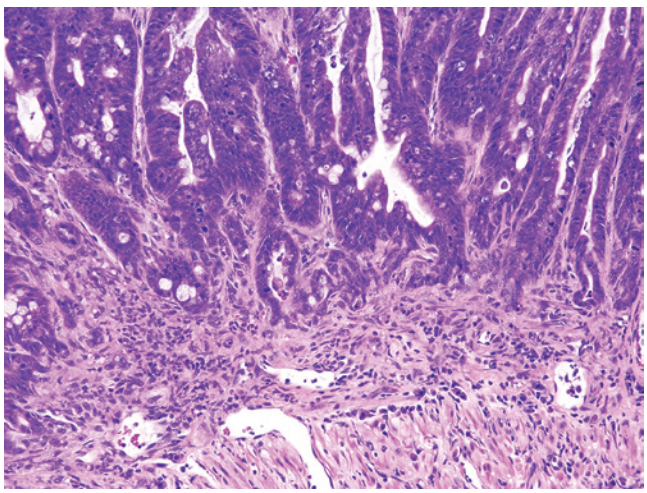


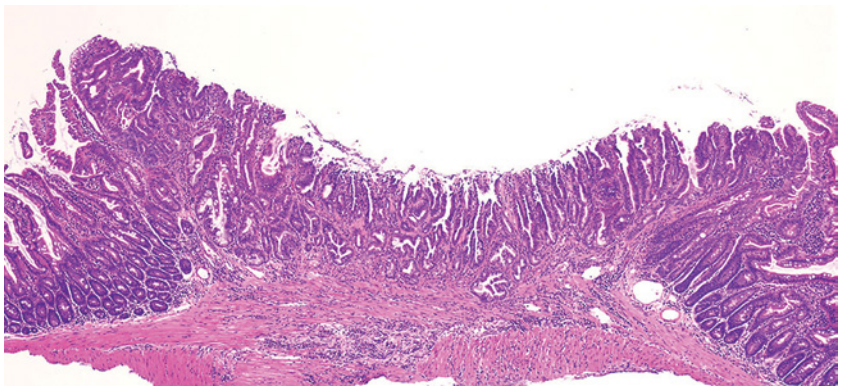
Figure 13.30 Adenocarcinoma, small intestine. Early invasion through muscularis mucosae. There is a stromal inflammatory response to the invasive tumor cells.

colonic epithelial structure, apparent invasion of lymphatics (Figure 13.35), has been reported in the suppression of tumorigenicity (*St14*) mutant mice carrying one $St14^{tm1Bug}$ allele, and a villin 1-*cre*-recombinase transgene driver ($vil1\text{-}cre^{+/0}$) on a mixed B6,129, Black Swiss background [121]. Although these lesions have evidence of malignancy, invasion of adjacent tissue, and lymphatic invasion, no tumor masses were seen. They were very unusual and the tumors have not been transplanted to prove neoplasia. Similar diffuse organ atypical proliferative epithelial lesions have been reported in GEM for other tissues.

Other Intestinal Tumors

Besides GIST in the cecum (Figure 13.36) and other stromal tumors noted in the stomach section previously, other primary intestinal tumors include follicular B-cell lymphomas, which may arise within the Peyer's patches of the small intestine of mice or may arise multifocally in the spleen, mesenteric lymph nodes, and Peyer's patches [11, 122].

Figure 13.31 Adenocarcinoma, small intestine. Invasion into the tunica muscularis.



Vet-ebooks.com

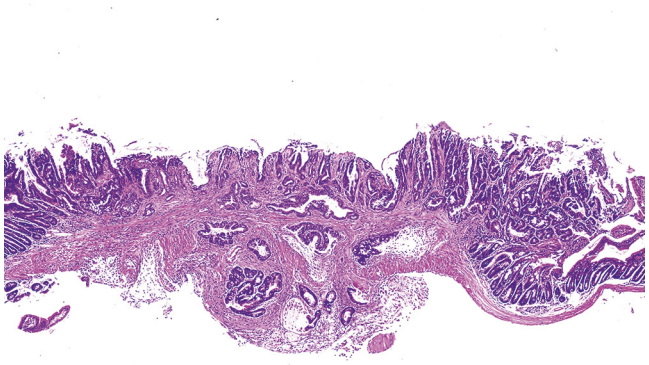


Figure 13.32 **Adenocarcinoma, small intestine, mouse**. Invasion to the serosa.

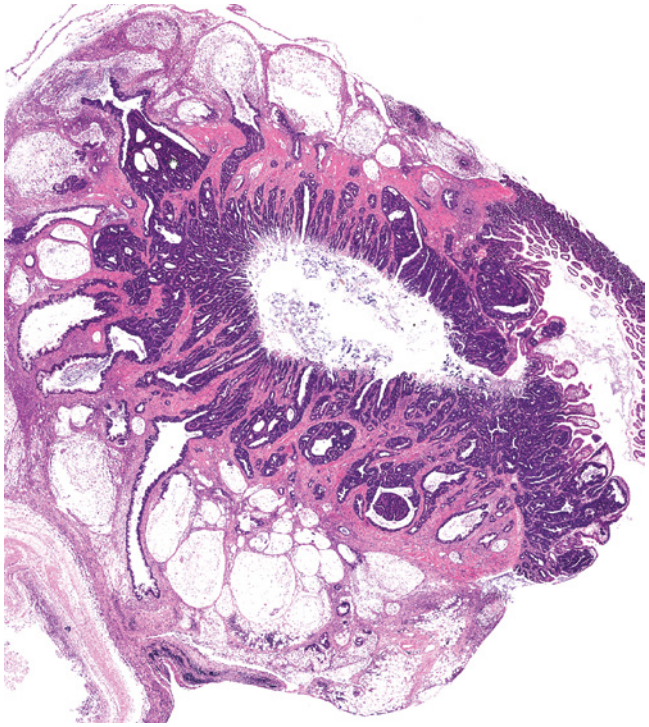


Figure 13.33 **Colon**. Adenocarcinoma, mucinous, with cystic mucinous areas in deeper layers and serosa, and basophilic cellular tumor areas in luminal areas.

Specific Intestinal Tumor Models

GEM models of intestinal neoplasia may be broadly divided into four groups, reflecting the most prevalent pathways of tumorigenesis identified in human colorectal cancer: *APC*-related models, mismatch repair deficient models, models with alterations in transforming growth factor β and its pathways, and colitis-associated neoplasia arising in immune-deficient models such as the *Il10* null mouse [59, 60, 101].

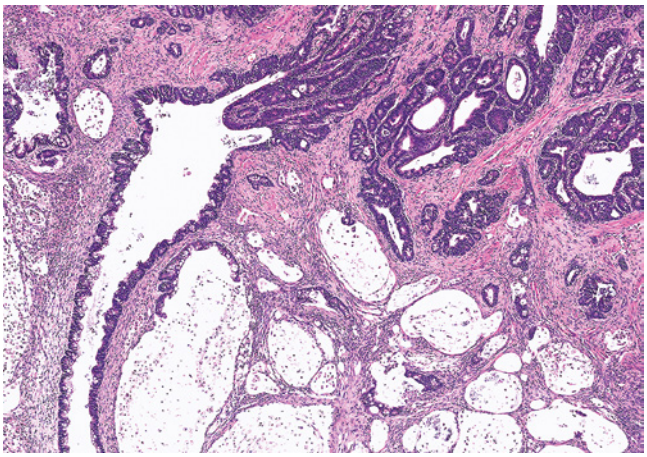


Figure 13.34 **Colon**. High magnification of 13.33 showing the cystic areas developing from the basophilic glandular and ductular areas.

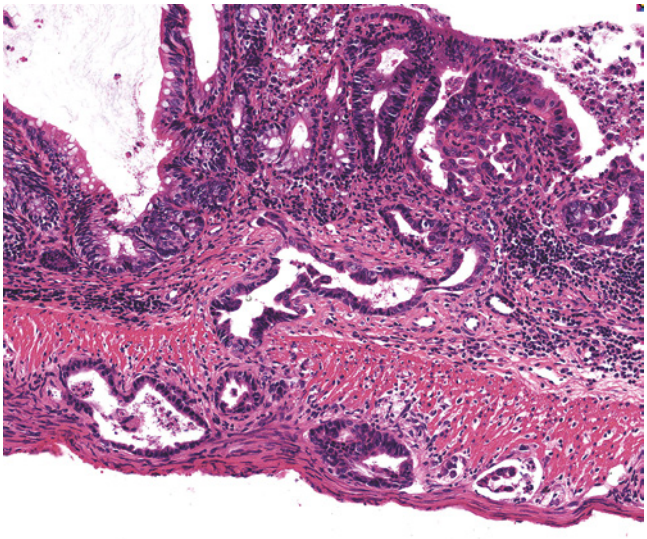


Figure 13.35 **Colon**. Diffuse invasive adenocarcinoma showing muscle and lymphatic invasion in *St14*^{tm1Bug} mutant mouse.

Apc$^{Min/+}$ and Related Models

The *Apc*$^{Min/+}$ mouse [103], originally called the multiple intestinal neoplasia mouse, one of the most widely used GEM models for human intestinal neoplasia, carries an autosomal dominant loss of function mutation at *Apc* codon 850 and serves as a model for FAPFAP coli. Because the most common drive mutation in human CRC is mutation in the tumor suppressor gene *APC*, the *Apc*-related GEM models have proven particularly useful in elucidating the role of loss of functionality of *Apc* in intestinal neoplasia, and in chemoprevention studies designed to prevent polyp formation. In contrast to humans with FAP, *Apc*$^{Min/+}$ mice develop primarily small intestinal adenomas that do not progress to adenocarcinoma; some GEM with other *Apc* mutations, such as the *Apc*^{tm1Rfo} (formerly called *Apc*$^{1638N/+}$) mouse, develop

Vet-ebooks.com

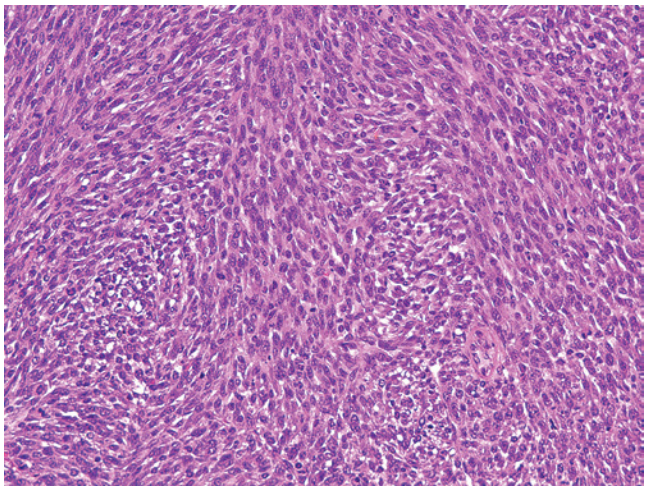


Figure 13.36 Cecum, gastrointestinal stromal tumor (GIST) in a mutant mouse. Note resemblance to leiomyosarcoma. Source: Jerry Rehg, St. Jude.

fewer small intestinal and more colonic adenomas [104] and thus tend to survive longer. Many of the *Apc*-related GEM also display other phenotypic characteristics of FAP such as the development of fibromatosis, gastric carcinoma, duodenal adenomas, and cutaneous cysts [102]. The adenomas in the various *Apc* models closely resemble human colorectal adenomas with low-grade dysplasia, with the exception that $Apc^{Min/+}$ adenomas may be covered by a layer of normal intestinal mucosa. The adenomas are made up of cells showing differentiation along multiple epithelial cell lines; in addition to absorptive-type cells, endocrine cells, goblet cells, and Paneth cells may be identified. Adenomas in these models rarely develop high-grade dysplasia and rarely progress to invasive adenocarcinoma. However, they become numerous and large in some inbred strains causing obstruction and death.

Apc models may display differences in the phenotype due to the genetic background as well as the specific genetic alteration, indicating the presence of modifying genetic factors [123]. In addition to modifier gene loci, diet, and the intestinal microbiome [123] influence polyp multiplicity, progression, and size in these models. Spontaneous small intestinal adenomas (polyps), often in the duodenum, are also strain related [56].

The $Apc^{Pirc/+}$ rat model develops adenomas and adenocarcinomas in the small and large intestines; tumor multiplicity depends upon the strain and sex of the animal, with male rats developing more neoplasms [124]. This model has the advantage of being longer lived than most *Apc*-related GEM models; because the lesions in the large intestine are exophytic and often bulky, they are amenable to colonoscopy with serial biopsy.

Mismatch Repair Deficiency Models

Intestinal neoplasms, including carcinomas, are predominantly located in the small intestine in several GEM models with deficiencies in mismatch repair proteins, such as the $Msh3^{-/-}$, $Msh6^{-/-}$, and $Mlh^{-/-}$ models and those crossed with various *Apc*-related models [59]. The mismatch repair GEM models also develop other neoplasms such as lymphomas, skin tumors, and sarcomas. In humans, colorectal and small intestinal carcinomas arising through this carcinogenic pathway often display unusual subtypes, such as signet ring cell, medullary, or mucinous features and are heavily infiltrated by lymphocytes. Similarly, the intestinal carcinomas in these models may display mucinous differentiation.

Models with Alterations in *Tgfb1* Signaling

Representative GEM models with alterations in *Tgfb1* pathway include the $Tgfb1^{-/-}Rag2^{-/-}$ mouse and models with deficiencies in the *Smad* family of proteins, which are downstream effectors of *Tgfb1* [59, 105] and *Pten* [106]. A *Smad*-deficient models, $Smad3^{tm1Par}$ [125] develops intestinal lesions, ranging from mucosal hyperplasia to adenomas, to adenocarcinoma, often mucinous, with a dense inflammatory infiltrate in desmoplastic tumor stroma. However, not all $Smad3^{-/-}$ GEM develop intestinal tumors, a finding attributed to differences in mouse strains, intestinal flora, and mutations.

Immunodeficiency Models

GEM characterized by immunodeficiencies with or without bacterial infections, such as the $Il10^{-/-}$ mouse, develop colorectal neoplastic lesions that lack overt cytologic dysplasia [59]. Rather, these neoplasms arise in plaque-like hyperplastic lesions that develop because of colitis, and frequently have a mucinous component. The distribution and morphology of the colitis vary depending upon the model, and the intestinal flora plays an important role in the development of both colitis and neoplasia [72, 126]. Herniation in rectal prolapse is common in these models and may be difficult to distinguish from invasive carcinoma [10, 59].

Pitfalls in Interpretation of Intestinal Carcinogenesis

Mucosal herniation, or displacement of intestinal epithelium into deeper layers of the intestinal and stomach wall, occurs in mice, spontaneously, and in GEM (Figures 13.15, 13.37). The displaced epithelium may be neoplastic (adenomatous) but non-invasive, or may be non-neoplastic, typically seen in the setting of colitis (Table 13.6). The mucosa is easily herniated into the submucosa or deeper layers because the muscularis mucosae is thin and offers little resistance, although the exact mechanism to account for mucosal displacement has not been elucidated; theories include herniation through weak points of the intestinal wall where blood vessels penetrate the muscularis propria [51], and inward pressure from a mucosal mass lesion such as a polyp. In one study of a mouse mutant ($Cdx2^{tm1Mmt}$), it was shown that anomalous duplication of the embryonic gut epithelium caused colon hamartomas in the adult mice, which resemble herniation (Figure 13.37) [50]. Without knowing the history of this lesion, it may have been diagnosed as a herniation, cystadenoma, or even cystic adenocarcinoma.

Vet-ebooks.com

Table 13.6 Features helpful in distinguishing invasive adenocarcinoma from mucosal herniation.

Feature	Favors invasive carcinoma	Favors mucosal herniation
Comparison with overlying mucosa	More advanced dysplasia/atypia in invasive cells, exceeding low-grade dysplasia	Dysplasia is absent or low grade, similar to the overlying mucosa
Desmoplasia	Present	Absent; minor degrees of stromal alteration may be seen in association with a prominent inflammatory infiltrate
Crypt/gland architecture	Irregular, angulated, pointed, or infiltrative gland profiles	Rounded profiles; may be cystically dilated
Spread relative to mucosal surface	Lateral spread deep to mucosal surface component	No lateral spread in deeper layers
Cell loss from leading edge	Present; invading crypts/glands are incompletely lined by epithelium	Absent; displaced crypts are completely lined by epithelial cells
Number of displaced/invading crypts	More than 2	1 or 2
Basement membrane around displaced/invading crypts	Discontinuous	Continuous
Findings in other mice of the same phenotype	Evidence of progression to invasive carcinoma in other mice	No invasive cancer in other mice
Biology	Transplanted with malignant growth in recipient	Not transplanted or if transplanted does not grow as a tumor

Source: Modified from [59, 60].

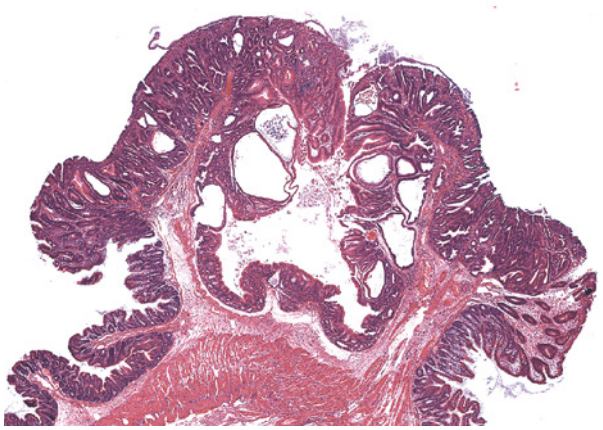


Figure 13.37 Colon hamartoma in a *Cdx2*^{tm1Mmt} mouse. The cystic proliferative area arose from a reduplication embryonal defect.

Herniated displaced gastric or intestinal crypts in GEM [59] are analogous to similar lesions occurring in humans (Table 13.6). In human intestinal neoplastic lesions, mucosal herniation most commonly occurs in large polyps with an elongated stalk. These lesions undergo twisting and torsion, which can result in displacement of the adenomatous crypts into the stalk of the polyp. Such crypts are surrounded by lamina propria, lack a stromal desmoplastic response, and display an identical degree of dysplasia as the overlying mucosa. In addition, stromal hemosiderin, evidence of prior trauma, is present in the stroma of the stalk.

In the setting of ulcerative colitis, cystically dilated displaced non-neoplastic crypts may be seen, a condition known as colitis cystica profunda. A similar lesion was seen in *A4gnt*^{tm1Jnaka} and other mutant mice [34].

To classify a lesion as invasive carcinoma, most of the features as outlined in Table 13.6 should be present. If the displaced crypts are few in number, occur in prolapsing mucosa, are not associated with stromal desmoplasia, and do not show more advanced dysplasia than the overlying mucosa, the lesion should not be interpreted as showing invasion.

Regeneration Adjacent to Ulcer

Regenerating intestinal mucosa at the edge of an acute or chronic ulcer or a focus of diffuse chronic inflammatory lesion may be difficult to distinguish from adenomatous change, especially in mouse colitis models [10, 52]. The mucosa adjacent to an ulcer is often thicker than the more normal mucosa because of epithelial regeneration. More problematic, however, is the histologic appearance of the regenerating crypts, which may have aberrant, distorted, complex architecture mimicking the crowded architecture of an adenoma (Figures 13.23 and 13.24). The regenerating cells have a more primitive appearance resembling dysplasia seen in preneoplastic or precancerous lesions, with basophilic cytoplasm, increased nucleus-to-cytoplasm ratio, increased mitotic figures, and little cytoplasmic mucin. In problematic cases, unequivocal classification of a lesion as neoplastic may need to be deferred until more advanced neoplastic lesions and evidence for tumor progression in the GEM are observed later in the experiment.

Vet-ebooks.com

References

1 Treuting, P.M., Arends, M.J., and Dintzis, S.M. (2018). Upper gastrointestinal tract. In: Comparative Anatomy and Histology: A Mouse, Rat and Human Atlas (eds. P.M. Treuting, M.J. Arends and S.M. Dintzis), 191–211. London: Elsevier.

2 Ruberte, J.C. and Navarro, M. (eds.) (2017). Morphological Mouse Phenotyping. Amsterdam: Academic Press.

3 Fu, D.J., Wang, L., Chouairi, F.K. et al. (2020). Gastric squamous-columnar junction contains a large pool of cancer-prone immature osteopontin responsive $Lgr5^{-}CD44^{+}$ cells. *Nat. Commun.* 11: 84.

4 Fu, D.J., Miller, A.D., Southard, T.L. et al. (2018). Stem cell pathology. *Annu. Rev. Pathol.* 13: 71–92.

5 Mahler, M., Rozell, B., Mahler, J.F. et al. (2000). Pathology of the gastrointestinal tract of genetically engineered and spontnaeous mutant mice. In: Pathology of Genetically Engineered Mice (eds. J.M. Ward, J.F. Mahler, R.R. Maronpot and J.P. Sundberg), 269–297. Ames, IA: Iowa State University Press.

6 Rogers, A.B. and Houghton, J. (2009). Helicobacter-based mouse models of digestive system carcinogenesis. *Methods Mol. Biol.* 511: 267–295.

7 Rogers, A.B. (2012). Gastric *Helicobacter* spp. in animal models: pathogenesis and modulation by extragastric coinfections. *Methods Mol. Biol.* 921: 175–188.

8 Rogers, A.B. (2012). Histologic scoring of gastritis and gastric cancer in mouse models. *Methods Mol. Biol.* 921: 189–203.

9 Kumar, V., Abbas, A.K., and Aster, J.C. (eds.) (2015). Robbins and Cotran Pathologic Basis of Disease. Philadelphia: Elsevier.

10 Nolte, T., Brander-Weber, P., Dangler, C. et al. (2016). Nonproliferative and proliferative lesions of the gastrointestinal tract, pancreas and salivary glands of the rat and mouse. *J. Toxicol. Pathol.* 29 (1 Suppl): 1S–125S.

11 Maronpot, R.R. (1999). Pathology of the Mouse. Vienna, IL: Cache River Press.

12 Ward, J.M., Yoon, M., Anver, M.R. et al. (2001). Hyalinosis and Ym1/Ym2 gene expression in the stomach and respiratory tract of 129S4/SvJae and wild-type and CYP1A2-null B6, 129 mice. *Am. J. Pathol.* 158 (1): 323–332.

13 Kurtzman, C.P., Robnett, C.J., Ward, J.M. et al. (2005). Multigene phylogenetic analysis of pathogenic candida species in the Kazachstania (Arxiozyma) telluris complex and description of their ascosporic states as *Kazachstania bovina* sp. nov., *K. heterogenica* sp. nov., *K. pintolopesii* sp. nov., and *K. slooffiae* sp. nov. *J. Clin. Microbiol.* 43 (1): 101–111.

14 D'Costa, K., Chonwerawong, M., Tran, L.S., and Ferrero, R.L. (2018). Mouse models of helicobacter infection and gastric pathologies. *J. Vis. Exp.* 140: 56985.

15 Ge, Z., Sheh, A., Feng, Y. et al. (2018). Helicobacter pylori-infected C57BL/6 mice with different gastrointestinal microbiota have contrasting gastric pathology, microbial and host immune responses. *Sci. Rep.* 8 (1): 8014.

16 O'Rourke, J.L., Dixon, M.F., Jack, A. et al. (2004). Gastric B-cell mucosa-associated lymphoid tissue (MALT) lymphoma in an animal model of '*Helicobacter heilmannii*' infection. *J. Pathol.* 203 (4): 896–903.

17 Floch, P., Izotte, J., Guillemaud, J. et al. (2017). A new animal model of gastric lymphomagenesis: APRIL transgenic mice infected by *Helicobacter* species. *Am. J. Pathol.* 187 (7): 1473–1484.

18 Jiang, Y. and Yu, Y. (2017). Transgenic and gene knockout mice in gastric cancer research. *Oncotarget* 8 (2): 3696–3710.

19 Dahlhoff, M., Gerhard, M., Rad, R. et al. (2012). A new mouse model for studying EGFR-dependent gastric polyps. *Biochim. Biophys. Acta* 1822 (8): 1293–1299.

20 Bakkelund, K.E., Waldum, H.L., Nordrum, I.S. et al. (2010). Long-term gastric changes in achlorhydric H(+)/K(+)-ATPase beta subunit deficient mice. *Scand. J. Gastroenterol.* 45 (9): 1042–1047.

21 Takagi, H., Jhappan, C., Sharp, R., and Merlino, G. (1992). Hypertrophic gastropathy resembling Menetrier's disease in transgenic mice overexpressing transforming growth factor alpha in the stomach. *J. Clin. Invest.* 90 (3): 1161–1167.

22 Inoue, S.I., Takahara, S., Yoshikawa, T. et al. (2017). Activated Braf induces esophageal dilation and gastric epithelial hyperplasia in mice. *Hum. Mol. Genet.* 26 (23): 4715–4727.

23 Shimada, S., Mimata, A., Sekine, M. et al. (2012). Synergistic tumour suppressor activity of E-cadherin and p53 in a conditional mouse model for metastatic diffuse-type gastric cancer. *Gut* 61 (3): 344–353.

24 Till, J.E., Yoon, C., Kim, B.J. et al. (2017). Oncogenic KRAS and p53 loss drive gastric tumorigenesis in mice that can be attenuated by E-cadherin expression. *Cancer Res.* 77 (19): 5349–5359.

25 Kinoshita, H., Hayakawa, Y., Konishi, M. et al. (2019). Three types of metaplasia model through *Kras* activation, *Pten* deletion, or *Cdh1* deletion in the gastric epithelium. *J. Pathol.* 247 (1): 35–47.

26 Seidlitz, T., Chen, Y.T., Uhlemann, H. et al. (2019). Mouse models of human gastric cancer subtypes with stomach-specific CreERT2-mediated pathway alterations. *Gastroenterology* 157 (6): 1599–1614.e2.

27 Fox, J.G., Rogers, A.B., Ihrig, M. et al. (2003). Helicobacter pylori-associated gastric cancer in INS-GAS mice is gender specific. *Cancer Res.* 63 (5): 942–950.

28 Rogers, R., Eastham-Anderson, J., DeVoss, J. et al. (2016). Image analysis-based approaches for scoring mouse models of colitis. *Vet. Pathol.* 53 (1): 200–210.

29 Park, J.W., Kim, M.S., Voon, D.C. et al. (2018). Multi-omics analysis identifies pathways and genes involved in diffuse-type gastric carcinogenesis induced by E-cadherin, p53, and Smad4 loss in mice. *Mol. Carcinog.* 57 (7): 947–954.

30 Takeda, H., Rust, A.G., Ward, J.M. et al. (2016). Sleeping Beauty transposon mutagenesis identifies genes that

Vet-ebooks.com

cooperate with mutant Smad4 in gastric cancer development. *Proc. Natl. Acad. Sci. U.S.A.* 113 (14): E2057–E2065.
31 Liu, W., Pan, H.F., Wang, Q., and Zhao, Z.M. (2018). The application of transgenic and gene knockout mice in the study of gastric precancerous lesions. *Pathol. Res. Pract.* 214 (12): 1929–1939.
32 Suarez, G., Romero-Gallo, J., Piazuelo, M.B. et al. (2019). Nod1 imprints inflammatory and carcinogenic responses toward the gastric pathogen *Helicobacter pylori*. *Cancer Res.* 79 (7): 1600–1611.
33 Zavros, Y., Eaton, K.A., Kang, W. et al. (2005). Chronic gastritis in the hypochlorhydric gastrin-deficient mouse progresses to adenocarcinoma. *Oncogene* 24 (14): 2354–2366.
34 Kawakubo, M., Komura, H., Goso, Y. et al. (2019). Analysis of *A4gnt* knockout mice reveals an essential role for gastric sulfomucins in preventing gastritis cystica profunda. *J. Histochem. Cytochem.* 67 (10): 759–770.
35 Fukayam, M., Rugge, M., and Washington, M.K. (2019). Tumors of the stomach. In: Digestive System Tumours, WHO Classification of Tumours Series, 5ee, vol. 1 (ed. WHO Classification of Tumours Editorial Board), 59–110. Lyon (France): International Agency for Research on Cancer.
36 Gold, L.S., Manley, N.B., Slone, T.H., and Ward, J.M. (2001). Compendium of chemical carcinogens by target organ: results of chronic bioassays in rats, mice, hamsters, dogs, and monkeys. *Toxicol. Pathol.* 29 (6): 639–652.
37 Olson, W.A., Habermann, R.T., Weisburger, E.K. et al. (1973). Induction of stomach cancer in rats and mice by halogenated aliphatic fumigants. *J. Natl. Cancer Inst.* 51 (6): 1993–1995.
38 Tamano, S., Jakubczak, J., Takagi, H. et al. (1995). Increased susceptibility to N-nitrosomethylurea gastric carcinogenesis in transforming growth factor alpha transgenic mice with gastric hyperplasia. *Jpn. J. Cancer Res.* 86 (5): 435–443.
39 Tsukamoto, T., Mizoshita, T., and Tatematsu, M. (2007). Animal models of stomach carcinogenesis. *Toxicol. Pathol.* 35 (5): 636–648.
40 Potter, C.S., Wang, Z., Silva, K.A. et al. (2014). Chronic proliferative dermatitis in Sharpin null mice: development of an autoinflammatory disease in the absence of B and T lymphocytes and IL4/IL13 signaling. *PLoS One* 9 (1): e85666.
41 Sundberg, J.P., France, M., Boggess, D. et al. (1997). Development and progression of psoriasiform dermatitis and systemic lesions in the flaky skin (fsn) mouse mutant. *Pathobiology* 65 (5): 271–286.
42 Sundberg, J.P., Kenty, G.A., Beamer, W.G., and Adkison, D.L. (1992). Forestomach papillomas in flaky skin and steel-Dickie mutant mice. *J. Vet. Diagn. Invest.* 4 (3): 312–317.
43 Janardhan, K.S., Venkannagari, P., Jensen, H. et al. (2019). Do GISTs occur in rats and mice? Immunohistochemical characterization of gastrointestinal tumors diagnosed as smooth muscle tumors in The National Toxicology Program. *Toxicol. Pathol.* 47 (5): 577–584.
44 Nakai, N., Ishikawa, T., Nishitani, A. et al. (2008). A mouse model of a human multiple GIST family with KIT-Asp820Tyr mutation generated by a knock-in strategy. *J. Pathol.* 214 (3): 302–311.
45 Sommer, G., Agosti, V., Ehlers, I. et al. (2003). Gastrointestinal stromal tumors in a mouse model by targeted mutation of the Kit receptor tyrosine kinase. *Proc. Natl. Acad. Sci. U.S.A.* 100 (11): 6706–6711.
46 Sundaresan, S., Kang, A.J., Hayes, M.M. et al. (2017). Deletion of Men1 and somatostatin induces hypergastrinemia and gastric carcinoids. *Gut*. [Research Support, N.I.H., Extramural] 66 (6): 1012–1021.
47 Andervont, H.B. and Stewart, H.L. (1937). Adenomatous lesion in stomach of strain I mice. *Science* 86 (2242): 566–567.
48 Fernandez-Salguero, P.M., Ward, J.M., Sundberg, J.P., and Gonzalez, F.J. (1997). Lesions of aryl-hydrocarbon receptor-deficient mice. *Vet. Pathol.* 34 (6): 605–614.
49 Boorman, G., Crabbs, T.A., Kolenda-Roberts, H. et al. (2012). Proceedings of the 2011 National Toxicology Program Satellite Symposium. *Toxicol. Pathol.* 40 (2): 321–344.
50 Tamai, Y., Nakajima, R., Ishikawa, T. et al. (1999). Colonic hamartoma development by anomalous duplication in *Cdx2* knockout mice. *Cancer Res.* 59 (12): 2965–2970.
51 Treuting, P.M., Arends, M.J., and Dintzis, S.M. (2018). Lower gastrointestinal tract. In: Comparative Anatomy and Histology: A Mouse, Rat, and Human Atlas (eds. P.M. Treuting, S.M. Dintzos and K.S. Montine), 213–228. London: Academic Press.
52 Ward, J.M. and Treuting, P.M. (2014). Rodent intestinal epithelial carcinogenesis: pathology and preclinical models. *Toxicol. Pathol.* 42 (1): 148–161.
53 Pereira, E.S.A., Lourenco, A.L., Marmello, B.O. et al. (2019). Comparison of two techniques for a comprehensive gut histopathological analysis: Swiss Roll versus Intestine Strips. *Exp. Mol. Pathol.* 111: 104302.
54 Yoneda, M., Molinolo, A.A., Ward, J.M. et al. (2015). A simple device to rapidly prepare whole mounts of the mouse intestine. *J. Vis. Exp.* 27 (105): e53042.
55 Barthold, S.W., Griffey, S.M., and Percy, D.H. (2016). Pathology of Laboratory Rodents and Rabbits, 4e. Oxford, UK: Wiley Blackwell.
56 Sundberg, J.P., Berndt, A., Sundberg, B.A. et al. (2016). Approaches to investigating complex genetic traits in a large-scale inbred mouse aging study. *Vet. Pathol.* 53 (2): 456–467.
57 Radaelli, E., Castiglioni, V., Recordati, C. et al. (2016). The pathology of aging 129S6/SvEvTac mice. *Vet. Pathol.* 53 (2): 477–492.
58 Mohr, U. (ed.) (2001). International Classification of Rodent Tumors: The Mouse. Berlin: Springer.
59 Boivin, G.P., Washington, K., Yang, K. et al. (2003). Pathology of mouse models of intestinal cancer: consensus report and recommendations. *Gastroenterology* 124 (3): 762–777.

Vet-ebooks.com

60 Washington, M.K., Powell, A.E., Sullivan, R. et al. (2013). Pathology of rodent models of intestinal cancer: progress report and recommendations. *Gastroenterology* 144 (4): 705–717.

61 Arends, M.J., Lam, A.K., Nagtegaal, I.D., and Odze, R.D. (2019). Tumours of the colon and rectum. In: Digestive System Tumors, WHO Classification of Tumours Series, 5ee, vol. 1 (ed. WHO Classification of Tumours Editorial Board), 157–192. Lyon (France): International Agency for Research on Cancer.

62 Allen, I.C., Wilson, J.E., Schneider, M. et al. (2012). NLRP12 suppresses colon inflammation and tumorigenesis through the negative regulation of noncanonical NF-kappaB signaling. *Immunity* 36 (5): 742–754.

63 Caruso, R., Mathes, T., Martens, E.C. et al. (2019). A specific gene-microbe interaction drives the development of Crohn's disease-like colitis in mice. *Sci. Immunol.* 4 (34): 19.

64 Conway, K.L., Kuballa, P., Song, J.H. et al. (2013). Atg16l1 is required for autophagy in intestinal epithelial cells and protection of mice from Salmonella infection. *Gastroenterology* 145 (6): 1347–1357.

65 Lavoie, S., Conway, K.L., Lassen, K.G. et al. (2019). The Crohn's disease polymorphism, ATG16L1 T300A, alters the gut microbiota and enhances the local Th1/Th17 response. *Elife* 8: e39982.

66 Hue, S., Ahern, P., Buonocore, S. et al. (2006). Interleukin-23 drives innate and T cell-mediated intestinal inflammation. *J. Exp. Med.* 203 (11): 2473–2483.

67 Ey, B., Eyking, A., Klepak, M. et al. (2013). Loss of TLR2 worsens spontaneous colitis in MDR1A deficiency through commensally induced pyroptosis. *J. Immunol.* 190 (11): 5676–5688.

68 Kullberg, M.C., Ward, J.M., Gorelick, P.L. et al. (1998). *Helicobacter hepaticus* triggers colitis in specific-pathogen-free interleukin-10 (IL-10)-deficient mice through an IL-12- and gamma interferon-dependent mechanism. *Infect. Immun.* 66 (11): 5157–5166.

69 Kasper, S.H., Spalinger, M.R., Leonardi, I. et al. (2016). Deficiency of protein tyrosine phosphatase non-receptor type 2 in intestinal epithelial cells has no appreciable impact on dextran sulphate sodium colitis severity but promotes wound healing. *Digestion* 93 (4): 249–259.

70 Szabo, R., Callies, L.K., and Bugge, T.H. (2019). Matriptase drives early-onset intestinal failure in a mouse model of congenital tufting enteropathy. *Development* 146 (22): dev183392.

71 Guerra, E., Lattanzio, R., La Sorda, R. et al. (2012). mTrop1/Epcam knockout mice develop congenital tufting enteropathy through dysregulation of intestinal E-cadherin/beta-catenin. *PLoS One* 7 (11): e49302.

72 Nguyen, D.D., Muthupalani, S., Goettel, J.A. et al. (2013). Colitis and colon cancer in WASP-deficient mice require helicobacter species. *Inflamm. Bowel Dis.* 19 (10): 2041–2050.

73 Perse, M. and Cerar, A. (2012). Dextran sodium sulphate colitis mouse model: traps and tricks. *J. Biomed. Biotechnol.* 2012: 718617.

74 Clapper, M.L., Cooper, H.S., and Chang, W.C. (2007). Dextran sulfate sodium-induced colitis-associated neoplasia: a promising model for the development of chemopreventive interventions. *Acta Pharmacol. Sin.* 28 (9): 1450–1459.

75 Cooper, H.S., Murthy, S., Kido, K. et al. (2000). Dysplasia and cancer in the dextran sulfate sodium mouse colitis model. Relevance to colitis-associated neoplasia in the human: a study of histopathology, B-catenin and p53 expression and the role of inflammation. *Carcinogenesis* 21 (4): 757–768.

76 DeVoss, J. and Diehl, L. (2014). Murine models of inflammatory bowel disease (IBD): challenges of modeling human disease. *Toxicol. Pathol.* 42 (1): 99–110.

77 Klopfleisch, R. (2013). Multiparametric and semiquantitative scoring systems for the evaluation of mouse model histopathology – a systematic review. *BMC Vet. Res.* 9: 123.

78 Ward, J.M., Fox, J.G., Anver, M.R. et al. (1994). Chronic active hepatitis and associated liver tumors in mice caused by a persistent bacterial infection with a novel *Helicobacter* species. *J. Natl. Cancer Inst.* 86 (16): 1222–1227.

79 Mizoguchi, A., Takeuchi, T., Himuro, H. et al. (2016). Genetically engineered mouse models for studying inflammatory bowel disease. *J. Pathol.* 238 (2): 205–219.

80 Takahashi, D., Hase, K., Kimura, S. et al. (2011). The epithelia-specific membrane trafficking factor AP-1B controls gut immune homeostasis in mice. *Gastroenterology* 141 (2): 621–632.

81 Lees, C.W., Barrett, J.C., Parkes, M., and Satsangi, J. (2011). New IBD genetics: common pathways with other diseases. *Gut* 60 (12): 1739–1753.

82 Khor, B., Gardet, A., and Xavier, R.J. (2011). Genetics and pathogenesis of inflammatory bowel disease. *Nature* 474 (7351): 307–317.

83 Bleich, A., Mahler, M., Most, C. et al. (2004). Refined histopathologic scoring system improves power to detect colitis QTL in mice. *Mamm. Genome* 15 (11): 865–871.

84 Seamons, A., Treuting, P.M., Brabb, T., and Maggio-Price, L. (2013). Characterization of dextran sodium sulfate-induced inflammation and colonic tumorigenesis in Smad3(−/−) mice with dysregulated TGFbeta. *PLoS One* 8 (11): e79182.

85 Sundberg, J.P., Elson, C.O., Bedigian, H., and Birkenmeier, E.H. (1994). Spontaneous, heritable colitis in a new substrain of C3H/HeJ mice. *Gastroenterology* 107 (6): 1726–1735.

86 Arthur, J.C., Perez-Chanona, E., Muhlbauer, M. et al. (2012). Intestinal inflammation targets cancer-inducing activity of the microbiota. *Science* 338 (6103): 120–123.

87 Mahler, M., Bristol, I.J., Leiter, E.H. et al. (1998). Differential susceptibility of inbred mouse strains to dextran sulfate sodium-induced colitis. *Am. J. Phys* 274 (3): G544–G551.

88 Mahler, M., Bristol, I.J., Sundberg, J.P. et al. (1999). Genetic analysis of susceptibility to dextran sulfate sodium-induced colitis in mice. *Genomics* 55 (2): 147–156.

Vet-ebooks.com

89 Means, A.L., Freeman, T.J., Zhu, J. et al. (2018). Epithelial Smad4 deletion up-regulates inflammation and promotes inflammation-associated cancer. *Cell Mol. Gastroenterol. Hepatol.* 6 (3): 257–276.

90 Meyerholz, D.K. and Beck, A.P. (2018). Fundamental concepts for semiquantitative tissue scoring in translational research. *ILAR J.* 59 (1): 13–17.

91 Suzuki, R., Kohno, H., Sugie, S. et al. (2006). Strain differences in the susceptibility to azoxymethane and dextran sodium sulfate-induced colon carcinogenesis in mice. *Carcinogenesis* 27 (1): 162–169.

92 Sellon, R.K., Tonkonogy, S., Schultz, M. et al. (1998). Resident enteric bacteria are necessary for development of spontaneous colitis and immune system activation in interleukin-10-deficient mice. *Infect. Immun.* 66 (11): 5224–5231.

93 Maggio-Price, L., Treuting, P., Bielefeldt-Ohmann, H. et al. (2009). Bacterial infection of Smad3/Rag2 double-null mice with transforming growth factor-beta dysregulation as a model for studying inflammation-associated colon cancer. *Am. J. Pathol.* 174 (1): 317–329.

94 Maggio-Price, L., Treuting, P., Zeng, W. et al. (2006). Helicobacter infection is required for inflammation and colon cancer in SMAD3-deficient mice. *Cancer Res.* 66 (2): 828–838.

95 Becker, C., Neurath, M.F., and Wirtz, S. (2015). The intestinal microbiota in inflammatory bowel disease. *ILAR J.* 56 (2): 192–204.

96 Peloquin, J.M. and Nguyen, D.D. (2013). The microbiota and inflammatory bowel disease: insights from animal models. *Anaerobe* 24: 102–106.

97 Lencioni, K.C., Seamons, A., Treuting, P.M. et al. (2008). Murine norovirus: an intercurrent variable in a mouse model of bacteria-induced inflammatory bowel disease. *Comp. Med.* 58 (6): 522–533.

98 Vogel, P., Janke, L., Gravano, D.M. et al. (2018). Globule leukocytes and other mast cells in the mouse intestine. *Vet. Pathol.* 55 (1): 76–97.

99 Paik, J., Meeker, S., Hsu, C.C. et al. (2020). Validation studies for germ-free Smad3(−/−) mice as a bio-assay to test the causative role of fecal microbiomes in IBD. *Gut Microbes* 11 (1): 21–31.

100 Ma, H., Brosens, L.A.A., Offerhaus, G.J.A. et al. (2018). Pathology and genetics of hereditary colorectal cancer. *Pathology* 50 (1): 49–59.

101 Taketo, M.M. and Edelmann, W. (2009). Mouse models of colon cancer. *Gastroenterology*. [Review]. 136 (3): 780–798.

102 Washington, K. and Zemper, A.E.D. (2019). Apc-related models of intestinal neoplasia: a brief review for patholgists. *Surg. Exp. Pathol.* 2: 11.

103 Moser, A.R., Pitot, H.C., and Dove, W.F. (1990). A dominant mutation that predisposes to multiple intestinal neoplasia in the mouse. *Science* 247 (4940): 322–324.

104 Fodde, R., Edelmann, W., Yang, K. et al. (1994). A targeted chain-termination mutation in the mouse Apc gene results in multiple intestinal tumors. *Proc. Natl. Acad. Sci. U.S.A.* 91 (19): 8969–8973.

105 Takeda, H., Wei, Z., Koso, H. et al. (2015). Transposon mutagenesis identifies genes and evolutionary forces driving gastrointestinal tract tumor progression. *Nat. Genet.* 47 (2): 142–150.

106 Yu, M., Trobridge, P., Wang, Y. et al. (2014). Inactivation of TGF-beta signaling and loss of PTEN cooperate to induce colon cancer in vivo. *Oncogene* 33 (12): 1538–1547.

107 Sakamoto, N., Feng, Y., Stolfi, C. et al. (2017). BRAF(V600E) cooperates with CDX2 inactivation to promote serrated colorectal tumorigenesis. *Elife* 6: e20331.

108 Belhadj, S., Mur, P., Navarro, M. et al. (2017). Delineating the phenotypic spectrum of the NTHL1-associated polyposis. *Clin. Gastroenterol. Hepatol.* 15 (3): 461–462.

109 Rengifo-Cam, W., Shepherd, H.M., Jasperson, K.W. et al. (2018). Colon pathology characteristics in Li-Fraumeni syndrome. *Clin. Gastroenterol. Hepatol.* 16 (1): 140–141.

110 Valle, L., Vilar, E., Tavtigian, S.V., and Stoffel, E.M. (2019). Genetic predisposition to colorectal cancer: syndromes, genes, classification of genetic variants and implications for precision medicine. *J. Pathol.* 247 (5): 574–588.

111 Ward, J.M. and Weisburger, E.K. (1975). Intestinal tumors in mice treated with a single injection of N-nitroso-N-butylurea. *Cancer Res.* 35 (8): 1938–1943.

112 Ward, J.M. and Devor-Henneman, D.E. (2004). Mouse models of human familial cancer syndromes. *Toxicol. Pathol.* 32 (Suppl 1): 90–98.

113 Roper, J., Tammela, T., Akkad, A. et al. (2018). Colonoscopy-based colorectal cancer modeling in mice with CRISPR-Cas9 genome editing and organoid transplantation. *Nat. Protoc.* 13 (2): 217–234.

114 Tang, J., Feng, Y., Kuick, R. et al. (2019). Trp53 null and R270H mutant alleles have comparable effects in regulating invasion, metastasis, and gene expression in mouse colon tumorigenesis. *Lab. Invest.* 99 (10): 1454–1469.

115 Klimstra, D.D., Nagtegaal, I.D., Rugge, M., and Salto-Tellez, M. (2019). Tumours of the small intestine and ampulla. In: WHO Classification of Tumours of the Digestive System (ed. Tumours WCoTEBDS), 66. Lyon: International Agency for Research on Cancer.

116 Roberts, R.B., Min, L., Washington, M.K. et al. (2002). Importance of epidermal growth factor receptor signaling in establishment of adenomas and maintenance of carcinomas during intestinal tumorigenesis. *Proc. Natl. Acad. Sci. U.S.A.* 99 (3): 1521–1526.

117 Wendling, O., Champy, M.F., Jaubert, S. et al. (2017). Atp6ap2 ablation in adult mice impairs viability through multiple organ deficiencies. *Sci. Rep.* 7 (1): 9618.

118 Cardiff, R.D., Anver, M.R., Boivin, G.P. et al. (2006). Precancer in mice: animal models used to understand, prevent, and treat human precancers. *Toxicol. Pathol.* 34 (6): 699–707.

119 Caderni, G., Femia, A.P., Giannini, A. et al. (2003). Identification of mucin-depleted foci in the unsectioned colon of azoxymethane-treated rats: correlation with carcinogenesis. *Cancer Res.* 63 (10): 2388–2392.

Vet-ebooks.com

120 O'Rourke, K.P., Loizou, E., Livshits, G. et al. (2017). Transplantation of engineered organoids enables rapid generation of metastatic mouse models of colorectal cancer. *Nat. Biotechnol.* 35 (6): 577–582.

121 Kosa, P., Szabo, R., Molinolo, A.A., and Bugge, T.H. (2012). Suppression of tumorigenicity-14, encoding matriptase, is a critical suppressor of colitis and colitis-associated colon carcinogenesis. *Oncogene* 31 (32): 3679–3695.

122 Ward, J.M., Mahler, J.F., Maronpot, R.R., and Sundberg, J.P. (eds.) (2000). Pathology of Genetically Engineered Mice. Ames, IA: Iowa State University Press.

123 Moskowitz, J.E., Andreatta, F., and Amos-Landgraf, J. (2019). The gut microbiota modulates differential adenoma suppression by B6/J and B6/N genetic backgrounds in Apc(Min) mice. *Mamm. Genome* 30 (9-10): 237–244.

124 Amos-Landgraf, J.M., Kwong, L.N., Kendziorski, C.M. et al. (2007). A target-selected Apc-mutant rat kindred enhances the modeling of familial human colon cancer. *Proc. Natl. Acad. Sci. U.S.A.* 104 (10): 4036–4041.

125 Zhu, Y., Richardson, J.A., Parada, L.F., and Graff, J.M. (1998). Smad3 mutant mice develop metastatic colorectal cancer. *Cell* 94 (6): 703–714.

126 Ward, J.M., Anver, M.R., Haines, D.C. et al. (1996). Inflammatory large bowel disease in immunodeficient mice naturally infected with *Helicobacter hepaticus*. *Lab. Anim. Sci.* 46 (1): 15–20.

Vet-ebooks.com

14

Cardiovascular System

Kathleen L. Gabrielson, Akash Behera, Polina Sysa-Shah, Tyler J. Creamer, and Timothy K. Cooper

Mouse Anatomy, Histology, and Physiology

This chapter focuses on spontaneously occurring cardiovascular lesions observed in routine background strains of mice, genetically engineered cardiovascular models, and methods utilized for characterizing cardiovascular disease in mice. The gross and histologic anatomy of the normal mouse cardiovascular system is covered in detail elsewhere, and readers are encouraged to review these sources [1–11]. Major salient features are briefly reviewed in the following text. Precise morphological descriptions of age-, strain-, and sex-dependent differences and associated disease in genetically engineered mice (GEM) are important for understanding pathogenesis and how these alterations impact structure and function in the cardiovascular system.

Heart

The weight of the heart in the adult male mouse is approximately 0.5–0.6% of the body weight (BW) and is age-, strain-, and sex-dependent [12]. The musculature of the heart is organized in bundles running in three distinct myofiber orientation patterns observed from epicardium to endocardium surfaces (transverse, oblique-longitudinal, and transverse) easily observed at the mid-papillary level. Coronary artery anatomy may vary significantly within or between strains [13]. This may be important in modeling myocardial infarction in mice. There are significant anatomic differences between mouse and human hearts including the great veins and conduction system [12].

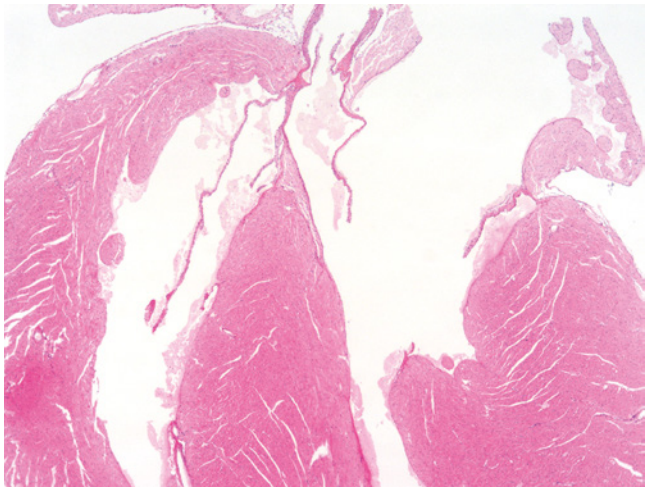
As in typical mammalian hearts, there are four valves in the mouse. The right atrioventricular (AV, tricuspid) valve separates the right atrium and ventricle. The semilunar pulmonic valve in the right ventricular outflow tract (pulmonary root) controls flow to the lungs. The left AV (bicuspid or mitral) valve separates the left atrium and ventricle. The aortic valve in the left ventricular outflow tract (aortic root) controls the release of blood to the general circulation. Unlike in humans, the AV valves show no obvious commissures and appear as a continuous sheet of tissue. As illustrated in Figure 14.1, the AV valves have a loose myxomatous matrix (lamina spongiosa) on the atrial aspect and a dense fibrous matrix (lamina fibrosa) on the ventricular aspect, while semilunar valves have a loose myxomatous matrix on the ventricular aspect and a dense fibrous matrix on the arterial aspect. Fibrous chordae tendineae attach the distal free edge of the AV valves to the papillary muscle. The fibrotic appearance and transition of the tendinous insertion into the papillary muscle should not be misinterpreted as myocardial fibrosis. The endocardial cells covering the valve cusps and chordae tendineae should be continuous, squamoid, and inconspicuous.

Cardiac Conduction System

The mouse cardiac conduction system (CCS) is difficult to observe and should not be confused with the numerous ganglia. The CCS is responsible for the regulation of contractions in the atria and ventricles via electrical signals [14]. Anatomically there are several primary areas: the sinoatrial node (SAN), the atrioventricular node (AVN), the bundle of His, and the Purkinje fiber network [14–16]. The SAN is the pacemaker of the heart, controlling atrial contractions. Located between the cranial vena cava and the right atrium, in larger species the SAN is recognizable as an oval-shaped mass with a fibrous tissue matrix. The head of the SAN projects towards the interatrial groove, and its tail extends to the caudal vena cava. Its vasculature consists of the particularly protrusive sinus node artery, which normally stems from the right coronary artery, although in some cases is seen originating from the left circumflex coronary artery [17]. Nodal cells are oval shaped, do not exhibit the striation present in typical myocardial cells, and are gap junction protein alpha 1 (GJAP1, formerly called connexin 43) negative in rodents [18].

Pathology of Genetically Engineered and Other Mutant Mice, First Edition. Edited by John P. Sundberg, Peter Vogel, and Jerrold M. Ward.
© 2022 John Wiley & Sons, Inc. Published 2022 by John Wiley & Sons, Inc.

(a)



(b)

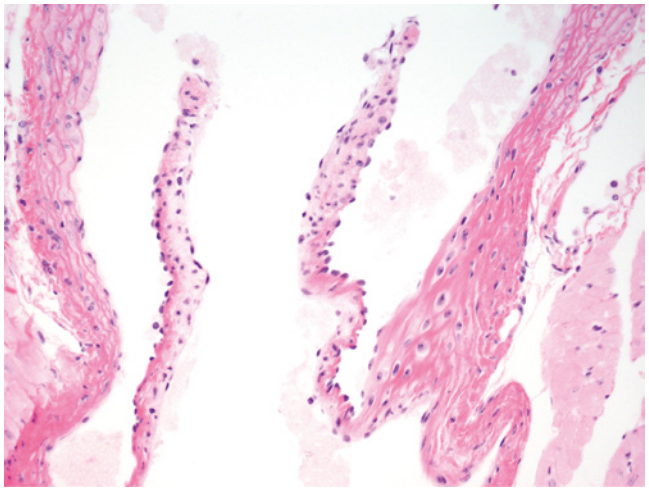


Figure 14.1 Longitudinal section of HE stained heart from a NZW/LacJ mouse demonstrating normal tricuspid, aortic, and mitral valve cusps (a). Higher magnification of aortic semilunar valve with a loose myxomatous matrix (spongiosa) on the ventricular aspect and a dense fibrous matrix (fibrosa) on the arterial aspect (b).

After passing through the SAN, electrical signals are conducted through the AVN, located in the atrial septum. The AVN causes a delay in myocardial contractions to allow for ventricular filling [19]. The AVN then leads into the bundle of His, which is split into left and right branches, leading to the Purkinje fiber network. Purkinje fibers are made of larger cells, dense with mitochondria, and are capable of efficient transfer of action potentials [17].

Development of CCS in mice has been studied with CCS-lacZ transgenic mice, including histological mapping using X-gal staining, optical mapping, and *in situ* hybridization [14, 15, 18, 20, 21]. Multiple micro-ganglia are present in the mouse heart, located on the epicardial surface and extending axons to the CCS; these should not be confused with the CCS [22].

Resident Immune Cells of the Heart

The role of inflammatory cells in heart failure is well known [23]. The heart has a resident macrophage population. These myocardial resident macrophages are established during embryonic development and persist into adulthood independent of blood monocyte input. Resident cardiac macrophages represent 6–8% of the non-cardiomyocyte population in the healthy adult mouse heart, with higher numbers in the developing heart [24].

Resident T cells impact inflammatory pathways in cardiac injury, controlling cardiomyocyte health [23]. The heart contains tissue-resident effector memory T cells, specifically resident memory signatures CD69 and ITGAE (formerly CD103) [25]. T cells from the heart contribute to heart failure, characterized by chronic inflammation [26, 27]. When studying heart inflammation, it is important to consider isolating, freezing, and fixing spleens to capture other immune cell such as CD4+ T lymphocytes that are globally expanded and activated due to chronic ischemic heart failure, with Th2 (vs. Th1) and Th17 (vs. Treg) predominance in failing hearts, and with an expansion of memory T cells in the spleen. For example, cardiac and splenic T cells in heart failure are primed to induce cardiac injury and remodeling, and retain this memory upon adoptive transfer [26].

Mast cells are also present in mouse hearts and easily identified with toluidine blue or Wright–Giemsa stain [28]. Cardiac mast cells are a potent mediator of adverse myocardial remodeling [29] and can modulate the effect of pharmacological interventions, such as ACE inhibitors [30]. Mast cells also regulate myofilament calcium sensitization and heart function after myocardial infarction [31].

Circulatory System: Vasculature

Blood vessels are composed of three layers: the inner tunica intima, middle tunica media, and outer tunica adventitia. The intima consists of a continuous, fenestrated, or discontinuous lining of endothelial cells on a basement membrane (including type IV collagen and laminin); the cells are squamoid and flattened when quiescent. Although endothelial cells are morphologically similar across vessels and organs, they are functionally highly distinct in different locations [32, 33]. The intima is separated from the media by an internal elastic lamina (IEL). In normal mouse vessels the distance between the endothelial cells and the IEL (subendothelial lamina) is imperceptibly small. In many large species, some large muscular arteries (e.g. extramural coronary or renal artery in macaques) have a moderate amount of well-differentiated collagen between the endothelium and IEL; this feature is absent in mice. Accumulation of fibrous matrix between the endothelium and IEL (inaccurately referred to as the subintima) is a stereotyped response to vascular injury from a variety of causes. The media is composed of concentrically oriented smooth muscle cells with variable amounts of elastic fibers and scant fibrillar collagen (types III and I). In arteries, an external elastic lamina (EEL) demarcates between

the muscular media and fibrous adventitia, the latter of which may blend inconspicuously into adjacent soft tissues. Arteries are classified as elastic or muscular according to the composition of the media, and as large, medium, or small, or arterioles according to size and location. Large vessels are the aorta and its major branches (e.g. renal artery) and corresponding veins, while medium vessels are extra-parenchymal distributing arteries and major intraparenchymal branches (e.g. renal interlobular, arcuate, and cortical radial arteries) and corresponding veins [34].

Elastic Arteries

Elastic arteries in the mouse include the aorta and its major proximal branches (brachiocephalic trunk, subclavian, common carotid, common iliac). The normal mouse aorta in cross section should consist of multiple (usually 4–6) regular undulating sawtooth elastic lamellae usually spanning the entire circumference of the vessel with only rare splitting, fragmentation, or disorganization. Lamellae are separated by quiescent interlamellar smooth muscle cells in a scant and fine collagenous matrix. Around ostia of branching arteries, the intima of the aorta will take on a winged polypoid appearance, which projects into the lumen with a basketweave of elastin (bolster). The adventitia will also appear thicker around these branch points. In longitudinal section, the elastic lamellae form a distinct and regular basketweave around medial smooth muscle cells, with little collagen. As major branches of the aorta extend centrifugally, the number of elastic lamellae becomes fewer and the smooth muscle cells increase in thickness and prominence. In mice there are no medial vasa vasorum in either the thoracic or the abdominal aorta; these are limited to the adventitia [35, 36]. Figure 14.2 shows examples of elastic arteries.

Muscular Arteries and Veins

In the mouse, medium and large pulmonary veins have striated cardiac muscle in the media, with smooth muscle in the media of pulmonary arteries [37]. Pulmonary arteries have less smooth muscle and a thinner media than a comparably sized systemic artery, consistent with the lower systolic pressures in the pulmonary circulation. Figure 14.3 provides a vessel comparison. Intrapulmonary bronchial arteries are underdeveloped in the mouse relative to other species, and express endothelial tissue plasminogen activator [38–40]. Figure 14.4 demonstrates an example of a systemic muscular artery. While mice have separate left and right cranial venae cava, they lack a right azygos vein.

Special Necropsy Organ Protocols

This next section will focus on anatomical and histological methods for characterizing vessels and hearts. For reproducible sectioning of the heart, either longitudinal or transverse

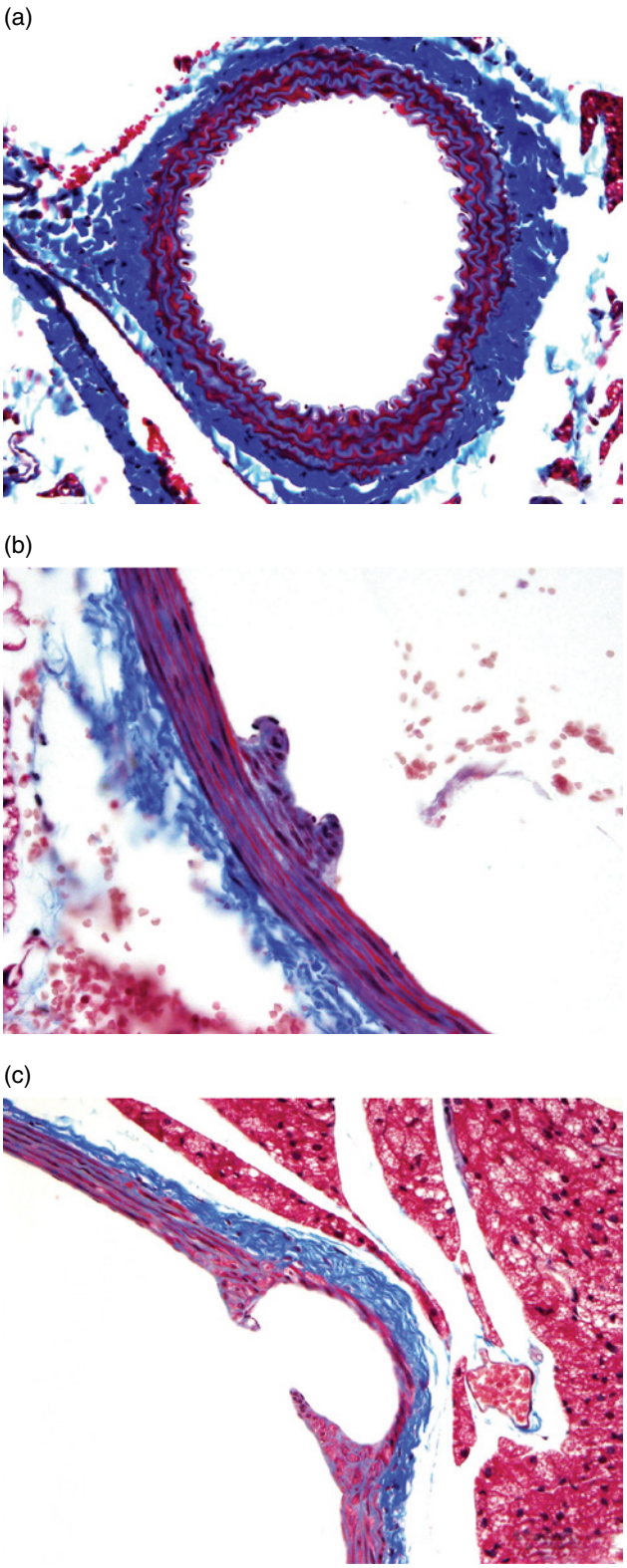
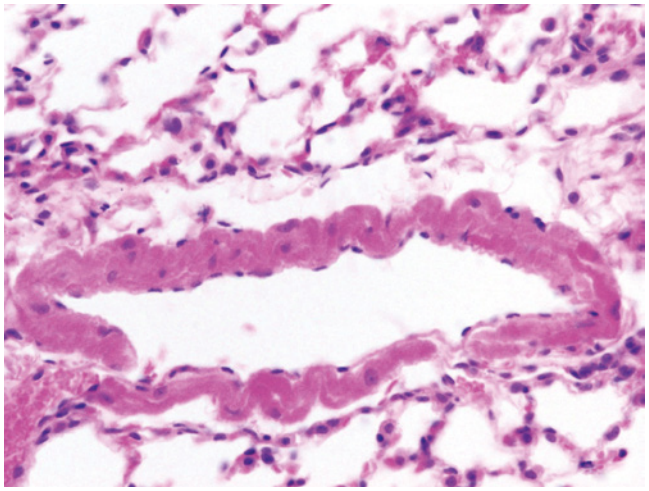


Figure 14.2 Cross section of Masson's trichrome stained normal large elastic artery (aorta) with regular medial elastic lamellae and intervening smooth muscle cells with scant collagen. The adventitia is collagen rich, and the endothelium sits imperceptibly upon the internal elastic lamina (a). Intimal bolster proximal to an arterial branch (ostium) (b). Normal arterial branch (ostium) (c).

(a)



(b)

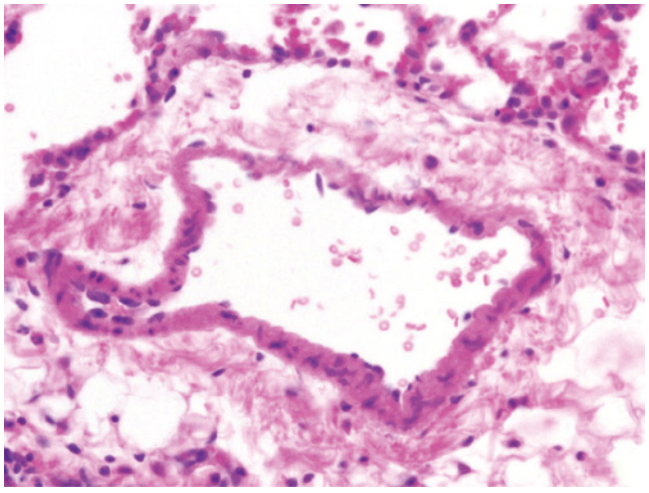


Figure 14.3 Normal mouse medium pulmonary vein with abundant striated cardiac muscle in the media (a). Comparably sized normal mouse medium pulmonary artery with abundant smooth muscle in the media (b).

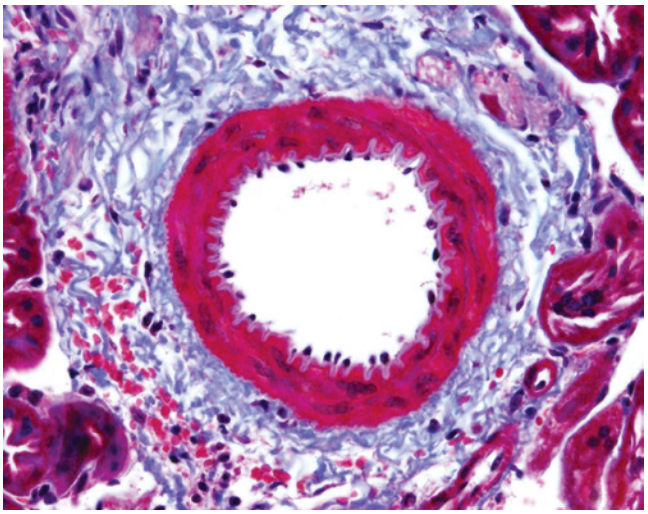


Figure 14.4 Cross section of Masson's trichrome stained normal medium muscular artery. Only the internal and external elastic laminae are visible, with abundant circumferentially oriented smooth muscle between. The collagen-rich adventitia blends into surrounding tissue, and the endothelium sits imperceptibly upon the internal elastic lamina.

sections are useful for gross and microscopic examination. The mouse heart is sufficiently small that it can completely fix in 48 hours in neutral buffered 10% formalin (NBF) without opening and/or removal of intracardiac blood. For routine screening type phenotyping necropsies, the heart may remain attached to the thoracic pluck, either removed from the chest or fixed *in situ* in the opened thoracic cavity with the breastplate sternum removed. Following 48–72 hours fixation, the heart is dissected free by transecting the great vessels. For longitudinal sections, after the heart has been weighed after fixation, it can be positioned on a cutting board to examine the anatomy. The right atrium is identified and a blade is positioned to cut from the middle of the atrium longitudinally to the apex. For routine screening, the heart may be sectioned in a longitudinal (base–apex, perpendicular to the IVS- using right atrium as a marker) or cross sectioned (transverse) (perpendicular to the long axis approximately half way between LV apex and the annulus fibrosus of the AV valves). An example of a longitudinal cut is shown in Figure 14.1. Transverse sections are useful at the mid-papillary level to compare wall thickness of the left ventricular free wall (LVFW), septum, and RVFW as seen in Figure 14.5 of a hypertrophied heart compared with a normal strain-, age-, and sex-matched heart. Both methods allow for evaluation or relative and absolute wall thickness and chamber diameter, while each has specific advantages.

For reproducible embedding, with multiple heart levels to be examined, heart sections are placed face down in the tissue cassette. It is conventional that the section surface placed faced down will be the surface cut first by the histotechnologist. For transverse sections of the mouse heart, three or four sections are made from apex to base. Tissue dye could be used to mark the section face needed to be cut first as these sections are small and can turn over in the cassette. Alternatively, a small sponge can be placed on top of the tissue sections to keep sections in place.

Compared with heart weight/BW, the heart weight/tibia length is considered more accurate to follow disease processes in the heart such as hypertrophy. Always include controls for appropriate age, sex, and strain/genetic background to provide objective relative measures of heart enlargement. Obesity, cachexia, or edema/effusions may mask or inflate enlargement, and atrial thrombosis and other non-myopathic conditions may also increase heart weight. Hearts can be also dissected into regions and ratios of ventricular weights ([LVFW + IVS]/RVFW, [LVFW + IVS]/BW, and RVFW/BW) can provide quantitative data, but dissection of the unfixed heart may result in reduced histology quality with frequent hypercontracted cardiomyocytes. If hearts are to be weighed,

(a)



(b)

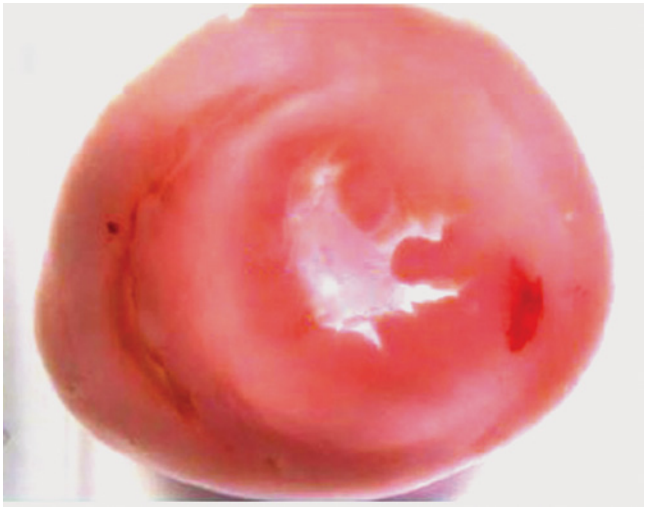


Figure 14.5 Transverse sections of the heart can be performed at mid papillary muscle level to compare ventricular wall thickness after perfusion of solution that stops hearts in diastole. (a) Normal wildtype littermate cross section of heart. (b) Hypertrophic heart from ErbB2- cardiac specific overexpression.

they should be perfused or washed with saline to remove any post-mortem blood clots that may vary in size according to whether the animal died in systole or diastole.

Longitudinal section (Figure 14.1) allows good evaluation of outflow tracts and valves (tricuspid, mitral, aortic, +/− pulmonic), atrial and ventricular septae (to evaluate for septal defects), and both atria. Transverse cross section (Figure 14.5) is preferred for evaluation of ventricular myocardial lesions such as hypertrophy, fibrosis, myofiber disarray, atrophy, or myocyte loss. As a compromise, hearts can be cross-sectioned just below or at mid-papillary level (cut one) and the remaining apex used for histology or frozen. The base half of the heart can be first fixed and then longitudinally sectioned using the right atrium as a marker to make the longitudinal second cut. Mouse heart trimming (mold) matrices, in either longitudinal or cross-sectional orientation, are available commercially (e.g. Zivic Instruments, Pittsburgh, PA) and facilitate repeatable sampling/trimming. Longitudinal sections in Figure 14.6 show the right-sided hypertrophy (due to pulmonary hypertension) compared with the normal heart section. Note the double apex in the hypertrophied longitudinal section. More detailed gross dissection (preferably under a dissection microscope following perfusion and fixation) or specialized sectioning (e.g. cross-sectioning through the aortic root to evaluate for atherosclerosis) may be necessary, particularly following input from in vivo imaging or functional studies (such as ultrasound/echocardiography).

Transcardial perfusion can improve tissue quality by removing luminal contents and fixing vessels (particularly arteries) in a more physiologically distended state, and can be done post-mortem without necessitating anesthesia in a still living animal. Blood in normal healthy mice generally only begins to clot more than three to five minutes after death by carbon dioxide euthanasia. This allows sufficient time for unhurried perfusion post-mortem. Intraperitoneal injection of heparin can be administered 10 minutes before euthanasia to prevent microvascular clotting. After CO_2 euthanasia, the thorax is opened and butterfly needle is inserted in left ventricle, while the right atrium or iliac vein is cut to allow an outflow of perfusate. Saline or PBS followed by formalin or electron microscopy fixatives can be infused by either pump or slow rate syringe infusion. Alternatively, after euthanasia or under anesthesia, hearts can be removed quickly and aortas cannulated then connected to a Langendorff apparatus for a 10–20 minutes infusion of buffer and collagenase enzymes to digest interstitial collagen for isolation of individual cells of the heart, such as rod shaped cardiomyocytes. This method can also be used for immune cell isolation for flow cytometry characterization. Alternatively, Miltenyi kits and equipment are used to isolate immune cells [41]. Isolated hypertrophied myocytes can be measured and compared with wild type cells [42]. Additionally, for comparative studies of mid-papillary level transverse section, a salt solution with cadmium can be perfused into the heart, to stop contractions in diastole as shown in Figure 14.5, so that multiple hearts can be compared for wall thickness in hypertrophy models [43].

For routine screening, cross sections of the thoracic aorta may be included with the trachea and esophagus. Alternatively, descending thoracic and abdominal aorta may remain attached to the spinal column and evaluated in decalcified tissue sections. Other vessels will generally be collected with relevant organs, but may be dissected and embedded in agar as necessary. For atherosclerosis lesion quantification, the aorta (root to iliac bifurcation) is grossly dissected from the mouse, opened longitudinally, and pinned flat with insect pins in a Petri dish containing a small amount of paraffin wax at the bottom as in Figure 14.7. The aorta may then be stained with oil red O for gross

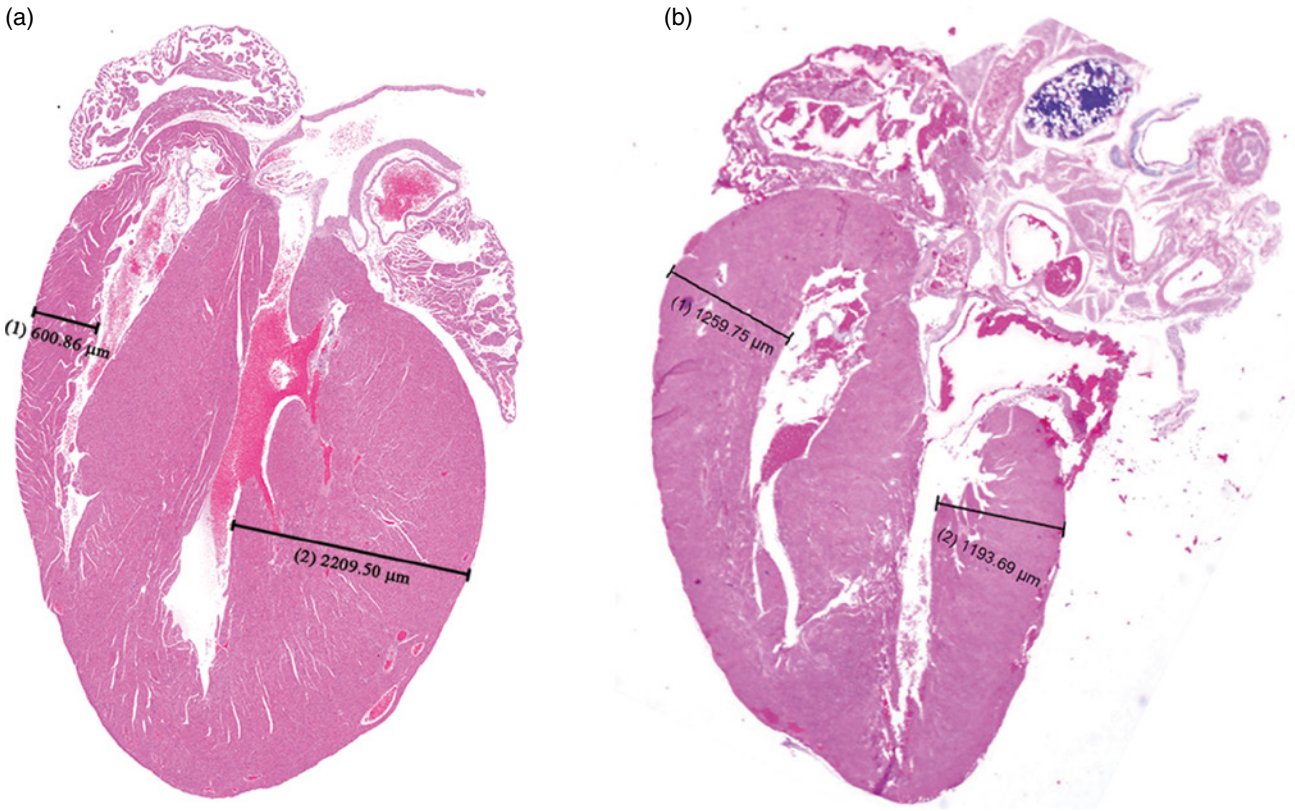


Figure 14.6 Longitudinal section of HE stained normal heart showing the LVFW and IVS are ⩾3 the thickness of the RVFW at the same apex-base level (a). A mouse with severe pulmonary hypertension causing right ventricular hypertrophy (b). The RVFW is approximately the same thickness as the LVFW and IVS.

plaque lesion quantification. For detailed analysis of mural aortic lesions, multiple cross sections are preferred. Following saline perfusion, a solution of either 50% (v/v) latex (e.g. Ward's Science latex injection medium diluted with water) injection or 3% (w/v) low melting temperature agarose (e.g. Lonza SeaPlaque GTG Agarose) is infused into the mouse. Latex has the advantage of being brightly colored, providing excellent gross photos (figure S2 in Habashi et al.) [44], but has a limited shelf life. Agarose is easier to work with, and often produces better histology sections [45]. Once injected, the mouse is kept moist with saline soaked towels at 4 °C for one to several hours, followed by immersion fixation in NBF. After 48 hours, the aorta is dissected out and transected in 2 mm thickness cross sections, ordered from cranial to caudal in 3% agarose in an embedding tray. Other techniques for gross/subgross vascular preparations have been described [46]. In Figure 14.8, the latex filled aortas in the wild type control (normal) and the Marfan mouse are compared, with aneurysmal dilatation of the root in the latter.

Although hematoxylin and eosin stained sections are adequate for routine screening, they are suboptimal for detailed evaluation of the cardiac, and particularly the vascular systems. For both the heart and blood vessels, Masson's trichrome provides excellent contrast between cells and extracellular matrix, particularly fibrillar collagens (blue) but will also delineate elastic fibers. Elastic fibers are better visualized by the Verhoeff–van Gieson elastin stain, Luna's stain, or Movat's pentachrome as in Figure 14.9. The latter also allows identification of mucin in the aorta, as does



Figure 14.7 Atherosclerosis lesion stained with Oil Red O for image quantification. The aorta (root to iliac bifurcation) is grossly dissected from the mouse, opened longitudinally, and pinned flat with insect pins in a Petri dish containing a small amount of paraffin wax at the bottom.

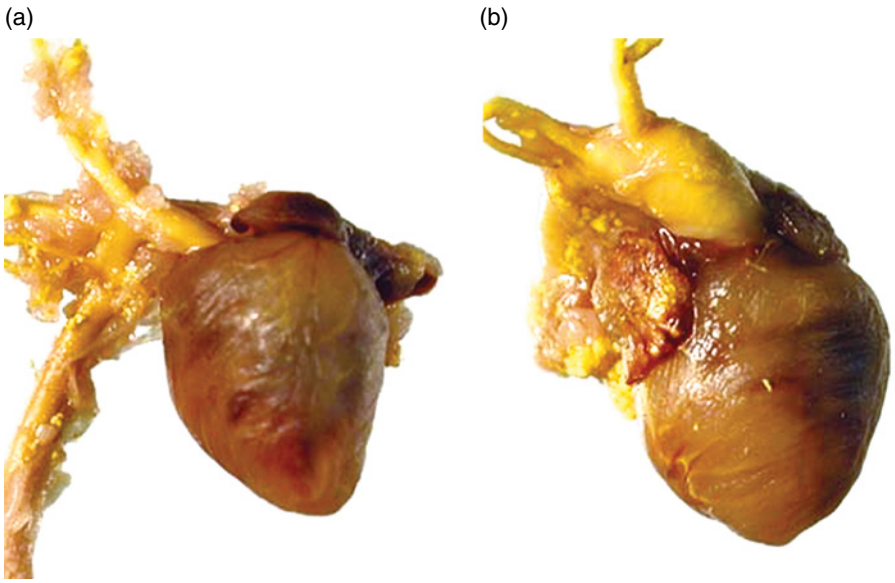


Figure 14.8 **Heart, aorta, and branches from a normal mouse**. The mouse was perfused with saline followed by yellow latex, and formalin fixed (a). Marked aneurysmal dilatation of the aortic root and ascending aorta in a B6.129-*Fbn1*^{tm1Hcd}/J model of Marfan syndrome (b).

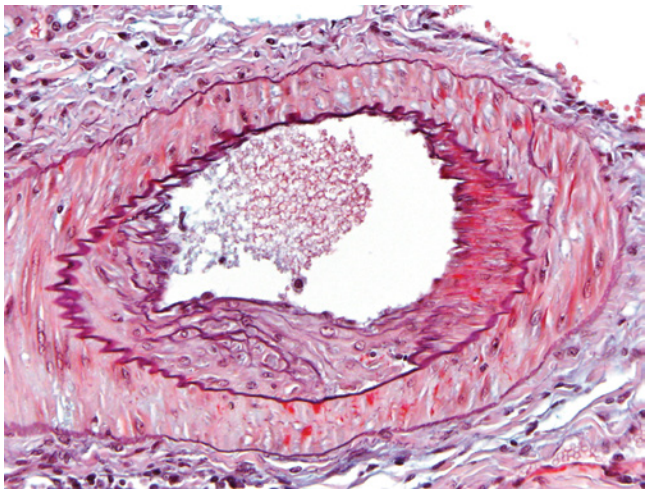


Figure 14.9 Cross section of a Movat's pentachrome stained medium muscular artery from a BUB/BnJ mouse with an eccentric fibroelastic and cellular proliferation luminal to the internal elastic lamina (intimal hyperplasia). Verhoeff–van Gieson elastin or Luna's stains can also be utilized to demonstrate elastic laminae.

Alcian blue. Periodic acid Schiff (PAS) is excellent for demonstrating hyaline or fibrinoid material in vascular media, while Congo red will demonstrate amyloid. Carstair's stain provides excellent visualization of fibrin for thrombi, although Mauritius scarlet blue trichrome and phosphotungstic acid hematoxylin (PTAH) can also be used. Fixation in Bouin's or Fekete's fixative may provide better detail of matrix in valves and blood vessels, and luminal erythrocytes (if present) are pale (ghosts). Triphenyltetrazolium chloride or Barbeito–Lopez trichrome stain can be used to demonstrate non-viable cardiomyocytes in acute infarctions.

Table 14.1 provides suggestions for immunohistochemistry (IHC) markers for endothelium [47], pericytes [48, 49], cardiomyocytes, conduction system, fibroblasts, and smooth muscle cells [50]. Antibodies against cardiac troponin (TNNC1) will delineate viable from non-viable cardiomyocytes in acute infarcts. Antibodies against type IV collagen will label the intima but not the media of muscular arteries. Antibodies against fibrin will label insudated protein in fibrinoid necrosis and hyaline arteriolosclerosis, as well as vascular leak (e.g. cytokine storm).

When evaluating hearts, the wall thickness of the LVFW, IVS, and RVFW should be evaluated at approximately the same level between apex and valve annulus, and should be done along a straight line drawn across the walls (in either orientation). A good rule of thumb is that the LVFW and IVS should be similar in thickness and approximately threefold thicker than the RVFW (post-natal). When evaluating for ventricular cardiomyocyte disarray, the junction of the LVFW and RVFW with the IVS should be avoided, as some degree of "disarray" or basket weaving is normal at these sites [42]. Disarray fiber orientation can be quantified [51].

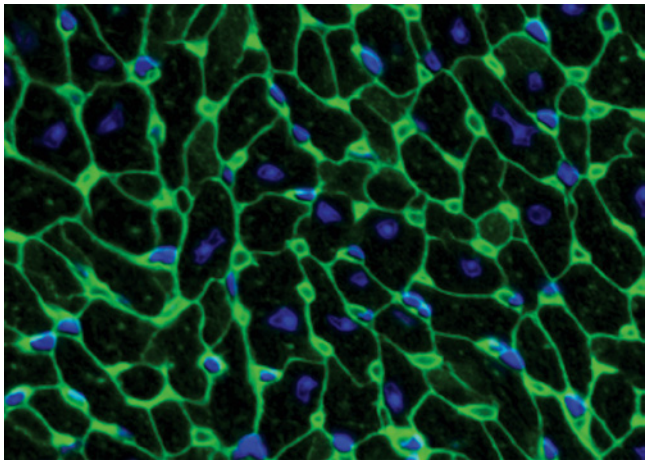
For visualization of hypertrophied myocytes, Wheat Germ Agglutinin (WGA) binds to glycoproteins of the cell membrane and is used for the staining cardiac sarcolemma to determine cross sectional area or myocyte density especially useful in hypertrophy models [42] seen in Figure 14.10. Fibrosis is a common sequela in many cardiovascular diseases and special stains accentuate these interstitial features allowing for quantification using picrosirius red [52] or Masson's trichrome [53] to demonstrate fibrosis.

Table 14.1 Immunohistochemical markers useful for evaluating the cardiovascular system.

Cell type	Positive marker(s)	Negative marker(s)
Endothelium (vascular) [47]	PECAM1/CD31, CD34, VWF, THBD/CD141, FLI1, EDN1, KDR/VEGFR2/FLK1, TEK/TIE2, ERG, VIM, CLDN5, ENG/CD105	
Pericytes [48, 49]	PDGFRB, DES, CSPG4/NG2, ANPEP/CD13, NGFR	SMTN +/− PECAM1/CD31, NES, ACTA2
Cardiomyocytes	DES, MB, MYH7, TNNI3, TNNT2	VIM
Purkinje cells	GJA5, CNTN2	
Cardiovascular fibroblasts	VIM	DES
Vascular smooth muscle [50]	ACTA2, MYH11, TAGLN, CNN1, CALD1, SMTN, VCL, DES	

Source: Based on Ismail et al. [47], Armulik et al. [48], and Attwell et al. [49]. © John Wiley & Sons.

(a)



(b)

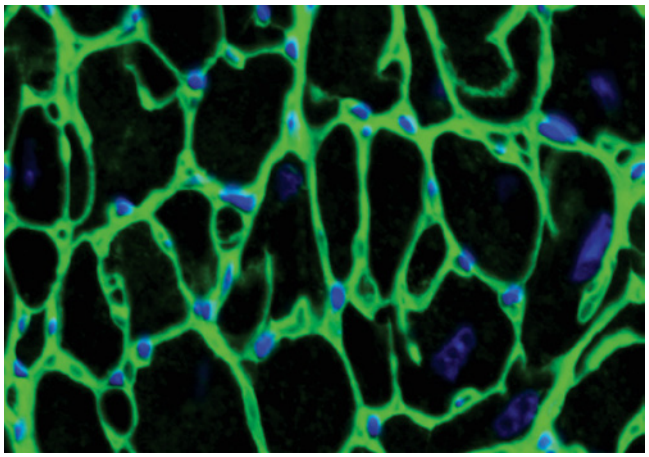


Figure 14.10 Wheat Germ Agglutinin (WGA) binds to glycoproteins of the cell membrane and is used for the staining cardiac sarcolemma to determine cross sectional area or myocyte density especially useful in hypertrophy models. (a) Normal wildtype littermate cross section of heart. (b) Hypertrophic heart from ErbB2- cardiac specific overexpression.

Detection of miRNAs of Cardiovascular System

MicroRNAs (miRNAs) are potent post-transcriptional regulators of gene expression through translational repression or transcript degradation of target messenger RNAs (mRNAs). Conveying mRNA target specificity through complimentary binding of nucleotides 2–8, or the seed sequence, of the ~21–24nt mature miRNA sequence, miRNAs can be transcribed from self-contained miRNA genes or introns of protein coding genes as individual miRNAs or as polycistronic clusters [54, 55]. Deletion of cardiac-associated miRNAs (including miR-1, miR-133, miR-143, miR-145, miR-208, miR-499) leads to several different phenotypes of varying severity [55]. For example, deletion of miR-1 in mice causes significant cardiac defects and 50% lethality rate suggesting a role in cardiac development [55]. The co-detection of miRNA and proteins of heart tissue can be accomplished with a combination of fluorescent *in situ* hybridization (FISH) and immunostaining with digoxigenin-labeled locked nucleic acid (DIG-LNA) and immunostaining with antibodies for proteins of interest like cardiac troponin T (TNNT2), respectively [56]. Refer to a recent review on miRNAs in cardiovascular development and disease [57].

Aging/Spontaneous Strain Specific Lesions

A brief overview and examples of common naturally occurring and misdiagnosed strain specific lesions for the organ system is discussed. For more information, the Society of Toxicologic Pathology International Harmonization of Nomenclature and Diagnostic Criteria (INHAND) consensus paper on proliferative and non-proliferative lesions is a very useful resource with photographs and methods for the mouse cardiovascular system [58]. Additionally, the National Toxicology Program has a digital histologic atlas of non-neoplastic lesions of the cardiovascular system (https://ntp.niehs.nih.gov/nnl/cardiovascular/index.htm).

Osseous Metaplasia (Os Cordis)

Mice may have an os cordis within the annulus fibrosus skeleton of the heart. Nodular masses of well-differentiated hyaline cartilage, mineralized cartilage, and/or bone (including marrow with hematopoietic elements) may be present, usually around the aortic valve/root in the trigone (Figure 14.11) [59].

Polyarteritis Nodosa

Polyarteritis nodosa (PAN) is a common chronic-active systemic arteritis in various C57BL/6 and 129 strains. Mesenteric/abdominal, coronary (including near aortic root/sinus), and musculoskeletal medium and small arteries most commonly affected are seen in Figure 14.12 [60–62]. Pulmonary arteries are spared. Typical features include fibrinoid necrosis, mononuclear leukocyte infiltration of the adventitia and media, and tortuosity.

Epicardial/Myocardial Mineralization

Mineralization is epicardial in BALB/c (and C.B.-17-*scid*) and epi- and myocardial in C3H and DBA mice [61, 63]. It is also reported in BALB/cByJ, KK/HIJ, A/J, C57BL/10J, and most, but not all, 129 substrains [64–67]. Lesions consist of basophilic mineralized concretions in a nascent to mature fibrous matrix with variable bland granulomatous foreign-body type inflammation as shown in Figure 14.13. Mineralization may also be seen as medial mineralization of the aorta (particularly elastic laminae) or other arteries. Quantitative trait loci (QTL) associated with the *Abcc6* gene are implicated in the strain specific mineralization phenotype [67, 68] and a targeted knock out of *Abcc6* (*Abcc6*^{tm1Jfk})

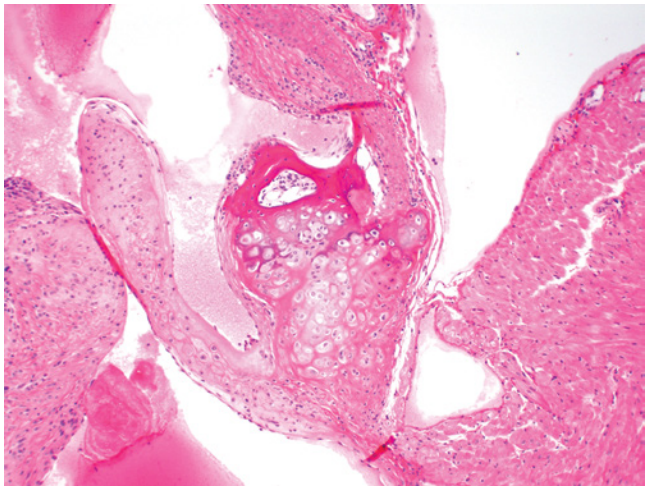


Figure 14.11 Normal mice may have an os cordis within the annulus fibrosus skeleton of the heart. Nodular masses of well differentiated hyaline cartilage, mineralized cartilage, and/or bone (including marrow with hematopoietic elements) may be present, most often around the aortic valve/root within the trigone.

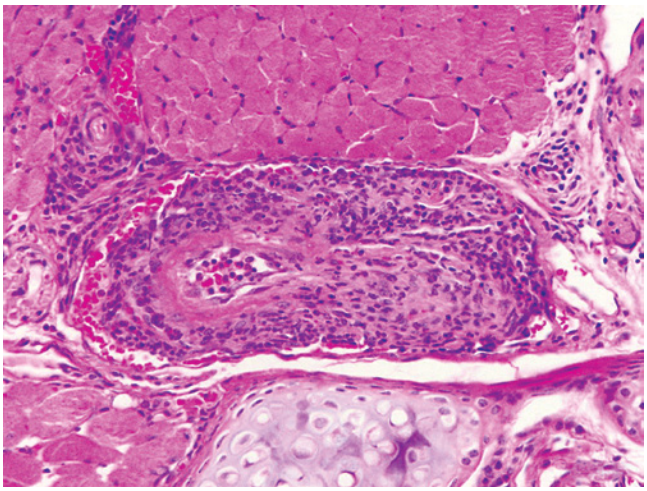
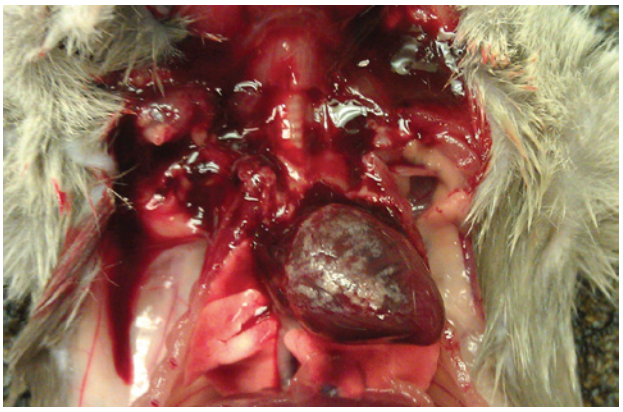


Figure 14.12 **Polyarteritis Nodosa is a common background lesion in a number of mouse strains, including C57BL/6 and 129 substrains**. Mesenteric/abdominal, coronary (including near aortic root/sinus), and musculoskeletal medium and small arteries are most commonly affected. Typical features include fibrinoid medial necrosis and florid acute to chronic leukocytic infiltrates.

(a)



(b)

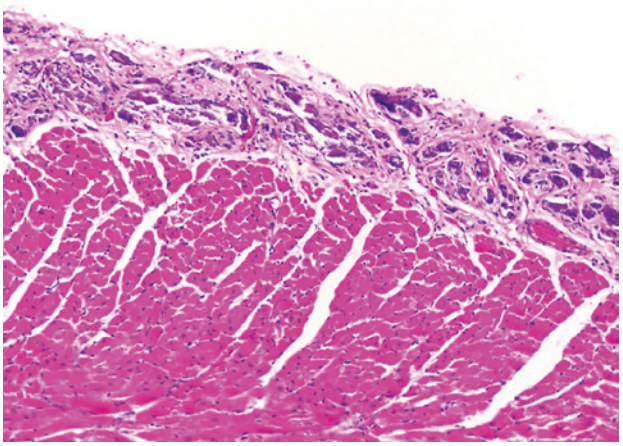


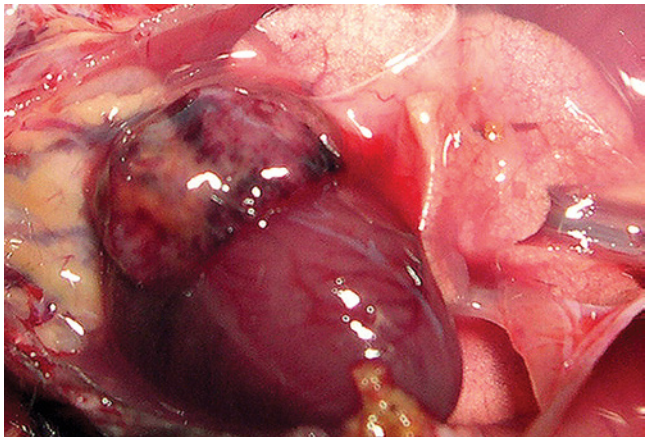
Figure 14.13 Gross (a) and histologic (b) images of epicardial mineralization in D2.B6-*Ins2*^{Akita}/MatbJ mice. Note abundant mature fibrosis.

have also been used as mouse models of pseudoxanthoma elasticum (PXE) with ectopic mineralization in the skin, arterial vessels, and vibrissae of *Abcc6* null mice [69]. Although mineralized lesions were initially linked to alopecia areata, this was shown to be due to the QTLs of the strain of mice used in the study, highlighting the importance of recognizing genetic variation between the commonly used inbred mouse strains [70].

Atrial Thrombosis

Atrial thrombosis can be acute or chronic, with generally large adherent thrombi in the atrium, giving a rounded appearance to the atrium grossly shown in Figure 14.14. Acute thrombi often have prominent lines of Zahn. Chronic thrombi may have cartilaginous or osseous metaplasia, and recanalization. This may co-occur with renal glomerular amyloidosis (due to loss of antithrombin III), but often occurs as an isolated lesion. Atrial thrombosis is also seen with doxorubicin toxicity [71]. Atrial involvement in many types of heart disease is reviewed [72].

(a)



(b)

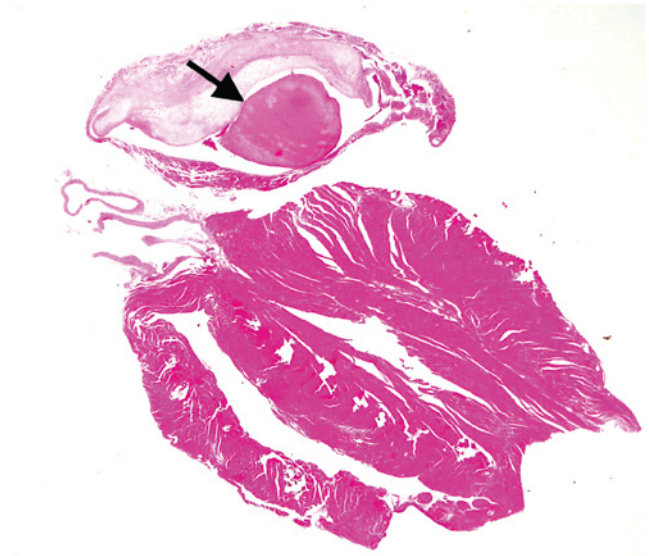


Figure 14.14 Gross image of a large pale thrombus in the atrium (a) creating a rounded appearance. Chronic-active atrial thrombus (b) in a BALB/cJ mouse with fibrin, fibrosis, and osseous and cartilaginous metaplasia.

Hyaline Arteriolosclerosis

Hyaline arteriolosclerosis is the accumulation of hyaline brightly eosinophilic, PAS positive, acellular proteinaceous material in the media of small arteries and arterioles of the spleen, kidney, and uterus most commonly, and less commonly in the heart, pancreas, testes, or intestine [73, 74].

Myxomatous Degeneration of the Cardiac Valves (Endocardiosis)

Accumulation of pale, loose, fibromyxoid stroma and increased cellularity in the distal cusps of the heart valves, often creating a nodular appearance and distorting the normal valve profile is illustrated in Figure 14.15. Material is alcianophilic, but may also include significant fibrillar collagen. Pulmonic valves are reported to be most commonly affected, followed by mitral (bicuspid), then aortic [75]. This is predominantly a lesion of older mice (>1 year). Secondary cardiac hypertrophy or failure may potentially occur as a result of regurgitant flow or stenosis.

Bicuspid Aortic Valve (BAV)

A very low incidence of spontaneous bicuspid aortic valve (BAV) has been reported in C57BL/6J x BALB/cByJ and Crl:OFI mice [76]. These were all of the human B type, resulting in right

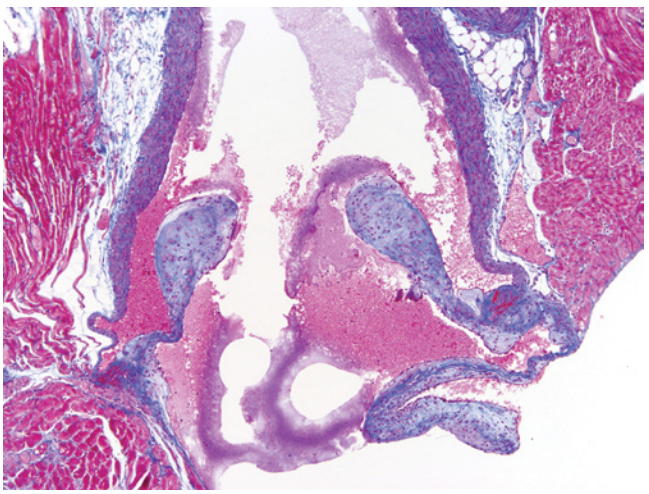


Figure 14.15 Longitudinal section of Masson's trichrome stained heart. The aortic valve cusps as well as the septal cusp of the mitral valve are nodular and distorted by abundant loose myxomatous matrix as well as plump spindled cells (endocardiosis).

and left septae, but lacking a discernible raphe. A literature review by the same authors showed BAV as a phenotype in 27 genetically modified mouse strains as well, including the homeobox genes *Nkx2–5*, *Pbx1*, and *Pbx2*. Valve morphology may be best appreciated in an *en face* view of the aortic root by either dissecting microscope or scanning electron microscopy.

Melanosis

Pigmented subendocardial melanocytes are common in the valves of mice, particularly C57BL/6 substrains, as shown in Figure 14.16 [77, 78]. AV and aortic valve cusps and chordae tendineae are commonly involved, and the aortic root may also be variably affected; the pulmonic valve is spared. The cells are presumed to have a neural crest origin in common with the great vessels and heart base. Discrimination of melanosomes from 3,3'-diaminobenzidine (DAB) chromogen in IHC is important.

Aortitis

There is a single report of a high incidence of chronic transmural inflammation without fibrinoid material in the aortic root of BALB/c mice (source not specified) [79]. One of the authors (TKC) has seen a similar lesion in the ascending thoracic aorta of a BALB/cJ mouse. Polyarteritis of the proximal coronary arteries/aortic root, a common age-related finding, should be excluded.

Opportunistic Bacteremia/Endocarditis/ Myocarditis in Immune-Incompetent Mice

Bacterial septicemias, including valvular and mural endocarditis shown in Figure 14.17 and myocarditis, are rare in immunocompetent mice but not uncommon spontaneous findings in immune-incompetent mice, particularly when not housed in a manner appropriate for their immune status [80, 81]. Bacteria are often opportunist flora or saprophytes such as *Pseudomonas aeruginosa* or *Stenotrophomonas maltophilia*. Lesions may result in secondary changes including cardiac enlargement, heart failure, or embolic showers. In contrast to rhesus and cynomolgus macaques, spontaneous (background) chronic mononuclear leukocytic infiltrates in the myocardium are uncommon in mice.

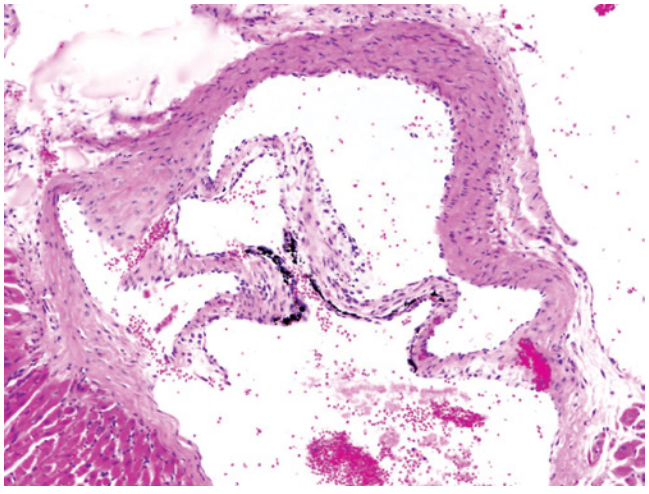


Figure 14.16 Oblique cross section of HE stained aortic valve showing numerous black pigmented melanocytes in the subendocardium. This is a common finding in a number of non-albino strains, particularly C57BL/6J.

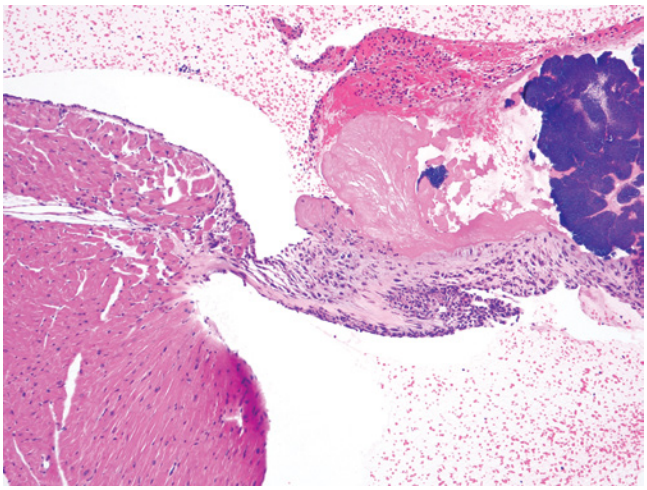


Figure 14.17 Abundant fibrin with enmeshed degenerate neutrophils and large colonies of large bacterial cocci distort the atrial surface of the mitral valve in an immunoincompetent NU/J mouse.

Neoplasia

Spontaneous hemangioma/hemangiosarcoma (Figure 14.18) is uncommon in mice (about 5% incidence) [62, 82, 83]. They are usually cutaneous in aged mice, but can be multicentric (including spleen, liver, and lung). Telangiectatic osteosarcoma has been reported in B6,129Sv-*Trp53*^{tm1Tyj} *Hic1*^{tm1Sbb} mice [84]. Mice with *Trp53* mutations are prone to sarcomas, including hemangiosarcomas. Hemangioma and hemangiosarcomas have been described in Tg(HRAS)2Jic (HRAS) transgenic mice [85].

Genetically Engineered Mice (GEMs) Models of Heart and Vessel Disease

The next section features GEM models developed to study cardiovascular disease. Tables 14.2 and 14.3 list genes in the various categories of cardiovascular disease and review article references. Gene nomenclature for humans (all upper case italicized) and mouse genes (first letter uppercase, subsequent letters lower case, italicized) are listed. We have provided some examples of genetic variants provided by MGI (Mouse Genome Informatics).

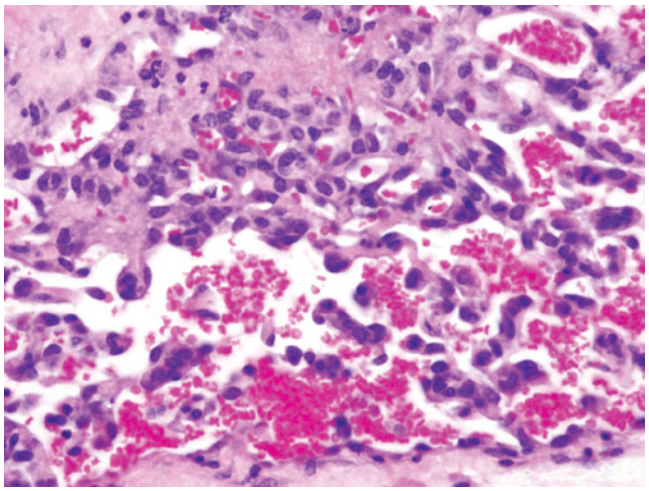


Figure 14.18 Spontaneous hemangiosarcoma characterized by poorly formed vascular spaces lined by atypical endothelial cells from pelvic adipose tissue of a 13 month old NOD.Cg-*Prkdc*^{scid} *Il2rg*^{tm1Wjl} Tg(CMV-IL3,CSF2,KITLG)1Eav/MloySzJ mouse. Thrombosis and invasion are common.

Septation

Trisomy 21 has been shown to lead to a number of congenital heart defects, including septal defects [125, 126]. Trisomy 16 mice have also been shown to have abnormal AV septation [127]. Lesions in spinal muscular atrophy models include septal defects, outflow irregularities, and rhythm disorders [128].

Aortic Stenosis

The aortic valve is a tricuspid valve made of cusps or leaflets that control unidirectional movement of blood flow out of the left ventricle [129]. Stenosis of the aortic valve is caused by calcification and fibrosis of the normal valve or the congenital bicuspid phenotype [130]. Throughout the progression of the disease, the stiffening of the leaflets causes turbulent blood flow through the valve with left ventricle hypertrophy. Staining with alizarin red is used to identify mineral. Alizarin red only labels mineral so without an element analysis you do not know what salts are present in deposits of the affected valve [131].

Cardiomyopathies

Diagnosis of cardiomyopathy requires exclusion of other predisposing causes of (compensatory) cardiac hypertrophy (e.g. aortic or pulmonic valve stenosis). It must be noted that many of the same genes are associated with different classes of cardiomyopathies, and there remains debate about overlap between these classifications [132].

Hypertrophic Cardiomyopathy

Key diagnostic features include hypertrophy of the ventricular myocardium (symmetric or asymmetric), hypertrophy of cardiomyocytes (increased cell size with large "boxcar" nuclei), and cardiomyocyte atrophy/degeneration/loss/replacement fibrosis. The *sine qua non* feature of hypertrophic cardiomyopathy (HCM) in humans and domestic species is cardiomyocyte disarray. Intimal hyperplasia of medium mural coronary arteries is a common concomitant lesion.

In humans, *MYPBC3* and *MYH7* are the most commonly implicated genes (80%). Also observed are mutations in the *TNNI3*, *TNNT2*, *ACTC1*, *MYL2*, *MYL3*, *TPM1*, *PLN*, *ALPK3*, and *PKP2* genes. Syndromic genes include *LAMP2* (Danon disease, *GSDIIB*), *GLA* (Fabry), *FXN, PRKAG2* (glycogen storage disorder), *TTR*, and *GAA* (Pompe, GSDIIA).

Table 14.2 Genetically engineered mice (GEMs) models of heart disease: reviews.

CV disease	Mutant genes	References
Congenital heart diseases – wall	*Actc1*, *Avc2*	[86, 87]
Congenital heart diseases – valve	*Nkx2-5*, *Dp(16Ifnar1-Kcnj6)10Yey*	[88–90]
Myocarditis autoimmune	*Myh10*, *H2-Ab1*, *HLA-DQ8*	[91–93]
Cardiomyopathies		
HCM	*Mypbc3, Myh7, Tnni3, Tnn2, Actc1, Myl2, Myl3, Tpm1, Pln, Alpk3, Pkp2*	[94, 95]
Dilative	*Ttn, Lmna, Mypbc3, Myh7, Tnni3, Tnnt2, Actc1, Scn5a, Abcg5*	[96–98]
Restrictive	*Taz, Dtnb, Ldb3*, *Lmna*, *Scn5a*, *Myh7, Mybpc3*	[99–101]
Mitochondrial	*Ctnna2*, *Slc25a4, Tfam*, *Ppargc1a*, *Ppara*, *Ppargc1a*, *Sod2*	[102, 103]
Storage disease	*Arsa*	[104–106]
Duchene's muscular dystrophy	*Dmd*	[107–110]
Neoplasia	*Trp53*	

Table 14.3 Genes that have been engineered in mice to produce models of vascular disease: reviews.

Disease	Mutant genes	References
Atherosclerosis	*Apoe*, *Ldlr*	[111–114]
Arteriosclerosis	*Icam1*, *Trem2*	[115]
Artery rupture/aneurysm	*Timp1*, *Tgfb1*	[116, 117]
Arterial thrombosis	*Apoe*, *Fpr2*, *Ifnar1*, *Vps13a*	[118–120]
Vasculitis	*Tgfbr1*	[121–123]
Vascular neoplasms	*Trp53N5T*	[124]

The DBA/2J strain, with variant (mostly intronic or synonymous coding) single nucleotide polymorphisms (SNPs) in the *Mybpc3* and *Myh7* genes, has been proposed as a spontaneous model for HCM [94]. Significantly, cardiomyocyte disarray was not reported as a feature. Disarray is reported in other models of HCM [42] but does not reach the level as observed in human HCM hearts. Cardiac-specific overexpression of epidermal growth factor receptor 2 (*ErbB2*) induces pro-survival pathways and HCM in mice associated with disarray [42], arrhythmias [133], and hypertrophic obstructive cardiomyopathy [43] but is not a known gene mutated in human HCM. Mouse models with cardiomyocyte disarray have had fiber orientation quantified [51].

Dilated Cardiomyopathy

In contrast to overexpression of *Erbb2* in the mouse heart, lack of receptors or ligands in this family is detrimental to the heart. Several studies employed animal models of deletion of *Erbb2* or ERBB4 receptors or neuregulin 1 (*Nrg1*), showing that disruption in cardiac EGFR family signaling leads to the significant alterations in cardiac development, and predisposes to dilated cardiomyopathy. *Erbb2* inactivation disrupts cardiac valves development in mouse embryos [134]. *Erbb2*-null, expressing kinase-dead ERBB2, or *Erbb4*-null mouse embryos die before E11 due to the defects in cardiac development [135–137]. Over 50% of HB-EGF null mice (*Hbegf*$^{tm1.1Mek}$) die in the first postnatal week, while the survivors develop severe heart failure and dilated ventricular chambers [138]. Conditional knock-out of *Erbb2* (*Erbb2*^{tm2Cbm}) resulted in dilated cardiomyopathy and increased sensitivity to anthracyclines in mice [139, 140]. Similarly, *Erbb4*-knockout mice develop severe dilated cardiomyopathy and die prematurely [141]. The blockade of endogenous ERBB1 (EGFR) phosphorylation and ERBB2 transphosphorylation by expression of mutant ERBB1 receptor causes a phenotype of cardiac dilation and increased mortality after transverse aortic constriction [142].

Mutated human genes identified in dilated cardiomyopathy include *TTN* (truncating mutations), *LMNA*, *MYPBC3*, *MYH7*, *TNNI3*, *TNNT2*, *ACTC1*, and *SCN5A*. Syndromic DCM includes mutations in *TAZ*, *DSP*, *DMD*, *EMD*, *FHL1*, *LMNA*, *HFE*, and *MYH7*. Mouse models of dilated cardiomyopathy utilize knock-in mutations in these genes encoding cytoskeletal, sarcomere, and nuclear envelope proteins found in patients. Some examples include *Ttn* (B6.Cg–*Ttn*^{tm1Brge}), *Lmna* (*Lmna*^{tm1Gbon}), and *Tnnt2* (*Tnnt2*^{tm2Mmto}) [96, 143–145]. Pathological manifestations of these mutations include chamber dilation, sarcomere formation defects, and conduction defects. The knock-in mutations created in mice, genetically similar to those found in patients, produce a phenocopy of human disease making these mouse models very useful for interrogation of disease mechanism and testing therapeutic interventions. Mice with *Lmna*^{tm1Gbon} display similar histological malformations of heart chamber dilation and interstitial fibrosis of the myocardium as seen in human disease on a time scale analogous to human disease [145].

Mouse models of Duchenne's muscular dystrophy have both skeletal and cardiac phenotypes [107]. These mice are very sensitive to isoproterenol [146] and social stress [147]. Fibrosis is a common feature in these models as shown in Figure 14.19. A Duchenne muscular dystrophy model working group noted the problem of the lack of standardized methods to characterize models and created a series of Standard Operating Procedures (SOPs) to improve research reproducibility [148]. For access to protocols go to link: (http://www.parentprojectmd.org/site/PageServer?pagename=Advance_researchers_sops).

Arrhythmogenic Cardiomyopathy

Arrhythmogenic cardiomyopathy, formerly called arrhythmogenic right ventricular dysplasia or arrhythmogenic right ventricular cardiomyopathy (ARVD or ARVC), has key diagnostic features including infiltration and replacement of the myocardium by fibrosis and abundant mature white adipocytes [149]. The process separates, surrounds, and replaces cardiomyocytes, which are themselves degenerate (often vacuolated), distinguishing it from the interstitial adiposity of obesity (adipositas cordis). RVFW involvement is often predominant, but LV dominant forms may occur [150]. Genetic defects in genes encoding intercalated disc proteins (predominantly desmosomes), calcium regulating factors, and growth factors identified in human patients include *PKP2* (most common), *DSP*, *DSG2*, *JUP*, and *DCS2* [151]. This phenotype has not been recapitulated in mouse models with *Pkp2* mutations without additional perturbation [152], although ventricular arrhythmias (Brugada syndrome) have been recorded. Fibrotic

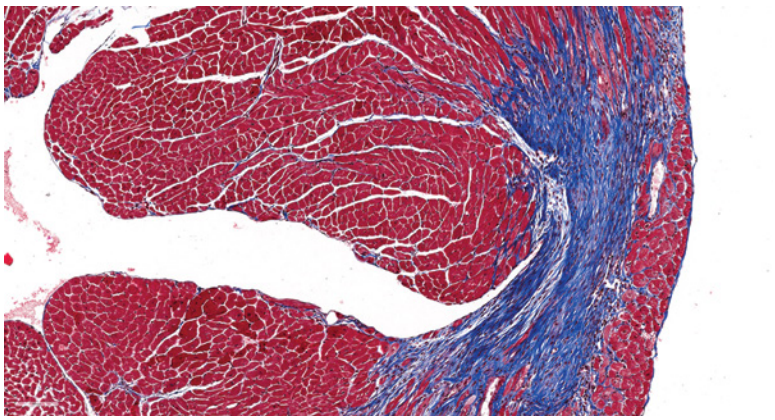


Figure 14.19 Masson's trichrome stain demonstrating abundant replacement fibrosis in a cross section of heart. This is a common feature in Duchenne muscular dystrophy model (dystrophin, muscular dystrophy; X linked muscular dystrophy [Dmd^{mdx}] model).

lesions and abnormal echocardiograms have been variably described in Dsp^{rul} mice [153] and more consistently in a *Dsg2* null (one of three possible floxed alleles not specified by the authors) mouse model [154]. Recapitulation of a human phenotype in a mouse with similar genetic perturbations gives great clinical value to this model to evaluate pathophysiology and possible treatments for human disease.

Other Cardiomyopathies

Mutant mouse models have been used to determine basic mechanisms of toxicities such as doxorubicin-induced cardiomyopathy [155]. Models with over-expression or deletion of proteins that combat oxidative stress have been consistently utilized. Additionally, collaborative crosses of mice strains with more defined genetic backgrounds have revealed sex differences and strain sensitivities that are useful in dissecting the genetics behind the susceptibility to this well-known cardiac mitochondrial toxin, used for over 40 years as chemotherapeutic agent [71].

Mouse models of mitochondrial cardiomyopathy are tools to understand the role of mitochondria in all types of cardiomyopathy [102, 103, 156–158]. For example, in the mouse model of Barth syndrome, a disease with cardiolipin deficiency as a result of mutations in *Taz* ($ROSA26^{H1/tetO\text{-}shRNA:taz}$), morphologic characterization is done by electron microscopy to reveal abnormalities in mitochondria and increased mitophagy [159].

Dilative cardiomyopathy in mice can also be induced by viral induced inflammation, and in some cases, as the immune system reacts against the myocardial proteins. The cardiac phenotype in mouse models of systemic autoimmunity has been reviewed [160]. Currently, several animal models are available that closely resemble human myocarditis. Cardiac autoimmunity mouse models have been made using a combination of induction methods. Some mouse strains show a syndrome of acute cardiac inflammation and sudden death induced by direct viral damage (using human Coxsackie B virus) and 70% of animals die within the first week after infection. Other mouse strains are used where inflammation is triggered by injections of adjuvant with cardiac myosin peptide or virus (heart-passaged) resulting in acute myocarditis, with no deaths, which progresses to chronic heart disease and dilative cardiomyopathy. In Figure 14.20, a BALB/c/J mouse was immunized [161] with myosin peptide and euthanized at 21 days post injection. Numerous macrophages and neutrophils are observed in areas of myocardial necrosis. Pericarditis and dilative cardiomyopathy are strain- and sex-dependent features of this model. Restrictive cardiomyopathy may result with significant pericarditis with resulting chronic fibrosis. Flow cytometry, rather than IHC, is frequently used to quantify heart inflammatory infiltrate. Mouse models (e.g. $Il17a^{tm1Yiw}$, a deletion of *Il17a*) have been used to further describe the pathogenesis of autoimmune myocarditis [162–165].

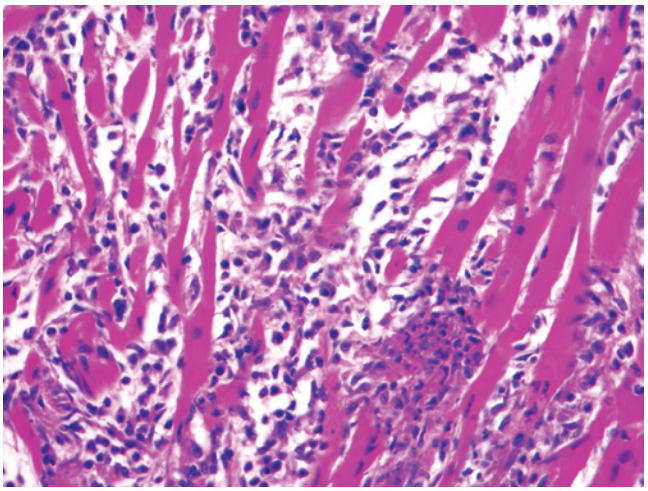


Figure 14.20 HE stain of myocardial necrosis with infiltration of numerous neutrophils and macrophages in a BALB/c/J mouse injected with myosin preparation with adjuvant to elicit autoimmune myocarditis.

Restrictive Cardiomyopathies

Restrictive cardiomyopathies in humans, due to genetic mutations (*TNNI3*), can result in left ventricular non-compaction (LVNC), a rare congenital cardiomyopathy characterized by excessive or prominent trabeculation of the luminal aspect of the left ventricle with deep recesses, creating a spongiform appearance. The proposed pathophysiology is failure of normal trabecular regression during embryonic development. There exist no consensus diagnostic criteria for LVNC in humans (or mice), and non-compaction may occur in conjunction with other cardiac abnormalities, so proposed mouse models may be difficult to rigorously validate [166]. Human gene associations include tafazzin (*TAZ*), β-dystrobrevin (*DTNB*), Cypher/ZASP (*LDB3*), *LMNA*, *SCN5A*, *MYH7*, and *MYBPC3*.

Lysosomal Storage Diseases

Lysosomal storage diseases affecting the heart have been modeled in mice [167]. In Fabry disease, inflammation is a controlling factor of cardiomyopathy, leading to cell death and fibrosis of the left ventricle. Cleaved caspase-3-positive cytoplasmic labeling is used to identify apoptotic cardiomyocytes [168]. IHC to identify CD68+ macrophages, or labeling for ubiquitin or p62 (sequestosome-1, SqSTM1; formerly called p62) indicating involvement of autophagy dysregulation. Autophagy pathways are useful to probe in other lysosomal storage diseases such as, GM2 gangliosidosis [104].

Markers of Cardiovascular Disease in Other Organs

Sequela to heart failure including alveolar hemosiderin-laden macrophages (siderophages, heart failure cells), acute/chronic passive hepatic congestion (nutmeg liver), ascites, hydropericardium, hydrothorax, etc. may be observed if the entire mouse is necropsied and evaluated by histopathology. Unfortunately, frequently the whole mouse is not analyzed and genetically modified mouse studies often focus only on the organ of interest, in this case, the heart.

Aorta

The features of inflammatory and non-inflammatory aortic lesions of significance in humans are well-described and are often translatable to mice [169, 170]. Because many of the non-inflammatory degenerative lesions of the aorta overlap to some extent with the nature and spectrum of normal aging changes, the use of appropriate age-, sex-, and strain-matched controls is essential [171, 172]. Elastic fiber degeneration, fragmentation, thinning, loss, and/or disorganization is a main feature of aortic lesions and elastic fiber degeneration is a typical feature of mouse models of human genetic aortopathy, including Marfan syndrome (MFS, B6.129-*Fbn1*^{tm1Hcd}/J) [44], Loeys–Dietz syndrome (LDS, 129S(Cg)-*Tgfbr2*$^{tm1.1Hcd}$/J and 129S6(Cg)-*Tgfbr1*$^{tm1.1Hcd}$) [173], and vascular Ehlers–Danlos syndrome (vEDS, C.129S4(B6)-*Col3a1*^{tm1Jae}/J, C57BL/6J-*Col3a1*$^{G938D/+}$, and C57BL/6J-*Col3a1*$^{G209S/+}$) [45, 174]. Vascular changes in vEDS can be subtle and special stains are needed [174]. Mucoid extracellular matrix accumulation (MEMA, aka cystic medial necrosis or mucoid degeneration) may be prominent in these vascular diseases. Medial fibrosis can occur as well and is highlighted with special stains.

Aneurysm and Dissection

Aneurysm refers to an abnormal dilatation of the vessel caliber as shown earlier in Figure 14.8, accompanied by degenerative changes in the wall. Classic histologic features include degeneration/loss, fragmentation, and thinning of elastic fibers with replacement fibrosis in the aneurysmal segment. Variable MEMA may be present between laminae. Although there may be infiltrating macrophages or synthetic phenotype VSMCs, cellularity is reduced with chronicity. Additionally, aneurysmally dilated vessels have functionally abnormal walls with increased stiffness and/or reduced strength and are prone to dissection. Dissection may occur with or without preceding dilatation, and gross examination may only reveal acute hemorrhage around the aorta. Dissection (sometimes inaccurately referred to as pseudoaneurysm) is a partial or full thickness tear in the wall, almost invariably involving the intima and communicating with the lumen. As blood is forced into the tear it will separate layers of the wall, which can create an enlargement of the vessel resembling an aneurysm when viewed externally. In acute dissections, erythrocytes are present in a non-endothelial lined space in the media/adventitia. With chronicity, these channels may become endothelium-lined, and there will be evidence of prior hemorrhage (e.g. hematoidin- or hemosiderin-laden macrophages). Aneurysms of the aortic root are a typical feature recapitulated in the mouse model of MFS [44] and LDS [173], although unlike humans, these do not naturally proceed to dissection. On the other hand, dissections without preceding aneurysm are common in homozygous but not heterozygous null mutations vEDS mice as well as heterozygous, patient identified knock-in mutations [174, 175]. A number of other genes have been implicated in human familial thoracic aortic aneurysm and dissection syndromes as well [176]. Specifically, aneurysms can occur in brain and other organs similar to humans with a heterozygous deletion of exon 40 of the *Col4a1* gene (B6.129S--*Col4a1*^{deltaex40}), which presents with vascular fragility and propensity for perinatal cerebral hemorrhage [177].

Tortuosity

Vascular tortuosity manifests as corkscrews, spirals, and other non-linear vessels grossly, with redundant and reduplicated vessels that (histologically) enter and exit the tissue plane of section. Tortuosity is a feature of polyarteritis, but may also be seen in non-inflammatory vascular disorders

such as LDS due to mutations in *Tgfbr1* (M318R) and *Tgfbr2* (G357W) that disrupt pathway signaling [173, 178].

Systemic hypertension

The classical histologic features of systemic hypertension include hyaline and proliferative (onion-skin) arteriolosclerosis (Figure 14.21) of the small arteries and arterioles [179]. Lesions may occur anywhere in the systemic arterial bed, but involvement of the afferent arterioles of the kidneys is pathognomonic. The lesions of acute severe hypertension (e.g. induced by angiotensin infusion or renal artery banding) can resemble those of PAN, including medial fibrinoid necrosis and adventitial fibroplasia and mononuclear leukocyte infiltrates [180]. Genetically modified mouse models of pulmonary hypertension induce plexiform lesions (Figure 14.22) and may be primary or may develop secondary to chronic interstitial lung disease or lung neoplasia.

Systemic hypertension can be modeled in mice using knockouts of *Kcnj1*, *Slc12a1*, or *Scnn1b* (also known as *Romk*, *Nkcc2*, and *βENaC*, respectively) [181]. Inactivation of mouse potassium inwardly-rectifying channel, subfamily J, member 1 gene (*Kcnj1*^{tm1Ges}) or NaK2Cl cotransporter (*Slc12a1*^{tm1Tkh}) can be used to study Bartter syndrome, while null mutations in *Scnn1b* (B6;129P2-*Scnn1b*$^{tm1.1Hum}$) mimic Liddle syndrome, causing hypertension and hypokalemia [182–184].

Vasculitis

Immunocompetent mouse strains have been used to study infectious diseases that can affect cardiovascular system, such as the Lyme disease [185]. Stationary phase persistent/biofilm microcolony of *Borrelia burgdorferi* cause more severe disease in a mouse model of Lyme. Figure 14.23 is an example of inflammation in the aortic root due to *Borrelia* infection.

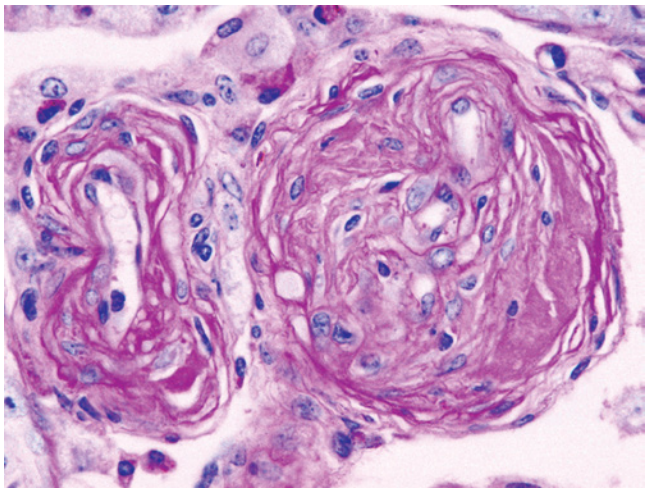


Figure 14.21 HE stain from a mouse with arteriolosclerosis with a narrowed lumen blood vessel termed "onion-skin" thickened concentric smooth muscle cell layer and thickened, duplicated basement membrane.

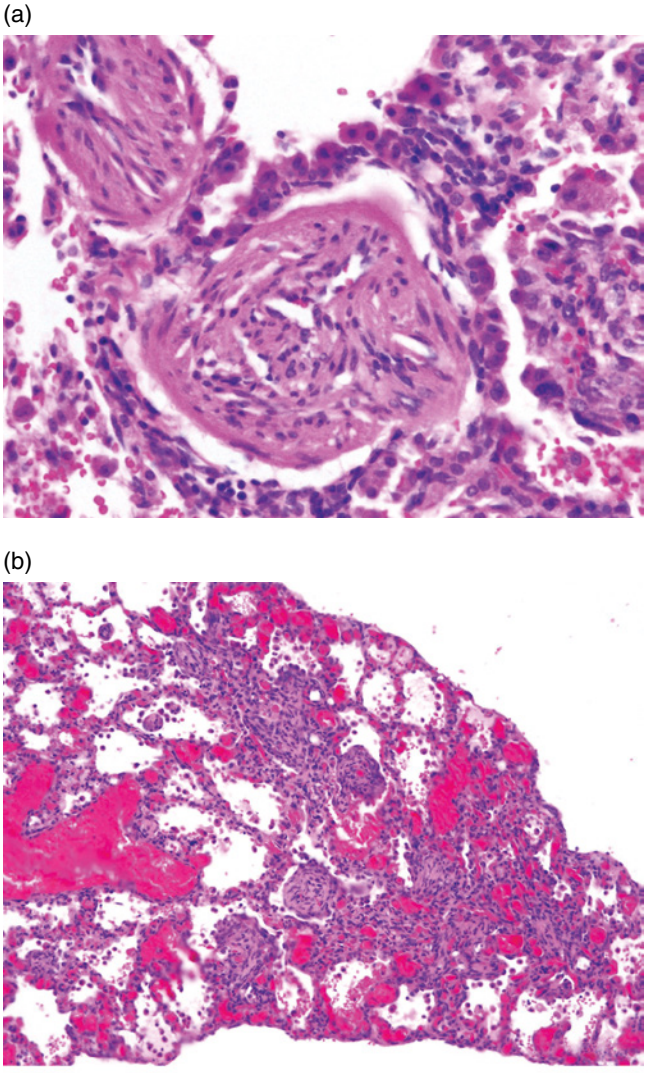


Figure 14.22 Florid pulmonary hypertension lesions in a transgenic mouse with abundant small artery and arteriole medial hyperplasia and intimal and adventitial fibrosis (a). The characteristic finding of pulmonary hypertension is the plexiform lesion illustrated here, a glomeruloid mass with multiple slit-like lumina (b).

Atherosclerosis

Atherosclerosis mouse models include B6.129P2-*Apoe*^{tm1Unc}/J, B6.129S7-*Ldlr*^{tm1Her}/J strains and are reviewed for applications and limitations to understand human atherosclerosis [111]. Oil red O is a useful stain to highlight the degree of plaque formation in dissected aortas. In mice, embedding heart base or aorta in gelatin or agar enables better sectioning of the specimen so that the normal anatomy and lesions can be analyzed systematically to quantify aortic valve plaque (Figure 14.24). IHC labeling for allograft inflammatory factor 1 (AIF1, formerly

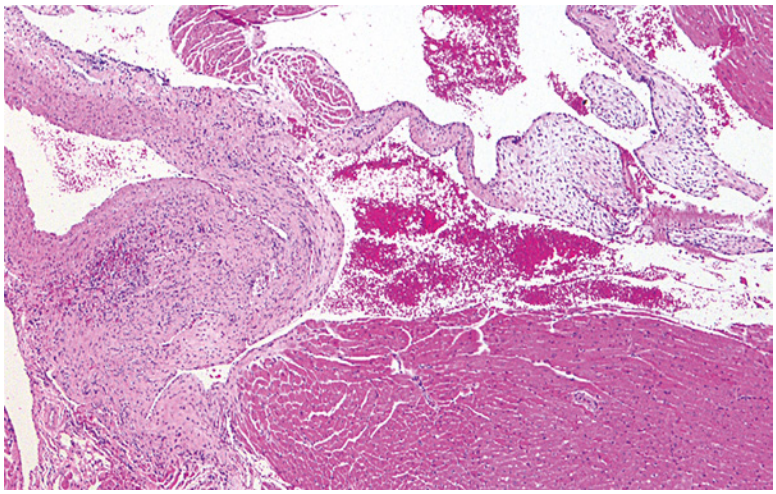


Figure 14.23 In this HE stain, the aortic root has a mononuclear infiltrate and the valve has myxomatosis degeneration, valvular endocardiosis and inflammation due to a stationary phase persistent/biofilm microcolony of *Borrelia burgdorferi* infection in a mouse model of the Lyme disease.

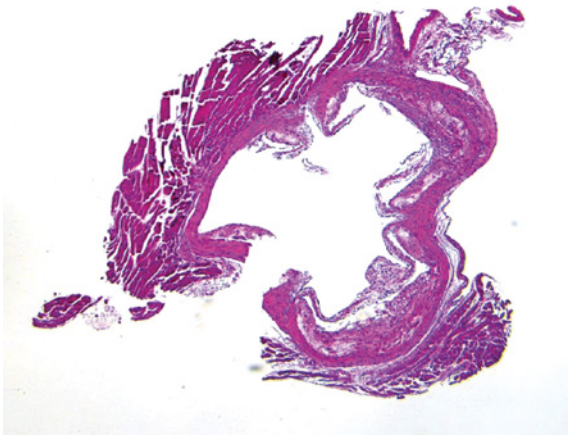
known as ionized calcium-binding adapter molecule 1 or IBA1) can identify plaque macrophages as seen in Figure 14.24 [186].

Summary

Tables 14.2 and 14.3 offer a quick reference to reviews for selected cardiovascular diseases with multiple varied etiologies. The heart and the vasculature have limited pathological responses. For the heart, epicardium, endocardium, or myocardium, the majority of lesions that occur includes cardiomyocyte degeneration, cell death, mineralization, inflammation, cardiomyocyte hypertrophy, and fibrosis. The same pathologic response, such as fibrosis, could be induced by multiple different etiologies from viral diseases to genetic diseases. Since many etiologies may share the same gross and microscopic lesion, molecular and functional studies are often included in characterizing the disease.

Fortunately, the cardiovascular system has many functional testing methods that are used in conjunction with histopathologic evaluation. Echocardiography characterization has become a primary non-invasive method for many laboratories. Since there are strain-, sex-, and age-dependent differences in the heart, all cardiovascular phenotypes require matched controls for these parameters. When presenting pathologic data in figures, the resolution needs to be adequate so that the morphology is clear in the figure. An inset with a higher magnification image at higher resolution can be used and paired with a low-resolution image. There are resources and cores at most institutions with experienced pathologists (DVM or MD) who can help investigators with microscopic evaluation. To increase research reproducibility, standard operation procedures should be developed and shared among scientists for improved outcomes for phenotyping and testing novel drugs or developing novel cardiovascular models.

(a)



(b)

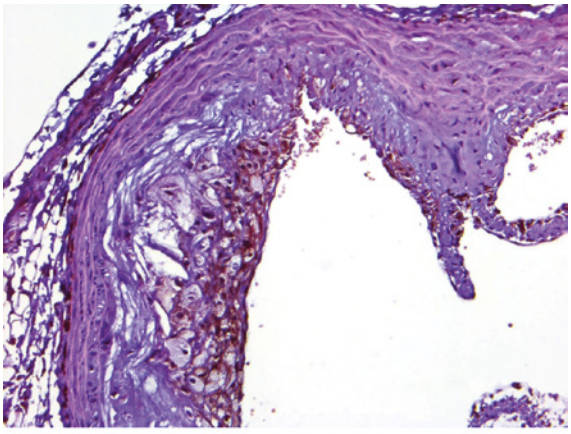


Figure 14.24 HE staining of the aortic root from an B6.129P2-*Apoe*^{tm1Unc}/J mouse with atherosclerosis (a). In a second mouse, AIF1 (formerly IBA1) immunohistochemistry of an aortic root marks the monocyte and macrophage population in the atherosclerotic plaque (b).

Acknowledgments

The authors are extremely grateful for the leadership of Dr. John Sundberg and Dr. Jerry Ward for their consistent support, multiple manuscript edits and figure contributions for this chapter. We also wish to thank Dr. Hal Dietz, Dr. Elena Gallo MacFarland, Dr. Daniella Cihakova, Dr. David Kass, and Dr. Brian Lin for examples of mouse cardiovascular diseases featured in figures.

References

1 Froud, M.D. (1959). Studies on the arterial system of three inbred strains of mice. *J. Morphol.* 104: 441–478.
2 Iwaki, T., Yamashita, H., and Hayakawa, T. (2001). A Color Atlas of Sectional Anatomy of the Mouse, p. 185. Tokyo: Maruzen Company.
3 Laflamme, M.A., Sebastian, M.M., and Buetow, B.S. (2012). Cardiovascular. In: Comparative Anatomy and Histology: A Mouse and Human Atlas (eds. P.M. Treuting and S.M. Dintzis), 135–153. San Diego: Academic Press.
4 Ruberte, J., Navarro, M., Carretero, A., and Koenig, H.E. (2017). Circulatory system. In: Morphological Mouse Phenotyping: Anatomy, Histology and Imaging (eds. J. Ruberte, A. Carretero and M. Navarro), 269–347. Academic Press.
5 Miquerol, L., Meysen, S., Mangoni, M. et al. (2004). Architectural and functional asymmetry of the His-Purkinje system of the murine heart. *Cardiovasc. Res.* 63 (1): 77–86.
6 Forbes, M.S., Van Niel, E.E., and Purdy-Ramos, S.I. (1990). The atrial myocardial cells of mouse heart: a structural and stereological study. *J. Struct. Biol.* 103 (3): 266–279.
7 Hinton, R.B. Jr., Alfieri, C.M., Witt, S.A. et al. (2008). Mouse heart valve structure and function: echocardiographic and morphometric analyses from the fetus through the aged adult. *Am. J. Physiol. Heart Circ. Physiol.* 294 (6): H2480–H2488.
8 Icardo, J.M. and Colvee, E. (1995). Atrioventricular valves of the mouse: II. Light and transmission electron microscopy. *Anat. Rec.* 241 (3): 391–400.
9 Lev, M. and Thaemert, J.C. (1973). The conduction system of the mouse heart. *Acta Anat. (Basel)* 85 (3): 342–352.
10 Savolainen, S.M., Foley, J.F., and Elmore, S.A. (2009). Histology atlas of the developing mouse heart with emphasis on E11.5 to E18.5. *Toxicol. Pathol.* 37 (4): 395–414.
11 Viragh, S. and Challice, C.E. (1982). The development of the conduction system in the mouse embryo heart. *Dev. Biol.* 89 (1): 25–40.
12 Doevendans, P.A., Daemen, M.J., de Muinck, E.D., and Smits, J.F. (1998). Cardiovascular phenotyping in mice. *Cardiovasc. Res.* 39 (1): 34–49.
13 Lopez-Garcia, A., Soto-Navarrete, M.T., Fernandez, M.C. et al. (2016). Unusual anatomical origins of the coronary arteries in C57BL/6 mice. Are they strain-specific? *J. Anat.* 229 (5): 703–709.
14 Hua, L.L., Vedantham, V., Barnes, R.M. et al. (2014). Specification of the mouse cardiac conduction system in the absence of Endothelin signaling. *Dev. Biol.* 393 (2): 245–254.
15 Hu, W., Xin, Y., Zhao, Y., and Hu, J. (2018). Shox2: the role in differentiation and development of cardiac conduction system. *Tohoku J. Exp. Med.* 244 (3): 177–186.
16 Patra, C., Zhang, X., and Brady, M.F. (2020). Physiology, Bundle of His. Treasure Island, FL: StatPearls.
17 Sanchez-Quintana, D. and Yen Ho, S. (2003). Anatomy of cardiac nodes and atrioventricular specialized conduction system. *Rev. Esp. Cardiol.* 56 (11): 1085–1092.
18 Oosthoek, P.W., Viragh, S., Mayen, A.E. et al. (1993). Immunohistochemical delineation of the conduction system. I: The sinoatrial node. *Circ. Res.* 73 (3): 473–481.
19 George, S.A., Faye, N.R., Murillo-Berlioz, A. et al. (2017). At the atrioventricular crossroads: dual pathway electrophysiology in the atrioventricular node and its underlying heterogeneities. *Arrhythm. Electrophysiol. Rev.* 6 (4): 179–185.
20 Rentschler, S., Vaidya, D.M., Tamaddon, H. et al. (2001). Visualization and functional characterization of the developing murine cardiac conduction system. *Development* 128 (10): 1785–1792.
21 Zhang, W., Li, X., Sun, S., and Zhang, X. (2019). Implantation of engineered conduction tissue in the rat heart. *Mol. Med. Rep.* 19 (4): 2687–2697.
22 Christoffels, V.M. and Moorman, A.F. (2009). Development of the cardiac conduction system: why are some regions of the heart more arrhythmogenic than others? *Circ. Arrhythm. Electrophysiol.* 2 (2): 195–207.
23 Strassheim, D., Dempsey, E.C., Gerasimovskaya, E. et al. (2019). Role of inflammatory cell subtypes in heart failure. *J. Immunol. Res.* 2019: 2164017.
24 Lavine, K.J., Pinto, A.R., Epelman, S. et al. (2018). The macrophage in cardiac homeostasis and disease: JACC macrophage in CVD series (Part 4). *J. Am. Coll. Cardiol.* 72 (18): 2213–2230.
25 Casey, K.A., Fraser, K.A., Schenkel, J.M. et al. (2012). Antigen-independent differentiation and maintenance of effector-like resident memory T cells in tissues. *J. Immunol.* 188 (10): 4866–4875.
26 Bansal, S.S., Ismahil, M.A., Goel, M. et al. (2017). Activated T lymphocytes are essential drivers of pathological remodeling in ischemic heart failure. *Circ. Heart Fail.* 10 (3): e003688.
27 Schenkel, J.M. and Masopust, D. (2014). Tissue-resident memory T cells. *Immunity* 41 (6): 886–897.
28 Bruno, K.A., Mathews, J.E., Yang, A.L. et al. (2019). BPA alters estrogen receptor expression in the heart after viral infection activating cardiac mast cells and T cells leading to perimyocarditis and fibrosis. *Front. Endocrinol. (Lausanne)* 10: 598.

29 Janicki, J.S., Brower, G.L., and Levick, S.P. (2015). The emerging prominence of the cardiac mast cell as a potent mediator of adverse myocardial remodeling. *Methods Mol. Biol.* 1220: 121–139.

30 Wei, C.C., Hase, N., Inoue, Y. et al. (2010). Mast cell chymase limits the cardiac efficacy of Ang I-converting enzyme inhibitor therapy in rodents. *J. Clin. Invest.* 120 (4): 1229–1239.

31 Ngkelo, A., Richart, A., Kirk, J.A. et al. (2016). Mast cells regulate myofilament calcium sensitization and heart function after myocardial infarction. *J. Exp. Med.* 213 (7): 1353–1374.

32 Kalluri, A.S., Vellarikkal, S.K., Edelman, E.R. et al. (2019). Single cell analysis of the normal mouse aorta reveals functionally distinct endothelial cell populations. *Circulation* 140: 147–163.

33 Garlanda, C. and Dejana, E. (1997). Heterogeneity of endothelial cells. Specific markers. *Arterioscler. Thromb. Vasc. Biol.* 17 (7): 1193–1202.

34 Jennette, J.C., Falk, R.J., Bacon, P.A. et al. (2013). 2012 revised International Chapel Hill Consensus Conference Nomenclature of Vasculitides. *Arthritis Rheum.* 65 (1): 1–11.

35 Wolinsky, H. and Glagov, S. (1967). Nature of species differences in the medial distribution of aortic vasa vasorum in mammals. *Circ. Res.* 20 (4): 409–421.

36 Wolinsky, H. and Glagov, S. (1969). Comparison of abdominal and thoracic aortic medial structure in mammals. Deviation of man from the usual pattern. *Circ. Res.* 25 (6): 677–686.

37 Best, P.V. and Heath, D. (1961). Interpretation of the appearances of the small pulmonary blood vessels in animals. *Circ. Res.* 9: 288–294.

38 Verloop, M.C. (1949). On the arteriae bronchiales and their anastomosing with the arteria pulmonalis in some rodents; a micro-anatomical study. *Acta Anat. (Basel)* 7 (1-2): 1–32.

39 Mitzner, W., Lee, W., Georgakopoulos, D., and Wagner, E. (2000). Angiogenesis in the mouse lung. *Am. J. Pathol.* 157 (1): 93–101.

40 Levin, E.G., Santell, L., and Osborn, K.G. (1997). The expression of endothelial tissue plasminogen activator in vivo: a function defined by vessel size and anatomic location. *J. Cell Sci.* 110 (Pt 2): 139–148.

41 Diny, N.L., Hou, X., Barin, J.G. et al. (2016). Macrophages and cardiac fibroblasts are the main producers of eotaxins and regulate eosinophil trafficking to the heart. *Eur. J. Immunol.* 46 (12): 2749–2760.

42 Sysa-Shah, P., Xu, Y., Guo, X. et al. (2012). Cardiac-specific over-expression of epidermal growth factor receptor 2 (ErbB2) induces pro-survival pathways and hypertrophic cardiomyopathy in mice. *PLoS One* 7 (8): e42805.

43 Sorensen, L.L., Bedja, D., Sysa-Shah, P. et al. (2016). Echocardiographic characterization of a murine model of hypertrophic obstructive cardiomyopathy induced by cardiac-specific overexpression of epidermal growth factor receptor 2. *Comp. Med.* 66 (4): 268–277.

44 Habashi, J.P., Judge, D.P., Holm, T.M. et al. (2006). Losartan, an AT1 antagonist, prevents aortic aneurysm in a mouse model of Marfan syndrome. *Science* 312 (5770): 117–121.

45 Cooper, T.K., Zhong, Q., Krawczyk, M. et al. (2010). The haploinsufficient Col3a1 mouse as a model for vascular Ehlers–Danlos syndrome. *Vet. Pathol.* 47 (6): 1028–1039.

46 Westerweel, P.E., Rookmaaker, M.B., van Zonneveld, A.J. et al. (2005). A study of neovascularization in the rat ischemic hindlimb using Araldite casting and Spalteholtz tissue clearing. *Cardiovasc. Pathol.* 14 (6): 294–297.

47 Ismail, J.A., Poppa, V., Kemper, L.E. et al. (2003). Immunohistologic labeling of murine endothelium. *Cardiovasc. Pathol.* 12 (2): 82–90.

48 Armulik, A., Genove, G., and Betsholtz, C. (2011). Pericytes: developmental, physiological, and pathological perspectives, problems, and promises. *Dev. Cell* 21 (2): 193–215.

49 Attwell, D., Mishra, A., Hall, C.N. et al. (2016). What is a pericyte? *J. Cereb. Blood Flow Metab.* 36 (2): 451–455.

50 Rensen, S.S., Doevendans, P.A., and van Eys, G.J. (2007). Regulation and characteristics of vascular smooth muscle cell phenotypic diversity. *Neth. Heart J.* 15 (3): 100–108.

51 Kartasalo, K., Polonen, R.P., Ojala, M. et al. (2015). CytoSpectre: a tool for spectral analysis of oriented structures on cellular and subcellular levels. *BMC Bioinf.* 16: 344.

52 Hanif, W., Alex, L., Su, Y. et al. (2017). Left atrial remodeling, hypertrophy, and fibrosis in mouse models of heart failure. *Cardiovasc. Pathol.* 30: 27–37.

53 Sysa-Shah, P., Tocchetti, C.G., Gupta, M. et al. (2016). Bidirectional cross-regulation between ErbB2 and beta-adrenergic signalling pathways. *Cardiovasc. Res.* 109 (3): 358–373.

54 Thompson, R.C., Deo, M., and Turner, D.L. (2007). Analysis of microRNA expression by in situ hybridization with RNA oligonucleotide probes. *Methods* 43 (2): 153–161.

55 Park, C.Y., Choi, Y.S., and McManus, M.T. (2010). Analysis of microRNA knockouts in mice. *Hum. Mol. Genet.* 19 (R2): R169–R175.

56 Memi, F., Tirziu, D., and Papangeli, I. (2018). Tissue-specific miRNA expression profiling in mouse heart sections using in situ hybridization. *J. Vis. Exp.* 139: 57920.

57 Kalayinia, S., Arjmand, F., Maleki, M. et al. (2020). MicroRNAs: roles in cardiovascular development and disease. *Cardiovasc. Pathol.*: 107296.

58 Berridge, B.R., Mowat, V., Nagai, H. et al. (2016). Non-proliferative and proliferative lesions of the cardiovascular system of the rat and mouse. *J. Toxicol. Pathol.* 29 (3_ Suppl): 1S–47S.

59 Hueper, W.C. (1939). Cartilaginous foci in the hearts of white rats and mice. *Arch. Pathol.* 27: 466–468.

60 Sundberg, J.P., Berndt, A., Sundberg, B.A. et al. (2016). Approaches to investigating complex genetic taits in a large-scale inbred mouse aging study. *Vet. Pathol.* 53 (2): 456–467.

61 Barthold, S.W., Griffey, S.M., and Percy, D.H. (2016). Mouse. In: Pathology of Laboratory Rodents and Rabbits, 4e (eds. S.W. Barthold, S.M. Griffey and D.H. Percy), 1–118. Ames, IA: Wiley Blackwell.

62 Pettan-Brewer, C. and Treuting, P.M. (2011). Practical pathology of aging mice. *Pathobiol. Aging Age Relat. Dis.* 1: 22953032.

63 Maeda, N., Doi, K., and Mitsuoka, T. (1986). Development of heart and aortic lesions in DBA/2NCrj mice. *Lab. Anim.* 20 (1): 5–8.

64 Li, Q., Berndt, A., Sundberg, B.A. et al. (2016). Mouse genome-wide association study identifies polymorphisms on chromosomes 4, 11, and 15 for age-related cardiac fibrosis. *Mamm. Genome* 27 (5-6): 179–190.

65 Berndt, A., Sundberg, B.A., Silva, K.A. et al. (2014). Phenotypic characterization of the KK/HlJ inbred mouse strain. *Vet. Pathol.* 51 (4): 846–857.

66 Glass, A.M., Coombs, W., and Taffet, S.M. (2013). Spontaneous cardiac calcinosis in BALB/cByJ mice. *Comp. Med.* 63 (1): 29–37.

67 Berndt, A., Li, Q., Potter, C.S. et al. (2013). A single-nucleotide polymorphism in the Abcc6 gene associates with connective tissue mineralization in mice similar to targeted models for pseudoxanthoma elasticum. *J. Invest. Dermatol.* 133 (3): 833–836.

68 Li, Q., Philip, V.M., Stearns, T.M. et al. (2019). Quantitative trait locus and integrative genomics revealed candidate modifier genes for ectopic mineralization in mouse models of pseudoxanthoma elasticum. *J. Invest. Dermatol.* 139 (12): 2447. 57 e7.

69 Klement, J.F., Matsuzaki, Y., Jiang, Q.J. et al. (2005). Targeted ablation of the abcc6 gene results in ectopic mineralization of connective tissues. *Mol. Cell. Biol.* 25 (18): 8299–8310.

70 Sundberg, J.P., Chevallier, L., Silva, K.A. et al. (2014). Mouse alopecia areata and heart disease: know your mouse! *J. Invest. Dermatol.* 134 (1): 279–281.

71 Zeiss, C.J., Gatti, D.M., Toro-Salazar, O. et al. (2019). Doxorubicin-induced cardiotoxicity in collaborative cross (CC) mice recapitulates individual cardiotoxicity in humans. *G3 (Bethesda)* 9 (8): 2637–2646.

72 Goette, A., Kalman, J.M., Aguinaga, L. et al. (2016). EHRA/HRS/APHRS/SOLAECE expert consensus on atrial cardiomyopathies: definition, characterization, and clinical implication. *Europace* 18 (10): 1455–1490.

73 Cooper, T.K., Silva, K.A., Kennedy, V.E. et al. (2019). Hyaline arteriolosclerosis in 30 strains of aged inbred mice. *Vet. Pathol.* 56 (5): 799–806.

74 Plendl, J., Kolle, S., Sinowatz, F., and Schmahl, W. (1996). Non-neoplastic lesions in blood vessels. In: Pathobiology of the Aging Mouse (eds. U. Mohr, D.L. Dungworth, C.C. Capen, et al.), 361–372. Washington, DC: ILSI Press.

75 Elangbam, C.S., Colman, K.A., Lightfoot, R.M. et al. (2002). Endocardial myxomatous change in Harlan Sprague-Dawley rats (Hsd:S-D) and CD-1 mice: its microscopic resemblance to drug-induced valvulopathy in humans. *Toxicol. Pathol.* 30 (4): 483–491.

76 Fernandez, B., Soto-Navarrete, M.T., Lopez-Garcia, A. et al. (2020). Bicuspid aortic valve in 2 model species and review of the literature. *Vet. Pathol.*:300985819900018.

77 Haines, D.C., Chattopadhyay, S., and Ward, J.M. (2001). Pathology of aging B6;129 mice. *Toxicol. Pathol.* 29 (6): 653–661.

78 Mjaatvedt, C.H., Kern, C.B., Norris, R.A. et al. (2005). Normal distribution of melanocytes in the mouse heart. *Anat. Rec. A Discov. Mol. Cell Evol. Biol.* 285 (2): 748–757.

79 Ramot, Y., Manno, R.A., Okazaki, Y. et al. (2009). Spontaneous aortitis in the Balb/c mouse. *Toxicol. Pathol.* 37 (5): 667–671.

80 Villano, J.S., Rong, F., and Cooper, T.K. (2014). Bacterial infections in Myd88-deficient mice. *Comp. Med.* 64 (2): 110–114.

81 Foreman, O., Kavirayani, A.M., Griffey, S.M. et al. (2011). Opportunistic bacterial infections in breeding colonies of the NSG mouse strain. *Vet. Pathol.* 48 (2): 495–499.

82 Booth, C.J. and Sundberg, J.P. (1995). Hemangiomas and hemangiosarcomas in inbred laboratory mice. *Lab. Anim. Sci.* 45 (5): 497–502.

83 Chandra, M. and Frith, C.H. (1992). Spontaneous neoplasms in B6C3F1 mice. *Toxicol. Lett.* 60 (1): 91–98.

84 Chen, W., Cooper, T.K., Zahnow, C.A. et al. (2004). Epigenetic and genetic loss of Hic1 function accentuates the role of p53 in tumorigenesis. *Cancer Cell* 6 (4): 387–398.

85 Nambiar, P.R., Turnquist, S.E., and Morton, D. (2012). Spontaneous tumor incidence in rasH2 mice: review of internal data and published literature. *Toxicol. Pathol.* 40 (4): 614–623.

86 Fattahi, F. and Ward, P.A. (2017). Complement and sepsis-induced heart dysfunction. *Mol. Immunol.* 84: 57–64.

87 Ma, X. and Adelstein, R.S. (2012). in vivo studies on nonmuscle myosin II expression and function in heart development. *Front. Biosci.* 17: 545–555.

88 Gittenberger-de Groot, A.C., Bartelings, M.M., Deruiter, M.C., and Poelmann, R.E. (2005). Basics of cardiac development for the understanding of congenital heart malformations. *Pediatr. Res.* 57 (2): 169–176.

89 Judge, D.P., Rouf, R., Habashi, J., and Dietz, H.C. (2011). Mitral valve disease in Marfan syndrome and related disorders. *J. Cardiovasc. Transl. Res.* 4 (6): 741–747.

90 Weiss, R.M., Miller, J.D., and Heistad, D.D. (2013). Fibrocalcific aortic valve disease: opportunity to understand disease mechanisms using mouse models. *Circ. Res.* 113 (2): 209–222.

91 Bacmeister, L., Schwarzl, M., Warnke, S. et al. (2019). Inflammation and fibrosis in murine models of heart failure. *Basic Res. Cardiol.* 114 (3): 19.

92 Blyszczuk, P. (2019). Myocarditis in humans and in experimental animal models. *Front. Cardiovasc. Med.* 6: 64.

93 Muller, A.M., Fischer, A., Katus, H.A., and Kaya, Z. (2015). Mouse models of autoimmune diseases – autoimmune myocarditis. *Curr. Pharm. Des.* 21 (18): 2498–2512.

94 Zhao, W., Zhao, T., Chen, Y. et al. (2015). A murine hypertrophic cardiomyopathy model: The DBA/2J strain. *PLoS One* 10 (8): e0133132.

95 Mosqueira, D., Smith, J.G.W., Bhagwan, J.R., and Denning, C. (2019). Modeling hypertrophic cardiomyopathy: mechanistic insights and pharmacological intervention. *Trends Mol. Med.* 25 (9): 775–790.

96 Du, C.K., Morimoto, S., Nishii, K. et al. (2007). Knock-in mouse model of dilated cardiomyopathy caused by troponin mutation. *Circ. Res.* 101 (2): 185–194.

97 Ikeda, Y. and Ross, J. Jr. (2000). Models of dilated cardiomyopathy in the mouse and the hamster. *Curr. Opin. Cardiol.* 15 (3): 197–201.

98 Tripathi, R., Sullivan, R., Fan, T.M. et al. (2017). Enhanced heart failure, mortality and renin activation in female mice with experimental dilated cardiomyopathy. *PLoS One* 12 (12): e0189315.

99 Houser, S.R., Margulies, K.B., Murphy, A.M. et al. (2012). Animal models of heart failure: a scientific statement from the American Heart Association. *Circ. Res.* 111 (1): 131–150.

100 Liu, X., Zhang, L., Pacciulli, D. et al. (2016). Restrictive cardiomyopathy caused by troponin mutations: application of disease animal models in translational studies. *Front. Physiol.* 7: 629.

101 McCauley, M.D. and Wehrens, X.H. (2009). Animal models of arrhythmogenic cardiomyopathy. *Dis. Models Mech.* 2 (11-12): 563–570.

102 Russell, L.K., Finck, B.N., and Kelly, D.P. (2005). Mouse models of mitochondrial dysfunction and heart failure. *J. Mol. Cell Cardiol.* 38 (1): 81–91.

103 Irwin, M.H., Parameshwaran, K., and Pinkert, C.A. (2013). Mouse models of mitochondrial complex I dysfunction. *Int. J. Biochem. Cell Biol.* 45 (1): 34–40.

104 Cachon-Gonzalez, M.B., Zaccariotto, E., and Cox, T.M. (2018). Genetics and therapies for GM2 gangliosidosis. *Curr. Gene Ther.* 18 (2): 68–89.

105 Pastores, G.M., Torres, P.A., and Zeng, B.J. (2013). Animal models for lysosomal storage disorders. *Biochemistry (Mosc).* 78 (7): 721–725.

106 Suzuki, K., Proia, R.L., and Suzuki, K. (1998). Mouse models of human lysosomal diseases. *Brain Pathol.* 8 (1): 195–215.

107 McGreevy, J.W., Hakim, C.H., McIntosh, M.A., and Duan, D. (2015). Animal models of Duchenne muscular dystrophy: from basic mechanisms to gene therapy. *Dis. Models Mech.* 8 (3): 195–213.

108 Yucel, N., Chang, A.C., Day, J.W. et al. (2018). Humanizing the mdx mouse model of DMD: the long and the short of it. *NPJ Regen. Med.* 3: 4.

109 Nakamura, A. and Takeda, S. (2011). Mammalian models of Duchenne Muscular Dystrophy: pathological characteristics and therapeutic applications. *J. Biomed. Biotechnol.* 2011: 184393.

110 Lim, K.R.Q., Yoon, C., and Yokota, T. (2018). Applications of CRISPR/Cas9 for the treatment of Duchenne Muscular Dystrophy. *J. Pers. Med.* 8 (4): 38.

111 von Scheidt, M., Zhao, Y., Kurt, Z. et al. (2017). Applications and limitations of mouse models for understanding human atherosclerosis. *Cell Metab.* 25 (2): 248–261.

112 Burke, A.C. and Huff, M.W. (2018). Regression of atherosclerosis: lessons learned from genetically modified mouse models. *Curr. Opin. Lipidol.* 29 (2): 87–94.

113 Emini Veseli, B., Perrotta, P., De Meyer, G.R.A. et al. (2017). Animal models of atherosclerosis. *Eur. J. Pharmacol.* 816: 3–13.

114 Getz, G.S. and Reardon, C.A. (2015). Use of mouse models in atherosclerosis research. *Methods Mol. Biol.* 1339: 1–16.

115 Xu, Q. (2004). Mouse models of arteriosclerosis: from arterial injuries to vascular grafts. *Am. J. Pathol.* 165 (1): 1–10.

116 Patelis, N., Moris, D., Schizas, D. et al. (2017). Animal models in the research of abdominal aortic aneurysms development. *Physiol. Res.* 66 (6): 899–915.

117 Wilson, N.K., Gould, R.A., and Gallo MacFarlane, E., Mibava Leducq Consortium (2016). Pathophysiology of aortic aneurysm: insights from human genetics and mouse models. *Pharmacogenomics* 17 (18): 2071–2080.

118 Baaten, C., Meacham, S., de Witt, S.M. et al. (2018). A synthesis approach of mouse studies to identify genes and proteins in arterial thrombosis and bleeding. *Blood* 132 (24): e35–e46.

119 Grover, S.P. and Mackman, N. (2019). Intrinsic pathway of coagulation and thrombosis. *Arterioscler. Thromb. Vasc. Biol.* 39 (3): 331–338.

120 Kiouptsi, K. and Reinhardt, C. (2018). Contribution of the commensal microbiota to atherosclerosis and arterial thrombosis. *Br. J. Pharmacol.* 175 (24): 4439–4449.

121 Gan, P.Y., Ooi, J.D., Kitching, A.R., and Holdsworth, S.R. (2015). Mouse models of anti-neutrophil cytoplasmic antibody-associated vasculitis. *Curr. Pharm. Des.* 21 (18): 2380–2390.

122 Luzina, I.G. and Handwerger, B.S. (2000). Lessons from animal models of vasculitis. *Curr. Rheumatol. Rep.* 2 (5): 369–375.

123 Salama, A.D. and Little, M.A. (2012). Animal models of antineutrophil cytoplasm antibody-associated vasculitis. *Curr. Opin. Rheumatol.* 24 (1): 1–7.

124 Carmichael, N.G., Debruyne, E.L., and Bigot-Lasserre, D. (2000). The p53 heterozygous knockout mouse as a model for chemical carcinogenesis in vascular tissue. *Environ. Health Perspect.* 108 (1): 61–65.

125 Das, I. and Reeves, R.H. (2011). The use of mouse models to understand and improve cognitive deficits in Down syndrome. *Dis. Model Mech.* 4 (5): 596–606.

126 Li, H., Edie, S., Klinedinst, D. et al. (2016). Penetrance of congenital heart disease in a mouse model of down syndrome depends on a trisomic potentiator of a disomic modifier. *Genetics* 203 (2): 763–770.

127 Anderson, R.H., Webb, S., and Brown, N.A. (1998). The mouse with trisomy 16 as a model of human hearts with

common atrioventricular junction. *Cardiovasc. Res.* 39 (1): 155–164.

128 Wijngaarde, C.A., Blank, A.C., Stam, M. et al. (2017). Cardiac pathology in spinal muscular atrophy: a systematic review. *Orphanet. J. Rare Dis.* 12 (1): 67.

129 Sider, K.L., Blaser, M.C., and Simmons, C.A. (2011). Animal models of calcific aortic valve disease. *Int. J. Inf. Secur.* 2011: 364310.

130 Czarny, M.J. and Resar, J.R. (2014). Diagnosis and management of valvular aortic stenosis. *Clin. Med. Insights Cardiol.* 8 (Suppl 1): 15–24.

131 Miller, J.D., Weiss, R.M., and Heistad, D.D. (2011). Calcific aortic valve stenosis: methods, models, and mechanisms. *Circ. Res.* 108 (11): 1392–1412.

132 d'Amati, G. and Giordano, C. (2016). Cardiomyopathies. In: Cardiovascular Pathology, Chapter 11, 4e (eds. L.M. Buja and J. Butany), 435–483. San Diego: Academic Press.

133 Sysa-Shah, P., Sorensen, L.L., Abraham, M.R., and Gabrielson, K.L. (2015). Electrocardiographic characterization of cardiac hypertrophy in mice that overexpress the ErbB2 receptor tyrosine kinase. *Comp. Med.* 65 (4): 295–307.

134 Camenisch, T.D., Schroeder, J.A., Bradley, J. et al. (2002). Heart-valve mesenchyme formation is dependent on hyaluronan-augmented activation of ErbB2-ErbB3 receptors. *Nat. Med.* 8 (8): 850–855.

135 Lee, K.F., Simon, H., Chen, H. et al. (1995). Requirement for neuregulin receptor erbB2 in neural and cardiac development. *Nature* 378 (6555): 394–398.

136 Gassmann, M., Casagranda, F., Orioli, D. et al. (1995). Aberrant neural and cardiac development in mice lacking the ErbB4 neuregulin receptor. *Nature* 378 (6555): 390–394.

137 Chan, R., Hardy, W.R., Laing, M.A. et al. (2002). The catalytic activity of the ErbB-2 receptor tyrosine kinase is essential for embryonic development. *Mol. Cell. Biol.* 22 (4): 1073–1078.

138 Iwamoto, R., Yamazaki, S., Asakura, M. et al. (2003). Heparin-binding EGF-like growth factor and ErbB signaling is essential for heart function. *Proc. Natl. Acad. Sci. U.S.A.* 100 (6): 3221–3226.

139 Ozcelik, C., Erdmann, B., Pilz, B. et al. (2002). Conditional mutation of the ErbB2 (HER2) receptor in cardiomyocytes leads to dilated cardiomyopathy. *Proc. Natl. Acad. Sci. U.S.A.* 99 (13): 8880–8885.

140 Crone, S.A., Zhao, Y.Y., Fan, L. et al. (2002). ErbB2 is essential in the prevention of dilated cardiomyopathy. *Nat. Med.* 8 (5): 459–465.

141 Garcia-Rivello, H., Taranda, J., Said, M. et al. (2005). Dilated cardiomyopathy in Erb-b4-deficient ventricular muscle. *Am. J. Physiol. Heart Circ. Physiol.* 289 (3): H1153–H1160.

142 Rajagopalan, V., Zucker, I.H., Jones, J.A. et al. (2008). Cardiac ErbB-1/ErbB-2 mutant expression in young adult mice leads to cardiac dysfunction. *Am. J. Physiol. Heart Circ. Physiol.* 295 (2): H543–H554.

143 Weintraub, R.G., Semsarian, C., and Macdonald, P. (2017). Dilated cardiomyopathy. *Lancet* 390 (10092): 400–414.

144 Gramlich, M., Michely, B., Krohne, C. et al. (2009). Stress-induced dilated cardiomyopathy in a knock-in mouse model mimicking human titin-based disease. *J. Mol. Cell Cardiol.* 47 (3): 352–358.

145 Arimura, T., Helbling-Leclerc, A., Massart, C. et al. (2005). Mouse model carrying H222P-Lmna mutation develops muscular dystrophy and dilated cardiomyopathy similar to human striated muscle laminopathies. *Hum. Mol. Genet.* 14 (1): 155–169.

146 Parvatiyar, M.S., Marshall, J.L., Nguyen, R.T. et al. (2015). Sarcospan regulates cardiac isoproterenol response and prevents Duchenne Muscular Dystrophy-associated cardiomyopathy. *J. Am. Heart Assoc.* 4 (12): e002481.

147 Razzoli, M., Lindsay, A., Law, M.L. et al. (2020). Social stress is lethal in the mdx model of Duchenne muscular dystrophy. *EBioMedicine.* 55: 102700.

148 Duan, D., Rafael-Fortney, J.A., Blain, A. et al. (2016). Standard Operating Procedures (SOPs) for evaluating the heart in preclinical studies of Duchenne Muscular Dystrophy. *J. Cardiovasc. Transl. Res.* 9 (1): 85–86.

149 Corrado, D., Link, M.S., and Calkins, H. (2017). Arrhythmogenic right ventricular cardiomyopathy. *N. Engl. J. Med.* 376 (1): 61–72.

150 Marcus, F.I., McKenna, W.J., Sherrill, D. et al. (2010). Diagnosis of arrhythmogenic right ventricular cardiomyopathy/dysplasia: proposed modification of the task force criteria. *Circulation* 121 (13): 1533–1541.

151 Costa, S., Cerrone, M., Saguner, A.M. et al. (2020). Arrhythmogenic cardiomyopathy: an in-depth look at molecular mechanisms and clinical correlates. *Trends Cardiovasc. Med.* https://doi.org/10.1016/j.tcm.2020.07.006.

152 van Opbergen, C.J.M., Noorman, M., Pfenniger, A. et al. (2019). Plakophilin-2 haploinsufficiency causes calcium handling deficits and modulates the cardiac response towards stress. *Int. J. Mol. Sci.* 20 (17).

153 Herbert Pratt, C., Potter, C.S., Fairfield, H. et al. (2015). Dsp rul: a spontaneous mouse mutation in desmoplakin as a model of Carvajal–Huerta syndrome. *Exp. Mol. Pathol.* 98 (2): 164–172.

154 Chelko, S.P., Asimaki, A., Andersen, P. et al. (2016). Central role for GSK3beta in the cardiomyopathy. *JCI Insight* 1 (5): e85923.

155 Octavia, Y., Tocchetti, C.G., Gabrielson, K.L. et al. (2012). Doxorubicin-induced cardiomyopathy: from molecular mechanisms to therapeutic strategies. *J. Mol. Cell Cardiol.* 52 (6): 1213–1225.

156 Huang, Y., Powers, C., Madala, S.K. et al. (2015). Cardiac metabolic pathways affected in the mouse model of barth syndrome. *PLoS One* 10 (6): e0128561.

157 Torraco, A., Diaz, F., Vempati, U.D., and Moraes, C.T. (2009). Mouse models of oxidative phosphorylation defects: powerful tools to study the pathobiology of

mitochondrial diseases. *Biochim. Biophys. Acta* 1793 (1): 171–180.

158 Torraco, A., Peralta, S., Iommarini, L., and Diaz, F. (2015). Mitochondrial diseases part I: mouse models of OXPHOS deficiencies caused by defects in respiratory complex subunits or assembly factors. *Mitochondrion* 21: 76–91.

159 Acehan, D., Vaz, F., Houtkooper, R.H. et al. (2011). Cardiac and skeletal muscle defects in a mouse model of human Barth syndrome. *J. Biol. Chem.* 286 (2): 899–908.

160 Sanghera, C., Wong, L.M., Panahi, M. et al. (2019). Cardiac phenotype in mouse models of systemic autoimmunity. *Dis. Model Mech.* 12 (3): dmm036947.

161 Pummerer, C.L., Luze, K., Grassl, G. et al. (1996). Identification of cardiac myosin peptides capable of inducing autoimmune myocarditis in BALB/c mice. *J. Clin. Invest.* 97 (9): 2057–2062.

162 Cihakova, D., Sharma, R.B., Fairweather, D. et al. (2004). Animal models for autoimmune myocarditis and autoimmune thyroiditis. *Methods Mol. Med.* 102: 175–193.

163 Wu, L., Ong, S., Talor, M.V. et al. (2014). Cardiac fibroblasts mediate IL-17A-driven inflammatory dilated cardiomyopathy. *J. Exp. Med.* 211 (7): 1449–1464.

164 Nakae, S., Komiyama, Y., Nambu, A. et al. (2002). Antigen-specific T cell sensitization is impaired in IL-17-deficient mice, causing suppression of allergic cellular and humoral responses. *Immunity* 17 (3): 375–387.

165 Barin, J.G., Baldeviano, G.C., Talor, M.V. et al. (2013). Fatal eosinophilic myocarditis develops in the absence of IFN-gamma and IL-17A. *J. Immunol.* 191 (8): 4038–4047.

166 Rhee, J.W., Grove, M.E., and Ashley, E.A. (2017). Navigating genetic and phenotypic uncertainty in left ventricular noncompaction. *Circ. Cardiovasc. Genet.* 10 (4).

167 Nair, V., Belanger, E.C., and Veinot, J.P. (2019). Lysosomal storage disorders affecting the heart: a review. *Cardiovasc. Pathol.* 39: 12–24.

168 Rozenfeld, P. and Feriozzi, S. (2017). Contribution of inflammatory pathways to Fabry disease pathogenesis. *Mol. Genet. Metab.* 122 (3): 19–27.

169 Halushka, M.K., Angelini, A., Bartoloni, G. et al. (2016). Consensus statement on surgical pathology of the aorta from the Society for Cardiovascular Pathology and the Association For European Cardiovascular Pathology: II. Noninflammatory degenerative diseases – nomenclature and diagnostic criteria. *Cardiovasc. Pathol.* 25 (3): 247–257.

170 Stone, J.R., Bruneval, P., Angelini, A. et al. (2015). Consensus statement on surgical pathology of the aorta from the Society for Cardiovascular Pathology and the Association for European Cardiovascular Pathology: I. inflammatory diseases. *Cardiovasc. Pathol.* 24 (5): 267–278.

171 Wheeler, J.B., Mukherjee, R., Stroud, R.E. et al. (2015). Relation of murine thoracic aortic structural and cellular changes with aging to passive and active mechanical properties. *J. Am. Heart Assoc.* 4 (3): e001744.

172 Schlatmann, T.J. and Becker, A.E. (1977). Histologic changes in the normal aging aorta: implications for dissecting aortic aneurysm. *Am. J. Cardiol.* 39 (1): 13–20.

173 Gallo, E.M., Loch, D.C., Habashi, J.P. et al. (2014). Angiotensin II-dependent TGF-beta signaling contributes to Loeys–Dietz syndrome vascular pathogenesis. *J. Clin. Invest.* 124 (1): 448–460.

174 Bowen, C.J., Calderon Giadrosic, J.F., Burger, Z. et al. (2020). Targetable cellular signaling events mediate vascular pathology in vascular Ehlers–Danlos syndrome. *J. Clin. Invest.* 130 (2): 686–698.

175 Liu, X., Wu, H., Byrne, M. et al. (1997). Type III collagen is crucial for collagen I fibrillogenesis and for normal cardiovascular development. *Proc. Natl. Acad. Sci. U.S.A.* 94 (5): 1852–1856.

176 Renard, M., Francis, C., Ghosh, R. et al. (2018). Clinical validity of genes for heritable thoracic aortic aneurysm and dissection. *J. Am. Coll. Cardiol.* 72 (6): 605–615.

177 Gould, D.B., Phalan, F.C., van Mil, S.E. et al. (2006). Role of COL4A1 in small-vessel disease and hemorrhagic stroke. *N. Engl. J. Med.* 354 (14): 1489–1496.

178 MacFarlane, E.G., Parker, S.J., Shin, J.Y. et al. (2019). Lineage-specific events underlie aortic root aneurysm pathogenesis in Loeys–Dietz syndrome. *J. Clin. Invest.* 129 (2): 659–675.

179 van Hoeven, K.H. and Factor, S.M. (1990). A comparison of the pathological spectrum of hypertensive, diabetic, and hypertensive-diabetic heart disease. *Circulation* 82 (3): 848–855.

180 Mullink, J.W. and Haneveld, G.T. (1979). Polyarteritis in mice due to spontaneous hypertension. *J. Comp. Pathol.* 89 (1): 99–106.

181 Lerman, L.O., Kurtz, T.W., Touyz, R.M. et al. (2019). Animal models of hypertension: a scientific statement from the American Heart Association. *Hypertension* 73 (6): e87–e120.

182 Takahashi, N., Chernavvsky, D.R., Gomez, R.A. et al. (2000). Uncompensated polyuria in a mouse model of Bartter's syndrome. *Proc. Natl. Acad. Sci. U.S.A.* 97 (10): 5434–5439.

183 Lorenz, J.N., Baird, N.R., Judd, L.M. et al. (2002). Impaired renal NaCl absorption in mice lacking the ROMK potassium channel, a model for type II Bartter's syndrome. *J. Biol. Chem.* 277 (40): 37871–37880.

184 Pradervand, S., Wang, Q., Burnier, M. et al. (1999). A mouse model for Liddle's syndrome. *J. Am. Soc. Nephrol.* 10 (12): 2527–2533.

185 Feng, J., Li, T., Yee, R. et al. (2019). Stationary phase persister/biofilm microcolony of Borrelia burgdorferi causes more severe disease in a mouse model of Lyme arthritis: implications for understanding persistence, Post-treatment Lyme Disease Syndrome (PTLDS), and treatment failure. *Discov. Med.* 27 (148): 125–138.

186 Li, L., Du, Z., Rong, B. et al. (2020). Foam cells promote atherosclerosis progression by releasing CXCL12. *Biosci. Rep.* 40 (1).

15

Liver and Pancreas

Maria L.Z. Dagli, Lucas M. Chaible, and Katja Steiger

Liver

The liver is a central organ for detoxification of xenobiotics and other important functions. Genetically engineered mice (GEM) have been created to understand the role of cells and molecular routes involved in liver function and to establish models to study human diseases. The objective of this chapter is to describe the existing models for hepatic and pancreatic human diseases and explain in detail what should be done to complete pathologic phenotyping of the liver and pancreas of GEM and provide some examples. Humanized mice are also good tools to understand the liver function using human hepatocytes/cells. Their characteristics will also be depicted in this chapter.

Anatomy, Histology, and Physiology

The anatomical aspects of the rodent livers share more similarities than differences with human livers.

The liver is one of the largest internal organ in mammals that exerts numerous metabolic and endocrine functions [1]. These include production of bile, metabolism of dietary compounds, detoxification, regulation of glucose levels through glycogen storage, and control of blood homeostasis by secretion of clotting factors and serum proteins such as albumin (ALB). The embryology of the liver has been nicely described in Swartley et al. [2], and elsewhere (https://discovery.lifemapsc.com/in-vivo-development/liver). The mouse liver has five lobes: the right and left lateral lobes (developed from both embryonic dorsolateral lobes), the right and left medial lobes (developed from the incompletely divided ventromedial lobe), and the caudate lobe. The mouse liver weighs approximately 2 g, representing about 6 percent of the mouse body weight [3].

The basic gross architecture of the liver can change by further subdivisions of the lobes or by the merging of the fissures. Thus, the caudate lobe often has caudate and papillary processes, and the right lateral lobe upper and lower sublobes. Interestingly, there is also a fifth lobe, the quadrate lobe, which is found between the gallbladder and the round ligament (postnatal remnant of the umbilical vein) and is very variable in its development between species. It is virtually absent in rodents, small in pigs, and well developed in dogs, cows, and horses. In humans, a quadrate lobe is normally present, but quantitative differences, including complete absence, have been reported. Histologically, the hepatocytes in mouse liver are organized in the form of "classic liver lobules." Hepatic plates in mice are less apparent than in human liver, and generally most prominent in zones 1 and 2. In portal spaces, the small triads are not apparent, and fibrous connective tissues are not prominent in health or disease; special stains, such as Masson, Mallory's, or Picrosirius red, for the staining of collagens, are required. As in other species, sinusoids are fenestrated and discontinuous, and bile canaliculi are not easily detectable in normal liver [3]. Endothelial cells, perisinusoidal cells (also called stellate cells or Ito cells), and macrophages (Kupffer cells) are part of the mouse liver sinusoidal wall.

The cell types present in mouse livers and their immunostaining characteristics are described in Table 15.1.

Hepatoblasts are embryonal bipotential precursor cells, which give rise to hepatocytes and biliary epithelial cells (BECs; also known as cholangiocytes), the two major liver cell types. Hepatoblasts are considered as the embryonal liver stem cells [12] and are sited within the canals of Hering, or intrahepatic bile ductules, located near portal tracts (Figure 15.1). The canal of Hering cells are the link between the hepatocyte canalicular system and the biliary tree. These cells are positive for keratin 19 (KRT19) and or ALB (Table 15.1) and may increase in number in many forms of liver disease, especially in cholestasis and liver necrosis [19].

The Hering canal stem cells can generate small round cells referred to as oval cells, which express markers of both fetal hepatocytes and biliary cells and are capable of generating both hepatocytes and bile duct cells. Because of these properties oval cells are considered to be bipotential progenitor cells in adult livers. Oval cell lines have been derived from livers of rodents exposed to toxic chemicals or carcinogens [19].

Hepatocytes comprise about 70% of hepatic cells. BECs line the lumen of the intrahepatic bile ducts (IHBDs). The remaining 30% of the adult liver is comprised of

Pathology of Genetically Engineered and Other Mutant Mice, First Edition. Edited by John P. Sundberg, Peter Vogel, and Jerrold M. Ward.
© 2022 John Wiley & Sons, Inc. Published 2022 by John Wiley & Sons, Inc.

Table 15.1 Mouse liver immunohistochemistry.

Cell type	Mouse	Staining/ immunostaining method	Gene names[a]	Protein symbol	References
Hepatocyte	52% of liver cells;	Albumin + Alexa 488	*Alb*	ALB, albumin	[4]
		Biotin + Alexa 488			[4]
		HepPar1 (Human)	*Foxa2*	F2R, coagulation factor II (thrombin) receptor	[5]
		Cytokeratin 18	*Krt18*	KRT18, keratin 18	[6]
		Cytokeratin 8/18	Krt8 /Krt18	KRT8, keratin 8, KRT18, keratin 18	[7]
		CK 8 and CK 18		KRT8, keratin 8, KRT18, keratin 18	[8]
		Glutamine synthetase	*GluI*	GLUl, glutamate-ammonia ligase (glutamine synthetase)	[9]
Bi-nucleated hepatocytes	35% of all hepatocytes	CK 8 and CK 18		KRT18, keratin 18	[4]
Kupffer cells	18%, sinusoidal	F4-80 + Alexa 488	*Adgre1*	ADGRE1, adhesion G protein-coupled receptor E1 (formerly F4-80); Cd68, CD68 antigen; GJB6, gap junction protein, beta 6; SRA-E5 (nothing in MGI); IBA1, induction of brown adipocytes 1; AIF1, allograft inflammatory factor 1 human Gene name: *ED2*	[4] [8]
		CD68, F4-80, ED2, SRA-E5, IBA1	*Cd68, Gjb6, Iba1*		
Stellate (Ito) cells	8%, perisinusoidal	GFAP + Alexa 488	*Gfap*	GFAP, glial fibrillary acidic protein	[4]
Activated stellate (Ito) cells		Alpha-smooth muscle actin (SMA)	*Acta*	ACTA2, actin, alpha 2, smooth muscle, aorta	[8]
Sinusoid endothelial cells		CD34 + Alexa 488	*Cd34*	CD34, CD34 antigen	[4]
		CD31, Factor VIII	*Pecam1*	PECAM1, platelet/endothelial cell adhesion molecule 1 (formerly CD31)	[8]
Stem cells	Mouse, postnatal	$CD133^{+}CD49f(low)$ CD107b(low)	*Prom1* and *Itga6*	PROM1, prominin 1 (formerly CD133) CD49 not in MGI	[10]
	Mouse, fetal (hepatoblasts)	c-Kit-(CD45/TER119)-liver stem/progenitor cells in mouse fetal liver	*Kit*, *Ptprc* and *Ly76*	KIT, KIT proto-oncogene receptor tyrosine kinase LEUF1, leukocyte filtration 1 (CD45+) but could be PTPRC, protein tyrosine phosphatase, receptor type, C (CD45) LY76, lymphocyte antigen 76 (formerly TER119)	[11]
Hering canal cells	Mouse	Cytokeratin 19, HepPar1, c-kit, and α-fetoprotein (AFP)	*Krt19*, *Foxa2*, *Kit* and *Afp*	KRT19, keratin 19 AFP, alpha fetoprotein	[12]
Bile canaliculi		Polyclonal carcinoembryonic antigen (CEA)		CEA, carcinoembryonic antigen gene family (this is a cluster of genes)	[8]
Bile duct epithelium		CK7, CK19, AE1/AE3	*Krt7*, *Krt19*, *Slc4a1*, *Slc4a3*	KRT7, keratin 7; KRT19; AE1/AE3 the stringent, but broad, specificity of pooled AE1/AE3 antibody has made this preparation very useful as a general stain for normal and neoplastic cells of epithelial origin. Anti-Keratin AE1 recognizes the 56.5, 50, 50′, 48, and 40 kD keratins of the acidic subfamily. Anti-keratin AE3 recognizes all members of the basic subfamily (65, 67, 64, 59.59, 56, 52 human basic cytokeratins). Epitope/region recognizes acidic and basic cytokeratins	[8, 13]

Table 15.1 (Continued)

Cell type	Mouse	Staining/ immunostaining method	Gene names[a]	Protein symbol	References
Oval cells		AFP, CK20	*Afp* and *Krt20*	AFP; KRT20, keratin 20	[14]
		A6		TWF1, twinfilin actin binding protein 1	[15]
Cell proliferation markers		PCNA or BrDU	*Pcna*	PCNA, proliferating cell nuclear antigen; BrdU, Bromodeoxyuridine	[16], [17]
		Ki67 (clone SP6 for mice)	*Mki67*	MKI67, antigen identified by monoclonal antibody Ki 67	[18]

[a] Symbols listed in Mouse Genome Informatics (http://www.informatics.jax.org/; searched 19 January 2021).

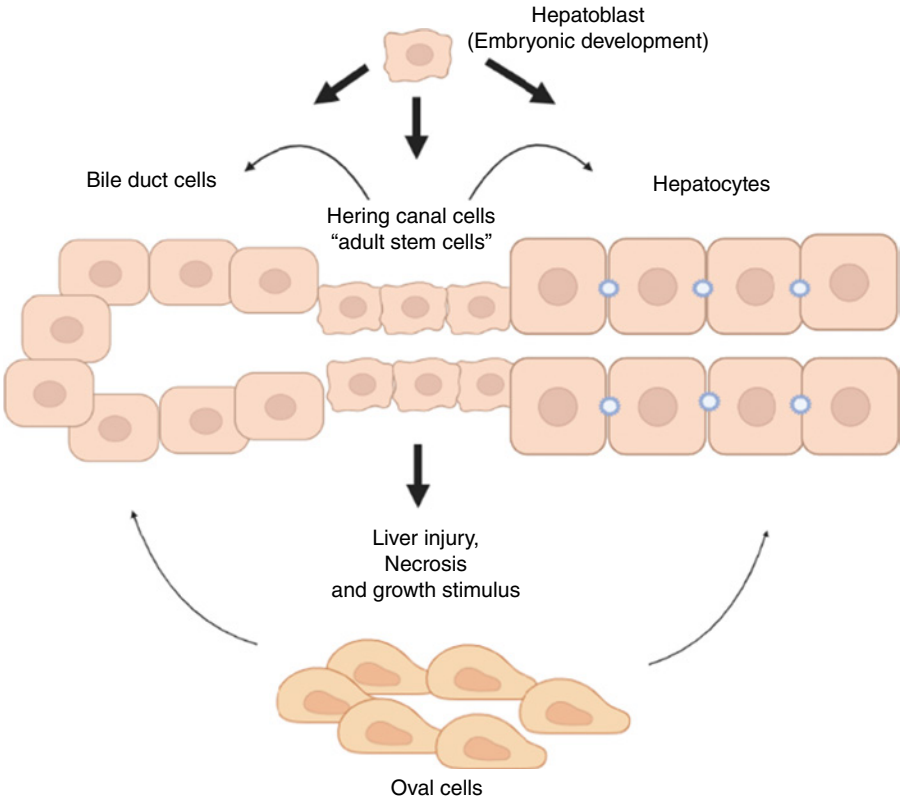


Figure 15.1 Role of hepatoblasts in liver. Differentiation of hepatoblasts into Hering canal cells and their relationship with bile duct cells, hepatocytes, and oval cells. Source: Modified from Refs. [11] and [18].

nonparenchymal cells, including Kupffer cells, stromal cells, and stellate cells of mesodermal origin.

The portal vein and hepatic artery, formed from segments of the vitelline and the umbilical veins of the fetus, are two major blood vessels that supply the liver. Within the adult liver, the bile duct, portal vein, and hepatic artery run in parallel and form the "portal triad." The portal triad is surrounded by hepatocytes arranged in single-cell sheets, the hepatic plates, separated by sinusoidal spaces that are connected to a network of capillaries.

The hepatic circulatory system is composed of the portal vein and the hepatic artery. Blood from the portal vein enters the sinusoidal space and comes into direct contact with the basal surface of hepatocytes, and these absorb metabolites and toxins. Bile is secreted from the apical surface of the hepatocytes into the bile canaliculi (grooves in the cell surface) and then flows toward the gall bladder, where it is stored before release into the duodenum.

The liver also has a lymphatic drainage system, which has been recently characterized in mouse liver. Intrahepatic lymphatic vessels are exclusively situated near portal triads. Lymphatic drainage in right lobe goes mainly to hepatoduodenal ligament lymph node 1 (LN1); left lobe lymphatic drainage goes to hepatoduodenal ligament LN1 + LN2 concurrently; median lobe shows a more variable LN1/LN2 drainage pattern with increased (sometimes exclusive) mediastinal thoracic lymph node involvement, indicating that part of the liver lymph can drain directly to the mediastinum [20].

Special Necropsy Organ Protocols

The pathological evaluation of GEM liver and pancreas is not different from what is recommended in conventional rodent studies. Body weight/liver ratios are often used in liver research studies. Best practices recommendations for obtaining liver weights can be obtained in Sellers et al. [21].

Liver samples can be obtained as described for routine toxicological studies (https://reni.item.fraunhofer.de/reni/trimming/) with one section of left lobe and median lobe with gallbladder, or with special liver protocols. Representative slices of mouse liver can be obtained as depicted in Figure 15.2.

Specifically for cancer studies, grossly visible focal or nodular lesions should be noted as to the location, measured, and recorded separately for each lobe. Small nodules (generally <1 cm) are usually foci of cellular alteration (FCA) or adenomas while larger nodules with irregular borders and prominent vascularization are usually hepatocellular carcinomas (HCCs) (Figures 15.3 and 15.4). It is often important to sample every nodule and its surrounding liver in order to get all possible information on the nature of the lesion. In addition, larger gross lesions should be examined for evidence of local invasion. Other organs, such as lungs or kidneys, should be examined for the presence of metastases when a potential neoplasm has been observed in the liver.

Whole liver should be fixed, and after fixation, representative slices of each liver lobe should be sampled. It is important to consistently sample from the same positions in the liver lobes, especially when comparative quantification will be undertaken, e.g. quantitation of altered foci or measurement of replicative DNA synthesis from histologic sections. If samples are needed for laboratory analysis, they can be taken at the time of necropsy and the whole liver not fixed.

The most commonly used fixatives are neutral buffered 10% formalin and Bouin's solution. However, if it is necessary to preserve the hepatic glycogen, nonaqueous alcoholic (coagulative) fixatives are preferred. The proper choice of fixative and prompt embedment may be critical for subsequent immunohistochemistry or *in situ* hybridization staining. In general, a good tactic is to fix separate and contiguous liver slices in one of at least two alternative fixatives followed by embedment in paraffin as soon as the slices are fixed. Methacarn (60% methanol, 30% chloroform, and 10% acetic acid) is an excellent fixative for the immunostaining of intermediate filaments in hepatic or stromal cells, as well as and for other immunohistochemical methods and for RNA analysis. For some studies, it may be necessary to have frozen liver slices for immunostaining or enzymatic histochemistry,

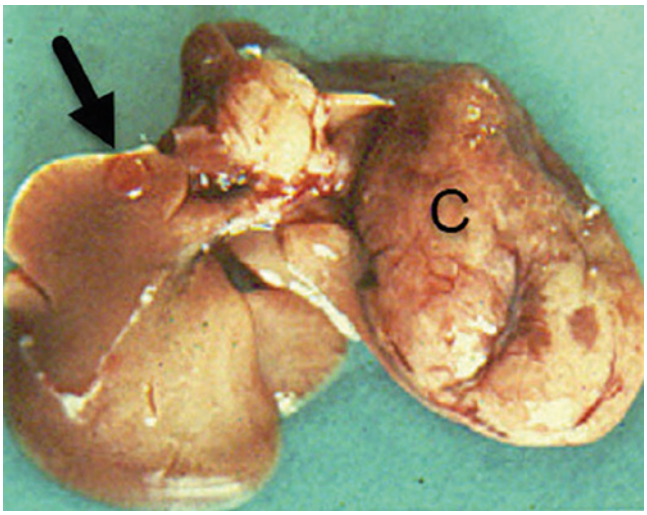


Figure 15.3 **HCC in mouse liver**. Gross liver tumors in a two-year-old mouse. Arrow points to small hepatocellular adenoma and mass is a hepatocellular carcinoma.

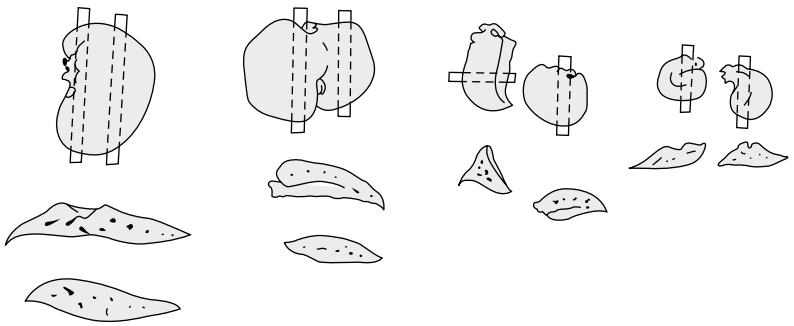




Figure 15.2 **Trimming the liver**. How to obtain mouse liver sections for histopathological analysis, especially for counting lesions and image analysis. The gall bladder can be included, if necessary.



Figure 15.4 **HCC in mouse liver**. Liver masses in a Liver-Onc3/HBsAg mouse. Multiple coalescing tumors are seen.

e.g. glucose-6 phosphatase staining. Frozen liver slices may also be collected and kept at −80 °C for molecular analyses.

Histopathological reports must be adequately prepared and fundamental elements of histopathological examinations that are necessary for the best practice of histopathology, along with appropriate techniques to minimize observational bias, can be found at Crissman et al. [22]. It is clear that the qualifications and experience of the pathologist clearly represent the most essential factors in determining the quality of the pathology evaluation and the interpretation.

Aging/Spontaneous Strain Specific Lesions

Described as a decline of biological functions related to the advancement of age, aging is characterized by progressive declines in multiple organ systems; increases in neoplastic and chronic degenerative nonneoplastic diseases may occur according to mouse strain and the genetic modification in genetically modified strains. Data on inbred strain cancer frequency can be found on the tumor frequency grid for inbred strains by organ (http://tumor.informatics.jax.org/mtbwi/dynamicGrid.do).

In aging studies, mice present hepatocellular tumors at variable average incidences that vary by strain or stock, and in general, there is higher incidence in males. Incidence of neoplasms in liver of lines of C57BL/6, 129, and B6/129 mice (combining benign and malignant) vary from 0 (C57BL/6J) to 22.5% (129S4/SvJae). Among others, liver neoplasms are commonly found in the following strains in long-term studies (after one year): BALB/c, C3H, and CBA. Liver neoplasms were commonly found in the following noninbred strains of mice in two-year studies: B6/129, B6C3F1, SENCAR, and Swiss CD1 and Swiss NMRI [23].

According to Pettan-Brewer and Treuting [24], only 1% of the aged C57BL/6J presented spontaneous hepatocellular adenoma, 3% presented biliary hyperplasia, and 3% presented biliary cysts.

Genetically Engineered Mice (GEM)

Mice have long been used as models to study liver diseases, and a large amount of knowledge has been acquired on these animals, especially on their susceptibility to develop spontaneous or induced liver cancers. Many models to study liver diseases have been created, using different chemicals, protocols, or surgical procedures, aiming at the detection of pathological or molecular alterations.

The study of the pathogenesis of liver lesions has benefited enormously from the advent of transgenic technology. The genetic manipulation of mice represents another step of biological discovery in which the genetic defect is known: foreign genes can be introduced into the genome or endogenous genes can be silenced [25]. The goal of genetic manipulation is to evaluate the consequences on animal or organ behavior, appreciating that the obtained responses can validate or even change current concepts.

Aberrant gene expression is frequently found in human cancers. Overexpression of genes, mutations in some genes, mutations that abolish the expression of genes important for cell growth control, or even translocations that generate new genes have all been implicated as genetic defects found in cancer cells. It is known that chronic viral hepatitis (hepatitis B and C) is associated with the majority of HCCs worldwide. However, there are many individuals in whom no obvious cause of HCC can be identified. Some inherited diseases are well known to be risk factors for the development of HCC. Among them are the hemochromatosis, alpha-1-antitrypsin deficiency, glycogen storage disease, porphyria cutanea tarda, and tyrosinemia. Alcoholic cirrhosis may result in HCC, although it is not clear whether alcohol is intrinsically carcinogenic, or whether associated hepatocellular injury and regeneration, iron accumulation, or coexistent infection with the hepatitis C virus (HCV) are required [25].

Development of transgenic and gene-targeting technologies facilitated the generation of GEM to study tumor biology. The most common ways to generate mouse models of cancers are activating oncogenes or inactivating tumor-suppressor genes (or both) *in vivo* through the use of transgenic and gene-targeting approaches. Transgenic and knockout models have been developed to answer critical questions about human HCC, aberrant gene effects and gene-environmental interactions. By combining transgenic and embryonic stem cell technologies, it is possible to explore many of the critical questions regarding the mechanisms of liver growth regulation in the intact animal. Several transgenic mouse models have been developed in which introduction of transgene constructs leads to development of HCC [25].

The Mouse Models of Human Cancers Database (formerly called the Mouse Tumor Biology Database) (http://tumor.informatics.jax.org/), a compendium on *in vivo* mouse models, was created in the fall of 1998 [26]. So far a total of 3252 mouse models of human liver cancers are available to date. Among these, 85 models of hepatocyte tumors, 262 models of bile duct tumors, 25 models of oval cell tumors, and 8 models of sinusoid tumors.

Genetically Engineered Mouse Models for Liver Diseases

Many genetically modified models are available nowadays to study nonneoplastic and neoplastic liver diseases. The suggested criteria to create and use a GEM model to understand and manipulate liver diseases, in particular cancers, have been described [25, 27]. The GEM model must recapitulate the etiology of the disease so that it bears genetic alterations that are similar to human disease. The model must also reflect the stages of the diseases progression. Microenvironmental aspects are also important, and therefore the pathological analysis is essential to inform about parenchymal cell types, extracellular matrix, inflammatory infiltrates, and alterations in blood and lymphatic vessels.

Mouse Models of Nonneoplastic Liver Diseases

Among the most important diseases of human liver, nonalcoholic steatohepatitis (NASH), nonalcoholic fatty liver disease (NAFLD), together with fibrosis and cirrhosis are currently the most relevant and prevalent.

Liver fibrosis and liver cirrhosis are the end-stage states of most chronic liver diseases. The cellular and molecular mechanisms of liver fibrogenesis have been extensively investigated using a wide variety of animal models. Mice are more resistant to liver fibrosis than rats, and susceptibility to fibrosis is highly variable among mouse strains; severe fibrosis can be induced in several strains by optimizing experimental procedures.

The classical models of liver fibrosis in mice include the following procedures and/or chemicals: common bile duct ligation, carbon tetrachloride (CCl_4), diethyl nitrosamine (DEN), dimethyl nitrosamine (DMN), or thioacetamide (TAA) [28].

Conventional and genetically modified animal models for primary biliary cholangitis (PBC), primary sclerosing cholangitis, autoimmune hepatitis, alcoholic liver disease (ALD), NAFLD, hepatitis C, and hepatitis B have been recently described [28].

Nowadays, there are a few genetic models of NAFLD available. The spontaneous obese allele of the leptin gene (Lep^{ob}; there are now 16 mutant alleles) and the diabetes allele of the leptin receptor gene ($Lepr^{db}$; there are now 58 mutant alleles) are classic mouse models (http://www.informatics.jax.org/), and the Zucker rat model ($Lepr^{fa}$; a spontaneous allele of the leptin receptor; https://rgd.mcw.edu) provides another rodent species; heterozygous agouti gene (KK-Ay/a) mutation model (there are 118 allelic mutations in the A) (nonagouti gene), Mc4r knockout mice model (melanocortin 4 receptor-deficiency) and *Srebf2* knock-out mice model (Sterol Regulator Element-Binding Protein 1c). All these models are used to display metabolic abnormalities such as overweight, diabetic phenotype, insulin resistance, and macro-vesicular steatosis. These symptoms do not lead to spontaneous progression of the liver disease and need additional side intervention by high-fat diet (HFD) or methionine–choline deficient diet (MCD) in animal models [29].

Gap junctions are communicating junctions that are present in almost all cell types, except striated skeletal muscle cells and erythrocytes. Hepatocytes express 2 types of gap junction proteins, the connexins (Cx): gap junction protein, beta 1(*Gjb1*), formerly Cx32 and gap junction protein, beta 2 (*Gjb2*; formerly Cx26). On the other hand, biliary cells express gap junction protein, alpha 1 (*Gja1*, formerly Cx43) [30]. Several strains of genetically modified mice deficient in connexins have been created in order to understand the role of these communicating junctions in liver function, like regeneration and cancer. Transgenic mice expressing a mutated $Gjb1^{V139M}$ under an *Alb* promoter has been generated in order to coexpress *Gjb1* and *Gjb2* in hepatocytes (Figures 15.5 and 15.6). When these mice were submitted to a liver regeneration protocol through 30% partial hepatectomy, it has been verified that the transgenic mice had impaired cell-to-cell communicating capacity and had a delay in liver regeneration. Interestingly, *Gjb1* disappears from proliferating hepatocytes during the peak of liver regeneration (48 hours) [31].

$Gjb1^{tm1Kwi}$ null mice were generated by Klaus Willecke's group [32]. These mice do not express GJB1 and have a low expression of GJB2. They spontaneously develop liver cancer and have a high incidence of liver tumors in DEN hepatocarcinogenesis model [33]. Liver fibrosis was chemically induced by carbon tetrachloride (CCl_4) in *Gjb1*-deficient mice, the major liver gap junction constituent. Collagen (stained with Picrosirius red) morphometric analysis has shown that more pronounced liver damage, and thus enhanced collagen deposition, was observed in GJB1-deficient mice compared to wild-type animals [34], as depicted in Figure 15.7. In addition, the role of *Gja1* heterologous deletion on carbon tetrachloride (CCl_4)-induced hepatic fibrosis in mice was also investigated through the quantification of collagen deposition by histological and ultrastructural analyses. Hemizygous mice for the gene $Gja1^{+/-}$ mice developed excessive liver fibrosis compared with wild-type mice after CCl_4-induced chronic hepatic injury, with thick and irregular collagen fibers [35].

The most relevant GEM models for nonneoplastic liver diseases are described in Table 15.2 and Figures 15.8–15.12.

The most relevant GEM models of neoplastic liver diseases, in particular HCC are presented in Table 15.3. Multiple liver insults including alcohol and metabolic syndrome synergize to accelerate experimental HCC.

A list of mice with constitutive or conditional expressions of genes involved in HCC can be seen in He et al. [43].

Histogenesis of HCC and Other Hepatic Tumors

It is known that HCC is highly heterogeneous in cellular morphology, genetic landscape, and response to therapeutic interventions. There are several hypotheses about the cell(s)

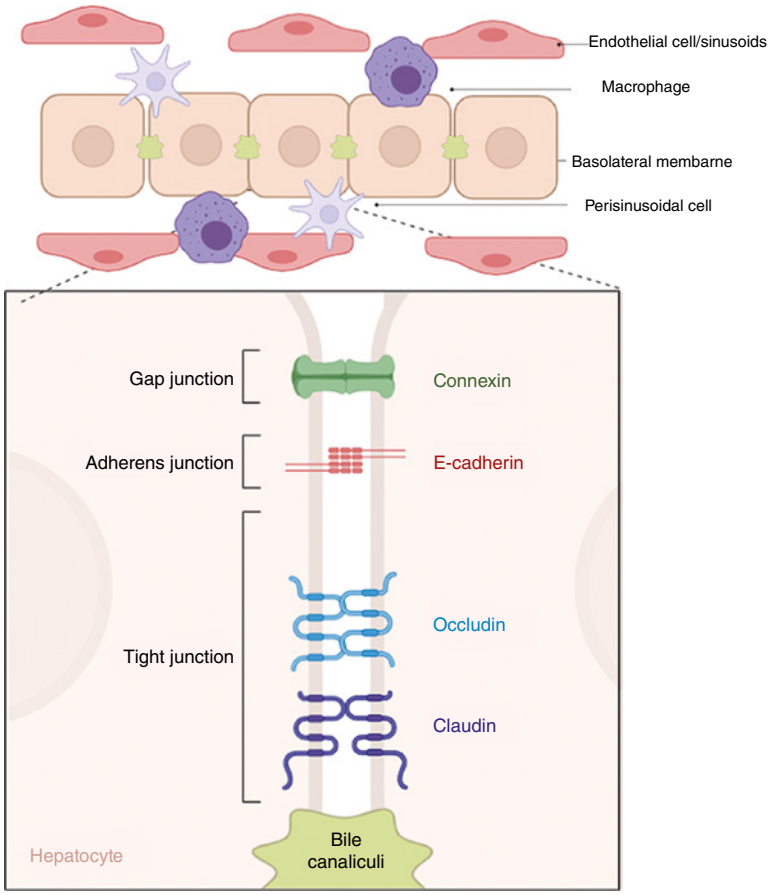


Figure 15.5 **Liver microenvironment**. The liver microenvironment is composed of hepatocyte plates, endothelial cells forming fenestrated sinusoids, perisinusoidal stellate cells, and macrophages (Kupffer cells). Cell junctions between adjacent hepatocytes include gap junctions (containing connexins 32 and 26, *Gjb1* and *Gjb2*), adherens junctions and tight junctions. Source: Created by the author with BioRender.

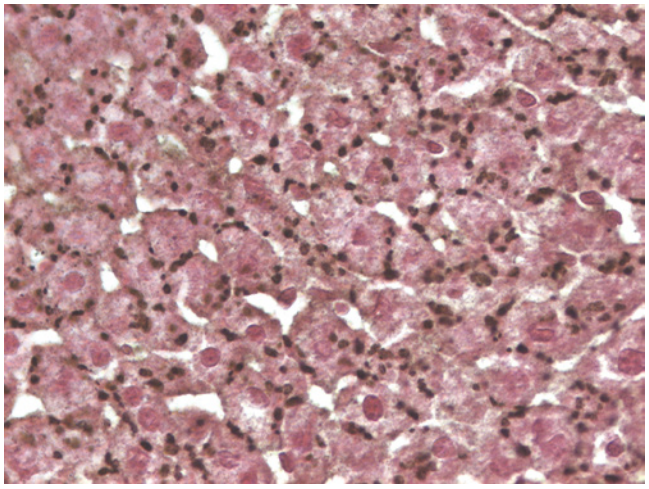


Figure 15.6 **Connexin 32 (GJB1) immunostaining**. Connexin 32 (GJB1) in the liver of transgenic mice expressing a mutant *Gjb1* (Cx 32) only in liver. Anti-Cx 32 antibody and amplification with DAB-Nickel. Source: Maria Dagli [31].

of origin of liver cancer, and hepatocytes and hepatic progenitor cells (HPCs) are the main cellular elements whose malignant transformation could initiate hepatocarcinogenesis.

In general, mouse primary HPCs, lineage-committed hepatoblasts, and differentiated adult hepatocytes were shown to be targetable by oncogenic transformation and to enable tumorigenesis via activation of diverse cell-specific pathways. However, the nature of target cells affected susceptibility to transformation, tumor histopathology, and global gene expression profiles.

Tumors of HCC-like pattern predominantly derived from mature adult hepatocytes underlined that tumorigenic cells keep at least part of the differentiation program typically seen in the original cell, while HPC tumors adopt a more primitive mesenchymal-like state [49].

Genetically modified mouse strains have been helping to understand the possible origin of liver cancer, but there is still a need to gain a much deeper insight into the mechanisms responsible for liver cancer initiation, that is, the cellular origin and progression, propagation and maintenance, in order to facilitate the detection of more reliable tumor markers for diagnostic and prognostic applications, and the development of new targeted therapy approaches for liver cancer [49].

By using human data and hepatocarcinogenesis mouse models, it has been shown [50] that transformed hepatocytes activate HPC expansion. Most evidences go toward the fact that HCC originates from hepatocytes and HPCs can generate benign lesions (regenerative nodules and adenomas) and aggressive HCCs (Figure 15.13).

It is necessary to integrate the morphology to the molecular profiles in rodent liver models in order to understand the role of FCA into the hepatocyte or HPC models.

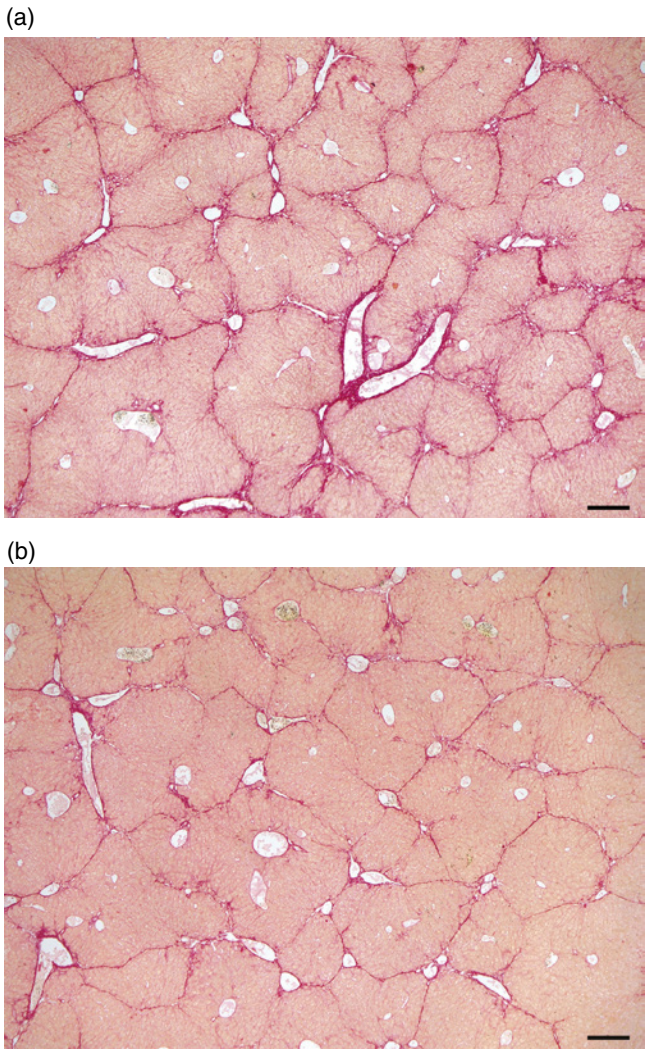


Figure 15.7 **Fibrosis/cirrhosis in mouse livers**. Photomicrograph of the liver of a *Gjb1* (Cx32) KO mouse (a) and wild-type mouse (b) submitted to a cirrhosis model with CCl4. Source: Cogliati et al. [34], *Gjb1* deficient mice (7A) present exacerbated carbon tetrachloride-induced hepatocellular injury and liver fibrosis (when compared to 7B). Picrosirius red staining. Source: Cogliati et al. [34]

The classification of mouse hepatocellular proliferative nonneoplastic, preneoplastic, and neoplastic lesions has been reported in several studies. Examples of preneoplastic hepatocellular foci, adenomas, and carcinomas can be found [18]. Other spontaneous primary tumors in the liver of mice include vascular tumors and histiocytic sarcomas [8].

The classification criteria for proliferative liver lesions are described in Table 15.4. Examples of hepatocellular adenoma (Figures 15.14 and 15.15), HCC developing in an adenoma (Figure 15.16), and lung metastases (Figures 15.17 and 15.18) are illustrated (Figure 15.19).

Induction of Mouse Liver Tumors

A number of mouse models have been developed in order to clarify the pathogenesis of HCC and investigate the effects of potential therapies. Conventional mouse strains differ in susceptibility to spontaneous hepatocellular neoplasia; as mentioned above, C3H mice and CBA mice are recognized as being prone to spontaneous liver tumors, while LP, 129, DBA/2, BALB/c, and C57BL are mouse strains with low incidence of spontaneous hepatocellular neoplasms [43].

The experimental study of liver tumors may require the induction by chemical carcinogens in conventional strains of mice. The DEN-induced hepatocarcinogenesis model is the most frequently used. DEN alone is effective to induce liver cancer in mice. In general, 15-days old male B6C3F1 mice are given a single intraperitoneal (i.p.) injection of DEN in a nontoxic dose ranging from 1.25 to 100 μg/g of body weight, as originally described by Vesselinovitch and Mihailovitch [51], the so-called "infant mouse model." Other doses and protocols using DEN for hepatocarcinogenesis in mice can be found at He et al. [43]. Preneoplastic lesions appear in about 15 weeks and liver tumors appear around 45 weeks after DEN [31]. The DEN infant mouse hepatocarcinogenesis model presents several advantages, since it can easily be administered to mice from different genetic backgrounds and of different genotypes, it induces a high incidence of HCC and is highly reproducible [52]. This model can also be applied to induce HCC in GEM [31].

In addition to DEN, 9,10-dimethyl-1,2-benzanthracene (DMBA) is a chemical carcinogen that can cause a mutation in the oncogene *Ras* when given to neonatal mice and can be used to induce HCC [53].

Overall, chemically induced liver tumors in animals share many of the morphological, histogenic, and biochemical features of human HCC.

Pathways to Human HCC

Since most cases of HCC develop in the setting of chronic hepatic inflammation, such as cirrhosis, ALD, and NAFLD or NASH, in order to fully recapitulate human disease, combination of models of HCC induction with liver disease models can be performed. HBV or HCV, alcohol, and other causes of liver disease (NAFLD or NASH) contribute to approximately 54%, 30%, and 16% of cases leading to HCC, respectively. Several methods of inducing liver diseases through diet, alcohol, inducing fibrosis, or cirrhosis can be found in Brown et al. [53].

Many genetic and epigenetic alterations, chromosomal aberrations, gene mutations, and altered molecular pathways were described. As such, chromosomal alterations could be attributed to certain genes potentially involved in hepatocarcinogenesis, such as *Myc* (8q), *Ccna2* (4q), *Ccnd1* (11q), *Rb1* (13q), *Axin1* (16p), *Trp53* (17p), *Igf2r/M6pr* (6q), *Cdkn2a* (9p), *Cdh1* (16q), *Cish* (16p), and *Pten* (10q) [52]. Further, chromosomal alterations could be described in HCC, of which amplifications of 1q (58–78%), 6p, 8q, 17q, and 20q, and deletions in 4q, 8p, 13q, 16q, and 17p represented the most frequent ones [52].

Some of the pathways involved in human HCC are the following: tumor suppressors genes (*TP53, AXIN1, RB1*), WNT pathway – Catenin Beta1 (*CTNNB1*), chromatin remodeling

Table 15.2 Relevant GEM models for human nonneoplastic liver diseases.

Human disease	Relevant human phenotype	Mouse model	Mouse phenotype	References
Cystic fibrosis	Cholestasis, focal biliary cirrhosis, micro gallbladder, steatosis	*Cftr*^{G551D} mutant	Low-grade steatosis, biliary abnormalities in a small percentage of G551D mice, macro gallbladder	[36]
Autoimmune hepatitis	Progressive destruction, liver fibrosis, elevated aminotransferase levels Interface hepatites, piecemeal necrosis, plasmacytosis, bridging fibrosis	*PD1 KO*	Fatal hepatitis, elevated aminotransferases, piecemeal necrosis, antinuclear autoantibodies (ANA), anti-smooth muscle (anti-SMA) autoantibodies antibodies, periportal antibodies, anti soluble liver antigen (anti-SLA)	[37]
Cholestasis, primary sclerosing cholangitis (PSC)	Peribiliary inflammation, to ductular reaction, myofibroblast activation with intense and early deposition of fibrotic tissue around the inflammed ducts that in the long-term may play pro-tumorigenic functions	*Abcb4* KO	Cholangiopathy caused by a primary defect of a translocase (flippase) expressed not by cholangiocytes, but by hepatocytes at the canalicular pole	[38]
Primary biliary cholangitis (PBC)	PBC liver phenotype-selective destruction of the small interlobular intrahepatic bile ducts, lymphocytic infiltrate in the portal tract, portal fibrosis that may progress to biliary cirrhosis and to end-stage liver disease; presence of anti-mitochondrial antibodies (AMA)	*Congenic NOD. c3c4-scid*	PBC liver phenotype, with periportal infiltrates PBC-specific AMA	[38]
NAFLD, NASH, fibrosis, cirrhosis, portal hypertension	Portal hypertension (PHT), prehepatic (noncirrhotic) PHT is mostly caused by portal vein thrombosis, while intrahepatic (sinusoidal) PHT caused by liver cirrhosis is by far the most common cause of PHT in patients [15]. Cirrhotic and intrahepatic portal hypertension can be induced by bile duct ligation (BDL), intoxication by CCl4, intoxication by thioacetamide (TAA), or by metabolic triggers	No specific gene detected	Cirrhosis by metabolic liver injury • NAFLD/NASH models [39] • Mc4r KO mice model (melanocortin 4 receptor-deficiency) [40] • Srebp KO mice model (Sterol Regulator Element-Binding Protein 1c) • ApoE$^{-/-}$ plus Western Diet • Ldlr$^{-/-}$ targeted mutation of the Ldlr gene encoding the low–density lipoprotein receptor; usually used in combination with high-fat/high-cholesterol feeding	[29]
Bile acid biosynthesis and metabolism	Bile acid biosynthetic defects	Several genes	• Mouse models of bile acid biosynthesis defects *Cyp7a1* knockout mice *Cyp8b1* knockout mice *Cyp27a1, Cyp46a1, Ch25h, Cyp7b1, Hsd3b7, Akr1d1, Amacr, Acox2, Hsd17b4, Scp2, Slc27a5*, and *Abcd3* KO mice • Mouse models to study bile acid transport Nulls – *Ntcp, Oatp, Bsep, Mdr2, Atp8b1, Atp11c, Atp8bq, Atp1x Asbt, Osta*	[41]

(*Continued*)

Table 15.2 (Continued)

Human disease	Relevant human phenotype	Mouse model	Mouse phenotype	References
Neutral lipid mobilization – tryacyl glycerol or steatosis	Steatosis, fatty liver disease	*ATGL, ATGL* co-regulators (*CGI-58, Plin5, G0S2*), *Pnpla3*	Several mouse models	[42]
Cirrhosis	Cirrhosis	*Gjb1 KO* *Gja1 KO* *Gjb2 KO*	*Develop cirrhosis upon treatment with CCl4*	[35]
			Gjb1 KO treated with CCl4 *Gja1* hemizygous treated with CCl4	[34]

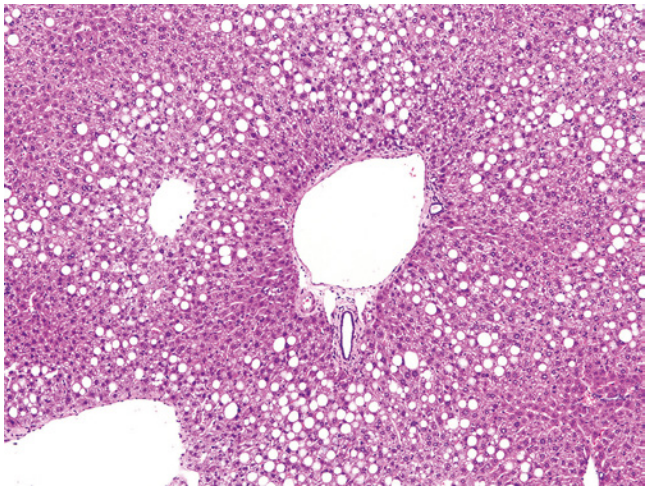


Figure 15.8 **Fatty change in mouse liver**. Fatty change, centrilobular, mouse on a high-fat diet.

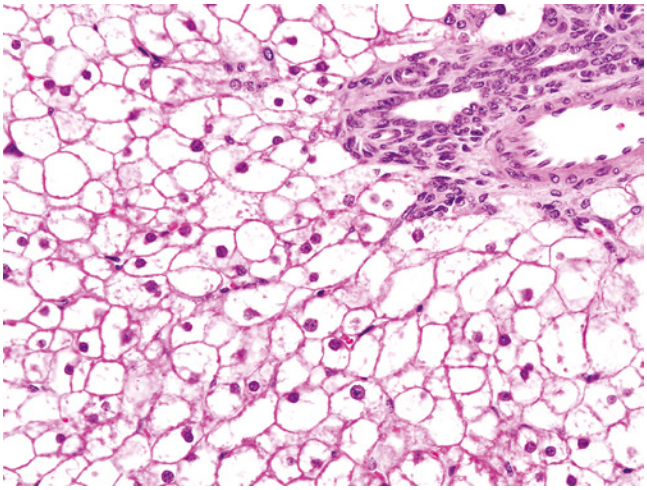


Figure 15.10 **Glycogen in mouse liver**. Glycogen storage disease in the liver of a four-week-old *G6pc*^{tm1lyc} mouse.

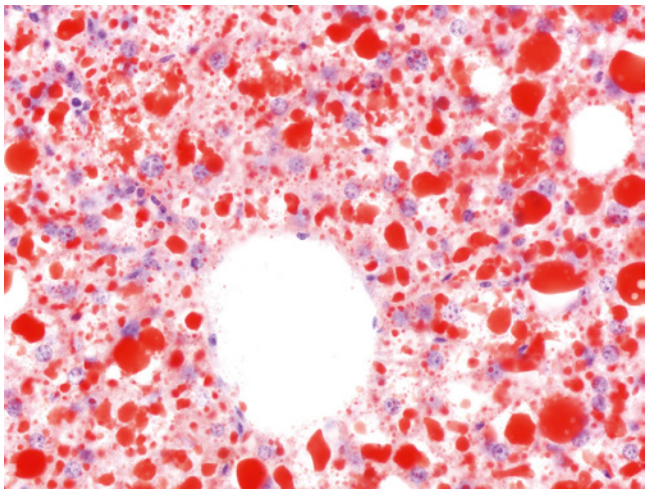


Figure 15.9 **Fatty change in mouse liver**. Fatty change, oil red oil stain, shows abundant fat in hepatocytes of a mouse on a high-fat diet.

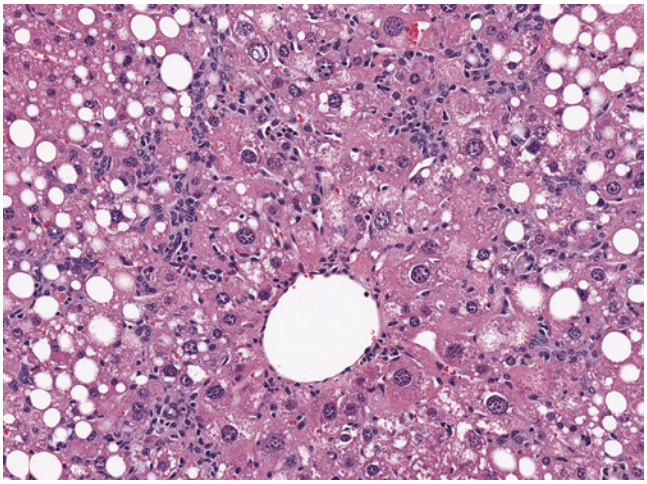


Figure 15.11 **Fatty change and inflammation in mouse liver**. Choline deficient diet, four months, fatty change, and inflammation.

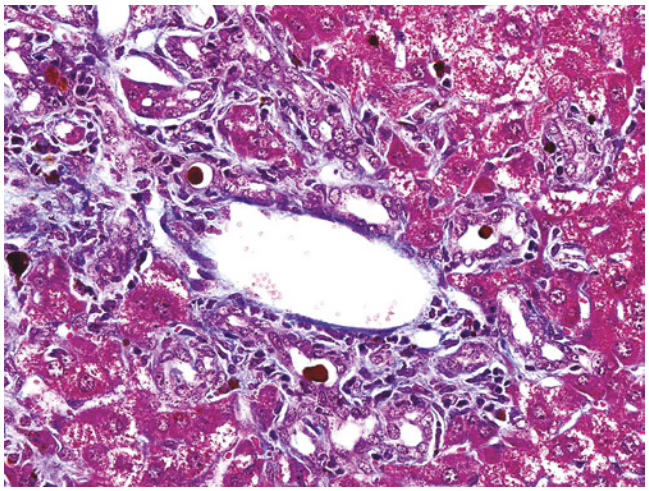


Figure 15.12 **Fibrosis in mouse liver**. Hepatic periportal fibrosis in a mouse model of primary biliary sclerosing cholangitis induced by 3,5-diethoxycarbonyl-1,4-dihydrocollidine (DDC) (Masson's trichrome).

(*ARID1A, ARID2, BAP1*), anti-oxidation (*NFE2L2, KEAP1*), metabolic pathways Afamin (AFM), apoptogenic protein 1, mitochondrial (APOP), oncogenes (*MYC, MET*), TGF beta pathway (Osteopontin) (*SPP1*), G2/mitotic-specific cyclin-B2 (*CCNB2*), cyclin-dependent kinase 1 (*CDK1*), lymphoid enhancer-binding factor 1 (*LEF1*) [53].

Animal models for HCC offer a unique possibility to study mechanistic and cellular aspects of tumor biology, including genetics of tumor initiation and promotion, tumor progression, and spreading (metastasis) *in vivo*.

The spontaneous and chemically induced mouse tumors have molecular profiles related to the etiologic chemical. Recently, Auerbach et al. [54], evaluated mutations in mouse HCC arising either spontaneously or due to chronic chemical exposure through the exome sequencing. Mutational spectra were obtained by examining the trinucleotide context. In order to classify the mutational signatures, the known signatures for mutational processes in human cancers were obtained from COSMIC (https://cancer.sanger.ac.uk/cosmic). Hierarchical clustering based on the

Table 15.3 Relevant GEM models for human neoplastic liver diseases.

Human disease/phenotype	Gene (transgenic or knockout, KO)	Mouse phenotype	References
Hepatocellular carcinoma	***Viral genes of*** Hepatitis B virus, Hepatitis C virus (HBV, HCV)	Hepatocellular carcinoma (also adenomas and preneoplastic lesions)	[43]
	Oncogenes *Myc, E2f1*, *Ctnnb1,Ctnnb1*, and *Hras*		[44]
	Growth factors *Tgfa, Myc Egf, Egf +Myc, Fgf19*		
	Fibrosis and cirrhosis that lead to HCC *Serpina1a, Pten, Pdgfa, Tgfb1*		
Hepatocellular carcinoma and/or adenoma and/or cholangiocarcinoma	*Pten/Tgfr2* *Pten* *Pten/Idh1* *Kras* *Kras/Pten*	Hepatocellular carcinoma Hepatocellular adenoma Cholangiocarcinoma Foci of cellular alterations Oval cells	[18]
Hepatocellular carcinoma	*Gjb1tm1Kw* null mice	Hepatocellular adenoma Hepatocellular carcinoma Other neoplasms: hemangiossarcoma, hemangioma, lymphoma, histiocytic sarcoma	[33] [45] [46]
Hepatocellular carcinoma	*Gib1* transgenic, expressing a mutated *Gjb1* only in liver	Hepatocellular carcinoma Hepatocellular adenoma Foci of cellular alterations Oval cells (Not spontaneous, upon exposure to DEN)	[33]
Hepatocellular carcinoma	Humanized mice (NOD-*Prkdc*^{scid} *Il2rg*$^{-/-}$ (NSG)) bearing Human Hematopoietic Stem Cells, into which HCC cells were orthotopically implanted – PDX humanized mice	Human HCC – PDX model in which human HCC cells were xenotransplanted into NOD-*scid Il2rg*$^{-/-}$ (NSG) mice and in "humice," which have been transplanted with Human Hematopoietic Stem Cells	[47] [48]

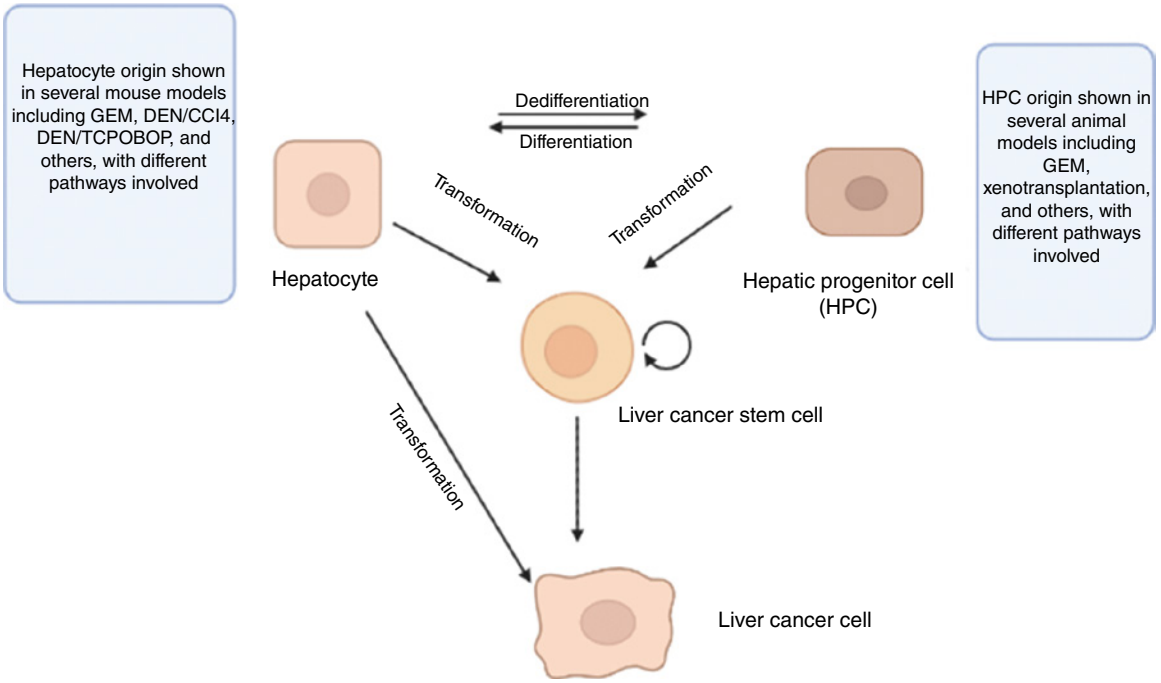


Figure 15.13 **On the origin of liver cancer**. Hepatocyte and Hepatic Progenitor Cells (HPC) are being investigated regarding the origin of liver cancer; however, the pathway seems to converge to a liver cancer stem cell that, when transformed, may generate the liver cancer cell. Source: Created by the author with BioRender, modified from [50].

Table 15.4 Most commonly diagnosed hepatic proliferative lesions found in mice.

Liver proliferative lesion	Characteristics
Hepatocellular hyperplasia	Comprised of slightly enlarged hepatocytes, tinctorially similar to surrounding parenchyma, minimal to mild compression of adjacent parenchyma, lobular architecture maintained
Bile duct hyperplasia	Increased number of small, well-differentiated bile ducts arising in portal region
Cholangiofibrosis	Consisting of dilated to cystic bile ducts filled with mucus and debris, surrounded by inflammatory cell infiltrates and connective tissue, the epithelium is usually single layered, epithelial cells sometimes showed a certain degree of cellular pleomorphism
Oval cell hyperplasia	Single or double row of oval to round cells along sinusoids often forming small ductules streaming into the hepatic parenchyma
Foci of cellular alteration	No or only minimal compression of the surrounding liver tissue, sharply demarcated from the adjacent normal hepatocytes by the appearance and staining reaction of its cells, lobular architecture preserved basophilic, eosinophilic, mixed, clear cell, amphophilic types were described [7]
Hepatocellular adenoma	Nodular lesion compressing (at least on two quadrants) the adjacent normal hepatocytes, sharply demarcated; loss of the normal lobular architecture with irregular growth pattern, liver plates often impinged obliquely on surrounding liver parenchyma
Hepatocellular carcinoma	Local infiltrating growth and/or lack of distinct demarcation, loss of normal lobular architecture, trabeculae with three or more cell-layers
Hepatoblastoma	Unknown but origin from liver blastema cells, neoplastic hepatocytes, oval cells, and biliary epithelial cells proposed
Bile duct adenoma	Uniform and well-circumscribed neoplasm with a single layer of cuboidal cells, growing expansively with compression
Cholangiocarcinoma	Glandular structures lined by single or multilayered cuboidal or cylindrical cells, invading into vascular or lymphatic structures and/or surrounding parenchyma
Hemangioma/hemangiosarcoma	Arises from endothelial cells lining vascular spaces, most commonly of the hepatic sinusoids
Perisinusoidal/Ito cell neoplasm	Arises from fat-storing perisinusoidal cells, so-called “Ito cells.” unicentric or multicentric unencapsulated mass, focal or diffuse accumulation of tumor cells. Differential diagnosis must be done with Ito cell hyperplasia

Source: Modified from Thoolen et al. [8] and Steiger et al. [18].

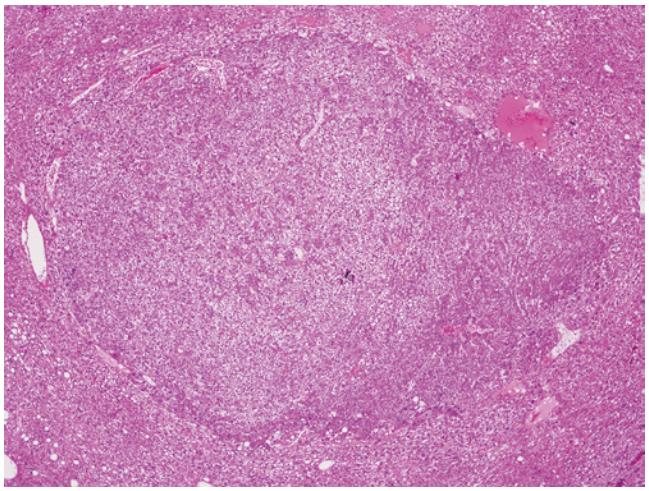


Figure 15.14 **Hepatocellular adenoma, basophilic with clear cells.**

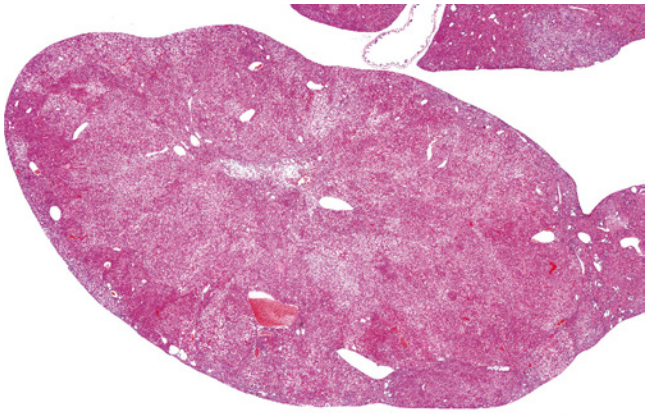


Figure 15.15 **Large hepatocellular adenoma with clear cell and lipid areas.**

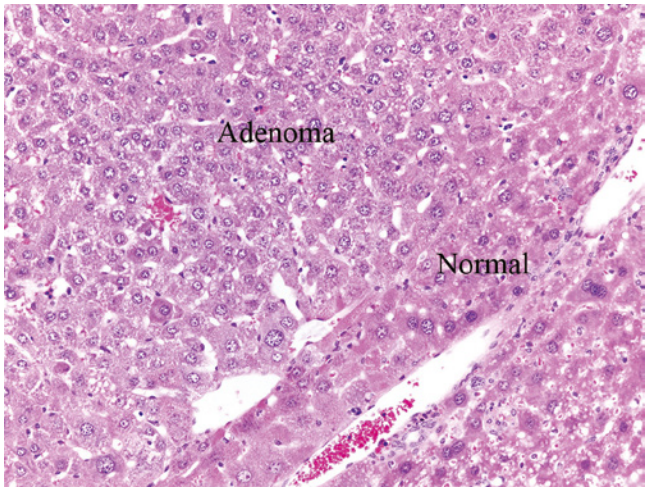


Figure 15.16 **Mouse liver parenchymal compression by adenoma.** Edge of hepatocellular adenoma showing compression of adjacent normal liver parenchyma.

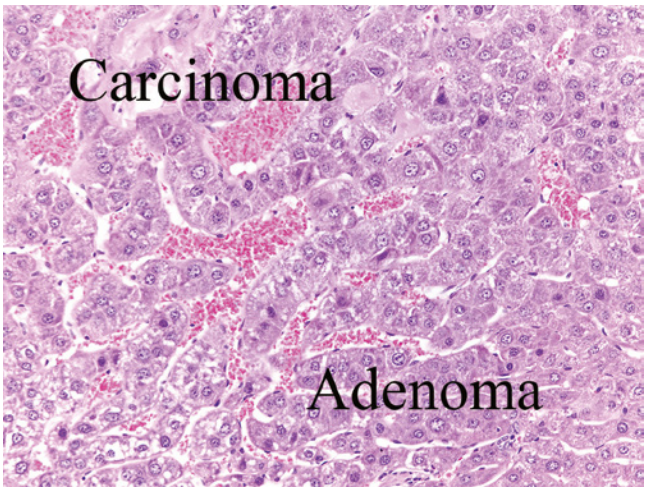


Figure 15.17 **Mouse liver – trabecular hepatocellular carcinoma developing in a hepatocellular adenoma.**

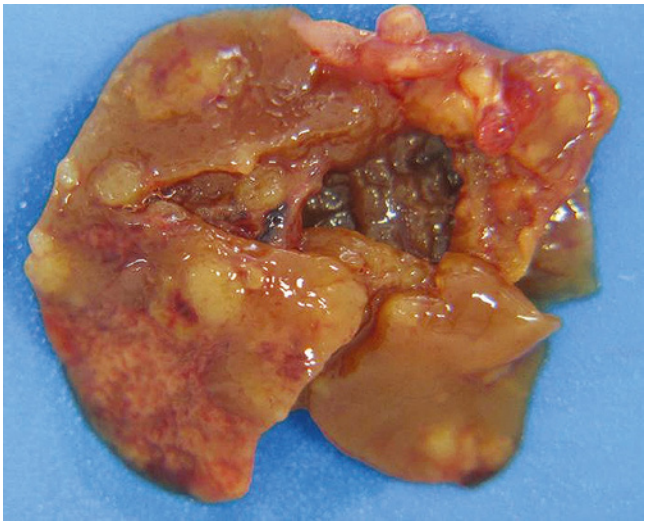


Figure 15.18 **Mouse lung with metastases of hepatocellular carcinoma.**

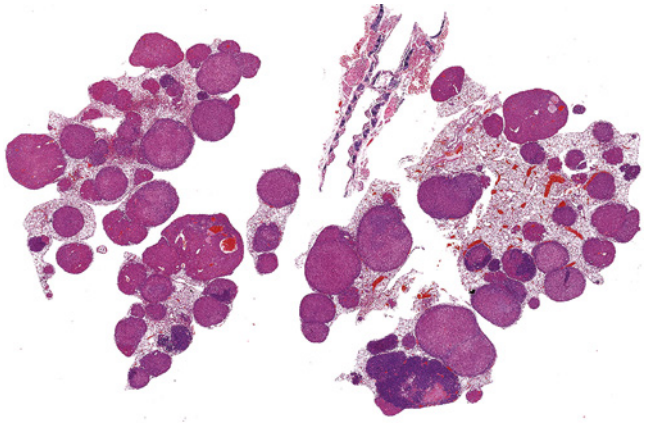


Figure 15.19 **Metastases of hepatocellular carcinoma in lung.** Basophilic areas in metastases are from a liver hepatoblastoma.

Kullback–Leibler distance method was used to compare the mutational signatures in human cancers to the mutational spectra from the mouse HCC FF/FFPE exome sequencing data after accounting for the differences in the trinucleotide composition of the human and mouse exomes. Multiple known (e.g. *Ctnnb1*^{T41A}, *Braf* ^{V637E}) and novel (e.g. *Erbb4*C559S, *Card10*A700V, *Klf11*P358L) mutations in cancer-related genes were identified. This is a novel approach for classifying liver carcinogens and understanding the mechanisms of hepatocellular carcinogenesis.

Humanized Mouse Liver Models for Liver Diseases

In addition to the animal models discussed above, mouse models with "humanized" livers are being used to study several aspects of liver function and pathology. These models are distinct from the GEM where individual or small groups of genes are replaced by their human orthologs. In chimeric or humanized liver mouse models, the population of endogenous mouse hepatocytes are selectively damaged and replaced with human hepatocytes. The approach involves engrafting human hepatocytes from donors with specific features, such as from healthy donors to model normal metabolism or from patients to model different forms of liver disease or from hepatocytes derived from human-induced pluripotent stem cells (iPSCs). In these models, repopulation of the mouse liver with >95% human hepatocytes has been achieved [55].

Genetically Edited Mouse Models for Liver Disease

The study of physiological and pathological processes in liver has gone through several increasingly complex phases. In particular, carcinogens, human tumors-derived cell lines, xenograft tumors, and genetically engineered cellular and animal models have been used for the study of liver cancer. Gene targeting was based on the use of a targeting construct containing target gene sequences to induce homologous recombination (HR) and specific modification, resulting in the introduction, inactivation, or mutation of a specific gene of interest. This technique is more technically difficult than transgenesis and takes longer to perform. It is used to generate knockout (inactivation of a gene) and knockin (insertion or substitution of a DNA sequence).

Genome engineering tools make it possible to edit target genome sequences by adding, replacing, or removing DNA bases [56]. Genome editing relies on the creation of double strand breaks (DSBs) (write out then abbreviate) in DNA, which cells attempt to repair via the homology-directed repair (HDR) pathway or by the error prone nonhomologous-end joining (NHEJ). Gene editing methods that exploit the repair mechanism of the cell (ZNFs, TALENs, and CRISPRs) make it possible to directly manipulate the genome of many different species, including bacteria, plants, fishes, and mammals. Genome editing techniques allow for precise modifications in the genome [57].

The liver is also amenable to somatic genome editing, and some delivery methods already allow for efficient editing in the whole liver. These techniques have expanded the repertoire of animal models available for the study of human liver disease, advancing our understanding of their pathophysiology and providing new opportunities to develop novel therapeutic approaches. CRISPR animal models of human disorders are now available (mouse, rat, or zebra fish) and can be used to study NAFLD, HCC, cholangiocarcinoma, and other diseases [58].

Exocrine Pancreas

Anatomy and Histology

During embryogenesis, the pancreas is formed by fusion of its dorsal and ventral buds originating from the embryonic foregut/midgut junction. In general, the pancreas is an organ with dual function exerted by exocrine and endocrine cell compartment. It is invested by a thin connective tissue capsule and consists of lobules formed by dense accumulations of exocrine glands.

Depending on the species, the pancreas presents as either a "mesenteric" or a "compact" type. The mouse pancreas represents a mesenteric type with a relatively diffuse dispersion of the lobules and segments within the mesentery. Thus, the lobules are separated by abundant mesenteric fat and stromal elements including also lymphoid aggregates [59]. The human pancreas (as the one in pigs, dogs, and other animals) is of the compact type, allowing for a differentiation of distinct regions termed head, neck, body, and tail in humans. The mouse pancreas consists of three lobes – splenic, duodenal, and gastric. It is surrounded by loose connective tissue of the mesentery and divided into lobules by connective tissue septae. Separation between the lobules is commonly seen histologically.

The mouse has a common hepatic (biliary)/pancreatic duct that enters the duodenum in the duodenal papilla. In addition, in mice, there are some large interlobular ducts that open directly into the duodenum [60, 61].

Histologically, the exocrine pancreas is a compound tubuloalveolar or compound acinar gland. Each pancreatic acinus is surrounded by a thin basal lamina, scant reticular stroma, and pancreatic stellate cells (akin to the hepatic stellate cells). Located centrally within the acinus, the centroacinar cells form an interface between the acinus and the intercalated duct. The intercalated duct continues into intralobular ducts formed by the ductular cells. The ducts are lined by cuboidal to columnar, sometimes ciliated epithelial cells with occasional goblet cells in the larger ducts. The intralobular ducts fuse to form the interlobular ducts that finally open into the pancreato-hepatic (biliary) duct [60, 61]. The islets of Langerhans are discussed in Chapter 17, the endocrine. A list of the different cell types

Table 15.5 Useful immunohistochemical markers and their reactivity in different cell types and pathological changes in murine pancreas.

Marker	Cell types	Pathological change	Comment
CK19	Ductal cells, centro-acinar cells	Acinar-to-ductal metaplasia/ PDAC	KRT19 is also expressed in several other nonpancreatic cell lines. Not useful to differentiate liver or lung metastases of PDAC from primary neoplasms at these sites
SOX9	Ductal cells, centro-acinar cells	Acinar-to-ductal metaplasia/ PDAC	
E-cadherin	All epithelial cell types (incl. islets of Langerhans)		Often retained in sarcomatoid PDAC
Amylase	Acinar cells	Expression lost in acinar-to-ductal metaplasia	
CPA1	Acinar cells		
MUC1	Ductal cells	Mucinous metaplastic cells (MTC and PanIN)/PDAC/CPN	
MUC4	Not expressed		
MUC5A	Not expressed		
α-smooth muscle actin	Activated stellate cells	Pancreatitis/PDAC	

and often used (immunohistochemical methods/markers) is provided in Table 15.5.

Latest findings have revealed that different cell types in the pancreas are heterogeneous, and they harbor different plasticity potential, histologically visible as metaplasia. The most relevant event in the exocrine pancreas in the context of mouse models used in research of the exocrine pancreas is the induction of acinar cell proliferation and a switch to a ductal-like progenitor phenotype with ductular morphology (acinar-to-ductal metaplasia, *ADM*) when challenged by inflammation or oncogenic stress. Depending on the severity and type of injury, distinct transcriptional and protein alterations, and epigenetic factors are obvious [62, 63]. In some cases, pancreatic acinar cells even attain an endocrine phenotype. Different terms are used to describe these events, morphologically they should be described as metaplasia.

Notch, WNT, and Hedgehog signaling pathways play important roles in these metaplastic pathways [60, 62].

Necropsy, Trimming, and Embedding

As mentioned above, the pancreas of the mouse has a mesenteric pattern with a fine dispersion of the elements within the duodenal mesentery, making it difficult to accurately collect and weigh completely if there are no pathological changes. In mice, the left lobe of the pancreas, located close to the spleen, represents a major part of pancreatic tissue, and is easier to localize and remove. For routine microscopic evaluation, the left lobe should be cut longitudinally in the horizontal plane, making the cut surface as large as possible. The left lobe can also be embedded together with the spleen. Usually, the pancreatic tissue can be put into cassettes immediately, no separate trimming is necessary. When putting into the cassette, one should make sure, that the pancreatic tissue lies flat on the bottom of the cassette. The right lobe can be removed, fixed, and embedded together with the adjacent small intestine [60, 64]. For a detailed analysis and morphometry (i.e. in experimental models of pancreatitis) the entire pancreas should be carefully dissected free and laid flat on filter paper prior to fixation [65]. For specific research questions on pancreatic diseases, especially in cases of models of neoplastic diseases, location and measures of nodular lesions have to be recorded. In GEM of neoplastic pancreatic diseases, often multiple primary neoplasms occur with multiple nodules in one organ. In such cases, the lesions can be sampled separately (especially if additional tissue needs to be cryofixed or used for other methods) or they should be marked with ink to allow for assignment of histological findings. In addition, larger gross lesions should be examined for evidence of local invasion into adjacent organs (i.e. duodenum, spleen, liver, or kidney). Other distant organs, especially lungs, should be examined for the presence of metastases when a potential neoplasm has been observed in the pancreas. The occurrence of distant metastases especially in liver and lungs should be validated by histology. Usually, hematoxylin and eosin (H&E) staining is sufficient for the first morphological evaluation of the pancreas. For detailed investigation of mucinous metaplasia, PAS reaction or PAS-Alcian blue staining might be useful.

The normal pancreatic weight/body ration is 8×10^{-3} [66].

Aging/Spontaneous Strain-Specific Lesions

Ectopic pancreatic tissue is occasionally seen in the gastrointestinal tract or abdominal cavity [61, 67]. These foci are composed of normal exocrine pancreatic tissue. Spontaneous

exocrine pancreas hypoplasia has been reported in C3HeB/FeJ and 101/H mice [68]. *Depletion* of exocrine pancreatic zymogen granules is a common finding in mice with concurrent inanition. *Atrophic change*s are among the most commonly occurring degenerative changes in the aging mouse pancreas [61, 67]. Atrophy can be focal, lobular, or diffuse. There is a reduction in the size and number of acini, occasionally accompanied by an inflammatory infiltrate. In early exocrine atrophy, the reduction in the cytoplasmic content of the acini, and the more basophilic appearance, can give the impression of ductular hyperplasia. As atrophy becomes more extensive, the acini are replaced with adipose tissue, and in extensive atrophy, only normal islets are left embedded in an adipose tissue stroma. The etiology of exocrine atrophy is unclear. *Acinar foci of cytological alteration* with basophilic or eosinophilic appearance are occasionally seen in the pancreas [61, 67]. Pancreatic *cysts* can appear in the interlobular ducts or as ectatic intralobular ducts. These cysts are lined with cuboidal to flattened epithelium and can be observed macroscopically. *Hyalinosis* (Figure 15.20) is rare in the larger pancreatic ducts.

Arteritis is occasionally seen in pancreatic vessels, despite an absence of this change in other tissues [69]. The changes observed are typical of those seen in blood vessels throughout the body, with fibrinoid necrosis of vessel walls and a florid inflammatory reaction.

As animals normally age, septal, and parenchymal connective tissue increases, particularly as an accompaniment to spontaneously occurring focal duct dilation and acinar cell atrophy. A higher incidence of spontaneously occurring pancreatic *lipomatosis* has been reported in C3HeB/FeJ and C57Bl6/NTac (especially in females) compared to other mouse strains [70]. Pancreatic lipomatosis in general can occur as an age-associated lesion [71].

Spontaneous *pancreatitis* is not commonly seen in mice and may be an indication of an underlying autoimmune disorder. Spontaneous *hyperplastic* and *neoplastic* lesions of the exocrine compartment are rare in mice. Islet cell hyperplasias are common in some mouse strains (discussed in Chapter 17, Endocrine System). Pancreatic cancer in mice is usually of endocrine and not – as in humans of ductal – origin [61]. Hyperplasia, adenoma, or carcinoma can occur in the acinar as well as in the endocrine compartment.

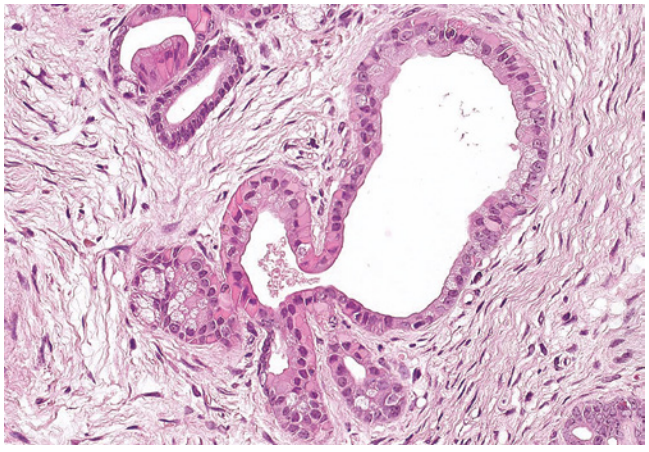


Figure 15.20 Hyaline droplets in pancreatic duct. Hyalinosis in an interlobular duct in a *Ptf1a*$^{tm1(cre)Hnak}$;*Kras*^{tm4Tyi} mouse.

The mouse pancreas frequently contains *leukemic* infiltrates, leukemias, and lymphomas are the most common neoplasm involving the pancreas [61].

Infectious diseases that have been described to involve the mouse pancreas are infections with *Proteus mirabilis, Encephalitozoon cuniculi, Rodentolepsis microstoma*, Mouse Adenovirus 1, and Mouse cytomegalovirus (CMV; Cytomegaly) [72].

Pathology of the Human Pancreas

Human diseases that are frequently investigated by using genetically modified mice are pancreatitis including inherited diseases of the pancreas (i.e. cystic fibrosis) and pancreatic neoplasia and its precursor lesions.

Pancreatitis in human patients is most often caused by gallstones/biliary sludge or excessive alcohol consumption. In critical cases, the mortality rate can range from 5% to 10% up to even 30% depending on the varying degree of disease severity [73]. Acute pancreatitis is a severe condition where the pancreas encounters a sudden and severe form of inflammation, which injures the organ leading to an inappropriate activation of its digestive enzymes in or derived from pancreatic acinar cells. Chronic pancreatitis is a progressive, inflammatory disease of the pancreas that leads to irreversible damage to the organ, histopathologically characterized by pancreatic atrophy, fibrosis, duct alterations, calcifications, and dysplasia [74, 75]. Depending on the etiology, the histomorphology of human chronic pancreatitis differs. Relevant histopathologic parameters are pseudocysts (in alcoholic pancreatitis), the arrangement of the fibrotic lesions (intralobular might be indicative for autoimmune pancreatitis), ductal dilatation or obstruction, and the specific occurrence of the ductal epithelium (degenerated in autoimmune and paraduodenal pancreatitis) [76]. Risk factor for chronic pancreatitis are environmental-toxic ones, as well as autoimmune and genetic factors. GEM for modeling of chronic pancreatitis, therefore, were based on mutations that increased the risk for chronic pancreatitis in human patients, additionally in the last years, further GEMs for chronic pancreatitis were developed with a more mechanistic approach [75] (Table 15.7).

Neoplasms and Other Proliferative Lesions

The 2019 World Health Organization classification of the gastrointestinal system provides the most recent classification of human pancreatic neoplasms [84]. It separates the tumors in *epithelial* (including exocrine and neuroendocrine tumors) and *nonepithelial* neoplasms and subtypes them according to their biological behavior in benign, premalignant, and malignant.

Nearly 90% of adult pancreatic neoplasms are pancreatic ductal adenocarcinoma (PDAC) [84] (Figure 15.21), but other malignant neoplasms (acinar cell carcinoma, solid pseudopapillary tumors, and pancreatoblastoma) also exist. There are several morphological subtypes of human PDAC (i.e. medullary, adenosquamous (Figure 15.22), colloid, hepatoid, rhabdoid, and others) with prognostic and molecular differences (Table 15.6).

The most frequent gene mutations in human PDAC are (somatic) oncogenic point mutations of *KRAS* on codon 12, 13, or 61 (and *Kras* mutations are also frequently used in GEM). The tumor suppressor gene *CDKN2A* (P16) is inactivated in about 95%, the *TP53* gene in 75%, and *SMAD4* (DPC4) in 55% of pancreatic carcinomas.

In addition to these four major and most frequent driver mutations, many genomic alterations are observed at a lower frequency in pancreatic cancer. Alterations in germline *BRCA* and *PALB2* are detected in approximately 5–9% of patients with PDAC and can lead to homologous repair deficiency (HRD) which is currently discussed as a predictive diagnostic criterion in several human cancers.

The major genetic alterations, their major occurrence (somatic or germline) and their correlation to different PDAC subtypes are depicted in Table 15.6.

Human pancreatic cancer develops from preinvasive neoplasms, typically pancreatic intraepithelial neoplasia (PanIN) (Figure 15.23), although intraductal papillary mucinous neoplasia (IPMN) and mucinous cystic neoplasms (MCN) can also give rise to adenocarcinoma [90]. The majority of pancreatic adenocarcinoma is of ductal morphology and contains a prominent desmoplastic component Oncogenic *KRAS* mutations – typically in codon 12, 13, or 61 – are found in 90% of human tumors, and they appear in early PanIN [91]. The accumulation of additional inactivating driver mutations in *P16/CDKN2A*, *TP53*, and *SMAD4* occurs with high frequency in later-stage PanIN, and these mutations are likely required for tumor progression to invasive adenocarcinoma. Microsatellite instability can also occur; however, it is more common in colloid and medullary variants [92].

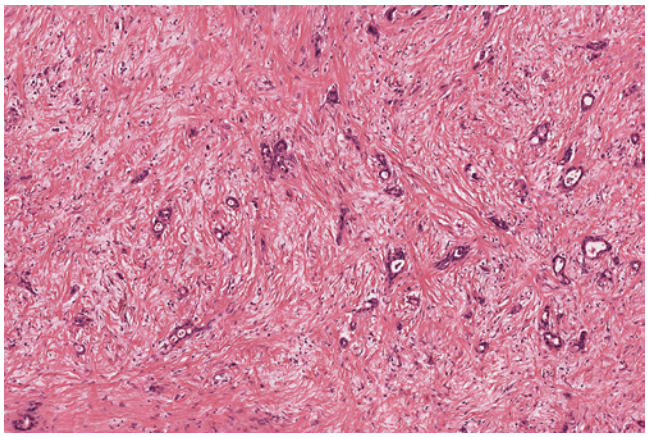


Figure 15.21 **Human PDAC**. Human PDAC showing ductal morphological and extensive desmoplasia.

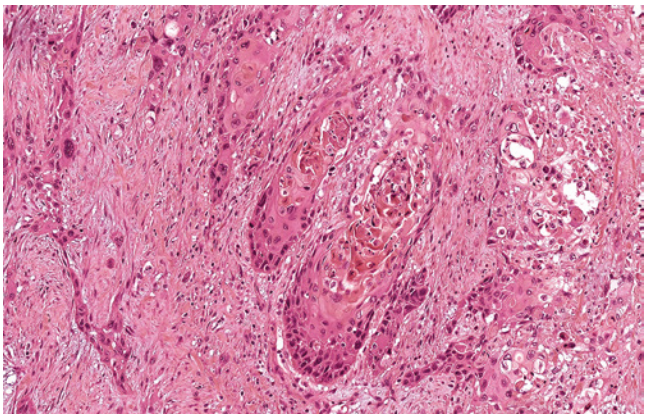


Figure 15.22 **Human PDAC – adenosquamous variant**. Adenosquamous variant of human PDAC.

Table 15.6 Major genetic alterations, their type of mutation, and their occurrence in specific pancreatic ductal adenocarcinoma (PDAC) subtypes.

Gene	Type of mutation	Subtype/variant	References
KRAS	Somatic	All (not in medullary variant)	[84]
TP53	Somatic	All	
SMAD4	Somatic	All	
CDKN2A	Somatic	All	
ATM	Germline	n.a.	[85]
BRCA1, BRCA2	Germline	n.a.	[86]
ARID1A		n.a.	[87]
GNAS	Somatic	Colloidal (also often mutated in IPMN)	[88]
MLH1, MLH2, PMS2, MSH6	Germline	Medullary	[84]
POLE	Somatic	Medullary	[89]

n.a. = not available.
Source: Based on Merry and Petrov [83].

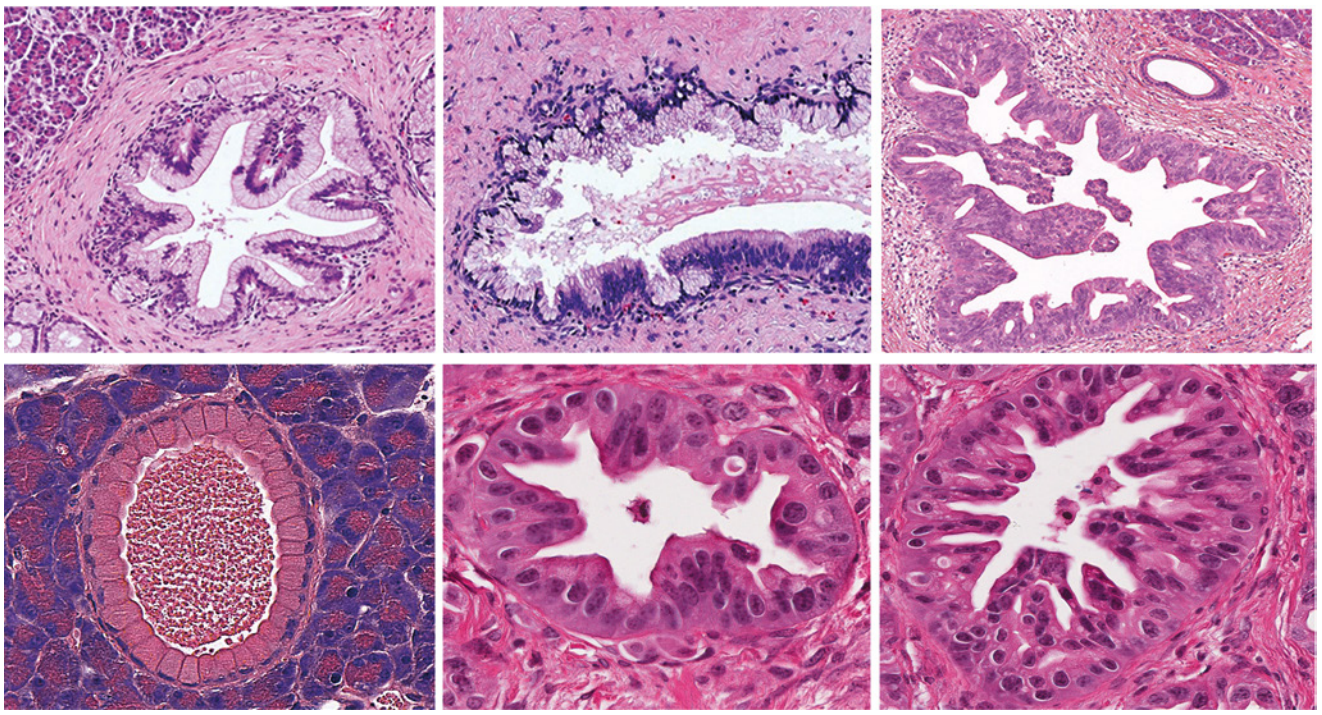


Figure 15.23 **Human and mouse PanIN**. From left to right: PanIN1, 2 (both now low grade) and 3 in human (upper row) and *Ptf1a*$^{tm1(cre)Hnak}$;*Kras*^{tm4Tyi} mice (lower row).

Familial and Hereditary Pancreatic Cancer

Pancreatic carcinomas arising in the context of familial pancreatic cancer (i.e. patients with PDAC having at least two first-degree relatives with confirmed PDAC and who do not fulfill the criteria of other inherited tumor syndromes) or another hereditary syndrome are usually conventional ductal adenocarcinomas and are indistinguishable from sporadic PDAC. It has been shown that familial and hereditary PDAC is associated with the appearance of multiple precursor lesions, including PanINs with low-grade or rarely high-dysplasia, and IPMNs, which in some cases are so numerous that they can even be appreciated grossly [93, 94]. Most of the IPMNs are small side-branch lesions of gastric type [95] and show high-grade dysplasia in up to one-fourth of the cases [96]. These precursor lesions are often associated with so-called "lobulocentric atrophy" of the pancreatic parenchyma, characterized by lobular fibrosis with loss of acinar tissue and slight inflammation. These findings may provide a basis for screening of patients at risk, because the patchy heterogeneity of the pancreatic parenchyma may be detected by endoscopic ultrasound [93, 97, 98].

Risk Factors of PDAC

Epidemiological studies point to several risk factors for developing pancreatic cancer. The best-known risk factor is tobacco smoking with a two to three times risk compared to nonsmokers. Also nutritional and dietary factors (i.e. obesity, low physical activity, high intake of saturated fats, and low intake of vegetables and fruits) have been suggested to be related to pancreatic cancer. Heavy alcohol consumption seems to have a weak effect on the development of pancreatic neoplasms [84]. Patients with chronic pancreatitis owing to protease, serine 1 (*PRSS1*) or serine peptidase inhibitor, Kazal type 1 (*SPINK1*) mutations have a well-documented increased risk of developing pancreatic cancer [99]. About 10% of PDAC cases in humans occur in familial clusters [100]. In this context, few major PDAC risk genes have been identified, including the tumor suppressors *CDKN2A* and *BRCA2* that are frequently altered during "sporadic" PDAC progression. These genes have also been validated as familial PDAC susceptibility genes in genetically engineered mouse models [101, 102], but they only account for a minority of familial PDAC cases. Additional risk alleles of lower penetrance, but more widespread in the population have been identified by genome wide-association studies (GWAS). With these agnostic gene-mapping approaches conducted in large numbers of case and control subjects, until today, 26 pancreatic cancer risk loci have been identified reaching genomewide significance in at least one study [103]. The relevance for the development of pancreatic cancer of some of these genes (as *NR5A2*) has also been validated in genetically engineered mouse models.

Chronic pancreatitis (which often occurs in connection with heavy alcohol use and smoking) is linked with an increased risk of pancreatic cancer. Other epidemiologically identified risk factors are obesity and type-2 diabetes which might promote PDAC through elevated systemic inflammation [104]. Additional risk factors for PDAC development are cigarette smoking [105] and periodontal disease [106].

Interestingly, exposure to pesticides, asbestos, benzene, and chlorinated hydrocarbons may increase the pancreatic cancer risk in humans [107], but chemicals as *N*-nitrosobis(2-oxopropyl)amine (BOP) or DMBA do not or only by direct implantation of the carcinogen into the pancreas induce precursor lesions or PDAC in mice [108, 109]. Of note, Syrian hamsters were a well-recognized PDAC model before genetically engineered animals became widely available by using a single injection of BOP inducing PDACs in up to 90% of the animals [110].

Genetically Engineered Mice

As mentioned above, the two major entities in the exocrine pancreas that are modeled by using GEM are pancreatitis and pancreatic cancer (usually not only targeting PDAC modeling but also other neoplastic alterations of the mouse pancreas can occur).

GEM for Inflammatory Lesions of the Pancreas

In animal (mostly rodent) models, the *inflammatory change of the pancreas* is most often induced by various chemical or surgical strategies [111], but genetically modified animals of pancreatitis also exist (Table 15.7). A detailed review on these models has been published by Merry and Petrov [83]. The most commonly used genes to drive expression in GEM of pancreatic diseases are summarized in Table 15.8.

Often, tissue-based grading of the occurring changes is used not only as the gold standard for validation of the model system but also for evaluation of therapeutic efficiency. Therefore, a lot of semiquantitative histopathological scoring systems have been developed and applied and are requested from the comparative pathologist on a regular base. All available scoring systems for application in acute pancreatitis are based on the first one from Schmidt, Rattner [113]. It uses five parameters: edema, acinar necrosis, hemorrhage, fat necrosis, inflammation, and perivascular infiltrate. Other scoring systems usually have been modified only marginally with the omission of a single parameter or including acinar cell vacuolization as an additional parameter. Besides

Table 15.8 Common genes used to drive expression in genetic models of exocrine pancreatic diseases.

Gene	Common expression systems	Target cell population(s)
Pdx1	Cre CreERT	Acinar, ductal, endocrine, centro-acinar
Ptf1a (syn. *bHLHa29, Ptf1-p48*)	Cre CreERT	Acinar, ductal, endocrine, centro-acinar
Nestin	Cre	Acinar, acinar progenitor
Elastase-1 (*Cela1* as in Tg(*Cela1*-cre/ERT)^{1Lgdn} animals or using a rat elastase gene promoter)	Cre CreERT2 tTA	Acinar
Cpa1	CreERT2	Acinar
Bhlha15	CreERT2	Acinar

Source: Modified from Saloman, Albers [112].

Table 15.7 Mouse models of human hereditary pancreatitis.

Human/mouse gene or mutation	Gene function	System	Tissue/cell target	Pancreatic phenotype	Type of pancreatitis
PRSS1/Prss1 [77, 78]	Trypsinogen production	Different variants available (transgenic expression of human or mouse R122H or N921 variant)	Pancreatic acinar cells	Acinar cell vacuolization, fibrosis, apoptosis (no pancreatic atrophy)	Chronic pancreatitis
PRSS1/Tg(CAG-GFP,-*Prss2**)$^{\#Bji}$ [79]	Trypsinogen activation	Cre/lox; elastase CreErT	Pancreatic acinar cells	Inflammation, edema, acinar cell injury	Acute pancreatitis
PRSS1/2210010C04Rik $^{tm1.1Satom}$ [80]	Trypsin activation	Knockin	Global	Inflammation, edema, acinar cell loss, lipomatosis	Acute and chronic pancreatitis
SPINK1/Spink1^{tm1Kymm} [81]	Pancreatic trypsin inhibitor	Knockout	Global	Acinar cell autophagy, nuclear chromatin disruption, acinar cell vacuolization	Acute pancreatitis
CPA1.pN256K/Cpa1$^{tm1.1Satom}$ [82]	Carboxypeptidase enzyme	Knockin	Global	Acinar cell atrophy, inflammation, fibrosis, and ADM	Chronic pancreatitis

Source: Selected from Merry and Petrov [83].

pancreatic evaluation (edema, inflammatory infiltration, parenchymal necrosis, and hemorrhage), some authors also assessed the liver, kidney, and lung for histological changes to compare these events to the systemic disease occurring in some human patients [114]. However, an accepted severity scoring related to the revised Atlanta Classification for human patients [115] is not available for mouse specimens.

Parameters used for semiquantitative scoring of chronic pancreatitis in mouse models include inflammatory cell infiltration, intensity of stromal fibrosis, and extent of acinar loss [116]. Other authors use glandular atrophy, presence of "pseudotubular complexes" (i.e. [mucinous] tubular complexes), and fibrosis as semiquantitative parameters and take the area of affected parenchyma into account [117]. Spatial allocation with respect to the major compartment affected by fibrosis or inflammation is usually not performed. Thus, a comparison of histopathological changes in pancreatitis in a degree of granularity as in human pathology is not common. Genetically engineered mouse models of pancreatitis, for example used not only on targeted mutations in *Cftr*, *Krt8/18*, *Lt*, *Mrl*, *Perk*, *Ctnbb1*, *E2f*, and *Itgb1* but also several GEM of pancreatic cancer (i.e. *Kras* based) also develop pancreatic changes comparable to chronic pancreatitis.

GEM for PDAC

Efforts to model PDAC via carcinogen treatment have produced robust success only in the Syrian hamster, where a single injection of the mutagen BOP induces invasive PDAC in up to 90% of animals. In mice, only direct implant of carcinogens into the pancreas induces pancreatic neoplasms [109]. Thus, mechanistic-functional studies of PDAC development in a larger scale were only possible after successful development of GEM of PDAC.

Genetically engineered mouse models of PDAC are mainly based on expression of a mutant KRAS which corresponds to the by far most frequent and "earliest" human genetic alteration, a mutation in the *Kras* gene. This is usually modeled by a targeted mutation (i.e. $Kras^{tm1Bbd}$ or $Kras^{tm4Tyj}$ and others), usually as a loxP-Stop-loxP construct or (in earlier publications) as a transgenic insertion of the human *KRAS* gene usually with a point mutation in codon 12 (G→D or G→V). Interestingly, targeted models using the duct-specific Cytokeratin-19 or the acinar-specific Elastase 1 promoter were not successful. *Krt19-KRASG12V* transgenic (Tg(*Krt19-KRAS**G12V)^{Aaru}) animals develop only mild inflammation, no cancer or dysplasia [118]. *Ela1-KRAS*^{G12D} (Tg(*Ela-KRAS**G12D)^{9Eps}) mice exhibit premalignant lesions of a mixed acinar and ductal phenotype [119]. These last findings showed that duct-like tumor precursors in mice might arise from acinar cells [120]. The majority of published PDAC mouse model experiments use strains in which *cre*-recombinase is expressed in multipotent progenitor cells of the embryonic pancreas. These are *Pdx1-cre* (often used: Tg(*Pdx1*-cre)^{6Tuv}, Tg(*Pdx1*-cre)^{6Cvw} or Tg(*Pdx1*-cre)$^{89.1Dam}$, and others) and $Ptf1a^{cre}$ (often used: $Ptf1a^{tm1.1(cre)Cvw}$ or $Ptf1a^{tm1(cre)Hnak}$). But also models with adult or inducible recombination in specific cell types (for example Tg(*Sox9*-cre/ERT2)^{1Msan} in ductal cells or Tg(*Cela*1-cre/ERT)^{1Dam} and $Ptf1a^{tm2(cre/ESR1)Cvw}$ in acinar cells) and inducible models using a tetracycline-responsive promoter element (Tg(tetO-*Kras2*)^{12Hev}) exist [121]. It should be noted, that all models based on purely mutant KRAS expression mostly develop pancreatic remodeling with extensive *ADM* and PanIN (Figures 15.23–15.26) starting after birth/some months of age, invasive carcinoma usually occur late and not with full penetrance.

The development of mouse PDAC is dramatically accelerated when additionally a heterozygous or homozygous mutation (or a knock-out) in a tumor suppressor gene (i.e. *Cdkn2a*, *Trp53*, *Smad4,* or *Brca2*) is introduced [120]. PDAC development can also be accelerated by adding an inflammatory reaction, for example by Cerulein injections.

Morphologically, the criteria defined for GEMs of PDAC by Hruban and Adsay [122] follow the human classification, underscoring the close similarities of the lesions on the morphologic level. Mouse (mPanIN), as their human counterparts, is noninvasive lesions graded according to their degree of dysplasia. PanIN always occur in the setting of a preexisting interoder intralobular duct. Morphologically, they cannot be differentiated from mucinous tubular complexes which occur in the context of *ADM* with subsequent mucinous metaplasia (Figures 15.24–15.26). At least in mice, PDACs may not only develop from ductal progenitor cells via PanINs or CPNs (cystic papillary neoplasms, see below), but also or predominantly from *ADM* lesions [123–125] that convert into ductal structures referred to as tubular complexes [126]. *ADM* is characterized by a loss zymogen granules and a loss of expression of acinar markers, such as chymotrypsin, carboxypeptidase A1 and amylase, as well as an increased expression of ductal markers such as KRT19 [127–129] (Table 15.5). In 2012, also the term acinar-to-ductal reprogramming (ADR) has been introduced [130], which refers to the acinar induction of the ductal gene *Sox9*. Morphologically, this cannot be distinguished from the (often-reversible) *ADM* that is observed in pancreatitis models. The processes of *ADM* and *ADR* in mouse models of pancreatic cancer have been reviewed in detail by Murtaugh [120].

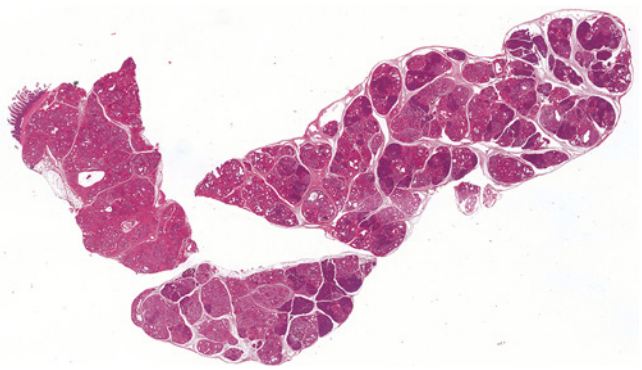


Figure 15.24 **Pancreatic remodeling**. Remodeling of the acinar compartment of the pancreas in a $Ptf1a^{tm1(cre)Hnak}$;$Kras^{tm4Tyj}$ mouse six months of age.

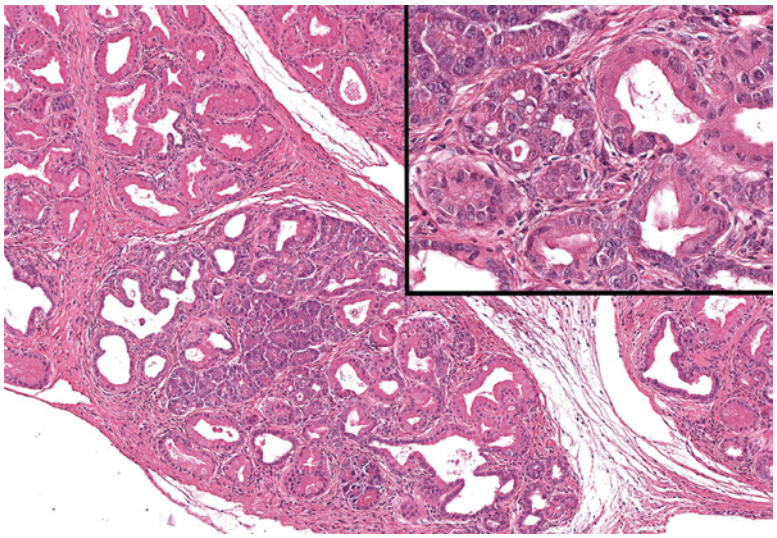


Figure 15.25 **Acinar-to-ductal metaplasia**. The acinar cells of the mouse of figure 5 undergo acinar-to-ductal metaplasia with loss of zymogen granules (inset) and switch to a ductal morphology with sometimes mucinous metaplasia.

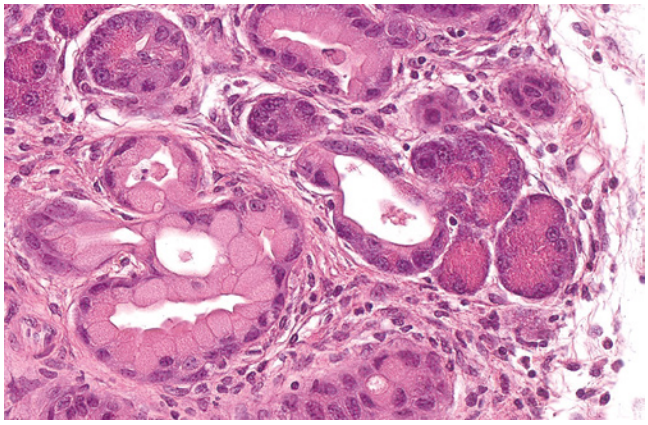


Figure 15.26 **Acinar-to-ductal and mucinous metaplasia**. Acinar-to-ductal metaplasia (right) and mucinous metaplasia of these metaplastic ducts (left, mucinous tubular complexes).

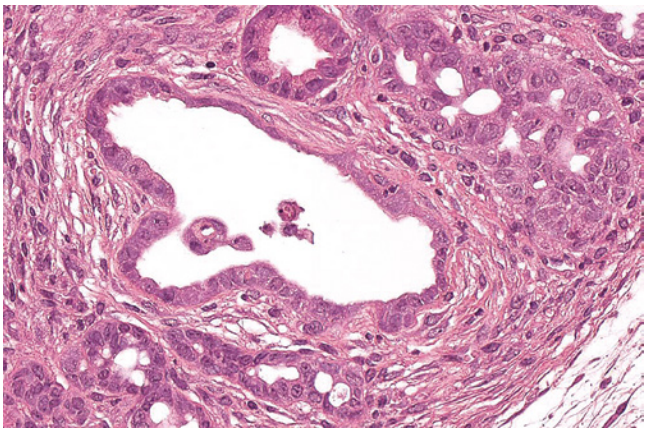


Figure 15.27 **Atypical flat lesion**. Atypical flat lesion (AFL) (center) adjacent to an early invasive carcinoma (upper right) in a *Ptf1a*$^{tm1(cre)Hnak}$;*Kras*^{tm4Tyi} mice.

Atypical flat lesions (AFL*s*) are recently described microscopic (<0.5 cm) mostly nonmucinous tubular structures [123, 131] arising in areas of lobulocentric atrophy in association with ADM and often bearing *KRAS* mutations [132] (Figure 15.27).

AFLs are therefore discussed as another precursor lesion of PDAC and seem to represent the link between ADM and ductal carcinogenesis. Presently, AFLs have been found in human familial pancreatic cancer, but their existence in sporadic PDAC remains to be shown. In GEM of PDAC, ductular-insular complexes (Figure 15.28) can occur which should not be identified as PanIN or PanIN-like lesions [122].

Grading of PanIN in mice has been done comparable to human PanIN (PanIN1A, 1B, 2, and 3) [122] but should now be adopted to the new, simplified grading of human PanIN (low grade and high grade, with previous grade 1 and 2 being low grade and grade 3 being high grade) [133] (Table 15.9).

Invasive ductal adenocarcinoma in mice are composed of well to poorly developed glandular and duct-like structures

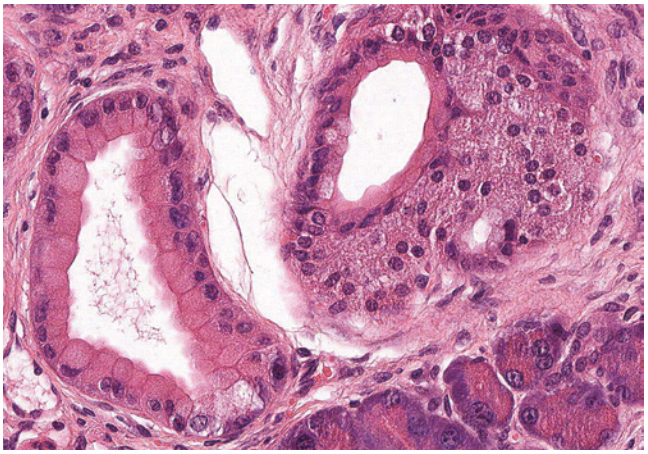


Figure 15.28 **Ductular-insular complex**. Ductular-insular complex (right) and low grade PanIN in a *Ptf1a*$^{tm1(cre)Hnak}$;*Kras*^{tm4Tyi} mouse.

Table 15.9 Classification and grading of mouse and human pancreatic intraductal neoplasia (PanIN and mPanIN).

Mouse classification [122]	Human classification [133]	Morphology
Normal duct	Normal duct	Flat, cuboidal, or low-columnar epithelium without mucin accumulation, nuclear crowding or atypia
PanIN 1A	Low-grade PanIN	Tall columnar cells, organized in flat epithelium, with basal nuclear localization and mucin-rich cytoplasm
PanIN 1B	Low-grade PanIN	Identical cellular morphology to PanIN 1A, but organized in papillary, micropapillary, to basally pseudostratified arrangements
PanIN 2	Low-grade PanIN	Flat or (more commonly) papillary architecture, with nuclear abnormalities that may include loss of polarity, crowding, enlargement, pseudostratification, and hyperchromatism. Mitoses are rare, and if present, are not atypical
PanIN 3	High-grade PanIN	Papillary or (less commonly) flat architecture, with loss of nuclear polarity, dystrophic goblet cells, occasionally abnormal mitoses, and prominent nuclear abnormalities. Cribriform architecture or luminal "shedding" of viable or necrotic cells frequently observed. Resemble carcinoma at the cytonuclear level, but invasion through the basement membrane is absent

expressing KRT19 and mucins [122], and are also associated with a fibroinflammatory response. They should be graded using the criteria that are applied to human cancers [122]. Briefly, well-differentiated adenocarcinoma form well-defined glands with only minimal nuclear pleomorphism. Moderately differentiated adenocarcinoma show a disorganized growth pattern and a less well-defined gland formation with more prominent nuclear pleomorphism (Figure 15.29). Poorly differentiated adenocarcinomas form small poorly defined glands, individual infiltrating cells and solid areas (Figure 15.30). In general, mouse PDAC do not show mucin production as frequently as human PDAC do (at least aborted). Subtypes or variants of PDAC that have been described in GEM are mainly the undifferentiated ones, with a variety of appearances. Especially sarcomatoid PDAC occur quite frequently (Figure 15.31). Anaplastic giant cell carcinomas or carcinomas with metaplastic cartilage or bone

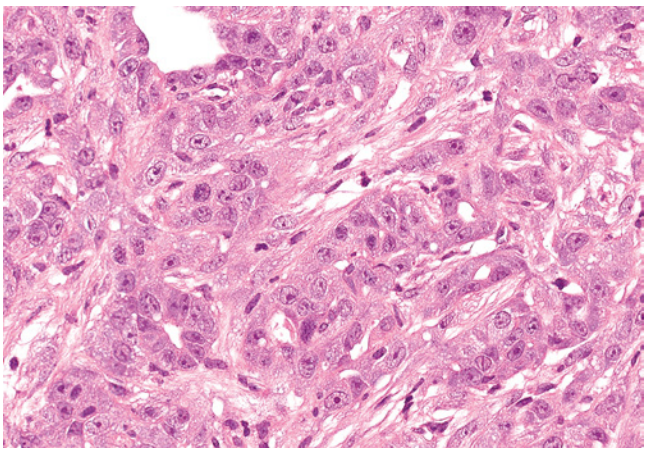


Figure 15.30 **Mouse PDAC G3**. Poorly differentiated PDAC in a Tg(*Pdx1*-cre)^{6Tuv};*Krast*^{m4Tyi}; *Trp53*^{tm1Brn} mouse.

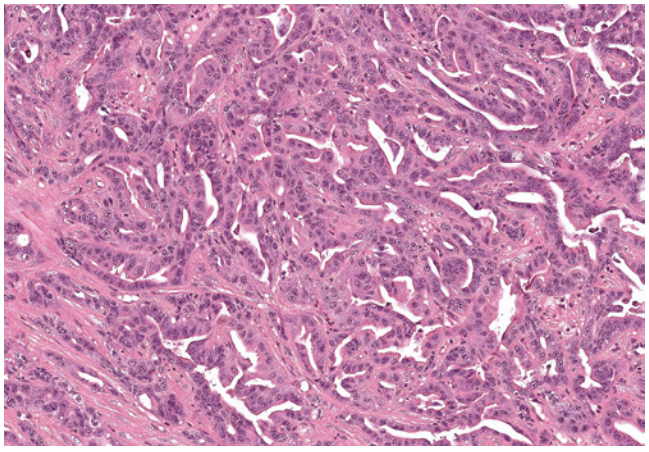


Figure 15.29 **Mouse PDAC G2**. Moderately differentiated PDAC in a Tg(*Pdx1*-cre)^{6Tuv};*Kras*^{tm4Tyi}; *Trp53*^{tm1Brn} mouse.

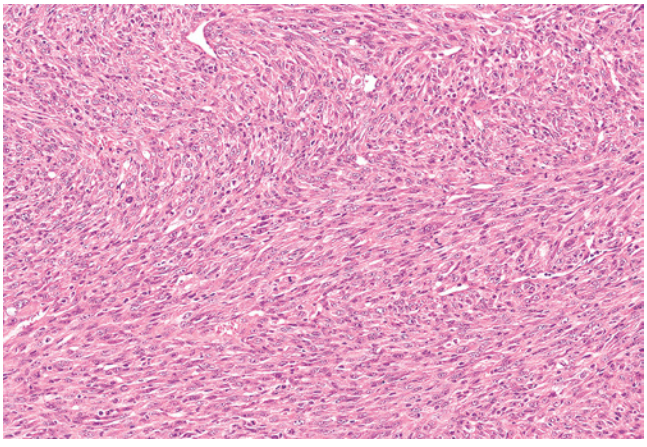


Figure 15.31 **Sarcomatoid mouse PDAC**. Sarcomatoid PDAC in a Tg(*Pdx1*-cre)^{6Tuv};*Kras*^{tm4Tyi}; *Trp53*^{tm1Brn} mouse.

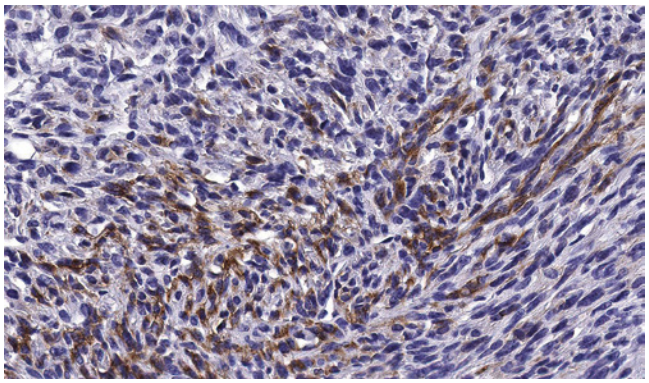


Figure 15.32 E-cadherin expression in sarcomatoid mouse PDAC. Retained E-cadherin expression in 30% of neoplastic cells in a sarcomatoid PDAC in a Tg(*Pdx1*-cre)^{6Tuv};*Kras*^{tm4Tyi}; *Trp53*^{tm1Brn} mouse.

can also be observed. In undifferentiated, anaplastic or sarcomatoid neoplasms, their epithelial and pancreatic origin might be questionable especially in newly introduced genetic constructs. In such cases, immunohistochemistry using an E-cadherin antibody often is still positive even in neoplasms with a distinct mesenchymal appearance (Figure 15.32, Table 15.5). Cytokeratin 19 labeling is often negative in such cases.

Intra- and interindividual heterogeneity of tumor differentiation and growth patterns can be observed in mouse models of PDAC. Grading of PDAC should always refer to the most poorly differentiated part of the neoplasm. Studies with respect to transcriptome signatures of PDAC in GEM revealed distinct expression-based clusters comparable to the subtypes in human patients [134] and with a clearly distinct "mesenchymal" subtype (i.e. undifferentiated neoplasms) and an epithelial subtype which again might consist of two or three different subclusters.

An overview of the most popular GEM and their relevance for the human disease is provided in Table 15.10.

Local invasion of the pancreatic neoplasm into the liver, the diaphragm, spleen, or kidney occurs frequently, tumor cell invasion into blood or lymphatic vessels is rarely visible in the histological specimen (Figure 15.33). Distant PDAC metastases in mice (especially to the liver and the lung) are often reported by researchers based on macroscopic appearance. Histologically, liver metastases of PDAC are sometimes hard to distinguish from cholangiofibrosis (which can occur as a separate entity), for lung metastases (Figure 15.34) the most important differential diagnosis are primary lung neoplasms (Figure 15.35). Here, if not possible on H&E, NKX-2.1 (also known as TTF-1) IHC can be performed to eliminate all doubts.

Table 15.10 Human pancreatic cancer genetics and mouse models of human PDAC.

First alteration	Second/third alteration	Mouse pancreatic phenotype	Human	References
Tg(*Pdx1*-cre)^{6Tuv};*Kras*^{tm4Tyi} and *Ptf1a*$^{tm1.1(cre)Cvw}$;*Kras*^{tm4Tyi}	None	PanIN/late PDAC; G12D (tm4Tyi) slightly more transforming [120]	Most prevalent *KRAS* mutations in human PDAC; G12D with tendency toward lower survival [135]	[136]
Ptf1a$^{tm1.1(cre)Cvw}$;*Kras*^{tm1Bbd}	None			[137]
Tg(*Pdx1*-cre)^{6Tuv};*Kras*^{tm4Tyi}	*Trp53*^{tm2Tyj}	Metastatic PDAC (*Trp53* missense mutation in exon 5)	P53 inactivation has low prognostic impact in human PDAC [135]	[138]
Tg(*Pdx1-cre*)$^{89.1Dam}$;*Kras*^{tm4Tyi}	*Trp53*^{tm1Brn}	Accelerated PDAC development (*Trp53* floxed)		[101]
Tg(*Cela1-tTA*)$^{\#Eps}$; *Kras*^{tm1Bbd}	*Trp53*^{tm1Brd}	Metastatic PDAC		[139]
Tg(*Pdx1-cre*)$^{89.1Dam}$;*Kras*^{tm4Tyi}	*Cdkn2a*^{tm4Rdp}	Undifferentiated PDAC	Loss of P16 expression is associated with poorer survival [140]; no genotype-phenotype correlation reported	[141]
Ptf1a$^{tm1.1(cre)Cvw}$;*Kras*^{tm4Tyi}	*Smad4*$^{tm2.1Cxd}$	IPMN derived PDAC	Loss of SMAD4 expression is an independent poor prognostic factor in PDAC [140] and a late event in human IPMN and MCN [142]	[141, 143]
		MCN derived PDAC		[144]
Tg(*Pdx1*-cre)^{6Tuv};*Kras*^{tm4Tyi}	*Brca2*^{tm1Cam} and *Brca2*^{tm1Brn}	Slightly accelerated PDAC development	Model for familial PDAC	[102]
	Trp53^{tm3Tyi}; *Brca2*^{tm1Cam} and *Trp53*^{tm3Tyi}; *Brca2*^{tm1Brn}	Accelerated PDAC development		

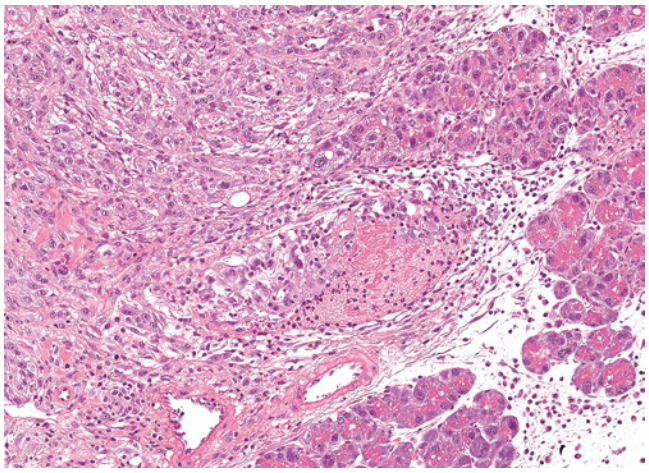


Figure 15.33 **Intravascular tumor cells**. Tumor cell invasion into an intrapancreatic venule in a Tg(*Pdx1*-cre)^{6Tuv};*Kras*^{tm4Tyi}; *Trp53*^{tm1Brn} mouse.

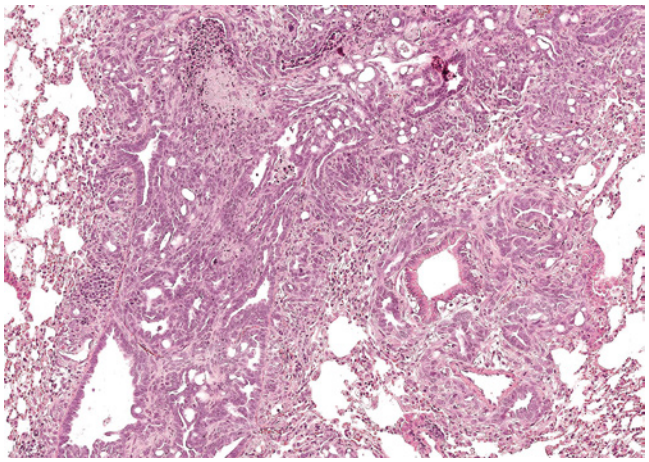


Figure 15.34 **Pulmonary metastasis**. Pulmonary metastasis of a PDAC in a Tg(*Pdx1*-cre)^{6Tuv};*Kras*^{tm4Tyi}; *Trp53*^{tm1Brn} mouse.

CPNs in mouse models have been defined by Hruban et al. [122] as cystic structures (>1 mm) with a papillary, noninvasive epithelial proliferation showing varying degrees of cellular atypia. CPNs arising in the larger ducts may resemble human IPMNs and can be subclassified similarly to human IPMN subtypes by their mucin expression pattern [145].

MCN with a mucinous epithelium and a dense ovarian-type stroma with wavy nuclei expressing estrogen- and progesterone receptors, as defined by Hruban et al. [122], have been described in mice after additional ablation of *Notch2* or

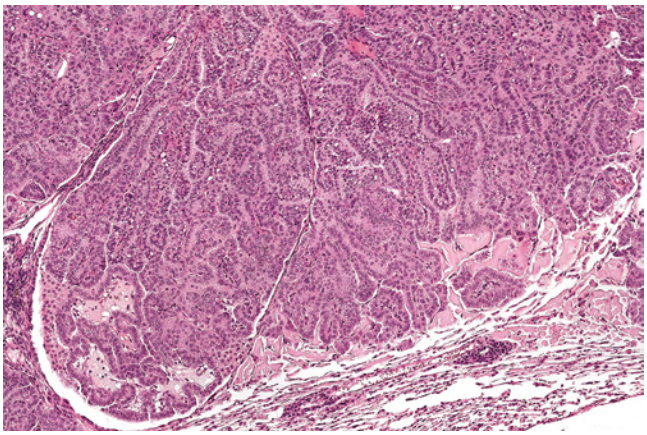


Figure 15.35 **Primary lung adenoma**. Primary lung adenoma in a Tg(*Pdx1*-cre)^{6Tuv};*Kras*^{tm4Tyi}; *Trp53*^{tm1Brn} mouse.

Smad4 in mice with *cre*-driven pancreas specific *Kras* mutation [144, 146]. Progression from MCN to PDAC occurred in the *Ptf1a*$^{tm1(cre)Hnak}$; *Kras*^{tm4Tyi}; *Notch2*^{tm1Frad} model developed by Mazur, Einwachter [146].

Acinar cell carcinoma in mouse models are solid to cystic invasive epithelial neoplasms with acinar differentiation that can be demonstrated by immunostaining for exocrine enzymes such as chymotrypsin and amylase [122].

Different primary multiple or mixed ductal and acinar neoplasms of the pancreas occur and have been described in several genetically engineered mouse models, for example described by Skoulidis, Cassidy [102] in Tg(*Pdx1*-cre)^{6Tuv}; *Kras*^{tm4Tyj}; *Trp53*^{tm3Tyj}; *Brca2*^{tm1Brn} animals. If different components are detected, they should be described and the percentage of the different neoplasms should be noted.

Neoplasms consisting of a single layer of uniform low cuboidal cells, separated by a region of stromal cells, thus closely resembling human *serous cystic neoplasms*, have been described by Bardeesy et al. using *MT-TGFα Ink4a/Arf* and *MT-TGFA TP53* models [147], mutations that seem not be relevant in the human tumors. Lesions resembling serous cystic neoplasms were also observed in a model with Keratin 5 (*Krt5*) driven *Cox2* expression [148]. *Vhl* inactivation, as one of the most frequent genetic events in human serous cystic neoplasms, has not yet been successfully developed in GEMs.

Tumors with necrosis and pseudopapillae consisting of small, polygonal cells resembling *solid-pseudopapillary neoplasms* were induced in a mouse model with stabilization of ß-catenin (*Ptf1a-Cre;ß-cat*^{act}), demonstrating the previously detected mutations in ß-catenin as the proximate cause of human solid pseudopapillary neoplasm [149].

References

1 Goldsmith, L.A. (1990). My organ is bigger than your organ. *Arch. Dermatol.* 126 (3): 301–302. PMID: 2310204.

2 Swartley, O.M., Foley, J.F., Livingston, D.P. 3rd et al. (2016). Histology atlas of the developing mouse hepatobiliary

hemolymphatic vascular system with emphasis on embryonic days 11.5–18.5 and early postnatal development. *Toxicol. Pathol.* 44 (5): 705–725.

3 Roger, A.B. and Dintzis, R.Z. (2017). Hepatobiliary system. In: *Comparative Anatomy and Histology, a Mouse, Rat and Human Atlas*, 2e (eds. P.M. Treuting, S.M. Dintzis and K.S. Montine), London: Elsevier/Academic Press. pp. 229–239. https://doi.org/10.1016/B978-0-12-802900-8.00013-0.

4 Baratta, J.L., Ngo, A., Lopez, B. et al. (2009). Cellular organization of normal mouse liver: a histological, quantitative immunocytochemical, and fine structural analysis. *Histochem. Cell Biol.* 131 (6): 713–726.

5 Salleng, K.J., Revetta, F.L., Deane, N.G., and Washington, M.K. (2015). The applicability of a human immunohistochemical panel to mouse models of hepatocellular neoplasia. *Comp. Med.* 65 (5): 398–408.

6 Gabriel, E., Schievenbusch, S., Kolossov, E. et al. (2012). Differentiation and selection of hepatocyte precursors in suspension spheroid culture of transgenic murine embryonic stem cells. *PLoS One* 7 (9): e44912.

7 Fickert, P., Fuchsbichler, A., Wagner, M. et al. (2009). The role of the hepatocyte cytokeratin network in bile formation and resistance to bile acid challenge and cholestasis in mice. *Hepatology* 50 (3): 893–899.

8 Thoolen, B., Maronpot, R.R., Harada, T. et al. (2010). Proliferative and nonproliferative lesions of the rat and mouse hepatobiliary system. *Toxicol. Pathol.* 38 (7 Suppl): 5S–81S.

9 Friemel, J., Frick, L., Unger, K. et al. (2019). Characterization of HCC mouse models: towards an etiology-oriented subtyping approach. *Mol. Cancer Res.* 17 (7): 1493–1502.

10 Jin, L., Feng, T., Chai, J. et al. (2014). Colony-forming progenitor cells in the postnatal mouse liver and pancreas give rise to morphologically distinct insulin-expressing colonies in 3D cultures. *Rev. Diabet. Stud.* 11 (1): 35–50.

11 He, Y.F., Liu, Y.K., Lu, H.J. et al. (2007). Comparative proteomic analysis of primary mouse liver c-Kit-(CD45/TER119)- stem/progenitor cells. *J. Cell. Biochem.* 102 (4): 936–946.

12 Theise, N.D., Saxena, R., Portmann, B.C. et al. (1999). The canals of Hering and hepatic stem cells in humans. *Hepatology* 30 (6): 1425–1433.

13 Davenport, M., Gonde, C., Redkar, R. et al. (2001). Immunohistochemistry of the liver and biliary tree in extrahepatic biliary atresia. *J. Ped. Surg.* 36: 1017–1025.

14 Faa, G., Van, E.P., Roskams, T. et al. (1998). Expression of cytokeratin 20 in developing rat liver and in experimental models of ductular and oval cell proliferation. *J. Hepatol.* 29: 628–633.

15 Developmental Studies Hybridoma Bank. DSHB. https://dshb.biology.uiowa.edu/ (Accessed 15th June, 2021).

16 Moser, G.J., Wolf, D.C., Harden, R. et al. (1996). Cell proliferation and regulation of negative growth factors in mouse liver foci. *Carcinogenesis* 17 (9): 1835–1840.

17 da Silva, T.C., Cogliati, B., da Silva, A.P. et al. (2010). Pfaffia paniculata (Brazilian ginseng) roots decrease proliferation and increase apoptosis but do not affect cell communication in murine hepatocarcinogenesis. *Exp. Toxicol. Pathol.* 62 (2): 145–155.

18 Steiger, K., Gross, N., Widholz, S.A. et al. (2020). Genetically engineered mouse models of liver tumorigenesis reveal a wide histological spectrum of neoplastic and non-neoplastic liver lesions. *Cancers (Basel)* 12 (8): 2265.

19 Fausto, N. and Campbell, J.S. (2003). The role of hepatocytes and oval cells in liver regeneration and repopulation. *Mech. Dev.* 120 (1): 117–130.

20 Frenkel, N.C., Poghosyan, S., Verheem, A. et al. (2020). Liver lymphatic drainage patterns follow segmental anatomy in a murine model. *Sci. Rep.* 10 (1): 21808.

21 Sellers, R.S., Morton, D., Michael, B. et al. (2007). Society of Toxicologic Pathology position paper: organ weight recommendations for toxicology studies. *Toxicol. Pathol.* 35 (5): 751–755.

22 Crissman, J.W., Goodman, D.G., Hildebrandt, P.K. et al. (2004). Best practices guideline: toxicologic histopathology. *Toxicol. Pathol.* 32 (1): 126–131.

23 Brayton, C.F., Treuting, P.M., and Ward, J.M. (2012). Pathobiology of aging mice and GEM: background strains and experimental design. *Vet. Pathol.* 49 (1): 85–105.

24 Pettan-Brewer, C. and Treuting, P.M. (2011). Practical pathology of aging mice. *Pathobiol. Aging Age Relat. Dis.* 1.

25 Chaible, L.M., Kinoshita, D., and Dagli, M.L. (2017). Genetically modified animal models. In: *Animal Models for the Study of Human Diseases*, 2e (ed. P.M. Conn), 703–720. Academic Press/Elsevier.

26 Bult, C.J., Krupke, D.M., and Eppig, J.T. (1999). Electronic access to mouse tumor data: the Mouse Tumor Biology Database (MTB) project. *Nucleic Acids Res.* 27 (1): 99–105. https://doi.org/10.1093/nar/27.1.99. PMID: 9847151; PMCID: PMC148106.

27 Krupke, D.M., Begley, D.A., Sundberg, J.P. et al. (2008). Mouse models of human cancer database. *Nat. Rev. Cancer* 8 (6): 459–465.

28 Takahashi, Y. and Fukusato, T. (2017). Animal models of liver diseases. In: *Animal Models for the Study of Human Diseases*, 2e (ed. P.M. Conn), 313–333. Academic Press/Elsevier.

29 Königshofer, P., Brusilovskaya, K., Schwabl, P., and Reiberger, T. (2019). Animal models of portal hypertension. *Biochim. Biophys. Acta Mol. Basis Dis.* 1865 (5): 1019–1030.

30 Mesnil, M., Aasen, T., Boucher, J. et al. (2018). An update on minding the gap in cancer. *Biochim. Biophys. Acta Biomembr.* 1860 (1): 237–243.

31 Dagli, M.L., Yamasaki, H., Krutovskikh, V., and Omori, Y. (2004). Delayed liver regeneration and increased susceptibility to chemical hepatocarcinogenesis in transgenic mice expressing a dominant-negative mutant of connexin32 only in the liver. *Carcinogenesis* 25 (4): 483–492.

32 Nelles, E., Bützler, C., Jung, D. et al. (1996). Defective propagation of signals generated by sympathetic nerve stimulation in the liver of connexin32-deficient mice. *Proc. Natl. Acad. Sci. U.S.A.* 93 (18): 9565–9570.

33 Temme, A., Buchmann, A., Gabriel, H.D. et al. (1997). High incidence of spontaneous and chemically induced liver tumors in mice deficient for connexin32. *Curr. Biol.* 7 (9): 713–716.

34 Cogliati, B., Crespo Yanguas, S., da Silva, T.C. et al. (2016). Connexin32 deficiency exacerbates carbon tetrachloride-induced hepatocellular injury and liver fibrosis in mice. *Toxicol. Mech. Methods* 26 (5): 362–370.

35 Cogliati, B., Da Silva, T.C., Aloia, T.P. et al. (2011). Morphological and molecular pathology of CCl_4-induced hepatic fibrosis in connexin43-deficient mice. *Microsc. Res. Tech.* 74 (5): 421–429.

36 Fiorotto, R., Amenduni, M., Mariotti, V. et al. (2019). Animal models for cystic fibrosis liver disease (CFLD). *Biochim. Biophys. Acta Mol. Basis Dis.* 1865 (5): 965–969.

37 Christen, U. (2019). Animal models of autoimmune hepatitis. *Biochim. Biophys. Acta Mol. Basis Dis.* 1865 (5): 970–981.

38 Mariotti, V., Cadamuro, M., Spirli, C. et al. (2019). Animal models of cholestasis: an update on inflammatory cholangiopathies. *Biochim. Biophys. Acta Mol. Basis Dis.* 1865 (5): 954–964.

39 Jahn, D., Kircher, S., Hermanns, H.M., and Geier, A. (2019). Animal models of NAFLD from a hepatologist's point of view. *Biochim. Biophys. Acta Mol. Basis Dis.* 1865 (5): 943–953.

40 Denk, H., Abuja, P.M., and Zatloukal, K. (2019). Animal models of NAFLD from the pathologist's point of view. *Biochim. Biophys. Acta Mol. Basis Dis.* 1865 (5): 929–942.

41 Li, J. and Dawson, P.A. (2019). Animal models to study bile acid metabolism. *Biochim. Biophys. Acta Mol. Basis Dis.* 1865 (5): 895–911.

42 Haemmerle, G. and Lass, A. (2019). Genetically modified mouse models to study hepatic neutral lipid mobilization. *Biochim. Biophys. Acta Mol. Basis Dis.* 1865 (5): 879–894.

43 He, L., Tian, D.A., Li, P.Y., and He, X.X. (2015). Mouse models of liver cancer: progress and recommendations. *Oncotarget* 6 (27): 23306–23322.

44 Heindryckx, F., Colle, I., and Van Vlierberghe, H. (2009). Experimental mouse models for hepatocellular carcinoma research. *Int. J. Exp. Pathol.* 90 (4): 367–386.

45 Evert, M., Ott, T., Temme, A. et al. (2002). Morphology and morphometric investigation of hepatocellular preneoplastic lesions and neoplasms in connexin32-deficient mice. *Carcinogenesis* 23: 697–703.

46 Igarashi, I., Makino, T., Suzuki, Y. et al. (2013). Background lesions during a 24-month observation period in connexin 32-deficient mice. *J. Vet. Med. Sci.* 75 (2): 207–210.

47 De La Rochere, P., Guil-Luna, S., Decaudin, D. et al. (2018). Humanized mice for the study of immuno-oncology. *Trends Immunol.* 39 (9): 748–763.

48 Zhao, Y., Shuen, T.W.H., Toh, T.B. et al. (2018). Development of a new patient-derived xenograft humanised mouse model to study human-specific tumour microenvironment and immunotherapy. *Gut* 67 (10): 1845–1854.

49 Schneller, D. and Angel, P. Cellular origin of hepatocellular carcinoma. In: *Hepatocellular Carcinoma*, Chapter 1 [Internet] (ed. T.-P. JEE). Brisbane: Codon Publications. https://www.ncbi.nlm.nih.gov/books/NBK549196/ https://doi.org/10.15586/hepatocellularcarcinoma.2019.ch1.

50 Tummala, K.S., Brandt, M., Teijeiro, A. et al. (2017). Hepatocellular carcinomas originate predominantly from hepatocytes and Benign lesions from hepatic progenitor cells. *Cell Rep.* 19 (3): 584–600.

51 Vesselinovitch, S.D. and Mihailovich, N. (1983). Kinetics of diethylnitrosamine hepatocarcinogenesis in the infant mouse. *Cancer Res.* 43: 4253–4259.

52 Vucur, M., Roderburg, C., Bettermann, K. et al. (2010). Mouse models of hepatocarcinogenesis: what can we learn for the prevention of human hepatocellular carcinoma? *Oncotarget* 1 (5): 373–378.

53 Brown, Z.J., Heinrich, B., and Greten, T.F. (2018). Mouse models of hepatocellular carcinoma: an overview and highlights for immunotherapy research. *Nat. Rev. Gastroenterol. Hepatol.* 15 (9): 536–554.

54 Auerbach, S.S., Xu, M., Merrick, B.A. et al. (2018). Exome sequencing of fresh-frozen or formalin-fixed paraffin-embedded B6C3F1/N mouse hepatocellular carcinomas arising either spontaneously or due to chronic chemical exposure. *Toxicol. Pathol.* 46 (6): 706–718.

55 Tian, H., Lyu, Y., Yang, Y.G., and Humanized Rodent, H.Z. (2020). Models for cancer research. *Front. Oncol.* 10: 1696.

56 Ma, Y., Zhang, L., and Huang, X. (2014). Genome modification by CRISPR/Cas9. *FEBS J.* 281 (23): 5186–5193.

57 Salsman, J. and Dellaire, G. (2017). Precision genome editing in the CRISPR era. *Biochem. Cell Biol.* 95 (2): 187–201.

58 Alves-Bezerra, M., Furey, N., Johnson, C.G., and Bissig, K.D. (2019). Using CRISPR/Cas9 to model human liver disease. *JHEP Rep.* 1 (5): 392–402.

59 Liggit, D. and Dintzis, S.M. (2018). Pancreas. In: *Comparative Anatomy and Histology: A Mouse, Rat, and Human Atlas*, 2e (eds. P.M. Treuting, S.M. Dintzis and K.S. Montine), 241–250. London: Elsevier/Academic Press.

60 Nolte, T., Brander-Weber, P., Dangler, C. et al. (2016). Nonproliferative and proliferative lesions of the gastrointestinal tract, pancreas and salivary glands of the rat and mouse. *J. Toxicol. Pathol.* 29 (1 Suppl): 1S–125S.

61 Boorman, G.A. and Sills, R.C. (1999). Exocrine and endocrine pancreas. In: *Pathology of the Mouse: Reference and Atlas*, 1e (ed. R.R. Maronpot), 185–205. Cache River Press.

62 Stanger, B.Z. and Hebrok, M. (2013). Control of cell identity in pancreas development and regeneration. *Gastroenterology* 144 (6): 1170–1179.

63 Demcollari, T.I., Cujba, A.M., and Sancho, R. (2017). Phenotypic plasticity in the pancreas: new triggers, new players. *Curr. Opin. Cell Biol.* 49: 38–46.

64 Kittel, B., Ruehl-Fehlert, C., Morawietz, G. et al. (2004). Revised guides for organ sampling and trimming in rats and mice--Part 2. A joint publication of the RITA and NACAD groups. *Exp. Toxicol. Pathol.* 55 (6): 413–431.

65 Kilimnik, G., Kim, A., Jo, J. et al. (2009). Quantification of pancreatic islet distribution in situ in mice. *Am. J. Physiol. Endocrinol. Metab.* 297 (6): E1331–E1338.

66 Dore, B.A., Grogan, W.M., Madge, G.E., and Webb, S.R. (1981). Biphasic development of the postnatal mouse pancreas. *Biol. Neonate* 40 (5-6): 209–217.

67 McInnes, E.F. (2012). *Background Lesions in Laboratory Animals: A Color Atlas*, p. ix, 130. Edinburgh: Saunders/Elsevier.

68 Cheeseman, M.T., Chrobot, N., Fray, M.D., and Deeny, A.A. (2007). Spontaneous exocrine pancreas hypoplasia in specific pathogen-free C3HeB/FeJ and 101/H mouse pups causes steatorrhea and runting. *Comp. Med.* 57 (2): 210–216.

69 Faccini, J.M., Abbott, D.P., Paulus, G.J.J., and Greaves, P. (1990). *Mouse Histopathology: A Glossary for Use in Toxicity and Carcinogenicity Studies*, p. xi, 225. Amsterdam/New York, NY: Elsevier; Sole distributors for the U.S.A. and Canada, Elsevier Science Pub. Co.

70 Serpi, R., Klein-Rodewald, T., Calzada-Wack, J. et al. (2013). Inbred wild type mouse strains have distinct spontaneous morphological phenotypes. *Histol. Histopathol.* 28 (1): 79–88.

71 Turner, P.V., Brash, M.L., and Smith, D.A. (2018). *Pathology of Small Mammal Pets*, xiii, 429 pages. Hoboken, NJ: Wiley.

72 Percy, D.H., Barthold, S.W., and Griffey, S.M. (2016). *Pathology of Laboratory Rodents and Rabbits*, ix, 371 pages, 4e. Ames, IA: Wiley.

73 Working Group IAPAPAAPG (2013). IAP/APA evidence-based guidelines for the management of acute pancreatitis. *Pancreatology* 13 (4 Suppl 2): e1–e15.

74 Whitcomb, D.C., Frulloni, L., Garg, P. et al. (2016). Chronic pancreatitis: an international draft consensus proposal for a new mechanistic definition. *Pancreatology* 16 (2): 218–224.

75 Klauss, S., Schorn, S., Teller, S. et al. (2018). Genetically induced vs. classical animal models of chronic pancreatitis: a critical comparison. *FASEB J.* 32: 5778–5792. https://doi.org/10.1096/fj.201800241RR.

76 Kloppel, G. (2007). Chronic pancreatitis, pseudotumors and other tumor-like lesions. *Mod. Pathol.* 20 (Suppl 1): S113–S131.

77 Archer, H., Jura, N., Keller, J. et al. (2006). A mouse model of hereditary pancreatitis generated by transgenic expression of R122H trypsinogen. *Gastroenterology* 131 (6): 1844–1855.

78 Athwal, T., Huang, W., Mukherjee, R. et al. (2014). Expression of human cationic trypsinogen (PRSS1) in murine acinar cells promotes pancreatitis and apoptotic cell death. *Cell Death Dis.* 5: e1165.

79 Gaiser, S., Daniluk, J., Liu, Y. et al. (2011). Intracellular activation of trypsinogen in transgenic mice induces acute but not chronic pancreatitis. *Gut* 60 (10): 1379–1388.

80 Geisz, A. and Sahin-Toth, M. (2018). A preclinical model of chronic pancreatitis driven by trypsinogen autoactivation. *Nat. Commun.* 9 (1): 5033.

81 Ohmuraya, M., Hirota, M., Araki, M. et al. (2005). Autophagic cell death of pancreatic acinar cells in serine protease inhibitor Kazal type 3-deficient mice. *Gastroenterology* 129 (2): 696–705.

82 Hegyi, E. and Sahin-Toth, M. (2019). Human CPA1 mutation causes digestive enzyme misfolding and chronic pancreatitis in mice. *Gut* 68 (2): 301–312.

83 Merry, T.L. and Petrov, M.S. (2018). The rise of genetically engineered mouse models of pancreatitis: a review of literature. *Biomol. Concepts* 9 (1): 103–114.

84 Gill, A.J., Klimstra, D., and Lam, A.K. (2019). Tumours of the pancreas. In: *Digestive System Tumours*, 5e (ed. Board WCoTE), 295–372. Lyon: IARC Press.

85 Roberts, N.J., Jiao, Y., Yu, J. et al. (2012). ATM mutations in patients with hereditary pancreatic cancer. *Cancer Discov.* 2 (1): 41–46.

86 Klein, A.P. (2012). Genetic susceptibility to pancreatic cancer. *Mol. Carcinog.* 51 (1): 14–24.

87 Jones, S., Li, M., Parsons, D.W. et al. (2012). Somatic mutations in the chromatin remodeling gene ARID1A occur in several tumor types. *Hum. Mutat.* 33 (1): 100–103.

88 Bazzichetto, C., Luchini, C., Conciatori, F. et al. (2020). Morphologic and molecular landscape of pancreatic cancer variants as the basis of new therapeutic strategies for precision oncology. *Int. J. Mol. Sci.* 21 (22): 8841.

89 Kryklyva, V., Ter Linden, E., Kroeze, L.I. et al. (2020). Medullary pancreatic carcinoma due to somatic POLE mutation: a distinctive pancreatic carcinoma with marked long-term survival. *Pancreas* 49 (7): 999–1003.

90 Maitra, A., Fukushima, N., Takaori, K., and Hruban, R.H. (2005). Precursors to invasive pancreatic cancer. *Adv. Anat. Pathol.* 12 (2): 81–91.

91 Hansel, D.E., Kern, S.E., and Hruban, R.H. (2003). Molecular pathogenesis of pancreatic cancer. *Annu. Rev. Genomics Hum. Genet.* 4: 237–256.

92 Luchini, C., Brosens, L.A.A., Wood, L.D. et al. (2021). Comprehensive characterisation of pancreatic ductal adenocarcinoma with microsatellite instability: histology, molecular pathology and clinical implications. *Gut.* 70: 148–156.

93 Brune, K., Abe, T., Canto, M. et al. (2006). Multifocal neoplastic precursor lesions associated with lobular atrophy of the pancreas in patients having a strong family history of pancreatic cancer. *Am. J. Surg. Pathol.* 30 (9): 1067–1076.

94 Shi, C., Hruban, R.H., and Klein, A.P. (2009). Familial pancreatic cancer. *Arch. Pathol. Lab. Med.* 133 (3): 365–374.

95 Bartsch, D.K., Dietzel, K., Bargello, M. et al. (2013). Multiple small "imaging" branch-duct type intraductal papillary mucinous neoplasms (IPMNs) in familial pancreatic cancer: indicator for concomitant high grade pancreatic intraepithelial neoplasia? *Fam. Cancer* 12 (1): 89–96.

96 Hruban, R.H., Canto, M.I., Goggins, M. et al. (2010). Update on familial pancreatic cancer. *Adv. Surg.* 44: 293–311.

97 Aimoto, T., Uchida, E., Nakamura, Y. et al. (2008). Multicentric pancreatic intraepithelial neoplasias (PanINs) presenting with the clinical features of chronic pancreatitis. *J. Hepatobiliary Pancreat. Surg.* 15 (5): 549–553.

98 Takaori, K., Matsusue, S., Fujikawa, T. et al. (1998). Carcinoma in situ of the pancreas associated with localized fibrosis: a clue to early detection of neoplastic lesions arising from pancreatic ducts. *Pancreas* 17 (1): 102–105.

99 Weiss, F.U. (2014). Pancreatic cancer risk in hereditary pancreatitis. *Front. Physiol.* 5: 70.

100 Maitra, A. and Hruban, R.H. (2008). Pancreatic cancer. *Annu. Rev. Pathol.* 3: 157–188.

101 Bardeesy, N., Aguirre, A.J., Chu, G.C. et al. (2006). Both p16(Ink4a) and the p19(Arf)-p53 pathway constrain progression of pancreatic adenocarcinoma in the mouse. *Proc. Natl. Acad. Sci. U.S.A.* 103 (15): 5947–5952.

102 Skoulidis, F., Cassidy, L.D., Pisupati, V. et al. (2010). Germline Brca2 heterozygosity promotes Kras(G12D) -driven carcinogenesis in a murine model of familial pancreatic cancer. *Cancer Cell* 18 (5): 499–509.

103 Gentiluomo, M., Canzian, F., Nicolini, A. et al. (2020). Germline genetic variability in pancreatic cancer risk and prognosis. *Semin. Cancer Biol.*, ISSN 1044-579X, https://doi.org/10.1016/j.semcancer.2020.08.003.

104 Greer, J.B. and Whitcomb, D.C. (2009). Inflammation and pancreatic cancer: an evidence-based review. *Curr. Opin. Pharmacol.* 9 (4): 411–418.

105 Bosetti, C., Lucenteforte, E., Silverman, D.T. et al. (2012). Cigarette smoking and pancreatic cancer: an analysis from the International Pancreatic Cancer Case-Control Consortium (Panc4). *Ann. Oncol.* 23 (7): 1880–1888.

106 Michaud, D.S., Izard, J., Wilhelm-Benartzi, C.S. et al. (2013). Plasma antibodies to oral bacteria and risk of pancreatic cancer in a large European prospective cohort study. *Gut* 62 (12): 1764–1770.

107 Antwi, S.O., Eckert, E.C., Sabaque, C.V. et al. (2015). Exposure to environmental chemicals and heavy metals, and risk of pancreatic cancer. *Cancer Causes Control* 26 (11): 1583–1591.

108 Takahashi, M., Hori, M., Mutoh, M. et al. (2011). Experimental animal models of pancreatic carcinogenesis for prevention studies and their relevance to human disease. *Cancers (Basel)* 3 (1): 582–602.

109 Osvaldt, A.B., Wendt, L.R., Bersch, V.P. et al. (2006). Pancreatic intraepithelial neoplasia and ductal adenocarcinoma induced by DMBA in mice. *Surgery* 140 (5): 803–809.

110 Pour, P., Althoff, J., Kruger, F.W., and Mohr, U. (1977). A potent pancreatic carcinogen in Syrian hamsters: N-nitrosobis(2-oxopropyl)amine. *J. Natl. Cancer Inst.* 58 (5): 1449–1453.

111 Lerch, M.M. and Gorelick, F.S. (2013). Models of acute and chronic pancreatitis. *Gastroenterology* 144 (6): 1180–1193.

112 Saloman, J.L., Albers, K.M., Cruz-Monserrate, Z. et al. (2019). Animal models: challenges and opportunities to determine optimal experimental models of pancreatitis and pancreatic cancer. *Pancreas* 48 (6): 759–779.

113 Schmidt, J., Rattner, D.W., Lewandrowski, K. et al. (1992). A better model of acute pancreatitis for evaluating therapy. *Ann. Surg.* 215 (1): 44–56.

114 Ding, S.P., Li, J.C., and Jin, C. (2003). A mouse model of severe acute pancreatitis induced with caerulein and lipopolysaccharide. *World J. Gastroenterol.* 9 (3): 584–589.

115 Banks, P.A., Bollen, T.L., Dervenis, C. et al. (2013). Classification of acute pancreatitis – 2012: revision of the Atlanta classification and definitions by international consensus. *Gut* 62 (1): 102–111.

116 Bai, H., Chen, X., Zhang, L., and Dou, X. (2012). The effect of sulindac, a non-steroidal anti-inflammatory drug, attenuates inflammation and fibrosis in a mouse model of chronic pancreatitis. *BMC Gastroenterol.* 12: 115.

117 Demols, A., Van Laethem, J.L., Quertinmont, E. et al. (2002). Endogenous interleukin-10 modulates fibrosis and regeneration in experimental chronic pancreatitis. *Am. J. Physiol. Gastrointest. Liver Physiol.* 282 (6): G1105–G1112.

118 Brembeck, F.H., Schreiber, F.S., Deramaudt, T.B. et al. (2003). The mutant K-ras oncogene causes pancreatic periductal lymphocytic infiltration and gastric mucous neck cell hyperplasia in transgenic mice. *Cancer Res.* 63 (9): 2005–2009.

119 Grippo, P.J., Nowlin, P.S., Demeure, M.J. et al. (2003). Preinvasive pancreatic neoplasia of ductal phenotype induced by acinar cell targeting of mutant Kras in transgenic mice. *Cancer Res.* 63 (9): 2016–2019.

120 Murtaugh, L.C. (2014). Pathogenesis of pancreatic cancer: lessons from animal models. *Toxicol. Pathol.* 42 (1): 217–228.

121 Collins, M.A., Bednar, F., Zhang, Y. et al. (2012). Oncogenic Kras is required for both the initiation and maintenance of pancreatic cancer in mice. *J. Clin. Invest.* 122 (2): 639–653.

122 Hruban, R.H., Adsay, N.V., Albores-Saavedra, J. et al. (2006). Pathology of genetically engineered mouse models of pancreatic exocrine cancer: consensus report and recommendations. *Cancer Res.* 66 (1): 95–106.

123 Aichler, M., Seiler, C., Tost, M. et al. (2012). Origin of pancreatic ductal adenocarcinoma from atypical flat lesions: a comparative study in transgenic mice and human tissues. *J. Pathol.* 226 (5): 723–734.

124 Murtaugh, L.C. and Leach, S.D. (2007). A case of mistaken identity? Nonductal origins of pancreatic "ductal" cancers. *Cancer Cell* 11 (3): 211–213.

125 Rooman, I. and Real, F.X. (2012). Pancreatic ductal adenocarcinoma and acinar cells: a matter of differentiation and development? *Gut* 61 (3): 449–458.

126 Bockman, D.E., Black, O. Jr., Mills, L.R., and Webster, P.D. (1978). Origin of tubular complexes developing during induction of pancreatic adenocarcinoma by 7,12-dimethylbenz(a)anthracene. *Am. J. Pathol.* 90 (3): 645–658.

127 Bockman, D.E., Guo, J., Buchler, P. et al. (2003). Origin and development of the precursor lesions in experimental pancreatic cancer in rats. *Lab. Invest.* 83 (6): 853–859.

128 Shi, G., DiRenzo, D., Qu, C. et al. (2013). Maintenance of acinar cell organization is critical to preventing Kras-induced acinar-ductal metaplasia. *Oncogene* 32 (15): 1950–1958.

129 Willemer, S. and Adler, G. (1989). Histochemical and ultrastructural characteristics of tubular complexes in human acute pancreatitis. *Dig. Dis. Sci.* 34 (1): 46–55.

130 Kopp, J.L., von Figura, G., Mayes, E. et al. (2012). Identification of Sox9-dependent acinar-to-ductal reprogramming as the principal mechanism for initiation of pancreatic ductal adenocarcinoma. *Cancer Cell* 22 (6): 737–750.

131 Esposito, I., Konukiewitz, B., Schlitter, A.M., and Kloppel, G. (2012). New insights into the origin of pancreatic cancer. Role of atypical flat lesions in pancreatic carcinogenesis. *Pathologe* 33 (Suppl 2): 189–193.

132 Konukiewitz, B., Schlitter, A.M., Berchtold, S. et al. (2013). Characterization of putative precursor lesions of familal pancreatic cancer. *Mod. Pathol.* 26 (Suppl. 2) (102nd USCAP Annual Meeting. March 2-8. 2013): 426A.

133 Basturk, O., Hong, S.M., Wood, L.D. et al. (2015). A revised classification system and recommendations from the baltimore consensus meeting for neoplastic precursor lesions in the pancreas. *Am. J. Surg. Pathol.* 39 (12): 1730–1741.

134 Mueller, S., Engleitner, T., Maresch, R. et al. (2018). Evolutionary routes and KRAS dosage define pancreatic cancer phenotypes. *Nature* 554 (7690): 62–68.

135 Shin, S.H., Kim, S.C., Hong, S.M. et al. (2013). Genetic alterations of K-ras, p53, c-erbB-2, and DPC4 in pancreatic ductal adenocarcinoma and their correlation with patient survival. *Pancreas* 42 (2): 216–222.

136 Hingorani, S.R., Petricoin, E.F., Maitra, A. et al. (2003). Preinvasive and invasive ductal pancreatic cancer and its early detection in the mouse. *Cancer Cell* 4 (6): 437–450.

137 Martinelli, P., Madriles, F., Canamero, M. et al. (2016). The acinar regulator Gata6 suppresses Kras*G12V*-driven pancreatic tumorigenesis in mice. *Gut* 65: 476–486.

138 Hingorani, S.R., Wang, L., Multani, A.S. et al. (2005). Trp53R172H and KrasG12D cooperate to promote chromosomal instability and widely metastatic pancreatic ductal adenocarcinoma in mice. *Cancer Cell* 7 (5): 469–483.

139 Guerra, C., Schuhmacher, A.J., Canamero, M. et al. (2007). Chronic pancreatitis is essential for induction of pancreatic ductal adenocarcinoma by K-Ras oncogenes in adult mice. *Cancer Cell* 11 (3): 291–302.

140 Oshima, M., Okano, K., Muraki, S. et al. (2013). Immunohistochemically detected expression of 3 major genes (CDKN2A/p16, TP53, and SMAD4/DPC4) strongly predicts survival in patients with resectable pancreatic cancer. *Ann. Surg.* 258 (2): 336–346.

141 Bardeesy, N., Cheng, K.H., Berger, J.H. et al. (2006). Smad4 is dispensable for normal pancreas development yet critical in progression and tumor biology of pancreas cancer. *Genes Dev.* 20 (22): 3130–3146.

142 Wood, L.D. and Hruban, R.H. (2012). Pathology and molecular genetics of pancreatic neoplasms. *Cancer J.* 18 (6): 492–501.

143 Kojima, K., Vickers, S.M., Adsay, N.V. et al. (2007). Inactivation of Smad4 accelerates Kras(G12D)-mediated pancreatic neoplasia. *Cancer Res.* 67 (17): 8121–8130.

144 Izeradjene, K., Combs, C., Best, M. et al. (2007). Kras(G12D) and Smad4/Dpc4 haploinsufficiency cooperate to induce mucinous cystic neoplasms and invasive adenocarcinoma of the pancreas. *Cancer Cell* 11 (3): 229–243.

145 von Figura, G., Fukuda, A., Roy, N. et al. (2014). The chromatin regulator Brg1 suppresses formation of intraductal papillary mucinous neoplasm and pancreatic ductal adenocarcinoma. *Nat. Cell Biol.* 16 (3): 255–267.

146 Mazur, P.K., Einwachter, H., Lee, M. et al. (2010). Notch2 is required for progression of pancreatic intraepithelial neoplasia and development of pancreatic ductal adenocarcinoma. *Proc. Natl. Acad. Sci. U.S.A.* 107 (30): 13438–13443.

147 Bardeesy, N., Morgan, J., Sinha, M. et al. (2002). Obligate roles for p16(Ink4a) and p19(Arf)-p53 in the suppression of murine pancreatic neoplasia. *Mol. Cell. Biol.* 22 (2): 635–643.

148 Muller-Decker, K., Furstenberger, G., Annan, N. et al. (2006). Preinvasive duct-derived neoplasms in pancreas of keratin 5-promoter cyclooxygenase-2 transgenic mice. *Gastroenterology* 130 (7): 2165–2178.

149 Heiser, P.W., Cano, D.A., Landsman, L. et al. (2008). Stabilization of beta-catenin induces pancreas tumor formation. *Gastroenterology* 135 (4): 1288–1300.

16

Neuromuscular System

Peter Vogel, Laura J. Janke, and Heather W. Sheppard

Introduction

Discovering the genetic causes of disease is key to understanding the underlying pathogenetic mechanisms and for developing mutation-specific therapies. Many mutant and genetically engineered mouse models of neuromuscular disease have already been discovered and proven useful in elucidating the pathogenesis of these diseases. The development of mouse models of neuromuscular disease that recapitulate the key genetic, clinical, and pathological features of human disease is critical to preclinical research because these types of models facilitate pharmacokinetic, pharmacodynamic, and safety studies, and testing the efficacy of novel therapeutic approaches (Tables 16.1 and 16.2). Mouse pathologists will play a key role in discovering novel myopathies while phenotyping genetically engineered mice.

In phenotyping genetically engineered mice, pathologists might be presented with mice that are stunted and shaky, appearing weak, or displaying postural or gait abnormalities associated with advanced neuromuscular disease. These obvious clinical signs of neuromuscular disease can be confirmed and measured using behavioral assays such as the inverted screen or grip strength tests. However, mild signs are not always clinically evident, particularly in younger mice, and it has become apparent that pathologists are well-positioned to discover and characterize subclinical neuromuscular disease. Through careful histopathologic examination of properly collected and prepared spinal cord and muscle, pathologists are often able to detect myopathies that cannot be demonstrated with commonly used behavioral screening tests. Histopathology is the most sensitive and specific method for detecting myopathies and pathologists can provide critical insights into the most likely underlying mechanisms involved in the development of any newly identified myopathies.

Most neuromuscular diseases present as myopathies, and these are broadly classified as either neurogenic or myogenic, based on the primary underlying pathogenic mechanisms involved. Neurogenic myopathies are caused by dysfunctional motor neurons, peripheral nerves, and/or neuromuscular junctions (NMJs). Clinical signs suggesting neurogenic myopathies include muscle atrophy associated with abnormal movement, circling, difficulty walking, lameness of unknown origin, generalized skeletal muscle weakness, paresis, paralysis, and proprioceptive defects. Tremors suggest myelination/peripheral nerve problems; an unstable lurching or staggering gait suggests cerebellar lesions; dragging legs with flaccid paralysis suggests lower motor neuron disease; while uncoordinated movements, writhing, and an inability to right oneself are associated with sensory receptor and nerve defects.

Transverse sections of the vertebral column processed *in situ* at the level of the lumbar and sacral spinal cord are particularly useful for determining the cause of neurogenic myopathies. Along with the spinal cord, these sections include the sciatic nerve and its branches, the dorsal root ganglia, and autonomic ganglia (Figure 16.1a). In addition, the epaxial and hypaxial muscles include abundant type 1 (red) and type 2 (brown) fiber dominant muscles (Figure 16.1b). Cross-sections of the hind leg permit evaluation of the femoral and peroneal nerves, bone, and muscles (Figure 16.1c,d). Evaluation of muscle in multiple locations is important because myopathies can preferentially affect specific muscle groups or muscle fiber types. In addition, it is often possible to differentiate neurogenic from myogenic disease by the distribution and appearance of atrophic/damaged muscle fibers.

With myogenic myopathies, the predominant clinical sign is muscle weakness, which often presents as abnormal gait, or in severe cases paralysis that is behaviorally indistinguishable from a neurogenic myopathy. The myogenic myopathies are due to intrinsic defects in myocytes, and may involve dysfunction of a wide range of proteins, including sarcolemmal (dystrophin, sarcoglycans, dysferlin), extracellular matrix (a2-laminin and collagen VI) sarcomeric (actin, telethonin), cytosolic (calpain3 and fukutin-related protein-FKRP), and nuclear (emerin and lamin A/C) proteins.

There are neuromuscular disease phenotypes with histopathologic lesions characteristic of both neurogenic and myogenic disease, and these generally involve dysfunction

Pathology of Genetically Engineered and Other Mutant Mice, First Edition. Edited by John P. Sundberg, Peter Vogel, and Jerrold M. Ward.
© 2022 John Wiley & Sons, Inc. Published 2022 by John Wiley & Sons, Inc.

Table 16.1 Mouse models: neurogenic myopathies.

Primary target	Human disease	Gene name (human/mouse) or mutation	Model disease summary with references
Motor neuron	Spinal muscular atrophy (SMA)	Survival motor neuron (*SMN1* and *SMN2/Smn1*^{tm1Msd})	−/− embryonic lethal (E12.5–E15.5) [1]. +/− progressive motor neuron loss at five weeks [2].
	Spinal muscular atrophy, lower extremity dominant (SMA-LED)	Cytoplasmic dynein heavy chain 1 (*DYNC1H1*/*Dync1h1*)	−/− abnormal CNS/perinatal death [3, 4]
			+/− altered neuronal migration [5]
		Legs at odd angles (*Dync1h1*^{Loa}) mutation [6]	Sensory neuropathy/striatal atrophy with axonopathy like CMT disease [7]
		Cramping 1 (*Dync1h1*^{Cra1}) mutation [8]	−/− progressive "fading" with hind limb then forelimb paralysis and decreased survival. +/− are morphologically and functionally normal [9].
	Spinal muscular atrophy with respiratory distress type 1 (SMARD1 or HMN type VI)	Immunoglobulin mu DNA binding protein 2 (*IGHMBP2*/*Ighmbp2*$^{nmd\text{-}2J}$)	−/− progressive paralysis at three weeks, death at six to seven weeks caused by motor neuron loss, dysfunction of motor endplates, axonal degeneration, and microtubule loss [10]
	Progressive motor and sensory neuropathy	Tubulin-specific chaperone E (*TBCE*/*Tbce*^{pmn})	−/− sterile and have brainstem and spinal cord motor neuron degeneration and muscle atrophy at three-weeks with progressive ataxia, tremors, and limb paralysis [11]
			+/− morphologically normal [12]
	Amyotrophic lateral sclerosis		
	ALS1	Superoxide dismutase 1 (*SOD1*/*Sod1*) Tg(SOD1*G93A)2Gur	Progressive motor neuron loss in spinal cord and paralysis in the tg*SOD1*^{G93A} model [13]
	Familial and sporadic FUS, ALS6/ALS10	FUS/TLS Tg(Prnp-FUS*R521C)3313Ejh	Transgenics have cytoplasmic accumulations of FUS correlating with motor and cognitive deficits [14, 15]
		Tg(Prnp-TARDBP*A315T)95Balo	Hemizygous develop fatal neurodegeneration comparable to ALS and FTLD [16]
	C9FTD/ALS	*C9orf72/C9orf72* Tg(C9orf72)500Lpwr	Hemizygous mice showed paralysis, muscle denervation, motor neuron loss, and decreased survival in initial study [17]
Peripheral nerve	Charcot–Marie–Tooth types 1A/1E, type 3	Peripheral myelin protein 22 (*PMP22*/*Pmp22*) Tg(PMP22)C61Clh	Mice develop myelinopathy dependent on PMP22 expression [18]
	Giant axonal neuropathy	Gigaxonin (*GAN*/*Gan*^{tm1Lpj})	Mild motor neuron loss, axonal degeneration, muscle atrophy with intermediate filament inclusions in CNS [19]
Neuromuscular junction			
Myasthenia gravis (MG), acquired	Autoantibodies against acetylcholine receptors (AChR)	Cholinergic receptor nicotinic epsilon subunit (*CHRNE*/*Chrne*^{tm1Vwi})	Mice have altered NMJ function and muscle weakness but normal lifespans [20]
	Autoantibodies against muscle-specific kinase (MuSK)-MG	Hemolytic complement/C5-deficient (*C5*/*Hc0*)	Complement 5 deficient mice develop muscle weakness following MuSK injection [21]
MG, congenital	Lambert–Eaton myasthenic syndrome: autoantibodies against voltage-gated calcium channels (VGCCs)	Calcium channel, voltage-dependent, P/Q type, alpha 1A subunit; rolling Nagoya (*CACNA1A*/*Cacna1a*$^{tg\text{-}rol}$)	Weakness in fast-twitch muscles in low calcium conditions [22]
	Congenital myasthenic syndrome 7	*Synaptotagmin 2* (*SYT2*/*Syt2tm1Sud*)	Severe motor dysfunction, and mortality starting at three weeks of age [23]
Mechanoreceptor	Failure of development of Pacinian corpuscles	Neuregulin 1 (*NRG1*/*Nrg1tm3Cbm*)	Poorly developed muscle spindles and proprioceptive deficits [24]
	Altered axon-Schwann cell interactions and myelination	erb-b2 receptor tyrosine kinase 2 (*ERBB*/*Erbb2*^{tm1Klee})	−/− mortality at E10.5 with motor neuron degeneration, absence of Schwann cells; dysmyelination in transgenic mice with mutant erbB4 receptor [25, 26]

Table 16.2 Mouse models: myogenic myopathies.

Primary target	Human disease	Gene name (human/mouse) or mutation	Model disease summary with references
Sarcolemma	Duchenne muscular dystrophy	Dystrophin (*DMD/Dmd*^{mdx})	*mdx* mutation on C57BL/10 background. Milder phenotype than in humans [27]
	Duchenne muscular dystrophy	Dystrophin (DMD/*Dmd*^{mdx})	*mdx* mutation on DBA/2 background. Increased severity, with fibrosis [28].
	Dysferlinopathy (limb-girdle muscular dystrophy type A)	Dysferlin (*DYSF/Dysf*^{tm1Kcam})	Muscles are defective in sarcolemma resealing following mechanical stress [29]
Sarcoplasmic reticulum	Core myopathy (Central core disease)	Type 1 ryanodine receptor/Ca^{2+} release channel (*RYR1/Ryr1*$^{tm1.1Dhm}$)	Progressive transformation from minicores to cores and nemaline rods [30]
	Marinesco–Sjögren syndrome	SIL1 Nucleotide Exchange Factor (*SIL1/Sil1*^{wz})	Woozy mouse (*wz*) carries a *Sil1* gene mutation [31]
Myofibrillar myopathies	Desminopathy	Desmin (*DES/Des*$^{tm1.1Ccrs}$)	Knock-in mice develop desmin+ protein aggregates [32]
	αB-crystallinopathy	αB-crystallin (*CRYAB/Cryab*$^{tm1.1Ady}$)	Myofibrillar disarray due to insoluble aggregates of αB-crystallin [33]
	Myotilinopathy	Myotilin (*MYOT/Myot*) Tg(ACTA1-MYOT*T57I)71Mah	Progressive myofibrillar vacuolization and aggregation [34]
	Filaminopathy	Filamin C (*FLCN/Flnc*$^{tm1.1Rsdf}$)	Knock-in mice develop myofibrillar instability [35]
	Zaspopathy	*LDB3* (*ZASP*)/*Ldb3*^{tm1Chen}	Neonatal lethality with disorganized and disrupted Z-lines [36]
Ion channel diseases	Myotonia congenita	Voltage-gated channel sodium channel 1 (*CLCN1/Clcn1*^{adr})	Myotonia, but no visible morphologic abnormalities [37]
	Hyper/hypokalemic periodic paralysis	Voltage-gated sodium channel type IV (*SCN4A/Scn4a*$^{tm1.1Ljh}$)	Myotonia with rare centralized nuclei as the only morphologic abnormality [38]
Autophagy/mitophagy		Autophagy related 7 (*ATG7/Atg7*^{tm1Tchi})	Vacuolation and atrophy of myofibers with centralized nuclei [39]
Mitochondrial diseases	Friedrich's ataxia	Frataxin (*FXN/Fxn*$^{tm2.1Mkn}$)	Conditional knockout results in degeneration of large sensory neurons of dorsal root ganglia [40]
	Mitochondrial myopathy	Mitochondrial transcription factor A (*TFAM/Tfam*^{tm1Lrsn})	Ragged-red fibers and accumulation of abnormal mitochondria [41]

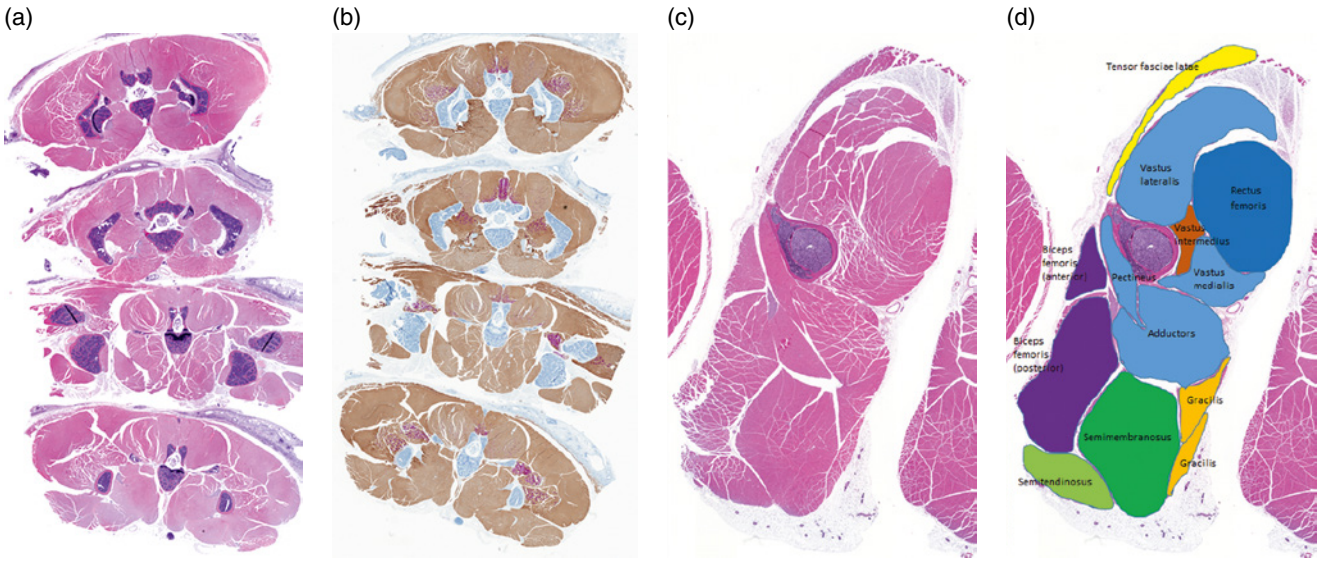


Figure 16.1 **Mouse skeletal muscle**. (a) Transverse section of spinal column showing epaxial and hypaxial muscles, spinal cord, vertebrae, and sciatic nerve. (b) Sequential section of spinal column with muscles immunohistochemically labeled for fast (brown) and slow (red) muscle fibers. (c) Transverse section of upper rear leg. (d) Transverse section of upper rear leg overlaid with muscle names.

of cellular processes that are critical in both neurons and myocytes (for example, autophagy). Neurogenic, myogenic, and mixed myopathies can all result in decreased muscle mass due to myocyte atrophy and/or loss. By combining histopathologic evaluations with appropriate immunohistochemical labeling, a pathologist can usually distinguish between neurogenic or myogenic origins of neuromuscular symptoms.

This chapter outlines approaches and methods that can be used to identify and better understand neuromuscular phenotypes in mice. Neuromuscular diseases can be conveniently categorized based on the location of the primary lesions as follows:

1) *Motor neuron diseases*: functional loss or death of lower motor neurons
2) *Peripheral neuropathies*: inflammation and/or demyelination of axons
3) *Myasthenias*: dysfunction of the neuromuscular junctions (motor end plates).
4) *Mechanoreceptor defects*: absence or dysfunction of proprioceptors located within joints, muscles, and tendons.
5) *Muscular dystrophies*: degeneration and/or necrosis of muscle fibers (myocytes).

General Guidelines

Neuromuscular diseases are frequently accompanied by lesions in spinal motor neurons, myelinated nerves, motor end plates, or the muscles themselves that are visible by light microscopy. Therefore, a thorough histopathologic examination of spinal cord and skeletal muscle is critically important in uncovering and understanding the presence and potential cause of any novel neuromuscular diseases. The histopathologic identification of the underlying cause of neuromuscular disease symptoms in mice depends on proper fixation and collection of target tissues. For comprehensive neuromuscular disease phenotyping, the following guidelines are provided:

1) Perfusion fixation is essential for preventing artifacts in motor neurons, dorsal root ganglia, and myelin.
2) Collect cross-sections of the spinal cord and limbs at multiple levels.
3) Comparisons with littermate controls (wild-type age and sex-matched) are essential.
4) Aging or challenge (treadmill, wheels) studies should be considered for cases where lesions are very mild.
5) To evaluate disease progression, collect tissues from weaned (3–4 weeks old), mature (3–4 months old), and geriatric (1–2+ years) mice.

Tissue Fixation

Whole body transcardial perfusion fixation with 10% neutral buffered formalin followed by paraffin-embedding (FFPE) is required to consistently identify many critical lesions associated with neuromuscular disease. If the spinal cord is fixed by immersion, artifactual cytoplasmic vacuolization and loss of nuclear and cytoplasmic detail (Figure 16.2a) can obscure subtle lesions in the nuclei and/or cytoplasm of spinal motor neurons that are preserved by rapid perfusion fixation (Figure 16.2b). Similarly, many lesions in peripheral nerves, motor endplates and skeletal muscle are not detectable in immersion fixed tissues.

Although frozen sections and whole mount tissues are used for some specific types of investigations, FFPE tissues

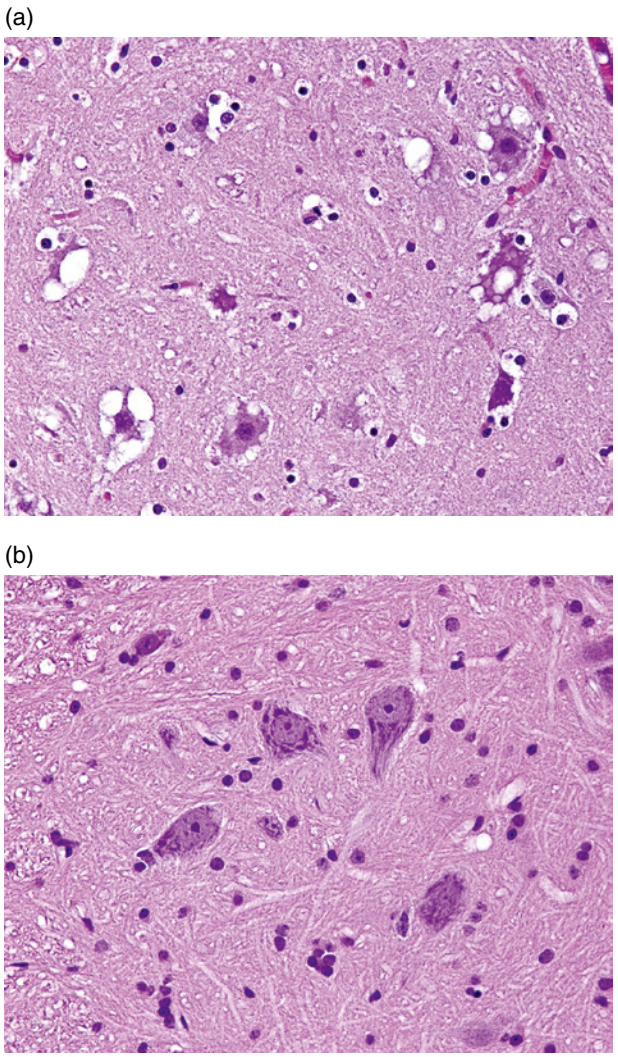


Figure 16.2 **Mouse spinal cord**. (a) Artifactual vacuolization of neurons and neuropil resulting from immersion fixation. (b) Preservation of neuron and neuropil fine structure due to perfusion fixation.

are generally adequate for most purposes. For example, frozen sections have traditionally been used to distinguish between Type 1 (slow) and Type 2 (fast) muscle fibers, with staining for ATPase at pH 9.4 and ATPase at pH 4.6 to detect glycolysis in fast fibers, and NADH-tetrazolium reductase to detect mitochondrial activity in slow fibers. Fortunately, frozen sections are no longer needed for this purpose given the availability of specific antibodies to fast, slow, and embryonic myosin heavy chain that specifically label Type 1 and Type 2 fibers in FFPE muscle (Figure 16.3a). These immunohistochemistry (IHC) labels can demonstrate instances where a myopathy preferentially affects a one of these fiber types (Figure 16.3b–d). Some other stains that may require frozen sections include Oil Red O and periodic acid Schiff (PAS), which are used to detect lipid or glycogen, respectively. However, in our experience these stains do not appear to be very useful in mouse skeletal muscle.

Tissue Samples

For high throughput screening, baseline neuromuscular phenotyping of genetically engineered mice only requires three FFPE tissue blocks. The first cassette contains multiple cross sections of the spinal column (one cervical, one thoracic, and at least two lumbar). The second cassette contains a rear leg trimmed to include the knee, with the medial surface down. The third cassette contains a cross-section of the quadriceps muscle (mid-femur) as well as sections of the heart.

For more complete pathology phenotyping, where neuromuscular disease is already known or suspected based on either clinical signs or the results of baseline histopathology, more extensive tissue collection is necessary in order to assess motor neurons, myocytes, dorsal root ganglia, peripheral nerves, NMJs, and mechanoreceptors. Since most lesions are more easily detected in transverse sections of both the spinal cord and skeletal muscle, we use at least six cassettes for adult mice; four of these contain maximal cross-sections of the

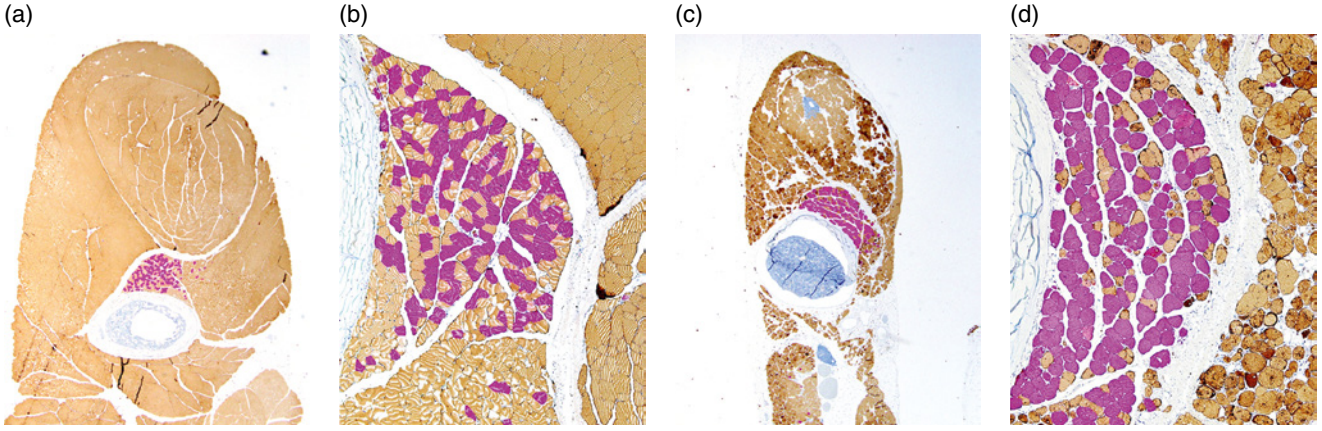


Figure 16.3 **Mouse quadriceps muscle**. (a) Transverse section of wild-type quadriceps muscle labeled for fast (brown) and slow (red) muscle fibers. (b) Higher magnification showing mixed distribution of fast and slow fibers in vastus intermedius head of quadriceps. (c) Transverse section of quadriceps muscle from GEM littermate showing overall reduction in muscle mass. (d) Higher magnification showing preservation of slow muscle fibers in vastus intermedius.

spinal cord, with two cassettes for the lateral and cross-sections of the rear legs. For the cervical and thoracic spinal cord, each cassette is loaded with at least four to six cross-sections. The lumbar/sacral region requires two cassettes, each containing six sections, with the first cut made at the level of the thoraco-lumbar junction and subsequent cuts at every second vertebral junction. For the rear legs, the usual sagittal section that includes longitudinal sections of skeletal muscle and the knee joint is supplemented by a second cassette that should contain at least six cross-sections of the contralateral leg (with three transverse sections above the knee and three more below the knee).

Histopathology

As with all other organ systems, it is essential to know normal histology in order to recognize any abnormalities that may exist. There are many other texts and resources that provide a comprehensive description of the normal histology, ultrastructure, and histochemistry of motor neurons, peripheral nerves, motor end plates, and muscle, so this chapter will focus only on those features most relevant to phenotyping neuromuscular disease in mice in specific anatomical sites.

The types and distribution of lesions in muscle can provide an early indication as to whether the myopathy is myogenic or neurogenic in origin. With neurogenic disease, the severity of atrophy can vary widely between different muscle groups, and distal muscles are often affected earlier, and are characterized by small rounded myocytes. Atrophic fibers may be restricted to specific muscles or appear in clusters next to normal or hypertrophic fibers (Figure 16.4a). Another important sign of neurogenic origin in atrophic fibers is that most cell nuclei remain at the periphery of the fibers (Figure 16.4b).

When the primary lesion affects motor neurons, the muscle lesion will often appear as atrophic and rounded myocytes affecting most fibers in a fascicle. Congenital motor neuron diseases show widespread atrophy with very small round myofibers in every fascicle. In neurogenic myopathies, myocyte nuclei are typically peripheral rather than internalized. The grouping of many small angular fibers, sometimes with fiber type conversion, are indications of chronic neurogenic atrophy following cycles of denervation and reinnervation. The atrophic fibers often appear in clusters surrounded by normal or hypertrophic fibers. The clustered distribution pattern of atrophic fibers reflects the innervation patterns of motor neurons. Since neurogenic myopathies tend to preferentially involve distal limb muscles at early stages, it is important to collect and examine cross-sections of the distal limbs.

Motor Neurons

Spinal cord lesions that cause neuromuscular disorders most often involve motor neurons in the ventral horn and/or the ventro-lateral myelinated white tracts. However, the dorsal root ganglia and sensory ascending tracts can also be affected. As mentioned previously, one of the most common problems in assessing gray matter lesions is the extensive vacuolization of neurons and neuropil caused by delayed or suboptimal fixation of the spinal cord. In fact, the primary reason for performing intracardiac perfusion fixation of mice is to prevent this artifact. In properly fixed tissues, degenerating or dying motor neurons can be distinguished by the loss of Nissl substance, swollen soma, and only rarely, pyknotic nuclei. Motor neurons with pale eosinophilic cytoplasm and a faintly or unstained nucleus appear as "ghost cells" and can be accompanied by nuclear and/cytoplasmic swelling or inclusions in motor neuron diseases (Figure 16.5a). Generally, neuronal spheroids are easily detected with hematoxylin and eosin (H&E) stains (Figure 16.5b), but swollen soma and axons can be

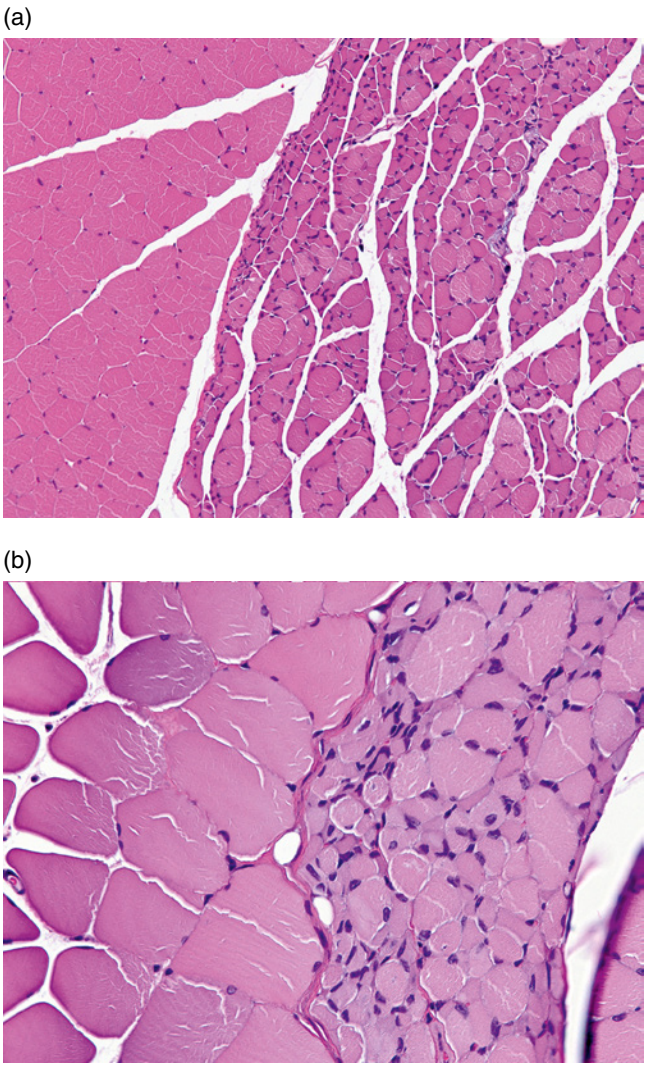


Figure 16.4 Mouse skeletal muscle – neurogenic myopathy. (a) Showing contrast between essentially normal muscle on left and extensive atrophy of muscle on right. (b) Higher magnification showing consistent peripheral location of myocyte nuclei associated with myogenic myopathies.

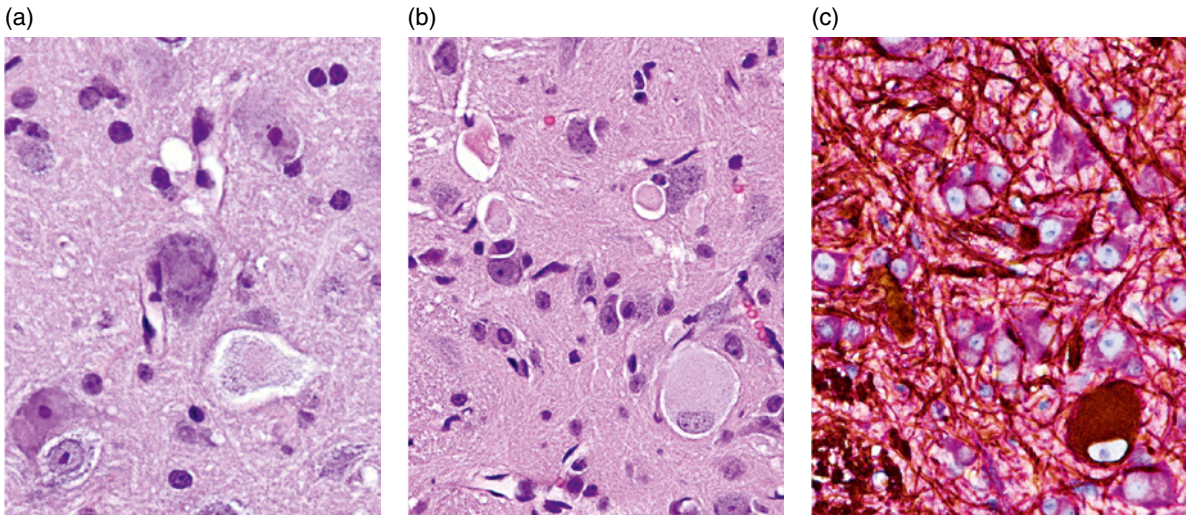


Figure 16.5 **Mouse spinal cord – lower motor neurons**. (a) "Ghost" motor neuron. (b) Axonal spheroids, cytoplasmic and nuclear alterations. (c) Sequential section labeled for neurofilament highlights neuronal and axonal enlargement.

highlighted by labeling for neurofilament protein (Figure 16.5c). However, it is important to remember that axonal swellings and spheroids often increase with age in normal mice, particularly within the lumbar spinal cord and in the gracile and cuneate nuclei in the brainstem.

Although an H&E stain is often sufficient to detect many types of lesions, there are several other useful histochemical and immunohistochemical methods that can be applied. For screening purposes, the most useful IHC markers for inflammatory reactions in the spinal cord include glial fibrillary acidic protein (GFAP) to detect reactive astrogliosis and Induction of Brown Adipocytes 1 (IBA1) to detect microglial activation. Cresyl violet stains motor neurons, but immunohistochemical labeling for the marker NeuN may be preferable for quantification of motor neurons since its labeling is restricted to neuronal nuclei. Regardless of the method used, assessing the extent and severity of motor neuron loss can be challenging because the number of motor neurons varies markedly at different levels of the spinal cord. For this reason, it is important to evaluate multiple sections of spinal cord that have been collected at strictly defined levels. The Luxol Fast Blue (LFB) stain is often used alone or in combination with cresyl violet to highlight demyelination in the white tracts and neurons, respectively (Figure 16.6a). Alternatively, immunohistochemical labeling of myelin basic protein (MBP) and neurofilament proteins enables assessment of both demyelination and axonal integrity, respectively, in the same tissue section (Figure 16.6b).

Peripheral Nerves

In pathology phenotyping, rapid perfusion fixation is key to identifying the location and type of lesions affecting the peripheral nerves. Collecting several cross-sections of the lumbosacral spinal column saves time by providing multiple undisturbed sections of sciatic nerve and dorsal root ganglia. Perfusion fixation prevents almost all necropsy-induced

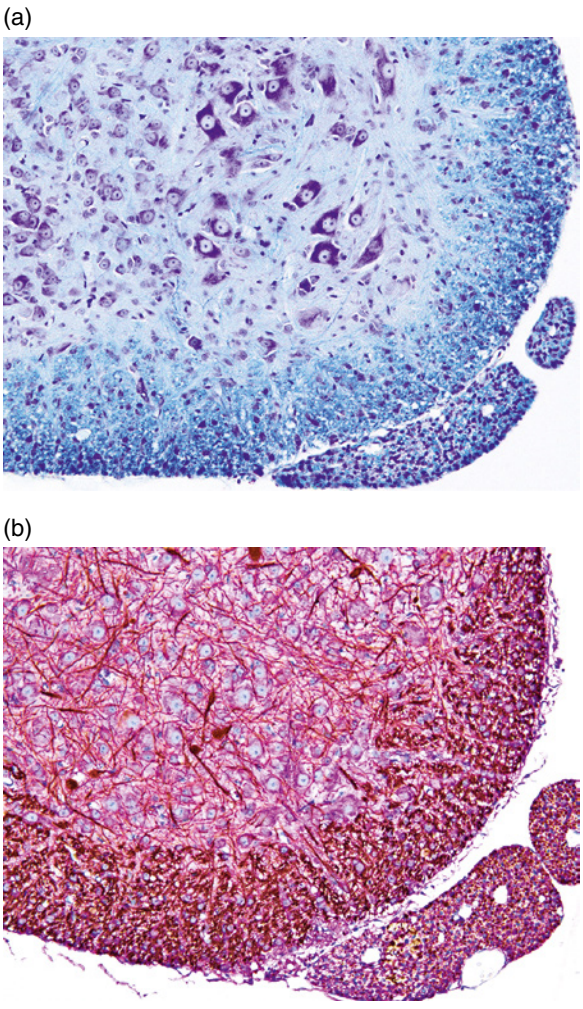


Figure 16.6 **Mouse spinal cord**. (a) Luxol fast blue stain highlight reduced myelin and cresyl violet stain facilitates neuron cell counts. (b) Double immunohistochemical stain for neurofilament (brown) and myelin (violet) on sequential section highlights axonopathy in spinal cord and adjacent spinal nerves.

artifacts, including the shrunken "dark neurons" in the brain and spinal cord that are produced when pressure is applied to unfixed or poorly fixed tissues. As implied by their name, shrunken dark neurons are characterized by deeply basophilic cytoplasm, reduced size, and irregular scalloped outlines. Well-demarcated cytoplasmic vacuoles in dorsal root ganglionic neurons and vacuolated myelin sheaths are artifacts that can occur following prolonged immersion in an alcohol-containing fixative during fixation or processing.

The sciatic nerve is the most frequently collected and evaluated nerve in studying peripheral nerve-related phenotypes. It is the largest peripheral nerve in mice and originates from spinal cord segment L3–L4. Evaluation of peripheral nerves can reveal abnormal axon profiles in the absence of motor neuron loss, which would indicate an axonopathy. In many studies, a relatively small section of sciatic nerve is dissected at time of necropsy from the lateral aspect of the thigh. However, this approach is time-consuming and misses a much longer, but unfortunately less accessible section of the nerve located in the lumbosacral area. Dissection also misses the more distal peroneal and tibial nerve branches. Since these peripheral nerve dissections are generally performed at time of necropsy, they involve handling of unfixed tissues, which can create artifacts that compromise the identification of potential lesions.

For example, the crushing or stretching of unfixed peripheral nerves during dissection can cause artefactual fragmentation and/or beading of axons that can be difficult to distinguish from pathological nerve fiber degeneration or axonal dystrophy. Even when real peripheral nerve lesions are present, it is important to remember that nerve fiber degeneration affecting a small number of fibers is often seen as a background change in control mice, especially in old mice. In contrast, gene-related peripheral nerve phenotypes typically affect numerous fibers in many different nerves, and often are present in young mice. Another artifact that can occur in peripheral nerves is the extensive vacuolization of myelin caused by extended exposure to alcohol-containing fixatives or dehydrating solutions during tissue processing; this change can be recognized as an artifact because it is almost always accompanied by widespread vacuolization of white tracts in the brain.

Collection and processing of perfusion-fixed cross-sections of the spinal column also facilitates the analysis of dorsal root and autonomic ganglia. In dorsal root ganglia, neurons are broadly classified as either large-diameter ("type A") or small-diameter ("type B") cells. The large-diameter neurons transmit nonnociceptive signals from the periphery to the spinal cord dorsal horn via large-caliber, thickly myelinated Aβ fibers, whereas the small-diameter ("type B") neurons carry mechanoreceptive, nociceptive, and thermal signals via thinly myelinated Aβ fibers or unmyelinated C-fibers. Lesions affecting the dorsal root ganglia (DRG) are increasingly recognized as causes of sensory loss and ataxia and are often accompanied by recognizable lesions in the gracile and cuneate fasciculi. In contrast to the DRG, autonomic ganglion neurons are small and more uniform in size, and lesions are not associated with signs of neuromuscular dysfunction.

H&E is the most common histological stain used to evaluate the peripheral nerves and white tracts. A combined LFB/cresyl violet stain is particularly useful for evaluating spinal cord and peripheral nerves. Other commonly used stains include LFB or modified Gomori's Trichrome (for myelin), and Bielschowsky's silver (for axons). Particularly useful immunohistochemical markers include neuronal nuclear antigen (NeuN, used to visualize neurons), glutamine synthetase (to label satellite glial cells in ganglia), and toluidine blue (typically used to stain osmicated, resin-embedded sections). These special stains may aid identification of lesions that are difficult to discern on routine H&E-stained sections. However, whenever myelin or axonal lesions are found or suspected in FFPE tissues, additional mice can be fixed by perfusion with methanol-free 4% formaldehyde, followed by postfixation in glutaraldehyde and osmium tetroxide, embedding in hard plastic resin, sectioning at 1 μm, and staining with toluidine blue.

Both the motor and sensory nerves can be affected in peripheral nerve disease, resulting in impaired sensation, movement, or other functions. Clinically, damage to motor nerves is usually associated with muscle weakness, fasciculations, and atrophy, whereas damage to the large sensory fibers can affect gait by impeding motor reflexes and the ability to sense touch and vibrations. The majority of gene mutations responsible for peripheral neuropathies affect proteins that have roles in maintaining the structure or function of the two main cellular components of the peripheral nervous system. These are the axons (of ventral horn spinal motor neurons and dorsal root ganglia sensory neurons) and the Schwann cells, which produce the myelin sheaths.

Motor neuron loss is invariably associated with variable severity demyelination and axonopathy, which in advanced cases will result in reduced sciatic nerve diameter and histologically evident lesions (Figure 16.7a,d). In milder cases, it may be necessary to measure the diameter and count axons in spinal nerve roots or major nerves. As in the spinal cord, a LFB stain is often used to highlight demyelination in peripheral nerves (Figure 16.7b,e), whereas immunohistochemical labeling of MBA and neurofilament proteins can highlight axonal lesions not easily detected in H&E or LFB stained sections (Figure 16.7c,f). Although the sciatic nerve is typically used to evaluate neuropathies, lesions are often more advanced and easier to detect in the distal nerves of the leg and feet (Figure 16.8a–d).

The axon is the primary target in axonopathies, whereas Schwann cells and/or myelin sheath are the primary target in myelinopathies. Usually, the primary site of damage can only be discriminated at the earliest stages of nerve fiber degeneration because reciprocal interactions between axon and myelin result in degeneration of both structures as well as the motor neurons that give rise to peripheral nerve axons. Lesions in peripheral nerves are typically accompanied by secondary changes in motor neurons, dorsal root ganglionic neurons, NMJs, and myocytes. For example, primary

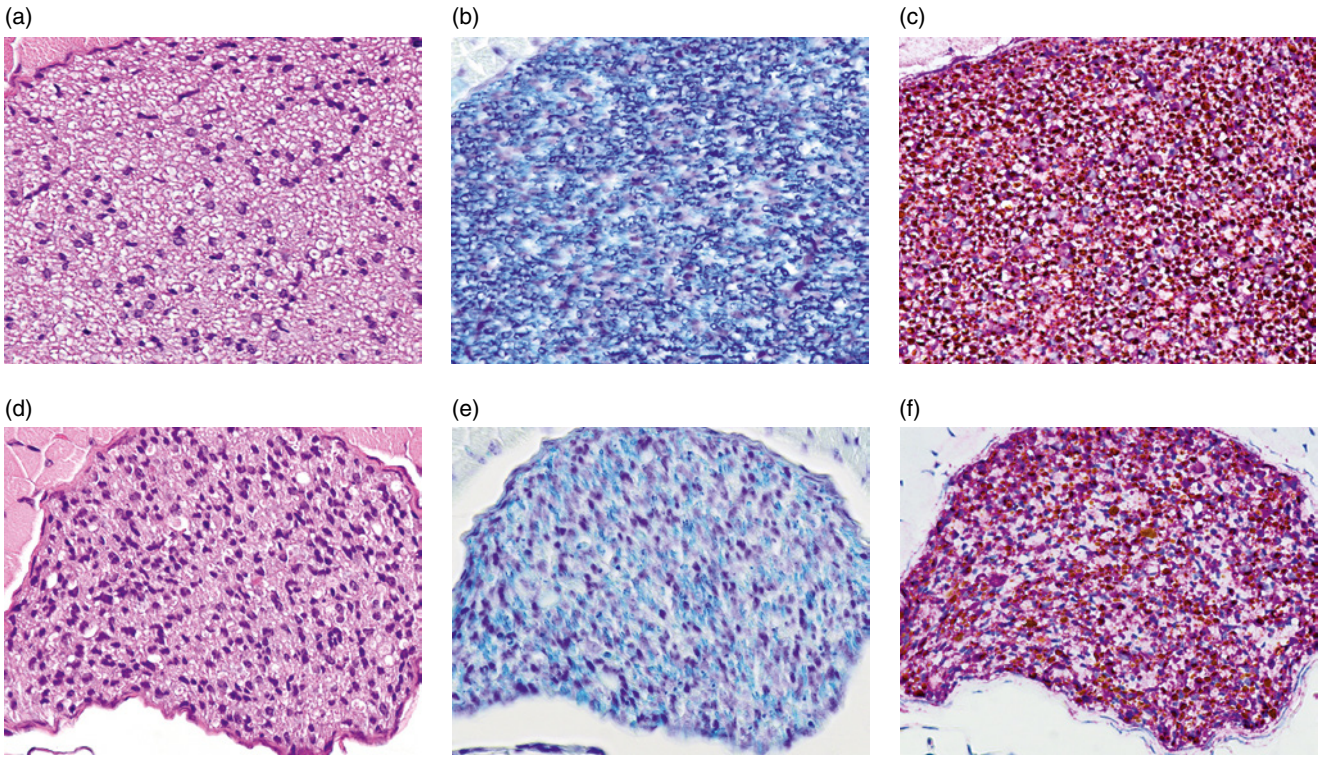


Figure 16.7 **Mouse sciatic nerve**. (a–c) Transverse sections show normal sciatic nerve stained with H&E, Luxol fast blue, and labeled with neurofilament/myelin basic protein, respectively. (d) Sciatic nerve from a mouse with peripheral neuropathy show reduced size of sciatic nerve and increased cell density with H&E. (e) Sequential section show reduced myelination with LFB stain. (f) IHC for neurofilament protein demonstrates reduced numbers and disruption of axons.

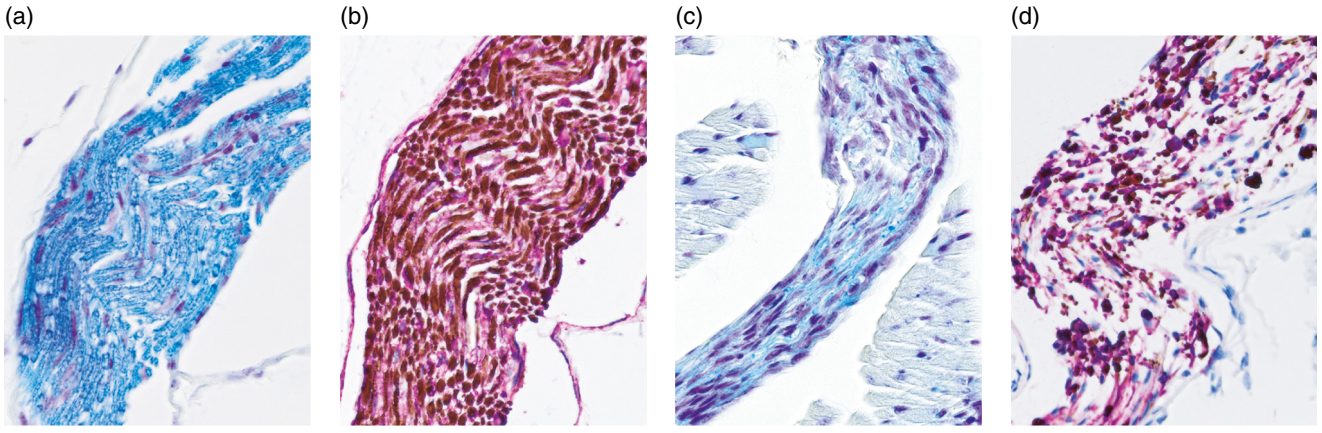


Figure 16.8 **Mouse femoral nerv**e. (a, b) Longitudinal sections show normal appearance of a femoral nerve stained with Luxol Fast Blue (a), and labeled with neurofilament/myelin basic protein (b). (c) The femoral nerve from a mouse with peripheral neuropathy stained with LFB shows reduced size and myelination of the femoral nerve. (d) Sequential section labeled for neurofilament (brown) and myelin basic protein (violet) shows reduced myelin and fragmentation of axons.

axonopathies and myelinopathies often result in motor neuron chromatolysis, which is characterized by dissolution of basophilic Nissl substance and expanded cytoplasm.

Most inherited neuropathies involving damage to the peripheral nerve as the primary target are included within a heterogenous group of diseases classified as Charcot–Marie–Tooth disease (CMT). Mutations in over 120 genes have been found to be associated with the pathogenesis of CMT, and numerous rodent models for CMT subtypes are available. Many genes that are highly expressed in Schwann cells or motor neurons have been linked to CMT, which typically manifests as a distal muscle atrophy that is both symmetric and progressive.

CMT is divided into two major groups based on pathological and electrophysiological findings. Cross-sections of distal

limbs and the feet may show muscle-specific atrophy that can be helpful in making a diagnosis by histopathology. In CMT1, scattered or grouped angular atrophic fibers are typical, whereas both atrophic and hypertrophic fibers with fiber splitting are more common in CMT2. These differences are most likely due to more active denervation/re-innervation processes where damage to myelin can be repaired by Schwann cells. In contrast, damage to axons is often irreversible, and hypertrophy of surviving myocytes compensates for the absence of re-innervation. However, histopathologic findings are somewhat variable so measurement of motor nerve conduction velocities are generally required to differentiate between the myelinopathies (CMT1) and axonopathies (CMT2). Demyelination in CMT1 results in markedly reduced nerve conduction velocities, whereas axonal neuropathy in CMT2 is typically associated with normal to near-normal nerve conduction velocities. In both types of CMT, the progressive length-dependent lesions typically affect both motor and sensory peripheral nerves. Lesions in the upper motor neurons in the cerebral cortex should be considered when the myelin/axons in the corticospinal tract and dorsal columns of the spinal cord are affected (for example in hereditary spastic paraplegia).

Axonal lesions in the peripheral nervous system and DRG are often associated with lesions in the spinal cord, and the distribution of these lesions can be helpful in understanding a disease process. The cranial cervical cord (C_1–C_2) sections are particularly useful for this because the spinal cord at this level contains the greatest concentration of sensory and motor fibers dedicated to PNS functions. In these sections, axonal degeneration and gliosis caused by primary sensory neuropathies are concentrated in the dorsal funiculi (gracile and cuneate fasciculi), whereas lesions are located in the dorsolateral tracts (i.e. spinocerebellar fibers) when caused by secondary sensory neuropathies. With combined primary and secondary sensory and motor neuropathy, white tract lesions occur in the dorsal funiculi, dorsolateral tracts (containing spinocerebellar fibers and crossed pyramidal fibers), and ventromedial tracts. These tract-specific patterns of spinal cord damage are characteristic of axonopathies, whereas pure demyelinating lesions usually involve all white tract columns in the spinal cord.

Neuromuscular Junctions

The NMJ is the synapse between a lower motor neuron and a skeletal muscle fiber. NMJ disorders result from the destruction, malfunction, or absence of key proteins involved in the transmission of signals between muscles and nerves.

Myasthenia gravis (MG) is the most common NMJ disease, and it is most often caused by autoantibodies that bind acetylcholine receptors in the postsynaptic membrane or less often, a receptor-associated muscle specific tyrosine kinase (MuSK). Clinical signs of myasthenia gravis are accentuated with exercise, and include tremor, hunched posture, muscle weakness, and fatigue. Much of what has been learned about the pathogenesis of MG comes from mouse models that involve the passive transfer of autoantibodies against acetylcholine receptors or MuSK protein, or active immunization against the same targets. Similarly, antibodies directed against calcium channels on nerve endings are responsible for another myasthenic syndrome (Lambert–Eaton). Another group of NMJ diseases, the congenital myasthenic syndromes (CMSs), have been linked to mutations in over 15 different genes that code for proteins involved in neuromuscular transmission at presynaptic (nerve), postsynaptic (muscle), or synaptic locations. Presynaptic CMS involves insufficient release of ACh; postsynaptic CMS is caused by ACh receptors that are missing or dysfunctional, whereas synaptic CMS is associated with reduced acetylcholinesterase activity.

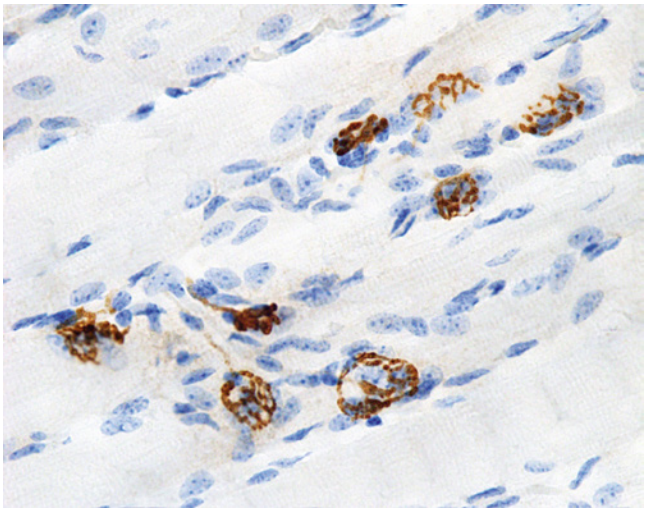
In adult mice, NMJs have a complex pretzel-shaped structure and tend to be concentrated near the middle of the muscle. In FFPE tissues, the NMJs are best visualized by using immunohistochemical labels for neurofilaments and synaptophysin on 10 µm thick longitudinal sections of muscle. When evaluating possible NMJ phenotypes, it is essential to compare them with controls from the same muscle, because NMJs in different muscles vary in size and shape. Immunohistochemical labels can reveal morphologic changes such as smaller nerve terminals and reduced complexity and area of endplates (Figure 16.9a,b). NMJ defects may lead to marked variation in muscle fiber size, but electron microscopy is required to detect the reduced postsynaptic folding and widened synaptic clefts associated with NMJ specific diseases such as MG. Other NMJ changes that can be recognized with light microscopy include shrunken NMJs, atrophied axons, and swollen or dystrophic axons or terminals. However, none of these morphologic changes are specific to NMJ disease, as they are also seen in nervous system disorders such as amyotrophic lateral sclerosis (ALS), CMT disease, and spinal muscular atrophy (SMA).

The small size and limited numbers of NMJs in standard longitudinal sections of hind limbs can hinder histopathological assessments in high throughput phenotype screening protocols so any suspected findings in routinely collected and processed tissues may justify the use of more specialized dissection and staining protocols on whole-mount or frozen sections of NMJ-rich muscles. With frozen sections and whole mounts, the most consistent histological finding in MG is a marked reduction in acetylcholinesterase (ACHE) activity at the end plates. Other components of the NMJ can be labeled for neurofilament (axons), synaptic vesicle 2 (pre-synaptic nerve terminals), and α-bungarotoxin (postsynaptic receptors). Transmitter release sites at the endplate can be specifically labeled with antibodies to the protein bassoon, which is a scaffolding protein in the presynaptic cytoskeleton.

Mechanoreceptors

The mechanoreceptors are specialized sensory organs located within joints, muscles, and tendons. The most important mechanoreceptors are the muscle spindles and the Pacinian corpuscles. Given their functions, problems

(a)



(b)

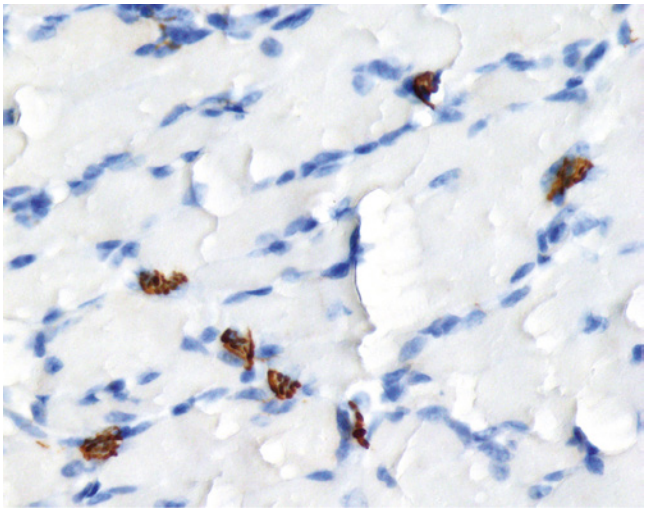


Figure 16.9 Mouse skeletal muscle – neuromuscular junction (NMJ). (a) Normal NMJs labeled for synaptophysin have a complex shape. (b) NMJs are small and distorted in this mouse with peripheral nerve disease.

with these mechanoreceptors typically present clinically as spasticity or exaggerated tendon reflexes (hyperreflexia). Despite their anatomic and functional complexity, surprisingly few pathologic phenotypes have been identified in mechanoreceptors.

Muscle spindles are complex fusiform stretch-sensitive organs located within the belly of skeletal muscles (Figure 16.10a). In adult mice, muscle spindles are 200–400 μm long and consist of three to eight specialized intrafusal muscle fibers that are oriented parallel to the regular (extrafusal) muscle fibers. Muscle spindles are most numerous in muscles where accurate proprioception is important, such in the forepaws and neck, where they play important roles in integrating information on the position of digits and the head, respectively. They contain two types of specialized intrafusal muscle fibers that are richly innervated by both sensory and motor neurons. The central (equatorial) regions of intrafusal fibers contain numerous nuclei that are either aggregated (in nuclear bag fibers) or form beaded rows (in nuclear chain fibers). The polar regions of both types contain normal contractile myofibrils, which stain for slow twitch myosin in nuclear bag fibers or for type II (fast twitch) myosin in nuclear chain fibers (Figure 16.10b). These intrafusal fibers and nerves are supported by a delicate fibrillar matrix and enclosed in a connective capsule, which is surrounded by extrafusal myocytes.

The muscle spindles are rapidly adapting sensorimotor receptors innervated by large sensory axons and γ motor axons. The cell bodies of the afferent sensory axons are located in the dorsal root ganglion and form annulospiral nerve endings over the central (equatorial) regions of the intrafusal fibers (Figure 16.10c). The sensory fibers can be labeled with antibodies raised against synaptophysin or vesicular glutamate transporter 1 (VGluT1). The efferent axons of γ-motor neurons innervate the intrafusal muscle fibers at both ends (polar regions) via cholinergic synapses that are functionally similar to the NMJs formed by γ-motor neurons on extrafusal muscle fibers. The intrafusal fibers monitor changes in the extent and rate of stretching of surrounding skeletal muscles and relay this information to the central nervous system, which communicates corrective adjustments to the tonicity of both agonistic and antagonistic muscle groups.

The muscle spindle's sensorimotor functions are important for proprioception, balance, gait, and postural responses; therefore, muscle spindle phenotypes should be considered in mice with clinical signs of ataxia, hypotonia, reduced or absent tendon reflexes, incoordination, and floppiness. These types of clinical signs are common in humans with congenital core myopathies, suggesting muscle spindle involvement. It is likely that the rarity of these tiny organs in human biopsy or autopsy-derived muscle samples has hindered the identification of lesions in human muscle spindles.

However, since relatively large numbers of mechanoreceptors are consistently present in routinely collected mouse tissues, mouse pathologists are well-positioned to discover mechanoreceptor lesions through careful evaluation of mice with clinical signs of neuromuscular disease. In mice, it is possible to evaluate both major types of mechanoreceptors – the muscle spindles located in muscles and the lamellar/Pacinian corpuscles located in the interosseous membranes (between tibia and fibula, or radius and ulna).

There are a few human diseases and mouse models that have been directly linked to mechanoreceptor defects. The markedly ataxic gait in humans affected with familial dysautonomia (also known as Riley–Day syndrome) has been attributed to impaired proprioception caused by the absence of muscle spindle function. *Egr3*-deficient mice ($Egr3^{tm1Jmi}$) lack muscle spindles and display sensory ataxia, abnormal limb positioning, and muscle tremors at rest. Neuregulin1 (*Nrg1*) and Erbb2 are also required for muscle spindle and Pacinian corpuscles development in mice. Mice with disrupted muscle spindles are ataxic and show spasticity and

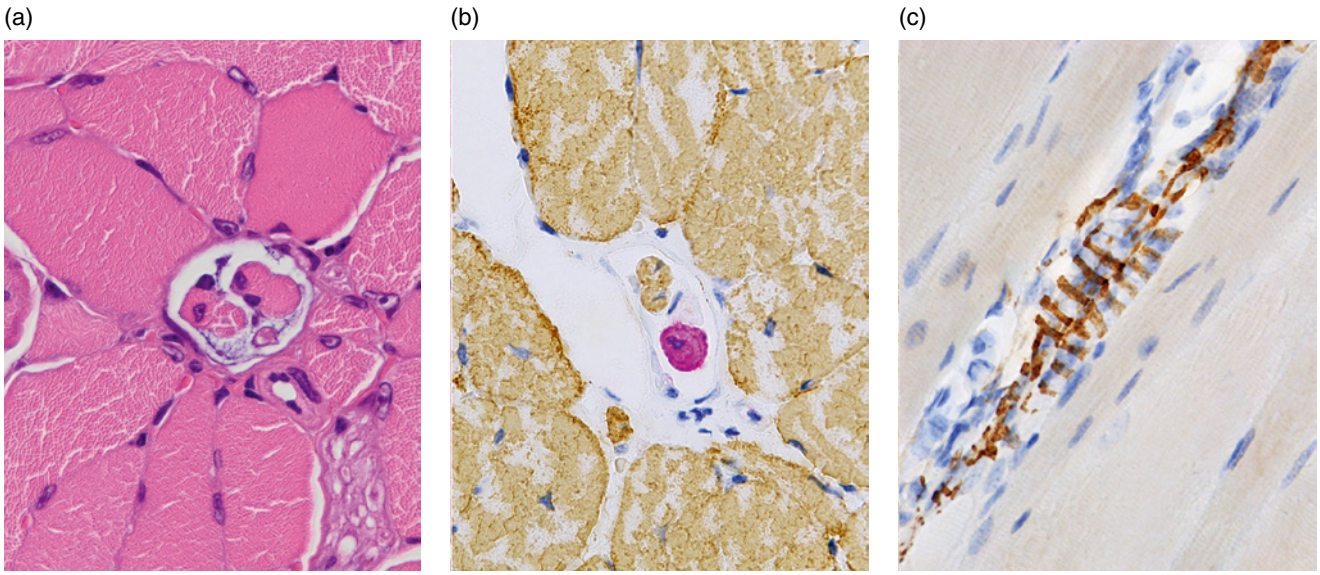


Figure 16.10 Mouse skeletal muscle – muscle spindle. (a) Normal muscle spindle. (b) Muscle spindle showing chain fibers labeled for fast (brown) and bag fiber labeled for slow (red) myosin. (c) IHC labeling for synaptophysin shows annulospiral nerves surrounding fusiform muscle spindle fibers.

abnormal hind limb reflexes. Interestingly, muscle spindles are resistant to degeneration in dystrophin- and dysferlin-related myopathies in humans, and the numbers and morphology of muscle spindles also appear to be normal in both dystrophin- and dysferlin-deficient mice.

Pacinian corpuscles represent another mechanoreceptor that is easy to evaluate consistently in mice. Pacinian corpuscles are relatively large mechanosensory organs located within the interosseous membranes of the lower limbs (Figure 16.11a). They have an inner core containing a single myelinated mechanosensory axon and a much thicker outer capsule composed of thin concentric lamellae composed of flattened nonmyelinating Schwann cells (Figure 16.11b). Pacinian corpuscles are defective or fail to develop in mice having defects affecting any part of the RET-ER81-Neuregulin 1 signaling pathway [42].

Myocytes

Some myopathies can be detected by tests that reveal muscle weakness, such as the grip strength or inverted screen tests while others can alter body composition or lean muscle mass enough to be detectable by dual-energy X-ray absorptiometry (DEXA) assays. However, histopathology is clearly the most sensitive and specific method for discovering myopathies. Routine H&E staining is sufficient for recognizing almost all myopathies in high-throughput screening programs, but there are several immunohistochemical markers that can help identify underlying pathogenetic mechanisms.

Transverse sections of the spinal column and legs are used to characterize myogenic myopathies, and internalization of myocyte nuclei is a very sensitive early indicator of a myogenic myopathy (Figure 16.12a,b). These internalized nuclei are better seen in muscle cross-sections than in longitudinal sections. In cross-sections of normal skeletal muscles in the adult mouse, myocytes appear as closely apposed polygonal cells with peripheral subsarcolemmal nuclei. Although internalized nuclei are an important early sign of muscle damage, it is important to remember that small numbers of internalized nuclei can be found in normal muscle, especially near myotendinous junctions. In early stages of myopathy, internalized nuclei may be accompanied by myocyte degeneration, inflammation, atrophy, fatty infiltration, and fibrosis.

Common lesions associated with advanced myogenic myopathies include myofibril disarray, with degeneration and necrosis of myofibers (Figure 16.12c). Coagulation and fragmentation of sarcoplasm are often associated with inflammatory infiltrates (Figure 16.12d). Cluster of degenerating fibers can also be present with myogenic myopathies, but nuclei in affected fibers are generally centralized or absent (Figure 16.12e). Mineralization, fibrosis, and inflammation are common findings in some chronic myogenic myopathies (Figure 16.12f).

Although sometimes interpreted as such, internalized nuclei in normal-sized myocytes are in fact not indicators of regeneration. Myocyte regeneration is characterized by thin basophilic fibers with nuclei that are intensely labeled for desmin and express nuclear proliferation markers such as MyoD1 (myogenic differentiation 1) and Myogenin (Figure 16.13a–d).

Evidence of myocyte regeneration (small diameter basophilic myocytes with rowed nuclei) is more common at earlier stages, whereas interstitial inflammation/fibrosis and adipose tissue infiltration and replacement of muscle are features of late-stage disease. These lesions may be diffuse or scattered, so it is important to examine all available muscle sections since lesion severity can vary markedly between individual muscles.

(a)



(b)

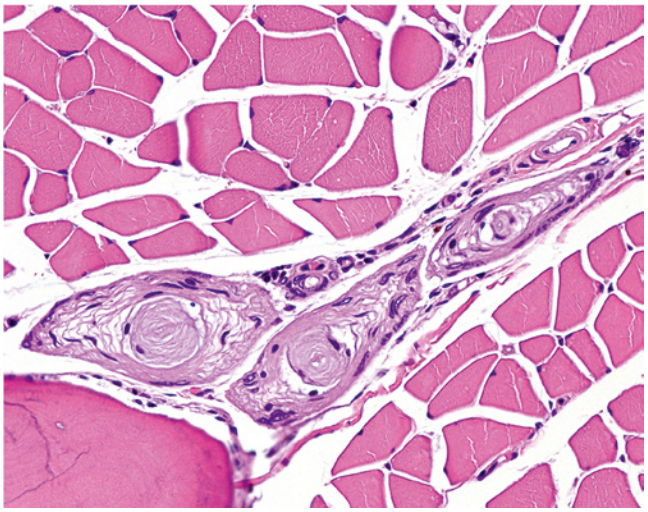


Figure 16.11 Mouse skeletal muscle – interosseous membrane and Pacinian corpuscles. (a) An interosseous membrane consisting of loose fibrous connective tissue connects the tibia and fibula in the rear leg. (b) Pacinian corpuscles are located with the interosseous membrane.

In addition to occasional internalized nuclei in normal skeletal muscle, there are other relatively common incidental findings in mouse muscle that pathologists should be aware of when evaluating potential myopathies. For example, contraction bands are artifacts characterized by dark hypercontracted regions interspersed with pale areas of disrupted myofibrils (Figure 16.14a). Contraction bands are most found near the cut ends of longitudinal sections of muscle. They are caused by handling and sectioning of unfixed or incompletely fixed tissues. Many standard myology texts recommend the use of muscle clamps to keep muscles at isometric length during fixation in order to prevent contraction bands. Fortunately for the mouse pathologist, muscle clamps are not needed since contraction bands do not develop in perfusion-fixed mice when dissection is delayed until fixation is complete.

Mouse pathologists need to be aware of a common incidental lesion that develops in the skeletal muscle of older male mice (over 12 months of age) that closely resembles central core disease in humans. In mice, these lesions are termed tubulovesicular inclusions (TVIs). By light microscopy, TVIs typically appear as central cores of pale amorphous material in type II muscle fibers (Figure 16.14b,c). TVIs are shown by electron microscopy to consist of massed tubulovesicular structures. Although TVIs are common in aged male mice of most strains, similar lesions in young mice or in female mice of any age or strain would most likely represent a true pathologic phenotype.

Myogenic myopathies in mice typically affect many different muscles in the body. Widespread internalization of myocyte nuclei appears to be a reaction to virtually any type of muscle injury. In longitudinal sections of muscle, internalized nuclei form long chains, and this finding is sometimes misinterpreted as evidence of muscle regeneration. Other lesions commonly associated with myogenic myopathies include scattered foci of myocyte degeneration/necrosis, inflammation, fatty infiltration, and fibrosis. Of these lesions, segmental degeneration of myocytes is the most common, with myocytes at early stages appearing as hypereosinophilic swollen fibers lacking striations (hyaline or waxy degeneration). Degenerating/necrotic myocytes may also undergo vacuolar or hydropic degeneration and appear as swollen pale mottled/fragmented fibers. These lesions may progress to globular or granular degeneration, where small basophilic granules (mineralized mitochondria) fill the myotube. In some types of myogenic myopathy, disarray of myofibrils may present, with occasional ring fibers, which are characterized by the circumferential orientation of peripheral myofibrils. Atrophy and variations in fiber diameters are commonly present, and some hypertrophic fibers may divide into smaller subunits (fiber splitting), creating a clefted multilobular appearance. Nuclear inclusions are associated with inclusion body myositis and sarcoplasmic inclusions with myofibrillar myopathies.

As much as possible, the collection of leg cross-sections should be standardized in order to make valid comparisons in fiber number, fiber size, and composition, all of which vary along the longitudinal axis in limb muscles. By itself, variation in muscle fiber size is not a particularly reliable indicator of neuromuscular disease because myocytes sectioned at the middle of each muscle have larger diameters than those sectioned closer to the ends. Also, myofibers in proximal limb muscles have larger mean fiber diameters than those in the distal limb, surrounding the spine, or on the head. These normal variations must be accounted for in morphometric studies intending to compare average muscle fiber diameters. In addition, because muscle fibers are often smaller and often more rounded in both very young, and very old mice it is essential to use age-matched littermate controls for any morphometric studies on muscle.

Myogenic myopathies are frequently accompanied by changes in surrounding stroma. In normal muscle, individual

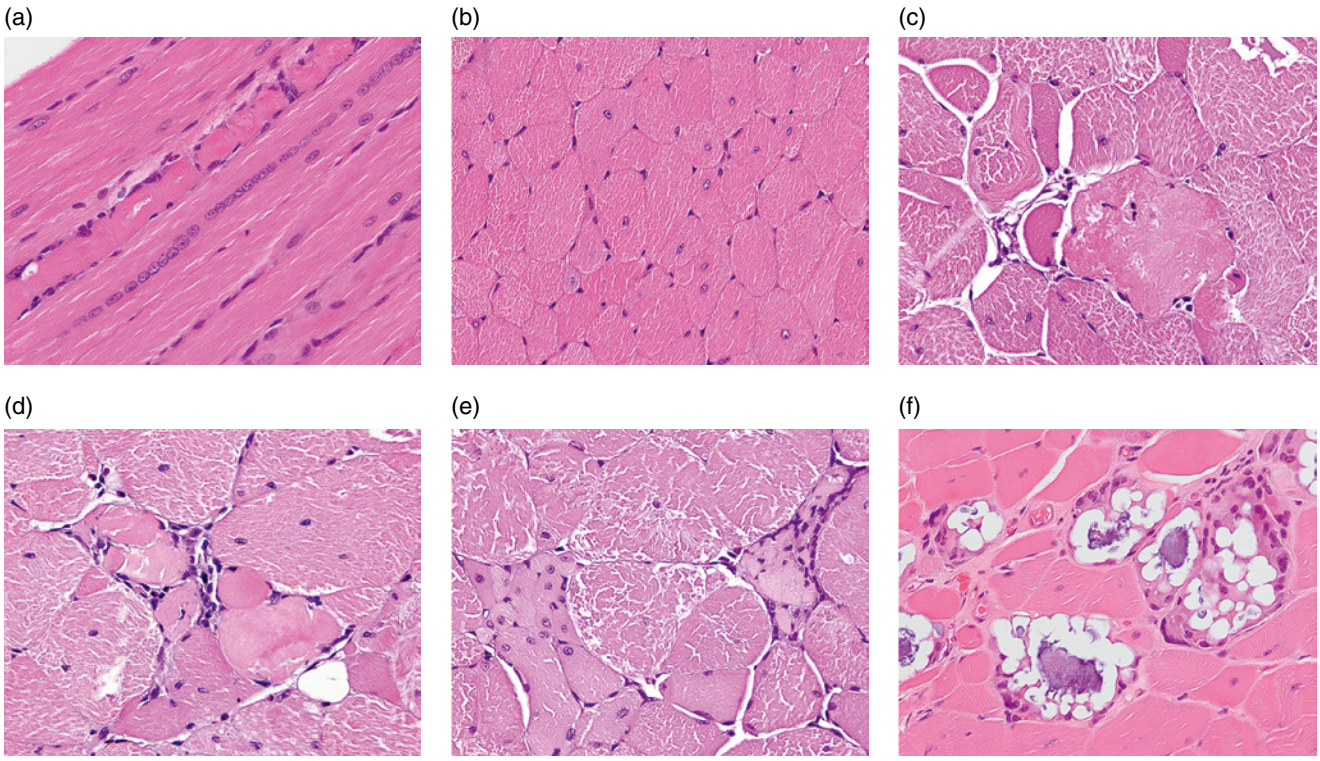


Figure 16.12 **Mouse skeletal muscle – myogenic myopathy**. (a) Internalization of myocyte nuclei in longitudinal section. (b) Internal/Central nuclei in cross-sectioned muscle fibers. (c) Rounded and irregular fibers, myofibrillar disarray, hypereosinophilic sarcoplasm, and fiber splitting. (d) Inflammatory cell surrounding and within degenerating myocytes with coagulated sarcoplasm. (e) There are clusters of degenerating fibers, but they show central nuclei and inflammatory cell infiltrates. (f) Mineralization of necrotic sarcoplasm surrounded by macrophages. Interstitial fibrosis and inflammation are also present.

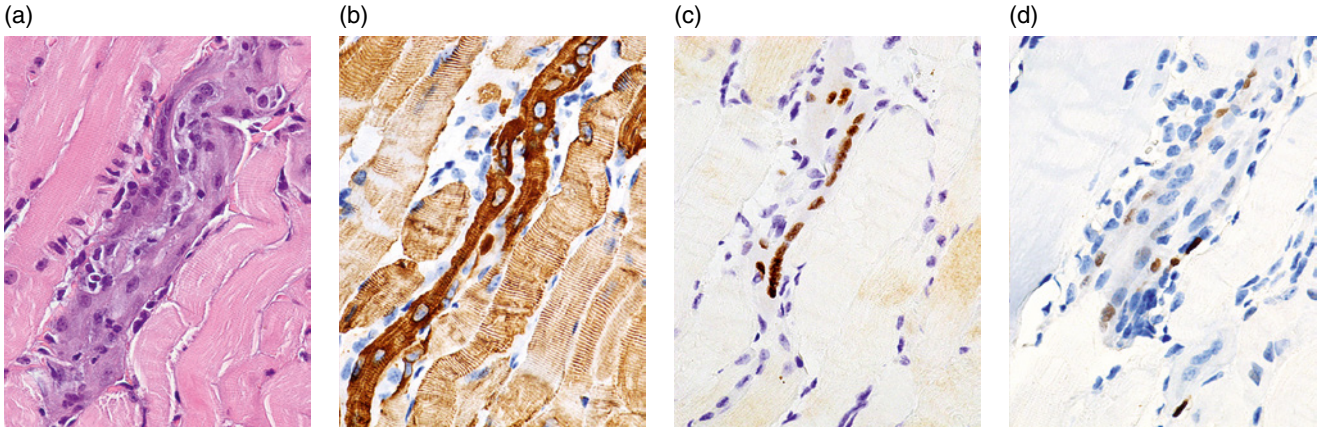


Figure 16.13 **Mouse skeletal muscle – regeneration**. (a) Regenerating fibers are thin and have basophilic cytoplasm and abundant nuclei in H&E stained tissues. (b) Desmin IHC shows intense labeling of regenerating fibers. (c) IHC labels myogenin in nuclei of regenerating muscle. (d) IHC labels MyoD in nuclei of regenerating muscle.

myocytes are surrounded by inconspicuous connective tissue (endomysium) containing capillaries. With myopathies, there is often detectable thickening of the endomysium, which is best visualized with Sirius Red or Trichrome stains. The epimysium divides groups of muscle fibers into fascicles while individual muscles are separated and defined by the perimysium, which contains the intramuscular nerves, veins, and arteries, and merges with the dense collagenous connective tissue of tendons and fascia. In transitional areas, where muscle and connective tissues meet, the increased variation in muscle fiber size and small numbers of internalized nuclei should not be interpreted as pathologic changes.

Although most lesions of myogenic myopathies can be identified with routine H&E staining, the full extent and types of muscle lesions are better demonstrated by immunohistochemical labeling for desmin (Figure 16.15a,b), which

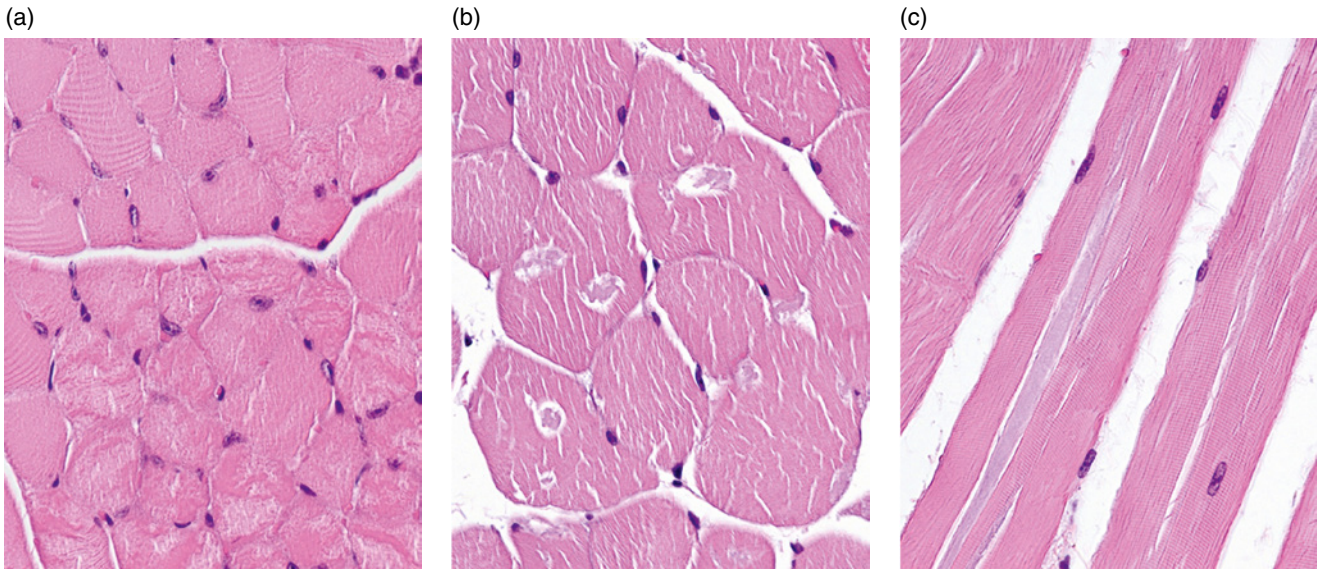


Figure 16.14 **Mouse skeletal muscle – old male mice**. (a) Prominent contraction bands. (b) Cross-section showing tubulovesicular aggregates/inclusions. (c) Longitudinal sections showing tubulovesicular aggregates/inclusions.

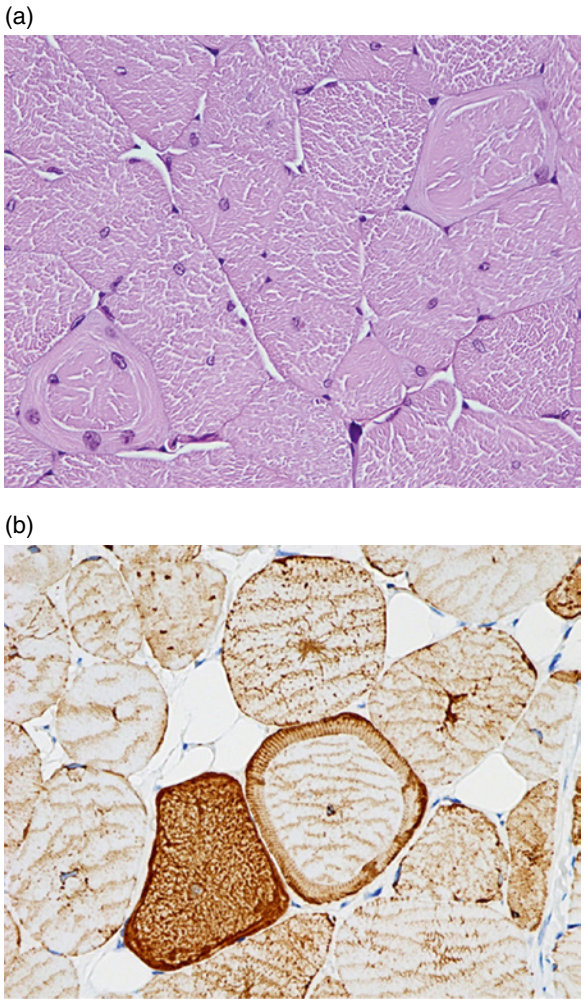


Figure 16.15 **Mouse skeletal muscle**. (a) Centralized nuclei and ring fibers. (b) IHC for desmin highlight myofibrillar disarray and disruption.

is an intermediate filament protein that is a major component of the three-dimensional cytoskeleton of myocytes. Desmin is involved in aligning and anchoring myofibrils, positioning mitochondria and nuclei, and cell signaling. In normal muscle, desmin forms delicate cross-striations that mirror the staining pattern of myosin. In almost all myogenic myopathies, these cross-striations are disrupted at early stages of disease development, and desmin-positive protein aggregates appear in the sarcoplasm with increasing lesion severity. Desmin labeling highlights disruptions in myofibril alignment and is also helpful in detecting necrotic/degenerating fibers, since those usually label negatively for desmin. In regenerating muscle, the cytoplasm of hypertrophic satellite cells/myoblasts located at the periphery of myotubes is often intensely labeled for desmin. There are several other markers other than desmin that can help pinpoint which dysfunctional cellular process or structure in myocytes is involved in the pathogenesis of a newly identified myopathy. These include structural defects affecting the sarcolemma, sarcoplasmic reticulum, mitochondria, and myofibrils, or functional defects affecting cellular processes that are critical for muscle function.

Sarcolemma

Some of the most common and serious muscular dystrophies in humans are related to defects involving the sarcolemma. The myocyte's sarcolemma consists of the outer basement membrane, basal lamina, plasma membrane, and associated sarcoplasmic cytoskeleton. Defective proteins in any of these layers of the sarcolemma can compromise sarcolemmal integrity and most forms of congenital muscular dystrophy involve proteins that either make up or interact with the sarcolemma or extracellular matrix. The best studied involve defects in dystrophin (*Dmd*), several sarcoglycans, dystroglycan (Dag1), or dysferlin (Dysf).

Dystrophin was the first protein identified as a cause of muscular dystrophy. It is a large cytoskeletal protein that is connected to a complex of cell membrane proteins that link it to the basal lamina. Defects in this complex or the extracellular matrix can result in degeneration/regeneration of myocytes, fiber hypertrophy, fibrosis, and replacement with adipose tissue. The mdx mouse (Dmd^{mdx}) lacks the protein dystrophin and is the most widely used model for Duchenne muscular dystrophy. However, this model has a much milder phenotype than seen in humans, so it is being replaced in preclinical trials by newer mouse models that more closely replicate the human disease phenotype.

Dysferlin is thought to have a role in repairing strain-related damage to the sarcolemma. The absence of dysferlin activity is responsible for Limb–Girdle Muscular Dystrophy type 2B in humans, and mouse models have been critical in understanding the pathogenesis of various dysferlinopathies. Mouse pathologists should be aware the SJL/J ($Dysf^{^{2J}m}$) and A/J ($Dysf^{prmd}$) mouse strains, which are widely used as models for multiple sclerosis (experimental autoimmune encephalomyelitis) research, also have a spontaneous mutation in the dysferlin gene. These mice develop a myopathy characterized by internalized nuclei, degeneration/necrosis, inflammation, marked variations in fiber size and fiber splitting (divided hypertrophic fibers), and eventual replacement by adipose tissue. The A/J mice are also prone to developing rhabdomyosarcoma [43]. Mouse models exist for many, but not all, forms of progressive muscular dystrophy in humans that are caused by mutations affecting sarcolemma-related proteins [44, 45]. These include defects in type VI collagen (*Col6a1, Col6a2, Col6a3*), laminin A/C, titin (*Ttn*), selenon (*Sepn1*), Secisbp2 (*Sbp2*), integrin alpha 7 (*Itga7*), plectin (*Plec*), Fukutin, FKRP, and many others [46].

When evaluating new myopathy models in mice, it is possible to test sarcolemmal membrane integrity by administering Evan's blue dye, which binds to albumin, and is normally excluded from intact cells. To perform this assay, dissolve Evan's blue dye in sterile saline at 10 mg/ml, inject the solution intraperitoneally in live mice at 0.1 ml per 10 g of body weight, and after 12 hours exposure, examine dissected muscles for blue coloration. An alternative approach for detecting permeabilized membranes (or necrotic myocytes) is to use IHC to detect albumin or immunoglobulins within myocytes in FFPE muscle sections from perfused mice.

Sarcoplasmic Reticulum and Transverse Tubules

The core myopathies comprise a group of nonprogressive congenital myopathies characterized histologically by the presence of variably sized amorphous pale areas within the sarcoplasm characterized histochemically by the absence of oxidative enzyme and phosphorylase activity. Ultrastructurally, these cores are created by proliferating sarcoplasmic reticulum and T-tubule networks that disrupt myofibrils. Although mutations in many different genes can be involved in central core disease in humans, most cases appear to be linked to mutations in the calcium channel protein ryanodine receptor 1 (*Ryr1*), which is also involved in an ion channel disease described below.

Ion channel diseases (channelopathies) are associated with mutations in genes encoding the calcium, sodium, chloride, or potassium channels located in the sarcoplasmic reticulum and T-tubules. Clinically, these diseases can present as muscle weakness, reduced muscle tone, or episodic muscle paralysis. Skeletal muscle lesions in channelopathies are generally absent, or limited at most to myocyte hypertrophy. However, malignant hyperthermia in humans is associated with mutations in *RYR1*, which normally controls the release of calcium ions from the sarcoplasmic reticulum into the transverse tubular systems. The uncontrolled release of calcium ions under certain conditions (e.g. anesthesia) causes diffuse muscle contractions and a very rapid severe rise in body temperature. The end result is massive rhabdomyolysis, where disintegration of cytoplasmic membranes and myofilaments results in the release of myoglobin and other skeletal muscle components into circulation. This process is often fulminant, but any survivors will display damage to kidneys (due to myoglobinuria) and widespread necrosis and inflammation in skeletal muscle.

Myofibrils

Myofibrillar myopathies involve proteins that play a role in the structure, maintenance, and protein quality control involving the Z-disc. The genes responsible for most myofibrillar myopathies have not yet been identified, but those that have code for proteins involved in the assembly of sarcomeres. Myofibrillar myopathies are characterized by disorganization of myofibrils and aggregates consisting of degraded myofibrillar products. Morphologically similar myopathies are caused by mutations in several different genes that code for structural components of the myofibrils [47]. For example, defects in desmin itself result in a typical myofibrillar myopathy, characterized by the presence of desmin-positive protein aggregates and degenerative changes in myofibrils. Similarly, the myofibrillar myopathy caused by mutations affecting filamin C (*Flnc*) is characterized by disintegration of myofibrils and the massive accumulation of protein aggregates within myocytes. The progressive muscle damage in these diseases is primarily caused by disruption of the intermediate filament network rather than the accumulated protein aggregates.

Mitochondria

Normal muscle structure and function is dependent on continual turnover of mitochondria, with mitochondrial quality being controlled by a balance of mitochondrial production (biogenesis) and destruction. Mitophagy is the process by which aged, damaged, and dysfunctional mitochondria are removed. In normal type I fibers stained for mitochondrial markers, a majority of mitochondria are concentrated as a thin band near the subsarcolemmal nuclei, with the remainder appearing within indistinct bands between myofibrils. In type II fibers, numerous small mitochondria colocalize

with the desmin intermediate filament network between microfibrils.

In conditions where mitophagy is reduced, a massive accumulation of enlarged dysfunctional mitochondria in the sarcoplasm results in impaired muscle metabolism and repair, which culminates in extensive myodegeneration. The appearance of so-called "ragged red fibers" is due to accumulations of abnormal mitochondria that stain red with modified Gomori trichrome. Although ragged red fibers are rarely seen in mouse tissues, IHC with mitochondrial markers can reveal the replacement of normal cross-striation staining pattern of small mitochondria in type II fibers by coarsely clumped large mitochondria. Irregular dense aggregates within subsarcolemmal and sarcoplasmic protein aggregates in affected myocytes often label for desmin.

Autophagy

Muscle is a metabolically dynamic tissue, and an imbalance between protein synthesis and protein degradation can lead to myocyte damage/loss. The turnover of proteins and organelles in muscle is mediated by both the ubiquitin-proteasome system and autophagy. The ubiquitin-proteasome system is the major pathway responsible for the degradation of contractile proteins in skeletal muscle and disruption of this pathway leads to the aggregation of sarcomere proteins such as myosin and myosin-associated proteins and microtubule disarray. The statin- or chloroquine-mediated myopathies may also involve inhibition of the ubiquitin-proteasome system.

However, the role of autophagosome–lysosome degradation is increasingly recognized as having an important role in both myogenic and neurogenic myopathies. Mice with mutations that impair autophagy are weak and show muscle atrophy and a degenerative myopathy characterized by distended sarcoplasmic reticulum, disorganized myofibrils, internalized nuclei, irregular vacuoles, decreased myofiber size, and accumulations of protein aggregates, abnormal mitochondria, and membrane bodies [48, 49]. The dysmorphic mitochondria accumulate in the sub-sarcolemma region in type I fibers and diffusely in type II fibers [48]. There are some particularly useful immunohistochemical markers in diagnosing autophagy-related myopathies. These include sequestosome 1 (p62/SQSTM1), microtubule-associated protein 1 light chain 3 beta (LC3B), and ubiquitin. Normally, these markers are barely detectable in myocytes because they are sequestered into autophagosomes and digested when the autophagosomes fuse with lysosomes. But accumulations of SQSTM1, LC3B, and ubiquitin all are indicative of reduced autophagy (Figure 16.16a–d). Some affected myocytes stain for albumin or immunoglobulin due to membrane permeabilization or degeneration/necrosis. In type I fibers, the abnormal mitochondria typically accumulate in large subsarcolemmal caps, whereas mitochondrial aggregates in affected type II fibers are dispersed between myofibrils.

Mixed Myopathies

We previously described important features that can help differentiate neurogenic from myogenic myopathies. However, there are numerous proteins and processes that appear to be important in virtually all cell types. Relatively small disruptions of certain processes, such as energy production by mitochondria and recycling of organelles and proteins, appear to be particularly likely to result in damage to long-lived cells such as neurons and myocytes (both skeletal and cardiac). One example of this occurs with mutations in the gene that codes for the protein frataxin (*Fxn*), which regulates levels of iron inside mitochondria. When frataxin is deficient or dysfunctional, excessive free iron accumulates in and damages mitochondria, leading to secondary damage to neurons and myocytes seen in Friedrich's ataxia [50]. Similarly, valosin-containing protein (VCP) plays an important role in neuron and myocyte development and mutations in VCP result in the accumulation of TDP-43 in neuromuscular diseases such as ALS and inclusion body myopathy [51]. Marinesco–Sjögren syndrome is a mixed neurogenic/myogenic is caused by mutations in a gene coding for the endoplasmic reticulum chaperone protein SIL1,

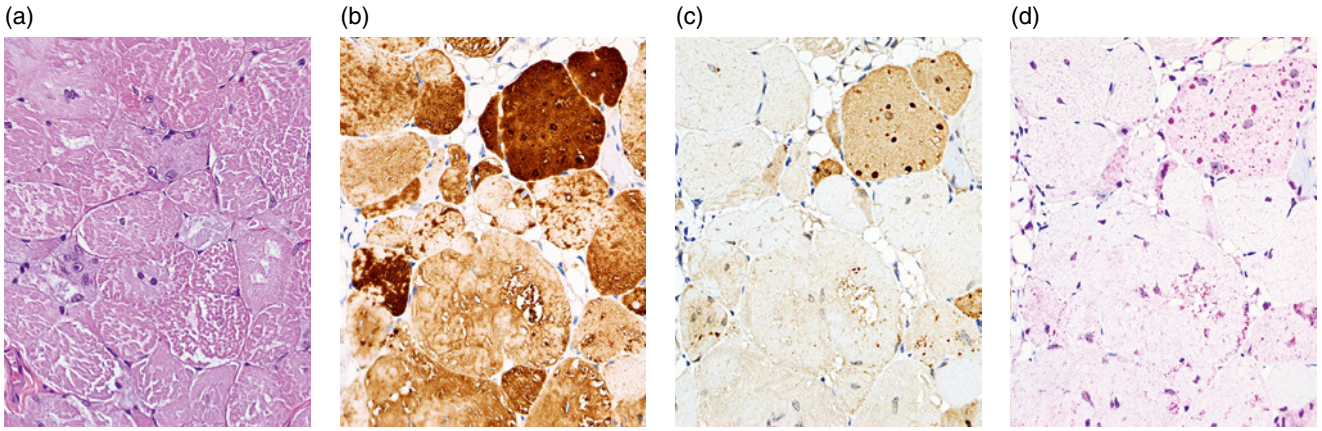


Figure 16.16 **Mouse skeletal muscle – autophagy myopathies**. (a) Internalized nuclei and separation of myofibrils are visible with H&E stain. (b) IHC labeling of SQSTM1. (c) IHC labeling of LC3B. (d) IHC labeling of ubiquitin.

which is involved in the process of protein folding. A lack of SIL1 protein impairs protein folding which results in the accumulation of misfolded proteins in the endoplasmic reticulum. This buildup occurs in both neurons and myocytes and results in a disease characterized by ataxia and a mixed neurogenic/myogenic myopathy [52].

References

1 Schrank, B.G.R., Gunnersen, J.M., Ure, J.M. et al. (1997). Inactivation of the survival motor neuron gene, a candidate gene for human spinal muscular atrophy, leads to massive cell death in early mouse embryos. *Proc. Natl. Acad. Sci. U.S.A.* 94 (18): 9920–9925.

2 Jablonka, S., Schrank, B., Kralewski, M. et al. (2000). Reduced survival motor neuron (Smn) gene dose in mice leads to motor neuron degeneration: an animal model for spinal muscular atrophy type III. *Hum. Mol. Genet.* 9 (3): 341–346.

3 Hafezparast, M., Klocke, R., Ruhrberg, C. et al. (2003). Mutations in dynein link motor neuron degeneration to defects in retrograde transport. *Science* 300 (5620): 808–812.

4 Harada, A., Takei, Y., Kanai, Y. et al. (1998). Golgi vesiculation and lysosome dispersion in cells lacking cytoplasmic dynein. *J. Cell Biol.* 141 (1): 51–59.

5 Ori-McKenney, K.M. and Vallee, R.B. (2011). Neuronal migration defects in the Loa dynein mutant mouse. *Neural Dev.* 6: 26.

6 Rogers, D.C., Peters, J., Martin, J.E. et al. (2001). SHIRPA, a protocol for behavioral assessment: validation for longitudinal study of neurological dysfunction in mice. *Neurosci. Lett.* 306 (1–2): 89–92.

7 Eschbach, J.S.J., Bouitbir, J., Fergani, A. et al. (2013). Dynein mutations associated with hereditary motor neuropathies impair mitochondrial morphology and function with age. *Neurobiol. Dis.* 58: 220–230.

8 Hrabe de Angelis, M.H., Flaswinkel, H., Fuchs, H. et al. (2000). Genome-wide, large-scale production of mutant mice by ENU mutagenesis. *Nat. Genet.* 25 (4): 444–447.

9 Grohmann, K., Rossoll, W., Kobsar, I. et al. (2004). Characterization of Ighmbp2 in motor neurons and implications for the pathomechanism in a mouse model of human spinal muscular atrophy with respiratory distress type 1 (SMARD1). *Hum. Mol. Genet.* 13 (18): 2031–2042.

10 Schmalbruch, H., Jensen, H.J., Bjaerg, M. et al. (1991). A new mouse mutant with progressive motor neuronopathy. *J. Neuropathol. Exp. Neurol.* 50 (3): 192–204.

11 Kaupmann, K., Simonchazottes, D., Guenet, J.L., and Jockusch, H. (1992). Wobbler, a mutation affecting motoneuron survival and gonadal functions in the mouse, maps to proximal chromosome-11. *Genomics* 13 (1): 39–43.

12 Reaume, A.G., Elliott, J.L., Hoffman, E.K. et al. (1996). Motor neurons in Cu/Zn superoxide dismutase-deficient mice develop normally but exhibit enhanced cell death after axonal injury. *Nat. Genet.* 13 (1): 43–47.

13 Gurney, M.E., Pu, H., Chiu, A.Y. et al. (1994). Motor neuron degeneration in mice that express a human Cu,Zn superoxide dismutase mutation. *Science* 264 (5166): 1772–1775.

14 Qiu, H., Lee, S., Shang, Y. et al. (2014). ALS-associated mutation FUS-R521C causes DNA damage and RNA splicing defects. *J. Clin. Invest.* 124 (3): 981–999.

15 Lopez-Erauskin, J., Tadokoro, T., Baughn, M.W. et al. (2018). ALS/FTD-linked mutation in FUS suppresses intra-axonal protein synthesis and drives disease without nuclear loss-of-function of FUS. *Neuron* 100 (4) 816–30 e7.

16 Wegorzewska, I., Bell, S., Cairns, N.J. et al. (2009). TDP-43 mutant transgenic mice develop features of ALS and frontotemporal lobar degeneration. *Proc. Natl. Acad. Sci. U.S.A.* 106 (44): 18809–18814.

17 Liu, Y., Pattamatta, A., Zu, T. et al. (2016). C9orf72 BAC mouse model with motor deficits and neurodegenerative features of ALS/FTD. *Neuron* 90 (3): 521–534.

18 Huxley, C., Passage, E., Robertson, A.M. et al. (1998). Correlation between varying levels of PMP22 expression and the degree of demyelination and reduction in nerve conduction velocity in transgenic mice. *Hum. Mol. Genet.* 7 (3): 449–458.

19 Dequen, F., Bomont, P., Gowing, G. et al. (2008). Modest loss of peripheral axons, muscle atrophy and formation of brain inclusions in mice with targeted deletion of gigaxonin exon 1. *J. Neurochem.* 107 (1): 253–264.

20 Cossins, J., Webster, R., Maxwell, S. et al. (2004). A mouse model of AChR deficiency syndrome with a phenotype reflecting the human condition. *Hum. Mol. Genet.* 13 (23): 2947–2957.

21 Mori, S., Kubo, S., Akiyoshi, T. et al. (2012). Antibodies against muscle-specific kinase impair both presynaptic and postsynaptic functions in a murine model of myasthenia gravis. *Am. J. Pathol.* 180 (2): 798–810.

22 Molenaar, P.C. (2008). A relative weak leg muscle in the rolling Nagoya mouse as a model for Lambert–Eaton myasthenic syndrome. *J. Neuroimmunol.* 201: 166–171.

23 Pang, Z.P., Melicoff, E., Padgett, D. et al. (2006). Synaptotagmin-2 is essential for survival and contributes to Ca2+ triggering of neurotransmitter release in central and neuromuscular synapses. *J. Neurosci.* 26 (52): 13493–13504.

24 Cheret, C., Willem, M., Fricker, F.R. et al. (2013). Bace1 and Neuregulin-1 cooperate to control formation and maintenance of muscle spindles. *EMBO J.* 32 (14): 2015–2028.

25 Crone, S.A., Negro, A., Trumpp, A. et al. (2003). Colonic epithelial expression of ErbB2 is required for postnatal maintenance of the enteric nervous system. *Neuron* 37 (1): 29–40.

26 Chen, S., Velardez, M.O., Warot, X. et al. (2006). Neuregulin 1-erbB signaling is necessary for normal

myelination and sensory function. *J. Neurosci.* 26 (12): 3079–3086.
27 Tanabe, Y., Esaki, K., and Nomura, T. (1986). Skeletal muscle pathology in X chromosome-linked muscular dystrophy (mdx) mouse. *Acta Neuropathol.* 69 (1–2): 91–95.
28 Hammers, D.W., Hart, C.C., Matheny, M.K. et al. (2020). The D2.mdx mouse as a preclinical model of the skeletal muscle pathology associated with Duchenne muscular dystrophy. *Sci. Rep.* 10 (1): 14070.
29 Bansal, D., Miyake, K., Vogel, S.S. et al. (2003). Defective membrane repair in dysferlin-deficient muscular dystrophy. *Nature* 423 (6936): 168–172.
30 Zvaritch, E., Kraeva, N., Bombardier, E. et al. (2009). Ca2+ dysregulation in Ryr1(I4895T/wt) mice causes congenital myopathy with progressive formation of minicores, cores, and nemaline rods. *Proc. Natl. Acad. Sci. U.S.A.* 106 (51): 21813–21818.
31 Roos, A., Buchkremer, S., Kollipara, L. et al. (2014). Myopathy in Marinesco–Sjögren syndrome links endoplasmic reticulum chaperone dysfunction to nuclear envelope pathology. *Acta Neuropathol.* 127 (5): 761–777.
32 Clemen, C.S., Stockigt, F., Strucksberg, K.H. et al. (2015). The toxic effect of R350P mutant desmin in striated muscle of man and mouse. *Acta Neuropathol.* 129 (2): 297–315.
33 Andley, U.P., Hamilton, P.D., Ravi, N., and Weihl, C.C. (2011). A knock-in mouse model for the R120G mutation of αB-crystallin recapitulates human hereditary myopathy and cataracts. *PLoS One* 6 (3): e17671.
34 Garvey, S.M., Miller, S.E., Claflin, D.R. et al. (2006). Transgenic mice expressing the myotilin T57I mutation unite the pathology associated with LGMD1A and MFM. *Hum. Mol. Genet.* 15 (15): 2348–2362.
35 Chevessier, F., Schuld, J., Orfanos, Z. et al. (2015). Myofibrillar instability exacerbated by acute exercise in filaminopathy. *Hum. Mol. Genet.* 24 (25): 7207–7220.
36 Zhou, Q., Chu, P.H., Huang, C. et al. (2001). Ablation of Cypher, a PDZ-LIM domain Z-line protein, causes a severe form of congenital myopathy. *J. Cell Biol.* 155 (4): 605–612.
37 Reininghaus, J., Fuchtbauer, E.M., Bertram, K., and Jockusch, H. (1988). The myotonic mouse mutant ADR: physiological and histochemical properties of muscle. *Muscle Nerve* 11 (5): 433–439.
38 Hayward, L.J., Kim, J.S., Lee, M.Y. et al. (2008). Targeted mutation of mouse skeletal muscle sodium channel produces myotonia and potassium-sensitive weakness. *J. Clin. Invest.* 118 (4): 1437–1449.
39 Masiero, E., Agatea, L., Mammucari, C. et al. (2009). Autophagy is required to maintain muscle mass. *Cell Metab.* 10 (6): 507–515.
40 Simon, D., Seznec, H., Gansmuller, A. et al. (2004). Friedreich ataxia mouse models with progressive cerebellar and sensory ataxia reveal autophagic neurodegeneration in dorsal root ganglia. *J. Neurosci.* 24 (8): 1987–1995.
41 Wredenberg, A., Wibom, R., Wilhelmsson, H. et al. (2002). Increased mitochondrial mass in mitochondrial myopathy mice. *Proc. Natl. Acad. Sci. U.S.A.* 99 (23): 15066–15071.
42 Fleming, M.S., Li, J.J., Ramos, D. et al. (2016). A RET-ER81-NRG1 signaling pathway drives the development of Pacinian corpuscles. *J. Neurosci.* 36 (40): 10337–10355.
43 Sher, R.B., Cox, G.A., Mills, K.D., and Sundberg, J.P. (2011). Rhabdomyosarcomas in aging A/J mice. *PLoS One* 6 (8): e23498.
44 Zhang, H., Kieckhaefer, J.E., and Cao, K. (2013). Mouse models of laminopathies. *Aging Cell* 12 (1): 2–10.
45 Stewart, C.L., Kozlov, S., Fong, L.G., and Young, S.G. (2007). Mouse models of the laminopathies. *Exp. Cell. Res.* 313 (10): 2144–2156.
46 Durbeej, M. and Campbell, K.P. (2002). Muscular dystrophies involving the dystrophin-glycoprotein complex: an overview of current mouse models. *Curr. Opin. Genet. Dev.* 12 (3): 349–361.
47 Batonnet-Pichon, S., Behin, A., Cabet, E. et al. (2017). Myofibrillar myopathies: new perspectives from animal models to potential therapeutic approaches. *J. Neuromuscul. Dis.* 4 (1): 1–15.
48 Wang, B., Maxwell, B.A., Joo, J.H. et al. (2019). ULK1 and ULK2 regulate stress granule disassembly through phosphorylation and activation of VCP/p97. *Mol. Cell* 74 (4) 742–57 e8.
49 Nemazanyy, I., Blaauw, B., Paolini, C. et al. (2013). Defects of Vps15 in skeletal muscles lead to autophagic vacuolar myopathy and lysosomal disease. *EMBO Mol. Med.* 5 (6): 870–890.
50 Britti, E., Delaspre, F., Feldman, A. et al. (2018). Frataxin-deficient neurons and mice models of Friedreich ataxia are improved by TAT-MTScs-FXN treatment. *J. Cell. Mol. Med.* 22 (2): 834–848.
51 Custer, S.K., Neumann, M., Lu, H. et al. (2010). Transgenic mice expressing mutant forms VCP/p97 recapitulate the full spectrum of IBMPFD including degeneration in muscle, brain and bone. *Hum. Mol. Genet.* 19 (9): 1741–1755.
52 Ichhaporia, V.P., Kim, J., Kavdia, K. et al. (2018). SIL1, the endoplasmic-reticulum-localized BiP co-chaperone, plays a crucial role in maintaining skeletal muscle proteostasis and physiology. *Dis. Models Mech.* 11 (5): 1–13.

17

Endocrine System

Krista M. D. La Perle

Overview

Endocrine organs are composed of ductless islands of polygonal secretory epithelial cells, arranged in nests and cords by a fine connective tissue stroma, that synthesize, store, and directly release their polypeptides, steroids, and amino acid derivatives into an interweaving network of capillaries to act on distant target cells upon receptor binding. An ensuing physiologic response is feedback inhibition whereby target organs secrete factors to downregulate production of stimulating hormones from the upstream gland. Endocrine diseases are typically categorized as those that result in hormone deficiency or excess due to diseases within (primary) or outside of (secondary) the specific endocrine gland, and those that result in the development of masses which may (functional) or may not (nonfunctional) be associated with hormone production. This chapter addresses the pituitary, thyroid, parathyroid, adrenal, and pineal glands, as well as the endocrine pancreas. Paraganglia are briefly addressed in conjunction with the adrenal medulla; neuroendocrine cell populations in other organs (i.e. gastrointestinal (13), respiratory (12), reproductive (19–20) tracts; thymus (7)) are discussed in their respective chapters. The anatomy and histology of each endocrine tissue covered herein have been reviewed [1–3].

General Phenotypic Considerations for the Endocrine System

An important consideration for the phenotypic characterization of mouse models of endocrine disease is the determination of hormones and other biochemical markers. As such, it is imperative to minimize biological (i.e. strain, age, sex, genotype, dietary/pharmacological interventions, diurnal variation), preanalytical (i.e. sample type, sampling technique, handling, processing, and storage), and analytical (i.e. analytical method) variability in order to obtain meaningful and reproducible results [4].

In general, with exceptions noted below for respective organs, tiny mouse endocrine organs are fixed prior to weighing to prevent destruction and/or loss. The organs are submitted for processing in mesh or multichamber cassettes, and embedded *in toto* for careful microtomy of all representative parts [5]. Standardized nomenclature should be used for classifying proliferative and nonproliferative microscopic lesions in the endocrine organs [6]. Biomarker localization in normal and neoplastic endocrine tissues is an essential complement to biochemical and morphologic evaluations and is facilitated by both histochemical and antibody-based labeling methods. The hallmark of neuroendocrine cells (i.e. thyroid C cells, parathyroid chief cells, adrenal medullary chromaffin cells, and pancreatic islets) is the membrane-bound electron dense-core secretory granule which is argyrophilic and can therefore be detected histochemically by silver stains such as Churukian–Schenk or Grimelius, as well as antibodies including neuron-specific enolase, chromogranin A, and synaptophysin [7, 8]. The ultrastructural size, density, and configuration of the granules also vary among the different cell types [9].

Given that many hormones produced by endocrine glands have multisystemic effects, body and organ weights should be obtained at the time of necropsy, and various imaging modalities such as radiography, computerized tomography (CT), magnetic resonance imaging (MRI), and dual energy X-ray absorptiometry should be employed antemortem to assess bone density, mineral content, percent body fat, and lean body mass. Numerous endocrine diseases also manifest as skin conditions. Additionally, noninvasive imaging is necessary to assess tumor progression and response to therapy.

Endocrine tumors are inherently heterogeneous on multiple levels: location and cell of origin; hormone production/functionality; clinical presentation; and molecular genetics. While the majority of tumors are sporadic, a significant percentage is associated with hereditary cancer syndromes (Table 17.1), often characterized by tumors in multiple organs, such as the classical prototypical multiple endocrine neoplasia (MEN) syndromes, which are frequently reproduced in mouse models [39–41]. The key genetically engineered mice used to investigate human endocrine tumors have recently been reviewed, a selection of which will be highlighted in the respective sections below [10]. With

Pathology of Genetically Engineered and Other Mutant Mice, First Edition. Edited by John P. Sundberg, Peter Vogel, and Jerrold M. Ward.
© 2022 John Wiley & Sons, Inc. Published 2022 by John Wiley & Sons, Inc.

Table 17.1 Selected hereditary human endocrine cancer syndromes and GEM[a] phenotypes.

Syndrome	Gene	Main endocrine organ tumor spectrum	Endocrine lesions in GEM	References
Carney complex	*PRKAR1A*	Pituitary, adrenal cortex, thyroid follicles	Pituitary, thyroid follicles	[10–17]
Cowden syndrome	*PTEN*	Thyroid follicles	Thyroid follicles, adrenal medulla	[13, 16–23]
MEN[b]1 (Wermer's syndrome)	*MEN1*	Parathyroid, pancreatic islets, pituitary, adrenal cortex	Parathyroid, pancreatic islets, pituitary, adrenal, thyroid follicles	[10–12, 14–16, 24–31]
MEN2	*RET*			
MEN2A (Sipple's syndrome)		Thyroid medulla, adrenal medulla, parathyroid	Thyroid medulla	[32–34]
FMTC[c]		Thyroid medulla		
MEN2B (MEN3)		Thyroid medulla, adrenal medulla	Thyroid medulla, adrenal medulla	[18, 32–35]
MEN4	*CDKN1B*	Parathyroid, pituitary	Pituitary	[10, 36]
Neurofibromatosis 1	*NF1*	Adrenal medulla, paraganglia, pancreatic islets	Adrenal medulla	[10, 12, 18, 35, 37]
von Hippel Lindau disease	*VHL*	Adrenal medulla, pancreatic islets	Paraganglia	[10, 37, 38]

[a] Genetically engineered mice.
[b] Multiple endocrine neoplasia.
[c] Familial medullary thyroid carcinoma.

specific regard to proliferative endocrine lesions in mice, it should be noted that there is often a continuum between hyperplasia, adenoma, and carcinoma across all the endocrine organs. Hyperplastic lesions typically involve one cell type, cells do not display atypia, lesions are not well demarcated, and do not cause compression of adjacent tissues. Adenomas may be encapsulated and cause compression. Carcinomas exhibit pleomorphism, atypia, mitotic figures, hemorrhage, and necrosis, infiltrate surrounding tissues, and may metastasize to distant sites. Around the start of the twenty-first century, a number of fundamental references were published in conjunction with the National Cancer Institute Mouse Models of Human Cancer Consortium, which develop criteria for the definition and classification of neoplastic diseases affecting various organ systems in mice, and recommend a standardized nomenclature which parallels the World Health Organization (WHO) classification of human tumors [42, 43]; however, the endocrine system was not included. For mice, several references [6, 44–48] and an online general guide [49] provide guidelines for mouse tumor nomenclature.

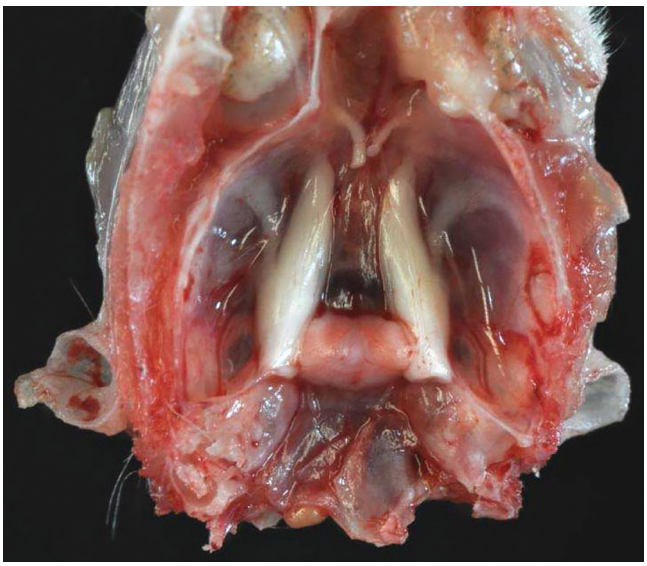


Figure 17.1 Pituitary gland *in situ* observed within the sella turcica upon removal of the brain.

Pituitary Gland

Anatomy, Histology, and Physiology

The pituitary gland, or hypophysis, is located subjacent to the brain within the sella turcica on the dorsal surface of the basisphenoid bone (Figures 17.1 and 17.2) [1, 3]. It is composed of an anterior lobe, or adenohypophysis derived from ectoderm, and a posterior lobe, or neurohypophysis derived from neuroectoderm; both are attached to the hypothalamus in the overlying brain via an infundibular stalk. The adenohypophysis encompasses the larger pars distalis that cradles the more central pars intermedia and the pars tuberalis, which is not apparent histologically. The pars

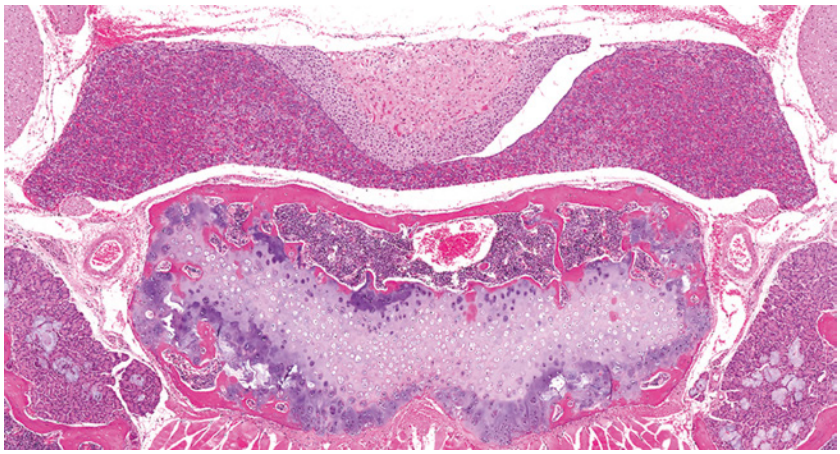


Figure 17.2 Photomicrograph of the pituitary gland *in situ* overlying the basisphenoid bone. Source: La Perle et al. [1].

intermedia is delineated by a residual lumen (cleft) of Rathke's pouch, which is lined by a single layer of low cuboidal epithelium. Epithelial cells in the anterior pituitary synthesize and secrete pituitary trophic hormones in response to releasing hormones or factors secreted by the hypothalamus (hypothalamic–pituitary axis). By routine hematoxylin and eosin staining, these cells are either chromophilic and classified as acidophils and basophils, or chromophobes, which lack cytoplasmic staining and represent degranulated chromophils, folliculo-stellate cells and/or undifferentiated stem cells. Acidophils include somatotrophs, which secrete growth hormone or somatotropin (~50% of pars distalis cells) and lactotrophs, which secrete prolactin (15–25% of pars distalis cells). Basophils comprise thyrotrophs which secrete thyroid stimulating hormone (TSH, ~5% of pars distalis cells), corticotrophs which secrete adrenocorticotropic hormone (ACTH, 15% of pars distalis cells), and gonadotrophs which secrete follicle-stimulating hormone (FSH) and luteinizing hormone (LH) (~10% of pars distalis cells). Most of the polygonal cells in the pars intermedia are melanotrophs which produce melanocyte-stimulating hormones (α-MSH and ß-MSH), with fewer corticotrophs; additional bioactive products generated in the pars intermedia have been identified.

The neurohypophysis includes the pars nervosa and the histologically inapparent infundibulum. As its name would imply, it histologically resembles nervous tissue due to its composition of unmyelinated axons belonging to hypothalamic neurons in the supraoptic and paraventricular nuclei, interspersed with pituicytes. In contrast to the anterior pituitary, the posterior pituitary is not an endocrine gland, but rather a storage site for neurosecretory vesicles that are synthesized in the hypothalamic nuclei, contain oxytocin and vasopressin or anti-diuretic hormone, and aggregate as Herring bodies.

The pituitary gland has a tremendous capacity for plasticity, which enables it to adjust to the systemic demands of growth, metabolism, reproduction, and stress. While mechanisms continue to be elucidated, it is now clear that populations of single and multihormone expressing trophic cells in the anterior pituitary exist during normal physiologic states and tumorigenesis, and their numbers fluctuate due to proliferation and metaplasia of mature cells as well as activation and differentiation of stem cells [50–52].

Special Necropsy Organ Protocols

Coronal (transverse) sections of the decalcified skull are often obtained to assess the brain, cranial nerves, and pituitary and pineal glands *in situ*, as well as the nasal cavity and eyes. In instances when this is not warranted, the pituitary gland is often fixed *in situ* before removal and embedding *in toto* for sectioning of all three portions [5, 53]. Alternatively, the pituitary gland may remain *in situ* and a coronal section made that includes decalcified basisphenoid bone (Figure 17.2) [5]. Orange G and periodic acid-Schiff (PAS) special histochemical staining facilitates the differentiation of acidophils (orange G positive), basophils (PAS positive), and chromophobes (no staining) in the anterior pituitary. Further subclassification of cells in the pars distalis and pars intermedia require immunostaining with antibodies directed against the specific hormones noted above. Folliculo-stellate cells are immunoreactive for S100 as well as markers of dendritic cells [54, 55]. Markers of stemness in the pars distalis include SOX2 and SOX9 as well as the lineage-specific markers POU1F1 (formerly called PIT1; somatotrophs, lactotrophs, and thyrotrophs), nuclear receptor subfamily 5, group A, member 1 (Nr5a1; formerly called SF1; gonadotrophs), and TBX19 (formerly called TPIT; corticotrophs and melanotrophs) [50, 56].

Aging/Spontaneous Strain-Specific Lesions

Cysts may occasionally be seen in the pituitary glands of mice, more commonly in the pars distalis or pars intermedia. Cysts may be unilocular or multilocular, lined by cuboidal to columnar epithelium with or without cilia, and often contain eosinophilic proteinaceous material. Cysts arising near

or within Rathke's cleft may represent remnants of Rathke's pouch; however, the origin is usually indeterminate.

Female FVB/N mice demonstrate a high prevalence (~46%) of proliferative changes in the pars distalis of the pituitary gland, which is influenced by age and parity. Pituitary lesions include hyperplasia and more commonly, lactotrophinomas, while concurrent mammary gland lesions include squamo-inflammatory nodules, lobuloalveolar hyperplasia, and adenocarcinomas [57].

Genetically Engineered Mice

Hypopituitarism

Pituitary hormone deficiency, in which one or more pituitary hormones are lacking, is typically secondary to lesions that destroy ≥75% of the pituitary gland. However, a subset of cases may lack predisposing lesions or present after birth. Genetically engineered mice have been essential to our understanding of pituitary development and congenital hypopituitarism. At the forefront are mice with deletions in transcription factors essential to the development of the pituitary and brain such as *Pou1f1*, *Tbx19*, *Lhx3*, *Prop1*, *Gli2*, and *Rax* [56, 58, 59]. Phenotypes in conventional targeted mutant mice include aplastic to hypoplastic pituitaries which often result in multiple hormone deficiencies, and may be associated with other defects in the central nervous system and skeleton.

Hyperpituitarism

Functional neoplasms arising in the anterior pituitary are the most common cause of hyperpituitarism in humans and animals. Given the evolving information regarding cell plasticity in the pituitary, classification of tumors now focuses on the pituitary cell lineage in conjunction with hormone secretion [60, 61]. Immunohistochemistry for pituitary hormones and lineage markers will aid in the diagnosis into seven subtypes: somatroph, lactotroph, thyrotroph, corticotroph, gonadotroph, null cell, and plurihormonal. Over 99% of human tumors are adenomas, and approximately half are lactotrophinomas. While the majority are sporadic, about 5% are associated with hereditary syndromes and mutations in *MEN1* (MEN1), *CDKN1B* ($p27^{kip1}$; *MEN4*), and *PRKAR1A* encoding the regulatory subunit 1α of the protein kinase A (PKA) pathway (Carney complex), *GNAS1* (McCune–Albright syndrome), and aryl hydrocarbon receptor interacting protein (*AIP*; familial isolated pituitary adenoma). As such, numerous mouse models have been engineered, many of which develop adenomas that vary in their cellular lineage, site of origin within the anterior pituitary and hormone production [11, 12]. Several different *Men1* mutant mouse models have been developed [24]. Homozygosity is embryonic lethal in conventional knockouts, but heterozygotes develop a tumor spectrum in the pituitary, parathyroid, and adrenal glands as well as the neuroendocrine pancreas, similar to humans. Pars distalis tumors of all lineages have been reported in *Men1* mice as have nonfunctioning tumors (Figures 17.3 and 17.4). Gender-related differences in human patients with mutations in the *MEN1* gene include a higher frequency of pituitary tumors in females, which has been recapitulated in some *Men1* mouse constructs. *Cdkn1b* mutant mice develop hyperplasia of the pars intermedia, with progression to adenoma that varies in prevalence and latency according to strain (Figure 17.5); additional and often multiple tumor types beyond the endocrine system are induced upon carcinogen administration [36]. Mice with combined heterozygosity for *Rb1* and *Trp53* also develop tumors of endocrine origin, most commonly pituitary adenomas as well as medullary thyroid carcinomas (MTCs) and to a lesser extent, pancreatic islet carcinomas and parathyroid adenomas [62].

Craniopharyngiomas

Craniopharyngiomas (CP) are benign but clinically aggressive, nonendocrine tumors that arise in the pituitary gland and often present with hypothalamic/pituitary deficiencies. The papillary subtype craniopharyngioma (PCP) arises from metaplasia of squamous epithelial rests that are remnants of buccal mucosa precursors. PCP is very rare, found almost exclusively in human adults, and is associated with

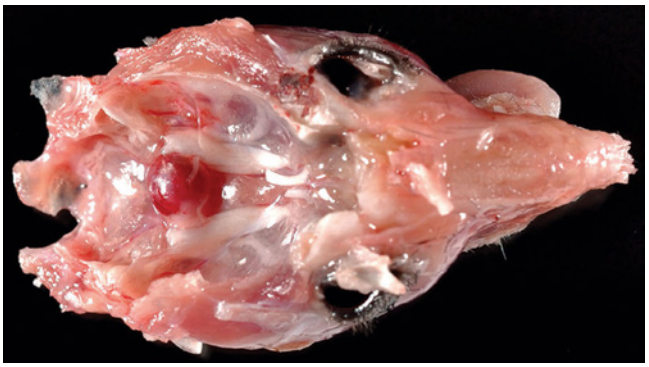


Figure 17.3 The pituitary gland is enlarged and red due to the presence of a pituitary gland adenoma.

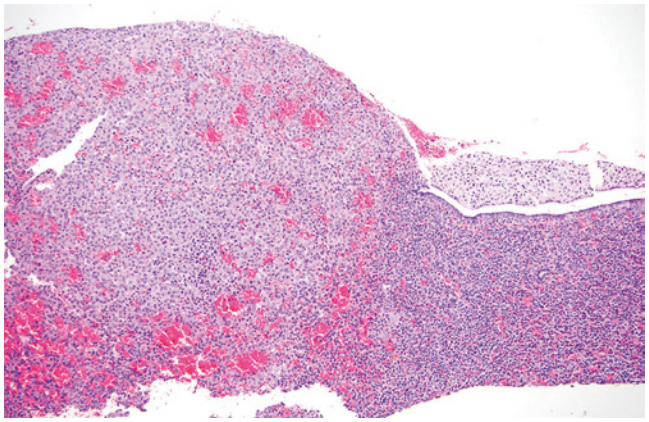


Figure 17.4 A focal adenoma (left) within the pars distalis is associated with congested vascular sinuses.

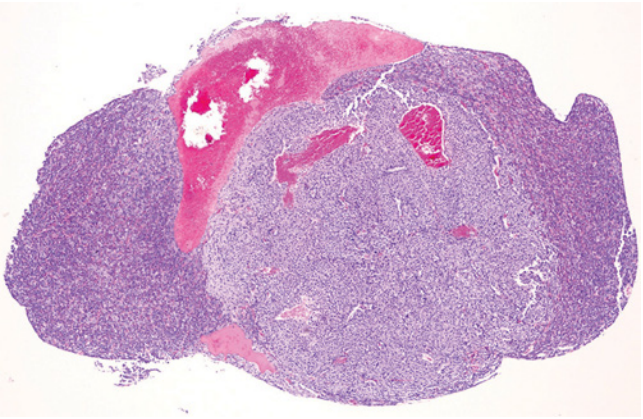


Figure 17.5 Centrally, an adenoma of the pars intermedia is compressing the pars distalis (right) and inducing hemorrhage.

overacting mutations in *BRAF* V600E. The adamantinomatous subtype craniopharyngioma (ACP) originates from epithelial remnants of the craniopharyngeal duct or Rathke's pouch with well described onsets in childhood (5–14 years) and adulthood (65–74 years). ACP is associated with mutations in *CTNNB1* which encodes ß-catenin, a central effector of the canonical Wnt signaling pathway, resulting in degradation resistance, prolonged half-life, and nucleocytoplasmic accumulations of mutant ß-catenin. Two different mouse models develop tumors that are histologically similar to human ACP, including clusters of neoplastic cells with nucleocytoplasmic ß-catenin [63]. The embryonic ACP model ($Hesx1^{tm1(cre)Jpmb}$; $Ctnnb1^{tm1Mmt}$) expresses mutant ß-catenin in Rathke's pouch, whereas expression in the inducible or adult ACP model is exclusively in $Sox2^{+}$ stem cells of the adult pituitary ($Sox2^{tm1.1(CreERT2)Jpmb}$; $Ctnnb1^{tm1Mmt}$).

Thyroid Gland

Anatomy, Histology, and Physiology

The thyroid gland, a reddish-brown organ with right and left lobes joined by an isthmus on the ventral aspect, is located along the first three to four tracheal rings [1, 3]. It is comprised predominately of thyrocytes or follicular cells forming spherical follicles of various sizes, and calcitonin-producing C (parafollicular) cells (Figure 17.6). While C cells have long thought to be derived from the neural crest, recent lineage tracing evidence in mice supports their origin from SOX17+ endoderm, similar to follicular cells [64]. Follicles are lined by a single layer of cuboidal epithelial cells aligned on a basement member, and contain colloid, consisting of the glycoprotein thyroglobulin (TG). The follicular epithelial cells are responsible for TG synthesis, sodium–iodide symporter (SLC5A5)-mediated uptake of iodide, and oxidization of iodide to iodine by thyroperoxidase (TPO). Iodine is released into the follicular lumen where it iodinates TG, the storage form of the thyroid hormones, triiodothyronine (T3), and tetraiodothyronine (T4) , also known as thyroxine. TSH secreted from thyrotrophs in the anterior pituitary stimulates release of T3 and T4. Calcitonin contributes to calcium homeostasis, working in direct opposition to parathyroid hormone (PTH) by decreasing blood calcium.

Special Protocols

Transverse sections of the thyroid gland attached to the trachea and adjacent esophagus are preferable (Figure 17.6), unless lobes are removed from the trachea for weighing and/or ancillary testing and then longitudinal sections are acceptable [5]. Detailed recommendations to aid in the characterization of thyroid hormone action in mouse models of hypothyroidism, hyperthyroidism, and thyroid cancer have been reported [65]. Measurement of hormone levels (T3, T4, TSH) and thyroid imaging via ultrasound or with pertechnetate or iodide isotopes via micro-positron emission tomography (PET)-CT or single-photon emission computed tomography (SPECT) helps to predict disease progression, results of which should be correlated with follicular morphology and immunostaining (TG, SLC5A5, TPO, PAX8, NKX2-1, and FOXE1) [66, 67]. T4 in mice has a much shorter half-life (<12 hours) than in humans and exists primarily in an unbound state which is more prone to metabolism. Serum calcitonin levels should be measured basally as well as following stimulation with calcium or pentagastrin, and assessed in conjunction with serum levels of calcium, phosphorus, PTH, and/or calcitriol, the active form of vitamin D. C cells account for 0.1% of thyroid epithelial cells, and argyrophilic histochemical or antibody-based (calcitonin, calcitonin gene-related peptide) stains are necessary to identify



Figure 17.6 Bilaterally, the lobes of the thyroid gland are attached to the trachea, which overlies the esophagus. Unilaterally (left), the parathyroid gland is noted peripheral to the thyroid lobe, just beneath the capsule. Colloid-filled follicles are of variable diameter and lined by flattened to cuboidal thyrocytes.

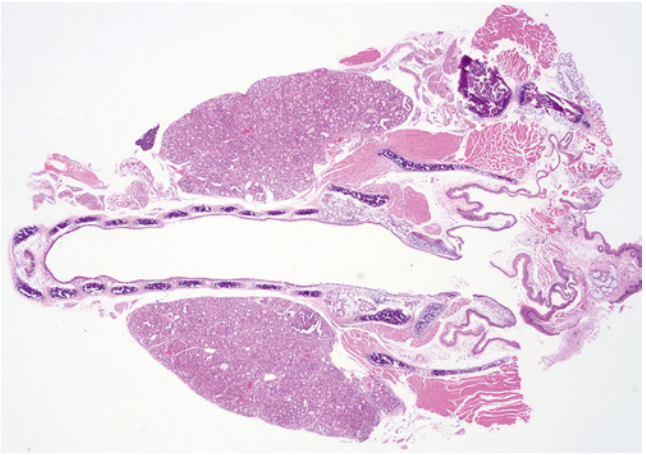


Figure 17.7 Diffuse bilateral follicular hyperplasia (goiter) secondary to iodine deficiency.

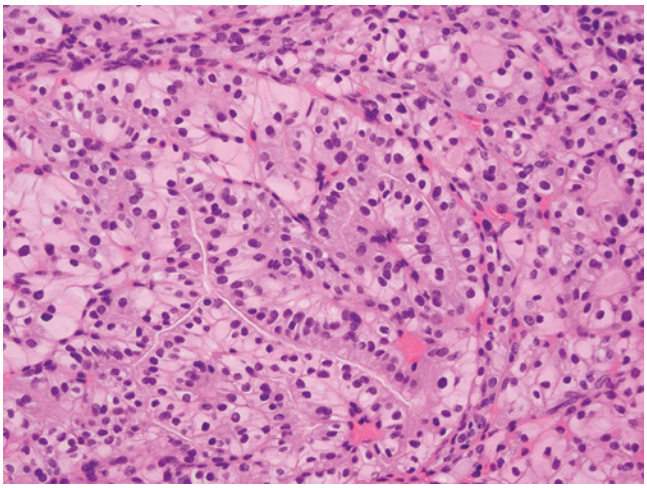


Figure 17.8 Thyroid follicular hyperplasia and dysplasia characterized by collapsed follicular lumina lined by columnar epithelial cells with basally oriented nuclei and apical vacuoles containing colloid.

them in their central location within the lobe [68]. Hormones produced by the thyroid have wide-reaching effects on skeletal muscle, adipose tissue, bone, the brain, and heart, so functional and morphologic evaluation of those systems may also be indicated.

Iodine deficiency as well as goitrogens, including numerous foods, drugs, and chemicals, interferes with thyroid hormone synthesis, secretion, and/or metabolism. Disruption of the thyroid-pituitary axis with a compensatory increase in TSH secretion results in hypertrophy and hyperplasia of thyrocytes (Figure 17.7), manifested as increased thyroid weight and goiter. Mutant mice may be more susceptible to tumor development under the influence of iodine deficiency or goitrogens; low iodine diets are commonly employed to amplify subtle phenotypes [65, 69].

Aging/Spontaneous Strain-Specific Lesions

A number of variables, including age, sex, diet, and endocrine status, affect the histologic appearance of follicular epithelial cells and colloid. Active glands are characterized by cuboidal epithelial cells with basophilic colloid and absorption droplets at the epithelial interface, whereas inactive follicles are lined by flattened epithelial cells and distended with eosinophilic colloid. As mice age, follicles become larger (cystic) and more variable in size (Figure 17.6), and may contain exfoliated cells. Aberrant or remnant tissue resulting from embryologic development may be observed in the thyroid gland and include ectopic thymic tissue and ultimobranchial cysts lined by ciliated, nonciliated, or attenuated epithelium and containing eosinophilic to mucinous material. The thyroid gland is also a site of deposition for APOA2 amyloid, which typically does not result in dysfunction, especially in CD-1 and C57BL/6 strains.

Thyroid follicular dysplasia in which follicular epithelial cells with large intracytoplasmic pale eosinophilic material and apically located nuclei has been observed in wild-type and mutant mice of different genetically engineered constructs (Figure 17.8). This lesion has been extensively characterized in Hannover Wistar GALAS rats and reported in rare untreated control cynomolgus macaques [70, 71]. Cytoplasmic vacuoles in follicular epithelial cells of mice and rats have been confirmed to contain colloid by TG immunohistochemistry and electron microscopy. The lesion in rats was attributed to an unidentified spontaneous genetic mutation resulting in defective TG production and/or secretion, which results in hypothyroidism and growth retardation in 20–25% of animals. Furthermore, follicular adenomas and adenocarcinomas have been documented in rats approaching one year of age and the incidence of these proliferative lesions increased upon administration of five carcinogens [72, 73]. Although microadenomas, as well as grossly nodular adenomatous lobes, have been occasionally noted in aged wild-type and mutant mice, carcinomas have yet to be documented.

Genetically Engineered Mice

Hypothyroidism

Congenital hypothyroidism is a prevalent neonatal endocrine disorder that can result in growth retardation and significant, irreversible neurodevelopmental impairment, also known as cretinism, if not promptly recognized and treated with hormone replacement therapy. Causes include dysgenesis, encompassing agenesis, hypoplasia, and ectopy, whereby the thyroid gland fails to develop normally, and dyshormonogenesis in which a morphologically normal thyroid gland fails to produce normal amounts of thyroid hormone [74]. Spontaneous mutant mice exist for both categories of congenital hypothyroidism and include the hypothyroid mouse carrying a $Tshr^{hyt}$ inactivating point mutation and the congenital goiter mouse carrying a Tg^{cog} mutation which results in defective homodimerization,

respectively [75, 76]. Both models are characterized by growth retardation, reduced serum T3 and T4, and elevated serum TSH, but exhibit distinct differences. As the name implies, hypothyroid mice have hypoplastic glands, and the resultant hypofunction causes cerebrocortical abnormalities with pathological motor behavior [75]. Congenital goiter mice demonstrate progressively increased thyroidal volume starting at E18, while T4 levels progressively increase to normal concentrations by 10 months of age [76].

Since these initial spontaneous mutants were characterized, a number of mouse models of primary (thyroid) and central (pituitary) congenital hypothyroidism have been genetically engineered and reviewed [77–79]. Most involve global or thyroid-targeted deletions or point mutations of thyroid-specific transcription factors (*Nkx2-1, Pax8, Ttf1, Hoxa3, Foxe1, Hhex*, and *Hes1*) expressed during development, or thyroid-specific genes (*Tg, Tpo, Tshr*, and *Slc5a5*) critical for thyroid hormone production. Models that are not embryonic lethal typically exhibit dwarfism and reduced life spans, often with brain defects and hearing impairment. Thyroid lesions range from aplasia and hypoplasia to goiters characterized by colloid accumulation or hyperplastic follicles. In some instances, mice can be fed diets supplemented with thyroxine or iodide to partially rescue the mutant phenotype.

The most common cause of primary hypothyroidism in adults is chronic autoimmune thyroiditis, with Hashimoto's thyroiditis (HT) being the most prevalent. HT is characterized by lymphocytic infiltration, destruction, and replacement by fibrous connective tissue, with the majority of patients developing autoantibodies against TPO and TG detectable in sera. Numerous susceptibility genes have been reported in humans, in which Th1-mediated cytotoxicity and apoptosis are important in the pathogenesis [80].

While the spontaneous polygenic mutant NOD/ShiLtJ (NOD) strain is popular for its utility as a model for autoimmune type I diabetes (see below), upwards of 20% of mice before two years of age also develop lymphocytic infiltrates in the thyroid which is not associated with hormonal dysfunction [81]. Haplotypes of the mouse major histocompatibility complex, *H2* influence this phenotype as evidenced by an increased incidence in NOD.$H2^{k}$ and a decreased incidence in NOD.$H2^{b}$ vs. the original NOD.$H2^{g7}$ [81]. NOD.$H2^{h4}$ mice also spontaneously develop thyroiditis, and rare mice present concurrently with thyroid hemiagenesis [82, 83]. In contrast to humans in which autoimmune disease is more in common in females, NOD mice do not exhibit a sex bias. Anti-TG and -TPO antibodies in sera from various haplotypes of NOD mice have been sporadically detected in spontaneous thyroiditis but are consistently detected when experimental autoimmune thyroiditis (EAT) is induced following immunization with mouse TG [81, 84]. EAT, indistinguishable in NOD and NOD.$H2^{k}$ mice, is characterized by marked lymphocytic infiltrations, organized lymphoid follicles, intraepithelial lymphocytes, fibrosis, and necrosis (Figure 17.9), and thereby closely resembles the disease in humans. Interestingly, when

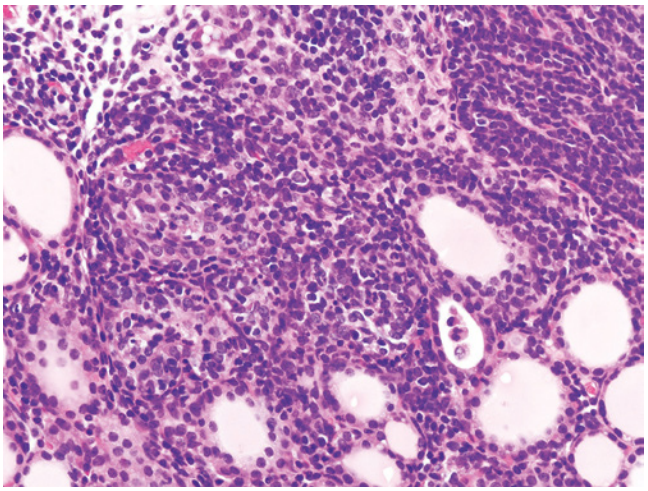


Figure 17.9 Marked lymphocytic infiltrates are disrupting normal thyroid follicular architecture. Intraepithelial lymphocytes are noted, as is intraluminal cellular debris. The parathyroid gland is evident in the upper right.

$Il12b^{tm1Jm}$ null mice are used as donor and recipient mice of mTG-sensitized splenocytes activated with mTG and IL12, granulomatous thyroiditis develops that is associated with Th2 cytokines [85].

Transgenic mice with expression of IFNG targeted to thyroid follicular cells by the rat TG promoter develop growth retardation associated with disrupted follicular architecture, and decreased serum T4, SLC5A5 expression, and radioiodide uptake [86]. Although these mice exhibit limited infiltration by CD4+ T cells, subsequent separate matings to *Rag2* null mice and *Ifngr* null mice attributed the phenotype to IFNγ signaling and not the lymphocytic inflammation [86].

Hyperthyroidism

Like HT, Graves' disease (GD) is an autoimmune disease of the thyroid gland, but Th2-mediated and causes hyperthyroidism resulting from thyroid stimulating antibodies (TSA) against the A-subunit of the thyroid stimulating hormone receptor (TSHR). In addition to thyroid follicular hyperplasia, patients exhibit weight loss, tachycardia, hyperthermia, and ophthalmopathy. Transgenic mice constitutively expressing an agonistic TSA from a GD patient have been developed using a 5′ flanking region of the original human antibody as a promoter, and a human Cμ segment for the constant region of the heavy chain [87]. Mice developed elevated T4 and reduced TSH serum levels, hyperthermia, increased thyroidal technetium uptake, and follicular hyperplasia. TSHR immunization strategies, resulting in the production of stimulating antibodies and hyperthyroidism, often in the absence of lymphocytic thyroiditis, are commonly employed to model GD [88]. NOD.Cg-$H2^{h4}$ Tg(TG-TSHR)51.9Smcl/Mmmh mice were developed by crossing NOD.$H2^{h4}$ mice that develop HT with transgenics expressing the human TSHR [89]. While these mice developed TSHR autoantibodies, and in 44% of mice tested, these stimulated

cAMP generation via an *in vitro* TSA bioassay, autoantibodies to the human TSHR had no effect on the mouse TSHR nor serum T4 levels. Interestingly, mice with overexpression of the human A-subunit TSHR driven by the bovine TG promoter had normal thyroid function [90]. Distinct transgenic lines exhibited low and high TSHR expression. Only low expressors developed autoantibodies after high dose A-subunit adenovirus, and upon Treg depletion with anti-CD25 (CD4+) but not –CD122 (CD8+), all mice developed massive lymphocytic thyroiditis consistent with a shift from GD to HT.

Neoplasms of Thyrocytes

Thyroid cancer is the most common endocrine cancer, and its incidence has been rising over the past several decades. The majority of thyroid neoplasms are derived from thyrocytes, and histologically classified as papillary thyroid carcinomas (PTCs, 80–85%) and follicular thyroid carcinomas (FTCs, 10–15%) which are well differentiated, as well as poorly differentiated thyroid carcinomas (PDTCs) and anaplastic thyroid carcinomas (ATCs). Metastasis occurs in approximately 30% of cases, typically to regional lymph nodes with ≤5% spreading beyond the neck to lung and bone. As the name implies, PTC are characterized by papillary growth in which neoplastic thyrocytes line a fibrovascular core and display distinct nuclear features, including nuclear grooves, pseudoinclusions, and open chromatin; numerous variants, including follicular and tall cell, are reported. Human PTCs are associated with genetic alterations in *BRAF*, *RET, RAS*, *TRK*, and *ALK*, all of which activate the RAS/RAF/MEK/ERK pathway. $BRAF^{V600E}$ mutations, which result in its constitutive activation, are the most common. Chromosomal rearrangements which disrupt *RET* and cause its fusion to various genes, resulting in ~19 different *RET/PTC* chimeric oncogenes reported to date, are prevalent in radiation-induced PTC as well as sporadic PTC in children and adolescents. Mutations of all three *RAS* isoforms have been documented in PTC, especially the follicular variant, as well as FTC and close to 50% of follicular adenomas. FTC has also been associated with the *PAX8-PPARG* gene fusion, as well as *PTEN* and *PRKAR1A* mutations in sporadic and hereditary (Cowden syndrome and Carney complex, respectively) PTC. The accumulation of several mutations, including in *TP53* and *TERT* are associated with progression to PDTC and ATC.

Numerous mouse models of thyroid cancer have been developed, including those with various mutations in $BRAF^{V600E}$, *RET/PTC*, *Prkar1a*, and *Pten* restricted to thyrocytes by the TG promoter, that develop a spectrum of lesions ranging from follicular hyperplasia and adenoma to FTC or PTC [13, 91]. Carcinomas (Figures 17.10 and 17.11) feature capsular fibrosis/invasion and less frequently, extrathyroid extension to adjacent skeletal muscle and intratumoral vascular invasion (Figure 17.12). Typically, the thyroid is diffusely involved and tumors, which are often bilateral in these genetically engineered models, may grow so large as to cause tracheal and esophageal compression resulting in dyspnea and dysphagia, respectively. Conventional models may present with mild-to-severe hypothyroidism, which has been largely overcome by conditional gene expression with inducible systems. Combining mutations by crossing multiple lines in an attempt to model multiple genetic hits has resulted in limited instances of micrometastasis. An interesting model of FTC which develops metastasis to lungs in approximately a third of mice >6 months of age is the $Thrb^{tm1.1Syc}$ knock-in mouse [92]. These mice express a dominant negative *TRB* mutation, *PV*, derived from a patient with severe thyroid hormone resistance syndrome. Lung metastases (Figure 17.13) often appear as distinct rafts of follicular structures that express TG. Differences in tumor latency and prevalence of metastasis between various genotypes that incorporate $Thrb^{tm1.1Syc}$ mice are objective endpoints to complement thyroid tumor morphology [93].



Figure 17.10 Bilateral follicular thyroid carcinomas.

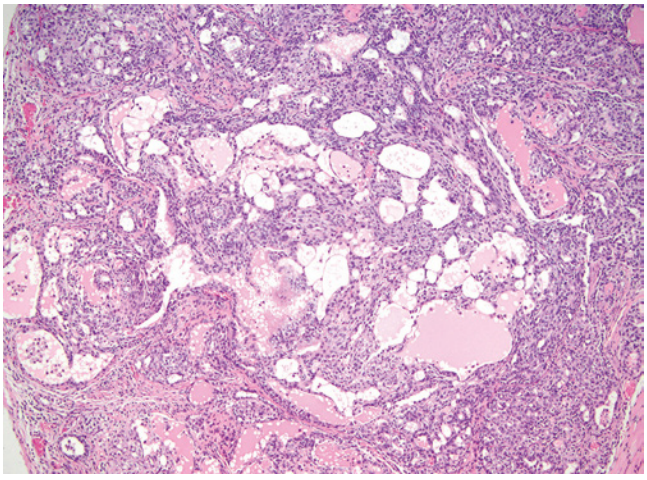


Figure 17.11 Follicular thyroid carcinoma.

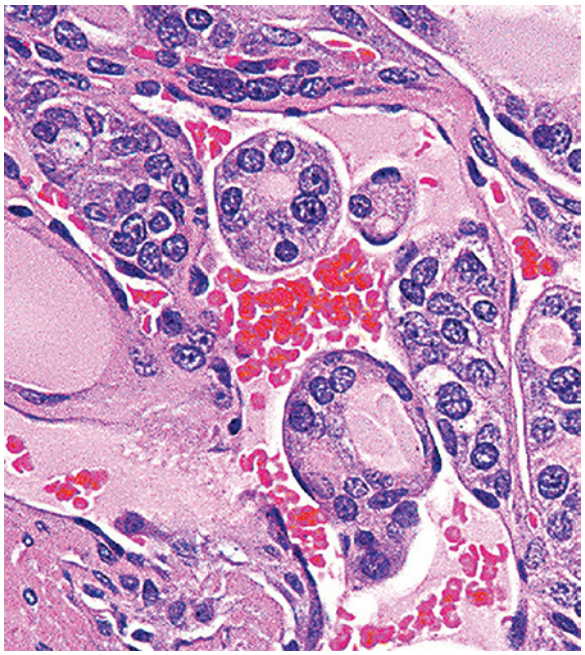


Figure 17.12 Intravascular rafts of follicular thyroid carcinoma cells.

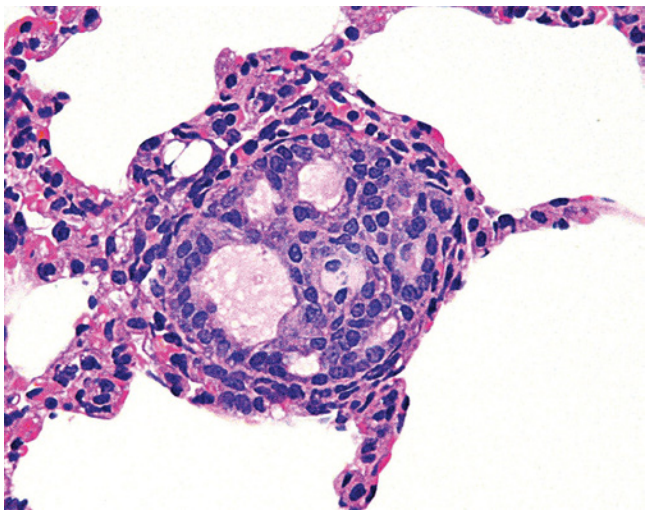


Figure 17.13 Pulmonary metastasis of follicular thyroid carcinoma.

Thyroid C Cell Neoplasms

C cells give rise to MTCs, which represent <5% of all thyroid carcinomas. MTC occurs sporadically in >70% of cases, with the remainder being hereditary as part of the MEN2 syndromes, which include MEN2A and its variant, familial medullary thyroid carcinoma (FMTC), as well as MEN2B (MEN3). The hallmark in all MEN2 syndromes is the development of MTC caused by various activating germline mutations in the human *RET* proto-oncogene, encoding a receptor tyrosine kinase of the glial cell line-derived neurotrophic factor family. Sporadic MTCs are associated with the somatic *RET* mutation M918T (40–60%) as well as *RAS* mutations and overexpression of *CDK5*; loss of *CDKN2C* has been linked to distant metastasis. Pheochromocytomas are features of both MEN2A and MEN2B patients. Additionally, MEN2A is characterized by hyperparathyroidism, whereas MEN2B is associated with a Marfanoid habitus, ganglioneuromatosis, and skeletal abnormalities. MTCs in humans exhibit various morphologies including round, polygonal, plasmacytoid, or spindle cells, and up to 90% are associated with amyloid deposits. MEN2-associated tumors are usually bilateral, multicentric, and associated with the precursor lesion, primary C cell hyperplasia, which may represent thyroid intraepithelial neoplasia of C cells (THINC). Preneoplastic C cell hyperplasia is focal to multifocal as opposed to diffuse C cell hyperplasia, which represents a pathophysiological response to hypercalcemia-induced C cell stimulation. In sporadic and familial cases, sites of metastasis typically include lymph nodes, lung, liver, and bone. Serum calcitonin is an accurate and sensitive biomarker for preoperative diagnosis and postsurgical disease recurrence/progression.

Historically, genetically engineered mice have informed the pathogenesis of sporadic and familial MTC as opposed to being utilized to evaluate the efficacy of targeted chemotherapeutics. Recent reviews reveal the majority of models express various *RET* mutations under control of human calcitonin or rat calcitonin/CGRP promoters, and develop C cell hyperplasia/adenoma (Figure 17.14) which frequently progresses to MTC, some associated with documented calcitonemia [32, 33]. Tumor penetrance has also been shown to vary by genetic background when a single transgenic line was backcrossed to four different strains, resulting in MTC incidences ranging from 0% in FVB/N mice to 98% in CBA/Ca mice [94]. Constitutive knock-in mice expressing the mouse ortholog of M918T, found in both sporadic MTC and MEN2B, developed C cell hyperplasia which does not progress to MTC, with concurrent pheochromocytomas in a subset of hemizygous and 100% of homozygous mutants;

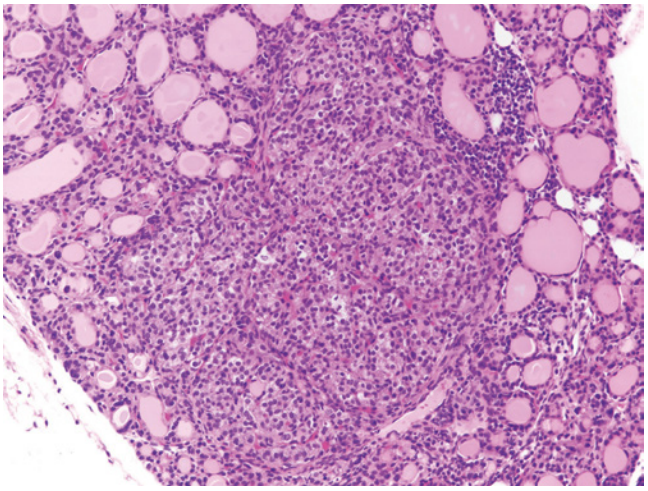


Figure 17.14 Thyroid C cell adenoma.

homozygous mutants also developed ganglioneuromas restricted to the adrenal medulla [34]. Transgenic lines expressing *v-Ha-ras* driven by the rat calcitonin/CGRP promoter developed MTCs of variable morphology, including with amyloid deposits, occasional mixed medullary-follicular tumors, and rare metastases to lymph nodes and lung. Although not necessarily associated with MTC in humans, a single mutant *Rb1* allele is sufficient to induce pituitary tumors in mice as well as C cell hyperplasia or unilateral MTC. Concurrent loss of *E2f,* a downstream target of *Rb1*, via breeding to *E2f3*^{tm1Lees} null mice, is sufficient to suppress pituitary tumorigenesis, resulting in almost completely penetrant bilateral MTCs which are highly invasive and metastasize in over a third of mice, most commonly to lung and liver [95]. As noted above, a portion of mice heterozygous for *Rb1* and *Trp53* develop MTCs. Multistep tumorigenesis has been demonstrated in a subset of these MTCs as evidenced by the identification of mutant *Ret* alleles, the majority of which correspond to activating mutations reported in people, and loss of heterozygosity of the remaining *Rb1* allele [96].

Parathyroid Gland

Anatomy, Histology, and Physiology

Mice have a single pair of parathyroid glands which are challenging to discern grossly due to their asymmetrical and subcapsular location within the cranial-lateral thyroid gland (Figure 17.6) [1, 3]. The parathyroid glands of mice are composed of sheets of chief or principal cells which produce PTH, an important regulator of calcium homeostasis through its action on bone, kidneys, and the intestines to increase blood calcium in opposition to calcitonin. Mouse chief cells are classified as active dark or inactive light cells; oxyphil cells, which are larger cells with eosinophilic cytoplasm rich in mitochondria and reported in humans to represent inactive chief cells, are not present in mice.

Special Protocols

Sequential sections of the thyroid gland are often required in order to capture the parathyroid glands in section. In addition to parathyroid gland histology, serum PTH levels should be assessed in conjunction with serum levels of calcium, phosphorus, calcitonin, and/or calcitriol; all should be correlated with morphologic and functional evaluations of kidney and bone. In addition to PTH, chief cells express glial cell missing 2 (GCM2), the calcium-sensing receptor (CASR), and vitamin D receptor (VDR).

Aging/Spontaneous Strain-Specific Lesions

Aberrant or remnant tissue resulting from embryologic development may be observed in the parathyroid gland as Kursteiner's cysts, which are lined by ciliated, nonciliated, or attenuated epithelium and contain eosinophilic to mucinous material. APOA2 amyloid may be deposited in the parathyroid gland interstitium of mice, especially in CD-1 and C57BL/6 strains (Figure 17.15). Diffuse chief cell hyperplasia is a pathophysiological response to hypocalcemia or decreased calcitriol associated with dietary or renal-induced secondary hyperparathyroidism.

Genetically Engineered Mice

Hypoparathyroidism

A number of congenital developmental abnormalities resulting in agenesis or dysgenesis of the human parathyroid gland with subsequent primary hypoparathyroidism have been described [97]. Unfortunately, many mouse models constructed with genetic mutations associated with these diseases are embryonic lethal and/or do not express the same phenotype, if any, in the parathyroid gland. The exception to this is constitutive or conditional loss of *Gcm2*. *Gcm2* is the mouse ortholog of *GCMB*, a parathyroid-specific transcription factor essential for its development. *Gcm2* deficient mice (*Gcm2*^{tm1Kry} and *Gcm2*^{tm1Malx}) are viable, lack parathyroid glands, and exhibit hypocalcemia and hyperphosphatemia, with or without detectable PTH levels [98, 99]. In tamoxifen-inducible *Gcm2* conditional null mice, decreased Ki67 positive cells were noted in the parathyroid gland after one month, whereas seven months later, the parathyroid glands were undetectable, serum calcium and PTH levels were significantly decreased, and serum phosphorus levels were increased [100]. *Mafb* is a transcription factor important in the development process of multiple tissues, including the parathyroid gland where it is downstream of *Gcm2*. Late stage (E18.5) *Mafb*^{em1Staka} deficient embryos possess ectopic parathyroid glands, with PTH- and CASR-expressing cells located between the thyroid and thymus near the carotid arteries in heterozygous mice, but only CASR-expressing (early differentiation) cells found within the

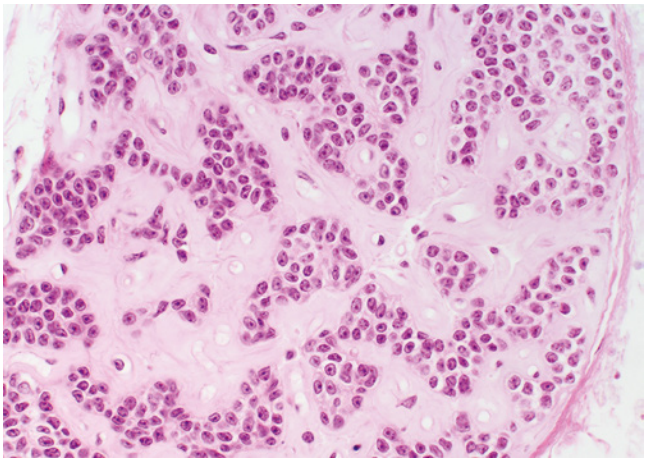


Figure 17.15 Chief cells within the parathyroid gland are widely separated by pale eosinophilic, amorphous, acellular amyloid.

anterior region of each thymus lobe in homozygous mice. Postnatally, both genotypes had decreased serum PTH levels, but only homozygous mice exhibited skeletal abnormalities [101]. Interestingly, mice homozygous for a disrupted *Pth*^{tm1Dgo} allele have pronounced parathyroid gland hyperplasia that accompanies typical biochemical changes associated with primary hypoparathyroidism [102]. Systemic administration of diphtheria toxin to mice in which expression of the diphtheria toxin receptor is limited to the parathyroid gland results in selective ablation of chief cells, thereby serving as a suitable model for secondary or acquired hypoparathyroidism [103].

Hyperparathyroidism

Hyperparathyroidism, characterized by elevated serum levels of PTH, is either primary, due typically to a benign parathyroid gland adenoma and associated with hypercalcemia, or secondary, in which disease outside of the parathyroid gland causes its hyperactivity in response to hypocalcemia. The majority of primary hyperparathyroidism cases are due to sporadic neoplasms, with 5–10% associated with hereditary syndromes. *Cyclin D1 (CCND1,* formerly called *PRAD1), MEN1,* and *MEN4* are specific genes implicated in the pathogenesis of human parathyroid gland adenomas. Secondary hyperparathyroidism is associated with dietary vitamin D deficiency or renal failure. Mouse models of parathyroid diseases characterized by abnormal calcium and phosphorus homeostasis have been reviewed [25].

Mice separately constructed with parathyroid gland-specific overexpression of *Ccnd1* and deletion of *Men1* both develop parathyroid gland hyperplasia progressing to adenomas, with hypercalcemia (Figure 17.16) [24, 26, 104, 105]. Mouse models of additional genes associated with deficient calcium-sensing and disrupted feedback to PTH include transgenic mice overexpressing *Rgs5* [*Tg(Rgs5-EGFP)JM24Gsat*] in the parathyroid gland. Serum PTH was elevated in males at 6 months of age and in females at 12 months, with variable calcium levels as well as parathyroid gland hyperplasia noted in 8/45 mice at 6 months and parathyroid gland adenomas in 9 of 42 mice at 12 months [106]. Genetically engineered mice with parathyroid gland-specific deletions in *Casr* and *Klotho*, alone and in combination, were constructed to further the understanding of mechanisms controlling progression of secondary hyperparathyroidism associated with renal failure. KLOTHO, a transmembrane protein in the renal tubules and parathyroid glands, binds to FGFR1; this binding is necessary for FGF23 signaling, which is induced by PTH. Mice lacking *Casr* as well as those lacking both *Casr* and *Klotho* have elevated serum PTH and $1,25(OH)_2D_3$, hypercalcemia, hypophosphatemia, hypercalciuria, and hypophosphaturia as well as parathyroid gland hyperplasia with nodular formations and a skeletal phenotype [107].

Familial hypocalciuric hypercalcemia (FHH) is an exceedingly rare cause of elevated serum PTH due to genetic mutations in *CASR*, *GNA11*, or *AP2S1*, or the production of autoantibodies against CASR. While renal and bone lesions frequently accompany primary or secondary hyperparathyroidism, they are often absent in FHH. Mouse models with mutations in these three FHH-associated genes, introduced via homologous recombination, CRISPR/Cas9-mediated gene editing and chemical mutagenesis have been produced. All recapitulate the respective FHH phenotype except *Ap2s1*^{m3Rvt} mutants in which homozygosity resulted in embryonic lethality and heterozygous mutants had no biochemical abnormalities [108–111].

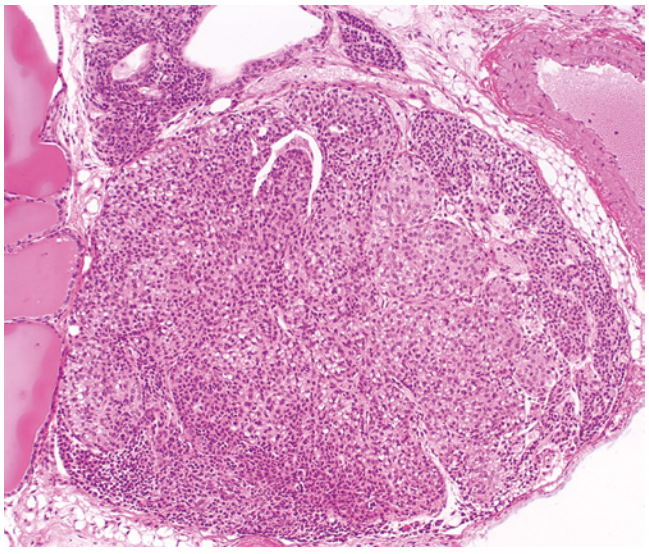


Figure 17.16 Parathyroid chief cell adenoma.

Adrenal Gland

Anatomy, Histology, and Physiology

The paired adrenal glands are located cranial to the cranial pole of the kidneys and are arranged into the mesodermal-derived cortex and central medulla of neural crest origin [1, 3]. Hormone production in the mouse adrenal cortex is limited to the mineralocorticoid aldosterone in the outermost zona glomerulosa, arranged in an arcuate pattern, and corticosteroids, primarily corticosterone, in the zona fasciculata which comprises the majority of the cortex. ACTH produced by corticotrophs in the anterior pituitary gland regulates glucocorticoid production in the zona fasciculata and can transiently stimulate aldosterone secretion in the zona glomerulosa, which is primarily regulated by the renin–angiotensin system. Adrenal cortical cells are rich in lipid and lack secretory granules due to direct secretion. The adrenal cortex of mice is unique among mammals in that it lacks 17α-hydroxylase (CYP17A1), thereby forcing production of corticosterone, rather than cortisol and precluding androgen production by the inapparent zona reticularis. Additionally, mice have an innermost X-zone, analogous to the human fetal zone which disappears soon after birth; the X-zone

develops postnatally and is evident as a distinct layer of smaller basophilic cells around day 10, reaches full development by weaning, and undergoes a sexually dimorphic and strain-dependent pattern of regression [112]. Regression of the X-zone in females occurs via lipid vacuolization (Figure 17.17) by 5–15 days of pregnancy or in the absence of pregnancy, slowly disappears between three and seven months of age, whereas in males, it disappears by puberty without undergoing lipid vacuolization. The presence and absence of the X-zone in both sexes corresponds to the enzymatic activity of 20α-hydroxysteroid dehydrogenase, a progesterone-metabolizing enzyme; additional X-zone markers include phosphatidylinositol-4-phosphate 3-kinase C2 domain-containing gamma polypeptide (PIK3C2G), and THRB.

The medulla is primarily composed of polygonal chromaffin cells also known as pheochromocytes and variable numbers of ganglion cells. Chromaffin cells dispersed throughout the body are referred to as paraganglia and are classified as sympathetic, exemplified by the adrenal medulla, or parasympathetic. The majority (75–85%) of medullary chromaffin cells in mice produce epinephrine compared to norepinephrine and can be differentiated ultrastructurally by the core density of their secretory granules.

Special Protocols

Due to the exceedingly small size of mouse adrenal glands, care must be taken to isolate the glands from the kidneys, not only to facilitate their combined weighing for the detection of stress-induced increases but also for embedding *in toto* to obtain longitudinal histologic sections that include both the cortex and medulla [5]. Dynamic testing via ACTH stimulation or dexamethasone suppression +/– corticotropic-releasing hormone challenge, with special consideration to diurnal variation, is typically utilized to evaluate the hypothalamic–pituitary–adrenal and sympathetic–adrenal–medullary axes, including in response to stressors such as restraint/handling, fasting/food restriction, exercise, and social stimuli [113]. A variety of behavioral testing paradigms also model acute and chronic stress in mice and may be incorporated into phenotypic strategies [114]. Measurement of hormones in urine and feces represents a noninvasive alternative to blood in which collection/handling is associated with stress, but is similarly influenced by strain, sex, and diurnal variation [115–117]. Fractionated catecholamine metabolites, known as metanephrines, in blood and/or urine are more sensitive biomarkers than fractionated catecholamines. Stress may also be manifested in results of routine clinical pathology testing as well as evaluation of the immune and reproductive systems [113].

All cortical cells express sonic hedgehog (SHH) while cells of steroidogenic origin, whether in the adrenal cortex or gonads, express NR5A1. GATA4 is expressed in fetal adrenocortical cells and gonadectomy-induced adrenal tumors, while GATA6 is expressed in the fetal and adult cortex [118]. Medullary chromaffin cells are immunoreactive for chromogranin A, synaptophysin, neuron-specific enolase, as well as tyrosine hydroxylase (TH), necessary for the conversion of tyrosine to dopamine, the first step in catecholamine synthesis. Variable expression of dopamine ß-hydroxylase (DBH) which converts dopamine to norepinephrine, and phenylethanolamine-*N*-methyl-transferase (PMNT) which produces epinephrine from norepinephrine, has also been reported [119]. Schwannian stroma may be immunoreactive for S100B.

Aging/Spontaneous Strain-Specific Lesions

A number of spontaneous findings are commonly observed in mouse adrenal glands, of which it is important to be aware, particularly when characterizing a phenotype and assessing the impact of genotype and background strain on the incidence of these findings [120]. Accessory cortical nodules, attached to the adrenal cortex or dispersed in the adjacent adipose tissue, should be distinguished from adrenocortical tumors. Lipogenic pigmentation (Figure 17.18) appears as yellowish-brown, granular to foamy, ceroid pigment within macrophages at the corticomedullary junction and may be associated with enlarged cortical epithelial cells as well as angiectasis. This is commonly seen as a consequence of physiologic regression of the X-zone, subsequent to lipid vacuolation (Figure 17.17), degeneration, and necrosis. Subtle phenotypes in adrenal models may manifest as persistence or delayed regression of the X-zone in mice. Extramedullary hematopoiesis may be observed in the adrenal gland, incidentally or as a physiologic response to anemia or systemic inflammation. When present in the adrenal gland, extramedullary hematopoiesis is typically also pronounced in the spleen and liver. APOA2 amyloid may also be deposited in the adrenal gland, especially at the corticomedullary junction in CD-1 and C57BL/6 strains.

A population of cells commonly proliferates in the mouse adrenal gland, initially in a subcapsular pattern and then a centripetal pattern between columns of the zona fasciculata

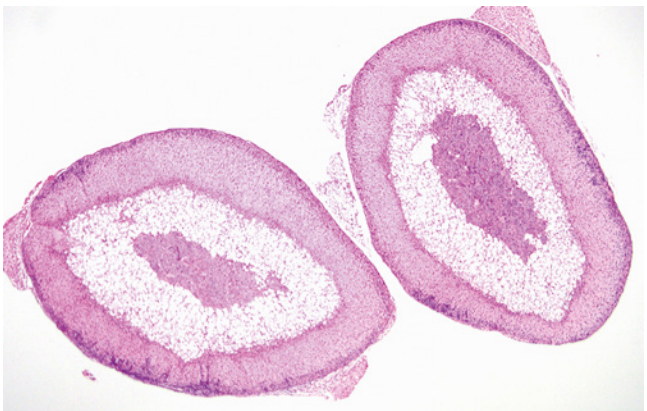


Figure 17.17 Bilateral regression of the adrenocortical X-zone as evidenced by lipid vacuolization in a female mouse.

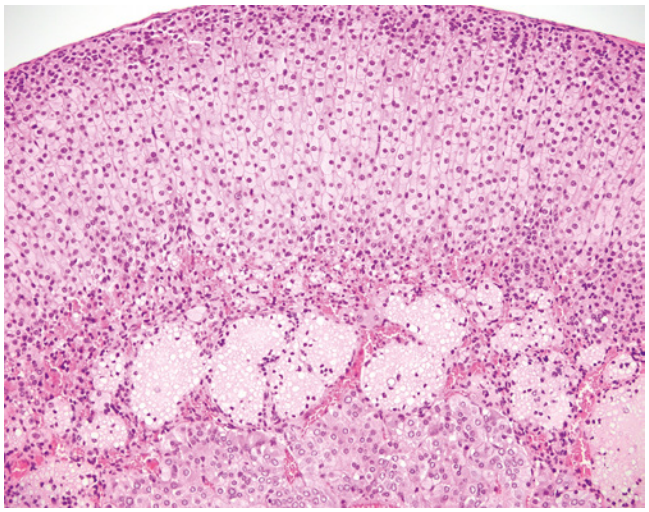


Figure 17.18 Large macrophages containing yellowish-brown pigment are associated with angiectasis at the corticomedullary junction of the adrenal gland.

to the corticomedullary junction (Figure 17.19). Type A spindle cells with indistinct cytoplasm predominate but type B polygonal cells with abundant, eosinophilic to vacuolated cytoplasm are occasionally observed. In addition to strain [121], numerous factors such as social stressors (crowding and isolation), gonadectomy, irradiation, and compound administration result in increased incidences as well as the formation of tumors, usually of type B cells (Figure 17.19). As evidenced by lineage studies, these cells represent stem/progenitor cells in the complex adrenocortical niche [122]. Recent results document the existence of nestin+ cells beneath the capsule and throughout the cortex, which are distinct but interconnected to SHH/GLI1+ capsular progenitor cells responsible for daily renewal and nestin+ progenitors in the medulla, that can differentiate into steroidogenic cells and are responsive to ACTH and a luteinizing hormone releasing hormone agonist [123].

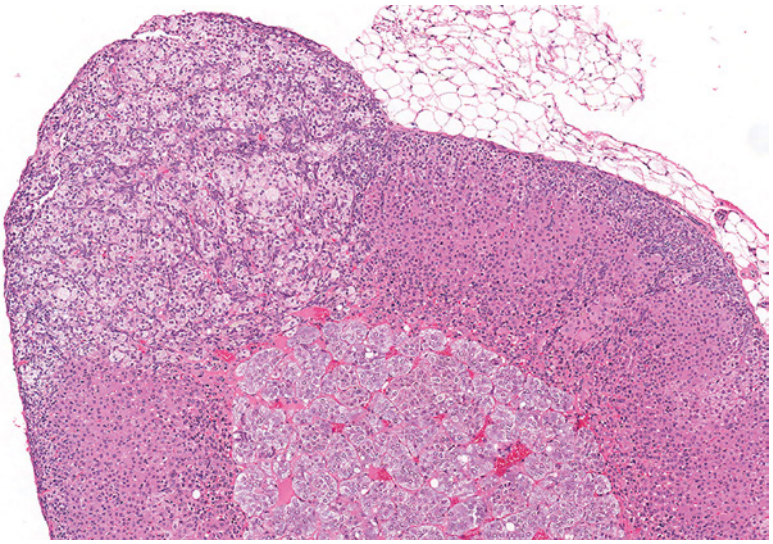
Genetically Engineered Mice

Adrenal Insufficiency

Adrenocortical hypofunction may be caused by primary adrenal disease (Addison disease) or secondary conditions resulting in decreased adrenal stimulation due to inadequate secretion or synthesis of ACTH. The latter can be associated with hypopituitarism and pituitary corticotroph adenomas, described above, as well as exogenous corticosteroids.

Causes of primary adrenal insufficiency include impaired steroidogenesis, adrenal dysgenesis/hypoplasia, and adrenal destruction. Familial glucocorticoid deficiency (FGD) is an autosomal recessive condition characterized by decreased glucocorticoids, elevated ACTH, and variable aldosterone levels in the blood. Less than half of FGD cases are associated with mutations in the melanocortin-2-receptor (*MCR2*, type 1), also known as the ACTH receptor, which is expressed in all zones of the adrenal cortex, as well as the melanocortin-2-receptor accessory protein (*MRAP*, type 2). Mice separately deficient in $Mcr2^{tm1Dchi}$ and $Mrap^{tm1Geno}$ have been developed, and homozygous mutants invariably die within one to two days of birth due to marked hypoglycemia, complicated by lung immaturation [124]. Mice also exhibited low to undetectable levels of corticosterone, aldosterone, and epinephrine, the latter exemplifying the glucocorticoid-dependent PMNT-mediated conversion of norepinephrine to epinephrine. Adrenal glands were indistinguishable from wild types at birth but were smaller in adulthood. Mutations in steroidogenic acute regulatory protein (*STAR*) can result in type 3 FGD with patients exhibiting normal genitalia, or lipoid congenital adrenal hyperplasia in which gonadal steroidogenesis is also defective and accompanied by disordered sexual differentiation. In addition to the phenotypic presentation described above, genetically male and female

Figure 17.19 Subcapsular proliferation of type A spindle cells (right) and a cortical adenoma composed primarily of type B polygonal cells in the adrenal gland.



Star^{tm1Klp} knockout mice exhibited female external genitalia [125]. Patients with adrenal hypoplasia congenita have adrenal insufficiency due to hypoplastic or aplastic adrenal glands, and those with the X-linked form of the disease due to gene deletions or mutations in *NR0B1* (formerly *DAX1*) also have hypogonadotropic hypogonadism. In contrast, *Nr0b1*$^{tm1Lja/Y}$ knockout mice initially exhibited adrenocortical hyperfunction with onset of progressive insufficiency after 15 weeks of age, characterized by decreased basal and ACTH-stimulated corticosterone, ACTH, steroidogenic enzymes, and adrenal volume [126].

The most common cause of primary adrenal insufficiency in humans is autoimmune adrenalitis, in which steroidogenic enzymes in the cortex, especially 21-hydroxylase, are subject to Th1-mediated destruction. Autoimmune adrenalitis is a key feature of autoimmune polyendocrinopathy syndromes (APSs). Type 1 APS results from mutations in the *AIRE* gene, which is normally expressed in a subset of medullary thymic epithelial cells and participates in negative selection of developing thymocytes. While *Aire*^{tm1Doi} knockout mice develop characteristic lymphocytic infiltrations in multiple organs, adrenal involvement has yet to be reported [127].

Adrenocortical Hyperplasia and Tumors

Proliferations of the adrenal cortex encompass hyperplastic conditions, which affect bilateral adrenal glands, as well as cortical adenomas and carcinomas, which tend to be unilateral; most lesions are benign adenomas. Functional lesions, while uncommon, may be associated with hyperadrenalism, manifesting as elevated mineralocorticoids (Conn's syndrome) or glucocorticoids (Cushing's syndrome), and can be ACTH-dependent or independent. Cortisol secretion is due to increased activation of the PKA pathway while abnormal calcium–calmodulin-dependent kinase signaling results in aldosterone secretion. Somatic and germline mutations in leak-type (TASK) potassium channels (*KCNJ5*), voltage-gated calcium channels (*CACNA1D* and *CACNA1H*), and Na^+/K^+ pumps (*ATP1A1* and *ATP2B3*) cause primary aldosteronism, cortical hyperplasia or adenoma, and hypertension. Multiple mouse models with potassium channel deletions develop hyperaldosteronism in the absence of proliferative adrenocortical lesions [14, 15, 128]. Hereditary cortisol-secreting lesions include primary bilateral macronodular adrenal hyperplasia (PBMAH) and primary pigmented nodular adrenocortical disease (PPNAD). Many genes are associated with the development of PBMAH, including *MEN1*, *APC*, *FH*, *ARMC5*, and multiple genes in the cAMP/PKA signaling pathway. Phenotypes vary among mouse models, ranging from cortical hyperplasia, adenomas, and carcinomas in whole body *Men1* knockout mice to abnormal corticosterone levels only that vary with age in heterozygous *Armc5*^{tm1Stra} mutant mice [14, 15, 129]. PPNAD is the most common manifestation of Carney complex associated with *PRKAR1A* mutations. *Prkar1a* mutant mice lack overt proliferative adrenocortical lesions, and autonomous corticosterone secretion is only seen in adrenocortical-specific knockouts [14, 15]. Adrenocortical carcinomas develop in humans with *APC* mutations and elevated Wnt/ß-catenin signaling (familial adenomatous polyposis), overexpression of *IGF2* (Beckwith–Wiedemann syndrome), and inactivation of *TP53/RB1* (Li–Fraumeni syndrome); however, mice with these mutations do not develop carcinomas [15].

Tumors of the Adrenal Medulla

While cancer of the adrenal gland is rare, tumors originating in the adrenal medulla are even rarer and include the more common catecholamine-producing pheochromocytomas as well as neuroblastomas. Similar tumors can also originate in extra-adrenal paraganglia, often in conjunction with the respective adrenal tumor. Pheochromocytomas and paragangliomas have a variable clinical presentation, but many presenting symptoms are associated with excess catecholamine release, such as tachycardia, hyperhidrosis, and hypertension. Seventy percent of pheochromocytomas and paragangliomas are due to germline and/or somatic mutations identified in 22 susceptibility genes described to date, with the most frequent in subunits of the succinate dehydrogenase gene (*SDHX*) [130]. The most clinically relevant hereditary syndromes include MEN2 (*RET*); von Hippel Lindau disease (*VHL*); neurofibromatosis type 1 (*NF1*); hereditary paraganglioma syndrome (*SDHA, SDHB, SDHC, SDHD, SDHAF2*); familial pheochromocytoma (*TMEM127, MAX*); and, Reed syndrome (*FH*). Associated susceptibility genes to date have been organized into two broad transcription signatures, including a pseudohypoxic cluster as well as a cluster rich in kinase receptor signaling and associated downstream pathways. A limited number of genetically engineered mouse models have been described that develop pheochromocytomas (Figure 17.20), some unexpectedly when modeling other diseases (i.e. *Rb1, Erbb2,* and *BRAF*^{V600E}) [18, 34, 35, 37]. Only a subset of susceptibility genes involved in kinase receptor signaling have resulted in chromaffin cell hyperplasia or neoplasia when introduced into the mouse genome and, with the exception of *RET* M918T and *Nf1* mutants, require concurrent mutations (i.e. *Pten*) to induce pheochromocytomas with or without metastasis.

Peripheral neuroblastomas are the most common solid, extracranial childhood neoplasm, with the diagnosis in most patients occurring before the age of five. Given that these tumors include a histologic spectrum based on the degree of cellular (blastic to ganglion) and stromal (Schwannian to neuropil) differentiation, it is preferable to collectively refer to these as peripheral neuroblastic tumors of neural crest origin. A number of genetically engineered constructs have been described which utilize the TH or DBH promoters to model *ALK* mutations with or without amplifications seen in familial and sporadic tumors, *MYCN* amplifications occurring in a quarter of all cases, and *LIN28B* overexpression [131, 132]. These mice develop tumors in adrenal glands and ganglia that exhibit the spectrum of differentiation noted in humans with variable latent periods and metastatic patterns influenced by

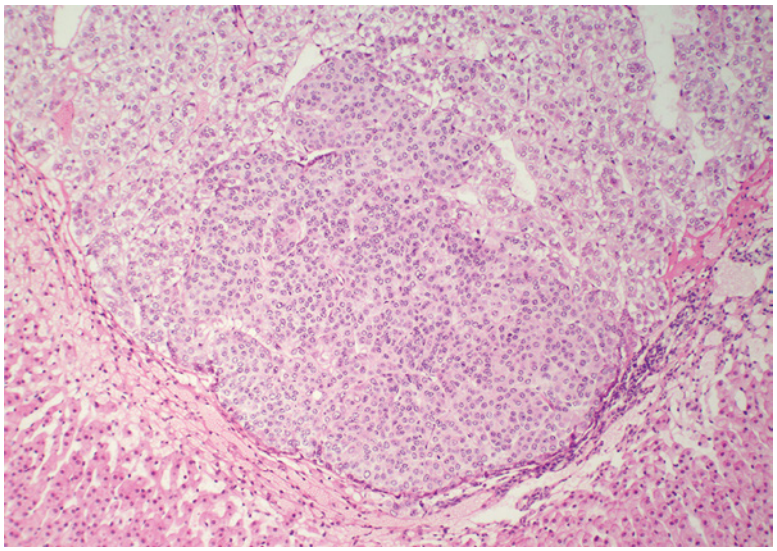


Figure 17.20 Focal pheochromocytoma at the cortical-medullary junction that disrupts nonneoplastic chromaffin cells within the adrenal medulla.

background strain. One of the first and best characterized models, the *Tg(Th-MYCN)41Waw* mouse, has also been utilized to investigate numerous modifier genes, metastasis, and drug resistance, while subcutaneous and orthotopic engraftments of their tumors in syngeneic mice have been used for preclinical testing of immunotherapeutics.

Pancreatic Islets

Anatomy, Histology, and Physiology

The endocrine pancreas accounts for just 1–2% of the adult pancreas and is arranged into islets composed of cells that produce multiple hormones important for glucose homeostasis and digestion [1, 3]. In contrast to human islets, mouse islets are primarily interlobular and comprised of a central core of ß cells (60–80%) which produce insulin and amylin surrounded by glucagon-secreting α cells (15–20%), somatostatin-secreting δ cells (<10%), ghrelin-secreting ε cells (<1%), and PP cells which produce pancreatic polypeptide (<1%) [133, 134]. Reminiscent of the anterior pituitary, islet plasticity and multihormonality have been documented through the transition from insulin-sensitivity to insulin resistance and diabetes, as well as in insulinomas [27, 135].

Special Protocols

The pancreas in rodents is widely dispersed within the duodenal mesentery, as opposed to being arranged in compact lobe(s), and as such may be visualized in histologic sections attached to the duodenum as well as the large intestine. Given that islets are variably distributed throughout the pancreas and associated with mesenteric adipose tissue, assessment of a large portion of the pancreas is necessary and facilitated by dissection and trimming recommendations previously reviewed [136, 137]. Beyond evaluating serum and urine glucose levels antemortem and/or at the time of necropsy, blood levels of the hormones noted above may be measured and tissue expression assessed via immunostaining. Various histochemical stains are also available for the identification of islet cells types, including the aldehyde fuchsin method for ß cells (Figure 17.21) [138]. Metabolic testing should also be undertaken during the phenotypic characterization of diabetic mouse models [139]. More specialized approaches include measurement of glycated hemoglobin (HbA1c), glucose and insulin tolerance tests, assessment of food intake and energy expenditure, as well as characterization of liver, skeletal muscle, and adipose tissue (brown and white). Use of controls, age-matched within one week is necessary because of age-related changes in the hormonal control of glucose homeostasis. Some tests such as the tolerance tests require frequent blood sampling, so body weight and blood volume should be considered when selecting mice for these tests. Among the additional considerations is the impact of overnight fasting and anesthesia on body weight, liver glycogen content, and stress [140]. Metabolic phenotypes may be subtle and require the feeding of a high fat diet to manifest.

Aging/Spontaneous Strain-Specific Lesions

Histologically, there is tremendous variability in the size of mouse islets (Figure 17.22), as well as the number of islets by strain [141]. Additionally, islet cell hyperplasia occurs in numerous strains with age [121]. Aggregates of small lymphocytes are commonly seen as perivascular cuffs in various mouse tissues, including the pancreas between islets, exocrine acini and ducts as well as within the mesenteric adipose tissue. C57BL/6J mice are predisposed to obese and diabetic phenotypes with impaired insulin secretion due to a mutation in the nicotinamide nucleotide transhydrogenase gene which disrupts glucose-stimulated insulin secretion; this mutation is not found in C57BL6/N mice [139].

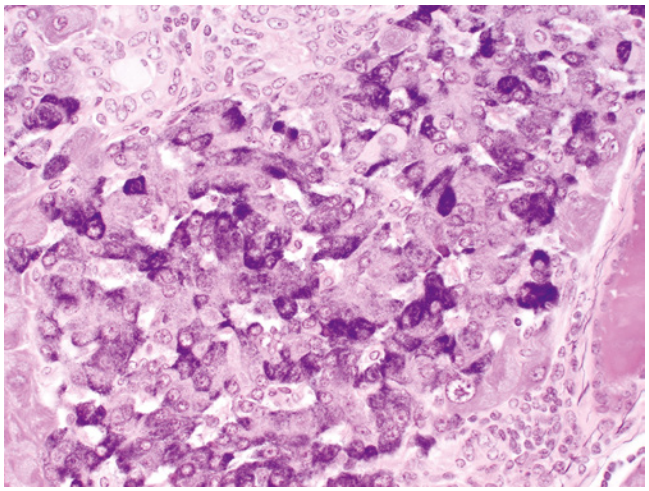


Figure 17.21 Aldehyde fuchsin histochemical staining of insulin within ß cells, which demonstrates reduced ß cell density in the islet of a diabetic mouse.

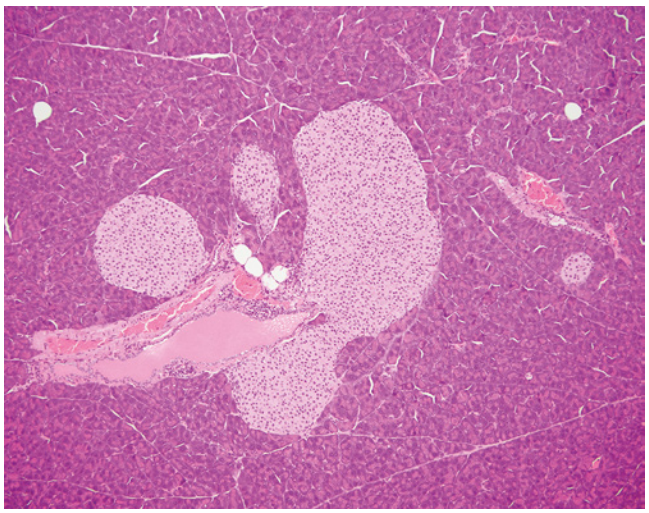


Figure 17.22 Mouse islets of variable sizes can be organized in close proximity or widely dispersed within the pancreas.

Genetically Engineered Mice

Diabetes Mellitus

Three interrelated processes tightly regulate normal glucose homeostasis: glucose production in the liver; glucose uptake, and utilization by peripheral tissues; and, the counter-regulatory actions of insulin and glucagon. Diabetes mellitus (DM) is a multifactorial group of metabolic disorders sharing the underlying feature of hyperglycemia due to insulin resistance, insufficient insulin secretion, or both. There are numerous forms of diabetes, but most commonly, it is classified as type 1 (T1DM), in which immune-mediated destruction of ß cells results in insulin deficiency, or type 2 (T2DM), characterized by insulin resistance and islet exhaustion. Monogenic and polygenic mouse models with spontaneous and induced mutations resulting in type 1 or type 2 diabetic phenotypes are reviewed elsewhere [140, 142, 143].

As noted above, NOD mice have served as the primary rodent model for T1DM diabetes for close to 40 years [143]. Insulitis presents as early as four to five weeks of age and begins at the periphery before progressing to involve entire islets. While T1DM is the only autoimmune disease without a female bias, insulitis is more severe in female NOD mice resulting in an earlier onset of nonfasting hyperglycemia and glucosuria, and higher incidences of diabetes compared to male mice. NOD mice have also been used to develop gene-targeted models, often restricted to ß cells utilizing the rat insulin promoter (RIP; INS1 or INS2) [144].

T2DM mouse models, including but not limited to those deficient in leptin (*Lep*; also known as *ob*) and the leptin receptor (*Lepr*; also known as *db*), are variable with regard to development of obesity, blood glucose and insulin levels, and pathology in other tissues such as liver, muscle, adipose, vasculature, and nerves [140]. As in people, ß cell morphology and function in mice vary according to disease stage as defined by responsiveness to insulin, with histopathologic findings ranging from ß cell hypertrophy and hyperplasia to death and loss (Figure 17.21). Islets in humans with T2DM are also commonly disrupted by amyloid derived from islet amyloid polypeptide (IAPP, amylin) which is secreted by ß cells and stored together with insulin in secretory vesicles. While IAPP is highly conserved across species, IAPP in the mouse is not amyloidogenic due to proline residues in the middle 20–29 fragment, which are not present in human IAPP. Consequently, only mice expressing human IAPP develop islet amyloidosis, which has been shown to promote ß cell death [145].

Islet Neoplasia

Tumors of the endocrine pancreas are rare and only account for ~2% of tumors involving the pancreas. Tumors may be functional and associated with the elaboration of specific hormones, but a majority are nonfunctional. Among islet neoplasms, insulinomas are most common and can result in clinically significant hypoglycemia; however, any cell type in the islets can undergo neoplastic transformation with or without hormone production. While most insulinomas are sporadic, <5% are associated with MEN1, as discussed above.

Most mouse models of pancreatic neuroendocrine tumors develop insulinomas through altered gene expression targeted to the ß cells via the RIP [28]. RIP is also weakly expressed in the pituitary gland so models incorporating loss of *Men1* also tend to develop lactotrophinomas in the anterior pituitary gland [29, 30]. An alternative model characterized by biallelic inactivation of *Men1* and *Pten* limited to ß cells by the mouse INS1 promoter develops islet cell hyperplasia and insulinomas (Figures 17.23–17.25) in over 25% of mice at 7 weeks and 100% at 13 weeks or later [30]. A popular model, *Tg(RIP1-Tag)2Dh*, utilizes RIP to drive expression of the SV40 T antigen (Tag) in ß cells [28]. The result is multistep tumor progression which begins as



Figure 17.23 Numerous hyperplastic and neoplastic islets distributed throughout the pancreas in a *Men1* heterozygous mutant mouse.

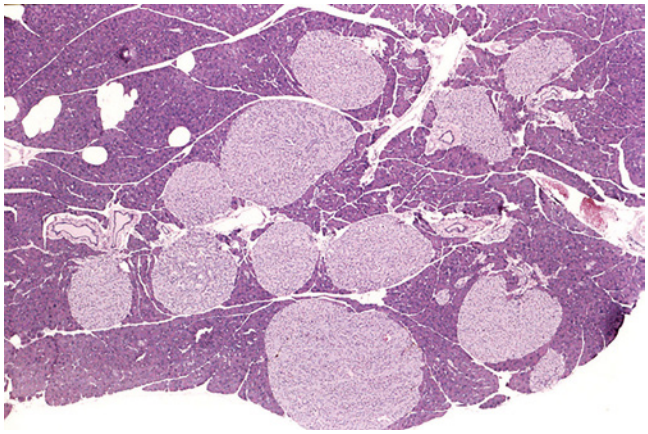


Figure 17.24 Hyperplastic and neoplastic islets in the pancreas of a *Men1* heterozygous mutant mouse.

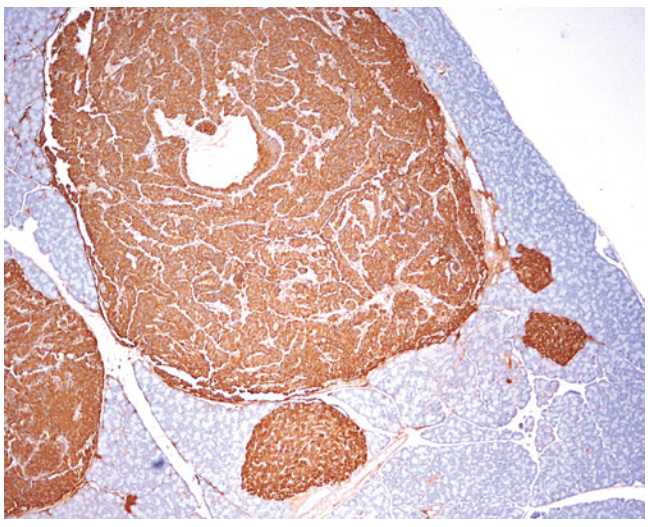


Figure 17.25 Hyperplastic and neoplastic islets in the pancreas of a *Men1* heterozygous mutant mouse are immunoreactive for insulin.

hyperplasia, followed by enhanced angiogenesis, formation of benign encapsulated adenomas, and ultimately invasive carcinomas. Most tumors produce insulin, causing mice to succumb to severe hypoglycemia prior to the formation of distant metastases. Interestingly, nonfunctioning pancreatic neuroendocrine tumors develop in *Tg(RIP1-Tag)2Dh* mice on a hybrid AB6F1 background instead of a C57BL/6 background [146]. These mice did not develop hyperinsulinemia or hypoglycemia, but their tumors were larger and metastasized more frequently to the liver; these differences were attributed to a locus in chromosome 2qG1 tightly linked to *Insm1*, which drives metaplasia of pancreatic ductal cells to endocrine cells through a stem cell intermediate. Comparable multistage tumorigenesis with the addition of neoplastic cells present in blood vessels, pancreatic ducts, and pancreatic lymph nodes is seen with the *Tg(Ins-MYC/Er)1Gev*; *Tg(Ins-BCL2L1)2Ksp* mouse in which coexpression of Bcl2l1 (formerly Bcl-XL) and c-Myc is induced in ß cells upon treatment with daily intraperitoneal administration of 4-hydroxytamoxifen (4-OHT) [28]. With c-Myc-induced apoptosis blocked by Bcl2l1, islets become hyperplastic within a week of 4-OHT treatment, insulinomas are noted within two weeks, and metastases detected by eight weeks.

Glucagonomas similarly develop through multistep progression when Tag is overexpressed in α cells by the rat preproglucagon promoter [147]. Hyperplastic/dysplastic islets were observed at 6–7 months, and overt tumors were present by 18 months, with retroperitoneal and lymph node metastases in at least one mouse. Interestingly, when this promoter is used to ablate *Men1* in α cells, pancreatic neuroendocrine tumors develop that express glucagon, insulin or both [27]. Highly penetrant metastases to liver and pancreatic lymph nodes develop in mice with glucagonomas due to conditional deletion of *Trp53* and *Rb1* using the renin 1 promoter [28]. Glucagonomas resulting in glucagonemia also unexpectedly developed concurrent with or independent of anterior pituitary adenomas in mice transgenic for *MYCN* in GFAP-expressing cells (*Gt(ROSA)26Sor*$^{tm1(CAG-MYCN,-luc)Jhsc}$; *Tg(GFAP-cre)25Mes)* [148].

Pineal Gland

The pineal gland is a photo-neuro-endocrine organ that produces melatonin through sequential conversions of tryptophan and serotonin by arylalkylamine-*N*-acetyl transferase (AANAT) and acetylserotonin *O*-methyltransferase (ASMT; formerly hydroxyindole-*O*-methyl transferase, HIOMT), respectively. Extra-pineal melatonin production exceeds that of the pineal gland and occurs in a number of cells and tissues, including but not limited to the retina, Harderian gland, enterochromaffin cells, thymus, mast cells, natural killer cells, platelets, and endothelial cells. Published data concerning melatonin levels in mice is contradictory and has been reviewed [149]. The majority of common laboratory

mouse strains are deficient in pineal melatonin production due to mutations in AANAT and ASMT with the exception of C3H/HeJ, CBA/J, DBA/1J, and SM/J mice. Similar to humans, melatonin-proficient strains produce melatonin at night, but peak levels occur late in the dark phase as opposed to humans in which it is earlier. Extra-pineal melatonin production has been documented in some melatonin-deficient strains [150].

The exceedingly small size of the mouse pineal gland restricts its evaluation to histologic coronal sections (Figure 17.26). A majority of cells are pinealocytes with eosinophilic, often foamy cytoplasm, and fewer, elongated, hyperchromatic glial cells. Spontaneous lesions of the mouse pineal gland are extremely rare. Reports of tumors originating in the pineal gland of genetically engineered mice are isolated, and limited to transgenic mice with expression of Tag restricted to the pineal gland due to the tryptophan hydroxylase promoter or the Moloney murine sarcoma virus enhancer and SV40 promoter [151, 152]. Reduced levels of melatonin have been observed in human aging and various diseases; most relevant preclinical studies utilizing genetically engineered mice involve models of Alzheimer's disease.

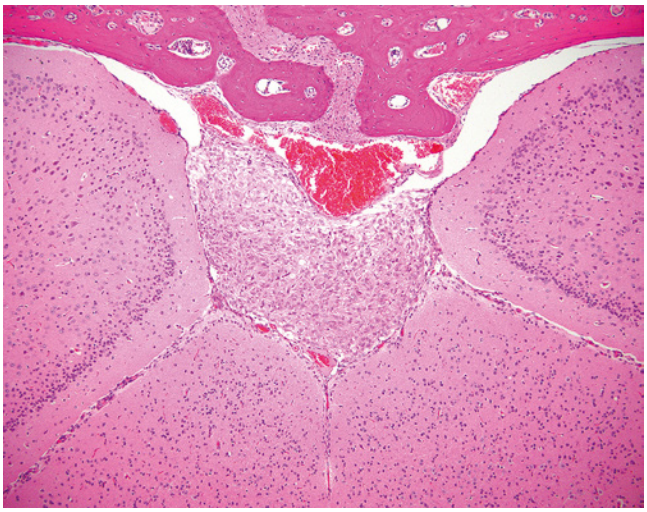


Figure 17.26 The pineal gland is located dorsally in a coronal section of the skull through the parietal cerebral cortex and midbrain.

References

1 La Perle, K. and Dintzis, S. (2018). Endocrine system. In: *Comparative Anatomy and Histology: A Mouse, Rat, and Human Atlas*, 2e (eds. P. Treuting, S. Dintzis and K. Montine), 251–273. San Diego, CA: Academic Press.

2 Liggitt, D. and Dintzis, S. (2018). Pancreas. In: *Comparative Anatomy and Histology: A Mouse, Rat, and Human Atlas* (eds. P. Treuting, S. Dintzis and K. Montine), 241–250. San Diego, CA: Academic Press.

3 Nacher, V., Ruberte, J., Navarro, M., and Carretero, A. (2017). The endocrine glands. In: *Morphological Mouse Phenotyping: Anatomy, Histology and Imaging* (eds. J. Ruberte, A. Carretero and M. Navarro), 349–375. Amsterdam: Academic Press.

4 Bielohuby, M., Popp, S., and Bidlingmaier, M. (2012). A guide for measurement of circulating metabolic hormones in rodents: pitfalls during the pre-analytical phase. *Mol. Metab.* 1 (1–2): 47–60.

5 Kittel, B., Ruehl-Fehlert, C., Morawietz, G. et al. (2004). Revised guides for organ sampling and trimming in rats and mice – part 2. A joint publication of the RITA and NACAD groups. *Exp. Toxicol. Pathol.* 55 (6): 413–431.

6 Brandli-Baiocco, A., Balme, E., Bruder, M. et al. (2018). Nonproliferative and proliferative lesions of the rat and mouse endocrine system. *J. Toxicol. Pathol.* 31 (3 Suppl): 1S–95S.

7 Grimelius, L. (2008). Methods in neuroendocrine histopathology, a methodological overview. *Upsala J. Med. Sci.* 113 (3): 243–260.

8 Baudin, E., Gigliotti, A., Ducreux, M. et al. (1998). Neuron-specific enolase and chromogranin A as markers of neuroendocrine tumours. *Br. J. Cancer* 78 (8): 1102–1107.

9 Crivellato, E., Nico, B., Bertelli, E. et al. (2006). Dense-core granules in neuroendocrine cells and neurons release their secretory constituents by piecemeal degranulation (review). *Int. J. Mol. Med.* 18 (6): 1037–1046.

10 Gahete, M.D., Jimenez-Vacas, J.M., Alors-Perez, E. et al. (2019). Mouse models of endocrine tumors. *J. Endocrinol.* 240 (3): R73–R96.

11 Cano, D.A., Soto-Moreno, A., and Leal-Cerro, A. (2014). Genetically engineered mouse models of pituitary tumors. *Front. Oncol.* 4: 203.

12 Lines, K.E., Stevenson, M., and Thakker, R.V. (2016). Animal models of pituitary neoplasia. *Mol. Cell. Endocrinol.* 421: 68–81.

13 Kirschner, L.S., Qamri, Z., Kari, S., and Ashtekar, A. (2016). Mouse models of thyroid cancer: a 2015 update. *Mol. Cell. Endocrinol.* 421: 18–27.

14 Basham, K.J., Hung, H.A., Lerario, A.M., and Hammer, G.D. (2016). Mouse models of adrenocortical tumors. *Mol. Cell. Endocrinol.* 421: 82–97.

15 Leccia, F., Batisse-Lignier, M., Sahut-Barnola, I. et al. (2016). Mouse models recapitulating human adrenocortical tumors: what is lacking? *Front. Endocrinol.* 7: 93.

16 Jones, G.N., Manchanda, P.K., Pringle, D.R. et al. (2010). Mouse models of endocrine tumours. *Best Pract. Res. Clin. Endocrinol. Metab.* 24 (3): 451–460.

17 Pringle, D.R., Vasko, V.V., Yu, L. et al. (2014). Follicular thyroid cancers demonstrate dual activation of PKA and mTOR as modeled by thyroid-specific deletion of Prkar1a and Pten in mice. *J. Clin. Endocrinol. Metab.* 99 (5): E804–E812.

18 Korpershoek, E., Pacak, K., and Martiniova, L. (2012). Murine models and cell lines for the investigation of pheochromocytoma: applications for future therapies? *Endocr. Pathol.* 23 (1): 43–54.

19 Lee, Y.R. and Pandolfi, P.P. (2020). PTEN mouse models of cancer initiation and progression. *Cold Spring Harbor Perspect. Med.* 10 (2): a037283.

20 Mirantes, C., Eritja, N., Dosil, M.A. et al. (2013). An inducible knockout mouse to model the cell-autonomous role of PTEN in initiating endometrial, prostate and thyroid neoplasias. *Dis. Models Mech.* 6 (3): 710–720.

21 Wang, H., Karikomi, M., Naidu, S. et al. (2010). Allele-specific tumor spectrum in pten knockin mice. *Proc. Natl. Acad. Sci. U.S.A.* 107 (11): 5142–5147.

22 Caserta, E., Egriboz, O., Wang, H. et al. (2015). Noncatalytic PTEN missense mutation predisposes to organ-selective cancer development in vivo. *Genes Dev.* 29 (16): 1707–1720.

23 Russo, M.A., Antico Arciuch, V.G., and Di Cristofano, A. (2012). Mouse models of follicular and papillary thyroid cancer progression. *Front. Endocrinol.* 2: 119.

24 Mohr, H. and Pellegata, N.S. (2017). Animal models of MEN1. *Endocr. Relat. Cancer* 24 (10): T161–T177.

25 Imanishi, Y., Nagata, Y., and Inaba, M. (2012). Parathyroid diseases and animal models. *Front. Endocrinol.* 3: 78.

26 Libutti, S.K., Crabtree, J.S., Lorang, D. et al. (2003). Parathyroid gland-specific deletion of the mouse Men1 gene results in parathyroid neoplasia and hypercalcemic hyperparathyroidism. *Cancer Res.* 63 (22): 8022–8028.

27 Lu, J., Herrera, P.L., Carreira, C. et al. (2010). Alpha cell-specific Men1 ablation triggers the transdifferentiation of glucagon-expressing cells and insulinoma development. *Gastroenterology* 138 (5): 1954–1965.

28 Buicko, J.L., Finnerty, B.M., Zhang, T. et al. (2019). Insights into the biology and treatment strategies of pancreatic neuroendocrine tumors. *Ann. Pancreatic Cancer* 2.

29 Crabtree, J.S., Scacheri, P.C., Ward, J.M. et al. (2003). Of mice and MEN1: insulinomas in a conditional mouse knockout. *Mol. Cell. Biol.* 23 (17): 6075–6085.

30 Wong, C., Tang, L.H., Davidson, C. et al. (2020). Two well-differentiated pancreatic neuroendocrine tumor mouse models. *Cell Death Differ.* 27 (1): 269–283.

31 Crabtree, J.S., Scacheri, P.C., Ward, J.M. et al. (2001). A mouse model of multiple endocrine neoplasia, type 1, develops multiple endocrine tumors. *Proc. Natl. Acad. Sci. U.S.A.* 98 (3): 1118–1123.

32 Paragliola, R.M., Torino, F., Papi, G. et al. (2016). Mouse models of medullary thyroid cancer and developing new targeted therapies. *Expert Opin. Drug Discovery* 11 (10): 917–919.

33 Vitale, G., Gaudenzi, G., Circelli, L. et al. (2017). Animal models of medullary thyroid cancer: state of the art and view to the future. *Endocr. Relat. Cancer* 24 (1): R1–R12.

34 Smith-Hicks, C.L., Sizer, K.C., Powers, J.F. et al. (2000). C-cell hyperplasia, pheochromocytoma and sympathoadrenal malformation in a mouse model of multiple endocrine neoplasia type 2B. *EMBO J.* 19 (4): 612–622.

35 Tischler, A.S., Powers, J.F., and Alroy, J. (2004). Animal models of pheochromocytoma. *Histol. Histopathol.* 19 (3): 883–895.

36 Payne, S.R. and Kemp, C.J. (2003). p27(Kip1) (Cdkn1b)-deficient mice are susceptible to chemical carcinogenesis and may be a useful model for carcinogen screening. *Toxicol. Pathol.* 31 (4): 355–363.

37 Lepoutre-Lussey, C., Thibault, C., Buffet, A. et al. (2016). From Nf1 to Sdhb knockout: successes and failures in the quest for animal models of pheochromocytoma. *Mol. Cell. Endocrinol.* 421: 40–48.

38 Shen, H.C., Adem, A., Ylaya, K. et al. (2009). Deciphering von Hippel–Lindau (VHL/Vhl)-associated pancreatic manifestations by inactivating Vhl in specific pancreatic cell populations. *PLoS One* 4 (4): e4897.

39 Walls, G.V. (2014). Multiple endocrine neoplasia (MEN) syndromes. *Semin. Pediatr. Surg.* 23 (2): 96–101.

40 Alrezk, R., Hannah-Shmouni, F., and Stratakis, C.A. (2017). MEN4 and CDKN1B mutations: the latest of the MEN syndromes. *Endocr. Relat. Cancer* 24 (10): T195–T208.

41 Ward, J.M. and Devor-Henneman, D.E. (2004). Mouse models of human familial cancer syndromes. *Toxicol. Pathol.* 32 (Suppl 1): 90–98.

42 Lloyd, R., Osamura, R., Kloppel, G., and Rosai, J. (eds.) (2017). *WHO Classification of Tumors of Endocrine Organs*, 4e. Lyon: International Agency for Research on Cancer (IARC).

43 Rindi, G., Klimstra, D.S., Abedi-Ardekani, B. et al. (2018). A common classification framework for neuroendocrine neoplasms: an International Agency for Research on Cancer (IARC) and World Health Organization (WHO) expert consensus proposal. *Mod. Pathol.* 31 (12): 1770–1786.

44 Mahler, J.F. and Elwell, M.R. (1999). Pituitary gland. In: *Pathology of the Mouse* (ed. R.R. Maronpot), 491–507. Vienna, IL: Cache River Press.

45 Hardisty, J.F. and Boorman, G.A. (1999). Thyroid and parathyroid glands. In: *Pathology of the Mouse* (ed. R.R. Maronpot), 537–554. Vienna, IL: Cache River Press.

46 Nyska, A. and Maronpot, R.R. (1999). Adrenal gland. In: *Pathology of the Mouse* (ed. R.R. Maronpot), 509–536. Vienna, IL: Cache River Press.

47 Boorman, G.A. and Sills, R.C. (1999). Exocrine and endocrine pancreas. In: *Pathology of the Mouse* (ed. R.R. Maronpot), 185–205. Vienna, IL: Cache River Press.

48 Capen, C.C., Karbe, E., Deschl, U. et al. (2001). Endocrine system. In: *International Classification of Rodent Tumors: The Mouse* (ed. U. Mohr), 269–322. Berlin: Springer.

49 Frith, C.H. and Ward, J.M. (1988). *Color Atlas of Neoplastic and Non-neoplastic Lesions in Aging Mice*. Elsevier. http://www.informatics.jax.org/frithbook

50 Haston, S., Manshaei, S., and Martinez-Barbera, J.P. (2018). Stem/progenitor cells in pituitary organ homeostasis and tumourigenesis. *J. Endocrinol.* 236 (1): R1–R13.

51 Ho, Y., Hu, P., Peel, M.T. et al. (2020). Single-cell transcriptomic analysis of adult mouse pituitary reveals sexual dimorphism and physiologic demand-induced cellular plasticity. *Protein Cell* 11 (8): 565–583.

52 Childs, G.V., MacNicol, A.M., and MacNicol, M.C. (2020). Molecular mechanisms of pituitary cell plasticity. *Front. Endocrinol.* 11: 656.

53 Cao, D., Ma, X., Zhang, W.J., and Xie, Z. (2017). Dissection and coronal slice preparation of developing mouse pituitary gland. *J. Visualized Exp.* 129.

54 Allaerts, W. and Vankelecom, H. (2005). History and perspectives of pituitary folliculo-stellate cell research. *Eur. J. Endocrinol.* 153 (1): 1–12.

55 Pires, M. and Tortosa, F. (2016). Update on pituitary folliculo-stellate cells. *Int. Arch. Endocrinol. Clin. Res.* 2: 006.

56 Rizzoti, K. (2015). Genetic regulation of murine pituitary development. *J. Mol. Endocrinol.* 54 (2): R55–R73.

57 Radaelli, E., Arnold, A., Papanikolaou, A. et al. (2009). Mammary tumor phenotypes in wild-type aging female FVB/N mice with pituitary prolactinomas. *Vet. Pathol.* 46 (4): 736–745.

58 Arnhold, I.J., Franca, M.M., Carvalho, L.R. et al. (2015). Role of GLI2 in hypopituitarism phenotype. *J. Mol. Endocrinol.* 54 (3): R141–R150.

59 Brachet, C., Kozhemyakina, E.A., Boros, E. et al. (2019). Truncating RAX mutations: anophthalmia, hypopituitarism, diabetes Insipidus, and cleft palate in mice and men. *J. Clin. Endocrinol. Metab.* 104 (7): 2925–2930.

60 Mete, O. and Lopes, M.B. (2017). Overview of the 2017 WHO classification of pituitary tumors. *Endocr. Pathol.* 28 (3): 228–243.

61 Lopes, M.B.S. (2017). The 2017 World Health Organization classification of tumors of the pituitary gland: a summary. *Acta Neuropathol.* 134 (4): 521–535.

62 Harvey, M., Vogel, H., Lee, E.Y. et al. (1995). Mice deficient in both p53 and Rb develop tumors primarily of endocrine origin. *Cancer Res.* 55 (5): 1146–1151.

63 Apps, J.R. and Martinez-Barbera, J.P. (2017). Genetically engineered mouse models of craniopharyngioma: an opportunity for therapy development and understanding of tumor biology. *Brain Pathol.* 27 (3): 364–369.

64 Johansson, E., Andersson, L., Ornros, J. et al. (2015). Revising the embryonic origin of thyroid C cells in mice and humans. *Development* 142 (20): 3519–3528.

65 Bianco, A.C., Anderson, G., Forrest, D. et al. (2014). American thyroid association guide to investigating thyroid hormone economy and action in rodent and cell models. *Thyroid* 24 (1): 88–168.

66 Liu, H. and Lin, F. (2015). Application of immunohistochemistry in thyroid pathology. *Arch. Pathol. Lab. Med.* 139 (1): 67–82.

67 Greco, A., Auletta, L., Orlandella, F.M. et al. (2017). Preclinical imaging for the study of mouse models of thyroid cancer. *Int. J. Mol. Sci.* 18 (12): 2731.

68 Sawicki, B. and Zabel, M. (1999). Immunocytochemical study of parafollicular (C) cells of the thyroid in some wild rodents. *Ann. Anat.* 181 (2): 173–180.

69 Hoshi, S., Hoshi, N., Okamoto, M. et al. (2009). Role of NKX2-1 in N-bis(2-hydroxypropyl)-nitrosamine-induced thyroid adenoma in mice. *Carcinogenesis* 30 (9): 1614–1619.

70 Weber, K., Ernst, R., Fankhauser, H. et al. (2009). Thyroid dysplasia in Wistar Hannover GALAS rats. *J. Toxicol. Pathol.* 22 (4): 247–254.

71 Hatakeyama, H., Takei, Y., Cruz, Y. et al. (2011). Spontaneous vacuolar degeneration of the thyroid follicular epithelium in cynomolgus monkeys. *J. Toxicol. Pathol.* 24 (4): 229–232.

72 Kokoshima, H., Doi, T., Yamada, N., and Tsuchitani, M. (2014). Proliferative lesions in thyroid follicular cells of dwarfs derived from Wistar Hannover GALAS rats. *Toxicol. Pathol.* 42 (3): 565–572.

73 Abe, M., Hayashi, S., Usuda, K. et al. (2012). Carcinogen-induced thyroid proliferative lesions in Wistar Hannover GALAS rats with thyroid dysplasia. *J. Toxicol. Pathol.* 25 (1): 11–17.

74 Cherella, C.E. and Wassner, A.J. (2017). Congenital hypothyroidism: insights into pathogenesis and treatment. *Int. J. Pediatr. Endocrinol.* 2017: 11.

75 Biesiada, E., Adams, P.M., Shanklin, D.R. et al. (1996). Biology of the congenitally hypothyroid hyt/hyt mouse. *Adv. Neuroimmunol.* 6 (4): 309–346.

76 Adkison, L.R., Taylor, S., and Beamer, W.G. (1990). Mutant gene-induced disorders of structure, function and thyroglobulin synthesis in congenital goitre (cog/cog) in mice. *J. Endocrinol.* 126 (1): 51–58.

77 Lof, C., Patyra, K., Kero, A., and Kero, J. (2018). Genetically modified mouse models to investigate thyroid development, function and growth. *Best Pract. Res. Clin. Endocrinol. Metab.* 32 (3): 241–256.

78 Mio, C., Grani, G., Durante, C., and Damante, G. (2020). Molecular defects in thyroid dysgenesis. *Clin. Genet.* 97 (1): 222–231.

79 Ferrandino, G., Kaspari, R., Reyna-Neyra, A. et al. (2017). An extremely high dietary iodide supply forestalls severe hypothyroidism in Na+/I− symporter (NIS) knockout mice. *Sci. Rep.* 7 (1): 5329.

80 Zaletel, K. and Gaberscek, S. (2011). Hashimoto's thyroiditis: from genes to the disease. *Curr. Genomics* 12 (8): 576–588.

81 Damotte, D., Colomb, E., Cailleau, C. et al. (1997). Analysis of susceptibility of NOD mice to spontaneous and experimentally induced thyroiditis. *Eur. J. Immunol.* 27 (11): 2854–2862.

82 McLachlan, S.M., Lesage, S., Collin, R. et al. (2017). Genes outside the major histocompatibility complex locus are linked to the development of thyroid autoantibodies and thyroiditis in NOD.H2h4 mice. *Endocrinology* 158 (4): 702–713.

83 McLachlan, S.M., Aliesky, H.A., Garcia, P. et al. (2018). Thyroid hemiagenesis in a thyroiditis prone mouse strain. *Eur. Thyroid J.* 7 (4): 187–192.

84 Kong, Y.-c.M. (2007). Experimental autoimmune thyroiditis in the mouse. *Curr. Protoc. Immunol.* (Supplement 78). Chapter 15:Unit 15 7.

85 Chen, K., Wei, Y., Sharp, G.C., and Braley-Mullen, H. (2001). Induction of experimental autoimmune thyroiditis in IL-12−/− mice. *J. Immunol.* 167 (3): 1720–1727.

86 Caturegli, P., Hejazi, M., Suzuki, K. et al. (2000). Hypothyroidism in transgenic mice expressing IFN-gamma in the thyroid. *Proc. Natl. Acad. Sci. U.S.A.* 97 (4): 1719–1724.

87 Kim-Saijo, M., Akamizu, T., Ikuta, K. et al. (2003). Generation of a transgenic animal model of hyperthyroid Graves' disease. *Eur. J. Immunol.* 33: 2531–2538.

88 Moshkelgosha, S., So, P.W., Diaz-Cano, S., and Banga, J.P. (2015). Preclinical models of Graves' disease and associated secondary complications. *Curr. Pharm. Des.* 21 (18): 2414–2421.

89 Rapoport, B., Aliesky, H.A., Banuelos, B. et al. (2015). A unique mouse strain that develops spontaneous, iodine-accelerated, pathogenic antibodies to the human thyrotrophin receptor. *J. Immunol.* 194 (9): 4154–4161.

90 McLachlan, S.M., Nagayama, Y., Pichurin, P.N. et al. (2007). The link between Graves' disease and Hashimoto's thyroiditis: a role for regulatory T cells. *Endocrinology* 148 (12): 5724–5733.

91 Landa, I. and Knauf, J.A. (2019). Mouse models as a tool for understanding progression in Braf(V600E)-driven thyroid cancers. *Endocrinol. Metab.* 34 (1): 11–22.

92 Suzuki, H., Willingham, M.C., and Cheng, S.Y. (2002). Mice with a mutation in the thyroid hormone receptor beta gene spontaneously develop thyroid carcinoma: a mouse model of thyroid carcinogenesis. *Thyroid* 12 (11): 963–969.

93 Saji, M., Kim, C.S., Wang, C. et al. (2020). Akt isoform-specific effects on thyroid cancer development and progression in a murine thyroid cancer model. *Sci. Rep.* 10: 18316.

94 Cranston, A.N. and Ponder, B.A. (2003). Modulation of medullary thyroid carcinoma penetrance suggests the presence of modifier genes in a RET transgenic mouse model. *Cancer Res.* 63 (16): 4777–4780.

95 Ziebold, U., Lee, E.Y., Bronson, R.T., and Lees, J.A. (2003). E2F3 loss has opposing effects on different pRB-deficient tumors, resulting in suppression of pituitary tumors but metastasis of medullary thyroid carcinomas. *Mol. Cell. Biol.* 23 (18): 6542–6552.

96 Coxon, A.B., Ward, J.M., Geradts, J. et al. (1998). RET cooperates with RB/p53 inactivation in a somatic multi-step model for murine thyroid cancer. *Oncogene* 17: 1625–1628.

97 Garfield, N. and Karaplis, A.C. (2001). Genetics and animal models of hypoparathyroidism. *Trends Endocrinol. Metab.* 12 (7): 288–294.

98 Gunther, T., Chen, Z.F., Kim, J. et al. (2000). Genetic ablation of parathyroid glands reveals another source of parathyroid hormone. *Nature* 406 (6792): 199–203.

99 Yuan, Z., Opas, E.E., Vrikshajanani, C. et al. (2014). Generation of mice encoding a conditional null allele of Gcm2. *Transgenic Res.* 23 (4): 631–641.

100 Yamada, T., Tatsumi, N., Anraku, A. et al. (2019). Gcm2 regulates the maintenance of parathyroid cells in adult mice. *PLoS One* 14 (1): e0210662.

101 Kamitani-Kawamoto, A., Hamada, M., Moriguchi, T. et al. (2011). MafB interacts with Gcm2 and regulates parathyroid hormone expression and parathyroid development. *J. Bone Miner. Res.* 26 (10): 2463–2472.

102 Miao, D., He, B., Lanske, B. et al. (2004). Skeletal abnormalities in Pth-null mice are influenced by dietary calcium. *Endocrinology* 145 (4): 2046–2053.

103 Bi, R., Fan, Y., Lauter, K. et al. (2016). Diphtheria toxin- and GFP-based mouse models of acquired hypoparathyroidism and treatment with a long-acting parathyroid hormone analog. *J. Bone Miner. Res.* 31 (5): 975–984.

104 Imanishi, Y., Hosokawa, Y., Yoshimoto, K. et al. (2001). Primary hyperparathyroidism caused by parathyroid-targeted overexpression of cyclin D1 in transgenic mice. *J. Clin. Invest.* 107 (9): 1093–1102.

105 Mallya, S.M., Gallagher, J.J., Wild, Y.K. et al. (2005). Abnormal parathyroid cell proliferation precedes biochemical abnormalities in a mouse model of primary hyperparathyroidism. *Mol. Endocrinol.* 19 (10): 2603–2609.

106 Balenga, N., Koh, J., Azimzadeh, P. et al. (2019). Parathyroid-targeted overexpression of regulator of G-protein signaling 5 (RGS5) causes hyperparathyroidism in transgenic mice. *J. Bone Miner. Res.* 34 (5): 955–963.

107 Fan, Y., Liu, W., Bi, R. et al. (2018). Interrelated role of Klotho and calcium-sensing receptor in parathyroid hormone synthesis and parathyroid hyperplasia. *Proc. Natl. Acad. Sci. U.S.A.* 115 (16): E3749–E3758.

108 Ho, C., Conner, D.A., Pollak, M.R. et al. (1995). A mouse model of human familial hypocalciuric hypercalcemia and neonatal severe hyperparathyroidism. *Nat. Genet.* 11 (4): 389–394.

109 Howles, S.A., Hannan, F.M., Gorvin, C.M. et al. (2017). Cinacalcet corrects hypercalcemia in mice with an inactivating Galpha11 mutation. *JCI Insight* 2 (20): e96540.

110 Gorvin, C.M., Rogers, A., Stewart, M. et al. (2017). *N*-ethyl-*N*-nitrosourea-induced adaptor protein 2 sigma subunit 1 (Ap2s1) mutations establish Ap2s1 loss-of-function mice. *JBMR Plus* 1 (1): 3–15.

111 Hannan, F., Stokes, V., Gorvin, C. et al. (2019). Mice harboring a germline heterozygous AP2S1 mutation, Arg15Leu, are a model for familial hypocalciuric hypercalcemia type 3 (FHH3). *J. Endocr. Soc.* 3:MON-539.

112 Huang, C.C. and Kang, Y. (2019). The transient cortical zone in the adrenal gland: the mystery of the adrenal X-zone. *J. Endocrinol.* 241 (1): R51–R63.

113 Everds, N.E., Snyder, P.W., Bailey, K.L. et al. (2013). Interpreting stress responses during routine toxicity studies: a review of the biology, impact, and assessment. *Toxicol. Pathol.* 41 (4): 560–614.

114 Lezak, K.R., Missig, G., and Carlezon, W.A. Jr. (2017). Behavioral methods to study anxiety in rodents. *Dialogues Clin. Neurosci.* 19 (2): 181–191.

115 Touma, C., Sachser, N., Mostl, E., and Palme, R. (2003). Effects of sex and time of day on metabolism and excretion of corticosterone in urine and feces of mice. *Gen. Comp. Endocrinol.* 130 (3): 267–278.

116 Rowland, N.E. and Toth, L.A. (2019). Analytic and interpretational pitfalls to measuring fecal corticosterone metabolites in laboratory rats and mice. *Comp. Med.* 69 (5): 337–349.

117 Smith, E.A., Schwartz, A.L., and Lucot, J.B. (2013). Measurement of urinary catecholamines in small samples for mice. *J. Pharmacol. Toxicol. Methods* 67 (1): 45–49.

118 Bielinska, M., Parviainen, H., Porter-Tinge, S.B. et al. (2003). Mouse strain susceptibility to gonadectomy-induced adrenocortical tumor formation correlates with the expression of GATA-4 and luteinizing hormone receptor. *Endocrinology* 144 (9): 4123–4133.

119 Tischler, A.S., Sheldon, W., and Gray, R. (1996). Immunohistochemical and morphological characterization of spontaneously occurring pheochromocytomas in the aging mouse. *Vet. Pathol.* 33 (5): 512–520.

120 Petterino, C., Naylor, S., Mukaratirwa, S., and Bradley, A. (2015). Adrenal gland background findings in CD-1 (Crl:CD-1(ICR)BR) mice from 104-week carcinogenicity studies. *Toxicol. Pathol.* 43 (6): 816–824.

121 Sundberg, J.P., Berndt, A., Sundberg, B.A. et al. (2016). Approaches to investigating complex genetic traits in a large-scale inbred mouse aging study. *Vet. Pathol.* 53 (2): 456–467.

122 Penny, M.K., Finco, I., and Hammer, G.D. (2017). Cell signaling pathways in the adrenal cortex: links to stem/progenitor biology and neoplasia. *Mol. Cell. Endocrinol.* 445: 42–54.

123 Steenblock, C., Rubin de Celis, M.F., Delgadillo Silva, L.F. et al. (2018). Isolation and characterization of adrenocortical progenitors involved in the adaptation to stress. *Proc. Natl. Acad. Sci. U.S.A.* 115 (51): 12997–13002.

124 Maharaj, A., Maudhoo, A., Chan, L.F. et al. (2019). Isolated glucocorticoid deficiency: genetic causes and animal models. *J. Steroid Biochem. Mol. Biol.* 189: 73–80.

125 Caron, K.M., Soo, S.C., Wetsel, W.C. et al. (1997). Targeted disruption of the mouse gene encoding steroidogenic acute regulatory protein provides insights into congenital lipoid adrenal hyperplasia. *Proc. Natl. Acad. Sci. U.S.A.* 94 (21): 11540–11545.

126 Scheys, J.O., Heaton, J.H., and Hammer, G.D. (2011). Evidence of adrenal failure in aging Dax1-deficient mice. *Endocrinology* 152 (9): 3430–3439.

127 Devoss, J.J., Shum, A.K., Johannes, K.P. et al. (2008). Effector mechanisms of the autoimmune syndrome in the murine model of autoimmune polyglandular syndrome type 1. *J. Immunol.* 181 (6): 4072–4079.

128 Aragao-Santiago, L., Gomez-Sanchez, C.E., Mulatero, P. et al. (2017). Mouse models of primary aldosteronism: from physiology to pathophysiology. *Endocrinology* 158 (12): 4129–4138.

129 Berthon, A., Faucz, F.R., Espiard, S. et al. (2017). Age-dependent effects of Armc5 haploinsufficiency on adrenocortical function. *Hum. Mol. Genet.* 26 (18): 3495–3507.

130 Alrezk, R., Suarez, A., Tena, I., and Pacak, K. (2018). Update of pheochromocytoma syndromes: genetics, biochemical evaluation, and imaging. *Front. Endocrinol.* 9: 515.

131 Ornell, K.J. and Coburn, J.M. (2019). Developing preclinical models of neuroblastoma: driving therapeutic testing. *BMC Biomed. Eng.* 1: 33.

132 Kamili, A., Atkinson, C., Trahair, T.N., and Fletcher, J.I. (2020). Mouse models of high-risk neuroblastoma. *Cancer Metastasis Rev.* 39 (1): 261–274.

133 Kim, A., Miller, K., Jo, J. et al. (2009). Islet architecture: a comparative study. *Islets* 1 (2): 129–136.

134 Steiner, D.J., Kim, A., Miller, K., and Hara, M. (2010). Pancreatic islet plasticity: interspecies comparison of islet architecture and composition. *Islets* 2 (3): 135–145.

135 Mezza, T., Cinti, F., Cefalo, C.M.A. et al. (2019). Beta-cell fate in human insulin resistance and type 2 diabetes: a perspective on islet plasticity. *Diabetes* 68 (6): 1121–1129.

136 Veite-Schmahl, M.J., Regan, D.P., Rivers, A.C. et al. (2017). Dissection of the mouse pancreas for histological analysis and metabolic profiling. *J. Visualized Exp.* 126.

137 Ruehl-Fehlert, C., Kittel, B., Morawietz, G. et al. (2003). Revised guides for organ sampling and trimming in rats and mice – part 1. *Exp. Toxicol. Pathol.* 55 (2–3): 91–106.

138 Baskin, D.G. (2015). A historical perspective on the identification of cell types in pancreatic islets of Langerhans by staining and histochemical techniques. *J. Histochem. Cytochem.* 63 (8): 543–558.

139 Lee, H.Y., Jeong, K.H., Choi, C.S., and International Mouse Phenotyping Consortium (2014). In-depth metabolic phenotyping of genetically engineered mouse models in obesity and diabetes. *Mamm. Genome* 25 (9–10): 508–521.

140 Kleinert, M., Clemmensen, C., Hofmann, S.M. et al. (2018). Animal models of obesity and diabetes mellitus. *Nat. Rev. Endocrinol.* 14 (3): 140–162.

141 Carter, J.D., Dula, S.B., Corbin, K.L. et al. (2009). A practical guide to rodent islet isolation and assessment. *Biol. Proced. Online* 11: 3–31.

142 King, A.J. (2012). The use of animal models in diabetes research. *Br. J. Pharmacol.* 166 (3): 877–894.

143 Chatzigeorgiou, A., Halapas, A., Kalafatakis, K., and Kamper, E. (2009). The use of animal models in the study of diabetes mellitus. *in vivo* 23 (2): 245–258.

144 Adorini, L., Gregori, S., and Harrison, L.C. (2002). Understanding autoimmune diabetes: insights from mouse models. *Trends Mol. Med.* 8 (1): 31–38.

145 Matveyenko, A.V. and Butler, P.C. (2006). Islet amyloid polypeptide (IAPP) transgenic rodents as models for type 2 diabetes. *ILAR J.* 47 (3): 225–233.

146 Kobayashi, S., Contractor, T., Vosburgh, E. et al. (2019). Alleles of Insm1 determine whether RIP1-Tag2 mice produce insulinomas or nonfunctioning pancreatic neuroendocrine tumors. *Oncogenesis* 8 (3): 16.

147 Rindi, G., Efrat, S., Ghatei, M.A. et al. (1991). Glucagonomas of transgenic mice express a wide range of general neuroendocrine markers and bioactive peptides. *Virchows Arch A Pathol. Anat. Histopathol.* 419 (2): 115–129.

148 Fielitz, K., Althoff, K., De Preter, K. et al. (2016). Characterization of pancreatic glucagon-producing tumors and pituitary gland tumors in transgenic mice overexpressing MYCN in hGFAP-positive cells. *Oncotarget* 7 (46): 74415–74426.

149 Kennaway, D.J. (2019). Melatonin research in mice: a review. *Chronobiol. Int.* 36 (9): 1167–1183.

150 Gomez-Corvera, A., Cerrillo, I., Molinero, P. et al. (2009). Evidence of immune system melatonin production by two pineal melatonin deficient mice, C57BL/6 and Swiss strains. *J. Pineal Res.* 47 (1): 15–22.

151 Son, J.H., Chung, J.H., Huh, S.O. et al. (1996). Immortalization of neuroendocrine pinealocytes from transgenic mice by targeted tumorigenesis using the tryptophan hydroxylase promoter. *Mol. Brain Res.* 37 (1–2): 32–40.

152 Gotz, W., Theuring, F., Schachenmayr, W., and Korf, H.W. (1992). Midline brain tumors in MSV-SV 40-transgenic mice originate from the pineal organ. *Acta Neuropathol.* 83 (3): 308–314.

18

Kidney and Urinary Bladder

Jeffrey B. Kopp, Avi Z. Rosenberg, Cory F. Brayton, Jeffrey I. Everitt, and Jerrold M. Ward

Introduction

Diseases of the human urinary system include congenital defects of kidney and lower urinary tract, cystic kidney diseases, renal parenchymal diseases affecting glomeruli, vasculature, tubules, or interstitium, renal stones, obstructive disorders, and tumors. These disorders are caused by genetic, infectious, toxic, hemodynamic, and other mechanisms. Mice have been used to model these diseases in order to study mechanisms of disease and to develop methods of therapy and prevention strategies. This chapter reviews the mouse kidney and lower urinary tract as models for human diseases.

Mouse Kidney Development, Anatomy, and Histology

Each adult human kidney weighs about 150 g, which for a 80 kg adult is about 0.02% of body weight. By contrast, depending on strain, each adult mouse kidney weight is 360–700 mg, which for a 30 g mouse is 1.2–2.3% of body weight. Each human kidney medulla has 10–18 conical subdivisions, with the broad part facing the cortex and the tip (papilla) entering the renal pelvis compared with the single papilla of the mouse kidney (Figure 18.1). The renal cortex occupies the outer portion of the kidney (cortical labyrinth, containing glomeruli and proximal, and distal tubules, both convoluted, i.e. twisting and turning) with medullary extensions called the medullary rays (consisting of straight tubular segments). The medulla is composed of three parts: the outer medulla, with outer stripe and inner stripe, and the inner medulla, composed of a single papilla. The general anatomy, histology, and imaging of the mouse kidney have been well described [1–3].

Embryologically, the nephron (composed of glomerulus, proximal tubule, and distal tubule) arises from the metanephrogenetic blastema and the collecting tubule arises from the ureteric bud. During fetal development, one nephron and one ureteric bud are connected by a connecting tubule to form the mature nephron. The glomerulus arises when a capillary tuft pushes into a blind expansion of the proximal renal tubule (Bowman space, surrounded by Bowman capsule).

Each mature mouse kidney contains approximately 2000 nephrons; Murawski and colleagues reported an average of 2060 nephrons in C57BL/6 mice and 2243 in C3H/HeJ mice [4]. Juxtamedullary glomeruli are larger than more superficially located glomeruli. Most of the cortex is occupied by proximal tubular segments, together with glomeruli, blood vessels, and nerves. The lengths of the loops of Henle differ in a systematic fashion, with superficial nephrons having longer loops compared to juxta-medullary nephrons.

Pathology of the Mouse Kidney

Many mouse strains develop spontaneous strain-specific lesions, which can be confused with outcomes or complications of particular experiments (Table 18.1) [6–10].

Among mouse strains commonly used for genetically engineered mice (GEM), renal physiologic and anatomic features may differ, but this topic has not been systematically described in the published literature. An important parameter that we should know more about is the average number of glomeruli (and thus, nephrons) in kidneys from male and female mice of different strains. Glomerular number numbers vary over a 10-fold range among humans, ranging from 210 000 to 2.7 million [11]. Low nephron endowment, either due to environment factors during fetal development, such as malnutrition, or possibly to genetic factors, and low nephron numbers are a risk for kidney disease adulthood. Similar data for range of mouse strains used in laboratory research is not readily available. See further discussion below under morphologic evaluation.

Pathology of Genetically Engineered and Other Mutant Mice, First Edition. Edited by John P. Sundberg, Peter Vogel, and Jerrold M. Ward.
© 2022 John Wiley & Sons, Inc. Published 2022 by John Wiley & Sons, Inc.

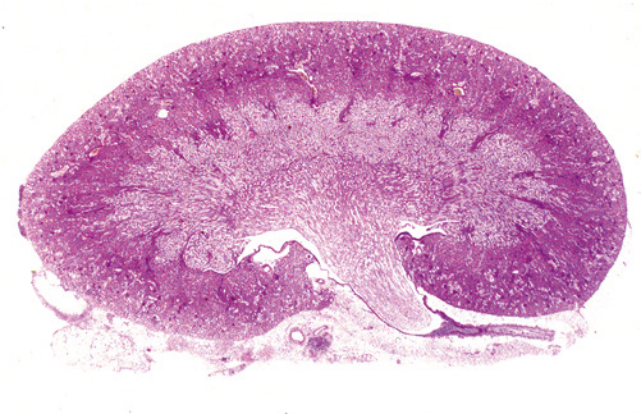


Figure 18.1 **Normal kidney**. Longitudinal section shows cortex, medulla, papillae, and pelvis.

Mouse strains differ in their propensity to develop fibrosis in response to injury stimuli, which has particular relevance for investigators interested in studying mechanisms, prevention, and treatment of fibrosis (Table 18.2); data are abstracted from the references cited above and based on the unpublished experience of the current authors. A systematic review has been published recently on strain differences in susceptibility to fibrosis [12]. Laouari et al. carried out backcrosses between fibrosis-sensitive and fibrosis-resistant strains and reported that the susceptibility of FVB/N mice was due to genetic variation that resulted in increased expression of transforming growth factor-α [13]. The genetic bases for these differences are not well understood, and this is a fruitful area for future research, given the power of whole genome approaches and the availability of inbred strains.

Characterization of Kidney Disease Phenotypes in Mice: Clinical Pathology

Kidney disease may be anticipated in some mouse lines because the transgene was generated in order to drive renal expression and renal injury. In other cases, mice from a particular line many develop kidney disease, as suggested by physical appearance, weight loss, behavior, clinical laboratory testing, and renal histopathology. In some mice with substantial proteinuria, a generalized puffiness is noted, although pitting edema is not usually present in mice but may occur in some cases. With the onset of uremia, mice may exhibit a hunched posture and manifest reduced food intake. At this point in disease progression, it is usually necessary to euthanize mice to reduce further animal suffering.

When kidney disease is anticipated, regular screening for proteinuria should be undertaken, perhaps every week or two weeks, depending on the pace of the kidney disease evolution. In humans, urinalysis dipsticks can measure multiple urinary parameters (if sufficient urine is available), in a semiquantitative fashion, including specific gravity, pH, and a semiquantitative concentration of blood, leukocytes,

Table 18.1 Examples of strain-specific lesions and phenotypes of the renal and excretory systems.[a]

Strain	Phenotype
129S2/SvPasCrl	Cystinuria, renal calculi
A/J	• Primary age-associated amyloid, due to *Apoa2c* (susceptibility) allele, and secondary SAA amyloid deposition Higuchi et al. (1991); may present as amyloid deposition in and necrosis of papilla, with cortex atrophy, loss • Strain is susceptible to urethane-induced glomerulonephritis • Males are susceptible to chloroform nephrosis
BALB/c, C3H, DBA/2	Considered resistant to amyloid (primary and secondary)
C57BL/6	B6 mice develop primary and secondary amyloid; associated with amyloid in other tissues, and chronic infection; involves glomeruli, sometimes interstitium, resistant to chloroform nephrosis
DBA/1, DBA/2	Giant lysosomes in proximal tubules
FVB/N	More susceptible to fibrosis, X C57BL/6 more resistant
129S1, C3H/HeJ, DBA/2J, KK/1J	*Abcc6* mutation associated with ectopic mineralization and renal tubule mineralization that can be severe
A/J, C3H, DBA, HR males	More tubular toxicity with chloroform compared to C57BL/6.
MRL/MpJ-*Fas*^{lpr}/J C3H/HeJ-*Fasl*^{gld}/J	Spontaneous mutations in in *Fas* and *Fasl*, respectively, result in lupus type nephritis and lymphoproliferative disease
NZBWF1/J	Glomerulonephritis

[a] Shown are strain-specific histologic lesions and pharmacologic sensitivities characteristic of the selected mouse strains. Source: Based on [5] and general sources.

Table 18.2 Common laboratory mouse strains: degree of susceptibility to experimentally induced fibrosis.[a]

Mouse strain	Pulmonary fibrosis	Cardiac fibrosis	Liver fibrosis	Renal fibrosis
BALB/c	Resistant	ND	Variable	Resistant
C57BL/6	Susceptible	Resistant	Variable	Resistant
C57BL/6J	Susceptible	ND	Variable	Susceptible
C3H	ND	ND	ND	Resistant
CD1	ND	ND	ND	Susceptible
FVB/NJ	ND	ND	Resistant	Susceptible
FVB/N	ND	ND	ND	Susceptible
129Sv	ND	ND	ND	Resistant
129S3	ND	ND	ND	Susceptible
129S1/SvJM	ND	ND	ND	Susceptible
ROP/GnLeJ	ND	ND	ND	Susceptible

[a] Data abstracted from the references cited above and based on the unpublished experience of the current authors.

nitrite, glucose, ketones (acetoacetate), bilirubin, urobilinogen, and protein. Full utilization of the strip requires more urine than can be obtained from a mouse. A convenient way to do this is to lift a mouse gently from the cage and place it on a piece of flexible film (e.g. Parafilm, Bemis, Veena, WI), on which the mouse may void spontaneously or after gentle stroking of the abdomen toward the bladder (Credé maneuver). The urine can then be transferred with a pipette to the analytic chips on a urine dipstick to obtain a semiquantitative measurement of albumin, protein, or glucose. If a laboratory can be found that works with limited volumes (<200 µl), urine from one or more voided urine samples, when pooled, may be sufficient to submit to a chemistry laboratory for measurement of urine total protein and/or albumin, and urine creatinine. If a more accurate determination of urine specific gravity is needed, urine can be transferred with a pipette to a refractometer.

Another approach is to use a specialized cage for a timed urine collection, typically for 24 hours, although shorter periods could also be used. The urine may be collected under light vegetable oil to minimize bacterial growth during the collection period, if contamination might comprise determination of an analyte of interest, such as glucose. Various analytes can be measured on this sample, including electrolytes (e.g. sodium, potassium, chloride, calcium, phosphate, protein, and albumin). By contrast, urinary bicarbonate is more labile, reaching equilibrium with atmospheric CO_2 and therefore some will be lost from the sample, unless vegetable oil is layered on to prevent CO_2 escape. Measuring urine creatinine is important, particularly for a random sample, where it can be used as a denominator (e.g. sodium/creatinine ratio) to adjust for differences in urine concentration between samples. The underlying principle is that generation of creatinine, and therefore its appearance in urine, is based on muscle mass and should be very similar in a given mouse from day; similarly, the amount of creatinine generated should be similar between mice, although differences in muscle mass can make comparisons between mice slightly less accurate.

If a kidney disease phenotype emerges at a relatively late age, or the age of onset is variable between mice, it may be desirable to induce glomerular damage by one or multiple interventions. Such interventions may include the following, as single elements or as combinations: saline solutions in place of drinking water (e.g. 0.9% or 0.45% sodium chloride for drinking), angiotensin II (administered by subcutaneous injection), uninephrectomy, and deoxycorticosterone acetate slow-release pellet (implanted subcutaneous). These four manipulations induce hypertension and reduce renal mass, both contributing factors to kidney disease. The full set of interventions (abbreviated as SAND) may be required to induce hypertensive glomerular injury in some strains. Lesser degrees of injury may be achieved with AND or ½ SAND (including 0.45% saline) or other subsets of these four interventions.

Glomerular proteinuria involves nonselective loss of plasma proteins into urine and so the urine albumin/total protein ratio is similar to that of plasma (approximately 0.4 g/g). With isolated tubular dysfunction, low molecular weight proteins (e.g. those <20–30 kDa) that are normally filtered through the glomerulus and reabsorbed into the circulation by the proximal tubule, are instead retained within the tubular lumen and excreted in the urine. Therefore, *tubular proteinuria* is typically characterized by a urine albumin/total protein ratio of <0.2 g/g. This difference in albuminuria vs. low molecular weight proteinuria can be readily seen on a Coomassie-stained gel.

A variety of analytes can be measured in serum or plasma and in urine that together provide information about glomerular function, tubular function, extracellular volume status, and calcium-phosphate homeostasis (the latter usually disturbed with advanced chronic kidney disease

Table 18.3 Clinical chemistry testing in evaluation of mice for kidney disease.[a]

Serum or plasma analyte	Comment	Urine analyte	Collection	Comment
Sodium	Reduced in water excess Increased in water deficit	Albumin/ creatinine ratio	Random or timed	Detect and monitor glomerular proteinuria
Chloride	Similar to sodium	Protein/ creatinine ratio	Random or timed	Detect and monitor all proteinuria
Potassium	Often elevated due to red cell or tissue injury while drawing blood	Albumin/ protein ratio	Random or timed	Tubular proteinuria tends to albumin/ protein ratio <0.4 g/g
Bicarbonate	Not reliable unless collection tube is sealed from air until assay, as CO_2 will diffuse out	Sodium/ creatinine Chloride/ creatinine	Random or timed	Reflect dietary intake, ECV status and tubular function
Creatinine	Less sensitive to reduced GFR in mice compared to humans	Sodium, chloride	Random or timed	As above
Cystatin C (CST3)	An alternative approach to assess GFR			
Kidney injury marker-1 (KIM1, HAVCR1)	Proximal tubular cell injury marker, and in urine			
Calcium	Falls in advanced CKD, due to reduced renal 1, 25-OH vitamin D production			
Phosphate	Elevated with CKD, due to decreased excretion			
Parathyroid hormone (PTH)	Parathyroid hormone 1–84 (intact) PTH is elevated in hyperparathyroidism, both primary and secondary; ELISA kits are available			
Vitamin D	1, 25, and 25-OH mouse vitamin D ELISA kits are available			

[a] Shown are analytes measured in serum or plasma and in urine, that together provide information about glomerular function, tubular function, extracellular volume status, and calcium-phosphate homeostasis (the latter usually disturbed with advanced chronic kidney disease). Unlike in humans, there are no nomograms that allow the investigator to estimate GFR from serum creatinine or cystatin C, especially given interstrain differences. Urine collections can be of random duration or can be timed (e.g. 8 or 24 hours).

(Table 18.3)). Unlike in humans, there are no nomograms that allow the investigator to estimate GFR from serum creatinine or cystatin C, especially given interstrain differences. Urine collections can be of random duration or can be timed (e.g. 8 or 24 hours).

Glomerular Numbers

Inspection of pathology slides from a new mouse model may suggest a paucity of glomeruli, or the mouse model may have been developed with the intention of reducing glomerular numbers, to study the effects of glomerular hyperfiltration or chronic kidney disease. Methods to estimate glomerular numbers include two approaches. First, the magnetic resonance imaging (MRI) approach uses particles that are injected intravenously and are trapped in the glomeruli, facilitating visualization of glomeruli [14]. Second, the physical dissector fractionator method is a histopathologic approach that involves removing precisely measured portions of the cortex, counting the glomeruli in those portions, and extrapolating to estimate the total glomerular numbers [15] (Table 18.5).

Preparation of Kidneys for the Histopathology

Many histologic and molecular studies can be performed on mouse kidneys, providing diverse types of information. While mice may be perfused with a fixative, most studies use immersion fixation. Especially if following this latter methodology, kidneys should be harvested, with minimal delay, after death. The prosector must avoid artifact when dissecting, as the kidney is particularly prone to compression artifacts. This is accomplished by gentle handling with

proper forceps technique and cutting using clean, sharp blades in a single motion. Every effort should be made to avoid desiccation artifact and osmotic injury by proper handling at necropsy. Tissue can be preserved for different microscopic purposes and analytical molecular techniques. One strategy used by some investigators is to fix one kidney in neutral buffered formalin or comparable fixative appropriate for routine light microscopy and to cut the second kidney sagittally ("bivalved") for (i) microscopic purposes not compatible with formalin fixation and (ii) downstream bioanalyte analysis. For example, one half kidney is placed in optimal cutting temperature (OCT, Sekura, Torrance, CA) compound on dry ice and stored at −80 °C for subsequent immunofluorescence staining, a minute piece ($1\,mm^3$) can be saved in glutaraldehyde for ultrastructural techniques, and the remainder snap frozen for molecular studies (e.g. genomic, transcriptomic, or proteomic analysis).

For routine examination of the kidney, fixation in 10% neutral buffered formalin or 4% paraformaldehyde followed by paraffin embedding is standard. Additional fixatives may be chosen depending on the epitope of interest when conducting immunohistochemistry. In all instances proper handling and conditions of fixation are required, with attention to adequate fixative volume, time, and temperature of fixation, and postfixation handling to prevent over-fixation and under-fixation of renal specimens. In most studies, mouse renal tissues are fixed for up to 48 hours and then trimmed (cross and longitudinal sections), processed, and embedded in paraffin allowing for the examination of cortex, outer medulla, and inner medulla, including the renal papilla (Figure 18.1).

Paraffin-embedded kidney sections are best cut as thinly as possible, ideally at close to 3 µm. The mouse glomerulus has a high volume-fraction of cells, appearing hypercellular when compared to the rat or human kidney, and thin sections are essential for evaluating proliferative glomerulonephritis (where increased cell numbers compared to normal may be harder to detect on thick sections). Alternatively, fixed tissue may be embedded in plastic (e.g. glycol methacrylate). This approach permits thinner sectioning at 2 µm facilitating detailed examination of renal structure, particularly with respect to the glomerulus and basement membranes in general.

Routine histologic analysis of the kidney can be made using hematoxylin and eosin (H&E) staining, and this technique is sufficient for structural assessment but is best for cytologic evaluation. Various additional histochemical stains are useful adjuncts for structural and compositional evaluation of glomeruli and tubules. Each stain has particular utility (Table 18.4). The periodic acid-Schiff stain (PAS) is particularly helpful in staining glycoprotein-rich structures such as glomerular and tubular basement membranes, mesangial matrix, and proteinaceous tubular material. In fact, some investigators rely largely on the PAS stained sections and omit the routine H&E stained sections but that omission is not recommended, as important histologic and cytologic detail may be missed. Sections individually stained or dual-stained with periodic acid and methenamine silver (PAMS) may help in visualizing basement membranes and matrix and facilitates visualization of immune deposits or hyaline which appear as a negative image contrasted with the uniform silver positivity. Masson's trichrome and picrosirius red stains for extracellular matrix proteins are also valuable in models with fibrosis. Congo red highlights amyloid deposits and is helpful in defining the pattern (glomeruli, blood vessels, and interstitium) as well as the abundance of amyloid. Special procedures including apoptosis assays, antigen staining, and *in situ* hybridization for gene expression may be valuable in some instances.

Table 18.4 Selected pathology stains and methods.

Technique	Use	Fixation	Comment
Hematoxylin and eosin stain (H&E)	General histology	Neutral buffered formaldehyde (Formalin)	Most commonly used, least expensive stain Excellent nuclear detail
Periodic acid-Schiff stain (PAS)	Glycoproteins/ Extracellular matrix	Same	
Masson's trichrome	Extracellular matrix	Same	
Silver stain	Basement membranes/ extracellular matrix	Same	Best visualized when sections are thin, e.g. 2–3 µm
Electron microscopy	Immune deposits, other deposits, basement membranes	Glutaraldehyde	Embed in methyl methacrylate Processing is expensive
Immunofluorescence	Characterizing immune deposits	None, to preserve antigenicity Quick frozen on dry ice using OCT or equivalent	Tissue frozen in OCT (optimal cutting compound) or tragacanth

Morphologic Examination

Evaluation of renal histology should include comprehensive and detailed consideration of the following aspects of four tissue compartments:

1) *Glomeruli:* Glomerular number, glomerular size, glomerular cellularity, mesangial matrix expansion, patency of capillary loops, and extracapillary epithelial proliferation (e.g. crescents within Bowman space). Male mouse kidney often has cuboidal epithelium lining Bowman capsule and it connects to the proximal tubule (Figure 18.2). Podocyte differentiation status can also be appreciated on H&E stained slides and by immunohistochemistry with a variety of antigens (Figures 18.3 and 18.4). While immunostaining can more specifically identify podocytes, when Bowman space is occupied by undifferentiated cells, they may have lost characteristic differentiated markers of podocytes or parietal epithelial cells. Metastatic tumor cells can also, rarely, be seen within glomeruli.
2) *Tubules:* Epithelial cell integrity and morphology, tubular atrophy and regenerative changes, and tubular casts.
3) *Interstitium:* Fibrosis and cellular infiltrates.
4) *Vessels:* Hypertrophy, intimal proliferation, and medial proliferation, cellular infiltrates.

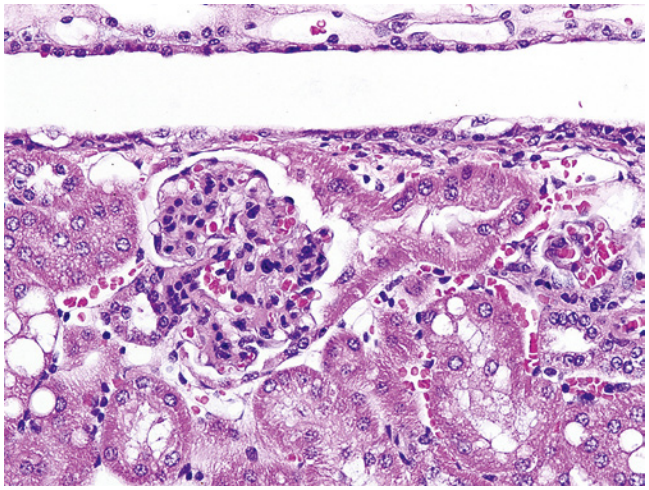


Figure 18.2 **Normal kidney**. Bowman capsule with flat or cuboidal epithelium is connected to the proximal tubule.

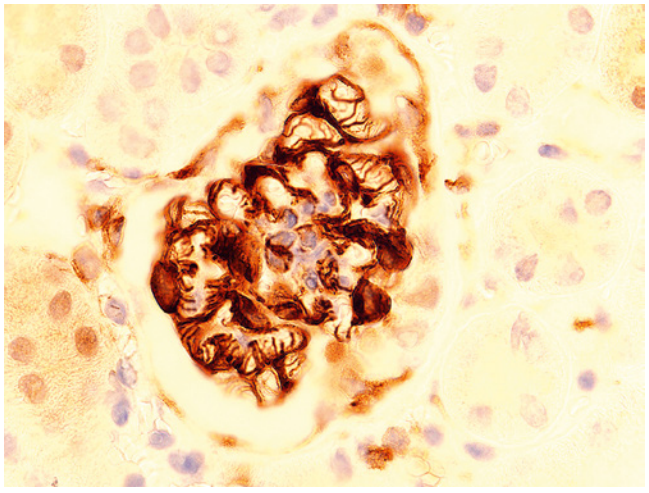


Figure 18.3 **Normal glomerulus**. Vimentin (VIM) IHC. Note foot processes of podocytes are seen.

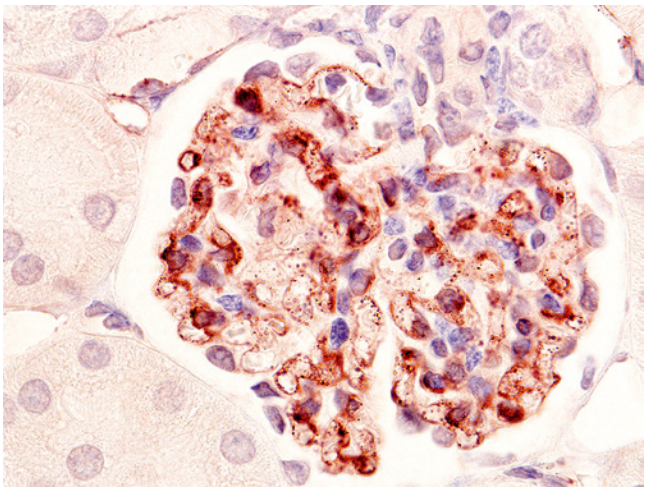


Figure 18.4 **Normal glomerulus**. Kinase insert domain protein receptor (KDR, formerly VEGFR2) IHC. Note focal punctate staining in podocytes.

Morphologic evaluation of renal structures may require ultrastructural examination for precise identification of specific lesions and immune and other acellular deposits. Tissue for transmission electron microscopy (TEM) should be fixed in freshly prepared 2.5% glutaraldehyde in either phosphate buffered saline or cacodylate buffer. Tissue specimens prepared for TEM must be small, ideally with all dimensions <2 mm. Following fixation, tissues are embedded in an appropriate plastic resin such as an epoxy resin (e.g. Epon812, Shell Chemicals, Houston, TX, or Araldite, Huntsman Advanced Materials, The Woodlands, TX) or glycol methacrylate. Thick sections (2 μm) can be stained with toluidine blue or trichrome stain, suitable for high-magnification light microscopy and particularly suitable for detailed examination of the glomeruli.

Renal structure is well suited to quantitative assessment of pathology, with regard to both light microscopy and electron microscopy. (i) Glomerulosclerosis, tubular dilatation/atrophy, and interstitial fibrosis may be assessed using a semi-quantitative scale. (ii) The number of glomerular cell nuclei may be counted. (iii) Using the light microscope and a point counting method, one can quantitate the volume of renal cortex occupied by glomeruli, tubules, interstitium, and fluid space. (iv) Light microscopic images may be digitized and the area of glomeruli or the extent of glomerulosclerosis defined as stained matrix exceeding a particular optical density threshold, may be measured. (v) Ultrastructural photographs may be subjected to direct measurement or point counting to determine glomerular basement membrane thickness or the volume density of glomerular components.

Table 18.5 Mean glomerular numbers per kidney in adult mice.[a]

Strain	Glomerular number (mean)	
C57BL/6	MRI R 14 163 L 12 449 [16]	Male mice PDI method R 13 877 L 11 180
C57BL/6	Sex not stated PDI method 28 000 [17]	Male mice PDI method 13 440 [18]
(C57BL/6 X 129Sv)	12 694 glomeruli Male mice Physical dissector/fractional method [19] [20]	
C3H/He X 101/H	18 880 glomeruli Male, female Stereology (dissector) [21]	
FVB/N	8000 glomeruli Sexes apparently pooled [19]	

MRI = magnetic resonance imaging, PDF = physical dissector fractionator method.
[a] Shown are data for glomerular numbers in adult wild-type mice from several commonly used strains; other strains have not been studied. Variation between strains may represent biological variability, although differences in experimental methods may also play a role.

Table 18.6 Major causes of nephrotic and nephritic syndromes in humans.[a]

Nephrotic	Nephritic
Primary diseases	
Minimal change disease	IgA nephropathy
Focal segmental glomerulosclerosis	Ant-GBM disease
Membranous nephropathy	
Secondary to systemic disease	
Lupus nephritis	Postinfectious, e.g. streptococcal infection
	Parainfectious, e.g. bacterial endocarditis, hepatitis B, C
	Lupus nephritis, rheumatoid arthritis, scleroderma
	ANCA associated vasculitis
	Anti-phospholipid syndrome
	Paraneoplastic syndrome
Drug induced	
NSAID	NSAID$^+$
	Cocaine, amphetamine abuse

Anti-GBM = anti-glomerular basement membrane disease, ANCA = anti-neutrophil cytoplasmic antibodies, NSAID = nonsteroidal anti-inflammatory drugs.
[a] Shown are some major causes of human nephrotic and nephritic syndromes.

In humans, glomerular numbers may be reduced in certain genetic disorders and acquired conditions, including maternal exposures (dietary deficiencies, hyperglycemia), prematurity (glomerulogenesis ceases at approximately 36 weeks of gestation), and low birth weight. Presumably most if not all of these factors would have similar effects in mice. As shown in Table 18.5, mean glomerular numbers in adult mice can vary from 8000 to 19 000 per kidney, as assessed by various means, including MRI and physical dissector/fractionator (PDI) combination method, for a detailed protocol for the latter [22]. References for the glomerular numbers are also noted in Table 18.5 [16–21].

Glomerular Diseases

Human glomerular diseases can be classified into two general categories: *primary* (affecting only the kidney) or *secondary* (associated with systemic disease). Clinically, diseases of either of these categories can present as nephrotic, nephritic, or mixed nephrotic/nephritic diseases (Table 18.6).

In humans, nephrotic syndrome manifests with a urine protein/creatinine ratio >2 g/g, scant blood cells in urine, low plasma albumin, hyperlipidemia, and peripheral edema. In *nephritic* syndrome, urinary leukocytes, and/or erythrocytes are frequently present, and the urine contains cellular casts containing either or both cell types while the urine protein/creatinine ratio can be variable.

There are many glomerular diseases that are associated with *systemic diseases*. These glomerular diseases can be nephrotic or nephritic. Associations include diabetes mellitus, chronic infection (HIV-1, hepatitis B and C, and syphilis, among others), systemic lupus, vasculitis, preeclampsia, and deposition disorders (including amyloid deposition and immunoglobulin light-chain deposition). AL amyloid refers to amyloid composed of immunoglobulin light chains and AA amyloid refers to amyloid due to deposition of plasma amyloid A protein.

There are four major forms of *primary* glomerular diseases. Three diseases present with nephrotic syndrome, or less commonly, subnephrotic proteinuria: minimal change disease (MCD), focal segmental glomerulosclerosis (FSGS), and membranous nephropathy. IgA nephropathy is primarily nephritic and is probably the most common primary glomerular disease in the world.

MCD manifests nephrotic syndrome, normal glomeruli on light microscopy, and diffuse foot process effacement on electron microscopy. Pathogenic mechanisms are poorly understood. It is sensitive to immunosuppressive therapy, and when a case of MCD is glucocorticoid-resistant, unsampled FSGS is

suspected. Various interventions in mice may mimic MCD pathology, but it is doubtful whether any recapitulate the molecular process underlying reversible podocyte injury in this disease, which indeed is not well characterized.

FSGS is perhaps the most complex of the nephrotic entities in humans. Fundamentally, FSGS is a histopathologic pattern of glomerular injury wherein segmental glomerular scarring is present in less than 50% of the glomeruli. It can present as a primary/syndromic form or more commonly is part of the evolution to chronicity of an underlying condition, such as membranous nephropathy, lupus nephritis, or systemic vasculitis.

FSGS in human patients is diagnosed when at least one glomerulus manifests segmental scarring, while other glomeruli may be normal or have progressed to global glomerulosclerosis. Immunostaining for IgM and C3 may be robust and reflect nonspecific insudation of serum proteins, though this is an area of investigation to better understand whether the presence of these reactants contribute to disease progression [23]. Electron microscopy can demonstrate variable foot process effacement with more limited segmental effacement in maladaptive and high-penetrance genetic forms of FSGS or more diffuse effacement in the setting of primary, APOL1 and virus-associated forms of FSGS [24].

FSGS can be partitioned into six syndromes, each comprising distinct entities [25]:

- Primary FSGS, likely due to a plasma factor, evidenced by recurrence following kidney transplant. Candidate molecules include serum plasminogen activator, urokinase receptor (PLAUR), and cardiotrophin-like cytokine factor 1 (CLCF1).
- Postadaptive FSGS, also known as maladaptive FSGS, due to a mismatch between increased glomerular load (associated with morbid obesity, and extreme muscular development, typically associated with androgen abuse) and glomerular capacity (associated with a nephron deficit in association with premature birth); cyanotic heart disease, reflux nephropathy, surgical kidney mass reduction, cholesterol emboli, and renal toxin exposure (e.g. heavy metals, certain medications). The underlying pathophysiology is an increased single nephron glomerular filtration that is achieved by efferent arteriolar vasoconstriction, resulting in increased glomerular capillary pressures, which also put increased stress on podocytes. In the long run, this is a maladaptive process and some have termed this maladaptive FSGS.
- *APOL1*-related FSGS due to coding variants in the gene encoding apolipoprotein L1 that are uniquely seen in individual with sub-Saharan ancestry; only a minority of individuals, perhaps 20%, with two *APOL1* risk alleles will develop kidney disease in their lifetime. The *APOL1* gene is unique to humans and certain other primates, and therefore is absent from mice.
- High-penetrance genetic FSGS caused by coding variants in >50 nuclear and mitochondrial genes.
- Viral-infection associated FSGS associated with HIV-1, cytomegalovirus (probable), and possibly Epstein–Barr, parvovirus B19, and hepatitis C virus infections. These associations are most likely mediated by high levels of circulating interferons and for which there may be some overlap with *APOL1*-related FSGS.
- Drug-associated FSGS, following the use of interferon (drives *APOL1* expression), lithium (tubular toxin), and bisphosphonates.

Therapy for FSGS depends on the particular form; for primary FSGS, immunosuppressive therapy (e.g. glucocorticoids, calcineurin inhibitors, or mycophenolate mofetil), although their benefit may be chiefly due to direct effects on restoring podocyte phenotype; for maladaptive and high-penetrance genetic FSGS, renin–angiotensin–aldosterone system antagonists plus low-dose thiazide diuretic and dietary sodium restriction; and for APOL1 FSGS, therapy based on whether the phenotype appears more similar to primary FSGS or to maladaptive FSGS.

Membranous nephropathy, the third major form of primary nephrotic syndrome, is characterized by nephrotic proteinuria and immune deposits composed of IgG and C3 along the glomerular basement membrane. The disease can be primary (occurring in isolation) or may accompany systemic disease, including systemic lupus and cancer. In primary membranous nephropathy, the major pathogenic antigens are phospholipase A2 receptor (PLA2R), thrombospondin type-1 domain-containing 7A protein (THSD7A), and most recently, neural epidermal growth factor-like protein 1 (NELL1).

Tissue Assessment of Immunologic Disease in Mouse Models

Immunologic renal disease is typically associated with the deposition of one or more immunoglobulins, sometimes in association with complement [26]. These molecules can be identified using immunofluorescence of frozen sections or by brightfield microscopy using immunohistochemistry on formalin-fixed, paraffin embedded tissue, and chromogen detection. Detection of immune reactants by immunofluorescence is routinely performed on medical kidney biopsies, as the staining protocols for using this approach are easy to use and may produce lower background staining and more precise localization as compared to chromogenic techniques, especially for multiplex assays (i.e. those involving detection of multiple antigens on one tissue section). Chromagenic detection is slightly less sensitive and may be harder to interpret. To detect IgG, IgA, and IgM, antibodies directed against the appropriate heavy chain (γ, α, and μ, respectively) are used. Immunoglobulin light chain is detected with antibodies specific for κ or λ light chain. The use of fluorescence-tagged antibodies is sensitive but requires access to a fluorescence microscope.

Since the classical and alternate complement activation cascades unite with the activation and deposition of C3 convertase, it is common to screen for complement deposition using an antibody that identifies tissue C3 and for C1q, the latter most frequently positive in lupus nephritis. The presence of extracapillary fibrinogen, particularly within Bowman space, indicates severe disruption of capillary

integrity, such as seen with florid glomerulonephritis, and is often associated with extracapillary epithelial proliferation (i.e. cellular crescents). Finally, albumin staining is performed as its normally minimal linear detection along glomerular capillary walls provides a control for the specificity of the deposition of other proteins within the glomerulus and as an index for comparing linear IgG staining, for example in the setting of anti-GBM disease.

Mouse Models of Human Glomerular Diseases

Transgenic mouse models, and to a lesser extent knockout mouse models, have been developed for a wide range of human glomerular and tubular diseases (Tables 18.7–18.9), although gaps remain with some human disease lacking a phenocopy in mouse.

MCD models shown in Table 18.7 replicate the pathologic findings in human patients, but it is unclear how well these models relate to human disease pathways, in large part because the mechanism of podocyte injury in MCD is uncertain.

As noted above, there are no validated mouse models of primary FSGS because the mechanisms remain to be defined. Some strains are more susceptible to the FSGS pattern of injury than others. For the resistant strains, higher doses of the injurious agents may be sufficient to induce sclerosing lesions, or several agents may be used in combination. In general, strain differences in susceptibility are poorly understood, and thus, this is a fertile area for further investigation. For example, in the case of doxorubicin (trade name Adriamycin), a Mendelian locus on chromosome 16 determines susceptibility to glomerular injury, although the gene has not been identified [27].

There are numerous mouse models of genetic FSGS, derived by the deletion of podocyte proteins, specifically those involved in regulating slit diaphragm integrity. Lesions may vary in type, but segmental and global glomerular lesions are seen (Figures 18.5 and 18.6). Niculovic et al. recently described a mouse deficient in sialyation, achieved by deleting CMP-sialic synthetase [28]. This is of particular interest now, as *N*-acetyl mannosamine, a precursor of sialic acid, is being developed as a novel therapy for human FSGS.

The classic animal model of membranous nephropathy (Heymann nephritis) involves immunizing rats with a tissue extract containing mouse proximal tubule brush border. This model has received renewed attention with the recognition of rare cases of anti-brush border antibodies in clinical practice. Recently, Meyer-Schwesinger and colleagues described a transgenic mouse model of membranous nephropathy, which involves transgenic expression mouse phospholipase 2A receptor (PLA2R) in mouse podocytes [29]. Perhaps not surprisingly, there was no immunologic response to this (endogenous) antigen. However, following administration of rabbit anti-mouse PLA2R antibody, the mice developed nephrotic syndrome, with antibody and complement deposition along podocyte cell membranes, although foot process effacement was not observed.

Table 18.7 Nephrotic and other proteinuric glomerular diseases modeled in transgenic mice or interventions used in mice.[a]

Disease entity	Human subtype	Mouse model
Minimal change disease	NA	None are ideal, as the mechanism is unknown Lipopolysaccharide, doxorubicin
Focal segmental glomerulosclerosis	Primary FSGS	None, as mechanism is unknown
	Postadaptive FSGS	5/6 nephrectomy SAND model: oral saline, angiotension II infusion, uninephrectomy, DOCA
	APOL1 FSGS	APOL1 transgenic mice Tg(tetO-GFP,-APOL1)#Susz TRE-APOL1-G0 Tg(tetO-GFP,-APOL1*)#Susz TRE-APOL1-G2 Tg(tetO-GFP,-APOL1*S342G*I384M)#Susz TRE-APOL1-G1
	Viral FSGS	HIV-associated nephropathy: FVB/N-Tg(HIV)26Aln/PkltJ
	High-penetrance genetic FSGS, now>50 loci	Various models
Membranous nephropathy	PLAR2R antibody+	Transgenic expression of in mouse podocytes combined with rabbit anti-murine PLA2R
Diabetic mellitus	Noninsulin dependent	Nonobese diabetic mouse (NOD/ShiLtJ)
Glomerulocystic phenotype		Endonuclease Dicer1 knock-out

[a] Shown are the mouse models of human disease which manifest primarily proteinuria, often reaching nephrotic levels. Three primary forms of human nephrotic disease: minimal change disease, focal segmental glomerulosclerosis and membranous nephropathy. Diabetic kidney disease is modeled by several transgenic lines.

Table 18.8 *Cre*-recombinase transgenic strain expression in particular kidney cells and tissue compartments.

Metanephric mesenchyme	Podocyte	Mesangial cell	Glomerular endothelial cells	Proximal tubule	Loop of Henle	Distal convoluted tubule	Collecting tubule
Foxd1	*Nphs1*	*Foxd1*	*Cdh5*^{tm9Dvst} (all endothelial cells)	*SLC34A1 (S1, S2)*	*Chd16*	*Chd16*	*Chd16*
	Nphs2						*Aqp2*
							Nek8
							Pax8

Table 18.9 Examples of mouse models of human glomerular nephritic diseases.[a]

Disease	Mouse model	Comments
IgA nephropathy	Strain DDY	High-IgA DDY substrain
	CD89 transgenic (Tg(Itgam-FCAR)83Rcmo)	
	BAFF transgenic (Tg(Tnfsf13b)1Fma)	
	β-1,4-Galactosyl transferase knockout (*B4galt1*^{tm1Yiw})	
Rapidly progressive GN	NZB X NZW (NZBWF1/J)	MPO-ANCA antibodies
	SCG/Knj	Anti-double stranded DNA
	PD-L1 (*Cd274)* knockout	More severe nephrotoxic serum nephritis
	Pdgfd mutants	More severe nephrotoxic serum nephritis
Lupus nephritis	MRL/MpJ-*Fas*^{lpr}/J	Lymphoproliferative condition may interfere with assessing glomerulonephritis phenotypes
	C3H/HeJ-*Fasl*^{gld}/J	
Post-infectious GN	Group A streptococci	Not a genetic model
Membranoproliferative GN	*Cfh-/- mutants*	

BAFF = B cell activating factor, PD-L1 = programmed death ligand L1, PDGF = platelet-derived growth factor.
[a] This is a nonexhaustive list of genetically engineered mice that spontaneously develop glomerulonephritis, some at particular ages. The ddY strain shows considerable variability in age of onset and severity; the substrains show more consistency.

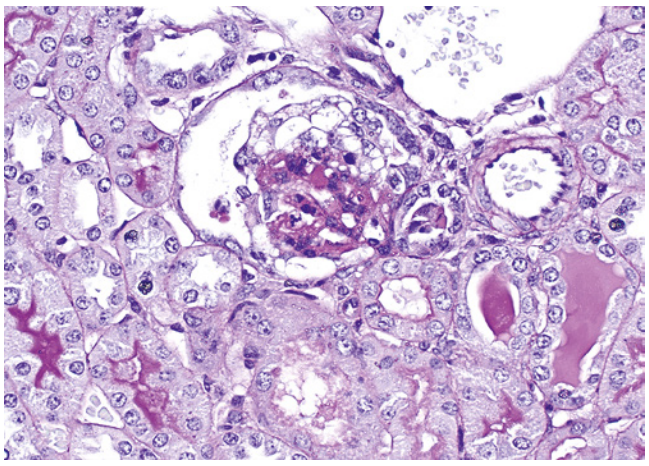


Figure 18.5 Focal segmental glomerular sclerosis (FSGS), SAND model, 36 experimental weeks. There is glomerular consolidation with prominent podocyte hypertrophy and hyperplasia with resulting podocyte cap. PAS stain.

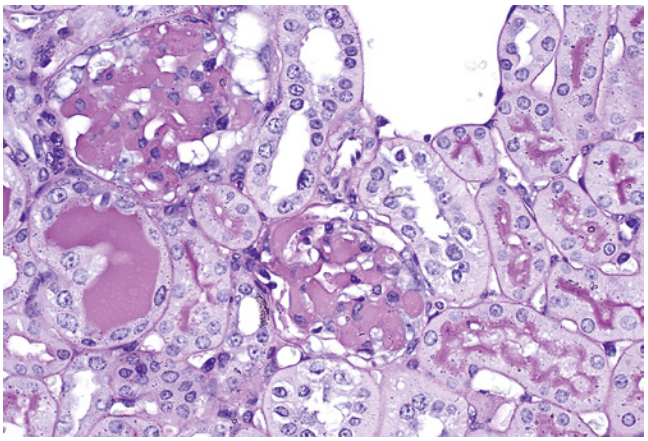


Figure 18.6 Focal segmental glomerular sclerosis (FSGS), SAND model, 36 weeks. Glomeruli show segmental consolidation with insudation of PAS-positive material consistent with hyalinosis.

Pathology and Scoring of Mouse Renal Glomerular Lesions

Classification schema have been devised for many human glomerular diseases, and these are impactful for diagnosis, therapy, and prevention. However, translation of these schema to mouse models has not been rigorously documented and evaluated for utility and reproducibility.

In veterinary pathology, standards for the diagnosis of canine glomerular disease have been well described (https://ohiostate.pressbooks.pub/vetrenalpathatlas), also to be used also for comparative glomerular clinical diagnosis and therapy [30]. The canine classification systems do have potential applications for diagnosis of mouse glomerular disease.

Mouse renal lesions represent a similar spectrum of glomerular lesions as seen in humans and dogs, but causes and prognosis are often different. In mice, diagnostic terms are simplified compared to those in human renal pathology and are used mostly to provide a mouse model for evaluating methods of therapy and prevention. Scoring methods reported vary by mouse model and pathologist [8, 31–33]. See discussion on scoring of mouse lupus models below. It is best to use what is easiest, reproducible, and applicable for the specific model and investigator to reach an endpoint. Thus, we recommend either following what is published by others or devising a custom solution for each situation. One can score for lesion extent in a tissue, severity of each lesion, and type of each lesion. For example, categories include extent of renal cortex or medulla occupied by any lesion (total organ score); and the presence of glomerular lesions including proliferative (Figure 18.7), membranous, (Figure 18.8), membranoproliferative (Figure 18.9), FSGS (Figures 18.5 and 18.6), and sclerotic patterns of injury (Figure 18.10). Most common examples of such lesions may be scored using discontinuous/ordinal semiquantitative system (0–4). One approach is to generate two scores for each tissue sample, one that estimates fraction of glomeruli with the lesion and another score that captures the severity of the lesions (which could be the most severe lesion present or other approaches). Tubular lesions often develop in later stages of glomerular disease models.

H&E stain is often generally very helpful, but some publications do not report H&E stain findings but use only PAS stain, and/or with silver stains, Masson's trichrome, immunohistochemistry, or immunofluorescence for immunoglobulins and antigens. Each may be of value in a particular model. A good general guide for evaluation of glomerular lesions is available for dogs but is applicable to mice and other species (https://ohiostate.pressbooks.pub/vetrenalpathatlas).

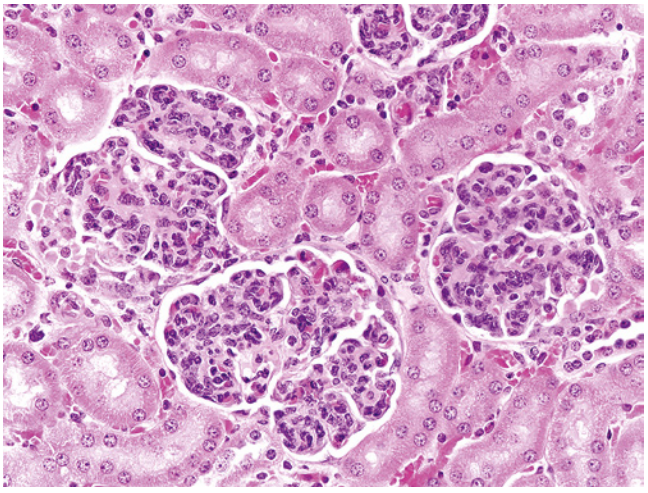


Figure 18.7 **Proliferative glomerulonephritis**. Increased cellularity of glomerulus. In a *Cyp1b1*^{tm1Gonz} mouse.

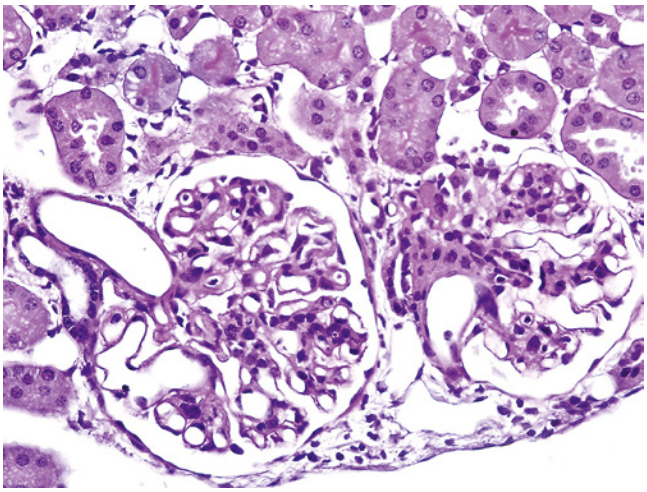


Figure 18.8 **Membranous glomerulonephritis**. Thickened glomerular capillary basement membranes. MRL/MpJ-*Fas*^{lpr}/J mouse.

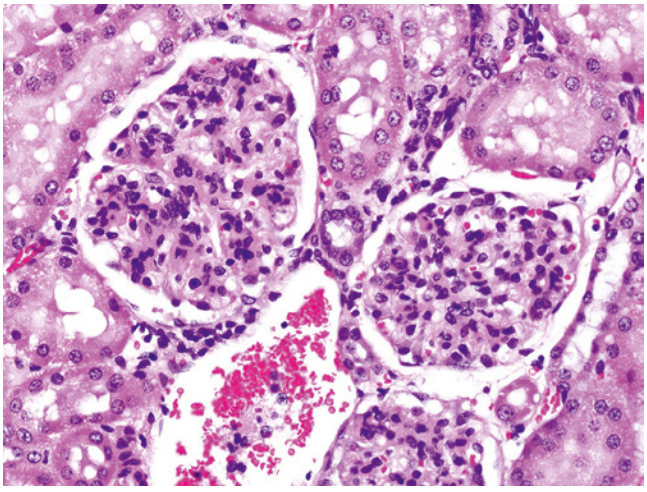


Figure 18.9 **Membranoproliferative glomerulonephritis**. Increased cellularity and thickened glomerular basement membranes, NZBWF1/J mouse, 26 weeks old.

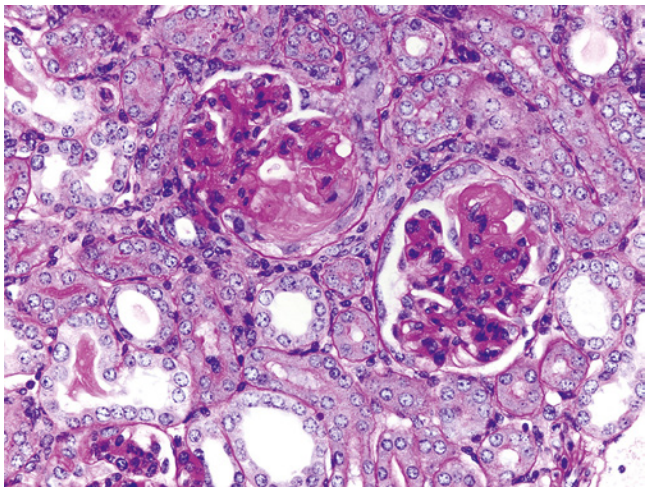


Figure 18.10 **Sclerotic glomerulus**. PAS stain shows positive material in mesangium and adhesions to capsule. NZBWF1/J mouse, 26 weeks old.

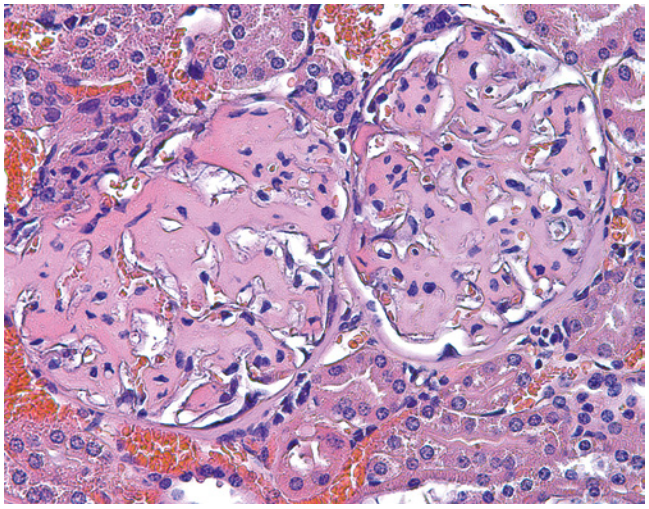


Figure 18.11 **Amyloid.** Hyaline material throughout the glomerulus, adhesions to capsule. Aged C57BL/6J mouse.

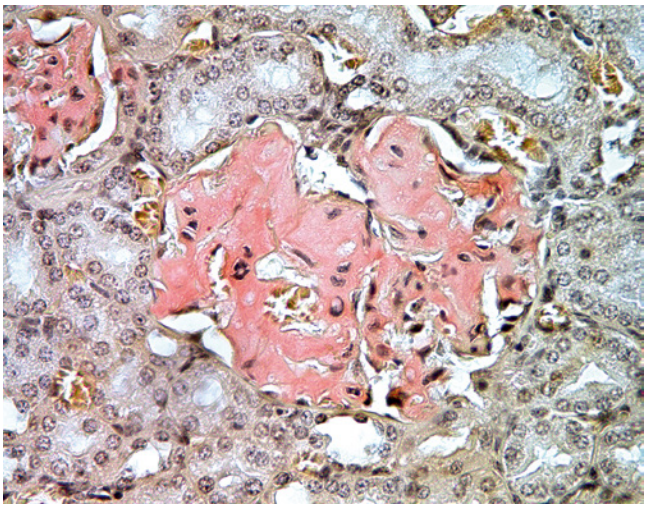


Figure 18.12 **Amyloid**. Congo Red stain reveals amyloid. Aged C57BL/6J mouse.

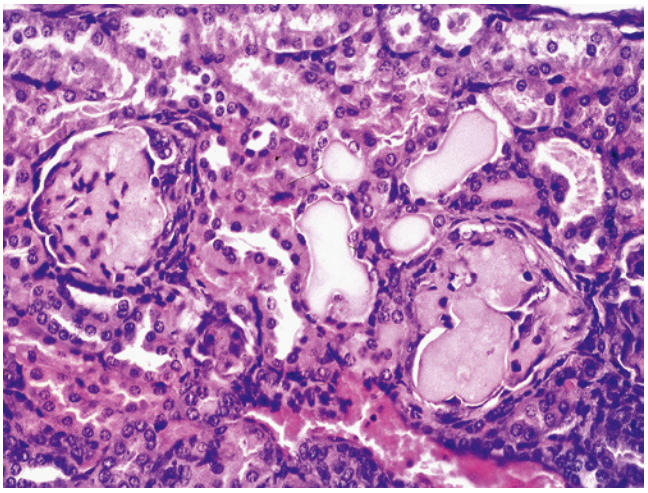


Figure 18.13 **Collagenopathy**. Note abundant eosinophilic material in glomeruli and casts in tubules. *Col1a2*^{oim} mouse.

In specific GEM and also in certain wild-type mice, deposition of eosinophilic material (hyaline or hyaline-like) be seen within the glomerulus [10]. The material deposition can be caused by interruption in normal homeostasis of excretory products through the kidney, endothelial injury, or a new protein product created in GEM. In contrast to hyaline-like material, there can be a variety of pathogenic materials deposited in the glomerulus. These include exogenous materials such as amyloid (Figures 18.11 and 18.12), aberrant extracellular matrix such as collagen deposition in osteogenesis imperfecta mice (*Col1a2*^{oim} mice) resembling human collagen Type III glomerulopathy (Figures 18.13 and 18.14), immunoglobulin complexes in a *Cyp1b1*^{tm1Gonz} null mouse (Figures 18.15) [34], fibronectin (Figure 18.16) [35], and drugs or other chemicals [8, 36]. Basophilic DNA material (Figure 18.17), generated due to tumor cell necrosis in other tissues, is seen in some cases of mouse leukemia or lymphoma, sometimes in mutant mice [37–39]. Metastases may also occur to glomeruli, especially in hematopoietic diseases (Figures 18.18 and 18.19).

Systemic Lupus Erythematosus

Systemic lupus erythematosus (SLE, lupus) syndromes occur in many species and are characterized by the production of autoantibodies to nuclear antigens, including DNA, RNA, and nucleoproteins. This causes immune complex deposition (Figure 18.20) or *in situ* formation, leading to systemic manifestations, of which kidney disease is highly prevalent. Factors promoting disease in humans include particular medications, female sex, and ethnicity.

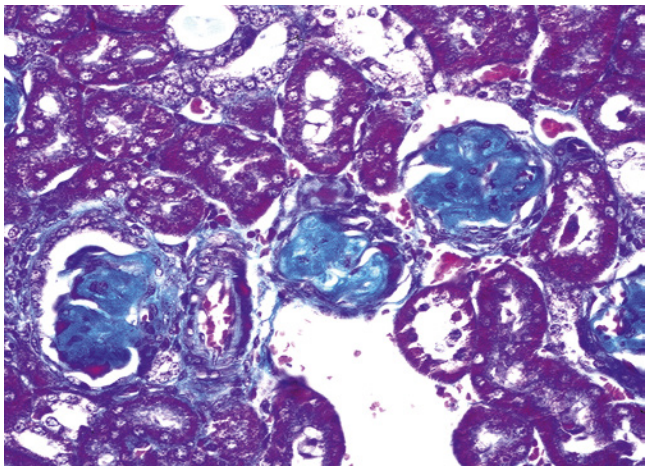


Figure 18.14 **Collagenopathy**. Note abundant collagen (blue) in glomeruli. Masson's trichrome. *Col1a2*^{oim} mouse.

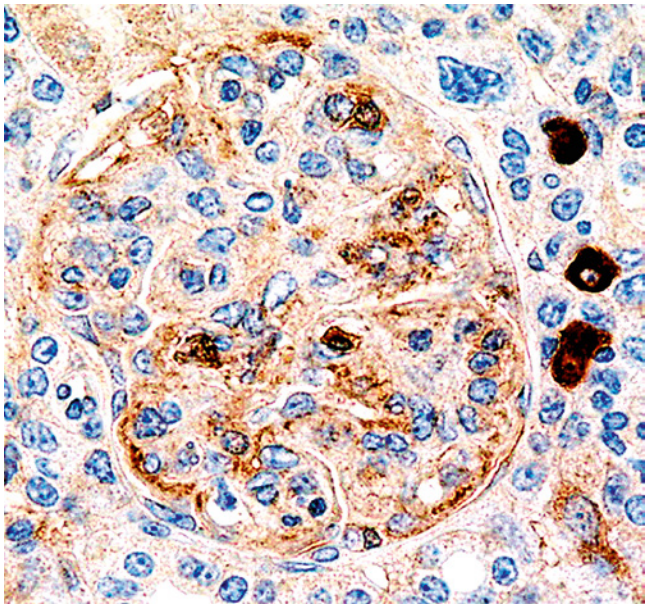


Figure 18.15 **Immune-mediated glomerulonephritis**. Human kappa light chains in glomerular basement membranes. *Cyp1b1*^{tm1Gonz} mouse. (Source: Ward et al. [34]).

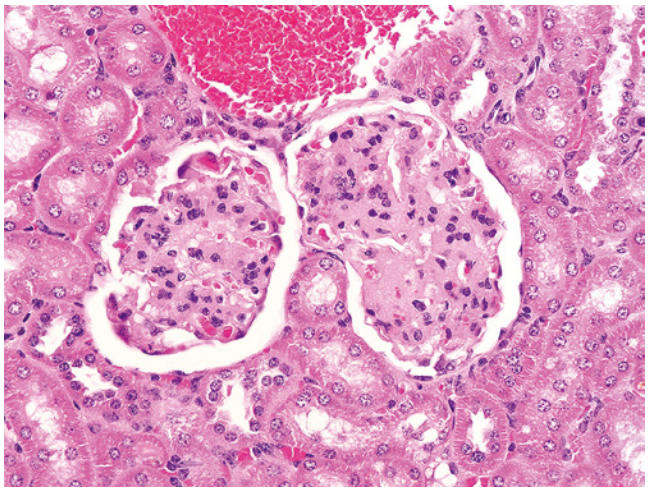


Figure 18.16 **Fibronectin glomerulopathy**. Increased focal and diffuse mesangial matrix (containing fibronectin). *Scgb1a1*^{tm1Abm} mouse.

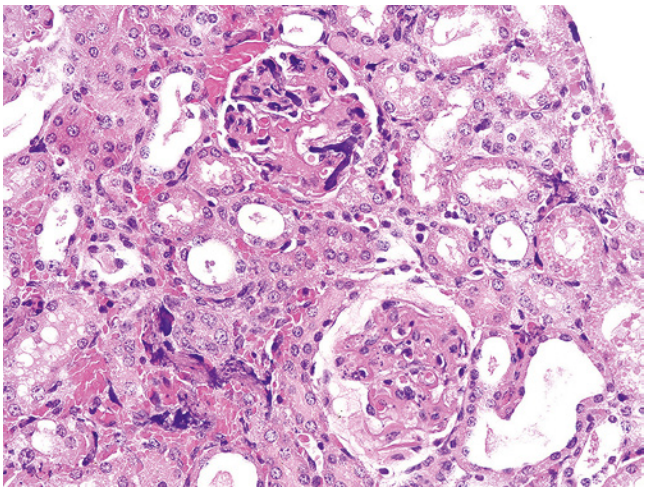


Figure 18.17 **Tumor lysis syndrome**. Blue material is DNA from a necrotic T-cell lymphoblastic lymphoma cells in other tissues. Other sclerotic glomerular lesions.

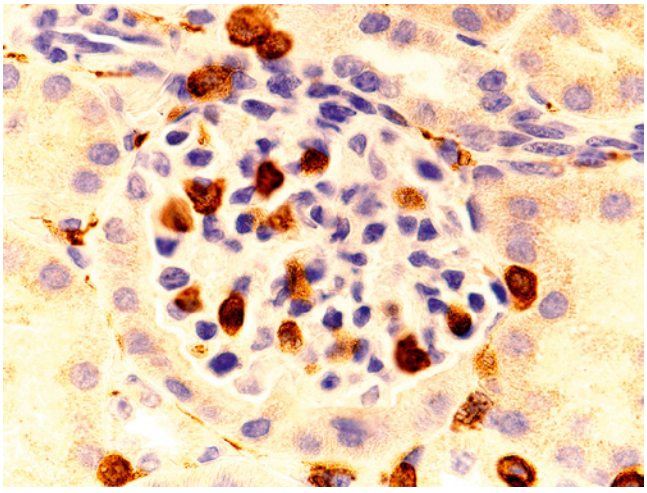


Figure 18.18 **Tumor metastases within glomerulus**. Metastatic CD3^{+} (CD3E) lymphoblastic lymphoma cells in glomerulus and in cortex.

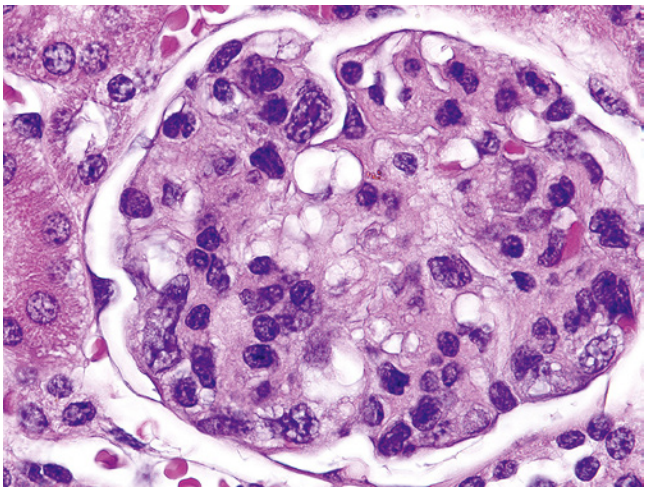


Figure 18.19 **Tumor metastases within glomerulus**. Histiocytic sarcoma cells within the glomerulus. Note large atypical nuclei.

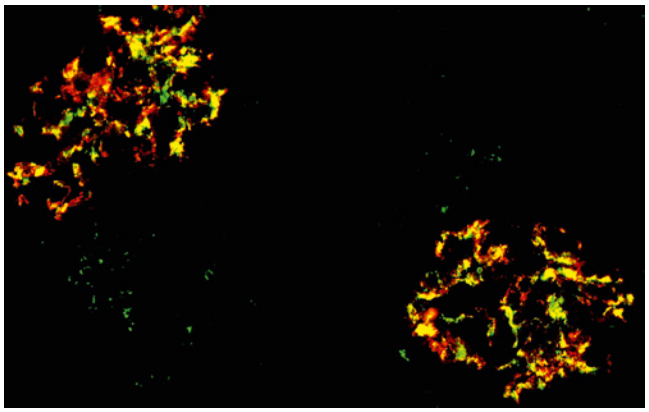


Figure 18.20 **Lupus glomerulonephritis**. IgG (green) and C3 (red) fluorescence in a MRL/MpJ-*Fas*^{lpr}/J mouse.

Mouse models have been used to study mechanisms of autoimmune disease and to evaluate potential preventive and therapeutic strategies. In reviews of the mouse models of lupus and human disease, the strengths and weaknesses of these various models have been reviewed [40–42] [43]. There are 8709 publications on lupus in mice (Pubmed accessed 31 January 2021, https://pubmed.ncbi.nlm.nih.gov/?term=lupus+mice&sort=date).

Some mouse strains, e.g. NZM2410/J, NZBWF1/J, and MRL/MpJ-*Fas*^{lpr}/J, are prone to spontaneous autoimmune kidney diseases with lupus-like features, particularly in strains prone to autoimmune disease [44]. Interventions to produce a lupus-like syndrome in susceptible mouse strains include exposure to pristane (a terpinoid alkane), resiquimod (an immune-stimulating compound), anti-glomerular basement membrane antibodies, graft versus host disease, and humanized models.

Virus-Associated Kidney Diseases

In humans, several viruses cause renal diseases, including HIV-1 (collapsing glomerulopathy, also termed HIV-associated nephropathy, and FSGS), parvovirus B-19 (mesangial proliferative glomerulonephritis, FSGS), cytomegalovirus (FSGS), and Epstein–Barr virus (crescentic glomerulonephritis, membranous nephropathy). Mouse models of nephrotic disease are summarized in Table 18.7. The most widely studied mouse model of HIV-associated nephropathy involves a transgenic mouse bearing a *gag-pol* deleted HIV genome that develops collapsing glomerulopathy [45], and other studies have examined the role of particular HIV genes, including *Vpr* [46]. Retroviruses have been implicated in mouse lupus nephritis [44, 47, 48], and retroviral complexes have been found in mouse lupus models [47].

Cell-type specific promoters, with a high degree of specificity for particular cell types include the following: metanephric mesenchyme (*Pax3, Eya1, Foxd1*), podocyte (*Nphs1*, *Nhps2, Foxd1*), all endothelial cells, as there is not yet a renal endothelial-cell specific knockout approach (*Cdh5* (formerly VEcad), *Icam2*), proximal tubule (*Kap*, male mice), loop of Henle/distal tubule/collecting duct (*Cdh16)*, principal cells of collecting ducts (*Aqp2*, *Hsd11b2*), type A intercalated cell of the collecting duct (*Aqp6),* and type B intercalated cells of the collecting duct (*Slc26a4, Insrr*).

Renal Tubular Disease

Pathologic conditions of human and mouse renal tubules occur not only from many causes, especially aging, toxins, and infectious disease, but also from genetic causes. Spontaneous tubular lesions of mice will be discussed later (Table 18.10), and genetic disorders of humans and mice are discussed next (Tables 18.11 and 18.12).

Human Genetic Disorders of Tubules

Human genetic disorders of the renal tubule are uncommon, with the major exception being autosomal dominant polycystic kidney disease (due to variants in *ADPKD1* and *APKD2*), which together affect 500,000 individuals in the USA (Table 18.11). There are also autosomal recessive forms of human polycystic disease. The most common genetic mutations are in *PKHD1* (encoding fibrocystin, also known as polyductin) and *MCDK1*, encoding medullary cystic kidney disease type 1 (which despite its name, exhibits nephronophthisis and predominantly cortical cysts).

Mouse Models of Cystic Kidney Disease

As gene knockout for these genes are embryonic and lethal in humans, various other classes of mouse models have been made (Tables 18.11 and 18.12). Furthermore, there appear to be strain differences in penetrance in cystic phenotypes, and the suggestion is a modifier affect based on genetic background [69].

Models include conditional knockout mice (involving deletion of one more exons), hypomorphic models carrying genetic variants with reduced function, and over-expressing models [70]. Conditional cystic models have been generated in which floxed exons have been introduced; when these mice are bred with a *cre*-recombinase transgenic mouse, expressing the transgene in a tissue-specific manner (e.g. proximal tubule or distal tubule), cell-specific manner, or particular tubular cell types in kidney or in extra-renal tissues.

Patterns of cysts in the kidney of mice and humans may be described as single, multiple, or polycystic. In addition to genetic etiologies, renal cysts can result from chronic renal disease, or from obstruction of the ureters, bladder, or urethra. Occurrence in young people or mice suggested a developmental defect that may start at nephron maturation in utero. Postnatal multiple or diffuse cysts suggest genetic

Table 18.10 Spontaneous tubular lesions in mice.[a]

Degenerative	• Autolysis/decomposition can mimic features of degeneration/necrosis in tubules, including focal, zonal, or diffuse pallor, vacuolation, loss of cytoplasmic and nuclear detail, detached/sloughing epithelial cells • Amyloidosis, glomerular, interstitial, (papilla in A/J) • Tubular degeneration; changes can include cell swelling, cytoplasmic vacuolation, pale or fragmented cytoplasm • Tubular regeneration characterized by relatively basophilic, hypercellular tubules • Hyaline casts; eosinophilic, homogeneous protein content in dilated tubules • Tubule necrosis; unusual in naive mice; must be differentiated from autolytic changes • Granular casts • Aging nephropathy
Metabolic	Cytoplasmic vacuolation, incidental finding more likely in males • Mineralization in tubules (more in strains carrying an *Abcc6* hypomorphic mutation associated with ectopic mineralization 129S1/SvImJ, C3H/HeJ, DBA/2J, KK/HlJ) • Crystals in tubules, may be associated with tubule dilatation, damage, macrophages, or multinucleated giant cells; may be birefringent and not clearly associated with tubule damage; the 129S2/SvPasCrl spontaneous mutation in *Slc3a1* causes cystinuria, hydronephrosis, early death
Infectious	• Chapparvovirus (MKPV mouse kidney parvovirus) • Inclusion body nephropathy (IBN) in older immune deficient mice • Bacterial urinary tract infection (UTI); Gram negative or Gram-positive bacteria related to lower UTI (cystitis, urethritis), • Adenovirus – rare; MAdV-1(FL) intranuclear inclusion bodies • Herpesvirus – rare; murine cytomegalovirus experimental infection caused karyocytomegaly and intranuclear inclusion bodies in tubules • Polyomavirus – rare; MPyV1experimental infections causes intranuclear inclusion bodies in tubules • Leptospirosis – rare in vivaria; a zoonotic expected in feral mice • *Klossiella muris* – rare in vivaria; expected in feral mice; renal coccidian parasite; most developmental stages manifest in tubular epithelium
Other	• Hyaline droplet change – intracytoplasmic acidophilic droplets (lysozyme) associated with histiocytic sarcoma in mice

[a] Some of these phenotypes arise spontaneously on particular genetic backgrounds, as shown. Information derived from various references including [5–10].

causes, often manifesting as developmental defect that compromises nephron maturation in utero or postnatal development. In humans, multiple or polycystic kidneys are caused by mutations in various genes, including *PKD1, PKD2, PKHD1, MCKD1,* or *REN*.

In mice, over 160 genotypes manifesting cystic renal diseases have been found, as listed in the JAX laboratory website (http://www.informatics.jax.org/vocab/mp_ontology/MP:0008528). These phenotypes include kidney cortex cysts (60 genotypes), corticomedullary cysts (5 genotypes), medullary cyst (24 genotypes), polycystic kidney (163 genotypes), and glomerular cysts (31 genotypes). Some manifest as polycystic kidney, many of which are probably due to development defects. Specific examples include mice with ciliopathy (*Tmem218* and *Flcn*^{tm1Baba}) conditional mutants (a gene associated with renal cancer in humans) (Figure 18.21). At birth, the earliest stages of tubular dilatation were found in these *Flcn*^{tm1Baba} mutant mice (J. Ward, unpublished). In the polycystic kidney diseases, mouse inheritance patterns do not always track those of human diseases. Thus, human autosomal dominant kidney disease is most frequently the result of mutations in *PKD1*, encoding fibrocystin (also known as polyductin).

Spontaneous Tubular Lesions of Mice

Tubular lesions occur sporadically in mice [5, 8–10] (Table 18.10) and are discussed in greater detail in Chapter 9 of this book. Tubular injury also occurs in immunodeficient mice. Changes arising as a consequence of transgene expression must be distinguished from autolytic change. Modest degenerative and regenerative tubular changes are unsurprising in older mice and are also typical of chronic renal disease of any etiology. Tubular necrosis is unusual in naive mice; these must be differentiated from autolytic changes. Cytoplasmic vacuolation is usually in outer cortical tubules, typically an incidental finding more likely in males and related to resorption of major urinary proteins but can be related to autolysis or interventions. Vacuolization due to glycogen storage is seen in storage diseases including the *G6pc*^{tm1Jyc} mouse (Figure 18.22) and can also be observed in cases of osmotic diuresis or drugs (e.g. calcineurin inhibitors). Mineralization (i.e. calcification) in tubules or in collecting ducts can be identified in various strains, sometimes in association with ectopic mineralization, and can be severe in strains (e.g. 129S1/SvImJ, C3H/HeJ, DBA/2J, KK/HlJ) that carry a mutation in *Abcc6,* encoding multidrug resistance protein 6.

Table 18.11 Selected genetic tubular diseases, including cystic diseases, modeled in genetically engineered mice.[a]

Disease Human gene Human protein	Major human disease features	Inheritance patterns in genetically engineered mice	Examples of GEM
Autosomal dominant polycystic kidney disease *PKD1* Polycystin 1	Kidney cysts	Autosomal recessive (dissimilar from human)	Null, unstable hypomorphic, and conditional alleles
Autosomal dominant polycystic kidney disease *PKD2* Polycystin2	Kidney cysts	Autosomal recessive (dissimilar from human)	Null, unstable, and conditional alleles
Autosomal recessive polycystic kidney disease *PKHD1* Fibrocystin1	Kidney cysts	Autosomal recessive	Null, conditional, and microdeletion alleles
Medullary cystic kidney disease type 1 *MCKD1*	Kidney cysts, hyperuricemia	Autosomal dominant	*Muc1*^{tm1Gend}
Autosomal dominant polycystic kidney disease: Hajdu–Cheney syndrome *NOTCH2* Notch receptor2	Kidney cysts	Autosomal recessive	Null, *Notch2* gain of function
Cystinosis *CTNS* Cystinosin	Eye, brain, kidney Lysosomal storage disease	Autosomal recessive	*Ctns*^{tm1Antc}
Joubert (ciliopathy) *INPP5E* Inositol 5-phosphate phosphatase	Cerebellum, eye, liver, kidney	Autosomal recessive	*Inpp5e*$^{tm1.1(KOMP)Vlcg}$
Methylmalonic aciduria *MMUT* and other genes Malonyl *co*-A decarboxylase (mitochondrial enzyme)	Tubular dysfunction, stroke, seizures, encephalopathy	Autosomal recessive	*Mmut*^{tm1Pai}/ *Mmut*$^{tm1.1Mrb}$
Multicentric carpotarsal osteolysis syndrome *MAFB* Transcription factor	Bone, kidney (focal segmental glomerulosclerosis)	Autosomal dominant; sporadic	*Mafb*^{em1Staka}
Lowe syndrome/Dent disease *OCRL1* Inositol 5-phosphate phosphatase	Brain, eye, kidney (Fanconi syndrome)	X-linked	*Ocrl*^{tm1Nbm}

[a] Shown are genetically engineered mouse models of selected tubular diseases, listed by inheritance pattern in mice. All mice have phenotypes that resemble human disease, at least to some extent. Gene mutations include null alleles (gene knockouts), hypomorphic alleles, gain of (dys)function alleles, and unstable alleles, as well as conditional alleles that can be deleted by breeding with an Cre deleter mouse, driven by a promoter sequence that targets the sequence of interest. Unstable (mutable) alleles are those that may convert to another allele, either in somatic or germline tissues. In the case of methylmalonic aciduria, the knockout mouse is embryonic lethal and is rescued by coexpressing the *Mut* gene under the control of the muscle-specific *Mck* promoter. Renal Fanconi syndrome involves defective proximal tubule function, manifesting as renal wasting of glucose, amino acids, phosphate, and uric acid. Note that autosomal dominant polycystic kidney disease, when modeled in mice, has autosomal recessive inheritance.

Table 18.12 Phenotypes of selected human kidney cancer genes and of genetically engineered mice bearing gene knockout or conditional deleted genes.[a]

Human gene/ disease	Human tumors/lesions	Mouse null	Mouse heterozygous deletion and other GEM	References
VHL	Renal cysts, renal clear cell cancer, CNS, retinal angiomas, hemangioblastomas, pheochromocytomas, in other tissues	Embryonic lethal	Conditional model: renal cysts, adenomas, fibrosis, tumors, including hemangiomas, in other organs, *Hif1a* transgenic	[49–55]
BAP1	Renal clear cell carcinoma, uveal melanoma, mesothelioma, skin tumors	NA	Conditional model-renal cysts, cystic, and solid tumors	[54, 56]
MET	Papillary renal cancer	No null mutation mouse	Targeted *Met* activating mutations manifest carcinoma, lymphoma, sarcoma	[57]
FLCN (BHD)	Hybrid oncocytic renal tumors and chromophobe renal cancer; spontaneous pneumothorax, fibrofolliculomas	Embryonic lethal	Conditional model ($Flcn^{tm1Baba}$) manifests polycystic kidneys, solid tumors with low penetrance and long latency	[58–60]
FH	Papillary type 2 renal cancer, skin and uterine leiomyomas	Embryonic lethal	Conditional model manifests renal cysts	[61]
SDHB/C/D	Renal cancer, paragangliomas, extra-renal pheochromocytomas	Embryonic lethal	No tumors	[62]
TSC1/2	Tuberous sclerosis, hamartomas, renal tumors, angiomyolipomas	Embryonic lethal	Cysts, adenomas, renal cancer, other tumors	[63, 64]
BAP1	Clear cell renal cancer, uveal and cutaneous melanoma, malignant mesothelioma	Ovarian tumors	Renal cysts, ovarian tumors	[54, 56, 65]
WT1	Juvenile nephroblastoma (sporadic)	Embryonic lethal	Conditional *Wt1* with *Ctnnb1* and other genes-renal tumors	[66, 67]
CDC73	Hyperparathroidism, Jaw syndrome, tumors, renal hamartomas, Wilms tumors	Embryonic lethality	Parathyroid and uterine tumors	[68]

NA, not applicable. Other references noted in renal/urinary system phenotype Mammalian Phenotype Term (MP:0005367) (http://jax.org).
[a] Shown are 10 genetic loci that have been associated with human cancers and the genetically modified mice that model these conditions.

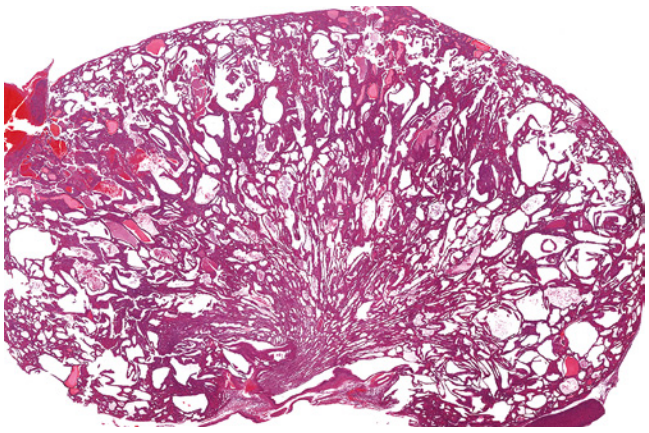


Figure 18.21 **Polycystic kidney**. Note numerous dilated and cystic tubules occurring due to defective development. $Flcn^{tm1Baba}$ mouse, three weeks old.

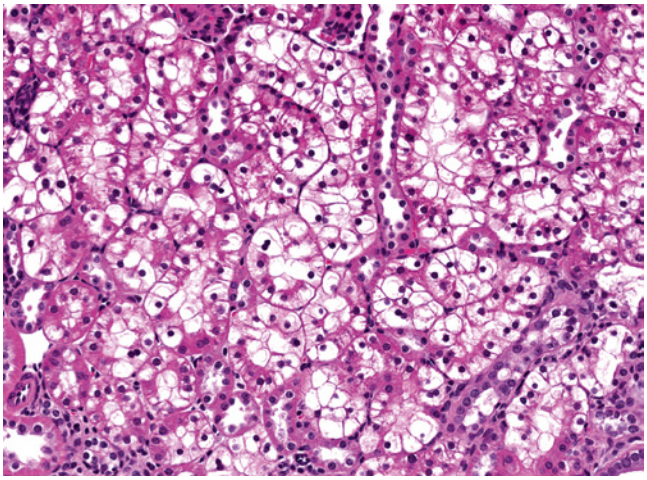


Figure 18.22 **Glycogen storage disease**. There is abundant glycogen in tubular epithelium. $G6pc^{tm1Iyc}$ mouse.

Crystals within tubular lumens or the interstitium are fairly unusual in mice. They may be associated with tubule dilatation and damage and the presence of macrophages or multinucleated giant cells in the interstitium. Crystals may become birefringent and not clearly associated with tubule damage or may be lost in tissue processing.

In humans, nephronophthisis in humans is an autosomal recessive chronic kidney disease that manifests as progressive interstitial fibrosis and is the most common genetic cause of kidney failure in children. This condition manifests genetic heterogeneity. Six genes have been implicated, *NPHP1-6*, and there are ciliopathy genes and other genes that can cause a similar phenotype. A limited number of GEM models have been made for these syndromes. This topic is also discussed under bladder urolithiasis.

The presence of chronic tubular damage warrants analysis of urine sediment. 129S2/SvPasCrl mice carry a spontaneous mutation in *Slc3a1*, encoding the neutral and basic amino acid transporter, causes cystinuria, hydronephrosis, early death. Hyaline droplet change (hypereosinophilic intracytoplasmic acidophilic droplets) has been associated with lymphoma and histiocytic sarcoma in mice.

Infections may manifest tubular injury. Viral tubule lesions in contemporary colonies are particularly associated with a recently identified with the nephrotropic Chapparvovirus (MKPV, mouse kidney parvovirus) (Figure 18.23). This virus causes prominent intranuclear inclusion bodies in tubular epithelial cells, and degenerative changes, particularly in older immunodeficient mice. Intranuclear inclusion bodies associated with adenovirus, herpesvirus, and polyomavirus infections have been seen in the past but are not common in most contemporary colonies. However, these infections may occur with the increasing use of immunodeficient mice, with the use of feral mice, and following administration of biological materials, including patient-derived xenografts. Vacuolated nuclei with PAS-positive inclusions, resembling viral inclusions, have been seen in mice exposed to streptozotocin (Figure 18.24).

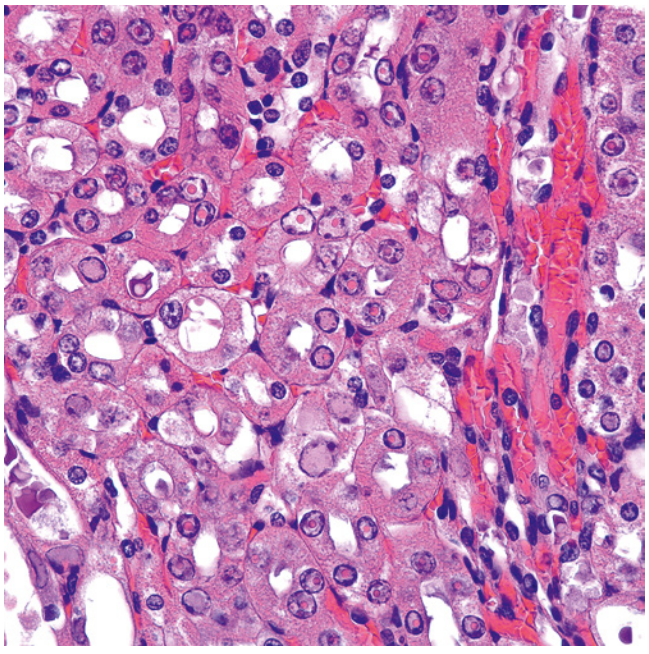


Figure 18.23 Chapparvovirus (MKPV, mouse kidney parvovirus) infection. Many eosinophilic intranuclear tubule cell inclusions fill the nucleus or halos are seen.

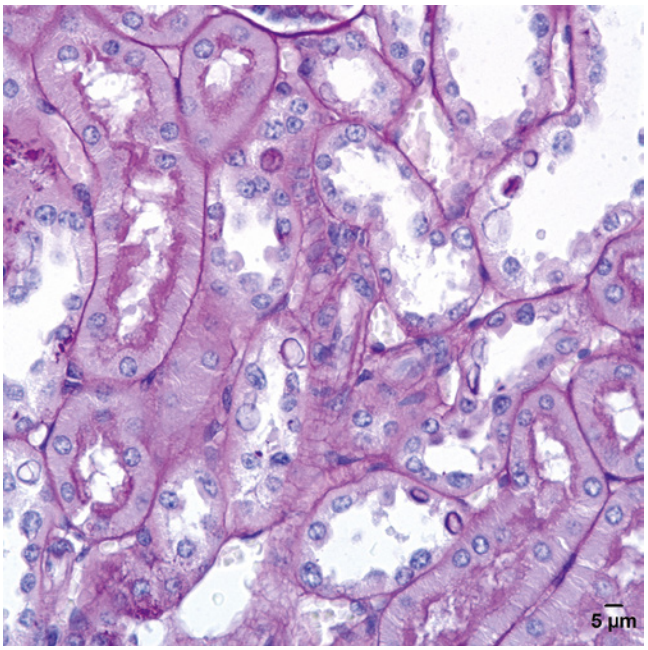


Figure 18.24 Streptozocin-induced clear intranuclear tubule cell inclusions. Note some are PAS$^+$.

Bacterial urinary tract infection (UTI) with Gram-negative or Gram-positive bacteria can be produce lower tract UTI (cystitis, urethritis) or kidney infection (pyelonephritis). Both, but especially the latter, give rise to bacteremia, particularly in immunodeficient mice. Leptospirosis, rarely seen with contemporary colony husbandry, is common in feral mice and is therefore a zoonotic concern. Similarly, the renal coccidian parasite, *Klossiella muris* is not expected with contemporary colony husbandry, but this can present feral mice in the tubular epithelium.

Renal Tumors

Renal epithelial tumors are a common human cancer [66] though they do not frequently occur spontaneously in mice but may be induced in mice with chemicals [67] and genetic engineering. A comparison of human genes associated with renal cancer and GEM are shown below. Human renal cancer genes used to create GEM include the following specific reviews: *VHL* [49–54], *MET* [57], *FLCN* [58–60], *FH* [61]; *SDHb/c/d* [62], *TSC1/2* [63, 64], *BAP1* [54, 56, 65], *WT1* [55, 71], and *CDC73* [68].

A common finding for the heritable human renal cancer genes is that the mouse null (knockout) is embryonic lethal (Table 18.12). The pathology of the mouse renal tumors varies from well differentiated to poorly differentiated. Clear cell renal cell carcinomas have been induced in mice [60], but they are not as common as in humans. When a detailed pathology study is reported, the tumors often arise from a preneoplastic precursor lesion, histomorphologically appreciated as atypical hyperplasia (Figure 18.25) [8]. These tumors often evolve to adenomas (Figures 18.25–18.27) and then adenocarcinomas (Figures 18.28 and 18.29). Metastatic progression has been reported in mouse *Tsc1* mutants [63].

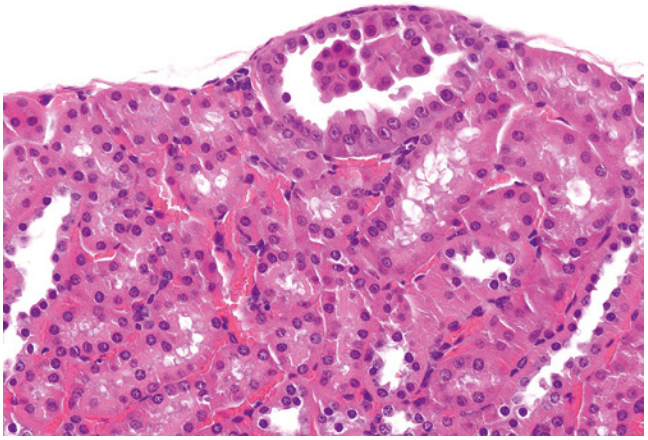


Figure 18.25 Preneoplastic renal tubule cell atypical hyperplasia. A single tubule is dilated and contains hypertrophic tubule cells. *Tsc2*^{tm1Djk} mouse mutant.

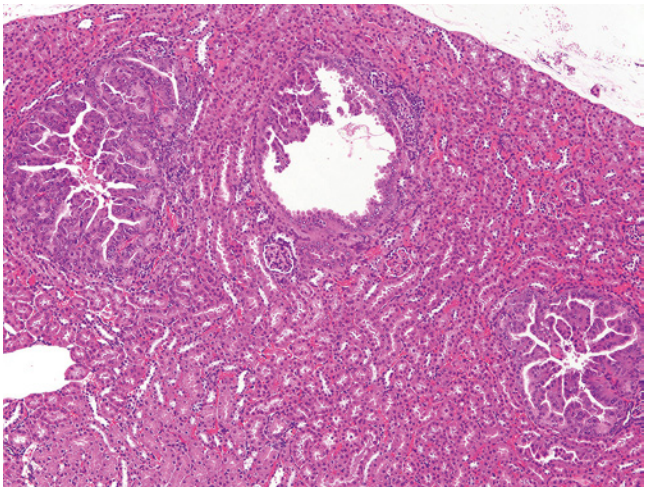


Figure 18.26 Multiple renal tubular adenomas. Tumors are small and papillary. *Tsc2*^{tm1Djk} mouse mutant.

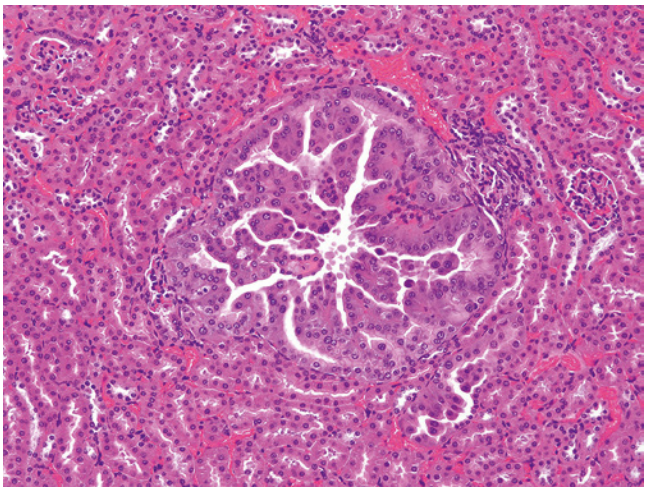


Figure 18.27 Renal papillary tubular adenoma. There is compression of adjacent normal kidney. *Tsc2*^{tm1Djk} mouse mutant.

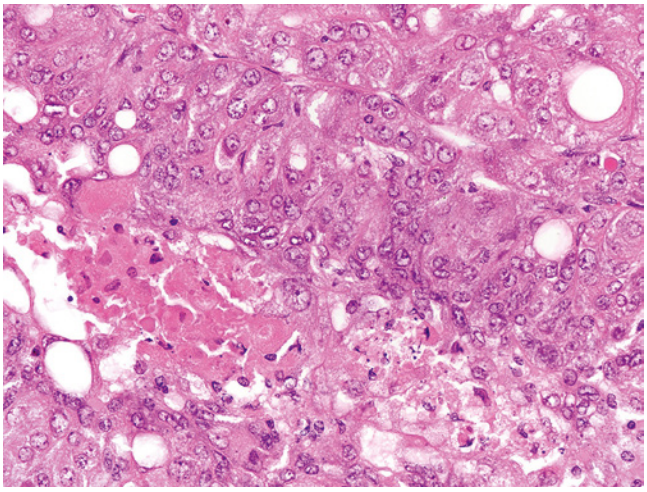


Figure 18.28 Solid renal tubular cell adenocarcinoma. Necrosis is seen. Chemically induced.

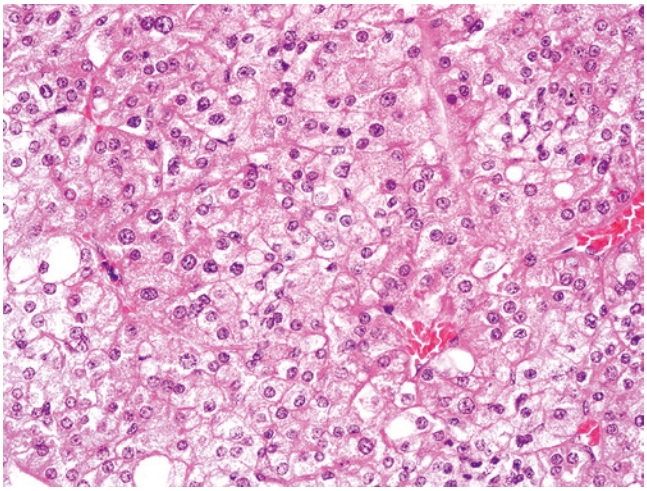


Figure 18.29 Renal clear cell carcinoma. Glycogen-like clear cytoplasm. Chemically induced.

Urinary Bladder: Anatomy and Histology

The mouse urinary bladder is a hollow musculomembranous organ that varies greatly in size and shape depending on the quantity of urine that it contains. Several anatomic regions are present including a cranial vertex, a body, and a neck that is continuous with the urethra. The microscopic morphology has been well described [2] and is similar across strains. The urinary bladder when devoid of urine is an ovoid approximately 4 mm structure lined throughout by a three-cell thick lining of urothelium with basal, intermediate, and luminal cell layers. The urothelium, a transitional epithelium, overlies a highly vascular lamina propria and is surrounded by multiple layers of smooth muscle. In the contracted state, there are numerous mucosal folds. Increases in submucosal lymphoid aggregates can be noted as a spontaneous age-related change in mice. During sectioning in tumor studies, it is important that the trim scheme collects the bladder neck with the trigone region since although most of the urinary bladder is of endodermal origin, the trigone is derived from the mesoderm of the Wolffian ducts and can be the site of specialized neoplasms.

Fixation and Trimming of Urinary Bladder

The mouse bladder is optimally fixed with infusion of fixative through the bladder wall with a small needle so that it is fixed in a distended state after ligation of the urethra. The organ is filled by injection of approximately 50 µl of fixative. Infusion of fixative is not performed if the urinary bladder is distended with urine. Choice of fixative depends on the purpose of the study and the type of tissue examination. It should be recognized that for some types of studies that employ scanning electron microscopy (SEM) to evaluate the surface urothelium, autolytic changes can occur rapidly following death and specific fixation methods must be employed [72]. Following fixation, tissue trim is performed. Multiple schemes for fixation and trim of the organ have been described. Many rodent pathologists fix the urinary bladder in males *en bloc* to preserve relationships with prostate, seminal vesicles, and accessory sex organs. It may be helpful to mark the ventral side of the bladder with a colored marker dye. For oncogenicity studies, a good method of trim is that recommended by the RENI guidelines [73]. In this method, the bladder is cut vertically through the ventral ligature where the urethra is ligated and allows to access to all parts of the organ. Another suggested trim method after bladder inflation and for oncogenicity studies is shown in Figure 18.30.

Urinary Bladder Physiology

Mice of many strains and many GEM models manifest a variety of spontaneous changes in the urinary bladder and urinary outflow tract associated with alterations in micturition, as reviewed in a textbook chapter [74]. As described there, this can lead to urinary retention and subsequent bladder distension, eventually manifesting as hydroureter and in some cases, hydronephrosis. As one example, B6.129S6-*Naglu*^{tm1Efn}/J mice, which were generated to develop mucopolysaccharidosis type IIIB, develop obstructive uropathy, which is not a typical feature of the human disease [75]. This condition leads to bladder hyperdistension and unscheduled deaths, which complicates experimental research.

A relatively common finding in male mice of various genetic backgrounds is obstructive genitourinary disease related to urethral obstruction due to a coagulum of seminal fluid. A multifactorial etiology has been postulated for this condition linked to various hormonal and environmental factors including certain forms of anesthesia [76]. Urethral obstruction with bladder distension and urologic dysfunction leads to hydroureter, hydronephrosis, pyelonephritis, cystitis, and urethritis. Urologic dysfunction with urethral obstruction has been noted in certain GEM models such as those of Rett syndrome associated with the loss of MeCP2 [77]. GEM models have been used to study vesicoureteral reflux and congenital abnormalities of the kidney and urinary tract [78].

Urolithiasis

Urolithiasis occurs spontaneously in many mouse strains and is often associated with environmental factors such as diet and bacterial infection as well as hormonal factors such as estrogen implants. GEM models have been used for genetic studies of crystalluria and urolithiasis. Also see discussion under tubular diseases in this chapter. Many GEM models of crystalluria do not lead to overt cystic calculi but instead result in interstitial calcinosis of the renal papilla, as reviewed by Wu [79]. Uromodulin (UMOD), also known as Tamm–Horsfall protein, is a protein product of distal tubular cells and the most abundant protein in normal urine. The primary function of uromodulin appears to be to inhibit urine crystal formation, and *Umod*^{tm1Xrw} mice have demonstrated the importance of UMOD in inhibiting calcium oxalate crystal formation [80]. Furthermore, genetic variants in *Umod* have been described to result in an autosomal dominant tubulointerstitial kidney disease and may behave similarly in mouse models.

Various GEM models have been described for studies of primary hyperoxaluria, often in conjunction with the administration of lithogenic agents. Transporter knockout models have been used to induce hyperoxaluria, hypercalciuria,

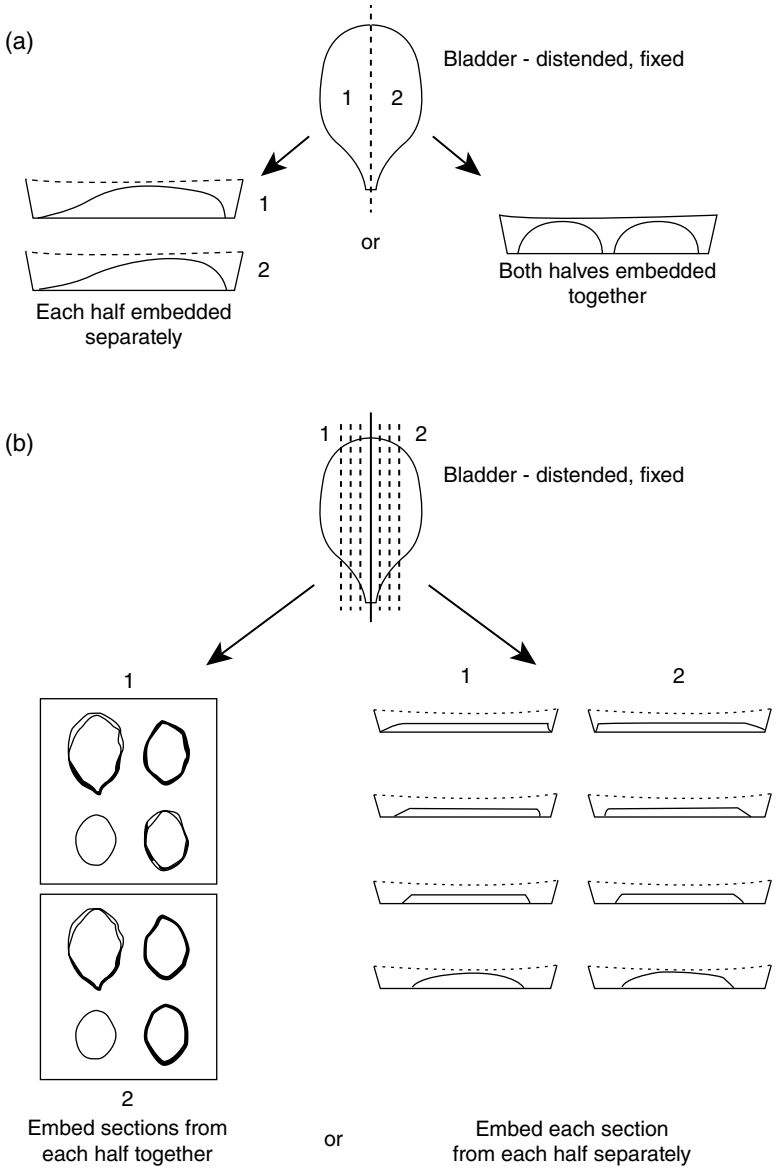


Figure 18.30 Bladder fixation and trimming protocol. Inflate bladder with 50 ml of fixative. Let fix for several days. For specific studies, trim as shown by one of two methods and embed multiple sections.

hyperuricosuria, and cystinuria. The relevant genes are reviewed by Tzou et al. [81]. Most of these models result in nephrolithiasis, accompanied by various degrees of intratubular crystal formation, and manifest progressive tubular degenerative, regenerative changes and tubulo-interstitial inflammatory lesions.

Urinary Bladder Neoplasia

Human bladder cancer is associated with cigarette smoking, workplace chemical exposures, particular medications, dietary supplements containing aristolochic acid, and arsenic in drinking water (www.cancer.org). Mouse bladder pathology has been reviewed [82].

The mouse has proven to be a useful model for the study of urothelial carcinogenesis. Spontaneous neoplasms of the mouse urinary bladder are very rare, but a variety of chemicals, particularly genotoxic compounds that have been associated with human urothelial carcinogenesis, have proven to cause urothelial neoplasms in mice (reviewed by [83]). The best-studied chemical carcinogen in mice is the nitrosamine, *N*-butyl-*N*-(4-hydroxybutyl) nitrosamine (BBN). BBN-induced urothelial carcinogenesis resembles the morphologic spectrum of lesions seen in human muscle-invasive bladder cancer and recapitulates many of the molecular alterations, as reviewed by Fantini and colleagues [84]. These urothelial changes range from simple hyperplasia to nodular hyperplasia (Figure 18.31), papilloma (Figure 18.32), through stages of dysplasia,

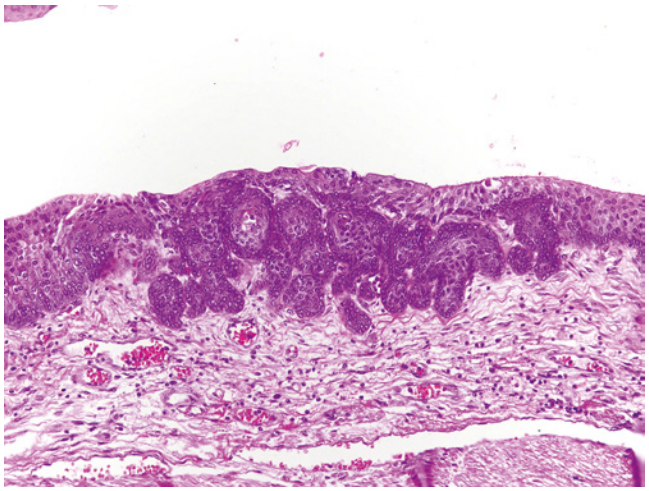


Figure 18.31 Bladder diffuse and nodular hyperplasia. Note diffuse and nodular thickening of epithelium. Chemically induced.

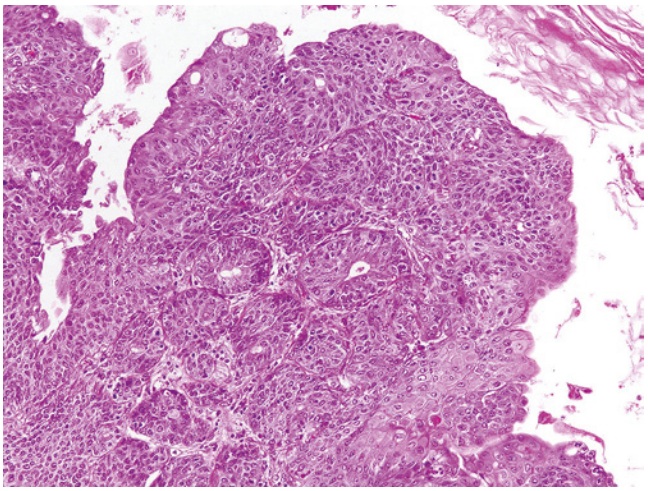


Figure 18.33 Bladder transitional cell carcinoma. Invasion of the bladder wall is observed also with growth into the bladder lumen. Chemically induced.

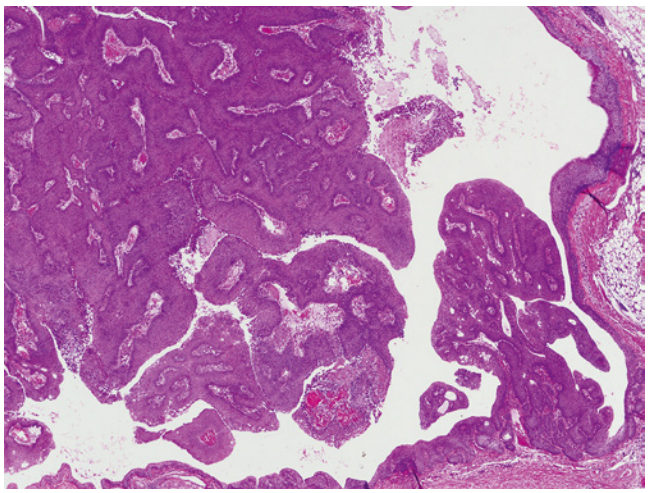


Figure 18.32 Large and small bladder papillomas. The adjacent epithelium is hyperplastic. Chemically induced.

carcinoma *in situ,* and invasive carcinoma (Figure 18.33), sometimes with squamous metaplasia.

Various GEM models have been used to explore the molecular genetics and oncogenic pathways associated with human bladder carcinogenesis [85]. Two distinct forms of urothelial tumors occur in humans, a low-grade recurring papillary neoplasm of the urothelium characterized by mutations in *FGFR3* or *HRAS*, and high-grade muscle-invasive neoplasms with metastatic potential. The latter tumors generally have alterations in pathways controlled by the tumor suppressor 53 (*TP53*) and retinoblastoma (*RB1*) genes. Various GEM models of urothelial cell carcinoma have been developed using mutations in various genes believed important in urothelial cell carcinoma pathways. These include, alone or in combination, *Hras*, *Egfr*, *Trp53*, *Pten, Rb1*, and *β-catenin* (*Ctnnb1*) using promoters expressed in the basal layer of the urothelium such as mouse uroplakin II (*Upk2*). These models have contributed greatly to our understanding of how dysregulation of oncogenic pathways in urothelial cell carcinoma contribute to biological outcomes. In humans, metastatic urothelial cell carcinoma is primarily observed in bone, lung, and liver, whereas in mouse GEM models of metastatic urothelial cancer, osseous lesions are not observed, for reasons yet to be elucidated.

Conclusion

Precision medicine requires precision diagnosis and precision therapeutics. Underpinning this is a precise understanding of the relevant molecular pathways that contribute to the pathogenesis of specific, often molecularly defined diseases. Precision mouse models of human disease are those that can be shown to manifest, to a reasonably accurate degree, alterations in the activity of disease-associated pathways and the expression or form of molecules that have been implicated in human disease. GEM mice have an important part to play in providing precision models for genetic diseases and also for nongenetic diseases. The combination of modern murine models of kidney disease with evolving molecular techniques including deep bulk RNAseq and single cell RNAseq technologies is driving the discovery of novel innate cellular compartments of the kidney as well as cellular differentiation states and infiltrating cells resulting from injury. If the molecular pathways in particular GEM disease models are be shown to resemble those in human diseases, to a sufficiently close extent, then these models can be used to test the efficacy and toxicity of novel therapies.

References

1 Carretero, A., Ruberte, J., Navarro, M. et al. (2017). Urinary organs. In: *Morphological Mouse Phenotyping: Anatomy, Histology and Imaging* (eds. J. Ruberte, A. Carretero and M. Navarro), 179–194. Amsterdam: Academic Press.

2 Delaney, M., Kowalewska, J., and Treuting, P. (2017). Urinary system. In: *Mouse, Rat and Human Atlas* (eds. P.M. Treuting, S. Dintzis and K. Montine), 275–301. Academic Press.

3 Khan, K.M.N., Hard, G.C., Li, X., and Alden, C.L. (2018). Urinary system. In: *Fundamentals of Toxicologic Pathology* (eds. M.A. Wallig, W.M. Haschek, C.G. Rousseaux, et al.), 213–271. London: Academic Press.

4 Murawski, I.J., Maina, R.W., and Gupta, I.R. (2010). The relationship between nephron number, kidney size and body weight in two inbred mouse strains. *Organogenesis* 6 (3): 189–194.

5 Barthold, S.W., Griffey, S.M., and Percy, D.H. (2016). *Pathology of Laboratory Rodents and Rabbits*. Wiley-Blackwell.

6 Brayton, C.F., Treuting, P.M., and Ward, J.M. (2012). Pathobiology of aging mice and GEM: background strains and experimental design. *Vet. Pathol.* 49 (1): 85–105.

7 Sundberg, J.P., Berndt, A., Sundberg, B.A. et al. (2016). Approaches to investigating complex genetic traits in a large-scale inbred mouse aging study. *Vet. Pathol.* 53 (2): 456–467.

8 Frazier, K.S., Seely, J.C., Hard, G.C. et al. (2012). Proliferative and nonproliferative lesions of the rat and mouse urinary system. *Toxicol. Pathol.* 40 (4 Suppl): 14S–86S.

9 Seely, J. (1999). Kidney. In: *Pathology of the Mouse* (ed. R. Maronpot), P208–P234. Vienna, IL: Cache River Press.

10 Eckhaus, M. and Kopp, J.B. (2000). Renal diseases in genetically-engineered mice. In: *Pathology of Genetically Engineered Mice* (eds. J.M. Ward, J.F. Mahler, R.R. Maronpot and J.P. Sundberg), 347–364. Iowa State University Press.

11 Charlton, J.R., Baldelomar, E.J., Hyatt, D.M., and Bennett, K.M. (2020). Nephron number and its determinants: a 2020 update. *Pediatr. Nephrol.* 36: 797–807.

12 Walkin, L., Herrick, S.E., Summers, A. et al. (2013). The role of mouse strain differences in the susceptibility to fibrosis: a systematic review. *Fibrogenesis Tissue Repair.* 6 (1): 18.

13 Laouari, D., Burtin, M., Phelep, A. et al. (2011). TGF-alpha mediates genetic susceptibility to chronic kidney disease. *J. Am. Soc. Nephrol.* 22 (2): 327–335.

14 Baldelomar, E.J., Charlton, J.R., deRonde, K.A., and Bennett, K.M. (2019). in vivo measurements of kidney glomerular number and size in healthy and Os(/+) mice using MRI. *Am. J. Physiol. Renal Physiol.* 317 (4): F865–F873.

15 Peterson, S.M., Wang, X., Johnson, A.C. et al. (2019). Estimation of nephron number in whole kidney using the acid maceration method. *J. Vis. Exp.* 147 https://doi.org/10.3791/58599.

16 Geraci, S., Chacon-Caldera, J., Cullen-McEwen, L. et al. (2017). Combining new tools to assess renal function and morphology: a holistic approach to study the effects of aging and a congenital nephron deficit. *Am. J. Physiol. Renal Physiol.* 313 (3): F576–F584.

17 Qiao, J., Uzzo, R., Obara-Ishihara, T. et al. (1999). FGF-7 modulates ureteric bud growth and nephron number in the developing kidney. *Development* 126 (3): 547–554.

18 Cullen-McEwen, L.A., Kett, M.M., Dowling, J. et al. (2003). Nephron number, renal function, and arterial pressure in aged GDNF heterozygous mice. *Hypertension* 41 (2): 335–340.

19 Godley, L.A., Kopp, J.B., Eckhaus, M. et al. (1996). Wild-type p53 transgenic mice exhibit altered differentiation of the ureteric bud and possess small kidneys. *Genes Dev.* 10 (7): 836–850.

20 Ruta, L.A., Dickinson, H., Thomas, M.C. et al. (2010). High-salt diet reveals the hypertensive and renal effects of reduced nephron endowment. *Am. J. Physiol. Renal Physiol.* 298 (6): F1384–F1392.

21 Fogelgren, B., Yang, S., Sharp, I.C. et al. (2009). Deficiency in Six2 during prenatal development is associated with reduced nephron number, chronic renal failure, and hypertension in Br/+ adult mice. *Am. J. Physiol. Renal Physiol.* 296 (5): F1166–F1178.

22 Cullen-McEwen, L.A., Armitage, J.A., Nyengaard, J.R., and Bertram, J.F. (2012). Estimating nephron number in the developing kidney using the physical disector/fractionator combination. *Methods Mol. Biol.* 886: 109–119.

23 Strassheim, D., Renner, B., Panzer, S. et al. (2013). IgM contributes to glomerular injury in FSGS. *J. Am. Soc. Nephrol.* 24 (3): 393–406.

24 De Vriese, A.S., Sethi, S., Nath, K.A. et al. (2018). Differentiating primary genetic, and secondary FSGS in adults: a clinicopathologic approach. *J. Am. Soc. Nephrol.* 29 (3): 759–774.

25 Rosenberg, A.Z. and Kopp, J.B. (2017). Focal segmental glomerulosclerosis. *Clin. J. Am. Soc. Nephrol.* 12 (3): 502–517.

26 Sethi, S. and Fervenza, F.C. (2019). Standardized classification and reporting of glomerulonephritis. *Nephrol. Dial. Transplant.* 34 (2): 193–199.

27 Zheng, Z., Schmidt-Ott, K.M., Chua, S. et al. (2005). A Mendelian locus on chromosome 16 determines susceptibility to doxorubicin nephropathy in the mouse. *Proc. Natl. Acad. Sci. U.S.A.* 102 (7): 2502–2507.

28 Niculovic, K.M., Blume, L., Wedekind, H. et al. (2019). Podocyte-specific sialylation-deficient mice serve as a model for human FSGS. *J. Am. Soc. Nephrol.* 30 (6): 1021–1035.

29 Meyer-Schwesinger, C., Tomas, N.M., Dehde, S. et al. (2020). A novel mouse model of phospholipase A2 receptor 1-associated membranous nephropathy mimics podocyte injury in patients. *Kidney Int.* 97 (5): 913–919.

30 Cianciolo, R.E. and Jennette, J.C. (2018). Glomerulonephritis in animal models and human medicine: discovery, pathogenesis, and diagnostics. *Toxicol. Pathol.* 46 (8): 898–903.

31 Klopfleisch, R. (2013). Multiparametric and semiquantitative scoring systems for the evaluation of mouse model histopathology – a systematic review. *BMC Vet. Res.* 9: 123.

32 Meyerholz, D.K., Tintle, N.L., and Beck, A.P. (2019). Common pitfalls in analysis of tissue scores. *Vet. Pathol.* 56 (1): 39–42.

33 Watson, M.L., Rao, J.K., Gilkeson, G.S. et al. (1992). Genetic analysis of MRL-lpr mice: relationship of the Fas apoptosis gene to disease manifestations and renal disease-modifying loci. *J. Exp. Med.* 176 (6): 1645–1656.

34 Ward, J.M., Nikolov, N.P., Tschetter, J.R. et al. (2004). Progressive glomerulonephritis and histiocytic sarcoma associated with macrophage functional defects in CYP1B1-deficient mice. *Toxicol. Pathol.* 32 (6): 710–718.

35 Zhang, Z., Kundu, G.C., Yuan, C.J. et al. (1997). Severe fibronectin-deposit renal glomerular disease in mice lacking uteroglobin. *Science* 276 (5317): 1408–1412.

36 Hoane, J.S., Johnson, C.L., Morrison, J.P., and Elmore, S.A. (2016). Comparison of renal amyloid and hyaline glomerulopathy in B6C3F1 mice: an NTP retrospective study. *Toxicol. Pathol.* 44 (5): 687–704.

37 Treuting, P.M., Albertson, T.M., and Preston, B.D. (2010). Case series: acute tumor lysis syndrome in mutator mice with disseminated lymphoblastic lymphoma. *Toxicol. Pathol.* 38 (3): 476–485.

38 Vogel, P., Gelfman, C.M., Issa, T. et al. (2015). Nephronophthisis and retinal degeneration in tmem218−/− mice: a novel mouse model for Senior-Loken syndrome? *Vet. Pathol.* 52 (3): 580–595.

39 Vogel, P., Pletcher, J.M., and Liang, Y. (2010). Spontaneous acute tumor lysis syndrome as a cause of early deaths in short-term carcinogenicity studies using p53 +/− mice. *Vet. Pathol.* 47 (4): 719–724.

40 Halkom, A., Wu, H., and Lu, Q. (2020). Contribution of mouse models in our understanding of lupus. *Int. Rev. Immunol.* 39 (4): 174–187.

41 Moore, E. and Putterman, C. (2020). Are lupus animal models useful for understanding and developing new therapies for human SLE? *J. Autoimmun.* 112: 102490.

42 Perry, D., Sang, A., Yin, Y. et al. (2011). Murine models of systemic lupus erythematosus. *J. Biomed. Biotechnol.* 2011: 271694.

43 Li, W., Titov, A.A., and Morel, L. (2017). An update on lupus animal models. *Curr. Opin. Rheumatol.* 29 (5): 434–441.

44 Alexander, J.J., Saxena, A.K., Bao, L. et al. (2002). Prominent renal expression of a murine leukemia retrovirus in experimental systemic lupus erythematosus. *J. Am. Soc. Nephrol.* 13 (12): 2869–2877.

45 Kopp, J.B., Klotman, M.E., Adler, S.H. et al. (1992). Progressive glomerulosclerosis and enhanced renal accumulation of basement membrane components in mice transgenic for human immunodeficiency virus type 1 genes. *Proc. Natl. Acad. Sci. U.S.A.* 89 (5): 1577–1581.

46 Dickie, P., Roberts, A., Uwiera, R. et al. (2004). Focal glomerulosclerosis in proviral and c-fms transgenic mice links Vpr expression to HIV-associated nephropathy. *Virology* 322 (1): 69–81.

47 Izui, S., McConahey, P.J., Theofilopoulos, A.N., and Dixon, F.J. (1979). Association of circulating retroviral gp70-anti-gp70 immune complexes with murine systemic lupus erythematosus. *J. Exp. Med.* 149 (5): 1099–1116.

48 Kihara, M., Leroy, V., Baudino, L. et al. (2011). Sgp3 and Sgp4 control expression of distinct and restricted sets of xenotropic retroviruses encoding serum gp70 implicated in murine lupus nephritis. *J. Autoimmun.* 37 (4): 311–318.

49 Fu, L., Wang, G., Shevchuk, M.M. et al. (2011). Generation of a mouse model of Von Hippel-Lindau kidney disease leading to renal cancers by expression of a constitutively active mutant of HIF1alpha. *Cancer Res.* 71 (21): 6848–6856.

50 Guinot, A., Lehmann, H., Wild, P.J., and Frew, I.J. (2016). Combined deletion of Vhl, Trp53 and Kif3a causes cystic and neoplastic renal lesions. *J. Pathol.* 239 (3): 365–373.

51 Haase, V.H. (2005). The VHL tumor suppressor in development and disease: functional studies in mice by conditional gene targeting. *Semin Cell Dev Biol.* 16 (4–5): 564–574.

52 Kleymenova, E., Everitt, J.I., Pluta, L. et al. (2004). Susceptibility to vascular neoplasms but no increased susceptibility to renal carcinogenesis in Vhl knockout mice. *Carcinogenesis* 25 (3): 309–315.

53 Pritchett, T.L., Bader, H.L., Henderson, J., and Hsu, T. (2015). Conditional inactivation of the mouse von Hippel-Lindau tumor suppressor gene results in wide-spread hyperplastic, inflammatory and fibrotic lesions in the kidney. *Oncogene* 34 (20): 2631–2639.

54 Wang, S.S., Gu, Y.F., Wolff, N. et al. (2014). Bap1 is essential for kidney function and cooperates with Vhl in renal tumorigenesis. *Proc. Natl. Acad. Sci. U.S.A.* 111 (46): 16538–16543.

55 Hooper, M.L. (1998). Tumour suppressor gene mutations in humans and mice: parallels and contrasts. *EMBO J.* 17 (23): 6783–6789.

56 Gu, Y.F., Cohn, S., Christie, A. et al. (2017). Modeling renal cell carcinoma in mice: Bap1 and Pbrm1 inactivation drive tumor grade. *Cancer Discov.* 7 (8): 900–917.

57 Graveel, C.R., DeGroot, J.D., Sigler, R.E., and Vande Woude, G.F. (2010). Germline met mutations in mice reveal mutation- and background-associated differences in tumor profiles. *PLoS One* 5 (10): e13586.

58 Chen, J., Huang, D., Rubera, I. et al. (2015). Disruption of tubular Flcn expression as a mouse model for renal tumor induction. *Kidney Int.* 88 (5): 1057–1069.

59 Baba, M., Furihata, M., Hong, S.B. et al. (2008). Kidney-targeted Birt-Hogg-Dube gene inactivation in a mouse model: Erk1/2 and Akt-mTOR activation, cell hyperproliferation, and polycystic kidneys. *J. Natl. Cancer Inst.* 100 (2): 140–154.

60 Hasumi, Y., Baba, M., Ajima, R. et al. (2009). Homozygous loss of BHD causes early embryonic lethality and kidney tumor development with activation of mTORC1 and mTORC2. *Proc. Natl. Acad. Sci. U.S.A.* 106 (44): 18722–18727.

61 Pollard, P.J., Spencer-Dene, B., Shukla, D. et al. (2007). Targeted inactivation of fh1 causes proliferative renal cyst development and activation of the hypoxia pathway. *Cancer Cell.* 11 (4): 311–319.

62 Lepoutre-Lussey, C., Thibault, C., Buffet, A. et al. (2016). From Nf1 to Sdhb knockout: successes and failures in the quest for animal models of pheochromocytoma. *Mol. Cell Endocrinol.* 421: 40–48.

63 Wilson, C., Idziaszczyk, S., Colley, J. et al. (2005). Induction of renal tumorigenesis with elevated levels of somatic loss of heterozygosity in Tsc1+/− mice on a Blm-deficient background. *Cancer Res.* 65 (22): 10179–10182.

64 Kobayashi, T., Minowa, O., Kuno, J. et al. (1999). Renal carcinogenesis, hepatic hemangiomatosis, and embryonic lethality caused by a germ-line Tsc2 mutation in mice. *Cancer Res.* 59 (6): 1206–1211.

65 Kadariya, Y., Cheung, M., Xu, J. et al. (2016). Bap1 is a bona fide tumor suppressor: genetic evidence from mouse models carrying heterozygous germline Bap1 mutations. *Cancer Res.* 76 (9): 2836–2844.

66 Linehan, W.M., Schmidt, L.S., Crooks, D.R. et al. (2019). The metabolic basis of kidney cancer. *Cancer Discov.* 9 (8): 1006–1021.

67 Lock, E.A. and Hard, G.C. (2004). Chemically induced renal tubule tumors in the laboratory rat and mouse: review of the NCI/NTP database and categorization of renal carcinogens based on mechanistic information. *Crit. Rev. Toxicol.* 34 (3): 211–299.

68 Walls, G.V., Stevenson, M., Lines, K.E. et al. (2017). Mice deleted for cell division cycle 73 gene develop parathyroid and uterine tumours: model for the hyperparathyroidism-jaw tumour syndrome. *Oncogene* 36 (28): 4025–4036.

69 Nagao, S., Hibino, T., Koyama, Y. et al. (1991). Strain difference in expression of the adult-type polycystic kidney disease gene, pcy, in the mouse. *Jikken Dobutsu* 40 (1): 45–53.

70 Happe, H. and Peters, D.J. (2014). Translational research in ADPKD: lessons from animal models. *Nat. Rev. Nephrol.* 10 (10): 587–601.

71 Huang, L., Mokkapati, S., Hu, Q. et al. (2016). Nephron progenitor but not stromal progenitor cells give rise to Wilms tumors in mouse models with beta-catenin activation or Wt1 ablation and Igf2 upregulation. *Neoplasia* 18 (2): 71–81.

72 Cohen, S.M., Ohnishi, T., Clark, N.M. et al. (2007). Investigations of rodent urinary bladder carcinogens: collection, processing, and evaluation of urine and bladders. *Toxicol. Pathol.* 35 (3): 337–347.

73 Ruehl-Fehlert, C., Kittel, B., Morawietz, G. et al. (2003). Revised guides for organ sampling and trimming in rats and mice – part 1. *Exp. Toxicol. Pathol.* 55 (2–3): 91–106.

74 Gaillard, E. (1999). Ureter, urinary bladder, and urethra. In: *Pathology of the Mouse: Reference and Atlas* (eds. R.R. Maronpot GAB and B.W. Gaul). Cache River Press.

75 Gografe, S.I., Sanberg, P.R., Chamizo, W. et al. (2009). Novel pathologic findings associated with urinary retention in a mouse model of mucopolysaccharidosis type IIIB. *Comp. Med.* 59 (2): 139–146.

76 Wells, S., Trower, C., Hough, T.A. et al. (2009). Urethral obstruction by seminal coagulum is associated with medetomidine-ketamine anesthesia in male mice on C57BL/6J and mixed genetic backgrounds. *J. Am. Assoc. Lab. Anim. Sci.* 48 (3): 296–299.

77 Ward, C.S., Huang, T.W., Herrera, J.A. et al. (2016). Loss of MeCP2 causes urological dysfunction and contributes to death by kidney failure in mouse models of Rett syndrome. *PLoS One* 11 (11): e0165550.

78 Liu, J., Sun, L., Shen, Q. et al. (2016). New congenital anomalies of the kidney and urinary tract and outcomes in Robo2 mutant mice with the inserted piggyBac transposon. *BMC Nephrol.* 17 (1): 98.

79 Wu, X.R. (2015). Interstitial calcinosis in renal papillae of genetically engineered mouse models: relation to Randall's plaques. *Urolithiasis* 43 (Suppl 1): 65–76.

80 Mo, L., Huang, H.Y., Zhu, X.H. et al. (2004). Tamm-Horsfall protein is a critical renal defense factor protecting against calcium oxalate crystal formation. *Kidney Int.* 66 (3): 1159–1166.

81 Tzou, D.T., Taguchi, K., Chi, T., and Stoller, M.L. (2016). Animal models of urinary stone disease. *Int. J. Surg.* 36 (Pt D): 596–606.

82 Gaillard, E. (1999). Ureter, bladder and urethra. In: *Pathology of the Mouse* (eds. R. Maronpot, G. Boorman and B. Gaul), 235–258. Cache River Press.

83 Gold, L.S., Manley, N.B., Slone, T.H., and Ward, J.M. (2001). Compendium of chemical carcinogens by target organ: results of chronic bioassays in rats, mice, hamsters, dogs, and monkeys. *Toxicol. Pathol.* 29 (6): 639–652.

84 Fantini, D., Glaser, A.P., Rimar, K.J. et al. (2018). A carcinogen-induced mouse model recapitulates the molecular alterations of human muscle invasive bladder cancer. *Oncogene* 37 (14): 1911–1925.

85 Ahmad, I., Sansom, O.J., and Leung, H.Y. (2012). Exploring molecular genetics of bladder cancer: lessons learned from mouse models. *Dis. Models Mech.* 5 (3): 323–332.

19

Female Reproductive System

Darlene Dixon and Alexander Yu. Nikitin
(In Memory of Dr. Joel Mahler)

The purpose of this chapter is to present an overview of the major wild-type and mutant mice with female reproductive phenotypes. This chapter will focus on gonadal phenotypes and will also include mutants whose effect is primarily at the level of the hypothalamus or pituitary leading to changes in reproductive function or structure. Also, models of common women's reproductive tract diseases will be highlighted. Due to the overwhelming amount of literature on these topics, this discussion cannot be totally comprehensive, but rather is intended to give the reader a sense of the diversity of phenotypes that may be found and the variety of pathogenetic mechanisms involved, in addition to their use to model common reproductive health conditions of women [1]. A brief summary of the key anatomical features and chemical mediators of the hypothalamic-pituitary-gonadal axis is presented in the following text, but for further details, the reader is referred to basic texts on these subjects. In addition to the normal anatomy and histology of organs of the female reproductive tract, it is also particularly important for the reader to know the spectrum of background lesions and normal physiologic changes that occur particularly in the mouse female reproductive tract in order to distinguish these changes from possible phenotypic effects of a mutation. For more in-depth coverage of background lesions, the reader is referred to mouse pathology texts, although we feel it important to briefly review the histology of physiologic events such as estrous cycle changes of the ovary, uterus, vagina, and cervix and to review a few background and aging lesions observed in commonly used strains for developing genetically engineered mice. Also, this chapter will outline specific recommendations on tissue collection of female reproductive tract organs, normal gross anatomy and histology observations of non-mutants, fixation, orientation, and a few immunohistochemical labels that can be used to define and differentiate hormone receptors, cell types, and compartments within the female reproductive tract.

In the evaluation of the female mouse, it is appropriate that a distinction is made between the reproductive tract and the reproductive system. The tract itself is composed of those anatomical parts needed for the basic performance of reproductive function occurs [ovary, oviduct, uterus, uterine cervix, and vagina] in the female mouse. However, in the broader sense, the reproductive system is more anatomically diverse and encompasses multiple tissue levels of control and interaction, in particular those involving the hypothalamus and pituitary gland [referred to as the hypothalamic-pituitary-gonadal axis]. The anatomical complexity is matched at the molecular level by the bewildering interactions and feedback mechanisms between numerous hormones and growth factor peptides, mediated by hormonal, autocrine, paracrine, and neurocrine mechanisms, which are essential for proper development and function of this system. Distinctions between the reproductive and endocrine systems also become blurred in view of the fact that the gonads are endocrine organs themselves, producing and responding to the effects of steroid sex hormones, and that the mammalian brain and pituitary are clearly target organs of these hormones [2–4]. The field of sex hormone biology is a particularly dynamic one with a broadening scope, as exemplified by the growing list of extragonadal tissues, such as the heart, adipose in breast tissue, aortic smooth muscle, and vascular endothelium in which estrogen has been shown to be critical for homeostasis [5–7].

The hypothalamus is the interface between the central nervous system and the endocrine system (pituitary). Hypothalamic hormonal factors that act as pituitary releasing or inhibiting factors are delivered to the pituitary by the specialized blood vessels of the hypothalamo-hypophyseal portal system. The anterior pituitary is composed of distinct cell types that produce and secrete various hormones in response to cell-specific hypothalamic factors, and most important to reproductive function are the pituitary gonadotrophs that secrete follicle stimulating hormone (FSH) and luteinizing hormone (LH) [9,10]. FSH and LH collectively called the gonadotropins and are composed of dimers of the common α-glycoprotein subunit with a distinct beta subunit (FSHB and LHB) that confers hormonal specificity. Their release under hypothalamic control is positively mediated by gonadotropin releasing hormone (GNRH).

The gonadotropins act on the gonads to regulate gametogenesis and synthesis of the gonadal sex steroid hormones, which in turn feed back to the hypothalamus and pituitary to modulate FSHB and LHB secretion by means of complex positive and negative feedback loops. Although the rate of

Pathology of Genetically Engineered and Other Mutant Mice, First Edition. Edited by John P. Sundberg, Peter Vogel, and Jerrold M. Ward.
© 2022 John Wiley & Sons, Inc. Published 2022 by John Wiley & Sons, Inc.

gonadotropin secretion by the pituitary is directly modulated by the hypothalamus via GNRH, the blood level of circulating sex steroids produced by the gonads is the most important physiologic determinant of serum gonadotropin levels. It should be noted that in addition to the hormones mentioned, a variety of other locally acting chemical mediators such as growth factors and prostaglandins play an important role in gonadal function by regulating processes of cell proliferation, differentiation, and apoptosis; for review, see [9, 10].

Embryology and Normal Anatomy of Organs of the Female Reproductive Tract

Embryology

The ovary is important for the synthesis of sex steroid hormones and growth factor peptides that impact tissues by autocrine, paracrine, and endocrine mechanisms to act locally or at distant organ sites, in addition to being the site of oocyte development and release. During embryonic development, at approximately 10 days *post coitum* (dpc), the genital ridge [or gonadal primordium], the structural precursor of the ovary emerges as a thickening of the coelomic epithelium that overlays the ventral aspect of the mesonephros in the mouse embryo (for review, see [11]). Primordial germ cells (PGCs) arise from the pluripotent primary proximal epiblast and move through the wall of the hindgut at ~9 dpc into the genital ridge at 10.5–11.5 dpc [12–14]. The PGCs colonize the genital ridges and form clusters that coalesce with somatic pregranulosa cells to form the ovigerous cords, which are loose tubular structures contained by the deposition of a basal lamina that separates the tubules from the stromal compartment [15, 16]. The ovigerous cords persist as nests or clusters of female germ cells that are loosely surrounded by somatic cells. At the time of birth, somatic cells begin to break down the germ cell nests by enclosing individual female germ cells or oocytes, resulting in the formation of primordial follicles [15, 16]. The germ cell nests and the forming primordial follicles localize predominantly to the outer region or cortex of the fetal ovary, similar to what is observed in the adult ovary where the development of follicles occurs mainly in the ovarian cortex. Prenatally, the embryonal oviduct (also known as, uterine tube or Fallopian tube) is composed of an epithelium encompassed by a delicate mesenchyme [17].

Much of the oviduct, uterus, and its cervical region, the upper vagina of the female reproductive tract in mice is derived from the paired tubular paramesonephric (Müllerian), which, similarly to the ovarian surface epithelium, derives from the coelomic epithelium [18]. The male reproductive tract originates from the mesonephric (Wolffian) ducts, which are parallel to the paramesonephric duct during embryonal development (for review, see [19]). It has been conventionally accepted that the Wolffian duct system regresses in females in the absence of the production of anti-Müllerian hormone (AMH) [also known as, Müllerian inhibiting substance, MIS] by Sertoli cells, and testosterone by the interstitial cells of the embryonic testes (for review, see [19]). However, more recently it has been suggested that regression of the Wolffian duct system in female mouse embryos is actively promoted by the transcription factor, chicken ovalbumin upstream promoter transcription factor II [COUP-TFII, Tg(Tek-Nr2f2)1Tsa] and is androgen-independent [20].

Normal Anatomy and Histology

Grossly, the adult ovaries are paired spherical structures located at the caudal end of the kidneys attached dorsally to the abdominal wall by the mesovarium at the hilum region (Figure 19.1). The ovary is entirely encapsulated by the ovarian bursa, which completely isolates it from the peritoneal cavity [21]. The medullary region primarily consists of stromal tissue and connects with the cortex that is comprised of follicles, corpora lutea. The division between the two regions is not always clearly distinct. In general, follicle development occurs mainly in the cortex, and the medulla is where blood vessels, lymphatics, and nerves enter and leave the ovary at the ovarian hilum [17, 21]. The histologic appearance of the ovary in a normal adult mouse varies with the age of the animal and the stage of the estrous cycle. In evaluating the ovary in a normal mouse, there is a range of developing follicles with degrees of atresia that may be observed. In the normal cycling mouse, the ovarian cortex contains follicles that consist of oocytes and surrounding somatic cells including theca and granulosa cells that produce steroids [in a temporal and cell-specific manner regulated by the gonadotropins]. Thecal cells possess the full complement of enzymes necessary for estradiol production, whereas granulosa cells are dependent on thecal-derived androgens as substrates for cytochrome P450, family 19, subfamily A, polypeptide 1 (CYP19A1) activity and conversion to estradiol under stimulation by FSH. Follicle rupture and ovulation occur in response to a surge in gonadotropins, at which time the thecal and granulosa cells differentiate into the corpus luteum, and there is a shift in steroid synthesis towards progesterone. In the adult cycling mouse, multiple follicles mature simultaneously in the ovary and several oocytes are released into the oviduct. One stage is the primordial follicle, which is characterized by an oocyte surrounded by a single layer of flattened pre-granulosa cells and has an outer basal lamina, which may be growing or atretic. Maturing follicles can be further defined by morphologic characteristics as: (i) primary, having a single layer of cuboidal to columnar granulosa cells surrounding the oocyte, (ii) secondary, which have two or more layers of granulosa cells, a theca cell layer and a zona pellucida between oocyte and granulosa cells, (iii) vesicular follicles, which are secondary follicles with fluid-filled spaces that have not coalesced into a single antrum, and (iv) tertiary follicles with an antrum and cumulus oophorus [granulosa cells surrounding oocyte] that forms a stalk extending into the antral cavity [22, 23]. The

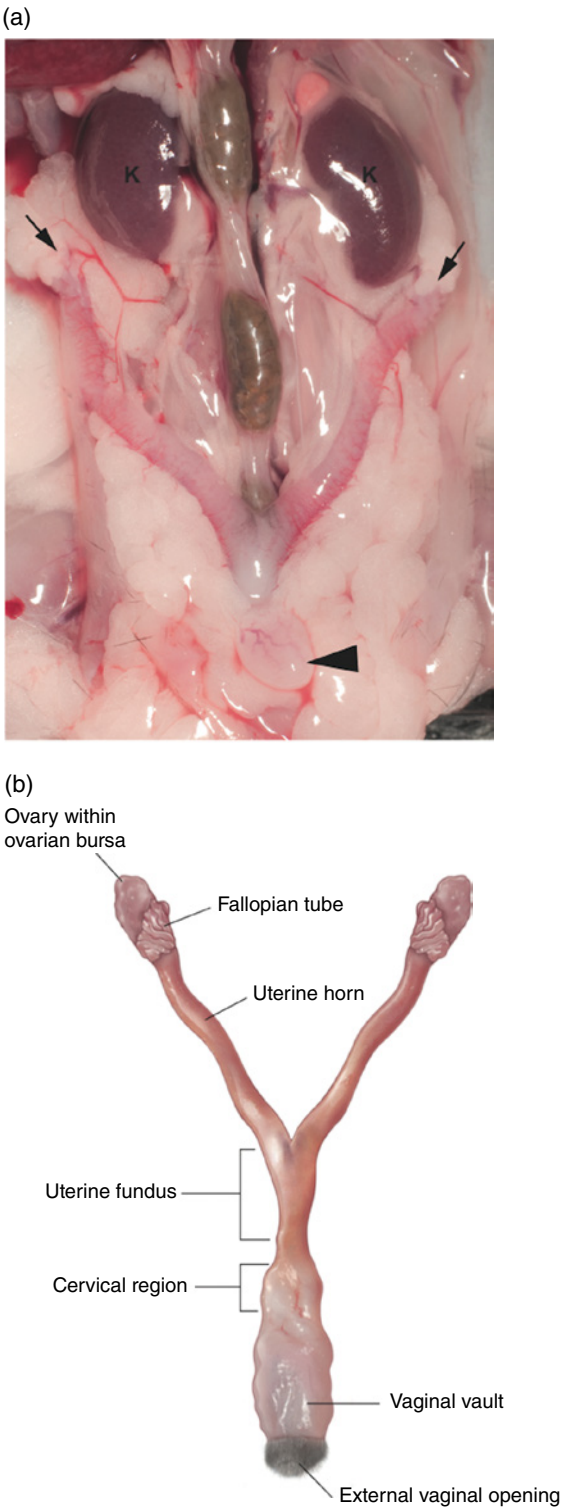


Figure 19.1 Mouse reproductive tract. (a) Mouse reproductive tract *in situ*. Note paired ovaries (arrows) located at the caudal poles of the kidneys (K) embedded in the ovarian fat pad. Paired uterine horns join at the fundus. Urinary bladder (arrowhead) is present. (b) *ex vivo* mouse reproductive tract showing paired ovaries and oviducts, uterus, vaginal vault, and external vaginal opening. Melanosis of uterine fundus can be observed in pigmented mouse strains. Source: Elsevier, Inc., www.netterimages.com. Source: Taken with permission from [17].

aforementioned terminology is considered adequate for evaluation of estrous cycle ovarian changes [see the following text] in rodents and is preferred by International Harmonization of Nomenclature and Diagnostic Criteria (INHAND) [22].

The mouse oviduct is a narrow, complexly coiled tube that transports oocytes and sperm, serves as the site of fertilization, supports early embryonic development, and is necessary for fertility [24]. As mentioned earlier, the oviduct develops from the embryonic Müllerian duct and development and differentiation occurs perinatally [24]. The mesotubarium suspends the oviduct from the dorsal body wall and is continuous with the mesovarium, ovarian bursa, and the uterine mesometrium that connects the uterine horn with the periovarian space [17]. The mouse oviduct consists of distal [the infundibulum and ampulla with ampullary–isthmic junction], and proximal [isthmus and intramuscular uterotubal junction] regions [24], in the adult mouse oviduct, the mucosa is folded throughout, more so extensively in the distal region, where the pseudostratified epithelium is being composed of a tall ciliated epithelium less frequent secretory cells marked by abundant eosinophilic cytoplasm, and an admix of intraepithelial T lymphocytes and peg cells. In the isthmus, pseudostratified epithelium contains a larger fraction of secretory cells [24], and simple columnar cells line the uterotubal intramural junction. The lamina propria of the oviduct is composed of a thin connective tissue layer, and elastic and smooth muscle [17].

Mice have a bicornuate uterus (Figure 19.1) consisting of two uterine horns that join distally into a single corpus (body). The rodent uterus is suspended from the dorsal body wall by the mesometria, which are heavy broad ligaments carrying blood and lymphatic vessels, as well as abundant nerves. The uterine body has a fundus and a cervix that is comprised of a single canal that protrudes into the vaginal opening [17]. The uterine horns join at the corpus and the columnar epithelium of the endometrium gradually changes to stratified squamous epithelium. The entire corpus and cervical canal are lined by stratified squamous epithelium that is continuous with the vaginal mucosa. The corpus has a more fibrous lamina propria compared with the uterine horns. The wall of the corpus consists of circular and longitudinal smooth muscle bundles surrounded by a serosa. The vaginal and cervical epithelium undergoes cyclic changes in thickness and morphology with phases of the estrous cycle. The myometrium is composed of smooth muscle cells that form an inner circular layer, an outer longitudinal layer separated by a highly vascularized middle oblique layer, called the stratum vasculosum [17]. The serosa lines the outer surface of the uterus and is continuous with the mesometrium.

Normal Estrous Cycle Changes

Histologic evaluation of the ovary is important in determining the pathologic changes in the female reproductive tract. When evaluating changes in the female reproductive organs it is often important to evaluate all organs including the

uterus, uterine cervix, and vagina in addition to the ovary. Additionally, it is prudent to remember in sexually mature mice, the female reproductive tract is consistently undergoing physiologic changes responding to sex steroid hormones during the normal estrous cycle. The rodent estrous cycle occurs every 4–5 days, and is subdivided in four subsequent phases, proestrus, estrus, metestrus, and diestrus [22]. It is not necessary to record the stage of the estrous cycle for routine screening; however, it is imperative that the pathologist evaluate tissues of the female reproductive tract with an awareness of normal cyclicity and an understanding of the morphologic features, representative of each phase so that deviations from normal can be detected [22]. Additionally, it is imperative to know the normal anatomy and histology of the cycling female mouse in order to detect ovarian phenotypes of mice with genetic mutations. In genetically altered mice, mutations can affect embryonal differentiation of the ovary, primordial follicle formation, follicular maturation, atresia, ovulation, and corpus luteum formation [25].

In the cycling ovary, follicles are numerous in all stages of the estrous cycle; however, large maturing tertiary follicles are most abundant in proestrus and disappear in estrus as a result of ovulation [17, 22]. During estrus there an absence of tertiary follicles with presence of smaller vesicular follicles is often observed. During metestrus there are numerous growing follicles of various stages present, whereas in diestrus there are more tertiary follicles present although they are smaller than those observed in proestrus before ovulation. Following ovulation, granulosa cells hypertrophy become luteinized (lutein cells) and become new corpora lutea and in a single ovary corpora lutea from several generations of ova may be seen. Immature or new corpora lutea are more basophilic and smaller in size and observed at the beginning of estrus, whereas mature corpora lutea are large and more eosinophilic cells arranged in cords around small sinusoids are often observed in proestrus and older [22].

In the cycling adult mouse uterus, the endometrium consists of endometrial epithelium and endometrial stroma. Endometrial epithelium is composed of simple columnar epithelium lining the uterine lumen (luminal epithelium) that connects with branched tubular glands (glandular epithelium) that are both responsive to sex steroid hormones, cytokines, and growth factors, although the effects are not as dramatic as observed in the vagina. The endometrial stroma may be loosely arranged and is composed of polyhedral small polyhedral cells with basophilic nuclei. During different stages of the estrous cycle, the uterus may become distended with fluid as observed during proestrus and the epithelium may show increased mitosis, or the epithelium may show evidence of apoptosis as observed during estrus, or both apoptosis and increased mitosis as seen with metestrus or inactive glands lined by low cuboidal epithelium as seen in diestrus in response to fluctuating levels of estrogen and progesterone [22]. Inflammatory cell infiltrates may also be observed in the endometrial stroma in addition to the myometrium of the uterus during proestrus and estrus. With the exception of the Spiny mouse [26, 27], mice do not shed the endometrium (menstruate) as occurs in humans.

In the cycling vagina, the epithelium is thickest during late diestrus, proestrus, and estrus and also contains a leukocytic infiltrate; for review, see [22]. The cells become cornified during late proestrus and estrus and these cells slough during metestrus. The epithelium is thinnest at the end of metestrus and the beginning of early diestrus. During late diestrus, the superficial cells begin to demonstrate clear cytoplasm containing mucus, which begins to form a distinct mucified layer during proestrus.

Biological Characterization of a New Mutation of Female Reproductive Tract

A thorough characterization of a phenotypic effect of a mutation requires a systematic review of sufficient numbers of mutant and control mice. Mice should be collected at specific ages and tissue samples collected over a period of time. Time periods to consider for sampling reflect when major changes occur in the lifespan of a mouse are: (i) at weaning [PND21 to PND28]; sexual maturity [PND42 to PND56]; mature adult [3–6 months]; middle aged [10–14 months] and reproductive senescence/middle aged [10–14 months]; and geriatric stages [18–24 months]. These major lifespan changes can have an impact on the phenotype induced by a mutation.

Collection of the Female Reproductive Tract Organs (Ovary/Oviduct/Uterus/Uterine Cervix and Vagina)

During necropsy of the female reproductive tract, attention should be given to examination of external genitalia and genital orifices as well as internal organs as detailed by the National Toxicology Program in their reproductive and developmental toxicity specifications [28]. All lesions, abnormalities, or malformations should be thoroughly evaluated. In describing observed phenotypes, descriptions and recordings should include the location of the abnormality, whether it is unilateral or bilateral, or complete or partial. Also, some malformations or lesions may be difficult to detect, especially in young animals, therefore careful comparisons to a known age-matched control may be necessary. The examination of the female reproductive tract should be done very carefully and thoroughly, especially when defining new genetically induced phenotypes.

The uterus, cervix, vagina, oviduct, and ovaries should be removed *en masse*. Each ovary with intact bursa, oviduct, and a tip of the uterus should be removed from each uterine horn (Figure 19.2). The ovaries should be embedded whole so that they can be sectioned parallel to their long axis [29]. For routine developmental and reproductive toxicology (DART) studies, when sectioning with a microtome, collect a first full-face section at approximately one-third of the way into the ovary. If needed, the residual ovarian tissue can be sectioned for ovarian follicle counts. As for the uterus, cervix, and vagina, they

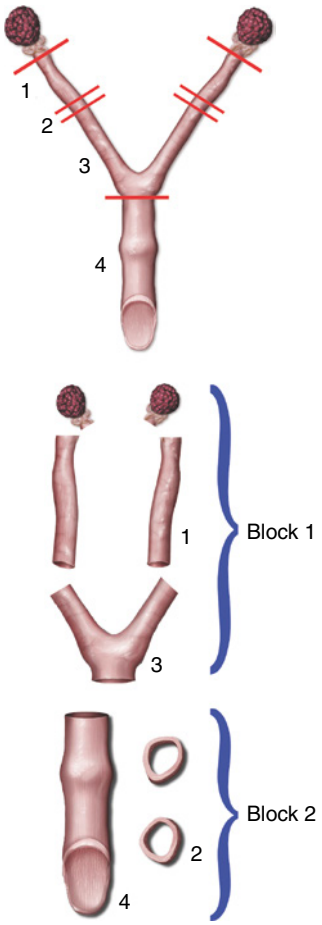


Figure 19.2 Protocol for longitudinal and cross sections of uterine tissue. Protocol for removal of the rodent ovaries and uterus, which obtains sections of the ovary, ovarian bursa, and oviduct in addition to longitudinal sections of the two free portions of uterine horn (1), two transverse sections of uterine horn (2), and a longitudinal section of uterine body (3) with attached portions of uterine horn, in addition to longitudinal sections of the uterine cervix and vagina (4). The sections are grouped into blocks 1 and 2 for sectioning.

should be mounted *en masse* on cardboard prior to fixation. For trimming, the cervix and vagina should be separated from the uterine horns immediately posterior to the uterine corpus. The uterine horns should be bisected at their midpoint and one transverse section from the midpoint of each horn should be collected (Figure 19.2). Embed the ovary, including intact bursa, oviduct and tip of uterine horn with the uterine body with attached portions of uterine horn and the two free linear portions of uterine horn in a single block (block 1) such that longitudinal sections of uterine tissue shall be presented for microscopic evaluation. Embed the cervix and vagina (as one piece) and the two transverse uterine sections in a second paraffin block (block 2) such that a longitudinal section of the cervix/vagina and cross sections of the uterine horns shall be presented for microscopic evaluation.

Special Stains for the Ovaries, Uterus, Cervix, and Vagina

The female reproductive tract is typically and routinely evaluated microscopically using hematoxylin and eosin-stained tissue sections. Many steroid hormone receptors in the cellular compartments of the ovary, uterus, and vagina (ESR1, ESR2, PGR) and transcription factor or glycoprotein markers of oviductal and endometrial epithelia (PAX8, FOXJ1, FOXA2, TACSTD2 [formerly TROP2]) can be identified using immunohistochemical staining and are listed in Table 19.1.

Spontaneous or Induced Mutant Phenotypes of the Gonads and Receptors

From the complex interdependent relationships outlined earlier, it is apparent that reproductive phenotypes may result from genetic manipulations affecting any one of the cellular or biochemical components of the hypothalamic-

Table 19.1 Common immunohistochemical markers.

Antibody	Target	Target cell type	References
ESR1	Steroid hormone receptor	Nucleus–**uterus**, epithelial; stromal; myometrial; **Oviduct**, epithelial; **Ovary**, granulosa; stromal	[30] [31] [32]
ESR2	Steroid hormone receptor	Nucleus–**ovary**, granulosa	[32]
PGR	Steroid hormone receptor	Nucleus–**uterus**, stromal; myometrial; epithelial; **Ovary**, theca; granulosa; stromal	[33] [34]
PAX8	Transcription factor	Nucleus–**uterus,** luminal and glandular epithelium; **Oviduct**, secretory cells	[35, 36]
FOXJ1	Transcription factor	Nucleus–**oviduct**, ciliated cells	[37]
TROP2	Transmembrane glycoprotein	Cell membrane and cytoplasm–**uterus**, luminal epithelium	[35]
FOXA2	Transcription factor	Nucleus–**uterus**, glandular epithelium	[35]

pituitary-gonadal axis. A review of the major phenotypes of spontaneous or induced mouse mutations in the literature permits a broad categorization into (i) steroid receptor-deficient mice, (ii) mutants with altered pituitary gonadotroph function, (iii) mutants with defective steroidogenesis, (iv) growth factor mutations, (v) mutations causing germ cell aplasia, (vi) mutations affecting gonadal apoptosis, and (vii) neoplastic gonadal phenotypes. Major examples in each of these categories are discussed in the following text and listed in Table 19.2.

Sex Steroid Receptor Deficient Mice

The proper function of the reproductive system is governed to a large degree by the gonadal sex steroid hormones, acting in concert with the peptide hormones of the anterior pitui-

Table 19.2 Major genetic alterations affecting gonadal structure or function.

Genetic alteration	Phenotype	References
Gnh1^{hpg}	Defective GNRH; hypogonadism	[38, 39]
Kitl (formerly Steel factor (*Stl*) and *Kit* (formerly Dominant white germ cell aplasia spotting (*W*)	Germ cell aplasia	[40]
Esr1 disruption	Disrupted mating behavior, lack of ovulation, hypoplastic uterus	[41, 42]
Esr2 disruption	Reduced ovulation	[42]
Esr1 and *Esr2* disruption	Infertile, follicles trans differentiate to seminiferous-like tubules, hypoplastic uterus	[41, 43]
Esr1$^{-/-}$-*Rosa26*$^{+/lslESR1}$-Tg(Cga-cre) disruption	Severe hemorrhagic and cystic ovaries	[44]
Pgr	Impaired ovulation	[45, 46]
Pgrmc1$^{tm1.1Ijp}$ / *Pgrmc2* $^{tm1.1Ijp}$	Infertility/subfertility, uterine cysts	[47, 48]
Fshb^{tm1Zuk} disruption	Impaired ovarian folliculogenesis	[49]
Fshrt^{m1Saco} disruption	Impaired ovarian folliculogenesis	[50]
Tg(Cga-LHB/CGB)94Jhn overexpression	Cystic ovaries; granulosa cell tumors	[51]
Prl disruption	Multiple (female)	[52, 53]
Cga^{tm1Sac} disruption	Hypogonadism	[54]
krox-24 disruption (*NGFI-A, Egr-1*)	Hypogonadism	[55, 56]
Nr5al (formerly *SF-1*) disruption	Female differentiation only due to lack of testosterone; gonadal and adrenal aplasia; absence of ventromedial hypothalamic nucleus	[57]
Wt1 disruption	Germ cell aplasia	[58]
Cyp19a1 disruption	Impaired ovulation	[59]
Igf1 disruption	Impaired ovarian folliculogenesis	[60, 61]
gdf-9 disruption	Impaired ovarian folliculogenesis	[62, 63]
Inha disruption	Hypogonadism; gonadostromal tumors	[64, 65]
Acvr2a^{tm1Zuk} disruption	Hypogonadism	[65]
Fst over- expression	Impaired ovarian folliculogenesis; seminiferous tubule degeneration	[66]
Ptgs2 (synonym *Cox2*) disruption	Impaired ovulation	[67, 68]
Cebpb disruption	Impaired ovulation	[69]
Sod1 disruption	Impaired ovulation	[70]
Bcl2 overexpression	Enhanced folliculogenesis; increased ovarian teratoma frequency	[71]
Bax disruption	Decreased ovarian follicular atresia	[72]
Tag overexpression	Ovarian granulosa cell tumors	[73]
mos disruption	Parthenogenesis; ovarian teratomas	[74, 75]
Lats1 disruption	Ovarian stromal cell tumors	[76]

tary gonadotrophs. The biologic effects of the sex steroid hormones are mediated by receptor proteins that have great specificity and high affinity for their respective steroid ligands. In the reproductive tract, the classical estrogen receptors (ESR1, ESR2) and the progesterone receptor (PGR) that are members of the nuclear receptor superfamily that includes the receptors for the sex and adrenal steroids, thyroid hormones, retinoids, vitamin D_3, and eicosanoids [77] [for review, see [78]]. These receptors are intracellular proteins acting as nuclear transcription factors, i.e. upon binding with the ligand they will be activated and result in transcription/translation of specific gene products and ultimately a cellular or tissue response. Considerable understanding of the role of hormones and their receptors in homeostasis of the reproductive tract has been derived from studies of mice that are deficient for these receptors. The action of estrogen as mediated by its receptor (ESR1) is arguably the most well characterized model of hormone receptor biology today. Decades of study on the role and mechanism of estrogen action preceded the development of the first genetically engineered mouse with a targeted disruption of the ERα gene [79]. The discovery of a second type of classical estrogen receptor, ESR2, and generation of mice deficient for this protein added further complexity to the field [80]. The two receptors are not isoforms of one another, but instead are distinct proteins encoded by separate genes on different chromosomes and with variable expression patterns. As summarized in the following text (for review, see [81]), studies with $Esr1^{tm3.1Ksk}/Esr1^{tm3.1Ksk}$ null mice have demonstrated numerous requirements for this protein in estrogenic action, in contrast to $Esr2^{tm1Unc}/Esr2^{tm1Unc}$ null mice that have shown no responses mediated solely by ESR2, indicating that ESR1 is the major biologically active form. There are also estrogen receptors that are membrane-associated and thought to be responsible for quick estrogenic signaling effects that occur in a matter of minutes and are grouped as receptors involved in activating nongenomic pathways in response to estrogen (for review, see [82]). The G protein-coupled estrogen receptor (GPER1, also originally known as GPR30; GPER) is one such receptor and is shown to be activated by estrogen (for review, see [83]). Deletion of GPER1 in $Gper1^{tm1.1Lmlf}$ mutant mice interferes with glucose tolerance, blood pressure parameters, and bone growth [84]; however, a reproductive tract phenotype does not appear to be apparent in female $Gper1^{tm1.1Lmlf}$ null mice [85]; for review, see Langer et al. [86]. $Gper1^{tm1.1Lmlf}$ mice also exhibit multiple adverse physiologic and metabolic diseases, which include obesity, cardiovascular dysfunction, insulin resistance, and glucose intolerance, in addition to a lack of estrogen-mediated responses in many tissues of $Gper1^{tm1.1Lmlf}$ mice; for review, see [82, 83].

Estrogens are not required for differentiation and initial development of the female reproductive tract (in contrast to testosterone which is essential to male differentiation); therefore ERα-deficient female mice have properly developed reproductive tracts. However, the estrogen insensitivity rendered by *Esr1* disruption does result in abnormal morphologic phenotypes in the ovary, uterus, and vagina of adult female ESR1 targeted mutant mice. The characteristic phenotype of the female ESR1 targeted mutant mouse reproductive tract is the presence of an ovary with numerous cystic and hemorrhagic follicles (Figure 19.3). Growing follicles are present but corpora lutea are notably absent, indicating follicular arrest and anovulation. Thecal cells are hypertrophied, consistent with stimulation by LHB, and elevated levels of this hormone are found in these mice. Increased LHB is likely due to increased serum estradiol concentrations and loss of normal hypothalamic-pituitary feedback inhibition controls. In aging ESR1 targeted mutant females, there is an approximately 40% incidence of ovarian granulosa cell tumors that may be related to the chronic overstimulation of follicle cells by estradiol or gonadotropins. When *Esr1*is reintroduced and exclusively expressed in the pituitary, $Esr1^{-/-}$-$Rosa26^{+/lslESR1}$-Tg(Cga-cre), of global ESR1 targeted mutant females, the mice (called PitERtgKO) show a more severe hemorrhagic and cystic ovarian phenotype compared with ESR1 targeted mutant littermates [44] (Figure 19.3).

The estrogen receptor is detectable in all components of the rodent uterus (epithelium, stroma, and myometrium) during early development, through puberty, and into adulthood. However, responses to estrogen, as measured by increases in uterine weight, cannot be seen until after weaning. Therefore, sexual maturation of the uterus is marked not only by the presence of ER but also by the acquisition of the capacity to respond to estrogen-induced signals for proliferation and differentiation. The requirement for a functioning ESR1 signaling pathway for sexual maturation of this tissue is indicated by the finding of hypoplastic uteri in female ESR1 targeted mutant mice, with reductions in both endometrial and myometrial compartments (Figure 19.4). Likewise, the requirement for this pathway for mitogenic and stimulatory uterine responses to estrogens is demonstrated in multiple studies in which there is failure to evoke agonist activity in ESR1 targeted mutant mice treated with estrogenic compounds. Similar to the uterus, the vagina is a highly sensitive estrogen target tissue that undergoes cyclic effects in response to the ovarian cycle and estradiol levels. The characteristic changes of vaginal mucosal estrogenization, such as stratification and cornification, are absent in ESR1 targeted mutant females, despite elevated serum levels of estradiol or administration of exogenous estrogens [87]. Reproductive phenotypes in ESR2 targeted mutant mice are not readily apparent morphologically. However, continuous mating studies have indicated a deficit in fertility that at present is attributed to ovarian dysfunction. Studies with $Esr2^{tm1Unc}$ females superovulated by administration of gonadotropins have indicated diminished ovulatory capacity. However, normal physiologic responses to estrogen are maintained in the uterus and vagina of ESR2 targeted mutant females, indicating that ESR1 is the predominant form responsible for mediating estrogen actions in these tissues. The ESR1/ESR2 targeted mutant females are homozygous null for both *Esr1* and *Esr2* genes and show normal uterine

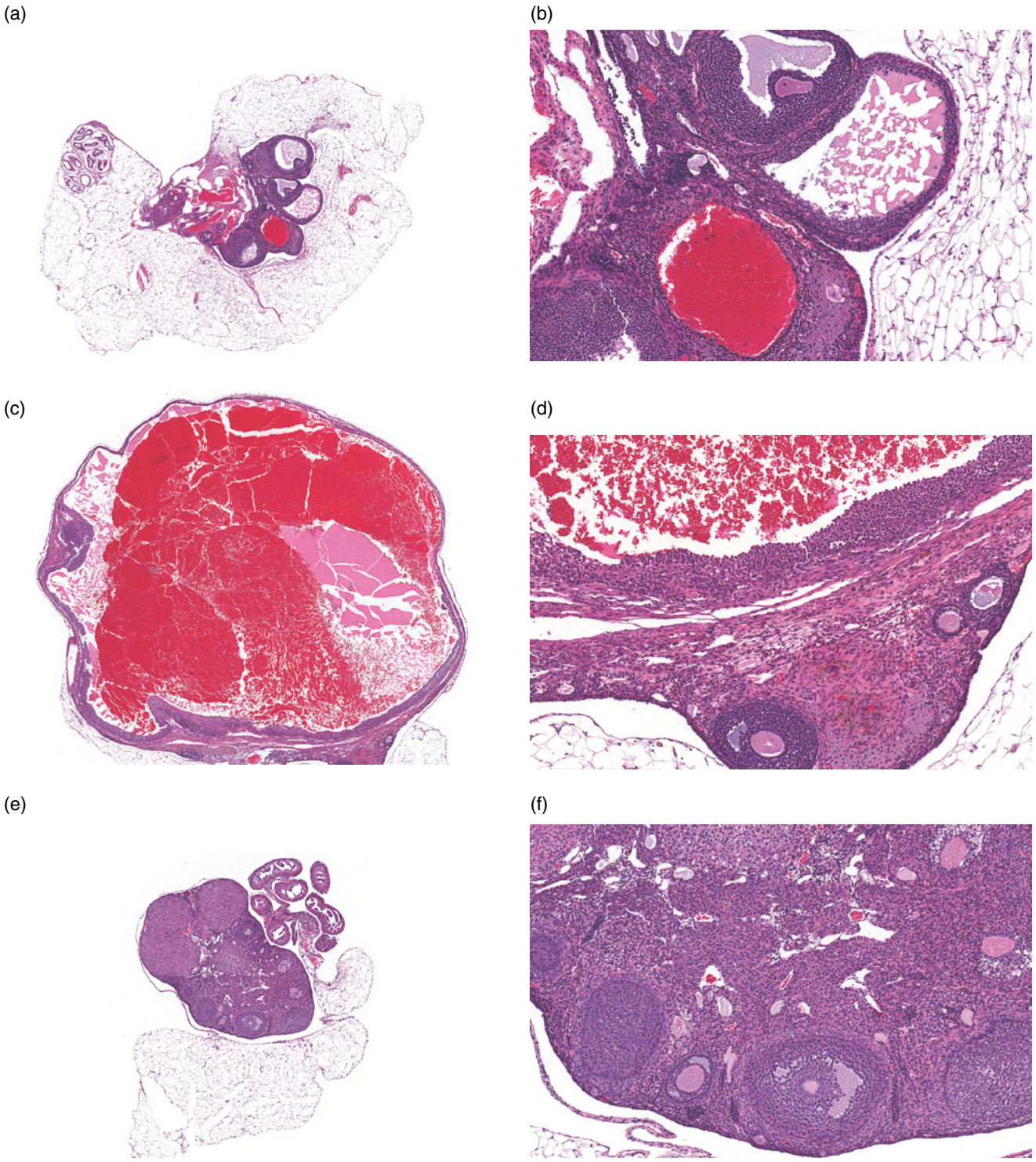


Figure 19.3 Cystic and hemorrhagic ovaries from *Esr1*$^{-/-}$-*Rosa26*$^{+/\text{lslESR1}}$-Tg(Cga-cre) (known as PitERtgKO) mice (A-D). Note, hemorrhagic and cystic ovarian follicles in an *Esr1*$^{-/-}$-*Rosa26*$^{+/\text{lslESR1}}$ mouse (a and b) and increased severity of changes in a PitERtgKO mouse (c and d). Also note, normal ovarian follicle development in a PitERtg wild-type mouse (e and f). Source: Scanned slides courtesy of Drs. Yukitomo Arao and Katherine J. Hamilton, NIEHS [44].

development; however, the uteri are hypoplastic similar to ESR1 targeted mutant mice, are insensitive to estrogen, and are infertile or subfertile [43]; for review, see Hewitt et al. [81]. Ovarian phenotypes consist of follicles that show trans-differentiation to structures resembling seminiferous tubules of the testis [41].

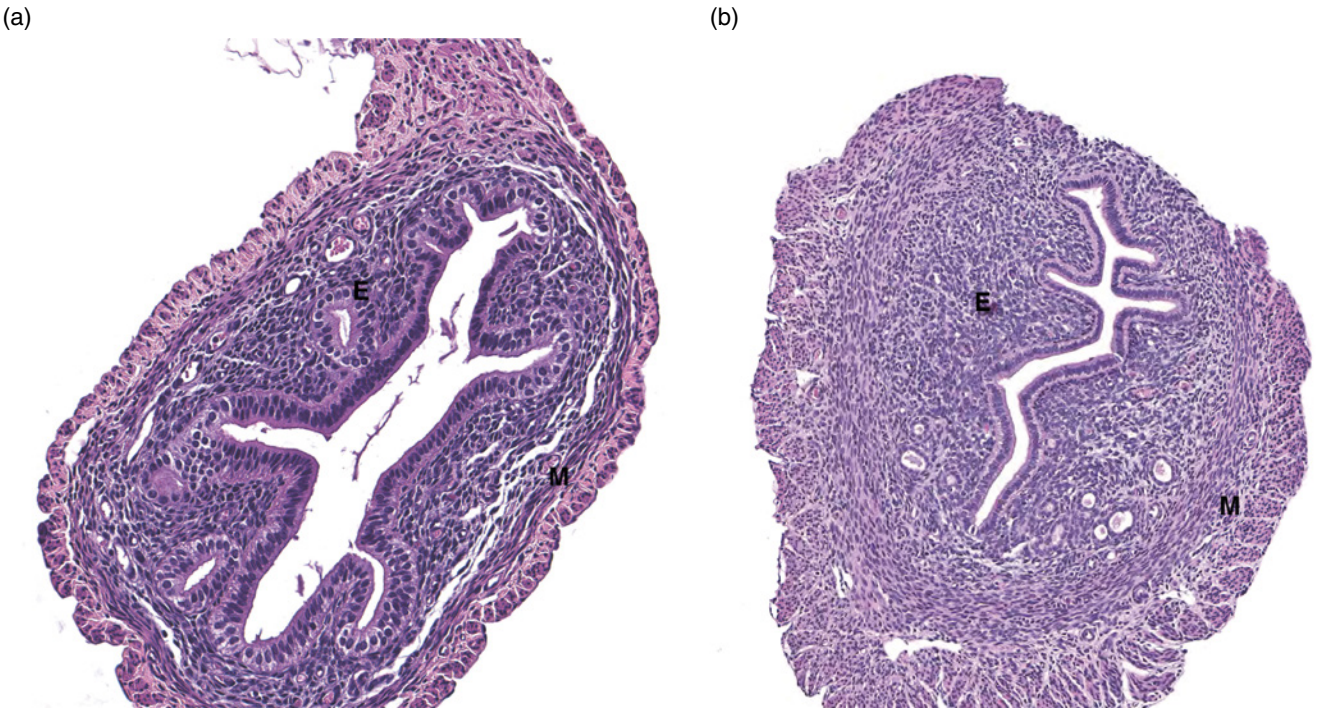


Figure 19.4 Hypoplastic uterus from an *Esr1*$^{tm3.1Ksk}$/*Esr1*$^{tm3.1Ksk}$ mouse. (a) ESR1 targeted mutant mouse showing atrophied endometrial (E) and myometrial (M) compartments compared to a uterus from an ESR1 wild-type mouse (b). Note reduction in both endometrial and myometrial compartments of the uterus in the ESR1 targeted mutant mouse. Source: Images courtesy of Dr. Sylvia Hewitt, NIEHS.

Another receptor-deficient mouse that has contributed insights into the field of reproductive biology is the classical PGR mutant [45]. Viability and sexual differentiation are not affected by the loss of PGR. However, homozygous null females are completely infertile. The uteri of PGR targeted mutant females develop normally and have normal architecture. However, as expected from the known role of progesterone in preparation of the uterus for pregnancy, the process of induced decidualization is completely abrogated in these mice. Furthermore, an ovarian phenotype develops after superovulation, similar to that of the ESR2-deficient ovary, characterized by numerous preovulatory but unruptured follicles, indicating roles for progesterone in ovulation and luteinization that were previously unsuspected. Hormonal characterizations of PGR-deficient mice have revealed dysregulation of gonadotropin secretions and resultant inability to effectively recognize ovulatory signals [46]. In addition to the classical PGR mutants, conditional ablation of the non-classical PGR membrane component 1 or 2 (i.e. *Pgrmc1*$^{tm1.1Jjp}$ and/or *Pgrmc2*$^{tm1.1Jjp}$) from female mouse reproductive tissues resulted in subfertility/infertility secondary to a possible lack of normal nutrient production within the decidua and transport to the embryo with loss of normal uterine histomorphology due to formation of uterine cysts [47, 48].

Mutants Affecting Pituitary Function

Normal reproductive function is clearly dependent on the release of pituitary hormones, in particular the gonadotropins, FSH and LH. In addition, although the pituitary hormone prolactin (PRL) is more closely related to growth hormone (GH) than the gonadotropins, and is primarily considered to be mammotrophic, numerous other functions have been attributed to this multifaceted hormone, including ones involved in gonadal homeostasis [52]; for review, see [88]. Therefore, abnormal reproductive phenotypes may result from mutations involving the production or action of either the pituitary gonadotropins or PRL. Spontaneous mutations demonstrated this fact prior to genetic engineering experiments. The first spontaneous endocrine mutant described was the autosomal recessive mutation Snell dwarf (*dw*), the locus of which was identified as encoding for a nuclear transcription factor (POU domain, class 1, transcription factor 1 (*Pou1f1*) formerly called *Pit1*), that activates the transcription of *Gh*, *Prl*, and *Tshb* genes [89]; for review, see [90]. Reproductive phenotypes in this mutant are likely associated with PRL deficiency. Another dwarf mouse, which has a recessive mutation a gene coding for the transcription factor termed paired lied homeodomain factor 1(PROP1, formerly called Prophet of Pit-1), is named the Ames dwarf (*Prop1*$^{df/df}$) mouse, which have the endocrine abnormalities as Snell dwarf mice, although the mutation is in another gene that is also involved in the differentiation of somatotrophs, thyrotrophs, and lactotrophs [91, 92]. Dwarf mice have retarded growth, are sterile due to luteal failure, and have extended longevity [92].

The spontaneous hypogonadal (*Gnrh1*^{hpg}) mutation [38] is an autosomal recessive mutant allele that proved to code for a

partial deletion of the gene for hypothalamic gonadotropin releasing hormone 1, GNRH1 [39]. The result of homozygosity for the *Gnrh1*^{hpg} allele is the production of a truncated mRNA and translation of an inactive GNRH1 peptide. Pituitary gonadotrophs are not stimulated to synthesize or release adequate amounts of LH and FSH. Consequently, the *Gnrh1*$^{hpg/hpg}$ females have infantile gonads throughout life and no detectable gonadal sex steroids [93]; for review, see [94].

A critical structural component of the pituitary glycoprotein hormones is the α-subunit, and disruption of this gene leads to infertility, hypogonadism, and hypothyroidism due to the absence of FSH, LH, and TSH [54]; for review, see [9]. Targeted inactivation of the gene for the early growth response 1 (*Egr1*, formerly called *A530045N19Rik*, *Egr-1*, *ETR103*, *Krox-1*, *Krox24*, *Krox-24*, *NGF1-A*, *NGFIA*, *NGFI-A*, *TIS8*, *Zenk*, *Zfp-6*, *Zif268*) leads to the inability of gonadotropes to synthesize the LHB, with resulting infertility of female mutant mice due to thyroid and ovarian dysfunction [55, 95]; for review, see [56]. To study the function of FSHB alone, mice deficient in this hormone were generated [49] and revealed infertile females due to a block in folliculogenesis prior to antrum formation and age-related hypertrophy of the uterus and ovary has been reported in FSHB subunit targeted mutant mice [96]. Overexpression of LH in transgenic mice leads to a phenotype of multiple hemorrhagic ovarian cysts, polycystic ovaries, and granulosa cell tumors [51]; for review, see [9], similar to that described earlier for ESR1 targeted mutant females [97].

Mice with null mutations of the PRL receptor (Prlr) gene have been generated [52]. In addition to the expected defects in mammary gland development and lactation, PRL-deficient females also exhibit multiple reproductive abnormalities in ovulation and embryo implantation; for review, see [53].

Mutants with Defective Steroidogenesis

Because of their essential roles in reproduction and many other diverse functions, the mechanisms that regulate the biosynthesis of steroids have been the subject of considerable study. One approach has been to study the cytochrome P450 steroid hydroxylases that catalyze most of the reactions in the steroidogenic pathways. Two notable examples of genetically engineered mouse models for this purpose are mice with targeted disruptions of the *Nr5al* (formerly called SF-1) and aromatase genes. NR5A1 is a nuclear hormone receptor and transcription factor that regulates the coordinated expression of the steroid hydroxylases within steroidogenic cells [57]; for review, see [98]. Consistent with their inability to synthesize steroids, NR5A1-deficient mice die shortly after birth, and all exhibit female sexual differentiation due to lack of testicular androgens. More unexpectedly, however, these mice also exhibit absence of the gonads, defects of pituitary gonadotroph function, and failure of the ventromedial hypothalamic nucleus to develop, revealing essential roles of NR5A1 in the development of the gonads and at all three levels of the hypothalamic-pituitary-gonadal axis. The role of NR5A1 in postnatal development has been not been fully explored; however, there is evidence that NR5A1 play a role in ovarian granulosa cell proliferation [99].

Aromatase (CYP19A1) catalyzes the final step in estrogen biosynthesis, and disruption of this gene is another approach to studying estrogen function by removing the source of the hormone rather than neutralizing its action as done by receptor-deficient mice [59]. CYP19A1 targeted mutant females have an ovarian phenotype of arrested folliculogenesis that has some similarities to that of ESR1 targeted mutant mice described previously. The phenotype is thought to be age-dependent and by 21–23 weeks of age mice have hemorrhagic and cystic ovarian follicles, and by 1 year the follicles are abnormal with absence of secondary and antral stages, and atretic primary follicles [100].

Growth Factor Mutations

Targeted manipulations of diverse growth factor genes are revealing their roles in reproduction. For example, various growth factors have been implicated as mediators of estrogen action, and this has been supported by studies with mutant mice such as those lacking the EGF receptor (EGFR) [101] and IGF1 [60], both of which display prominent reproductive phenotypes. The functional relationship between IGF1 and FSH has been examined in detail [60], revealing that IGF1 augments the expression of FSH receptors. Growth differentiation factor 9 (GDF9) is an oocyte-specific member of the TGFB superfamily; female mice with targeted deletions of the *Gdf9* gene are infertile and exhibit a hypogonadal phenotype with primary follicle arrest [62, 63]. Activins, inhibins, and follistatin are structurally related proteins also belonging to the TGFB family and recognized as peptides that stimulate or inhibit FSH production. Correspondingly, reproductive phenotypes and altered gonadotropin levels have been seen in mice that were generated lacking either inhibin or activin receptors [64] or overexpressing follistatin [66]. *Tgfbr1* KO (*Tgfbr1*^{tm1Dgen}) female mice are sterile thought to be secondary to diverticula of the oviduct that interferes with embryo transport and myometrial defects that may also contribute to maintaining a pregnancy [102].

Mutants with Germ Cell Aplasia

These include several spontaneous mutations at the kit ligand (*Kitl*, formerly called Steel factor) and KIT proto-oncogene receptor tyrosine kinase (*Kit*), formerly called Dominant white spotting, loci that may result in absence of germ cells in both sexes [40]. Other mutations at the *Kitl* gene result in ovaries with germ cells but with impaired folliculogenesis presumably due to an intrinsic defect in stromal cells [103]. Multiple roles for Wilm's tumor 1 homolog gene, *WT1*, have been identified in genitourinary development, and failure of gonadal and renal development is seen in *Wt1* null mice, reviewed in [58].

Mutants with Changes in Germ Cell Apoptosis

The fate of most ovarian follicles is atresia, and apoptosis plays a fundamental role in normal follicular atresia. Members of the BCL2 family of proteins may act as either positive or negative regulators of apoptotic cell death, and recent studies have shown that one of these proteins, BAX, is central to ovarian cell death [104]. A dramatic phenotype in *Baxtm1Sjk* females is the presence of threefold excess primordial follicles in their reserve than their wild-type female littermates at a young age, and an extended functional lifespan of the ovary, as indicated by recovery of fertilization-competent oocytes and absence of age-related ovarian and uterine atrophic changes in later years [72]. Therefore, BAX deficiency may lead to either increases or decreases in the apoptotic cell death pathway, depending on the cell type or lineage and presumably the composition and context of other BCL2 family members in that particular tissue. A potential role for the BCL2-dependent survival pathway in the ovarian follicle was further elucidated by studies that demonstrated decreased follicle apoptosis and enhanced folliculogenesis in transgenic mice (*Tg(Igk-V21-Bax)196Bvn*) with targeted overexpression of BCL2 [71]. Interestingly, these mice also display increased germ cell tumorigenesis (see the following text).

Phenotypes of Gonadal Neoplasia

Tumors of the reproductive system are relatively uncommon phenotypes in genetically altered mice [73]. Generally, a strong oncogenic stimulus is required, such as the large T antigens [108] of the SV40 and polyomaviruses. Expression of these oncogenes may be directed to the gonads by the use of promoters for genes endogenous to that tissue, such as that of the mouse *Inhba* gene. The *Inhba* gene is expressed in ovarian granulosa and theca cells and in testicular Sertoli and Leydig cells and functions as a feedback regulator of FSH synthesis in the pituitary. Utilizing an inhibin-α/Tag construct, transgenic mice were generated that developed gonadal tumors (granulosa and thecal cell tumors in females) at 4–9 months of age with a penetrance of 100% [106, 107]. Overexpression of the apoptosis suppression protein BCL2, again directed to the ovary by the inhibin-α gene promoter/enhancer, leads to the development of benign ovarian teratomas [71] presumably related to prolonged survival of ovarian cells. The transformation capacity of Tag is believed to be due to its ability to bind to the cellular tumor suppressor gene, *Trp53* [109]. Therefore, it is not unexpected that mice with disruptions of the *Trp53* gene may also be predisposed to gonadal tumors, as is the case. Malignant teratomas occurred with high incidence in $Trp53^{tm1Brd}$ null mice on the 129/Sv genetic background and with lower incidence in mice with the same genetic disruption on a mixed C57BL/6×129/Sv background [109].

As mentioned previously, inhibins, along with activins, are growth factor peptides that are produced and secreted intragonadally and regulate FSH production. Mice with a targeted deletion of the α-inhibin gene develop normally, but develop gonadal tumors as early as 4 weeks of age with virtually 100% penetrance in both sexes [64]. Histologically, the tumors are characterized as mixed or poorly differentiated gonadostromal neoplasms. These studies implicate inhibin as a critical intragonadal negative growth regulator and the first secreted protein to have been identified with tumor-suppressor activity.

Prolonged stimulation by gonadotropins is believed to contribute to ovarian cancer, and FSH dysregulation may contribute partly to the ovarian tumor phenotype in the inhibin-deficient mice described previously. Further support that hypergonadotropin stimulation plays a role in the development of ovarian granulosa cell tumors in the mouse is found in the increased incidences of this tumor seen in transgenic mice with overexpression of the *Lhb* subunit gene [51] and in ESR1 targeted mutant mice [7], both of which have significantly elevated levels of LH.

Another gene with tumor suppressor activity in the gonad has been described. Disruption of the mouse *Lats1* gene resulted in reduced neonatal viability and impaired fertility in both male and female survivors [76]. By three months of age, ovarian stromal tumors developed in all $Lats1^{tm1Tx}$ females examined. Similar to TRP53, LATS1 is thought to function as a negative cell cycle regulator. The *Mos* proto-oncogene product is implicated in the control of meiotic maturation events during gametogenesis. An unusual phenotype seen in female mice deficient for MOS was pathogenetic activation of the oocyte, as defined by completion of the second meiotic division, extrusion of the second polar body, and pronucleus formation without fertilization [74]. An apparent long-term consequence of this phenotype appearing in older Mos^{tm1Sia} null females was the development of ovarian teratomas at high frequency [75]. Miscellaneous transgenic mouse lines that exhibit gonadal tumorigenesis include female mice with an activated v-Ha--*ras* transgene (*Tg(Hba-x-v-Ha-ras)TG.ACLed*) that develops ovarian yolk sac carcinomas [110].

Miscellaneous Models with Reproductive Tract Phenotypes

Multiple actions of prostaglandins have been implicated in various female reproductive functions, particularly the ovulatory process. The rate-limiting enzyme in prostaglandin biosynthesis is cyclooxygenase [78], and mice deficient for one isoform of this enzyme, (prostaglandin-endoperoxide synthase 2, PTGS2, formerly called COX2), have been found to have ovulatory failure as well as abnormal implantation and decidualization reactions [67, 68]. CEBPB (CCAAT/enhancer binding protein beta) is a transcription factor that is specifically induced in the granulosa cells of antral follicles following LH receptor signaling. Impaired granulosa cell differentiation and ovulation in response to LH is seen in female mice with a null mutation of the *Cebpb* gene [69] and is attributed to failure to downregulate *Cebpb* and *Cyp19a1* genes. A loss of function

mutation in the superoxide dismutase 1, soluble (*Sod1*) gene is associated with reduced gonadotropin levels, lack of ovarian corpora lutea formation, and subfertility [70]. Abnormal ovarian phenotypes are also described in mice deficient for a diverse group of other gene products including cyclin D2 (CCND2) [111], gap junction protein, alpha 4 (GJA4, formerly connexin 37) [112], and vitamin D receptor (VDR) [113] among others; for review, see [114, 115].

Models of Diseases Affecting the Female Reproductive Tract

Models of Polycystic Ovarian Syndrome (PCOS)

Polycystic ovarian syndrome (PCOS) is a reproductive and metabolic disease affecting reproductive-aged women worldwide [116]. PCOS is characterized by two of the following three criteria: clinical or biochemical hyperandrogenism, menstrual dysfunction with anovulation, and polycystic ovary (PCO) morphology [117]. Women with PCOS are often obese, insulin-resistant, and at risk for type 2 diabetes and cardiovascular disease. The etiology of PCOS remains unknown, although androgens were considered the main drivers of PCOS, and therefore, androgenization of animals with hormones such as chronic dihydrotestosterone administration is a frequently used approach to induce symptoms and lesions that resemble PCOS [118] (for review, see [119]). However recently, PCOS is viewed as a multifactorial syndrome with metabolic, excessive ovarian hormone production, abnormal insulin signaling with genetic and environmental factors, and oxidative stress components [120].

The ERα null female mouse is used as a transgenic model for PCOS-like lesions and has increased LH levels although the metabolic phenotype has not been fully defined (for review, see [121]). Overexpression of a transgene that encodes for a chimeric LHB results in elevated LH and androgens, with anovulation and a PCO phenotype in female mice [51]. It is hypothesized that chronic prepubertal elevation of LH results in hyperandrogenemia with aberrant sexual development and ovarian changes consisting of precocious antral follicle formation, hypertrophy of the theca-interstitium with large and hemorrhagic cysts [122]. Knockout mice lacking leptin (*Lepr*) and insulin (*Insr*) receptors genes expressed in hypothalamic pro-opiomelanocortin (POMC) neurons (*Insr/LeprPOMC*) show insulin resistance, and female mice have increased serum testosterone levels, degeneration of the ovary with occasional cyst-like ovarian follicles, and reduced fertility [123]; for review, see [121]. The aforementioned models of PCOS are summarized in Table 19.3.

Models of Ovarian Cancer

About 90% of human ovarian cancers are carcinomas. The remaining malignancies are derived from germ cells and sex cord-stromal elements such as granulosa cells, theca cells, fibroblasts, and Sertoli and Leydig cells [151]. Human ovarian carcinomas have been traditionally divided in several types, such as serous, endometrioid, mucinous, clear cell, transitional cell, mixed, undifferentiated, and squamous [151]. However, more recently it has been noted that clinicopathological and molecular features of these neoplasms are more consistent with two broad categories: Type I and Type II [151, 152]. Type I neoplasms include low-grade serious and endometrioid carcinomas, clear cell carcinomas, and mucinous carcinomas. These tumors exhibit low chromosomal instability, rarely contain mutations in tumor suppressor gene *TP53* (mouse *Trp53*), and progress relatively slow. Type II tumors commonly feature *TP53* mutations and frequent alterations of Retinoblastoma 1 (RB1) pathway and are highly aggressive. This group largely consists of high-grade serous carcinoma (HGSC, ~70% of all epithelial carcinoma cases) and somewhat less defined categories of high-grade endometrial carcinoma, undifferentiated sarcoma, and carcinosarcoma. Many of the latter types are likely represent HGSC.

Majority of spontaneous mouse ovarian neoplasms are derived from sex cord-stromal elements, reviewed in [153]. Granulosa cell tumors and thecomas are also routinely observed in mice after chemical induction. These tumors are phenotypically similar to their human counterparts and can also be induced in genetically modified mice. For example, deletion of inhibin leads to gonadal stromal tumors [64]. Expression of SV40 T antigen targeted to the granulosa cells with inhibin α subunit promoter leads to formation of granulosa cell tumors [132].

Many ovarian carcinoma types have been modeled in genetically modified mice and/or cell transplantation systems [154]. These approaches are also complemented by 3D organoid cultures [155, 156]. Consistent with different natural history of the disease, *Trp53* mutations in a combination with inactivation of *Rb1*, *Brca1*, and/or *Brca2*, lead to HGSC [154, 157], while *K-ras* mutations and *Pten* inactivation lead to the initiation of endometrioid ovarian cancer similar to the endometrioid type of human ovarian carcinoma [135, 158].

Studies of ovarian carcinoma pathogenesis are complicated by continuous debates about the cell of cancer origin [155–157, 159, 160]. This has become a particularly important topic for HGSC, the most common and aggressive ovarian carcinoma type responsible for the majority of ovarian cancer related deaths. For an extended period of time, the ovarian surface epithelium (OSE) has been considered the main tissue giving rise to HGSC [151, 161].This view is supported by pathological observations of early atypical lesions in the inclusion cysts lined by the OSE and common location of overt carcinomas in the ovary. OSE role as a cell of origin is also supported by abundant experimental evidence. For example, inactivation of *Trp53* and *Rb1* in the OSE leads to formation of mouse carcinomas closely similar to human HGSC [134] (Figure 19.5). Such carcinomas are characterized by marked cellular atypia, high proliferation rate, expression of typical markers, such as PAX8 and WT1,

Table 19.3 Some major models for studying human female reproductive tract diseases.

Model	Features	References
Polycystic ovarian syndrome (PCOS)		
Genetically modified mouse (GMM)		
Esr1 disruption	Anovulation; absence of corpora lutea; hemorrhagic ovarian cysts; increased LH	[121, 124]
Esr1$^{-/-}$-*Rosa26*$^{+/lslESR1}$-Tg(Cga-cre) disruption	Severe hemorrhagic and cystic ovaries	[44]
Lhb overexpression	Cystic ovaries; hyperandrogenemia; Increased LH, testosterone, leptin and insulin	[51, 121]
Insr/Lepr^{POMC}	Cyst-like follicles; anovulation; increased LH, testosterone, and insulin	[121, 123]
Endometriosis		
Immunocompromised		
Foxn1^{nu}	Lack T cells; compromised B cell function; accepts human endometriotic patient-derived xenografts (PDX)	[125, 126]
Prkdcscid	Lack B and T cells; accepts humanendometriotic PDX	[8, 127, 128]
Rag2	Lack B, T. and NK cells; accepts human tissue-derived, cellular, and immune cell human endometriotic PDX	[125, 129]
GMM		
Pgr disruption	Lack PGR; syngeneic endometriosis model	[130]
Esr1 disruption	Lack ESR1 syngeneic endometriosis model	[131]
Ovarian tumors		
GMM		
Tg(inhα-Tag)	Granulosa cell tumor	[132]
Inha disruption	Gonadal stromal tumors	[64]
SV40TAg under the control of AMHR2 (MISIIR) promoter	Poorly differentiated carcinomas	[133]
Conditional *Trp53* and *Rb1* inactivation by AdCre in ovarian surface epithelium (OSE)	High-grade serous carcinoma	[134]
Conditional *Pten* inactivation and *K-ras* mutation by AdCre in the OSE	Endometrioid ovarian carcinoma	[135]
Conditional *Brca1*. *Brca2*, *Trp53*, and *Pten* inactivation in tubal (oviductal) epithelium (TE) of Pax8-rtTA TRECre mice	High-grade serous carcinoma	[136]
Brca1, *Trp53*, *Rb1*, and *Nf1* inactivation in TE of Ovgp1-iCreERT2 mice	High-grade serous carcinoma	[137]
Immunocompromised		
Expression of c-myc, K-ras, or Akt oncogenes in *Trp53* deficient TVA -expressing OSE	Transplantable ovarian carcinoma	[138]
Endometrial carcinoma		
GMM		
Disruption *Stk11* **(**formerly *Lkb1*)	Endometrial carcinoma	[139]
Pten disruption	Endometrial hyperplasia; endometrial carcinoma	[198]
*P*awr disruption (formerly *Par4*)	Endometrial hyperplasia; endometrial carcinoma	[140]
Terc disruption	*In situ* precursor of Type II serous carcinoma	[141]
Pax8-rtTA TRE-Cre*Trp53*$^{loxP/loxP}$ *Rb1*$^{loxP/loxP}$ Ai9	Serous endometrial carcinoma	[35]

(*Continued*)

Table 19.3 (Continued)

Model	Features	References
Uterine leiomyoma, fibroid		
Immunocompromised		
Foxn1^{nu}	Lack T cells; compromised B cell function; accepts human fibroid patient-derived xenografts (PDX)	[142]
Prkdc^{scid}	Lack B and T cells; accepts humanfibroid PDO	[143]
NOD.Cg-*Prkdc*^{scid}/J	Lack B, T, and NK cells; accepts human 3D fibroid cell culture PDX	[144]
GMM		
Ctnnb1 activation	Uterine leiomyoma; hyperplasia	[145]
Prlhr (formerly *Gpr*10) overexpression	Uterine leiomyoma	[146]
*Med*12, gain of function	Uterine leiomyoma; hyperplasia	[147]
Cervical cancer		
Immunocompetent		
FVB/N	Cervical cancer; murine papillomavirus infection	[148]
GMM		
Tg(KRT14-HPV16)wt1Dh overexpression	Cervical cancer; estradiol supplementation	[149, 150]

formation of ascites, and metastasis into the liver and lung. These observations have been confirmed both in genetically modified mice and in xenograft systems [155, 159, 162].

More recently, it has been proposed that a significant part of HGSC arises from the tubal epithelium (TE) of the uterine tube, also known as the fallopian tube or oviduct [151]. In familial HGSC cases, early atypical lesions, serous tubal intraepithelial carcinomas (STICs) are frequently observed in mutation carriers even without overt malignancies. Consistent with these observations, formation of STICs and HGSC has been reported in mice after inactivation of *Trp53*, *Brca1*, *Brca2*, *Pten*, *Nf1*, and *Rb1* [35, 136, 151, 157, 163] in the tubal (oviductal) epithelium (TE, Figure 19.6). However, frequency of STICs in non-familiar cases is low and is insufficient to explain all sporadic HGSC cases. Furthermore, some STICs found in patients with HGSC represent metastatic implants [164].

Several transcriptome analysis-based studies support a likely OSE origin for a subset of HGSC. It has been reported that a gene signature indicating OSE origin is associated with poor outcomes, and such tumors are both more resistant to chemotherapy and predisposed to a suboptimal debulking surgery as compared with TE-derived HGSC [160]. However, other studies claim that OSE-derived tumors are more similar transcriptionally to a relatively less aggressive proliferative subtype of human HGSC [155, 159]. A likely TE origin for mesenchymal and immunoreactive subtypes of human HGSC has been suggested [137, 159]. A recent study using single TE cell transcriptome analysis inferred that HGSC heterogeneity could be connected to diverse cell states present in TE cell lineages [165]. Based on deconvolution of non-cancer TE cell states, the authors identified an EMT-high molecular subtype, which is similar, but not identical, to a previously described mesenchymal subtype and predicts a poor HGSC prognosis. Inconsistency between reported gene signatures and course of diseases in different studies suggests that current stratifications of HGSC according to their molecular profiles alone are imprecise.

Recent advances in stem cell biology have shown that the phenotype and genetic make-up of HGSC may also depend on the cell differentiation state at the time of cancer-initiating events [29, 161]. This possibility has been directly supported by the discovery of OSE stem cells, which are highly susceptible to the malignant transformation [162, 166]. Several studies suggest that stem cell also exist in the TE [167–171]. However, it remains unclear if such cells have higher propensity to the malignant transformation. Developing of mouse models allowing targeting discrete differentiation states of a particular cell lineage should allow more careful recapitulations of a diverse group of ovarian carcinomas in future.

Models of Endometriosis

Endometriosis has been traditionally characterized as an estrogen-dependent inflammatory disorder characterized by endometrial tissue (glands and stroma) outside the uterus and is attributed to retrograde endometrial fragments that are shed at menses through a fallopian tube lumen [172, 173]. Retrograde menstruation occurs commonly in reproductive

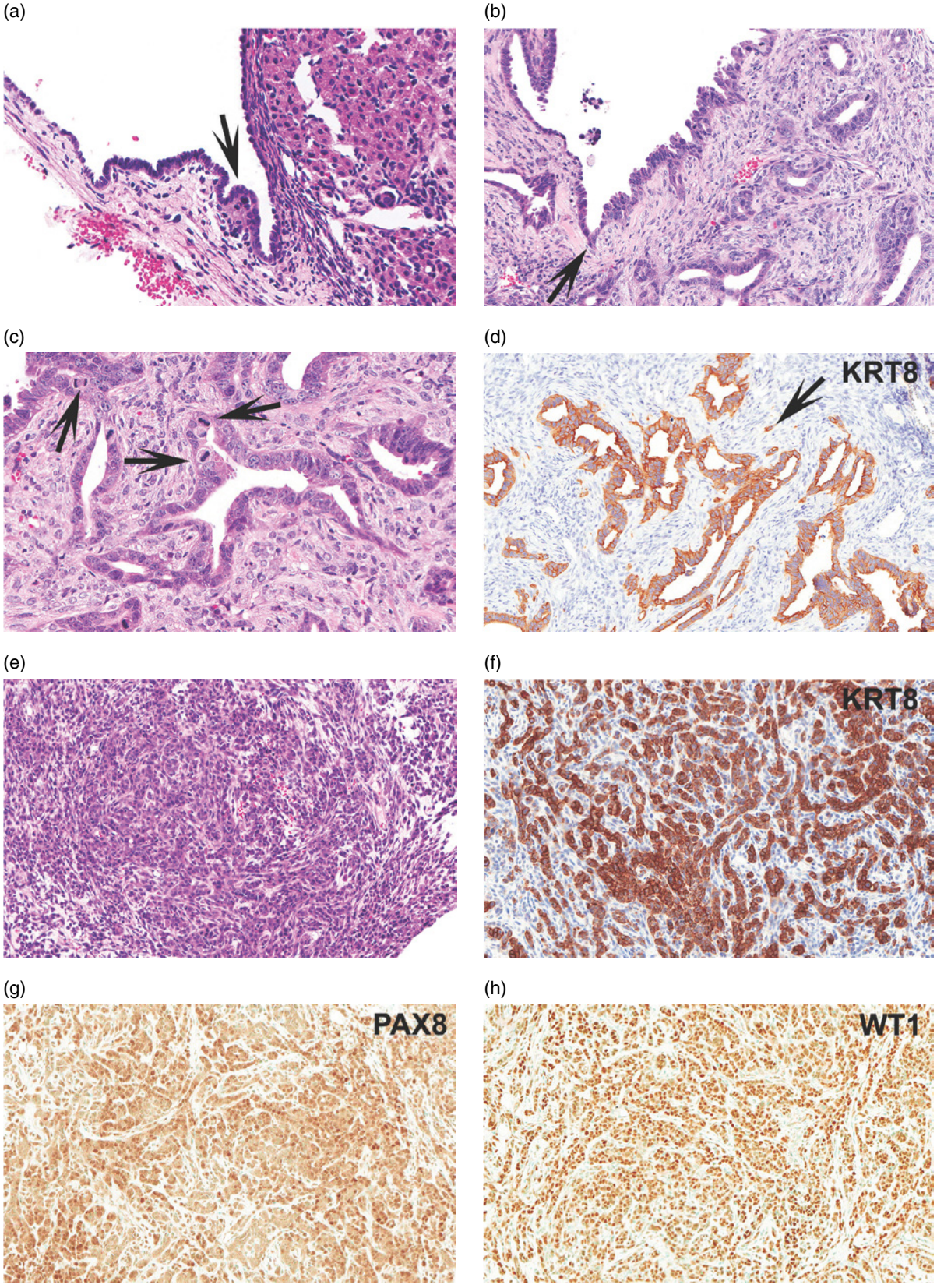


Figure 19.5 Mouse high-grade serous carcinoma arising from the ovarian surface epithelium (OSE). (a-d) Ovarian lesions in *Trp53*$^{loxP/loxP}$*Rb1*$^{loxP/loxP}$ mouse after a single transinfundibular intrabursal injection of AdCre. Atypical OSE cells located in the ovarian hilum (arrow) 60 days after AdCre administration (a). High-grade serous carcinoma located near the ovarian hilum (arrow) of *Trp53*$^{loxP/loxP}$*Rb1*$^{loxP/loxP}$ mouse 255 days after AdCre administration (b). Neoplastic cells with marked cytological atypia, high mitotic activity (arrows, c). KRT8 expression in invasive glandular structures and isolated groups (arrow) lying in dense fibrous tissue (d). (e–h) Neoplastic masses formed by *Trp53* and *Rb1* null hilum OSE cells transplanted into the mouse abdominal cavity. Neoplastic cells grow in solid and nested patterns (e), and express KRT8 (f), PAX8 (g) and Wilms tumor 1 protein (WT1). Hematoxylin and eosin (a–c, e) and immunostaining, Elite ABC method (d, f–h). Counterstaining with hematoxylin (d and f) and methyl green (g and h).

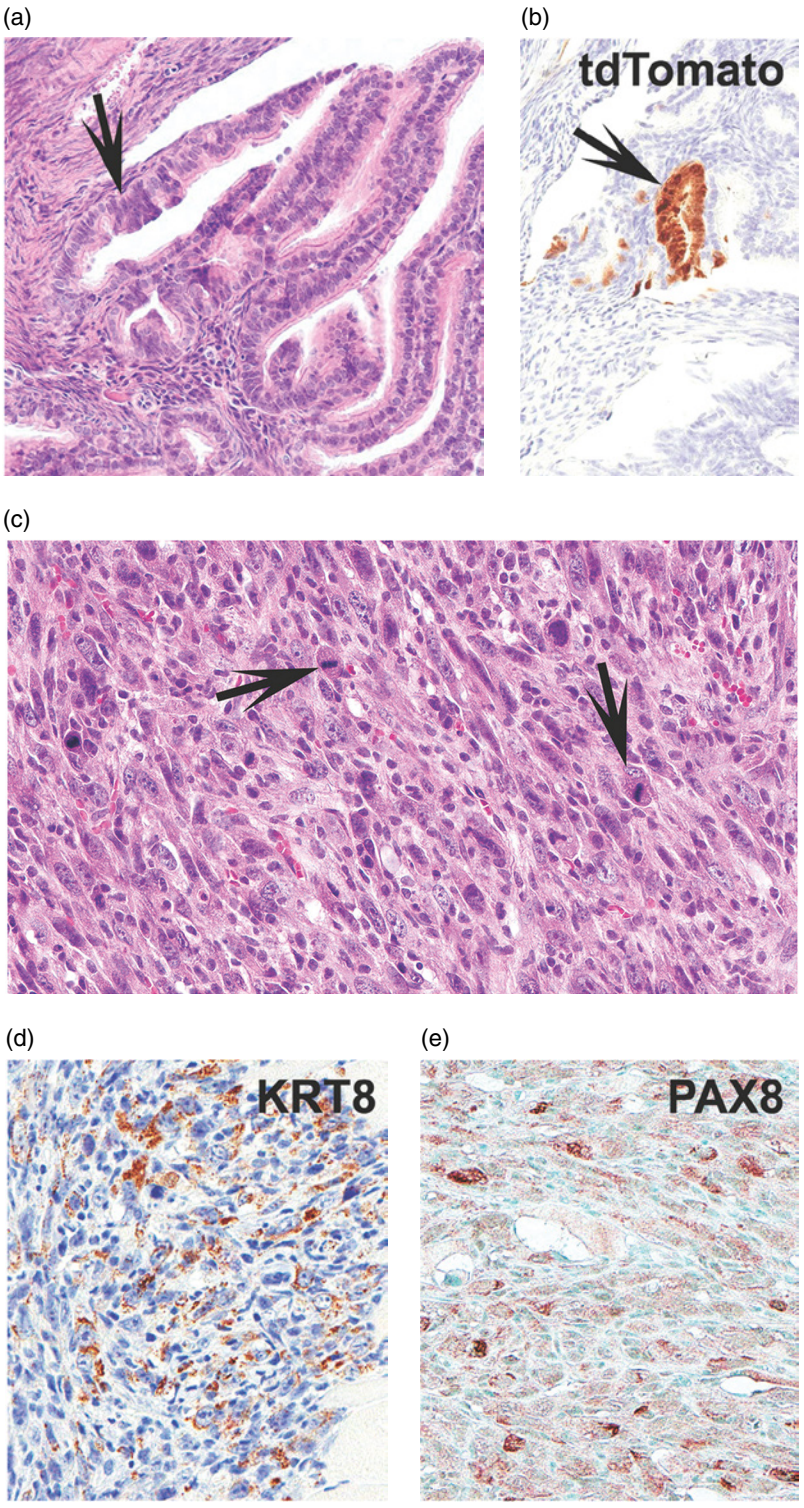


Figure 19.6 Mouse high-grade serous carcinoma arising from the tubal epithelium (TE). (a and b). Serous tubal intraepithelial carcinomas (STICs) (arrows) in the tubal epithelium of composite Krt5-creERT2 (*FVB.Cg-Tg(KRT5-cre/ERT2)2Ipc/JeldJ*) *Tr p53*$^{loxP/loxP}$ *Rb1*$^{loxP/loxP}$ Ai9 (B6.Cg-*Gt(ROSA)26-Sor*$^{tm9(CAG\text{-}tdTomato)Hze}$/J) mice. (c–e) Neoplastic masses formed by *Trp53* and *Rb1* null TE cells transplanted into the mouse abdominal cavity. Neoplastic cells are highly mitotic (arrows), grow in solid pattern, and express KRT8 (d), and PAX8 (e). Hematoxylin and eosin (a and c) and immunostaining, Elite ABC method (b, d, and e). Counterstaining with hematoxylin (b and d) and methyl green (e).

age women; however, approximately 10% of women will develop ectopic implants of endometrial tissue with formation of endometriotic lesions, which suggests other molecular mechanisms involving proinflammatory cytokines in addition to other factors are involved (for review, see [174]). Alternative suggestions for the origins of endometriosis include coelomic metaplasia [175, 176] and activation of embryonic cell rests in the peritoneum [177, 178]. More recently, speculations on a molecular basis of endometriosis suggest that it is estrogen-dependent (progesterone resistant) with an inflammatory component in addition to cellular (epi) genetic predisposition factors, and intercellular communica-

tion signaling mediated by exosomes (and miRNAs) that dictate the fate of cells comprising the disease cell [174]. It is thought that there are three distinct forms of endometriosis that may be present in the pelvic cavity, and occur as peritoneal, ovarian, and adenomyotic lesions [179].

Non-human primates offer a physiologically relevant model, due to the fact that they shed the endometrium during menses [17, 180, 181], unlike mice with the exception of the spiny mouse, which has a menstrual cycle [26]. However, the use of primates is limited by cost and ethical concerns. Of the different animal models used experimentally to study endometriosis, rodent models offer numerous advantages in comparison with other species currently considered for studying endometriosis. Some benefits include they are more cost effective than primates due to their small size and low housing costs, and they produce large litters with short gestation times. Several different endometriosis mouse model systems (for review, see [125]) have been developed with distinctive features shown in Table 19.3 that are typically selected based on the investigators needs.

Endometriosis is microscopically characterized by the presence of both endometrial glands and stromal cells with the glandular epithelium often being tall columnar cells with elongate nuclei. Stromal cells typically resemble normal endometrial stroma in the uterus. An inflammatory cell and vascular component is often present. In modeling endometriosis, the experimental animal system should represent all of the aforementioned histopathologic components observed in the disease [172]. There are several patient-derived xenograft (PDX) endometriosis models that employ immunocompetent rodents with transplantation of human endometrial cells into the peritoneal cavity of mice; however, kidney capsule models exist. Athymic nude mice with a spontaneous mutation of *Foxn1*^{nu} at chromosome 11 are commonly used due to their lack of T cells, and compromised B cell response and the ability of these mice to accept human xenografts with early lesion establishment; however, there is often age-related compensatory immunity, which may interfere with disease establishment [126, 182], usually dependent on strain background. Other immunocompromised models commonly are severe combined immunodeficiency mutant mice, available on a variety of congenic strain backgrounds, that have a spontaneous autosomal recessive mutation of the *Prkdc*^{scid} gene encoding for a DNA repair enzyme on chromosome 16, resulting in lack of both B and T cells, that allows for these mice to accept human xenografts and are good for establishing early lesions [127, 128, 183]. However, similar to nude mice, there is compensatory immunity with age, in addition to increased susceptibility to opportunistic infections; for review, see [184, 185]. The Rag2γ(c) immunocompromised mouse has a targeted double mutation that occurs as a result of crossing interleukin 2 receptor, gamma chain (*Il2rg*) null with a recombination activating gene 2 (*Rag2*) null mice [129]. These mice lack B, T, and natural killer (NK) cells in addition to loss of age-related compensatory immunity, which affords execution of studies of longer duration and transfer of solid tissue xenografts and even human immune cells [8, 186, 187]; however, immunocompetency is very strain dependent which is why many investigators now use NOD *Il2rg Prkdc* mutants, which have consistently low levels of NK cells. As mentioned earlier, endometriosis is thought to be estrogen dependent and progesterone resistant, therefore ESR1 and PGR targeted mutant mice with wild-types are often used in syngeneic endometriosis models to evaluate the effects of loss of steroid hormone receptor function on mediation of the disease progression [130, 131]. Endometriosis models described earlier are summarized in Table 19.3.

Models of Endometrial Cancer

Endometrial cancers have been often classified into two major divisions (types I and II) based on histopathologic, clinical, and epidemiologic parameters [188]. The more common sporadic endometrial carcinomas (~80%) are designated as type I. These cancers occur predominantly in peri- and pre-menopausal women in the presence of unopposed estrogen and are often preceded by endometrial hyperplasia [189, 190]. The majority of type I tumors are low grade, and usually well-differentiated endometrioid carcinomas and have characteristic genetic modifications such as microsatellite instability (MSI), *PTEN*, *KRAS*, and *CTNNB1* mutations; for review, see [191]. Type II endometrial carcinomas, alternatively, are commonly observed in menopausal women, are estrogen-independent, and upon histologic evaluation are diagnosed as predominantly HGSC, malignant mixed Müllerian tumor, or clear cell carcinoma. Unlike type I endometrioid carcinomas, MSI, *PTEN* and *KRAS* mutations occur infrequently in type II carcinomas with *TP53* mutations [192], enhanced ERBB2 amplification [193, 194], and chromosomal loss of heterozygosity (LOH) [195] observed more frequently in type II cancers.

Several mutant mouse models of endometrial cancer have targeted oncogenes and/or suppressor genes to better understand the role of gain or loss of function of gene products and their relevance to the development and progression of uterine endometrial cancer (see Table 19.3). The serine/threonine kinase 11 (*Stk11*, formerly *Lkb1*) mouse model of endometrial cancer is heterozygous for the mutant allele (*Stk11*$^{tm1.1Rdp}$). These mice develop endometrial adenocarcinomas that are observed grossly in at least half of the mice and histologically are well-differentiated, but highly invasive [139]. In studies of human endometrial cancer, it has been found that tumors that express lower levels of STK11 are likely to be more aggressive and highly invasive into the myometrium, indicating a possible tumor suppressor role of STK11. Another model of endometrial cancer is the phosphatase and tensin (PTEN) homolog model (*Pten*$^{+/-}$). *Pten* mutations are the most common genetic alteration in type I endometrioid carcinomas in women. Mutant mice develop a range of cancers that include endometrial, breast, prostate, and lymphomas. The vast array of tumor phenotypes is attributed to the genetic background of mice on which the mutation is made, with those on a C57BL/6×129Sv

background having a higher tendency for developing endometrial carcinomas versus mice on a CD1 background [196, 197]. *Pten*$^{+/-}$ female mice on a pure 129/Sv background developed endometrial hyperplasia by three months of age, and at 5–9 months the lesions progressed to *in situ* carcinoma with locally invasive carcinomas observed in ~30% of mice [198]. By ten months of age, most mice do not survive due to multifocal regions of uterine horn destruction as a result of expansive hemorrhage and necrosis. Endometrial cancer phenotypes are also described in mice deficient for a diverse group of other gene (*Pawr*, the PRKC, apoptosis, WT1, regulator gene) products including *Pawr* [140] and telomerase RNA component (*Terc*) gene product, TERC [141] involved in regulation of apoptosis and telomere length, respectively. Recently, conditional inactivation of tumor suppressor genes *Trp53* and *Rb1* in PAX8-positive endometrial cells in adult mice was found to result in the formation of uterine tumors with characteristics of highly malignant human serous endometrial cancer [35] (Figure 19.7).

Models of Uterine Fibroids

Uterine leiomyomas (fibroids; myomas) are benign smooth muscle tumors originating in the myometrium that clinically affect 25–30% of premenopausal women in the United States and worldwide [100]. Uterine fibroids are responsible for approximately 200 000 hysterectomies, 30 000 myomectomies, and thousands of selective uterine artery embolizations (UAE) per year at an estimated cost of US$5.9–34.4 billion annually in the United States [199]. These tumors are steroid hormone dependent (estrogen and progesterone) and may also be the target of environmental agents that mimic hormones [200]. Also, growth factors such as IGFI, TGFB, EGF, and VEGF [201] are important regulators of the growth of the smooth muscle cells and the extracellular matrix (ECM), with the latter commonly a major component of fibroids [202]; for review, see [203, 204]. Little is known of the etiology, (epi)genetic, and/or the molecular biology events important in the pathogenesis of fibroid although they are thought to be derived from a side population of stem cells that may give rise to tumor development; for review, see [205].

Fibroid models often use PDX approaches whereby human uterine leiomyoma tissue pieces are implanted subcutaneously [142] or more tumor site-specific patient-derived orthotopic xenograft (PDOX) models in that primary fibroid cells are injected into the uterus of immunocompromised mice and supplemented with growth factors and/or steroid hormones to support xenograft growth [143]. More recently a PDX model transplanted three-dimensional uterine fibroid cell cultures into NOD.Cg-*Prkdc*^{scid}/J ovariectomized mice to establish fibroid growth for at least 12 weeks with tumors showing ECM production up to 12 weeks [144]. Few genetically engineered mouse models exist for studying uterine fibroids although a mouse model that constitutively expresses activated beta-catenin (CTNNB1, catenin [cadherin associated protein], beta 1) in uterine mesenchyme with formation of uterine leiomyomas that consist of plump smooth muscle cells forming fascicles and an ECM component similar to human uterine fibroids [145], another model overexpressing *Prlhr* (formerly *Gpr*10) in the myometrium develop uterine fibroids [146], and more recently a mouse model that conditionally expresses a missense variant (c. 131G>A) of *Med12* in the uterus promotes uterine leiomyoma formation and hyperplasia [147].

Models of Cervical Cancer

Cervical cancer is reported as the fourth most common cancer diagnosed in women worldwide (for review, see [206]), and a causal relationship has been shown between human papillomavirus (HPV) infection and cervical cancer [207]. In the United States, HPV is one of the most common sexually transmitted infection among both men and women [208]. Sexually active people may be infected by HPV during their life; however, the vast majority of HPV infections are quickly cleared by the immune system; however, in some cases of HPV infections persist with progression to premalignant changes such cervical intraepithelial neoplasia (CIN) or carcinoma *in situ*. High-risk HPVs are mostly genotype 16, 18, 31, and 33 (in descending order of importance), and act as crucial etiologic agents in the progression of cervical cancer [209, 210]. The cervix in humans is lined by stratified squamous epithelium that covers the outer ectocervix and mucus-secreting columnar epithelium of the endocervix, with premalignant histologic changes are often observed at the squamocolumnar junction. Persistent infection and progression to malignant transformation in 70% of cervical cancer cases is associated with genotype 16 and 18 (for review, see [206]).

Models used to study the pathogenesis of cervical cancer include a mouse papilloma virus (MmuPV1) infection model whereby wild-type immunocompetent FVB/N mice infected with MmuPV1 develop low-grade dysplastic lesions in female mice at four months, and mice infected for six months develop progressively harmful disease, including squamous cell carcinoma (SCC) [148]. A transgenic mouse model expressing the oncogene of human papillomavirus type 16 (HPV16) targeted to the basal cells of the squamous epithelium, using a human keratin 14 (K14) enhancer/promoter supplemented with 17β-estradiol pellets develop cervical and vaginal squamous carcinomas [149]. Modifications of this model have been used to further define the role of HPV oncoproteins in cervical cancer progression [150].

Aging/Spontaneous Strain Specific Lesions

Spontaneous and aging lesions of the female reproductive tract of mice are not infrequent and are strain specific, therefore it is important to know what spontaneous and aging

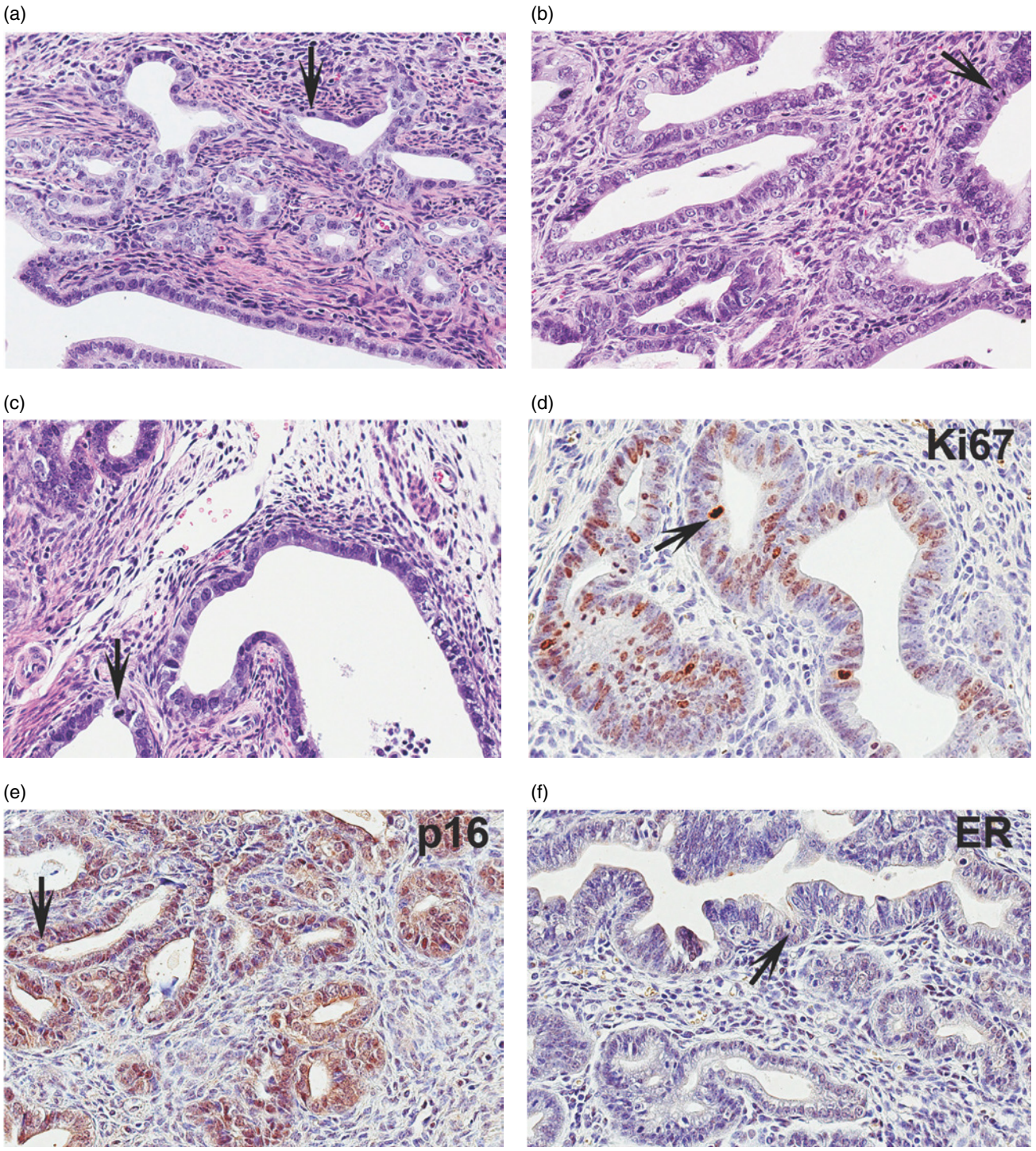
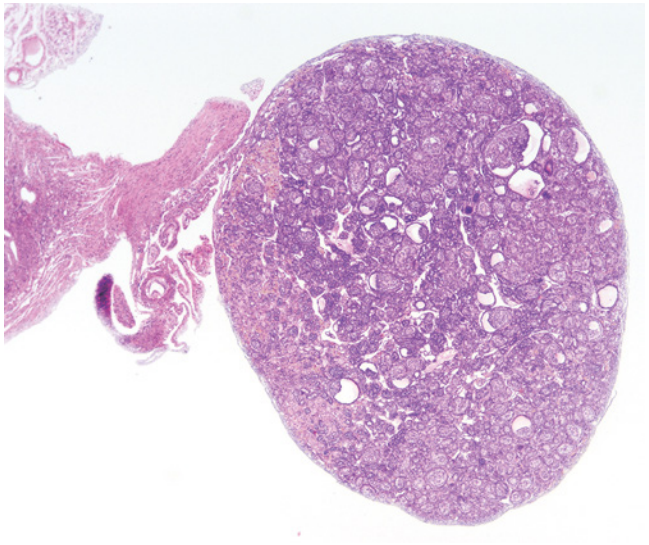


Figure 19.7 Mouse serous endometrial carcinoma. (a) Early atypical lesions 60 days after doxycycline treatment of 60 days old virgin Pax8-rtTA TRE-Cre *Trp53*$^{loxP/loxP}$ *Rb1*$^{loxP/loxP}$ Ai9 mouse. (b and c) Areas of neoplastic endometrial epithelium with marked cytologic atypia, mitoses and glandular pattern (b), and invasion into perimetrium (c) in advanced carcinoma 270 days after induction. (d–f) Detection of proliferation marker Ki67 (d), diffuse staining of p16 (e) and lack of ER expression (f). Arrows, mitotic figures. (a–c) Hematoxylin and eosin. (d–f) ABC Elite method, hematoxylin counterstaining.

changes that occur in strains often selected to create genetically engineered mice. It is also important when defining a phenotype that the change observed is directly related to the targeted gene effect and not a spontaneous lesion common to the background strain selected. Mice on a C57BL/6, 129, and FVB/N backgrounds have been widely used in the

(a)



(b)

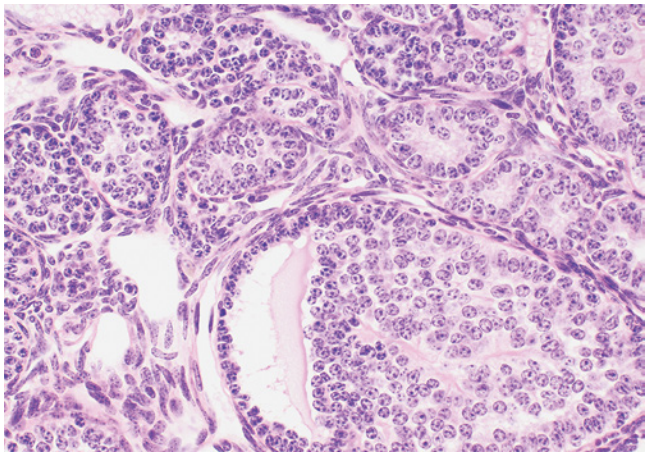
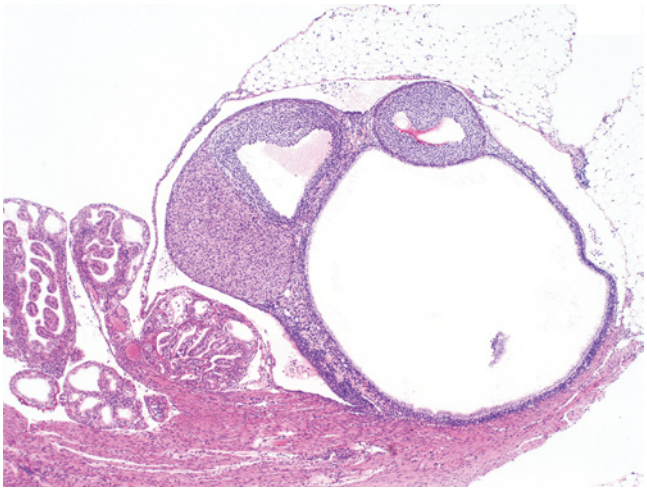


Figure 19.8 Spontaneous granulosa cell tumor in an aged FVB/NJ mouse (a and b). Neoplastic granulosa cells forming tubules that are replacing the entire ovary parenchyma.

(a)



(b)

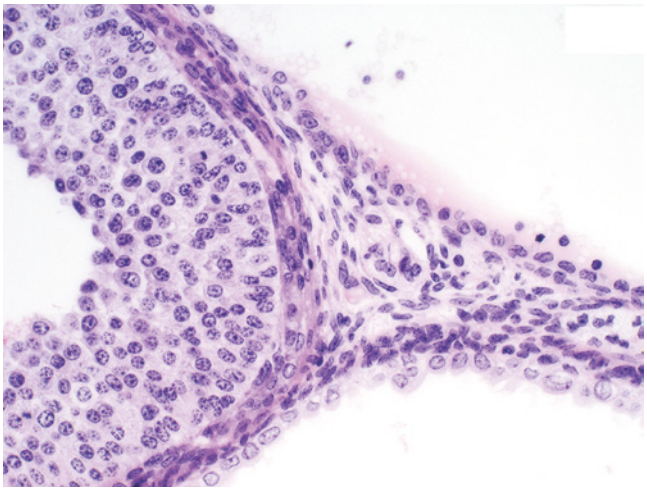


Figure 19.9 Spontaneous ovarian cysts in an aged C57L/J mouse (a and b). Cysts are lined by tall cuboidal to columnar epithelial cells.

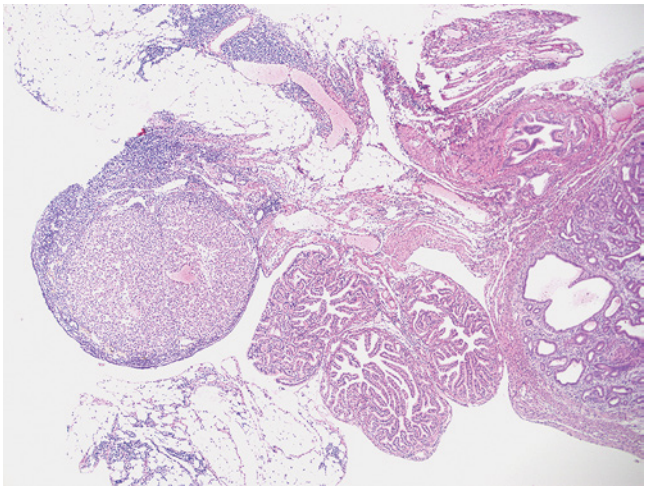
generation of targeted (knockout), transgenic, and conditional mutant genetically engineered mice [211]. In FVB/N female mice, ovarian tumors consisting mostly of granulosa cell tumors (Figure 19.8) or teratomas were the third most common spontaneous tumor type found in retired breeders [212]. Non-neoplastic lesions consisting of ovarian atrophy and cysts have been reported as aging changes in C57BL/6 mice maintained on long-term studies [211] with the latter being observed in an aging C57L/J mouse at Jackson laboratory (Figure 19.9). The uterus (in addition to the Harderian gland) was found to be the second most common site of tumor formation with endometrial sarcoma most often diagnosed in aging 129S6/SvEvTac mice [213]; however, a luteoma of the ovary was found in an aged 129S1/SvlmJ mouse (Figure 19.10).

Age-related changes observed in NOD.Cg-*Prkdc*^{scid} *Il2rg*^{tm1Wjl}/SzJ female mice (average age at necropsy 52 weeks) were characterized mostly by single or multiple stromal polyps of the uterus in 89% of aging NOD.Cg-*Prkdc*^{scid}/J mice although granulosa cell tumors were observed at an incidence of 11% [105].

Acknowledgments

We thank members of the Nikitin lab for their image contributions to Figures 19.5, 19.6, and 19.7. This work was supported by the Intramural Research Program of the NIH, NIEHS, and DNTP (ES021196-27) for DD and also has been supported by NIH (CA096823, CA197160, CA248524 and CA260115.) and NYSTEM (C023050 and C028125) grants to AYN.

(a)



(b)

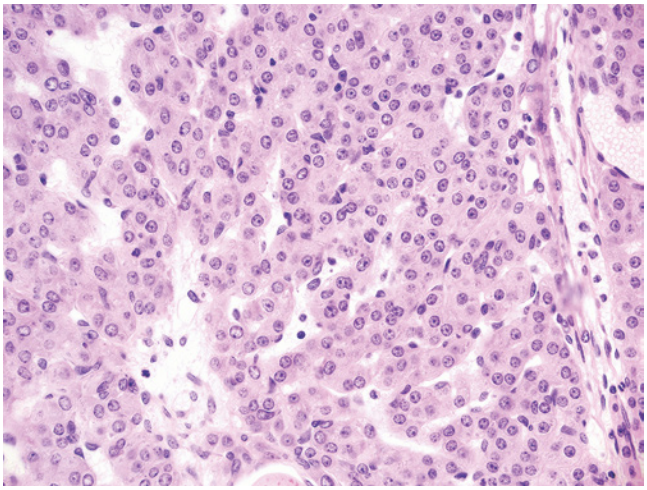


Figure 19.10 Spontaneous luteoma in the ovary of an aged 129S1/SvlmJ mouse (a and b). Note, presence of neoplastic luteoma cells with abundant eosinophilic cytoplasm and stippled nuclei.

References

1 Johnston-MacAnanny, E.B., Patel, B.G., and Taylor, R.N. (2019). Disorders of the female reproductive tract. In: *Pathophysiology of Disease: An Introduction to Clinical Medicine*, 8e (eds. G.D. Hammer and S.J. McPhee), 1–34. New York: McGraw-Hill Education.

2 Plant, T.M. (2015). 60 YEARS OF NEUROENDOCRINOLOGY: the hypothalamo-pituitary-gonadal axis. *J. Endocrinol.* 226 (2): T41–T54.

3 McEwen, B.S. (1992). Steroid hormones: effect on brain development and function. *Horm. Res.* 37 (Suppl. 3): 1–10.

4 Stefaneanu, L. (1997). Pituitary sex steroid receptors: localization and function. *Endocr. Pathol.* 8 (2): 91–108.

5 Simpson, E.R. (2003). Sources of estrogen and their importance. *J. Steroid Biochem. Mol. Biol.* 86 (3–5): 225–230.

6 Couse, J.F. and Korach, K.S. (1998). Exploring the role of sex steroids through studies of receptor deficient mice. *J. Mol. Med. (Berl.)* 76 (7): 497–511.

7 Couse, J.F. and Korach, K.S. (1999). Estrogen receptor null mice: what have we learned and where will they lead us? *Endocr. Rev.* 20 (3): 358–417.

8 Bruner-Tran, K.L., Carvalho-Macedo, A.C., Duleba, A.J. et al. (2010). Experimental endometriosis in immunocompromised mice after adoptive transfer of human leukocytes. *Fertil. Steril.* 93 (8): 2519–2524.

9 Gilbert, S.B., Roof, A.K., and Rajendra Kumar, T. (2018). Mouse models for the analysis of gonadotropin secretion and action. *Best Pract. Res. Clin. Endocrinol. Metab.* 32 (3): 219–239.

10 Spergel, D.J. (2019). Modulation of gonadotropin-releasing hormone neuron activity and secretion in mice by non-peptide neurotransmitters, gasotransmitters, and gliotransmitters. *Front. Endocrinol. (Lausanne)* 10: 329.

11 Liu, C.F., Liu, C., and Yao, H.H. (2010). Building pathways for ovary organogenesis in the mouse embryo. *Curr. Top. Dev. Biol.* 90: 263–290.

12 Anderson, R., Copeland, T.K., Scholer, H. et al. (2000). The onset of germ cell migration in the mouse embryo. *Mech. Dev.* 91 (1–2): 61–68.

13 Molyneaux, K.A., Stallock, J., Schaible, K., and Wylie, C. (2001). Time-lapse analysis of living mouse germ cell migration. *Dev. Biol.* 240 (2): 488–498.

14 Tam, P.P. and Snow, M.H. (1981). Proliferation and migration of primordial germ cells during compensatory growth in mouse embryos. *J. Embryol. Exp. Morphol.* 64: 133–147.

15 Merchant-Larios, H. and Chimal-Monroy, J. (1989). The ontogeny of primordial follicles in the mouse ovary. *Prog. Clin. Biol. Res.* 296: 55–63.

16 Pepling, M.E. and Spradling, A.C. (1998). Female mouse germ cells form synchronously dividing cysts. *Development* 125 (17): 3323–3328.

17 Boyd, K.L., Muehlenbachs, A., Rendi, M.H. et al. (2018). Female reproductive system. In: *Comparative Anatomy and Histology*, Chapter 17, 2e (eds. P.M. Treuting, S.M. Dintzis and K.S. Montine), 303–334. San Diego, CA: Academic Press.

18 Auersperg, N., Woo, M.M., and Gilks, C.B. (2008). The origin of ovarian carcinomas: a developmental view. *Gynecol. Oncol.* 110 (3): 452–454.

19 Kobayashi, A. and Behringer, R.R. (2003). Developmental genetics of the female reproductive tract in mammals. *Nat. Rev. Genet.* 4 (12): 969–980.

20 Zhao, F., Franco, H.L., Rodriguez, K.F. et al. (2017). Elimination of the male reproductive tract in the female

embryo is promoted by COUP-TFII in mice. *Science* 357 (6352): 717–720.
21 Kaufman, M.H. (2010). *Histologic Basis of Mouse Endocrine System Development: A Comparative Analysis*. Boca Raton, FL: CRC Press.
22 Dixon, D., Alison, R., Bach, U. et al. (2014). Nonproliferative and proliferative lesions of the rat and mouse female reproductive system. *J. Toxicol. Pathol.* 27 (3–4 Suppl): 1S–107S.
23 Rudmann, D.G. and Foley, G.L. (2018). Female reproductive system. In: *Fundamentals of Toxicologic Pathology*, Chapter 18, 3e (eds. M.A. Wallig, W.M. Haschek, C.G. Rousseaux and B. Bolon), 517–545. Academic Press.
24 Stewart, C.A. and Behringer, R.R. (2012). Mouse oviduct development. *Results Prob. Cell Differ.* 55: 247–262.
25 Barnett, K.R., Schilling, C., Greenfeld, C.R. et al. (2006). Ovarian follicle development and transgenic mouse models. *Hum. Reprod. Update* 12 (5): 537–555.
26 Bellofiore, N., Ellery, S.J., Mamrot, J. et al. (2017). First evidence of a menstruating rodent: the spiny mouse (*Acomys cahirinus*). *Am. J. Obstet. Gynecol.* 216 (1): 40e1–e11.
27 Bellofiore, N., Rana, S., Dickinson, H. et al. (2018). Characterization of human-like menstruation in the spiny mouse: comparative studies with the human and induced mouse model. *Hum. Reprod.* 33 (9): 1715–1726.
28 National Toxicology Program (2011). Reproductive and Developmental Toxicity Specifications May 2011. https://ntp.niehs.nih.gov/ntp/test_info/finalntp_reprospecsmay2011_508.pdf (accessed 15 March 2021).
29 Fu, D.J., Miller, A.D., Southard, T.L. et al. (2018). Stem cell pathology. *Annu. Rev. Pathol.* 13: 71–92.
30 Korach, K.S., Horigome, T., Tomooka, Y. et al. (1988). Immunodetection of estrogen receptor in epithelial and stromal tissues of neonatal mouse uterus. *Proc. Natl. Acad. Sci. U.S.A.* 85 (10): 3334–3337.
31 Tibbetts, T.A., Mendoza-Meneses, M., O'Malley, B.W., and Conneely, O.M. (1998). Mutual and intercompartmental regulation of estrogen receptor and progesterone receptor expression in the mouse uterus. *Biol. Reprod.* 59 (5): 1143–1152.
32 Jefferson, W.N., Couse, J.F., Banks, E.P. et al. (2000). Expression of estrogen receptor beta is developmentally regulated in reproductive tissues of male and female mice. *Biol. Reprod.* 62 (2): 310–317.
33 Gava, N., Clarke, C.L., Byth, K. et al. (2004). Expression of progesterone receptors A and B in the mouse ovary during the estrous cycle. *Endocrinology* 145 (7): 3487–3494.
34 Teilmann, S.C., Clement, C.A., Thorup, J. et al. (2006). Expression and localization of the progesterone receptor in mouse and human reproductive organs. *J. Endocrinol.* 191 (3): 525–535.
35 Fu, D.J., De Micheli, A.J., Bidarimath, M. et al. (2020). Cells expressing PAX8 are the main source of homeostatic regeneration of adult mouse endometrial epithelium and give rise to serous endometrial carcinoma. *Dis. Model. Mech.* 13 (10) https://doi.org/10.1242/dmm.047035.
36 Ghosh, A., Syed, S.M., and Tanwar, P.S. (2017). In vivo genetic cell lineage tracing reveals that oviductal secretory cells self-renew and give rise to ciliated cells. *Development* 144 (17): 3031–3041.
37 Ning, G., Bijron, J.G., Yamamoto, Y. et al. (2014). The PAX2-null immunophenotype defines multiple lineages with common expression signatures in benign and neoplastic oviductal epithelium. *J. Pathol.* 234 (4): 478–487.
38 Cattanach, B.M., Iddon, C.A., Charlton, H.M. et al. (1977). Gonadotrophin-releasing hormone deficiency in a mutant mouse with hypogonadism. *Nature* 269 (5626): 338–340.
39 Mason, A.J., Hayflick, J.S., Zoeller, R.T. et al. (1986). A deletion truncating the gonadotropin-releasing hormone gene is responsible for hypogonadism in the hpg mouse. *Science* 234 (4782): 1366–1371.
40 Witte, O.N. (1990). Steel locus defines new multipotent growth factor. *Cell* 63 (1): 5–6.
41 Couse, J.F., Hewitt, S.C., Bunch, D.O. et al. (1999). Postnatal sex reversal of the ovaries in mice lacking estrogen receptors alpha and beta. *Science* 286 (5448): 2328–2331.
42 Hewitt, S.C. and Korach, K.S. (2018). Estrogen receptors: new directions in the new millennium. *Endocr. Rev.* 39 (5): 664–675.
43 Dupont, S., Krust, A., Gansmuller, A. et al. (2000). Effect of single and compound knockouts of estrogen receptors alpha (ERalpha) and beta (ERbeta) on mouse reproductive phenotypes. *Development* 127 (19): 4277–4291.
44 Arao, Y., Hamilton, K.J., Wu, S.P. et al. (2019). Dysregulation of hypothalamic-pituitary estrogen receptor alpha-mediated signaling causes episodic LH secretion and cystic ovary. *FASEB J.* 33 (6): 7375–7386.
45 Lydon, J.P., DeMayo, F.J., Funk, C.R. et al. (1995). Mice lacking progesterone receptor exhibit pleiotropic reproductive abnormalities. *Genes Dev.* 9 (18): 2266–2278.
46 Chappell, P.E., Lydon, J.P., Conneely, O.M. et al. (1997). Endocrine defects in mice carrying a null mutation for the progesterone receptor gene. *Endocrinology* 138 (10): 4147–4152.
47 Clark, N.C., Pru, C.A., Yee, S.P. et al. (2017). Conditional ablation of progesterone receptor membrane component 2 causes female premature reproductive senescence. *Endocrinology* 158 (3): 640–651.
48 McCallum, M.L., Pru, C.A., Niikura, Y. et al. (2016). Conditional ablation of progesterone receptor membrane component 1 results in subfertility in the female and development of endometrial cysts. *Endocrinology* 157 (9): 3309–3319.
49 Kumar, T.R., Wang, Y., Lu, N., and Matzuk, M.M. (1997). Follicle stimulating hormone is required for ovarian follicle maturation but not male fertility. *Nat. Genet.* 15 (2): 201–204.
50 Dierich, A., Sairam, M.R., Monaco, L. et al. (1998). Impairing follicle-stimulating hormone (FSH) signaling in vivo: targeted disruption of the FSH receptor leads to aberrant gametogenesis and hormonal imbalance. *Proc. Natl. Acad. Sci. U.S.A.* 95 (23): 13612–13617.

51 Risma, K.A., Clay, C.M., Nett, T.M. et al. (1995). Targeted overexpression of luteinizing hormone in transgenic mice leads to infertility, polycystic ovaries, and ovarian tumors. *Proc. Natl. Acad. Sci. U.S.A.* 92 (5): 1322–1326.

52 Bole-Feysot, C., Goffin, V., Edery, M. et al. (1998). Prolactin (PRL) and its receptor: actions, signal transduction pathways and phenotypes observed in PRL receptor knockout mice. *Endocr. Rev.* 19 (3): 225–268.

53 Gorvin, C.M. (2015). The prolactin receptor: diverse and emerging roles in pathophysiology. *J. Clin. Transl. Endocrinol.* 2 (3): 85–91.

54 Kendall, S.K., Samuelson, L.C., Saunders, T.L. et al. (1995). Targeted disruption of the pituitary glycoprotein hormone alpha-subunit produces hypogonadal and hypothyroid mice. *Genes Dev.* 9 (16): 2007–2019.

55 Topilko, P., Schneider-Maunoury, S., Levi, G. et al. (1998). Multiple pituitary and ovarian defects in *Krox-24* (*NGFI-A*, *Egr-1*)-targeted mice. *Mol. Endocrinol.* 12 (1): 107–122.

56 Thackray, V.G., Mellon, P.L., and Coss, D. (2010). Hormones in synergy: regulation of the pituitary gonadotropin genes. *Mol. Cell. Endocrinol.* 314 (2): 192–203.

57 Parker, K.L. (1998). The roles of steroidogenic factor 1 in endocrine development and function. *Mol. Cell. Endocrinol.* 145 (1–2): 15–20.

58 Schedl, A. and Hastie, N. (1998). Multiple roles for the Wilms' tumour suppressor gene, WT1 in genitourinary development. *Mol. Cell. Endocrinol.* 140 (1–2): 65–69.

59 Fisher, C.R., Graves, K.H., Parlow, A.F., and Simpson, E.R. (1998). Characterization of mice deficient in aromatase (ArKO) because of targeted disruption of the *cyp19* gene. *Proc. Natl. Acad. Sci. U.S.A.* 95 (12): 6965–6970.

60 Baker, J., Hardy, M.P., Zhou, J. et al. (1996). Effects of an IGF1 gene null mutation on mouse reproduction. *Mol. Endocrinol.* 10 (7): 903–918.

61 Zhou, J., Kumar, T.R., Matzuk, M.M., and Bondy, C. (1997). Insulin-like growth factor I regulates gonadotropin responsiveness in the murine ovary. *Mol. Endocrinol.* 11 (13): 1924–1933.

62 Dong, J., Albertini, D.F., Nishimori, K. et al. (1996). Growth differentiation factor-9 is required during early ovarian folliculogenesis. *Nature* 383 (6600): 531–535.

63 Carabatsos, M.J., Elvin, J., Matzuk, M.M., and Albertini, D.F. (1998). Characterization of oocyte and follicle development in growth differentiation factor-9-deficient mice. *Dev. Biol.* 204 (2): 373–384.

64 Matzuk, M.M., Finegold, M.J., Su, J.G. et al. (1992). Alpha-inhibin is a tumour-suppressor gene with gonadal specificity in mice. *Nature* 360 (6402): 313–319.

65 Matzuk, M.M., Kumar, T.R., Shou, W. et al. (1996). Transgenic models to study the roles of inhibins and activins in reproduction, oncogenesis, and development. *Recent. Prog. Horm. Res.* 51: 123–154; discussion 55–7.

66 Guo, Q., Kumar, T.R., Woodruff, T. et al. (1998). Overexpression of mouse follistatin causes reproductive defects in transgenic mice. *Mol. Endocrinol.* 12 (1): 96–106.

67 Lim, H., Paria, B.C., Das, S.K. et al. (1997). Multiple female reproductive failures in cyclooxygenase 2-deficient mice. *Cell* 91 (2): 197–208.

68 Davis, B.J., Lennard, D.E., Lee, C.A. et al. (1999). Anovulation in cyclooxygenase-2-deficient mice is restored by prostaglandin E_2 and interleukin-1beta. *Endocrinology* 140 (6): 2685–2695.

69 Sterneck, E., Tessarollo, L., and Johnson, P.F. (1997). An essential role for C/EBPbeta in female reproduction. *Genes Dev.* 11 (17): 2153–2162.

70 Matzuk, M.M., Dionne, L., Guo, Q. et al. (1998). Ovarian function in superoxide dismutase 1 and 2 knockout mice. *Endocrinology* 139 (9): 4008–4011.

71 Hsu, S.Y., Lai, R.J., Finegold, M., and Hsueh, A.J. (1996). Targeted overexpression of BCL-2 in ovaries of transgenic mice leads to decreased follicle apoptosis, enhanced folliculogenesis, and increased germ cell tumorigenesis. *Endocrinology* 137 (11): 4837–4843.

72 Perez, G.I., Robles, R., Knudson, C.M. et al. (1999). Prolongation of ovarian lifespan into advanced chronological age by Bax-deficiency. *Nat. Genet.* 21 (2): 200–203.

73 Rahman, N.A., Kananen Rilianawati, K., Paukku, T. et al. (1998). Transgenic mouse models for gonadal tumorigenesis. *Mol. Cell. Endocrinol.* 145 (1–2): 167–174.

74 Colledge, W.H., Carlton, M.B., Udy, G.B., and Evans, M.J. (1994). Disruption of c-*mos* causes parthenogenetic development of unfertilized mouse eggs. *Nature* 370 (6484): 65–68.

75 Hashimoto, N., Watanabe, N., Furuta, Y. et al. (1994). Parthenogenetic activation of oocytes in c-*mos*-deficient mice. *Nature* 370 (6484): 68–71.

76 St John, M.A., Tao, W., Fei, X. et al. (1999). Mice deficient of Lats1 develop soft-tissue sarcomas, ovarian tumours and pituitary dysfunction. *Nat. Genet.* 21 (2): 182–186.

77 Varga, T., Czimmerer, Z., and Nagy, L. (2011). PPARs are a unique set of fatty acid regulated transcription factors controlling both lipid metabolism and inflammation. *Biochim. Biophys. Acta* 1812 (8): 1007–1022.

78 Mazaira, G.I., Zgajnar, N.R., Lotufo, C.M. et al. (2018). The nuclear receptor field: a historical overview and future challenges. *Nucl. Recept. Res.* 5 https://doi.org/10.11131/2018/101320.

79 Lubahn, D.B., Moyer, J.S., Golding, T.S. et al. (1993). Alteration of reproductive function but not prenatal sexual development after insertional disruption of the mouse estrogen receptor gene. *Proc. Natl. Acad. Sci. U.S.A.* 90 (23): 11162–11166.

80 Krege, J.H., Hodgin, J.B., Couse, J.F. et al. (1998). Generation and reproductive phenotypes of mice lacking estrogen receptor beta. *Proc. Natl. Acad. Sci. U.S.A.* 95 (26): 15677–15682.

81 Hewitt, S.C., Winuthayanon, W., and Korach, K.S. (2016). What's new in estrogen receptor action in the female reproductive tract. *J. Mol. Endocrinol.* 56 (2): R55–R71.

82 Prossnitz, E.R. and Hathaway, H.J. (2015). What have we learned about GPER function in physiology and disease from knockout mice? *J. Steroid Biochem. Mol. Biol.* 153: 114–126.

83 Prossnitz, E.R. and Barton, M. (2011). The G-protein-coupled estrogen receptor GPER in health and disease. *Nat. Rev. Endocrinol.* 7 (12): 715–726.

84 Martensson, U.E., Salehi, S.A., Windahl, S. et al. (2009). Deletion of the G protein-coupled receptor 30 impairs glucose tolerance, reduces bone growth, increases blood pressure, and eliminates estradiol-stimulated insulin release in female mice. *Endocrinology* 150 (2): 687–698.

85 Otto, C., Fuchs, I., Kauselmann, G. et al. (2009). GPR30 does not mediate estrogenic responses in reproductive organs in mice. *Biol. Reprod.* 80 (1): 34–41.

86 Langer, G., Bader, B., Meoli, L. et al. (2010). A critical review of fundamental controversies in the field of GPR30 research. *Steroids* 75 (8–9): 603–610.

87 Couse, J.F., Dixon, D., Yates, M. et al. (2001). Estrogen receptor-alpha knockout mice exhibit resistance to the developmental effects of neonatal diethylstilbestrol exposure on the female reproductive tract. *Dev. Biol.* 238 (2): 224–238.

88 Horseman, N.D. and Gregerson, K.A. (2014). Prolactin actions. *J. Mol. Endocrinol.* 52 (1): R95–R106.

89 Camper, S.A., Saunders, T.L., Katz, R.W., and Reeves, R.H. (1990). The Pit-1 transcription factor gene is a candidate for the murine Snell dwarf mutation. *Genomics* 8 (3): 586–590.

90 Bartke, A. and Quainoo, N. (2018). Impact of growth hormone-related mutations on mammalian aging. *Front. Genet.* 9: 586.

91 Brown-Borg, H.M., Borg, K.E., Meliska, C.J., and Bartke, A. (1996). Dwarf mice and the ageing process. *Nature* 384 (6604): 33.

92 Bartke, A. and Brown-Borg, H. (2004). Life extension in the dwarf mouse. *Curr. Top. Dev. Biol.* 63: 189–225.

93 Mannan, M.A. and O'Shaughnessy, P.J. (1988). Ovarian steroid metabolism during post-natal development in the normal mouse and in the adult hypogonadal (hpg) mouse. *J. Reprod. Fertil.* 82 (2): 727–734.

94 Peltoketo, H., Zhang, F.P., and Rulli, S.B. (2011). Animal models for aberrations of gonadotropin action. *Rev. Endocr. Metab. Disord.* 12 (4): 245–258.

95 Tremblay, J.J. and Drouin, J. (1999). Egr-1 is a downstream effector of GnRH and synergizes by direct interaction with Ptx1 and SF-1 to enhance luteinizing hormone beta gene transcription. *Mol. Cell. Biol.* 19 (4): 2567–2576.

96 Abel, M.H., Huhtaniemi, I., Pakarinen, P. et al. (2003). Age-related uterine and ovarian hypertrophy in FSH receptor knockout and FSHbeta subunit knockout mice. *Reproduction* 125 (2): 165–173.

97 Couse, J.F., Yates, M.M., Sanford, R. et al. (2004). Formation of cystic ovarian follicles associated with elevated luteinizing hormone requires estrogen receptor-beta. *Endocrinology* 145 (10): 4693–4702.

98 Schimmer, B.P. and White, P.C. (2010). Minireview: steroidogenic factor 1: its roles in differentiation, development, and disease. *Mol. Endocrinol.* 24 (7): 1322–1337.

99 Pelusi, C., Ikeda, Y., Zubair, M., and Parker, K.L. (2008). Impaired follicle development and infertility in female mice lacking steroidogenic factor 1 in ovarian granulosa cells. *Biol. Reprod.* 79 (6): 1074–1083.

100 Britt, K.L., Drummond, A.E., Dyson, M. et al. (2001). The ovarian phenotype of the aromatase knockout (ArKO) mouse. *J. Steroid Biochem. Mol. Biol.* 79 (1–5): 181–185.

101 Hom, Y.K., Young, P., Wiesen, J.F. et al. (1998). Uterine and vaginal organ growth requires epidermal growth factor receptor signaling from stroma. *Endocrinology* 139 (3): 913–921.

102 Li, Q., Agno, J.E., Edson, M.A. et al. (2011). Transforming growth factor beta receptor type 1 is essential for female reproductive tract integrity and function. *PLoS Genet.* 7 (10): e1002320.

103 Kuroda, H., Terada, N., Nakayama, H. et al. (1988). Infertility due to growth arrest of ovarian follicles in Sl/Sl^t mice. *Dev. Biol.* 126 (1): 71–79.

104 Tilly, J.L. (1996). Apoptosis and ovarian function. *Rev. Reprod.* 1 (3): 162–172.

105 Santagostino, S.F., Arbona, R.J.R., Nashat, M.A. et al. (2017). Pathology of aging in NOD scid gamma female mice. *Vet. Pathol.* 54 (5): 855–869.

106 Kananen, K., Markkula, M., el-Hefnawy, T. et al. (1996). The mouse inhibin alpha-subunit promoter directs SV40 T-antigen to Leydig cells in transgenic mice. *Mol. Cell. Endocrinol.* 119 (2): 135–146.

107 Kananen, K., Markkula, M., Rainio, E. et al. (1995). Gonadal tumorigenesis in transgenic mice bearing the mouse inhibin alpha-subunit promoter/simian virus T-antigen fusion gene: characterization of ovarian tumors and establishment of gonadotropin-responsive granulosa cell lines. *Mol. Endocrinol.* 9 (5): 616–627.

108 Dilworth, S.M. (1990). Cell alterations induced by the large T-antigens of SV40 and polyoma virus. *Semin. Cancer Biol.* 1 (6): 407–414.

109 Donehower, L.A., Harvey, M., Vogel, H. et al. (1995). Effects of genetic background on tumorigenesis in p53-deficient mice. *Mol. Carcinog.* 14 (1): 16–22.

110 Hansen, L.A., Trempus, C.S., Mahler, J.F., and Tennant, R.W. (1996). Association of tumor development with increased cellular proliferation and transgene overexpression, but not c-Ha-*ras* mutations, in v-Ha-*ras* transgenic Tg.AC mice. *Carcinogenesis* 17 (9): 1825–1833.

111 Sicinski, P., Donaher, J.L., Geng, Y. et al. (1996). Cyclin D2 is an FSH-responsive gene involved in gonadal cell proliferation and oncogenesis. *Nature* 384 (6608): 470–474.

112 Simon, A.M., Goodenough, D.A., Li, E., and Paul, D.L. (1997). Female infertility in mice lacking connexin 37. *Nature* 385 (6616): 525–529.

113 Yoshizawa, T., Handa, Y., Uematsu, Y. et al. (1997). Mice lacking the vitamin D receptor exhibit impaired bone formation, uterine hypoplasia and growth retardation after weaning. *Nat. Genet.* 16 (4): 391–396.

114 Elvin, J.A. and Matzuk, M.M. (1998). Mouse models of ovarian failure. *Rev. Reprod.* 3 (3): 183–195.

115 Sullivan, S.D. and Castrillon, D.H. (2011). Insights into primary ovarian insufficiency through genetically engineered mouse models. *Semin. Reprod. Med.* 29 (4): 283–298.

116 Norman, R.J., Dewailly, D., Legro, R.S., and Hickey, T.E. (2007). Polycystic ovary syndrome. *Lancet* 370 (9588): 685–697.

117 Williams, T., Mortada, R., and Diagnosis, P.S. (2016). Treatment of polycystic ovary syndrome. *Am. Fam. Phys.* 94 (2): 106–113.

118 van Houten, E.L., Kramer, P., McLuskey, A. et al. (2012). Reproductive and metabolic phenotype of a mouse model of PCOS. *Endocrinology* 153 (6): 2861–2869.

119 Ryu, Y., Kim, S.W., Kim, Y.Y., and Ku, S.Y. (2019). Animal models for human polycystic ovary syndrome (PCOS) focused on the use of indirect hormonal perturbations: a review of the literature. *Int. J. Mol. Sci.* 20 (11): 2720.

120 El Hayek, S., Bitar, L., Hamdar, L.H. et al. (2016). Poly cystic ovarian syndrome: an updated overview. *Front. Physiol.* 7: 124.

121 van Houten, E.L. and Visser, J.A. (2014). Mouse models to study polycystic ovary syndrome: a possible link between metabolism and ovarian function? *Reprod. Biol.* 14 (1): 32–43.

122 Risma, K.A., Hirshfield, A.N., and Nilson, J.H. (1997). Elevated luteinizing hormone in prepubertal transgenic mice causes hyperandrogenemia, precocious puberty, and substantial ovarian pathology. *Endocrinology* 138 (8): 3540–3547.

123 Hill, J.W., Elias, C.F., Fukuda, M. et al. (2010). Direct insulin and leptin action on pro-opiomelanocortin neurons is required for normal glucose homeostasis and fertility. *Cell Metab.* 11 (4): 286–297.

124 Schomberg, D.W., Couse, J.F., Mukherjee, A. et al. (1999). Targeted disruption of the estrogen receptor-alpha gene in female mice: characterization of ovarian responses and phenotype in the adult. *Endocrinology* 140 (6): 2733–2744.

125 Bruner-Tran, K.L., Mokshagundam, S., Herington, J.L. et al. (2018). Rodent models of experimental endometriosis: identifying mechanisms of disease and therapeutic targets. *Curr. Womens Health Rev.* 14 (2): 173–188.

126 Flanagan, S.P. (1966). Nude', a new hairless gene with pleiotropic effects in the mouse. *Genet. Res.* 8 (3): 295–309.

127 Bosma, G.C., Custer, R.P., and Bosma, M.J. (1983). A severe combined immunodeficiency mutation in the mouse. *Nature* 301 (5900): 527–530.

128 Shultz, L.D., Schweitzer, P.A., Christianson, S.W. et al. (1995). Multiple defects in innate and adaptive immunologic function in NOD/LtSz-scid mice. *J. Immunol.* 154 (1): 180–191.

129 Shinkai, Y., Rathbun, G., Lam, K.P. et al. (1992). RAG-2-deficient mice lack mature lymphocytes owing to inability to initiate V(D)J rearrangement. *Cell* 68 (5): 855–867.

130 Fang, Z., Yang, S., Lydon, J.P. et al. (2004). Intact progesterone receptors are essential to counteract the proliferative effect of estradiol in a genetically engineered mouse model of endometriosis. *Fertil. Steril.* 82 (3): 673–678.

131 Burns, K.A., Rodriguez, K.F., Hewitt, S.C. et al. (2012). Role of estrogen receptor signaling required for endometriosis-like lesion establishment in a mouse model. *Endocrinology* 153 (8): 3960–3971.

132 Rahman, N.A. and Huhtaniemi, I.T. (2001). Ovarian tumorigenesis in mice transgenic for murine inhibin alpha subunit promoter-driven Simian Virus 40 T-antigen: ontogeny, functional characteristics, and endocrine effects. *Biol. Reprod.* 64 (4): 1122–1130.

133 Connolly, D.C., Bao, R., Nikitin, A.Y. et al. (2003). Female mice chimeric for expression of the simian virus 40 TAg under control of the MISIIR promoter develop epithelial ovarian cancer. *Cancer Res.* 63 (6): 1389–1397.

134 Flesken-Nikitin, A., Choi, K.C., Eng, J.P. et al. (2003). Induction of carcinogenesis by concurrent inactivation of *p53* and *Rb1* in the mouse ovarian surface epithelium. *Cancer Res.* 63 (13): 3459–3463.

135 Dinulescu, D.M., Ince, T.A., Quade, B.J. et al. (2005). Role of *K-ras* and *Pten* in the development of mouse models of endometriosis and endometrioid ovarian cancer. *Nat. Med.* 11 (1): 63–70.

136 Perets, R., Wyant, G.A., Muto, K.W. et al. (2013). Transformation of the fallopian tube secretory epithelium leads to high-grade serous ovarian cancer in *Brca;Tp53;Pten* models. *Cancer Cell* 24 (6): 751–765.

137 McCool, K.W., Freeman, Z.T., Zhai, Y. et al. (2020). Murine oviductal high-grade serous carcinomas mirror the genomic alterations, gene expression profiles, and immune microenvironment of their human counterparts. *Cancer Res.* 80 (4): 877–889.

138 Orsulic, S., Li, Y., Soslow, R.A. et al. (2002). Induction of ovarian cancer by defined multiple genetic changes in a mouse model system. *Cancer Cell* 1 (1): 53–62.

139 Contreras, C.M., Gurumurthy, S., Haynie, J.M. et al. (2008). Loss of Lkb1 provokes highly invasive endometrial adenocarcinomas. *Cancer Res.* 68 (3): 759–766.

140 Garcia-Cao, I., Duran, A., Collado, M. et al. (2005). Tumour-suppression activity of the proapoptotic regulator Par4. *EMBO Rep.* 6 (6): 577–583.

141 Akbay, E.A., Contreras, C.M., Perera, S.A. et al. (2008). Differential roles of telomere attrition in type I and II endometrial carcinogenesis. *Am. J. Pathol.* 173 (2): 536–544.

142 Suzuki, Y., Ii, M., Saito, T. et al. (2018). Establishment of a novel mouse xenograft model of human uterine leiomyoma. *Sci. Rep.* 8 (1): 8872.

143 Drosch, M., Bullerdiek, J., Zollner, T.M. et al. (2013). A novel mouse model that closely mimics human uterine leiomyomas. *Fertil. Steril.* 99 (3): 927–935.e6.

144 Malik, M., Britten, J., and Catherino, W.H. (2020). Development and validation of hormonal impact of a mouse xenograft model for human uterine leiomyoma. *Reprod. Sci.* 27 (6): 1304–1317.

145 Tanwar, P.S., Lee, H.J., Zhang, L. et al. (2009). Constitutive activation of beta-catenin in uterine stroma and smooth muscle leads to the development of mesenchymal tumors in mice. *Biol. Reprod.* 81 (3): 545–552.

146 Varghese, B.V., Koohestani, F., McWilliams, M. et al. (2013). Loss of the repressor REST in uterine fibroids promotes aberrant G protein-coupled receptor 10 expression and activates mammalian target of rapamycin pathway. *Proc. Natl. Acad. Sci. U.S.A.* 110 (6): 2187–2192.

147 Mittal, P., Shin, Y.H., Yatsenko, S.A. et al. (2015). *Med12* gain-of-function mutation causes leiomyomas and genomic instability. *J. Clin. Invest.* 125 (8): 3280–3284.

148 Spurgeon, M.E., Uberoi, A., McGregor, S.M. et al. (2019). A novel in vivo infection model to study papillomavirus-mediated disease of the female reproductive tract. *mBio* 10 (2).

149 Arbeit, J.M., Howley, P.M., and Hanahan, D. (1996). Chronic estrogen-induced cervical and vaginal squamous carcinogenesis in human papillomavirus type 16 transgenic mice. *Proc. Natl. Acad. Sci. U.S.A.* 93 (7): 2930–2935.

150 Riley, R.R., Duensing, S., Brake, T. et al. (2003). Dissection of human papillomavirus E6 and E7 function in transgenic mouse models of cervical carcinogenesis. *Cancer Res.* 63 (16): 4862–4871.

151 Seidman, J.D., Ronnett, B.M., Shih, IeM. et al. (2019). Epithelial tumors of the ovary. In: *Blaustein's Pathology of the Female Genital Tract* (eds. R.J. Kurman, L. Hedrick Ellenson and B.M. Ronnett), 841–966. Cham: Springer International Publishing.

152 Cho, K.R. and Shih, I.M. (2009). Ovarian cancer. *Annu. Rev. Pathol.* 4: 287–313.

153 Vanderhyden, B.C., Shaw, T.J., and Ethier, J.F. (2003). Animal models of ovarian cancer. *Reprod. Biol. Endocrinol.* 1: 67.

154 Zakarya, R., Howell, V.M., and Colvin, E.K. (2020). Modelling epithelial ovarian cancer in mice: classical and emerging approaches. *Int. J. Mol. Sci.* 21 (13): 4806.

155 Zhang, S., Dolgalev, I., Zhang, T. et al. (2019). Both fallopian tube and ovarian surface epithelium are cells-of-origin for high-grade serous ovarian carcinoma. *Nat. Commun.* 10 (1): 5367.

156 Lohmussaar, K., Kopper, O., Korving, J. et al. (2020). Assessing the origin of high-grade serous ovarian cancer using CRISPR-modification of mouse organoids. *Nat. Commun.* 11 (1): 2660.

157 Kim, J., Park, E.Y., Kim, O. et al. (2018). Cell origins of high-grade serous ovarian cancer. *Cancers (Basel)* 10 (11): pii: E433.

158 Wu, R., Hendrix-Lucas, N., Kuick, R. et al. (2007). Mouse model of human ovarian endometrioid adenocarcinoma based on somatic defects in the Wnt/beta-catenin and PI3K/Pten signaling pathways. *Cancer Cell* 11 (4): 321–333.

159 Lawrenson, K., Fonseca, M.A.S., Liu, A.Y. et al. (2019). A study of high-grade serous ovarian cancer origins implicates the SOX18 transcription factor in tumor development. *Cell Rep.* 29 (11): 3726–3735.e4.

160 Hao, D., Li, J., Jia, S. et al. (2017). Integrated analysis reveals tubal- and ovarian-originated serous ovarian cancer and predicts differential therapeutic responses. *Clin Cancer Res.* 23 (23): 7400–7411.

161 Flesken-Nikitin, A., Odai-Afotey, A.A., and Nikitin, A.Y. (2014). Role of the stem cell niche in the pathogenesis of epithelial ovarian cancers. *Mol. Cell. Oncol.* 1: e963435. 1–7.

162 Flesken-Nikitin, A., Hwang, C.I., Cheng, C.Y. et al. (2013). Ovarian surface epithelium at the junction area contains a cancer-prone stem cell niche. *Nature* 495 (7440): 241–245.

163 Zhai, Y., Wu, R., Kuick, R. et al. (2017). High-grade serous carcinomas arise in the mouse oviduct via defects linked to the human disease. *J. Pathol.* 243 (1): 16–25.

164 McDaniel, A.S., Stall, J.N., Hovelson, D.H. et al. (2015). Next-generation sequencing of tubal intraepithelial carcinomas. *JAMA Oncol.* 1 (8): 1128–1132.

165 Hu, Z., Artibani, M., Alsaadi, A. et al. (2020). The repertoire of serous ovarian cancer non-genetic heterogeneity revealed by single-cell sequencing of normal fallopian tube epithelial cells. *Cancer Cell* 37 (2): 226–242.e7.

166 Yamulla, R.J., Nalubola, S., Flesken-Nikitin, A. et al. (2020). Most commonly mutated genes in high-grade serous ovarian carcinoma are nonessential for ovarian surface epithelial stem cell transformation. *Cell Rep.* 32 (9): 108086.

167 Paik, D.Y., Janzen, D.M., Schafenacker, A.M. et al. (2012). Stem-like epithelial cells are concentrated in the distal end of the fallopian tube: a site for injury and serous cancer initiation. *Stem Cells* 30 (11): 2487–2497.

168 Rose, I.M., Bidarimath, M., Webster, A. et al. (2020). WNT and inflammatory signaling distinguish human Fallopian tube epithelial cell populations. *Sci. Rep.* 10 (1): 9837.

169 Xie, Y., Park, E.S., Xiang, D., and Li, Z. (2018). Long-term organoid culture reveals enrichment of organoid-forming epithelial cells in the fimbrial portion of mouse fallopian tube. *Stem Cell Res.* 32: 51–60.

170 Schmoeckel, E., Odai-Afotey, A.A., Schleissheimer, M. et al. (2017). LEF1 is preferentially expressed in the tubal-peritoneal junctions and is a reliable marker of tubal intraepithelial lesions. *Mod. Pathol.* 30 (9): 1241–1250.

171 Fu, D.J., Wang, L., Chouairi, F.K. et al. (2020). Gastric squamous-columnar junction contains a large pool of cancer-prone immature osteopontin responsive $Lgr5^{-}CD44^{+}$ cells. *Nat. Commun.* 11 (1): 84.

172 Greaves, E., Cousins, F.L., Murray, A. et al. (2014). A novel mouse model of endometriosis mimics human phenotype and reveals insights into the inflammatory contribution of shed endometrium. *Am. J. Pathol.* 184 (7): 1930–1939.

173 McLeod, B.S. and Retzloff, M.G. (2010). Epidemiology of endometriosis: an assessment of risk factors. *Clin. Obstet. Gynecol.* 53 (2): 389–396.

174 Klemmt, P.A.B. and Starzinski-Powitz, A. (2018). Molecular and cellular pathogenesis of endometriosis. *Curr. Womens Health Rev.* 14 (2): 106–116.

175 El-Mahgoub, S. and Yaseen, S. (1980). A positive proof for the theory of coelomic metaplasia. *Am. J. Obstet. Gynecol.* 137 (1): 137–140.

176 Nakamura, M., Katabuchi, H., Tohya, T. et al. (1993). Scanning electron microscopic and immunohistochemical studies of pelvic endometriosis. *Hum. Reprod.* 8 (12): 2218–2226.

177 Batt, R.E. and Smith, R.A. (1989). Embryologic theory of histogenesis of endometriosis in peritoneal pockets. *Obstet. Gynecol. Clin. North Am.* 16 (1): 15–28.

178 Batt, R.E., Smith, R.A., Buck, G.M. et al. (1990). Mullerianosis. *Prog. Clin. Biol. Res.* 323: 413–426.

179 Nisolle, M. and Donnez, J. (1997). Peritoneal endometriosis, ovarian endometriosis, and adenomyotic nodules of the rectovaginal septum are three different entities. *Fertil. Steril.* 68 (4): 585–596.

180 Martin, R.D. (2007). The evolution of human reproduction: a primatological perspective. *Am. J. Phys. Anthropol.* (Suppl. 45): 59–84.

181 Tirado-Gonzalez, I., Barrientos, G., Tariverdian, N. et al. (2010). Endometriosis research: animal models for the study of a complex disease. *J. Reprod. Immunol.* 86 (2): 141–147.

182 Zamah, N.M., Dodson, M.G., Stephens, L.C. et al. (1984). Transplantation of normal and ectopic human endometrial tissue into athymic nude mice. *Am. J. Obstet. Gynecol.* 149 (6): 591–597.

183 Aoki, D., Katsuki, Y., Shimizu, A. et al. (1994). Successful heterotransplantation of human endometrium in SCID mice. *Obstet. Gynecol.* 83 (2): 220–228.

184 Shultz, L.D., Ishikawa, F., and Greiner, D.L. (2007). Humanized mice in translational biomedical research. *Nat. Rev. Immunol.* 7 (2): 118–130.

185 Walsh, N.C., Kenney, L.L., Jangalwe, S. et al. (2017). Humanized mouse models of clinical disease. *Annu. Rev. Pathol.* 12: 187–215.

186 Greenberg, L.H. and Slayden, O.D. (2004). Human endometriotic xenografts in immunodeficient RAG-2/gamma(c)KO mice. *Am. J. Obstet. Gynecol.* 190 (6): 1788–1795; discussion 95–6.

187 Mazurier, F., Fontanellas, A., Salesse, S. et al. (1999). A novel immunodeficient mouse model--RAG2 x common cytokine receptor gamma chain double mutants--requiring exogenous cytokine administration for human hematopoietic stem cell engraftment. *J. Interferon Cytokine Res.* 19 (5): 533–541.

188 Bokhman, J.V. (1983). Two pathogenetic types of endometrial carcinoma. *Gynecol. Oncol.* 15 (1): 10–17.

189 Sherman, M.E. (2000). Theories of endometrial carcinogenesis: a multidisciplinary approach. *Mod. Pathol.* 13 (3): 295–308.

190 Sherman, M.E., Sturgeon, S., Brinton, L.A. et al. (1997). Risk factors and hormone levels in patients with serous and endometrioid uterine carcinomas. *Mod. Pathol.* 10 (10): 963–968.

191 Hong, B., Le Gallo, M., and Bell, D.W. (2015). The mutational landscape of endometrial cancer. *Curr. Opin. Genet. Dev.* 30: 25–31.

192 Lax, S.F., Kendall, B., Tashiro, H. et al. (2000). The frequency of p53, *K-ras* mutations, and microsatellite instability differs in uterine endometrioid and serous carcinoma: evidence of distinct molecular genetic pathways. *Cancer* 88 (4): 814–824.

193 Berchuck, A., Rodriguez, G., Kinney, R.B. et al. (1991). Overexpression of HER-2/neu in endometrial cancer is associated with advanced stage disease. *Am. J. Obstet. Gynecol.* 164 (1 Pt. 1): 15–21.

194 Rolitsky, C.D., Theil, K.S., McGaughy, V.R. et al. (1999). HER-2/neu amplification and overexpression in endometrial carcinoma. *Int. J. Gynecol. Pathol.* 18 (2): 138–143.

195 Tritz, D., Pieretti, M., Turner, S., and Powell, D. (1997). Loss of heterozygosity in usual and special variant carcinomas of the endometrium. *Hum. Pathol.* 28 (5): 607–612.

196 Suzuki, A., de la Pompa, J.L., Stambolic, V. et al. (1998). High cancer susceptibility and embryonic lethality associated with mutation of the PTEN tumor suppressor gene in mice. *Curr. Biol.* 8 (21): 1169–1178.

197 Stambolic, V., Tsao, M.S., Macpherson, D. et al. (2000). High incidence of breast and endometrial neoplasia resembling human Cowden syndrome in *Pten*$^{+/-}$ mice. *Cancer Res.* 60 (13): 3605–3611.

198 Vilgelm, A., Lian, Z., Wang, H. et al. (2006). Akt-mediated phosphorylation and activation of estrogen receptor alpha is required for endometrial neoplastic transformation in *Pten*$^{+/-}$ mice. *Cancer Res.* 66 (7): 3375–3380.

199 Cardozo, E.R., Clark, A.D., Banks, N.K. et al. (2012). The estimated annual cost of uterine leiomyomata in the United States. *Am. J. Obstet. Gynecol.* 206 (3): 211.e1–211.e9.

200 Katz, T.A., Yang, Q., Trevino, L.S. et al. (2016). Endocrine-disrupting chemicals and uterine fibroids. *Fertil. Steril.* 106 (4): 967–977.

201 Dixon, D., He, H., and Haseman, J.K. (2000). Immunohistochemical localization of growth factors and their receptors in uterine leiomyomas and matched myometrium. *Environ. Health Perspect.* 108 (Suppl. 5): 795–802.

202 Flake, G.P., Moore, A.B., Sutton, D. et al. (2018). The life cycle of the uterine fibroid myocyte. *Curr. Obstet. Gynecol.* 7 (2): 97–105.

203 Segars, J.H., Parrott, E.C., Nagel, J.D. et al. (2014). Proceedings from the Third National Institutes of Health International Congress on Advances in Uterine Leiomyoma Research: comprehensive review, conference summary and future recommendations. *Hum. Reprod. Update* 20 (3): 309–333.

204 Flake, G.P., Andersen, J., and Dixon, D. (2003). Etiology and pathogenesis of uterine leiomyomas: a review. *Environ. Health Perspect.* 111 (8): 1037–1054.

205 Carneiro, M.M. (2016). Stem cells and uterine leiomyomas: what is the evidence? *JBRA Assist. Reprod.* 20 (1): 33–37.

206 Small, W. Jr., Bacon, M.A., Bajaj, A. et al. (2017). Cervical cancer: a global health crisis. *Cancer* 123 (13): 2404–2412.

207 Bosch, F.X., Lorincz, A., Munoz, N. et al. (2002). The causal relation between human papillomavirus and cervical cancer. *J. Clin. Pathol.* 55 (4): 244–265.

208 Palefsky, J.M. (2010). Human papillomavirus-related disease in men: not just a women's issue. *J. Adolesc. Health* 46 (4 Suppl): S12–S19.

209 Waggoner, S.E. (2003). Cervical cancer. *Lancet* 361 (9376): 2217–2225.

210 Lee, S.J., Yang, A., Wu, T.C., and Hung, C.F. (2016). Immunotherapy for human papillomavirus-associated disease and cervical cancer: review of clinical and translational research. *J. Gynecol. Oncol.* 27 (5): e51.

211 Brayton, C.F., Treuting, P.M., and Ward, J.M. (2012). Pathobiology of aging mice and GEM: background strains and experimental design. *Vet. Pathol.* 49 (1): 85–105.

212 Huang, P., Duda, D.G., Jain, R.K., and Fukumura, D. (2008). Histopathologic findings and establishment of novel tumor lines from spontaneous tumors in FVB/N mice. *Comp. Med.* 58 (3): 253–263.

213 Radaelli, E., Castiglioni, V., Recordati, C. et al. (2016). The pathology of aging 129S6/SvEvTac mice. *Vet. Pathol.* 53 (2): 477–492.

20

Male Reproductive System

Sue E. Knoblaugh, Hibret A. Adissu, Colin McKerlie, and Robert D. Cardiff

Introduction

The purpose of this chapter is to provide an introduction and overview of the normal anatomy, histology, and physiology of the mouse male reproductive system, unique necropsy and trimming protocols relevant to phenotyping the male reproductive tract, and to provide an overview of spontaneous phenotypes, as well as major genetically engineered mice (GEM) and other mutant model phenotypes of specific genetic mutations modeling human male reproductive diseases.

Male Reproductive System

The mouse male reproductive system consists of the paired testes with attached epididymides, efferent ducts, and vas deferens; and accessory sex glands consisting of paired seminal vesicles with attached coagulating glands, prostate gland, bulbourethral glands, ampullary glands, preputial glands, and the urethra and penis (Figure 20.1). The mouse prostate is divided into the anterior (coagulating gland), dorsal, ventral, and lateral lobes [1].

Accessory Sex Glands

Anatomy and Histology

The mouse male accessory sex glands consist of paired seminal vesicles with attached coagulating glands (also referred to as the anterior prostate), prostate gland, bulbourethral glands, ampullary glands, urethral glands, and preputial glands (Figure 20.1). Detailed anatomy and histology have been reviewed [1].

Special Necropsy and Trimming Protocols

The prostate with attached accessory sex glands may be removed together and placed flat on moist paper or in a cassette prior to fixation. It is important to maintain the orientation of the attached accessory sex glands because they are often included in sections of the prostate and allow for a complete evaluation.

To avoid misidentification, the prostate and associated organs can be submitted *en bloc* to maintain normal orientation (Figure 20.2). The urinary bladder and seminal vesicles with attached coagulating glands (anterior prostate) are removed, and a transverse section is made through the seminal vesicle and coagulating gland at the widest point and both sections are embedded and processed together. Specific protocols for trimming the prostate lobes are described under the prostate section. The bulbourethral glands can be fixed whole with the penis and a cross section may be embedded. Alternatively, they can be excised and fixed separately [2].

Preputial Glands

Necropsy and Trimming Protocols

The preputial glands lie in the inguinal subcutaneous region along the length of the penis. At necropsy, these glands may be gently collected by blunt dissection between the glands and the abdominal connective tissue and muscles. Both glands may be removed whole and embedded flat.

Anatomy and Histology

The preputial glands (like the clitoral glands in females) are paired modified sebaceous glands that are flattened, tan-yellow, and located subcutaneously on the caudoventral

Pathology of Genetically Engineered and Other Mutant Mice, First Edition. Edited by John P. Sundberg, Peter Vogel, and Jerrold M. Ward.
© 2022 John Wiley & Sons, Inc. Published 2022 by John Wiley & Sons, Inc.

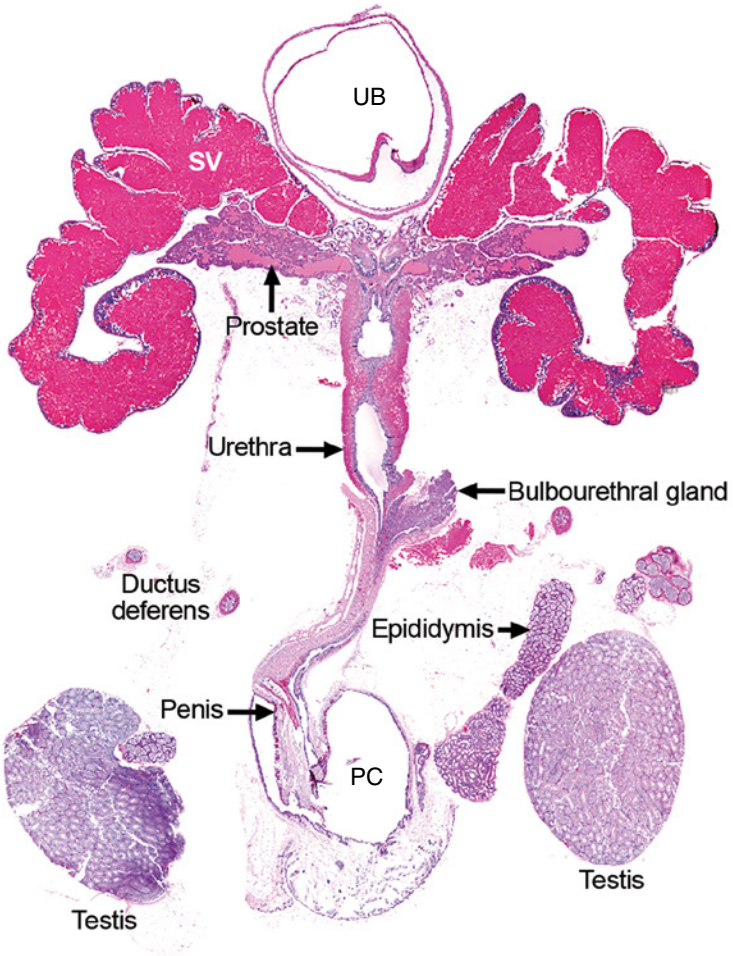


Figure 20.1 **Mouse male reproductive system**. Seminal vesicles (SV), preputial cavity (PC), urinary bladder (UB), ductus deferens (DD).

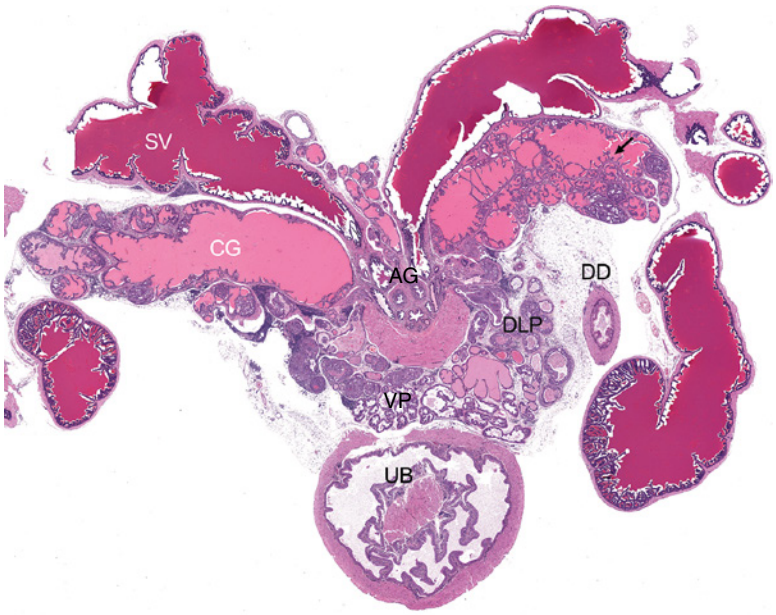


Figure 20.2 **Mouse prostate and associated accessory sex glands en bloc**. Seminal vesicles (SV), ampullary glands (AG), coagulating gland (CG), dorsolateral prostate (DLP), ventral prostate (VP), urinary bladder (UB), and ductus deferens (DD). Note the mPIN/ early adenocarcinoma of anterior prostate (coagulating gland).

abdomen. Glands are lobulated and consist of acini composed of eosinophilic, pale, foamy, secretory sebaceous cells with dark nuclei and peripheral, flat, elongated basal cells, and large ducts lined by stratified squamous epithelium (Figure 20.3). The secretions are intensely eosinophilic and contain pheromones and glucuronidase [3].

Pathology of Preputial Glands

Enlargement of the glands or preputial swelling present as firm swellings lateral to the penis that are typically secondary to proliferative lesions or abscesses. Enlarged glands are often associated with ductal ectasia, cysts, and hyperkeratosis. Ductal ectasia with acinar atrophy is a common age-associated finding with no clinical significance. Bacteria can become entrapped within the ducts, leading to inflammation and even abscessation and rupture of both preputial glands. Numerous genera of bacteria are associated with this lesion. Tumors are not common but can be induced with some chemicals.

Bulbourethral Glands (Cowper's Glands)

Anatomy and Histology

The bulbourethral glands are paired glands embedded within the ischiocavernosus and bulbocavernosus muscles located near the base of the penis. The glands consist of a main body, tail, and secretory duct.

Histologically, the multilobular glands are composed of acini opening into a central canal with ducts lined by cuboidal epithelium. Acini are line by tall columnar epithelium with abundant, foamy cytoplasm in the secretory state and eosinophilic, granular cytoplasm in the resting state (Figure 20.4). The secretory cells are found most commonly in the body and the resting cells are more commonly found in the tail. The ductular epithelium is cuboidal.

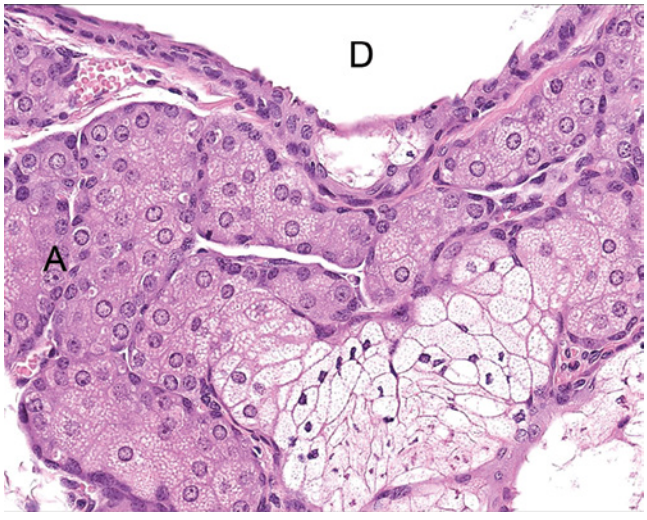


Figure 20.3 The mouse preputial glands are composed of acini (A) and large, cavernous, excretory ducts lined by squamous epithelium (D).

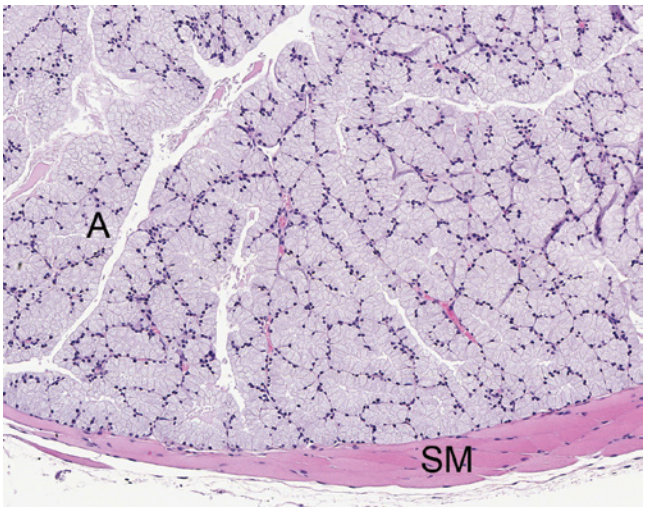


Figure 20.4 The Bulbourethral glands (Cowper's glands) are multilobular glands composed of acini (A) lined by tall columnar epithelium embedded in skeletal muscle (SM).

Pathology of Bulbourethral Glands

Older mice may develop dilation of the bulbourethral glandular acini or ducts that may progress to cystic atrophy and may result in swelling of the perineal region and impaired reproductive performance [2]. Bacterial infection with *Staphylococcus aureus* and *Pasteurella pneumotropica* is also common and may result in abscessation.

Genetically Engineered Mice

GEM models of prostate carcinoma may also result in expression of transgenes in the bulbourethral and other accessory sex glands. An example are the SV40 transgenic models developed as GEM models of prostatic adenocarcinoma such as the early non-prostate specific *Tg(C3-1-Tag)cJeg* transgenic mouse model that develops adenocarcinomas of the periurethral and bulbourethral glands [4]. Familiarity with the normal histological features of these accessory sex glands is key to accurate evaluation of GEM models.

Ampullary Glands

The AGs are paired outpouchings of the ductus deferens (DD) lined by a cuboidal epithelium. They are distinguished from prostate glands by their characteristic eosinophilic, vacuolated secretions and dense, fibromuscular stroma and flat epithelium (Figure 20.5). Similar to the periurethral glands, they may also be included in *en bloc* sections of the prostate.

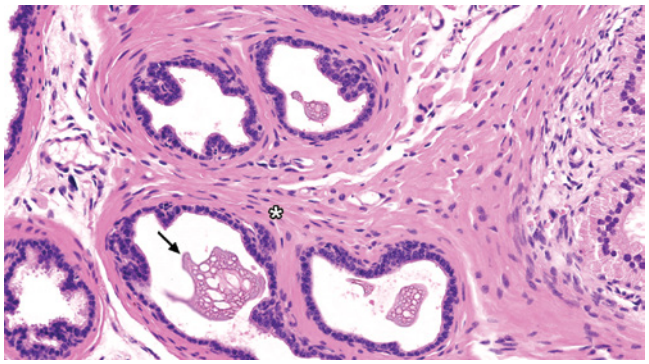


Figure 20.5 Ampullary glands are lined by a cuboidal epithelium with characteristic eosinophilic, vacuolated secretions (arrow) and dense, fibromuscular stroma (*).

Periurethral Glands (Glands of Littré)

The periurethral glands (glands of Littré) are small mucus-secreting glands located in the suburethral tissue and should be distinguished from glands of the prostate and other accessory tissues because they are commonly seen in *en bloc* sections of the prostate.

Genetically Engineered Mice

The SV40 transgenic models developed as GEM models of prostatic adenocarcinoma may also develop hyperplasias and tumors in the periurethral glands. An example includes the early non-prostate specific *Tg(C3-1-Tag)cJeg* transgenic mouse model that develops adenocarcinomas of the periurethral and bulbourethral glands [4].

Seminal Vesicles

Anatomy and Histology

The seminal vesicles are large, paired sacculated glands located dorsolateral to the urinary bladder. Histologically the glands have characteristic intensely bright eosinophilic secretions and are lined by a columnar epithelium that forms characteristic branching mucosal folds (Figure 20.6).

Pathology of Seminal Vesicles

One or both glands can become quite distended with secretions and associated with thinning of the vesicle wall in older animals. The secretions may become hardened and inspissated and may result in abdominal distension and possible infarction of the seminal vesicles. This is very common in aging C57BL/6J and CB6F1 mice. They may also become blocked and distended in mouse models of prostatic cancer. Grossly, the seminal vesicular fluid is normally white, but will discolor to tan or brown with infection, infarction, or blockage. Contraction (atrophy) of one or both seminal vesicles is also common.

Genetically Engineered Mice

The TRansgenic Adenocarcinoma of Mouse Prostate (TRAMP) *Tg(TRAMP)8247Ng* mouse model may develop neuroendocrine carcinoma affecting the seminal vesicles and may also develop benign epithelial stromal tumors or polyps. This tumor develops from both mesenchymal and epithelial components of the seminal vesicle and is characterized by papillary or polypoid growth with a prominent stromal component, low mitotic rate, and is considered benign with no evidence of invasion (Figure 20.7). A myxomatous expansion of the stroma may also be seen. It should be noted that this lesion was previously misdiagnosed as a malignant phyllodes tumor of prostatic origin [5].

Prostate

Anatomy and Histology

The mouse prostate is divided into the anterior (coagulating gland), dorsal, lateral (sometimes grouped as dorsolateral lobe), and ventral lobes separated by a thin fibromuscular

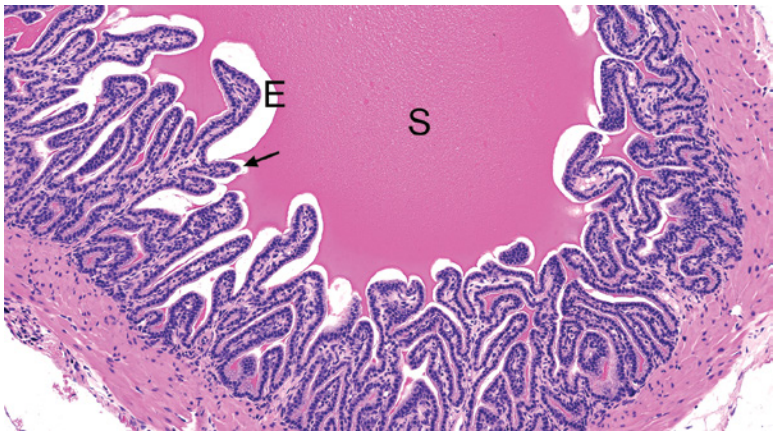


Figure 20.6 The Seminal vesicles are composed of tall columnar epithelium (E) with delicate branching mucosal folds (arrow) and intensely eosinophilic intraluminal secretions (S).

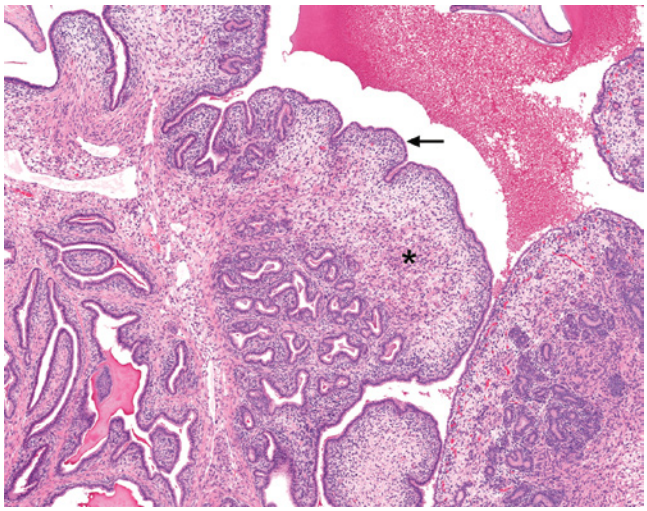


Figure 20.7 Benign polyp of the seminal vesicles in the TRAMP (Tg(TRAMP)8247Ng) model characterized by polyploid growth with a mixture of epithelial cells (arrow) and myomatous stroma (*).

stroma (Figure 20.8a,b). This differs from the single gland human prostate divided into histologically distinct zones consisting of peripheral, transition, and central zones separated by a robust fibromuscular stroma [6]. Unlike many GEM models of prostatic cancer whereby multiple lobes are affected or several lesions may be present in a single lobe, the peripheral zone is the most commonly affected zone in human prostatic neoplastic disease.

Detailed anatomy and histology have been reviewed [1]. Briefly, each lobe of the mouse prostate may be distinguished by characteristic epithelium and secretions (Figure 20.9a–d). The CGs (anterior prostate) are lined by a cuboidal to columnar epithelium with a papillary or cribriform growth pattern and contain homogeneous, light eosinophilic secretions. The lateral prostate glands are lined by mostly cuboidal to low columnar epithelium with sparse infoldings, and contain amorphous, particulate, eosinophilic secretions. The ventral prostate glands are lined by cuboidal to columnar epithelium with sparse infolding, focal tufting, and abundant pale homogeneous serous secretion. The dorsal prostate glands are lined by columnar epithelium with moderate infolding and contain homogeneous eosinophilic secretions. Individual glands are surrounded by a distinct fibromuscular stroma.

Special Necropsy and Trimming Protocols

As previously stated, identification and analysis of individual prostate lobes are essential for the characterization of GEM prostatic cancer models and analysis for progression of disease. Depending on the genetic alteration, GEM models may have varying lesions in different prostate lobes, as well as the accessory sex glands including the periurethral glands, seminal vesicles, and bulbourethral glands. It is also important to evaluate all accessory sex glands for neoplastic lesions that may extend into the prostate. Evaluation requires careful necropsy and dissection protocols to include the prostate and associated accessory sex glands *en bloc* and preparation of tumors and surrounding tissues (Figure 20.2). A transverse section through the prostate lobes includes the dorsolateral and ventral lobes and urethra may be made and both sections may be embedded cut-face down [7, 8]. Alternatively, microdissection of the individual prostate lobes has been described, but care must be taken when orienting for embedding [9]. Chambered cassettes are often utilized for this purpose. Artifacts such as oblique sections and out-foldings of epithelial structures may occur and confound diagnosis. Such artifacts must be distinguished from true areas of

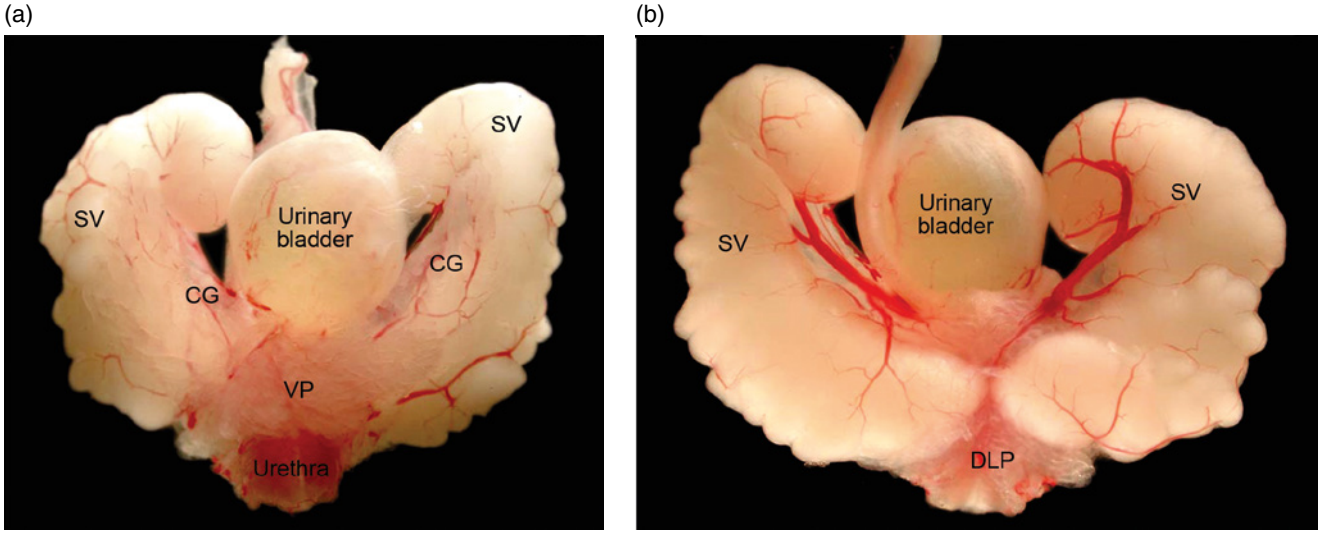


Figure 20.8 **Gross prostate lobes and Seminal vesicles**. (a) Ventral view, (b) Dorsal view. The seminal vesicles (SV) and murine prostate lobes. The coagulating gland (CG) (anterior), dorsolateral prostate (DLP), and ventral prostate (VP).

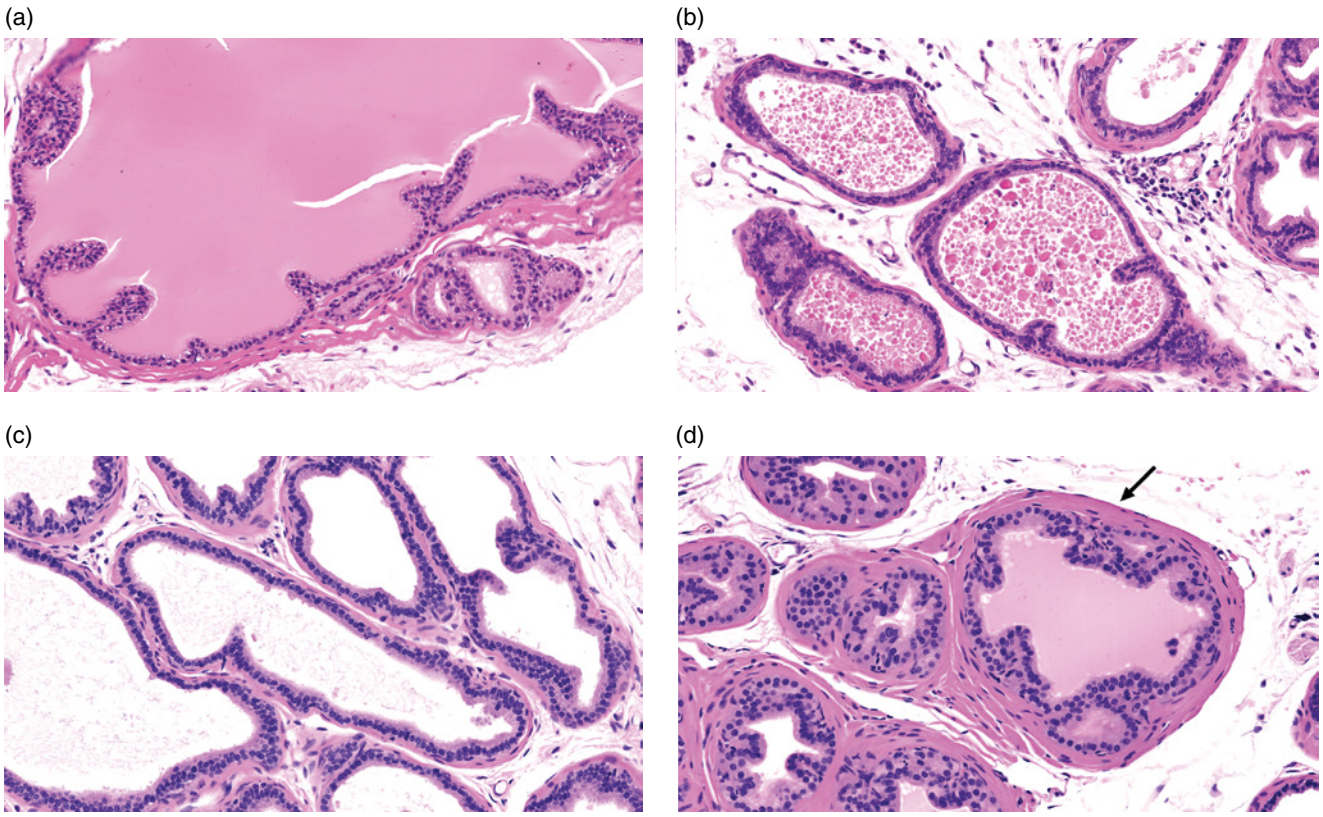


Figure 20.9 **The four mouse prostate lobes are histologically distinct**. (a) Coagulating gland (Anterior prostate): The epithelium is cuboidal to columnar with a papillary or cribriform growth pattern (arrows) with abundant, homogenous, eosinophilic secretions. (b) Lateral prostate: Lined by mostly cuboidal to low columnar epithelium with sparse infolding, with amorphous, particulate, eosinophilic secretions. (c) Ventral prostate: Lined by mostly cuboidal epithelium with homogenous, pale, serous secretions. (d) Dorsal prostate: Lined by columnar epithelium, with moderate infolding with homogenous, eosinophilic secretions. Individual glands are surrounded by a distinct fibromuscular stroma (arrow).

invasion or microcarcinomas. Step and serial sections may be performed to avoid misdiagnosis in early disease and to avoid misclassification of section artifacts.

Background strain-specific lesions and spontaneous tumors in non-prostatic tissues must be distinguished from metastatic lesions. It is essential to examine age-matched littermate controls of the same genetic background and housed under the same conditions. Transgene expression should be interpreted with caution in nonprostate tissues as a prostate-specific promoter may have transformative activity in nonprostate cells. This is particularly problematic in mice with global germline expression or when using non-prostate specific promoters.

Special Histochemical Stains and Immunohistochemical Markers

Immunohistochemical markers have broad utility in characterization of GEM models. Some of these include markers of epithelial differentiation (pancytokeratin, E-cadherin, cadherin 1, CDH1, KRT14, KRT5, KRT8, TRP63) vascular density (CD31 (PCAM1), CD34, CD105 (ENG), neuroendocrine differentiation (Synaptophysin (SYP)), Chromogranin A (CHGA)) and other useful markers such as androgen receptor (AR) and Ki-67. As previously stated, expression of particular transgenes (i.e. Tag or SV40) for specific GEM models and relevant proteins or activated signaling pathways may be evaluated by immunohistochemistry. Indeed, transgene immunostains must not be used as evidence of metastasis from primary prostatic neoplasms because even with prostate specific promoters, it is known that transgene expression may occur in non-prostate sites. This is particularly common and known with specific transgenes (e.g. large T antigen in the case of SV40 or Tag-based models) [7]. In some instances, immunostains such as thyroid transcription factor-1 (TTF-1/NKX2-1) for primary lung neoplasms should be used to assist in interpretation of possible metastatic lesions. Many useful markers and assays have been published in model specific literature; however, it should be emphasized that while immunohistochemistry is helpful it is not a replacement for histopathologic evaluation of step or serial H&E stained sections.

Pathology of Prostate Glands

Spontaneous lesions are rare in the wild type mouse prostate [7, 8]. The low incidence of lesion in the prostate of wild type mice suggests that any lesion in the GEM prostate could

be a consequence of the genetic manipulation involved either due to systemic effects (e.g. immunological or endocrinologic effects) or as a direct consequence of a genetic alteration in the prostate [7].

Mononuclear or lymphocytic infiltration is the most common background finding affecting the various lobes, while pronounced inflammation (prostatitis) is uncommon [7, 8]. Inflammation in the prostate, spontaneous or experimental, can be accompanied by reactive epithelial proliferation and nuclear atypia [8, 10]. Such secondary epithelial changes in the GEM prostate should be classified as inflammatory, with specification of reactive atypia, rather than proliferative [7]. This distinction could present a challenge; hence it is recommended that attention should be given to areas relatively free or devoid of inflammation, where recognition of epithelial hyperplasia can be made with more confidence [7].

Genetically Engineered Mouse Models

Genetic abnormalities are believed to underlie a large percentage of human prostatic cancer. GEM models are instrumental in understanding the cause, prevention, and treatment of prostate cancer. Several essential genes for human cancer have been modeled in mice and the models have led to the identification of additional genes and pathways associated with the development of prostatic neoplasia. The Mouse Tumor Biology Database maintained by The Jackson Laboratory contains information on a number of GEM models in a searchable database for a variety of tumor types, including prostatic carcinoma (see http://tumor.informatics.jax.org/). Most GEM models of human prostatic cancer are associated with expression of transgenes, overexpression of genes, or deletion or inactivation of tumor suppressor genes with limited or restriction of expression to the prostate (see http://www.informatics.jax.org/vocab/mp_ontology/MP:0009220).

Pathology and Classification of Lesions of the Prostate in Genetically Engineered Mouse Models

Prostate pathology for many GEM models has been previously reviewed, described, and updated in detail by The Mouse Models of Human Cancers Consortium Prostate Pathology Committee and should be referenced for histopathologic analysis and classification of GEM models of prostate cancer (Figure 20.10a–d; Table 20.1) [7, 11]. There are several important points to keep in mind when using GEM to model the human disease. First, it has been shown and should be noted that genetic background may influence lesion development and progression in GEM models of prostate cancer [7]. GEM models may have a range of changes with variable severity in the same prostatic lobe or gland (e.g. Mouse prostatic intraepithelial neoplasia [mPIN] to adenocarcinoma) [11]. In general, neoplastic progression may be secondary to activation of transgenes or loss of tumor suppressors of individual cells at variable rates.

Epithelial Hyperplasia

Epithelial hyperplasia in the prostate is defined as an increase in prostatic epithelial cells and may be focal, multifocal, or diffuse and vary from simple to more complex forms with tufting, papillary, and cribriform patterns. Cellular nuclear atypia may be noted but is typically mild and associated with inflammation.

Mouse Prostatic Intraepithelial Neoplasia (mPIN)

Prostatic intraepithelial neoplasia (PIN) is the proliferation of atypical epithelial cells within glands. In humans, PIN is distinguished as low grade and high grade and it is thought that high-grade prostatic intraepithelial neoplasia (HGPIN) is a precursor lesion to invasive carcinoma. Such lesions have been shown to progress to invasive carcinoma in GEM models and are thought of as preinvasive neoplastic lesions unlike in humans where only a fraction of HGPIN lesions continue to invasive carcinoma. In GEM models, the lesion is classified as mPIN. mPIN has been shown to affect all lobes of the mouse prostate and its morphology may be GEM model specific. Classification of mPIN has been described [12]. Briefly, mPIN is graded on a 4-point scale with increasing cytologic and architectural abnormality. This scale equates mPIN1 and 2 to low grade prostatic intraepithelial neoplasia (LGPIN) in humans, whereas mPIN3 and 4 are similar to human high grade HGPIN (Figure 20.10a,b).

Adenocarcinoma

Invasive adenocarcinoma is identified by atypical glandular cells with an invasive growth pattern and a characteristic stromal desmoplasia (fibrosis) and associated inflammation (Figure 20.10c) [7]. Intraductal carcinoma is an entity that occurs in human disease and has been shown in some GEM models. Intraductal carcinoma is characterized by proliferating atypical cells expanding the preexisting epithelium and structures, but without infiltration. This is an aggressive disease in humans, but the significance is unclear in GEM models. Within some mouse models, adenocarcinomas have focal squamous and intestinal metaplasia, which is rare in human prostatic cancer.

Sarcomatoid Carcinoma

Some GEM models have shown extensive sarcomatoid differentiation within adenocarcinomas that are characterized by atypical spindle cells admixed with, or adjacent to, invasive adenocarcinoma [11]. Sarcomatoid lesions have been shown to coexpress immunohistochemical epithelial and mesenchymal markers and have been classified as epithelial–mesenchymal tumors (EMTs) (Figure 20.10d).

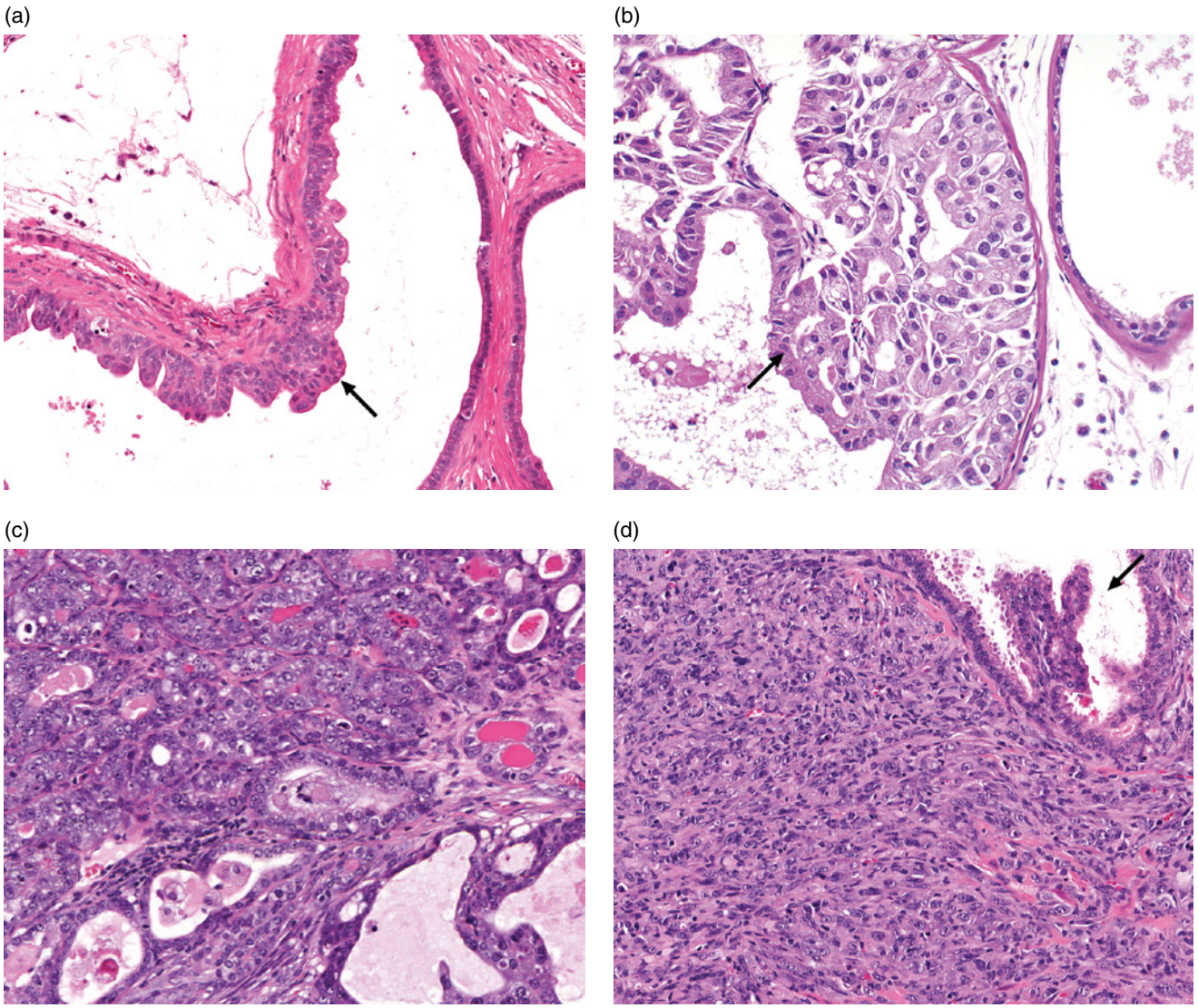


Figure 20.10 **Classification of lesions of the prostate in genetically engineered mouse models**. (a) Mouse prostatic intraepithelial neoplasia (mPIN)-low-grade with focal epithelial proliferation and mild atypia (arrow). (b) Mouse prostatic high-grade intraepithelial neoplasia (mPIN) with proliferation of atypical cells filling the duct (arrow). (c) Adenocarcinoma. (d) Sarcomatoid carcinoma with atypical proliferating spindle cells shown adjacent to a residual gland with mPIN (arrow).

Neuroendocrine Carcinoma

Malignant neuroendocrine tumor or NE is noted in GEM models, especially the *Tg(TRAMP)8247Ng* (TRAMP) model of prostatic neoplasia and outcrosses of TRAMP to other GEM. They are the most widely metastatic and aggressive of mouse prostate cancers [11]. This tumor often forms in the ventral prostate or submucosal urethral glands and is characterized by expansile masses of neoplastic cells forming packets, sheets, and multifocal pseudorosettes separated by a fine fibrous stroma (Figure 20.11). Neoplastic cells have marked cellular and nuclear pleomorphism with atypical mitoses. Multifocal masses often contain entrapped prostatic acini. There are also angiocentric cells separated by large zones of necrosis, invasion into surrounding tissue, and metastases to the lung and other tissues such as the adrenal glands, liver, lymph nodes, and kidney. Tumors typically do not express AR but are positive for the neuroendocrine markers synaptophysin and chromogranin A (Figure 20.11). Neuroendocrine tumors have also been reported in FVB/N mice containing the SV40 T-Ag and development may be affected by the background strain of the mouse.

Specific Prostatic Tumor Models

There are numerous GEM models of prostate cancer, all with varying features of the human disease, and are associated with mutations in several genes (Table 20.2) [12, 14]. The majority of prostate models either express oncogenes or

Table 20.1 Classification of lesions of the prostate in genetically engineered mouse models.

Classification	Histopathologic changes	References
Epithelial hyperplasia	Nonneoplastic increase in prostatic epithelial cells Simple: a single epithelial cell lining with increased cells Complex: increased epithelial cells with tufting, papillary, and cribriform growth patterns	[7, 11]
Mouse prostatic intraepithelial neoplasia (mPIN)	Proliferation of atypical epithelial cells within glandular spaces and without invasion Low-grade (mPIN 1,2) – Focal epithelial proliferation with mild atypia High-grade (mPIN 3,4) – Proliferation of atypical cells that may fill glands but maintain well-demarcated border. Atypia is often pronounced.	[7, 11]
Adenocarcinoma	Malignant neoplasm that is invasive with epithelial glandular formation. Often associated with stromal desmoplasia and chronic inflammation. Metaplasia- focal squamous or intestinal differentiation may occur within adenocarcinoma	[7, 11]
Sarcomatoid carcinoma (EMT)	Adenocarcinoma with sarcomatoid differentiation. May coexpress mesenchymal and epithelial immunohistochemistry (IHC) markers to variable degrees.	[7, 11]
Neuroendocrine carcinoma	Invasive malignant epithelial neoplasm with NE differentiation- formation of gland-like spaces and rosettes without true gland formation. Cells have round to oval nuclei with finely granular chromatin and cytoplasm containing neurosecretory-type granules. Tumors are immunopositive for NE markers (synaptophysin, chromogranin). Ultrastructural NE features: focal or multifocal dense core (NE type) secretory granules.	[7, 11]

delete known tumor suppressors specifically within the prostatic epithelium. It should be noted that mouse prostate lobes may respond differently to genetic manipulation whereby different genetic manipulations may result in specific lobes being affected and at various rates of progression [15]. GEM models that affect the dorsolateral prostate (DLP) may develop rather large tumors that may block the ejaculatory duct and result in massive dilatation of the anterior prostate. This typically leads to edema and inflammation that may not only be misdiagnosed as a neoplasm macroscopically but could also confound immunoinflammatory end points. This is commonly seen with the probasin (*Pbsn-cre*) models. Early models targeted many proteins and are based off SV40, which is not present in human prostate disease. Later models are prostate specific and are based on human genetic mutations. Several models have been previously reviewed [7, 11, 13].

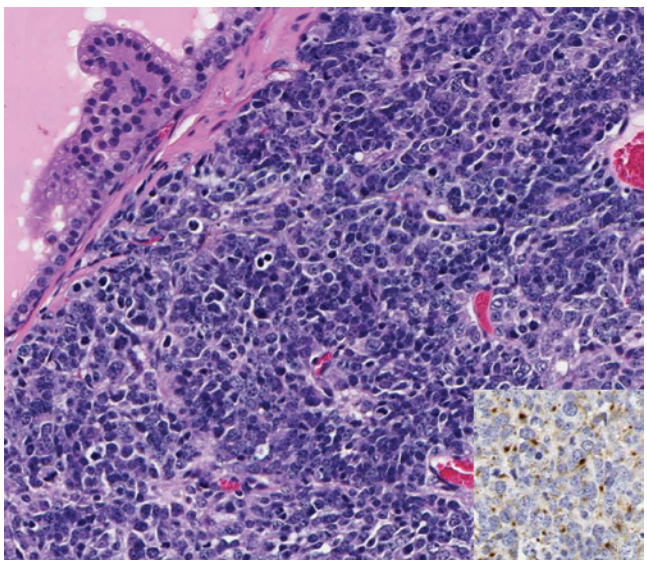


Figure 20.11 TRAMP (Tg(TRAMP)8247Ng) mouse model with neuroendocrine carcinoma. H&E stained TRAMP tumor characterized by expansile masses of neoplastic cells forming packets, sheets, and multifocal pseudorosettes separated by a fine fibrous stroma. Inset: Synaptophysin immunolabeling for neuroendocrine cells.

Models with Alterations in PTEN/AKT Signaling

PTEN is a negative regulator of the PI3K/AKT pathway known to be activated in most late-stage human prostate cancers. Homozygous deletion of *Pten* is embryonic lethal. *Pten* heterozygous mice develop mPIN but encounter many health problems before progression to adenocarcinoma. Prostate-specific homozygous deletion of *Pten* (*Pten*^{tm1Hwu}; Tg(Pbsn-cre)4Prb) mice develop mPIN and invasive adenocarcinoma with involvement of all prostate lobes and metastasis as seen in humans [11]. A number of mouse *Pten* deletion models combined with additional genetic alterations form sarcomatoid carcinomas in addition to invasive adenocarcinoma and HGPIN lesions. Examples include the *Pten* (*Pten*^{tm1Rdp})/*Trp53* (*Trp53*^{tm1Brn}) and *Pten*/*Smad4* (*Smad4*$^{Tn(sb\text{-}Pten)1.1Jcad}$) null mouse models and *Pten* null

Table 20.2 Select GEM models of prostate cancer.

Disease-associated gene	Human disease and pathology	GEM models	Mouse phenotype	References
Pten	*PTEN* deletions occur in 23% of HGPIN, 69% of localized PCa, and 86% of metastatic CRPC.	*Pten*$^{+/-}$ (*Pten*^{tm1Ppp})	Hyperplasia, mPIN, small % adenocarcinoma	[11, 13]
		Pten$^{+/-}$*Nkx3.1*$^{-/-}$ (Nkx3-1$^{tm4(cre/ERT2)Mms}$) (*Pten*^{tm1Hwu})	HGPIN, adenocarcinoma, LN mets	[11, 13]
			HGPIN, adenocarcinoma, mets.	[11, 13]
		Pten $^{flox/flox}$ (prostate specific) (*Pten*^{tm1Hwu}; Tg(Pbsn-cre)4Prb)	HGPIN,	[11, 13]
		Pten$^{flox/flox}$; *p53*$^{flox/flox}$ *Pten*(*Pten*^{tm2Hwu})/*Trp53* (*Trp53*^{tm1Brn})	Adenocarcinoma with reactive stroma, sarcomatoid carcinoma	[11, 13]
		Pten$^{flox/flox}$; *Smad4*$^{flox/flox}$ *Smad4*$^{Tn(sb-Pten)1.1Jcad}$	Adenocarcinoma, aggressive with reactive stroma, mets to LN and Lung	[11, 13]
		Pten$^{flox/flox}$ (*Pten*^{tm1Rdp}) *p53*$^{flox/flox}$ (*Trp53*^{tm1Brn}) *telomerase* (*Tert*^{tm3Rdp})	Adenocarcinoma and highly pleomorphic sarcomatoid carcinomas with invasion/ extension into vertebra	
MYC	Increased copy number and overexpression in human PCa.	Hi-*MYC* (Tg(ARR2/Pbsn-MYC)7Key)	mPIN, invasive adenocarcinoma (DLP, VP)	[11, 13]
		MYC; Pten$^{flox/+}$; *p53*$^{flox/flox\ (alleles\ not\ specified)}$	Adenocarcinoma (all lobes), mets to LN	[11, 13]
TMPRSS2/ERG	*TMPRSS2/ERG* fusion gene present 50% PCa.	*TMPRSS2-ERG* (*Gt(ROSA)26Sortm1(TMPRSS2/ERG)Key*)	mPIN	[11, 13]
SV40-Tag (Large T antigen)	N/A	LADY model (*Tg(Pbsn-Tag)12T10Rjm*)	mPIN, adenocarcinoma, NED	[11, 13]
		PB-Hepsin (*Tg(Pbsn-Hpn,-GFP)DVv)*	NE with mets to lung, liver, and bone	
SV40-Tag (Small and large-T).	N/A	TRAMP model (*Tg(TRAMP)8247Ng*)	NE with visceral met (FVB); NED to NE (C57)	[11, 13]

mPIN = prostatic intraepithelial neoplasia; NE = Neuroendocrine; NED = Neuroendocrine differentiation; HGPIN = High grade prostatic intraepithelial neoplasia; LGPIN = Low grade prostatic intraepithelial neoplasia; Mets = Metastases; DLP = Dorsolateral prostate; VP = Ventral prostate; LN = lymph node.

(*Pten*$^{tm2.1Ppp}$) with *ERG* overexpression (*Gt(ROSA)26Sor*$^{tm1(TMPRSS2/ERG)Key}$) model. The pathology is similar in these models and includes stromal fibrosis (desmoplasia) with invasive progression [11] (Figure 20.12). The loss of both *Pten* and *Trp53* in combination with telomerase *Pten*$^{flox/flox}$ (*Pten*^{tm1Rdp})*Trp53*$^{flox/flox}$ (*Trp53*^{tm1Brn}) *telomerase* (*Tert*^{tm3Rdp}) reactivation results in aggressive adenocarcinoma and sarcomatoid carcinomas with metastasis to the spine. Homozygous deletion of *Smad4* and *Pten* (*Smad4*$^{Tn(sb-Pten)1.1Jcad}$) in the mouse prostate results in early-onset glandular adenocarcinomas with metastasis to lumbosacral lymph nodes and later metastasis to the lung. Overexpression models such as the *Pten* null/*Sox9* model show enhanced cancer progression. Similarly, *Pten* (*Pten*^{tm2Mak}) deletion in combination with mutant *Kras* heterozygous (*Tg(tetO-Kras2)12Hev*) mice promotes accelerated progression of disease when compared with *Pten* deletion alone or *Kras* alone.

Pten deletion models have been developed and studied to determine the cell origins of prostate cancer. Nkx3.1CreERT2 (*Nkx3-1*$^{tm4(cre/ERT2)Mms}$)/*Pten* deletion (*Pten*^{tm1Hwu}) mice have *Pten* deletion specific to the luminal cells and develop HGPIN and microinvasive carcinoma. Tumors regress following castration, but eventually regress to microinvasive adenocarcinoma with AR positivity [13].

Models with Alterations in *MYC* Signaling

In human prostate cancer, overexpression or increased copy number of *MYC* are common findings in up to 50% of tumors [16]. Using GEM models, the role of *MYC* in the initiation and progression of disease has shown that direct MYC transgene expression (*Tg(ARR2/Pbsn-MYC)7Key*) results in mPIN and progression to invasive adenocarcinoma without requiring additional genetic mutations [11, 16]. Invasive adenocarcinoma in these models often exhibits stromal fibrosis and inflammation (Figure 20.13). Metastatic disease is seen with a combination of *Pten* loss (Specific allele unknown) and *MYC* activation (*Tg(ARR2/Pbsn-MYC)7Key*) and *Pten* (Specific allele unknown)/*Trp53* (Specific allele unknown) deficiency where *MYC* is a known driver [16].

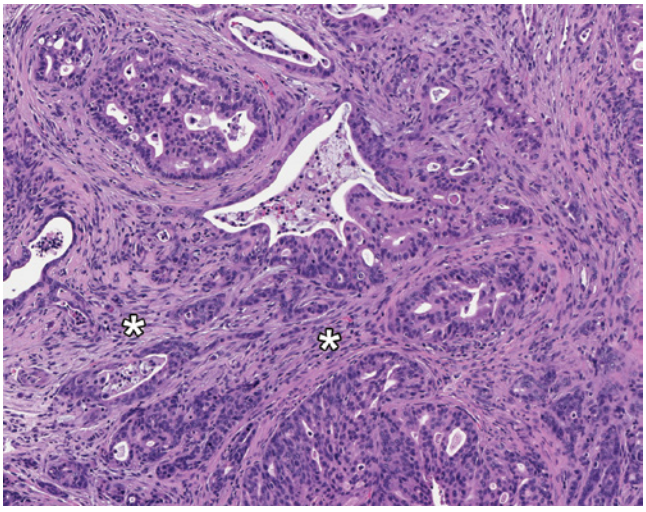


Figure 20.12 **Prostatic adenocarcinoma from a mouse with conditional prostate-specific deletion of *Pten*.** The tumor cells form irregular glands and solid masses, which are embedded in an abundant stroma (*).

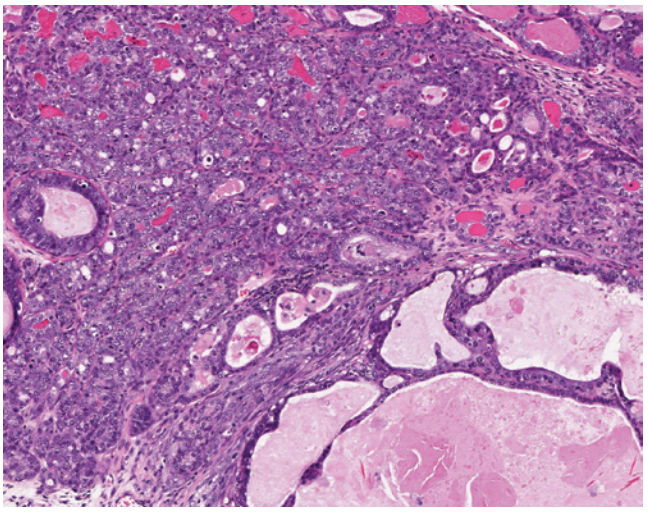


Figure 20.13 Adenocarcinoma from an overexpressing MYC (FVB-Tg(ARR2/Pbsn-MYC)7Key) model with characteristic large basophilic nuclei and prominent nucleoli.

Models with Alterations in *ERG* Signaling

Half of all human prostate cancers include the *TMPRSS2/ERG* fusion gene. GEM models with overexpression of *ERG* (*Gt(ROSA)26Sortm1(TMPRSS2/ERG)Key*) are characterized by mPIN lesions with no evidence of HGPIN or adenocarcinoma. As previously noted, *ERG* overexpression (*Gt(ROSA)26Sortm1(TMPRSS2/ERG)Ke*) in combination with *Pten* deletion (*Ptentm2.1Ppp*) promotes a more advanced phenotype with sarcomatoid carcinomas.

Models with Alterations in Fibroblast Growth Factor (*FGF*) Signaling

Fibroblast growth factors (FGFs) and FGF receptors are required for normal prostate development. Aberrant activation has been implicated in prostate cancer. The ligand-inducible human *FGFR1* (*Tg(Pbsn-Fgfr1/Fkbp1a)#aDmsp*) transgenic mouse model, *JOCK1* (juxtaposition of CID and kinase1) mice are treated with dimerizing drug to oligomerize and activate FGFR1 signaling. Upon activation, the mice develop hyperplasia, mPIN, adenocarcinoma, and sarcomatoid carcinomas with a marked desmoplastic stromal response [11].

Models with Alterations in Androgen Receptor (*AR*) Signaling

Androgen receptor (*AR*) is essential and a marker for growth and differentiation of the epithelium in the normal human prostate. Aberrant expression of AR is implicated in metastatic human prostate cancer and is implicated in treatment failure of castration resistant disease [14]. A mouse model with conditionally activated human *AR* transgene expression (*Gt(ROSA)26Sortm1(CAG-AR)Zsu*) in the prostate epithelium develops low grade and high grade mPIN with development of large intracystic adenocarcinoma with occasional squamous metaplasia [11, 13]. Because this is a conditionally activated and prostate-specific model, the AR transgene expression is persistent in intact or castrated mice.

Models with Alterations in *TGF-b* Signaling

Similar to *AR*, Transforming Growth Factor Beta (TGFB) signaling is implicated in human prostate carcinoma where it contributes as a stromal growth factor driving the initial stages of prostate carcinogenesis. Crossing (*Tgfbr2tm1.2Hlm*) and *Tg(Col1a2-cre/ERT,-ALPP)7Cpd* mice in a C57BL/6 background resulted in partial *Tgfbr2* deletion in stromal fibroblasts. The deficiency in TGFBR2 stromal signaling resulted in HGPIN and chronic stromal inflammation [13]. As previously stated, *Smad4*, a central mediator of TGFB signaling, in combination with *Pten* deficiency, causes adenocarcinoma with metastasis.

SV40 T-antigen

The earliest GEM models of prostatic adenocarcinoma used the prostate steroid binding protein (C3-1) promoter to express the SV40 early region (*Tg(C3-1-Tag)cJeg*) and resulted in mammary gland adenocarcinoma and prostatic adenocarcinoma. Older male *Tg(C3-1-Tag)cJeg* transgenic mice also developed tumors of the bulbourethral gland, urethra, and salivary glands. Although not present in human prostate carcinoma, the Simian Virus 40 (SV40) large tumor antigen (Tag) is an exogenous oncogene that may be targeted to the murine prostate and will bind and inhibit the tumor suppressors *Trp53* and *Rb1*. In mouse models, SV40 T121 (*Tg(Pbsn-TAg)15Tvd*) expression and *Pten* ($Pten^{tm1Ppp}$) / *Trp53* ($Trp53^{tm1Tyj}$) deletion results in development of HGPIN in all lobes with adenocarcinoma and sarcomatoid carcinoma in mice older than 21 weeks. The anterior prostate is characteristic with intracystic carcinoma and occasional metastases to the lung. It should be noted that there may be periurethral gland lesions in addition to the prostate lobes in SV40 transgenic models.

The LADY model expresses SV40 large T-antigen, which inactivates *Rb1* and *Trp53* and the phenotype is line dependent. The *Tg(Pbsn-Tag)12T10Rjm* (LADY) mouse model develops mPIN and limited locally invasive adenocarcinoma with involvement of all prostate lobes, some of which develop adenocarcinoma-neuroendocrine biphasic carcinoma that do not metastasize [13]. The LADY models induce a reactive stromal proliferation during tumorigenesis that can be quite pronounced. Interestingly, crossing PBhepsin (*Tg(Pbsn-Hpn,-GFP)DVv*) with LADY mice results in NE tumor metastasis including bone [15].

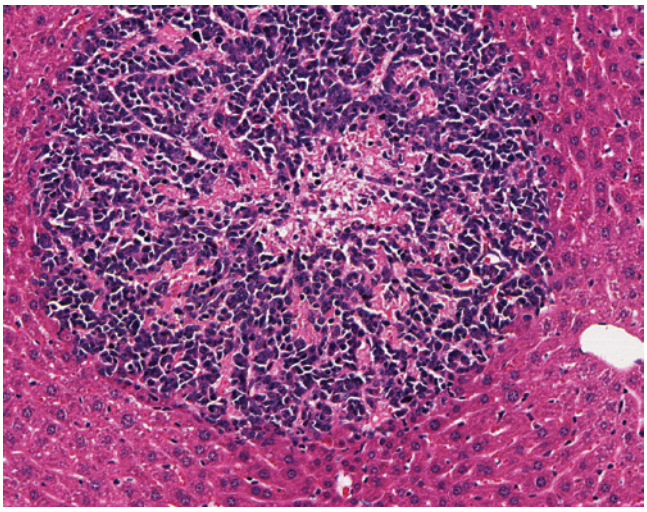


Figure 20.14 Neuroendocrine carcinoma metastasis to the liver from TRAMP model characterized by expansile masses of neoplastic cells forming packets, sheets and multifocal pseudorosettes separated by a fine fibrous stroma.

The TRansgenic Adenocarcinoma Mouse Prostate (TRAMP) *Tg(TRAMP)8247Ng* model expresses a complete SV40-T antigen (small and large-T) under control of a rat probasin promoter with high levels of transgene expression in the ventral and dorsal prostate lobes. There are over 700 publications on the TRAMP model (see https://pubmed.ncbi.nlm.nih.gov/?term=mouse+prostate+tramp&sort=date). The TRAMP model phenotype is highly dependent on background strain and includes predominantly neuroendocrine tumors that originate in the prostate and are highly metastatic to lymph nodes, liver, lung, and adrenal glands (Figure 20.14). On an FVB background, tumors are predominantly neuroendocrine carcinoma, but on a C57BL/6 background, neuroendocrine carcinomas are reported to form in only 20% of mice in which progression from mPIN to adenocarcinoma with metastasis to regional lymph nodes and lung has been described. Some models have been described to develop an atypical epithelial hyperplasia rather than adenocarcinoma [17]. Neuroendocrine tumors are immunopositive for synaptophysin and chromogranin but are often negative for AR and cytokeratin markers. Tumors are reported to be 100% neuroendocrine post castration [13]. Crossing additional genetic mutations to the TRAMP model may also suppress the development of neuroendocrine carcinomas. TRAMP mice may also develop benign tumors of the seminal vesicles that are polyploid and are a mixture of epithelial cells and myomatous stroma (Figure 20.6).

Cyclin Dependent Kinase Inhibitor 2A (*CDKN2A*)

The tumor suppressor cyclin dependent kinase inhibitor 2A (*Cdkn2a*) also known as *p16INK4a* is an inhibitor of cyclin D-dependent kinases 4 and 6 (CDK4, CDK6), which prevents the phosphorylation of the retinoblastoma protein probasin (RB) and the inhibition of the transcription of E2F-regulated genes required for cell cycle entry at the G1/S checkpoint [18]. The deletion, mutation, or epigenetic silencing of *CDKN2A* is frequently observed in human prostate cancer. A mouse model with conditional deletion of *p16Ink4a* ($Cdkn2a^{em2Hwl}$) in prostatic luminal epithelium developed mPIN but did not progress to adenocarcinoma. Compound mice with deletion of $p16^{Ink4a}$ ($Cdkn2a^{em2Hwl}$) and conditional expression of the human *AR* transgene ($Gt(ROSA)26Sor^{tm1(CAG-AR)Zsu}$) within prostatic luminal epithelial cells showed early onset of HGPIN, prostatic adenocarcinoma, and metastatic lesions. Sarcomatoid carcinomas were noted with intermixed focal regions reminiscent of the human signet ring cell carcinoma and featured characteristics of epithelial to mesenchymal transition [18].

Testes and Epididymis

Anatomy, Histology, Physiology

Detailed anatomy and histology of the testis [1] and the detailed process of spermatogenesis have been reviewed elsewhere [19, 20]. The testes are paired bilateral organs, covered by a dense fibrous capsule (tunica albuginea) and composed of arrays of convoluted seminiferous tubules that produce spermatozoa and an interstitium composed of Leydig cells that produce and secrete the androgenic steroid hormone, testosterone, under the regulation of pituitary luteinizing hormone. Each seminiferous tubule is surrounded by a basement membrane of basal lamina and myoid cells and lined by Sertoli cells and germ cells (spermatogonia, spermatocytes, spermatids, and spermatozoa) arranged in thick layers at varying stages of maturation with immature cells located basally and more mature cells located towards the lumen. Residual bodies are dense, basophilic, globular bodies that are intermixed with mature spermatids at the luminal surface of stage VII and VIII tubules (Figure 20.15). They are generally resorbed by Sertoli cells upon completion of spermiation in the basal region of stage IX and X tubules. Abnormally enlarged residual bodies can be an incidental background finding. Multinucleated cells may be normally be seen in small numbers in immature mice (pre- or peripubertal) (Figure 20.16) but are indicative of pathology when increased in number and associated with degenerative changes [21]. Tubuli recti are the terminal ends of the seminiferous tubules that transition to the rete testis (Figure 20.17), and should not be misinterpreted as atrophic tubules [21].

The paired epididymides consist of the head (caput), body (corpus), and tail (cauda) and are responsible for maturation and storage of mature spermatozoa. Final maturation of spermatozoa occurs in the epididymis and the presence of mature sperm is indicative of normal spermatogenesis. Epididymal tubules are lined by an epithelium that varies between the head and tail with the head having the tallest epithelium (pseudostratified columnar) and smallest lumen and the tail having the shortest epithelium (cuboidal to simple columnar) and the largest diameter lumen (Figure 20.18). Megalokaryocytosis of the epithelial lining of the epididymis and ductus deferens characterized by large polyploid nuclei could be seen in aged mice (Figure 20.19).

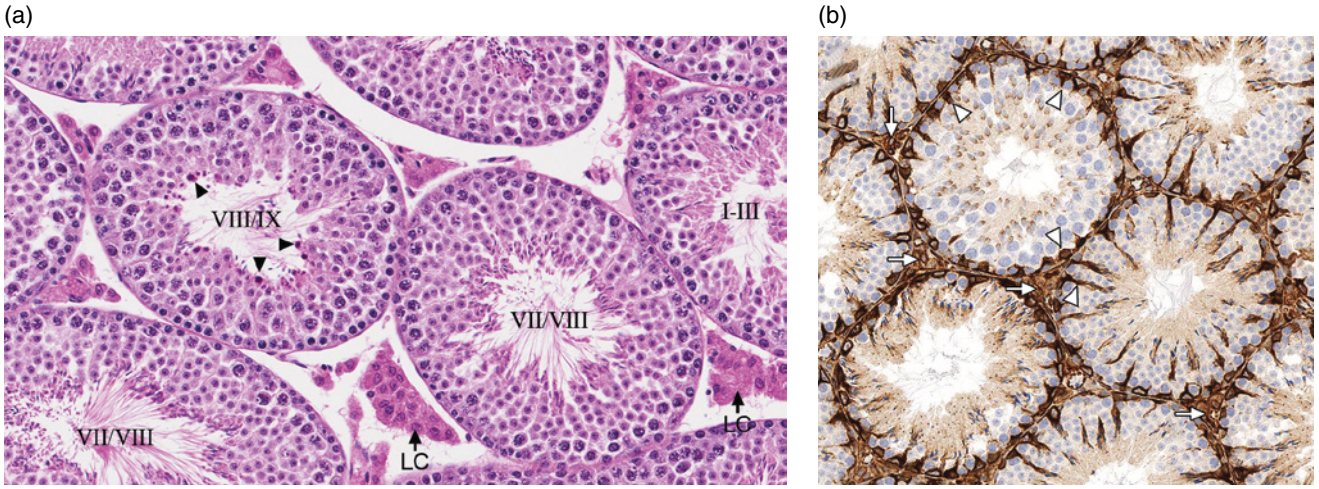


Figure 20.15 **Testis**. (a) Normal seminiferous tubules (arrowheads) separated by interstitial cells (Leydig cells)= LC. Most tubules are at release stage (VII/VIII). A tubule in transition between release and elongation (stage VIII/IX) with residual bodies (arrow heads) and one at maturation stage (I-III) are also in view. (b) Vimentin immunolabeling of testis highlighting Sertoli cells (arrowheads) and Leydig cells (arrows).

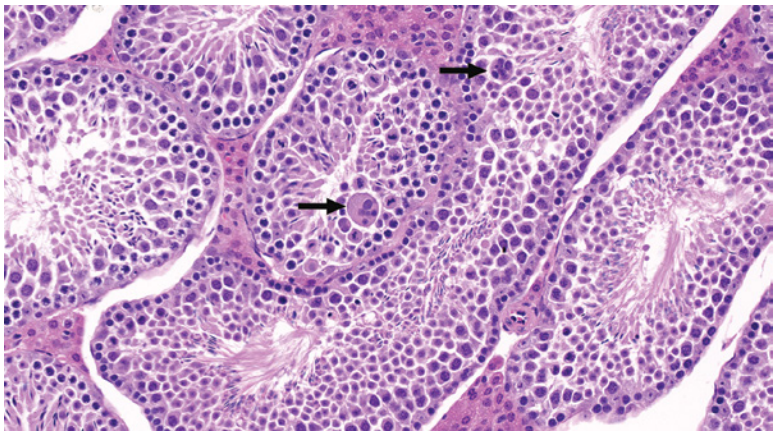


Figure 20.16 **Testis**. Multinucleate germ cells (symplasts). Symplasts (arrows) are occasionally seen in some tubules of wild type mice.

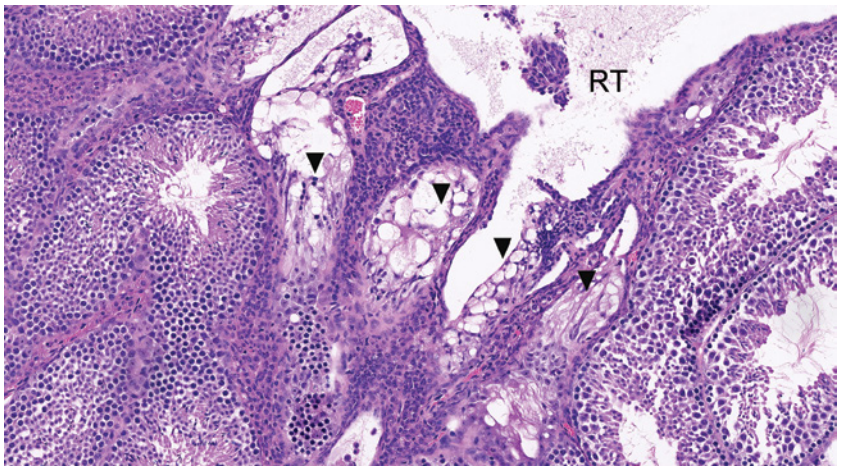


Figure 20.17 **Testis**. Straight seminiferous tubules (tubuli recti) are lined only by Sertoli cells and converge on the rete testis (RT).

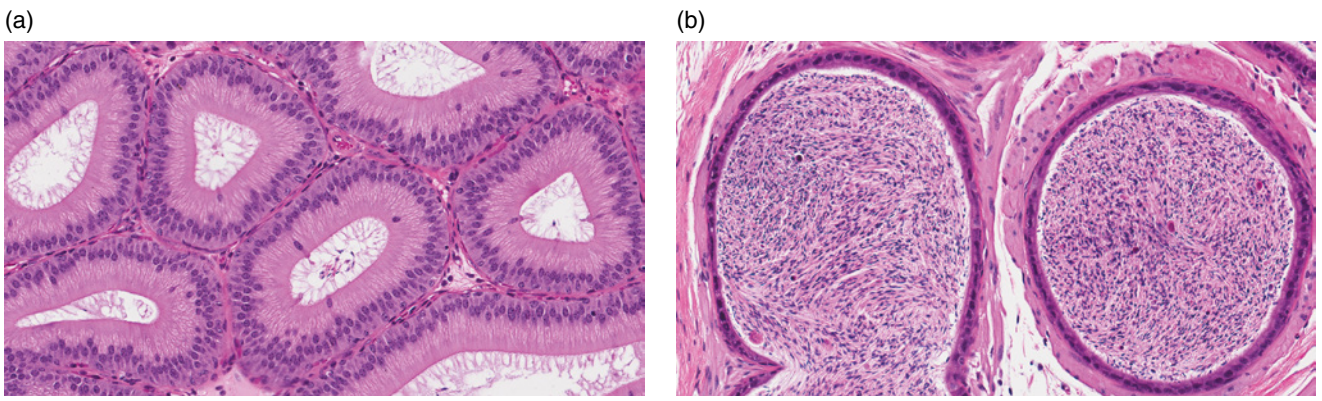


Figure 20.18 **Epididymis**. (A) The head of the epididymis has small lumen lined by tall pseudostratified columnar epithelium. (b) The tail of the epididymis has large lumen lined by cuboidal to low columnar epithelium.

Special Necropsy and Trimming Protocols

Each testis and epididymis should be weighed at necropsy. Littermate/concurrent wild type mice should always be processed in parallel in order to account for age and strain-to-strain variations in the efficiency of spermatogenesis [22]. Each testis with attached epididymis should be fixed whole. The tunica albuginea may be carefully and shallowly pierced at each pole to enable better fixative penetration. Care should be taken to avoid handling or compression artifact of the

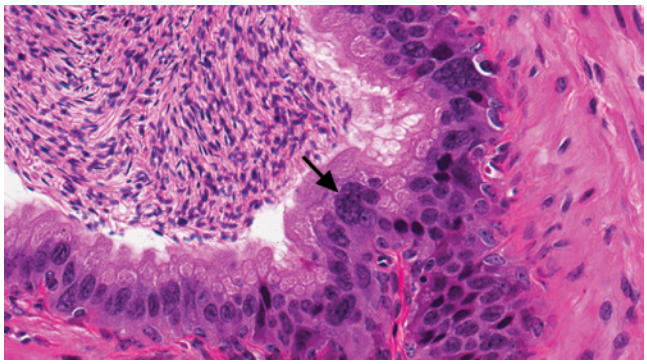


Figure 20.19 Epididymis, Epithelium with focal karyomegaly. An atypical enlarged nucleus (arrow) in the epididymal epithelium.

seminiferous tubules. Formalin (neutral buffered 10% formalin) will suffice for routine examination; however, formalin fixation may cause shrinkage artifact of the seminiferous tubules. Optimal fixation is achieved with Bouin's solution or modified Davidson's fixative [23]. Modified Davidson's fixative is recommended for optimal antigen preservation for immunohistochemistry. A transverse section through the middle of each testis is recommended for histological assessment of spermatogenesis in the rete testis and seminiferous tubules and a longitudinal section including the poles will best enable assessment of the entire testis, rete testis, and the isthmus, head, body, and tail of the epididymis [24]. The epididymides may be gently teased away from the testes and embedded separately.

For routine assessment, hematoxylin and eosin staining will enable morphological assessment and qualitative staging of spermatogenesis [21]. For accurate semi-quantitative staging of spermatogenesis, periodic acid–Schiff (PAS) stained sections allow visualization of the acrosome. Plastic embedding to generate thin sections stained with PAS may be required to detect subtle changes especially those involving acrosome dysregulation [25]. Other useful immunohistochemical markers may be found in Table 20.3.

Aging and Spontaneous Strain-Specific Lesions

Testis

The classification of spontaneous and induced lesions of the testes and epididymides of mice and rats have been extensively reviewed (Maronpot, https://ntp.niehs.nih.gov/nnl, http://www.informatics.jax.org/frithbook).

Degeneration, Atrophy, and Germ Cell Depletion

With aging, focal or diffuse testicular atrophy may occur. Grossly, the testis may be reduced in size. There is reduction in the number of seminiferous tubules and germinal epithelial cells and a relative increase in Sertoli cells and interstitial cells. Multinucleated cells and ceroid pigment within tubule lumens may also be associated with atrophy. Seminiferous tubule degeneration/atrophy or germ cell depletion can be a focal, multifocal, unilateral, or bilateral incidental finding affecting occasional tubules and must be distinguished from normal tubuli recti (Figure 20.17). Focal interstitial cell hyperplasia may be seen and may be indicative of early or pre-neoplasia.

Table 20.3 Selected immunohistochemical markers to identify different cell types in the mouse testis.

Cell type	Antigen	References
Sertoli cell	SRY-Box Transcription Factor 9 (Sox 9)	[26]
	GATA-4 (GATA-binding protein 4)	[27]
	Claudin 11 (CLDN11)	[27]
	Anti-Müllerian hormone (prepubertal)	[28]
	Vimentin	J. Ward, unpublished (Figure 20.15b).
Leydig cell	Cytochrome P450 17A1 (CYP17A1)	[26]
	17β-Hydroxysteroid dehydrogenases (17β-HSD)	[29]
	3β-Hydroxysteroid dehydrogenase (3βHSD)	[26]
	Vimentin	J. Ward, unpublished (Figure 20.15b).
Germ cell		
Spermatogonia	Octamer-binding transcription factor 4 (Oct 4)	[30]
	Cadherin-1 (Cdh1) – AKA E-cadherin	[31]
	Ethinylestradiol induced gene (EE2)	[32]
Spermatids/spermatocytes	TRA54, TRA55	[33]
All germ cells	TRA104, TRA98	[32, 34]
Peritubular myoid cell	p75 neurotrophin receptor (p75NTR)	[35]

Tubular Necrosis

Testicular tubular necrosis may be a consequence of ischemic injury secondary to torsion which is uncommon in mice [36]. Tubular necrosis is distinguished from tubular degeneration/atrophy because it involves coagulative necrosis (rather than apoptosis) of germ cells (Figure 20.20a,b). There is generally disruption and necrosis of the Sertoli cells and disruption of the blood–testis barrier (BTB) resulting in inflammation. Germ cell loss by necrosis is also possible, although rarely seen in GEM models [22].

Miscellaneous Changes

Mineralization

Occasionally, focal basophilic mineralization of the seminiferous tubules may occur. The mineralization is thought to be dystrophic and secondary to areas of previous injury and is composed of amorphous or concentric laminated basophilic masses. Mineralization is often associated with tubular necrosis (Figure 20.20a,b).

Amyloid

Amyloid deposition around testicular or epididymal blood vessels or within the basal lamina of seminiferous tubules may occur spontaneously, be an age-related change, or as a consequence of systemic amyloidosis.

Pigment

Pigment may be seen in the mouse testes at various stages of life. Hemosiderin is seen in all ages secondary to breakdown of erythrocytes at sites of hemorrhage. Hemosiderin is positive with Perls Prussian blue histochemical stain for iron. In aging mice, lipofuscin may be a breakdown product of lipid peroxidation and is positive with Periodic acid–Schiff (PAS) and Schmorl histochemical stains.

Mononuclear Aggregates

Lymphoid aggregates are a common incidental finding in mice in many organs, including the testes and male accessory sex glands. The testes are also a particularly common site for necrotizing arteriopathy; an age-related spontaneous background finding affecting medium sized vessels in the male reproductive system.

Epididymis

The rodent epididymis commonly forms spermatic granulomas and spermatoceles secondary to spermatozoa penetrating the duct and tubule epithelium into the interstitial tissues inciting an inflammatory reaction composed of epithelioid macrophages and/or foreign body giant cells and lymphocytes centered on aggregated sperm. Sperm granulomas are an incidental finding and can occur anywhere in the epididymis but more commonly in the tail (Figure 20.21). Disruption and rupture of the epithelial lining may be evident with presence of sperm cells within the interstitium. Dilation of the proximal segments of the epididymis and/or seminiferous tubules often accompanies sperm granulomas (Figure 20.21) and sperm stasis (Figure 20.22). Aggregates of mononuclear cells, mainly lymphocytes, are a common background finding in the epididymal interstitium and should not be confused with sperm granuloma.

The prominent presence of mast cells is a common background finding in various tissues in mice including the epididymis. This should not be misdiagnosed as inflammation. Tubular epithelial vacuolation is another common finding in the murine epididymis. Epithelial vacuolation may be exacerbated in some GEM (Figure 20.23).

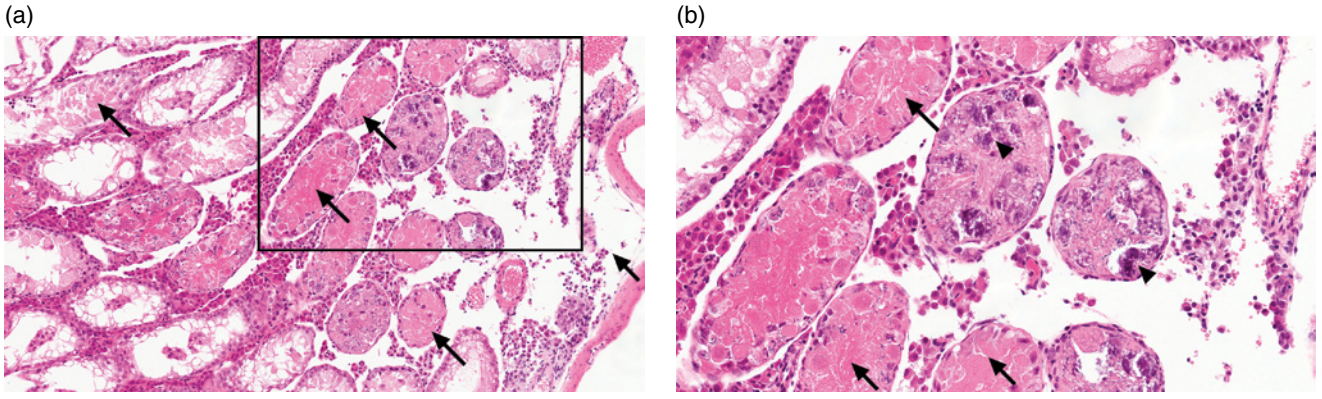


Figure 20.20 **Testis**. (a) Tubular necrosis. (b) A higher magnification of inset in 'a' shows disruption of normal tubular architecture.

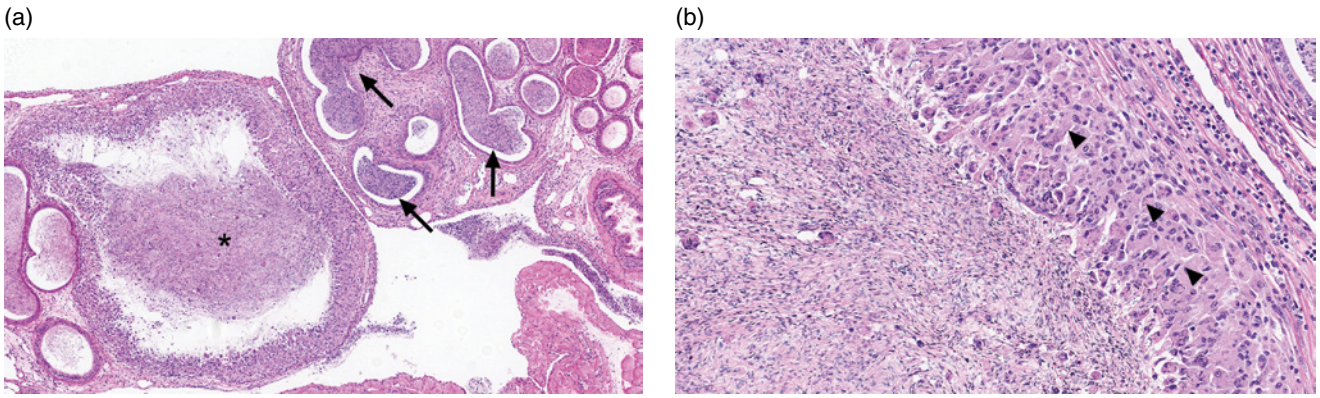


Figure 20.21 **Epididymis, tail**. Dilation, sperm stasis, and granuloma. (a) Segmental dilation of the tail of the epididymis (asterix) and sperm stasis in proximal segments (arrows); (b) Granulomatous inflammation (intraductal granuloma) characterized by layers of epithelioid macrophages lining the duct wall (arrow heads).

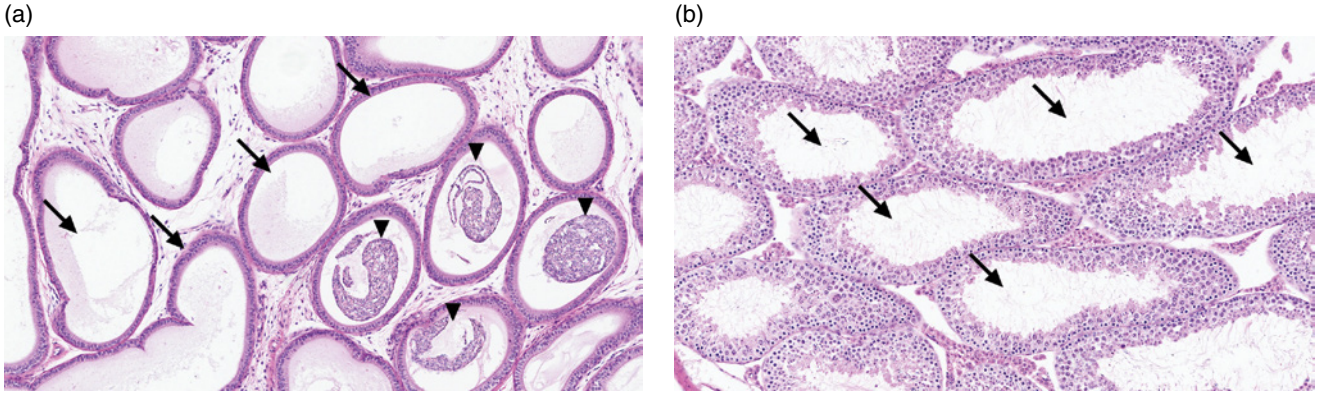
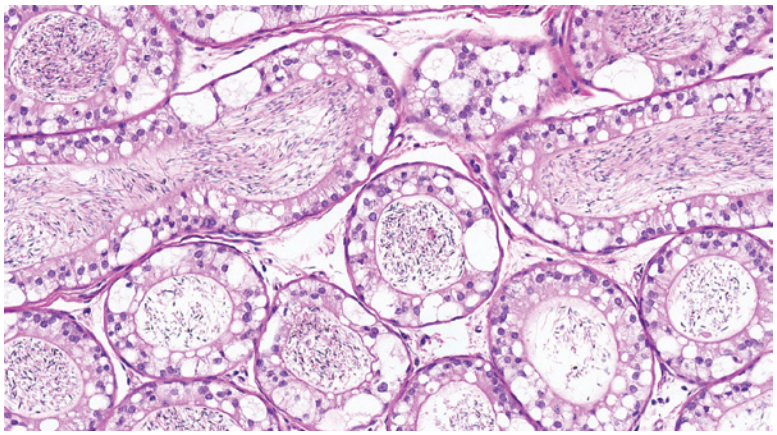


Figure 20.22 (a) Epididymis-segmental dilation (arrows) with luminal aggregation/concentration of sperm (stasis) distal to the dilated segment (arrow heads); note absence of sperm store. (b) Testis-tubular dilation – the corresponding (ipsilateral) testis exhibits secondary tubular dilation (arrows) with associated thinning of the seminiferous epithelium.

Figure 20.23 **Epididymis, body**. Epithelial vacuolation. This finding was not associated with infertility.



Genetically Engineered Mouse Models of Male Infertility

Histopathology Classification and Mechanisms of Action

Human infertility is a global health problem. Fifteen percent of couples are affected by some form of infertility and nearly half are attributed to male infertility [22]. The underlying cause and molecular mechanism of most male infertility remain unknown and are classified as idiopathic infertility [22, 37]. Genetics is believed to contribute to, or cause, a large proportion of testicular failure (complete failure of spermatogenesis), not surprising considering that thousands of genes are involved in spermatogenesis [37]. Understanding the function and consequences of dysfunction of these genes would inform male idiopathic infertility and provide potential diagnostic and treatment options. Knowledge about these genes and the protein products they produce might also identify potential targets for male contraceptives [38]. Given the complex cellular interactions that are involved in gonad development and spermatogenesis, GEM provide a biologically relevant model system to study male infertility [38]. Examples of GEM models of male infertility/subfertility with corresponding human condition(s) caused by abnormalities in spermatogenesis and sperm function are shown in Tables 20.4 and 20.5. Mouse spermatogenesis is comparable with human spermatogenesis and is well defined in developmental and histological terms [70]. It is estimated that nearly 50% of mouse genes are involved in testis development and over 4000 human genes may be associated with male infertility [93]. Mouse models of several hundred putative human fertility genes have identified genes involved in spermatogenesis, sperm maturation, capacitation, and fertilization and have provided insight into male idiopathic infertility and potential genetic diagnosis [37, 94]. An example is testis expressed gene 11 (*Tex11*^{tm1Jw}) that was confirmed as essential for meiosis in a knockout mouse model [72]. Subsequent work identified pathogenic mutations in the human orthologue *TEX11* among a large cohort of azoospermic men [71]. GEM models of human male infertility include expression of transgenic vectors and humanized genes, overexpression of endogenous genes, and deletion or inactivation of genes known to have limited or restricted expression in the testes (see http://www.informatics.jax.org/vocab/mp_ontology/MP:0001145).

Consistent with the complexity of spermatogenesis and that thousands of genes are involved [95], GEM produced for research unrelated to fertility frequently present with a male infertility phenotype [22]. Also, more male than female GEM models of infertility have been identified [96]. Data from large scale mouse knockout projects show male

Table 20.4 Examples of GEM models of male infertility/subfertility with corresponding human condition(s) caused by abnormalities in sex differentiation or testis development.

Disease-associated gene	Gene function	Human disease phenotype and pathology	GEM model phenotype and pathology
SOX8	Sertoli cell differentiation and function	Disorders/differences in sex development (DSD), gonad dysgenesis [39]	Sperm agenesis [40]
SOX9	Sertoli cell differentiation and function	Testicular differentiation defect, sex reversal (ovaries instead of testes) [41]	Lack of testis sex cord development, reduced number of seminiferous tubules [42]
GNRHR	Production of gonadotrophins (LH and FSH)	Hypogonadotropic hypogonadism, testicular failure [43, 44]	Spermatogenesis arrested at pachytene stage [45, 46]
LHR	Leydig cell production of testosterone	Hypoplasia/agenesis of Leydig cells and female external genitalia [47]	Testes growth arrest and descent, immature genitalia and accessory sex glands, decreased number of Leydig cells [48]
FSHR	Sertoli cell replication and function	Variable impairment of spermatogenesis [49]	Delayed sexual maturity, absent or reduced round spermatids, absent elongated spermatids [50]
AR	Secondary sex characteristics, initiation and maintenance of spermatogenesis	Androgen insensitivity syndrome (AIS) characterized by feminized external genitalia, intra-abdominal testes, lack of Secondary Sex Characteristics (SCO) syndrome [51]	Feminized external genitalia, intra-abdominal testis, lack of secondary sex characteristics, spermatogenesis arrest [52, 53]
KISS1 or *KISS1R*	Activation of hypothalamic pituitary gonadal axis, initiating secretion of GnRH	Hypogonadotropic hypogonadism and testicular failure [54, 55]	Hypogonadotropic hypogonadism with small testes, immature secondary sex glands, spermatogenesis arrest [56, 57]

Table 20.5 Examples of GEM models of male infertility/subfertility with corresponding human condition(s) caused by abnormalities in spermatogenesis and sperm function.

Disease-associated gene	Gene function	Human disease phenotype and pathology	GEM model phenotype and pathology
Premeiotic germ cell development, proliferation, and differentiation			
FANCA or FANCC	Chromosomal stability, primordial germ cell proliferation	Hypogonadism, Sertoli Cell-Only (SCO) syndrome, Leydig cell hyperplasia [58, 59]	Hypogonadism-seminiferous atrophy, Leydig cell hyperplasia [60, 61]
ETV5	Chemoattractant and spermatogonia self-renewal	SCO syndrome, azoospermia [110]	SCO phenotype [62]
DAZL	RNA-binding essential for spermatogenesis	Oligozoospermia, maturation arrest, SCO syndrome [63]	Defective spermatogonia differentiation [64]
Meiosis			
SYCP1 or SYCP3	Meiotic recombination/synaptonemal complex	Azoospermia, meiotic, and maturation arrest [65]	Germ cell apoptosis [66, 67]
ATM	DNA double strand break sensing and repair	Meiosis arrest, germ cell apoptosis [68]	Meiosis arrest, germ cell apoptosis absent round & elongated spermatids [69]
TEX11	Meiotic double strand DNA repair/ crossover formation	Azoospermia, meiotic arrest at pachytene stage [70, 71]	Meiosis arrest, germ cell apoptosis, spermatocyte loss [72]
TEX14	Germ cell intercellular bridges	Non-obstructive azoospermia [73]	Meiotic defect; arrest at pachytene stage [74]
Spermiogenesis			
CREM	Transcriptional regulation of germ-cell-specific genes	Azoospermia, arrest at round spermatid stage [75, 76]	Failure of spermatids to differentiate into sperm [77, 78]
PRM1 or PRM2	Sperm chromatin condensation	Late spermiogenesis defect, sperm penetration defect [79, 80]	Abnormal sperm morphology and motility [81]
SPINK2	Neutralize the action of acrosomal proteases	Azoospermia/oligospermia, reduced number of round spermatids, immotile spermatozoa [82]	Arrest at the round-spermatid stage, round spermatids and symplasts within tubular lumen [83]
Spermatozoa morphology and function			
TEKT2	Axonemal protein-formation, movement of flagella/cilia	Asthenozoospermia (abnormal sperm motility) [84]	Abnormal structure and motility of spermatozoa [85]
DNAH1	Biogenesis of the axoneme	Abnormal spermatozoa motility due to flagellar abnormalities (MMAF) [86, 87]	Abnormal spermatozoa motility [88]
CATSPER1/2	Flagellar function, Sperm motility and fertilization	MMAF [89, 90]	Abnormal spermatozoa motility [91]
CFAP43/44	Flagellar structure and function	MMAF [63, 92]	Abnormal spermatozoa motility [82]

infertility as one of the most common phenotypes infertility as one of the most common phenotypes [97] (IMPC[1]), and testicular lesions as one of the most common abnormalities [98]. Fertility data from the International Mouse Phenotyping Consortium reported male infertility in 239 of 4205 (5.68%) unique knockout strains tested and female infertility in 110 of 4205 (2.62%) unique knockout strains (IMPC Data Release 13.0 published 17 December 2020).

Male bias in infertility may be attributed to many more genes being required for testis differentiation and spermatogenesis than for ovary differentiation and ovogenesis [99]. Furthermore, infertile male mice are almost exclusively homozygous knockouts [97, 98], consistent with human fertility data that shows the majority of male infertility is caused by autosomal-recessive mutations [94, 100].

Male mice with infertility or subfertility generally present with testicular and/or epididymal morphological changes. This section highlights common histopathological patterns in the testis and epididymis. Recognizing and categorizing the pattern of lesions often provide some insight into the genotype-phenotype correlation. Common age-related background findings and incidental lesions are also described. The material presented here is far from a comprehensive and growing list of testis and epididymis pathology in GEM. Readers are referred to other publications [37, 96] and resources (IMPC[1]).

Pathology of the Testis in Infertile GEM

Infertile male mice often present with microscopic changes in the testis. However, light microscopic changes may not be detectable as infertility can also result from ultrastructural defects, abnormal terminal differentiation, functional deficiencies of spermatozoa, or a physical inability to copulate [101–103]. A diversity of genetic mutations can produce similar histological phenotype, most often presenting as degeneration/atrophy of seminiferous tubules. In many instances, however, unique morphological features are present in specific germ cell stages that provide insight into a genotype–phenotype correlation and the mechanism of action of the gene in question. Therefore, it is essential to recognize and capture these specific microscopic features in the morphological diagnosis and narrative pathology report (e.g. seminiferous tubular degeneration/atrophy with germ cell dissociation and frequent multinucleated spermatids).

Detailed qualitative evaluation of spermatogenesis requires a sound knowledge of the spermatogenic cycle, its kinetics, and the morphological features of the different stages of the cycle [21]. Deviation from normal morphology and relative quantity of germ cells of each stage often reveals stage-specific developmental changes due to overexpression or absence of expression of one or more genes and may provide insight into the mechanism of action in question [25]. Therefore, the testis should be carefully and systematically evaluated for the presence or absence of all germ cell types, cellular organization, and morphological integrity in comparison with age-matched wild type mice.

Seminiferous Tubule Degeneration/Atrophy

Degeneration/atrophy is the most common but least specific finding in the testis of infertile or subfertile mice. Seminiferous tubular degeneration with atrophy is an end-stage lesion characterized by complete loss of germ cells as a result of progressive degeneration and phagocytosis/exfoliation of germ cells or cumulative depletion of germ cells and collapse of tubular size [21, 104]. The combined term degeneration/atrophy is recommended in rodents because, in many instances, a mixture of atrophic and degenerating tubules is present [21]. However, degeneration/atrophy may manifest as germ cell loss, spermatid retention, vacuolation of Sertoli cells, multinucleated germ cell (MNG) syncytia formation, disorder within the germ cell layers, and exfoliation of germ cells into the tubular lumen [21, 104]. These changes are usually accompanied by grossly small testes, decreased testis and/or epididymis weight, and by absent or reduced sperm store with cellular debris in the tubules of the epididymis (Figure 20.24). Most GEM with male infertility present with marked germ cell depletion characterized by tubules lined only by Sertoli cells (Figure 20.24a). These tubules are considered the human equivalent of Sertoli cell only phenotype [105]. In some GEM models, degeneration/atrophy may be incomplete where spermatogonia and a few spermatocytes remain. The difference in extent of germ cell depletion may reflect a stage-specific gene effect and/or the stage of progression of the lesion at termination of the animal. For example, genes involved in cell division and DNA repair are typically associated with complete germ cell loss, whereas genes involved in germ cell differentiation may have various degrees of germ cell depletion at any stage of spermatogenesis. It is also important to recognize the age of the mouse at analysis. Most GEM are typically analyzed between puberty and mature adulthood by which time early or precursor degenerative changes in the seminiferous tubules have likely progressed to complete germ cell depletion.

Distinguishing tubular atrophy from hypoplasia is challenging as both represent an end stage change in seminiferous tubules. Without a thorough time course study with timed periodic termination, it is not possible to establish whether the tubular changes resulted from a collapse of tubule integrity (atrophy) or germ cells have not populated the tubules or proliferated in the first place (hypoplasia). Hence a descriptive diagnostic term of “germ cell depletion” with severity grade is more appropriate for routine evaluation. It is important to note that atrophy is often associated with actual or relative (perceived) increase in the number or size of interstitial Leydig cells (Figure 20.24a). Therefore, caution should be exercised when diagnosing interstitial cell hyperplasia in testes with seminiferous atrophy.

1 IMPC - International Mouse Phenotyping Consortium: https://www.mousephenotype.org/data/phenotypes/MP:0001925

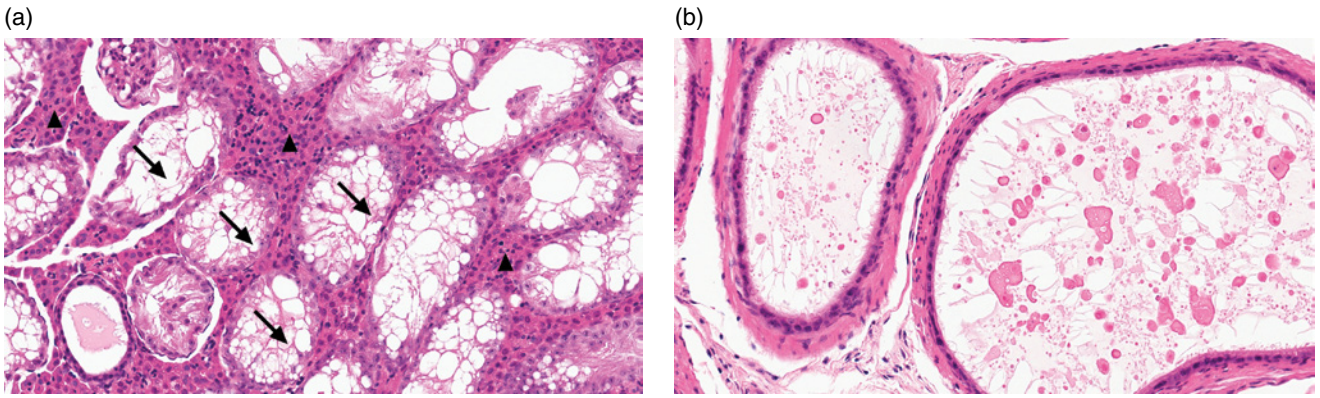


Figure 20.24 Testis. Diffuse tubular atrophy/hypoplasia. (a) Complete germ cell depletion characterized by tubules containing only Sertoli cells (arrows). Note the unmasked, vacuolated, and lacy cytoplasm of Sertoli cells. There is a relative or actual Leydig cell hyperplasia (arrow heads). (b) The ducts of the epididymis are devoid of sperm and contain proteinaceous debris. The deleted gene is critical determinant of the germ cell lineage.

Tubular degeneration/atrophy may be diffuse (Figure 20.24) or focal to multifocal (Figure 20.25) and the severity may range from degeneration of a single generation of germ cells to the entire seminiferous tubule epithelium including Sertoli cells. Often the post proliferative Sertoli cells are spared. Because mice have massive reserve capacity for spermatogenesis [3], focal, segmental, or multifocal degenerate and atrophic tubules may not affect fertility, although they may be accompanied by a decreased sperm store in the epididymis (Figure 20.25b). For example, multifocal tubular atrophy associated with decreased sperm store was observed in *Nsun2* knockout mice (*Nsun2tm1a(EUCOMM)Wtsi*, unpublished); Nsun2 is a methyltransferase required for testis differentiation [106]. It is not certain whether focal lesions progress with age to diffuse changes that do affect fertility because most GEM are terminated at a relatively young to mature adult age and longitudinal studies with analysis-over-time are rarely undertaken. Nonetheless, genetic mutations that result in focal or segmental tubular degeneration/atrophy may be comparatively of greater significance in humans because of the potential for age-associated progression and the relatively low reserve and efficiency of spermatogenesis in humans [3, 22].

Tubular degeneration/atrophy could be the result of defects in germ cells or Sertoli cells. Regardless of the mechanism, spermatogenesis is dependent on coordinated function by all other cell types and processes within the testis, and any disturbance in this interaction typically results in germ cell death or exfoliation into the tubular lumen [21].

Spermatogenesis Arrest and Spermiation Defects

Male infertility in GEM can be caused by spermatogenesis arrest from early spermatogonia to spermiation [37]. Arrest at the spermatogonia stage may result from defects in premeiotic germ cell development [64], at the spermatocyte stage because of arrest in meiosis [107, 108], or at the stage of round spermatids because of post meiotic or spermiogenesis defects [77, 81, 109]. Spermatogenesis arrest results in the stage-dependent phenomenon of "maturation depletion" of the germinal epithelium, whereby spermatogenesis is normal at one stage of maturation, but the population of germ cells in subsequent stages are absent [25]. Examples are mutant alleles in ets variant 5 (*Etv5*) mice ($Etv5^{sco}/Etv5^{sco}$

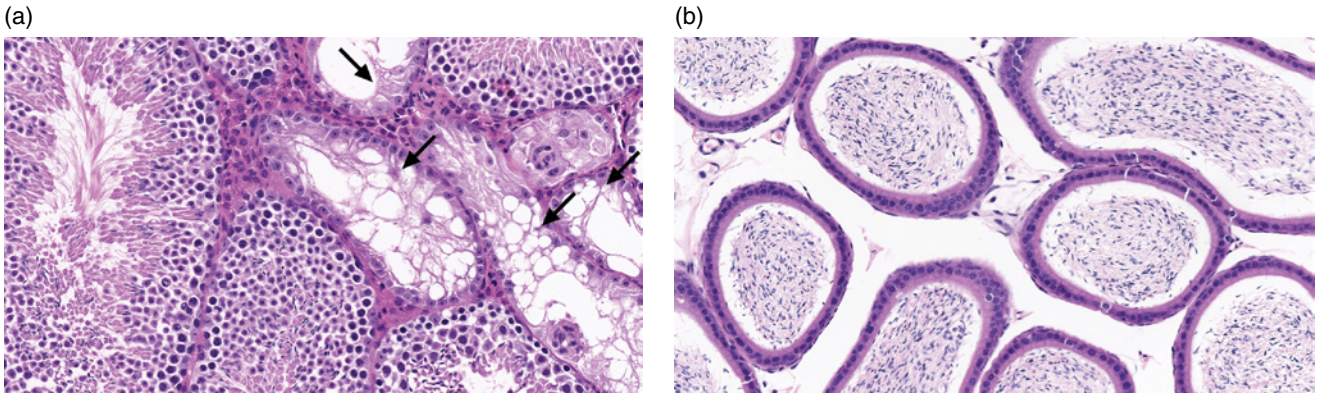


Figure 20.25 Testis. Multifocal tubular atrophy/hypoplasia, multifocal. (a) Multifocal atrophy characterized by complete depletion of germ cells in some tubules (arrows). (b) Corresponding decreased sperm density in the epididymis.

and *Etv5*^{tm1Kmm}) in which maintenance of spermatogonial stem cell self-renewal is lost without a block in normal spermatogenic differentiation resulting in progressive germ-cell depletion and a Sertoli-cell-only syndrome [110]. Defects in meiosis typically manifest as tubules with spermatocytes arrested prior to the pachytene stage and a lack of spermatids (Figure 20.26). Arrest at a later stage such as spermiogenesis results in normal numbers of spermatogonia, spermatocytes, and round spermatids with no or very few elongating spermatids and no sperm in the epididymides (Figure 20.27). In some cases, defective spermiogenesis may manifest as degeneration with enlargement of elongated spermatids as observed in gametogenetin binding protein 2 knockout mice (*Ggnbp2*$^{tm1c(KOMP)Wtsi}$) (Figure 20.28). This gene is expressed in the adult testis from late pachytene spermatocytes to round spermatids and knockout males are infertile and show extensive defects in spermatogenesis [111]. Evidence from rodent toxicity studies show that degeneration of elongating spermatids may result from Sertoli cell toxicity or direct germ cell injury [104]. Care should be taken not to confuse these enlarged and degenerate elongated spermatids with the large residual bodies in the apical lumen that are a common background finding in mice.

Among post meiotic defects, spermiation failure (retention of mature elongated spermatids) is relatively challenging to detect. In normal tubules there should be only one generation of elongated spermatids. The presence of more than one generation confirms spermiation defect [36]. Spermiation defect is most apparent in stage IX tubules, following spermiation at stage VIII. At stage IX, elongated spermatids have already been released and round spermatids have begun elongation. Appearance of elongated spermatids at the tubular lumen beyond stage VIII is indicative of spermiation defect [36, 104]. Spermatids that fail to be released are phagocytosed by Sertoli cells [22, 36] and some

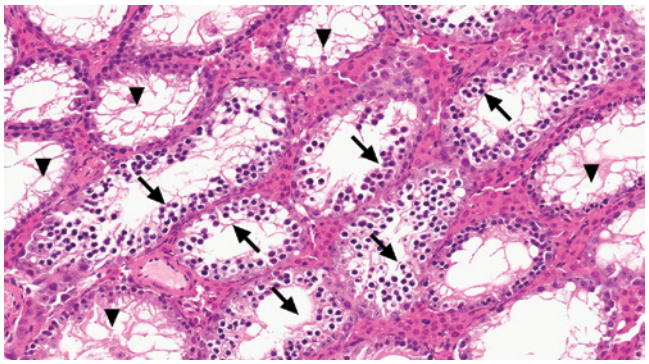


Figure 20.26 Testis. Failure of meiosis. Seminiferous tubules show spermatocytes arrested prior to pachytene stage; clusters of cells morphologically similar to zygotene spermatocytes (arrows) are admixed with tubules containing no germ cells (arrow heads). Note the absence of germ cells with pachytene spermatocyte morphology. The deleted gene is involved in the initiation of meiotic recombination.

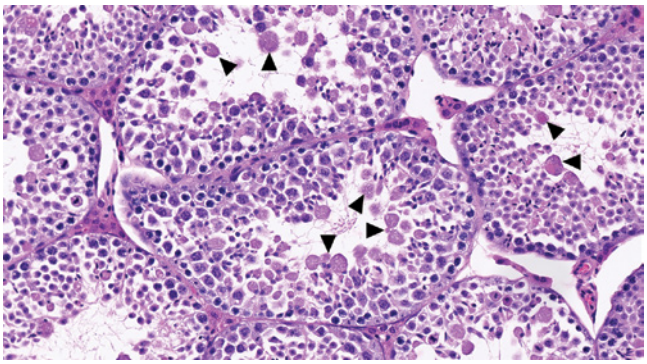
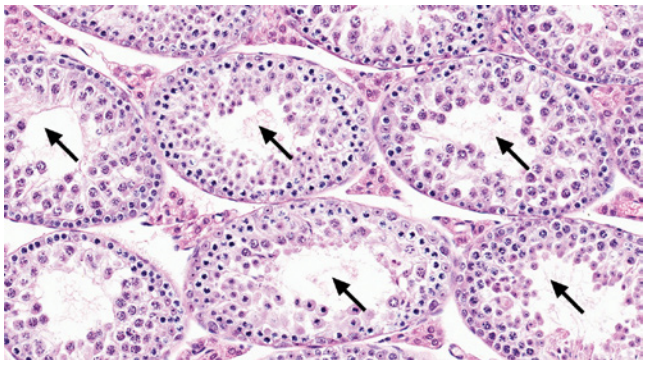


Figure 20.28 Testis. Degeneration of elongated spermatids. Large structures with granular eosinophilic cytoplasm (degenerated elongated spermatids) line the lumen (arrow heads). Note the absence of normal elongating spermatids and mature spermatozoa.

(a)



(b)

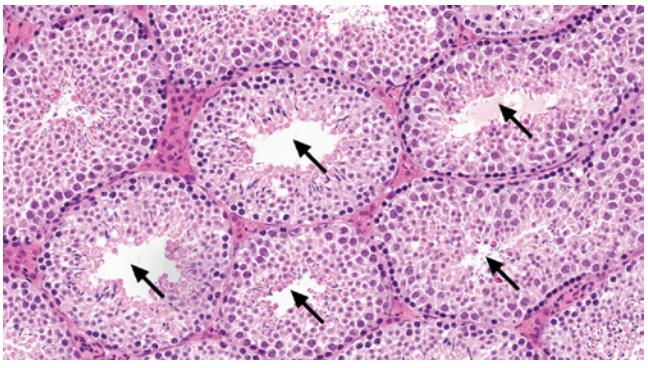


Figure 20.27 Testis, Defects in spermiogenesis and spermiation. (a) Defect in spermiogenesis. Elongated spermatids and mature spermatozoa are missing (arrows). Note that spermatogonia, spermatocytes, and round spermatids are present. The deleted gene is involved in chemotaxis function. (b) Defect in spermiation. Mature spermatozoa are rare or missing (arrows). Mature elongated spermatids are few. The deleted gene is a microtubule binding protein that localizes to the sperm tail and motile cilia.

of these resorbed spermatids can be seen basally in parallel orientation to the tubular basal lamina rather than in their normal radial orientation [22, 36]. A number of genetic mutations that alter cellular adhesion, androgen signaling, and Sertoli cell function can result in spermiation defect and several GEM models with dysregulation of these processes have been described [22].

Multinucleated Spermatids; Symplasts

Germ cells develop in a syncytium connected to their sister cells as well as preceding and succeeding generations of germ cells via cytoplasmic bridges. Consequently, degenerative changes often include aberrant formation of syncytia known as multinucleated germ cells (MNGs), or symplasts [22, 37]. These MNGs may indicate a slow degenerative process of breakdown in cytoskeletal fibers supporting the interconnecting cytoplasmic bridges with subsequent detachment from the seminiferous epithelium [3, 105, 112]. Symplasts are most frequently composed of round spermatids but can also be formed by fusion of neighboring spermatocytes or elongating spermatids [22, 37, 105]. Varying degrees of MNG formation have been described in GEM models with mutation of genes involved in transcription regulation, apoptosis, and flagellar biogenesis/spermiogenesis [70, 112–114]. MNGs appear to be a striking or dominant feature of tubular degeneration in select GEM models suggesting a specific underlying mechanism. For example, tubular degeneration in peroxisomal biogenesis factor 3 (*Pex3*$^{tm1a(EUCOMM)Wtsi}$) knockout mice is characterized by marked increase in MNGs number and size (Figure 20.29) both at 16 and 24 weeks of age. Similar morphology was observed in other *Pex* knockout mice [115]. Morphologically MNGs may appear viable or degenerating with dark staining apoptotic-like nuclei (Figure 20.29) [113, 115]. In *Pex3* knockouts, a minor proportion of MNGs, are apoptotic (Figure 20.29b). Viable or non-viable MNGs may also be present within the lumen of epididymis. The presence of rare MNGs in the tubules of sexually immature or young males is considered a normal finding (Figure 20.17) as part of the degenerative and apoptotic cell death associated with first and often faulty early waves of spermatogenesis.

Germ Cell Exfoliation

Spermatozoa are released from Sertoli cells into seminiferous lumens through progressive loss of cell adhesion junctions between these cell types [94]. Premature release occurs in some pathological conditions commonly referred to as germ cell exfoliation. This lesion may be a primary abnormality or secondary to tubular degeneration. The term "exfoliation, germ cell" should be used only when this feature is interpreted as a primary change [21]. The pathogenesis of primary germ cell exfoliation or premature release is generally attributed to Sertoli cell dysfunction [40], or Sertoli cell-germ cell adhesion or association, and has been extensively reviewed [21, 22, 116]. Most GEM models with germ cell exfoliation phenotype have dysregulation of genes involved in cell adhesion or association. These include genes involved in Sertoli cell-germ cell adhesion such as cell adhesion molecule 1 (*Cadm*$^{tm1a(EUCOMM)Wtsi}$) (Figure 20.30) [117] and mannosidase 2, α 2 (*Man2a2tm1Mfu*) that encodes alpha-mannosidase 2x [118], genes involved in anchoring germ cells to the basal lamina such as endothelial PAS domain protein 1 (*Epas1, Epas1*$^{tm1.1Mcs}$) [119], and genes involved in forming the BTB, such as cadherin 2 (*Amh-Cre;Cdh2*$^{fl/fl}$) [120]. Primary germ cell exfoliation is characterized by non-degenerated germ cells in the seminiferous lumen and sloughed germ cells in the rete testis or epididymal lumen. Caution should be exercised not to diagnose germ cell exfoliation based on germ cell dissociation and presence of exfoliated cells in the lumens of seminiferous tubules which can be an artifact of tissue sample processing. Presence of exfoliated spermatocytes and spermatids within the epididymal lumen (Figure 20.30b) helps distinguish *bona fide* primary germ cell exfoliation from artifact [3, 105]. Some degree of germ cell apoptosis and exfoliation is also normal in peripubertal animals, and to a lesser extent in wild type sexually

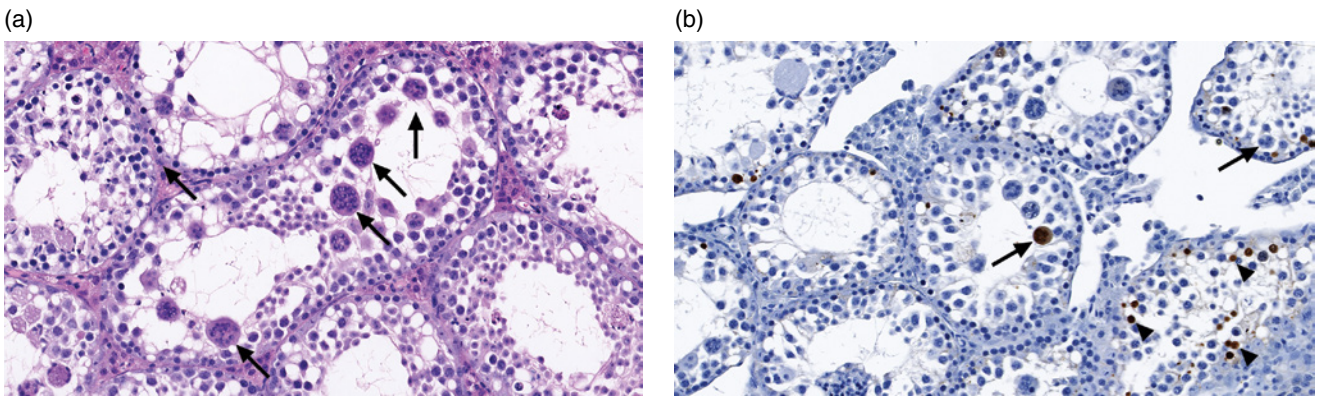


Figure 20.29 Testis. Tubular degeneration/atrophy with multinucleate germ cells (symplasts). (a) Numerous symplasts (arrows) in depleted and vacuolated tubules. (b) Apoptotic symplast (arrow) and germ cells (arrow heads) are confirmed by TUNEL (terminal deoxynucleotidyl transferase dUTP nick end labeling). Deleted gene is *Pex3* = peroxisomal biogenesis factor 3. (*Pex3*$^{tm1a(EUCOMM)Wtsi}$).

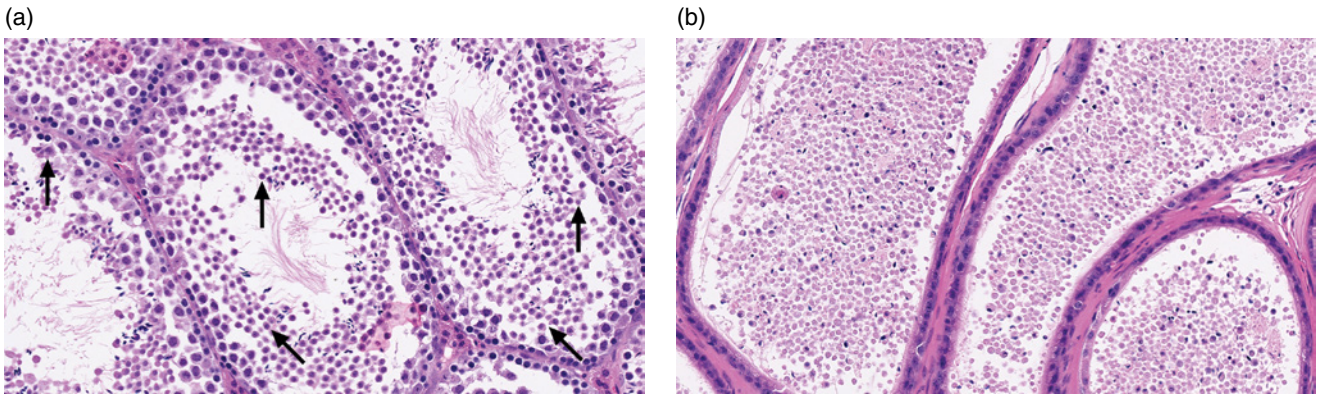


Figure 20.30 Testis. Germ cell dissociation. (a) Germ cells are dissociated (arrows), and elongated spermatid or mature spermatocytes are rare. (b) Epididymis, tail; abundant immature germ cells, viable and non-viable, are present in the epididymis. Mouse knockout for *Cadm1* – Cell adhesion molecule 1 (*Cadm1*$^{tm1a(EUCOMM)Wtsi}$).

mature mice [3, 105]. Apoptotic germ cells are readily observed as early as post-natal day 14 (PN14) in wild type mice but dropping to barely detectable by PN60 [114]. Secondary exfoliation is typically accompanied by sloughed degenerate germ cells and cell debris within the epididymis [121].

Tubule and Sertoli Cell Vacuolation

Vacuolation within seminiferous tubules and Sertoli cells accompanying degenerative/atrophic changes in infertile GEM appear in all layers of tubular epithelium and may result from germ cell depletion. Unless vacuolation is considered a primary or singular change, it is not recommended to use a diagnosis of tubular vacuolation in rodents [21]. Toxicity studies have shown that primary Sertoli cell cytoplasmic vacuolation consists of variably sized, discrete, clear, round structures predominantly located toward the tubular basement membrane [104]. Primary vacuolation of Sertoli cells is rare in GEM but has been reported with consequent abnormal sperm shape and motility in infertile mice with glycolipid storage disease caused by mutation of glucosidase beta 2 (*Gba2, Gba2*^{tm1Rus}) [122]. However, primary vacuolation as part of other lipid storage disorders with no other testis abnormality has resulted in no adverse effect on fertility [98]. Note that minimal nonspecific vacuolation within tubules can be observed as an incidental background finding or as a processing artifact [21].

Tubular Dilation

Dilation of seminiferous tubules is occasionally seen as a background finding, typically unilateral, and due to blockage of efferent ducts (Figure 20.22b). Anatomically, mouse efferent tubules are oriented so the proximal efferent ductules merge to form a single, common duct that enters the isthmus then head of the epididymis, increasing the likelihood of dilation secondary to downstream efferent tubular blockage [123]. Tubular dilation appears as enlarged seminiferous tubule diameter with thinning of the seminiferous epithelium, dilated rete testis and efferent ducts, sperm stasis, or sperm granulomas in the efferent ducts. It may be associated with upstream germ cell degeneration secondary to increased hydrostatic luminal pressure. The efferent ducts are the major site of reabsorption of seminiferous tubular fluid; hence inadequate resorption may lead to a backup of fluid accumulation and tubular dilation, whereas excessive resorption can result in sperm stasis and blockage [124]. Male infertility as a direct consequence of fluid dysregulation of fluid absorption and dilation of seminiferous tubules has also been reported [125, 126]. In some GEM models, dilation of tubules may be caused by obstruction of excurrent ducts by sloughed germ cells secondary to seminiferous tubular degeneration [18], and infertility in estrogen receptor 1 (*Esr1*^{tm1Ksk}) knockout mice has been associated with seminiferous tubular dilation and subsequent pressure atrophy [127]. Hence, careful analysis of the testis and efferent ducts is important to determine primary or secondary seminiferous tubular dilation.

Primary Ciliary Dyskinesia (Immotile Cilia Syndrome)

Primary ciliary dyskinesia (PCD), also known as "immotile-cilia syndrome" or "ciliopathy," is a genetically heterogeneous disorder of motile cilia. PCD is characterized by ciliary dysfunction and impaired mucociliary clearance that result in an array of clinical manifestations, including male infertility [128]. Ciliopathies in GEM, including those associated with testis lesions, are described in Chapter 6.

Leydig Cell Abnormalities

Abnormalities in interstitial Leydig cells are not common in GEM. Normal variability in Leydig cell size and the effects of tissue fixation present a challenge to evaluate size by qualitative examination unless the change is marked or severe [3].

Image analysis combined with immunohistochemical markers has been used to quantify subtle alterations in Leydig cell size [3]. Normal mouse Leydig cells have a vacuolated cytoplasm that should not be confused with degeneration.

Atrophy, hyperplasia, or hypertrophy of Leydig cells is rarely seen in wild type mice. Decreased size or number may occur in GEM in response to decreased Luteinizing Hormone (LH) stimulation or as a result of decreased testosterone production by Sertoli cells. Luteinizing hormone/choriogonadotropin receptor (*Lhcgr*^{tm1Hht}) knockout mice may have reduced number and size of Leydig cells and arrested spermatogenesis [48]. Leydig cell hyperplasia (LCH) can be focal, multifocal, or diffuse. Focal LCH has a diameter smaller than or equal to three seminiferous tubules [21, 36], whereas diffuse LCH has bridging strands of Leydig cells several layers thick between seminiferous tubules or as locally extensive involving a large portion of the testis [21]. In mice, LCH is characteristically diffuse and often most severe in the subcapsular region [21]. LCH presents a diagnostic challenge because it may be difficult to distinguish a real increase in the number of Leydig cells from a relative prominence of cells secondary to seminiferous tubular atrophy and contraction due to germ cell loss [21, 105]. Most GEM models with LCH present with concomitant seminiferous tubular changes such as hypoplasia, atrophy, and/or degeneration [103, 108].

Pathology of the Epididymis in Infertile GEM

A common sequela of testis pathology is changes in epididymal content. Absence (aspermia), reduced sperm number (hypospermia), and increased cellular debris in epididymal duct are the most common findings in infertile or subfertile GEM. Aspermia or hypospermia may indicate subtle stage-specific spermatogenesis defects that would otherwise be missed. Detecting abnormalities in late-stage spermatogenesis (spermiation) for example, may present a challenge without a corroborating change in the epididymal sperm store. Mild to moderate reduction in sperm quantity is challenging to identify definitively by qualitative evaluation and may require quantitative sperm analysis to confirm [21]. The epididymal body and tail are good locations to assess epididymal sperm content, recognizing that reduction in sperm content may be throughout the epididymis or limited to a specific segment depending on the time after perturbed spermatogenesis [21]. It is important to consider that sperm content in the tail reflects the output of the testis one to two weeks earlier while content in the head reflects sperm just released from the testis [3]. The quantity of sperm in epididymal duct also varies with age. Sperm are normally absent or scarce in the tail of the epididymis of mice younger than 5 weeks of age and do not reach normal quantity until ~9 weeks of age. Sperm content can vary significantly in peripubertal animals. Care should be taken when interpreting reduction of sperm quantity in the tail of the epididymis because sperm loss may be an artifact of tissue processing. Sloughed germ cells and cell debris in the epididymal duct are also good indicators of defective spermatogenesis and may provide insight to the underlying mechanism. For example, intact round spermatids in the epididymis indicate primary germ cell exfoliation. Note that degenerate germ cells and germ cell debris are a normal finding in peripubertal and young adult mice, particularly in the tail of the epididymis.

Epithelial vacuolation of the epididymis is occasionally seen as an insignificant background finding. Vacuolation can present as prominent clear cells or as a sequela of aspermia or hypospermia [21]. This change may be present in some GEM with no apparent effect on fertility (Figure 20.23). Infertility caused by a primary epididymal defect has been reported in GEM [129, 130]. For example, immunohistochemistry has identified abnormal differentiation of epididymal epithelium as the only histological change in the subfertile double *Crisp1*/*Crisp4* knockout mice that were generated by mating *Crisp1*$^{-/-}$ (*Crisp1*^{tm1Pasc}) and *Crisp4*$^{-/-}$ (*Crisp4*$^{tm1.1Pasc}$) [48]. Because morphologic and immunohistochemical characteri-

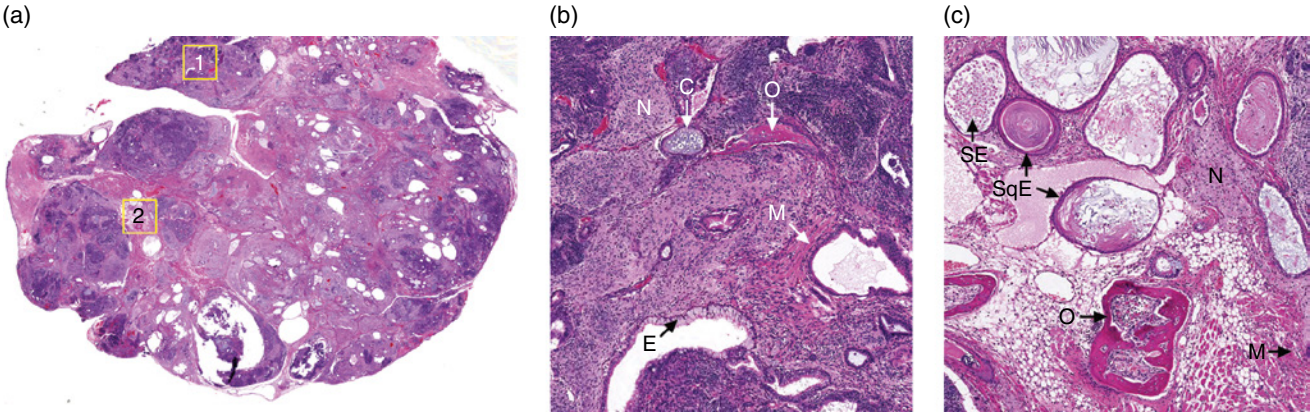


Figure 20.31 **Mouse testis. Teratoma**. (a) Differentiation into epithelial, mesenchymal, and neural tissues. (b) Top inset [1] show neuronal (N), epithelial (E), osseous (O), chondroid (C), and muscle (M) differentiation. (c) Bottom inset [2] show neuronal (N), osseous (O), muscle (M), secretory epithelial (SE), and squamous epithelial (SqE) differentiation.

zation of all regions of the epididymis are not commonly done, the contribution of structural or functional abnormalities in the epididymis as a primary cause of male infertility is likely underestimated.

Neoplasms of the Testis

Proliferative lesions of the testis and the epididymis are rare in rodents [21] with the exception of testicular teratomas in 129/Sv mice [131] (Figure 20.31). Testicular tumors reported in GEM are classified as either germ cell tumors (seminomas) or sex cord-stromal tumors, which include Leydig cell tumors, Sertoli cell tumors, granulosa cell tumors, and mixed sex cord-stromal tumors.

Sex Cord-Stromal Tumors

Leydig Cell Tumors

Leydig cell tumors are rare in mice with a spontaneous incidence of 0.7–1.2% in B6C3F1 and CD1 strains [132]. Estrogen is implicated in Leydig cell tumorigenesis in certain strains of mice based on the effects of estrogen agonists [133]. Increased production of estrogen by overexpression of aromatase results in Leydig cell tumors in MMTV-int-5/aromatase transgenic mice [134]. Transgenic mice expressing the SV40 oncogene under the anti-Müllerian hormone (AMH) promotor develop LCH at one to three months of age and tumors of mixed differentiation (Leydig cell and Sertoli cell tumors) at a later age [135]. This is compatible with the common origin of Leydig and Sertoli cells from the specific stroma of the gonadal ridge [135]. Since both Leydig and Sertoli cells express AMH [136], the mixed tumor phenotype in the latter model is not unexpected.

Distinguishing Leydig cell adenoma from focal LCH is a challenge. Definitive diagnosis is based on the presence of adjacent tubular compression and tubular diameter. A lesion with a diameter larger than the cumulative diameter of three seminiferous tubules should be diagnosed as adenoma [21, 36]. Leydig cell adenomas are composed of uniform polyhedral cells with abundant eosinophilic, finely granular, or vacuolated cytoplasm, and central round nucleus with prominent nucleolus. Larger nuclei and polyploidy may be observed, and some tumors may also contain elongated and spindle shaped Leydig cells [21, 36]. Large tumors may have areas of less well differentiated basophilic cells with scant cytoplasm or elongated spindle-shaped cells. Some tumors are moderately vascular, containing dilated, thin-walled blood vessels, hemorrhage, and focal areas of necrosis and cystic change [21]. Leydig cell carcinoma (malignant interstitial cell tumor) is distinguished from adenoma by polymorphism, cellular atypia, and invasion of testicular capsule or blood vessels [21, 36].

Sertoli Cell Tumors

Sertoli cell tumors, also known as sustentacular cell tumor, sex cord stromal tumor, or gonadal stromal tumor [21], originate from sex-cord stromal cells. GEM models have been developed to study Sertoli cell tumor biology including transgenic mice expressing the large T protein of polyoma virus in the seminiferous epithelium [137], a transgenic model expressing the SV40 oncogene under Anti-Müllerian Hormone (AMH) promotor (AT mice) [135], and a model that expresses a constitutively active form of beta-catenin in Sertoli cells (*Ctnnb1*$^{tm1Mmt/+}$*;Tg(AMH-cre)1Flor*) [138]. Benign Sertoli cell tumors are characterized by palisading Sertoli-like cells admixed with a delicate fibrovascular stroma [21, 36]. Malignant Sertoli cell tumors are distinguished by invasion of the interstitium, poorly differentiated cells, or increased mitotic rate [21].

Granulosa Cell Tumors

Various GEM models of testicular granulosa cell tumors (GrTs) have been developed [139–141]. Transgenic mice with constitutively active human transforming growth factor, beta receptor 1 (*TGFBR1*) in the testes developed tumors resembling human testicular GrTs *(TGFBR1*$^{CA\ flox/+}$*; Amhr2-cre)* [141]. Interestingly, overexpression of the same gene in mouse granulosa cells resulted in the development of ovarian GrTs [142]. GrTs form follicle-like nests and nodules, a growth pattern reminiscent of ovarian granulosa cells [21, 141]. Tumor cells are small, basophilic, round or spindle-shaped, similar to ovarian granulosa cell tumors with scant cytoplasm and nuclei with a single nucleolus and stippled chromatin [21].

Germ Cell Tumors

Seminoma

Seminoma is a germ cell tumor also referred to as spermatocytoma, and spermatocytic seminoma. Seminomas retain morphological features of pluripotent, primitive germ cells. Tumors are composed of cells arranged in sheets and localized within the confines of one or a few seminiferous tubular profiles. Tumor cells have cytological features resembling spermatogonia or spermatocytes. Occasional multinucleated cells and numerous mitotic figures may be present [21]. Malignant seminoma invades through the tubular basement membrane and distributes throughout the testicular interstitium [21].

Spontaneous seminomas are extremely rare in mice and only a few GEM models have been described [32]. Targeted overexpression of human glial cell derived neurotrophic factor (GDNF) in mice induced aberrant proliferation of spermatogonial stem cells and eventually seminoma-like tumors [32], consistent with GDNF's role in regulating spermatogonial stem cell renewal [143]. Tumors were composed of round spermatogonia with scant cytoplasm that were locally invasive but did not metastasize [32]. This is the first reported GEM model for seminoma; the most common testicular germ cell tumor in men [32].

References

1 Knoblaugh, S. and True, L. (2018). Male reproductive system. In: *Comparative Anatomy and Histology: A Mouse, Rat, and Human Atlas*, 2e (eds. P.M. Treuting and S.M. Dintzis), 335–363. London: Academic Press.

2 Kiupel, M., Brown, K.S., and Sundberg, J.P. (2000). Bulbourethral (Cowper's) gland abnormalities in inbred laboratory mice. *J. Exp. Anim. Sci.* 40 (4): 178–188.

3 Creasy, D. and Chapin, R. (2018). Male reproductive system. In: *Fundamentals of Toxicologic Pathology*, 3e (eds. M.A. Walling, W.M. Hascheck, C.G. Rousseaux, et al.), 459–516. London, UK: Academic Press.

4 Shibata, M.A., Ward, J.M., Devor, D.E. et al. (1996). Progression of prostatic intraepithelial neoplasia to invasive carcinoma in C3(1)/SV40 large T antigen transgenic mice: histopathological and molecular biological alterations. *Cancer Res.* 56 (21): 4894–4903.

5 Tani, Y., Suttie, A., Flake, G.P. et al. (2005). Epithelial-stromal tumor of the seminal vesicles in the transgenic adenocarcinoma mouse prostate model. *Vet. Pathol.* 42 (3): 306–314.

6 Oliveira, D.S.M., Dzinic, S., Bonfil, A.I. et al. (2016). The mouse prostate: a basic anatomical and histological guideline. *Bosn. J. Basic Med. Sci.* 16 (1): 8–13.

7 Shappell, S.B., Thomas, G.V., Roberts, R.L. et al. (2004). Prostate pathology of genetically engineered mice: definitions and classification. The consensus report from the Bar Harbor meeting of the Mouse Models of Human Cancer Consortium Prostate Pathology Committee. *Cancer Res.* 64 (6): 2270–2305.

8 Suwa, T., Nyska, A., Haseman, J.K. et al. (2002). Spontaneous lesions in control B6C3F1 mice and recommended sectioning of male accessory sex organs. *Toxicol. Pathol.* 30 (2): 228–234.

9 Zingiryan, A., Farina, N.H., Finstad, K.H. et al. (2017). Dissection of individual prostate lobes in mouse models of prostate cancer to obtain high quality RNA. *J. Cell. Physiol.* 232 (1): 14–18.

10 Elkahwaji, J.E., Zhong, W., Hopkins, W.J., and Bushman, W. (2007). Chronic bacterial infection and inflammation incite reactive hyperplasia in a mouse model of chronic prostatitis. *The Prostate* 67 (1): 14–21.

11 Ittmann, M., Huang, J., Radaelli, E. et al. (2013). Animal models of human prostate cancer: the consensus report of the New York meeting of the Mouse Models of Human Cancers Consortium Prostate Pathology Committee. *Cancer Res.* 73 (9): 2718–2736.

12 Park, J.-H., Walls, J.E., Galvez, J.J. et al. (2002). Prostatic intraepithelial neoplasia in genetically engineered mice. *Am. J. Pathol.* 161 (2): 727–735.

13 Grabowska, M.M., DeGraff, D.J., Yu, X. et al. (2014). Mouse models of prostate cancer: picking the best model for the question. *Cancer Metastasis Rev.* 33 (2–3): 377–397.

14 Taylor, B.S., Schultz, N., Hieronymus, H. et al. (2010). Integrative genomic profiling of human prostate cancer. *Cancer Cell* 18 (1): 11–22.

15 Adissu, H.A., McKerlie, C., Di Grappa, M. et al. (2015). Timp3 loss accelerates tumour invasion and increases prostate inflammation in a mouse model of prostate cancer. *The Prostate* 75 (16): 1831–1843.

16 Wang, G., Zhao, D., Spring, D.J., and DePinho, R.A. (2018). Genetics and biology of prostate cancer. *Genes Dev.* 32 (17–18): 1105–1140.

17 Chiaverotti, T., Couto, S.S., Donjacour, A. et al. (2008). Dissociation of epithelial and neuroendocrine carcinoma lineages in the transgenic adenocarcinoma of mouse prostate model of prostate cancer. *Am. J. Pathol.* 172 (1): 236–246.

18 Lee, D.-H., Yu, E.-J., Aldahl, J. et al. (2019). Deletion of the p16INK4a tumor suppressor and expression of the androgen receptor induce sarcomatoid carcinomas with signet ring cells in the mouse prostate. *PLoS One* 14 (1): e0211153.

19 Creasy, D.M. (1997). Evaluation of testicular toxicity in safety evaluation studies: the appropriate use of spermatogenic staging. *Toxicol. Pathol.* 25 (2): 119–131.

20 Russell, L.D., Ettlin, R.A., Hikim, A.P.S., and Clegg, E.D. (1990b). Staging for the Mouse. In: *Histological and Histopathological Evaluation of the Testis*, 119–161. Clearwater, FL: Cache River Press.

21 Creasy, D., Bube, A., de Rijk, E. et al. (2012). Proliferative and nonproliferative lesions of the rat and mouse male reproductive system. *Toxicol. Pathol.* 40 (6 Suppl): 40S–121S.

22 Borg, C.L., Wolski, K.M., Gibbs, G.M., and O'Bryan, M.K. (2010). Phenotyping male infertility in the mouse: how to get the most out of a "non-performer". *Hum. Reprod. Update* 16 (2): 205–224.

23 Latendresse, J.R., Warbrittion, A.R., Jonassen, H., and Creasy, D.M. (2002). Fixation of testes and eyes using a modified Davidson's fluid: comparison with Bouin's fluid and conventional Davidson's fluid. *Toxicol. Pathol.* 30 (4): 524–533.

24 Kittel, B., Ruehl-Fehlert, C., Morawietz, G. et al. (2004). Revised guides for organ sampling and trimming in rats and mice--Part 2. A joint publication of the RITA and NACAD groups. *Exp. Toxicol. Pathol. Off. J. Ges. Toxikol. Pathol.* 55 (6): 413–431.

25 Meistrich, M.L. and Hess, R.A. (2013). Assessment of spermatogenesis through staging of seminiferous tubules. *Methods Mol. Biol.* 927: 299–307.

26 Liu, C., Rodriguez, K., and HH-C, Y. (2016). Mapping lineage progression of somatic progenitor cells in the mouse fetal testis. *Dev. Camb. Engl.* 143 (20): 3700–3710.

27 Anagawa-Nakamura, A., Kakimoto, K., Miyajima, K. et al. (2015). Immunohistochemical characterization of spontaneous sertoli cell clusters in the seminiferous tubules of C57BL/6J Mice. *Toxicol. Pathol.* 43 (5): 743–746.

28 Al-Attar, L., Noël, K., Dutertre, M. et al. (1997). Hormonal and cellular regulation of Sertoli cell anti-Müllerian

hormone production in the postnatal mouse. *J. Clin. Invest.* 100 (6): 1335–1343.

29 O'Shaughnessy, P.J., Baker, P.J., Heikkilä, M. et al. (2000). Localization of 17beta-hydroxysteroid dehydrogenase/17-ketosteroid reductase isoform expression in the developing mouse testis – androstenedione is the major androgen secreted by fetal/neonatal leydig cells. *Endocrinology* 141 (7): 2631–2637.

30 Kubota, H., Avarbock, M.R., and Brinster, R.L. (2004). Growth factors essential for self-renewal and expansion of mouse spermatogonial stem cells. *Proc. Natl. Acad. Sci. U.S.A.* 101 (47): 16489–16494.

31 Tokuda, M., Kadokawa, Y., Kurahashi, H., and Marunouchi, T. (2007). CDH1 is a specific marker for undifferentiated spermatogonia in mouse testes. *Biol. Reprod.* 76 (1): 130–141.

32 Meng, X., de Rooij, D.G., Westerdahl, K. et al. (2001). Promotion of seminomatous tumors by targeted overexpression of glial cell line-derived neurotrophic factor in mouse testis. *Cancer Res.* 61 (8): 3267–3271.

33 Ling, X., Tanaka, H., Tsuchida, J., and Nishimune, Y. (2000). Identification of differentiation antigens in mouse testicular germ cells recognized by monoclonal antibody TRA 55. *Int. J. Androl.* 23 (1): 29–35.

34 Tanaka, H., Pereira, L.A., Nozaki, M. et al. (1997). A germ cell-specific nuclear antigen recognized by a monoclonal antibody raised against mouse testicular germ cells. *Int. J. Androl.* 20 (6): 361–366.

35 Campagnolo, L., Russo, M.A., Puglianiello, A. et al. (2001). Mesenchymal cell precursors of peritubular smooth muscle cells of the mouse testis can be identified by the presence of the p75 neurotrophin receptor. *Biol. Reprod.* 64 (2): 464–472.

36 Radovsky, A., Mitsumori, K., and Chapin, R.E. (1999). Male reproductive tract. In: *Pathology of the Mouse, Reference and Atlas* (eds. R.R. Maronpot, G.A. Boorman and B.W. Gaul), 381–407. Vienna, IL: Cache River Press.

37 Jamsai, D. and O'Bryan, M.K. (2011). Mouse models in male fertility research. *Asian J. Androl.* 13 (1): 139–151.

38 Neto, F.T.L., Bach, P.V., Najari, B.B. et al. (2016). Genetics of male infertility. *Curr. Urol. Rep.* 17 (10): 70.

39 Portnoi, M.-F., Dumargne, M.-C., Rojo, S. et al. (2018). Mutations involving the SRY-related gene SOX8 are associated with a spectrum of human reproductive anomalies. *Hum. Mol. Genet.* 27 (7): 1228–1240.

40 O'Bryan, M.K., Takada, S., Kennedy, C.L. et al. (2008). Sox8 is a critical regulator of adult Sertoli cell function and male fertility. *Dev. Biol.* 316 (2): 359–370.

41 Wagner, T., Wirth, J., Meyer, J. et al. (1994). Autosomal sex reversal and campomelic dysplasia are caused by mutations in and around the SRY-related gene SOX9. *Cell* 79 (6): 1111–1120.

42 Chaboissier, M.-C., Kobayashi, A., Vidal, V.I.P. et al. (2004). Functional analysis of Sox8 and Sox9 during sex determination in the mouse. *Dev. Camb. Engl.* 131 (9): 1891–1901.

43 Lin, L., Conway, G.S., Hill, N.R. et al. (2006). A homozygous R262Q mutation in the gonadotropin-releasing hormone receptor presenting as constitutional delay of growth and puberty with subsequent borderline oligospermia. *J. Clin. Endocrinol. Metab.* 91 (12): 5117–5121.

44 Layman, L.C., Cohen, D.P., Xie, J., and Smith, G.D. (2002). Clinical phenotype and infertility treatment in a male with hypogonadotropic hypogonadism due to mutations Ala129Asp/Arg262Gln of the gonadotropin-releasing hormone receptor. *Fertil. Steril.* 78 (6): 1317–1320.

45 Cattanach, B.M., Iddon, C.A., Charlton, H.M. et al. (1977). Gonadotrophin-releasing hormone deficiency in a mutant mouse with hypogonadism. *Nature* 269 (5626): 338–340.

46 Pask, A.J., Kanasaki, H., Kaiser, U.B. et al. (2005). A novel mouse model of hypogonadotrophic hypogonadism: N-ethyl-N-nitrosourea-induced gonadotropin-releasing hormone receptor gene mutation. *Mol. Endocrinol.* 19 (4): 972–981.

47 Bruysters, M., Christin-Maitre, S., Verhoef-Post, M. et al. (2008). A new LH receptor splice mutation responsible for male hypogonadism with subnormal sperm production in the propositus, and infertility with regular cycles in an affected sister. *Hum. Reprod. Oxf. Engl.* 23 (8): 1917–1923.

48 Zhang, F.P., Poutanen, M., Wilbertz, J., and Huhtaniemi, I. (2001). Normal prenatal but arrested postnatal sexual development of luteinizing hormone receptor knockout (LuRKO) mice. *Mol. Endocrinol.* 15 (1): 172–183.

49 Tapanainen, J.S., Aittomäki, K., Min, J. et al. (1997). Men homozygous for an inactivating mutation of the follicle-stimulating hormone (FSH) receptor gene present variable suppression of spermatogenesis and fertility. *Nat. Genet.* 15 (2): 205–206.

50 Krishnamurthy, H., Babu, P.S., Morales, C.R., and Sairam, M.R. (2001). Delay in sexual maturity of the follicle-stimulating hormone receptor knockout male mouse. *Biol. Reprod.* 65 (2): 522–531.

51 Ferlin, A., Vinanzi, C., Garolla, A. et al. (2006). Male infertility and androgen receptor gene mutations: clinical features and identification of seven novel mutations. *Clin. Endocrinol. (Oxf)* 65 (5): 606–610.

52 Wang, R.-S., Yeh, S., Tzeng, C.-R., and Chang, C. (2009). Androgen receptor roles in spermatogenesis and fertility: lessons from testicular cell-specific androgen receptor knockout mice. *Endocr. Rev.* 30 (2): 119–132.

53 Tsai, M.-Y., Yeh, S.-D., Wang, R.-S. et al. (2006). Differential effects of spermatogenesis and fertility in mice lacking androgen receptor in individual testis cells. *Proc. Natl. Acad. Sci. U.S.A.* 103 (50): 18975–18980.

54 Seminara, S.B., Messager, S., Chatzidaki, E.E. et al. (2003). The GPR54 gene as a regulator of puberty. *N. Engl. J. Med.* 349 (17): 1614–1627.

55 de Roux, N., Genin, E., Carel, J.-C. et al. (2003). Hypogonadotropic hypogonadism due to loss of function of the KiSS1-derived peptide receptor GPR54. *Proc. Natl. Acad. Sci. U.S.A.* 100 (19): 10972–10976.

56 d'Anglemont de Tassigny, X., Fagg, L.A., Dixon, J.P.C. et al. (2007). Hypogonadotropic hypogonadism in mice lacking a

functional Kiss1 gene. *Proc. Natl. Acad. Sci. U.S.A.* 104 (25): 10714–10719.

57 Funes, S., Hedrick, J.A., Vassileva, G. et al. (2003). The KiSS-1 receptor GPR54 is essential for the development of the murine reproductive system. *Biochem. Biophys. Res. Commun.* 312 (4): 1357–1363.

58 Krausz, C., Riera-Escamilla, A., Chianese, C. et al. (2019). From exome analysis in idiopathic azoospermia to the identification of a high-risk subgroup for occult Fanconi anemia. *Genet. Med. Off. J. Am. Coll. Med. Gen.* 21 (1): 189–194.

59 Bargman, G.J., Shahidi, N.T., Gilbert, E.F., and Opitz, J.M. (1977). Studies of malformation syndromes of man XLVII: disappearance of spermatogonia in the Fanconi anemia syndrome. *Eur. J. Pediatr.* 125 (3): 163–168.

60 Nadler, J.J. and Braun, R.E. (2000). Fanconi anemia complementation group C is required for proliferation of murine primordial germ cells. *Genesis* 27 (3): 117–123.

61 Cheng, N.C., van de Vrugt, H.J., van der Valk, M.A. et al. (2000). Mice with a targeted disruption of the Fanconi anemia homolog Fanca. *Hum. Mol. Genet.* 9 (12): 1805–1811.

62 Chen, C., Ouyang, W., Grigura, V. et al. (2005). ERM is required for transcriptional control of the spermatogonial stem cell niche. *Nature* 436 (7053): 1030–1034.

63 Tang, S., Wang, X., Li, W. et al. (2017). Biallelic mutations in CFAP43 and CFAP44 cause male infertility with multiple morphological abnormalities of the sperm flagella. *Am. J. Hum. Genet.* 100 (6): 854–864.

64 Schrans-Stassen, B.H., Saunders, P.T., Cooke, H.J., and de Rooij, D.G. (2001). Nature of the spermatogenic arrest in Dazl$^{-/-}$ mice. *Biol. Reprod.* 65 (3): 771–776.

65 Ferguson, K.A., Chow, V., and Ma, S. (2008). Silencing of unpaired meiotic chromosomes and altered recombination patterns in an azoospermic carrier of a t(8;13) reciprocal translocation. *Hum. Reprod. Oxf. Engl.* 23 (4): 988–995.

66 de Vries, F.A.T., de Boer, E., van den Bosch, M. et al. (2005). Mouse Sycp1 functions in synaptonemal complex assembly, meiotic recombination, and XY body formation. *Genes Dev.* 19 (11): 1376–1389.

67 Yuan, L., Liu, J.G., Zhao, J. et al. (2000). The murine SCP3 gene is required for synaptonemal complex assembly, chromosome synapsis, and male fertility. *Mol. Cell.* 5 (1): 73–83.

68 Xu, Y., Ashley, T., Brainerd, E.E. et al. (1996). Targeted disruption of ATM leads to growth retardation, chromosomal fragmentation during meiosis, immune defects, and thymic lymphoma. *Genes Dev.* 10 (19): 2411–2422.

69 Barlow, C., Liyanage, M., Moens, P.B. et al. (1998). Atm deficiency results in severe meiotic disruption as early as leptonema of prophase I. *Dev. Camb. Engl.* 125 (20): 4007–4017.

70 Yang, F., Silber, S., Leu, N.A. et al. (2015). TEX11 is mutated in infertile men with azoospermia and regulates genome-wide recombination rates in mouse. *EMBO Mol. Med.* 7 (9): 1198–1210.

71 Yatsenko, A.N., Georgiadis, A.P., Röpke, A. et al. (2015). X-linked TEX11 mutations, meiotic arrest, and azoospermia in infertile men. *N. Engl. J. Med.* 372 (22): 2097–2107.

72 Yang, F., Gell, K., van der Heijden, G.W. et al. (2008). Meiotic failure in male mice lacking an X-linked factor. *Genes Dev.* 22 (5): 682–691.

73 Gershoni, M., Hauser, R., Yogev, L. et al. (2017). A familial study of azoospermic men identifies three novel causative mutations in three new human azoospermia genes. *Genet. Med.* 19 (9): 998–1006.

74 Greenbaum, M.P., Yan, W., Wu, M.-H. et al. (2006). TEX14 is essential for intercellular bridges and fertility in male mice. *Proc. Natl. Acad. Sci. U.S.A.* 103 (13): 4982–4987.

75 Behr, R. and Weinbauer, G.F. (2000). CREM activator and repressor isoforms in human testis: sequence variations and inaccurate splicing during impaired spermatogenesis. *Mol. Hum. Reprod.* 6 (11): 967–972.

76 Vouk, K., Hudler, P., Strmsnik, L. et al. (2005). Combinations of genetic changes in the human cAMP-responsive element modulator gene: a clue towards understanding some forms of male infertility? *Mol. Hum. Reprod.* 11 (8): 567–574.

77 Blendy, J.A., Kaestner, K.H., Weinbauer, G.F. et al. (1996). Severe impairment of spermatogenesis in mice lacking the CREM gene. *Nature* 380 (6570): 162–165.

78 Nantel, F., Monaco, L., Foulkes, N.S. et al. (1996). Spermiogenesis deficiency and germ-cell apoptosis in CREM-mutant mice. *Nature* 380 (6570): 159–162.

79 Steger, K., Failing, K., Klonisch, T. et al. (2001). Round spermatids from infertile men exhibit decreased protamine-1 and -2 mRNA. *Hum. Reprod. Oxf. Engl.* 16 (4): 709–716.

80 Carrell, D.T. and Liu, L. (2001). Altered protamine 2 expression is uncommon in donors of known fertility, but common among men with poor fertilizing capacity, and may reflect other abnormalities of spermiogenesis. *J. Androl.* 22 (4): 604–610.

81 Cho, C., Willis, W.D., Goulding, E.H. et al. (2001). Haploinsufficiency of protamine-1 or -2 causes infertility in mice. *Nat. Genet.* 28 (1): 82–86.

82 Kherraf, Z.-E., Conne, B., Amiri-Yekta, A. et al. (2018). Creation of knock out and knock in mice by CRISPR/Cas9 to validate candidate genes for human male infertility, interest, difficulties and feasibility. *Mol. Cell. Endocrinol.* 15 (468): 70–80.

83 Kherraf, Z.-E., Christou-Kent, M., Karaouzene, T. et al. (2017). SPINK2 deficiency causes infertility by inducing sperm defects in heterozygotes and azoospermia in homozygotes. *EMBO Mol. Med.* 9 (8): 1132–1149.

84 Zuccarello, D., Ferlin, A., Garolla, A. et al. (2008). A possible association of a human tektin-t gene mutation (A229V) with isolated non-syndromic asthenozoospermia: case report. *Hum. Reprod. Oxf. Engl.* 23 (4): 996–1001.

85 Tanaka, H., Iguchi, N., Toyama, Y. et al. (2004). Mice deficient in the axonemal protein Tektin-t exhibit male infertility and immotile-cilium syndrome due to impaired

inner arm dynein function. *Mol. Cell. Biol.* 24 (18): 7958–7964.

86 Amiri-Yekta, A., Coutton, C., Kherraf, Z.-E. et al. (2016). Whole-exome sequencing of familial cases of multiple morphological abnormalities of the sperm flagella (MMAF) reveals new DNAH1 mutations. *Hum. Reprod. Oxf. Engl.* 31 (12): 2872–2880.

87 Ben Khelifa, M., Coutton, C., Zouari, R. et al. (2014). Mutations in DNAH1, which encodes an inner arm heavy chain dynein, lead to male infertility from multiple morphological abnormalities of the sperm flagella. *Am. J. Hum. Genet.* 94 (1): 95–104.

88 Neesen, J., Kirschner, R., Ochs, M. et al. (2001). Disruption of an inner arm dynein heavy chain gene results in asthenozoospermia and reduced ciliary beat frequency. *Hum. Mol. Genet.* 10 (11): 1117–1128.

89 Avenarius, M.R., Hildebrand, M.S., Zhang, Y. et al. (2009). Human male infertility caused by mutations in the CATSPER1 channel protein. *Am. J. Hum. Genet.* 84 (4): 505–510.

90 Avidan, N., Tamary, H., Dgany, O. et al. (2003). CATSPER2, a human autosomal nonsyndromic male infertility gene. *Eur. J. Hum. Genet.* 11 (7): 497–502.

91 Qi, H., Moran, M.M., Navarro, B. et al. (2007). All four CatSper ion channel proteins are required for male fertility and sperm cell hyperactivated motility. *Proc. Natl. Acad. Sci. U.S.A.* 104 (4): 1219–1223.

92 Sha, Y.-W., Wang, X., Xu, X. et al. (2019). Novel mutations in CFAP44 and CFAP43 cause multiple morphological abnormalities of the sperm flagella (MMAF). *Reprod. Sci. Thousand Oaks Calif.* 26 (1): 26–34.

93 Chen, H., Yi, M., Sheng, Y. et al. (2013). A novel testis-enriched gene Spata33 is expressed during spermatogenesis. *PLoS One* 8 (7): e67882.

94 Cooke, H.J. and Saunders, P.T.K. (2002). Mouse models of male infertility. *Nat. Rev. Genet.* 3 (10): 790–801.

95 Schultz, N., Hamra, F.K., and Garbers, D.L. (2003). A multitude of genes expressed solely in meiotic or postmeiotic spermatogenic cells offers a myriad of contraceptive targets. *Proc. Natl. Acad. Sci. U.S.A.* 100 (21): 12201–12206.

96 Matzuk, M.M. and Lamb, D.J. (2008). The biology of infertility: research advances and clinical challenges. *Nat. Med.* 14 (11): 1197–1213.

97 White, J.K., Gerdin, A.-K., Karp, N.A. et al. (2013). Genome-wide generation and systematic phenotyping of knockout mice reveals new roles for many genes. *Cell* 154 (2): 452–464.

98 Adissu, H.A., Estabel, J., Sunter, D. et al. (2014). Histopathology reveals correlative and unique phenotypes in a high-throughput mouse phenotyping screen. *Dis. Model Mech.* 7 (5): 515–524.

99 Raymond, C.S., Murphy, M.W., O'Sullivan, M.G. et al. (2000). Dmrt1, a gene related to worm and fly sexual regulators, is required for mammalian testis differentiation. *Genes Dev.* 14 (20): 2587–2595.

100 Lilford, R., Jones, A.M., Bishop, D.T. et al. (1994). Case-control study of whether subfertility in men is familial. *BMJ* 309 (6954): 570–573.

101 Cho, C., Bunch, D.O., Faure, J.E. et al. (1998). Fertilization defects in sperm from mice lacking fertilin beta. *Science* 281 (5384): 1857–1859.

102 Nishimura, H., Cho, C., Branciforte, D.R. et al. (2001). Analysis of loss of adhesive function in sperm lacking cyritestin or fertilin beta. *Dev. Biol.* 233 (1): 204–213.

103 Kissel, H., Georgescu, M.-M., Larisch, S. et al. (2005). The Sept4 septin locus is required for sperm terminal differentiation in mice. *Dev. Cell* 8 (3): 353–364.

104 Vidal, J.D. and Whitney, K.M. (2014). Morphologic manifestations of testicular and epididymal toxicity. *Spermatogenesis* 4 (2): e979099.

105 Lanning, L.L., Creasy, D.M., Chapin, R.E. et al. (2002). Recommended approaches for the evaluation of testicular and epididymal toxicity. *Toxicol. Pathol.* 30 (4): 507–520.

106 Hussain, S., Tuorto, F., Menon, S. et al. (2013). The mouse cytosine-5 RNA methyltransferase NSun2 is a component of the chromatoid body and required for testis differentiation. *Mol. Cell. Biol.* 33 (8): 1561–1570.

107 Celeste, A., Petersen, S., Romanienko, P.J. et al. (2002). Genomic instability in mice lacking histone H2AX. *Science* 296 (5569): 922–927.

108 Yeh, S., Tsai, M.-Y., Xu, Q. et al. (2002). Generation and characterization of androgen receptor knockout (ARKO) mice: an in vivo model for the study of androgen functions in selective tissues. *Proc. Natl. Acad. Sci. U.S.A.* 99 (21): 13498–13503.

109 Bhandari, R., Juluri, K.R., Resnick, A.C., and Snyder, S.H. (2008). Gene deletion of inositol hexakisphosphate kinase 1 reveals inositol pyrophosphate regulation of insulin secretion, growth, and spermiogenesis. *Proc. Natl. Acad. Sci. U.S.A.* 105 (7): 2349–2353.

110 Jamsai, D., Clark, B.J., Smith, S.J. et al. (2013). A missense mutation in the transcription factor ETV5 leads to sterility, increased embryonic and perinatal death, postnatal growth restriction, renal asymmetry and polydactyly in the mouse. *PLoS One* 8 (10): e77311.

111 Chen, A., Li, J., Song, L. et al. (2017). GGNBP2 is necessary for testis morphology and sperm development. *Sci. Rep.* 7 (1): 2998.

112 Print, C.G., Loveland, K.L., Gibson, L. et al. (1998). Apoptosis regulator bcl-w is essential for spermatogenesis but appears otherwise redundant. *Proc. Natl. Acad. Sci. U.S.A.* 95 (21): 12424–12431.

113 Martianov, I., Fimia, G.M., Dierich, A. et al. (2001). Late arrest of spermiogenesis and germ cell apoptosis in mice lacking the TBP-like TLF/TRF2 gene. *Mol. Cell.* 7 (3): 509–515.

114 Wu, Y., Hu, X., Li, Z. et al. (2016). Transcription factor RFX2 is a key regulator of mouse spermiogenesis. *Sci. Rep.* 6: 20435.

115 Brauns, A.-K., Heine, M., Tödter, K. et al. (2019). A defect in the peroxisomal biogenesis in germ cells induces a

spermatogenic arrest at the round spermatid stage in mice. *Sci. Rep.* 9 (1): 9553.

116 Hess, R.A. and Nakai, M. (2000). Histopathology of the male reproductive system induced by the fungicide benomyl. *Histol. Histopathol.* 15 (1): 207–224.

117 Wakayama, T. and Iseki, S. (2009). Role of the spermatogenic-Sertoli cell interaction through cell adhesion molecule-1 (CADM1) in spermatogenesis. *Anat. Sci. Int.* 84 (3): 112–121.

118 Akama, T.O., Nakagawa, H., Sugihara, K. et al. (2002). Germ cell survival through carbohydrate-mediated interaction with Sertoli cells. *Science* 295 (5552): 124–127.

119 Gruber, M., Mathew, L.K., Runge, A.C. et al. (2010). EPAS1 is required for spermatogenesis in the postnatal mouse testis. *Biol. Reprod.* 82 (6): 1227–1236.

120 Jiang, X., Ma, T., Zhang, Y. et al. (2015). Specific deletion of Cdh2 in Sertoli cells leads to altered meiotic progression and subfertility of mice. *Biol. Reprod.* 92 (3): 79.

121 Ali, A., Mistry, B.V., Ahmed, H.A. et al. (2018). Deletion of DDB1- and CUL4- associated factor-17 (Dcaf17) gene causes spermatogenesis defects and male infertility in mice. *Sci. Rep.* 8 (1): 9202.

122 Yildiz, Y., Matern, H., Thompson, B. et al. (2006). Mutation of beta-glucosidase 2 causes glycolipid storage disease and impaired male fertility. *J. Clin. Invest.* 116 (11): 2985–2994.

123 La, D.K., Creasy, D.M., Hess, R.A. et al. (2012). Efferent duct toxicity with secondary testicular changes in rats following administration of a novel leukotriene A_4 hydrolase inhibitor. *Toxicol. Pathol.* 40 (5): 705–714.

124 Hess, R.A. (1998). Effects of environmental toxicants on the efferent ducts, epididymis and fertility. *J. Reprod. Fertil. Suppl.* 53: 247–259.

125 Danielian, P.S., Hess, R.A., and Lees, J.A. (2016). E2f4 and E2f5 are essential for the development of the male reproductive system. *Cell Cycle Georget. Tex.* 15 (2): 250–260.

126 Davies, B., Baumann, C., Kirchhoff, C. et al. (2004). Targeted deletion of the epididymal receptor HE6 results in fluid dysregulation and male infertility. *Mol. Cell. Biol.* 24 (19): 8642–8648.

127 Eddy, E.M., Washburn, T.F., Bunch, D.O. et al. (1996). Targeted disruption of the estrogen receptor gene in male mice causes alteration of spermatogenesis and infertility. *Endocrinology* 137 (11): 4796–4805.

128 Leigh, M.W., Pittman, J.E., Carson, J.L. et al. (2009). Clinical and genetic aspects of primary ciliary dyskinesia/Kartagener syndrome. *Genet. Med. Off. J. Am. Coll. Med. Gen.* 11 (7): 473–487.

129 Sonnenberg-Riethmacher, E., Walter, B., Riethmacher, D. et al. (1996). The c-ros tyrosine kinase receptor controls regionalization and differentiation of epithelial cells in the epididymis. *Genes Dev.* 10 (10): 1184–1193.

130 Carvajal, G., Brukman, N.G., Weigel Muñoz, M. et al. (2018). Impaired male fertility and abnormal epididymal epithelium differentiation in mice lacking CRISP1 and CRISP4. *Sci. Rep.* 8 (1): 17531.

131 Stevens, L.C. and Little, C.C. (1954). Spontaneous testicular teratomas in an inbred strain of mice. *Proc. Natl. Acad. Sci. U.S.A.* 40 (11): 1080–1087.

132 Mähler, M. and Sundberg, J.P. (1997). Spontaneous Leydig cell tumors in inbred laboratory mice. *Lab. Anim. Sci.* 47 (2): 148–152.

133 Clegg, E.D., Cook, J.C., Chapin, R.E. et al. (1997). Leydig cell hyperplasia and adenoma formation: mechanisms and relevance to humans. *Reprod. Toxicol.* 11 (1): 107–121.

134 Fowler, K.A., Gill, K., Kirma, N. et al. (2000). Overexpression of aromatase leads to development of testicular leydig cell tumors: an in vivo model for hormone-mediated TesticularCancer. *Am. J. Pathol.* 156 (1): 347–353.

135 Quintana, S., Venara, M., Rey, R. et al. (2010). Origin and evolution of somatic cell testicular tumours in transgenic mice. *J. Pathol.* 221 (4): 443–451.

136 Racine, C., Rey, R., Forest, M.G. et al. (1998). Receptors for anti-müllerian hormone on Leydig cells are responsible for its effects on steroidogenesis and cell differentiation. *Proc. Natl. Acad. Sci. U.S.A.* 95 (2): 594–599.

137 Paquis-Flucklinger, V., Rassoulzadegan, M., and Michiels, J.F. (1994). Experimental Sertoli cell tumors in the mouse and their progression into a mixed germ cell-sex cord proliferation. *Am. J. Pathol.* 144 (3): 454–459.

138 Chang, H., Guillou, F., Taketo, M.M., and Behringer, R.R. (2009). Overactive beta-catenin signaling causes testicular sertoli cell tumor development in the mouse. *Biol. Reprod.* 81 (5): 842–849.

139 Boyer, A., Paquet, M., Laguë, M.-N. et al. (2009). Dysregulation of WNT/CTNNB1 and PI3K/AKT signaling in testicular stromal cells causes granulosa cell tumor of the testis. *Carcinogenesis* 30 (5): 869–878.

140 Richards, J.S., Fan, H.-Y., Liu, Z. et al. (2012). Either Kras activation or Pten loss similarly enhance the dominant-stable CTNNB1-induced genetic program to promote granulosa cell tumor development in the ovary and testis. *Oncogene* 31 (12): 1504–1520.

141 Fang, X., Ni, N., Gao, Y. et al. (2018). A novel mouse model of testicular granulosa cell tumors. *Mol. Hum. Reprod.* 24 (7): 343–356.

142 Gao, Y., Vincent, D.F., Davis, A.J. et al. (2016). Constitutively active transforming growth factor β receptor 1 in the mouse ovary promotes tumorigenesis. *Oncotarget.* 7 (27): 40904–40918.

143 Huleihel, M., Fadlon, E., Abuelhija, A. et al. (2013). Glial cell line-derived neurotrophic factor (GDNF) induced migr of spermatogonial cells in vitro via MEK and NF-kB pathways. *Differ. Res. Biol. Divers.* 86 (1–2): 38–47.

21

Nervous System

Jessica M. Snyder, Katherine N. Gibson-Corley, and Enrico Radaelli

Anatomy, Histology, and Physiology

Grossly, the mouse brain is lissencephalic and oriented along a linear axis. Broadly, the brain is divided into the prosencephalon (forebrain), mesencephalon (midbrain), and rhombencephalon (hindbrain). The prosencephalon is further subdivided into the telencephalon (paired cerebral hemispheres), diencephalon (thalamus) and hypothalamus. The rhombencephalon is further subdivided into the metencephalon (pons and cerebellum) and myelencephalon (medulla oblongata) [1, 2]. Large olfactory bulbs are present at the cranial aspect of the cerebrum. Dorsally, there is a prominent longitudinal fissure that separates the cerebral hemispheres. The cerebellum is present overlying the pons and medulla, and the rostral and caudal colliculi are visible between the occipital lobes and the cerebellum (Figure 21.1). Ventrally, the optic tract, infundibulum, and mammillary bodies are present on midline in the center of the brain. The pons and medulla, with the pyramids separated by the ventral fissure, are visible on the ventral aspect of the brainstem (Figure 21.2).

On the cut section of the brain, the distinction between white and gray matter is apparent. Rodents have relatively little white matter compared with many larger mammals including primates. In rodents, the caudate and putamen are not separated by the internal capsule, but rather are combined into the striatum. The corpus callosum is visible dorsally on midline on coronal sections at the levels of the striatum and thalamus. The lateral ventricles, which are typically small in mice, are also apparent in these sections. The hippocampus tends to be present dorsally in more cranial sections and curves ventrolaterally in more caudal sections (Figures 21.3, and 21.4).

The ventricular system is composed of two lateral ventricles, the third ventricle, the mesencephalic aqueduct, and the fourth ventricle. Cerebrospinal fluid (CSF) production and flow may be interrupted in a number of disease processes such as hydrocephalus, inflammatory diseases, and neoplastic processes [3–5]. The vascular system of the mouse nervous system may vary slightly by strain and is described in detail elsewhere [1, 6]. Major surface arteries include the rostral cerebral artery, middle cerebral artery, internal carotid artery, caudal cerebral artery, rostral cerebellar artery, basilar artery, and caudal cerebellar artery [1]. The mouse central nervous system (CNS) (and the mammalian CNS more in general) was thought to lack lymphatic drainage. However, lymphatic vessels have been discovered in the dura mater of mice [7]. Lymphatic vessels provide a route for immune cells trafficking and toxic substances clearing from the CNS. In the mouse brain, basal, but not dorsal, lymphatic vessels specialize in fluid uptake draining to the cervical lymph nodes [8]. This mechanism becomes progressively dysfunctional as mice age. In this context, impairment of lymphatic drainage from the CNS has been proposed as a possible contributory cause of senile neurofunctional decline [8, 9]. The glymphatic system is a recently described system that clears waste via a series of perivascular channels formed by astroglial cells. The glymphatic system may also play a role in the distribution of compounds such as glucose, lipids, and neurotransmitters to the brain [10].

The rodent brain physiology is similar to that of other mammalian species. Broadly, the cerebrum is responsible for cognition, including interpretation of visual, auditory, olfactory, tactile, and other stimuli, and for memory and learning. The basal ganglia function via connections with other brain regions to coordinate movement, posture, and some forebrain functions. The brainstem contains nuclei responsible for balance, awareness, and respiration. The cerebellum functions to coordinate and refine movement. Functional regions of the brain that are especially relevant for comparative studies include cerebral cortex; basal nuclei (striatum, globus pallidus, substantia nigra); hippocampus; and cerebellum. Unique histological features of these regions and common disease models involving these areas are presented (Table 21.1).

Brain atlases are critical to correctly identify relevant anatomical structures, and many good references exist [1, 2, 11–13; and online http://atlas.brain-map.org/)]. The *Nervous System* chapter in *Comparative Anatomy and Histology: A Mouse, Rat and Human Atlas* provides a reference for comparative anatomy and histology of the mouse and human brain and spinal cord [14]. Embryological development of the mouse CNS is described elsewhere [2, 15].

The mouse has 7 cervical, 13 thoracic, 6 lumbar, 4 sacral, and 27–30 caudal vertebrae, although there may be some variation in number of lumbar vertebrae by strain [16].

Pathology of Genetically Engineered and Other Mutant Mice, First Edition. Edited by John P. Sundberg, Peter Vogel, and Jerrold M. Ward.
© 2022 John Wiley & Sons, Inc. Published 2022 by John Wiley & Sons, Inc.



Figure 21.1 **Dorsal view of brain**. Source: Reproduced from Comparative Anatomy and Histology – A Mouse, Rat, and Human Atlas, with permission of Elsevier.



Figure 21.2 **Ventral view of brain**. Source: Melanin (an incidental finding in pigmented strains) is present on the ventral surface of the olfactory lobes. Reproduced from Comparative Anatomy and Histology – A Mouse, Rat, and Human Atlas, with permission of Elsevier.

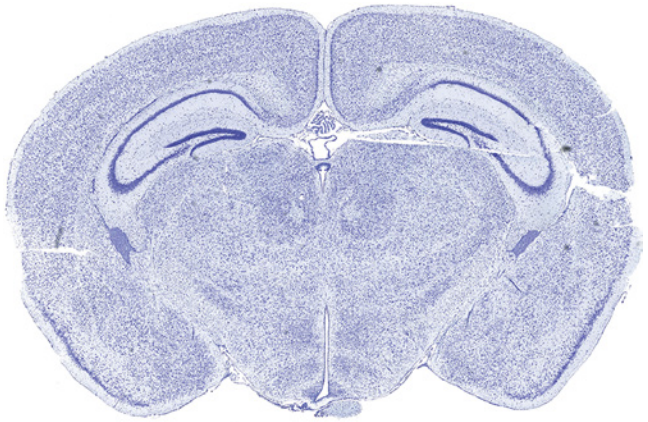


Figure 21.3 **Coronal (cross) section of brain at the level of the thalamus, with the body of the hippocampus in its more dorsal location**. Nissl stain. Source: Reproduced from Comparative Anatomy and Histology – A Mouse, Rat, and Human Atlas, with permission of Elsevier.



Figure 21.4 **Coronal (cross) section of brain at the level of the midbrain, with the hippocampus in a more ventrolateral location**. Tear artifacts are present. Nissl stain. Source: Reproduced from Comparative Anatomy and Histology – A Mouse, Rat, and Human Atlas, with permission of Elsevier.

Within the vertebral canal, there are 8 cervical spinal cord segments (C1–C8), 13 thoracic segments (T1–T13), 6 lumbar segments (L1–L6), 4 sacral segments (S1–S4), and 3 coccygeal segments (Co1–Co3). The spinal cord is composed of an inner central canal and butterfly-shaped region of gray matter, which is surrounded by white matter. The spinal cord is functionally divided into four segments in the mouse: C1–C5 (axons of the upper motor neuron to both the thoracic and pelvic limbs); C5–T1 (cervical enlargement, lower motor neuron to the thoracic limbs); T1–L2 (axons of the upper motor neuron to the pelvic limbs); and L2–L6 (lumbosacral enlargement, lower motor neuron to the pelvic limbs). The spinal cord occupies the vertebral canal such that in the adult mouse the C5–T1 spinal cord segments are associated with the C5–C7 vertebral bodies and the L2–L6 spinal cord segments are associated with the T12–L1 vertebral bodies. The S1–S4 segments are associated with vertebral bodies L1–L2, and the Co1–Co3 segments are associated with the L3–L4 vertebral bodies [16].

The gray matter of the spinal cord is composed of a dorsal horn, responsible for sensation, and the ventral horn, responsible for motor function. In the thoracic and cranial lumbar spinal cord, there is a lateral column of gray matter, which contains preganglionic neurons of the sympathetic nervous system. According to the Rexed's classification of the spinal gray matter, 10 anatomico-functional laminae are recognized [17, 18]. Laminae are organized in a series of

Table 21.1 Functional regions of the central nervous system.

Region	Unique histological features	Common disease models
Cerebrum	Laminae (six parallel layers) [less distinct in many parts of the rodent cerebral cortex compared to human]	Alzheimer's disease Autism Epilepsy
Basal ganglia – striatum	Bundles of finely myelinated small diameter axons (pencil fibers)	Huntington's disease
Basal ganglia – substantia nigra	Neuromelanin; in mice neurons have a narrow halo of cytoplasm bordered by a basophilic band and pigment is not visible	Parkinson's disease
Hippocampus	Dentate gyrus – dense granule cells Ammon's horn CA1–CA4 – pyramidal neurons	Epilepsy
Cerebellum	Granular layer, Purkinje cell layer, molecular layer	Spinocerebellar ataxia
White matter	Oligodendrocytes in linear rows between nerve fibers (brain); myelinated axons (spinal cord)	Multiple sclerosis
Motor neuron, spinal cord ventral horn	Large pyramidal neurons	Amyotrophic lateral sclerosis

layers from dorsal to ventral, with the exception of lamina 10 located around the central canal. The white matter of the spinal cord is organized into somatotopically arranged descending and ascending fiber tracts within the dorsal, lateral, and ventral funiculi.

The peripheral nervous system is composed of the ganglia, peripheral nerve, neuromuscular junction, and skeletal muscle and is discussed in further detail in Chapter 16.

Histologically, cell types of the CNS include neurons, glial cells (astrocytes, oligodendrocytes, and microglia), choroid plexus epithelial cells, ependymal cells, meningothelial cells, vascular endothelium, and pericytes [10, 19]. Histochemical stains and immunohistochemical labels to differentiate some of these cell types are listed (Table 21.2).

Neurological phenotypes commonly target specific areas of the brain, and even with pronounced clinical changes, histological changes may be subtle or even nonexistent [20]. Thorough evaluation of multiple levels of brain and spinal cord and careful comparison with age matched (ideally, littermate) controls should be performed. Following gross evaluation, hematoxylin and eosin (HE) histology is the first step in the diagnosis of a neurological phenotype. Changes may include decreased numbers of neurons with or without a secondary tissue response (to distinguish from normal regional variation in neuronal numbers advanced morphometric analysis may be needed); neuronal death; decreased myelination; and increased numbers of astrocytes, microglia, and other inflammatory cells. Depending on changes observed on HE, special stains and immunohistochemistry may provide further information on the cell types of interest.

Neuroanatomic Localization

Neuroanatomic localization helps to guide sampling of appropriate regions within the central and peripheral nervous system for histological analysis [21]. Neurological examination is more difficult in mice compared with domestic species such as dogs and cats; however, brief examination coupled with evaluation of gait and balance may provide an estimate of where in the CNS a lesion is located.

Specific Signs Related to Neuroanatomic Localization

Prosencephalon

Mice with forebrain disease seldom have specific signs, although seizures or a tendency to walk in very large circles around the perimeter of the cage is consistent with a lesion in this location.

Brainstem Lesions in the brainstem may affect the vestibular nuclei. Mice with vestibular disease often have a head tilt and vestibular ataxia characterized by leaning, tilting, or rolling towards the side of a lesion. The vestibular system is divided into peripheral (inner ear, cranial nerve VIII) and central (brainstem) components, and differentiating between peripheral and central vestibular disease in mice may be challenging. The presence of proprioceptive deficits, pronounced mental dullness, and multiple cranial nerve deficits suggest central vestibular disease. In a mouse with a head tilt and vestibular ataxia, evaluation of both the inner/middle ear and brain should be performed.

Cerebellum Symptoms of cerebellar disease include a tremor, side to side sway, and hypermetria. Mutant mice called "lurchers" or "staggerers" have cerebellar abnormalities (see Table 21.7). Mice with diffuse hypomyelination may also tremor, although this tends to be a generalized rapid tremor.

Spinal Cord Precise neuroanatomic localization of spinal cord lesions is also challenging in mice, given the difficulty performing complete reflex analysis in this species. Upper motor neuron disease can broadly be differentiated from lower motor neuron disease on the basis of limb tone and

Table 21.2 Main cell types of the central nervous system.

Cell type	Histological characteristics (HE)	Key histological features in disease (HE)	Examples of histochemical stains and immunohistochemistry (IHC)
Neuron	Vary in number and appearance by location, but classically large soma with dendrites and central circular to ovoid nucleus and Nissl substance	Reduced numbers of neurons may be a result of hypoplasia; abiotrophy; or neuronal necrosis/ apoptosis and other modalities of cell death or aging (atrophy). Histological changes to neurons: 1) Acute eosinophilic neuron degeneration ("red dead"; acute necrosis) 2) Fading neurons ("ghost cells") 3) Vacuolated neurons (spongiform encephalopathies and storage diseases) 4) Central chromatolysis 5) Accumulated material	*Histochemical*: Nissl; Flouro Jade B or C for neuronal necrosis; Luxol fast blue or PAS may be used to visualize material within vacuolated neurons; Bielschowsky's silver stain for axon integrity; Gallyas staining for neurofibrillary tangles *IHC*: Mature neurons: RNA binding protein fox-1 homolog 3 (RBFOX3, also known as NeuN), Gamma enolase (ENO2, also known as NSE); Microtubule-associated protein 2 (MAP2); ubiquitin carboxyl-terminal hydrolase isozyme L1 (UCHL1, also known as PGP9.5) Neuronal precursor cells: Neuronal migration protein doublecortin (DCX); Nestin (NES) in neural stem cells Functional markers: Dopaminergic – Tyrosine 3-monoxygenase (TH, also known as tyrosine hydroxylase); Glutamatergic – Vesicular glutamate transporter 2 (VGLUT2, also known as SLC17A6); GABAergic – Parvalbumin (PVALB), Glutamine decarboxylase (GAD1, also known as GAD67) Synapses: Synaptophysin Additional markers: Calretinin; Calbindin
Astrocytes	Nonreactive astrocytes appear on HE as "naked nuclei" with little cytoplasm (long cytoplasmic extensions are not visible on HE)	Gemistocytic when activated (hypertrophic and eosinophilic); Type II astrocytes are the hallmark of hepatic encephalopathy; fibrous (in white matter), protoplasmic (in gray matter), and radial (Bergmann in the cerebellum and Muller in the retina)	*IHC*: Glial fibrillary acidic protein (GFAP); Glutamine synthetase (GLUL, also known as GS); protein S100-B (S100B); 10-formyltetrahydrofolate dehydrogenase (10-FTHFDH, also known as ALDH1L1)
Oligodendrocytes	Small round nuclei, condensed chromatin, halo artifact, arranged in rows	In gray matter often found adjacent to neuron cell bodies; satellitosis with neuronal injury consists of clusters of glial cells around a degenerating neuron	*IHC*: Precursors: PDGFRA; CSPG4 (also known as NG2) Mature: Myelin basic protein (MBP); myelin-oligodendrocyte glycoprotein (MOG); Carbonic anhydrase II (CA2); 2',3'-cyclic-nucleotide 3'-phosphodiesterase (CNPase)
Microglia	Small; cigar shaped nuclei; elongate, spindle cell appearance	With activation, ramified processes are initially only observed on IHC, although chronically may develop increased cytoplasm ("Gitter cells"); ramified and ameboid microglia	*IHC*: Allograft inflammatory factor 1 (AIF1, also known as Iba1); integrin alpha-M (ITGAM, also known as CD11b); Receptor-type tyrosine-protein phosphatase C (also known as CD45); Adhesion G protein-coupled receptor E1 (ADGRE1, also known as F4/80); Transmembrane protein 119 (TMEM119)
White matter Myelinated axons		Dystrophic axons are hypereosinophilic and swollen ("spheroids") in secondary demyelination; myelin ovoids may be present; remyelination occurs in the peripheral nervous system	*Histochemical*: Luxol Fast Blue, Bielschowsky and Bodian stain (to visualize axons) *IHC*: MBP; MOG; Myelin proteolipid protein (PLP1); S100B (Schwann cells [peripheral nervous system])

reflexes. Increased tone and spasticity of the limbs and tail suggests an upper motor neuron lesion (either cranial to the cervical intumescence if all four limbs are involved or cranial to the lumbar intumescence if only the pelvic limbs are affected). In contrast, flaccid limbs and tail are characteristics of lower motor neuron disease (involving the intumescence or peripheral nerve[s]).

A nonspecific sign of neurological disease in mice is to clasp the hind limbs in to the body when picked up by the tail [21, 24].

Necropsy Protocols

The CNS is exquisitely sensitive to artifact during removal, fixation, and processing. Autolysis occurs rapidly after death, so mice should be euthanized immediately prior to necropsy. Euthanasia by cervical dislocation should be avoided as this disrupts anatomy of the skull and spinal cord [21]. For initial screening and phenotyping, the brain may be left *in situ* within the calvarium and coronal sections obtained following decalcification, which allows for the identification of large or pronounced lesions. For evaluation of CNS phenotypes, however, removal of the brain from the skull prior to processing is generally recommended. If samples of fresh brain are required for molecular testing in addition to histology, then the brain may be removed, and portions intended for histology may be immersion fixed in the fixative of choice. Common fixatives for nervous tissue include 10% neutral buffered formalin (NBF), 1–4% paraformaldehyde (PFA), 2.5–5% glutaraldehyde, and glutaraldehyde and paraformaldehyde combinations [25]. Bouin's solution also provides high quality fixation. Acid–alcohol based fixatives, such as Fekete's solution, can produce many artifacts and should be avoided (Sundberg and Ward, unpublished data) (Figure 21.5). The fixative choice should be based on the desired outcome and when transmission electron microscopy is necessary, glutaraldehyde should be utilized. The whole brain may also be removed from the calvarium and immersion fixed in formalin. However, for optimal central nervous histology, designation of specific animals for histology and intravascular perfusion with fixative (which can be preceded by phosphate buffered saline perfusion) is recommended to minimize artifact. In general, for routine light microscopy assessment of brain and spinal cord, the use of either 4% PFA or 10% NBF for perfusion provides excellent morphology [26]. Following perfusion, brains may be removed from the skull or may be left *in situ* in the skull and post fixed for 24–72 hours, after which the brain can be removed to further reduce artifact. Leaving the brain in the skull for at least 48 hours has been described to best reduce the incidence of tissue artifact, especially dark neuron artifact (DNA). Protocols for terminal intracardial perfusion using either a gravity fed system or pump have been previously described [27, 28]. During perfusion, care should be taken to avoid increased intravascular perfusion pressures as this may also create artifact (Figure 21.6).

Typically, sagittal or coronal (cross sectional) sections of brain are obtained. Sagittal sections may be useful to visualize the entire brain in a single section (Figure 21.7), and are particularly useful for cerebellum [29]. Coronal sections provide more information on specific neuroanatomic regions

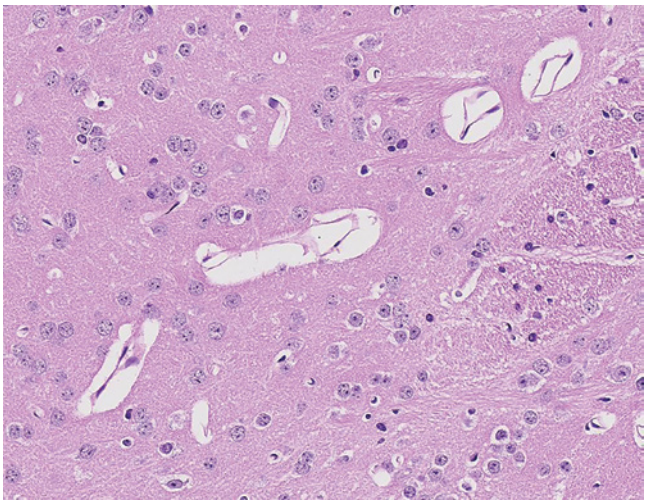


Figure 21.6 Artifactual spaces surrounding the vessels following intravascular perfusion using excessive perfusion pressure. HE.

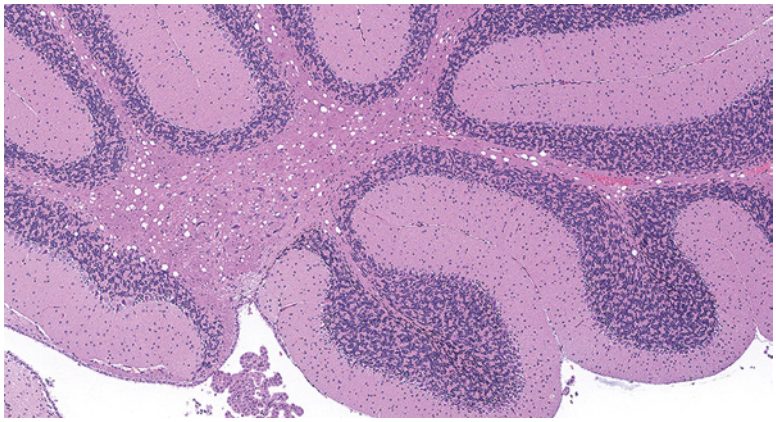


Figure 21.5 Artifactual vacuolation of the white matter of the cerebellum following storage of the brain in alcohol based fixative. Hematoxylin and eosin (HE).

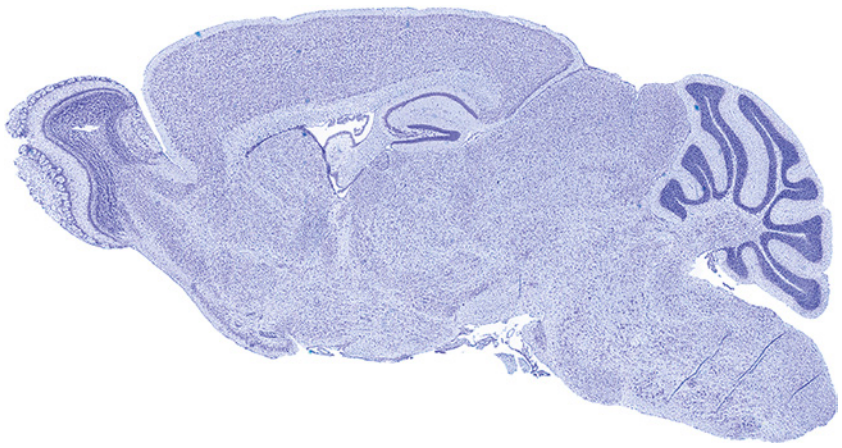


Figure 21.7 Parasagittal (lateral of midline) section of brain. Nissl stain. Source: Reproduced from Comparative Anatomy and Histology – A Mouse, Rat, and Human Atlas, with permission of Elsevier.

and asymmetric lesions (Figures 21.3, and 21.4). Guidelines for trimming brain have been previously reported [26, 30]. For experimental studies, consistent sections must be obtained, which may be facilitated by the use of brain molds, rodent brain matrices; [15, 30, 31] as long as brain sizes are consistent between experimental groups. Sagittal and coronal sections can be also combined [32, 33].

For evaluation of the spinal cord, sagittal sections through the cervical, thoracic, and lumbar spine when left *in situ* will show the spinal cord in relation to the vertebral bodies (Figure 21.8). This technique is efficient and especially useful for the evaluation of focal or multifocal lesions in the spinal cord for which the precise location is unknown. If a lesion is widespread throughout the spinal cord, or if evaluation of specific locations throughout the spinal cord is performed, then cross sectional images provide more information regarding white and gray matter involvement or diseases affecting the lateral spinal cord or nerve roots (Figures 21.9, and 21.10). Following euthanasia, the spinal cord can be removed from the vertebral column [26].

Histological Artifacts

Artifacts are common in the CNS, may be subject to misinterpretation, and include the DNA, which may mimic neuronal necrosis [15]. This change is characterized by spiky, shrunken, basophilic neurons [19]. Dark neurons are most commonly observed in regions of brain that have been manipulated with instruments during removal, in hippocampus, and involving the Purkinje cells of the cerebellum [21] (Figures 21.11, and 21.12). These neurons may label non-specifically with immunohistochemical antibodies. By contrast, necrotic neurons are slightly shrunken to angular with hypereosinophilic cytoplasm and may be surrounded by activated glial cells (Figure 21.13). Artifactual neuronal vacuolation may also occur.

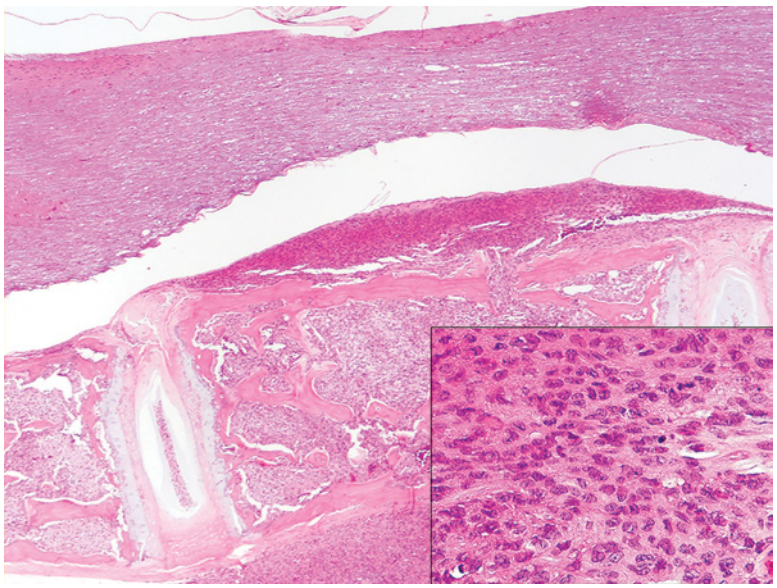


Figure 21.8 Sagittal section of spine, showing the orientation of the spinal cord in relation to the vertebral bodies and intervertebral disks. A large amount of artifactual space is present between the spinal cord and vertebral canal due to shrinkage and decalcified preparation. A hematopoietic neoplasm (histiocytic sarcoma suspected based on cellular morphology and other organs affected) is present in the vertebral canal. Inset shows higher magnification of the neoplastic cells. HE.

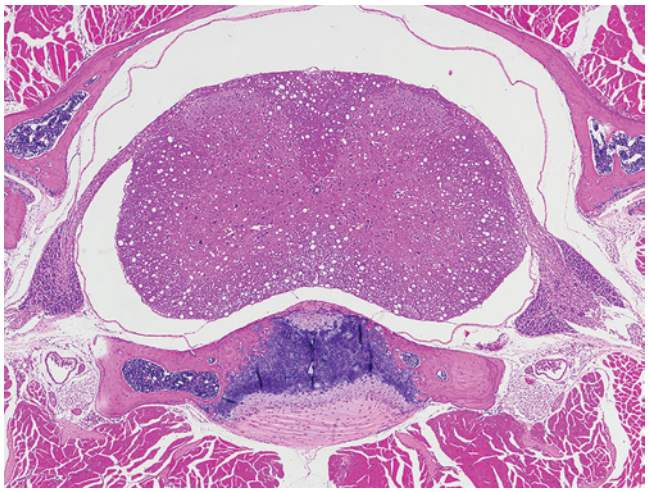


Figure 21.9 Cross section of the spinal cord *in situ* with nerves and ganglia included. This spinal cord was stored in alcohol, which creates artifactual vacuolation in the gray and white matter. HE.

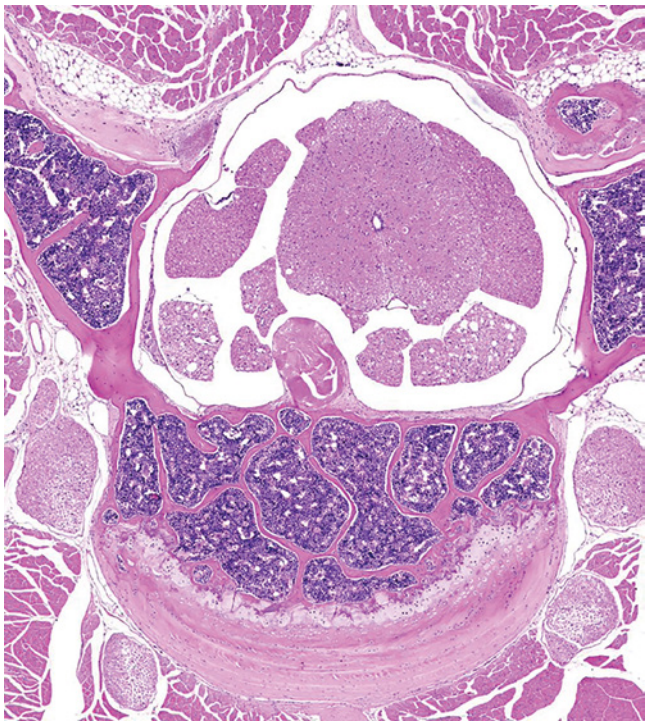


Figure 21.10 Cross section of spinal cord *in situ* in an aged C57BL/6 mouse with intervertebral disk protrusion at the level of the caudal spinal cord (cauda equina). HE.

Artifactual white matter vacuolation may be seen as randomly distributed holes in densely myelinated areas including corpus callosum, internal capsule, and cerebellar white matter [19]. These holes may be empty or contain pale blue material, and this change can be worsened by storage of fixed tissues in ethanol [19, 21] (Figure 21.5). Other artifacts seen in immersion fixed brain samples include clear halos surrounding oligodendrocytes (Figure 21.14), perivascular

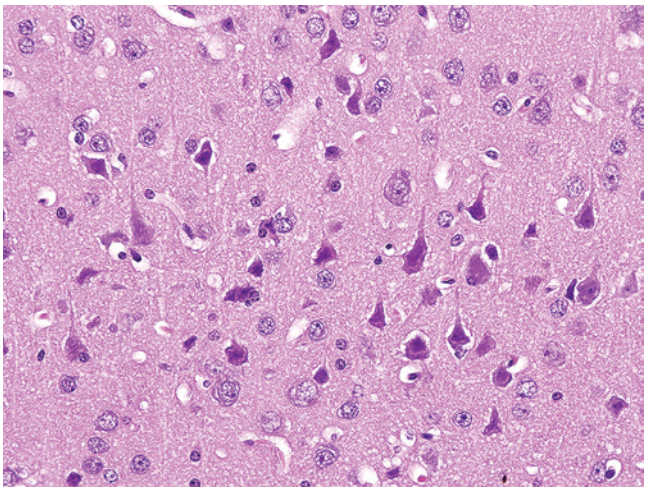


Figure 21.11 Dark neuron artifact in mouse cerebrum. HE.

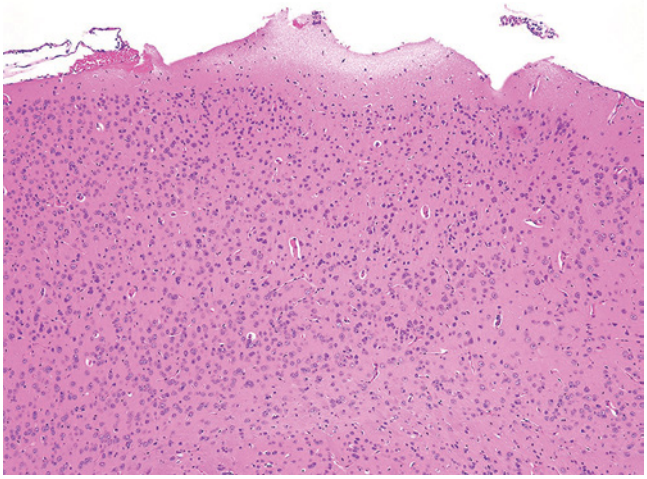


Figure 21.12 Touch artifact at the surface of the mouse cerebrum due to handling during removal of the brain. Dark neuron artifact is also present. HE.

cleft formation (Figure 21.15), and retraction spaces, the latter of which are particularly prominent in the regions of the Purkinje layer of the cerebellum and dentate gyrus of the hippocampus [34] (Figure 21.16). Figures 21.11–21.16 show common artifacts of the CNS.

Aging/Spontaneous Strain Specific Lesions

Spontaneous strain-specific lesions of the CNS occur (Table 21.3, Figures 21.17–21.19) [15]). Notably, several strains have an increased incidence of absent or incomplete corpus callosum [Table 21.3; [35, 49–51]]. FVB/NJ, C3H/HeJ, CBA/J, and other mice have a homozygous mutation of *Pde6b* (*Pde6b*^{rd1}), which leads to retinal degeneration and blindness by sexual maturity. Retinal degeneration associated with the *Crb1*^{rd8} mutation is also a feature in C57BL/6NJ but not C57BL/6J mice [42, 52–54]. FVB/NJ, SJL/J, SWR/J,

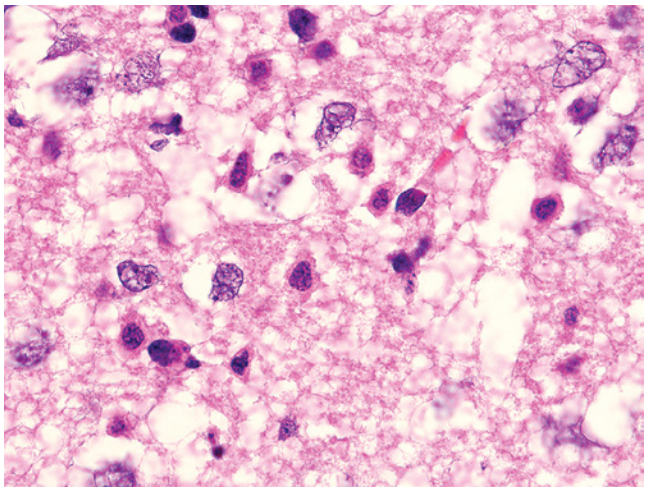


Figure 21.13 Hypereosinophilic, dead neurons in the cerebrum of an FVB mouse following seizure activity. HE.

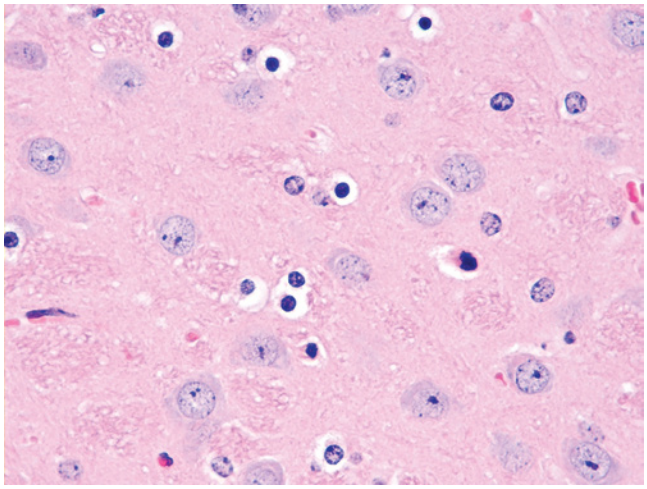


Figure 21.14 Artifactual clear space (halos) surrounding oligodendrocytes in an immersion fixed brain. HE.

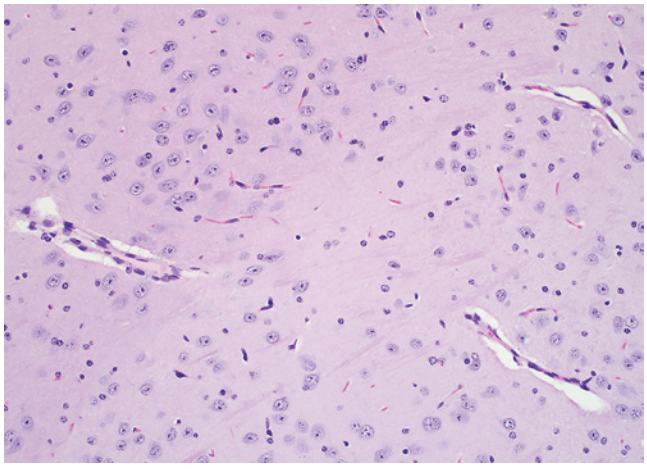


Figure 21.15 Artifactual clear space (perivascular clefts) surrounding blood vessels in an immersion fixed brain. HE.

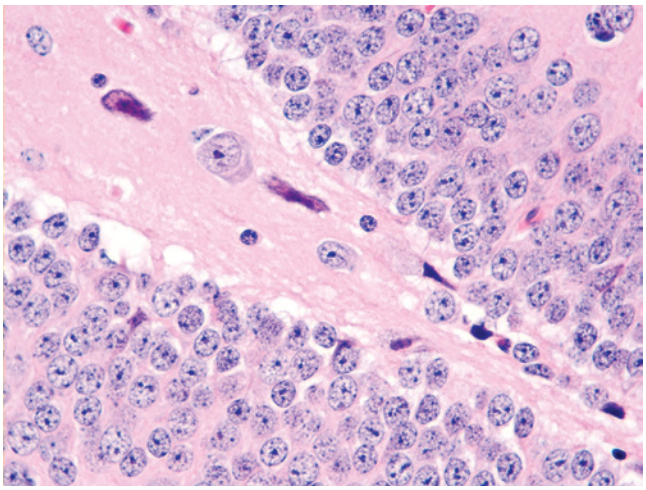


Figure 21.16 Artifactual clear space and separation of the dentate gyrus of the hippocampus in an immersion fixed brain. HE.

and most of the 129 mouse substrains also have deletion mutation of *Disc1*, which has been implicated in learning [55–57]. C57BL/6J mice have age-related hearing loss due to a *Cdh23* mutation, which affects cochlear hair cells [46, 47]. Malformation of the posterior cerebellar vermis with heterotopia of granule cells in the molecular layer is also reported in genetically engineered mice on this background strain [58, 59]. Many strains have early onset or age-related hearing loss [48] (Table 21.3).

Some mouse strains such as DBA/2J have a predisposition to audiogenic seizures (Table 12.10) [60–64].

Vasculature may vary by strain, and this and other factors may contribute to differences in susceptibility between strains to experimental insults such as carotid or middle cerebral artery occlusion and hypoxic–ischemic brain injury [65–67]. While some studies have not demonstrated obvious differences in gross anatomy [65], others have shown a higher incidence of hypoplastic or absent caudal communicating artery in C57BL/6J and other C57BL/6 substrains and BALB/cAnNCrl mice compared with 129X1/SvJ mice [67–69]. Rates of congenital hydrocephalus also differ by strain [36].

There is strain specific susceptibility to many CNS infections, including *Listeria monocytogenes*, *Toxoplasma gondii*, Scrapie, and several viral infections [70–75]. Strain-related outcomes following infection may be related to differential immune responses [76]. Immunodeficient mice are more susceptible to systemic bacterial infections, which may affect the CNS (Figure 21.20).

Several aging lesions of the CNS also occur and may vary in frequency by strain (Table 21.4, Figures 21.21, and 21.22). Spontaneous primary brain tumors are uncommon in mice, but pituitary tumors occur as an age-related lesion in mice (particularly in females) and may represent a cause of death [86–88]. Hematopoietic neoplasms such as lymphoma and histiocytic sarcoma, which commonly occur in older mice of many strains, may also occasionally involve

Table 21.3 Examples of spontaneous strain-specific lesions in the mouse.

Strain specific lesions	Notes/genetics
Absent/incomplete corpus callosum	Occasional in BALB/cByJ and other BALB/c substrains; common in 129S1/SvImJ (6/20 mice); corpus callosum absent in most I/LnJ and BTBR T^{+} *Itpr3*^{tf}/J mice [35]
Hydrocephalus	C57BL strains; reference provides information in relative ventricle size in several strains [36]
Pigmentation of meninges	All C57BL/6 substrains as well as other pigmented strains; typically frontal lobes and olfactory bulbs [37]
Meningeal hamartomas	Lipomatous hamartomas described in C57BL/6J and C3H/HeJ mice [19, 38]
Audiogenic seizures	DBA/2J; see Table 20.10 (Epilepsy models)
Squamous cysts (dermoid/epidermoid cysts)	C57BL/6J, C57BR/cdJ, SJL/OlaHsd; occur on midline in brain and in spinal canal [19, 39–41]
Retinal degeneration	*Pde6b*^{rd1}: FVB/NJ, C3H/HeJ, CBA/J, SJL/J, others; blindness by 1 month of age; *Crb1*^{rd8}: C57BL/6N; slower onset of blindness [42] See also https://www.jax.org/research-and-faculty/resources/eye-mutant-resource/retinal-degeneration-genes
Neurodegenerative disease (space cadet syndrome)	Syndrome of behavioral changes and gliosis in the cerebrum of aged FVB/NTac and FVB/NCr mice [43–45]
Hearing loss	*Cdh23*^{ahl} (age-related hearing loss) present in over 20 strains including C57BL/6J, BALB/cByJ, and DBA/2J [46, 47]; significantly increased ABR thresholds before three months of age in several strains [48]

the CNS (Figures 21.9, and 21.23). Ependymomas have been reported to affect 7% of male 129S6/SvEvTac mice at end of life [77]. Common incidental aging lesions in the brain of many strains of mice include mineralization in the thalamus and, to a lesser degree, brainstem [32, 77, 78]. Incidental aging lesions in the brain include intracytoplasmic inclusion bodies in neurons of the thalamus (Figure 21.21); progressive neuroinflammation characterized by microgliosis and astrogliosis (Figure 21.24); periodic acid–Schiff–positive granular deposits in the neuropil of the hippocampus; and neuroaxonal dystrophy in the medulla oblongata [32] (Figure 21.22). Intervertebral disk degeneration and less often herniation occur in the vertebral column of old mice and are common by 20 months of age, although there may not be clinically apparent neurological signs (Figure 21.10).

Genetically Engineered Mice (GEM) Disease Models: Degenerative

Based on the increasing frequency of neurodegenerative diseases in the human population, these diseases comprise the vast majority of mouse models of neurological disease in terms of funding and publications in recent years. Mouse models are valuable to study disease pathogenesis and in preclinical testing. However, when considering neurodegenerative diseases such as Alzheimer's disease, Parkinson's disease, and amyotrophic lateral sclerosis, it is important to realize that most cases in patients represent sporadic disease with a complex multifactorial pathogenesis. By contrast, most mouse models are the result of manipulation of one or more specific genes implicated in familial forms of the diseases. This, combined with inherent differences in neuroanatomy, lifespan, and physiology, impairs the ability of mice models to completely and faithfully recapitulate the full spectrum of pathologic and behavioral abnormalities observed in human patients with many neurodegenerative diseases. In some cases, genetically engineered mice are combined with pharmacologic or other interventions, such as inoculation of abnormal or misfolded proteins into the brain. Additionally, for degenerative CNS disease models in particular, behavioral testing is a common end point read out. Behavioral tests frequently used to measure cognitive decline include the Morris water maze, radial arm water maze, Barnes maze, novel object recognition, passive avoidance, fear conditioning, and others [98, 99]. It is important to realize that strain related visual deficits unrelated to cognitive defects may affect performance on these tests. Behavioral testing provides useful data, which can be interpreted with pathological and biochemical changes; however, behavior testing in mice may be challenging to translate to measurement of cognitive decline in human patients. To test changes in mobility and strength in mouse models of PD and ALS, tests such as the open field test, stepping test, pole test, grip test, grip coordination test, and rotarod are used [100]. There are numerous publications of mouse models and the use of mice for studying human neurological diseases with references found in Pubmed by keywords for mouse and Alzheimer's (14 533); Parkinson's (4858); and brain trauma (3084). We can only review select models.



Figure 21.17 Histologic appearance of the normal corpus callosum in a BALB/c mouse. HE.

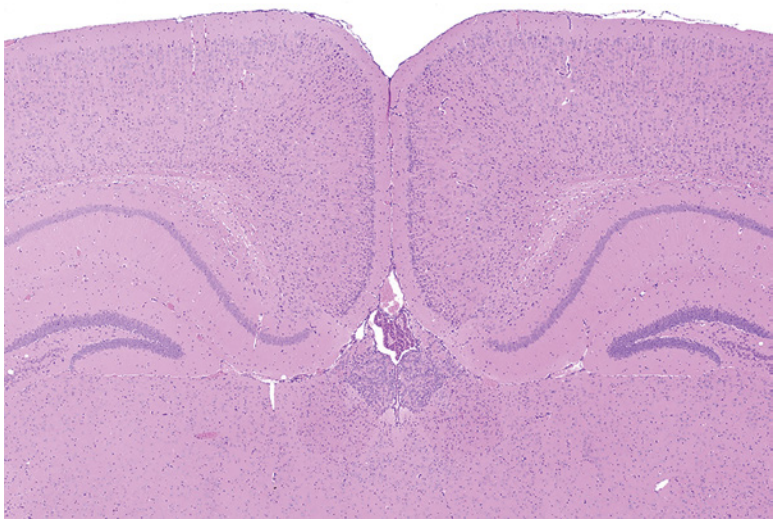


Figure 21.18 Histologic appearance of an incomplete corpus callosum in a BALB/c mouse. HE.

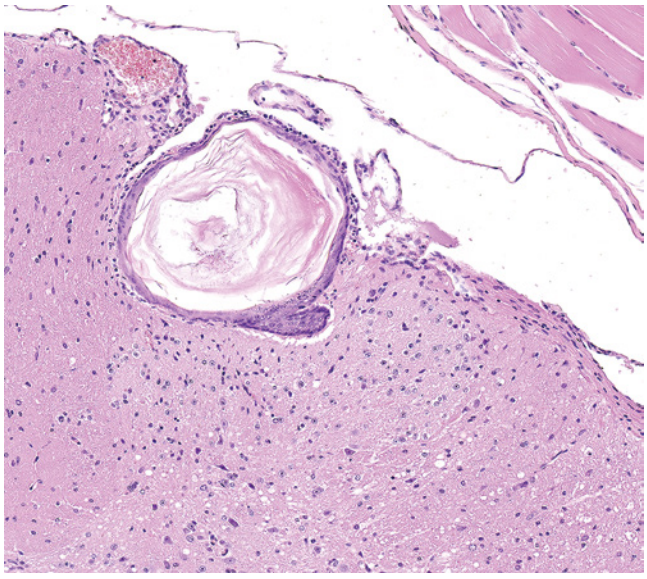


Figure 21.19 Dermoid cyst in the spinal cord of a B6SJL-*Tg(SOD1*G93A)1Gur*/J as an incidental finding. HE.

Alzheimer's Disease (AD)

An in-depth discussion of Alzheimer's neuropathology and mouse models is beyond the scope of this text. Numerous publications are devoted to this topic, including several reviews [98, 101]. Approximately 170 transgenic rodent models of AD have been described; the mouse models most commonly used in Alzheimer's research are presented (Table 21.5). Mouse models are generated to recapitulate one or more of the pathological hallmarks of AD in patients, including senile plaques, neurofibrillary tangles, and neurodegeneration in the cortex and hippocampus [101, 102] (Figures 21.25–21.28). Plaques are composed of amyloid beta (Aβ) aggregates of 40 or 42 amino acids formed by cleavage of the amyloid precursor protein (APP), and neurofibrillary tangles are composed of hyperphosphorylated, misfolded tau proteins [101, 102]. Few mouse models recapitulate all of these neuropathological findings, and the age at which mouse models develop lesions also varies by model [101]. Neuropathology and cognitive decline of the most

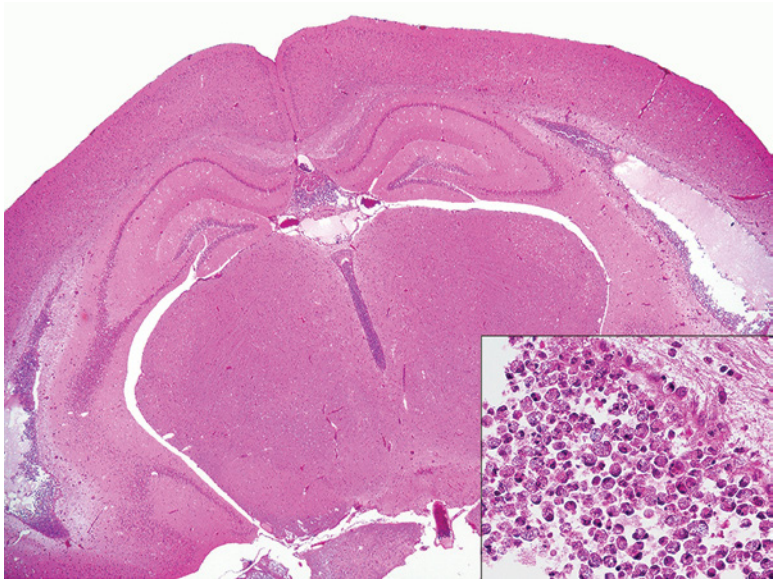


Figure 21.20 Encephalitis and abscesses in an immunosuppressed *Myd88tm1Aki* mouse. Inset shows higher magnification of inflammatory cells with intracellular bacteria. HE.

commonly used mouse models of AD is summarized [103]. Most cases of AD are sporadic and late onset (late onset Alzheimer's disease [LOAD]); rarely, early-onset genetic AD occurs. Genetic risk factors in familial AD include mutations of *APP*, presenilin 1 (*PSEN1*) and 2 (*PSEN2*) [102]. Other implicated genes in human patients include microtubule associated protein tau (*MAPT*); the allele E4 of apolipoprotein E (*APOE*); triggering receptor expressed on myeloid cells 2 (*TREM2*); and beta-site APP cleaving enzyme (beta secretase) 1 (*BACE1*) [98]. The *APOE4* allele and mutations

Table 21.4 Examples of age-related lesions in the mouse.

Age related lesions	Affected strains	References
Thalamic (globoid) mineralization, brainstem mineralization	B6C3F1; C57BL/6J; 9–11% 129S6/SvEvTac	[32, 77, 78]
Intracytoplasmic inclusion bodies (Hirano-like), neurons of thalamus	C57BL/6J; B6C3F1; SAMP8/TaHSD	[32, 79, 80]
White matter gliosis	Cerebrum of aged female mice; CBA/HT6J, C57BL/6J, B6CBAT6F1J, and B6C3F1	[19, 81]
Senile neuroaxonal dystrophy – spinal cord and brainstem	C57BL/6 J; SAMP8/TaHSD; B6C3F1	[32, 80, 82–84]
Intracytoplasmic pigment (lipofuscin), neurons	C57BL/6J; SAMP8/TaHSD; B6C3F1	[19, 80, 85]
Pituitary tumor	C57BL/6J; C57BL/6NHsd	[86–89]
Intervertebral disk degeneration/herniation	Progressive degeneration beginning at 14 months of age and progressing to 80% of mice with chondrification of disk and single or multiple disk herniation >2 years of age [90]; >20% of 129S6/SvEvTac mice have disk degeneration and 7% of males have herniation at end of life [77]	Progeroid and some genetically engineered mice show premature intervertebral disk degeneration [91–93]
PAS-positive granular deposits (mainly hippocampus)	Several C57BL/6J, C57BL/6NCrl, AKR/J, SAMP8-TaHsd, and SJL/J	[94–96]
Chronic arteritis, meninges (as part of polyarteritis)	Mouse lines predisposed to lupus-like conditions	[97]

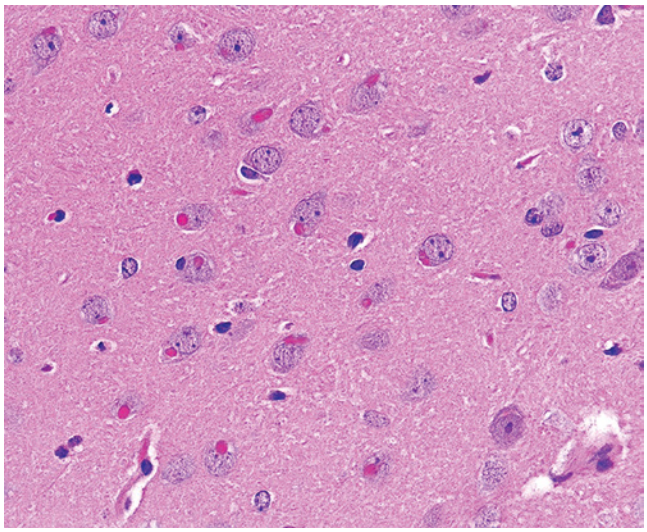


Figure 21.21 Eosinophilic intracytoplasmic neuronal inclusions in the thalamus of an aged C57BL/6J mouse. HE.

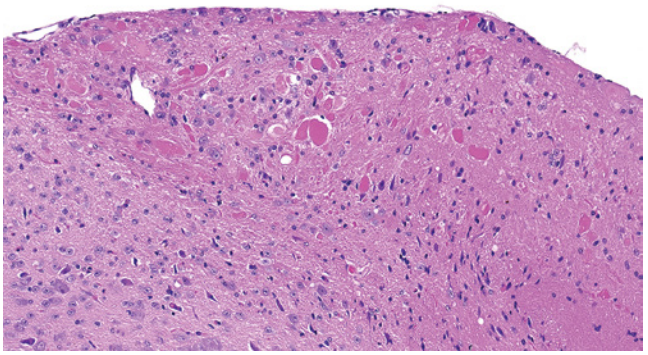


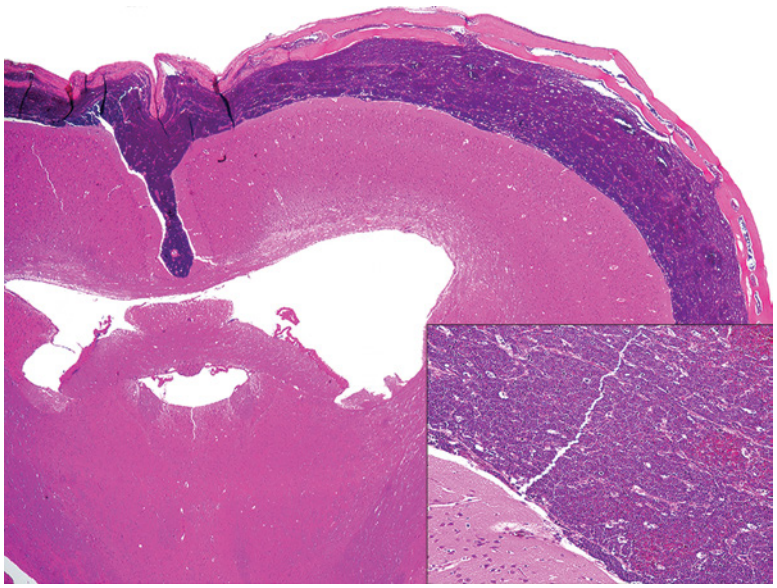
Figure 21.22 Neuroaxonal dystrophy in the medulla oblongata (gracilis nucleus) of an aged C57BL/6J mouse. HE.

in *TREM2* predispose humans to develop LOAD (A Table of APOE and TREM models, including availability and references, is present in reference [101]). Genetically engineered mouse models involve manipulation and expression of these wild type or mutant human or analogous mouse genes.

Amyloid Plaques/Models of Amyloid Pathology

APP is cleaved by the β-APP cleaving enzyme (BACE1) at the N-terminus and by γ-secretase at the C-terminus to form Aβ [101]. Many *APP* mouse models overexpress various forms of mutated human *APP* to either increase total Aβ or increase the amount of certain forms of Aβ produced, and this can be accelerated in combination with *PSEN1* and *PSEN2* mutations by increasing the proportion of Aβ42, which is more prone to aggregation and pathogenic [101, 102] (Figures 21.25–21.27). The Swedish mutation involves a two amino acid substitution adjacent to the β secretase cleavage site, increasing APP processing through the β secretase pathway and total Aβ produced [101]. By contrast, mutations such as the Indiana mutation at the γ secretase cleavage site increase the ratio of Aβ42 to Aβ40. Histologically, mouse models with *APP* mutations tend to have diffuse and fibrillary Aβ deposits best visualized using Aβ immunohistochemistry or Congo red or thioflavin-S staining [101] (Figures 21.26, and Figure 21.27). Plaques may be associated with gliosis and swollen axons [101] (Figure 21.27). By contrast with AD patients, mouse APP models generally do not have neurofibrillary tangles from misfolded tau proteins, nor do they demonstrate substantial neurodegeneration [102]. While these mice generally do have some degree of cognitive decline, they may not display progressive behavioral abnormalities that correlate with Aβ accumulation [102], and performance varies depending on cognitive test used [101].

Figure 21.23 Neoplastic lymphocytes (lymphoma) expanding the meninges of an Crl:CD1 (ICR) mouse. This mouse had lymphoma effacing many internal organs. HE.



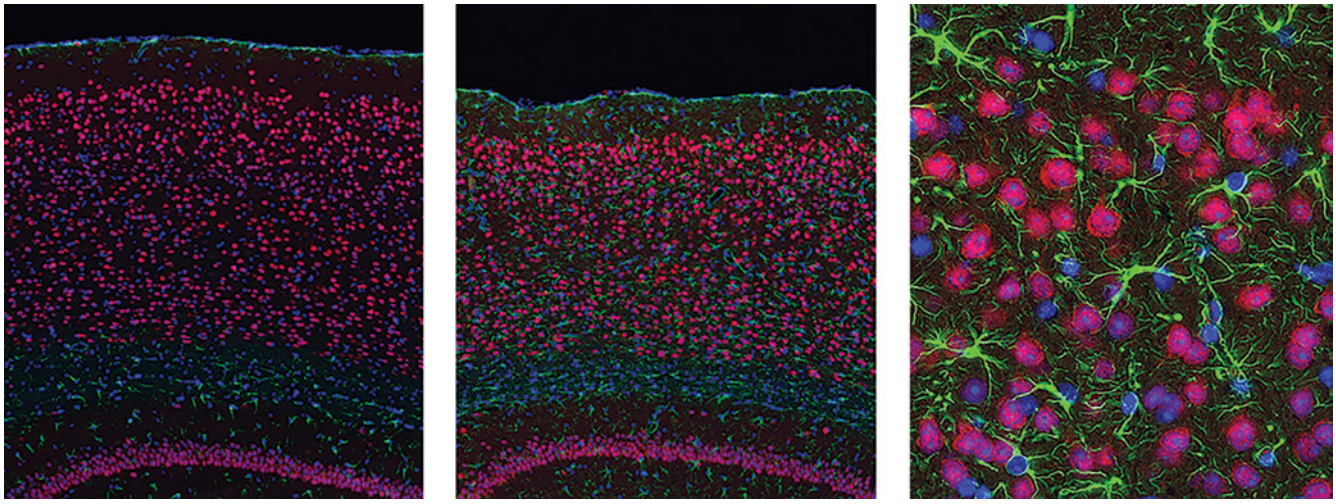


Figure 21.24 **Neuronal loss with astrogliosis in a mouse with a conditional null mutation in the *Aph1* gene in the excitatory neurons of the forebrain (center) compared with a control mouse (left)**. In the affected mouse, there is cortical collapse with neuronal loss and accompanying astrogliosis (higher magnification, right). Neurons labeled in pink (NeuN), astrocytes labeled in green (GFAP), and nuclei labeled in blue (DAPI). NeuN mouse monoclonal antibody, EMD Millipore, MAB377; GFAP rabbit polyclonal antibody, Agilent/DAKO, Z0334.

Table 21.5 Quick guide to the pros and cons of commonly used AD mouse models.

Model	Main features	Pros	Cons
Tg2576	Mid-life amyloid pathology (10–14 mo)	Well-characterized, maintains aging feature of AD	High lethality on C57 background, Tg male aggressive and needs to be single-housed
APP/PS1	Early-onset (~6 mo) amyloid pathology	Well-characterized, co-integrated transgenes breed as a single allele	Like other co-integrated models, cannot control for independent transgene effects
5XFAD	Juvenile-onset amyloid pathology (~3 mo)	Rapid onset phenotype, co-integrated transgenes breed as a single allele	Non-physiological combination of FAD mutations, marked intracellular Aβ accumulation
3xTg-AD	Early- to mid-life amyloid pathology plus hyperphosphorylated tau	Captures both Aβ and phospho-tau features of AD	Variable pathology between colonies and sexes, genetic drift has been observed
rTg4510	Early-onset neurofibrillary tangles (~5–6 mo), severe neurodegeneration	Temporally controllable, rapid onset phenotype, develops true NFT pathology, well-characterized	Breeding complicated by need for two independent transgenes, 13-fold overexpression of tau protein
PS19	Mid-life neurofibrillary tangles (6–9 mo), marked neurodegeneration	Single-transgenic model, mid-life on set allows use in experiments expected to either delay or exacerbate pathology	Transgene expression in spinal cord causes paralysis by mid-life
APP^{NLF}	Mid-life amyloid pathology (~12 mo for homozygote, but note >24 mo for heterozygote allele)	Endogenous APP level, native human Aβ sequence	Limited cognitive impairment, requires homozygous allele for mid-life onset
APP^{NLGF}	Juvenile-onset amyloid pathology (~3–4 mo for homozygote, ~9 mo for heterozygote)	Endogenous APP level, can be used as heterozygote	Non-native Aβ sequence, mild cognitive phenotype
hTau	Mid-life hyperphosphorylated tau (~6 mo)	Near-endogenous level expression of all six human wild-type tau isoforms	Complicated breeding of transgene on null background, mild phenotype variable between colonies
APOE2, E3, E4 Targeted replacement	Allele-specific effects on Aβ, tau, brain atrophy, and neuroinflammation; both central and peripheral functions influenced by allele	Widely-studied, expressed at endogenous levels, mouse ApoE deleted	Cannot distinguish central vs. peripheral effects; available through Taconic but with restrictions on usage

Source: Reproduced from Jankowsky and Zheng [101] under permission of the Creative Commons Attributions 4.0 International License [http://creativecommons.org/license/by/4.0/]. Table has been modified slightly from the original by removing column "Examples of use in AD research" with references from original text.

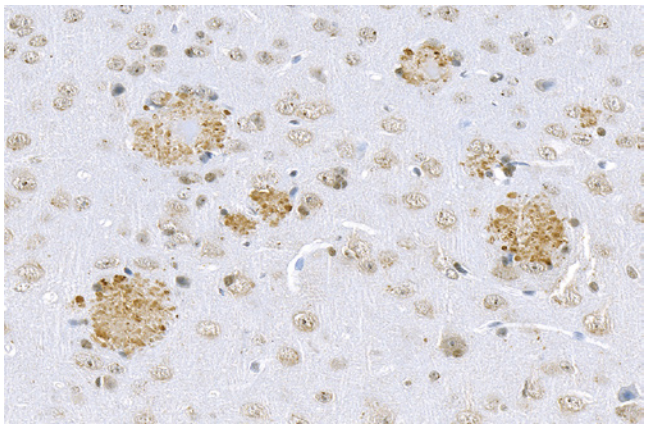


Figure 21.25 Ubiquitin positive plaques in the cortex of a seven-month-old female B6.Cg-Tg*(Thy1-APPSw,Thy1-PSEN1*L166P)21Jckr*. Ubiquitin positive plaques labeled brown; hematoxylin counterstain. Ubiquitin mouse monoclonal antibody Cell Signaling Technology, Catalog# 3936.

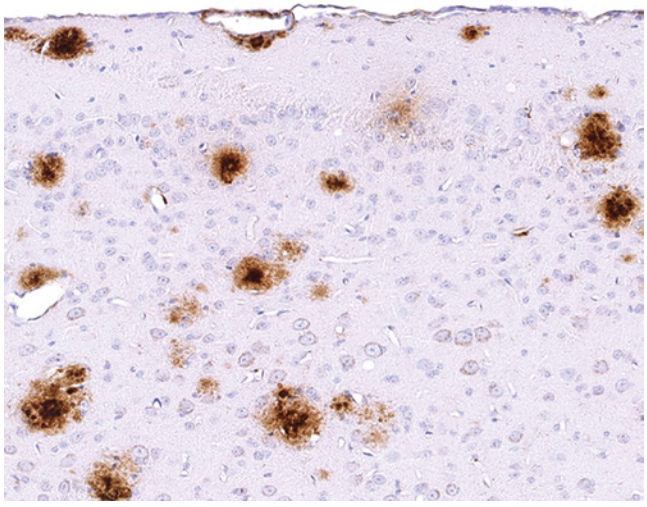


Figure 21.26 Amyloid beta positive plaques in the cortex of a seven-month-old female B6.Cg-Tg*(Thy1-APPSw,Thy1-PSEN1*L166P)21Jckr*. Amyloid beta positive plaques labeled brown; hematoxylin counterstain. Amyloid beta mouse monoclonal Clone 6E10 (Covance SIG-39320).

Neurofibrillary Tangles and Neurodegeneration/ Models of Tau Pathology

Tau is an axonal protein that normally stabilizes microtubules. In an abnormal state, tau becomes hyper-phosphorylated, dissociating from microtubules and redistributing to neuronal soma and apical dendrites to form neurofibrillary tangles [101]. In humans, three-repeat and four-repeat isoforms of tau are formed by splicing of *MAPT*; in adult mice, only the four-repeat form is expressed [101]. Mouse models of tau abnormalities largely result from mutations which cause overexpression of mutated human 4R tau. The most common models are based on P301L or P301S *MAPT* mutations [101, 102] (Figure 21.28). A humanized tau model has also been created [104], which preserves the human 3R/4R tau ratio, although the phenotype is mild. Because other neurodegenerative conditions in addition to AD are associated with tau inclusions, and because mutations in *MAPT* in

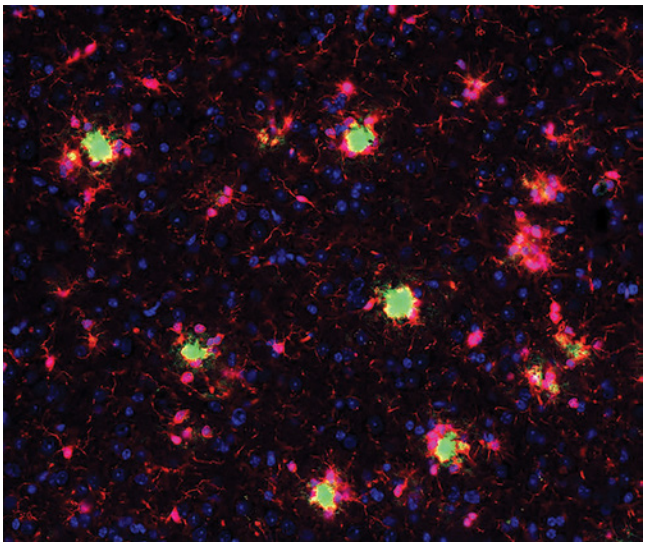


Figure 21.27 Amyloid plaques and microgliosis in the cortex of a six-month-old B6.Cg-Tg*(Thy1-APPSw,Thy1-PSEN1*L166P)21Jckr*. Microglia are labeled pink (Iba1), plaques are labeled green (Thioflavin S), and nuclei are labeled blue (DAPI). Iba1 rabbit polyclonal antibody WAKO, 019-19741.

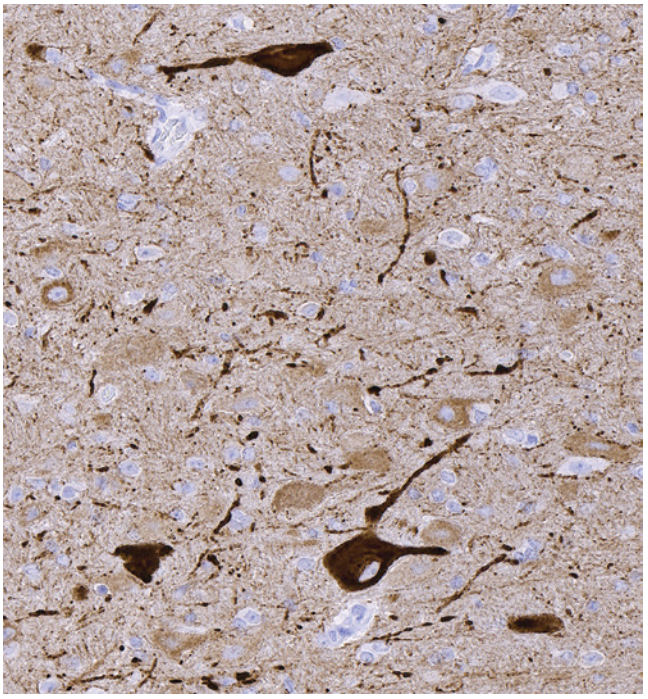


Figure 21.28 Tauopathy and neurofibrillary tangles in the medulla oblongata of a four-month-old B6;C3-Tg*(Prnp-MAPT*P301S)PS19Vle/J*. Tau positive structures labeled brown; hematoxylin counterstain. Phospho-Tau rabbit monoclonal antibody, CST, #12885.

human patients cause a subtype of frontotemporal lobar degeneration (FTLD) rather than AD [101], there is concern that mouse models based on *MAPT* mutations do not accurately model the neurofibrillary tangles observed in AD and instead represent models of FLTD [102].

Histologically, mouse models of mutant tau show neurofibrillary tangle formation and neurodegeneration. STOCK Tg(Camk2a-tTA)1Mmay *Fgf14*$^{Tg(tetO\text{-}MAPT*P301L)4510Kha}$ (synonym rTg4510) mice develop mature neurofibrillary tangles in the cortex and hippocampus, significant forebrain atrophy, and >50% loss of CA1 neurons by 6 months of age [101, 105, 106]. Tau lesions, forebrain atrophy, and neuronal loss also occur in B6;C3-Tg*(Prnp-MAPT*P301S)PS19Vle* (synonym PS19) mice, although at a later age, and these mice develop hind limb dysfunction at approximately 10 months as a result of transgene expression in spinal cord [101, 107] (Figure 21.28). Mice with multiple mutations (for example, mutations in *APP* and mutations in *PS1* such as the B6.SJL-Tg*(APPSwFlLon,PSEN1*M146L*L286V)6799Vas* (synonym 5XFAD) also show neuronal loss [108].

Mouse Factors

Background strain, animal source, and sex may affect disease phenotypes, and female mice have an earlier onset of lesions in several models [43, 101, 109].

Online Resources

Several commercial repositories for Alzheimer's models exist, including The Jackson Laboratory's Alzheimer's Mouse Model Resource https://www.jax.org/research-and-faculty/research-centers/alzheimers-disease-center/alzheimers-mouse-model-repository or Taconic Bioscience's Neuroscience Portfolio at https://taconic.com/find-your-model/neuroscience-portfolio/alzheimers-disease-models.

A list of 179 mouse models of AD is available at https://www.alzforum.org/research-models, with information on the presence and time course of several phenotypes in the various models including: plaques; tangles; neuronal loss; gliosis; synaptic loss; changes in LTP/LTD; and cognitive impairment. This website also has links to relevant publications.

Parkinson's Disease (PD)

Parkinson's disease is a neurodegenerative disorder associated with tremor and bradykinesia and involves the dopaminergic pathway (Figure 21.29). In PD, there is accumulation of misfolded α-synuclein in Lewy bodies and neurites with loss of dopamine neurons in the substantia nigra [102, 110]. Lewy bodies are 2–5 μm diameter intracytoplasmic eosinophilic neuronal inclusions, which represent a pathological hallmark of PD, although they are not unique to PD [110]. In patients with PD, the Braak staging scheme suggests that Lewy Bodies first appear in the dorsal motor nucleus of the vagus nerve and anterior olfactory bundle and in a sequential fashion affect other brain regions prior to the substantia nigra, at which point they are associated with the characteristic motor clinical signs [110, 111]. Genetic risk factors in PD include mutations of α-synuclein (*SNCA*), leucine rich repeat kinase 2 (LRRK2), Parkin (PRKN, also known as PARK2), PTEN induced putative kinase 1 (PINK1), and Parkinson disease protein 7 (PARK7, also known as *DJ-1*) [102, 110].

α-Synuclein Models

Duplication or mutations in the *SCNA* gene can cause familial PD. Many mouse models are based on overexpression of human wild type or A53T, A30P, or other mutant forms of α-synuclein using various promoters [110, 112, 113]. For a comparison of α-synuclein mouse models, see Table 1 in reference [110] or Table 2 in reference [114].

Many α-synuclein models are characterized histologically by the presence of α-synuclein inclusions, although these lack the typical fibrillar halo appearance of Lewy bodies in human patients [114]. Although some α-synuclein models

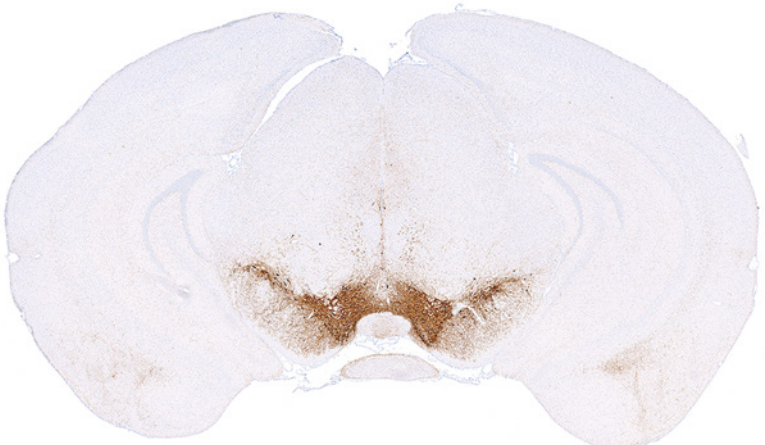


Figure 21.29 Constitutive tyrosine hydroxylase expression in the substantia nigra of an adult C57BL/6J. Tyrosine hydroxylase positive cells labeled brown; hematoxylin counterstain. Tyrosine Hydroxylase (TH) rabbit polyclonal antibody, EMD Millipore, AB152.

show dopaminergic neurodegeneration and neuron loss in the striatum and substantia nigra, substantial dopaminergic cell loss is not a feature of most models [113]. Some motor deficits are present, depending on the model. With viral transfection of α-synuclein, more robust dopaminergic neurodegeneration and motor deficits are present, although rats are often used for these studies [100, 102, 113]. With intracranial seeding of α-synuclein aggregates, mild dopaminergic neurodegeneration and some motor deficits may be present [100].

LRRK2 Models

Genetically engineered mice overexpressing WT LRRK2 protein or mutations of G2019S, R1441G, or R1441C have been created and show some age-related hypoactivity and mild dopaminergic degeneration, although generally little to no consistent loss of dopaminergic neurons or motor deficits are present in these models [102, 110, 113].

Other Genetic Models: Prkn, Pink1, and Park7 (Synonym DJ-1)

Mouse models of *Prkn* and *Pink1* also largely fail to show robust dopaminergic neurodegeneration or motor deficits. FVB/NJ-*Tg(Slc6a3-PARK2*Q311X)AXwy* mice show age-dependent dopaminergic neurodegeneration and some motor deficits [112, 113, 115].

Background strain for some PD models may affect the motor phenotype and degree of loss of dopaminergic neurons [113].

Pharmacologic and Toxic Models

In addition to genetic models of PD, induced (pharmacologic and toxic) models are common, although the toxic models typically do not include synucleinopathy [110, 113]. Mouse models are variably successful at modeling neurodegeneration, motor deficits and non-motor deficits.

Online Resources Commercial repositories for PD models exist, including The Jackson Laboratory's Parkinson's Disease Mouse Model Resource at https://www.jax.org/research-and-faculty/resources/parkinsons-resource.

A list of 14 mouse models of PD is available at https://www.alzforum.org/research-models, with information on the presence and time course of several phenotypes in the various models including neuronal loss; dopamine deficiency; α-synuclein inclusions; neuroinflammation; mitochondrial abnormalities; motor impairment; and non-motor impairment. This website also has links to relevant publications.

Amyotrophic Lateral Sclerosis (ALS)

Amyotrophic lateral sclerosis is characterized by progressive motor neuron degeneration and loss of motor neurons leading to paralysis, with more widespread neuron degeneration including the frontal and temporal lobes (frontotemporal dementia) in some patients [102, 116]. In approximately 10% of patients, the disease is familial; whereas 90% of cases are sporadic. Mutations in more than 20 genes have been associated with disease, including superoxide dismutase 1 (*SOD1*); Chromosome 9 open reading frame 72 (*C9orf72*); transactive response (TAR) DNA binding protein (*TARDBP*, *synonym TDP-43*), and fused in sarcoma (*FUS*) [116–119]. In all forms of ALS, there are cytoplasmic inclusions, which affect RNA metabolism and result in dysfunctional axonal transport [119]. In the majority of ALS cases, there are ubiquitin positive TARDBP (TDP-43) protein inclusions within the neurons and glia, although in *SOD1* mutations there is cytoplasmic accumulation of misfolded SOD1 [116].

The *SOD1* gene was the first causative gene identified in ALS, and mouse models based on SOD1-G93A mutation [ex B6SJL-Tg*(SOD1*G93A)1Gur*] are most widely used to model ALS [102, 116, 119] (Figure 21.30). These mice express the human SOD1 protein with the G93A mutation, show motor neuron loss and axonal degeneration, and, depending on genetic background, may develop paralysis and death within five months of life [116, 119]. Other models of ALS are based on mutations of *C9orf72*, the most common gene mutation associated with familial ALS and FTD in Western Countries, and *FUS*, the second most common mutation in ALS [119]. Mouse models of *C9orf72* hexanucleotide repeat expansion have been reviewed [120], and rodent models of FUS-associated ALS and FTD have also been reviewed [121]. Finally, *TARDBP* mutations are attractive in their potential to model TARDBP (TDP-43) associated lesions in ALS. Selected commonly used genetic mouse models of ALS are listed in Table 21.6. Many models of ALS suffer from promoter and strain-related effects, and some show sexually dimorphic phenotypes.

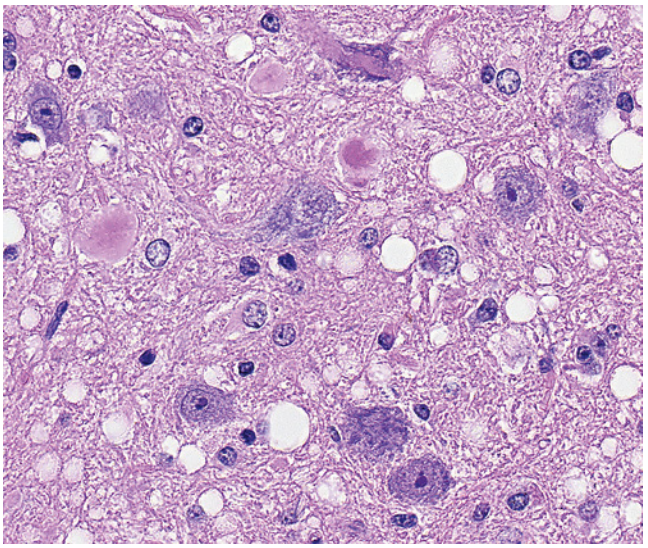


Figure 21.30 Neurodegenerative changes with Lewy body-like inclusions in the ventral horn of the spinal cord of a 19-week-old B6SJL-Tg(*SOD1*G93A)1Gur/J*. HE.

Table 21.6 Commonly used mouse models of amyotrophic lateral sclerosis and their clinicopathological characteristics.

Mouse model (common name)	Pathology	Progression	References
SOD1 related models Examples: B6SJL-Tg *(SOD1*G93A)1Gur*/J (G93A-SOD1)	Cytoplasmic inclusions of misfolded SOD1 Cortical and spinal motor neuron loss Impaired NMJ integrity Gliosis Limitation: No TDP-43 inclusions	Hind limb tremors from 14 weeks and progressive motor dysfunction (paralysis); Reduced lifespan (50% survival at 130–160 days depending on genetic background)	[102, 122, 123]
C9orf72 related models Example: FVB/NJ-Tg *(C9orf72)500Lpwr* (C9-500)	Impaired NMJ integrity Cortical and spinal motor neuron loss (depending on model) Gliosis (depending on model)	+/− Paralysis depending on model/study; *Tg(C9orf72)500Lpwr* develop paralysis with males surviving longer than females	[119, 124–126]
Mice overexpressing human WT FUS and human mutant FUS^{R521C} and FUS^{P525L} Examples: B6;SJL-Tg *(Prnp-FUS*R521C)3313Ejh* B6J.129P2(129S)-*$Mapt^{tm3.1(FUS)Neas}$* STOCK Tg *(Prnp-FUS)WT3CShw* (hFUS)	Spinal cord motor neuron loss (most models) Impaired NMJ integrity Gliosis Inclusions of FUS in cytoplasm of neurons in some models	Paresis/paralysis in most models with death between 2 and 12 mo *Tg(Prnp-FUS*R521C)3313Ejh*, show 55% loss of motor neurons by 2–3 months of age	[119, 121, 127–129]
TARDBP related models Examples: B6.Cg-Tg *(Prnp-TARDBP*A315T)95Balo* (Prp-$TDP43^{A315T}$) *Tg(TARDBP*A315T)#Jpj* B6N.Cg-Tg *(Prnp-TARDBP*Q331K)103Dwc* (Prp-$TDP43^{Q331K}$)	Motor neuron loss Impaired NMJ integrity Gliosis (depending on model) Limitation: TDP-43 cytoplasmic inclusions not present in all models	*Tg(Prnp-TARDBP*A315T) 95Balo:* Average survival 153 days; gait abnormality at 3–4 mo of age (varies with genetic background) *Tg(Prnp-TARDBP*Q331K)103Dwc*: Progressive motor dysfunction (until ten months of age); Limitation: No UMN defects	[117, 119, 130–134]

Source: Adapted from Additional Table 1 of Morrice et al. [117], Table 1 of De Giorgio et al. [118], and Amyotrophic Lateral Sclerosis Mouse Model Resource, Comparison table of featured ALS models, The Jackson Laboratory https://www.jax.org/jax-mice-and-services/solutions-by-therapeutic-area/neurobiology/amyotrophic-lateral-sclerosis-efficacy-studies/als-mouse-model-resource.

Online Resources

Commercial repositories for ALS models exist, including The Jackson Laboratory's Amyotrophic Lateral Sclerosis Mouse Model Resource at https://www.jax.org/jax-mice-and-services/solutions-by-therapeutic-area/neurobiology/amyotrophic-lateral-sclerosis-efficacy-studies/als-mouse-model-resource.

A list of 44 models of ALS is available at https://www.alzforum.org/research-models, with information on the presence or absence of several phenotypes in the various models, including cortical neuron loss; lower motor neuron loss; cytoplasmic inclusions; gliosis; neuromuscular junction abnormalities; muscle atrophy; motor impairment; body weight; and premature death. This website also has links to relevant publications.

Spinocerebellar Ataxias

The spinocerebellar ataxias (SCA) are a group of approximately 30 autosomal dominant, late-onset slowly progressive disorders predominantly affecting the cerebellum, brainstem, and spinal cord and characterized by a cerebellar ataxia [22, 135]. Most are caused by trinucleotide repeat expansions of a CAG-repeat sequence in genes, which result in an expanded tract of glutamine residues within a mutated protein [22, 135]. Within the cerebellum, all regions are involved in many SCAs, including the Purkinje cells, molecular cells, granule cells, and deep cerebellar nuclei [135]. In some spinocerebellar ataxias, the cortex, basal ganglia, and peripheral nervous system also are affected [22]. The most common are SCA 1, 2, 3, 6, and 7. Table 21.7 presents features of relevant mouse models of these spinocerebellar ataxias and mouse models of other cerebellar ataxias.

Table 21.7 Mouse models of spinocerebellar ataxia and cerebellar mutants.

Disease/mouse name	Genetic abnormality (Human/mouse gene)	Histologic lesions and clinical phenotype of selected models
SCA 1	Ataxin 1 (*ATXN1/ Atxn1*) Multiple models	*Tg(PcP2-ATXN1*82Q)5Horr*: Cerebellar atrophy with abnormal morphology and loss of PC; progressive ataxia by 12 w *Atxn1*^{tm1Hzo}: Uniform brain atrophy; PC loss; muscle wasting, ataxia, kyphosis, early death
SCA 2	Ataxin 2 (*ATXN2/ Atxn2*) Multiple models	Phenotype ranges from none to poor rotarod performance and progressive motor abnormalities/death; depending on model may see PC reduction or abnormal morphology
SCA 3 Machado-Joseph disease	Ataxin 3 (*ATXN3/ Atxn3*) Multiple models	Phenotype includes gait abnormality, tremors, limb clasping, and ataxia; depending on model may see neuronal loss, neuronal intranuclear inclusions, demyelination
SCA 6	*CACNA1A / Cacna1a*	*Cacna1a*^{tm3Hzo}: Hypoactivity at 17 mo and poor performance on rotarod without cell loss
SCA 7	Ataxin 7 (*ATXN7/ Atxn7*) Multiple models	*Atxn7*^{tm1Hzo}: Ataxia, visual impairment, premature death *Tg(Prnp-ATXN7*92Q)6076Als*: PC degeneration, blindness; ataxia
Lurcher	*Grid2*^{Lc} spontaneous mutation; homozygous lethal in early PN life; heterozygotes survive with neurologic deficits	Degeneration of PC beginning P8-11; >95% PC loss by P90 Ataxia; loss of motor skills, motor learning, and spatial learning
Hotfoot	*Grid2*^{ho} Spontaneous mutation	PC have ectopic spines with no presynaptic innervation Abnormal gait, especially of hind limbs
Purkinje cell degeneration	*Agtpbp1*^{pcd} Several spontaneous mutant alleles and induced mutants; autosomal recessive; males are sterile	Loss of PC beginning at P20 and severe by P28; secondary loss of GC; activation of microglia and astrocytes; degeneration in olfactory bulb after 13 w; thalamic nuclei after P50 Retinal degeneration; cerebellar ataxia beginning at P21
Nervous	*nr* (gene unknown) Spontaneous; autosomal recessive	PC degeneration beginning at P23 and severe by P50; retinal degeneration Ataxia and hyperactivity
Staggerer	*Rora*^{sg} Spontaneous recessive mutation but heterozygotes also affected less severely	Delayed development of PC spines; severe PC loss by P30; severe GC loss by P28; secondary degeneration of inferior olive neurons Ataxia; behavioral and motor abnormalities
Weaver	*Kcnj6*^{wv} Spontaneous mutation; males are sterile; heterozygotes affected to lesser degree	Disorganized cerebellar structure; marked developmental defects by P10; cell loss other parts of CNS; homozygotes die early Ataxia; behavior, motor, and learning abnormalities
Reeler	*Reln*^{rl} Spontaneous autosomal recessive; heterozygotes have behavioral abnormalities	Disordered cell migration; disorganization and ectopic cells in cerebellum and other parts of CNS Ataxia; behavioral abnormalities
Scrambler	*Dab1*^{scm} Spontaneous autosomal recessive	Cerebellum hypoplastic and devoid of folia at 1 mo; markedly reduced GC; PC reduced and abnormally located Ataxia and whole body tremor by P8

w = weeks; mo = months; P = postnatal day; GC = granule cells; PC = Purkinje cells; CNS = central nervous system.
Source: Adapted from Table 1 of Ingram et al. [22] and text of Cendelin [23].

Huntington's Disease (HD)

Huntington's disease is an autosomal dominant disease characterized by a CAG repeat expansion (>35 repeats) in the Huntington's disease gene (*HTT*), which encodes huntingtin HTT protein [136, 137]. Beginning in middle age, patients develop progressive cognitive impairment and motor deficits with neuronal loss in the striatum (particularly the caudate and putamen), with cell loss in the cortex and brain atrophy in later stages [137].

Mouse models are variably successful at replicating neuropathological changes similar to the human phenotype, including loss of striatal volume and neurons, intracellular

inclusions, and cognitive and motor deficits as measured on behavioral and rotarod testing [136]. Commonly used models that express truncated mutant HTT are the B6CBA-Tg*(HDexon1)62Gpb* (synonym R 6/2), in which seizures, tremors, and motor impairment with progressive accumulation of neuronal intranuclear inclusions occurs at approximately 10 weeks with death by 13 weeks [138], the B6CBA-Tg*(HDexon1)61Gpb* (synonym R6/1), which survives to a later age, and the B6C3-Tg*(HD82Gln)81Gschi* (N171-Q2Q model), in which progressive motor impairment occurs after 8–12 weeks, intranuclear inclusions are present, and death occurs at 16–30 weeks [139, 140]. Other transgenic mouse models of HD that express full-length human mutant HTT include FVB/N-Tg*(YAC72)2511Hay* [YAC 72; [141]], FVB/N-Tg*(YAC128)53Hay* [YAC 128; [142]], and FVB-Tg*(HTT*97Q)LXwy* [BACHD; [143]]. Various knock-in models also exist. Mouse models of Huntington's disease are summarized in detail elsewhere [136, 144–147].

Commercial repositories for HD models include the Jackson Laboratory's Huntington's Disease Mouse Model Resource at https://www.jax.org/jax-mice-and-services/solutions-by-therapeutic-area/neurobiology/huntingtons-disease-mouse-model-resource.

Autoimmune

Experimental Allergic Encephalitis

Experimental autoimmune encephalitis (EAE) is an inducible rodent disease model used to study multiple sclerosis (MS). MS is characterized by four key histopathological lesions; inflammation of the CNS, demyelination, axonal loss, and degeneration as well as gliosis [148]. The cause(s) and mechanism(s) of MS has/have yet to be determined but it is associated with both environmental factors such as infectious agents, toxins, and diet, as well as genetics. Differences in expression of the class II region of the human leukocyte antigen (HLA), which functions to present peptides to T cells have been linked to disease susceptibility [149]. Clinically, there are several subtypes of MS, many of which have been modeled in EAE systems, including relapsing–remitting MS, progressive MS and chronic MS (Table 21.8) [148].

EAE recapitulates many of the disease manifestations of MS including myelin sheath destruction and inflammation of the CNS leading to impaired axonal conduction and progressive paralysis [150–152] (Figure 21.31). EAE is classically induced in mice by immunization with CNS tissue or purified myelin protein(s) along with an adjuvant followed by clinical disease onset within 9–12 days [148]. There are many different myelin proteins that can induce EAE and, depending on the mouse strain utilized, lead to different disease phenotypes (Table 21.8). Strain variations are often

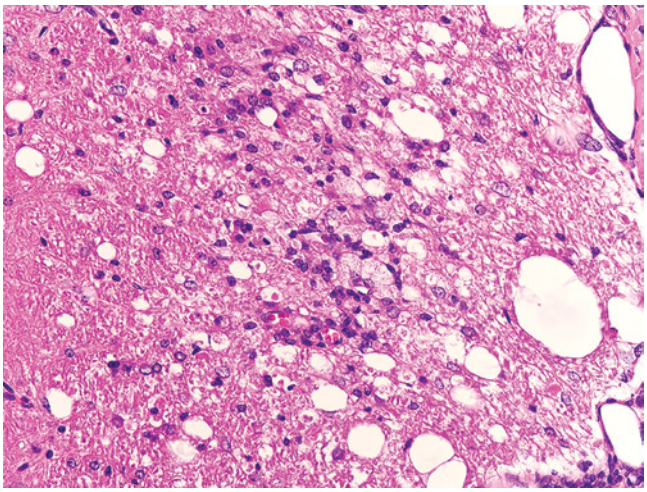


Figure 21.31 Inflammation and demyelination in the spinal cord of a mouse model of experimental autoimmune encephalomyelitis. Artifactual vacuolation is also present. HE.

Table 21.8 Selected mouse models for study of EAE.

Type of EAE disease	MHC *H2* haplotypes	Mouse strain	Inducer (s)	Pathology
Acute	Carry $H2^{dq1}$ MHC haplotype and express mouse I-A^{g7} MHC class II molecule	ABH /BiozDbak	MAG, MBP	Mild demyelination
Chronic	$H2^{b}$	C57BL/6J; C57BL/6NTac; C57BL/6NCrl	MOG_{35-55}	Inflammation and neuron loss
Relapsing, Remitting	$H2^{s}$	SJL/JCrNTac; SJL/JCrHsd; SJL/J	SCH, PLP, MBP or MOG_{92-106}	Inflammation, demyelination, remyelination
Progressive	see above $H2^{g7}$	ABH NOD/ShiLtJ[a]	SCH MOG_{35-55}	Gliosis, demyelination, remyelination, and inflammation
Spontaneous	Humanized transgenics for HLAs, TCR or BCR	Most commonly B6 background	None	Inflammation and demyelination

Spinal cord homogenate (SCH), myelin associated glycoprotein (MAG), myelin basic protein (MBP), myelin oligodendrocyte protein (MOG), proteolipid protein (PLP), non-obese diabetic mice (NOD mice), human leukocyte antigen (HLA), T cell receptor (TCR), B cell receptor (BCR)
[a] Some authors state that the NOD/ShitLtJ model represents a relapsing/remitting model.
Source: Adapted from Tables 2 and 3 from Kipp et al. [150].

associated with what histocompatibility system (H2) is expressed in that strain, which is analogous to HLA in humans. EAE resistance or susceptibility is further modified by a number of binary and quantitative trait loci (BTL/QTL) in the various strains [153]. EAE can also be induced by adoptive transfer of stimulated myelin protein-primed T cells injected into naïve or immunodeficient mice, which allows for more in-depth study of specific T cell populations. More recently, transgenic mice have been developed, which have been humanized for the T cell receptor complex (TCR), B cell receptor complex (BCR) specific for myelin epitopes or for susceptible HLA phenotypes [152, 154, 155]. Although EAE is a useful model system to study disease mechanisms of MS as well as the effectiveness of disease-modifying therapies, it does not fully model this complex disease and comes with its own limitations, as do all animal models of human diseases [156]. More information about mouse models of EAE is available at: taconic.com/taconic-insights/neuroscience/eae-mouse-models-of-multiple-sclerosis.

Developmental:

Lysosomal Storage Diseases

Lysosomal storage disorders (LSDs) are a collection of 50–70 distinct genetic diseases that result from mutations in genes encoding proteins that are critical for lysosomal function [157, 158]. Such mutations lead to accumulation within lysosomes of lipids, glycoproteins, and other substances [157] (Figure 21.32). Often cells in multiple systems are involved, and more than 50% of LSDs involve the CNS. While neurons throughout the CNS are involved, different susceptibilities may result in clinical signs referable to a specific location (for example, increased susceptibility of Purkinje cells causing cerebellar ataxia).

References summarizing mouse models of lysosomal storage disease [159] and the glycosaminoglycan storage disorders in particular [160] are available. Use of mouse models in the development of therapies for lysosomal storage disease is discussed in Desnick and Schuchman [161], among other references.

Mouse models of lysosomal storage diseases (Table 21.9) are useful to inform pathogenesis/pathophysiology and evaluate initial response to treatments such as gene therapy and enzyme replacement [157]. However, many genetically engineered models of lysosomal storage diseases do not recapitulate human disease, causing either minimal phenotypes in the mouse model or far more severe phenotypes [162]. Large animal models for many lysosomal storage diseases may better model human disease and are more similar to humans in size and metabolism, which are benefits in some preclinical analyses and drug development [157].

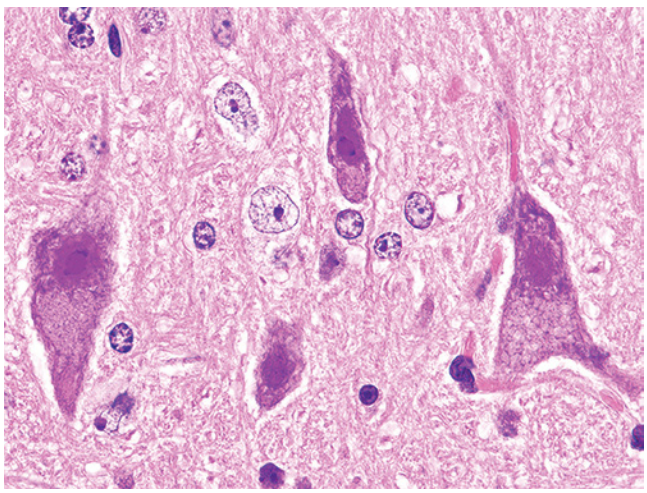


Figure 21.32 Neurons with accumulated intracytoplasmic vacuolated material in a mouse model of a lysosomal storage disease. HE.

Epilepsy

The term epilepsy includes seizure disorders of multiple causes, including idiopathic or genetic, infectious, structural (neoplasm, stroke, trauma), metabolic, immune, or unknown [178–180]. Types of seizure activity include generalized, which may be characterized by motor activity (such as tonic–clonic) or nonmotor (absence), and focal (also known as partial), depending on clinical presentation and pattern of abnormal activity on electroencephalography [180]. Status epilepticus is defined as sustained seizure activity for longer than 5 minutes. Temporal lobe epilepsy is the most common form of human epilepsy, with the origin of seizures in the hippocampus.

Animal models are used to develop anti-epileptic drugs and to model particular types of epilepsy [181]. Many animal models of epilepsy involve electroconvulsive or chemically induced seizures in wild type mice and rats, which is beyond the scope of this chapter. These models are discussed extensively elsewhere [see 178, 179]. Strain-related differences in epileptic phenotype and degree of hippocampal damage are observed in some induced models [182–185].

Approximately 1000 genes have been associated with epilepsy in human patients [186–188]. Genetic models of epilepsy include reflex models such as audiogenic seizures in DBA/2J and DBA/1OlaHsd mice as well as spontaneous recurrent seizures related to defects of ion channels and ligand gated channels, among other causes [(Table 21.10), [63, 195]]. Genetically engineered mice with mutations in genes important in epileptogenesis (such as genes involved in inhibitory neurotransmitter [GABA] synthesis, voltage or ligand-gated receptor function, and transport) and genes implicated in severe congenital seizure disorders and inherited human epilepsy are increasingly common [188, 196]. Table 21.10 lists mouse models of reflex epilepsy and pediatric epilepsy. Epilepsy is also associated with some mouse models of AD [see 197, 198] and autism spectrum disorders (involving mutations of the genes *Mecp2*; *Ube3a*; and *Shank3*) [193]. For a review of epilepsy genes in the human and mouse see [194]. A list of 900 genotypes with an annotated term of seizures and references can be found (informatics.jax.org/mp/annotations/MP:0002064).

Table 21.9 Selected mouse models of lysosomal storage diseases.

Disease	Enzyme/protein deficiency	Human Gene	Characteristics of mouse model and references
Aspartylglucosaminuria	Aspartylglucosaminidase	*AGA*	Ataxia and motor incoordination from 5 mo; dilated urinary bladder from 10 mo; vacuolation of cells in CNS; similar to human disease [159]
Gaucher II,III	β-Glucocerebrosidase	*GBA*	Severe type 2; die within 24 hours; severe skin pathology [159]; conditional knockout also exists [158]
GM1 gangliosidosis	β-Galactosidase	*GLB1*	Ataxia and tremor from 4 to 5 mo; widespread PAS positive storage material in neurons; similar to infantile form of GM1 gangliosidosis [159]
GM2-gangliosidosis (Tay-Sachs)	β-Hexosaminidase	*HEXA*	Neurons in prosencephalon have membranous cytoplasmic bodies; mice phenotypically normal and fertile until at least 1 year of age [159, 162]
GM2-gangliosidosis (Sandhoff)	β-Hexosaminidase	*HEXB*	Severe phenotype (infantile form); motor function declines from 12 w; PAS positive storage material in neurons throughout CNS [159, 162]
Fucosidosis	α-L-Fucosidase	*FUCA1*	Similar to mild form of human disease; ataxia, tremor, and large urinary bladder from 6 mo; euthanized at 9–11 mo; storage throughout CNS with PC loss; axon spheroids [163]
Galactosialidosis	Interferes with normal function of cathepsin A	*CTSA*	Late onset ataxia and cutaneous edema; die by 12 mo; vacuolated cells in brain (perivascular and perineuronal) and neuronal storage [159]
Globoid cell leukodystrophy (Krabbe)	Galactosylceramidase	*GALC*	Spontaneous Twitcher mouse *Galc*^{twi} (example B6.CE-*Galc*^{twi}/J)
Niemann–Pick A/B	Sphingomyelin phosphodiesterase	*SMPD1*	Tremor and ataxia from 8 w; die at 4–8 m; accumulation of sphingomyelin; loss of Purkinje cells; similar to Niemann-Pick A [159]
Niemann-Pick C1/2	NPC intracellular cholesterol transporter	*NPC1/2*	Various mouse models summarized [164]
α-Mannosidosis	α –Mannosidase	*MAN2B1*	Spheroids; cytoplasmic vacuoles in neurons in CNS and PNS [165]
B-Mannosiosis	β-Mannosidase	*MANBA*	Normal growth, appearance and lifespan; neuronal vacuolation (severity depends on background strain) [166]
Mucopolysaccharidosis (MPS) I; (Hurler, Scheie)	α-L-Iduronidase	*IDUA*	Cytoplasmic vacuolation of glial cells by 4 w and neurons by 8 w (among other organs); resembles severe MPS I [159]
MPS II (Hunter)	Iduronate sulfatase	*IDS*	Hemizygous males have vacuolization in many cells including PC; neuronal necrosis by 60 w [167]
MPS IIIA (Sanfilippo)	N-sulfoglucosamine sulfohydrolase	*SGSH*	Spontaneous (B6.Cg-*Sgsh*^{mps3a}/PstJ); die 7–10 m; severe brain involvement; "zebra bodies" on EM [168, 169]
MPS IIIB (Sanfilippo)	N-acetyl-α-glucosaminidase	*NAGLU*	Vacuolation in neurons increases with age; abnormal behavior by 4.5 mo [168, 170]
MPS IV A (Morquio)	N-acetylgalactosamine 6- sulfatase	*GALNS*	Variable storage in neurons and glial cells depending on model [171, 172]
MPS VII (Sly)	β-Glucuronidase	*GUSB*	Spontaneous (*Gusb*^{mps}) and induced; behavioral deficits, shortened lifespan; cytoplasmic vacuolation glia, neurons, leptomeninges by 3–4 w [173]
Neuronal ceroid lipofuscinosis (Batten)	Several	Several	Mouse models summarized [174] and [175]
Mucolipidosis II (alpha/beta)	GlcNAc-1-phosphotransferase	*GNPTAB*	Described in [176, 177]
Metachromatic leukodystrophy	Arylsulfatase A/prosaposin	*ARSA* *PSAP*	Milder phenotype than human disease; late onset of mild tremor; storage of sulfatide through WM [159, 162]

w = weeks; mo = months.
Source: Adapted from Table 1 of Xu et al. [157], Table 1 of Suzuki et al. [159] and Table 1 of Coutinho et al. [160].

Table 21.10 Spontaneous and genetically engineered mouse models of epilepsy.

Category	Mouse models/gene
Reflex	
Monogenic audiogenic seizure susceptible	Spontaneous BUB/BnJ mice *Adgrv1*^{frings} (synonyms frings, Mass1^{frings})
Audiogenic seizure prone 1 and 2 (Asp-1 and Asp-2)	Spontaneous DBA/2J mice
Juvenile audiogenic monogenic seizures (Jams1)	Spontaneous Black Swiss mice
Leucine rich, glioma inactivated 1 (Lgi1)	B6.Cg-*Lgi1* $^{tm1.1Ics}$/Orl; other *Lgi1* Tg models
Handling/vestibular	EL/SuzSeyFrkJ mice [EL-inbred; [189]]
Spontaneous recurrent seizures	
Ion channels	See [190] for models of calcium channel defects
Cacna1a^{tg}	Spontaneous, recessive; Tottering
Cacnb4^{lh}	Spontaneous, recessive; Lethargic
Cacna2d2^{du} *and Cacna2d2*$^{du\text{-}td}$	Spontaneous, recessive; Ducky and torpid
Cacng2^{stg}	Spontaneous, recessive; Stargazer
Kcnj6^{wv}	Spontaneous, recessive; Weaver [191]
Kcnq2, *Kcnq3* *Kcna1*, *Kcna2* *Kcnmb4* *Scn1a, Scn1b, Scn2b, Scn8a*	Various genetically engineered models See [192] and [193] for tables of models
Ligand-gated channels	*Gria2*, *Chrna4*, *Gabrg2*
Models of mTOR dysregulation	*Tsc1/2*; regulators of mTOR complex 1 activity; several genetically engineered models (see [192])

Source: Adapted from Table 2 of Italiano et al. [64], Table 1 of Gu and Dalton [193], and Table 2 of Meisler et al. [194].

Traumatic Brain Injury and Post-Traumatic Epilepsy

Traumatic brain injury is a leading cause of morbidity and mortality, especially in people less than 40 years of age, with sequelae including post-traumatic epilepsy and cognitive and motor deficits. Mouse models of traumatic brain injury include focal or diffuse injury induced by techniques such as fluid percussion, weight-drop, rigid indentation, dynamic cortical deformation, and blast injury [199]. In this context, genetically engineered mice enable researchers to investigate the role of specific genes in the response to traumatic brain injury [200].

Malformation

Malformations include neural tube closure defects such as exencephaly [the mouse equivalent of human anencephaly [201]]; spina bifida; myelomeningocele; encephalocele; and Chiari malformation [202]. Malformations also include abnormalities of neuronal proliferation, differentiation, and histogenesis; migration; myelination; or secondary injury to normally formed structures, such as hydrocephalus [202]. Mouse models of neural tube defects have been described [203–206; among others].

In mice, congenital hydrocephalus is a complex polygenic trait, with strain-associated genetic modifiers [5]. In this context, C57BL strains have increased predisposition for the development of congenital hydrocephalus if compared to other inbred strains of mice. Congenital hydrocephalus also is associated with both spontaneous mutations and genetically engineered mice [5, 207–211]. Hydrocephalus can be either communicating (caused by reduced absorption of CSF) or noncommunicating (caused by an interruption in CSF circulation) [5]. Most cases of congenital hydrocephalus are noncommunicating and involve an obstruction at the level of the cerebral aqueduct, which results in dilation of the lateral and third ventricles with a normal fourth ventricle [5, 21, 212, 213]. In mice, ciliary defects appear to be a common cause of hydrocephalus, in addition to abnormal

neuronal migration or brain morphogenesis [5]. Neoplasms and infectious diseases can also cause obstructive hydrocephalus in older mice.

Neoplasia

Intracranial neoplasms are common in humans, and a classification system has been developed by the World Health Organization [214]. By contrast, spontaneous brain tumors in non-genetically manipulated mice are uncommon. One reference studying four strains of mice found the frequency of CNS neoplasms to be less than 0.25% [215]. Other studies have found similar results [216, 217]. Astrocytoma has been reported to occur at a 1% incidence in male mice of some strains, with spread throughout the CNS [19, 218].

Intracranial neoplasms in rodents can be induced at higher frequency via carcinogen exposure and/or genetic manipulation [219, 220]. Immunodeficient or wild-type mice may also be implanted with primary tumor cells from patients (either fresh or from tumors passaged serially in the flanks of mice) or mouse or human immortalized tumor cell lines [221–223]. Common mouse and human cells lines used to create mouse models of glioblastoma are summarized [222].

Reviews on mouse models of intracranial neoplasia are available [224–226]. In particular, mouse models of glioma are common and information regarding genetic manipulation, morphology, and incidence of glioma (astrocytoma, oligodendroglioma) and medulloblastoma has been summarized [227]. Medulloblastoma, the most common malignant pediatric brain neoplasm, can be classified in patients by histologic characteristics as well as molecular/genetic and immunohistochemical markers [228]. These tumors are thought to arise from neuronal stem or progenitor cells in the cerebellum and may involve amplifications of oncogenes such as *MYC*, defective WNT signaling, or mutations in regulators of the sonic hedgehog pathway such as *PTCH1* and *SUFU* [229]. Genetically engineered mice models of medulloblastoma include mice with mutations of Hedgehog pathway gene patched 1 (*Ptch1*); the tumor suppressor gene transformation related protein 53 (*Trp53*); and the DNA repair enzyme ADP-ribosyltransferase (*Parp1*, synonym *Adprt1*) [227, 230] (Figure 21.33). Mice with these mutations often show tumor growth by 6 months of age, and irradiation can increase tumor frequency [227]. Retroviral gene transfer to generate medulloblastoma and glioma models is also used [222, 227].

Genetically engineered mouse models of glioma involve mutations of *Nf1*, *Trp53*, *Pten*, and *Cdkn2a*, with some under control of a GFAP or nestin promoter, among others [222, 227, 231]. Astrocytomas in genetically engineered mice do not always express GFAP and may resemble glioblastoma multiforme [216, 232, 233]. Immunohistochemical markers to evaluate glial and neuronal differentiation when characterizing a GEM glioma or medulloblastoma model include GFAP, protein S100B, synaptophysin, RBBOX3 (NeuN), nestin, and neurofilament (heavy, medium, light) proteins [234]. Recommendations regarding evaluation of GEM models of tumors of the nervous system are summarized in Weiss et al. [234].

Patients with neurofibromatosis type 1 and type 2 have mutations in the NF1 and NF2 tumor suppressor genes and are predisposed to develop benign peripheral nerve sheath tumors (neurofibromas) and multiple Schwann cell tumors (schwannomas), respectively [234]. Mice with mutations of *Nf1*, *Nf2*, and *Trp53* develop malignant peripheral nerve sheath tumors among other tumor types [234–236].

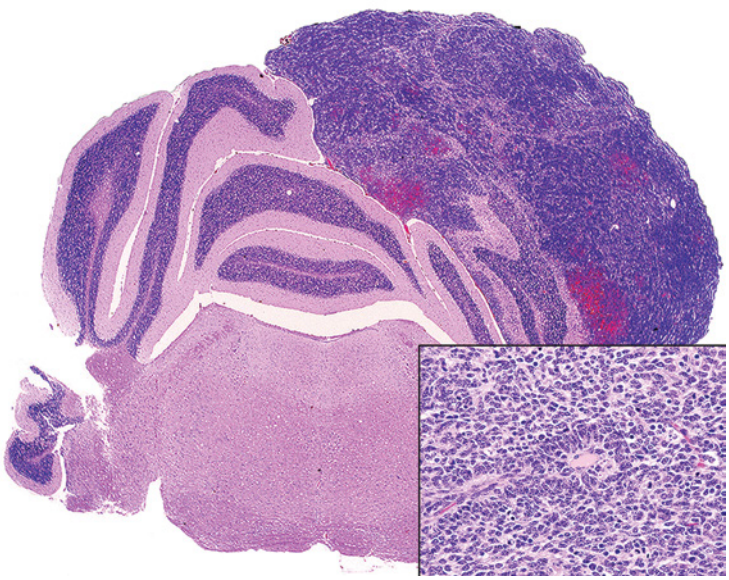


Figure 21.33 Medulloblastoma at the level of the medulla and cerebellum. Inset at higher magnification shows rosette formation characteristic of this neoplasm. HE.

References

1 Ruberte, J., Navarro, M., Carretero, A. et al. (2017). Nervous system. In: *Morphological Mouse Phenotyping: Anatomy, Histology, and Imaging* (eds. J. Ruberte, A. Carretero and M. Navarro), 377–474. Spain: Elsevier.

2 Chen, V.S., Morrison, J.P., Southwell, M.F. et al. (2017). Histology atlas of the developing prenatal and postnatal mouse central nervous system, with emphasis on prenatal days E7.5 to E18.5. *Toxicol. Pathol.* 45 (6): 705–744.

3 Johanson, C., Stopa, E., McMillan, P. et al. (2011). The distributional nexus of choroid plexus to cerebrospinal fluid, ependyma and brain: toxicologic/pathologic phenomena, periventricular destabilization, and lesion spread. *Toxicol. Pathol.* 39 (1): 186–212.

4 Bruni, J.E., Del Bigio, M.R., Cardoso, E.R., and Persaud, T.V. (1988). Hereditary hydrocephalus in laboratory animals and humans. *Exp. Pathol.* 35 (4): 239–246.

5 Vogel, P., Read, R.W., Hansen, G.M. et al. (2012). Congenital hydrocephalus in genetically engineered mice. *Vet. Pathol.* 49 (1): 166–181.

6 Dorr, A., Sled, J.G., and Kabani, N. (2007). Three-dimensional cerebral vasculature of the CBA mouse brain: a magnetic resonance imaging and micro computed tomography study. *Neuroimage* 35 (4): 1409–1423.

7 Aspelund, A., Antila, S., Proulx, S.T. et al. (2015). A dural lymphatic vascular system that drains brain interstitial fluid and macromolecules. *J. Exp. Med.* 212 (7): 991–999.

8 Ahn, J.H., Cho, H., Kim, J.H. et al. (2019). Meningeal lymphatic vessels at the skull base drain cerebrospinal fluid. *Nature* 572 (7767): 62–66.

9 Ma, Q., Ineichen, B.V., Detmar, M., and Proulx, S.T. (2017). Outflow of cerebrospinal fluid is predominantly through lymphatic vessels and is reduced in aged mice. *Nat. Commun.* 8 (1): 1434.

10 Jessen, N.A., Munk, A.S., Lundgaard, I., and Nedergaard, M. (2015). The glymphatic system: a beginner's guide. *Neurochem. Res.* 40 (12): 2583–2599.

11 Sidman, R.L., Angevine, J.B. Jr., and Pierce, E.T. (1971). *Atlas of the Mouse Brain and Spinal Cord*. Cambridge: Harvard University Press.

12 Ero, C., Gewaltig, M.O., Keller, D., and Markram, H. (2018). A cell atlas for the mouse brain. *Front. Neuroinform.* 12: 84.

13 Paxinos, A. and Franklin, K.B.J. (2019). *The Mouse Brain in Stereotaxic Coordinates*, 5e. New York: Academic Press.

14 Snyder, J., Hagan, C.E., Bolon, B., and Keene, C.D. (2018). Nervous system. In: *Comparative Anatomy and Histology: A Mouse, Rat, and Human Atlas* (eds. P.M. Treuting, S.M. Dintzis and K.S. Montine), 403–444. San Diego, CA: Elsevier.

15 Roulois, A. (2014). Nervous system. In: *A Practical Guide to the Histology of the Mouse*, 1e (ed. C. Scudamore), 123–148. West Sussex: Wiley Blackwell.

16 Harrison, M., O'Brien, A., Adams, L. et al. (2013). Vertebral landmarks for the identification of spinal cord segments in the mouse. *NeuroImage* 68: 22–29.

17 Watson, C., Paxinos, G., Kayalioglu, G., and Heise, C. (2009). An atlas of the mouse spinal cord. In: *The Spinal Cord: A Christopher and Dana Reeve Foundation Text and Atlas* (eds. C. Watson, G. Paxinos and G. Kayalioglu), 308–379. San Diego, CA: Elsevier Academic Press.

18 Sengul, G., Puchalski, R.B., and Watson, C. (2012). Cytoarchitecture of the spinal cord of the postnatal (P4) mouse. *Anat. Rec. (Hoboken)* 295 (5): 837–845.

19 Kaufmann, W., Bolon, B., Bradley, A. et al. (2012). Proliferative and nonproliferative lesions of the rat and mouse central and peripheral nervous systems. *Toxicol. Pathol.* 40 (4 Suppl): 87S–157S.

20 Al Khazal, F., Holte, M.N., Bolon, B. et al. (2019). A conditional mouse model of complex II deficiency manifesting as Leigh-like syndrome. *FASEB J.* 33 (12): 13189–13201.

21 Bronson, R.T. (2000). Pathologic characterization of neurological mutants. In: *The Pathology of Genetically Engineered Mice* (eds. J. Ward, J.F. Mahler, R.R. Maronpot and J.P. Sundberg). Ames, IA: Iowa State University Press.

22 Ingram, M.A., Orr, H.T., and Clark, H.B. (2012). Genetically engineered mouse models of the trinucleotide-repeat spinocerebellar ataxias. *Brain Res. Bull.* 88 (1): 33–42.

23 Cendelin, J. (2014). From mice to men: lessons from mutant ataxic mice. *Cerebellum Ataxias* 1: 4.

24 Sicinski, P., Donaher, J.L., Parker, S.B. et al. (1995). Cyclin D1 provides a link between development and oncogenesis in the retina and breast. *Cell* 82 (4): 621–630.

25 Jortner, B.S. (2011). High-definition microscopic analysis of the nervous system. In: *Fundamental Neuropathology for Pathologists and Toxicologists: Principles and Techniques* (eds. B. Bolon and M.T. Butt), 203–207. Hoboken, NJ: Wiley.

26 Jordan, W.H., Hall, D.G., Hyten, M.J., and Young, J.K. (2011). Practical neuropathology of the rat and other species. In: *Fundamental Neuropathology for Pathologists and Toxicologists: Principles and Techniques* (eds. B. Bolon and M.T. Butt), 159–170. Hoboken, NJ: Wiley.

27 Butt, M.T. (2011). Evaluation of the adult nervous system in preclinical studies. In: *Fundamental Neuropathology for Pathologists and Toxicologists: Principles and Techniques* (eds. B. Bolin and M.T. Butt), 321–338. Hoboken, NJ: Wiley.

28 Gibson-Corley, K.N., Boyden, A.W., Leidinger, M.R. et al. (2016). A method for histopathological study of the multifocal nature of spinal cord lesions in murine experimental autoimmune encephalomyelitis. *PeerJ* 4: e1600.

29 Cook, S.A., Bronson, R.T., Donahue, L.R. et al. (1997). Cerebellar deficient folia (*cdf*): a new mutation on mouse chromosome 6. *Mamm. Genome* 8 (2): 108–112.

30 Morawietz, G., Ruehl-Fehlert, C., Kittel, B. et al. (2004). Revised guides for organ sampling and trimming in rats and mice--Part 3. A joint publication of the RITA and NACAD groups. *Exp. Toxicol. Pathol.* 55 (6): 433–449.

31 Garman, R.H., Li, A.A., Kaufmann, W. et al. (2016). Recommended methods for brain processing and quantitative analysis in rodent developmental neurotoxicity studies. *Toxicol. Pathol.* 44 (1): 14–42.

32 Tarrant, J.C., Savickas, P., Omodho, L. et al. (2019). Spontaneous incidental brain lesions in C57BL/6J mice. *Vet. Pathol.* https://doi.org/10.1177/0300985819859878.

33 Bolon, B., Garman, R.H., Pardo, I.D. et al. (2013). STP position paper: recommended practices for sampling and processing the nervous system (brain, spinal cord, nerve, and eye) during nonclinical general toxicity studies. *Toxicol. Pathol.* 41 (7): 1028–1048.

34 Garman, R.H. (2011). Histology of the central nervous system. *Toxicol. Pathol.* 39 (1): 22–35.

35 Wahlsten, D., Metten, P., and Crabbe, J.C. (2003). Survey of 21 inbred mouse strains in two laboratories reveals that BTBR T/+ *tf/tf* has severely reduced hippocampal commissure and absent corpus callosum. *Brain Res.* 971 (1): 47–54.

36 Hino, K., Otsuka, S., Ichii, O. et al. (2009). Strain differences of cerebral ventricles in mice: can the MRL/MpJ mouse be a model for hydrocephalus? *Jpn. J. Vet. Res.* 57 (1): 3–11.

37 Gudjohnsen, S.A., Atacho, D.A., Gesbert, F. et al. (2015). Meningeal melanocytes in the mouse: distribution and dependence on *Mitf*. *Front. Neuroanat.* 9: 149.

38 Adkison, D.L. and Sundberg, J.P. (1991). "Lipomatous" hamartomas and choristomas in inbred laboratory mice. *Vet. Pathol.* 28 (4): 305–312.

39 Nobel, T.A., Nyska, A., Pirak, M. et al. (1987). Epidermoid cysts in the central nervous system of mice. *J. Comp. Pathol.* 97 (3): 357–359.

40 Stroop, W.G. (1984). Spinal leptomeningeal epidermoid cysts in inbred mouse strains. *Acta Neuropathol.* 63 (4): 301–305.

41 Hansmann, F., Herder, V., Ernst, H., and Baumgartner, W. (2011). Spinal epidermoid cyst in a SJL mouse: case report and literature review. *J. Comp. Pathol.* 145 (4): 373–377.

42 Peirson, S.N., Brown, L.A., Pothecary, C.A. et al. (2018). Light and the laboratory mouse. *J. Neurosci. Methods* 300: 26–36.

43 Carlson, G.A., Borchelt, D.R., Dake, A. et al. (1997). Genetic modification of the phenotypes produced by amyloid precursor protein overexpression in transgenic mice. *Hum. Mol. Genet.* 6 (11): 1951–1959.

44 Goelz, M.F., Mahler, J., Harry, J. et al. (1998). Neuropathologic findings associated with seizures in FVB mice. *Lab. Anim. Sci.* 48 (1): 34–37.

45 Kohnken, R.A. and Schwahn, D.J. (2016). Lack of chronic histologic lesions supportive of sublethal spontaneous seizures in FVB/N mice. *Comp. Med.* 66 (2): 105–111.

46 Noben-Trauth, K., Zheng, Q.Y., and Johnson, K.R. (2003). Association of cadherin 23 with polygenic inheritance and genetic modification of sensorineural hearing loss. *Nat. Genet.* 35 (1): 21–23.

47 Kane, K.L., Longo-Guess, C.M., Gagnon, L.H. et al. (2012). Genetic background effects on age-related hearing loss associated with *Cdh23* variants in mice. *Hear. Res.* 283 (1–2): 80–88.

48 Zheng, Q.Y., Johnson, K.R., and Erway, L.C. (1999). Assessment of hearing in 80 inbred strains of mice by ABR threshold analyses. *Hear. Res.* 130 (1–2): 94–107.

49 Bohlen, M.O., Bailoo, J.D., Jordan, R.L., and Wahlsten, D. (2012). Hippocampal commissure defects in crosses of four inbred mouse strains with absent corpus callosum. *Genes Brain Behav.* 11 (7): 757–766.

50 Livy, D.J. and Wahlsten, D. (1991). Tests of genetic allelism between four inbred mouse strains with absent corpus callosum. *J. Hered.* 82 (6): 459–464.

51 Sellers, R.S. (2012). The gene or not the gene--that is the question: understanding the genetically engineered mouse phenotype. *Vet. Pathol.* 49 (1): 5–15.

52 Bowes, C., Li, T., Danciger, M. et al. (1990). Retinal degeneration in the rd mouse is caused by a defect in the beta subunit of rod cGMP-phosphodiesterase. *Nature* 347 (6294): 677–680.

53 Bowes, C., Li, T., Frankel, W.N. et al. (1993). Localization of a retroviral element within the rd gene coding for the beta subunit of cGMP phosphodiesterase. *Proc. Natl. Acad. Sci. U.S.A.* 90 (7): 2955–2959.

54 Pittler, S.J. and Baehr, W. (1991). Identification of a nonsense mutation in the rod photoreceptor cGMP phosphodiesterase beta-subunit gene of the rd mouse. *Proc. Natl. Acad. Sci. U.S.A.* 88 (19): 8322–8326.

55 Koike, H., Arguello, P.A., Kvajo, M. et al. (2006). *Disc1* is mutated in the 129S6/SvEv strain and modulates working memory in mice. *Proc. Natl. Acad. Sci. U.S.A.* 103 (10): 3693–3697.

56 Clapcote, S.J. and Roder, J.C. (2006). Deletion polymorphism of *Disc1* is common to all 129 mouse substrains: implications for gene-targeting studies of brain function. *Genetics* 173 (4): 2407–2410.

57 Ritchie, D.J. and Clapcote, S.J. (2013). *Disc1* deletion is present in Swiss-derived inbred mouse strains: implications for transgenic studies of learning and memory. *Lab. Anim.* 47 (3): 162–167.

58 Cuoco, J.A., Esposito, A.W., Moriarty, S. et al. (2018). Malformation of the posterior cerebellar vermis is a common neuroanatomical phenotype of genetically engineered mice on the C57BL/6 background. *Cerebellum* 17 (2): 173–190.

59 Tanaka, M. and Marunouchi, T. (2005). Abnormality in the cerebellar folial pattern of C57BL/6J mice. *Neurosci. Lett.* 390 (3): 182–186.

60 Schreiber, R.A. and Graham, J.M. Jr. (1976). Audiogenic priming in DBA/2J and C57BL/6J mice: interactions among age, prime-to-test interval and index of seizure. *Dev. Psychobiol.* 9 (1): 57–66.

61 Neumann, P.E. and Seyfried, T.N. (1990). Mapping of two genes that influence susceptibility to audiogenic seizures in crosses of C57BL/6J and DBA/2J mice. *Behav. Genet.* 20 (2): 307–323.

62 Buchhalter, J.R. (1993). Animal models of inherited epilepsy. *Epilepsia* 34 (Suppl. 3): S31–S41.

63 De Sarro, G., Russo, E., Citraro, R., and Meldrum, B.S. (2017). Genetically epilepsy-prone rats (GEPRs) and DBA/2

mice: two animal models of audiogenic reflex epilepsy for the evaluation of new generation AEDs. *Epilepsy Behav.* 71 (Pt. B): 165–173.

64 Italiano, D., Striano, P., Russo, E. et al. (2016). Genetics of reflex seizures and epilepsies in humans and animals. *Epilepsy Res.* 121: 47–54.

65 Connolly, E.S. Jr., Winfree, C.J., Stern, D.M. et al. (1996). Procedural and strain-related variables significantly affect outcome in a murine model of focal cerebral ischemia. *Neurosurgery* 38 (3): 523–531; discussion 32.

66 Maeda, K., Hata, R., and Hossmann, K.A. (1998). Differences in the cerebrovascular anatomy of C57black/6 and SV129 mice. *Neuroreport* 9 (7): 1317–1319.

67 Fujii, M., Hara, H., Meng, W. et al. (1997). Strain-related differences in susceptibility to transient forebrain ischemia in SV-129 and C57black/6 mice. *Stroke* 28 (9): 1805–1810; discussion 11.

68 Majid, A., He, Y.Y., Gidday, J.M. et al. (2000). Differences in vulnerability to permanent focal cerebral ischemia among 3 common mouse strains. *Stroke* 31 (11): 2707–2714.

69 Barone, F.C., Knudsen, D.J., Nelson, A.H. et al. (1993). Mouse strain differences in susceptibility to cerebral ischemia are related to cerebral vascular anatomy. *J. Cereb. Blood Flow Metab.* 13 (4): 683–692.

70 Bruce, M.E., McConnell, I., Fraser, H., and Dickinson, A.G. (1991). The disease characteristics of different strains of scrapie in Sinc congenic mouse lines: implications for the nature of the agent and host control of pathogenesis. *J. Gen. Virol.* 72 (Pt. 3): 595–603.

71 Wang, K. and Deubel, V. (2011). Mice with different susceptibility to Japanese encephalitis virus infection show selective neutralizing antibody response and myeloid cell infectivity. *PLoS ONE* 6 (9): e24744.

72 Snyder-Keller, A., Kramer, L.D., Zink, S., and Bolivar, V.J. (2019). Mouse strain and sex-dependent differences in long-term behavioral abnormalities and neuropathologies after developmental zika infection. *J. Neurosci.* 39 (27): 5393–5403.

73 Brinkmeyer-Langford, C.L., Rech, R., Amstalden, K. et al. (2017). Host genetic background influences diverse neurological responses to viral infection in mice. *Sci. Rep.* 7 (1): 12194.

74 Czuprynski, C.J., Faith, N.G., and Steinberg, H. (2003). A/J mice are susceptible and C57BL/6 mice are resistant to Listeria monocytogenes infection by intragastric inoculation. *Infect. Immun.* 71 (2): 682–689.

75 Schluter, D., Buck, C., Reiter, S. et al. (1999). Immune reactions to Listeria monocytogenes in the brain. *Immunobiology* 201 (2): 188–195.

76 Kulcsar, K.A., Baxter, V.K., Abraham, R. et al. (2015). Distinct immune responses in resistant and susceptible strains of mice during neurovirulent alphavirus encephalomyelitis. *J. Virol.* 89 (16): 8280–8291.

77 Radaelli, E., Castiglioni, V., Recordati, C. et al. (2016). The pathology of aging 129S6/SvEvTac mice. *Vet. Pathol.* 53 (2): 477–492.

78 Morgan, K.T., Johnson, B.P., Frith, C.H., and Townsend, J. (1982). An ultrastructural study of spontaneous mineralization in the brains of aging mice. *Acta Neuropathol.* 58 (2): 120–124.

79 Yanai, T., Masegi, T., Yoshida, K. et al. (1995). Eosinophilic neuronal inclusions in the thalamus of ageing B6C3F1 mice. *J. Comp. Pathol.* 113 (3): 287–290.

80 Akiguchi, I., Pallas, M., Budka, H. et al. (2017). SAMP8 mice as a neuropathological model of accelerated brain aging and dementia: Toshio Takeda's legacy and future directions. *Neuropathology* 37 (4): 293–305.

81 Bronson, R.T., Lipman, R.D., and Harrison, D.E. (1993). Age-related gliosis in the white matter of mice. *Brain Res.* 609 (1–2): 124–128.

82 Bronson, R.T., Sweet, H.O., Spencer, C.A., and Davisson, M.T. (1992). Genetic and age related models of neurodegeneration in mice: dystrophic axons. *J. Neurogenet.* 8 (2): 71–83.

83 Johnson, J.E., Mehler, W.R., and Miquel, J. (1975). A fine structural study of degenerative changes in the dorsal column nuclei of aging mice. Lack of protection by vitamin E. *J. Gerontol.* 30 (4): 395–411.

84 Radovsky, A. and Mahler, J. (1999). Nervous system. In: *Pathology of the Mouse: Reference and Atlas* (eds. R. Maronpot, G.A. Boorman and B.W. Gaul), 445–470. Vienna, IL: Cache River Press.

85 Reichel, W. (1968). Lipofuscin pigment accumulation and distribution in five rat organs as a function of age. *J. Gerontol.* 23 (2): 145–153.

86 Blackwell, B.N., Bucci, T.J., Hart, R.W., and Turturro, A. (1995). Longevity, body weight, and neoplasia in ad libitum-fed and diet-restricted C57BL6 mice fed NIH-31 open formula diet. *Toxicol. Pathol.* 23 (5): 570–582.

87 Brayton, C.F., Treuting, P.M., and Ward, J.M. (2012). Pathobiology of aging mice and GEM: background strains and experimental design. *Vet. Pathol.* 49 (1): 85–105.

88 Treuting, P.M., Linford, N.J., Knoblaugh, S.E. et al. (2008). Reduction of age-associated pathology in old mice by overexpression of catalase in mitochondria. *J. Gerontol. A Biol. Sci. Med. Sci.* 63 (8): 813–822.

89 Wijnhoven, S.W., Beems, R.B., Roodbergen, M. et al. (2005). Accelerated aging pathology in ad libitum fed Xpd^{TTD} mice is accompanied by features suggestive of caloric restriction. *DNA Repair (Amst)* 4 (11): 1314–1324.

90 Ohnishi, T., Sudo, H., Tsujimoto, T., and Iwasaki, N. (2018). Age-related spontaneous lumbar intervertebral disc degeneration in a mouse model. *J. Orthop. Res.* 36 (1): 224–232.

91 Vo, N., Niedernhofer, L.J., Nasto, L.A. et al. (2013). An overview of underlying causes and animal models for the study of age-related degenerative disorders of the spine and synovial joints. *J. Orthop. Res.* 31 (6): 831–837.

92 Vo, N., Seo, H.Y., Robinson, A. et al. (2010). Accelerated aging of intervertebral discs in a mouse model of progeria. *J. Orthop. Res.* 28 (12): 1600–1607.

93 Harkema, L., Youssef, S.A., and de Bruin, A. (2016). Pathology of mouse models of accelerated aging. *Vet. Pathol.* 53 (2): 366–389.

94 Manich, G., Cabezon, I., Auge, E. et al. (2016). Periodic acid-Schiff granules in the brain of aged mice: from amyloid aggregates to degenerative structures containing neo-epitopes. *Ageing Res. Rev.* 27: 42–55.

95 Jucker, M., Walker, L.C., Kuo, H. et al. (1994). Age-related fibrillar deposits in brains of C57BL/6 mice. A review of localization, staining characteristics, and strain specificity. *Mol. Neurobiol.* 9 (1–3): 125–133.

96 Cana, A., Herder, V., Hansmann, F. et al. (2015). Characterization of periodic acid-Schiff-positive granular deposits in the hippocampus of SJL/J mice. *Toxicol. Pathol.* 43 (5): 737–742.

97 Wigley, R.D., Couchman, K.G., and Maule, R. (1970). Polyarteritis nodosa: the natural history of a spontaneously occurring model in outbred mice. *Australas. Ann. Med.* 19 (4): 319–327.

98 Mullane, K. and Williams, M. (2019). Preclinical models of Alzheimer's disease: relevance and translational validity. *Curr. Protoc. Pharmacol.* 84 (1): e57.

99 Webster, S.J., Bachstetter, A.D., Nelson, P.T. et al. (2014). Using mice to model Alzheimer's dementia: an overview of the clinical disease and the preclinical behavioral changes in 10 mouse models. *Front. Genet.* 5: 88.

100 Konnova, E.A. and Swanberg, M. (2018). Animal models of Parkinson's disease. In: *Parkinson's Disease: Pathogenesis and Clinical Aspects* (eds. T.B. Stoker and J.C. Greenland), 83–106. Brisbane (AU): Codon Publications.

101 Jankowsky, J.L. and Zheng, H. (2017). Practical considerations for choosing a mouse model of Alzheimer's disease. *Mol. Neurodegener.* 12 (1): 89.

102 Dawson, T.M., Golde, T.E., and Lagier-Tourenne, C. (2018). Animal models of neurodegenerative diseases. *Nat. Neurosci.* 21 (10): 1370–1379.

103 Drummond, E. and Wisniewski, T. (2017). Alzheimer's disease: experimental models and reality. *Acta Neuropathol.* 133 (2): 155–175.

104 Duff, K., Knight, H., Refolo, L.M. et al. (2000). Characterization of pathology in transgenic mice over-expressing human genomic and cDNA tau transgenes. *Neurobiol. Dis.* 7 (2): 87–98.

105 Ramsden, M., Kotilinek, L., Forster, C. et al. (2005). Age-dependent neurofibrillary tangle formation, neuron loss, and memory impairment in a mouse model of human tauopathy (P301L). *J. Neurosci.* 25 (46): 10637–10647.

106 Santacruz, K., Lewis, J., Spires, T. et al. (2005). Tau suppression in a neurodegenerative mouse model improves memory function. *Science* 309 (5733): 476–481.

107 Yoshiyama, Y., Higuchi, M., Zhang, B. et al. (2007). Synapse loss and microglial activation precede tangles in a P301S tauopathy mouse model. *Neuron* 53 (3): 337–351.

108 Oakley, H., Cole, S.L., Logan, S. et al. (2006). Intraneuronal beta-amyloid aggregates, neurodegeneration, and neuron loss in transgenic mice with five familial Alzheimer's disease mutations: potential factors in amyloid plaque formation. *J. Neurosci.* 26 (40): 10129–10140.

109 Krezowski, J., Knudson, D., Ebeling, C. et al. (2004). Identification of loci determining susceptibility to the lethal effects of amyloid precursor protein transgene overexpression. *Hum. Mol. Genet.* 13 (18): 1989–1997.

110 Breger, L.S. and Fuzzati Armentero, M.T. (2019). Genetically engineered animal models of Parkinson's disease: from worm to rodent. *Eur. J. Neurosci.* 49 (4): 533–560.

111 Braak, H., Muller, C.M., Rub, U. et al. (2006). Pathology associated with sporadic Parkinson's disease--where does it end? *J. Neural Transm. Suppl.* 70: 89–97.

112 Leung, C. and Jia, Z. (2016). Mouse genetic models of human brain disorders. *Front. Genet.* 7: 40.

113 Blesa, J. and Przedborski, S. (2014). Parkinson's disease: animal models and dopaminergic cell vulnerability. *Front. Neuroanat.* 8: 155.

114 Antony, P.M., Diederich, N.J., and Balling, R. (2011). Parkinson's disease mouse models in translational research. *Mamm. Genome* 22 (7–8): 401–419.

115 Lu, X.H., Fleming, S.M., Meurers, B. et al. (2009). Bacterial artificial chromosome transgenic mice expressing a truncated mutant parkin exhibit age-dependent hypokinetic motor deficits, dopaminergic neuron degeneration, and accumulation of proteinase K-resistant alpha-synuclein. *J. Neurosci.* 29 (7): 1962–1976.

116 Lutz, C. (2018). Mouse models of ALS: past, present and future. *Brain Res.* 1693 (Pt. A): 1–10.

117 Morrice, J.R., Gregory-Evans, C.Y., and Shaw, C.A. (2018). Animal models of amyotrophic lateral sclerosis: a comparison of model validity. *Neural Regen. Res.* 13 (12): 2050–2054.

118 De Giorgio, F., Maduro, C., Fisher, E.M.C., and Acevedo-Arozena, A. (2019). Transgenic and physiological mouse models give insights into different aspects of amyotrophic lateral sclerosis. *Dis. Model. Mech.* 12 (1): 1–16.

119 Alrafiah, A.R. (2018). From mouse models to human disease: an approach for amyotrophic lateral sclerosis. *In Vivo* 32 (5): 983–998.

120 Batra, R. and Lee, C.W. (2017). Mouse models of C9orf72 hexanucleotide repeat expansion in amyotrophic lateral sclerosis/frontotemporal dementia. *Front. Cell. Neurosci.* 11: 196.

121 Nolan, M., Talbot, K., and Ansorge, O. (2016). Pathogenesis of FUS-associated ALS and FTD: insights from rodent models. *Acta Neuropathol. Commun.* 4 (1): 99.

122 Nardo, G., Trolese, M.C., Tortarolo, M. et al. (2016). New insights on the mechanisms of disease course variability in ALS from mutant SOD1 mouse models. *Brain Pathol.* 26 (2): 237–247.

123 Tu, P.H., Raju, P., Robinson, K.A. et al. (1996). Transgenic mice carrying a human mutant superoxide dismutase transgene develop neuronal cytoskeletal pathology resembling human amyotrophic lateral sclerosis lesions. *Proc. Natl. Acad. Sci. U.S.A.* 93 (7): 3155–3160.

124 Liu, Y., Pattamatta, A., Zu, T. et al. (2016). C9orf72 BAC mouse model with motor deficits and neurodegenerative features of ALS/FTD. *Neuron* 90 (3): 521–534.

125 Jiang, J., Zhu, Q., Gendron, T.F. et al. (2016). Gain of toxicity from ALS/FTD-linked repeat expansions in C9ORF72 is alleviated by antisense oligonucleotides targeting GGGGCC-containing RNAs. *Neuron* 90 (3): 535–550.

126 O'Rourke, J.G., Bogdanik, L., Muhammad, A. et al. (2015). C9orf72 BAC transgenic mice display typical pathologic features of ALS/FTD. *Neuron* 88 (5): 892–901.

127 Qiu, H., Lee, S., Shang, Y. et al. (2014). ALS-associated mutation FUS-R521C causes DNA damage and RNA splicing defects. *J. Clin. Invest.* 124 (3): 981–999.

128 Sharma, A., Lyashchenko, A.K., Lu, L. et al. (2016). ALS-associated mutant FUS induces selective motor neuron degeneration through toxic gain of function. *Nat. Commun.* 7: 10465.

129 Mitchell, J.C., McGoldrick, P., Vance, C. et al. (2013). Overexpression of human wild-type FUS causes progressive motor neuron degeneration in an age- and dose-dependent fashion. *Acta Neuropathol.* 125 (2): 273–288.

130 Wegorzewska, I., Bell, S., Cairns, N.J. et al. (2009). TDP-43 mutant transgenic mice develop features of ALS and frontotemporal lobar degeneration. *Proc. Natl. Acad. Sci. U.S.A.* 106 (44): 18809–18814.

131 Swarup, V., Phaneuf, D., Bareil, C. et al. (2011). Pathological hallmarks of amyotrophic lateral sclerosis/frontotemporal lobar degeneration in transgenic mice produced with TDP-43 genomic fragments. *Brain* 134 (Pt. 9): 2610–2626.

132 Philips, T. and Rothstein, J.D. (2015). Rodent models of amyotrophic lateral sclerosis. *Curr. Protoc. Pharmacol.* 69: 5.67.1–5.67.21.

133 Arnold, E.S., Ling, S.C., Huelga, S.C. et al. (2013). ALS-linked TDP-43 mutations produce aberrant RNA splicing and adult-onset motor neuron disease without aggregation or loss of nuclear TDP-43. *Proc. Natl. Acad. Sci. U.S.A.* 110 (8): E736–E745.

134 Ditsworth, D., Maldonado, M., McAlonis-Downes, M. et al. (2017). Mutant TDP-43 within motor neurons drives disease onset but not progression in amyotrophic lateral sclerosis. *Acta Neuropathol.* 133 (6): 907–922.

135 Paulson, H.L. (2009). The spinocerebellar ataxias. *J. Neuroophthalmol.* 29 (3): 227–237.

136 Ehrnhoefer, D.E., Butland, S.L., Pouladi, M.A., and Hayden, M.R. (2009). Mouse models of Huntington disease: variations on a theme. *Dis. Model. Mech.* 2 (3–4): 123–129.

137 Chang, R., Liu, X., Li, S., and Li, X.J. (2015). Transgenic animal models for study of the pathogenesis of Huntington's disease and therapy. *Drug Des. Devel. Ther.* 9: 2179–2188.

138 Mangiarini, L., Sathasivam, K., Seller, M. et al. (1996). Exon 1 of the HD gene with an expanded CAG repeat is sufficient to cause a progressive neurological phenotype in transgenic mice. *Cell* 87 (3): 493–506.

139 Schilling, G., Becher, M.W., Sharp, A.H. et al. (1999). Intranuclear inclusions and neuritic aggregates in transgenic mice expressing a mutant N-terminal fragment of huntingtin. *Hum. Mol. Genet.* 8 (3): 397–407.

140 Zhunina, O.A., Yabbarov, N.G., Orekhov, A.N., and Deykin, A.V. (2019). Modern approaches for modelling dystonia and Huntington's disease in vitro and in vivo. *Int. J. Exp. Pathol.* 100 (2): 64–71.

141 Hodgson, J.G., Agopyan, N., Gutekunst, C.A. et al. (1999). A YAC mouse model for Huntington's disease with full-length mutant huntingtin, cytoplasmic toxicity, and selective striatal neurodegeneration. *Neuron* 23 (1): 181–192.

142 Slow, E.J., van Raamsdonk, J., Rogers, D. et al. (2003). Selective striatal neuronal loss in a YAC128 mouse model of Huntington disease. *Hum. Mol. Genet.* 12 (13): 1555–1567.

143 Gray, M., Shirasaki, D.I., Cepeda, C. et al. (2008). Full-length human mutant huntingtin with a stable polyglutamine repeat can elicit progressive and selective neuropathogenesis in BACHD mice. *J. Neurosci.* 28 (24): 6182–6195.

144 Rangel-Barajas, C. and Rebec, G.V. (2018). Overview of Huntington's disease models: neuropathological, molecular, and behavioral differences. *Curr. Protoc. Neurosci.* 83 (1): e47.

145 Pouladi, M.A., Morton, A.J., and Hayden, M.R. (2013). Choosing an animal model for the study of Huntington's disease. *Nat. Rev. Neurosci.* 14 (10): 708–721.

146 Menalled, L.B. and Chesselet, M.F. (2002). Mouse models of Huntington's disease. *Trends Pharmacol. Sci.* 23 (1): 32–39.

147 Ramaswamy, S., McBride, J.L., and Kordower, J.H. (2007). Animal models of Huntington's disease. *ILAR J.* 48 (4): 356–373.

148 Constantinescu, C.S., Farooqi, N., O'Brien, K., and Gran, B. (2011). Experimental autoimmune encephalomyelitis (EAE) as a model for multiple sclerosis (MS). *Br. J. Pharmacol.* 164 (4): 1079–1106.

149 Hollenbach, J.A. and Oksenberg, J.R. (2015). The immunogenetics of multiple sclerosis: a comprehensive review. *J. Autoimmun.* 64: 13–25.

150 Kipp, M., van der Star, B., Vogel, D.Y. et al. (2012). Experimental in vivo and in vitro models of multiple sclerosis: EAE and beyond. *Mult. Scler. Relat. Disord.* 1 (1): 15–28.

151 Baxter, A.G. (2007). The origin and application of experimental autoimmune encephalomyelitis. *Nat. Rev. Immunol.* 7 (11): 904–912.

152 Robinson, A.P., Harp, C.T., Noronha, A., and Miller, S.D. (2014). The experimental autoimmune encephalomyelitis (EAE) model of MS: utility for understanding disease pathophysiology and treatment. *Handb. Clin. Neurol.* 122: 173–189.

153 Blankenhorn, E.P., Butterfield, R., Case, L.K. et al. (2011). Genetics of experimental allergic encephalomyelitis supports the role of T helper cells in multiple sclerosis pathogenesis. *Ann. Neurol.* 70 (6): 887–896.

154 Luckey, D., Bastakoty, D., and Mangalam, A.K. (2011). Role of HLA class II genes in susceptibility and resistance

to multiple sclerosis: studies using HLA transgenic mice. *J. Autoimmun.* 37 (2): 122–128.

155 Bettelli, E. (2007). Building different mouse models for human MS. *Ann. N. Y. Acad. Sci.* 1103: 11–18.

156 Glatigny, S. and Bettelli, E. (2018). Experimental autoimmune encephalomyelitis (EAE) as animal models of multiple sclerosis (MS). *Cold Spring Harb. Perspect. Med.* 8 (11): a028977.

157 Xu, M., Motabar, O., Ferrer, M. et al. (2016). Disease models for the development of therapies for lysosomal storage diseases. *Ann. N. Y. Acad. Sci.* 1371 (1): 15–29.

158 Platt, F.M., d'Azzo, A., Davidson, B.L. et al. (2018). Lysosomal storage diseases. *Nat. Rev. Dis. Primers.* 4 (1): 27.

159 Suzuki, K., Proia, R.L., and Suzuki, K. (1998). Mouse models of human lysosomal diseases. *Brain Pathol.* 8 (1): 195–215.

160 Coutinho, M.F., Lacerda, L., and Alves, S. (2012). Glycosaminoglycan storage disorders: a review. *Biochem. Res. Int.* 2012: 471325.

161 Desnick, R.J. and Schuchman, E.H. (2012). Enzyme replacement therapy for lysosomal diseases: lessons from 20 years of experience and remaining challenges. *Annu. Rev. Genomics Hum. Genet.* 13: 307–335.

162 Elsea, S.H. and Lucas, R.E. (2002). The mousetrap: what we can learn when the mouse model does not mimic the human disease. *ILAR J.* 43 (2): 66–79.

163 Wolf, H., Damme, M., Stroobants, S. et al. (2016). A mouse model for fucosidosis recapitulates storage pathology and neurological features of the milder form of the human disease. *Dis. Model. Mech.* 9 (9): 1015–1028.

164 Fog, C.K. and Kirkegaard, T. (2019). Animal models for Niemann-Pick type C: implications for drug discovery & development. *Expert Opin. Drug Discovery* 14 (5): 499–509.

165 Stinchi, S., Lullmann-Rauch, R., Hartmann, D. et al. (1999). Targeted disruption of the lysosomal alpha-mannosidase gene results in mice resembling a mild form of human alpha-mannosidosis. *Hum. Mol. Genet.* 8 (8): 1365–1372.

166 Zhu, M., Lovell, K.L., Patterson, J.S. et al. (2006). Beta-mannosidosis mice: a model for the human lysosomal storage disease. *Hum. Mol. Genet.* 15 (3): 493–500.

167 Muenzer, J., Lamsa, J.C., Garcia, A. et al. (2002). Enzyme replacement therapy in mucopolysaccharidosis type II (hunter syndrome): a preliminary report. *Acta Paediatr. Suppl.* 91 (439): 98–99.

168 Wilkinson, F.L., Holley, R.J., Langford-Smith, K.J. et al. (2012). Neuropathology in mouse models of mucopolysaccharidosis type I, IIIA and IIIB. *PLoS ONE* 7 (4): e35787.

169 Bhaumik, M., Muller, V.J., Rozaklis, T. et al. (1999). A mouse model for mucopolysaccharidosis type III A (Sanfilippo syndrome). *Glycobiology* 9 (12): 1389–1396.

170 Li, H.H., Yu, W.H., Rozengurt, N. et al. (1999). Mouse model of Sanfilippo syndrome type B produced by targeted disruption of the gene encoding alpha-N-acetylglucosaminidase. *Proc. Natl. Acad. Sci. U.S.A.* 96 (25): 14505–14510.

171 Tomatsu, S., Orii, K.O., Vogler, C. et al. (2003). Mouse model of *N*-acetylgalactosamine-6-sulfate sulfatase deficiency (*Galns*$^{-/-}$) produced by targeted disruption of the gene defective in Morquio A disease. *Hum. Mol. Genet.* 12 (24): 3349–3358.

172 Tomatsu, S., Montano, A.M., Nishioka, T. et al. (2005). Mutation and polymorphism spectrum of the GALNS gene in mucopolysaccharidosis IVA (Morquio A). *Hum. Mutat.* 26 (6): 500–512.

173 Vogler, C., Birkenmeier, E.H., Sly, W.S. et al. (1990). A murine model of mucopolysaccharidosis VII. Gross and microscopic findings in beta-glucuronidase-deficient mice. *Am. J. Pathol.* 136 (1): 207–217.

174 Shacka, J.J. (2012). Mouse models of neuronal ceroid lipofuscinoses: useful pre-clinical tools to delineate disease pathophysiology and validate therapeutics. *Brain Res. Bull.* 88 (1): 43–57.

175 Bond, M., Holthaus, S.M., Tammen, I. et al. (2013). Use of model organisms for the study of neuronal ceroid lipofuscinosis. *Biochim. Biophys. Acta* 1832 (11): 1842–1865.

176 Paton, L., Bitoun, E., Kenyon, J. et al. (2014). A novel mouse model of a patient mucolipidosis II mutation recapitulates disease pathology. *J. Biol. Chem.* 289 (39): 26709–26721.

177 Idol, R.A., Wozniak, D.F., Fujiwara, H. et al. (2014). Neurologic abnormalities in mouse models of the lysosomal storage disorders mucolipidosis II and mucolipidosis III gamma. *PLoS ONE* 9 (10): e109768.

178 Kandratavicius, L., Balista, P.A., Lopes-Aguiar, C. et al. (2014). Animal models of epilepsy: use and limitations. *Neuropsychiatr. Dis. Treat.* 10: 1693–1705.

179 Becker, A.J. (2018). Review: animal models of acquired epilepsy: insights into mechanisms of human epileptogenesis. *Neuropathol. Appl. Neurobiol.* 44 (1): 112–129.

180 Pack, A.M. (2019). Epilepsy overview and revised classification of seizures and epilepsies. *Continuum (Minneap Minn)* 25 (2): 306–321.

181 Loscher, W. (2002). Animal models of epilepsy for the development of antiepileptogenic and disease-modifying drugs. A comparison of the pharmacology of kindling and post-status epilepticus models of temporal lobe epilepsy. *Epilepsy Res.* 50 (1–2): 105–123.

182 Almeida Silva, L.F., Engel, T., Reschke, C.R. et al. (2016). Distinct behavioral and epileptic phenotype differences in 129/P mice compared to C57BL/6 mice subject to intraamygdala kainic acid-induced status epilepticus. *Epilepsy Behav.* 64 (Pt. A): 186–194.

183 Schauwecker, P.E. (2011). The relevance of individual genetic background and its role in animal models of epilepsy. *Epilepsy Res.* 97 (1–2): 1–11.

184 Loscher, W., Ferland, R.J., and Ferraro, T.N. (2017). The relevance of inter- and intrastrain differences in mice and rats and their implications for models of seizures and epilepsy. *Epilepsy Behav.* 73: 214–235.

185 Schauwecker, P.E. (2002). Modulation of cell death by mouse genotype: differential vulnerability to excitatory

amino acid-induced lesions. *Exp. Neurol.* 178 (2): 219–235.

186 Grone, B.P. and Baraban, S.C. (2015). Animal models in epilepsy research: legacies and new directions. *Nat. Neurosci.* 18 (3): 339–343.

187 Wang, J., Lin, Z.J., Liu, L. et al. (2017). Epilepsy-associated genes. *Seizure* 44: 11–20.

188 Demarest, S.T. and Brooks-Kayal, A. (2018). From molecules to medicines: the dawn of targeted therapies for genetic epilepsies. *Nat. Rev. Neurol.* 14 (12): 735–745.

189 King, J.T. Jr. and LaMotte, C.C. (1989). El mouse as a model of focal epilepsy: a review. *Epilepsia* 30 (3): 257–265.

190 Burgess, D.L. and Noebels, J.L. (2000). Calcium channel defects in models of inherited generalized epilepsy. *Epilepsia* 41 (8): 1074–1075.

191 Eisenberg, B. and Messer, A. (1989). Tonic/clonic seizures in a mouse mutant carrying the weaver gene. *Neurosci. Lett.* 96 (2): 168–172.

192 Galanopoulou, A.S. and Moshe, S.L. (2015). Neonatal and infantile epilepsy: acquired and genetic models. *Cold Spring Harb. Perspect. Med.* 6 (1): a022707.

193 Gu, B. and Dalton, K.A. (2017). Models and detection of spontaneous recurrent seizures in laboratory rodents. *Zool. Res.* 38 (4): 171–179.

194 Meisler, M.H., Kearney, J., Ottman, R., and Escayg, A. (2001). Identification of epilepsy genes in human and mouse. *Annu. Rev. Genet.* 35: 567–588.

195 Maxson, S.C. (2017). A genetic context for the study of audiogenic seizures. *Epilepsy Behav.* 71 (Pt. B): 154–159.

196 Upton, N. and Stratton, S. (2003). Recent developments from genetic mouse models of seizures. *Curr. Opin. Pharmacol.* 3 (1): 19–26.

197 Palop, J.J., Chin, J., Roberson, E.D. et al. (2007). Aberrant excitatory neuronal activity and compensatory remodeling of inhibitory hippocampal circuits in mouse models of Alzheimer's disease. *Neuron* 55 (5): 697–711.

198 Minkeviciene, R., Rheims, S., Dobszay, M.B. et al. (2009). Amyloid beta-induced neuronal hyperexcitability triggers progressive epilepsy. *J. Neurosci.* 29 (11): 3453–3462.

199 Johnson, V.E., Meaney, D.F., Cullen, D.K., and Smith, D.H. (2015). Animal models of traumatic brain injury. *Handb. Clin. Neurol.* 127: 115–128.

200 Brady, R.D., Casillas-Espinosa, P.M., Agoston, D.V. et al. (2019). Modelling traumatic brain injury and posttraumatic epilepsy in rodents. *Neurobiol. Dis.* 123: 8–19.

201 Juriloff, D.M. and Harris, M.J. (2000). Mouse models for neural tube closure defects. *Hum. Mol. Genet.* 9 (6): 993–1000.

202 van der Knaap, M.S. and Valk, J. (1988). Classification of congenital abnormalities of the CNS. *AJNR Am. J. Neuroradiol.* 9 (2): 315–326.

203 Greene, N.D. and Copp, A.J. (2005). Mouse models of neural tube defects: investigating preventive mechanisms. *Am. J. Med. Genet. C Semin. Med. Genet.* 135C (1): 31–41.

204 Harris, M.J. and Juriloff, D.M. (2010). An update to the list of mouse mutants with neural tube closure defects and advances toward a complete genetic perspective of neural tube closure. *Birth Defects Res. A Clin. Mol. Teratol.* 88 (8): 653–669.

205 Juriloff, D.M. and Harris, M.J. (2018). Insights into the etiology of mammalian neural tube closure defects from developmental, genetic and evolutionary studies. *J. Dev. Biol.* 6 (3): 22.

206 van Straaten, H.W. and Copp, A.J. (2001). Curly tail: a 50-year history of the mouse spina bifida model. *Anat. Embryol. (Berl.)* 203 (4): 225–237.

207 Kume, T., Deng, K.Y., Winfrey, V. et al. (1998). The forkhead/winged helix gene Mf1 is disrupted in the pleiotropic mouse mutation congenital hydrocephalus. *Cell* 93 (6): 985–996.

208 Lyon, M.F., Quinney, R., Glenister, P.H. et al. (1996). Doublefoot: a new mouse mutant affecting development of limbs and head. *Genet. Res.* 68 (3): 221–231.

209 Rolf, B., Kutsche, M., and Bartsch, U. (2001). Severe hydrocephalus in L1-deficient mice. *Brain Res.* 891 (1–2): 247–252.

210 Cohen, A.R., Leifer, D.W., Zechel, M. et al. (1999). Characterization of a model of hydrocephalus in transgenic mice. *J. Neurosurg.* 91 (6): 978–988.

211 Bronson, R.T. and Lane, P.W. (1990). Hydrocephalus with hop gait (*hyh*): a new mutation on chromosome 7 in the mouse. *Brain Res. Dev. Brain Res.* 54 (1): 131–136.

212 Lindeman, G.J., Dagnino, L., Gaubatz, S. et al. (1998). A specific, nonproliferative role for E2F-5 in choroid plexus function revealed by gene targeting. *Genes Dev.* 12 (8): 1092–1098.

213 Bruni, J.E. (1998). Ependymal development, proliferation, and functions: a review. *Microsc. Res. Tech.* 41 (1): 2–13.

214 Louis, D.N., Perry, A., Reifenberger, G. et al. (2016). The 2016 World Health Organization classification of tumors of the central nervous system: a summary. *Acta Neuropathol.* 131 (6): 803–820.

215 Weber, K., Garman, R.H., Germann, P.G. et al. (2011). Classification of neural tumors in laboratory rodents, emphasizing the rat. *Toxicol. Pathol.* 39 (1): 129–151.

216 Krinke, G.J., Kaufmann, W., Mahrous, A.T., and Schaetti, P. (2000). Morphologic characterization of spontaneous nervous system tumors in mice and rats. *Toxicol. Pathol.* 28 (1): 178–192.

217 Bertrand, L., Mukaratirwa, S., and Bradley, A. (2014). Incidence of spontaneous central nervous system tumors in CD-1 mice and Sprague-Dawley, Han-Wistar, and Wistar rats used in carcinogenicity studies. *Toxicol. Pathol.* 42 (8): 1168–1173.

218 Fraser, H. (1986). Brain tumours in mice, with particular reference to astrocytoma. *Food Chem. Toxicol.* 24 (2): 105–111.

219 Oda, H., Zhang, S., Tsurutani, N. et al. (1997). Loss of p53 is an early event in induction of brain tumors in mice by transplacental carcinogen exposure. *Cancer Res.* 57 (4): 646–650.

220 Kim, Y., Hong, H.H., Lachat, Y. et al. (2005). Genetic alterations in brain tumors following 1,3-butadiene exposure in B6C3F1 mice. *Toxicol. Pathol.* 33 (3): 307–312.

221 Wu, X., Northcott, P.A., Croul, S., and Taylor, M.D. (2011). Mouse models of medulloblastoma. *Chin. J. Cancer* 30 (7): 442–449.

222 Miyai, M., Tomita, H., Soeda, A. et al. (2017). Current trends in mouse models of glioblastoma. *J. Neurooncol.* 135 (3): 423–432.

223 Kijima, N. and Kanemura, Y. (2017). Mouse models of glioblastoma. In: *Glioblastoma* (ed. S. De Vleeschouwer), 131–139. Brisbane (AU): Codon Publications.

224 Simeonova, I. and Huillard, E. (2014). In vivo models of brain tumors: roles of genetically engineered mouse models in understanding tumor biology and use in preclinical studies. *Cell. Mol. Life Sci.* 71 (20): 4007–4026.

225 Fomchenko, E.I. and Holland, E.C. (2006). Mouse models of brain tumors and their applications in preclinical trials. *Clin. Cancer Res.* 12 (18): 5288–5297.

226 Kalamarides, M., Peyre, M., and Giovannini, M. (2010). Meningioma mouse models. *J. Neurooncol.* 99 (3): 325–331.

227 Huse, J.T. and Holland, E.C. (2009). Genetically engineered mouse models of brain cancer and the promise of preclinical testing. *Brain Pathol.* 19 (1): 132–143.

228 Pietsch, T. and Haberler, C. (2016). Update on the integrated histopathological and genetic classification of medulloblastoma - a practical diagnostic guideline. *Clin. Neuropathol.* 35 (6): 344–352.

229 Northcott, P.A., Robinson, G.W., Kratz, C.P. et al. (2019). Medulloblastoma. *Nat. Rev. Dis. Primers.* 5 (1): 11.

230 Eberhart, C.G. (2003). Medulloblastoma in mice lacking p53 and PARP: all roads lead to Gli. *Am. J. Pathol.* 162 (1): 7–10.

231 Noorani, I. (2019). Genetically engineered mouse models of gliomas: technological developments for translational discoveries. *Cancers (Basel)* 11 (9): 1335.

232 Koso, H., Takeda, H., Yew, C.C. et al. (2012). Transposon mutagenesis identifies genes that transform neural stem cells into glioma-initiating cells. *Proc. Natl. Acad. Sci. U.S.A.* 109 (44): E2998–E3007.

233 Reilly, K.M., Loisel, D.A., Bronson, R.T. et al. (2000). *Nf1;Trp53* mutant mice develop glioblastoma with evidence of strain-specific effects. *Nat. Genet.* 26 (1): 109–113.

234 Weiss, W.A., Israel, M., Cobbs, C. et al. (2002). Neuropathology of genetically engineered mice: consensus report and recommendations from an international forum. *Oncogene* 21 (49): 7453–7463.

235 Carroll, S.L. (2016). The challenge of cancer genomics in rare nervous system neoplasms: malignant peripheral nerve sheath tumors as a paradigm for cross-species comparative oncogenomics. *Am. J. Pathol.* 186 (3): 464–477.

236 Williams, K.B. and Largaespada, D.A. (2020). New model systems and the development of targeted therapies for the treatment of neurofibromatosis type 1-associated malignant peripheral nerve sheath tumors. *Genes (Basel)* 11 (5).

22

Eye and Ear

Heather W. Sheppard, Laura J. Janke, Jerold E. Rehg, and Peter Vogel

Anatomy, Histology, and Physiology of the Eye

Evolutionary divergence caused by the domestication of the mouse has not caused drastic changes to the structure of the eye unlike in other domestic species [1]. However variations in the size parameters of eye structures and pigmentation among different strains of mice have been documented, and this variation between inbred strains should be taken into account when conducting morphologic phenotyping [2]. Knowledge of the embryology and anatomic organization of the mouse eye is essential for understanding normal development and physiology and how to approach the characterization and description of any potential lesions in prenatal, neonatal, juvenile, and adult mice. The eye is derived from a combination of surface ectoderm (cornea, lens), mesoderm (cornea, sclera, and uvea), and neuroectoderm (retina) [3]. A detailed review of the embryology of the eye is beyond the scope of this chapter, and Kaufman provided an excellent review, with detailed lineage diagrams and references describing the morphologic and molecular details of mouse eye development [3].

The outermost layer of the eye includes the anterior cornea, the transitional limbus zone, and the sclera. The sclera maintains the overall shape of the eye. Unlike the vision-specific cornea, this structure is opaque in appearance and connects with extraocular structures, including the extraocular eye muscles that facilitate eye movements. The sclera also contacts the dura matter at the entry point of optic nerve through the posterior scleral foramen. Both the cornea and the sclera are composed mostly of type I collagens in the mouse and human [4]. In contrast to the sclera, the cornea is a translucent structure derived from cranial ectoderm. It consists of a cornified, stratified epithelial layer that is approximately 4–6 cell layers in thickness, which is supported by a thin, acellular basal lamina comparable with Bowman's membrane in other mammals. The corneal stromal layer, which is a mesenchymal structure derived from periocular neural crest, is immediately beneath this membrane, and it is an avascular structure that is composed of multiple layers of uniform type I and type V collagen fibers and scattered keratinocytes [4]. Descemet's membrane is located immediately below the stromal layer. It is covered by a monolayer of corneal endothelium, which produces Descemet's membrane and engages in the active transportation of fluids and electrolytes that are essential for maintaining corneal transparency for light conductance [4].

The iris is a complex structure consisting of an outer bilayer of pigmented epithelium derived from embryonic neuroepithelium and a supporting fibrovascular stromal component that is derived from mesodermal neural crest [3]. The iris delineates the anterior and posterior eye chambers. The stroma contains dendritic melanocytes, capillaries, collagen, and extracellular matrix [5]. Eye color is determined by the relative numbers of melanocytes within the stroma. The gene named, oculocutaneous albinism II (*Oca2*, originally called *p*), is responsible for varying degrees of eye pigmentation and dilution depending on the allelic mutation and genetic background. A common mutant of the 72 allelic mutations that are described at this locus, *Oca2p*, is associated with reduced pigmentation and ocular albinism (*p/p*) [6, 7]. The ABJ/Le stock (#000004) carries this mutation [8]. Mice having eyes with two different colors also have been described (i.e. heterochromia iridis) [9]. A thin smooth muscle sphincter that regulates pupillary contraction is located at the pupillary border between the pigmented epithelium, from which it is derived, and the stroma. The junction between the iris and the cornea is referred to as the anterior chamber angle. This region contains a trabecular meshwork of collagen and elastic fibers that are lined by endothelium. The trabecular meshwork mediates the passive outflow of aqueous humor, which regulates intraocular pressure. Schlemm's canal connects the aqueous outflow to a series of episcleral veins that connect to the systemic vasculature [5].

The ciliary body lies directly behind the iris and is composed of a fibrovascular stroma called the ciliary processes that are covered by single layers of non-pigmented and pigmented epithelium. The ciliary processes connect to and suspend the lens by zonular fibers that may not always be apparent in histologic sections. A rudimentary ciliary muscle is visible in the mouse. The ciliary body is the site of

Pathology of Genetically Engineered and Other Mutant Mice, First Edition. Edited by John P. Sundberg, Peter Vogel, and Jerrold M. Ward.
© 2022 John Wiley & Sons, Inc. Published 2022 by John Wiley & Sons, Inc.

aqueous humor production [5]. Both the non-pigmented and pigmented epithelial layers of the ciliary body connect to the peripheral retina at the posterior aspect of the ciliary body. The pigmented ciliary epithelium is continuous with the retinal pigmented epithelium, while the non-pigmented epithelium merges with the sensory retina, with which it shares a common embryonic origin. The retina is organized into morphologically distinguishable layers in the mouse, which are often altered with retinal degeneration phenotypes. The outer nuclear layer is normally thicker than the inner nuclear layer, and early or mild retinal degeneration should be suspected if the outer nuclear layer is the same thickness or thinner than the inner nuclear layer. Bruch's membrane separates the retinal pigmented epithelium from the choroid, which directly contacts the sclera [5]. Albino mouse strains have no differences in retinal anatomy from pigmented mice except for a lack of melanosomes [10].

Astrocytes, microglia, and Müller cells provide homeostatic and metabolic support, direct the innate immune response, and aid in tissue repair functions within the retinal microenvironment. Macrophages and microglia are important for both physiological and pathological retinal angiogenesis. These populations are immunoreactive for F4/80 and OX42 and have a round or ameboid appearance with pseudopodial processes when immunolabeled [11]. Microglia localize near the vasculature within the inner plexiform layer (IPL), outer plexiform layer (OPL), and ganglion cell layers (GCLs) and are also closely associated with Müller cells. Müller cells are a specialized type of glial cell that extend radially across the length of the retina. Their cell bodies are present within the inner nuclear layer, with processes that extend out into the outer limiting membrane to form type junctions with the photoreceptors. Microglia clear cellular debris in the retina and increases in tangible body profiles within the inner or outer segments of the photoreceptors are consistent either with a physiological developmental change or are indicative of retinal degeneration in adult mice. Likewise, impairment of phagocytosis can result in an autoimmune disease [11]. Ganglion cells are few in number in the peripheral retina and become more numerous in the central retina, where the nerve fiber layer is visible and connects with the optic nerve, which traverses the lamina cribrosa, and connects with the central nervous system. The mouse retina possesses the typical rod scotopic and cone photopic systems for vision. Mice express S and M opsins that form visual pigments for the detection of light and visual signaling in cones, and there are strain dependent differences in opsin expression [12]. The visual system of the mouse is dichromatic, which is typical of nonprimate mammals [10]. Furthermore, mice lack a macula lutea and fovea, which is correlated with high-acuity color vision in primates [13].

A lens capsule surrounds lens epithelium, which produce the primary and secondary lens fibers forming the bulk of this structure. Lens fibers are composed of actin microfilaments to facilitate changes to shape for accommodation and for maintaining cell contacts [14]. Lens fibers also contain beaded filaments and crystallin proteins that help to maintain optical transparency for light conductance [15]. Zonular fibers arising from the pars plana and pars plicata of the ciliary body connect to the lens to hold it in place along with pressure from the posterior vitreous. Zonular fibers also assist shape accommodation of the anterior and posterior faces. As a whole the lens is not as metabolically active as other tissues. The aqueous humor and vitreous provide metabolites and ions and dispose of wastes through transport gradients controlled by lens cells [16].

Optic Nerve

Cranial nerve II, the optic nerve, develops from the growth of the retinal ganglion neuronal axons through the embryonic optic stalk to contact the developing brain structure [3]. The optic nerve contains neuroglial populations, with the exception of Schwann cells, and is surrounded by meninges. This structure is considered part of the central nervous system and connects each eye with the brain as it extends caudally through the orbit into the optic canals of the sphenoid bone along the ventral aspect of the brain stem at the optic chiasm to connect to the visual system [17].

Lids and Ocular Adnexa

The external surface of the eyelid is covered by haired skin with modified folliculoadnexal structures. The eyelids are lined by specialized hairs (cilia) produced by the folliculosebaceous units located near the ocular mucocutaneous junctions. Tarsal glands are associated with the eyelid cilia. Mucocutaneous junctions consisting of the bulbar and palpebral conjunctiva are areas of transition between the eyelids and the ocular structures [4]. Lymphoid follicles can be seen in the conjunctiva of older mice and are the result of antigenic stimulation. Meibomian glands are modified pilosebaceous glands that produce a lipid secretion that is essential to tear film formation and for maintaining hydration of keratinocytes on the lens. Lesions occurring to the eyelids, conjunctiva, and ocular adnexal structures can result in lesions affecting the cornea and anterior eye chambers with progression to more diffuse involvement of other ocular structures if the lesions are allowed to persist or are left untreated.

Gross Phenotyping Screen

Phenotyping should begin with a clinical examination and gross review of eye structures when possible. Eyelids and eyelid margins should be examined for conformation, movement, masses, or abnormally placed cilia, since all of these abnormalities can result in corneal irritation or exposure keratitis. Entropion is the inward rolling of the eyelid margin, while ectropion is the outward gaping of the eyelid margin that is often caused by skin laxity. Eyelash anomalies such as ectopic cilia (distichiasis) or misplacement of cilia (trichiasis) should be documented. The nictitating membrane should be elevated and examined by retropulsing the

globe through the upper eyelid. The palpebral and bulbar conjunctiva, sclera, and nictitating membrane should be evaluated for color, thickness, inflammation, foreign bodies, masses, and other abnormalities. The periocular regions and orbit should be visually examined and palpated for abnormalities including masses or other swellings. Periocular alopecia should also be recorded when present. The use of dry weights of ocular tissues to detect lesions, like edema, is prone to technical errors and not recommended as part of a standard phenotyping screen.

There are three main components that are essential to visual function in mice: the assessment of optic function, photoreceptor function, and nerve conductance. The optic function is reliant upon the transparency of cornea, aqueous humor, iris, lens, and vitreous humor for the conductance of visible light energy. The photoreceptors of the retina (rods and cones) undergo photolysis to convert light energy into electrical signals. The optic nerve then carries these signals to the visual cortex within the central nervous system. Several methods can be used to survey visual function at these three key points.

Optic Function Evaluations

Following a gross examination and clinical evaluation tear film formation should be measured by the Schirmer tear test or phenol red thread test (PRTT) before the application of any additional stains [18, 19]. The cornea is transparent with a smooth surface. Most corneal lesions have combinations of cloudiness and loss of clarity and/or changes in the corneal thickness that should be recorded. Evaluations of the corneal tear film and corneal epithelial integrity can then be performed by application of corneal vital stains including sodium fluorescein, rose bengal, or lissamine green [18]. Fluorescein staining of the cornea is more commonly used to visually assess for corneal epithelial damage and epithelial and endothelial permeability indicative of corneal erosions or ulcerations [18, 20]. Additionally, this stain can be used to determine if there are obstructions within the nasolacrimal drainage system, which may affect tear film formation and drainage. Fluorescein staining can also be used in applanation tonometry to measure intraocular pressure and to study retinal circulation [21].

Slit lamp biomicroscopy of the cornea is used to detect subtle gross lesions that may be missed on a physical visual examination [22]. Assessments of corneal curvature topography (keratometry) can also be performed [23]. Changes in intraocular pressure can cause stroma edema that thickens the cornea and results in a cloudy appearance on gross examination. There are three methods for measuring intraocular pressure (IOP): (i) digital palpation, (ii) indentation, and (iii) applanation, which uses fluorescein [24–26]. Measurements of the IOP of at least 30 different mice strains result in a reproducible range of 10–20 mmHg based on a diurnal pressure variation, which is comparable with humans. However, increased age and specific conditions, such as stress or having certain mutations in either the leptin receptor gene (*Leprdb*) or tyrosinase gene (*Tyrc*$^{-2}$*J*), result in higher IOPs. Interestingly the presence of pigmented macrophages at drainage angles is not correlative with increases in IOP [27]. The blood–aqueous barrier can be assessed by injecting Evan blue dye intravenously and measuring the aqueous humor concentration [28].

Posterior Eye Examination

Pharmacologic dilation of the pupil and examination by either direct or indirect ophthalmoscopy allows for examination of the fundus (e.g. vitreous, retina, choroid, and optic nerve) and the detection of specific conditions such as hemorrhage, cataracts, neoplasia, or other lesions. The vitreous is examined for clarity. Changes in retinal transparency (e.g. edema, infiltrates, hemorrhage, pigmentation), position (e.g. detachment, masses, colobomas), and vasculature (e.g. tortuosity, dilations) should be evaluated. The size, shape, and color of the optic nerve head should be recorded. Published photography of normal findings and pathologic changes of the mouse fundus are available [29, 30].

Photoreceptor Function Evaluations

Electroretinography and visually evoked occipital response (e.g. electroencephalogram) are specialized physiological tests of the functional integrity of the retina [31, 32].

Special Necropsy Organ Protocols

Collection

The eyes and associated extraocular structures can be sampled in a number of ways depending on the structures of interest and the design of the study. For initial morphologic phenotyping of mice, the revised guides for organ sampling and trimming in rats and mice can be used to ensure a standardized approach to the collection and review of all intra- and extraocular structures [33, 34]. This approach requires the total exenteration of the eye from the socket together with the optic nerve, eyelid, and the Harderian glands and other orbital supporting tissues after the whole head has been fixed. Alternatively, the eyes and associated structures may be left *in situ* in the fixed whole head with either coronal, sagittal, or transverse sections being made on decalcified samples. This latter method is preferred, especially for embryos, neonates, and weanling mice.

The eyes may also be dissected unfixed at the time of necropsy. However, handling unfixed ocular tissues is not recommended because it often causes tissue artifacts, especially in the retina and optic nerve. Sections of fixed embedded eyes are preferred in both research and diagnostic ophthalmic pathology because morphology is better preserved and pathologists are familiar with these types of sections, and also because of the inherent small size of eye and its associated structures. Frozen sections may be indicated for specific study needs, but this is not common. Excellent technical resources describing specialized techniques for the visualization and molecular analysis of specific eye components are available, including Smith et al. [35, 36].

Fixation and Decalcification

Whole body perfusion of the mouse is recommended at the time of necropsy for optimal preservation of all tissues. The eye tissues should be placed immediately into fixative for at least 24 hours at room temperature followed by storage in 70% ethanol until tissue processing and embedding can be performed. Unlike other larger animal species, fixative does not need to be injected into the mouse eye nor does the eye need to be opened to allow for penetration of the fixative because of its small size. A variety of different fixatives can be used for the eye, but Davidson's fixative is optimal for preserving retinal morphology. Nevertheless, for routine evaluation the use of 10% neutral buffered formalin or 4% paraformaldehyde is sufficient to preserve morphology for the detection of most lesions. If immunohistochemistry or molecular assays are needed downstream of the pathologic analyses, then the fixed tissues should be tested for any loss of or changes to antigenicity with any developed protocols. Changes to antigenicity or epitope loss are also possible if the eyes are left *in situ*, necessitating that the tissue be decalcified.

Tissue Processing and Sectioning – Paraffin Embedded Samples

Eye tissues can be processed as either paraffin or plastic sections or for electron microscopy. This subsection focuses on sectioning and processing for paraffin embedded samples, which is the most common method for specimen handling in research settings. If removed from the head, the eye should be sectioned in a vertical longitudinal plane through the optic nerve. The use of embedding molds helps to better orient and trim enucleated mouse eyes. Specific anatomic locations can be marked with indelible tissue ink.

Interpretation of Eye Sections

The anatomic structures of the eye are intimately related in proximity and interdependence on each other's functions. As a result, there is rarely an isolated lesion within an eye, and a detailed description of all morphologic changes affecting various eye components is useful for elucidating the pathogenesis of the disease in question. Careful examination of all structures is important because even subtle changes within the eye, such as the presence of thin fibrovascular membranes in the anterior chamber, may not be striking or involve large regions of the eye structures, but have very significant functional effects, and should be included in any morphologic description. An INHAND guide is available to facilitate a consistent description of ocular lesions [37].

Eye disease resulting from spontaneous disease or caused by an experimental manipulation can be a common reason for the removal of animals from a study. Congenital malformations and trauma to intraocular structures and secondary ocular infections are the cause for many well-described eye lesions in mice. However, metastatic neoplasia, systemic diseases, and central nervous system lesions can also result in ocular disease. Lesions in the central nervous system can be associated with related ocular disease. Hematoxylin and eosin (HE) stained sections are sufficient for the morphologic evaluation of the eye. Special stains like periodic acid–Schiff (PAS), Luxol fast blue, and Cresyl violet may be used to evaluate the optic nerve for lesions. PAS staining is also useful for evaluating Descemet's membrane and the lens capsule in conjunction with a HE stain. Pigmented mouse strains may have severe ocular melanosis and require bleaching of the eye section. The evaluation of eye sections should begin with the cranial structures, including the conjunctiva and cornea, progressing to caudally to the retinal and optic nerve, and end with an examination of extraocular structures and the orbit. Likewise, ocular diseases are commonly described by anatomic location and can be categorized by common morphologic features as follows:

Description/Lesions of the: Globe (as a Whole)

Changes to the size of one or both eyes should be recorded. Microphthalmia is a common background lesion in certain mouse strains, like the C57BL [38]. Anophthalmia is considered to be an extremely rare event that indicates eye development stopped at a very early stage in one or both eyes (Figures 22.1 and 22.2). Most cases of anophthalmia may be severe forms of microphthalmia, so this diagnosis should not be made without the histologic evaluation of the eyes in the context of the whole head to ensure that rudimentary ocular structures are truly absent. A key example is the anophthalmic mouse mutant called *eyeless* (*Raxey1*), retina and



Figure 22.1 Age-matched E13.5 littermates, in which the mouse on the right has a genetic modification that yields craniofacial defects, including anophthalmia, that is lethal at birth.



Figure 22.2 Histologic section of affected E13.5 embryo in Figure 22.1, which lacks rudimentary eye structures confirming that there is a true anophthalmia phenotype.

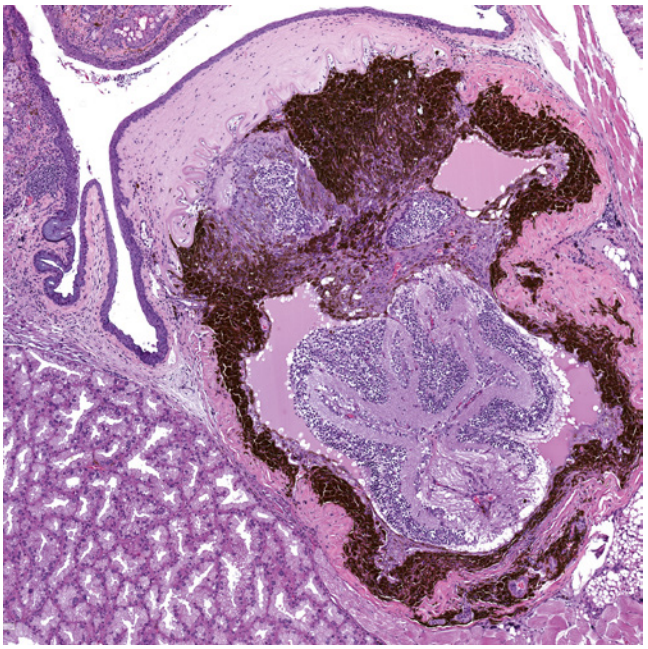


Figure 22.3 Phthisis bulbi resulting from a chronic, severe uveitis in a C57BL/6 mouse. Subgrossly, the eye is markedly shrunken and the cornea is markedly thickened by increased collagen deposition. There is midstromal corneal neovascularization. Portions of the bulbar and palpebral conjunctiva are inflamed (top left corner). All intraocular structures are distorted and disorganized, and there is abundant intraocular fibrosis. The lens is absent.

anterior neural fold homeobox; eyeless (i) that was identified by Herman Chase. This mutant also had severe microphthalmia as a phenotype [39]. Colobomas are a less severe congenital defect where there is failure of closure of the optic fissure resulting in outpouchings of pigmented structures such as the retina and optic nerve, which will appear grossly as regions of scleral ectasia. Choroid hypoplasia is an associated defect. Colobomas in mice are associated with mutations in coloboma deletion region (*Cm*), which is a heritable phenotypic marker [40, 41]. Phthisis bulbi (Figure 22.3) is another change to eye size that may also be the result of end stage lesions caused by a chronic pathoetiology such as trauma, chronic uveitis (Figure 22.3), persistent hyaloid vasculature, or Harderian gland lesions (Figure 22.4) and can be viewed in any strain. Microscopically the globe will be reduced in size with disorganization of optic structures and intraocular fibrosis. Changes to the overall size and structure of the eye affects tear duct secretions and spreading, and keratoconjunctivitis and secondary bacterial infections are common sequela [42].

Ocular Adnexa and Eyelids

Abnormalities affecting the Meibomian glands can affect tear film formation and result in conjunctival and corneal lesions. Chalazion describes a sterile, granulomatous inflammation directed towards the lipid secretions of the Meibomian gland. Lipid secretions within macrophages can be observed under polarized light. Blepharitis and conjunctivitis may be the result of either acute or chronic inflammation of the eyelids and bulbar and palpebral conjunctiva

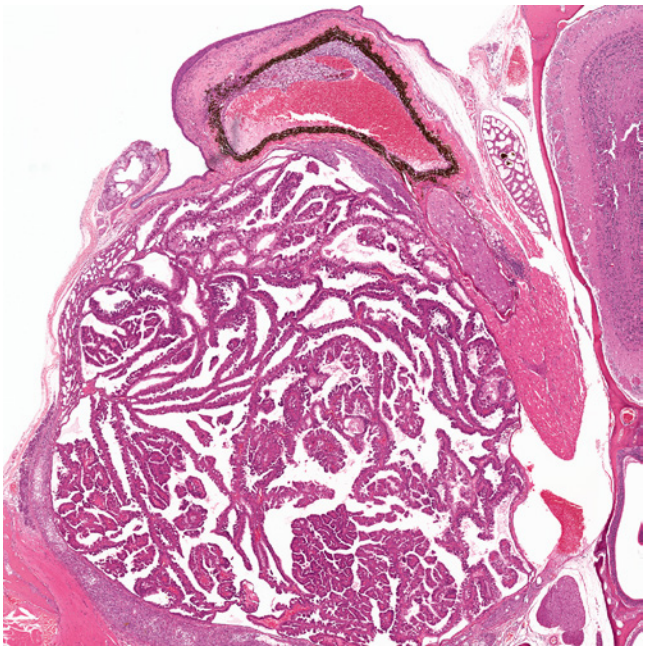


Figure 22.4 Phthisis bulbi resulting from the compression of the globe by an adjacent Harderian gland papillary adenocarcinoma in a one-year-old FVB mouse.

from a number of etiologies. Gross lesions consist of watery discharge that may become mucopurulent with chronicity or as a result of secondary bacterial infections. Histologically these lesions are characterized by increases in immune infiltrates, thickening of or erosion, or ulceration of mucocutaneous regions, and serocellular debris. Bacterial colonies may be present. Keratoconjunctivitis sicca is a sequela. Several strains with high incidence of this lesion include 129P3/J, A/HeJ, BALB/cJ, BALB/cByJ, and CBA/J [43]. Eyelids opened at birth are abnormal in mice. Grossly and histologically, there is an exposure keratitis characterized by corneal epidermal erosions and/or ulcerations. The corneal stroma is thickened due to stromal immune infiltrates, edema, and neovascularization. Blepharoconjunctivitis and secondary opportunistic bacterial infections are common when there is precocious opening of the eyelids. Abnormal eyelid development or development failure is associated with a spontaneous mutation in open eyelids 2 (protein phosphatase 1, regulatory subunit 13 like, *Ppp1r13lwoe2*). Failure of embryonic eyelid closure arising spontaneously has been described for mice on a mixed C57BL/6X129/SvJ background [44]. The A/J strain also has an increased incidence of cleft lip and palate, open eyelid, and embryonic death associated with the precocious eyelid phenotype [45].

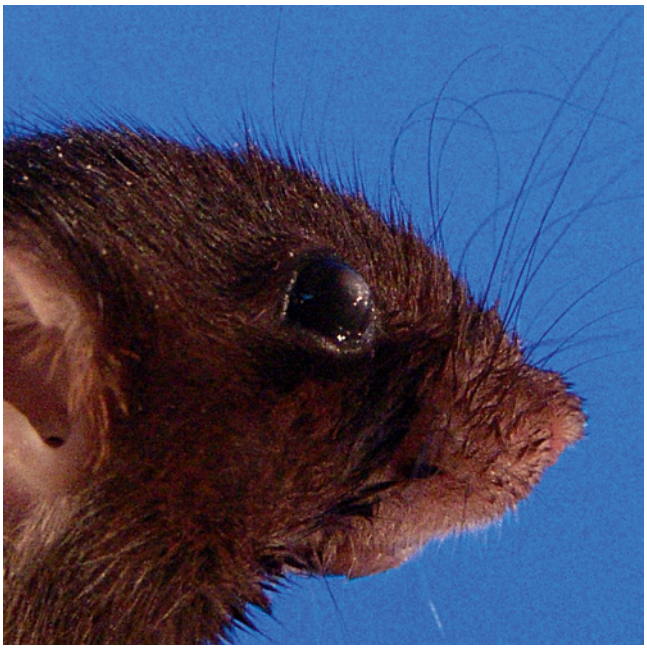


Figure 22.5 Corneal opacity in a C57BL/6 mouse arising from keratoconjunctivitis sicca caused by an experimental manipulation.

Anterior Segments Including the Conjunctiva, Cornea, Iris, and Ciliary Body

Morphologic lesions affecting the cornea should be described for the epithelium, stroma, and Descemet's membrane. The corneal epithelium should be 4–6 cell layers in thickness. Corneal opacities (Figure 22.5), including dystrophy or mineralization, are commonly observed in certain inbred strains including DBA/2 (29.1%), C3H (16.2%), CF1 (16.2%), BALB/c (10.0%), and C57BL/6 (4.1%), and some of these phenotypes are caused by mutations in *Abcc6*, *Enpp*1, and other genes associated with ectopic mineralization [46, 47]. Opacity of the cornea is also suggestive of a healed wound from a previous microtrauma. Decreases in layer thickness are suggestive for erosions and an absence of epithelium over a region of stroma is consistent with ulceration (Figure 22.6). Ulcerations progressing to the level of Descemet's membrane are considered to be deep ulcers. Therefore, the observation of reduplication or branching of Descemet's membrane is most consistent with a penetrating wound and changes should be expected in the corneal stroma and anterior chamber. Increases in clear space within the stroma correlate with edema. Immune cell infiltrates are not presence in the stroma and their presence should be diagnosed as keratitis. Likewise, neovascularization is considered to be abnormal and indicates a previous trauma and wound healing has occurred.

Changes within the anterior chamber of the mouse could be present as a result of penetrating corneal lesions, trauma, or from intraocular or systemic disease-causing inflammation. Abnormal wound healing responses to this inflammation

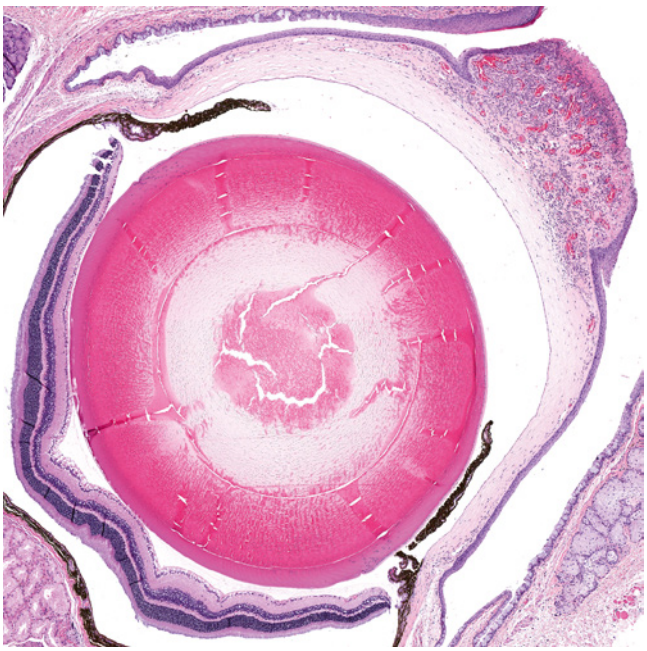


Figure 22.6 Healing corneal ulceration in a C57BL/6 mouse. Superficially the corneal epithelium is ulcerated and lined by serocellular debris. This ulcerated region is underlain by extensive stromal neovascularization, increased clear space representing edema, infiltrating immune cells and granulating fibrosis, which all together thickens the cornea subgrossly to create a distinct mass that reduces the opacity of this structure if viewed grossly (Figure 22.5). Intraocular structures are unaffected.

including altered angiogenesis and the formation of fibrovascular membranes will develop along the surfaces of the iris leaflets, drainage angles, and anterior lens are a common morphologic lesion [48]. Adhesion of the iris to other anterior chamber structures by fibrovascular membranes is called synechiae. Adherence to the cornea is referred to as peripheral anterior synechiae while adherence of the iris to the lens is called posterior synechiae. Forward folding of the iris leaflet upon itself from synechiae formation is called ectropion uvea while post-iridial fibrovascular membrane formation and folding backwards of the leaflet into the posterior eye is referred to as entropion uvea. Immune infiltrates (anterior uveitis), hemorrhage (hyphema), or acellular amphophilic material consistent with fibrin may be observed in the anterior chamber. Sometimes the corneal endothelium will become detached as a result of tissue handling and sectioning, and this should be distinguished from fibrovascular membrane formation due to inflammation. However, displacement of endothelium from Descemet's membrane may result in enhanced proliferation and endothelialization within the anterior chamber that blocks the drainage angle leading to glaucomatous lesions.

The trabecular meshwork may or may not be viewable in the eye depending on the section but should be free of debris and fibrous membranes. Low numbers of phagocytic cells are normally visible in the drainage angles and within the iris stroma and around the iris sphincter and near its root, and these cells may also contain melanin pigment depending upon the strain. Certain strains, like the DBA/2J mouse, may have ocular melanosis (Figure 22.7). This finding is characterized by the diffuse infiltration of large-sized pigmented cells within the iris and ciliary body with variable extension into the choroid and episcleral tissues. Glaucoma (Figure 22.8) is a common, age-related sequela [49, 50]. Glaucoma is a common lesion that develops from the blockage of the trabecular meshwork and Schlemm's canal and affects most segments of the eye especially in the later stages of this disease. Glaucoma is classified broadly as either congenital or acquired. Open angle, angle closure, and pigment-associated forms in mice are described and referenced in Tables 22.2 and 22.3.

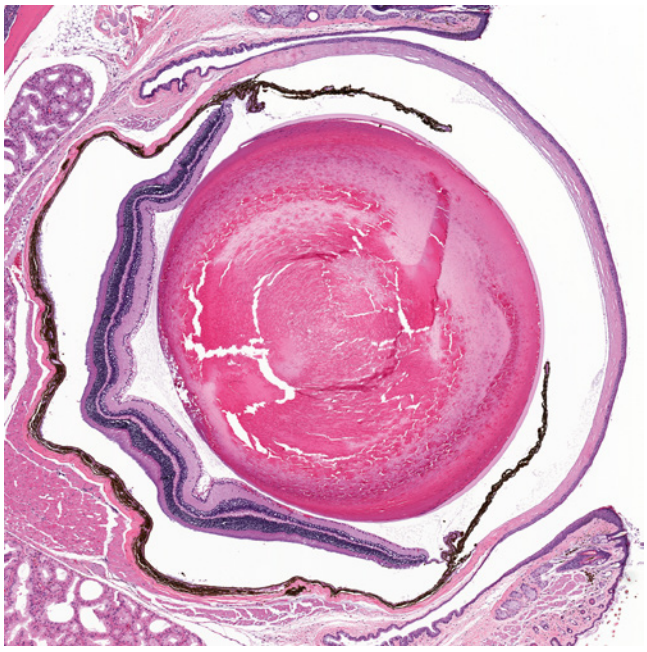


Figure 22.7 Ocular melanosis in the eye of a C57BL/6 mouse with no notable findings.

Lens

Focal and diffuse opacities within the lens that can be observed either grossly or histologically are described as cataracts. Histologically lenticular fibers may appear disrupted and displaced by variably sized and irregular globular eosinophilic aggregates called Morgagnian globules. Lens epithelial cells that appear swollen and have an abundant eosinophilic vacuolated cytoplasm are termed bladder cells. Alternatively, lens epithelia may undergo fibrous metaplasia and become spindle-shaped and separated by fine collagen fibers. Disruption and degradation of the lens can induce the

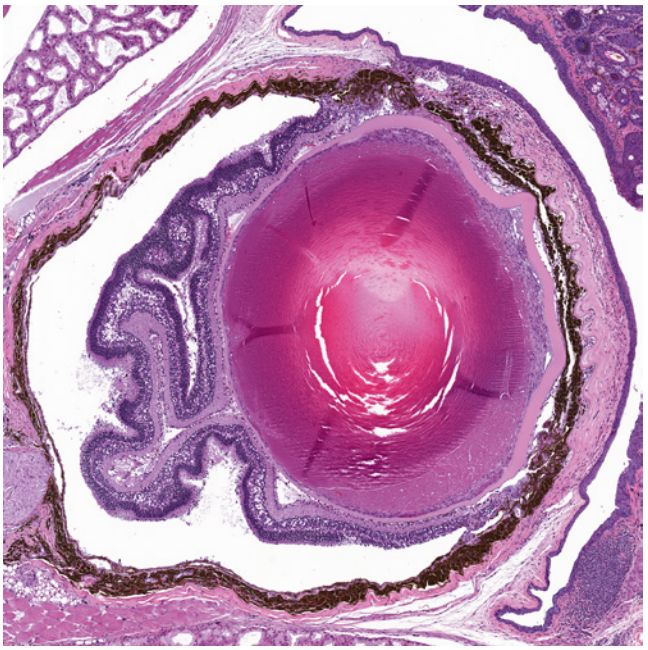


Figure 22.8 Pigment-associated glaucoma in an aged C57BL/6 mouse. There is a diffuse keratitis with stromal neovascularization and immune cell infiltration. Synechia adhere the lens to Descemet's membrane. There is drainage angle blockage and collapse caused by fibrovascular membrane formation. Cataractous changes are visible in the image including epithelial hyperplasia of the lens with fibroblastic metaplasia, formation of bladder cells and Morgagnian globules. There is a widespread dispersion of pigment and pigmented cells throughout the anterior chamber. There is also probable retinal detachment as evidenced by the presence of fibrovascular membranes adhering portions of the retina to the posterior lens capsule with concurrent hypertrophy of the retinal pigmented epithelium.

formation of fibrovascular membranes in the anterior chamber that result in the attachment of the iris to the lens, which is termed posterior synechia. Cataracts may be subclassified by location within the lens. Cataractous changes confined to the central portion of the lens are nuclear cataracts while lesions involving the lenticular surface are called cortical cataracts. Lesions arising on the posterior surface under the capsule are called posterior capsular cataracts. Cataracts in mice can be congenital, from spontaneous mutations, occur in conjunction with glaucoma (Figure 22.8), or be age-related when not associated with any particular experimental manipulation [71].

Posterior Segments in Cluing the Vitreous, Choroid, Retina, and Optic Nerve

The posterior chamber and vitreous should be free of any cellular debris. However, pigmented cells may be present when there is ocular melanosis. Degeneration of the retina is most commonly observed as a thinning of the photoreceptor layer of the outer retina that may be segmental or diffuse in anatomic distribution (Figure 22.9). Retinal degeneration that is associated with phototoxicity, especially in albino mice, will show initial lesions within the rod outer segment disks followed by degeneration and loss of the entire photoreceptor layer. Later stage lesions often show full thickness loss of the retinal layering closest to the optic disc with relative sparing of the interior portions of the retina. Additionally, fibrous connective tissue may form between the vitreous and the degenerating retina in long-standing phototoxicity lesions [72]. In contrast, retinal degeneration associated with glaucoma will more typically result in a diffuse thinning caused by atrophy and degeneration of all retinal layers due to the progressive increase in intraocular pressure. Scleral thinning may also occur with retinal thinning when glaucoma is the underlying cause. In contrast, retina dysplasia (Figure 22.10) is a congenital malformation that is morphologically characterized by the disorderly differentiation of the retinal layers that appear folded with rosette formation or atrophied with a blending of the inner and outer layers. Degeneration is also a common finding that is associated with dysplasia. Artifactual detachment of the retina may mimic morphologic changes that are similar to retinal dysplasia, but the retinal layers will retain organization and degeneration should be absent. Artifactual versus true retinal detachment is important to discern, especially if there are other ocular lesions. True retinal detachment is characterized by the separation of the retinal layers from the retinal pigmented epithelium, which will have a plump, hypertrophied appearance that is often described as "tombstoning" (Figure 22.8). Retinal and choroidal vessels may have a hyalinized appearance, and this is indicative of systemic vascular disease.

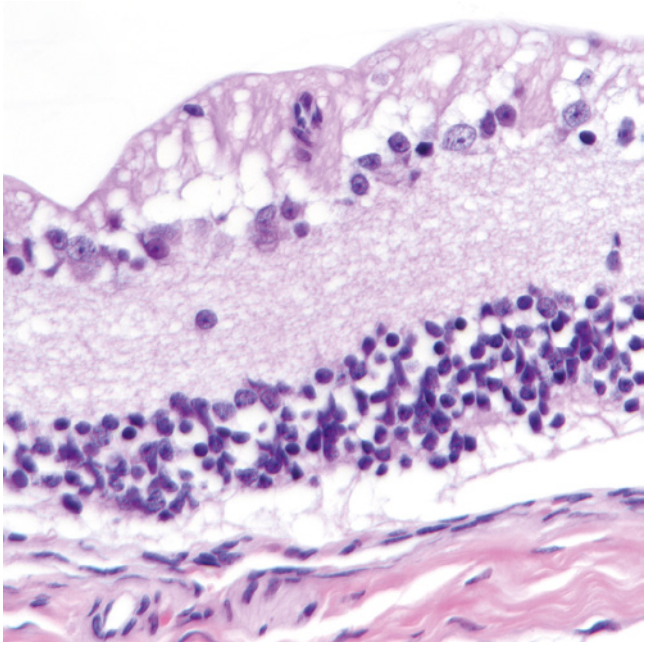


Figure 22.9 Retinal degeneration in a Swiss Webster outbred model from the Rockefeller Institute through Rockland Farms, Inc. known to carry the recessive mutation, Pde6b^{rd1}.

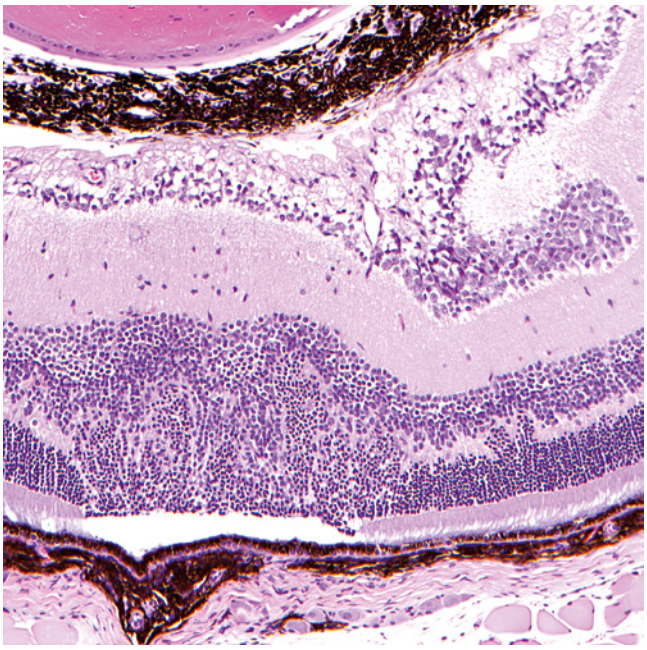


Figure 22.10 Retinal dysplasia. There is disorderly differentiation, blending and folding of the outer and inner retinal layers. Pigmented fibrovascular tissue connects the dysplastic retina to the posterior lens capsule.

Neoplasia

Neoplasia is an uncommon spontaneous lesion. Proliferative lesions and neoplasms of the Harderian and lacrimal glands occurring at increasing frequencies in aged mice are correlated with the development of exposure keratitis or the development of phthisis bulbi (Figure 22.4) [73]. Metastatic

neoplasia, such as lymphoma, may occur, especially in older mice in the uveal tract. However primary intraocular neoplasms are extremely rare in mice, although ocular melanoma has been reported as a spontaneous lesion in aged B6C3F1 mice (0.03%) [74]. Ocular melanosis and the accumulation of pigmented cells within the anterior chamber and at the level of the drainage angles, or when the uvea, choroid, limbal sclera, and episcleral, are markedly thickened by pigmentary cell infiltrates. However, this is a distinct and well-characterized lesion that is not considered to be pre-neoplastic.

Spontaneous Mutations Associated with Strain-Specific Eye Lesions

The effects of spontaneous or age-related lesions may result in unanticipated ocular effects that could confound the conclusions of a study. Therefore, it is essential to be aware of background disease so that it is not interpreted as being a result of the experimental manipulation. However, some genetic manipulations or mutations may actually increase the frequency or onset of ocular background lesions, so the documentation of any lesions is still warranted. In addition to the recognition of strain predilections for spontaneous mutations, it is also important to consider eye lesions arising in recombinant inbred strains. If one of the parental strains carries a mutation that will affect eye development or functions, then a subset of progeny lines is expected to develop comparable lesions. Stocks and strains with a genetic predisposition to developing ocular lesions may also develop secondary pathologies. C57BL inbred strains, hybrids, congenics, and recombinant inbred strains more frequently develop mesodermal dysgenesis syndromes from altered optic cup and lens vesicle formation, which morphologically manifests as unilateral anophthalmia or microphthalmia with higher frequencies being documented in female mice and in the right eye. In severely microphthalmic mice, there are alterations to tear drainage that can increase the incidence of secondary bacterial infections [38]. Varying global effects also include corneal opacities, iridocorneal and corneal–lenticular adhesions, abnormal formation of the iris and ciliary body, cataracts, extrusion of lens cortical material, failure of vitreous development, and retinal folding [38]. A summary of commonly encountered lesions resulting from spontaneous mutations in inbred mice is listed in Tables 22.1, 22.2, and 22.3 and others are discussed in the following text. There is also at least one published study of spontaneous ocular lesions in outbred Crl:CD-1(ICR)BR mice, which serves as a useful comparison to what is observed in the inbred strains [75].

Genetic anomalies of the eye occur in inbred mice, and some are considered to be common in certain strains. Eye lesions are often polygenic traits that are inherited with other craniofacial and otic abnormalities since eye development is under the regulation of master control genes including members of the *Six* and *Eya* gene families, and sonic hedgehog (*Shh)*, paired box 2 (*Pax2*), paired box 6 (*Pax6*) [76, 77]. Spontaneously encountered mutations in genes known to affect the eye are ectopic (*ec*; 1 allele), retina and anterior neural fold homeobox (formerly eyeless-1, *Rax*, 10 alleles), eyeless-2 (*ey2*; 1 allele), fidgetin (*fign*; 5 alleles), lens rupture (*lr*; 1 allele), visual system homeobox 2 (*Vsx2or*, formerly called ocular retardation; 16 alleles), and phosphodiesterase 6B, cGMP, rod receptor, beta polypeptide (*Pde6b*, formerly called retinal degeneration, *rd*, and Keeler rodless retina, *r*; 16 alleles), which are outside of perturbations affecting paired box 6 (*Pax6*, 71 alleles) or other master regulators of eye development [39, 51, 78–88]. Additionally, some strains of mice have persistent fetal hyaloid vasculature, which predisposes them to glaucoma from angle-closure and phthisis bulbi [89].

Some of these spontaneous mutant mice have been used to model human ocular diseases because the genetic basis and lesions in affected mice appear to be conserved and mirror many aspects of the human diseases. Disorders of pigment dispersion have been described as a spontaneous lesion, especially for DBA mice, and this strain has been used to study pigmentary-related glaucoma arising in human patients, which is referenced in Tables 22.2 and 22.3. However, models do not always share similar genetic changes with the human disease but are still useful as correlative models because of the shared morphologic and functional changes that can be observed. For example, the

Table 22.1 Select list of inbred mouse strains with a *Pde6b*^{rd1} mutation.

Strain name	JAX stock numbers
BDP/J, BUB/BnJ	000652, 000653
C3H sublines: C3H/HeJ, C3H/HeJSx, C3H/HeOuJ, C3H/HeSnJ, C3HeB/FeJ, C3HfB/Bi	000659, 001824, 000635, 000661, 000658, 001908
CBA/J[a], CBA/CaJ, CBA/CaGnLeJ	000656, 000654, 001143
DA/HuSnJ	000660
FL/1Re, FL/4Re	000023, 000025
FVB/NJ	001800
MOLF/EiJ, MOLD/RkJ, and MOLG/DnJ	000550, 000734, 000555
NON/LtJ	002423
P/J, PL/J	000679, 000680
SB/LeJ	000269
SJL/J	000686
ST/bJ	000688
SWR/J	000689
WB/ReJ-*KitW*/+	000692
WC/ReJ-*KitlfSl*/+	000693

Allele name: retinal degeneration 1, Allele symbol: *Pde6b*^{rd1}, MGI:1856373, [8]

[a] CBA/J is the only substrain reported to carry the *Pde6b*^{rd1}mutation [8]

Table 22.2 Genes and spontaneous mutations of the laboratory mouse eye that also model human diseases.

Anatomic location, Ocular defect and human disease correlation (if any)	Gene name and gene product and spontaneous mutation	Description of stock/strains with mutation	Mouse phenotype and reference
Iris, ciliary body, trabecular meshwork			
Iris stromal atrophy	Tyrosinase-related protein 1, (*Tyrp1)* 65 alleles/ mutations MGI:98881	DBA/2J, C57BR/cdJ, C57L/J, I/LnJ, SEA/GnJ, and SEC/1ReJ	Description in DBA mice [49]
Pigment dispersion, *Human pigment dispersion syndrome and pigmentary glaucoma*	Spontaneous mutation: tyrosinase-related protein 1, *Tyrp1b* MGI:1855960	DBA/2J	Description of pigment dispersion disorder in DBA mice [49, 50]
	Spontaneous mutation: tyrosinase-related protein 1, *Tyrp1b* MGI:1855960 Glycoprotein nmb, *Gpnmb* 9 alleles/ mutations MGI:1934765 Spontaneous mutation: glycoprotein (transmembrane) nmb; iris pigment dispersion, $Gpnmb^{R150X}$ MGI:2177814		
Lens			
Defective formation	Lens rupture, *lr* 1 allele MGI:96827	F1 hybrids of recombinant inbred (RI) strain, CXS4 or CXSD (D) crossed with BALB/cHeA(BALB/c or C) or STS/A(STS or S)	See [51]
Cataracts *Age-related human cataracts*		Senescence-accelerated mouse (SAM) derived from the AKR/J strain	Develop cataracts at 10 weeks of age and have a persistent hyaloid vascular system [52] See [53]
Human cataracts, not otherwise specified	Crystallin gamma complex (*Cryg*) MGI:88520 ENU induced point mutation: crystallin, gamma S; opacity due to poor secondary fiber cell junctions, $Crygs^{Opj}$ MGI:1861635	C3H	
Retina, Choroid			
Retinal atrophy, degeneration *Congenital stationary night blindness* *Hermansky–Pudlak syndrome 4* *Retinitis pigmentosa*	phosphodiesterase 6B, cGMP, rod receptor, beta polypeptide (*Pde6b*) 17 alleles/ mutations MGI:97525 Spontaneous mutation: phosphodiesterase 6B, cGMP, rod receptor, beta polypeptide; retinal degeneration 1 $(Pde6b^{rd1})$ MGI:1856373	For a list of strains with $Pde6b^{rd1}$ spontaneous mutation please see Table 22.1	Retinal dysplasia that is worsened by light exposure. Corneal stromal deposits, incipient nuclear cataracts, altered translucency of the anterior lens capsule, vitreous crystalline deposits, and vitreous pigment [54–59] Both homozygotes and heterozygotes develop a slow form of retinal degeneration with thinning and loss of the outer nuclear layer, loss of photoreceptor outer segments, and increased numbers of Muller cells and gliosis [60] See [58]

Table 22.2 (Continued)

Anatomic location, Ocular defect and human disease correlation (if any)	Gene name and gene product and spontaneous mutation	Description of stock/strains with mutation	Mouse phenotype and reference
Retinal dysplasia *Leber congenital amaurosis, human CRB1 retinopathies*	peripherin 2 *(Prph2)* 12 alleles/ mutations, MGI:102791 Spontaneous mutation: peripherin 2; retinal degeneration 2 (*Prph2*^{Rd2}) MGI:1856523 Retinal degeneration 8 *(Rd8)* 21 alleles/ mutations Spontaneous mutation: crumbs family member 1, photoreceptor morphogenesis associated; retinal degeneration 8 (*Crb1*^{rd8}) MGI:2676366	C57BL/6N strain (58%)	
Diffuse effects			
Anopthalmia/ Micropthalmia *Human anophthalmia*	Retina and anterior neural fold homeobox (*Rax)* 10 alleles/ mutations, MGI:109632 Spontaneous mutation: retina and anterior neural fold homeobox; eyeless 1 (*Raxey1*) MGI:1856862	ZRDCT inbred mouse strain	Most ZRDCT mice are born eyeless (est. 90%) and have orbits, eyelids, palpebral conjunctivae, Harderian glands, and periocular soft tissues are intact but lack eyes and optic tracts and have hypothalamic abnormalities [61].

human protein, Lysyl oxidase like 1 (LOX1) has been associated with exfoliation syndrome and pseudoexfoliation glaucoma in humans. However, oxidized low density lipoprotein (lectin-like) receptor 1 (*Olr1tm1Lex*) mutant mice have no abnormal eye phenotype [8]. Mice that are deficient for *Lox1* do not recapitulate key aspects of the human disease but do have ocular lesions [90]. The mouse gene lysosomal trafficking regulator; beige Jackson (*Lystbg−J*) appears to better mimic the human disease phenotype. Histologically B6--*Lystbg−J* mice have exfoliative-like material, pigment dispersion, and iris transillumination defects caused by altered cellular adhesion of the iris pigment epithelium making the argument that the LYST pathway may have a role in the human disease [65].

Spontaneously arising retinal diseases are well described for inbred stocks and strains. A key example of a background disease affecting the retinas of inbred laboratory mice is the prevalence of the gene for retinal degeneration 1 (*Pde6brd1*) in over 88 different mouse strains, especially C3H and FVB strains. Additionally, 117 strains or lines have been reported to carry any *Pde6b* mutation [91, 92]. Mice with the *Pde6brd1* mutation have normal, fully functional photoreceptors at birth, but start losing rods and cones and are blind by three weeks of age. There are 31 genotypes associated with the *Pde6brd1* allele [91]. At least 21 retinal dystrophy genes or quantitative trail loci (QTLs) have been reported when the Mouse Genome Informatics (MGI) website is searched under "retinal degeneration" indicating, not surprisingly, that spontaneous mutations arise causing this phenotype in production colonies over time [8]. Two examples involve retinal degeneration 8 (*Crb1rd8*) and cone photoreceptor function loss 3 (*Gnat2cpfl3*) [93]. Retinal dysplasia caused by a *Crb1rd8* mutation in the C57BL/6N is a frequently encountered lesion that results from the abnormal development of the pars optica retinae of the optic cup and is a model for Leber congenital amaurosis [94]. Ocular phototoxicity leading to retinal atrophy in albino mice is common and well described for certain strains like FVB mice. However, many albino mouse strains also have *Pde6brd1* mutations, which may enhance the susceptibility to phototoxicity [72]. Unlike with inherited retinal degeneration (Figure 22.9), which will appear in young mice by three weeks of age and affect the entire retina, phototoxic atrophy is characterized by variable cell loss and decreases in the thickness of the outer plexiform and nuclear layer and the photoreceptor layer that preferentially affects the superior retinal quadrants, particularly above and near the optic disc [72].

Table 22.3 Selected genetically engineered and mutant mice for glaucoma and retinal degeneration research.

Anatomic location, Ocular defect & Human disease correlation	Gene name (human/mouse) and gene product and transgene or mutation	Mouse phenotype and references
Iris, ciliary body, trabecular meshwork Glaucoma, secondary Primary open angle glaucoma (POAG)	Myocilin (*MYOC/Myoc*) 12 alleles/ mutations, MGI:1202864 transgene insertion, Val C Sheffield Tg-MYOC^{Y437H} MGI:5302242	Transgenic mice had cell detachment from the trabeculae in Schlemm's canal on EM that correlated with increased IOPs and retinal and optic nerve degeneration [62]
	transgene insertion 1, Simon John Tg(Myoc)1Sj MGI:6367838	See [63]
Primary closed-angle Glaucoma (PCAG)	calcitonin receptor-like receptor (*CALCRL/Calcrl*) transgene insertion 4688, Kazu Nakazawa Tg(Calcrl,cre)4688Nkza MGI:5523525	See [64]
Pigmentary-related	Tyrosinase-related protein 1 (TYRP1/Tyrp1) 65 alleles/ mutations, MGI:98881	See [49, 50]
	Spontaneous mutation: tyrosinase-related protein 1, *Tyrp1b* MGI:1855960	See [49] See [50]
	Spontaneous mutation: Glycoprotein nmb (*GPNMB/Gpnmb*) glycoprotein (transmembrane) nmb; iris pigment dispersion, *Gpnmb^{R150X}* MGI:2177814	
Exfoliation syndrome (XFS) and Pseudoexfoliation glaucoma	Human gene association with XFS is Lysyl oxidase like 1 (LOX1), which differs from the murine gene lysosomal trafficking regulator; beige Jackson *(Lyst^{bg-J})* MGI:1855969	Model recapitulates iris defects although genetics of the lesions differ [65]
Primary congenital glaucoma	cytochrome P450 family 1 subfamily B member 1 *(CYP1B1/Cyp1b1)* 3 alleles/ mutations, MGI:88590 Targeted allele: cytochrome P450, family 1, subfamily b, polypeptide 1; targeted mutation 1, Frank J Gonzalez (*Cyp1b1tm1Gonz*) MGI:2154690	Goniodysgenesis caused by drainage angle malformation with secondary glaucomatous changes resulting in bupthalmos [66]
Retina, choroid *Retinal degeneration, RPE-Photoreceptor layers*		
Early onset hereditary maculopathy: Stargardt's macular dystrophy	ATP-binding cassette transporter, retina-specific *(ABCR/Abcr)* 14 alleles/ mutations, MGI:109424	Homozygotes have increased RPE lipofuscin and A2E progressing to RPE and photoreceptor degeneration [67]
	Transgene insertion, Wojciech Kedzierski, Tg(IVL-Elovl4)#Wked MGI:6360307	
	Cathepsin D (*CTDS/Ctsd*) 9 alleles/ mutations, MGI:88562 cathepsin D; mutation 1, Jackson (Ctsd^{m1J}) MGI:5752221	Transgenic mice have increases in RPE lipofuscin and A2E [68] Aged mice have increases in RPE lipofuscin and RPE and photoreceptor degeneration [69]
Autosomal dominant Retinitis pigmentosa	peripherin 2 (*PRPH2/Prph2*) 12 alleles/ mutations, MGI:102791 Spontaneous mutation: peripherin 2; retinal degeneration 2 *(Prph2Rd2)* MGI:1856523	Progressive photoreceptor loss starting at two weeks of age [70]

Genetically Engineered and Mutant Mice (GEMs)

There are many similarities in the anatomy of the mouse and human eye as well as a shared molecular pathogenesis in lesion development that makes the mouse an ideal model for studying human ocular diseases. However, there are significant anatomic and functional differences, especially between the retinas, of humans and mice. Furthermore, there are genetic changes that drive types of ocular lesions in humans that have not yet been identified in the mouse making genetic engineering necessary to create certain human ocular disease models. There are several active research programs and numerous publications addressing the ophthalmic abnormalities of genetically engineered and mutant mice. The Eye Mutant Resource (EMR, https://www.jax.org/research-and-faculty/resources/eye-mutant-resource) and the Translational Vision Research Models (TVRMs) programs currently housed at The Jackson Laboratory provide genetically defined mouse models for vision research by screening for spontaneous mutations and using ENU mutagenesis methods, respectively [95]. Key examples of genetically engineered and mutant mice as human eye disease models for glaucoma and retinal diseases are summarized in Table 22.3.

Anatomy, Histology, and Physiology of the Ear

The mammalian auditory and vestibular structures and functional pathways of the auditory system are well conserved between mice and humans, and mouse mutants have had a pivotal role in the identification of numerous key genetic loci involved in hearing and balance [96, 97]. Findings in mice have helped elucidate the underlying mechanisms of human hearing and vestibular function, as well as the genetic bases of their impairment.

The highly complex structures of the inner ear are responsible for hearing and balance and include many components that must work in harmony. The perception of sound begins with the collection of incoming sound waves by the external ear, which directs the vibrations to the tympanic membrane. The ossicles of the middle ear transmit the vibration of the tympanic membrane to the fluid-filled inner ear. The auditory portion of the inner ear, the cochlea, transduces sound waves into nerve impulses. Defects in any of the components in this chain of events can result in hearing deficits or loss. Therefore, pathologists involved in phenotyping genetically engineered mice (GEM) must carefully examine each part of this system.

The parts of the auditory system are traditionally divided into three anatomic compartments, the external ear, the air-filled middle ear, and the fluid-filled inner ear. The external ear consists of the auricle (pinna), external auditory canal (or meatus), and the tympanic membrane at the medial aspect of the auditory canal. The middle ear cavity includes the ossicles and the Eustachian tube connecting the middle ear space to the nasopharynx. The inner ear consists of a membranous labyrinth which is surrounded by an osseous layer or bony shell within the petrous portion of the temporal bone. This bony shell is termed the otic capsule. Specialized cells within the inner ear communicate with neurons in the spiral ganglion, which then transmit information to the auditory cortex. Phenotyping of lesions in the auditory cortex of the brain will not be discussed here.

Regarding deafness, the primary lesion site defines the two types of hearing loss: conductive deafness is caused by lesions or dysfunction of the external or middle ear, while perceptive or sensorineural deafness is caused by defects within the cochlea or neural connections to the auditory cortex. In humans, genetic hearing loss accounts for approximately 50% of congenital deafness and is classified by whether it occurs as part of a recognized syndrome (syndromic hearing loss, 20%) or as an isolated finding (nonsyndromic hearing loss, 80%).

Phenotyping Screen

Performing a histopathology evaluation of the ear occurs in different contexts. As with all pathological phenotyping, not all mice in which a hearing impairment is identified will have an associated morphologic abnormality. In research programs specifically investigating mechanisms of hearing and balance, or as part of a guided phenotyping screen such as the International Mouse Phenotyping Consortium (IMPC), histologic evaluation is generally preceded by behavioral and electrophysiological auditory phenotyping. However, there are cases where vestibulocochlear lesions may be discovered first, and these findings should be confirmed by electrophysiological auditory testing.

A simple first-level screen for auditory dysfunction is the Preyer reflex, in which the pinnae flick backwards upon hearing a loud sound. This can be elicited by a simple hand clap or in a more precise manner using a click-box, which is a handheld unit that emits a high frequency tone stimulus at a level of 90 dB [98–100]. This is a quick screening test but detects only profound hearing loss in response to a suprathreshold stimulus. In one analysis of the IMPC auditory phenotyping data, this test was able to detect 80% of mutant phenotypes classified as having severe hearing loss [100]. However, more sophisticated techniques are required to detect milder hearing deficits, the most common and sensitive being the Auditory Brainstem Response (ABR) [101]. This test measures auditory activity in the auditory nerve and subsequent fiber tracts and nuclei within the auditory brainstem pathways. Specialized computerized systems have been developed to perform this analysis [102].

Vestibular phenotyping is initially performed via gross examination of mouse behavior, as histologic lesions are rarely evident. Unusual movements such as head tossing or bobbing and circling (shaker-waltzer behavior) are suggestive of vestibular dysfunction. Specific tests include the trunk curl test, a contact righting test, and the swim test [99]. Laboratories focusing on vestibular research perform advanced assessment of peripheral vestibular function via

far-field recording of vestibular compound action potentials. The vestibular sensory evoked potential (VsEP) is one such measure. Linear VsEPs provide a direct measure of peripheral vestibular function because they are compound action potentials generated by the vestibular portion of the eighth nerve and central vestibular relays in response to transient linear acceleration of the head. The neural responses can be recorded from the surface of the skull much like the widely used auditory brainstem response [103].

Gross Necropsy and Trimming

Often, abnormalities of the auricle can be identified by gross examination alone, and histopathology may be performed to identify specific cellular defects. Some middle ear lesions can be identified grossly. By examination with a dissecting microscope, one can examine the tympanic membrane for a serous or suppurative effusion behind the eardrum, which may be indicative of otitis media. Alternatively, one may remove the bulla to examine the middle ear cavity directly. Specialized dissection and gross examination of the ossicles may reveal abnormal development of the ossicular chain. These gross dissection techniques are generally employed in targeted research areas, whereas in most mouse phenotyping efforts, histologic examination is the only method whereby morphologic changes are identified. Many abnormalities of the inner ear or vestibular organs can only be identified by microscopic examination.

Most histological examinations are performed on formalin-fixed, paraffin-embedded (FFPE) sections stained with hematoxylin and eosin (HE). Although immersion fixation will permit detection of middle ear abnormalities and significant inner ear abnormalities, fixation via intracardiac perfusion is often necessary to detect mild to moderate inner ear lesions. Standard examination of the ears is possible on standard frontal sections of the whole head, which typically include six sections, with the key cut for visualizing all ear structures being made at the level of the external acoustic meatus. This section permits examination of the external ear canal, middle, and inner ears in one slide (Figure 22.11). However, when a higher degree of preservation and morphologic detail of the inner ear is required, tissues should be fixed in glutaraldehyde and sodium cacodylate, embedded in resin, with semi-thin sections (0.5–2 μm) stained with toluidine blue. Alternative orientations for sectioning the cochlea have been described [104]. Sectioning of bisected heads in the sagittal plane will produce a mid-modiolar section, which may be the most informative snapshot for assessing gross cochlear morphology. The modiolus is the central spiral bone of the cochlea, and a mid-modiolar section will show a cross-sectional view through the central axis of the modiolus, allowing visualization of the basal, mid, and apical turns of the cochlea and assessment of the organ of Corti and other structures of the membranous labyrinth.

For advanced examination of the inner ear, it is recommended that adult samples be processed by removing the inner ear and flushing the cochlear duct with fixative before decalcifying in EDTA and embedding for sectioning. Proper orientation of the isolated inner ear during embedding is important and requires practice. One method is to position the inner ear with the oval and round windows facing upwards and the cochlea pointing down toward the cutting face of the mold.

Advanced imaging techniques can be employed for a more in-depth analysis of hearing and vestibular organ morphology, particularly in the inner ear. These include the use of scanning electron microscopy (SEM) and immunofluorescent (IF) imaging of cochlear sections and whole-mount preparations [104]. Surface imaging of the cochlear sensory epithelium by SEM enables assessment of both hair cell

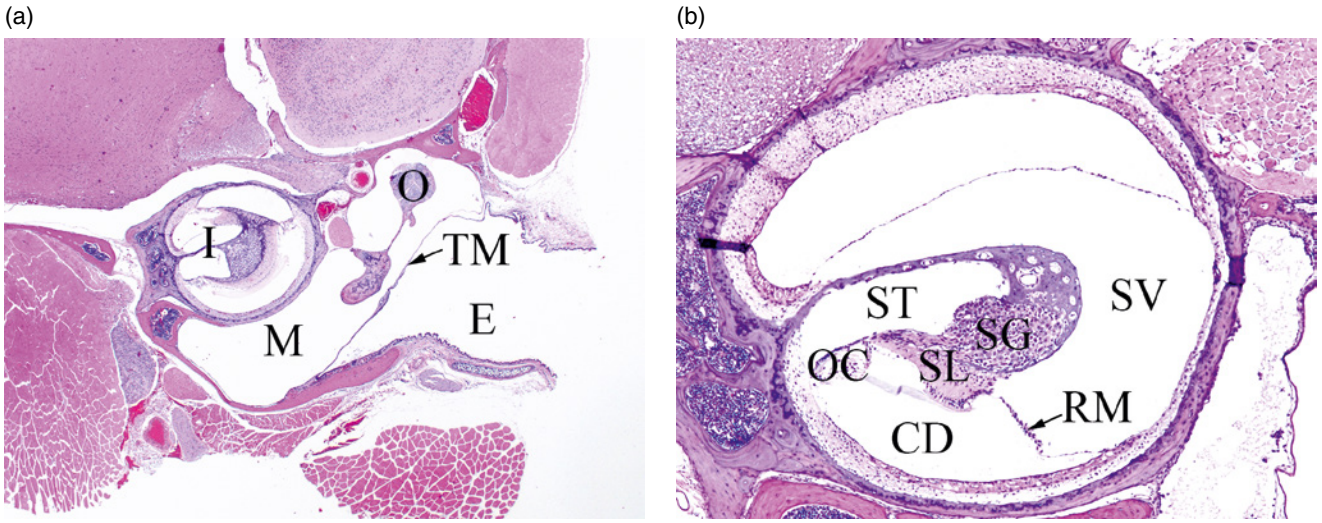


Figure 22.11 Coronal sections of mouse head. (a) Low magnification view showing single section with external (E), middle (M), and inner (I) ear. Ossicle (O) and tympanic membrane (TM) are indicated. (b) Section of inner ear. The organ of Corti (OC), cochlear duct (CD), Reissner's membrane (RM), scala vestibuli (SV), scala tympani (ST), spiral ganglion (SG), and spiral ligament (SL) are indicated.

number and stereocilia bundle morphology along the entire spiral (base to apex) [104, 105]. Immunofluorescence imaging allows for co-labeling of markers of hair cells and supporting cells with the protein of interest to define specific cell subsets affected by a genetic manipulation [106–109]. Detailed protocols for these techniques are available elsewhere [104, 110, 111].

Embryology

Embryonically, the external ear develops from a series of auditory hillocks, which develop on either side of the first pharyngeal groove (between the first and second branchial arches). The first pharyngeal groove itself becomes the external acoustic/auditory meatus. The tympanic membrane, which separates the external from the middle ear, differentiates after birth and like the external acoustic meatus is derived from the first branchial groove. The main components of the middle ear, the ossicles, are derived from two different pharyngeal arches, and thus genetic defects affecting one or the other can have differing effects. The malleus and incus differentiate from the first branchial arch, while the stapes differentiates from the second. The otic capsule, or the bony shell forming the outer wall of the middle ear, is derived from the second branchial arch, and the Eustachian tube from the first pharyngeal pouch. The inner ear is derived from the otic vesicle/otocyst.

Histology

The external ear is comprised of a central layer of elastic cartilage covered by haired epidermis with an intervening layer of thin connective tissue containing blood and lymph vessels and nerves. Zymbal's gland (a structure unique to rodents; see Chapter 10, Figure 10.15) is located between the cartilage at the base of the external ear and the tympanic bulla. The external auditory meatus is lined by non-haired cornified stratified squamous epithelium. The tympanic membrane separates the external ear from the middle ear. It is comprised of three layers that, in mice, are difficult to distinguish by light microscopy and routine histology. The outermost layer facing and continuous with the lining of the external auditory meatus is a thin squamous epithelium. The middle layer is comprised of collagen fibers, and the inner aspect facing the lumen of the middle ear is respiratory epithelium. The Eustachian tube, which connects the middle ear to the nasopharynx, is covered by respiratory epithelium which is continuous with the inner lining of the tympanic membrane.

The inner ear has a complex three-dimensional morphology, but this discussion will focus on those components that can develop lesions identifiable by light microscopy. The cochlea is composed of three fluid-filled canals that spiral together around the central modiolus bone in two and a half turns in mice. The three canals are the scala vestibuli, the scala tympani, and the intervening cochlear duct (also known as the scala media). The scala vestibuli and scala tympani are separated from the middle ear by membrane-covered openings, the oval and round windows, respectively. These two canals are filled with perilymph, a Na^{2+} rich, K^{+} poor fluid of ionic composition similar to cerebrospinal fluid (CSF). Perilymph is partly a filtration product from CSF (via the opening of the cochlear aqueduct to the subarachnoid and perilymphatic spaces), and partly a filtration product from blood vessels of the ear. The cochlear duct (which contains the organ of Corti) is filled with endolymph, a fluid that is K^{+} rich and Na^{2+} poor – an ionic composition close to that of intracellular fluid. Endolymph has a viscosity similar to the vitreous of the eye due to its high mucopolysaccharide content. Its main source is the stria vascularis, a structure lining the lateral aspect of the cochlear duct. The stria vascularis is a three-layer structure formed by marginal, intermediate, and basal cells and is highly vascularized by intraepithelial capillaries. The luminal facing marginal layer is composed of pseudostratified secretory epithelial marginal cells. On the other side of stria vascularis is the mesoderm-derived basal cell layer. Between these is the intermediate cell layer, which contains neural crest-derived melanocytes sometimes containing melanin pigments. This layer is highly vascularized by numerous capillaries. The stria vascularis is integral to maintaining the high K^{+} ion concentration of the endolymph and thereby the integral positive potential of the cochlear duct compared with scala tympani and scala vestibuli.

The ionic differentials are also maintained by membrane barriers that separate the cochlear duct from the scala vestibuli and scala tympani – Reissner's membrane and the basilar membrane, respectively. Reissner's membrane is thin and consists of two layers of cells – an inner epithelial-like layer derived from ectoderm and an outer layer of mesodermal origin. The basilar membrane is an acellular fibrous tissue that supports the base of organ of Corti. The cochlear duct houses the organ of Corti, the sensory structure of the cochlea. It sits upon the basilar membrane and is overlain by the tectorial membrane, an acellular membrane comprised of collagen and glycosaminoglycans. The cellular elements of the organ of Corti include three rows of outer hair cells (OHCs) and one row of inner hair cells (IHCs), and several types of supporting or pillar cells. OHCs provide sound amplification via mechanoelectrical transduction, while the IHCs are the genuine auditory sensory cells that release glutamate onto glutamate receptors present on auditory neurons upon stimulation of their hair bundles. At the base of each hair cell are efferent and afferent nerve endings that transmit impulses to the bipolar neurons of the spiral ganglion, which is located within the modiolus. Each IHC is synaptically connected to all type I spiral ganglion neurons, forming the radial afferent system, and each OHC synapses with a few small endings from type II spiral ganglion neurons, forming the spiral afferent system.

The vestibular portion of the inner ear is comprised of the vestibule, which contains the utricle and saccule, and the three semicircular canals. The semicircular canals arise from the posterior vestibule and lie at right angles to each other in

three planes and are filled with endolymph. These bony canals are lined by the membranous labyrinth, and the space between this and bone contains perilymph. At the base of each semicircular canal is a bulbous expansion called the ampulla, and at its base is the crista, which contains the hair cells. The apical projections of the hair cells are embedded in a gelatinous cap called the cupola, which is often indistinct in routinely processed tissue. Similar sensory epithelium is present in the utricle and saccule, each having a patch of hair cells termed the macula. Their hair cell projections are also embedded in a gelatinous membrane, but here it is termed the otolithic membrane because embedded within it are calcium bodies referred to as otoconia (or otoliths). These otoconia are visible in routinely processed sections as a layer of small roughly spherical masses overlying the maculae.

Aging/Spontaneous Strain Specific Lesions

There is a large phenotypic diversity between strains of mice in relation to the onset, degree, and progression of hearing loss [112], and background strain has been shown to influence the development of genetically induced hearing and associated phenotypes [113]. One of the most commonly encountered background lesions was initially identified in C57BL/6 mice. These mice have age-related hearing loss due to a base-to-apex progression of degeneration of cochlear hair cells, supporting cells, and the spiral ganglion neurons [114]. Later there is thinning of the stria vascularis. The causative mutation was mapped to the *ahl* locus on Chromosome 10 [115], which has been shown to be a splice variant of the cadherin 23 gene (*Cdh23*) [116]. This allele is present in many commonly used strains of mice, including A/J, DBA/2J, and NOD/LtJ [117].

Otitis media is a relatively common spontaneous finding in laboratory mice. It can occur in conjunction with other inflammatory conditions including bronchopneumonia with abscess formation due to *Pasteurella pneumotropica* [118]. The C3H/HeJ mouse strain has an increased susceptibility to infection with gram negative bacteria such as *Klebsiella oxytoca* due a spontaneous mutation in *Tlr4* [119, 120].

Abnormalities in Genetically Engineered Mice

External Ear Abnormalities

The most common genetic abnormalities of the external ear are developmental in origin. These can often be characterized grossly as abnormal size (hypoplastic or absent), abnormal shape/malformation [121–129], or abnormal placement [130, 131]. The condition of microtia is characterized by a small, abnormally shaped auricle. Rarely there can be a complete absence of the external ear and the auditory canal, which is termed anotia. Often when abnormalities of the external ear are noted grossly, it is important to additionally examine the middle ear, as their development is strongly linked due to their both being derived from the first and second branchial arches. It has long been recognized that a gross morphologic abnormality in the external ears can be a sign of multisystemic developmental defects. One such early description was of the "short ear" phenotype described first in 1921 [132] and further detailed in 1942 [133]. This phenotype was later determined to be due to a nonsense mutation in the gene for bone morphogenic protein 5 (*Bmp5*) [134]. In addition to numerous skeletal defects present in BMP5 null mice, they have abnormalities in the lungs, liver, urinary system, and gastrointestinal system. Mutation of genes that affect patterning and morphogenesis often results in malformation of all regions of the ear (external, middle, inner), such as occurs with the *Hox* family of genes [121–123, 135]. These mutations can result in malformed to absent auricles, a malformed external acoustic meatus, absence of second pharyngeal arch-derived structures such as the stapes and the otic capsule, duplication of first pharyngeal arch-derived elements such as the malleus and incus bones, and occasionally a malformed cochlea, which is derived from the otic vesicle (otocyst). Similarly, certain syndromes in humans are associated with abnormalities in all three ear regions, such as branchio-oto-renal syndrome [124], Kashin–Beck disease [129], DiGeorge syndrome [130, 131], and Treacher Collins syndrome [136]. Modeling of the genetic defects in mice has enhanced our understanding of the pathogenesis of these forms of syndromic deafness.

Middle Ear Abnormalities

Many of the developmental syndromes earlier include abnormalities such as absent [121–123], malformed [124], or duplicated ossicles [121, 122], with sometimes differential effects between the first pharyngeal arch-derived malleus and incus and the second pharyngeal arch-derived stapes. In other cases, defects are restricted to the middle ear and generally include abnormal ossicles [137]. Ossicle development begins as foci of endochondral ossification embedded within endomesenchymal tissue. Failure of ossicles to separate from one another within this mass, resulting in ossicle fusion, occurs with some genetic mutations. Once final mesenchymal condensation has occurred around the ossicles, remaining attachments form ligaments suspending the malleus and incus to the wall of the middle ear, but the mechanisms of this have not been well-studied. Failure of this complete mesenchymal condensation can result in malformed ligaments and therefore conduction deficits in hearing (Figure 22.12). Genetic mutations of factors involved in bone development can affect middle ear to varying degrees. For example, while mice with osteopetrosis have widespread skeletal defects, their ear abnormalities are localized to middle ear only and include thin, fragile bullae, abnormal otic capsules, and malformed ossicles [138]. Numerous mouse mutations affecting phosphate homeostasis that have associated conductive hearing loss are reported to have middle ear ossicle fusion [139].

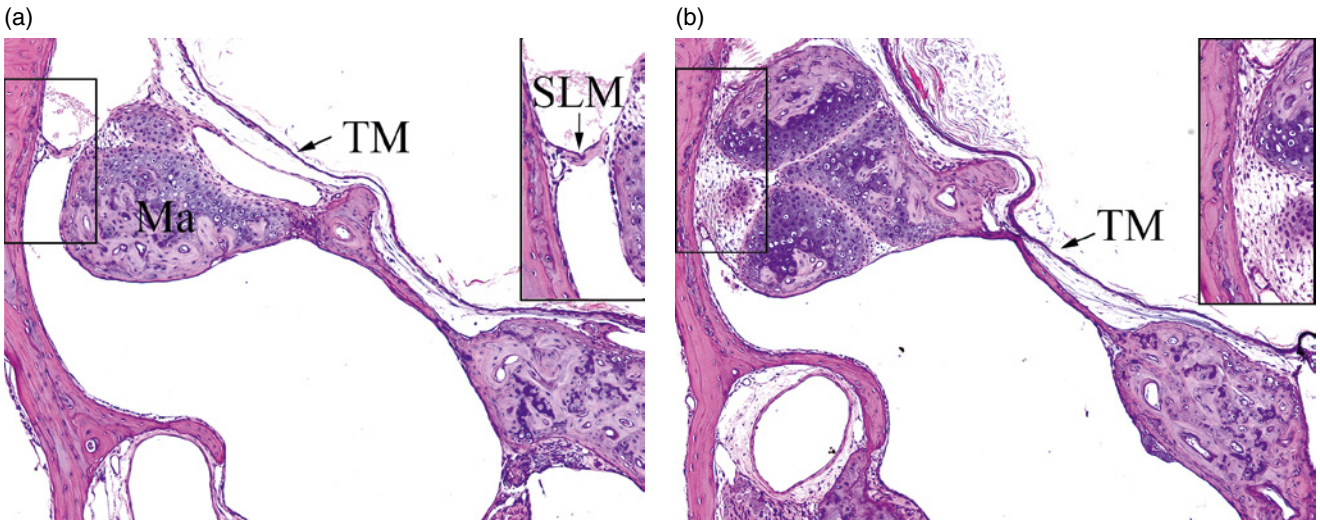


Figure 22.12 Failure of mesenchymal condensation and development of superior ligament of the malleus (SLM). (a) Normal morphology of the SLM. Inset shows higher magnification of attachment site. (b) The ligament has not condensed, leaving a broad-based sheet of mesenchymal tissue rather than a thin collagenous ligament. Malleus (Ma) and tympanic membrane (TM) are indicated.

Inflammation of the middle ear (otitis media) may occur as a spontaneous infection or as a secondary outcome due to genetic manipulation elsewhere. For example, an increased susceptibility to otitis media has been described in mice to due to genetic mutations causing abnormal development of the Eustachian tube [140–142], decreased production of secretory proteins from the mucosa [143], and ciliopathies [144]. In acute otitis media, lumens of the middle ear can become filled with serous exudate and degenerate neutrophils. With chronicity, the mucosal epithelium becomes hyperplastic with the occasional development of polyps, the lumen will additionally contain foamy macrophages and cholesterol clefts, and there is stromal fibrosis [139, 143, 145]. Similar histopathologic changes are seen in experimental models of otitis media, in which genetically modified mice have been used to elucidate host factors involved in immunity or susceptibility to specific pathogens [146–150].

Inflammation of the middle ear can be seen as one of the multisystemic manifestations of disease in mice with lysosomal storage disorders (Figure 22.13). Depending on the type of storage disorder, one can see changes including thickening of the mucosal lamina propria by highly vacuolated macrophages, and ossicles with highly vacuolated chondrocytes, osteoblasts, and osteocytes [151–153].

Inner Ear Abnormalities

The inner ear is comprised of the auditory organ the cochlea and the vestibular organs the vestibule and semicircular canals. These organs function similarly in that mechanical information is transmitted by fluid movements to neuroepithelial hair cells, which then relay this information to the nervous system. Therefore, it is not uncommon for hearing and vestibular deficits to occur concurrently if a mutation affects these important hair cells [154], but there are instances where only the cochlear or vestibular hair cells are affected. Unfortunately, most papers focused on deafness do not indicate whether the vestibular hair cells were examined. The importance of excellent tissue fixation when evaluating the inner ear cannot be overemphasized. Perfusion fixation is essential to preserve morphology of structures, especially the hair cells. The rapid autolysis of hair cells compared to other structures in the inner ear can cause the artifactual appearance of hair cell degeneration.

In humans, nearly 200 deafness-related loci and nearly 50 causative genes have been identified. Approximately half of these known causative genes encode proteins present in hair cells. It is difficult to study the impact of these mutations in humans because of the challenges associated with accessing the cochlea. This has made the study of mouse genetic models of hearing loss particularly important in this context. One of the most common locations to identify structural abnormalities underlying hearing loss is in the organ of Corti (Figure 22.14a). This can include complete agenesis or degeneration of the organ of Corti (Figure 22.14b) or be localized to the sensory hair cells. Often this affects both the OHCs and IHCs (Figure 22.14c) [108, 109, 155, 156], but sometimes involves only the OHCs (Figure 22.14d, e) [157, 158] or IHCs (Figure 22.14f). Hair cells may show lesions such as agenesis, immaturity, loss/degeneration, and disorganized or abnormal stereocilia. When hair cell function is compromised due to disorganized or abnormal cilia, this cannot be identified by light microscopy but can be examined by SEM [159]. Often with hair cell degeneration there is

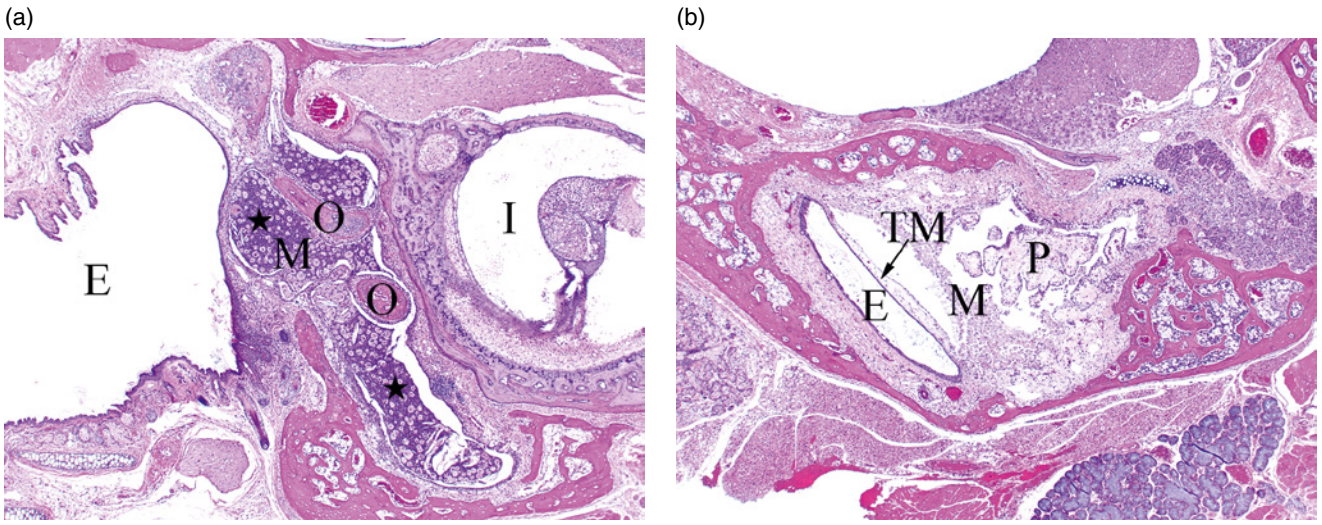


Figure 22.13 Otitis media in mouse with a lysosomal storage disease. (a) Middle ear (M) is filled predominantly by neutrophils with fewer macrophages (starred areas). (b) In a more rostral section, the lumen contains macrophages and there are fibrous polyps (P) present, indicative of chronicity. External ear (E), ossicles (O), and tympanic membrane (TM) are indicated.

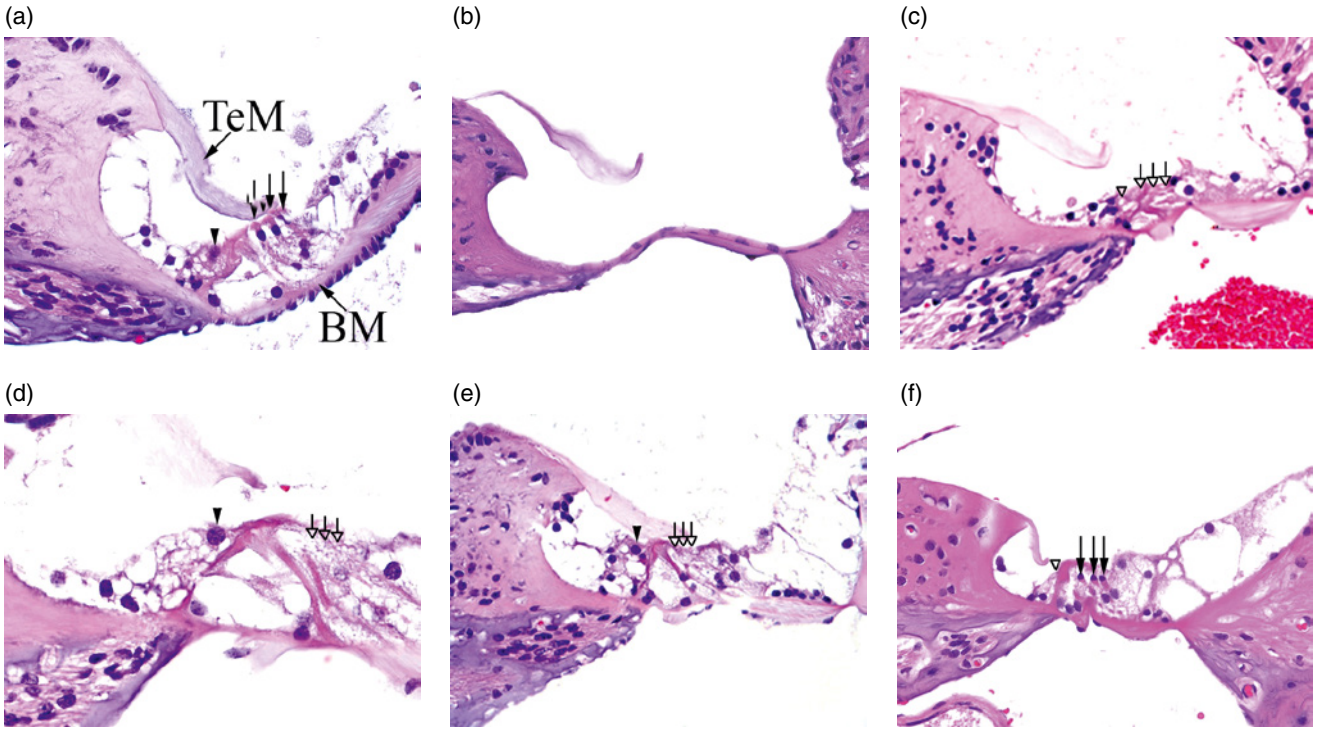


Figure 22.14 Lesions of the organ of Corti. Arrows indicate outer hair cells (OHCs) and arrowheads indicate inner hair cells (IHCs) Open arrows and open arrowheads indicate site of OHC and IHC loss, respectively. (a) Normal structure. (b) Complete atrophy of the organ of Corti. (c) Loss of both the outer hair cells (OHCs) and the inner hair cells (IHCs). (d, e) Loss of OHCs. (f) Loss of IHCs. Tectorial membrane (TeM) is indicated. It is artificially detached in b, c, and d.

a secondary atrophy of spiral ganglion cells. A less commonly encountered lesion of the hair cells is expansion and vacuolation of the cytoplasm in mouse models of some lysosomal storage disorders [151–153, 160]

Immunohistochemistry can be used to label and evaluate specific cell types within the organ of Corti. Both outer and inner hair cells can be detected by antibodies to myosin 6 [161] or myosin 7a, outer hair cells with anti-prestin

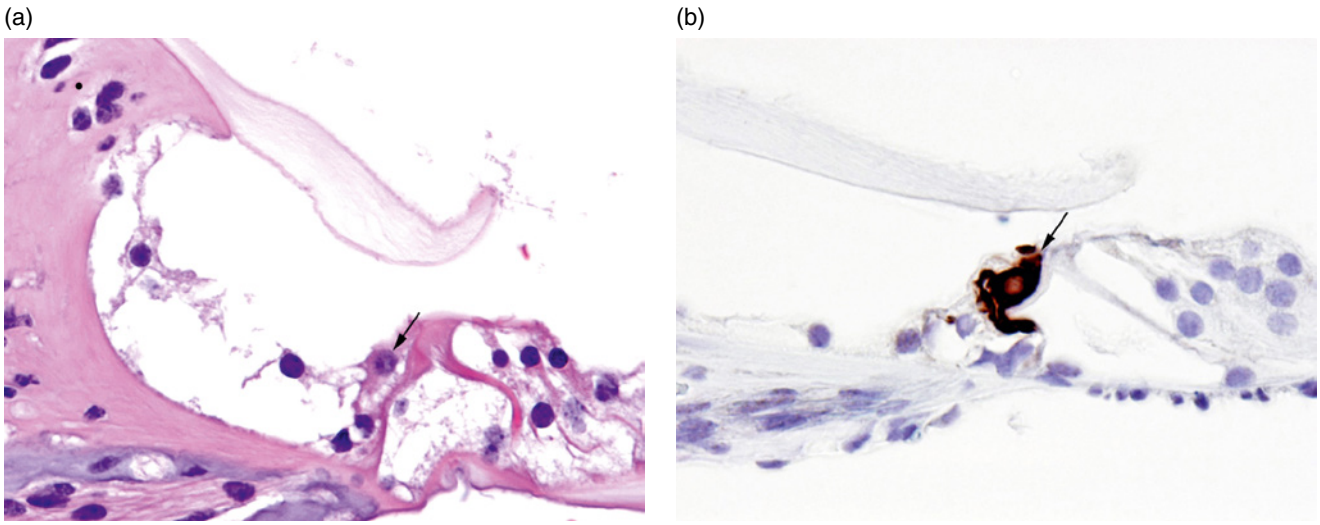


Figure 22.15 Deafness phenotype in mouse lacking vesicular glutamate transporter 3 (VGLUT3). (a) Inner ear of a mouse without VGLUT3. All structures are without morphologic abnormalities, including an intact organ of Corti, but this mouse was profoundly deaf. (b) VGLUT3 normal pattern of expression is limited to the inner hair cells, and its absence results in deafness.

antibodies, and supporting cells by antibodies to SOX2 [110]. Mutations of integral signaling components within the hair cells and between the hair cells and spiral ganglion neurons may result in deafness without any visible morphologic abnormalities in these cells. For example, mice with nonfunctional vesicular glutamate transporter 3 (*Slc17a8*) (Figure 22.15) have a morphologically normal organ of Corti but are profoundly deaf.

Other structures in the organ of Corti may show agenesis or degeneration, including the basal membrane, supporting cells, and the tectorial membrane (TM). Detachment of the TM from the spiral limbus has been shown to be the cause of one type of non-syndromic deafness [162]. Note that the detachment of the TM from the apical surface of the hair cells is a common processing artifact and should not be interpreted as an abnormality (Figure 22.14a). Given the central importance of the maintenance of endolymph potential, deafness can be caused by damage to the structure that generates this potential, the stria vascularis.

Degeneration/atrophy of the stria vascularis in advanced stages appears as marked flattening, but in early stages it is sometimes possible to identify specific degeneration of the marginal cells (epithelial) [163, 164] or intermediate (neuroectodermal) cells [165] by light microscopy or advanced methods. There are numerous mouse models of deafness in which mutations in ion transporters result in aberrant endolymph ionic composition. Mutations in a specific K^+ channel contributing to the delayed rectifier K^+ current result in reduced endolymph manifested by a collapsed Reissner's membrane and serve as a model of Jervell and Lange-Nielsen syndrome in humans [166–168]. A secondary loss of hair cells is seen in these models as well. Similar lesions are present when the secretory isoform of the Na–K–2Cl co-transporter (*Slc12a2*) is absent [169]. Conversely, loss of H^+-ATPase function leads to a developmental expansion of the cochlear duct, and rather than collapse of Reissner's membrane, it is expanded toward the scala vestibuli and there is secondary atrophy of the stria vascularis [170].

Vestibular System Abnormalities

Similar to the cochlea, gene mutations affecting morphogenesis and patterning can cause malformation of the structure of vestibular organs [123, 171], and can be seen in some mouse models of human syndromes such as branchio-oto-renal syndrome [124] and DiGeorge syndrome [131]. Many forms of syndromic and nonsyndromic deafness have an associated vestibular phenotype. Degeneration of the neuroepithelium of the ampullae and maculae can occur, and it presents as thinning or absence of the cell layers or a decreased number of cells. Degenerative lesions usually affect all of these locations, but in some cases may involve only one area, such as the macula of the saccule [172]. With mutations affecting the production of endolymph and the maintenance of its ionic composition, such as in models of Jervell and Lange-Nielsen syndrome, one may see a contraction of the membranous labyrinth lining the utricle and saccule with an increased space containing perilymph [167, 168, 173]. Abnormalities in otoconia can occur, such as a complete absence [174–176], a decreased number (Figure 22.16), and abnormal morphology [177] (Table 22.4).

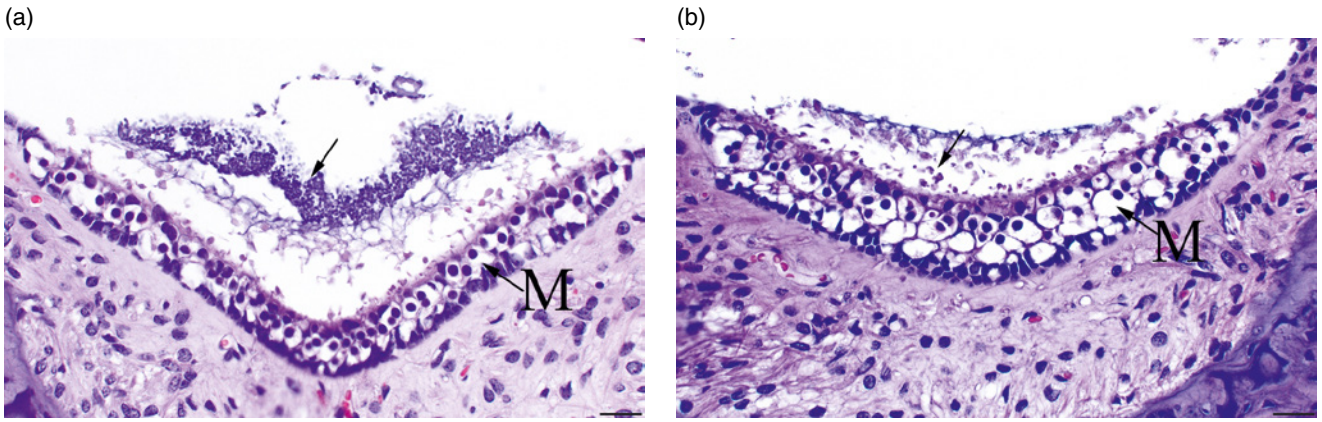


Figure 22.16 Decreased to absent otoconia over the macula (M). (a) Normal appearance of otoconia (arrow). (b) Otoconia are rare, and those present are malformed (arrow).

Table 22.4 Select genetically engineered and mutant mice for with hearing and vestibular phenotypes.

Syndrome	Gene name (human) and gene product	Mouse gene or mutant allele	Mouse phenotype
Craniofacial abnormalities			
Oto-auricular syndrome	*HMX1*, homeodomain transcription factor	H6 homeobox 1; dumbo (*Hmx1*^{dmbo}) MGI:3807705	Malformation of the external ear (and eye) [178]
Branchio-oto-renal (BOR) Syndrome	*EYA1*, EYA Transcriptional Coactivator and Phosphatase 1	EYA transcriptional coactivator and phosphatase 1; targeted mutation 1, Richard Maas (*Eya1*^{tm1Rilm}) MGI:2150426	Heterozygotes have malformed external and middle ears; knockout mice have absent external, middle, and inner ears [124]
DiGeorge Syndrome	*TBX1*, T-box transcription factor 1	T-box 1 (*Tbx1*) 34 alleles/ mutations MGI:98493	Malformed external, middle, and inner ears [130]
Treacher Collins syndrome	*TCOF1*, treacle ribosome biogenesis factor 1	treacle ribosome biogenesis factor 1; targeted mutation 1, Michael J Dixon (*Tcof1*^{tm1Mjd}) MGI:2386185	Malformed external and middle ears [136]
Defect in hair cells			
Usher 1B	*MYO7a*, myosin VIIA	myosin VIIA; shaker 1 (*Myo7a*^{sh1}) MGI:1856716 myosin VIIA; headbanger (*Myo7a*^{Hdb}) MGI:3511858	Near complete loss of inner and outer cochlear hair cells [156]
Usher 1C	*USH1c*, harmonin	USH1 protein network component harmonin; deaf circler (*Ush1c*^{dfcr}) MGI:2651858	Disorganized stereocilia with subsequent degeneration of the hair cells [108]
Usher 1D	*CDH23*, cadherin-23	cadherin 23 (otocadherin); waltzer (*Cdh23*^{v}) MGI:1856228	Cochlear hair cell degeneration [179, 180]
Usher 2D	*WHRN*, whirlin	whirlin; whirler (*Whrn*^{wi}) MGI:1857090	Abnormal development of stereocilia

Table 22.4 (Continued)

Syndrome	Gene name (human) and gene product	Mouse gene or mutant allele	Mouse phenotype
DFNB67	*LHFPL5*, lipoma HMGIC fusion partner-like 5	lipoma HMGIC fusion partner-like 5; hurry-scurry (*Lhfpl5*^{hscy}) MGI:3055797	Abnormal development of stereocilia [181]
DFNB49	*MARVELD2*, tricellulin	MARVEL (membrane-associating) domain containing 2; targeted mutation 1, Sachiko Tsukita (*Marveld2*^{tm1Sats}) MGI:6156852	Hair cell degeneration [109]
Stria vascularis			
Jervell and Lange-Nielsen Syndrome	*KCNE1*, potassium voltage-gated channel subfamily E regulatory subunit 1	potassium voltage-gated channel, Isk-related subfamily, member 1; punk rocker (*Kcne1*^{pkr}) MGI:1889639	Collapse of Reissner's membrane with secondary loss of hair cells [166]
Waardenburg syndrome Type 4	*EDNRB*, endothelin receptor type B	Endothelin receptor type B; Waardenburg syndrome 4 (*Ednrb*^{WS4}) MGI:2674291	Stria vascularis lacks intermediate cells [165]
Autosomal recessive nonsyndromic deafness 68	*S1PR2*, sphingosine-1-phosphate receptor 2	Sphingosine-1-phosphate receptor 2; stonedeaf (*S1pr2*^{stdf}) MGI:5423977	Stria vascularis degeneration [182, 183]
Tectorial membrane			
DFNB22	*OTOA*, otoancorin	Otoancorin; targeted mutation 1, Guy P Richardson (*Otoa*^{tm1Gpr}) MGI:5469411	Tectorial membrane is detached from the spiral limbus [162]
Vestibular system			
N/A	*ATG5*	autophagy related 5; targeted mutation 1, Noboru Mizushima (*Atg5*^{tm1Nmz}) MGI:3612279	Absence or malformation of otoconia [177]
N/A	*OTOP1*, otopetrin 1	Otopetrin 1 (*Otop1*) MGI:2388363 15 alleles/ mutations otopetrin 1; tilted (*Otop1*^{tlt}) MGI:1856638 otopetrin 1; mergulhador (*Otop1*^{mlh}) MGI:2655558	Absence of ototonia [175, 176]
N/A	*NOX3*, NADPH oxidase 3	NADPH oxidase 3; head-tilt (*Nox3*^{het}) MGI:1856606	Absence of otoconia [184]
Autosomal recessive nonsyndromic deafness	*SIPR2*, sphingosine-1-phosphate receptor 2	Sphingosine-1-phosphate receptor 2; targeted mutation 1, A John MacLennan (*S1pr2*^{tm1Ajml}) MGI:2180817	Degeneration of saccule epithelium and decreased otoconia [182]
N/A	*HMX3*, H6 family homeobox 3	H6 homeobox 3 (*Hmx3*) 6 alleles/ mutations MGI:107160	Degeneration of epithelium in saccule and utricle and fusion of the utricle and saccule endolymphatic spaces [185]

References

1 Shupe, J.M., Kristan, D.M., Austad, S.N., and Stenkamp, D.L. (2006). The eye of the laboratory mouse remains anatomically adapted for natural conditions. *Brain Behav. Evol.* 67 (1): 39–52.

2 Puk, O., Dalke, C., Favor, J. et al. (2006). Variations of eye size parameters among different strains of mice. *Mamm. Genome.* 17 (8): 851–857.

3 Kaufman, M.H. (1999). The eye and the ear. In: *The Anatomical Basis of Mouse Development* (eds. M.H. Kaufman and J.B. Bard), 194–207. San Diego, CA: Academic Press.

4 Smith, R.S., Sundberg, J.P., and John, S.W.M. (2001). The anterior segment and ocular adnexa. In: *Systematic Evaluation of the Mouse Eye: Anatomy, Pathology, and Biomethods* (eds. R.S. Smith, S.W.M. John, P.M. Nishina and J.P. Sundberg), 3–24. Boca Raton, FL: CRC Press.

5 Smith, R.S., John, S.W.M., and Nishina, P.M. (2001). The posterior segment and orbit. In: *Systematic Evaluation of the Mouse Eye: Anatomy, Pathology, and Biomethods* (eds. R.S. Smith, S.W.M. John, P.M. Nishina and J.P. Sundberg), 25–44. Boca Raton, FL: CRC Press.

6 Silvers WK. *The Coat Colors of Mice: A Model for Mammalian Gene Action and Interaction: Springer Verlag*; 1979.

7 Fairfield, H., Srivastava, A., Ananda, G. et al. (2015). Exome sequencing reveals pathogenic mutations in 91 strains of mice with Mendelian disorders. *Genome Res.* 25 (7): 948–957.

8 Bult, C.J., Blake, J.A., Smith, C.L. et al. (2019). Mouse Genome Database G. Mouse Genome Database (MGD) 2019. *Nucleic Acids Res.* 47 (D1): D801–D806.

9 Dunn, L.C. (1945). A new eye color mutant in the mouse with asymmetrical expression. *Proc. Natl Acad. Sci. U S A.* 31 (11): 343–346.

10 Peirson, S.N., Brown, L.A., Pothecary, C.A. et al. (2018). Light and the laboratory mouse. *J Neurosci Methods.* 300: 26–36.

11 Rathnasamy, G., Foulds, W.S., Ling, E.-A., and Kaur, C. (2019). Retinal microglia – A key player in healthy and diseased retina. *Prog. Neurobiol.* 173: 18–40.

12 Applebury, M.L., Antoch, M.P., Baxter, L.C. et al. (2000). The murine cone photoreceptor: a single cone type expresses both S and M opsins with retinal spatial patterning. *Neuron.* 27 (3): 513–523.

13 Thoreson, W.B. and Dacey, D.M. (2019). Diverse cell types, circuits, and mechanisms for color vision in the vertebrate retina. *Physiol. Rev.* 99 (3): 1527–1573.

14 Blankenship, T., Bradshaw, L., Shibata, B., and Fitzgerald, P. (2007). Structural specializations emerging late in mouse lens fiber cell differentiation. *Invest. Ophthalmol. Vis. Sci.* 48 (7): 3269–3276.

15 Ueda, Y., Duncan, M.K., and David, L.L. (2002). Lens proteomics: the accumulation of crystallin modifications in the mouse lens with age. *Invest. Ophthalmol. Vis. Sci.* 43 (1): 205–215.

16 Hejtmancik, J.F., Riazuddin, S.A., McGreal, R. et al. (2015). Lens biology and biochemistry. *Prog. Mol. Biol. Transl. Sci.* 134: 169–201.

17 Seabrook, T.A., Burbridge, T.J., Crair, M.C., and Huberman, A.D. (2017). Architecture, function, and assembly of the mouse visual system. *Ann. Rev. Neurosci.* 40 (1): 499–538.

18 Barabino, S., Chen, W., and Dana, M.R. (2004). Tear film and ocular surface tests in animal models of dry eye: uses and limitations. *Exp. Eye. Res.* 79 (5): 613–621.

19 Kilic, S. and Kulualp, K. (2016). Tear Production Rate in a Mouse Model of Dry Eye According to the Phenol Red Thread and Endodontic Absorbent Paper Point Tear Tests. *Comp Med.* 66 (5): 367–372.

20 Maurice, D.M. (1967). The use of fluorescein in ophthalmological research: The Jonas S. Friedenwald Memorial Lecture. *Invest. Ophthalmol. Vis. Sci.* 6 (5): 464–477.

21 Bellhorn, R.W. (1973). Fluorescein fundus photography in veterinary ophthalmology. *J. Am. Anim. Hosp. Assoc.* 9: 227–233.

22 McDonald, T.O., Baldwin, H.A., and Beasley, C.H. (1973). Slit-lamp examination of experimental animal eyes. I. Techniques of illumination and the normal eye. *J. Soc. Cosmet. Chem.* 24: 163–180.

23 Liu, A.S., Brown, D., Conn, R.E. et al. (2019). Mouse corneal topography, pachymetry, and keratometry utilizing OCT with keratometer validation. *Invest. Ophthal. Vis. Sci.* 60 (9): 185.

24 John, S.W., Hagaman, J.R., MacTaggart, T.E. et al. (1997). Intraocular pressure in inbred mouse strains. *Invest. Ophthalmol. Vis Sci.* 38 (1): 249–253.

25 SWM, J. and Savinova, O.V. (2001). Other techniques B. Intraocular pressure measurement in mice: technical aspects. In: *Systematic evaluation of the mouse eye: Anatomy, Pathology, and Biomethods* (eds. R.S. Smith, J. SWM, P.M. Nishina and J.P. Sundberg), 313–320. Boca Raton, FL: CRC Press.

26 Danias, J., Kontiola, A.I., Filippopoulos, T., and Mittag, T. (2003). Method for the noninvasive measurement of intraocular pressure in mice. *Invest. Ophthalmol. Vis. Sci.* 44 (3): 1138–1141.

27 Savinova, O.V., Sugiyama, F., Martin, J.E. et al. (2001). Intraocular pressure in genetically distinct mice: an update and strain survey. *BMC. Genet.* 2: 12.

28 Xu, Q.W., Qaum, T., and Adamis, A.P. (2001). Sensitive blood-retinal barrier breakdown quantitation using Evans blue. *Invest. Ophthal. Vis. Sci.* 42 (3): 789–794.

29 Hawes, N.L., Smith, R.S., Chang, B. et al. (1999). Mouse fundus photography and angiography: a catalogue of normal and mutant phenotypes. *Mol Vis.* 5: 22.

30 Paques, M., Guyomard, J.L., Simonutti, M. et al. (2007). Panretinal, high-resolution color photography of the mouse fundus. *Invest. Ophthalmol. Vis. Sci.* 48 (6): 2769–2774.

31 Peachey, N.S. and Ball, S.L. (2003). Electrophysiological analysis of visual function in mutant mice. *Doc. Ophthalmol.* 107 (1): 13–36.

32 Nusinowitz, S., Ridder III William, H., and Heckenlively, J. (2001). Chapter 14 Other techniques C. Electrophysiological testing of the mouse visual system. In: *Systematic evaluation of the mouse eye: Anatomy, Pathology, and Biomethods* (eds. R.S. Smith, S.W.M. John, P.M. Nishina and J.P. Sundberg), 320–344. Boca Raton, FL: CRC Press.

33 Ruehl-Fehlert, C., Kittel, B., Morawietz, G. et al. (2003). Revised guides for organ sampling and trimming in rats and mice--part 1. *Exp Toxicol Pathol.* 55 (2–3): 91–106.

34 Morawietz, G., Ruehl-Fehlert, C., Kittel, B. et al. (2004). Revised guides for organ sampling and trimming in rats and mice--Part 3. A joint publication of the RITA and NACAD groups. *Exp. Toxicol. Pathol.* 55 (6): 433–449.

35 Smith, R.S., Zabaleta, A., John, S.W.M. et al. (2001). General and special histopathology. In: *Systematic Evaluation of the Mouse Eye: Anatomy, Pathology, and Biomethods* (eds. R.S. Smith, S.W.M. John, P.M. Nishina and J.P. Sundberg), 251–297. Boca Raton, FL: CRC Press.

36 Escher, P. and Schorderet, D.F. (2011). Exploration of the visual system: Part 1: Dissection of the mouse eye for RNA, protein, and histological analyses. *Curr. Protoc. Mouse Biol.* 1 (4): 445–462.

37 Ramos, M.F., Baker, J., Atzpodien, E.A. et al. (2018). Nonproliferative and proliferative lesions of the Ratand mouse special sense organs(Ocular [eye and glands], olfactory and otic). *J. Toxicol. Pathol.* 31 (3 Suppl): 97S–214S.

38 Smith, R.S., Roderick, T.H., and Sundberg, J.P. (1994). Microphthalmia and associated abnormalities in inbred black mice. *Lab. Anim. Sci.* 44 (6): 551–560.

39 Chase, H.B. (1944). Studies on an anophthalmic strain of mice. IV. a second major gene for anophthalmia. *Genetics.* 29 (3): 264–269.

40 Hess, E.J., Collins, K.A., Copeland, N.G. et al. (1994). Deletion map of the coloboma (Cm) locus on mouse chromosome 2. *Genomics.* 21 (1): 257–261.

41 Theiler, K. and Varnum, D.S. (1981). Development of coloboma (Cm/+), a mutation with anterior lens adhesion. *Anat. Embryol. (Berl).* 162 (1): 121–126.

42 Frame, S.R. and Slone, T.W. (1996). Nonneoplastic and neoplastic changes in the eye. In: *Pathobiology of the Aging Mouse*, vol. 2 (eds. U.D.D.L. Mohr, C.C. Capen, W.W. Carlton, et al.), 97. Washington, D.C.: ILSI Press.

43 Sundberg, J.P., Brown, K.S., Bates, R. et al. (1991). Suppurative conjunctivitis and ulcerative blepharitis in 129/J mice. *Lab. Anim. Sci.* 41 (5): 516–518.

44 Toonen, J., Liang, L., and Sidjanin, D.J. (2012). Waved with open eyelids 2 (woe2) is a novel spontaneous mouse mutation in the protein phosphatase 1, regulatory (inhibitor) subunit 13 like (Ppp1r13l) gene. *BMC Genet.* 13: 76.

45 Kalter, H. (1975). Prenatal epidemiology of spontaneous cleft lip and palate, open eyelid, and embryonic death in A/J mice. *Teratology.* 12 (3): 245–257.

46 Van Winkle, T.J. and Balk, M.W. (1986). Spontaneous corneal opacities in laboratory mice. *Lab. Anim. Sci.* 36 (3): 248–255.

47 Li Q, Philip VM, Stearns TM, Bubier JA, King BL, Low BE, et al. Quantitative trait locus and integrative genomics revealed candidate modifier genes for ectopic mineralization in mouse models of Pseudoxanthoma elasticum. J Invest. Dermatol. 2019;139(12):2447–2457.e7.

48 Friedlander, M. (2007). Fibrosis and diseases of the eye. *J. Clin. Invest.* 117 (3): 576–586.

49 Chang, B., Smith, R.S., Hawes, N.L. et al. (1999). Interacting loci cause severe iris atrophy and glaucoma in DBA/2J mice. *Nat. Genet.* 21 (4): 405–409.

50 Anderson, M.G., Smith, R.S., Hawes, N.L. et al. (2002). Mutations in genes encoding melanosomal proteins cause pigmentary glaucoma in DBA/2J mice. *Nat. Genet.* 30 (1): 81–85.

51 Song, C.W., Okumoto, M., Mori, N. et al. (1997). A new hereditary cataract mouse with lens rupture. *Lab. Anim.* 31 (3): 248–253.

52 Takeda, T., Matsushita, T., Kurozumi, M. et al. (1997). Pathobiology of the senescence-accelerated mouse (SAM). *Exp. Gerontol.* 32 (1–2): 117–127.

53 Favor, J. (1983). A comparison of the dominant cataract and recessive specific-locus mutation rates induced by treatment of male mice with ethylnitrosourea. *Mutat. Res.* 110 (2): 367–382.

54 Tsang SH, Woodruff ML, Yamashita CK, Lee W, Goff SP, Gouras P, et al. A new animal model of congenital stationary night blindness (CSNB). Invest. Ophthal. Vis. Sci. 2003;44(13):4515–.

55 Ammann, S., Schulz, A., Krageloh-Mann, I. et al. (2016). Mutations in AP3D1 associated with immunodeficiency and seizures define a new type of Hermansky-Pudlak syndrome. *Blood.* 127 (8): 997–1006.

56 Cheng, L.L., Han, R.Y., Yang, F.Y. et al. (2016). Novel mutations in PDE6B causing human retinitis pigmentosa. *Int. J. Ophthalmol.* 9 (8): 1094–1099.

57 Hart, A.W., McKie, L., Morgan, J.E. et al. (2005). Genotype–phenotype correlation of mouse Pde6b mutations. *Invest. Ophthal. Vis. Sci.* 46 (9): 3443–3450.

58 Moore, B.A., Roux, M.J., Sebbag, L. et al. (2018). A population study of common ocular abnormalities in C57BL/6N rd8 mice. *Invest. Ophthalmol. Vis. Sci.* 59 (6): 2252–2261.

59 Mattapallil, M.J., Wawrousek, E.F., Chan, C.C. et al. (2012). The Rd8 mutation of the Crb1 gene is present in vendor lines of C57BL/6N mice and embryonic stem cells, and confounds ocular induced mutant phenotypes. *Invest. Ophthalmol. Vis. Sci.* 53 (6): 2921–2927.

60 van Nie, R., Iványi, D., and Démant, P. (1978). A new H-2-linked mutation, rds, causing retinal degeneration in the mouse. *Tissue Antigens.* 12 (2): 106–108.

61 Tucker, P., Laemle, L., Munson, A. et al. (2001). The eyeless mouse mutation (ey1) removes an alternative start codon from the Rx/rax homeobox gene. *Genesis.* 31 (1): 43–53.

62 Zode, G.S., Kuehn, M.H., Nishimura, D.Y. et al. (2011). Reduction of ER stress via a chemical chaperone prevents

disease phenotypes in a mouse model of primary open angle glaucoma. *J. Clin. Invest.* 121 (9): 3542–3553.
63 Gould, D.B., Miceli-Libby, L., Savinova, O.V. et al. (2004). Genetically increasing Myoc expression supports a necessary pathologic role of abnormal proteins in glaucoma. *Mol. Cell Biol.* 24 (20): 9019–9025.
64 Jinde, S., Zsiros, V., Jiang, Z. et al. (2012). Hilar mossy cell degeneration causes transient dentate granule cell hyperexcitability and impaired pattern separation. *Neuron.* 76 (6): 1189–1200.
65 Trantow, C.M., Mao, M., Petersen, G.E. et al. (2009). Lyst mutation in mice recapitulates iris defects of human exfoliation syndrome. *Invest. Ophthalmol Vis. Sci.* 50 (3): 1205–1214.
66 Libby, R.T., Smith, R.S., Savinova, O.V. et al. (2003). Modification of ocular defects in mouse developmental glaucoma models by tyrosinase. *Science.* 299 (5612): 1578–1581.
67 Weng, J., Mata, N.L., Azarian, S.M. et al. (1999). Insights into the function of Rim protein in photoreceptors and etiology of Stargardt's disease from the phenotype in abcr knockout mice. *Cell.* 98 (1): 13–23.
68 Karan, G., Lillo, C., Yang, Z. et al. (2005). Lipofuscin accumulation, abnormal electrophysiology, and photoreceptor degeneration in mutant ELOVL4 transgenic mice: a model for macular degeneration. *Proc. Natl Acad. Sci. U S A.* 102 (11): 4164–4169.
69 Rakoczy, P.E., Zhang, D., Robertson, T. et al. (2002). Progressive age-related changes similar to age-related macular degeneration in a transgenic mouse model. *Am. J. Pathol.* 161 (4): 1515–1524.
70 Sancho-Pelluz, J., Arango-Gonzalez, B., Kustermann, S. et al. (2008). Photoreceptor cell death mechanisms in inherited retinal degeneration. *Mol. Neurobiol.* 38 (3): 253–269.
71 Smith, R.S., Sundberg, J.P., and Linder, C.C. (1997). Mouse mutations as models for studying cataracts. *Pathobiology.* 65 (3): 146–154.
72 De Vera Mudry, M.C., Kronenberg, S., Komatsu, S., and Aguirre, G.D. (2013). Blinded by the light: retinal phototoxicity in the context of safety studies. *Toxicol. Pathol.* 41 (6): 813–825. doi: 10.1177/0192623312469308. Epub 2012 Dec 27.
73 Krinke GJ, Schaetti PR, Krinke A. Nonneoplastic and neoplastic changes in the Harderian and lacrimal glands. In: Mohr U DDL, Capen CC, Carlton WW, Sundberg JP, Ward JM, editor. Pathobiology of the Aging Mouse Vol 2. Washington, D.C.: ILSI Press; 1996. p. 139.
74 Ward, J.M., Goodman, D.G., Squire, R.A. et al. (1979). Neoplastic and nonneoplastic lesions in aging (C57BL/6N x C3H/HeN)F1 (B6C3F1) mice. *J. Natl Cancer Inst.* 63 (3): 849–854.
75 Mukaratirwa, S., Petterino, C., Naylor, S.W., and Bradley, A. (2015). Incidences and range of spontaneous lesions in the eye of Crl:CD-1(ICR)BR mice used in toxicity studies. *Toxicol. Pathol.* 43 (4): 530–535.
76 Carl, M., Loosli, F., and Wittbrodt, J. (2002). Six3 inactivation reveals its essential role for the formation and patterning of the vertebrate eye. *Development.* 129 (17): 4057–4063.
77 Purcell, P., Oliver, G., Mardon, G. et al. (2005). Pax6-dependence of Six3, Eya1 and Dach1 expression during lens and nasal placode induction. *Gene Expr. Patterns.* 6 (1): 110–118.
78 Chase, H.B. and Chase, E.B. (1941). Studies on an anophthalmic strain of mice I. Embryology of the eye region. *J. Morphol.* 68 (2): 279–301.
79 Chase, H.B. (1942). Studies on an anophthalmic strain of mice. III. Results of crosses with other strains. *Genetics.* 27 (3): 339–348.
80 Chase, H.B. (1945). Studies on an anophthalmic strain of mice; associated cranial nerves and brain centers. *J. Comp. Neurol.* 83 (2): 121–139.
81 Lima Cunha, D., Arno, G., Corton, M., and Moosajee, M. (2019). The spectrum of PAX6 mutations and genotype–phenotype correlations in the eye. *Genes (Basel).* 10 (12): 1050.
82 Keeler, C. (1966). Retinal degeneration in the mouse is rodless retina. *J. Hered.* 57 (2): 47–50.
83 Robb, R.M., Silver, J., and Sullivan, R.T. (1978). Ocular retardation (or) in the mouse. *Invest. Ophthalmol. Vis. Sci.* 17 (5): 468–473.
84 Konyukhov, B.V. and Vakhrusheva, M.P. (1969). Abnormal development of eyes in mice homozygous for the fidget gene. *Teratology.* 2 (2): 147–157.
85 Steingrimsson, E., Moore, K.J., Lamoreux, M.L. et al. (1994). Molecular basis of mouse microphthalmia (mi) mutations helps explain their developmental and phenotypic consequences. *Nat. Genet.* 8 (3): 256–263.
86 Packer, S.O. (1967). The eye and skeletal effects of two mutant alleles at the microphthalmia locus of Mus musculus. *J. Exp. Zool.* 165 (1): 21–45.
87 Beasley, A.B. (1963). Inheritance and development of a lens abnormality in the mouse. *J. Morphol.* 112 (1): 1–11.
88 Graw J. Mouse models of congenital cataract. Eye (Lond). 1999;13 (Pt 3b)(3):438–44.
89 Silva, R.L., Thornton, J.D., Martin, A.C. et al. (2005). Arf-dependent regulation of Pdgf signaling in perivascular cells in the developing mouse eye. *EMBO J.* 24 (15): 2803–2814.
90 Wiggs, J.L., Pawlyk, B., Connolly, E. et al. (2014). Disruption of the blood-aqueous barrier and lens abnormalities in mice lacking lysyl oxidase-like 1 (LOXL1). *Invest. Ophthalmol. Vis. Sci.* 55 (2): 856–864.
91 Eppig, J.T., Motenko, H., Richardson, J.E. et al. (2015). The International Mouse Strain Resource (IMSR): cataloging worldwide mouse and ES cell line resources. *Mamm. Genome.* 26 (9–10): 448–455.
92 Collin GB, Gogna N, Chang B, Damkham N, Pinkney J, Hyde LF, et al. Mouse models of inherited retinal degeneration with photoreceptor cell loss. Cells. 2020;9(4).
93 Chang, B., Hurd, R., Wang, J., and Nishina, P. (2013). Survey of common eye diseases in laboratory mouse strains. *Invest. Ophthalmol. Vis. Sci.* 54 (7): 4974–4981.
94 Low, B.E., Krebs, M.P., Joung, J.K. et al. (2014). Correction of the Crb1rd8 allele and retinal phenotype in C57BL/6N

mice via TALEN-mediated homology-directed repair. *Invest. Ophthalmol. Vis. Sci.* 55 (1): 387–395.

95 Won, J., Shi, L.Y., Hicks, W. et al. (2011). Mouse model resources for vision research. *J. Ophthalmol.* 2011: 391384.

96 Leibovici M, Safieddine S, Petit C. Chapter 8 Mouse Models for Human Hereditary Deafness. Mouse Models of Developmental Genetic Disease. Current Topics in Developmental Biology. 84: Academic Press; 2008. p. 385–429.

97 Ingham, N.J., Pearson, S.A., Vancollie, V.E. et al. (2019). Mouse screen reveals multiple new genes underlying mouse and human hearing loss. *PLoS Biol.* 17 (4): e3000194.

98 Jero, J., Coling, D.E., and Lalwani, A.K. (2001). The use of Preyer's reflex in evaluation of hearing in mice. *Acta Oto-Laryngol.* 121 (5): 585–589.

99 Hardisty-Hughes, R.E., Parker, A., and Brown, S.D. (2010). A hearing and vestibular phenotyping pipeline to identify mouse mutants with hearing impairment. *Nat. Protoc.* 5 (1): 177–190.

100 Bowl, M.R., Simon, M.M., Ingham, N.J. et al. (2017). A large scale hearing loss screen reveals an extensive unexplored genetic landscape for auditory dysfunction. *Nat. Commun.* 8 (1): 886.

101 Akil, O., Oursler, A.E., Fan, K., and Lustig, L.R. (2016). Mouse auditory brainstem response testing. *Bio. Protoc.* 6 (6): e1768.

102 Zhou, X., Jen, P.H., Seburn, K.L. et al. (2006). Auditory brainstem responses in 10 inbred strains of mice. *Brain Res.* 1091 (1): 16–26.

103 Jones, S.M. and Jones, T.A. (2014). Genetics of peripheral vestibular dysfunction: lessons from mutant mouse strains. *J. Am. Acad. Audiol.* 25 (3): 289–301.

104 Parker, A., Chessum, L., Mburu, P. et al. (2016). Light and electron microscopy methods for examination of cochlear morphology in mouse models of deafness. *Curr. Protoc. Mouse Biol.* 6 (3): 272–306.

105 Brown, S.D., Hardisty-Hughes, R.E., and Mburu, P. (2008). Quiet as a mouse: dissecting the molecular and genetic basis of hearing. *Nat. Rev. Genet.* 9 (4): 277–290.

106 Giese, A.P.J., Tang, Y.Q., Sinha, G.P. et al. (2017). CIB2 interacts with TMC1 and TMC2 and is essential for mechanotransduction in auditory hair cells. *Nat Commun.* 8 (1): 43.

107 Liu, Z., Dearman, J.A., Cox, B.C. et al. (2012). Age-dependent *in vivo* conversion of mouse cochlear pillar and Deiters' cells to immature hair cells by Atoh1 ectopic expression. *J. Neurosci.* 32 (19): 6600–6610.

108 Johnson, K.R., Gagnon, L.H., Webb, L.S. et al. (2003). Mouse models of USH1C and DFNB18: phenotypic and molecular analyses of two new spontaneous mutations of the Ush1c gene. *Hum. Mol. Genet.* 12 (23): 3075–3086.

109 Kamitani, T., Sakaguchi, H., Tamura, A. et al. (2015). Deletion of tricellulin causes progressive hearing loss associated with degeneration of cochlear hair cells. *Sci. Rep.* 5: 18402.

110 Montgomery, S.C. and Cox, B.C. (2016). Whole mount dissection and immunofluorescence of the adult mouse cochlea. *J. Vis. Exp.* 107.

111 Fang, Q.J., Wu, F., Chai, R., and Sha, S.H. (2019). Cochlear surface preparation in the adult mouse. *J Vis Exp.* 153: e60299.

112 Zheng, Q.Y., Johnson, K.R., and Erway, L.C. (1999). Assessment of hearing in 80 inbred strains of mice by ABR threshold analyses. *Hear Res.* 130 (1–2): 94–107.

113 Dixon, J. and Dixon, M.J. (2004). Genetic background has a major effect on the penetrance and severity of craniofacial defects in mice heterozygous for the gene encoding the nucleolar protein Treacle. *Dev. Dyn.* 229 (4): 907–914.

114 Han X, Ge R, Xie G, Li P, Zhao X, Gao L, et al. Caspase-mediated apoptosis in the cochleae contributes to the early onset of hearing loss in A/J mice. ASN Neuro. 2015;7(1).

115 Johnson, K.R., Erway, L.C., Cook, S.A. et al. (1997). A major gene affecting age-related hearing loss in C57BL/6J mice. *Hear. Res.* 114 (1–2): 83–92.

116 Noben-Trauth, K., Zheng, Q.Y., and Johnson, K.R. (2003). Association of cadherin 23 with polygenic inheritance and genetic modification of sensorineural hearing loss. *Nat Genet.* 35 (1): 21–23.

117 Noben-Trauth, K. and Johnson, K.R. (2009). Inheritance patterns of progressive hearing loss in laboratory strains of mice. *Brain Res.* 1277: 42–51.

118 Santagostino, S.F., Arbona, R.J.R., Nashat, M.A. et al. (2017). Pathology of aging in NOD scid gamma female mice. *Vet. Pathol.* 54 (5): 855–869.

119 MacArthur, C.J., Pillers, D.A., Pang, J. et al. (2008). Gram-negative pathogen Klebsiella oxytoca is associated with spontaneous chronic otitis media in Toll-like receptor 4-deficient C3H/HeJ mice. *Acta Otolaryngol.* 128 (2): 132–138.

120 Bleich, A., Kirsch, P., Sahly, H. et al. (2008). Klebsiella oxytoca: opportunistic infections in laboratory rodents. *Lab. Anim.* 42 (3): 369–375.

121 Gendron-Maguire, M., Mallo, M., Zhang, M., and Gridley, T. (1993). Hoxa-2 mutant mice exhibit homeotic transformation of skeletal elements derived from cranial neural crest. *Cell.* 75 (7): 1317–1331.

122 Rijli, F.M., Mark, M., Lakkaraju, S. et al. (1993). A homeotic transformation is generated in the rostral branchial region of the head by disruption of Hoxa-2, which acts as a selector gene. *Cell.* 75 (7): 1333–1349.

123 Chisaka, O., Musci, T.S., and Capecchi, M.R. (1992). Developmental defects of the ear, cranial nerves and hindbrain resulting from targeted disruption of the mouse homeobox gene Hox-1.6. *Nature.* 355 (6360): 516–520.

124 Xu, P.X., Adams, J., Peters, H. et al. (1999). Eya1-deficient mice lack ears and kidneys and show abnormal apoptosis of organ primordia. *Nat. Genet.* 23 (1): 113–117.

125 Rowe, T.M., Rizzi, M., Hirose, K. et al. (2006). A role of the double-stranded RNA-binding protein PACT in mouse ear development and hearing. *Proc. Natl Acad. Sci. U S A.* 103 (15): 5823–5828.

126 Selleri, L., Depew, M.J., Jacobs, Y. et al. (2001). Requirement for Pbx1 in skeletal patterning and programming chondrocyte proliferation and differentiation. *Development.* 128 (18): 3543–3557.

127 Pau, H., Fuchs, H., de Angelis, M.H., and Steel, K.P. (2005). Hush puppy: a new mouse mutant with pinna, ossicle, and inner ear defects. *Laryngoscope.* 115 (1): 116–124.

128 Newbern, J., Zhong, J., Wickramasinghe, R.S. et al. (2008). Mouse and human phenotypes indicate a critical conserved role for ERK2 signaling in neural crest development. *Proc. Natl Acad. Sci. U S A.* 105 (44): 17115–17120.

129 Downey, C.M., Horton, C.R., Carlson, B.A. et al. (2009). Osteo-chondroprogenitor-specific deletion of the selenocysteine tRNA gene, Trsp, leads to chondronecrosis and abnormal skeletal development: a putative model for Kashin-Beck disease. *PLoS Genet.* 5 (8): e1000616.

130 Paylor, R., Glaser, B., Mupo, A. et al. (2006). Tbx1 haploinsufficiency is linked to behavioral disorders in mice and humans: implications for 22q11 deletion syndrome. *Proc. Natl. Acad. Sci. U S A.* 103 (20): 7729–7734.

131 Moraes, F., Novoa, A., Jerome-Majewska, L.A. et al. (2005). Tbx1 is required for proper neural crest migration and to stabilize spatial patterns during middle and inner ear development. *Mech. Dev.* 122 (2): 199–212.

132 Lynch, C.J. (1921). Short ears, an autosomal mutation in the house mouse. *Am. Nat.* 55: 421–426.

133 Green ELaG, M.C. (1942). The development of three manifestations of the short ear gene in the mouse. *J. Morphol.* 70: 1–19.

134 King, J.A., Marker, P.C., Seung, K.J., and Kingsley, D.M. (1994). BMP5 and the molecular, skeletal, and soft-tissue alterations in short ear mice. *Dev. Biol.* 166 (1): 112–122.

135 Mentzer, S.E., Sundberg, J.P., Awgulewitsch, A. et al. (2008). The mouse hairy ears mutation exhibits an extended growth (anagen) phase in hair follicles and altered Hoxc gene expression in the ears. *Vet. Dermatol.* 19 (6): 358–367.

136 Dixon, J., Jones, N.C., Sandell, L.L. et al. (2006). Tcof1/Treacle is required for neural crest cell formation and proliferation deficiencies that cause craniofacial abnormalities. *Proc. Natl Acad. Sci. U S A.* 103 (36): 13403–13408.

137 Lv, K., Huang, H., Yi, X. et al. (2017). A novel auditory ossicles membrane and the development of conductive hearing loss in Dmp1-null mice. *Bone.* 103: 39–46.

138 Zehnder, A.F., Kristiansen, A.G., Adams, J.C. et al. (2006). Osteoprotegrin knockout mice demonstrate abnormal remodeling of the otic capsule and progressive hearing loss. *Laryngoscope.* 116 (2): 201–206.

139 Tian, C., Harris, B.S., and Johnson, K.R. (2016). Ectopic mineralization and conductive hearing loss in Enpp1asj mutant mice, a new model for otitis media and tympanosclerosis. *PLoS One.* 11 (12): e0168159.

140 Yang, B., Tian, C., Zhang, Z.G. et al. (2011). Sh3pxd2b mice are a model for craniofacial dysmorphology and otitis media. *PLoS One.* 6 (7): e22622.

141 Depreux, F.F., Darrow, K., Conner, D.A. et al. (2008). Eya4-deficient mice are a model for heritable otitis media. *J. Clin. Invest.* 118 (2): 651–658.

142 Zhang, Y., Yu, H., Xu, M. et al. (2012). Pathological features in the LmnaDhe/+ mutant mouse provide a novel model of human otitis media and laminopathies. *Am. J. Pathol.* 181 (3): 761–774.

143 Bartlett, J.A., Meyerholz, D.K., Wohlford-Lenane, C.L. et al. (2015). Increased susceptibility to otitis media in a Splunc1-deficient mouse model. *Dis. Model. Mech.* 8 (5): 501–508.

144 Voronina, V.A., Takemaru, K., Treuting, P. et al. (2009). Inactivation of Chibby affects function of motile airway cilia. *J. Cell Biol.* 185 (2): 225–233.

145 Parkinson, N., Hardisty-Hughes, R.E., Tateossian, H. et al. (2006). Mutation at the Evi1 locus in Junbo mice causes susceptibility to otitis media. *PLoS Genet.* 2 (10): e149.

146 Leichtle, A., Hernandez, M., Ebmeyer, J. et al. (2010). CC chemokine ligand 3 overcomes the bacteriocidal and phagocytic defect of macrophages and hastens recovery from experimental otitis media in TNF−/− mice. *J. Immunol.* 184 (6): 3087–3097.

147 Hernandez, M., Leichtle, A., Pak, K. et al. (2008). Myeloid differentiation primary response gene 88 is required for the resolution of otitis media. *J. Infect. Dis.* 198 (12): 1862–1869.

148 Tateossian, H., Morse, S., Parker, A. et al. (2013). Otitis media in the Tgif knockout mouse implicates TGFbeta signalling in chronic middle ear inflammatory disease. *Hum. Mol. Genet.* 22 (13): 2553–2565.

149 Leichtle, A., Hernandez, M., Pak, K. et al. (2009). The toll-Like receptor adaptor TRIF contributes to otitis media pathogenesis and recovery. *BMC Immunol.* 10: 45.

150 Leichtle, A., Hernandez, M., Lee, J. et al. (2012). The role of DNA sensing and innate immune receptor TLR9 in otitis media. *Innate Immun.* 18 (1): 3–13.

151 Schachern, P.A., Cureoglu, S., Tsuprun, V. et al. (2007). Age-related functional and histopathological changes of the ear in the MPS I mouse. *Int. J. Pediatr. Otorhinolaryngol.* 71 (2): 197–203.

152 Heldermon, C.D., Hennig, A.K., Ohlemiller, K.K. et al. (2007). Development of sensory, motor and behavioral deficits in the murine model of Sanfilippo syndrome type B. *PLoS One.* 2 (8): e772.

153 Wu, X., Steigelman, K.A., Bonten, E. et al. (2010). Vacuolization and alterations of lysosomal membrane proteins in cochlear marginal cells contribute to hearing loss in neuraminidase 1-deficient mice. *Biochim. Biophys. Acta.* 1802 (2): 259–268.

154 Longo-Guess, C.M., Gagnon, L.H., Cook, S.A. et al. (2005). A missense mutation in the previously undescribed gene Tmhs underlies deafness in hurry-scurry (hscy) mice. *Proc. Natl. Acad. Sci. U S A.* 102 (22): 7894–7899.

155 Johnson, K.R., Longo-Guess, C.M., and Gagnon, L.H. (2012). Mutations of the mouse ELMO domain containing 1 gene (Elmod1) link small GTPase signaling to actin cytoskeleton dynamics in hair cell stereocilia. *PLoS One.* 7 (4): e36074.

156 Calabro, K.R., Boye, S.L., Choudhury, S. et al. (2019). A novel mouse model of MYO7A USH1B reveals auditory and visual system haploinsufficiencies. *Front. Neurosci.* 13: 1255.

157 Huh, S.H., Jones, J., Warchol, M.E., and Ornitz, D.M. (2012). Differentiation of the lateral compartment of the cochlea requires a temporally restricted FGF20 signal. *PLoS Biol.* 10 (1): e1001231.

158 Lee, B., Baek, J.I., Min, H. et al. (2018). Exocyst complex member EXOC5 is required for survival of hair cells and spiral ganglion neurons and maintenance of hearing. *Mol. Neurobiol.* 55 (8): 6518–6532.

159 Holme, R.H., Kiernan, B.W., Brown, S.D., and Steel, K.P. (2002). Elongation of hair cell stereocilia is defective in the mouse mutant whirler. *J. Comp. Neurol.* 450 (1): 94–102.

160 Ohlemiller, K.K., Hennig, A.K., Lett, J.M. et al. (2002). Inner ear pathology in the mucopolysaccharidosis VII mouse. *Hear Res.* 169 (1–2): 69–84.

161 Laos, M., Sulg, M., Herranen, A. et al. (2017). Indispensable role of Mdm2/p53 interaction during the embryonic and postnatal inner ear development. *Sci. Rep.* 7: 42216.

162 Lukashkin, A.N., Legan, P.K., Weddell, T.D. et al. (2012). A mouse model for human deafness DFNB22 reveals that hearing impairment is due to a loss of inner hair cell stimulation. *Proc. Natl Acad. Sci. U S A.* 109 (47): 19351–19356.

163 Murillo-Cuesta, S., Camarero, G., Gonzalez-Rodriguez, A. et al. (2012). Insulin receptor substrate 2 (IRS2)-deficient mice show sensorineural hearing loss that is delayed by concomitant protein tyrosine phosphatase 1B (PTP1B) loss of function. *Mol. Med.* 18: 260–269.

164 Chen, J., Ingham, N., Kelly, J. et al. (2014). Spinster homolog 2 (spns2) deficiency causes early onset progressive hearing loss. *PLoS Genet.* 10 (10): e1004688.

165 Matsushima, Y., Shinkai, Y., Kobayashi, Y. et al. (2002). A mouse model of Waardenburg syndrome type 4 with a new spontaneous mutation of the endothelin-B receptor gene. *Mamm. Genome.* 13 (1): 30–35.

166 Letts, V.A., Valenzuela, A., Dunbar, C. et al. (2000). A new spontaneous mouse mutation in the Kcne1 gene. *Mamm. Genome.* 11 (10): 831–835.

167 Casimiro, M.C., Knollmann, B.C., Ebert, S.N. et al. (2001). Targeted disruption of the Kcnq1 gene produces a mouse model of Jervell and Lange-Nielsen Syndrome. *Proc. Natl Acad. Sci. U S A.* 98 (5): 2526–2531.

168 Lee, M.P., Ravenel, J.D., Hu, R.J. et al. (2000). Targeted disruption of the Kvlqt1 gene causes deafness and gastric hyperplasia in mice. *J Clin Invest.* 106 (12): 1447–1455.

169 Delpire, E., Lu, J., England, R. et al. (1999). Deafness and imbalance associated with inactivation of the secretory Na-K-2Cl co-transporter. *Nat. Genet.* 22 (2): 192–195.

170 Lorente-Canovas, B., Ingham, N., Norgett, E.E. et al. (2013). Mice deficient in H+-ATPase a4 subunit have severe hearing impairment associated with enlarged endolymphatic compartments within the inner ear. *Dis. Model Mech.* 6 (2): 434–442.

171 Edlund, R.K., Ohyama, T., Kantarci, H. et al. (2014). Foxi transcription factors promote pharyngeal arch development by regulating formation of FGF signaling centers. *Dev. Biol.* 390 (1): 1–13.

172 Alagramam, K.N., Kwon, H.Y., Cacheiro, N.L. et al. (1999). A new mouse insertional mutation that causes sensorineural deafness and vestibular defects. *Genetics.* 152 (4): 1691–1699.

173 Flagella, M., Clarke, L.L., Miller, M.L. et al. (1999). Mice lacking the basolateral Na-K-2Cl cotransporter have impaired epithelial chloride secretion and are profoundly deaf. *J. Biol. Chem.* 274 (38): 26946–26955.

174 Kozel, P.J., Friedman, R.A., Erway, L.C. et al. (1998). Balance and hearing deficits in mice with a null mutation in the gene encoding plasma membrane Ca2+-ATPase isoform 2. *J. Biol. Chem.* 273 (30): 18693–18696.

175 Hurle, B., Ignatova, E., Massironi, S.M. et al. (2003). Non-syndromic vestibular disorder with otoconial agenesis in tilted/mergulhador mice caused by mutations in otopetrin 1. *Hum. Mol. Genet.* 12 (7): 777–789.

176 Ornitz, D.M., Bohne, B.A., Thalmann, I. et al. (1998). Otoconial agenesis in tilted mutant mice. *Hear. Res.* 122 (1–2): 60–70.

177 Mariño, G., Fernandez, A.F., Cabrera, S. et al. (2010). Autophagy is essential for mouse sense of balance. *J. Clin. Invest.* 120 (7): 2331–2344.

178 Rosin, J.M., Li, W., Cox, L.L. et al. (2016). A distal 594 bp ECR specifies Hmx1 expression in pinna and lateral facial morphogenesis and is regulated by the Hox-Pbx-Meis complex. *Development.* 143 (14): 2582–2592.

179 Wilson, S.M., Householder, D.B., Coppola, V. et al. (2001). Mutations in Cdh23 cause nonsyndromic hearing loss in waltzer mice. *Genomics.* 74 (2): 228–233.

180 Palma, F.D., Holme, R.H., Bryda, E.C. et al. (2001). Mutations in Cdh23, encoding a new type of cadherin, cause stereocilia disorganization in waltzer, the mouse model for Usher syndrome type 1D. *Nature Genet.* 27 (1): 103–107.

181 Xiong, W., Grillet, N., Elledge, H.M. et al. (2012). TMHS is an integral component of the mechanotransduction machinery of cochlear hair cells. *Cell.* 151 (6): 1283–1295.

182 MacLennan, A.J., Benner, S.J., Andringa, A. et al. (2006). The S1P2 sphingosine 1-phosphate receptor is essential for auditory and vestibular function. *Hear. Res.* 220 (1–2): 38–48.

183 Ingham, N.J., Carlisle, F., Pearson, S. et al. (2016). S1PR2 variants associated with auditory function in humans and endocochlear potential decline in mouse. *Sci. Rep.* 6: 28964.

184 Bergstrom, R.A., You, Y., Erway, L.C. et al. (1998). Deletion mapping of the head tilt (het) gene in mice: a vestibular mutation causing specific absence of otoliths. *Genetics.* 150 (2): 815–822.

185 Wang, W., Van De Water, T., and Lufkin, T. (1998). Inner ear and maternal reproductive defects in mice lacking the Hmx3 homeobox gene. *Development.* 125 (4): 621–634.

23

Bones and Teeth

Peter Vogel, John P. Sundberg, and Cheryl Ackert-Bicknell

Introduction

Bones and teeth are composite structures consisting mostly of a collagenous organic matrix mineralized with a hydroxylapatite analog [1]. Bone and dentin are produced by osteoblasts and odontoblasts, respectively, whose main function is to form a mineralized matrix by secreting collagenous and noncollagenous proteins, as well as mediators of mineralization [2]. Most of the noncollagenous proteins in bone and dentin are phosphorylated [3], while those associated with enamel (amelogenins, ameloblastins, and enamelins) are not [4].

Pathologists should evaluate bones and teeth together because many bone abnormalities are accompanied by dentin defects in teeth. For example, mice with abnormalities in the genes that express or modify type I collagen develop both osteogenesis imperfecta (OI) and dentinogenesis imperfecta [5]. This is not entirely unexpected given that osteoblasts and odontoblasts both produce a mineralizing matrix and differentiate from the same types of mesenchymal stem cells. The differentiating developmental factor for these two cell types is that RUNX2 is downregulated for odontoblast differentiation, and it has been shown that increased levels of RUNX2 induces odontoblasts to transdifferentiate into osteoblasts [6, 7]. In addition, both osteoblasts and odontoblasts express the same growth factors belonging to the bone morphogenetic protein (BMP)/transforming growth factor beta (TGFB) superfamily, fibroblast growth factors (FGFs), and vascular endothelial growth factors [2], so the concurrent development of dentin and bone defects is not surprising. Many diseases involve the BMPs, growth factors that induce the formation of bone and cartilage [8] and are known to have a variety of functions in embryogenesis and skeletal development, as well as bone homeostasis and fracture healing [9, 10]. For the mouse pathologist, the presence of dentinal lesions is often the more easily detected and sensitive indicator of concurrent bone disease.

Bone

In humans, skeletal diseases comprise an extremely diverse and complex group of over 450 well-characterized disorders affecting the development and/or homeostasis of bone, with an overall prevalence of at least 1 per 4000 children [11, 12]. The 2019 International Skeletal Dysplasia Society nosology listed over 450 mutated genes linked to human skeletal disorders. These genes code for enzymes (33%), scaffolding proteins (18%), signal transduction proteins (16%), transcription factors (14%), cilia proteins (8%), extracellular matrix proteins (5%), and membrane transporters (4%). The resulting skeletal disorders were classified as aggrecanopathies, channelopathies, ciliopathies, cohesinopathies, laminopathies, linkeropathies, lysosomal storage diseases, protein-folding and RNA splicing defects, and ribosomopathies [13].

Bone Structure

Adult bone can be divided into two types: cortical bone, which is also referred to as compact or structural bone, and trabecular bone, which is also referred to as cancellous, spongy, or metabolic bone. In mice and rats, cortical bone constitutes the majority of bone mass. In larger mammals, trabecular bone plays a major role in adding structural strength to locations receiving high loads from various directions, such as near the joints. Mice have very few trabeculae per bone compartment and it is unclear how much of a structural role trabecular bone plays in locations such as the proximal tibia. The amount and shape of both cortical and trabecular bone varies widely among strains of inbred mice and can be considered polygenic traits [14–16]. For example, the commonly used C57BL/6J strain has very thin cortices in the long bone with relatively low amount of cortical bone relative to the size of the marrow cavity in the femur. The trabeculae of the distal femur and lumbar spine vertebral body in C57BL/6J mice are rod-shaped and thin. In contrast,

Pathology of Genetically Engineered and Other Mutant Mice, First Edition. Edited by John P. Sundberg, Peter Vogel, and Jerrold M. Ward.
© 2022 John Wiley & Sons, Inc. Published 2022 by John Wiley & Sons, Inc.

C3H/HeJ mice have thick cortical bone and thick plate-like trabeculae [17]. The strength of the long bones has been extensively studied as a quantitative trait; however, most of these studies have only found loci controlling bone size, which is the major determinant of bone strength in rodents [14].

Bone is a connective tissue composed of mineral, protein, water, and lipids. The proteinaceous extracellular matrix is highly ordered and is designed to withstand repetitive loads and dissipate the energy associated with loading in such a manner so as to prevent failure or fracture [18]. The proteinaceous matrix is mineralized, resulting in the rigid structure we consider as bone. The major constituent of both cortical and trabecular bone matrix is Type I collagen [19]. First, a procollagen molecule is assembled which is a triple helical protein composed of two polypeptide chains of collagen type I alpha I (COL1A1) and one chain of collagen, type I, alpha 2 (COL1A2). Each procollagen molecule is posttranslationally modified, including the removal of both N and C terminal residues to yield the final structural tropocollagen triple helix which is approximately 1.5 ηm in diameter [18]. The tropocollagen is mineralized with hydroxylapatite crystals arranged in a spiral fashion with repeat of the spiral occurring every 300 ηm. These fibrils are arranged in an antiparallel fashion with a strict 67 ηm offset in the arrangement to form fibers [18] which are in turn arranged in a lamellar sheet arrangement. Each lamellar sheet is approximately 1 μm thick, and these are layered in bone in a rotational twisted plywood arrangement [20]. In addition to collagen, 15% of the protein content of bone is noncollagenous and is composed of glycoproteins, growth factors, enzymes, and other noncollagenous structural proteins [21].

Bone Cells

Osteoblasts are cuboidal cells of mesenchymal origin that are found on the surface of bone [22]. These cells go through a complex and tightly controlled differentiation process, with terminal differentiation initiated by the transcription factor RUNX2 [23]. Mice lacking *Runx2* are not viable and are completely unable to form any calcified bony tissue. Expression of *Runx2* induces expression of Osterix (gene name is *Sp7*), a zinc finger containing transcription factor almost exclusively expressed in preosteoblast cells. Like *Runx2* null mice, mice lacking *Sp7* are not viable, although some mineralized elements are found in their skeletons [24]. The control over the final maturation and function of mature osteoblasts involves multiple signaling pathways including (but not limited to) the BMP pathway, both the canonical and noncanonical WNT pathways and hedgehog, Notch, FGF, IGF1, PTH, and TGFB signaling [25].

Osteocytes are former osteoblasts that have become embedded inside the bone matrix. The osteocytes remain in contact with each other and with cells on the bone surface through gap-junction-coupled cell processes that pass through the matrix via canaliculi [26]. Compared to the osteoblast, considerably less is known about the osteocytes, although it is generally agreed that osteocytes are the mechnosensing/load-sensing cells of bone and play a critical role in regulating osteoblast activity [26]. In addition, osteocytes are the major source of FGF-23, a hormone critical for phosphate metabolism [27]. Lastly, osteocytes are able to lyse/resorb bone and play a critical role in calcium mobilization in pregnancy and during lactation [28].

Osteoclasts are large multinuclear cells of myeloid origin that mediate bone resorption [22]. Bone resorption by osteoclasts occurs through a complex multistep process that requires proliferation and fusion of osteoclast precursors, establishing close contact with the bone surface, and the secretion of protons and enzymes that break down the inorganic and organic constituents of bone [29]. Mature osteoclasts on the bone surface normally form a sealing zone to create an isolated extracellular microenvironment or lacuna where the so-called "ruffled" membrane releases hydrogen ($H+$) and chloride ($Cl-$) ions via an ATPase proton pump and CLC chloride channel to dissolve bone mineral. Osteoclasts also release proteolytic enzymes such as Cathepsin K that degrade bone matrix. The degradation products of bone resorption are transported via transcytosis though the osteoclast and can be detected in both the serum and in the urine [29]. In research, serum levels of the phosphatase TRAP5B in mice is a useful indicator of osteoclast number, but this measure should be coupled with levels of collagen degradation products such as NTX or CTX, because these latter markers are indicative of osteoclastic activity/bone resorption. Bone mass is basically controlled by the balance between the bone forming activity of osteoblasts and bone resorption by osteoclasts [30].

Differences Between Mouse and Man

Mice provide useful bone disease models because their genome shares a high degree of homology with the human genome and their rapid development allows completion of long-term investigations in a 6- to 12-month period [31, 32]. Thus, mouse models are able to provide key insights into the pathophysiology of skeletal and dental diseases affecting humans [33–35]. A recent review showed that mouse skeletal phenotypes mimicked the human skeletal disorders in 249 of 260 genes (96%), clearly demonstrating the relevance of mouse models for identifying genes affecting bone mass, architecture, mineralization, and strength [36]. Another advantage of mouse models is that advanced genetic engineering approaches can be used to produce mice with the same hypomorphic, gain-of-function, dominant-negative, or intronic mutations involved in specific human diseases [36].

However, there are clear differences between mice and humans in the size, structure, development, and metabolism of bones [37]. In humans, lamellar bone is remodeled via internal Haversian systems while mouse bones undergo surface rather than intracortical remodeling. In humans, the epiphyses fuse shortly after puberty, whereas epiphyseal fusion remains incomplete in mice. The consequence of this is that there is the potential for longitudinal bone growth to

continue throughout life in mice. However, the amount of this growth is strain-specific, with some strains exhibiting up to 8% increase in body length between 6 and 12 months of age while others, such as C57BL/6J mice, have largely ceased growth by 6 months. Substantial body length increases have been observed in adult *Little* dwarf mice, which carry a mutation in the growth hormone releasing hormone receptor (*Ghrhr*) gene [38].

The pattern of bone loss and gain of trabecular bone in the long bones or axial skeleton is very different in humans compared to mice. In mice, trabecular bone mass can peak as early as eight weeks of age in C57BL/6J and DBA/2J mice, followed by rapid loss. In C3H/HeJ mice, trabecular bone mass peaks at five months of age, but these mice also experience rapid postpeak trabecular loss [39, 40]. In outbred mouse populations, such as the Diversity outbred, 100% of trabecular bone can be lost in the distal femur by six months of age with no association with fracture [14]. These findings suggest that trabecular bone in the appendicular skeleton of mice has little to no structural/strength role, unlike in humans and larger mammals.

Phenotyping Mouse Bone

Histomorphometry

Histomorphometry of bone and cartilage is an important tool with which to study the pathophysiology of bone disease in mice. Both static and dynamic histomorphometric assays are used to quantify changes in bone. Mice should always be age- and sex-matched for histomorphometry analyses. The distal femur is best suited for measurements of osteoid width and area, osteoblast number/perimeter, osteoclast number/perimeter, and bone turnover/resorption, and articular cartilage [41], but it should be noted that there is no guarantee of concordance between the long bones and vertebrae in trabecular bone measurements. Indeed, large GWAS in humans and reverse genetic studies in mice have shown that trabecular bone of the spine and of long bones are controlled by both overlapping and discrete genetic factors [42, 43]. The femoral midshaft is usually used for cortical bone measurements, including measures of bone strength.

Static histomorphometry involves the histological analysis and quantification of cells (osteoblasts and osteoclasts) and structures (trabeculae) in 2D tissue sections of bone. Because the amounts and thickness of both trabecular and cortical bone vary in different regions within a single bone, standardization of collection sites, and tissue orientation is essential for histomorphometry studies [42]. Although H&E staining is usually sufficient for evaluating static structures and cell numbers, histochemical staining for alkaline phosphatase (ALP) (osteoblasts) and tartrate-resistant acid phosphatase (TRAP) (osteoclasts) may be indicated. These enzymatic histochemical assays have traditionally required either ethylene diamine tetraacetic acid (EDTA) decalcification of bone before paraffin embedding or embedding undecalcified bones in plastic or resin. However, newer techniques such as cryo-histology on undecalcified bones can also yield satisfactory results [44].

Dynamic histomorphometry involves the *in vivo* labeling of bone with fluorochromes and is used to quantify the rate of bone formation and remodeling, and thus more directly assess the activity of osteoclasts and osteoblasts [45]. It requires the administration of calcium-chelating fluorochromes such as calcein, tetracycline, or Alizarin red complexome at predetermined time points before mice are euthanized and tissues collected. These compounds are fluorochromes that chelate with calcium in newly mineralized bone and fluoresce at wavelengths used with standard ultraviolet microscopy. The time-spaced administration of multiple labels that fluoresce at different wavelengths allows highly informative measures such as bone formation rate (BFR), mineral apposition rate (MAR), and the amount of mineralizing surface (MS/Bs) to be determined. The BFR and MAR slow as mice mature so the time intervals between the administration of the first label and the second label, and finally the time before euthanasia should all be extended in older mice. The American Society for Bone and Mineral Research has set standards for the nomenclature and units that should be used when reporting bone histomorphometry findings [46]. Unlike BFRs, bone resorption cannot be measured directly via histology, but a resorption rate can be estimated using certain assumptions based on change of bone volume [46]. There are large differences in bone formation and resorption between male and female mice, with the rate of turnover being much higher in females than males [42].

Dynamic histomorphometry studies have traditionally required embedding and sectioning of undecalcified bone, because the decalcification process removes the fluorochrome labels along with bone mineral. However, the preparation of undecalcified bone requires technically demanding procedures in which bone is embedded in plastic or resin (glycol methacrylate, methyl methacrylate, or Spurr's resin) and 50 μm sections cut with a tungsten carbide knife before being polished using high-precision grinding machines. The development of laser microtomes has made cutting serial 10–100 μm sections of nondecalcified bone, with better preservation of histological features, much easier and faster [47]. Nevertheless, these approaches require expensive equipment and techniques, which restricts their use to specialized laboratories. More recently, cryosectioning of undecalcified bones using a tape transfer method has proven to be a successful way to prepare samples for both static and dynamic bone histomorphometry studies [44]. Another new method of processing mineralized bones permits tissues to be embedded in paraffin and sectioned using standard histology equipment for both static and dynamic histomorphometry studies [48].

Whole Mounts

The entire skeleton of mice may be evaluated for gross defects by whole-mount staining with Alcian blue and Alizarin red to identify cartilage and bone, respectively.

Briefly, specimens are prepared by removing skin, organs, and brown fat and then are then dehydrated and fixed in 95% ethanol. For a more complete removal of adipose tissue and better tissue permeabilization, the specimens are immersed in acetone and then consecutively transferred to Alcian blue and Alizarin red staining solutions. The Alizarin red solution also contains potassium hydroxide, which hydrolyzes soft tissue and allows visualization of the stained bone and cartilage [49, 50]. Whole body mounts are used to characterize dysostoses affecting single bones, which are caused by mutations in early patterning genes, as well as the more widespread osteochondrodysplasias which are linked to genes involved in organogenesis [51].

Dual X-ray Absorptiometry (DXA)

Dual X-ray Absorptiometry (DXA) has been used clinically for the diagnosis of osteoporosis and osteopenia in human patients for decades [52] as it is strongly correlated to bone strength [53] and inversely correlated with fracture risk [54]. This method uses two energy levels to discriminate between bone and soft tissue [52], and while this method lacks the resolution of other methods, it remains widely used in research studies. In short, an X-ray source is placed above the animal and an array of detectors is placed below. The amount of attenuation of X-rays is recorded in a two-dimensional or areal array and interpreted as being bone, soft tissue (lean mass), or nonbone, nonsoft tissue (widely considered to be adipose tissue). From these measures, the bone mineral content (BMC), for the whole animal or a region of interest is calculated. This BMC measure is highly correlated to ash content of the bone [55]. Dividing BMC by the area considered to be bone (BA) yields the measure of bone mineral density (BMD). Fat mass is usually reported as the amount of measured adipose tissue divided by the total mass estimated from the total X-ray attenuation and is reported as a percent (% fat), and soft tissue mass is usually reported as the unadjusted mass considered to be soft tissue. While DXA is considered to be reasonably accurate for measuring BMD and BMC, it does tend to overestimate the % fat and underestimate lean mass, especially if the animal has a high fat mass [55]. The entire scan of a mouse using currently available commercial DXA instruments only takes minutes and an animal can be scanned multiple times, allowing for longitudinal study designs. DXA is the most commonly used method for high throughput screening of genetically engineered mouse (GEM) to quickly identify lines with BMC phenotypes [42]. However, whole-body DXA lacks the sensitivity of microcomputed tomography to distinguish between cortical from trabecular bone phenotypes [56] in the femur and selected lumbar vertebrae [57].

Microcomputed Tomography (μCT)

Unlike DXA, this method provides a high-resolution, three-dimensional reconstruction of bone. This method is considered the gold standard for the measure of architecture and size of cortical and trabecular bone. Instruments have been developed to allow for imaging of live animals, but at the cost of resolution. Higher-resolution measures can be obtained using machines designed solely for *ex vivo* specimens. For μCT, the specimen is placed between the X-ray source and a detector, and either the source or the detector moves around the sample, or the sample is rotated between the two. After a complete circuit of images is collected, the source/detector is moved on the z-plane relative to the sample, and the process is repeated, yielding "slices" of data used to reconstruct 3D images of cortical and trabecular bone.

Despite its sensitivity and precision, μCT does not accurately predict bone strength or provide much information about the underlying cause for altered bone density. While true measurements of bone strength are not possible using imaging techniques, it is possible to calculate estimated or geometrical strength of the diaphysis of the long bones [58]. The American Society for Bone and Mineral research has published detailed guidelines on the use and reporting of μCT derived measures for rodent bones [58].

Additional X-ray-Based Imaging Techniques

Peripheral Quantitative Computed Tomography (pQCT) is analogous in principle to μCT, albeit at substantially lower resolution [59], and most pQCT instruments that have been adapted for use with mice lack the resolution to accurately measure the trabecular compartment. Data from the use of pQCT for mice is found frequently in older literature, but this technique is not widely used in more recent studies.

Radiography remains a fast and simple method to scan the skeleton and teeth for abnormalities at time of necropsy. Symmetrical structures that overlap, such as bones and teeth in the skull, can be best visualized by bisecting the skull lengthwise and laying the halves side by side. This is especially useful for evaluating teeth [60]. Small enclosed units, such as the digital Faxitron® X-ray cabinet (https://www.faxitron.com/pre-clinical-imaging/) yield high-quality images that can be scanned quickly for obvious abnormalities. A new PATHBIO atlas will provide details of the normal mouse skeleton (anticipated 2021 public availability; www.pathbio.org/).

Biomechanical Testing

While BMD is correlated to strength, direct biomechanical tests are required to actually assess bone strength, and those used in mice include three-point bending of the radius for cortical bone strength [61], compression testing of lumbar vertebrae for cancellous bone strength [62], and torsion testing to assess healing of fractures, and other less commonly used mechanical tests for specific applications [63]. Depending on the test employed, one is able to measure bone strength, stiffness, fracture energy, and differences in elastic versus plastic deformation. These whole bone strength parameters can be coupled with measures of size

and shape obtained from high-resolution imaging, such as μCT, to calculate tissue level strength parameters [64].

Histology

Although histopathological evaluation of tissue sections cannot match the sensitivity of DEXA, μCT, or even pQCT in detecting bone phenotypes and quantifying changes in BMD, cortical bone thickness, or trabecular bone volume, it can nevertheless provide invaluable insights that explain the underlying pathogenetic processes responsible for structural changes in bone. There are hundreds of different genetic skeletal disorders affecting bones and joints, and histologic studies can help elucidate the pathophysiologic basis of many. Many bone phenotypes are the result of abnormal developmental processes, particularly those involving the differentiation and/or function of osteoblasts, osteoclasts, osteocytes, and cartilage, as well as the processes of extracellular matrix formation and biomineralization. The basic histological approach to assessing bone phenotypes is to focus on osteoclasts and osteoblasts and to assess changes affecting bone and cartilage.

Fixation and decalcification: As usual, the diagnostic value of histological specimens is improved markedly when mice are first fixed by intracardiac infusion at time of death followed by continued immersion fixation and decalcification. The most commonly used solutions for decalcification contain formic acid or EDTA. For screening purposes, aqueous formic acid in concentrations from 5% to 10% is generally considered to be the best overall choice for decalcification. However, when immunohistochemical or enzyme histochemical assays are planned on paraffin embedded sections of bones or teeth, we recommend perfusion fixation with either 10% neutral buffered formaldehyde or 95% ethanol 5% acetic acid (required for some immunohistochemistry (IHC) protocols), followed by decalcification in 20% EDTA pH 7.4 for no more than two weeks. EDTA is chelating agent that binds ionized calcium without destroying binding epitopes for IHC or inactivating enzymes for histochemical. Decalcification in EDTA can be a very slow compared to formic acid decalcification. In decalcifying bone specimens, the goal is to achieve sufficient decalcification to allow successful sectioning while avoiding over-decalcification that will obscure cellular details. As described earlier, immunohistochemical or enzyme histochemical assays can also be conducted on tape-supported cryosections from undecalcified bone [44].

Staining: Many different staining methods are available, but hematoxylin & eosin (H&E) are more than adequate for most studies, on both decalcified and undecalcified tissues. Goldner's or Masson's trichrome are also useful when staining bone and cartilage in both paraffin-embedded and plastic-embedded sections. Masson's trichrome clearly differentiates bone (dark blue) from cartilage (very pale blue) in decalcified samples. Goldner's trichrome and von Kossa's stains are used to differentiate osteoid from mineralized bone matrix in undecalcified bones.

Two enzymes involved in bone metabolism, TRAP and ALP, can be used to identify osteoclasts and osteoblasts, respectively. Special fixation and processing methods are required for the detection of ALP in decalcified formalin-fixed tissues [65], but histochemical detection of TRAP and immunohistochemical labeling of bone-specific ALP works well on formalin-fixed, EDTA decalcified bone (Figure 23.1). Other useful immunohistochemical markers include osteopontin (secreted phosphoprotein 1, SPP1), which is a noncollagenous bone matrix glycoprotein secreted by preosteoblasts/osteoblasts during bone remodeling [66]; osteocalcin, the protein product of the tandem genes *Bglap1* and *Bglap2*, which is highly expressed only in mature osteoblasts; and bone sialoprotein (integrin

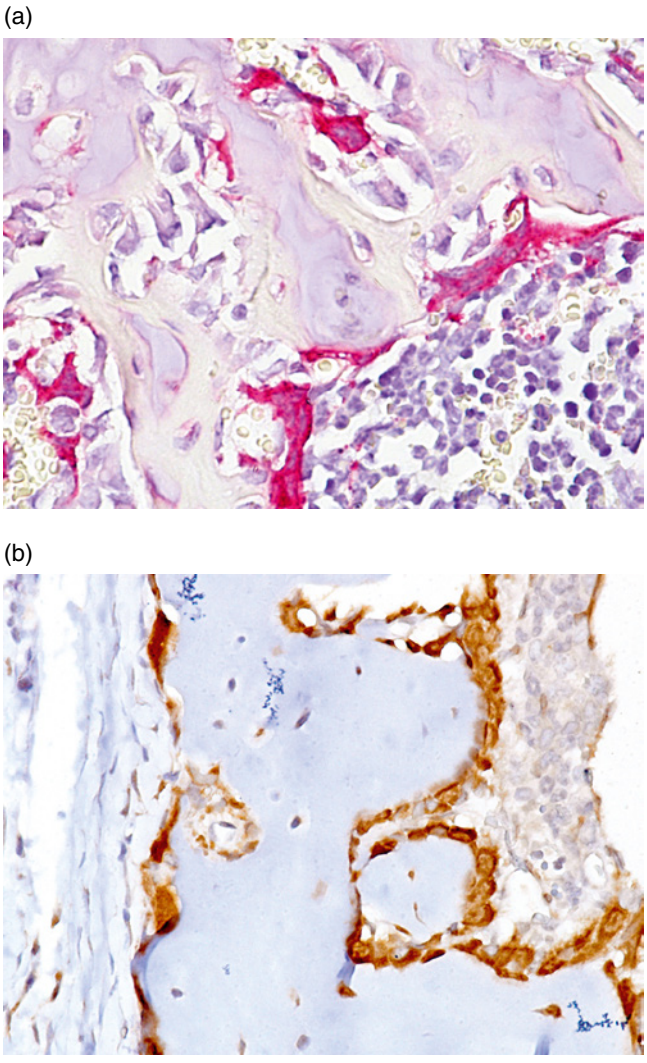


Figure 23.1 **Mouse bone**. (a) Enzyme histochemistry showing TRAP-positive osteoclasts (red). (b) Osteoblasts immunohistochemically labeled for alkaline phosphatase (brown).

binding sialoprotein, IBSP), and dentin matrix protein 1 (DMP1), which are additional markers of osteoblasts and preosteocytes/osteocytes, respectively [66].

Diseases of Bone

Fibro-osseous Lesions

Fibro-osseous lesions of bone represent a relatively common finding in many inbred mouse strains that increase in frequency and severity with age. Fibro-osseous lesions consist of a cytologically uniform fibrovascular stroma interspersed with fine irregular trabeculae of woven bone. There is no evidence of cytologic atypia, mitotic activity, osteonecrosis, permeative growth patterns, cortical transgression, associated inflammation, or osteoblastic rimming. These lesions can interfere with bone phenotyping if investigators are not aware of them as a background lesion that can affect all mice in some strains. In an aging study on 31 inbred strains mice [67], frequency in females ranged from 0% in 10 strains up to 100% in KK/HlJ and NZW/LacJ mice. For male mice, the frequency was significantly lower than in females, ranging from 0% for 23 strains up to 50% in BUB/BnJ mice. Histological features of murine fibro-osseous lesions resemble human Gorham–Stout syndrome or Gorham's massive osteolysis/angiomatosis [68, 69], but it remains unknown if these are truly orthologous conditions. Gorham–Stout syndrome is very rare and is not widely thought to be genetic, whereas fibro-osseous lesions in mice are clearly genetic and very reproducible in some inbred strains. Despite drastic cortical thinning, fibro-osseous lesions are not usually associated with spontaneous long bone fractures under normal laboratory husbandry conditions.

Diseases of High Bone Mass

Most high BMD and/or high bone mass phenotypes reflect impaired resorption by dysfunctional osteoclasts, which result in osteopetrosis or pycnodysostosis [1]. Mutations in any of the many different genes responsible for osteoclast differentiation and function can result in high bone mass phenotypes in mice. In affected mice, the most common histopathologic finding is retention of the primary spongiosa (cartilage cores in trabeculae) in the metaphysis of long bones (Figure 23.2). Osteoclast numbers can be reduced, normal, or increased in mice with high bone mass, depending on the nature of the underlying genetic defect, and newly formed bone can contain abundant microfractures (Figure 23.2). Although DXA and uCT analyses show that bones are typically very dense with osteoclast deficiencies, they are nevertheless brittle and prone to spontaneous fracture [70, 71]. Typical examples of high bone mass phenotypes caused by dysfunctional osteoclasts include mutations affecting *Clcn7* (human disease: autosomal dominant osteopetrosis 2 [72]) and *Lrrk1* (human disease: osteopetrosis [73]). Dental phenotypes are also associated with many different mutations affecting osteoclast development or function, often manifesting as blocked eruption of molar teeth in mice (discussed below). The result of decreased osteoclast mediated bone resorption is illustrated by the phenotype of the gray lethal mutation (*Ostm1*^{gl}) in mice. The *gl* allelic mutation consists of a 7.5 kb deletion on mouse chromosome 10, which includes the promoter and entire first exon of the osteopetrosis-associated transmembrane protein 1 gene (*Ostm1*) mice. These mice have a coat color defect, for which the allele was named, and have a defect in bone resorption [74]. Mature multinucleated osteoclasts are present in *Ostm1*$^{gl/gl}$ mice, but these osteoclasts are not functional [75]. This allele is completely penetrant and without a bone marrow transplant, null mice die by four weeks of age due to failure in bone marrow development [74]. This mouse is considered an appropriate model of the human condition of severe malignant autosomal recessive osteopetrosis (autosomal recessive osteopetrosis 5) [76]. The primary defect with osteoclast function in *Ostm1*$^{gl/gl}$ mice results from a failure in lysosomal dispersal [75].

A second much smaller group of sclerosing bone disorders are the result of increased bone formation by osteoblasts. Sclerostin deficient mice (*Sost*$^{tm1(KOMP)Vlcg}$ and *Sost*^{tm1Paz}; human disease: Sclerosteosis 1 and Van Buchem disease) show marked increase in BMD by DXA, and μCT analyses of the femur shows increased bone volume in both the trabecular and cortical compartments, which are also evident histologically (Figure 23.2). In contrast to the dense but weak bones with retained cartilage cores in trabeculae associated with dysfunctional osteoclasts, bone strength and trabecular bone are markedly increased in sclerostin-deficient mice [77]. The *Sost* gene is almost exclusively expressed by osteocytes and the SOST protein is a secreted factor that functions as an inhibitor of the pro-osteoblast maturation, probone formation WNT signaling pathway [78]. Indeed, blocking the function of this inhibitor of WNT signaling is the basis of Romosozumab, the newest anabolic agent approved by the FDA for the treatment of postmenopausal osteoporosis in humans [79]. A similar, albeit less dramatic phenotype is seen in humans with dominant activating mutations in the *LRP5* gene [78]. The LRP5 protein constitutes half of the heterodimer that acts as a canonical receptor for WNTs in osteoblasts [80] and transgenic mice heterozygous for the human G171V *Lrp5* activating mutation have high cortical bone volume and high trabecular bone volume fraction [81].

Diseases of Low Bone Mass

Low BMD diseases are typically associated with increased osteoclast activity or numbers (osteolysis), unbalanced bone turnover, defective bone matrix formation such as is seen in OI and with osteomalacia, or hypo-mineralization of bone (both described in the section below). Osteoporosis is the most common low bone mass disease in humans, and the correct use of this word as a diagnostic term is made using strict criteria set forth by the World Health Organization (WHO) and the National Osteoporosis Foundation (NOF). Because these WHO and NOF criteria are not applicable to mice, it is more appropriate to refer to a mouse model as having low BMD or low bone mass, depending on the method used for phenotyping.

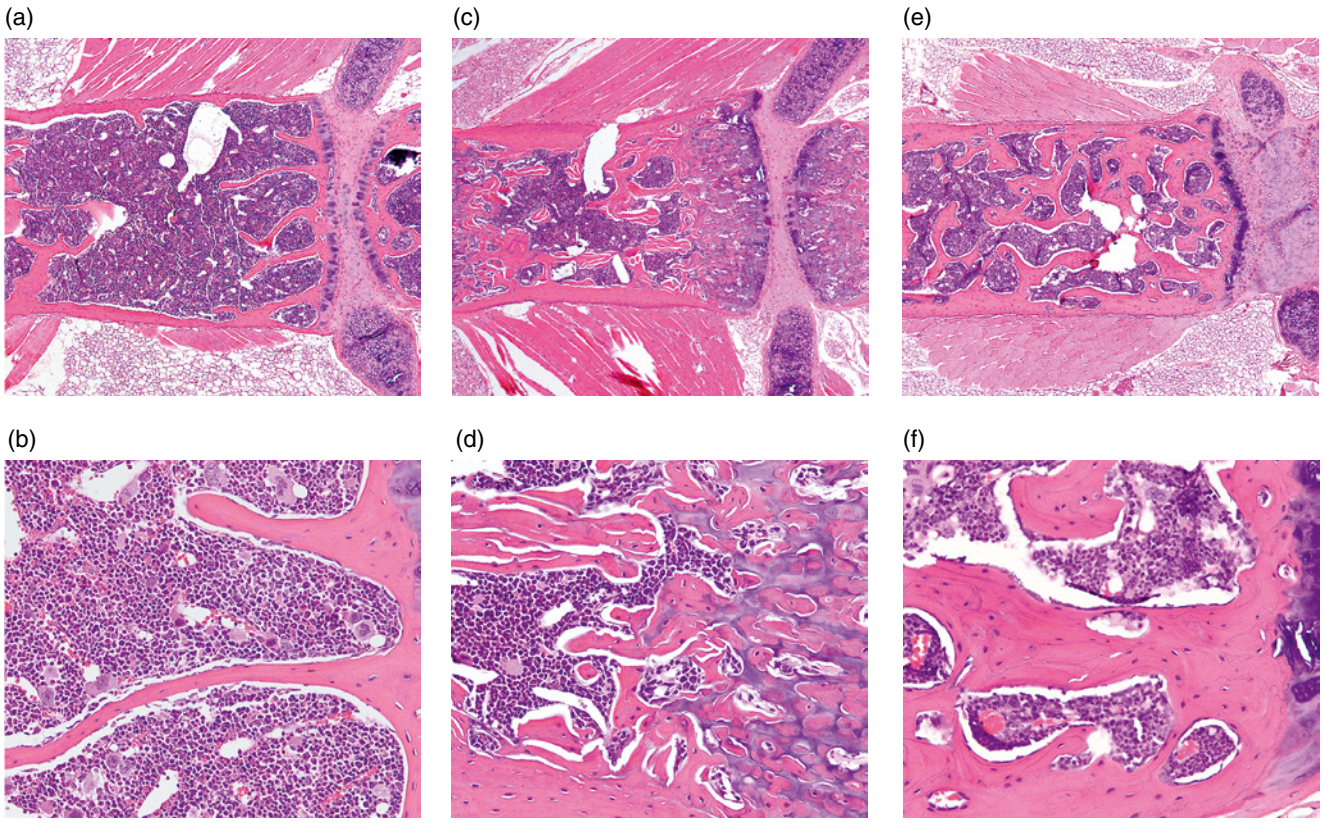


Figure 23.2 **Mouse sternebrae**. (a) Wild-type C57BL/6 mouse showing typical trabecular and cortical bone. (b) Normal bone at higher magnification. (c) Sternum from *Lrrk1* knockout mouse showing increased trabecular and cortical bone thickness. (d) Higher magnification of figure (c) showing retention of cartilage in primary spongiosa and poor attachment of new bone (microfractures) on trabecular and cortical bone. (e) Sternum from *Sost* knock-out mouse showing markedly increased thickness of trabecular and cortical bone. (f) Higher magnification of figure (e) showing normal structure of thickened trabecular and cortical bone.

Bone homeostasis depends on a balance between bone resorption by osteoclasts and bone formation by osteoblasts. Imbalances in this tightly controlled metabolic process can be due to increased osteoclast activity, decreased osteoblast activity, or a combination of both [82]. Osteoprotegerin (*Tnfrsf11b*, also commonly referred to as OPG) deficient mice (*Tnfrsf11b*^{tm1Eac} *Tnfrsf11b*^{tm1Wss}, and *Tnfrsf11b*^{tm1Wss}) display the classic histopathological lesions of low BMD disease in mice. These include decreased bone density, marked thinning of cortical and skull bones, reduced to absent trabeculae, a high incidence of spontaneous fractures, and medial calcification of the aorta and renal arteries [83]. In contrast, transgenic mice overexpressing *Tnfrsf11b* develop osteopetrosis [84]. Renal osteodystrophy associated with chronic kidney disease is also characterized by low BMD due to increased osteoclasia (Figure 23.3) and medial arterial calcification [85, 86]. Any disruption in the balance between bone resorption and formation can lead to reduced trabecular and cortical bone mass, which in turn increases bone fragility and fracture susceptibility [1].

Ascorbic acid (vitamin C) has a key role in bone homeostasis. Unlike humans, mice have the endogenous ability to synthesize ascorbic acid via the actions of gulonolactone (L-) oxidase (*Gulo*). The original spontaneous fracture (*sfx*) mutation arose spontaneously as a BALB/cBy inbred strain mice, and it was later determined that the *sfx* allele was in fact a deletion of the entire *Gulo* gene [87]. Homozygous *sfx* mice can be considered a model of genetically caused scurvy. They are normal at birth, but by

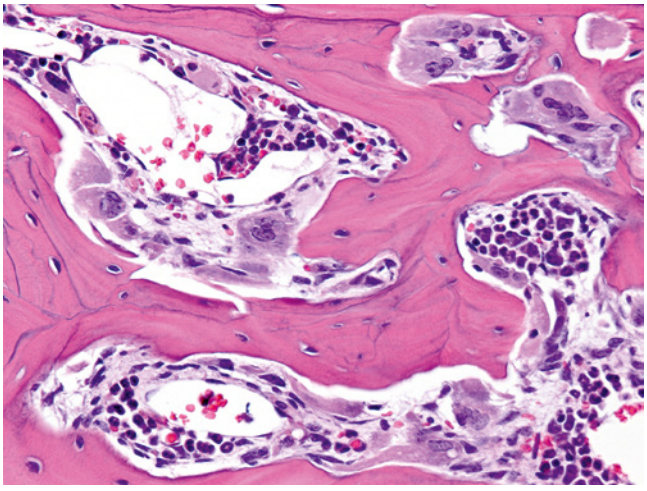


Figure 23.3 **Mouse bone – renal osteodystrophy**. Increased numbers of osteoclasts on bone surfaces.

~30 days, begin to show difficulties with ambulation, grooming, and are unable to reach food and water in suspended dispensers. These mice fail to gain weight, develop very low cortical bone mass (their femurs are approximately half the diameter of heterozygous littermate controls), and they do not live much longer than 50–60 days. Unsurprisingly, given the name of the allele, these mice will present with spontaneous fractures. Histological examination of the bone marrow of these mice shows evidence of a highly proliferative cell type (Figure 23.4a) [88]. These cells have since been identified as preosteoblasts because they are positive for osterix (Figure 23.4b), and they rapidly differentiate into bone forming osteoblasts with ascorbate supplemented diets (Figure 23.4c) [89]. Osteoblasts *in vitro* show impaired function that can be corrected by treatment with ascorbic acid [87]. The key role of ascorbate in osteoblast differentiation and function has been demonstrated in double knockout mice lacking the enzymes aldehyde reductase (*Akr1a1*$^{Gt(OST222400)Lex}$) and aldose reductase (*Akr1b3*$^{tm1.1Kgab}$), which both convert D-glucuronate to L-gulonate, a key step in the ascorbate synthesis pathway. These double knock-out mice are unable to synthesize ascorbate, develop scurvy, and present with spontaneous fractures [89]. Although the single knockout aldehyde reductase deficient mice develop and grow normally on standard diets, they will develop severe osteopenia and spontaneous fractures when challenged with physiological stresses that increase ascorbate requirements, such as pregnancy (Figure 23.5) [89].

Biomineralization Defects

Physiologic calcification or biomineralization of extracellular matrices is a normal process that is essential for the proper formation of bones and teeth, but any tissue can be abnormally mineralized as a result of mutations affecting a wide range of proteins. Biomineralization processes in bones and teeth involve complex, tightly regulated interactions between promoters and inhibitors of mineralization. Mouse models have helped elucidate many of the complex interactions between these inhibitors and promoters involved in regulating mineralization in bones and teeth as well as in preventing ectopic mineralization of soft tissues (Figure 23.6) [90].

Osteomalacia is the result of defective mineralization of the osteoid matrix and is characterized histologically by increased osteoid volume, osteoid surface, and osteoid thickness. Osteomalacia is often associated with vitamin D deficiencies, although chronic renal disease and hypophosphatemia can cause osteomalacia without affecting vitamin D levels [91]. Abnormal mineralization is also associated with a broad range of other mutations that result in hypophosphatemia, including hyperparathyroidism and mutations affecting fibroblast growth factor 23 (*Fgf23*) and Klotho (*Klo*). FAM20C, golgi-associated secretory pathway kinase (*Fam20c*) also affects phosphorus levels throughout the body. Bone lesions in FAM20C-deficient mice (*Fam20c*^{tm1Lex}) are typical of those associated with hypophosphatemic rickets. Long bones show thickened and irregular growth cartilage, with shortened and fused trabeculae lacking distinct cartilage cores at the growth plate. In aged mice, there is enlargement or flaring of the metaphysis, which are filled with broad bands of poorly mineralized osteoid (osteomalacia). FAM20C-deficient mice (*Fam20c*^{tm1Lex}) are hypophosphatemic and also show elevated serum ALP and FGF23 concentrations, all being changes consistent with a diagnosis of autosomal recessive hypophosphatemic rickets/osteomalacia [92].

Studies on hypophosphatemic disorders in mice have contributed immeasurably to our understanding of the physiological processes involved in phosphate homeostasis and their influence on biomineralization. Proteins that specifically regulate inorganic phosphate (P_i) homeostasis are called phosphatonins. The principal phosphatonin is fibroblast growth factor 23 (FGF23), a hormone secreted by osteocytes, which inhibits

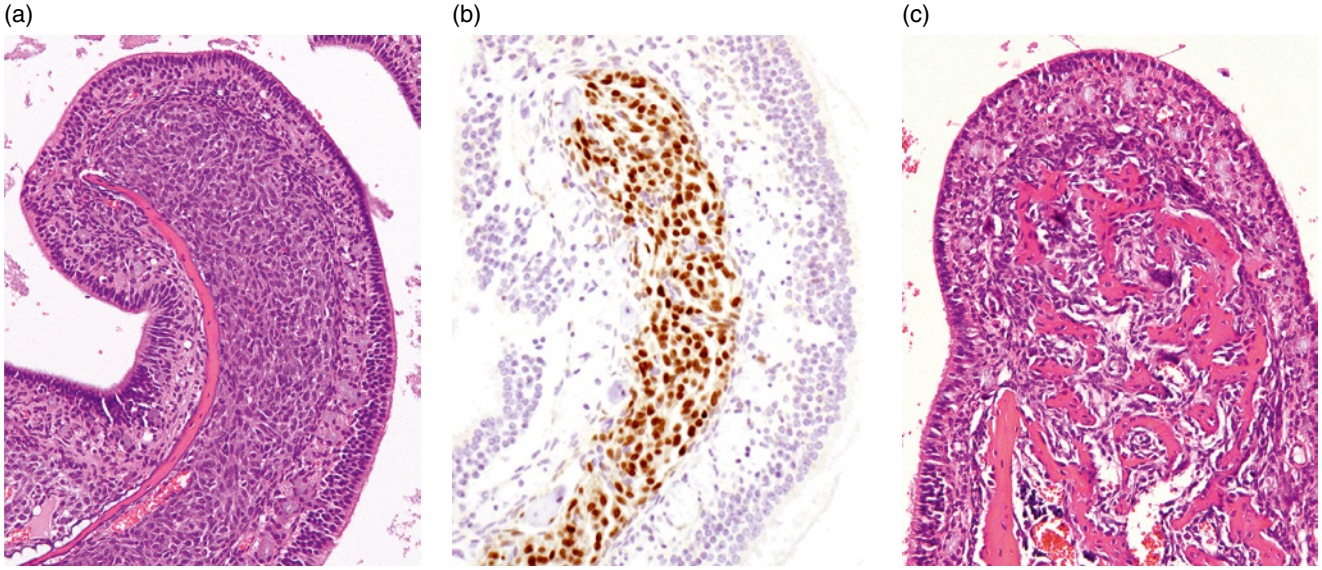


Figure 23.4 **Mouse turbinate**. (a) Proliferating cells in bones of ascorbate-deficient mice. (b) Positive nuclear labeling of proliferating cells for Osterix. (c) Differentiation of cells into bone-producing osteoblasts after ascorbate supplementation.

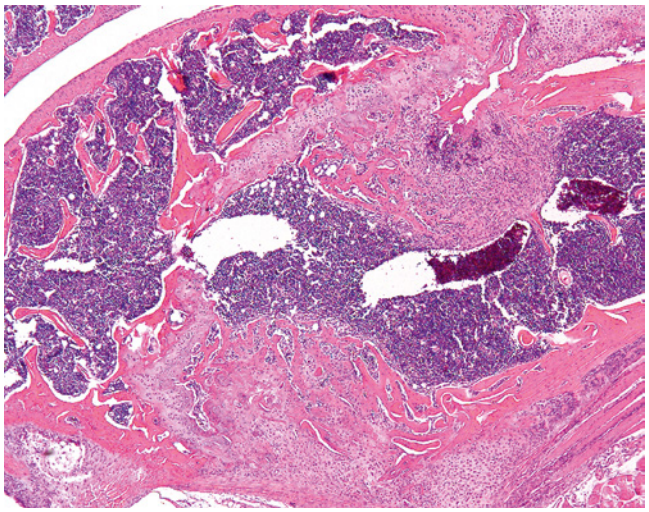
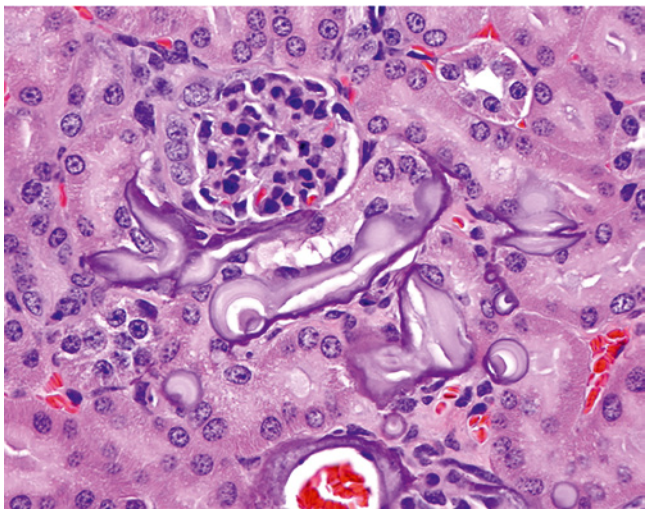


Figure 23.5 **Mouse femur**. Healing fracture in ascorbate-deficient mouse.

(a)



(b)

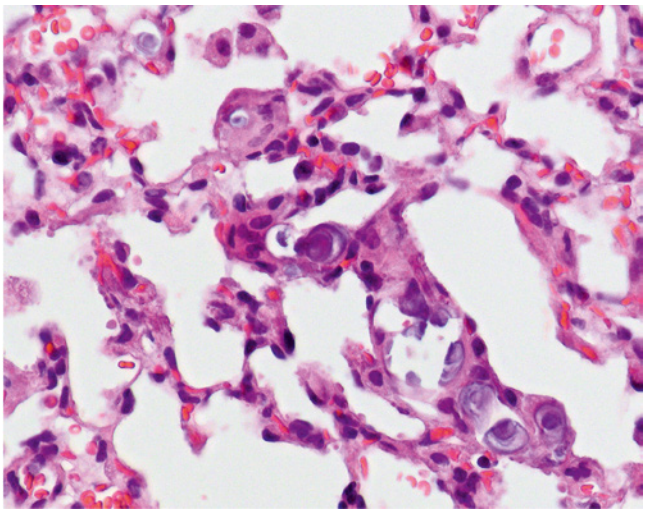


Figure 23.6 **Mouse kidney (a) and lung (b)**. Ectopic mineralization.

phosphate reabsorption by the sodium/phosphate cotransporter in the kidney, by acting through specific FGF receptors with the cofactor Klotho (KLO) protein [93]. Klotho-deficient mice, of which there are several different alleles, have flat osteoblasts and small osteoclasts on trabecular surfaces and accumulate broad bands of nonmineralized osteoid on metaphyseal trabeculae (Figure 23.7a) [94, 95]. Poorly defined basophilic material accumulates between osteoid (Figure 23.7b) and the osteocytes and their lacunae are enlarged and have a pale basophilic appearance (Figure 23.7c). FGF-deficient mice have a virtually identical phenotype. FGF23 activates KLO/FGFR1 receptor heterodimers in the kidney to inhibit phosphate reabsorption and 1,25-dihydroxyvitamin D synthesis in the proximal renal tubules [96, 97]. Hypophosphatemia in mice is characterized by defective calcification of cartilage and bone leading to rickets and osteomalacia [98].

In addition, to the physiologically normal process of matrix mineralization, aberrant or ectopic mineralization is part of human diseases such as fibrodysplasia ossificans progressiva (FOP) and calcification of other soft tissues such as the vasculature. Ectopic calcification is not a passive process, but rather can be triggered by the loss of mineralization inhibitors such as *Matrix-Gla protein* (*Tnfrsf11b*), *Osteoprotegerin* (*Tnfrsf11b*), *Osteopontin* (also known as *Secreted phosphoprotein*, Spp1), and Fetuin-A (*Alpha-2-HS-glycoprotein*, *Ahsg*). Inorganic pyrophosphate ($P_2O_7^{4-}$, abbreviated as PP_i) is perhaps the most potent inhibitor of ectopic mineralization [99]. Inorganic pyrophosphate levels are modulated by three different enzymes: Ectonucleotide pyrophosphatase/phosphodiesterase 1 (*Enpp1*) [100], ATP binding cassette, subfamily C, member 6 (*Abcc6*), and mouse progressive ankylosis protein (*Ank*) [101]. Lastly, extracellular PP_i is hydrolyzed to P_i by alkaline phosphatase (*Alpl*), and P_i then combines with calcium to generate hydroxyapatite [102]. Thus, deficiencies in *Enpp1* [103–105], *Abcc6*, or *Ank* [101] or increased *Alpl* activity can result in ectopic calcification [106].

It is important to note that a number of inbred mouse strains carry spontaneous allelic mutations of genes that can interfere with interpretation of phenotyping studies. Specifically, C3H/HeJ, DBA/2J, KK/HIJ, and most 129 substrains carry a hypomorphic allele of *Abcc6* [107]. Because 129 substrains have been used extensively to create targeted mutants (KOs), this has been a problem. For example, evaluation of B6;129 incipient congenic *Nt5e*^{tm1Jgsc} null mice have features of *Abcc6* mutant mice because they carry the 129 allele [108].

Osteogenesis Imperfecta

OI is a collection of monogenetic diseases in humans that can result in bone deformation and spontaneous fractures. There are 18 recognized types of this diseases that are categorized into two groups: (i) mutations in either the *COL1A1* or *COL1A2* genes or (ii) mutations in noncollagen genes that affect the posttranslational modification of collagen, the arrangement of collagen in bone, the mineralization of bone matrix, or the amount of collagen formed [109]. Osteogenesis imperfecta is distinct from other diseases of hypomineralization such as rickets and hypoascorbemia (scurvy).

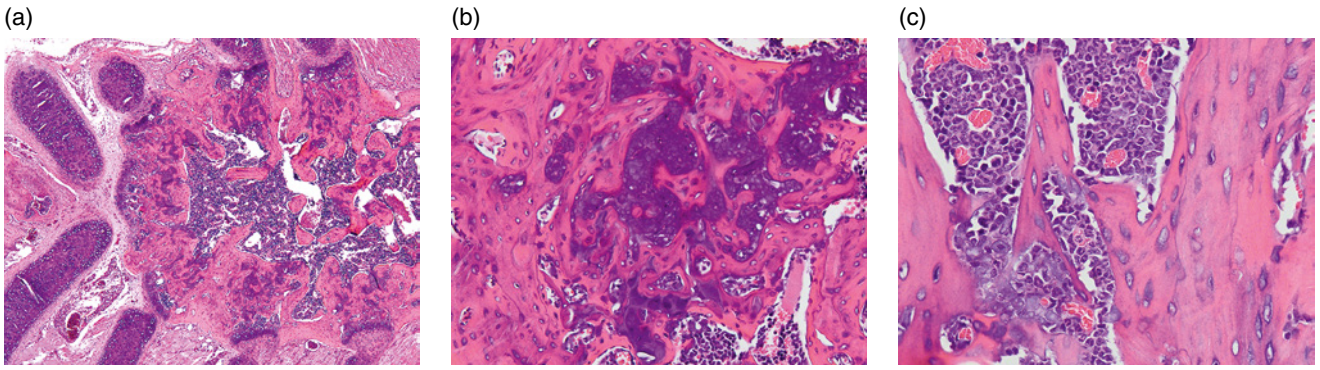


Figure 23.7 **Mouse sternum**. (a) Cortical and trabecular bone are disorganized and thick in *Klotho* knockout mice. (b) Higher magnification shows that the increased thickness is due to accumulation of osteoid and basophilic ground substance. (c) Osteocytes are enlarged, basophilic, and have prominent cytoplasmic extensions into surrounding bone.

The first four types of OI (Group 1 from above) all have mutations in collagen genes. In humans, Type 1 OI is usually due to a premature stop codon in one of the two Type 1 collagen genes and represents a haplo-insufficiency scenario. Types II–IV are all caused by coding mutations in either *COL1A1* or *COL1A2* that impact the ability to properly form the triple helical structure of tropocollagen [110]. The OI (*oim* allele; $Col1a2^{oim}$) is a spontaneous mutation that was found in a C3H/HeJ in a C57BL/6JLe F2 cross [111]. In these mice, a single base pair deletion at nucleotide 3983 of the *Col1a2* gene results in frame shift mutation and defective Type 1 collagen production. While these mice can live to ~18 months of age, they suffer spontaneous fractures, are very small in size, and have very short femurs. It should be noted that under normal modern laboratory animal conditions, spontaneous fractures should be nonexistent in "wild-type" mice, and when they are observed it is always indicative of either severe disease or negligence on the part of the husbandry staff. Spontaneous fractures are observed in homozygous $Col1a2^{oim}$ mice as these mice present with severe cortical thinning and low to nonexistent trabecular bone mass [111]. The bone matrix is poorly organized, is overmineralized with inappropriately small mineral crystals, and the bone is mineralized in a disordered fashion. Cortical bone in these mice has low stiffness and poor mechanical properties [112], likely contributing to the propensity for these mice to have spontaneous fractures. These mice are generally considered to be appropriate models of the human OI Type III disease and are now widely used for the study of this condition. Another commonly used mouse model of OI is the *Brittle IV* mouse. This is a genetically engineered model in which a glycine to cysteine mis-sense mutation was knocked into the *Col1a1* gene ($Col1a1^{tm1.1Jcm}$) [113]. Compared to the *oim* allele, the *Btrl* mutation is considered milder and homozygous *Btrl* mice represent a model of OI Type IV disease. While these mice do have low BMD, low whole bone strength, and defective matrix composition, they do not present with spontaneous fractures on a mixed 129Sv/CD-1/C57BL/6S mixed background [113].

The second group of OI disorders all tend to be moderate to severe in humans. Most of the genes linked to these types of OI are known and corresponding mouse models are available. This is the case for OI Type XI, which in humans is caused by mutations in *WNT1* [114]. The swaying mouse ($Wnt1^{sw}$) is the result of a spontaneous mutation and provides an excellent model of this disorder [115]. Compared to wild-type controls, these mice have drastically reduced trabecular bone, very thin cortical bone, very low bone strength, and they experience spontaneous fractures under normal laboratory husbandry conditions. They have slight reductions in bone collagen and mineral content and low osteoblast activity, but osteoclast number per unit bone surface is not affected in this mouse model [115].

Cartilage Defects

Cartilage is largely composed of extracellular matrix proteins such as highly sulfated macromolecule proteoglycans, small proteoglycans, and collagens 2, 6, 9, 10, and 11. There are hundreds of different chondrodysplasias that result in abnormal skeletal growth or deformations. Many have been linked to mutations affecting cartilage-related proteins [116], but the genetic causes of many others remain to be discovered [117–119]. Frequently used stains for cartilage include Alcian blue or Safranin O (for proteoglycans), and periodic acid–Schiff (for chondroitin sulfate and glycoproteins) (Figure 23.8). An alternate staining protocol for articular cartilage involves the use of Safranin O and fast green when cartilage erosion is expected, such as in osteoarthritis models. The degree to which cartilage degradation has occurred in such models can be quantified using a modified for rodent Osteoarthritis Research Society International (OARSI) scoring method [120].

It is generally classified as being either hyaline, elastic, or fibrous cartilage based on histological features. Of these, hyaline cartilage is the most widespread type and can be further classified into permanent cartilage and transient cartilage. Transient cartilage is involved in the proper formation,

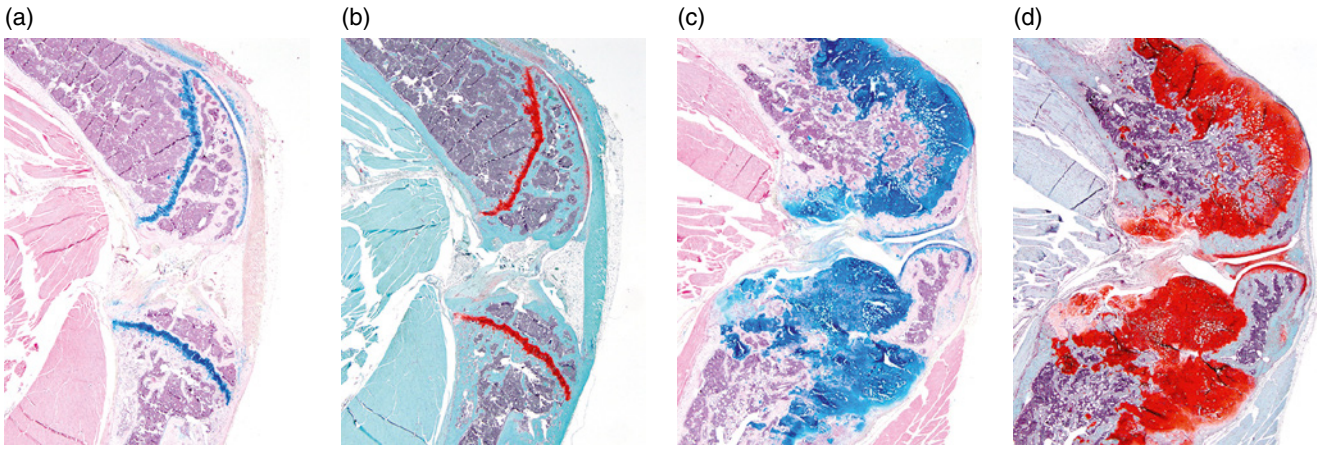


Figure 23.8 **Mouse femorotibial joint**. (a) Wild-type bone stained with Alcian blue showing normal cartilaginous growth plate (blue). (b) Sequential section of wild-type bone stained with Safranin O showing normal growth plate (red). (c) Dyschondroplasia affecting growth plates stained with Alcian blue. (d) Sequential section stained with Safranin O.

patterning, and growth of the skeleton, whereas permanent cartilage at joints and other locations is not replaced by bone. The transient growth plate cartilage in mice can be divided into a resting zone, a proliferating zone, a prehypertrophic zone, and a hypertrophic zone [119]. For consistency, mouse pathologists should compare the relative thickness and the alignment and numbers of chondrocytes in all four zones within the proximal tibial growth plates of age and sex-matched WT and GEM mice [118]. Lesions affecting growth plate cartilage include thickening and disorganization of chondrocytes [3, 117, 121] and hypoplasia [11, 118].

Permanent cartilage includes articular cartilage, which is roughly organized into four zones known as the tangential/superficial, transitional/intermediate, radial/deep, and calcified zones [122]. In the superficial or tangential zone located immediately below the surface of articular cartilage, the chondrocytes are very small and the fibers and matrix are aligned parallel to the articular surface [122]. Fibers in the intermediate/transitional zone arch over to become perpendicular to the articular surface in the deep or radial zone. The deep zone comprises the largest area of uncalcified cartilage in adult mice and contains large rounded chondrocytes orientated perpendicularly to the articular surface. The "tidemark" or calcification front defines the distinct line between the deep zone and the calcified zone, which forms a mechanical transition between the relatively deformable cartilage above and the hard subchondral bone [123].

Osteoarthritis is a degenerative disorder of synovial joints that culminates in the destruction of articular cartilage and subchondral bone. A wide range of genetic, developmental, metabolic, immunologic, and mechanical processes have been implicated in the pathogenesis of osteoarthritis, and the STR/ort mouse is widely used strain that spontaneously develops reproducible age-related degenerative changes of knee joints that closely resemble human osteoarthritis [124]. There are several other GEM that have helped elucidate underlying molecular mechanisms and genes that influence the pathogenesis and progression of osteoarthritis [125]. Many of genetic mutations linked to osteoarthritis disrupt the structure or homeostasis of extracellular matrix components, inflammatory processes, or chondrocyte homeostasis in articular cartilage [126, 127]. Pathology phenotyping protocols typically call for lateral sections of the rear leg that include the knee joint, and standardized methods for tissue collection and scoring lesion severity in bone and cartilage in this location are available [125]. The vertebral column and temporomandibular joint should also be assessed routinely for the presence of inflammatory and/or degenerative lesions when assessing GEM mice.

Teeth

Mice have proven to be particularly useful models for human dental disorders because the cell signaling pathways and processes involved in the development of teeth in mice and humans are essentially identical [128, 129]. Tooth development involves numerous complex interactions between neural crest-derived mesenchymal cells and the ectoderm-derived epithelial cells lining the oral cavity [130]. The continuous growth of rodent incisors permits detailed study of the highly conserved and complex interactions involved in tooth morphogenesis and enamel/dentin formation [131] and provides an easily accessible system to study organogenesis and mineralization defect diseases [132]. Studies on the epitheliomesenchymal interactions in mouse incisors have proven particularly useful in elucidating many of the molecular pathways and morphogenetic processes involved in tooth development and the pathogenesis of dental diseases [133–135]. The effects of deleting or altering specific genes

on tooth development can easily be assessed in incisors because longitudinal sections of these continuously growing teeth display all the spatiotemporal steps that occur during tooth development, and their cervical loops contain the stem cells capable of generating ameloblasts and odontoblasts. Tooth development involves complex reciprocal interactions between oral epithelium and dental pulp mesenchyme that engage the hedgehog (HH), wingless related MMTV integration site (WNT), fibroblast growth factor (FGF), and bone morphogenic protein (BMP) signaling pathways, and disruption of any one of these odontogenic-signaling pathways can cause developmental dental disorders [134].

The terms used to describe distinct stages of tooth development are the dental lamina, bud, cap, bell, and crown formation stages. In mice, the earliest morphological sign of odontogenesis appears on embryonic day 11 (E11) as localized thickenings of the oral epithelium (dental lamina) that express key signaling molecules such as *Shh* [136]. In the tooth bud stage at E12.5–E13.5, epithelial cells continue to proliferate and invaginate into the mesenchyme and express signaling molecules and transcription factors such as *Bmp4*, *Msx1*, and *Pax9* [133, 137]. During the cap stage starting at E14, the epithelial bud extends deeper into the mesenchyme to surround the mesenchymal dental papilla. By E16, the developing tooth starts to increase in size and attain its final shape during the so-called "bell stage," with the secondary enamel knots in molar teeth determining the sites of tooth cusps [131]. In the crown stage, epithelial cells derived from oral ectoderm differentiate into enamel-producing ameloblasts, whereas the primitive mesenchymal cells facing the epithelial basement membrane differentiate into dentin-producing odontoblasts. Immediately following initial predentin deposition, the adjacent layer of epithelial cells differentiates into ameloblasts, which are arranged in a single-cell row supported by the intermediate stratum and the stellate reticulum. The ameloblasts secrete organic enamel matrix in tightly packed, highly organized three-dimensional patterns in which the protein matrix is gradually replaced with enlarging hydroxyapatite crystals.

Mice develop only one set of teeth throughout life (monophyodont). Their continuously growing incisors are covered by enamel only on the labial surface, and typically have a smooth opalescent surface with yellow-brown coloration due to the high iron content in the outer and surface enamel layers. The lingual surface of the incisors is covered by thin cementum where periodontal ligament fibers attach. Incisor teeth with defective enamel often have a chalky white to opaque appearance with roughened/pitted surfaces from an early age. Histologically, the normal developing incisor tooth consists of distinctive and easily identifiable layers of cells and extracellular matrix. In decalcified sections, fully mineralized mature enamel is removed, leaving an empty space, but protein-rich enamel matrix remains visible in more caudal sections representing earlier stages of tooth development.

In mice, the maxillary and mandibular incisors are separated from three molar teeth by a toothless region called the diastema. The three molar teeth on each side are separated from the incisors by a toothless region called the diastema. The cusps of molars are not covered with enamel. Molar teeth with defective enamel show marked abrasion of the cusps in young mice which progresses to molars worn down to the gum line in adults. In decalcified sections of mature molar teeth of WT mice, the enamel layer appears as clear space, with the previous space occupied by fully mineralized enamel sometimes outlined by remnants of surface enamel proteins and attached plaque. Odontoblasts produce predentin which mineralizes to form acellular and avascular dentin. As additional dentin is produced, the odontoblasts move deeper into the pulp cavity but maintain connection with the dentin and via cytoplasmic processes located within dentinal tubules. Special stains such as Masson's Trichrome and Movat's Pentachrome are useful for accentuating structural defects present in enamel and dentin. Because enamel and dentin are produced by cells having different origins, developmental defects are often restricted to either enamel or dentin, but not both [92, 138].

Major dental abnormalities such as malocclusion, missing teeth, and variations in size, color, and shape can be found at necropsy. However, other than malocclusion, dental lesions are often missed or not evident at necropsy, so most dental phenotypes are discovered by light microscopy. Histologic sections of both incisor and molar teeth are present in the coronal sections of the head that include the nasal turbinates and nasal-associated lymphoid tissues. Ideally, mice are fixed by perfusion immediately after death and the head along with the axial and appendicular skeleton are transferred into a formic acid and formaldehyde solution (Cal-Rite, Thermo Fisher Scientific, Waltham, MA, USA) for simultaneous decalcification and fixation. Alternatively, decalcification in a buffered EDTA solution may be necessary to preserve both antigenicity and nucleic acids for IHC and *in situ* hybridization studies, respectively. Frontal sections of the head cut at the levels of the first and third molar teeth are suitable for routine histological evaluations, but longitudinal sections incisors within the mandible are used to evaluate the temporospatial development of tooth lesions.

Abnormal Tooth Numbers/Shapes

Defects in either the number or shape of teeth are best made at time of necropsy. Hypodontia/oligodontia/anodontia are the terms used to describe reduced numbers or complete absence of teeth. The complex process of tooth morphogenesis involves the integration of several different pathways in a highly conserved regulatory network [139–141]. The TGFB, fibroblast growth factor (FGF), sonic hedgehog (SHH), tumor necrosis factor (TNF), and WNT signaling pathways are all required repeatedly during tooth development, and disruption of any of these pathways can result in developmental arrest of teeth [139–141]. The numerous genes and pathways involved in tooth development contribute to the highly variable shape and size of teeth [134] and

this means that mutations in the same genes can result in different tooth phenotypes in humans and in mice [142].

The size and shape of teeth are determined by reiterative activation and patterning of the epithelial enamel knots [137, 140], while the cusps are generated by the formation of additional secondary enamel knots. Defects in the size or shape of the primary enamel knot can disrupt the arrangement of the secondary enamel knots in molars and lead to cusp defects. Expression of the genes *Eda*, *Edar*, and *Edaradd* during tooth development has been linked to the formation of primary enamel knots in *tabby*, *downless*, and *crinkled* mice [143–147]. These mouse strains have mutations in proteins involved in the same pathway: *tabby* mice have a mutation in ectodysplasin (*Eda*), *downless* mice have mutations in the receptor for EDA (*Edar*), while *crinkled* have mutations in the EDAR adaptor protein known as EDARADD [148, 149].

Given the central importance of the signaling pathways involved in tooth development, dental disorders are often associated with other congenital anomalies, including the ectodermal dysplasias that affect the development of hair, nails, salivary glands, mammary glands, and nasolacrimal ducts [150]. WNT signaling has important effects on tooth development and in regulating bone homeostasis, with activation of the canonical WNT pathway resulting in increased bone mass and strength while inhibition of WNT signaling has the opposite effect [80]. NOTUM is a highly conserved secreted feedback repressor of WNT activity that has been shown to suppress WNT signaling [133–135]. NOTUM-deficient mice ($Notum^{Gt(OST172035)Lex}$) have dental and bone phenotypes. Many tooth abnormalities are accompanied by skeletal disorders. For example, missing teeth due to eruption disorders (pseudoanodontia) caused by dysfunctional osteoclasts coexist with osteopetrosis in several mouse models [151], including Fos (formerly: c-Fos) knockout mice (Fos^{tm1Pa}, Fos^{tm1Wag}, $Fos^{tm2(Fosl1)Wag}$) which lack functional osteoclasts [152]. Similarly, mutations in the genes encoding collagen-1 and -2 cause both dentinogenesis imperfecta and OI in sphingomyelin phosphodiesterase 3, neutral ($Smpd3^{fro}$) mutant mice [5].

Enamel Defects

Because incisor teeth in rodents grow continuously, it is possible to see the development of the enamel defects at different stages of tooth development within individual animals. The process of amelogenesis on the labial surface of incisor teeth is generally subdivided into the presecretory, secretory, and maturation zones. In the presecretory zone, the ameloblasts proliferate, induce odontoblasts, differentiate into a columnar epithelium, and change their polarity. The presecretory stage can be subdivided into regions where the ameloblasts initially face pulp and then later, dentin. In the secretory zone, fully differentiated ameloblasts secrete enamel matrix proteins. During maturation, enamel matrix proteins are progressively removed and replaced by mineral.

Amelogenesis imperfecta (AI) is generally characterized by disorganization of the ameloblast cell layer and the decussating enamel rod substructures. Detached ameloblasts may form irregular nests of cells within a highly irregular mineralized crust arising from the fusion of variably sized and poorly calcified multilobulated and lamellated enamel bodies (Figure 23.9). AI is linked to mutations in several different genes whose loss results in abnormalities in the amount, composition, and/or structure of enamel. Generally, most morphological enamel defects can be characterized as having some combination of hypoplastic, hypomaturation, and hypomineralized enamel phenotypes [153, 154]. In the hypoplastic type, defective enamel matrix synthesis results in thin or weak enamel due to reduced apposition of enamel during tooth maturation. Hypoplastic enamel is thin, but its

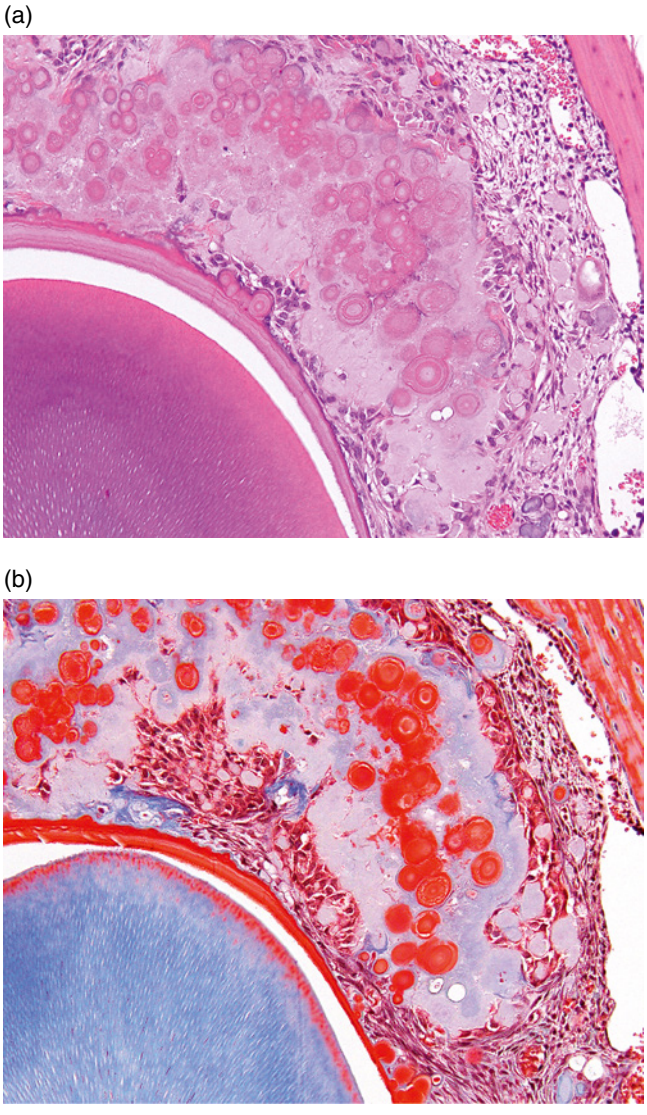


Figure 23.9 Mouse incisor tooth – Amelogenesis imperfecta. (a) Disorganized enamel with normal dentin, H&E stain. (b) Sequential section stained with Masson's trichrome highlights enamel protein elements (red) and dentin (blue).

radiodensity remains greater than that of the underlying dentin. Hypomature enamel can be of normal thickness, but it is soft because the incomplete removal of proteins during the maturation phase results in incomplete and defective development of enamel crystals. The radiodensity of hypomature enamel can be reduced to approximately the same as dentin. Due to defective mineralization of the matrix and crystals, hypomineralized enamel has lower radiodensity than dentin and is soft, rough, and rapidly lost by attrition. Hypoplastic or hypomineralized enamel is the most common type of AI seen in humans, but an overlap of these characteristics is often present [155].

Enamel differs from bone and dentin in its tissue origin, mineralization matrix, and mode of mineralization. Mineralization of bone and dentin proceeds within a collagenous matrix (osteoid and predentin, respectively) that is deposited by cells of mesenchymal origin, and requires coordinated interactions between Type I collagen matrix and several bone/dentin-specific noncollagenous proteins that help organize the matrix and regulate the mineralization process [156]. In contrast, enamel mineralization takes place within a noncollagenous protein matrix that is secreted by ameloblasts of epithelial origin. This enamel matrix consists of specialized proteins that regulate the structural development and mineralization of enamel [157]. These protein components include enamelin (ENAM) [158], amelogenin (AMELX) [159], ameloblastin (AMBN) [160], amelotin (AMELOTIN) [161], and dentin sialophosphoprotein (DSPP) [162].

Enamel phenotypes from rodents with genetically modified enamel genes have been analyzed using a wide range of methods to determine the physical properties of enamel such as mineral density, structure, mechanical integrity, and color; these include advanced and technically demanding methods such as microcomputed tomography (μCT), ashing, color analysis, scanning electron microscopy, and micro/nano-indentation [163–165]. However, histological evaluation of teeth is a relatively simple and effective approach to identifying enamel defects in GEM.

Most cases of AI in humans have been linked to mutations in six major enamel proteins and proteinases (ENAM, AMBN, AMELX, MMP20, KLK4, and AMELOTIN), but many cases do not have mutations in any of these protein coding genes [162, 166]. Heritable enamel defects that may be associated with lesions affecting other organ systems [167]. Deficiencies in any of the secreted ameloblast proteins result in the production of defective enamel, and mouse models deficient for amelogenin (*Amelx*^{Rgsc888}, *Amelx*^{tm1Kul}, *Tg(AMELX*P70T)2Gibs*) [168], kallikrein 4 (*Klk4*$^{tm1.1Jpsi}$) [169], matrix metalloproteinase 20 (*Mmp20*^{tm1Jdb}) [170] all are models for human AI. Ameloblastin (*Ambn*^{tm1Nid}) [171] and enamelin (*Enam*^{Rgsc395}, *Enam*^{Rgsc514}, *Enam*^{Rgsc521}, and *Enam*$^{tm1.1Jcch}$) [172] develop AI phenotypes. The dental lesions displayed by each of these models have helped elucidate the functions of these matrix components in enamel formation. For example, amelogenin-deficient mice have very thin and rodless enamel [168]. The two secreted proteinases, KLK4 and MMP20, enable the maturation (expansion) of enamel crystallites by removing matrix proteins [173]. Of these, MMP20 is an early protease secreted along with enamel proteins by secretory-stage ameloblasts [174], whereas the protease KLK4 is secreted later by transition- and maturation-stage ameloblasts and degrades the remaining organic matrix proteins following the termination of appositional growth of enamel rods [174]. The absence of KLK4 results in frail, hypomineralized enamel with normal rod/inter-rod organization and thickness [169], MMP20 deficiency produces thin enamel with disrupted rod patterns [170], while deficiencies in either ameloblastin or enamelin result in formation of an abnormally thin, disorganized, and poorly mineralized enamel layer [171, 172]. Interestingly, tooth fractures with foreign material and pulp necrosis/inflammation are generally absent in teeth with lesions restricted to the enamel layer. For these lesions to develop, the dentin layer must be compromised as well.

Dentin Defects

Dentinogenesis is an ongoing process where odontoblasts produce primary dentin during tooth development, and then generate secondary dentin throughout life. During the transition from cap stage to bell stage, some dental pulp mesenchyme cells undergo dentinogenesis, a process in which they differentiate into pre-odontoblasts, polarizing odontoblasts, secretory odontoblasts, and finally, terminally differentiated odontoblasts [175]. The secretory odontoblasts synthesize and secrete dentin extracellular matrix which includes many types of collagen and noncollagen proteins. DSPP and DMP1 are noncollagen proteins that are markers of odontoblast differentiation and defects in these proteins in humans and mice result in dentin-related diseases, such as dentinogenesis imperfecta and dentin dysplasia [176].

In older mice, odontoblasts produce tertiary dentin below the cusps as teeth wear down or in response to injury. Normal primary dentin is characterized by parallel dentin tubules that extend from the dentin-enamel junction to a base of linearly arranged columnar odontoblasts in the dental pulp. Dentin defects in both incisor and molar teeth are usually characterized by a disrupted odontoblast layer, with replacement of parallel dentin tubules by irregular disorganized and atubular stroma, sometimes containing entrapped odontoblasts within lacunae.

Defects in dentin formation can appear as dentinogenesis imperfecta or dentin dysplasia (DD), with disrupted or reduced dentin (Figure 23.10). The roots of molar teeth are often reduced in length and diameter and have root canals that are smaller than normal or completely obliterated. Dentin dysplasia is broadly classified based on the most severely affected areas of the tooth, with type I primarily involving the tooth roots (DDI; radicular dentin dysplasia) and type II affecting the tooth crowns (DDII; coronal dentin dysplasia) [154, 177]. In humans, DDI is characterized by normal appearing crowns but with defective dentin, short roots (resulting in hypermobility and premature loss), and

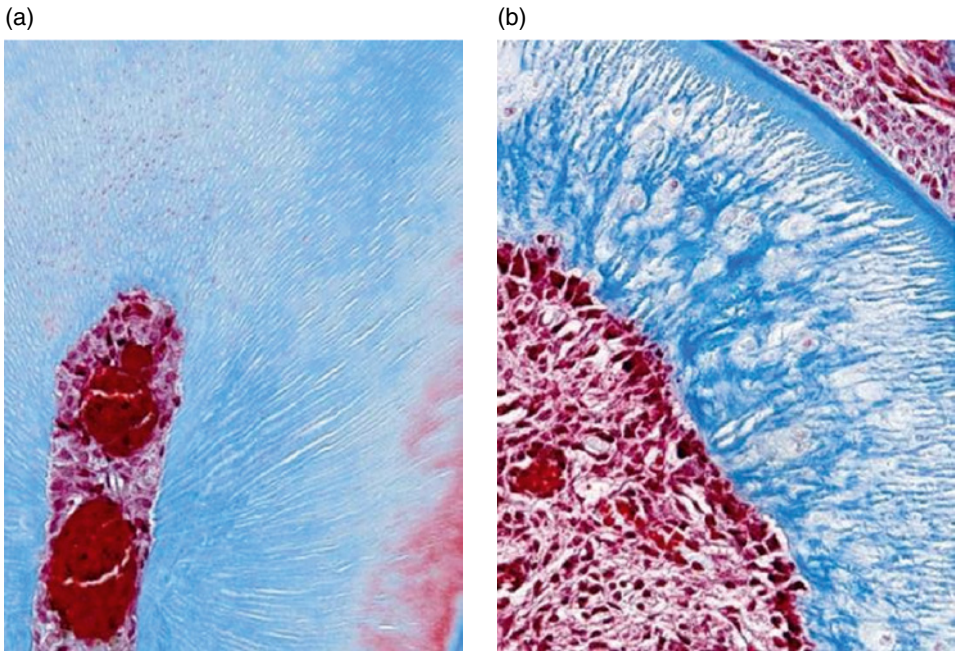


Figure 23.10 **Mouse molar teeth – Dentinogenesis imperfecta**. (a) Parallel arrangement of dentin tubules in normal tooth stained with Masson's trichrome. (b) Disorganized connective tissue and trapped cells in dentin layer.

frequent dental abscesses [178]. Tooth lesions in *Notum*$^{-/-}$ (*Notum*$^{Gt(OST172035)Lex}$) mice are very similar to those reported in human DDI, and are characterized by normal-shaped crowns, normal mantle dentin with underlying zone of dentin dysplasia, short blunt roots, hypermobility, and periodontal inflammation/abscesses.

The loss of dentin integrity in *Notum*$^{-/-}$ mice compromises the strength of the enamel, making the tooth prone to fracture and infection [138]. The presence of tooth fractures, intrapulpal food particles, inflammation, and necrosis are key histopathological findings suggestive of primary dentin defects because dentin that is dysplastic or poorly mineralized does not provide adequate structural support to enamel [138]. Since the cusps of molar teeth in mice are not covered with enamel, any clefts or fissures in poorly organized or mineralized dentin allow bacteria and food particles to enter the pulp, resulting in inflammation and necrosis, followed by periosteal proliferation, lysis of tooth roots, and periapical abscesses [92].

As mentioned earlier, mouse pathologists need to be aware that dentin defects are often accompanied by bone phenotypes. The frequent association of dentin and bone phenotypes in not surprising since similar signaling pathways is involved in the differentiation of odontoblasts and osteoblasts, and both bone and dentin are mineralized tissues built on a collagen framework. Dystrophic dentin has histological similarities to woven bone and can be described as osteodentin [138].

Incidental Lesions

Probably the three most common reported incidental dental diseases in mice are malocclusions, dental dysplasia of maxillary incisors, and foreign body periodontitis. When they occur sporadically, they most likely represent background lesions, but genetic causes are likely to be involved with increased prevalence, especially in young mice. Dental dysplasia is relatively common spontaneous background lesion affecting maxillary incisors in old mice [179, 180]. At early stages, there is clefting of the labial tooth surface with occasional intrapulpal denticles (Figure 23.11). In more advanced cases, dental dysplasia is characterized by severe malformations in the tooth structure, which can be accompanied by impactions, tooth fractures, pulp and periodontal inflammation and necrosis, and odontomas [180].

Malnourished or stunted mice should always be examined for the presence of malocclusion or overgrown incisors, which

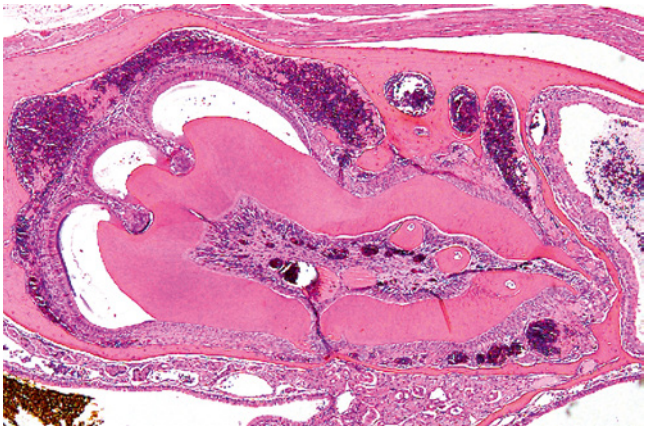


Figure 23.11 **Aged mouse incisor**. Deep clefting of enamel layer, intrapulpal denticles, and irregular dentin are present in this tooth.

are common incidental findings in mice [181]. Malocclusions caused by misalignment of incisors are more common in lines with craniofacial abnormalities [182]. Foreign body (hair shaft)-induced periodontitis is another very common lesion in some strains of mice [183]. However, wild-type mice are generally relatively well protected against periodontitis [184]. In GEM, increased susceptibility to periodontitis has been linked to mutations that disrupt the migration/killing capacities of polymorphonuclear neutrophils, block effective antigen presentation by dendritic cells, or dysregulate production of pro-inflammatory cytokines [184].

Acknowledgments

This work was supported by grants from the National Institutes of Health (R01-CA089713 and P30-CA034196 to JPS).

References

1 Boskey, A.L. (2007). Mineralization of bones and teeth. *Elements* 3 (6): 385–391.
2 Ravindran, S. and George, A. (2014). Multifunctional ECM proteins in bone and teeth. *Exp. Cell. Res.* 325 (2): 148–154.
3 Millan, J.L. (2013). The role of phosphatases in the initiation of skeletal mineralization. *Calcif. Tissue Int.* 93 (4): 299–306.
4 Margolis, H.C., Beniash, E., and Fowler, C.E. (2006). Role of macromolecular assembly of enamel matrix proteins in enamel formation. *J. Dent. Res.* 85 (9): 775–793.
5 Enderli, T.A., Burtch, S.R., Templet, J.N., and Carriero, A. (2016). Animal models of osteogenesis imperfecta: applications in clinical research. *Orthop. Res. Rev.* 8: 41–55.
6 Komori, T. (2020). Molecular mechanism of Runx2-dependent bone development. *Mol. Cells* 43 (2): 168–175.
7 Miyazaki, T., Kanatani, N., Rokutanda, S. et al. (2008). Inhibition of the terminal differentiation of odontoblasts and their transdifferentiation into osteoblasts in Runx2 transgenic mice. *Arch. Histol. Cytol.* 71 (2): 131–146.
8 Reddi, A.H. and Reddi, A. (2009). Bone morphogenetic proteins (BMPs): from morphogens to metabologens. *Cytokine Growth Factor Rev.* 20 (5–6): 341–342.
9 Bragdon, B., Moseychuk, O., Saldanha, S. et al. (2011). Bone morphogenetic proteins: a critical review. *Cell Signalling* 23 (4): 609–620.
10 Rider, C.C. and Mulloy, B. (2010). Bone morphogenetic protein and growth differentiation factor cytokine families and their protein antagonists. *Biochem. J* 429 (1): 1–12.
11 Briggs, M.D., Bell, P.A., and Pirog, K.A. (2015). The utility of mouse models to provide information regarding the pathomolecular mechanisms in human genetic skeletal diseases: the emerging role of endoplasmic reticulum stress (review). *Int. J. Mol. Med.* 35 (6): 1483–1492.
12 Briggs, M.D., Bell, P.A., Wright, M.J., and Pirog, K.A. (2015). New therapeutic targets in rare genetic skeletal diseases. *Expert. Opin. Orphan. Drugs* 3 (10): 1137–1154.
13 Mortier, G.R., Cohn, D.H., Cormier-Daire, V. et al. (2019). Nosology and classification of genetic skeletal disorders: 2019 revision. *Am. J. Med. Genet. A* 179 (12): 2393–2419.
14 Adams, D.J. and Ackert-Bicknell, C.L. (2015). Genetic regulation of bone strength: a review of animal model studies. *Bonekey Rep.* 4: 714.
15 Bouxsein, M.L., Uchiyama, T., Rosen, C.J. et al. (2004). Mapping quantitative trait loci for vertebral trabecular bone volume fraction and microarchitecture in mice. *J. Bone Miner. Res.* 19 (4): 587–599.
16 Koller, D.L., Schriefer, J., Sun, Q. et al. (2003). Genetic effects for femoral biomechanics, structure, and density in C57BL/6J and C3H/HeJ inbred mouse strains. *J. Bone Miner. Res.* 18 (10): 1758–1765.
17 Doolittle, M.L., Maynard, R.D., and Ackert-Bicknell, C.L. (2020). Inbred mouse strains in the study of bone disease. In: Encyclopedia of Bone Biology, 1e (ed. M. Zaidi), 150–159. Elsevier Inc.
18 Wegst, U.G., Bai, H., Saiz, E. et al. (2015). Bioinspired structural materials. *Nat. Mater.* 14 (1): 23–36.
19 Burgeson, R.E. and Nimni, M.E. (1992). Collagen types. Molecular structure and tissue distribution. *Clin. Orthop. Relat. Res.* 282: 250–272.
20 Zimmermann, E.A., Busse, B., and Ritchie, R.O. (2015). The fracture mechanics of human bone: influence of disease and treatment. *Bonekey Rep.* 4: 743.
21 Boskey, A.L. and Robey, P.G. (2013). The composition of bone. In: Primer on the Metabolic Bone Diseases and Disorders of Mineral Metabolism, 8e (ed. C.J. Rosen), 49–58. Wiley-Blackwell.
22 Hall, B.K. (2015). Vertebrate Skeletal Tissues. Bones and Cartilage: Developmental and Evolutionary Skeletal Biology, 2e, 3–40. Amsterdam: Elsevier.
23 Komori, T., Yagi, H., Nomura, S. et al. (1997). Targeted disruption of Cbfa1 results in a complete lack of bone formation owing to maturational arrest of osteoblasts. *Cell* 89 (5): 755–764.
24 Nakashima, K., Zhou, X., Kunkel, G. et al. (2002). The novel zinc finger-containing transcription factor osterix is required for osteoblast differentiation and bone formation. *Cell* 108 (1): 17–29.
25 de Gorter, D.J.J. and ten Dijke, P. (2013). Signal transduction cascades controlling osteoblast differentiation. In: Primer on the Methabolic Bone Diseases and Disorders of Mineral Metabolism, 8e (ed. C.J. Rosen), 15–24. Wiley-Blackwell.
26 Bonewald, L.F. (2013). Osteocytes. In: Primer on the Metabolic Bone Diseases and Disorders of Mineral Metabolism, 8e (ed. C.J. Rosen), 34–41. Wiley-Blackwell.
27 Goyal, R. and Jialal, I. (2020). Hyperphosphatemia. StatPearls.

28 Kovacs, C.S. (2000). Calcium and phosphate metabolism and related disorders during pregnancy and lactation. In: Endotext (eds. K.R. Feingold, B. Anawalt, A. Boyce, et al.). South Dartmouth, MA: MDText.com, Inc.

29 Ross, F.P. (2013). Osteoclast biology and bone resorption. In: Primer on the Metabolic Bone Diseases and Disorders of Mineral Metabolism, 8e (ed. C.J. Rosen), 25–33. Wiley-Blackwell.

30 Baron, R. and Hesse, E. (2012). Update on bone anabolics in osteoporosis treatment: rationale, current status, and perspectives. *J. Clin. Endocrinol. Metab.* 97 (2): 311–325.

31 Eppig, J.T., Smith, C.L., Blake, J.A. et al. (2017). Mouse Genome Informatics (MGI): resources for mining mouse genetic, genomic, and biological data in support of primary and translational research. *Methods Mol. Biol.* 1488: 47–73.

32 Law, M. and Shaw, D.R. (2018). Mouse Genome Informatics (MGI) is the international resource for information on the laboratory mouse. *Methods Mol. Biol.* 1757: 141–161.

33 Priemel, M., Schilling, A.F., Haberland, M. et al. (2002). Osteopenic mice: animal models of the aging skeleton. *J. Musculoskelet. Neuronal. Interact.* 2 (3): 212–218.

34 Rosen, C.J., Beamer, W.G., and Donahue, L.R. (2001). Defining the genetics of osteoporosis: using the mouse to understand man. *Osteoporos. Int.* 12 (10): 803–810.

35 Maynard, R.D. and Ackert-Bicknell, C.L. (2019). Mouse models and online resources for functional analysis of osteoporosis genome-wide association studies. *Front. Endocrinol.* 10: 277.

36 Brommage, R. and Ohlsson, C. (2019). High fidelity of mouse models mimicking human genetic skeletal disorders. *Front. Endocrinol.* 10: 934.

37 Allen, M.R. (2017). Preclinical models for skeletal research: how commonly used species mimic (or don't) aspects of human bone. *Toxicol. Pathol.* 45 (7): 851–854.

38 Godfrey, P., Rahal, J.O., Beamer, W.G. et al. (1993). GHRH receptor of little mice contains a missense mutation in the extracellular domain that disrupts receptor function. *Nat. Genet.* 4 (3): 227–232.

39 Glatt, V., Canalis, E., Stadmeyer, L., and Bouxsein, M.L. (2007). Age-related changes in trabecular architecture differ in female and male C57BL/6J mice. *J. Bone Miner. Res.* 22 (8): 1197–1207.

40 Glatt, V., Shultz, K.L., Beamer, W.G., and Bouxsein, M.L. (eds.) (2007). Age related changes in bone architecture vary among inbred strains of mice. *Bone* 40 (6): S194–S198.

41 Erben, R.G. and Glosmann, M. (1914). Histomorphometry in rodents. *Methods Mol. Biol.* 2019: 411–435.

42 Rowe, D.W., Adams, D.J., Hong, S.H. et al. (2018). Screening gene knockout mice for variation in bone mass: analysis by mu CT and histomorphometry. *Curr. Osteoporos. Rep.* 16 (2): 77–94.

43 Zheng, H.F., Forgetta, V., Hsu, Y.H. et al. (2015). Whole-genome sequencing identifies EN1 as a determinant of bone density and fracture. *Nature* 526 (7571): 112–117.

44 Dyment NA, Jiang X, Chen L, Hong SH, Adams DJ, Ackert-Bicknell C, et al. High-throughput, multi-image cryohistology of mineralized tissues. *J. Vis. Exp.* 2016 (115): 1–11. doi: 10.3791/54468.

45 Erben, R.G. (2003). Bone-labeling techniques. In: Handbook of Histology Methods for Bone and Cartilage (eds. Y.H. A and K.L. M), 99–117. Totowa, NJ: Humana Press.

46 Dempster, D.W., Compston, J.E., Drezner, M.K. et al. (2013). Standardized nomenclature, symbols, and units for bone histomorphometry: a 2012 update of the report of the ASBMR Histomorphometry Nomenclature Committee. *J. Bone Miner. Res.* 28 (1): 2–17.

47 Kunert-Keil, C., Richter, H., Zeidler-Rentzsch, I. et al. (2019). Histological comparison between laser microtome sections and ground specimens of implant-containing tissues. *Ann. Anat.* 222: 153–157.

48 Porter, A., Irwin, R., Miller, J. et al. (2017). Quick and inexpensive paraffin-embedding method for dynamic bone formation analyses. *Sci. Rep.* 7: 42505.

49 Mead, T.J. (2020). Alizarin red and alcian blue preparations to visualize the skeleton. *Methods Mol. Biol.* 2043: 207–212.

50 Rigueur, D. and Lyons, K.M. (2014). Whole-mount skeletal staining. *Methods Mol. Biol.* 1130: 113–121.

51 Hall, C.M. (2002). International nosology and classification of constitutional disorders of bone (2001). *Am. J. Med. Genet.* 113 (1): 65–77.

52 Miller, P.D. (2017). The history of bone densitometry. *Bone* 104: 4–6.

53 Lotz, J.C., Cheal, E.J., and Hayes, W.C. (1991). Fracture prediction for the proximal femur using finite element models: Part I – Linear analysis. *J. Biomech. Eng.* 113 (4): 353–360.

54 Marshall, D., Johnell, O., and Wedel, H. (1996). Meta-analysis of how well measures of bone mineral density predict occurrence of osteoporotic fractures. *BMJ* 312 (7041): 1254–1259.

55 Nagy, T.R. and Clair, A.L. (2000). Precision and accuracy of dual-energy X-ray absorptiometry for determining in vivo body composition of mice. *Obes. Res.* 8 (5): 392–398.

56 Gasser, J.A. (1995). Assessing bone quantity by pQCT. *Bone* 17 (4 Suppl): 145S–154S.

57 Brommage, R., Liu, J., Hansen, G.M. et al. (2014). High-throughput screening of mouse gene knockouts identifies established and novel skeletal phenotypes. *Bone Res.* 2.

58 Bouxsein, M.L., Boyd, S.K., Christiansen, B.A. et al. (2010). Guidelines for assessment of bone microstructure in rodents using micro-computed tomography. *J. Bone Miner. Res.* 25 (7): 1468–1486.

59 Schmidt, C., Priemel, M., Kohler, T. et al. (2003). Precision and accuracy of peripheral quantitative computed tomography (pQCT) in the mouse skeleton compared with histology and microcomputed tomography (microCT). *J. Bone Miner. Res.* 18 (8): 1486–1496.

60 Mahler, M., Roszell, B., Mahlter, J.F. et al. (2000). Pathology of the gastrointestinal tract of genetically engineered and spontaneous mutant mice. In: Pathology of Genetically Engineered Mice (eds. J.M. Ward, M. Mahler, R.R. Maronpot and J.P. Sundberg), 269–297. Ames, IA: Iowa State University Press.

61 Schriefer, J.L., Robling, A.G., Warden, S.J. et al. (2005). A comparison of mechanical properties derived from multiple skeletal sites in mice. *J. Biomech.* 38 (3): 467–475.

62 Akhter, M.P., Otero, J.K., Iwaniec, U.T. et al. (2004). Differences in vertebral structure and strength of inbred female mouse strains. *J. Musculoskelet. Neuronal. Interact.* 4 (1): 33–40.

63 Turner, C.H. and Burr, D.B. (2001). Experimental techniques for bone mechanics. In: Bone Mechanics Handbook, 8e (ed. S.C. Cowin), 1–35. Boca Raton, FL: CRC Press.

64 van der Meulen, M.C., Jepsen, K.J., and Mikic, B. (2001). Understanding bone strength: size isn't everything. *Bone* 29 (2): 101–104.

65 Miao, D. and Scutt, A. (2002). Histochemical localization of alkaline phosphatase activity in decalcified bone and cartilage. *J. Histochem. Cytochem.* 50 (3): 333–340.

66 Roeder, E., Matthews, B.G., and Kalajzic, I. (2016). Visual reporters for study of the osteoblast lineage. *Bone* 92: 189–195.

67 Berndt, A., Ackert-Bicknell, C., Silva, K.A. et al. (2016). Genetic determinants of fibro-osseous lesions in aged inbred mice. *Exp. Mol. Pathol.* 100 (1): 92–100.

68 Moller, G., Priemel, M., Amling, M. et al. (1999). The Gorham–Stout syndrome (Gorham's massive osteolysis). A report of six cases with histopathological findings. *J. Bone Joint Surg. Br.* 81 (3): 501–506.

69 van der, van der Linden-, Zwaag, H. and Onvlee, G.J. (2006). Massive osteolysis (Gorham's disease) affecting the femur. *Acta Orthop. Belg.* 72 (3): 261–268.

70 Ishimoto, T., Sato, B., Lee, J.W., and Nakano, T. (2017). Co-deteriorations of anisotropic extracellular matrix arrangement and intrinsic mechanical property in c-src deficient osteopetrotic mouse femur. *Bone* 103: 216–223.

71 Tuukkanen, J., Koivukangas, A., Jamsa, T. et al. (2000). Mineral density and bone strength are dissociated in long bones of rat osteopetrotic mutations. *J. Bone Miner. Res.* 15 (10): 1905–1911.

72 Kornak, U., Kasper, D., Bosl, M.R. et al. (2001). Loss of the ClC-7 chloride channel leads to osteopetrosis in mice and man. *Cell* 104 (2): 205–215.

73 Xing, W., Liu, J., Cheng, S. et al. (2013). Targeted disruption of leucine-rich repeat kinase 1 but not leucine-rich repeat kinase 2 in mice causes severe osteopetrosis. *J. Bone Miner. Res.* 28 (9): 1962–1974.

74 Chalhoub, N., Benachenhou, N., Rajapurohitam, V. et al. (2003). Grey-lethal mutation induces severe malignant autosomal recessive osteopetrosis in mouse and human. *Nat. Med.* 9 (4): 399–406.

75 Vacher, J., Bruccoleri, M., and Pata, M. (2020). Ostm1 from mouse to human: insights into osteoclast maturation. *Int. J. Mol. Sci.* 21 (16).

76 Pangrazio, A., Poliani, P.L., Megarbane, A. et al. (2006). Mutations in OSTM1 (grey lethal) define a particularly severe form of autosomal recessive osteopetrosis with neural involvement. *J. Bone Miner. Res.* 21 (7): 1098–1105.

77 Li, X., Ominsky, M.S., Niu, Q.T. et al. (2008). Targeted deletion of the sclerostin gene in mice results in increased bone formation and bone strength. *J. Bone Miner. Res.* 23 (6): 860–869.

78 Gregson, C.L. and Duncan, E.L. (2020). The Genetic Architecture of High Bone Mass. *Front. Endocrinol.* 11: 595653.

79 Kerschan-Schindl, K. (2020). Romosozumab: a novel bone anabolic treatment option for osteoporosis? *Wien. Med. Wochenschr.* 170 (5–6): 124–131.

80 Baron, R. and Kneissel, M. (2013). WNT signaling in bone homeostasis and disease: from human mutations to treatments. *Nat. Med.* 19 (2): 179–192.

81 Babij, P., Zhao, W., Small, C. et al. (2003). High bone mass in mice expressing a mutant LRP5 gene. *J. Bone Miner. Res.* 18 (6): 960–974.

82 Chen, X., Wang, Z., Duan, N. et al. (2018). Osteoblast-osteoclast interactions. *Connect. Tissue Res.* 59 (2): 99–107.

83 Bucay, N., Sarosi, I., Dunstan, C.R. et al. (1998). Osteoprotegerin-deficient mice develop early onset osteoporosis and arterial calcification. *Genes Dev.* 12 (9): 1260–1268.

84 Simonet, W.S., Lacey, D.L., Dunstan, C.R. et al. (1997). Osteoprotegerin: a novel secreted protein involved in the regulation of bone density. *Cell* 89 (2): 309–319.

85 Shobeiri, N., Adams, M.A., and Holden, R.M. (2010). Vascular calcification in animal models of CKD: a review. *Am. J. Nephrol.* 31 (6): 471–481.

86 Tani, T., Orimo, H., Shimizu, A., and Tsuruoka, S. (2017). Development of a novel chronic kidney disease mouse model to evaluate the progression of hyperphosphatemia and associated mineral bone disease. *Sci. Rep.* 7 (1): 2233.

87 Mohan, S., Kapoor, A., Singgih, A. et al. (2005). Spontaneous fractures in the mouse mutant sfx are caused by deletion of the gulonolactone oxidase gene, causing vitamin C deficiency. *J. Bone Miner. Res.* 20 (9): 1597–1610.

88 Beamer, W.G., Rosen, C.J., Bronson, R.T. et al. (2000). Spontaneous fracture (sfx): a mouse genetic model of defective peripubertal bone formation. *Bone* 27 (5): 619–626.

89 Gabbay, K.H., Bohren, K.M., Morello, R. et al. (2010). Ascorbate synthesis pathway: dual role of ascorbate in bone homeostasis. *J. Biol. Chem.* 285 (25): 19510–19520.

90 Kornak, U. (2011). Animal models with pathological mineralization phenotypes. *Joint Bone Spine*.

91 Goltzman, D. (2018). Functions of vitamin D in bone. *Histochem. Cell Biol.* 149 (4): 305–312.

92 Vogel, P., Hansen, G.M., Read, R.W. et al. (2012). Amelogenesis imperfecta and other biomineralization defects in Fam20a and Fam20c null mice. *Vet. Pathol.* 49 (6): 998–1017.

93 Razzaque, M.S. and Lanske, B. (2007). The emerging role of the fibroblast growth factor-23-klotho axis in renal regulation of phosphate homeostasis. *J. Endocrinol.* 194 (1): 1–10.

94 Sasaki, M., Hasegawa, T., Yamada, T. et al. (2013). Altered distribution of bone matrix proteins and defective bone mineralization in klotho-deficient mice. *Bone* 57 (1): 206–219.

95 Suzuki, H., Amizuka, N., Oda, K. et al. (2005). Histological evidence of the altered distribution of osteocytes and bone matrix synthesis in klotho-deficient mice. *Arch. Histol. Cytol.* 68 (5): 371–381.

96 Alizadeh Naderi, A.S. and Reilly, R.F. (2010). Hereditary disorders of renal phosphate wasting. *Nat. Rev. Nephrol.* 6 (11): 657–665.

97 Strom, T.M. and Juppner, H. (2008). PHEX, FGF23, DMP1 and beyond. *Curr. Opin. Nephrol. Hypertens.* 17 (4): 357–362.

98 Consortium, H. (1995). A gene (PEX) with homologies to endopeptidases is mutated in patients with X-linked hypophosphatemic rickets. The HYP Consortium. *Nat. Genet.* 11 (2): 130–136.

99 Murshed, M. and McKee, M.D. (2010). Molecular determinants of extracellular matrix mineralization in bone and blood vessels. *Curr. Opin. Nephrol. Hypertens.* 19 (4): 359–365.

100 Hessle, L., Johnson, K.A., Anderson, H.C. et al. (2002). Tissue-nonspecific alkaline phosphatase and plasma cell membrane glycoprotein-1 are central antagonistic regulators of bone mineralization. *Proc. Natl. Acad. Sci. U.S.A.* 99 (14): 9445–9449.

101 Ho, A.M., Johnson, M.D., and Kingsley, D.M. (2000). Role of the mouse ank gene in control of tissue calcification and arthritis. *Science* 289 (5477): 265–270.

102 Whyte, M.P. (2010). Physiological role of alkaline phosphatase explored in hypophosphatasia. *Ann. N.Y. Acad. Sci.* 1192: 190–200.

103 Harmey, D., Hessle, L., Narisawa, S. et al. (2004). Concerted regulation of inorganic pyrophosphate and osteopontin by akp2, enpp1, and ank: an integrated model of the pathogenesis of mineralization disorders. *Am. J. Pathol.* 164 (4): 1199–1209.

104 Johnson, K., Polewski, M., van Etten, D., and Terkeltaub, R. (2005). Chondrogenesis mediated by PPi depletion promotes spontaneous aortic calcification in NPP1−/− mice. *Arterioscler. Thromb. Vasc. Biol.* 25 (4): 686–691.

105 Rutsch, F., Ruf, N., Vaingankar, S. et al. (2003). Mutations in ENPP1 are associated with 'idiopathic' infantile arterial calcification. *Nat. Genet.* 34 (4): 379–381.

106 Suliman, M.E., Garcia-Lopez, E., Anderstam, B. et al. (2008). Vascular calcification inhibitors in relation to cardiovascular disease with special emphasis on fetuin-A in chronic kidney disease. *Adv. Clin. Chem.* 46: 217–262.

107 Berndt, A., Li, Q., Potter, C.S. et al. (2013). A single-nucleotide polymorphism in the Abcc6 gene associates with connective tissue mineralization in mice similar to targeted models for pseudoxanthoma elasticum. *J. Invest. Dermatol.* 133 (3): 833–836.

108 Li, Q.L., Price, T.P., Sundberg, J.P., and Uitto, J. (2014). Juxta-articular joint-capsule mineralization in CD73 deficient mice: similarities to patients with NT5E mutations. *Cell Cycle* 13 (16): 2609–2615.

109 Marini, J.C., Forlino, A., Bachinger, H.P. et al. (2017). Osteogenesis imperfecta. *Nat. Rev. Dis. Primers* 3: 17052.

110 Forlino, A. and Marini, J.C. (2016). Osteogenesis imperfecta. *Lancet* 387 (10028): 1657–1671.

111 Chipman, S.D., Sweet, H.O., DJ, M.B. Jr. et al. (1993). Defective pro alpha 2(I) collagen synthesis in a recessive mutation in mice: a model of human osteogenesis imperfecta. *Proc. Natl. Acad. Sci. U.S.A.* 90 (5): 1701–1705.

112 Vanleene, M., Porter, A., Guillot, P.V. et al. (2012). Ultra-structural defects cause low bone matrix stiffness despite high mineralization in osteogenesis imperfecta mice. *Bone* 50 (6): 1317–1323.

113 Kozloff, K.M., Carden, A., Bergwitz, C. et al. (2004). Brittle IV mouse model for osteogenesis imperfecta IV demonstrates postpubertal adaptations to improve whole bone strength. *J. Bone Miner. Res.* 19 (4): 614–622.

114 Laine, C.M., Joeng, K.S., Campeau, P.M. et al. (2013). WNT1 mutations in early-onset osteoporosis and osteogenesis imperfecta. *N. Engl. J. Med.* 368 (19): 1809–1816.

115 Joeng, K.S., Lee, Y.C., Jiang, M.M. et al. (2014). The swaying mouse as a model of osteogenesis imperfecta caused by WNT1 mutations. *Hum. Mol. Genet.* 23 (15): 4035–4042.

116 Lamande, S.R. and Bateman, J.F. (2020). Genetic disorders of the extracellular matrix. *Anat. Rec.* 303 (6): 1527–1542.

117 Miao, D., Bai, X., Panda, D.K. et al. (2004). Cartilage abnormalities are associated with abnormal Phex expression and with altered matrix protein and MMP-9 localization in Hyp mice. *Bone* 34 (4): 638–647.

118 Pirog, K.A., Irman, A., Young, S. et al. (2014). Abnormal chondrocyte apoptosis in the cartilage growth plate is influenced by genetic background and deletion of CHOP in a targeted mouse model of pseudoachondroplasia. *PLoS One* 9 (2): e85145.

119 Usami, Y., Gunawardena, A.T., Iwamoto, M., and Enomoto-Iwamoto, M. (2016). Wnt signaling in cartilage development and diseases: lessons from animal studies. *Lab. Invest.* 96 (2): 186–196.

120 Gerwin, N., Bendele, A.M., Glasson, S., and Carlson, C.S. (2010). The OARSI histopathology initiative – recommendations for histological assessments of osteoarthritis in the rat. *Osteoarthr. Cartil.* 18 (Suppl 3): S24–S34.

121 Koehne, T., Marshall, R.P., Jeschke, A. et al. (2013). Osteopetrosis, osteopetrorickets and hypophosphatemic rickets differentially affect dentin and enamel mineralization. *Bone* 53 (1): 25–33.

122 Hughes, L.C., Archer, C.W., and ap Gwynn, I. (2005). The ultrastructure of mouse articular cartilage: collagen orientation and implications for tissue functionality. A polarised light and scanning electron microscope study and review. *Eur. Cell Mater.* 9: 68–84.

123 Buckwalter, J.A. and Mankin, H.J. (1998). Articular cartilage: tissue design and chondrocyte-matrix interactions. *Instr. Course Lect.* 47: 477–486.

124 Staines, K.A., Poulet, B., Wentworth, D.N., and Pitsillides, A.A. (2017). The STR/ort mouse model of spontaneous osteoarthritis – an update. *Osteoarthr. Cartil.* 25 (6): 802–808.

125 Lorenz, J. and Grassel, S. (2014). Experimental osteoarthritis models in mice. *Methods Mol. Biol.* 1194: 401–419.

126 Kan, L.X. (2013). Animal models of bone diseases-A. *Anim. Models Study Hum. Dis.*: 353–390.

127 Veronesi, F., Della Bella, E., Cepollaro, S. et al. (2016). Novel therapeutic targets in osteoarthritis: narrative review on knock-out genes involved in disease development in mouse animal models. *Cytotherapy* 18 (5): 593–612.

128 Streelman, J.T., Webb, J.F., Albertson, R.C., and Kocher, T.D. (2003). The cusp of evolution and development: a model of cichlid tooth shape diversity. *Evol. Dev.* 5 (6): 600–608.

129 Ohazama, A., Blackburn, J., Porntaveetus, T. et al. (2010). A role for suppressed incisor cuspal morphogenesis in the evolution of mammalian heterodont dentition. *Proc. Natl. Acad. Sci. U.S.A.* 107 (1): 92–97.

130 Lesot, H. and Brook, A.H. (2009). Epithelial histogenesis during tooth development. *Arch. Oral Biol.* 54 (Suppl 1): S25–S33.

131 Jheon, A.H., Seidel, K., Biehs, B., and Klein, O.D. (2013). From molecules to mastication: the development and evolution of teeth. *Wiley interdisciplinary reviews Developmental biology.* 2 (2): 165–182.

132 Zhang, Y.D., Chen, Z., Song, Y.Q. et al. (2005). Making a tooth: growth factors, transcription factors, and stem cells. *Cell Res.* 15 (5): 301–316.

133 Caton, J. and Tucker, A.S. (2009). Current knowledge of tooth development: patterning and mineralization of the murine dentition. *J. Anat.* 214 (4): 502–515.

134 Fleischmannova, J., Matalova, E., Tucker, A.S., and Sharpe, P.T. (2008). Mouse models of tooth abnormalities. *Eur. J. Oral Sci.* 116 (1): 1–10.

135 Miletich, I. and Sharpe, P.T. (2003). Normal and abnormal dental development. *Hum. Mol. Genet.* 12 Spec No 1: R69–R73.

136 Hardcastle, Z., Mo, R., Hui, C.C., and Sharpe, P.T. (1998). The Shh signalling pathway in tooth development: defects in Gli2 and Gli3 mutants. *Development* 125 (15): 2803–2811.

137 Jernvall, J., Kettunen, P., Karavanova, I. et al. (1994). Evidence for the role of the enamel knot as a control center in mammalian tooth cusp formation: non-dividing cells express growth stimulating Fgf-4 gene. *Int. J. Dev. Biol.* 38 (3): 463–469.

138 Vogel, P., Read, R.W., Hansen, G.M. et al. (2016). Dentin dysplasia in notum knockout mice. *Vet. Pathol.* 53 (4): 853–862.

139 Fraser, G.J., Hulsey, C.D., Bloomquist, R.F. et al. (2009). An ancient gene network is co-opted for teeth on old and new jaws. *PLoS Biol.* 7 (2): e31.

140 Jernvall, J. and Thesleff, I. (2000). Reiterative signaling and patterning during mammalian tooth morphogenesis. *Mech. Dev.* 92 (1): 19–29.

141 Jernvall, J. and Thesleff, I. (2012). Tooth shape formation and tooth renewal: evolving with the same signals. *Development* 139 (19): 3487–3497.

142 Vogel, P., Liu, J., Platt, K.A. et al. (2015). Malformation of incisor teeth in grem2−/− mice. *Vet. Pathol.* 52 (1): 224–229.

143 Laurikkala, J., Mikkola, M., Mustonen, T. et al. (2001). TNF signaling via the ligand-receptor pair ectodysplasin and edar controls the function of epithelial signaling centers and is regulated by Wnt and activin during tooth organogenesis. *Dev. Biol.* 229 (2): 443–455.

144 Pispa, J., Jung, H.S., Jernvall, J. et al. (1999). Cusp patterning defect in Tabby mouse teeth and its partial rescue by FGF. *Dev. Biol.* 216 (2): 521–534.

145 Sofaer, J.A. (1979). Additive effects of the genes tabby and crinkled on tooth size in the mouse. *Genet. Res.* 33 (2): 169–174.

146 Tucker, A.S., Headon, D.J., Schneider, P. et al. (2000). Edar/Eda interactions regulate enamel knot formation in tooth morphogenesis. *Development* 127 (21): 4691–4700.

147 Ohazama, A., Courtney, J.M., Tucker, A.S. et al. (2004). Traf6 is essential for murine tooth cusp morphogenesis. *Dev. Dyn.* 229 (1): 131–135.

148 Headon, D.J., Emmal, S.A., Ferguson, B.M. et al. (2001). Gene defect in ectodermal dysplasia implicates a death domain adapter in development. *Nature* 414 (6866): 913–916.

149 Kere, J., Srivastava, A.K., Montonen, O. et al. (1996). X-linked anhidrotic (hypohidrotic) ectodermal dysplasia is caused by mutation in a novel transmembrane protein. *Nat. Genet.* 13 (4): 409–416.

150 Bailleul-Forestier, I., Berdal, A., Vinckier, F. et al. (2008). The genetic basis of inherited anomalies of the teeth. Part 2: syndromes with significant dental involvement. *Eur. J. Med. Genet.* 51 (5): 383–408.

151 Wang, Z. and McCauley, L.K. (2011). Osteoclasts and odontoclasts: signaling pathways to development and disease. *Oral Dis.* 17 (2): 129–142.

152 Alfaqeeh, S., Oralova, V., Foxworthy, M. et al. (2015). Root and eruption defects in c-Fos mice are driven by loss of osteoclasts. *J. Dent. Res.* 94 (12): 1724–1731.

153 Nusier, M., Yassin, O., Hart, T.C. et al. (2004). Phenotypic diversity and revision of the nomenclature for autosomal recessive amelogenesis imperfecta. *Oral Surg. Oral Med. Oral Pathol. Oral Radiol. Endod.* 97 (2): 220–230.

154 Witkop, C.J. Jr. (1988). Amelogenesis imperfecta, dentinogenesis imperfecta and dentin dysplasia revisited: problems in classification. *J. Oral Pathol.* 17 (9–10): 547–553.

155 Backman, B. and Holm, A.K. (1986). Amelogenesis imperfecta: prevalence and incidence in a northern Swedish county. *Community Dent. Oral Epidemiol.* 14 (1): 43–47.

156 He, G. and George, A. (2004). Dentin matrix protein 1 immobilized on type I collagen fibrils facilitates apatite deposition in vitro. *J. Biol. Chem.* 279 (12): 11649–11656.

157 Hu, J.C., Chun, Y.H., Al Hazzazzi, T., and Simmer, J.P. (2007). Enamel formation and amelogenesis imperfecta. *Cells Tissues Organs* 186 (1): 78–85.

158 Deutsch, D., Palmon, A., Dafni, L. et al. (1995). The enamelin (tuftelin) gene. *Int. J. Dev. Biol.* 39 (1): 135–143.

159 Snead, M.L., Lau, E.C., Fincham, A.G. et al. (1989). Of mice and men: anatomy of the amelogenin gene. *Connect. Tissue Res.* 22 (1–4): 101–109.

160 Krebsbach, P.H., Lee, S.K., Matsuki, Y. et al. (1996). Full-length sequence, localization, and chromosomal mapping of ameloblastin. A novel tooth-specific gene. *J. Biol. Chem.* 271 (8): 4431–4435.

161 Iwasaki, K., Bajenova, E., Somogyi-Ganss, E. et al. (2005). Amelotin – a novel secreted, ameloblast-specific protein. *J. Dent. Res.* 84 (12): 1127–1132.

162 Crawford, P.J., Aldred, M., and Bloch-Zupan, A. (2007). Amelogenesis imperfecta. *Orphanet. J. Rare Dis.* 2: 17.

163 Pugach, M.K. and Gibson, C.W. (2014). Analysis of enamel development using murine model systems: approaches and limitations. *Front. Physiol.* 5.

164 Pugach, M.K., Ozer, F., Mulmadgi, R. et al. (2014). Shear bond strength of dentin and deproteinized enamel of amelogenesis imperfecta mouse incisors. *Pediatr. Dent.* 36 (5): 130–136.

165 Schmitz, J.E., Teepe, J.D., Hu, Y. et al. (2014). Estimating mineral changes in enamel formation by ashing/BSE and microCT. *J. Dent. Res.* 93 (3): 256–262.

166 Santos, M.C., Hart, P.S., Ramaswami, M. et al. (2007). Exclusion of known gene for enamel development in two Brazilian families with amelogenesis imperfecta. *Head Face Med.* 3: 8.

167 Aldred, M.J., Savarirayan, R., and Crawford, P.J. (2003). Amelogenesis imperfecta: a classification and catalogue for the 21st century. *Oral Dis.* 9 (1): 19–23.

168 Gibson, C.W., Yuan, Z.A., Hall, B. et al. (2001). Amelogenin-deficient mice display an amelogenesis imperfecta phenotype. *J. Biol. Chem.* 276 (34): 31871–31875.

169 Simmer, J.P., Hu, Y., Lertlam, R. et al. (2009). Hypomaturation enamel defects in Klk4 knockout/LacZ knockin mice. *J. Biol. Chem.* 284 (28): 19110–19121.

170 Caterina, J.J., Skobe, Z., Shi, J. et al. (2002). Enamelysin (matrix metalloproteinase 20)-deficient mice display an amelogenesis imperfecta phenotype. *J. Biol. Chem.* 277 (51): 49598–49604.

171 Wazen, R.M., Moffatt, P., Zalzal, S.F. et al. (2009). A mouse model expressing a truncated form of ameloblastin exhibits dental and junctional epithelium defects. *Matrix Biol.* 28 (5): 292–303.

172 Hu, J.C., Hu, Y., Smith, C.E. et al. (2008). Enamel defects and ameloblast-specific expression in Enam knock-out/lacz knock-in mice. *J. Biol. Chem.* 283 (16): 10858–10871.

173 Lu, Y., Papagerakis, P., Yamakoshi, Y. et al. (2008). Functions of KLK4 and MMP-20 in dental enamel formation. *Biol. Chem.* 389 (6): 695–700.

174 Smith, C.E., Richardson, A.S., Hu, Y. et al. (2011). Effect of kallikrein 4 loss on enamel mineralization: comparison with mice lacking matrix metalloproteinase 20. *J. Biol. Chem.* 286 (20): 18149–18160.

175 Thesleff, I. (2003). Epithelial-mesenchymal signalling regulating tooth morphogenesis. *J. Cell Sci.* 116 (Pt 9): 1647–1648.

176 MacDougall, M., Dong, J., and Acevedo, A.C. (2006). Molecular basis of human dentin diseases. *Am. J. Med. Genet. A* 140 (23): 2536–2546.

177 Kim, J.W. and Simmer, J.P. (2007). Hereditary dentin defects. *J. Dent. Res.* 86 (5): 392–399.

178 Barron, M.J., McDonnell, S.T., Mackie, I., and Dixon, M.J. (2008). Hereditary dentine disorders: dentinogenesis imperfecta and dentine dysplasia. *Orphanet. J. Rare Dis.* 3: 31.

179 Fujihara, H., Nozaki, T., Tsutsumi, M. et al. (2019). Spontaneous development of dental dysplasia in aged Parp-1 knockout mice. *Cells* 8 (10).

180 Losco, P.E. (1995). Dental dysplasia in rats and mice. *Toxicol. Pathol.* 23 (6): 677–688.

181 Vasquez, S.X., Bahadur, A.N., Johnson, J.T. et al. (2007). Severe runting in a laboratory mouse (Mus musculus). *Lab. Anim.* 36 (1): 19, 22-3.

182 Peterkova, R., Peterka, M., and Lesot, H. (2003). The developing mouse dentition: a new tool for apoptosis study. *Ann. N.Y. Acad. Sci.* 1010: 453–466.

183 Sundberg, J.P., Rozell, B., and Everts, H. (2011). Association between hair-induced oronasal inflammation and ulcerative dermatitis in C57BL/6 mice. *Comp. Med.* 61 (3): 204–205, author reply 5.

184 de Vries, T.J., Andreotta, S., Loos, B.G., and Nicu, E.A. (2017). Genes critical for developing periodontitis: lessons from mouse models. *Front. Immunol.* 8: 1395.

Index

a

Abcc6 11, 44, 160, 249, 292, 528
accessory sex glands 431, 433, 435, 448
adenomas, pulmonary 152
adipocytes, brown 308, 342
adipocytes, white 296
adipose tissue 214, 219, 231, 322, 351, 360, 369, 523
adrenal glands 98, 149–51, 358, 365–68, 438, 442
agenesis 360, 364, 509, 511
aggregates 67, 113, 122, 338, 351–52, 369, 446, 471, 499
aging 3, 11, 84–85, 88, 92, 164, 188, 196, 231, 241, 259, 272, 311, 369, 392, 397, 422, 446, 525
A/J mice 184, 351
AKR/J mice 26–28, 99, 472
albinism 29, 175
alcoholic liver disease (ALD) 312, 314
allantois 50, 65
allograft 99, 107, 118, 299, 308, 465
alopecia 11, 149, 159, 177–80, 182, 185, 187
alopecia areata 164, 171, 176, 181, 187–88, 199, 293
alveolar macrophages 239, 242–43
  Type II cell 239, 245, 251–53
alveoli 21, 238–40, 242, 244–46, 252, 254
Alzheimer's disease 372, 470, 472
ameloblasts 531–33
ampullary glands (AG) 431–34
amyloid 88, 90, 92, 389, 446, 473, 475
anagen 160, 162–63, 166, 174, 176
anaplastic large cell lymphoma (ALCL) 118–19, 121
anophthalmia 496–97
anovulation 409, 414–15
anus 167, 259, 266
aortic lesions 289, 298
aortic valve 284, 293, 295
Apc^{Min} 226, 266, 269, 271–72, 276–77
apocrine sweat glands 164, 177
APP (amyloid precursor protein) 471–73, 476
aqueduct 74
aqueous humor 493–95
arteries 285–86, 288, 292, 349, 469
arterioles 91, 136, 246, 286, 293, 299
asthma 249–50
astrocytes 77, 464, 474, 479, 494
astrogliosis 470, 474
AT2 239, 252–51
ataxia 343, 346, 353, 478–79, 482
athymic nude mice 419
auditory brainstem response (ABR) 505–6
autoantibodies 194, 337, 345, 362, 365, 389
autoimmune diseases
  cell-mediated 176, 181
  humoral 187, 194, 196
autoimmune encephalomyelitis, experimental (EAE) 351
autoimmune myocarditis 297
autoimmune thyroiditis, experimental 361
autoimmunity, systemic 297
autophagy 325, 338–39, 352, 513
axon 339, 341, 343–45, 463
axonopathies 337, 343–45
azoospermia 449

b

backcrosses 23, 27, 29, 31–32, 74
background lesions 150, 403, 525, 534
BALB/c mice 99, 106, 111, 119, 250–51, 311, 314, 379–80, 471, 498, 502
basement membrane 50, 141, 162, 196, 198, 271, 278, 285, 328, 382, 443
basophils 99, 101–2, 108, 357
B-cells 97, 108–9, 118
B-cell lymphomas 97, 112, 116, 118, 121
  diffuse high-grade blastic 116–17
  diffuse large 109–10, 117
  follicular 275
  lymphoblastic 109, 116–17
  mature 121
  small 109–10
bile duct 260, 272, 309, 315, 318
blepharitis 497
BMC (bone mineral content) 523
BMD (bone mineral density) 523–25
body weight (BW) 53, 166, 285, 287, 314, 351, 369, 378, 478
bone development 77, 508
bone formation 522, 526
bone formation rate (BFR) 522
bone homeostasis 520, 526
bone marrow aplasia/failure 83, 142–43
bone marrow hypoplasia 83
bone mass 7, 16, 520–21
bone mineral content (BMC) 523
bone mineral density (BMD) 523–25
bone resorption 521–22, 525–26
bone strength 521–23, 525, 529
brain development 75
brain malformations 73, 75, 77
brain morphogenesis 74, 484
brain tumors, spontaneous 484
Brca 2, 217, 323–26, 414–16
bronchi 238, 252
bronchial-associated lymphoid tissue (BALT) 238, 241
bronchiolar club cells 240, 245, 251
bronchioles 238, 242, 244–45, 252, 254
bulbourethral glands 228, 431, 433–35, 442

c

cadherin 217, 420, 436, 453, 508
calcification 295, 322, 392, 526–30
carcinogenesis 1, 124, 188, 218, 262, 264, 270
carcinoids 272, 274
cardiac development 291, 296

Pathology of Genetically Engineered and Other Mutant Mice, First Edition. Edited by John P. Sundberg, Peter Vogel, and Jerrold M. Ward.
© 2022 John Wiley & Sons, Inc. Published 2022 by John Wiley & Sons, Inc.

cardiomyocytes 288, 290–91, 295–96
cardiomyopathy 295, 297–98
  dilative 296–97
  mitochondrial 297
  obstructive 296
cartilage 53, 56, 507, 520, 522–24, 526, 528–30
cataracts 190, 495, 499–502
CBC (complete blood count) 58, 102, 142
CD2 118, 122
CD3 98, 100, 103, 105–6, 109–10, 112, 114–15, 117–21, 136–37, 141–42, 232
CD4 109, 117, 119, 121–23
CD5 109–10, 118–19, 121
CD7 118, 122
CD8 109, 117–23, 140, 188–89, 231, 362
CD19 109–10, 112
CD30 119, 121–22
CD41 98, 100–101, 103, 105–6
CD43 98–100, 106, 109–10, 112, 115, 121
CD45R/B222 98, 105, 109–10, 112, 114–17, 121
CD47 134
CD49B 121
CD68 98–101, 103, 105–7, 239, 308
CD71 98, 101, 103, 106
CD117 98–100, 102, 105, 107–9, 118, 265, 272
CD163 100, 106–7
Cdkn2a 106, 191, 314, 323, 326, 443, 484
cecum 91, 144, 152, 265–66, 268, 275, 277
centroblasts 113–14
centrocytes 112–13
cerebellum 57–59, 393, 462, 464–68, 478–79, 484
cerebrospinal fluid 74, 462, 507
ceruminous glands 164
cervical cancer 189, 416, 420
cervix 403, 405–7, 420
chalazion 497
channelopathies 351, 520
Chediak-Higashi syndrome 41
Chil3 239, 241, 26, 272
chorion 50–52, 64–65
choroid 494–95, 499–502, 504
chronic lymphocytic leukemia (CLL) 109
cilia 72–78, 162, 164, 167, 177, 357, 494
  ectopic 494
  ependymal 74
ciliary body 493–94, 49, 451–502, 504
ciliopathies 72–73, 75–78, 241, 247, 392–93, 454, 509, 520
Cinderella effect 39–40, 42, 44
cirrhosis 312, 314–15
cleft lip 237, 498
cleft palate 59, 61, 77, 86, 237
clitoral glands 177, 182, 431
cochlea 77, 505–7, 509, 511
cochlear hair cells 469, 508
colitis models 266–68, 271, 274, 277
collaborative cross (CC) 23–24, 29, 33, 44
collagen 39, 196–97, 286, 307, 312, 493, 497, 507, 520–21, 528–29, 533
collagenopathy 389–90
collagen types 2, 521
colon adenocarcinomas 139, 275
colon adenomas 271, 274
complement 2, 133–34, 147, 385–86, 404
congenic mice 22–23, 29–32, 42, 159–60, 175, 196, 501
congenital heart diseases 77, 295
conjunctiva 177, 494, 496, 498
conjunctivitis 149, 497
contraction bands 348
cornea 177, 493–96, 498–99
corneal lesions 495, 497
corpus callosum 462, 468, 470
Corti, organ of 77, 506–7, 509–11
cortical bone 520, 522, 526, 529
corticotrophs 357–58, 365
craniopharyngioma 358
creatinine ratio 380–81, 384
Crohn's disease 267–68
Ctnnb1 273–74, 314, 317, 359, 394, 399, 420
cyclin 112, 191, 317, 365, 414, 443
cystic fibrosis 2, 147, 247–49, 266, 322
cystinosis 393
cysts 85–86, 189, 199, 225, 265, 322, 357, 391, 394, 422, 433
  dermal 182
  renal 391, 394
cytokines 82, 84, 87, 93, 102, 124, 160, 181–82, 231, 290, 406, 418, 535
cytotoxic T-cell 121

d

DBA/2J mice 11–12, 26–27, 29–30, 52, 99, 249, 379, 392, 469–70, 502, 508, 528
deafness 73, 77, 505, 509, 511
  non-syndromic 511
  syndromic 508
decidua 48, 50–52, 64–66, 411
Demodex musculi 147
demyelination 342, 345, 479–80
dendritic cell (DC) 84–85, 87–88, 91, 106–8, 113, 140, 148, 357, 535
dendritic cell tumors 107
dental diseases 521, 530
dentin 520, 531–34
dentinogenesis 533
dentinogenesis imperfecta 532–34
dermatitis
  chronic 147
  inflammatory 122
  necrotizing 179
  psoriasiform 184
dermis 122, 160, 162, 173, 177, 180, 184, 189, 198–99
Descemet's membrane 493, 498–99
desmin 107, 338, 347, 349–52
desmoglein 42, 159, 184–85, 187, 193–94
desmosomes 184–85, 191, 195, 296
DHGBL (Diffuse high-grade blastic lymphoma) 109, 115–17
diabetes 324, 361, 369–70, 414
diabetes mellitus 2, 370, 384
diaphragm 55, 241, 329
DiGeorge syndrome 86, 508, 511
diverticulum 265, 272
DLBCL (diffuse large B-cell lymphoma) 109–11, 113–18
dorsal root ganglia (DRG) 336, 338–40, 342–43, 345
Dual X-ray Absorptiometry. *See* DXA
Duchenne 2, 296–97, 338, 351
ducts
  collecting 391–92
  intercalated 320
duodenum 259, 265, 277, 309, 320–21, 369
DXA (Dual X-ray Absorptiometry) 523, 525
dysferlin 336, 338, 350–51
dyshormonogenesis 360
dysplasia 104–5, 215, 260, 262, 266, 268, 271–74, 279, 322, 326, 500
dyspnea 146, 149, 241, 362
dystrophin 2, 297, 336, 347, 350–51

e

EAE (experimental autoimmune encephalitis) 351, 480–81
ear 162, 166–67, 173, 179, 181, 190, 195–96, 493–94, 496, 498, 500, 505–12, 514
ear canal, external 176–77, 506
E-cadherin 313, 321, 329, 436, 445
eccrine glands 164, 167, 173, 177, 181
ectoderm 49, 356, 507
ectopic mineralization 42, 44, 160, 249, 293, 379, 392, 498, 528
edema 59, 146, 243, 325–26, 439, 495, 498
embryogenesis 161–62, 213, 320, 520
embryology 160, 307, 404, 493, 507

embryonic death/lethality 39, 58–60, 62–63, 65–66, 365, 394, 498
enamel 520, 531–34
endocrine glands 61, 355, 357
endoderm 49, 84, 86
endolymph 507–8, 511
endometriosis 415–16, 418–19
endothelium 51, 65, 148, 226, 285–87, 290–91, 493, 499
ENU mutagenesis 7, 13, 106
eosinophils 84, 98, 118, 122, 184, 231, 241, 250
epidermolysis bullosa 191, 196
  junctional 39, 41, 196–98
epididymis 75, 443–47, 450–51, 453–56
erroneous pathology 3
erythrocytosis 103–4
erythroid cells/precursors 98, 100–101, 105
erythroleukemia 100–101
erythropoiesis 82–84
esophagus 147, 259–60, 288, 359
estrus 228, 406
exencephaly 483
experimental autoimmune encephalitis. *See* EAE
eyelashes 152, 164

f

fat pad 213–14, 230–31
fertility 13, 74–75, 405, 409, 448, 451, 454–55
fibers
  elastic 173, 285, 289, 298, 493
  intrafusal 346
  nuclear bag 346
  nuclear chain 346
fibronectin 389–90
fibro-osseous lesions 83–84, 525
flagella 72–73
flow cytometry 83–85, 88, 98, 101–3, 105, 109–10, 112, 115, 117–18, 297
follicle development 161, 404
follicles 86, 88, 91, 93–94, 110, 160–62, 168, 177–78, 181, 183, 359–60, 403–4, 406, 410, 412
follicular cells 114, 359, 361
follicular lymphoma (FL) 110 112–15, 118, 392
folliculitis 149, 179
folliculogenesis 412
fracture 521–23, 534
FSH (follicle-stimulating hormone) 357, 403–4, 411–12, 448
FVB mice 222, 363, 379, 438, 503

g

gall bladder 260, 272, 309–10
gametogenesis 413
gastrointestinal neoplasia 272
gastrointestinal stromal tumors (GIST) 265, 272, 277
genetic modifiers 74, 78
genetic background 29, 31, 40, 78, 102, 159, 176, 219, 268, 297, 392, 419
gene redundancy 42, 78
gene trap 35–36, 177
genocopies 42, 159–60, 181, 183–84
germ cells 27, 412, 414, 443, 445–46, 450–54
germ cell tumors 456
germinal center (GC) 66, 86–88, 91, 93–94, 110, 112–14, 116, 123, 132, 479
GIN, see gastrointestinal neoplasia
GIST, see gastrointestinal stromal tumor
GFAP (glial fibrillary acidic protein) 308, 342, 465, 474, 484
glands
  ampullary 431–34
  coagulating 431–32, 434–36
  periurethral 433–35
  pineal 355, 371–72
glaucoma 499–501, 504–5
glial cells 363–64, 464–65, 482, 494
glial fibrillary acidic protein. *See* GFAP
glioma 483–84
gliosis 345, 470, 473, 476, 478, 480, 502
glomeruli 378–90
glomerulonephritis 150, 152, 379, 387–88, 390–91
glycogen 173, 340, 394
glycogen storage disease 295, 311, 316
goblet cells 239, 272, 277, 320
goiter 360–61
gonadal tumors 413
gonadotropins 403–4, 409, 411, 413
gonads 366, 402–4, 412–13
graft-versus-host disease. *See* GVHD
granular lymphocyte lymphomas 121
granule cells 469, 478–79
granulocytes 98, 102–3
granulosa cells 404, 413–14
  ovarian 456
granulosa cell tumors 151, 408, 412, 414–15, 422, 456
growth factors 83–84, 231, 296, 317, 404, 406, 412, 420, 520–21
GVHD (graft-versus-host disease) 139–41

h

hair abnormalities 159, 175
hair bulb 160, 162
hair cells 506–13
  inner 507, 510
  outer 507, 510
  sensory 77, 509
hair cycle 162–64, 166, 177–78, 181–82
hair development 532
hair follicles 16, 86, 160–63, 166–67, 169, 173, 176–77, 184–85, 187–89, 194, 196
hair follicle stem cells 168, 176
hairless 29, 181–82, 188, 199
hair loss 159, 171, 176
hair types 160–62, 164
hamartoma 265, 272, 394
haplotypes 361, 480
Harderian glands 141, 151, 218, 228, 371, 422, 495–97, 503
Hashimoto's thyroiditis 55, 361–62
heart failure 285, 294, 298
hedgehog 2, 72, 321, 366, 501, 521, 531
Helicobacter 149, 260–62, 264–68
hematolymphoid neoplasms 97–98, 110
hematopoietic cells 83–84, 132
hematopoietic neoplasms 97, 123, 467, 469
hematopoietic stem cells. *See* HSCs
hemosiderin 83, 88, 93, 446
hepatoblasts 307–9
hepatocarcinogenesis 313–14
hepatocellular adenoma 314, 317–19
hepatocellular carcinoma 139, 310, 317–19
Hering cells 307
herniation 241, 260, 262, 265–65, 268, 277, 470, 472
high-fat diet (HFD) 40, 312, 316
hippocampus 58, 462–64, 467–72, 476, 481
histiocytes 97, 106, 113–15, 122
histiocytic sarcoma 97, 106–8, 115, 151–52, 314, 317, 392, 395, 467, 469
hormone receptors 2, 222, 361, 402
hormones 355, 357, 360, 366, 369–70, 403–4, 409, 412, 414, 521, 527
Hras 191, 294, 317, 399
humanized mice 132, 134, 136, 140–52, 307, 317
Huntington's disease 464, 479–80
hyaline arteriolosclerosis 290, 293
hyalinosis 237, 241–42, 259–62, 272, 322, 387
  pulmonary 242
hybrids 6, 27, 29, 501–2
hydrocephalus 73–74, 77–78, 468–70, 483
  congenital 74, 469, 483

hydronephrosis 392, 395, 397
hypermobility 533–34
hyperpigmentation 176
hyperpituitarism 358
hyperplasia, atypical
adenomatous 252, 264
hyperreflexia 346
hyperthermia 361
hypocalcemia 364–65
hypogonadism 408, 412, 449
hyponychium 164, 167, 197–98
hypoparathyroidism 364
hypophosphatemia 365, 527–28
hypopituitarism 358, 367
hypothalamus 356–57, 403–4, 462
hypothyroidism 86, 359–60, 412

i

IBA1 98–101, 106–8, 300, 308, 342, 465, 475
IBD (inflammatory bowel disease) 266–68
ichthyosis 185–87, 199
idiopathic pulmonary fibrosis. *See* IPF
IgA 110, 112, 115, 384–85, 387
IgG 110, 112, 115, 385, 391
IKMC. *See* International Knockout Mouse Consortium
immune responses
adaptive 84, 88, 140, 267
innate 494
immunocompromised mice 99, 111, 119, 147, 149, 420
immunodeficient mice 9, 98, 105, 132, 134, 139–45, 147–49, 151, 267, 392, 395
immunophenotype 97–98, 100–103, 106–10, 112–19, 121–24
immunostaining 291, 310, 313, 330, 357, 359, 369, 383, 385, 417–18
IMPC (International Mouse Phenotyping Consortium) 7, 12–13, 43, 450, 505
implantation 48, 50, 58, 61, 63, 138–39
inbreeding 23, 27, 29, 32–33
incisors 531, 533, 535
maxillary 534
inclusions 341, 473, 477, 480
infertility 74, 412, 447–48, 450, 454–55
inflammatory bowel disease. *See* IBD
infundibulum 163, 357, 405, 462
insulin 2, 369–71, 414–15
interface dermatitis 141
International Knockout Mouse Consortium (IKMC) 16, 43
International Mouse Phenotyping Consortium. *See* IMPC
interstitial cells 265, 272, 404, 443, 445
intestinal cancer 269–70, 274
intranuclear inclusions 144, 189, 392, 395, 479–80
involution 85, 214, 218
IPF (idiopathic pulmonary fibrosis) 248–51
iris 493, 495, 498–502, 504
islets 355–56, 369–71
hyperplasia 322, 369–70
Ito cells 307, 318

j

joints 339, 345, 520, 524, 530
Joubert syndrome 77, 248, 393

k

keratins 107, 121, 123, 161–62, 169, 173, 187, 193, 196, 197–99, 218, 220, 307–9
keratitis 498–99
keratoconjunctivitis 497–98
kidney disease 379–80, 385, 389, 399
advanced chronic 380–81
autosomal dominant polycystic 391, 393
autosomal recessive polycystic 393
kinocilium 77
Klotho 249, 365, 527
KOMP (Knockout Mouse Program) 16–17, 43, 177, 186, 393, 452, 525
Kras 248, 251, 265, 269, 323, 326–27, 330, 419, 441
Krt5 107, 123, 162, 169, 198, 239, 330, 436
Kupffer cells 307–9, 313

l

labyrinth 50–52, 64–66, 378, 505–8
lacrimal duct-associated lymphoid tissue (LDALT) 88–91
lacrimal glands 141, 500
lactation 214, 218, 412, 520
lactotrophs 357–58, 411
laminopathies 520
Langerhans cells 320–21
Langerhans cell histiocytosis (LCH) 106–7, 455–56
Langerhans cell sarcomas 107
leiomyosarcoma 151, 265, 277
lens 493–95, 497, 499–502
leukemia 97–103, 109, 117, 121, 322
acute myeloid 105
chronic lymphocytic 109
chronic myelogenous 2
erythroid 98, 100–101
megakaryocytic 98, 101
monoblastic 99
mouse myeloid 97
leukemogenesis 97–98
leukocytes 82, 91, 93, 134, 246, 379
leukocytosis, reactive 103–4
Leydig cells 413–14, 443, 445, 448–49, 455–56
LH (luteinizing hormone) 357, 367, 403, 41–14, 448, 455
Li Fraumeni syndrome 217, 270
lipids 173, 176, 340, 365, 446, 462, 481, 521
liver cancer 312–14, 320
liver fibrosis 312, 314–15
lung adenocarcinoma 248
lung tumors 241–42, 251–52
lupus 389, 391
lupus nephritis 384–85, 387
luteinizing hormone. *See* LH
lymphatic 84, 87–94, 169, 215, 226, 272, 275, 404, 507
lymphoblastic lymphomas 98, 106, 109, 113, 116–18
lymphoblasts 100, 109, 115–17
lymphoid follicles 88, 91, 494
lymphoid neoplasms 97, 100, 111, 119
lymphoid organs
secondary 82, 84, 86, 93, 132, 134
tertiary 84, 93–94
lymphomas 9, 97, 101, 107–10, 112–18, 120–23, 142, 150–52, 259–60, 265, 394–95, 469, 473
lysosomal storage diseases 298, 393, 481–82, 520

m

MALT (Mucosa-associated lymphoid tissue) 84, 88, 110–11
MALT lymphomas 110
mammary bud 213–14, 230
mammary fat pad 139, 214–15, 218, 230
mammary intraepithelial neoplasia (MIN) 215, 226, 229
mammary tumorigenesis 42, 232
mantle cell lymphoma (MCL) 110, 112
Marfan syndrome 249, 290, 298
marginal zone lymphoma (MZL) 110, 112
marginal zone macrophages 92
mast cell hyperplasia 108
mast cells 99, 101–2, 106, 108, 180, 285, 371, 446
dermal 184
lamina propria 108
leukemic 102
mucosal 108, 268

mast cell tumors 107–8, 188, 193
malignant 108
mechanoreceptors 340, 345–47
medulla, adrenal 355–56, 364, 366, 368–69
medulloblastoma 484
megakaryocytes 82, 93, 98, 100–101, 103, 105
megakaryocytosis 443
Meibomian glands 167, 176–77, 494, 497
melanin 88, 93, 160, 175, 463
melanocytes 93, 175–76, 189, 191, 493
melanoma 115, 139, 189, 191, 195, 394
melanosis 294, 405, 499
membranous nephropathy 384–86, 391
Menetrier's disease 265
mesoderm 49, 82, 397, 493
mesothelioma 123, 394
metestrus 406
MGD (Mouse Genome Database) 8, 16–17
microbiota 93, 144, 147, 268
microglia 464, 475, 479, 494
microgliosis 470, 475
micrognathia 77
microphthalmia 76, 175, 496, 501
middle ear 464, 505, 507–9, 512
mineralization 292, 300, 347, 349, 392, 446, 470, 472, 520–21, 527–28, 533
mitochondria 285, 297, 338, 350–52, 364
mitophagy 351–52
mitoses 65, 67, 107–10, 112–13, 117, 123, 138, 278, 328, 356, 421, 456
MMHCC. *See* Mouse Models of Human Cancers Consortium
MMHCD. *See* Mouse Models of Human Cancer Database
MMTV (mouse mammary tumor virus) 36, 72, 214, 218, 223
molar teeth 525, 531, 533–34
monoblasts 99–100
monocytes 98–100, 107, 300
monocytic leukemia 99–101
disseminated 100
Morgagnian globules 499
motile cilia 72–74, 452, 454
motor neuron loss 337, 342–43, 477–78
motor neurons 339–44, 346, 464, 477–78
lower 339, 342, 345, 463
upper 345, 463
Mouse hepatitis virus (MHV) 148
mouse mammary tumor virus. *See* MMTV
Mouse Models of Human Cancer Database (MMHCD) 7–10, 251, 269
Mouse Models of Human Cancers Consortium (MMHCC) 97, 104–5, 233, 437
Mouse Phenome Database (MPD) 7, 15
Mouse Tumor Biology Database 10, 311, 437
MPD (Mouse Phenome Database) 7, 15
MTB (Mouse Tumor Biology) 10
mucinous metaplasia 321, 326–27
mucosa-associated lymphoid tissues (MALT) 84, 88, 110
Müller cells 494, 502
multinucleated giant cells 107, 152, 392, 395
mucus metaplasia 260, 262–63
muscle atrophy 336–37, 340, 352, 478
muscle fibers 339–40, 346, 348–49
specialized intrafusal 346
muscle fiber types 336
muscle spindles 345–47
muscular arteries 286–87, 290
muscular dystrophy 2, 197, 295–97, 339, 350–51
myasthenia gravis 337, 345
myelin 339, 342–45, 465, 480
myelin basic protein (MBP) 186, 342, 344, 465, 480
myelinopathies 337, 343–45
myelodysplastic syndromes, labeled 105
myeloid cells 84, 97–105, 134, 472
myeloid dysplasia (MD) 2, 104–6
myeloid leukemia 98–99, 101–2, 104–6
chronic 103
differentiated 101
myeloid proliferation 102
myeloid sarcomas 106
myocardium 294, 296, 300
myocytes 336, 339–40, 343, 347–53
myoepithelial cells 212
myosin 175, 346–47, 350, 352, 510, 512

n

NAFLD 312, 314–15
NALT (nasopharynx-associated lymphoid tissue) 88–91, 237
NASH 312, 314–15
neonates 48, 53–56, 58, 60–61, 67, 495
neovascularization 498
nerves
optic 493–97
sciatic 336, 339, 342–44
nestin 325, 367, 465, 484
NeuN 343, 465, 474, 484
neuregulin 296, 337, 346
neurodegeneration 470, 473, 475–76
neuroendocrine tumors 151, 255, 254, 265, 322, 434, 438–39, 442
neuroepithelium 75, 511
neurofibrillary tangles 465, 471, 473, 476
neurofilament 342, 342–45, 484
neuromuscular diseases 336, 339, 348, 352
neuromuscular junctions 336–37, 340, 345, 463
neurons 77, 339–43, 352–53, 414, 464–65, 467, 468–70, 472, 474, 477–79, 481–82
neutrophils 98, 100, 102–3, 145–47, 184, 231, 297, 510
NK cell lymphomas 117, 121
NK (natural killer) cells 52, 97, 108, 111, 116, 119, 121, 132–34, 147, 231, 371, 415–16, 419
NOD 24, 31, 99, 134, 152, 361, 370, 480
NOD.Cg-*Prkdcscid* 134–37, 141, 145
nomenclature 2–3, 8, 15, 22–23, 27, 31, 33–36, 82, 110, 222, 291
nose 88–90, 148, 237
Notch 72, 119, 177, 321, 330, 393, 521
NSG 88–89, 92, 99, 105, 119, 133–35, 140–41, 146–47, 149, 151, 317
nude mice 86, 132, 148–50, 419

o

obesity 73, 77–78, 287, 296, 324, 370, 409
ocular lesions 496, 500, 503, 505
ocular melanosis 499–500
odontoblasts 520, 530–34
oncogenesis 2, 98, 191, 217–19, 221, 224, 226, 269, 317, 413, 420, 438
organogenesis 49, 57–58, 523
ossicles 505–10
osteoarthritis 530
osteoblasts 82, 509, 520–22, 524–28, 534
osteoclasts 520–22, 524–26
osteocytes 509, 520, 524–25, 527–29
osteogenesis imperfecta (OI) 2, 520, 525, 528–29, 532
osteomalacia 525, 527–28
osteoporosis 523, 525
otitis media 73, 149, 506, 508–9
otoconia 508, 511–13
outer hair cell (OHC) 507, 509–10
outer segment 76, 494, 502
oval cells 307, 318
ovarian cancer 413–14
ovarian follicles 151, 406, 413–14
ovary 228, 232, 402–7, 409, 412–14, 422–22, 448
cystic 231, 408, 415

oviduct 48, 74, 403–7, 412, 416
ovulation 404, 406, 408, 411–13

p

Pacinian corpuscles 345–48
pancreatic acinar cells 321–22, 325
pancreatic cancer 323–27
pancreatic ductal adenocarcinoma (PDAC) 321, 323–30
pancreatic duct 260, 272, 320, 322, 371
pancreatic intraepithelial neoplasia (PanIN) 323
pancreatitis 321–22, 325–26
papillomas 148, 187, 189–90, 193, 252, 264, 398–98
paralysis 86, 336–37, 474, 477–78
parathyroid 355–56, 358–11, 364–65, 394
Parkinson's disease 464, 470, 476
pars distalis 357–59
pars intermedia 357–59
patient derived xenograft. *See* PDX
PAX5 98, 100, 103, 105–6, 109–10, 112, 114, 116, 118, 121
PAX8 359, 361, 387, 407, 414, 417–18
PCNA (proliferating cell nuclear antigen) 173, 309
PDAC 321, 323–30
PDX 8–9, 44, 98, 105–6, 136, 138–39, 142, 317, 415–16, 419–20
pemphigus 159, 192, 194–96
penis 431, 433
perforin 117–19
periodontitis 241, 535
peripheral nerves 336, 340–44, 464, 466
peripheral T-cell lymphoma (PTCL) 118, 120, 122
Peyer's patches 88, 91, 110, 117, 132, 265, 275
PGCs (primordial germ cells) 404
pharynx 237
photoreceptors 76, 494–95, 502
phototoxicity 500, 503
phthisis bulbi 497, 500–501
pigment/pigmentation 88, 92–93, 160, 175–76, 446, 464, 470, 493, 495, 499
pigment dispersion 500–503
pilosebaceous unit 176–77, 199
pituitary 221, 355–61, 366–70, 403–4, 409, 411, 413
pituitary adenomas 221, 358
PKD. *See* polycystic kidney disease
placenta 48, 50–53, 59, 63, 65, 67
plasma cells 82, 84, 87–88, 91, 110, 112, 114, 118, 247
plasticity 221, 321, 357
pneumonia, interstitial 149, 244, 246, 248–49
podocytes 383, 385, 391
polarity 271, 328, 532
polyarteritis 294, 298, 472
polycystic kidney disease (PKD) 75, 391–93
polydactyly 77
polyps 270–72, 275, 277–78, 434, 509–10
preeclampsia 384
pregnancy 52, 214, 221, 240, 366, 411–12, 521, 527
preneoplastic lesions 231, 268, 314, 317
preputial glands 431, 433
primary cilia 72–75, 77
primary ciliary dyskinesia 73, 247–48, 454
proestrus 406
prostate 397, 419, 431, 433–40, 442
  anterior 431–32, 435–36, 439, 442
  ventral 432, 435–36, 438, 440
prostate cancer 437–38, 440–41
prostatic intraepithelial neoplasia (PIN) 437–40
proteinuria 379, 381, 386
psoriasis 44, 159, 184, 199
Pten 191, 217, 224, 265, 270, 314, 317, 362, 368, 370, 416, 419–20, 439–42
puberty 164, 166, 366, 409, 450, 521
Pudlak syndrome 249, 502
pulmonary alveolar proteinosis 248–49
pulmonary fibrosis 247–48, 250–51
pulmonary hypertension 288, 299
pycnodysostosis 525
pyelonephritis 94, 149, 395, 397
pyogranulomas 183, 241, 244, 246–47

q

quantification 105, 290, 312, 310, 342, 522
QTLs (quantitative trait loci) 32, 292–93, 481, 513

r

Rag1 86, 88, 91–92, 132–34, 144, 152
Rag2 88, 91–92, 134, 150–52, 415, 419
Ras 214, 217, 223–24, 362
Rathke's pouch 357, 359
recombinant inbred (RI) 22–23, 27–30, 110, 501–2
rectal prolapse 149, 272, 277
regenerative changes/hyperplasia 272–73, 383, 398
Reissner's membrane 511, 513
renin 365, 371, 385
reproductive phenotypes 407, 411–12
respiratory syncytial virus (RSV) 247
rete testis 443–45, 453
reticular cells 97, 107
retina 371, 465, 493–97, 499–505
retinal atrophy 502–3
retinal degeneration 75–76, 468, 470, 479, 494, 500–504
retinal dysplasia 503
retinoblastoma 2, 399, 414

s

sarcolemma 338, 350–51
sarcomas 106, 265, 277, 294, 394, 477
sarcomatoid carcinomas 437–43
sarcomatoid PDAC 321, 328–29
SARS CoV 244–47
scala tympani 507
scala vestibuli 507, 511
scarring alopecia 176–79, 179
Schwann cells 343–45, 465, 494
SCID mice 134
sclera 493–95
sebaceous glands 148, 160, 163–64, 166–68, 176–79, 181, 221
seminal vesicles 397, 431–32, 434–35, 442
seminiferous tubules 443, 445–46, 448, 450, 452–56
seizures 217, 321, 464, 469–70, 480–81, 483
senescence 216, 230
sensory cilia 72–78
Sertoli cells 404, 443–45, 450–56
Sertoli Cell Tumors 456
severe combined immunodeficiency 2, 99, 119, 132–34, 149, 241
Sharpin 91, 132, 166, 184, 264
skeletal muscle (SM) 219, 339–40, 346, 348, 350–52, 360, 369, 433, 464
skin cancers 9, 187, 192
skin color 160
Smad4 265, 269–70, 323, 326, 330, 439, 441–42
smooth muscle cells 286, 290, 405, 420
SOD1 337, 414, 471, 477–78
sperm 43, 405, 447, 449, 450–52, 455
sperm agenesis 448
spermatocytes 443, 449–50, 452, 456
spermatogenesis 443, 445, 448–51, 453
sperm granulomas 446, 454
spermiogenesis 449, 452
spinal column 288, 339–40, 342–42, 347
spinal cord 16, 149, 336–37, 339–43, 345, 462–64, 466–68, 472, 478
spinocerebellar ataxia 464, 478–79
squamous cell carcinoma (SCC) 33, 123, 139, 189–89, 191, 193, 251–52, 260, 264, 420

steatosis 315–16
stellate cells 307, 309
stereocilia 77, 512–13
steroidogenic cells 367, 412
stomach 55, 91, 147, 241, 259–65, 272
storage disease 295, 392, 454, 465, 509
strain background 102, 159, 176, 419
strains, consomic 31–32
stratum corneum 161, 164, 187
striatum 462, 477, 479
stria vascularis 507–8, 511, 513
stromal cells 85–86, 97, 309–11, 330, 412, 419
substantia nigra 462, 464, 476–77
SV40 36, 123, 191, 370, 413–14, 436, 439, 442
symplasts 444, 449, 453
synaptophysin 272, 325–47, 355, 366, 436, 439, 442, 465, 484
synechiae 499

t

tau 474–75
T-cell anaplastic lymphoma 115
T-cell lymphoblastic lymphomas 109, 117–18, 121
T-cell lymphomas 97, 112–14, 118
  cutaneous 122
  peripheral 118
T cell receptor (TCR) 84, 86, 132, 134, 480–81
teeth 86, 179–80, 241, 520–34
tertiary lymphoid tissue 84, 87, 93–94
testis 152, 293, 410, 443–48, 450–56
tectorial membrane 507, 510–11, 513
Tgfb1 248, 277, 296, 317
thalamus 462, 470, 472–73
Theiler staging 48–49
thrombi 66, 149, 243, 290, 293, 295
thymic lymphomas 133, 151–52
thymomas 97, 107, 122–23
thymus 55, 58, 84–86, 88, 97, 117–18, 121–23, 132, 134–35, 140, 364, 371
thyroid 110, 355, 357, 359–64, 412
thyrotrophs 357–59, 411
T-lymphoblastic leukemia 117
tooth development 530–33
TP53 191, 251, 269–70, 314, 323, 362, 399
trabecular bone 520, 522–23, 525, 529
trachea 237–39, 288, 359
TRAMP (TRansgenic Adenocarcinoma of Mouse Prostate) 434–35, 438–40, 442
transcytosis 88, 148, 521
transgenes 27, 31, 35–36, 140, 191, 221, 379, 391, 414, 433, 436–37
transgenesis 33, 320
Transgenic Adenocarcinoma of Mouse Prostate. *See* TRAMP
transplantation 105, 134, 140, 215–16, 221, 230, 419
transposons 36, 43
tremors 336–37, 345, 464, 476, 479–80, 482
trichoblastoma 148, 189, 194
trophoblasts 50–52, 65–66
Trp53 22, 24, 217, 221, 223, 326, 329, 358, 364, 371, 413–16, 439–42, 484
tubular atrophy 383, 450, 455
tumor suppressor 2, 191, 213, 221, 269, 314, 326, 399, 419, 437
tumor lysis syndrome 400
tumors, spontaneous 150, 214, 231, 251, 436

u

ulcer 159, 179–80, 187, 278, 498
ulcerative colitis 267–68, 278
ulcerative dermatitis 160, 179, 187
ureter 272, 391
urethra 391, 397, 431, 435, 442
urinary bladder 397–98, 405, 431–32, 434
urinary tract infection (UTI) 392, 395
urine 75, 366, 379–81, 384, 397, 521
urolithiasis 397
urothelium 397, 399
uterine fibroids 420
uterine leiomyoma 394, 416, 420
uterus 48, 61, 107, 151, 293, 403–7, 409–12, 416, 419–20, 422
utricle 507–8, 511, 513

v

vagina 189, 194, 228, 403, 406–7, 409
valosin-containing protein (VCP) 352
vasculitis 148, 246, 250, 296, 299, 384
vibrissae 132, 162, 164, 173, 293
vimentin 221, 383, 445
vitamin 160, 179, 181, 359, 364, 381, 414, 536–37
vitamin D receptor (VDR) 181, 364, 414
vitreous 494–95, 500, 507
von Willebrand factor (VWF) 98, 100–101, 105, 291

w

Wilms tumor 91, 241, 394, 417
WGA (Wheat Germ Agglutinin) 290–91

x

xenograft 132, 139
xenograft tumors 139, 320
xenotransplantation 99, 101, 108, 119, 123, 136, 139, 141, 318

y

yeast 147, 260, 262
yolk sac 49–51, 64–65, 82

z

Zymbal's glands 164, 176–77, 507